

LTBD 2017

LONG-TERM BEHAVIOUR AND ENVIRONMENTALLY FRIENDLY REHABILITATION TECHNOLOGIES OF DAMS

Proceedings of the 4th International Conference

17th -19th October, 2017

Tehran, Iran

Edited by

Ali Noorzad

Faculty of Civil, Water & Environmental Engineering
Shahid Beheshti University, Tehran, Iran

Erich Bauer

Institute of Applied Mechanics
Graz University of Technology, Graz, Austria

Mohsen Ghaemian

The Department of Civil Engineering
Sharif University of Technology, Tehran, Iran

Babak Ebrahimian

Faculty of Civil, Water & Environmental Engineering
Shahid Beheshti University, Tehran, Iran

Published by

Verlag der Technischen Universität Graz
Graz University of Technology



© 2017 Verlag der Technischen Universität Graz

www.ub.tugraz.at/Verlag

ISBN (print) 978-3-85125-564-5

ISBN (e-book) 978-3-85125-565-2

DOI 10.3217/978-3-85125-564-5



This work is licensed under a Creative Commons Attribution 4.0 International License
<https://creativecommons.org/licenses/by-nc-nd/4.0/deed.en>

The authors are responsible for the content of their contributions. The texts of the papers in this volume were set individually by typists under the supervision of each of the authors concerned.

Printed by Iranian National Committee on Large Dams (IRCOLD)
No. 1, 3rd floor, Shahrshaz Alley, Kargozar St., Zafar Ave., Tehran, Iran

Layout by Fatemeh Farahani and Shirin Masoudian
Iranian National Committee on Large Dams (IRCOLD)

Cover design by Kaveh Moghissi
Iranian National Committee on Large Dams (IRCOLD)

Copyright of cover pictures by Iranian National Committee on Large Dams (IRCOLD)

PREFACE

The development of water resources is a key element in the socio-economic development of many regions in the world. Water availability and rainfall are unequally distributed both in space and time. Shifting weather patterns are predicted to further affect the amount of rainfall in many regions. Some areas will become drier while others will see an increase in precipitation events. These changes will have untold consequences for the freshwater supply of the people living there. Decisions in water management planning must take this development into account.

In this context dams play a vital role, there being only a few viable alternatives for storing water. Dams hold a prime place in satisfying the ever-increasing demand for power, irrigation and drinking water, in protecting human life, property and the environment from catastrophic floods, and in regulating the flow of water.

Dams have contributed to the development of civilization for over 2,000 years. Worldwide there are roughly 45,000 large dams listed by ICOLD, which have a height over 15 meters. Today, in many countries where most of the water resources have been developed, it is of prime concern to investigate the long term behaviour of the existing dams and measures to rehabilitate them in order to extend their economic life.

The proceedings of the 4th International Conference on Long-Term Behaviour and Environmentally Friendly Rehabilitation Technologies of Dams (LTBD 2017), which was held from 17 to 19 October 2017 at IRIB International Conference Centre in Tehran, IRAN, include contributions from 19 countries. They provide a state-of-the-art overview of the long term behaviour of dams covering aspects like load history and climate changes, uncertainties and risk-informed decision making in dam design, construction and operation, the time dependent behaviour of new construction materials, and new rehabilitation technologies. Traditional areas are also considered, such as concrete dams and embankment dams, methods of analysis and design, dam foundation, seismic analysis, design and safety, stability of dam and slope, dam safety monitoring and instrumentation, dam maintenance, and rehabilitation and heightening.

These proceedings will be an excellent piece of reference for scientists, researchers, engineers and students working in dam engineering, dam design, environmental engineering and structural hydraulics. We trust that the contributions will provide an impetus for further study and research in all the areas covered.

We thank all conference participants and the authors of the papers for their contributions. Furthermore, we are grateful for the support of the reviewers of the papers, the members of the International Advisory Committee, the Scientific and Organizing Committees and the IRCOLD Secretariat. We also express our sincere appreciation to the technical and financial co-sponsors: The Ministry of Energy, Shahid Beheshti University, the Water Resources Management Company, and Iran Water and Power Resources Development Company.

Tehran, October 2017

Ali Noorzad

Erich Bauer

Mohsen Ghaemian

Babak Ebrahimian

Table of Contents

Conference Organization

Acknowledgements

Overview of Keynote Abstracts and Technical Papers

Keynote Abstracts

Topic A:

Dam - Monitoring, Instrumentation and Safety Assessment

Topic B:

Environmental Issues

Topic C:

Interaction of Dam Foundation and Structure

Topic D:

Long-Term Behaviour of Dams with Respect to Loading History and Climate

Topic E:

Methods of Analysis and Design of Earth, Rockfill and Concrete Dams including experimental, Analytical and Numerical Investigations

Topic F:

Operation, Maintenance, Rehabilitation and Heightening

Topic G:

Seepage Under Saturated and Unsaturated Conditions

Topic H:

Seismic Aspects and Earthquake Analysis

Topic I:

Time - Dependent Properties of Construction Materials for Dams and Their Constitutive Modeling

Conference Organization

Universities Involved in the Conference Organization

The conference was jointly organized by

Shahid Beheshti University, Tehran, Iran

Graz University of Technology, Graz, Austria

Sharif University of Technology, Iran

Conference Organizing Committee

Conference Chairman

Ali Noorzad (Shahid Beheshti University, Iran)

Co-Chairman

Babak Ebrahiman (Shahid Beheshti University, Iran)

Secretary

Nima Tavakoli (Iranian National Committee on Large Dams, Iran)

Head of Scientific Committee

Mohsen Ghaemian (Sharif University of Technology, Iran)

Head of Workshops Committee

Eisa Bozorgzadeh (Iran water & Power Resources Development Company, Iran)

Head of Technical & Study tours Committee

Mohammadali Mirzaeei (Sharif University of Technology, Iran)

Head of Finance & support Manager Committee

Mojtaba Gharavy (Iran University of Science and Technology, Iran)

Head of Cultural & Social Events Committee

Bijan Farhangi (Mahab Ghodss Consulting Engineering Company, Iran)

Auspices and Supporting Organizations

Iran Ministry of Energy

Iranian National Committee on Large Dams (IRCOLD)

International Commission on Large Dams (ICOLD)

Iran Water Resources Management Company (WRM)

Iran water & Power Resources Development Company (IWPC)

Khuzestan Water and Power Authority (KWPA)

Korea National Committee on Large Dams (KNCOLD)

The International Society for Soil Mechanics and Geotechnical Engineering (ISSMGE)

The United States Society on Dams (USSD)

Embassy of the Republic of Korea in the Islamic Republic of Iran

Members of International Advisory Committee

Hakim Abdelgader (University of Teripoli, Lybia)

Markus Aufleger (University of Innsbruck, Austria)

Dennes T. Bergado (Asian Institute of Technology, Thailand)

Andreas Bieberstein (Karlsruhe Institute of Technology, Germany)

Erich Bauer (Graz University of Technology, Austria)

Gianluca Cusatis (Northwestern University, USA)

Bettina Detmann (Technical University of Berlin, Germany)

Jin Feng (Tsinghua University, China)

Zhongzhi Fu (Nanjing Hydraulic Research Institute, China)

Pierre-Yves Hicher (Ecole Centrale de Nantes, France)

Eduardo E. Alonso (Universidad Politècnica de Catalunya, Spain)

Wenxiong Huang (Hohai University, China)

Herbert Linsbauer (Austria)

Sihong Liu (Hohai University China)

David Masin (Charles University, Czech)

Eliane Portela (Portugal)

Peter Tschernutter (Vienna University of Technology, Austria)

Martin Wieland (Poyry Switzerland Ltd, Switzerland)

Peter von Wolffersdorff (Baugrund Wien, Austria)

Gerald Zenz (Graz University of Technology, Austria)

Acknowledgements

The editors are grateful to the following persons reviewed the manuscripts of the proceedings.

- Ahmad Abrishamchi** (Sharif University of Technology, Tehran, Iran)
Abbas Afshar (Iran University of Science & Technology, Tehran, Iran)
Kaveh Ahangari (Islamic Azad University, Tehran, Iran)
Mohammad Taghi Ahmadi (Tarbiat Modares University, Tehran, Iran)
Mohammadreza Askari (Bandab consulting Engineers Company, Tehran, Iran)
Mohammad Hassan Baziar (Iran University of Science & Technology, Tehran, Iran)
Babak Ebrahimian (Shahid Beheshti University, Tehran, Iran)
Behrouz Gatmiri (University of Tehran, Tehran, Iran)
Mohsen Ghaemian (Sharif University of Technology, Tehran, Iran)
Abbas Ghalandarzadeh (University of Tehran, Tehran, Iran)
Mojtaba Gharavi (Iran University of Science & Technology, Tehran, Iran)
Mohammad Hajrasouliha (Iran Water Resource Management Company, Tehran, Iran)
Vahid Lotfi (Amirkabir University of Technology, Tehran, Iran)
Ahmadreza Mahboubi Ardakani (Shahid Beheshti University, Tehran, Iran)
Rahim Meydani (Ministry of Energy, Tehran, Iran)
Ali Asghar Mirghasemi (University of Tehran, Tehran, Iran)
Behzad Mohaghegh Hazrati (Arsa International Construction Company, Tehran, Iran)
Seyed Jamshid Mousavi (Amirkabir University of Technology, Tehran, Iran)
Ali Noorzad (Shahid Beheshti University, Tehran, Iran)
Mohammad Reza Rezazadeh (Iran Water & Power Resources Company, Tehran, Iran)
Mohammadsadegh Sadeghian (Islamic Azad University, Tehran, Iran)
Abbas Soroush (Amirkabir University of Technology, Tehran, Iran)
Mohammad Masoud Tajrishi (Sharif University of Technology, Tehran, Iran)

Overview of Keynote Abstracts and Technical Papers

Keynote Abstracts

- K-1 Design, construction, monitoring and modelling of Albagés earthdam. A case history 1
Núria M. Pinyol, Eduardo E. Alonso
DOI 10.3217/978-3-85125-564-5-005
- K-2 Destructive phenomenon of dust storm and its mitigation measures on the global scale 2
Naser Tarkeshdooz
DOI 10.3217/978-3-85125-564-5-024
- K-3 Assessment of foundation mass and earthquake input mechanism effect on dam-reservoir-foundation system response 3
Mohsen Ghaemian, Ali Noorzad, Hamid Mohammadnezhad
DOI 10.3217/978-3-85125-564-5-029
- K-4 Ensuring worldwide long-term prosperity thanks to dams and reservoirs as vital water infrastructures - The important role of ICOLD 4
Anton Schleiss
DOI 10.3217/978-3-85125-564-5-035
- K-5 Constitutive modelling of wetting deformation of rockfill materials 5
Erich Bauer
DOI 10.3217/978-3-85125-564-5-064
- K-6 Internal erosion in dams. studies and rehabilitation 6
Laura Caldeira
DOI 10.3217/978-3-85125-564-5-073
- K-7 Models of earthquake ground shaking used in seismic design and safety checks of large dams 7
Martin Wieland
DOI 10.3217/978-3-85125-564-5-089
- K-8 Seismic response analysis of high Arch dams to spatially-varying ground motions 8
Jin-Ting Wang, Feng Jin, Chu-Han Zhang
DOI 10.3217/978-3-85125-564-5-118
- K-9 Assessment of newmark methods for the Prediction of deviatoric displacement of earth dams using energy approach 9
Reza Karimi Moghadam, Mohammad Hassan Baziar
DOI 10.3217/978-3-85125-564-5-119
- K-10 Research on rock-filled concrete dam 10
Feng Jin, Hu Zhou, Xuehui An
DOI 10.3217/978-3-85125-564-5-113

Topic A - Dam - Monitoring, Instrumentation and Safety Assessment

- A003 Quantifying seepage flow velocities in embankment dams from optical fibre distributed temperature measurements 11
Jean-Robert Courivaud, Nicolas Lorrain, Francois Martinot, Remi Beguin
DOI 10.3217/978-3-85125-564-5-001
- A004 System identification of concrete arch dam using frequency domain and time-frequency domain methods 18
Arman Roshanravan, Mohammad Manafpour, Hesaneh Ghanbari
DOI 10.3217/978-3-85125-564-5-002
- A006 Investigating the local arching phenomenon in total pressure cells located in clay core protective filters and comparison with numerical modeling results (Case Study: Mamlou Earth Dam) 25
Mohammad Salehian Zolbin, Maziar Mahmoudinia
DOI 10.3217/978-3-85125-564-5-003
- A007 Implementation of a web based platform for portfolio dam monitoring 32
Stefan Hoppe, Manuel G. de Membrillera Ortuño, Jürgen Fleitz
DOI 10.3217/978-3-85125-564-5-004
- A0023 The principles of deep alluvial drilling management on Borehole 40
Amin Mansouri, Maliheh Ghadiri
DOI 10.3217/978-3-85125-564-5-006
- A0024 Back Analysis of Banqiao Clay Core Dam Breaching 50
Qiming Zhong, Shengshui Chen, Shiang Mei
DOI 10.3217/978-3-85125-564-5-007
- A0025 Assessment of an Embankment Dam Break Warning System Based on Historical Dam Failures 58
López, Diana, Aufleger, Markus
DOI 10.3217/978-3-85125-564-5-008
- A0026 Performance and Safety Assessment of Seven Storage Dams in Khuzestan Province, Iran 65
Reza Esmaili, Morteza Rayati, Seyed Mehdi Hosseini Tehrani, Yaghoub Arab
DOI 10.3217/978-3-85125-564-5-009

- A0027 Numerical study on the effect of grout properties on the results of borehole
extensometers in earth dams 73
Afshin Gholinia, Majid Nikkhah, Reza Naderi
DOI 10.3217/978-3-85125-564-5-010

Topic B - Environmental Issues

- B001 Evaluation of Groundwater Management Techniques for the City of Mashhad 81
Mahdi Safdari Seh Gonbad, Poorya Nakhaei, Farzin Kalantary
DOI 10.3217/978-3-85125-564-5-011
- B002 The Mountain Water Reservoirs influence on Meteorological Conditions of 88
Coastal Area
Parviz Normatov, Bakhtiyor Markaev, Abulqosim Muminov, Inom Normatov
DOI 10.3217/978-3-85125-564-5-012
- B003 Defining a framework for integrating environmental and social aspects in dam 96
rehabilitation
Zahra Sobhaniyeh, Amin Sarang
DOI 10.3217/978-3-85125-564-5-013
- B007 The Effect of Saturated Lime Solution on Increasing the Strength of Silty Sandy 104
Soils
Forough Hassanvand, Mohammad Hadi Davoudi
DOI 10.3217/978-3-85125-564-5-014
- B009 Strategies for Greenhouse Gases Mitigation in Hydro-electrical Water Reservoir 111
Saeed Karbin, Hadi Karbin, Hossien Ali Alikahni
DOI 10.3217/978-3-85125-564-5-015
- B0010 Optimizing Selective Withdrawal System in Reservoir to Manage Downstream 118
Water Quality and Hydropower Energy Generation
Motahareh Saadatpour, Shima Javaheri
DOI 10.3217/978-3-85125-564-5-016
- B0011 Double-Stilling Basin Modelling, Pakistan – Case Study 126
Ubaid Ullah, Eric J Lesleighter, Muhammad Iqbal
DOI 10.3217/978-3-85125-564-5-017

B0013	Review of Reservoir Water Quality Monitoring and Modelling Nasser Talebbeydokhti, Shokoufeh Pourshahabi, Gholamreza Rakhshandehroo, Mohammad Reza Nikoo, Mehrab Amiri DOI 10.3217/978-3-85125-564-5-018	134
B0014	Smoothed Particle Hydrodynamics for morphology changes and a non-Newtonian fluid Pooyan Nikeghbali, Pourya Omidvar, Payam Rasooli, S. Mehdi Mohammadizadeh DOI 10.3217/978-3-85125-564-5-019	143
B0016	Rockfall Hazard Assessment in the Right Abutment of Sefidrud Dam, Gilan, Iran Mahnaz Firuzi, Ali Noorzad, Mohammad Hossein Ghobadi DOI 10.3217/978-3-85125-564-5-021	152
B0017	Positive and negative effects of damming industry MohammadAli Jaberi, Ghasem Shahparifar DOI 10.3217/978-3-85125-564-5-022	159
B0018	Environmental Impact Assessment of Dams at Construction and Operation Phases Abdolhosein Haddad, Maryam Naeimi, Ghasem Mohammadi DOI 10.3217/978-3-85125-564-5-023	167
B0020	Aerobiology, Biophysical studies through integration of Zigbee communication protocols in fixed wing air vehicle for Dam regions Syed Mohammed Shoaib, Shaik Abdul Khader Jilani DOI 10.3217/978-3-85125-564-5-025	174
B0021	Assessment of Hydrologic Alternation of flow due to dam construction in an arid basin (The case of the Gadar River in Urmia Basin) Somayeh Sima DOI 10.3217/978-3-85125-564-5-026	178

Topic C - Interaction of Dam Foundation and Structure

C001	Parametric Investigation of valley shape affects on seismic response of concrete gravity dams Behzad Nikkhakian, Mohammad AlemBagheri DOI 10.3217/978-3-85125-564-5-027	187
------	--	-----

C002	Dynamic Analysis of Dam-Reservoir-Intake Tower Considering Sediments Absorption Ali Mahdian Khalili, Bahram Navayi Neya, Leila Kalani Sarokolayi DOI 10.3217/978-3-85125-564-5-028	194
------	---	-----

Topic D - Long-Term Behaviour of Dams with Respect to Loading History and Climate

D002	Design and Performance of Drainage Systems for Long Term Stability Wynfrith Riemer, F. B. Samani DOI 10.3217/978-3-85125-564-5-030	203
D003	Impact of mining waste effluents on the shear strength of compacted lateritic soils used in waste containment dikes (DRC) Gustave Mukoko Kalenda, Gabriel Lile Amisi, Yannick Kiyukeno Kitwanyoka, Elie Musoya Kyulu, Ramiro Daniel Verastegui Flores, Jean-François Thimus, Kelly Guerrier DOI 10.3217/978-3-85125-564-5-031	213
D005	Climate Change Adaptation in Multi-Reservoir Systems through Revising Operation Policies Banafsheh Zahraie, Hamed Poorsepahy-Samian, Saeed Jamali, Baharch Noroozi, Mohsen Nasseri DOI 10.3217/978-3-85125-564-5-032	221
D006	Laouzas dam: behavior of a thin concrete arch dam located in a wide valley and foundation stability improvement Emmanuel Robbe, François Morel DOI 10.3217/978-3-85125-564-5-033	227
D007	Risk Assessment of Earth Dam Overtopping Using System Dynamics and Monte Carlo Simulation (case study: Hajilarchay Dam) Ali Ebrahimzadeh, Mahdi Zarghami, Vahid Nourani DOI 10.3217/978-3-85125-564-5-034	234

Topic E - Methods of Analysis and Design of Earth, Rockfill and Concrete Dams including experimental, Analytical and Numerical Investigations

E003	Optimum Characteristic Compressive Strength for CMDs (Case study: Dasht-e-Palang Dam) Abbas Mohammadian, Ahmad Ghezel Ayagh DOI 10.3217/978-3-85125-564-5-036	243
E008	Design Experience on Slope Stability for Rockfill Dams, Turkey Hasan Tosun DOI 10.3217/978-3-85125-564-5-037	251

E009	Investigation of the leakage and maximum stress in plastic concrete cut-off wall with 100 centimeter width instead of clay core in static state on embankment dam's Raz & jargalan Ahmad Sedighian, Abbas Ali Ghezel sooflo DOI 10.3217/978-3-85125-564-5-038	259
E0010	Evaluation of Long-term Settlement of Ghoocham Dam by Numerical Analysis Hooman Rezaee, Hamidreza Hajihassani, Shahram Mahzarnia DOI 10.3217/978-3-85125-564-5-039	266
E0011	Safety Evaluation of Concrete Gravity Dams Founded on Inhomogeneous Rock Media due to Static Loads Hamid Taghavi Ganji, Mohammad Alembagheri DOI 10.3217/978-3-85125-564-5-040	274
E0013	Behavior analysis of Ghaleeh Chay earth fill dam using instruments data Mohammad Manafpour, Mojtaba Ghahremannezhad DOI 10.3217/978-3-85125-564-5-041	282
E0014	Effective Parameters for Calculating the Discharge of Spillway with Radial Gates at Large Dams Hossein Khalili Shayan, Javad Farhoudi, Younes Aminpoor, Amin Seyedzadeh, Reza Roshan, Alireza Vatankhah DOI 10.3217/978-3-85125-564-5-042	289
E0015	Numerical simulation of post-construction deformation of a concrete face rockfill dam Mohammadkeya Khosravi, Linke Li, Erich Bauer DOI 10.3217/978-3-85125-564-5-043	307
E0017	Numerical Investigation of the Flow Characteristics in the vicinity of Pressure Conduit's Gates Mohammad Manafpour, Tohid Jamali Rovesht DOI 10.3217/978-3-85125-564-5-044	315

E0018	The Multiphase Capability of OpenFoam CFD Toolbox in Solving Flow Field in Hydraulic Structure Mohammad Manafpour, Hamzeh Ebrahimnezhadian DOI 10.3217/978-3-85125-564-5-045	323
E0022	Design of Neural Networks by Using Genetic Algorithm for the Prediction of Immersed CBR Index Mohammed el Amin Bourouis, Abdeldjalil Zadjoui, Abdelkader Djedid, Abderrahmen Bensenouci DOI 10.3217/978-3-85125-564-5-046	331
E0029	Long-term behavior of kinevars embankment dam using numerical model and compare it with the Instrumentation results Ahmad Ghezelayagh, Mansour Fadaei, Amin Bolouri DOI 10.3217/978-3-85125-564-5-047	339
E0031	Determination of Optimum Cross Section of Earth Dams by Using Artificial Intelligence Mohammad Davoodi, Mohammad Kazem Jafari, Amin Rezaeeian DOI 10.3217/978-3-85125-564-5-048	347
E0032	Numerical Investigation of Damage Types through Concrete Dam by Multi-laminate model upon Instrumentation Data Seyed Amirodin Sadrnejad DOI 10.3217/978-3-85125-564-5-049	357
E0033	Non-destructive Numerical Investigation of Local heave/liquefaction through Rock-fill Dam upon Instrumentation Data Seyed Amirodin Sadrnejad DOI 10.3217/978-3-85125-564-5-050	365
E0034	Evaluation of Collapse Deformation Behavior of a Rockfill Material Using Large Scale Triaxial Tests Ahmadreza Tabibnejad DOI 10.3217/978-3-85125-564-5-051	373

E0035	Study of Hydraulic Characteristics of Large Dam's Spillway (Case Study: Zola Dam Spillway) Mohammad Manafpour, Sevda Kafshdooz Salimy DOI 10.3217/978-3-85125-564-5-052	385
E0037	On the slices-based limit equilibrium method for the active earth pressure applied by soils with nonlinear strength behavior Zhongzhi Fu, Shengshui Chen, Guoying Li DOI 10.3217/978-3-85125-564-5-053	393
E0038	The Effect of Grout Curtain Efficiency on Abutments Stability of an Arch Dam Hasan Mostafaei, M. Sohrabi Gilani, M. Ghaemian DOI 10.3217/978-3-85125-564-5-054	412
E0039	Effect of Fine content on Lateral Wall Movement of Bearing Reinforcement Earth (BRE) Walls K. Sukmak, S. Horpibulsuk, P. Sukmak DOI 10.3217/978-3-85125-564-5-055	420
E0040	Effect of Hydraulic Properties of Fill and Geocomposite Drainage Materials on Seepage Response in Reinforced Earth Walls Avirut Chinkulkijniwat, Suksun Horpibulsuk, Duc Bui Van, Somjai Yubonchit, Thanakorn Rakkob DOI 10.3217/978-3-85125-564-5-056	428
E0041	Numerical simulation of sharp crested arced weir Saeid Azizi, Mojtaba Mehraein DOI 10.3217/978-3-85125-564-5-057	437
E0042	History and Overview of Self Compacting Grout and Concrete: Properties and Applications Hakim S. Abdelgader, Ali S. El-Baden, Hamdi A. Abdurrahman DOI 10.3217/978-3-85125-564-5-058	444

E0043	Numerical Study of the Passing Flow over Spillway with Emphasis on the Potential of Cavitation Occurrence Hamzeh Ebrahimnezhadian, Mir Ali Mohammadi, Ramin Abdullah Kookhi, Ako Seyedi DOI 10.3217/978-3-85125-564-5-059	451
E0044	Numerical investigation of Flow over Rectangular Side weir in a Circular Channel Sanaz Shoaie, Mojtaba Mehraein DOI 10.3217/978-3-85125-564-5-060	459
E0046	An investigation of the effects of explosive charge in different levels on the dynamic response of concrete arch dams Mirali Mohammadi, Mohammad Manafpour, Hesane Ghanbari DOI 10.3217/978-3-85125-564-5-061	466
E0047	Analysis and Design of Ferrocement Cut off Trench in Earthen Dam: A Case study of Bham Dam Sunil Kute, Patil N. P., Ebrahim Farajpour Bonab, Susmit Kute DOI 10.3217/978-3-85125-564-5-062	474
E0048	Laboratory Study of the effect of recycled fillers from coking and iron concentrates factories on the Roller Compacted Concrete properties in dams (RCC Dams) Jaber Mahmoudi, Kouros Qaderi, Mohammad Zounemat Kermani, Faeze Yazdi DOI 10.3217/978-3-85125-564-5-063	479

Topic F - Operation, Maintenance, Rehabilitation and Heightening

F001	Chambon dam reinforcement works Olivier Chulliat, Etienne Grimal, Emmanuel Robbe DOI 10.3217/978-3-85125-564-5-065	489
F002	Lessons learnt - Raising an earthfill dam: From the initial design to the dam-raising works - Ganguise Dam (France) Eric Vuillermet DOI 10.3217/978-3-85125-564-5-066	497

F003	<p>The Use of Geomembranes in Dams</p> <p>Alberto Scuero, Gabriella Vaschetti, Marco Bacchelli</p> <p>DOI 10.3217/978-3-85125-564-5-067</p>	506
F005	<p>Water-Filled Bladders, an Innovative Bearing Interface for Arch Dam Bracing</p> <p>Alexandre Lochu, Thomas Pinchard</p> <p>DOI 10.3217/978-3-85125-564-5-068</p>	515
F006	<p>Rockfill Dams Overtopping Risk Analysis</p> <p>Ali Komak Panah, Hamidreza Rahmani</p> <p>DOI 10.3217/978-3-85125-564-5-069</p>	521
F007	<p>Study of the Sarough dam fusegates</p> <p>Komeil Samet, Mojtaba Ahmadi, Mohammad Ashrafi, Khosrow Hoseini</p> <p>DOI 10.3217/978-3-85125-564-5-070</p>	530
F0010	<p>Design and Operation of Sustainable Reservoirs, a New Approach</p> <p>Esmacil Tolouie</p> <p>DOI 10.3217/978-3-85125-564-5-071</p>	537
F0011	<p>Rehabilitation of the Sylvenstein Dam, Germany – Success Proof by Major Flood 2013</p> <p>Peter Banzhaf</p> <p>DOI 10.3217/978-3-85125-564-5-072</p>	548
F0014	<p>Critical success factors in construction or rehabilitation contracts regarding dams</p> <p>Bettina Geisseler</p> <p>DOI 10.3217/978-3-85125-564-5-074</p>	555
F0015	<p>Analytical Solution for Level Pool Routing Equation Based on Various Inflow Hydrographs</p> <p>Banafshe Nematollahi Sarvestani, Majid Miazkar, Nasser Talebbeydokhti</p> <p>DOI 10.3217/978-3-85125-564-5-075</p>	562

F0016	Real Time Operation Model for Optimum Operation of Bukan Reservoir in Lake Urmia Basin Kayhan Gavahi, S. Jamshid Mousavi DOI 10.3217/978-3-85125-564-5-076	570
F0017	Erosion of channel beds covered by cohesive sediments Hesam Fouladfar, Mahmoud Shafai Bajestan DOI 10.3217/978-3-85125-564-5-077	578
F0018	Ageing Evaluation Model of Dams and Case Studies Dong-Hoon Shin DOI 10.3217/978-3-85125-564-5-078	583
F0020	Introducing a New Long-Lead Hydrologic Forecasting System for Improving Reservoir Operation Shahab Araghinjead, Saeed Jamali, Mohammad Hoseini Moughari, Fereshteh Modaresi DOI 10.3217/978-3-85125-564-5-079	590

Topic G - Seepage Under Saturated and Unsaturated Conditions

G001	Investigation on the Performance of Blanket, Cutoff Wall and Synthetic Cover for the Control of Seepage and Piping in Earth Dams Hossein Khalili Shayan, Maryam Jamal, Faraz Rabeii Gholami DOI 10.3217/978-3-85125-564-5-080	599
G002	Analyzing the effect of defect in the upstream impervious blanket on the seepage behavior of earthfill dam Hamed Farshbaf Aghajani, Majid Mahdavi-rad DOI 10.3217/978-3-85125-564-5-081	607
G005	Field seepage tests on discontinuity structural rocks in a hydropower project Sihong Liu, Bin Zhou, Liping Weng, Meiqi Jiang, Hanwen Xiong DOI 10.3217/978-3-85125-564-5-082	614
G006	The seepage behavior of a high concrete face rockfill dam on alluvium deposit Weijun Cen, Dengjun Li, Erich Bauer DOI 10.3217/978-3-85125-564-5-083	620

G007	Numerical analysis of elastic surface settlement due to seepage force Abdollah Rohani Hajiagha, Abolfazl Riahi Nouri DOI 10.3217/978-3-85125-564-5-084	627
------	---	-----

Topic H - Seismic Aspects and Earthquake Analysis

H001	Earthquake Safety Evaluation for Dams in Upper Aras Basin, Turkey Hasan Tosun DOI 10.3217/978-3-85125-564-5-085	631
H003	Seismic and Geotechnical Aspects of the Large Earthfill Dam in a Seismically Active Region Dariush Belashi, Saeed Nayeb DOI 10.3217/978-3-85125-564-5-086	638
H004	Seismic Safety Aspects of Gated Spillways of Large Storage Dams Martin Wieland, Sanaz Ahlehagh DOI 10.3217/978-3-85125-564-5-087	645
H005	Spectrum Response Analysis of Concrete Face Rock Fill Dam, case study Bakun Dam Behrouz Gordan, Azlan Adnan DOI 10.3217/978-3-85125-564-5-088	655
H007	Studying the effects of non-uniform earthquake excitations on dynamic response of concrete arch dams Fateme Esmaili Soureh, Alireza Manafpour, Mohammad Manafpour DOI 10.3217/978-3-85125-564-5-090	663
H008	Global sensitivity analysis of concrete gravity dams subjected to seismic excitation Mohammad Houshmand, Mohsen Ghaemian, Vahab Toufigh DOI 10.3217/978-3-85125-564-5-091	670
H009	Earthquake records on concrete dams in Japan: comparison with finite-element analyses Emmanuel Robbe DOI 10.3217/978-3-85125-564-5-092	677

H0010	Probabilistic-based analysis of concrete gravity dams under synthetic ground motion excitation Yasaman Afkhami, Mohammad Alembagheri DOI 10.3217/978-3-85125-564-5-093	684
H0011	Probabilistic Analysis of Concrete Gravity Dams Owing to Foundation Inhomogeneity Hamid Taghavi Ganji, Mohammad Alembagheri, Mohammad Houshmand DOI 10.3217/978-3-85125-564-5-094	691
H0013	Hydrodynamic sub-pressure incremental pattern in dam-reservoir interaction system subjected to far field and near field ground motions Mohammad Manafpour, Arman Roshanravan DOI 10.3217/978-3-85125-564-5-095	699
H0016	The Study of Site Effects on Seismic Response of Adjacent Rectangular Valleys Behrouz Gatmiri, Zahra Khakzad DOI 10.3217/978-3-85125-564-5-096	705
H0018	Comparison of 2D and 3D Seismic Analysis of Concrete Face Rockfill Dams in Narrow Canyons Babak Mahmoodi, Ali Asghar Mirghasemi DOI 10.3217/978-3-85125-564-5-097	710
H0021	Seismic Response Analysis of High Arch Dams to Spatially-Varying Ground motions Jin-Ting Wang, Feng Jin, Chu-Han Zhang DOI 10.3217/978-3-85125-564-5-098	717
H0022	Three-dimensional effects on the dynamic response of the Dariyan dam Davood Salehi DOI 10.3217/978-3-85125-564-5-099	725
H0023	Nonlinear Dynamic Analysis of Concrete Gravity Zavin Dam Behzad Najmoddini, Abbasali Ghezelsofloo DOI 10.3217/978-3-85125-564-5-100	732

H0024	Seismic vulnerability assessment of a set of concrete gravity dams Saeid Ghasemi Gavabar, Mohammad Alembagheri, Behrang Esmi DOI 10.3217/978-3-85125-564-5-101	739
H0025	Dynamic Analysis of Embankment Dams under Strong Seismic Excitation and a Case Study Hasan Tosun, Turgut Vatan Tosun DOI 10.3217/978-3-85125-564-5-102	747
H0026	Finite Element Analysis of Multi-tiered Reinforced Soil Walls of Gotvand Dam Powerhouse under Earthquake Loading Amir Mohsen Safaee, Ali Noorzad, Ahmad Reza Mahboubi-Ardakani DOI 10.3217/978-3-85125-564-5-103	754
H0027	Investigation of the Effect of Seismic Loading on Displacements of Multi-tiered Reinforced Soil Walls in Iran Major Hydropower Projects Amir Mohsen Safaee, Ali Noorzad, Ahmad Reza Mahboubi-Ardakani DOI 10.3217/978-3-85125-564-5-104	761
H0028	Dynamic Response of Concrete Dams Shiva Khosravi, Reza Kamyab Moghadas DOI 10.3217/978-3-85125-564-5-105	770
H0029	Seismic Analysis of Rockfill Dam, A Case Study of Ghoocham Dam Hooman Rezaee, Hamidreza Hajihassani, Shahram Mahzarnia DOI 10.3217/978-3-85125-564-5-106	777
H0030	Seismic performance evaluation of Salman Farsi dam with considering the influence of sediment Sahar Rezaei Koujani, Zahra Heirany DOI 10.3217/978-3-85125-564-5-107	783
H0031	Assessment of Newmark Methods for the Prediction of Deviatoric Displacement of Earth Dams Using Energy Approach Reza Karimi Moghadam, Mohammad Hassan Baziar DOI 10.3217/978-3-85125-564-5-108	790
H0032	Numerical Earthquake Response Analysis of the Earth Dams Babak Ebrahimian, Ali Noorzad DOI 10.3217/978-3-85125-564-5-109	805

H0033 Numerical Analysis of Soil Liquefaction Induced Failure of Earth Dams 818
Babak Ebrahimian, Ali Noorzad

DOI 10.3217/978-3-85125-564-5-110

H0034 Numerical Analysis of Granular Soil-structure Interface Behavior at Large Shearing 826
 Displacement: Evolution and Characterization
Babak Ebrahimian, Ali Noorzad

DOI 10.3217/978-3-85125-564-5-111

Topic I - Time - Dependent Properties of Construction Materials for Dams and Their Constitutive Modeling

I001 On sensitivity analysis of a nonlinear gravity dam model 839
M.A. Hariri-Ardebili, S.M. Seyed-Kolbadi

DOI 10.3217/978-3-85125-564-5-112

I003 Durability Enhancement of Concrete Dams by Controlling and Mitigating 847
 AAR Problem
AliAkbar Ramezani pour, Amirmohammad Ramezani pour

DOI 10.3217/978-3-85125-564-5-114

I005 A probabilistic approach to define the reliability of gates at dams and weirs 853
Adrian Lindermuth, Barbara Brinkmeier, Markus Aufleger

DOI 10.3217/978-3-85125-564-5-115

I006 A case study on the deformation behaviour of asphalt concrete core dams 857
 (ACRD) with different core inclinations
Peter Tschernutter, Adrian Kainrath

DOI 10.3217/978-3-85125-564-5-116

I007 Thermal Analysis of Roller Compacted Concrete Dams 864
Mohammad Mousavi, Majid Pasbani Khiavi, Mortaza Ali Ghorbani

DOI 10.3217/978-3-85125-564-5-117

Additional Conference Papers

B0015 Flow Pattern and Delta Characteristics in a Dam Reservoir 873
Kazem Gomar, Masoud Ghodsian, Seyed Ali Ayuobzadeh

DOI:10.3217/978-3-85125-564-5-020

Design, Construction, Monitoring and Modelling of Albagés Earthdam. A Case History

Núria M. Pinyol^{1,2}, Eduardo E. Alonso²

1- Centre Internacional de Mètodes Numèrics en Enginyeria (CIMNE), Spain

2- Civil Engineering School, UPC, Barcelona, Spain

Email: eduardo.alonso@upc.edu

Abstract

A zoned earth dam 40 m high is analyzed and modelled using a numerical code able to deal with unsaturated-saturated soils and the coupled hydro-mechanical phenomena. The paper discusses the selection of the materials for the design of the dam. The dam construction was modelled at the design stage (a type “A” calculation) and results are compared with actual measurements registered during construction until the time when the dam reached two-thirds of the total final height. The limitations of the type A model are discussed and an updated model is presented taking into account compaction data and field tests performed during construction

Keywords: Earth Dam, Unsaturated Soils, Compaction Conditions, Numerical Modelling, Real Case.

Destructive Phenomenon of Dust Storm and Its Mitigation Measures on the Global Scale

Naser Tarkeshdooz
Managing Director of Mahab Ghodss Consulting Engineering Company, Iran
Member of ICOLD Committee

Email: ntarkeshdooz@yahoo.com

Abstract

Today, “Air Pollution” especially the greenhouse gases generation; and dust storm, (known as dust cloud and dust layer) have become a severe problem of human’s life and a real threat to the public health. The issue is considered as a serious challenge for the societies, experts and etc. In this article, it is attempted first to define the phenomenon, (dust storm, dust layer or cloud), and then to give a brief summarized actual mechanism of their formation. Also secondly to describe their movement and travelling, together with the causes of their remaining partly in the sky and partly deposited. The article concludes that the excessive generations of the greenhouse gases are the main cause of pollution, and consequently the formation of the dust storm (or dust layer or cloud). Also the most logical and possible remedial measure is to decrease and mitigate the generation of the greenhouse gases. It is also concluded that the thermal power station is responsible for generating the biggest portion and percentage of the greenhouse gases and the transportation, industry and households uses are in descending order. To achieve the effective reduction in greenhouse gases generation, one must resort to replacement of the production of the thermal power plant by the renewable energy; and also allocate the largest possible share for the clean, green, renewable energy in the basket of energy future production. Among the renewable energies, the hydropower clean and green energy is the most logical, possible, economical alternative.

Keywords: Green House Gas Generation, Dust Storm, Health Problem, Mitigation, Hydropower as Solution.

Assessment of Foundation Mass and Earthquake Input Mechanism Effect on Dam-Reservoir-Foundation System Response

Mohsen Ghaemian¹, Ali Noorzad², Hamid Mohammadnezhad¹

1- Department of Civil Engineering, Sharif University of Technology, Tehran, Iran

2- Faculty of Civil, Water & Environmental Engineering, Shahid Beheshti University and President, Iranian Committee on Large Dams (IRCOLD), Tehran, Iran

Email: ghaemian@sharif.edu

Abstract

Concrete dams are one of the most important infrastructures in every country and the seismic safety assessment of them is a major task in dam engineering field. Dam-foundation-reservoir system analysis is a complex interaction problem because this system consists of three domains with different behaviors. For accurate analysis of this system some important factors should be considered such as foundation mass and earthquake input mechanism. In this paper the effect of foundation mass and earthquake input mechanism on seismic response of concrete gravity dam is investigated. For this purpose, 2 different methods are introduced for modeling of massed semi-infinite foundation in finite element method namely, Free-Field Boundary Condition (FFBC) and Domain Reduction Method (DRM). To verify the feasibility of proposed methods for seismic analysis of dam-foundation-reservoir system, the displacement and stress outputs using proposed methods are compared with EAGD-84 results. The obtained results indicate that both methods are accurate enough for finite element modeling of massed foundation. Finally, Koyna concrete gravity dam is analyzed for rigid, massless and massed foundation cases using DRM and it is concluded that the foundation has significant effect on dam response and the common massless foundation approach overestimates the dam response.

Keywords: Soil-Structure Interaction, Free-Field Boundary Condition, Domain Reduction Method, Massed Foundation, Boundary Condition, Seismic Wave Propagation, Radiation Damping.

Ensuring Worldwide Long-Term Prosperity Thanks Dams and Reservoirs as Vital Water Infrastructures The Important Role of ICOLD

Anton J. Schleiss

**Laboratory of Hydraulic Constructions (LCH), Ecole polytechnique fédérale de Lausanne (EPFL),
Switzerland
President of the International Commission on Large Dams (ICOLD)**

Email: anton.schleiss@epfl.ch

Abstract

History shows that the economic prosperity of a society and its cultural wealth was always closely related to the level of the development of the water infrastructures, including dams and reservoirs. In view of climate change, dams and reservoirs will and have to play an even more important role as mitigation and adaptation infrastructures in order to satisfy the vital needs in water, renewable energy and food in the different continents worldwide. It is also a worldwide political will to improve water, energy and food security on a global level through the so-called NEXUS approach that integrates management and governance across sectors and scales. Nevertheless, these political intentions have to be necessarily followed by a concrete translation into the urgently needed enhancement of the worldwide water infrastructure including reservoirs and dams. To gain wide acceptance and to obtain a win-win situation between all stakeholders, such large water infrastructures projects have to be designed as multi-purpose projects by multidisciplinary teams with a complex system approach. This needs excellence in engineering sciences and management. Through the excellent work of his technical committees, the International Commission on Large Dams (ICOLD) is contributing to the worldwide vision “better dams for a better world”.

Keywords: Dams, Reservoirs, Water, Food, Energy, Sustainable Development, Climate Change.

Constitutive Modelling of Wetting Deformation of Rockfill Materials

Erich Bauer

Institute of Applied Mechanics, Graz University of Technology, Graz, Austria

Email: erich.bauer@tugraz.at

Abstract

In this paper the constitutive framework of hypoplasticity is used to model long-term deformations and stress relaxations of weathered and moisture sensitive rockfill materials. The state of weathering of the material is represented by a so-called solid hardness in the sense of a continuum description. The time-dependent degradation of the solid hardness is a result of progressive weathering caused for instance by hydro-chemical reactions of fluid with the solid material. The degradation of the solid hardness can lead to collapse settlements and creep deformations, which are also called wetting deformations. In contrast to a previous version, a new evolution equation for a more refined modelling of the degradation of the solid hardness is proposed. With respect to a pressure-dependent relative density, the influence of the pre-compaction of the material and also the influence of the pressure level on the stiffness can be modelled in a unified manner using a single set of constants. The performance of the new model is validated by comparison of the numerical simulations with experiments data.

Keywords: Rockfill Material, Wetting Deformation, Solid Hardness, Creep, Hypoplasticity.

Internal Erosion in Dams. Studies and Rehabilitation

Laura Caldeira

National Laboratory for Civil Engineering, Av. do Brasil, 101, 1900-066 Lisboa, Portugal

Email: laurac@Inec.pt

Abstract

In embankment dams, filters/drain systems constitute a first line of defense against the phase of continuation of erosion. It is generally assumed by several authors that the continuation of internal erosion can be prevented by using adequate granular filters in areas where important hydraulic gradients may develop. This paper addresses the most important purpose and functions of filters. Once the internal erosion process initiates, for a given load condition, and there are no effective filters stopping eroded particles along the erosion path, the occurrence of progression of internal erosion should be assessed. In zoned dams, upstream zones may assist in controlling the phase of progression of erosion, before flows became excessively large for the downstream zone to discharge safely. The limitation of the progression of internal erosion in zoned dams, potentially caused by an upstream zone can be assessed using a new test cell. This device and correspondent test results are presented and analyzed. Two case studies of dams with internal erosion problems are described. The first is an embankment dam, Lapão dam, where due to design and construction problems an internal erosion process was developed. The other is Crestuma dam, a gated structure type. Since the dam started operating, the river bed in the vicinity of the dam has been subject to frequent monitoring that evidenced progressive erosion of the protective layer. This paper presents the results of the studies undertaken in relation to the hydraulic stability of the alluvial foundation of the dam's stilling basins and of the downstream rockfill, and the main features of the implemented solutions.

Keywords: Internal erosion, Filters, Laboratory tests, Case studies, Rehabilitation.

Models of Earthquake Ground Shaking Used in Seismic Design and Safety Checks of Large Dams

Martin Wieland

**Chairman, ICOLD Committee on Seismic Aspects of Dam Design, c/o Poyry Switzerland Ltd.,
Herostrasse 12, CH-8048 Zurich, Switzerland**

Email: martin.wieland48@gmail.com

Abstract

For the seismic design and seismic safety checks of large storage dams, dynamic analyses have to be carried in the time domain, as inelastic deformations have to be expected under the safety evaluation earthquake ground motion. As input for such analyses acceleration time histories are needed. The characteristics of these time histories are discussed. They may include features such as spectrum matching of recorded or artificial acceleration time histories, aftershocks, directivity effects, near fault effects, extended duration of strong ground shaking, number of earthquakes, and stochastic independence of earthquake components as listed in the new guideline on the Selection of Seismic Parameters of Large Dams of the International Commission on Large Dams. These acceleration time histories used for dam design are models of earthquake ground motions but have hardly anything in common with real earthquake acceleration time histories, but by using such records, the dam engineer can provide a safe design, which is the main objective of the design of any structure.

Keywords: Dam Design, Seismic Analysis, Acceleration Time Histories, Aftershocks, Ground Motion Modelling.

Seismic Response Analysis of High Arch Dams to Spatially-Varying Ground Motions

Jin-Ting Wang, Feng Jin, Chu-Han Zhang

Department of Hydraulic Engineering, Tsinghua University, Beijing 100084, China

Email: wangjt@tsinghua.edu.cn

Abstract

The failure of a large dam can be catastrophic to human life and property downstream. Therefore, the seismic safety is of particular concern for high dams in seismically active regions. This paper addresses the seismic response analysis of high arch dams due to spatially-varying ground motions. Firstly, a comprehensive analysis model developed at Tsinghua University is presented, which takes into account radiation damping effect of semi-unbounded canyons, dynamic interaction of dam-water, opening of contraction joints, seismic damage cracking and strengthening of dam concrete, and nonlinearity of foundation rock. Subsequently, the seismic damage of Pacoima dam during the 1994 Northridge earthquake is qualitatively analyzed by the developed analysis model. The results agree with the actual damage observed after the earthquake. Most of the contraction joints opened and closed during the earthquake, and a larger residual opening occurred at the thrust block joint after the earthquake. The cracks continue from the bottom of the thrust block joint in three directions: diagonal, horizontal, and vertical. Finally, a large-scale numerical simulation of seismic ground motion from source rupture to dam canyons is introduced, which can simulate the characteristics of near-field ground motions at dam sites by considering the effect of source mechanism, propagation media, and local site.

Keywords: Concrete Dam, Seismic Damage, Spatially-Varying Ground Motion, Source To Site.

Assessment of Newmark Methods for the Prediction of Deviatoric Displacement of Earth Dams Using Energy Approach

Reza Karimi Moghadam¹, Mohammad Hassan Baziar²

1- M.sc. Graduated Student, School of Civil Engineering, Iran University of Science and Technology, Tehran, Iran

2- Professor, School of Civil Engineering, Iran University of Science and Technology, Tehran, Iran

Email: baziar@iust.ac.ir

Abstract

In this research, permanent earthquake-induced deformations of earth dams using Newmark methods are investigated. For this purpose, the errors of all sliding block methods for the prediction of the permanent deformation of 25 real earth dams are discussed in the time domain. Also, the importance level of some related parameters, discussed by previous studies, is scrutinized using energy approach. The results of the study revealed that, the energy value, related to the velocity time history, not only acts as a separator parameter between conservative and non-conservative predictions of sliding block methods but also has a significant impact on the prediction of permanent earthquake-induced deformations of earth dams.

Keywords: Energy Approach, Earth Dams, Newmark Methods.

Research on Rock-Filled Concrete Dam

Feng JIN, Hu ZHOU, Xuehui AN

Department of Hydraulic Engineering, Tsinghua University, Beijing 100084, China

Email: jinfeng@tsinghua.edu.cn

Abstract

Rock-filled concrete dam is a new type of dams constructed by RFC technology. Dozens of RFC dam have been built in China. At first, a brief introduction to RFC dams is presented in this paper. Then, some researches of RFC are introduced. The research focus on mechanical properties and thermal-physical properties of RFC. Some data in situ are also presented. Research results demonstrated that the RFC has good properties to be employed to build dams.

Keywords: Rock-Filled Concrete, RFC dam, Properties of RFC.

Quantifying Seepage Flow Velocities in Embankment Dams from Optical Fibre Distributed Temperature Measurements

Jean-Robert Courivaud¹, Nicolas Lorrain², Francois Martinot³, Remi Beguin⁴

1- EDF CIH, Avenue du lac du bourget, Bourget du lac, France

2- Geophy Consult, 159 quai des Allobroges, 73000 Chambéry, France

3- EDF DTG, 21 avenues de l'Europe, BP 41, 38040 Grenoble, France

4- geophyConsult, 159 quai des Allobroges, 73000 Chambéry, France

Email: Jean-robot.courivaud@edf.fr

Abstract

Seepage flow velocities are a key parameter to assess the risk of internal erosion in embankment hydraulic structures, such as embankment dams, canal embankments or levees. Accurate orders of magnitude of these seepage flow velocities are difficult to assess via conventional monitoring technologies or numerical modelling. EDF and geophyConsult have developed for 15 years an innovative technology of seepage detection using optical fiber distributed temperature measurements. This technology has already demonstrated its capability to locate seepages through embankment hydraulic structures using passive temperature measurements without any constraint of the optical fiber cable location with respect to the ground water table elevation. The next step was to use this technology to quantify the seepage flow velocities after having located them. A specific numerical modelling and analysis of optical fiber temperature data was developed and applied to a canal embankment experiencing seepage. After having presented the main geometrical and geotechnical characteristics of this canal embankment and its foundation, this paper presents the optical fiber monitoring installation. Then, the hydraulic behaviour of this canal embankment is discussed, based on visual inspections and piezo metric measurements. In its third part, this paper presents the optical fiber temperature measurement analysis, allowing seepage location detection and seepage velocity quantification. This innovative technology still needs to be tested and implemented on other case studies but it has already shown a promising potential to significantly improve internal erosion assessment from monitoring data.

Keywords: embankment dams, monitoring, seepage flows, temperature measurements, optical fiber.

1. INTRODUCTION

Seepage flow velocities are a key parameter to assess the risk of internal erosion in embankment hydraulic structures, such as embankment dams, canal embankments or levees. Accurate orders of magnitude of these seepage flow velocities are difficult to assess via conventional monitoring technologies or numerical modelling. EDF and geophyConsult have developed for 15 years an innovative technology of seepage detection using optical fiber distributed temperature measurements. This technology has already demonstrated its capability to locate seepages through embankment hydraulic structures using passive temperature measurements without any constraint of the optical fiber cable location with respect to the ground water table elevation ([1], [2], [3], [4], [5], [6]). The next step was to use this technology to quantify the seepage flow velocities after having located them. A specific numerical modelling and analysis of optical fiber temperature data was developed and has been applied to an 800m-long portion of a canal embankment where seepages occurred at the downstream toe.

After having presented the main geometrical and geotechnical characteristics of this canal embankment and its foundation, this paper presents the optical fiber monitoring installation. Then, the hydraulic behaviour of this canal embankment is discussed, based on visual inspections and piezo metric measurements. In its third part, this paper presents the optical fiber temperature measurement analysis, allowing seepage location detection and seepage velocity quantification.

2. CANAL EMBANKMENT DESCRIPTION

The 15-km long canal embankment of interest is located on the right bank of the intake channel of an EDF's hydraulic power plant located in the South-East of France. Figure 1 shows a view of this canal from the top of the embankment.



Figure 1 : View of the canal embankment

The embankment's height above natural ground varies until 15m. Dam crest is 9m wide, downstream and upstream slopes are 3H/1V. The foundation is made of silty sandy alluviums. The embankment body includes a watertight upstream fill made of clay, sand and lime. The central and downstream part of the embankment body are made of sandy gravels. In some parts of the embankment, diaphragm walls have been realized from the crest to the upper part of the foundation (Fig. 2). However, this canal embankment which was originally built in the years 1890' has suffered for decades of seepages and low kinetics types of internal erosion (suffusion and contact erosion).

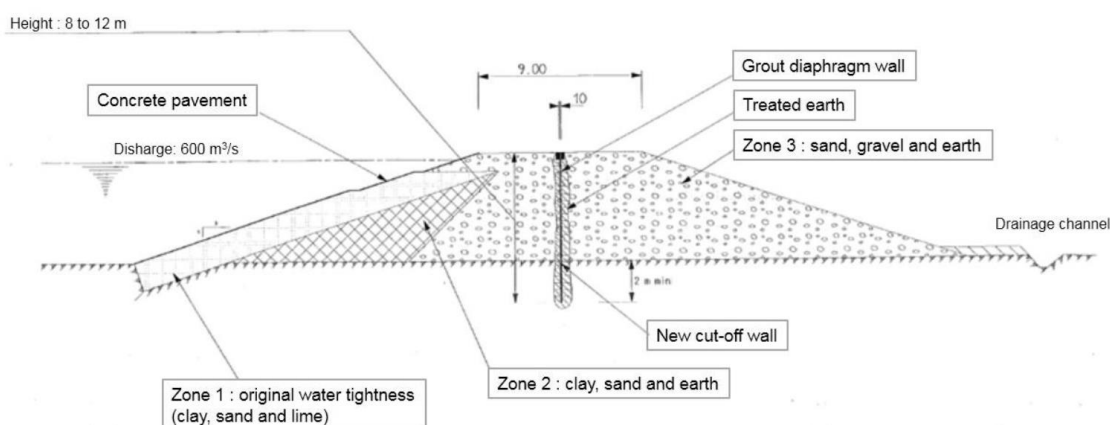


Figure 2: Cross section of the canal embankment before its rehabilitation 3

As this canal embankment is located in a high-density urban area where a breach due to internal erosion is a major safety issue, rehabilitation works have been carried out in 2014, following a safety assessment study. These works included the realization of a continuous diaphragm wall from the embankment crest to the upper part of the foundation and the rehabilitation of the drainage at the downstream toe of the embankment. The rehabilitation of the drainage included the recalibration and reinforcement of the existing drainage channel in addition to the realization of a new drainage ditch at the downstream toe of the embankment, in order to improve the resistance of the embankment against internal erosion and to enhance seepage monitoring. Taking advantage of the undergoing construction, optical cables were installed during the works of the new drainage ditch and the existing drainage channel (Fig. 3). The goal of this fiber optic monitoring system is to monitor the spatial distribution of seepages and to quantify the seepage flow velocities.

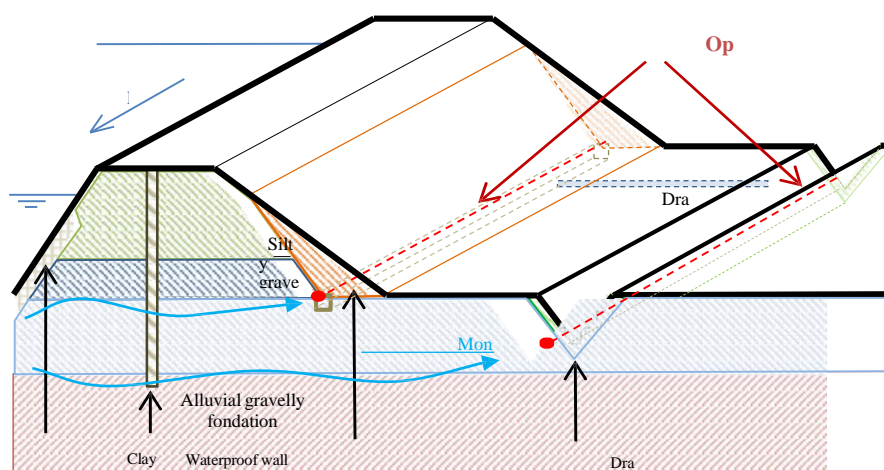


Figure 3: 3D view of the canal embankment after its rehabilitation

The monitoring system of this canal embankment includes piezometers which are located along the crest, behind the cut-off wall and along the berm between the downstream toe of the embankment and the drainage channel, flow weirs which measure drainage flows at drainage exits and optical fiber distributed temperature measurements located along the drainage ditch and channel.

The main potential failure mode of this embankment identified by the safety assessment study is contact erosion in the upper and lower part of the silty-sand layer associated with a defect in the cut-off wall. Through thermo-hydraulics modelling of seepages induced by this physical process, it was concluded that two optical fiber cables parallel to the embankment were needed to detect it. The first cable is located at the base of the draining ditch, just above the draining trench. The draining ditch is located at the base of the downstream slope. Flow from seepages, if any, is drained into the trench and then routes through the outlets along the berm to end up in the drainage channel. Some outlets are equipped with water flow sensors. The second cable is located parallel to the drainage channel, which is roughly 20 meters from the toe of the downstream slope.

These two optical fiber cables are connected to the optoelectronic instrument, configured for hourly data acquisition. Distributed temperature is computed using Raman spectra method.

Despite these rehabilitation works, seepages were observed along the downstream toe of the canal embankment during visual inspections performed during fall 2015 on an 800m-long section. In order to better understand the physical processes through a characterization of this seepage, an analysis of the optical fiber temperature measurements has been performed with the goals to quantify this seepage.

In this section of the embankment, the core is composed of different gravelly and silty-sand soils. A 1-meter-tall layer of silty-sand supports the core. The foundations are composed of sandy-silty-gravel (see Fig. 3).

3. EMBANKMENT HYDRAULIC BEHAVIOUR

To study the consistency of the optical fiber data processing results, conventional monitoring conclusion is previously presented. Visual inspection, piezometer and flow discharge data, as part of the conventional monitoring, give an insight of the embankment's hydraulic behaviour in this specific section.

First of all, during the optical fiber installation works in 2014, a 600-meter long area of saturated soil with the presence of very slight seepages has been highlighted during excavation of the draining ditch between locations KP (Kilometric Point) 9.5 and KP 10.1. Figure 3 is a picture of the draining ditch being excavated. A high water table level was also identified during drainage channel works in this area.



Figure 4: Picture of the draining ditch being excavated during works in 2014 (left picture), observation of humid soil (right picture).

During standard operation of the canal, a visual inspection is carried out along the whole embankment on a 15-day basis. During visual inspections in 2016 and 2017, areas of humid soil at the toe of the downstream slope around locations KP9.5 and 9.7 and a 180-meter wide area of high water level on the side of the drainage channel were identified.

The piezometers along the embankment, during the period from 2014 to 2015, are extremely stable in the area of interest and further with a standard deviation of about 20 cm. Figure 5 shows a piezo metric profile at location KP 9.670 compiled with a 2-year dataset. Maximum, minimum and average piezo metric levels are displayed in the French national reference unit. 5

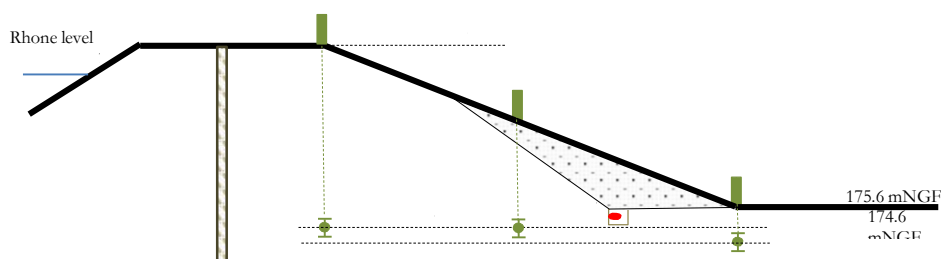


Figure 5: Piezo metric profile at KP 9.670. mNGF unit refers to the topographic level in the French national reference.

At location KP 9.670, the piezo metric profile shows that the optical fiber is located around 30 cm above the highest water line. At location KP 9.940, the water level is slightly above the level of the optical fiber, submerging it.

The draining ditch is composed of two drainage sub-sections as shown in Figure 6. The first sub-section drains the draining ditch from location KP 9.46 to 9.7 with an outlet located at KP 9.58. The average water discharge over the years 2015 and 2016 was 220 L.min⁻¹ with a maximum up to 400 L.min⁻¹. The second sub-section spans from KP 9.7 to KP 10.1 with a non-monitored outlet located at KP 9.7. The visual inspection of March 2017 gave an estimated discharge of about 100 L.min⁻¹.

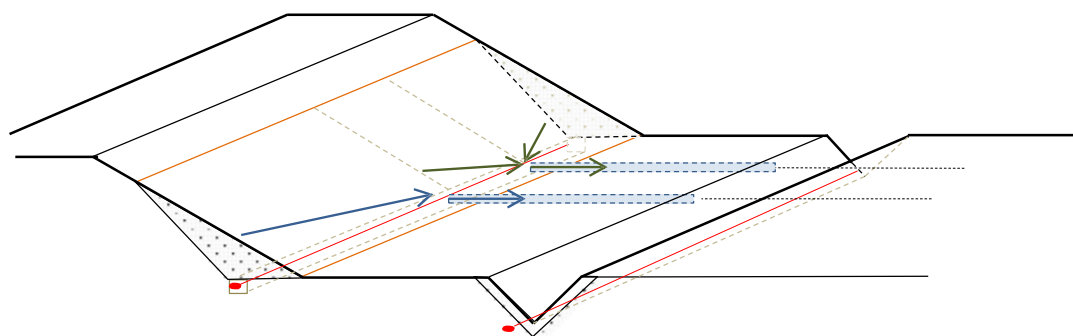


Figure 6: 3D view of the drainage slopes and outlets layout

The conventional monitoring concluded that the water table is generally high, as described by piezometric data and visual inspections. At KP 9.94, the water level was higher than the location of the optical fiber. The non-zero water discharge at the outlets showed that a flow ran in the draining trench and gave an insight on the potential presence of seepage in the area of interest. The conventional results are summarized in Table 1. 6

PK	9.4	9.45	9.5	9.55	9.6	9.65	9.7	9.75	9.8	9.85	9.9	9.95	10	10.05	10.1	10.15	10.2	
Visual inspection	Saturated soil during works in 2014																	
Piezometry	Humid soil					High water table												
Discharge	Optical fiber above water table			Optical fiber below water cable														
Seepage suspected from optical fiber measurement	225 L min ⁻¹			100 L min ⁻¹														
							Seepage suspected at ~5.10 ⁻⁵ m/s											

Table 1: Summary of the conventional monitoring results in the area of interest.

4. SEEPAGE FLOW VELOCITY QUANTIFICATION METHOD

The seepage flow velocity quantification method is a physically-based seepage detection method analyzing at each measurement point the optical fiber temperature measurements, using:

- A 1D energy numerical model to compute the temperature induced only by thermal advection as energy transportation process from the water in the canal to the location of the optical fiber. The water temperature and the distance between the canal and the optical fiber are the inputs of the computation. The model calculates the seepage flow velocity in order to optimize the modelled temperature with the temperature measured by the optical fiber.

- A 1D energy numerical model to compute the temperature induced only by thermal conduction as energy transportation process from the ground surface to the depth of the optical fiber. The air temperature and the optical fiber depth are the inputs of the computation. The model estimates the thermal parameters of the soil so that the computed temperature fits best with the measured optical fiber temperature.

An offset and a ratio correction are allowed as means to take into account the limitations of the models, such as the absence of solar radiative flux, the non-coupling of water and air effect, 2D or 3D problems, water and air temperature measured potentially far away from onsite location...etc.

These two temperature numerical models are compared together in terms of their performance to reproduce the measured optical fiber temperatures. When the air-based model gets less convincing, and the water-based model becomes better, a seepage flow from the canal is likely to exist. Figure 7 presents the example of a post-processing graph.

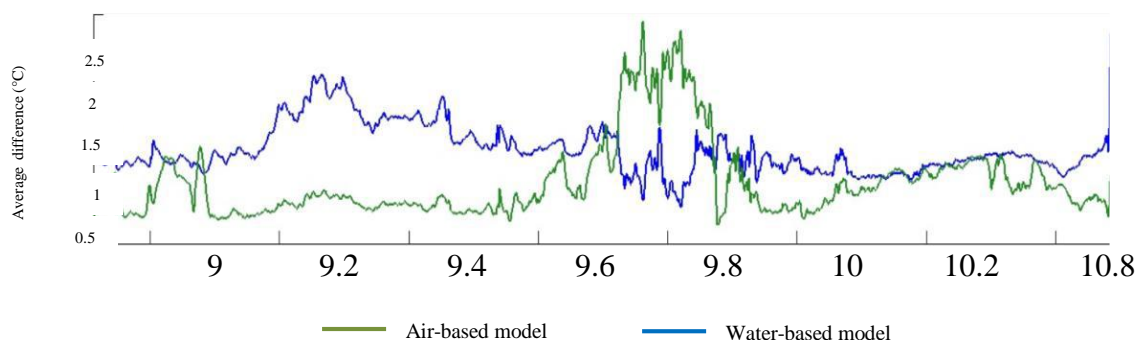


Figure 7: Temperature difference between the water-based model and the optic fiber temperature (blue line) and between the air-based model and the optic fiber data (green line)

This graph shows the average temperature difference between numerical results and measured temperatures, along the position of the optical fiber cable. Between KP 9.7 and 9.9, the average temperature difference between water-based model and measured temperature drops whereas the air-based model tends to divert from the measured temperature. This area is highlighted as a potential area of seepage. Between KP 9.7 and KP 9.9, the water-based model fits the measured temperature with a seepage flow velocity of about $5.10^{-5} \text{ m.s}^{-1}$ over a span of about 150 meters. Figure 8 shows the time evolution of the water-based model at PK 9.797 at the center of the area highlighted.

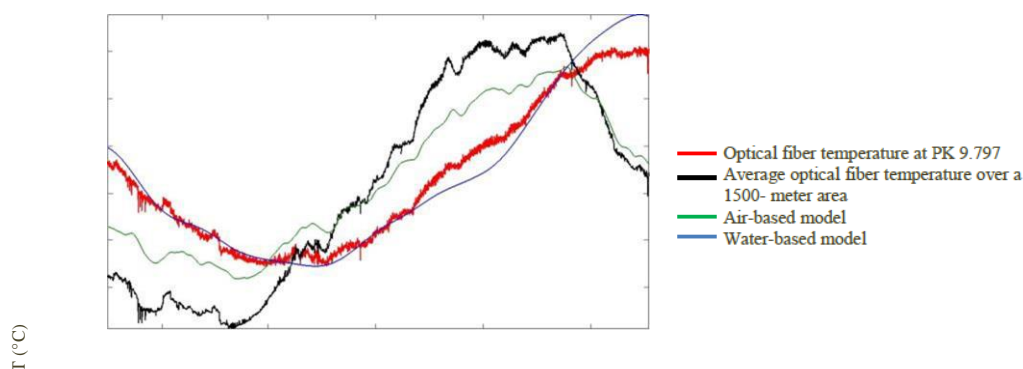


Figure 8: Air-based and water-based model temperature evolutions at PK 9.797 compared to optical fiber temperature evolution.

The seepage flow rate can be estimated from the width of the detected leaking area, from the estimation of the flow velocity and assuming a height of the seepage path in the dyke. If a 0.2 to 2-meter average height is assumed for the seepage, a total flow rate between 100 L.min^{-1} and 900 L.min^{-1} is calculated. This result is consistent with the estimated water discharge at the outlet 1 (100 L.min^{-1}). The monitoring of the water discharge at the outlet 1 would give better confidence in this comparison.

The seepage flow velocity quantification method detected an area of temperature disturbance, explained by the presence of seepage around KP 9.7 and 9.9 consistent with the conventional measurements. The analysis of the optical fiber temperature measurements gathered between KP 9.4 and 9.7, where a significant flow-rate is also collected from the drainage ditch is currently in progress.

5. CONCLUSIONS

A new method of quantification of seepage flow velocities by optical fiber temperature measurements has been used on a real case of seepage on a canal embankment operated by EDF. This method doesn't require to heat the optical fiber nor to locate the optical fiber cable below the water table. Being able to provide seepage flow velocities every one meter all along the embankment downstream toe, this method enables to envisage at short term to assess automatically in real time and at low cost the risk of internal erosion along canal embankments or levees for flood protection. This method is currently tested with data from other embankments in order to characterize properly its domain of use.

6. REFERENCES

1. J.-R. Courivaud, J.-J. Fry, “*Progress on Leakage Detection on Dykes Using Distributed Optic Fibre Temperature Measurements*”, Hydro Vision 2006 conference, Portland, USA, August 2006.
2. J.-R. Courivaud, J.-J. Fry, Y.-L. Beck, “*Feed-back after 10 years of Development and Deployment on EDF Hydraulic Structures of Optical Fiber Based Monitoring Systems*”, Hydro Vision Russia 2013 conference, Moscow, March 2013.
3. J.-R. Courivaud, P. Pinettes, Y.-L. Beck, “*Improvements in the Surveillance of Canal Embankments and Levees*”, ASDSO annual conference, San Diego, USA, September 2014.
4. J.-J. Fry, J.-R. Courivaud, R. Beguin, C. Guidoux, “*Application of fiber optics to the surveillance of canals at EDF*”, TKZ 2017, Warszawa, Poland, September 2017.
5. P. Cunat, “*Détection et évaluation des fuites à travers les ouvrages hydrauliques en remblai, par analyse de températures réparties, mesurées par fibre optique/Detection and analysis of leaks through hydraulic dykes, using distributed fiber optic temperature*”, thesis report, Grenoble, France, 2006.
6. C. Guidoux, J.-R. Courivaud, Y.-L. Beck, R. Beguin, “*80 km cumulative earth dams equipped with fiber optic monitoring systems: site experience feedback on the 4 past years*”, TKZ 2015, Warszawa, Poland, September 2015.

System Identification of Concrete Arch Dam Using Frequency Domain and Time-Frequency Domain Methods

Arman Roshanravan¹, Mohammad Manafpour², Hesaneh Ghanbari³

1- PhD student, Faculty of Civil Engineering, University of Urmia, Iran

2- Assistant Professor, Faculty of Civil Engineering, University of Urmia, Iran

3- MSc of Hydraulic Structures, Faculty of Civil Engineering, University of Tabriz, Iran

Email: Arman.roshanravan@gmail.com

Abstract

System identification is an effective and important method in health monitoring of structures especially in long term behaviors. It looks after any changes such as cracking or abutment instability in the behavior of structure. There are several methods of system identification which investigate dynamic parameters of the structure and each of them has advantages and disadvantages. The results in system identification process are reliable when it is done by several records and similar results are achieved. In this article, dynamic parameters of double curved Karun III dam was identified by different methods and different records. Peak Picking (PP), Frequency Domain Decomposition (FDD) and Wavelet Transform (WT) methods are used to identify the natural frequencies and extracting damping ratios of the Karun III dam. The similarity of the results for different records and different methods proves that the results are reliable.

Keywords: System identification, Wavelet transform, Frequency domain decomposition, Karun III.

1. INTRODUCTION

Operational modal analysis (OMA) is one of the best methods for health monitoring and detecting of probable damages in structures. OMA methods are based on only-output data [1]. Classical modal parameter identifications are usually based on frequency response functions or impulse response function that require measurement of both the input force and the resulting response. However, for some practical reasons, modal parameters must be extracted only from response data sometimes. In addition, ambient vibration testing (AVT) has advantages over forced vibration and free vibration methods such as low cost, multiplicity and variety of excitations and the continuous use of structure in real condition.

Several techniques are available for OMA such as pick picking (PP) from power spectral density (PSD) functions, least-square curve fitting technique, natural excitation technique (NExT), autoregressive moving average (ARMA), stochastic subspace identification (SSI), frequency domain decomposition (FDD) method and continuous wavelet transform (CWT) method. Frequency Domain Decomposition (FDD) method transforms signal to frequency domain and selects system frequencies during processes [2-4]. continuous Wavelet Transform (CWT) is a time-frequency domain method [5,6]. The advantage of the CWT than other time-frequency method is variability of time and frequency resolutions which made CWT to a multi resolution method. In this paper, PP, CWT and FDD methods were used to calculating frequencies and damping ratios of the recorded motions of the Karun III dam.

2. SYSTEM IDENTIFICATION

System identification is used to obtain modal characteristics of structures to observe any changes. OMA are output based methods which extract modal parameters based on dam responses regardless to input signal. Different methods were used to this purpose such as Pick Picking (PP), FDD and continuous Wavelet Transform (CWT). Here, system identification was used to identify modal parameters and dynamic behavior of the Karun III dam. PP, CWT and FDD methods were used as Operational Modal Analysis (OMA) method to calculating modal parameters. PP is a simple method based on power spectral density spectrum. FDD and CWT methods are more sophisticated and have special advantages. CWT is a multi-resolution time-frequency method that separate frequencies precisely. In the first step, the wavelet parameters should be selected in an optimization process. Then frequencies of the record are calculated. After that, the original signal is decomposed to single frequency signals that contain identified frequencies. The calculated single frequency signals do not have any modes interference so

they are appropriate to apply half power method to calculate damping ratios. So, the main advantage of CWT method is its ability to decompose signals. FDD method is a frequency domain method which decomposes power spectral density spectrum to its singular values. The peaks in first singular values shows frequencies of the record and second singular value's peaks are used to verify the weak peaks which appears at the first singular values. The main advantage of the FDD method is its accuracy to decompose signals and to distinguish frequencies.

2.1. CONTINUOUS WAVELET TRANSFORM (CWT) METHOD

CWT is a mathematical transform which can analyze signals in both time and frequency domain with variable resolution. The main equation of CWT is:

$$CWT_x^\psi(a, b) = \frac{1}{\sqrt{a}} \int_{-\infty}^{+\infty} x(t) \bar{\psi}\left(\frac{t-b}{a}\right) dt \quad (1)$$

Where b and a are translation and scale parameters respectively. x is signal and t indicates that the signal is in time domain and ψ is wavelet function. In this research the modified Morlet wavelet was used as wavelet function. Mathematical representation of modified Morlet wavelet is:

$$\psi(t) = \frac{1}{\sqrt{\pi f_b}} e^{i2\pi f_c t} e^{-t^2/f_b} \quad (2)$$

Where f_b and f_c are band pass and central frequency of wavelet respectively.

As mentioned above Wavelet transform is a multi-resolution transform that resolutions are depend on wavelet parameters. Wavelet time and frequency resolutions are represented as:

$$\Delta t_i = \frac{f_c \sqrt{f_b}}{f_i^2} \quad (3)$$

$$\Delta f_i = \frac{f_i}{f_c 2\pi \sqrt{f_b}} \quad (4)$$

As is clear by changing the value of f_b and f_c , different resolutions can be obtained. So these parameters should be optimized to obtain better results. Here, a trial and error process was applied to optimize wavelet parameters. The requested domain for wavelet parameters should satisfy Equation 5 [7].

$$\sqrt{f_b} f_c = (2\alpha) \frac{f_{i+1}}{2\pi \Delta f_{i+1}} \quad (5)$$

Where α is the parameter defining the overlap between the adjacent Gaussian windows of the modified Morlet wavelet. Kijewski and Kareem suggested the empirical value $\alpha=2$ which is generally sufficient to distinguish two adjacent frequency components [8].

2.2. FREQUENCY DOMAIN DECOMPOSITION (FDD) METHOD

In this method, Power Spectral Density (PSD) matrix of the response signal is calculated according to equation 1 [7].

$$G_{yy}(j\omega) = \bar{H}(j\omega) G_{xx}(j\omega) H(j\omega)^T \quad (6)$$

Where G_{xx} and G_{yy} are the PSD of input and output signal respectively and H is the matrix of frequency response function. The frequency response matrix can be written as:

$$H(j\omega) = \sum_{k=1}^n \frac{Q_k}{j\omega - \lambda_k} + \frac{\bar{Q}_k}{j\omega - \bar{\lambda}_k} \quad (7)$$

Where n is the number of modes, λ_k is the pole and Q_k is the residue. By combining equation 1 and 2, the relationship between PSD matrix of the input and output is derived as:

$$G_{yy}(j\omega) = \left[\sum_{k=1}^n \frac{Q_k}{j\omega - \lambda_k} + \frac{\bar{Q}_k}{j\omega - \bar{\lambda}_k} \right] \cdot G_{xx}(j\omega) \cdot \left[\sum_{s=1}^n \frac{Q_s}{j\omega - \lambda_s} + \frac{\bar{Q}_s}{j\omega - \bar{\lambda}_s} \right] \quad (8)$$

Assuming that the input is white noise, i.e. its PSD is a constant matrix, after some mathematical calculations the following equation can be obtained:

$$G_{yy}(j\omega) = \sum_{k=1}^n \frac{A_k}{j\omega - \lambda_k} + \frac{\bar{A}_k}{j\omega - \bar{\lambda}_k} + \frac{B_k}{-j\omega - \lambda_k} + \frac{\bar{B}_k}{-j\omega - \bar{\lambda}_k} \quad (9)$$

Where A_k is the k th residue matrix of the output PSD. As for the output PSD itself, the residue matrix is an $(m \times m)$ Hermitian matrix given by:

$$A_k = Q_k C \left[\sum_{s=1}^n \frac{Q_k^{-T}}{-\lambda_k - \lambda_s} + \frac{Q_k^T}{-\lambda_k - \lambda_s} \right] \quad (10)$$

The contribution to the residue from the k th mode is given by:

$$A_k = \frac{Q_k C \bar{Q}_k}{2\alpha_k} \quad (11)$$

Where α_k is the negative of the real part of the pole. When the damping is light, the remaining term is proportional to the mode shape and can be expressed as:

$$Q_k = \phi_k \gamma_k \quad (12)$$

Therefore,

$$A_k \propto Q_k C \bar{Q}_k = \phi_k \gamma_k C \gamma_k^T \phi_k^T = d_k \phi_k \phi_k^T \quad (13)$$

Where d_k is a scalar constant, and ϕ_k and γ_k are the mode shape vector and the modal participation vector, respectively. Thus, in the case of a lightly damped structure the response spectral density can always be written as:

$$G_{yy}(j\omega) = \sum_{k=1}^n \frac{d_k \phi_k \phi_k^T}{j\omega - \lambda_k} + \frac{\bar{d}_k \bar{\phi}_k \bar{\phi}_k^T}{j\omega - \bar{\lambda}_k} \quad (14)$$

This is a modal decomposition of the spectral matrix.

Then, the PSD matrix of output signal is decomposed by taking the SVD of the matrix.

$$\hat{G}_{yy}(j\omega_i) = U_i S_i U_i^H \quad (15)$$

Where the matrix $U_i = [u_{i1}, u_{i2}, \dots, u_{im}]$ is a unitary matrix holding the singular vectors u_{ij} , and S_i is a diagonal matrix holding the scalar singular values S_{ij} .

Frequencies of each pick in the first singular value are equal to frequencies of the record. In this method, to choose the correct picks, the Modal Assurance Criterion (MAC) was used [7]. The MAC compares the relationship between two complex mode shape vectors ϕ and ψ by linear comparing:

$$MAC = \frac{|\psi^T \phi|^2}{(\psi^T \psi)(\phi^T \phi)} \quad (16)$$

Continues Wavelet Transform (CWT) was used separately to decompose response signal to all identified frequencies. Eliminating of modes interference and considerably increasing the accuracy of calculated damping ratios are the advantages of this process. Then, half power method applied to PSD of each single frequency signal to calculate damping ratios

3. IDENTIFICATION OF MODAL PARAMETERS OF KARUN III DAM

Karun III is one of the biggest double curved arch dam in Iran. The height and the crest length are 205 m and 462 m respectively, and its thickness varies from 29 m at the base of the crown cantilever to 5.5 m at its crest level. An array of 15 accelerometers were installed on Karun III dam body to record dam responses to ground motions. As is represented in Figure 2, four accelerometers were selected to study identification of modal parameters of the dam.

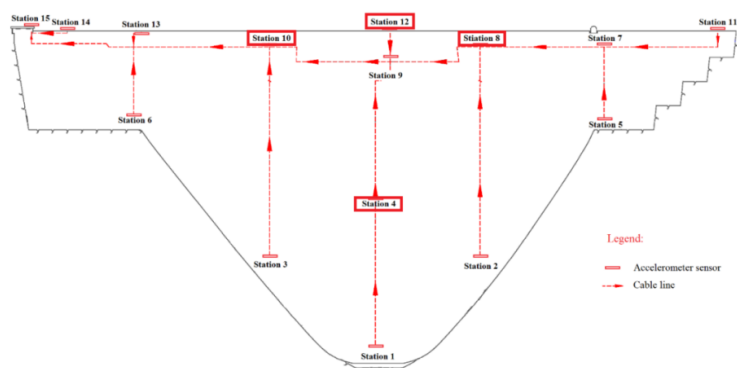


Figure 1- Location of accelerometers on Karun IV dam body

The recorded acceleration at 04 August 2012 was selected to investigate modal parameters. Two other recorded events also were selected to verify the results obtained by processing the records of the first motion. The recorded accelerations in stations 4,8,10 and 12 are shown in Figure 3.

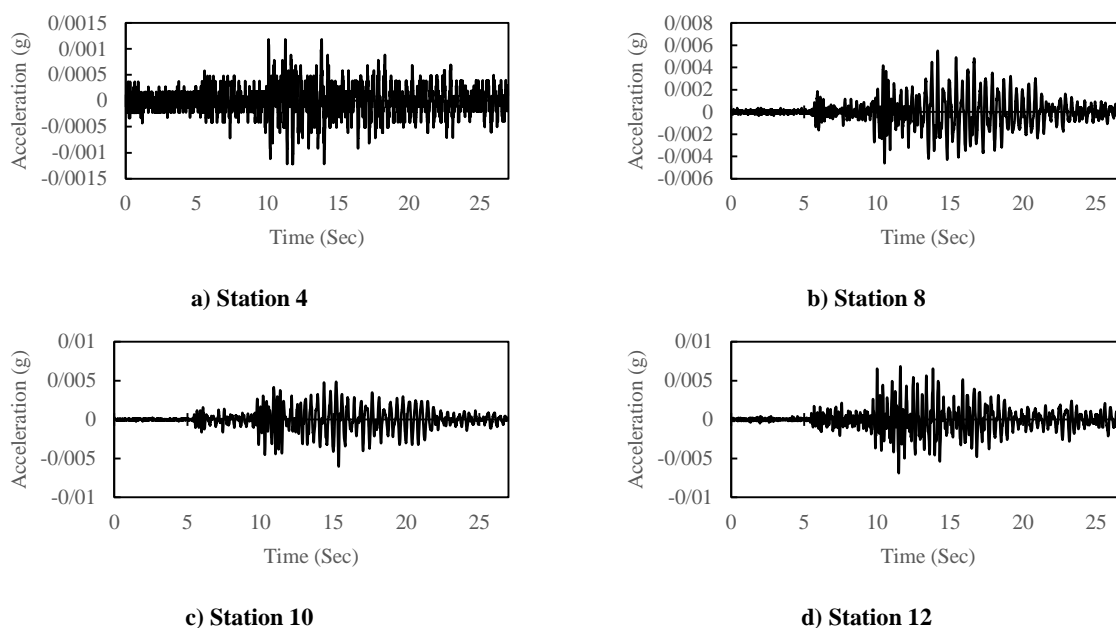


Figure 2- Recorded accelerations. A) station 4. B) station 8. C) station 10. D) station 12.

3.1. FREQUENCY IDENTIFICATION OF KARUN III DAM WITH PP METHOD

The peak picking (PP) method is the simplest method in system identification methods. It is based on power spectral density matrix of the accelerations. Here, there are four recorded motions from four different stations which have their own PSD spectrum. In the first step all four PSD spectrum should be normalized and then average spectrum should be calculated. The averaged normalized power spectral density (ANPSD) spectrum can be used to calculate frequencies of the structure as shown if figure 4.

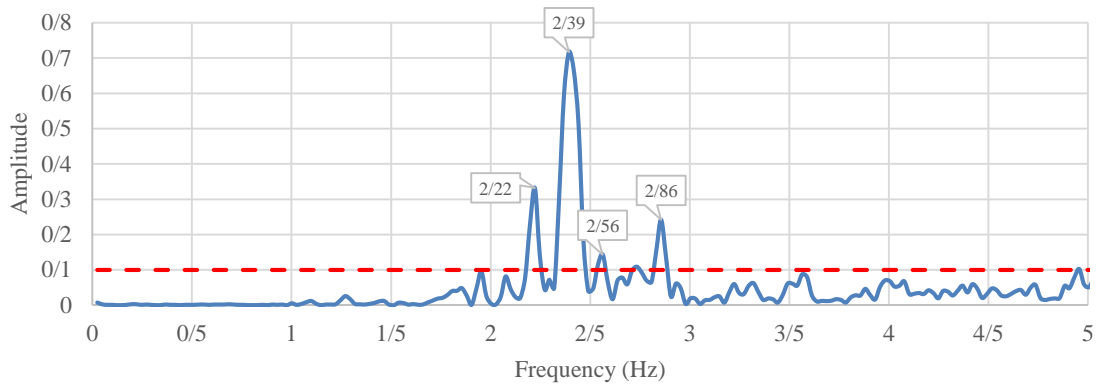


Figure 3- ANPSD of the recorded motion

3.2. FREQUENCY IDENTIFICATION OF KARUN III DAM WITH CWT METHOD

The calculated CWT for the record 1 is shown in Figure 5. As shown in Figure 5, there are four peaks of energy and each of them could be assumed system frequency, but the energy of the first identified mode is not as much as the others. Therefore, to find the first mode of the system accurately, two other records were used. Figure 6 and 7 represent the first mode which were identified with record 2 and 3 respectively. As it can be seen, these figures verify the selected modes of record 1.

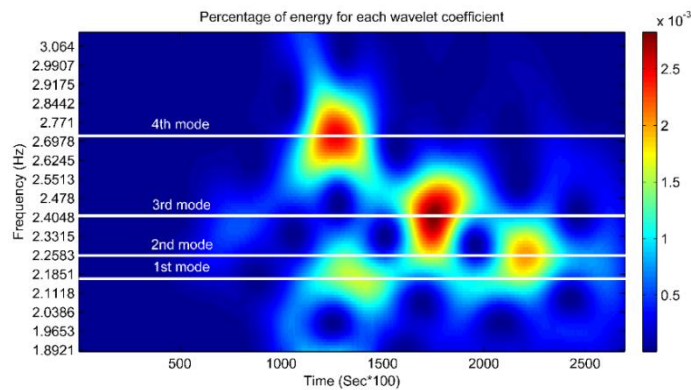


Figure 4- CWT of first motions and identified frequencies

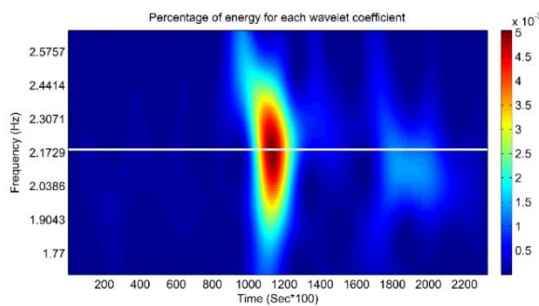


Figure 6- CWT of third motion and identifying first mode

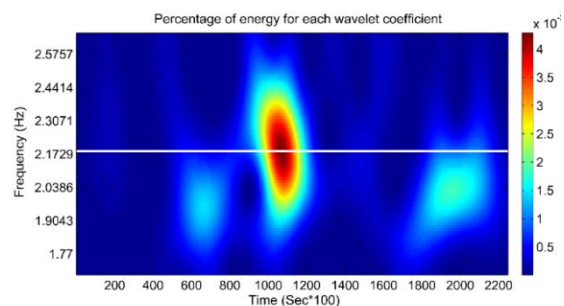


Figure 5- CWT of second motion and identifying first mode

The identified modes of the Karun III dam by CWT method due to ambient vibrations are briefly shown in Table 1.

3.3. FREQUENCY IDENTIFICATION OF KARUN III DAM BY FDD METHOD

Frequencies of the system with PP and CWT methods were extracted. Here, in this section, FDD method was applied to calculate frequencies of the Karun III dam. As explained, FDD method decomposes acceleration record to its singular values and the peaks which appear in first singular value represent frequencies. Figure 8 shows first singular value of recorded motion and four identified frequencies.

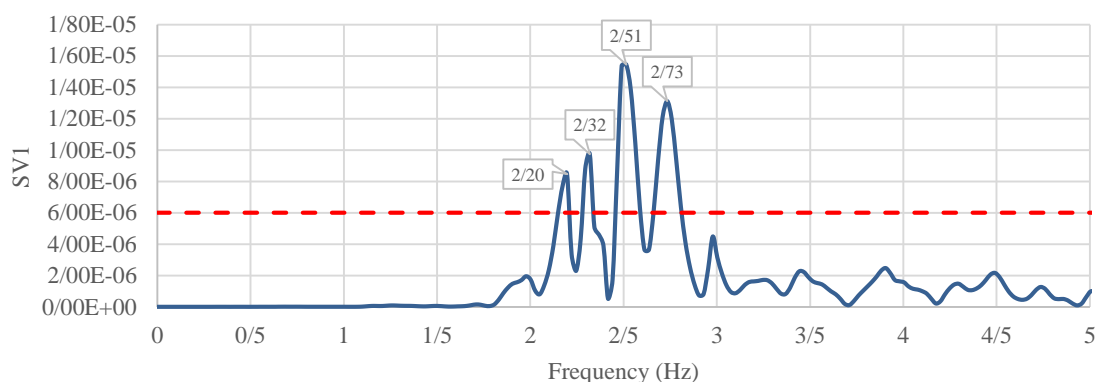


Figure 7- first singular value of recorded motion

Three different methods (PP, CWT and FDD) in frequency domain and time-frequency domain were used to calculate frequencies of the Karun III dam from recorded motions. The results of all three methods briefly are presented in table 1 below.

Table 1- identified modes of Karun III dam

Modes	Frequency (Hz)			Average (Hz)	Error(Percent)
	PP	WT	FDD		
1 st	2.22	2.18	2.20	2.20	1.80
2 nd	2.39	2.26	2.32	2.32	5.44
3 rd	2.56	2.42	2.51	2.50	5.47
4 th	2.86	2.72	2.73	2.77	4.89

3.4. CALCULATING DAMPING RATIOS

Half power method was applied to calculate damping ratios in four identified modes. Because the identified modes, especially the first two modes are close, modes interference causes significant errors in calculating damping ratios. Therefore, the dam responses were decomposed to identify frequencies. These frequencies were used to eliminate modes interference in order to use half power method to calculate damping ratios exactly. Damping ratios calculated are represented in Table 2.

Table 2- calculated damping ratios of Karun III dam

Modes	Damping ratio (%)
1 st	1.66
2 nd	1.58
3 rd	1.02
4 th	1.12

4. CONCLUSIONS

In this paper PP, CWT and FDD methods were used to calculate modal parameters of Karun III dam. Because the recorded responses on dam body are ambient vibrations and cannot excite all modes of the dam clearly, more than one motion was used to find weak modes.

The first identified frequency by three methods has 1.8% difference and its average magnitude is 2.2. the first mode is the most important one in system identification process and 1.8% error demonstrates that the all three methods have almost similar results. the second identified frequency and its tolerance are 2.32 Hz and 5.44% respectively. In all 4 identified modes, error tolerance percentage for different methods is lower than 5.47% which shows excellent accuracy for identification process.

The signal decomposition technique which was used to eliminate modes interference showed good results. In addition, damping ratios were calculated separately for each mode. This method significantly increases the accuracy of calculated damping ratios.

5. ACKNOWLEDGMENT

Iran Water and Power resources development Co. (IWPCO) and Mr. Basereh are thanked for providing databases for this project

6. REFERENCES

1. d Andersen, P. (2001), "*Damping estimation by frequency domain decomposition*," IMAC XIBrincker, R. and Ventura, C. anX, Kissimmee, USA.
2. Brincker, R. and Zhang, L. and Andersen, P. (2001), "*Modal identification of output-only systems using frequency domain decomposition*," Smart materials and structures.
3. Ventura, C. and Laverick, B. and Brincker, R. and Andersen, P. (2003) "*Comparison of dynamic characteristics of two instrumented tall buildings*," in Proceedings of the 21st International Modal Analysis Conference (IMAC).
4. Zhang, L. and Brincker, R. and Andersen, P. (2009), "*An overview of operational modal analysis: major development and issues*," Mechanical Systems and Signal Processing.
5. Daubechies, I. (1992), "*Ten lectures on wavelets*," SIAM.
6. Staszewski, W. (1997), "*Identification of damping in MDOF systems using time-scale decomposition*," Journal of Sound and Vibration, pp.283-305.
7. Tarinejad, R. and Damadipour, M. (2014), "*Modal identification of structures by a novel approach based on FDD-wavelet method*," Journal of Sound and Vibration, pp. 1024-1045.
8. Kijewski, T. and Kareem, A. (2003), "*Wavelet transforms for system identification in civil engineering*," Computer-Aided Civil and Infrastructure Engineering, pp. 339-355.

Investigating the Local Arching Phenomenon in Total Pressure Cells Located in Clay Core Protective Filters and Comparison with Numerical Modeling Results (Case Study: Mamlou Earth Dam)

Mohammad Salehian Zolbin¹, Maziar Mahmoudinia²

1- MSc in Civil Engineering Hydraulic Structures, Mamlou earth dam, Iran

2- MSc in Civil Engineering Geotechnical Engineering, Lar earth dam, Iran

Email: mdsalehian@gmail.com

Abstract

One of the most important factors affecting the safety and stability of earth dams is arching in a clay core. This phenomenon happens due to difference of elastic modulus of clay and filter materials, which, in turn, causes more settlement in clay core than the sides. This makes transmissions of stress in arched format to lateral filters; hence, stress recorded in pressure cells located in filters increases to more than the above material layers' weight. This led to an increase of arching factor (ratio of stress recorded of total pressure cells to materials weight over these cells) to higher than the unit. This implies that arching is of great importance during the initial impounding of dam reservoir, which should not exceed limited value. The problem happened in Mamlou earth dam is local arching in place of total pressure cells installed in filters which has caused decreasing of recorded stress. Accordingly, the factor of arching is less than one. The phenomenon has happened in most of pressure cells installed in filters. This paper, then, has studied the cases happened in the highest section of dam (section 14). In the next part, we have modelled the main section of the dam in finite difference method by FLAC2D. Finally, we have presented the results of comparison between instrument and model results.

Keywords: local arching, modulus of elasticity, FLAC2D, total pressure cells.

1. INTRODUCTION

Safety of large structures made by human always requires a comprehensive and detailed understanding of them. In the case of earth dams, as the most complex geotechnical structures, the best known structural failure reason is defect in construction, which, in turn, leads to instability in dam body [1], [2], [3] and [4]. Rock fill dams with clay core are desirable among engineers and societies largely due to protection against natural hazards and also cost-effectiveness. As a result, they have developed rapidly in recent decades [5], [6], [7] and [8]. Failure of high earth dams with central impermeable core and two permeable shell on both sides of core could cause risks for communities in downstream. This has led experts and scholars to carry out extensive studies on the same issue. Dam safety evaluation is a complex issue that requires a detailed analysis using instrumentation and analysis by different soft wares [9], [10] and [11].

One of the most important parameters to be taken into consideration is pressure. In order to monitor pressure, it is of great importance to place pressure cells in pre-determined locations in dam body. Recorded data in pressure cells is cyclically collected through data loggers and analyzed. Stability of dam body depends on different items including displacements, pressures, pore pressures. One usual phenomena that happens inside dam body is arching. Arching takes place as a result of settlement difference in clay and filter materials arises due to more filter modulus in comparison with clay. During this process, pressure transition happens from clay to filter. To put it another way, clay behaves like an arch bridge and the side filters act as pile of bridge and carry loads more than overhead load. Before dam construction, prediction is made in different methods to have safe and stable body. Moreover, monitoring is done during construction and in first impounding of reservoir. During our study on Mamlou earth dam, we observed strange phenomena happened in pressure cells located in filters. It was understood that arching factor in these regions is less than unit meaning that it not only does not apply greater burden on the region, but also, loading on the region is less than the overhead. This problem happened in many pressure clusters located in these regions. we called these phenomena as "local arching". In this paper we are going to investigate these phenomena.

¹ Mamlou earth dam Safety and sustainability expert

² Lar earth dam Safety and sustainability expert

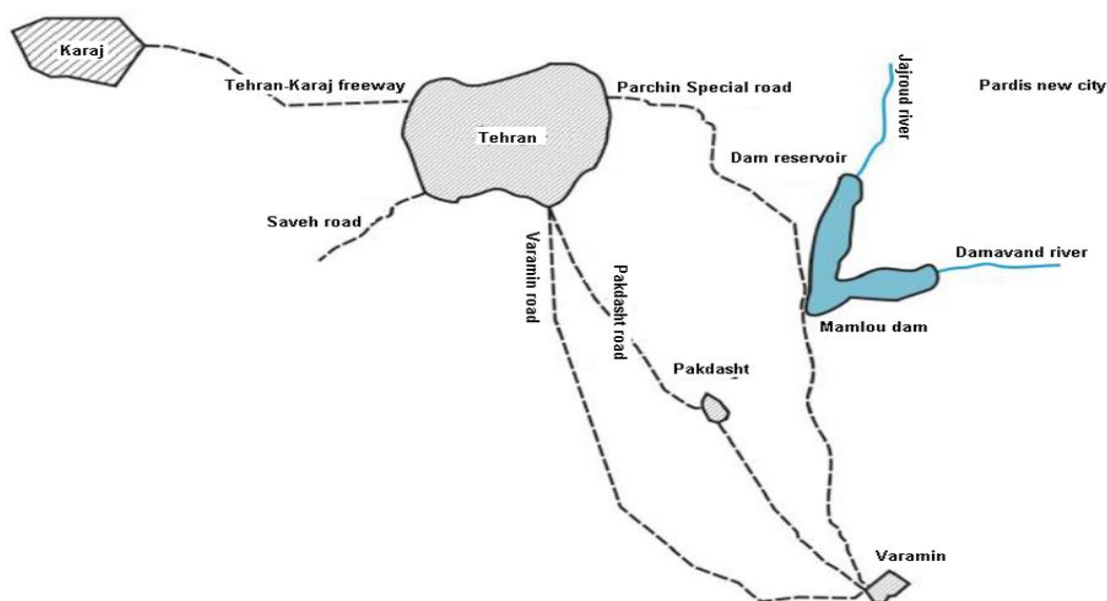
Technical studies concerning geotechnical complex structures such as dams is necessary and the related researchers considered instrumentation a factor for keeping economic interests, which helps to grow the construction and maintenance of development projects [12]. This is quite evident in Mamlou dam instrumentation. In order to accurately evaluate the dam during the construction and exploitation stage, a complete set of instrumentation were installed in 5 sections according to the length of the dam body .Mamlou dam instrumentation consists of total 384 numbers of different instruments. One of the main goals that can be followed through instrumentation of data at the end of dam construction is consideration of the correct Performance of construction and verifying design assumptions and providing alerts to solve the potential problems of the dam. The basic parameters necessary for this purpose in earth dams is measurement of pore water pressure, the amount of stresses in soil and lateral and vertical deformation in dam body [9], [10].

This paper reports the analysis of actual measured pressure in order to estimate arching factor in Mamlou earth dam. With rapid growth in computer processing power and speed, it is not surprising that many engineering problems are solved through analysis or modeling. Today, these soft wares are highly optimized (Siva Kumar and Singh, 2016) [13]. FLAC is a software is used for engineering calculations. FLAC software, which is known as an explicit finite difference based on lagrangian analysis functions, was used to model the main section of Mamlou earth dam (section 14-14) by using Mohr-Coulomb elasto-plastic model and also through data analysis instrumentation. Furthermore, through back analyses, the actual parameters of dam body materials were extracted. In this way, we were able to accurately assess our design assumptions with actual conditions. This analysis focuses on pressure and displacements, and the available monitoring data entails a total of nearly 8 years including part of the construction phase and stage of first filling of the reservoir (2 years), and 6 years of its operational Time.

2. MAMLOU EARTH DAM

Mamlou earth dam shown in Fig.1 is constructed about 2.5 km downstream the accession of Damavand river to Jajroud Rivers in a place called "gate" by Longitude and latitude of 51.7880° and 35.5840° , respectively which is about 45 km southeast of Tehran. In upstream of the dam is Pardis city and at the downstream of the dam is Pakdasht city located in about 17 and 15 Km distance respectively. Mamlou earth dam is 89m high from the base and 86m high from river bed and the length of crest is 807m (Table 1). The construction of dam began in 2002 and was completed in 2009. First impounding of reservoir started in 2008 February.

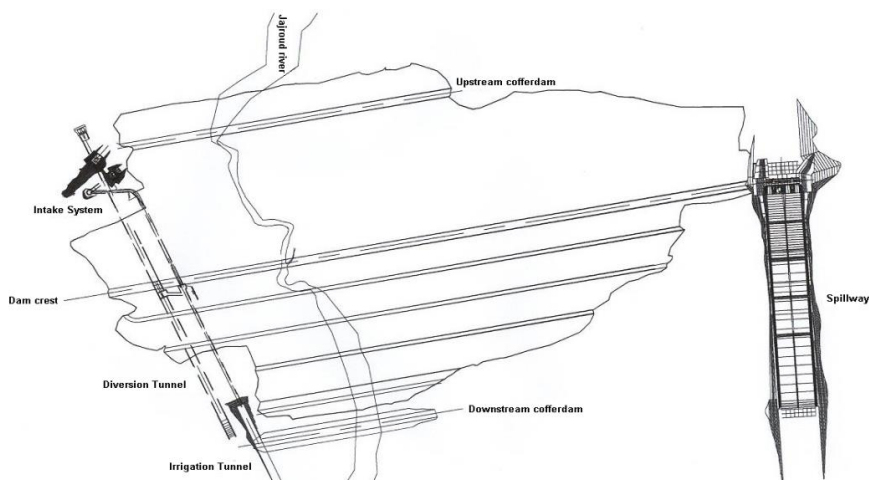
(a)



(b)



(c)



(d)

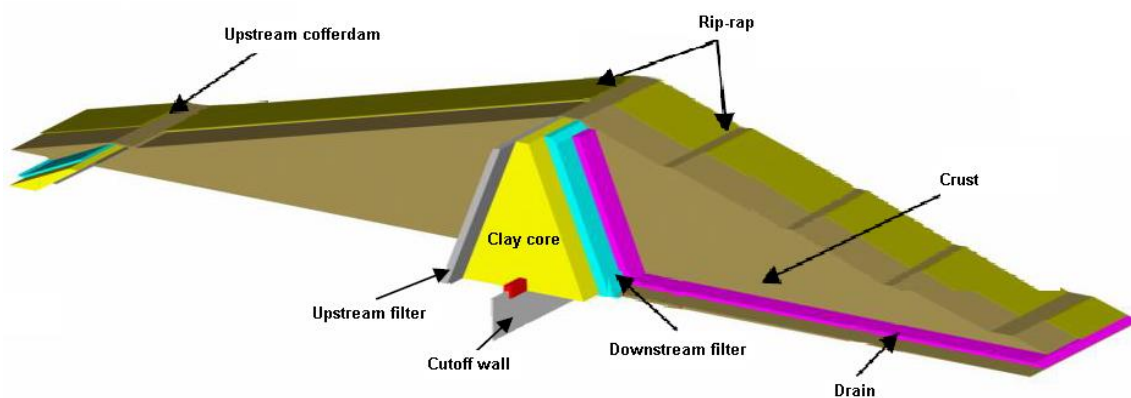


Fig 1. (a) Geographical location of Mamlou earth dam. (b) A general view of Mamlou earth dam. (c) General construction plan and layout of the Mamlou earth dam. (d) Zoning of Mamlou earth dam.

Table 1: General characteristics of the Mamlou dam.

characteristics	estimate
Maximum height	89m
Crest length	807m
Crest width	10m
Crest elevation	1308m
Dam volume	$7.17 \times 10^6 \text{ m}^3$
Reservoir volume	$2.5 \times 10^8 \text{ m}^3$
Normal water level	1303.5m

3. ANALYSIS OF MONITORING RESULTS

This section deals with dam behavior around the pressure clusters situated in filters. Data collected during dam construction, first impounding and then, operation period, is used for analysis. There are numerous pressure cells that are facing local arching. Therefore, we have chosen one critical instrument which is located in highest instrumentation section of dam body (section 14-14). Fig 2 shows the arching factor and stress changes in PC14-1 which is installed at upstream filter and is at bottom level interface of foundation and filter. As shown in fig 2, arching factor is less than unit which is unusual. According to equation 1, for arching factor (A) increases as with P_v . As a result, we can claim that arching factor should be more than unit while this is completely different. In this experiment, we found that this cannot happen while there is arching in clay core. In our argument, then, the only reason is local arching which happens locally around the instrument. In other words, materials around the instrument is in condition that settlement does not happens equally so stress transmitted to beside the cluster that, in turn, it causes less pressure on the pressure cells and accordingly, arching factor decreases less than unit.

$$A = \frac{P_v}{\gamma h} \tag{1}$$

Where P_v is vertical pressure, γ is special weight and h is height of building materials on the instrument.

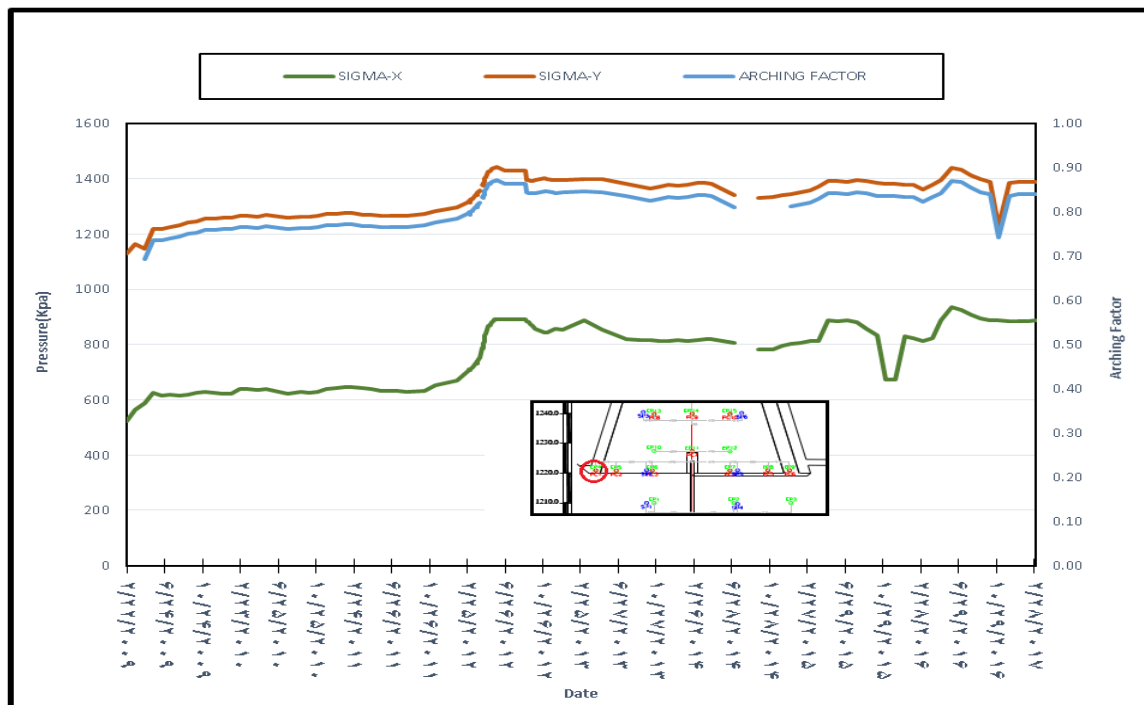


Fig 2. Arching factor and stress measured in pressure cells installed in PC 14-1 cluster

4. NUMERICAL ANALYSIS OF MAMLOO EARTH DAM

In this study, finite difference method was used for modeling dam behavior in order to obtain reliable stress-strain relationship. Mohr-coulomb model, as a conventional model for soil and stone materials, was used for earth dam that provided most adaption with real measurement. FLAC software, which is known as an explicit finite difference based on lagrangian analysis functions, was used to model the main section of Mamlou earth dam (section 14-14) by using Mohr-Coulomb elasto-plastic model. Fig 3 shows the numerical model created in FLAC. Fig 4 shows the vertical stress changes during construction of dam body. According to this graph, it is completely obvious that vertical stress recorded in instruments is lower than the numerical results. Thus, it directly affects arching factor to decrease less than unit.

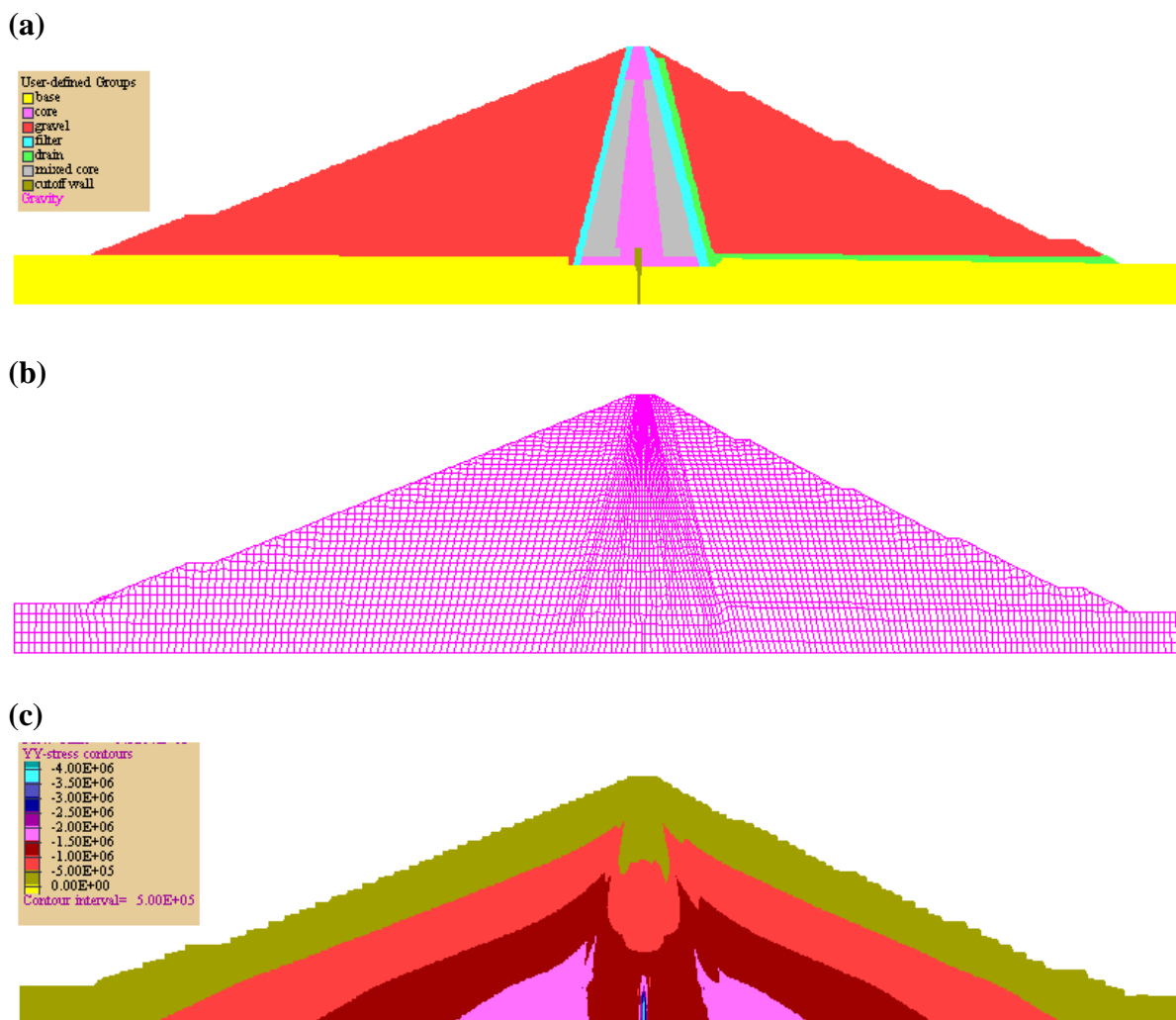


Fig 3. (a) Regions of dam body (b) meshing considered for numerical finite difference method (c) numerical result for vertical stress obtained in dam body at the end of construction.

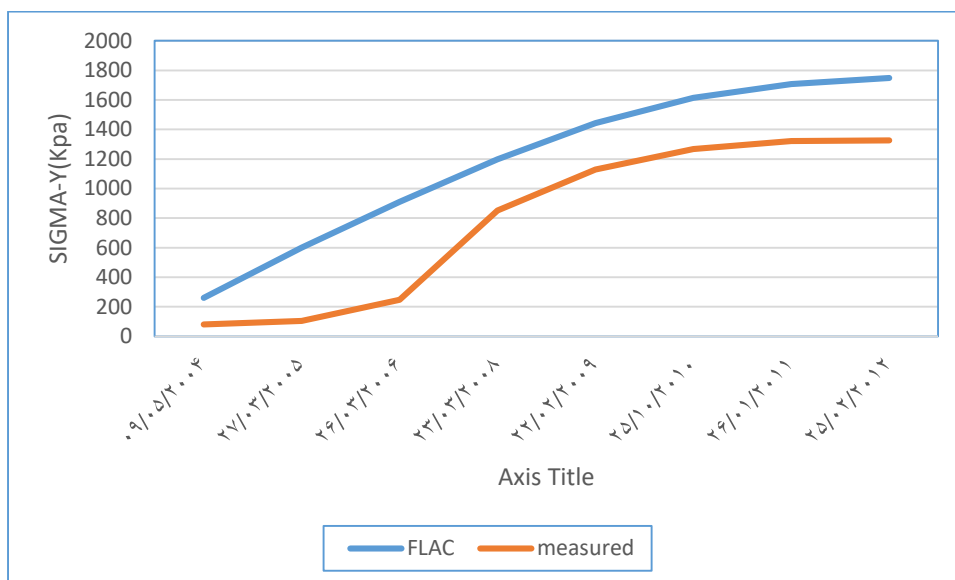


Fig 4. Vertical stress changes in modeling and measurement at the end of construction

5. CONCLUSIONS

The pressure characteristics of an earth dam during construction and operation phases were investigated in this research study. Monitoring was carried out for Mamloo earth dam in Tehran province. For comparison, monitoring records were collected during construction and operation phases which mostly focused on pressure and pore pressure records in pressure clusters located in filters. We observed unusual behaviors in pressure cells located in filters as they showed less pressure compared to overload materials weights while arching has happened in clay core and this is unreasonable. Thus, we understood that an unusual event went on around the pressure cells which decreased the stress on the pressure cell and arching factor becomes less than unit. Since this behavior occurs in clay core, we called it local arching. During our numerical study, we observed usual behaviors in dam body spatially in susceptible zones. These results confirmed our argument about local arching around the pressure cells. Differences between normal and unnormal pressure records were about 400kpa at the end of construction continued in operation phase.

6. REFERENCES

1. Sowers G, Sally H (1962), "*Earth and rock fill dam engineering*", London (UK): Asia Publishing House.
2. ICOLD. Lessons from dam incidents (1973) International commission of large dams. Abridged ed. MA (USA): USCOLD.
3. Gikas, Vassilis, and Michael Sakellariou (2008). "*Settlement analysis of the Mornos earth dam (Greece): evidence from numerical modeling and geodetic monitoring*" *Engineering Structures* 30.11: 3074-3081
4. ÖZEL, HALL FIRAT (2012). "*Comparison of the 2D and 3D Analyses Methods for CFRDS. Diss*". MIDDLE EAST TECHNICAL UNIVERSITY.
5. Singh R, Choudhury S, Singh B (2015). "*Wireless disaster monitoring and management system for Dams*". *Procedia Computer Science*.381-6.
6. Duncan JM, Chang CY (1970 Sep). "*Nonlinear analysis of stress and strain in soils*", *Journal of Soil Mechanics & Foundations Div*.
7. Xu B, Zou D, Liu H (2012 Jun 30). "*Three-dimensional simulation of the construction process of the Zipingpu concrete face rock fill dam based on a generalized plasticity model*", *Computers and Geotechnics*.;43:143-54.
8. Mahinroosta R, Alizadeh A, Gatmiri B (2015 Mar 17). "*Simulation of collapse settlement of first filling in a high rockfill dam*". *Engineering Geology*. 187:32-44.
9. Stewart M, Tsakiri M (2001). "*The application of GPS to dam surface monitoring*". *Journal of Geospatial Engineering*; 3(1):45-58.
10. Rohaninejad M, Zarghami M (2012 Mar 31). "*Combining Monte Carlo and finite difference methods for effective simulation of dam behavior*". *Advances in Engineering Software*; 45(1):197-202.
11. Athani SS, Solanki CH, Dodagoudar GR (2015 Dec 31). "*Seepage and Stability Analyses of Earth Dam Using Finite Element Method*". *Aquatic Procedia*. 4:876-83.
12. Wymore ML, Van Dam JE, Ceylan H, Qiao D (2015 Dec 31). "*A survey of health monitoring systems for wind turbines*". *Renewable and Sustainable Energy Reviews*. 52:976-90.
13. Zhang WG, Goh AT (2013 Mar 31). *Multivariate adaptive regression splines for analysis of geotechnical engineering systems*. *Computers and Geotechnics*; 48:82-95.

The Principles of Deep Alluvial Drilling Management on Borehole

Amin Mansouri¹, m. Ghadiri²

1- M. Sc engineering geology, Bu Ali Sina University, Hamedan, Iran

2- Professor of petrology, University of Golpayegan, Golpayegan, Iran

Emails: am.mansouri@yahoo.com¹, ABMco.ir@gmail.com

Abstract

Drilling borehole is one of the Geotechnical studies methods in land. The improvement of the procedure for and largely reinforcing the ground and injecting the material into the ground used. According to ground conditions and specify the desired goals of the depth of the borehole, which could include the borehole of the shallow, deep and profound. In this research, in the alluvial land drilling operations are studied on alluvial layers. Soils of fine-grained up to coarse-grained and even the structure of There is a very complicated that you should be sure of the direction of the drilling operation. Soft rock with rock areas of the organization that the cycle of diagenz there has to be complete and their effect on tectonic setting or location and climate of the region suffered alteration and alteration have been certain important also in drilling. In fact, drilling in the sand and stone strata loose organization, some of chemical- vaporize, because the coal and limestone rock component that compresses the soft sensitive work; and the necessary measures in this regard should be anticipated. A variety of machine tools for drilling, digging wells and the borehole in the world level used. In this research is based on the mechanism of action of the machine, drilling them into different groups, which is divided into the selection of the drilling system to each of these sets of factors, geographical location, gender, position, and depth of the well diameter materials and other factors are correlated.

Keywords: Drilling, Alluvium, New methods of speculation, Management.

1. INTRODUCTION

One of the methods Renovation and strengthening of the land, injection into the land, materials, mainly of the drilling method used to achieve this goal. now depends on the ground conditions and the goal of changes in soil texture, drilling can be carried out in various forms such as can be used to make the chips, holes drilled, dug the pit Borehole by drill point, drilling in order to dig here by car of the digger, in order to inject mixes of Within the different ground

2. THE METHOD OF BOREHOLE DRILLING

To perform the drilling operation first must specify the position of the Borehole, as well as the location of the work shall have been appropriated and not opponent as well as the access road to the site is possible by car and in the case of not having the necessary measures must be well access way. in some cases, because of the existence of legal problems or terrain can designer The location of the Borehole could be as much as possible and as far as an aims the project would not be entered, move.

After you determine the location of the Borehole, according to the coordinates of the position presented in the map of the borehole as with the mapping camera by a surveyor in the walk location. After being determined the exact location of the borehole by seating the team preparing drilling. prepare device for seating include preparing the way to access the flat, horizontal directional drilling and seating create a sturdy platform and prove by concrete for mounting the device. After preparing the drilling platform of the device must be in the form of Bob (perpendicular to the ground) in the desired location is fixed. Fixed to the device and its perpendicular on the ground is very important, especially during drilling that the device should not be moved to no or Off-Plumb and level. the error in each of these cases can cause wrong results or business failure of the drilling operation at that point. At the time of the start of drilling operations generally, the value soil, alluvium or manual categories may exist that must be of casing investment methods. Unless the desired level of concrete or stone and dig out the starting point (zero point) on a concrete or stone. Soft rock with rock areas of the organization that the cycle of diagenz there has to be complete and their effect on tectonic setting or location and climate of the region suffered alteration and alteration have been certain important also in drilling. In fact, dig in the sand and stone flowers loose organization, some of vapor and chemical because the coal and limestone rock component that compresses the soft sensitive work; and the necessary measures in this regard should be anticipated (Mansouri, 1385).

A variety of tools and devices Drilling for the well, and the Borehole in the world used the mechanism of action they are., drilling of the four following main classified group (Bell, 1983):

- 1- bits drilling
- 2-wash drilling
- 3-impact drilling A
- 4-Rotary drilling

Select each of these systems Drilling of the collection of the following factors are correlated (Bell, 2000):

- The position of the geographical location of the
- Genus earth materials
- Diameter and depth of the wells and drilling machine
- The device being available.
- The aim of the drilling operation
- Sampling quality.

2.1. SPIRAL BITS DRILLING

One of the methods Conventional drilling, in the activities of the development will count come the digging of wells in the rotation on their effect and spiral drill and go it on land obtained. application of this method of more drilling in soft and semi hard and depending on the type of drill, various used (Duncan, 2005). Drill drilling of the main two are divided into: 1. drill Manual of drill-2-mechanical indices.

2.1.1. HAND AUGERS

This drill These are manual by one or two people are slaves earning. overall the composition they include bit, bar or tube in the Middle, and handles the drill head can be could have different shapes, and practice of drilling and sampling done by them (Shafai, 1373).

This type of drill for drilling to a depth of 10 to 30 meters used in drilling depths by gender. land and water access level control in underground, drilling through the drill. Manual of tasks usually done for the prospect of another application, such as a declaration recognizing and water level basement and creating wells, drainage can also.

Frequently asked questions The most common type of drill Manual, the following are divided into three groups:

A: Post – hole Auger

This type of drill for example, soil sampling of fine seeds used in sticky and their diameter shall be between 100-200 mm.

B: Helical or Screw Auger

Spiral drill for samples Any of the soil (the non-sticky sticky or) use. of course, the soil should dry and above the level of the ground water located between 50 to 100 mm in diameter they are.

C: Spiral Auger

This drill Building simulation, springs, and according to their forms and their uses are as follows:

1. Closed spiral drill, 2. Open spiral drill;

The first type of soil for samples of the hard clay soil and Sandy heaped up in use. the second type of soil sampling for non-adherent of the sand used in slave of the drill diameter are between 50 to 100 mm.

2.1.2. MECHANICAL AUGER

The necessary resources for implementation of dropping this kind of drill Are supplied by a motor power consumption amounts to a kind of drills and drilling for the Earth in which sex may be depends. drill of its duty based on the mechanical properties of two group of drills and drill style of mechanical properties of heavy losses in the Division.

2.1.2.1. LIGHT MECHANICAL AUGER

This drill in terms of application interface limit of the drill of the drill manual and mechanical properties of heavy metals. Transport and work to get them done by one or two people from a small engine to power 10 horsepower for turning and sinking of land used in the drill. the depth of wells drilled by this type of drill between

10-15 m in diameter drilling, and between 75 to 300 mm. they further application in deposit that not soft and hard and toward the drill Manual of the higher speed.

2.1.2.2. HEAVY MECHANICAL AUGER

These drills are usually on trucks and by them to the desired locations in data transfer with them by force. A powerful engine and penetrating power supply (pressure) they may be caused by the weight of the drill and drill machine itself or by an external supply of hydraulic power or dynamic.

2.1.2.2.1. FLIGHT AUGERS

These drills Height are equal to 50 to 300 mm and drilling to a depth of 50 of them for up to 60 meters in use. The drill blade, depending on the application they have to drill two of the spokes of the drill and short blade of a continuous classified.

2.1.2.2.1.1. SHORT FLIGHT AUGERS

The composition of this drill Are in three sections:

A: blade in the lower part of the winning and the drilling operation is performed.

B: drill spiral-length limit in the middle section.

C: the axial Rod drill set to attach drilling machine.

During the drilling drill machine to spin and the spin by the middle bar (axial) are transferred to the winner of the blade It is done by drilling materials. in the middle part of the spiral instead of may be brought to the surface of the Earth in this and rotated in the reverse-discharge materials drill drilling and drilling wells are sent to the end again.

According to the type of blade used, drilling a winner may the following can be in.

1-spiral blade 600 mm maximum diameters: simple, drill for deposits of the soil surface and soft.

2-blade diameter 400 mm double spiral: maximum drilling, for deposits Hard rock of altered.

3-blade fish tail shape: maximum diameter 300 mm, for drilling in stone of loose soil and hard.

4-blade 300 mm maximum diameters, mounted: for drilling in stone of semi hard.

2.1.2.2.1.2. CONTINUOUS FLIGHT AUGERS

This drill Page spiral form head to head Kelly bar section [9] are unlikely to be seen as going a snail, a result of the on-going progress in drilling and drilling materials with rotation of the page brought up in spiral, and finally, at the level of the discharge in the Earth. the possibility of mixing sample Being brought up in the end in this kind of drilling is high and not obtained samples of the precise location of the drilling depth will be introducing. using this drill, then can be used to a depth of 60 m continuous drilling in. diameter drill this is between 60 to 110 mm. drill with this type may be found in the any land, though in different drilling will use them more on the sediment surface of and, like the loose shale. The middle part of the drill of the spokes going in May to the following distort.

A: bold Flight Augers

When of the drill of the blades used in bold is required after each time the drill has to be outside of the sample or part discharge of drilling has been performed in Australia and or drill, but tests of the blade of this score are you available during the drilling core sampling done also and the intact samples of a diameter of 75 mm to 150 mm and a will get that, no need to drag out the drill from the inside Wells.

B: Bucket Auger

This drill Includes a cylindrical steel container in the shape of the top and on the bottom of the page are open there is a metal on the blade of the winner has been anticipated in the vicinity immediately. this blade of the winner of the thread that is located within the open compartment bar compartment of steel -to connect the drill machine May drill during drilling operations. To rotate dermis and blade of the winning cause shatter and cut rock or sediment in your path may be crushed by materials. Thread are way into the Chamber to be filled when they and the Chamber is brought to the surface of the Earth, the drill and the discharge Chamber contents in this case and the practice of oil drilling continue. using this method, the well of a diameter of one meter and to a depth of 50 meters drilled. Of course, this drills for drilling in soft sediment not suitable hard.

2.2. WASH BORING DRILLING

Wash boring drilling method A simple exploration of the common Borehole and germination in one application of this type of more drilling. deposits of soft and hard stones and half are badly needed, altered drilling depth 30 m. and a diameter of wells drilling, to a limit of 15 cm. drilling speed in the sediment of the soft alluvium in about 6 meters per hour and in stiff clay, 5.2 meters per hour. the practice of drilling samples obtained from most of the hand and many are disrupted and distorted value for the activity of identifying the samples in order to have healthy examples of tools usually used by Drilling tools include the drill (drilling blade) The bar mounted on the drilling and steel through the cable (rope) attached to the drilling device may include drilling of telecommunications device. (Three or four foundations), engine, steel cable, pulley and the water pump is a device. drill (blade), drilling a three form of linear, sharp tip and a page there is a crossover of the two types of deposits for the first drilling soft clay to silts, for deposits of alluvial rock semi hard and loose use of this method of drilling are usually in the form of the tube wall of the need to protect the wall used in the well and be in the Borehole that the party does not have the necessity of at least two-walled pipe the first meters of the well by the pipe wall protecting the safety of the Earth around the well that the place of establishment Drill machine is guaranteed.

This drilling method for drill and drilling is the first bar to a certain height (30 to 100 cm) high by the motion of the motor is brought Then abandoned and drilling tools in effect force called free fall to the bottom of the well shall enter that causes the path of wisdom and shortening their materials into the water simultaneously. Wells drilling through injected bar and through a hole that had been anticipated with the pressure on the drill blade out. by pressing the crushed materials and parts for water through the gap between the pipe and that bar drilling the wall with wall Located well to the top of the well, along with the materials out of the water to the pond or tank shall discharge the alternatives. in these ponds are gradually destroying the bomb materials may have been pumping and water wells within the injected again.

2.3. PERCUSSION DRILLING

This method for soil drilling Soil heaped up, hard and stiff clay minerals and rocks are used an average drilling depth of 60 meters. and a maximum of more than 200 m and diameter of drilling between the Borehole-100-600 in mm. drilling speed according to the type of ground materials and sex that are drilling be different. Coarse of Soft surface and 2 to 4 meters per hour, in the semi hard materials 1 to 2 meters per hour and in rock hard maximum of 1 meter per hour may. in rock drilling when the sample represents the mentality of the soil, but are often examples of the obtained hand and drains me. this method more dug in deep water may be and its application in geotechnical exploration due to the high cost of doing it and the lack of access to healthy, is limited. The device Drilling tool set is included in the operation of drilling and sampling in two stages separately. Summary description of how to work in below.

1. Drilling operation: on the effect of high and low go drilling tool within the wells and the influence they have on earth are in effect if you hit Drill drilling tool included. (Blade), bar drilling and may be replaced by metal cable pulley and the motor is attached to the drilling machine can be moved by first drilling tools. the engine up to a height of 50 cm high to 100 cm. then release brought shall be. This tool since all are steel, as a result, many weight. so many during the fall energy (D) may blow in and enter and penetrate the Earth to cause drill bits. Drilling drill during the penetration on the land, located in the materials is cut and their continued resistance. If drilling beneath the surface of the water within the well water level, seeps, and mixed with chopped materials and flowers and will create a layer that bring in the next step (stage of sampling) shall discharge from wells drilling. Over the surface of the Earth, it is necessary to be entered into some water wells up with the crushed stone mixed materials has mud and earth and can be used to discharge after layer.

2- the practice of sampling material discharge: after finding out drilling tools and drilling operation status do Sample tools. the sampling Chamber or barrel including discharge and are depending on the gender of the specific and different types of drilling materials type are part of the lower Chamber are each one win and her heel is a side valve open. "thus allow crushed materials and flowers came into the Chamber layer may increase, but prevents their exit Sample tools. the sampling and bar are connected to discharge drilling and drilling device by cable to attach metal and move it by the motor adjustment, usually the discharge Chamber with a shot to the bottom of the well is imported and with his winning of the heel into the building materials and flowers and are down layer and high vacancies, while flower materials and layer to the level of the Earth.

Method The discharge of the other for flowers and used wells Te layer, for example when the bottom of the well and mud materials sand layer of lacking adhesion can be used from head method and when more materials are made of clay may be of the drill of the vane rotor movement that have spiral.

2.4. ROTARY DRILLING

This method of drilling in all types of land in earthy and stone and has taken to act too deep. Borehole diameter between 40 to 200 mm and has a sample of the obtained may be intact and represents or can depend on what purposes these are drilling are done.

Drilling on their speed of operation compared to other methods of it is, therefore, more extensive use of Borehole for digging deep and prospect of operating oil and gas. this method in the project application and exploration of high-cost geotechnical for the implementation of complex it systems and it limited drilling of this system is its duty according to the two groups of micro tool and the tool are divided into core study and a brief description of each of the following has come in.

2.4.1. CUTTING BIT

When these tools are used The main purpose of the action are in the Earth, and the influence of advance at drilling and sampling in the second priority is located in the samples obtained in this way have been routed and crushed in the drill included utility (blade) and the body of the drill is a drilling axial rod is mounted and connected to it by drilling machine may. A drill machine is equipped with hydraulic power generating engine that move the supply of drilling tools on their May drill drilling. Rotate and move on their own and cause rapid shortening of materials in the bottom of the well and drilling tool weight effect causes the sink into the Earth and water or drilling mud. compressed air simultaneously through the drilling of the well within the injected bar and ultimately through the holes and slots in the drill designed to drill around b.OBO very high pressure injected and thus in the meantime climbed and materials have been routed to the surface of the Earth. of water (drilling mud) or compressed air for cooling is used to keep drilling bit drilling in the flowers. the protection of the wall of the well in front of the drilling mud also loss. Of the mix to water with bentonite obtained in drilling and wide use of oil.

2.4.2. CORING TOOLS

The only difference between core tools Gear and tools in tools core barrel insult, core gear is installed after the bit and the sample during the 1960s dig into it driven and after completion of drilling, a thigh high along the sample. core barrel length is usually between 50 to 300 cm. two types of related core barrel and there is double core barrel related to the sample in the soil sample to take and double core barrel in the land of stone used It can be.

3. MODERN METHOD OF DRILLING

In addition to the items listed by need method New ways have been devised to drilling is a brief description of them.

3.1. THERMAL DRILLING

On the method of thermal, thermal radiation of energy helps the air with oxygen, or fuel type, white cementing, oil used for may Air or oxygen and fuel stone. of the two separate tract into the reservoir located on the back of the drill is added and after igniting the flame, heat the drill through the nozzle head to level the stones conveys and also heat the surface of the stone is ready for separation and laminate. Finally, to help the water pressure, laminate and parts of the Earth are transferred to the surface.

3.2. WATER DRILLING

In this method, using the water supply pressure at the surface, digging wells is possible here, with water pressure in wear resistance; surface rocks in may Breaks, and thus, will face drilling. This method applied with the increase of water pressure in coal mining and Placer reserves.

3.3. SHAKE DRILLING

This method of creating vibrations with high-frequency may be one of the most common stone broke. One of shake drilling method is ultrasonic drilling.

3.4 CHEMICAL DRILLING

In this method, the use of chemical action of explosive in explosion Be used in drilling classes. This method is usually used of two types of spending.

- 1) Cylinder that makes spending are digging cylinder hole.
- 2) Spend hole is the increased diameter of the hole.

3.5. ELECTRICAL DRILLING

In this method, with electrical production type or traits or spark drilling operations, done in stone In some of these methods, despite high temperatures, because of the call time short of being electric, the stone does not melt, but other methods are due to the high temperature and long time contact with the surface of the stone electric, after melting the surface of the stone, stone breaks.

3.6. LASER DRILLING

Electromagnetic radiation can be used with laser rays to be traits of production. This type of radiation is Be used for evaporation, or melting of rocks, creating fractures in rocks and digging hole. With strong waves phosphorous infrared thermometer can be used to surface traits, causing evaporation and melting the surface of the stone, and the stone fractures around the melting range. The function of the radius of the areas heavily depends on the laser radiation power.

4. DRILLING CATEGORY WITH FLUIDS

4.1. AIR FLOW

To dig in the ground such loose and soft can be from the air as drilling fluid. the only course to a depth of 300 meters can be benefited from this method because for the depths of most existing equipment cannot be used with the air volume required for the preparation of the cutting exit.

4.2. OIL BASE FLUID

The use of fluid with base oil which contains Automotive, petroleum and mining are to dig in the ground of salt rooms and the possibility of a dissolution of the clay and the Borehole it would, especially in the depths of the most high-temperature effect on clay may be used, these hydrated. so looking for a substitute fluid which does not react with clay and lowest effect on other samples can be used instead of the oil, the water that The lowest hand corrosion formation. One of the other benefits it resistance against salt pollution, chalk and acid gases CO₂ and H₂S can be. Of course, the cost of the above it should also be considered and only in special cases and sensitive use. In addition to the cost of maintenance and the cost of disposal of waste transportation is also high. It is therefore in terms of environmental and pollution that are in use, except for special cases It is not recommended and is prohibited.

4.3. WATER-BASE FLUID

Water-base drilling fluid more broadly than oil and gas. Construction and keeping it comfortable and simply can be low or high additive compounds it. For example, during the excavation until the Borehole in the sand Stone Data on the water before it is completely on the drilling, but in some parts of the limestone that as soon as the water reaches the full face excavation could not be found and in some other parts of the Red reverse in water There are caustic cavities of that with filling by Some clay minerals (Mansouri & Ghadiri & 2012).

5. DRILLING IN ALLUVIUM

For the land in the section of alluvial clay which consists of alluvium and is to be no investment casing up to 20 meters of drilling, but also because of the high risk are advised to be walled pipes or bentonite used. But in the weakening of alluvium, coarse grain zone penalties crushed stone for each meter of drilling requires the casing investment and for each 50 cm and less need to steer the casing in zone and casing be relevant.

5.1. DETERMINE THE PRESSURE DROP IN THE RODS

One of the issues which in drilling It is considered a deep calculation of pressure loss within the steel drilling rod. For this purpose, can be used with the graph of figure (1) the amount of pressure drop calculation for rods (Amoco).

For example:

$$d=19\text{mm}, q=150\text{l/m}, dp =1 \text{ Mpa}$$

$$d=19\text{mm}, q=1.5\text{l/m}, dp =10^{-4} \text{ Mpa}$$

If the diameter of the rods 19 mm for pressure drop on the 150 l/min flow equivalent to 1 MPa in the length of 10 meters and we so rod If Discharge is to reach the pressure drop 1.5 liters per minute for a length of 10 meters from the rods arrives to 0.1 Kpa.

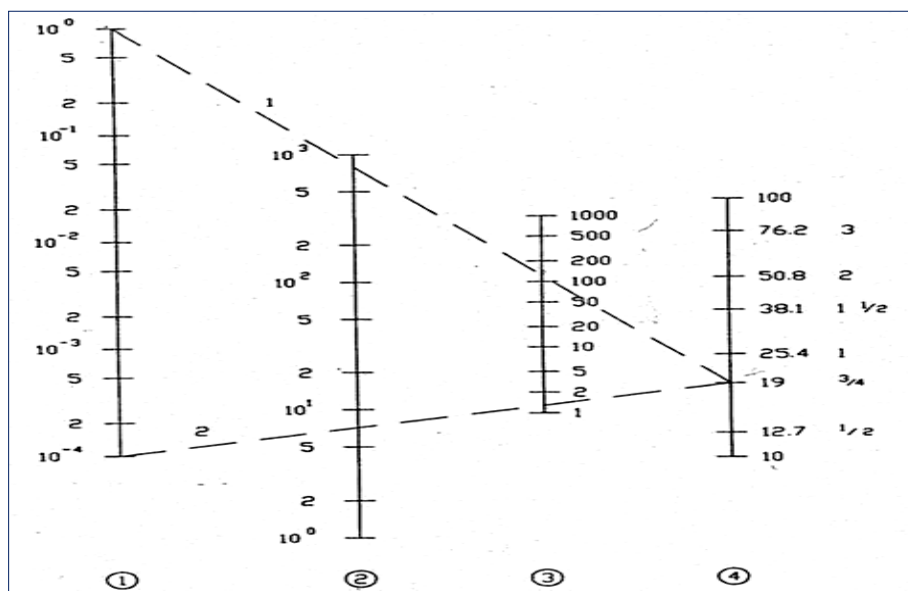


Figure 1: Determine The drop of pressure in rods (Amoco, 1994), (rods of metal and for length 10 m in comments taken made); 1-drop the pressure, dp (in MPa), 2-viscosity stream, v (Cm/S), 3-Discharge, Q (l/min), 4-diameter of pipe, D (mm, in)

6. THE BOREHOLE DEEP ALLUVIAL SYSTEMS:

In some areas the thickness of the layer Of the more than 300 meters of alluvial perhaps time. for drilling on this earth can be the method of casing telescopic investments. The best method of drilling to the total length of the dividing sections of 50 meters. This case up to a depth of 50 meters with two sizes of drilling core samples taken, placed in the sample box and the required tests during the Borehole. Is done Of course, during the excavation to prevent Borehole parapet loss of drilling mud (bentonite + water) or the casing will use investment. If testing of the penetration the use of drilling mud is prohibited and can only be of the casing investments. After completing the 50 meters high and rods all casing from borehole has to continue excavation work out with the initial drilling diameter stabilizer along with drilling mud from the point 0 to 50 yards, where small size is to start and to the end of the Borehole will continue. So it's casing (a casing size) to a depth of 50 meters can be laid, and the Borehole thumbs up is given, the Borehole had to start drilling next 50 meters. This process has any value in coring the depths of the Borehole can be continued.

The role of stabilizer in the prevention of the diversion of Borehole here. it is also to prevent too much rods thong in the depths can be used spacers spacers depreciation in casing Working efficiency, and to prevent the waste of energy in the direction of increased engine power, and to completely pass the boring head. the process of drilling the Borehole of deep alluvial briefly can be divided into several stages:

1. drilling to a depth of 151 possible size (30-40 m), sampling and do the necessary tests and casing.
2. continue drilling to a depth of 50 meters with 127 size, sampling and do the necessary tests and casing Widget
3. send out rods and casing Of Borehole and Borehole within the rim by 151 stabilizers, along with drilling mud to a depth of 50 meters.
4. install the casing to a depth of 50 meters inside the Borehole 146 by tension wire.

5. wash the Borehole and Borehole for preparing drilling 50 meters.
6. continue the process of working with a smaller size, such as the steps one to five and repeat these steps to achieve the desired depth.

7. BOREHOLE MANAGEMENT

Here are the questions before starting to dig the Borehole should be investigated. the answer to this question Can choose the appropriate size and performance management system for solid particles and help us (Growcock, 2005).

- 1-What are the parameters of the well?
- 2- Where do you dig?
- 3-What is the purpose of drilling?
- 4-What formations and geological effects expected?
- 5-well what is a teepee? (Straight, angled, horizontally)?
- 6-What is the foreseeable problems?

As well as the depth of underground water must be drilled in the location of the Borehole.

8. EQUIPMENT NEEDED FOR DRILLING

In addition to the drilling device and injection pump, most major equipment for the start of the drilling operation and the infusion is necessary to be prepared as follows: casing, drill heads, drilling rod, and water pump, dredge pump drilling mud, a strong pressure hose and push the breaker.

9. DISCUSSION AND CONCLUSIONS

At the end of the major issues that has arisen for the drilling operation may come and hole longing and it is necessary that the Geotechnical Engineer is aware of it has been brought to the summary.

9.1. DRILLING ISSUES

- 1-What is the expected final depth?
- 2-Where and what places the necessary investment of casing? (The amount of the required size and how much)
- 3- Do chisel specified parameters? (Borehole size, type of drill, drilling speed, speed penetration)
- 4-What kind of drilling mud used to?
- 5- The amount of solid material density inside the well tolerance how much will it be?
- 6- What is the ratio of a stream is designed?
- 7- What to cutting Borehole of nazel intended?
- 8- What other demands of the flowers is considered? (The weight of the flowers, the point of surrender, stability, viscosity, electric)

9.2. ABILITY TO THE EQUIPMENT

- 1- What kind of particle size Can be shipped?
- 2- What kind of equipment to the location of the cutting Suggested?
- 3- Is this equipment available? Where and who?
- 4- Weight and dimension of this equipment is how much?
- 5- The process of preparation of the equipment can be done how fast?
- 6- What is the efficiency of this equipment cannot be prospect?
- 7- How much drilling mud may be lost (go to waste)? (At ground level or within the well)?
- 8- What is the required fuel or power?
- 9- What are the experiences in this geographical area have already obtained? (The seller or the number of equipment units or branches)
- 10- The duration of a break machines?
- 11- Safety certificate vendors?
- 12- The degree of safety of the equipment, to what extent?
- 13- Safety and health plan is available?
- 14- The volume of what any well required?

12-3-mast design, equipment and its utility

What kind of pillar is selected?

How to install equipment?

Do not install correctly?

What repairs will be needed?

Do the layout and order the correct tanks do?

What does the conversion need to be corrected?

Do I need to add repositories or plumbing is required?

How section (Coupe divider) clean?

Where the mud volcano (mud gun) Take place?

Placement flower suction Volcano?

What is the size of the centrifugal pump which is available?

How to mix sucked and stirred added and check?

For each point of the Borehole for the preparation of the drilling mud on Earth spend time how long?

What are the changes and reforms is needed?

Do you have the desired space for modification and changes in the hands of clay?

What is the source of the force which is available?

9.4. LOGISTICS

1- The location of the project?

2- Building facilities, logistics and warehouse?

3- How many staffing needs?

4- Do they all over the place and need food?

5- The need for protection of the equipment is intended for people who have considered or available?

9.5. ENVIRONMENTAL EFFECTS

1- Do you cutting can be buried in the soil or that they will be empty without being a threat to the environment?

2- What are the functions of contraction for this case there?

3- When cutting they are clean; what decision have?

4- What to test Where should the need for analytical?

5. What period of time is required to determine their cleanliness?

For a special topic and that are:

1-There is a site on the inside or outside of the site?

2. What equipment is needed, which should be added? Where section?

3- What type of fuel and the necessary accommodations?

4-do in terms of climate change there are limitations?

5-What is the necessary permissions?

6-who is responsible to provide them?

9.6. ECONOMIC DIMENSION

1. The value of each barrel drilling mud?

2- Which is more expensive, solid or liquid?

3. To obtain the value and price of the equipment require what should we do?

4. The cost of the installation and what is reform?

5- The value of the prices and availability and how much is being important?

6- How much to save for it is intended?

10. REFERENCES

1. Amoco Production Company, Drilling fluids manual, Rev. 6/94, 444 pages.
2. Bell, F. G. (1983), Fundamentals of engineering geology, Butter Worths, UK.
3. Bell, F. G. (2000), Engineering Properties of Soils and Rocks, Fourth Edition, Black Well Sciences.
4. Duncan C., Wyllie, 2005, Foundations on rock, E & FN Spon, An Imprint of Chapman & Hall
5. Growcock F., Harvey T., (2005) Drilling Fluids Processing Handbook, Elsevier Inc., Chp. 2.
6. Mansouri A., Ghadiri M.,(2012), Important of expolation borehole in estimation of permability of dams foundation, case study, First symposium of Dams & light-water powerhouse, Tehran.
7. Mansouri Amin, (2006), The position of the Soft rocks in engineering classification, The 5th Conference of the engineering geology and the environment, Tehran.
8. Shafai bajestan, Mahmood, (1994)• Sedimentation hydraulic, Shahid Chamran University of Ahvaz.

Back Analysis of Banqiao Clay Core Dam Breaching

Qiming Zhong¹, Shengshui Chen², Shiang Mei³

1- Nanjing Hydraulic Research Institute, Key Laboratory of Failure Mechanism and Safety Control Techniques of Earth-rock Dam of the Ministry of Water Resources, Nanjing 210029, China

2- Nanjing Hydraulic Research Institute, Key Laboratory of Failure Mechanism and Safety Control Techniques of Earth-rock Dam of the Ministry of Water Resources, Nanjing 210029, China

3- Nanjing Hydraulic Research Institute, Nanjing 210029, China

E-mail: qmzhong@nhri.cn

Abstract

In this study, a numerical model is put forward to simulate the Banqiao reservoir dam breaching. Based on the breaching process records, a numerical model is put forward. In this model, two different erosion formulas are utilized to simulate the erosion process of dam shell and core materials, respectively; a mechanical equilibrium equation is adopted to simulate the shear failure of clay core; meanwhile, broad-crested weir formula is adopted to calculate breach flow discharge, the limit equilibrium method is utilized to analyze the stability of breach slope as well. In addition, according to the real situation, the model considers dam base erosion. Based on the surveyed records, the calculated results of the proposed model are in accordance with the measured data.

Keywords: Banqiao reservoir, overtopping, clay core dam, numerical model.

1. INTRODUCTION

Based on the Bulletin of First National Census for Water [1], by the end of 2011, there is 98002 reservoir dams in China; on the contrast, according to the statistical data of Dam Safety Management Center of the Ministry of Water Resources, P. R. China [2], from 1954 to 2014, there have been 3530 dam breach accidents happened in China. According to the statistics, the dam breach accidents of overtopping failure occupy over 50% of the total number. In August 1975, the clay core dam with a height of 24.5 m of Banqiao reservoir was failed due to overtopping flow, the dam breached resulting in catastrophic downstream flooding and over 26000 fatalities [3]. In order to evaluate the consequence of the core dam breaching, the mechanism of clay core dam breach due to overtopping failure requires in-depth research, as well as the mathematical model which can reasonably simulate the breach process.

As we know, for the homogeneous dam overtopping failure, numerous tests of different scales are carried out, an array of numerical models are put forward [4]. When it comes to core dam overtopping failure, owing to the complexity of the model test, only the IMPACT Project [5] and NHRI [6] held a large scale model test of moraine core rockfill dam with a height of 6.0 m and centrifugal model tests of clay core rockfill dam with a height of 16.0 m, respectively (see Figures 1 and 2).



Figure 1. Large scale model test of moraine core rockfill dam due to overtopping failure



Figure 2. Centrifugal model test of clay core rockfill dam due to overtopping failure

The model tests show that the overtopping flow first erodes the downstream dam shell. With the increasing erosion of the downstream dam shell, the downstream side of the core is gradually exposed and hollow. Under the co-action of the upstream water and soil pressures, shear failure occurs in the core. With the decrease of water head, the discharge through the breach gradually fall to zero.

Since 1980s, according to the soil erosion tests, some mathematical model for core dam breaching are put forward. Among these models, NWS BREACH model [7], HR BREACH model [8, 9], DLBreach model [10], and NHRI-CCOB model [6] are the representatives.

It is worth mentioning that the subbase erosion of the dam is not considered in the core dam breaching model tests at home and abroad. Figure 3 shows the final breach of the Banqiao reservoir dam, owing to the erodible base and large reservoir storage and relative small dam height, the base erosion depth is 5.04 m (see Figure 4(a)). Meanwhile, a scour hole which has a depth of 11.0 m is formed downstream, then the hole is filled with reservoir deposit (see Figure 4(b)). In order to simulate the clay core dam breaching process of Banqiao reservoir, a mathematical model is put forward, the technical details are described in the following sections.



Figure 3. Final breach of Banqiao reservoir dam

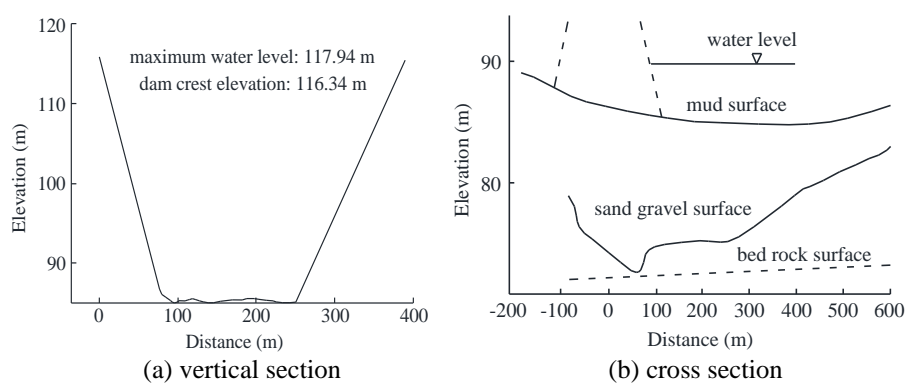


Figure 4. Breach sections of Banqiao reservoir

2. BREACHING PROCESS OF BANQIAO CLAY CORE DAM

Banqiao reservoir has a maximum storage of $4.92 \times 10^8 \text{ m}^3$, and a maximum dam height of 24.5 m as well. The length of the dam is 2020 m, and the crest width is 6 m. The dam crest and the wave wall elevations are 116.34 m and 117.64 m, respectively.

In August 1975, a heavy storm occurs in Henan. When it comes to Banqiao reservoir, there are two inflow process, the first inflow occurs during 14:00 August 5th to 2:00 August 6th, and the peak inflow is $7500 \text{ m}^3/\text{s}$; the second inflow occurs during 12:00 August 7th to 8:00 August 8th, and the peak inflow is $13000 \text{ m}^3/\text{s}$ (see Figure 5).

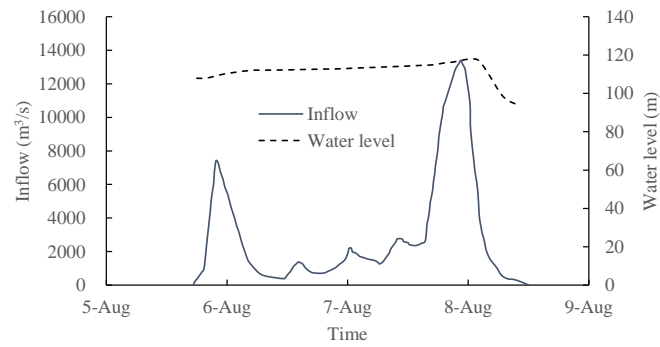


Figure 5. Inflow and water level variation of Banqiao reservoir during “75.8” flood

3. NUMERICAL MODEL FOR BANQIAO CLAY CORE DAM BREACHING PROCESS

In this section, a numerical model is proposed to simulate the breaching process of Banqiao clay core dam. Based on the model tests, the breach mechanism of clay core dam due to overtopping failure is revealed. The breach is divided into two reaches at the early stage before the clay core is exposed (see Figure 6, ①-②). Once the core is exposed, the breach is divided into three reaches (see Figure 6, ③-⑥); then, the clay core may fail due to significant erosion in the lower shoulder reach. After the core failure, the breach is divided into two reaches again (see Figure 6, ⑦-⑨). After the remaining material in the breach is washed out and the non-erodible foundation is exposed, the breach can still widen until the headwater is depleted or the tailwater is raised.

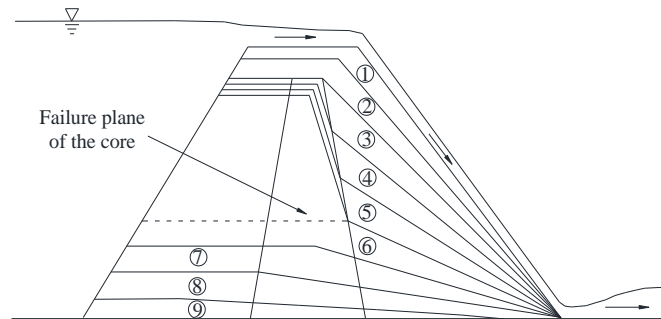


Figure 6. The breaching process of clay core dam due to overtopping failure

Based on the mechanism of dam breach process described above, a numerical model is put forward for clay core dam breach due to overtopping failure. The technical details are described as follows.

The water balance in the reservoir can be described by:

$$\frac{dV}{dt} = A_s \frac{dz_s}{dt} = Q_{in} - Q_b - Q_{spill} - Q_{sluice} \quad (1)$$

Where V =volume of water in the reservoir; t =time; A_s =surface area of reservoir; z_s =water surface elevation; Q_{in} =inflow discharge; Q_b =breach flow; Q_{spill} =flow through spillways; and Q_{sluice} =flow through sluice gates.

The reservoir geometric characteristics are represented by the surface area and water depth curve, $z_s(h)$. The curve is usually given as pair values of surface area and water depth in the reservoir.

The overtopping flow at the breach is estimated using the broad-crested weir equation:

$$Q_b = k_{sm} (c_1 b h^{1.5} + c_2 m h^{2.5}) \quad (2)$$

Where b =bottom width of the breach; $h=z_s-z_b$, z_b =elevation of breach bottom; m =side slope (horizontal/vertical) of the breach; $c_1=1.7$, $c_2=1.3$ [11]; and k_{sm} =submergence correction for tailwater effects on weir outflow. k_{sm} is determined with the empirical relationship [11, 12].

Two erosion formula are utilized to deal with the erosion of dam shell material and clay core material, respectively.

For the dam shell material, it is assumed to be a noncohesive material and the erosion is calculated using the following formula which is put forward based on the steep channel model tests [6]:

$$Q_s = 0.25 \left(\frac{d_{90}}{d_{30}} \right)^{0.2} B_b \sec \theta \frac{v_* (v_b^2 - v_c^2)}{g \left(\frac{\gamma_d}{\gamma_w} - 1 \right)} \quad (3)$$

Where Q_s =erosion volume; d_{90} =particle size for which 90 percent is finer by weight; d_{30} =particle size for which 30 percent is finer by weight; B_b =width of breach bottom; θ =downstream slope angle; v_* =friction velocity; v_b =flow velocity at breach bottom; v_c =incipient velocity of dam material; γ_d = specific gravity of soil, in this paper, it is assumed to be $2.65 \times 9.8 \text{ kN/m}^3$; and γ_w =specific gravity of water, in this paper, it is assumed to be 9.8 kN/m^3 .

The erosion rate of dam shell material can be calculated as follows:

$$(1 - p') \frac{dV_b}{dt} = \frac{dQ_s}{dt} \quad (4)$$

Where p' =porosity of dam shell material; and dV_b/dt =erosion rate of dam shell material.

It is assumed that the breach slope angle is equal to the internal friction angle, the relationship between horizontal expansion and vertical undercutting is determined by (see Figure 7):

$$\Delta b = \frac{n_{loc} \Delta z_b}{\sin \phi_1} \quad (5)$$

Where Δb =horizontal expansion value at each time step; Δz_b =vertical undercutting value at each time step; n_{loc} =indicator of breach location ($n_{loc}=1$ for one-sided breach and 2 for breach located at the middle of dam length); and ϕ_1 =internal friction of dam shell material.

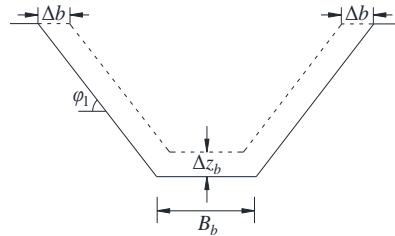


Figure 7. Breach development of dam shell

When it comes to the clay core, the erosion at the breach top flat section is computed using the following excess shear detachment rate relation [13]:

$$\frac{dz}{dt} = k_d (\tau_e - \tau_c) \quad (6)$$

Where dz/dt =erosion rate; k_d =erosion coefficient; τ_e =bed shear stress; and τ_c =critical stress required to initiate detachment for the material determined using Shields diagram.

The coefficient k_d usually needs to be measured [14-16] or utilizes the empirical formula [17]:

$$k_d = \frac{5.66 \gamma_w}{\gamma_d} \exp \left[-0.121 c\%^{0.406} \left(\frac{\gamma_d}{\gamma_w} \right)^{3.1} \right] \quad (7)$$

Where $c\%$ =clay ratio.

The bed shear stress is determined by using the Manning equation:

$$\tau_e = \frac{\rho_w g n^2 Q_b^2}{A^2 R^3} \quad (8)$$

Where ρ_w =water density; A =flow area; R =hydraulic radius. The Manning's n is relate to sediment median size d_{50} (m) by:

$$n = \frac{d_{50}^{\frac{1}{6}}}{A_n} \quad (9)$$

Where A_n is an empirical coefficient. In this model, $A_n=12$ for the field cases [10].

The width change of the breach can be assumed as follows:

$$\Delta b = n_{loc} \Delta z_b \quad (10)$$

With the erosion of dam shell and clay core, the downstream side of the core is gradually exposed and hollow. Under the co-action of the upstream water and soil pressures, shear failure occurs in the core (see Figure 8(a)). The stress state of the failure clay core is shown in Figure 8(b).

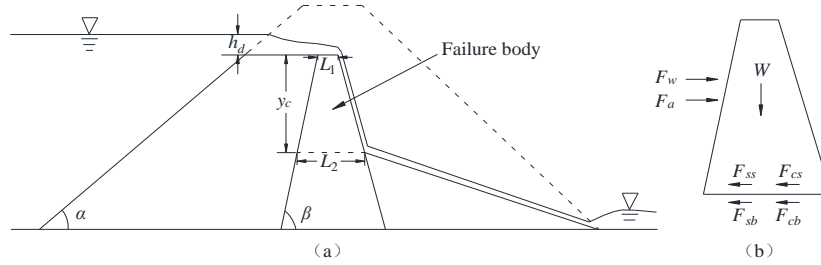


Figure 8. Shear failure of clay core

As shown in Fig. 9, the critical condition of clay core failure can be expressed as:

$$F_a + F_w = F_{sb} + F_{ss} + F_{cb} + F_{cs} \quad (11)$$

In which,

$$F_a = 0.5B_b y_c \left[\gamma_1 y_c \tan^2 \left(45^\circ - \frac{\varphi_1}{2} \right) - 2c_1 \tan \left(45^\circ - \frac{\varphi_1}{2} \right) \right] \quad (12)$$

$$F_w = 0.5\gamma_w B_b (y_c + h_d)^2 \quad (13)$$

$$F_{sb} = W \tan \varphi_2 \quad (14)$$

$$F_{ss} = \gamma_2 y_c^2 K L_2 \tan \varphi_2 \quad (15)$$

$$F_{cb} = C_2 B_b L_2 \quad (16)$$

$$F_{cs} = C_2 y_c (L_1 + L_2) \quad (17)$$

$$B_b = B_t - 2y_c \cot \varphi_1 \quad (18)$$

$$K = \frac{1 - \sin \varphi_2}{1 + \sin \varphi_2} \quad (19)$$

$$L_2 = L_1 + 2y_c \cot \beta \quad (20)$$

$$W = 0.5\gamma_2 (L_1 + L_2) B_b y_c \quad (21)$$

Where F_a =active earth pressure of the dam materials upstream the clay core; F_w =water pressure; F_{sb} =friction along the bottom of failure plane; F_{ss} =friction along the two sides of failure plane; F_{cb} =cohesion along the bottom of failure plane; F_{cs} =cohesion along the two sides of failure plane; h_d =the water head above the dam crest; y_c =the height between dam crest to failure plane of clay core; K =coefficient of static earth pressure; B_t =breach top width; B_b =breach width at the failure plane; L_1 =top width of clay core; L_2 =width of failure palne; W =clay core weight above failure plane; γ_1 =dry specific gravity of dam shell material; γ_2 =dry specific gravity of clay core material; C_1 =cohesion of dam shell material; C_2 =cohesion of clay core material; α =slope angle of dam upstream; β =slope angle of clay core upstream; φ_1 =internal friction angle of dam shell material; φ_2 =internal friction angle of clay core material.

In the case of erodible foundation, the model allows erosion into the foundation. The breach is assumed to have a flat horizontal bottom surface and can lower to a value predefined according to the foundation material properties, but the base erosion does not affect the upstream water volume and downstream channel flow. The breach flow discharge is determined using Eq. (2) with submergence coefficient considered. As erosion continues into the foundation, breach widens laterally until the breaching is finished.

4. CALCULATE RESULTS ANALYSIS

The following section analyzes the results of the breaching process of Banqiao reservoir dam failure using the model above-mentioned. The dam configurations, reservoir characteristics, and soil properties are shown in Table 2. The calculated results of peak breach flow (Q_p), breach top width (B_t), breach bottom width (B_b), time to peak discharge (T_p), failure time (T_f), and measured data (Xu and Zhang 2009; Ru and Niu 2001) are shown respectively in Table 3, Figures 9 and 10 also show the calculated breach flow hydrograph and the breach development of Banqiao reservoir dam.

Table 2- Conditions of Banqiao reservoir dam failure case

Parameter	Value
Dam height (m)	24.5
Dam length (m)	500
Crest width (m)	8
U/S slope (V/H)	0.384
D/S slope (V/H)	0.5
Reservoir storage (m ³)	6.08×10^8
Reservoir surface area (m ²)	A_s-h
Initial reservoir level (m)	26
Inflow (m ³ /s)	Q_{in-t}
Base erosion (m)	-5.04
k_d (cm ³ /N-s)	18
τ_c (Pa)	0.5
Clay core	
Height (m)	23 ^a
Crest width (m)	3 ^a
U/S slope (V/H)	4 ^a
D/S slope (V/H)	4 ^a
d_{50} (mm)	0.03 ^a
p'	0.3
C (kPa)	30 ^a
ϕ (°)	26.6 ^a
Clay ratio	0.4 ^a
d_{90}/d_{30}	10 ^a
Dam shell	
d_{50} (mm)	0.2
p'	0.35
C (kPa)	0
ϕ (°)	20 ^a
d_{90}/d_{30}	20 ^a

Note: U/S=upstream slope=vertical/horizontal, D/S=downstream slope=vertical/horizontal.

^aAssumed value.

Table 3- Results of Banqiao reservoir dam failure case

Calculated results					Measured data				
Q_p (m ³ /s)	B_t (m)	B_b (m)	T_p (h)	T_f (h)	Q_p (m ³ /s)	B_t (m)	B_b (m)	T_p (h)	T_f (h)
77085.1	432.4	286.4	1.72	3.03	78100	372	210	-	5.5

Note: The calculated failure time is defined as the time period from the beginning of dam breaching to the moment when 99% of the final breach width is reached.

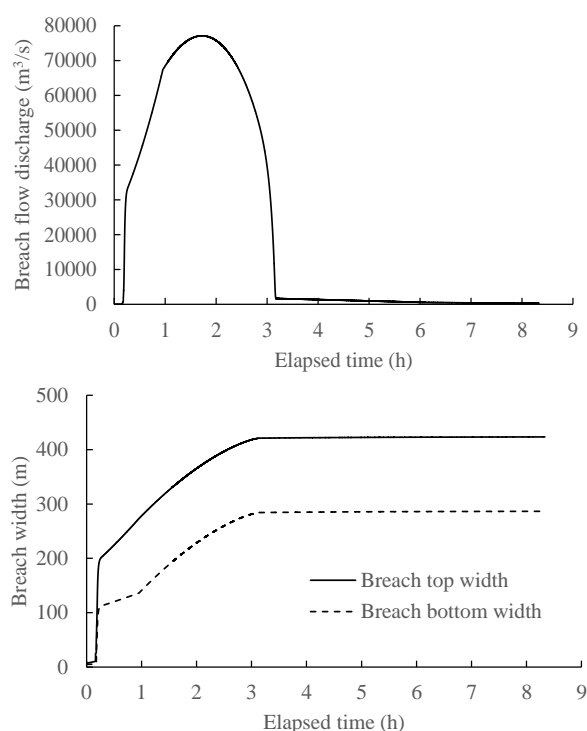


Figure 9. Calculated breach flow discharge Figure 10. Breach width development

Based on the contrast table and the figures, some conclusions can be drawn. According to Figures 9 and 10, owing to the collapse of wave wall, the overflow water head is about 1.5 m above the dam crest, the breach flow discharge increases immediately at the initial breaching period, as well as the top and bottom breach widths; after 1.72 h, the peak discharge occurs, then the breach flow decreases, and the breach width increases relatively small until the end of breaching. According to Table 3, the calculated peak breach flow is 77085.1 m³/s, which is 1.3% smaller than the measured data. To the breach widths, we can see that the breach top width and breach bottom width is 16.2% and 36.4% larger than the measured data, respectively. When it comes to the failure time, the calculated data is 44.9% smaller than the measured one. Overall, the calculated peak discharge is in accordance with the measured data; in contrast, the calculated breach widths are larger than measured data especially the bottom breach width, the possible reason is the drainage of reservoir sediment affects the development of breach; owing to the lacking of measured time to peak, the contrast of this parameter is ignored; with regard to failure time, the definitions of calculated and measured data are different, the documentary record is the duration of whole breaching process, which differs to the calculated failure time. From the above, the numerical model can meet the demands in calculating of Banqiao reservoir dam breaching process.

5. CONCLUSION

A numerical model is proposed to calculate the Banqiao reservoir breaching process in this study considering the erosion of different dam materials and the failure of clay core. Based on the calculated results, the following conclusions can be drawn: The clay core dam can be assumed as a composite dam with noncohesive and cohesive materials; a shear failure formula is adopted to calculate the time and height of failure clay core; for the dam with relatively small dam height and large reservoir storage, base erosion should be considered if the foundation is erodible. Based on the contrast of calculated and measured results, the proposed model can reproduce good results, and can be utilized for the breaching process of clay core dam due to overtopping failure.

6. ACKNOWLEDGMENT

This writers acknowledge the support from the Natural Science Foundation of China (Grant No. 51379129, 51539006) and the Natural Science Foundation of Jiangsu Province (Grant No. BK20161121).

7. REFERENCES

1. Ministry of Water Resources, P. R. China, National Bureau of Statistics, P. R. China. (2013), “*Bulletin of first national census for water*”, China Waterpower Press, China. (in Chinese)
2. Dam Safety Management Center of the Ministry of Water Resources. (2015), “*Dam breach register book of the national reservoirs*”, Dam Safety Management Center of the Ministry of Water Resources, China. (in Chinese)
3. Ru, N. and Niu, Y. (2001), “*Embankment dam · incidents and safety of large dams*”, China Waterpower Press, China. (in Chinese)
4. Chen, S. (2012), “*Breach mechanism and simulation of breach process for earth-rock dams*”, China Waterpower Press, China. (in Chinese)
5. Morris, M. W. (2008), “*IMPACT Project field tests data analysis*”, FLOODsite Rep. T04-08-04, HR Wallingford, UK.
6. Chen, S., Zhong, Q., and Cao, W. (2011), “*Centrifugal model test and numerical simulation of the breaching process of clay core dams due to overtopping*”, *Advances in Water Science*, 22(5), pp 674-679. (in Chinese)
7. Fread, D. L. (1988), “*BREACH: An erosion model for earthen dam failure*”, National Oceanic and Atmospheric Administration, National Weather Service, Silver Spring, USA.
8. Mohamed, A. A. A., Samuels, P. G., Morris, M. W., and Ghataora, G. S. (2002), “*Improving the accuracy of prediction of breach formation through embankment dams and flood embankments*”, *Proc. Int. Conf. on Fluvial Hydraulics (River Flow 2002)*, Louvain-la-Neuve, Belgium.
9. Morris, M. W. (2011), “*Breaching of earth embankments and dams*”, PhD thesis, the Open University, UK.
10. Wu, W. (2013), “*Simplified physically based model of earthen embankment breaching*”, *Journal of Hydraulic Engineering*, 139(8), pp 837-851.
11. Singh, V. P. (1996), “*Dam breach modeling technology*”, Kluwer Academic Publishes, Netherlands.
12. Fread, D. L. (1984), “*DAMBREAK: The NWS dam break flood forecasting model*”, National Oceanic and Atmospheric Administration, National Weather Service, Silver Spring, USA.
13. U.S. Dept. of Agriculture, Natural Resources Conservation Service (USDA-NRCS). (1997), “*Chapter 51: Earth spillway erosion model*”, Part 628 Dams, *National Engineering Handbook*, USA.
14. Briaud, J. L., Ting, F. C. K., Chen, H. C., Cao, Y., Han, S. W., and Kwak, K. W. (2001), “*Erosion function apparatus for scour rate prediction*”, *Journal of Geotechnical and Geoenvironmental Engineering*, 127(2), pp 105-113.
15. Hanson, G. J. and Cook, K. R. (2004), “*Determination of material rate parameters for headcut migration of compacted earthen materials*”. *Proceedings of Dam Safety 2004*, Association of State Dam Safety Officials (ASDSO), Inc. C. D. ROM, USA.
16. Wan, C. F. and Fell, R. (2004), “*Investigation of rate of erosion of soils in embankment dams*”, *Journal of Geotechnical and Geoenvironmental Engineering*, 130(4), pp 373-380.
17. Temple, D. M. and Hanson, G. J. (1994), “*Headcut development in vegetated earth spillways*”, *Applied Engineering in Agriculture*, 10(5), pp 677-682.

Assessment of an Embankment Dam Break Warning System Based on Historical Dam Failures

López, Diana¹, Aufleger, Markus²

1- Unit of Hydraulic Engineering, University of Innsbruck, Austria

2- Unit of Hydraulic Engineering, University of Innsbruck, Austria

Email: Diana.Lopez@uibk.ac.at

Abstract

Embankment dams offer many outstanding benefits to the society, but like any built structure, dams also pose potential risks for people or property, especially in densely populated areas. If a dam fails, it results in most of the cases in a catastrophic event. The negative consequences could entail not only large loss of property (besides the dam), but also loss of lives.

Principal causes of embankment dam failures are overtopping, internal erosion and problems associated with the foundation. A literature review of historical failure events indicates that there are multiple reasons for dam failure (e.g. a large precipitation, a human mistake, an intentionally act, etc.). Furthermore, most of the cases report that dam crest depressions and other signals were observed at an early failure phase. The conventional monitoring measurements could not give reliable information at the failure begin, in case they were available. Hence, in many cases the failure detection at the dam occurred too late, which reduced the time for executing the mitigation plan downstream.

Embankment dam warning systems are often part of large dams and some selected small dams. The investigation of historical failure events (including the reported warning times) showed that there is the need of an improved warning system detecting failures at an early stage. This paper proposes an embankment dam break warning system, which could be based on the distributed temperature and strain sensing technology (DTSS). The proposed concept offers not only a long term monitoring along the dam crest and the location of a problem, but also the possibility of extending the warning time by early failure detection.

Keywords: warning system, dam failure, dam crest.

1. INTRODUCTION

Embankment dam failures occur due to different processes. According to a conducted study [1] of 75 earth and rockfill embankment dam failures from 1979 to 2009, approximately 48% failed by overtopping, 42% by internal erosion and 9% by foundation problems. The number of embankment dams failed due to hostile actions was extremely low (around 1%) compared to the total number of failures, but they could occur instantaneously. Dams are possible targets in case of wars and terrorist attacks, because of their high damage potential [2].

Insufficient spillway capacities, extreme floods that exceed the design criteria, breaching of an upstream dam, quality construction problems around the spillway or the embedded structures are the most common reasons for embankment dam failures due to overtopping and internal erosion. In addition, foundation problems normally occur due to inadequate material selection and treatment, which finally allows an unwanted water flow. In most cases, these processes cause an important deformation or a local leak at the dam crest, followed by a dam crest overflow.

At the beginning or at least in a relatively early stage of a failure process, a damage or a significant deformation at the dam crest is typically visible. If water starts to leak through an initial breach, the failure progress proceeds quickly and a complete failure of the embankment cannot be prevented at all. The flood wave resulting from the breach depends on the interaction of many parameters (e.g. the velocity, the breach form, water supply and reservoir proportions). Commonly, it exceeds by far the magnitude of a flood event and causes catastrophic damages.

The consequences of an extreme event on dams are estimated by using flood wave methods. They assess the effects of a failure on the individuals living downstream as well as for the local infrastructure and sometimes for the environment. For this purpose, the flood wave models assume a hypothetical failure of a dam or suppose breach formation as a start point for the simulation.

The simulation of the flood wave caused by a dam failure is a complex task. Higher flood velocities and water depths (compared to one from an intense precipitation event), as well as uncertainties due the breach formation progress, sediment transport, topography accuracy, bank stability, roughness choice, model selection

or obstacles (e.g. bridge or other structures) make a simulation more difficult [3]. Thus, all these issues affect the results in diverse magnitude.

The flood wave arrival time together with the flood wave propagation (inundated area), water depth and flow velocities are the most relevant results of a simulation and the basis for developing evacuation plans. Typically, the warning time is defined with the time difference between the beginning of the breach development and the occurrence of a critical hydraulic condition (during flood wave propagation) at the downstream areas. Commonly, warning times are in the range of several minutes to a few hours.

2. DAM MONITORING AND WARNING TIME

2.1. EXPERIENCES FROM DAM FAILURES

The structural behavior of an embankment dam is generally monitored depending on the size and type-specific requirements of the structure. The monitoring of large embankment dams often includes the measurement of reservoir level, seepage flow, pore-water pressure, and deformations. Moreover, some of the related measuring systems include in many cases a relatively high number of measuring points, are automatized and provide a remote data transfer. An additional part of the monitoring plan includes frequent visual inspections of the whole dam including abutments, shoulders and the embankment crest. At other structures (e.g. control rooms and appurtenant structures), also facilities such as security cameras or access sensors are often available. As a result, the probability of observing an extreme situation at this type of embankment dams [4] is much higher compared with less monitored embankment dams.

General specifications for small embankments involve less measuring systems, less frequent data recording, and fewer measuring points. Only few structures have automatic data collection and remote data transfer [1]. In addition, seepage monitoring is not always an implicitness. Therefore, a reliable detection of an extreme situation in such cases could be problematic.

Warning times resulting from simulations usually assume an immediate detection of the start of the breaching process at the dam and an instantaneous alarm. To ensure the efficacy of the emergency action plans, real warning times should not fall below them significantly. In this context, the strong dependence between the reliable recognition of a critical condition at the dam (aid monitoring and surveillance equipment) and real warning time is evident.

However, not all embankment dams are monitored with the same frequency and measuring equipment. Often large dams are well monitored. They have generally not only more equipment, but also more measuring points, recurrent data collection, remote data transfer, etc. Hence, most probably an extreme situation could be detected earlier than at small dams. It can therefore be assumed that in general warning times at large embankment dams are longer.

19 documented embankment dam failures at the USA [5] shows that real warning times were extremely short and in most of the cases (84%) an alarm activation was just given after the complete failure (warning time = 0). According to the definition of the International Commission on Large Dams (ICOLD) for dam classification, 68% of affected embankment dams were small and in all of them the warning time was zero. Furthermore, warning times longer than 1 hour were only available at 50% of the large one.

2.2. SITUATIONAL WARNING TIME

The warning time is considered situational due to the close relationship with the monitoring plan, the detection of a problem at the embankment dam and the alarm activation downstream. This definition will be reviewed in this work using three potential situations shown in Figure 1. On top a well-monitored embankment dam (i.e. continuous seepage measurement with remote data transfer), in the middle one equipped with fewer elements (only reservoir level measuring with remote data transfer) and at the bottom the worst case, an embankment dam with no monitoring at all, are displayed.

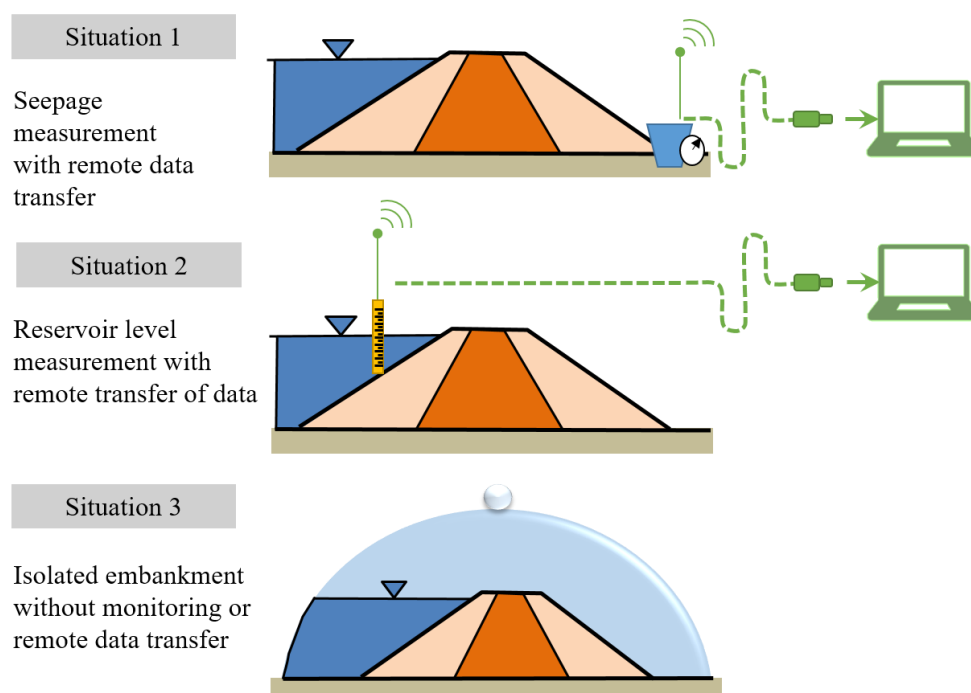


Figure 1: Embankment dam with three different monitoring plans

Figure 2 shows the cross-section from an embankment dam along the flood path to a residential area downstream. Furthermore, two gauges at different locations, one at the embankment dam and another at the residential area downstream, are marked in blue and green [4].

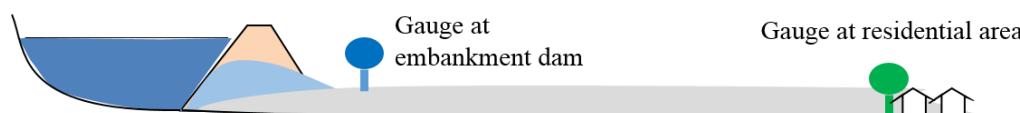


Figure 2: Cross-section with gauges and flood waves [4]

Figure 3 shows the situational warning times, the failure progress and the hydrographs at the gauging stations defined in Figure 2 for the three monitoring situations defined at Figure 1. Here a typical internal erosion process is shown also starting with the formation of an erosion tube that then expands until it collapses and the embankment dam breaches.

The first monitoring situation leads to a fast observation of seepage flow rise. Consequently, the occurrence of internal erosion is detected at a very early stage and the warning time is relatively long. The second situation represents an embankment dam with a water level monitoring with remote data transfer. It is supposed, that there are alarm values activated that allow the identification of unusual fast drops of the reservoir water level. In this case, the internal erosion detection happens at a later time (after the breach initiation and the start of an uncontrolled outflow from the reservoir) and the warning time is shorter compared to situation 1. The efficiency of an evacuation plan is reduced significantly compared with the first monitoring situation.

The third situation represents the worst case without any remote data transfer. The alarm will be activated after the whole breach, when the flood wave hits the residential area. Thus, the warning time at the residential area is missing, the mitigation plan could not be implemented and the negative repercussions downstream are most catastrophic than by the other situations.

The above considerations do assume that the development of the internal erosion process could not be detected within the scope of the regular dam surveillance procedures (e.g. visual inspection). Thus, in a certain way this comparison has to be considered as a schematic approach in order to present the fundamental relationships in a simple way.

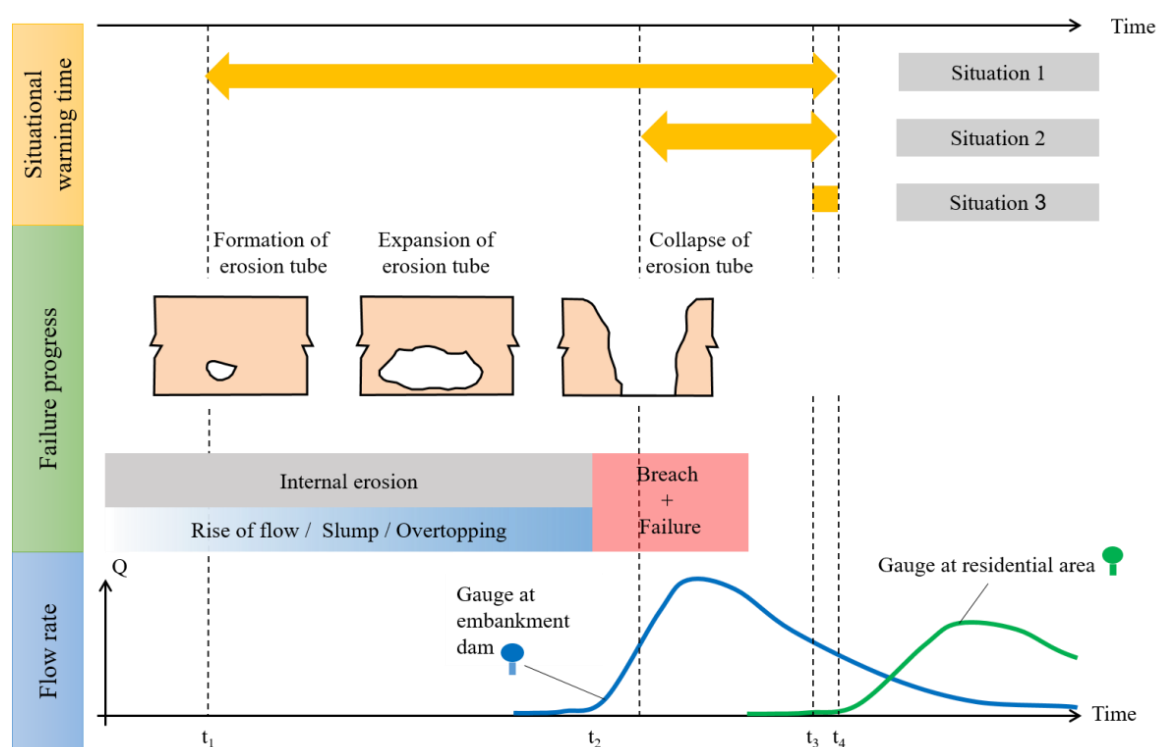


Figure 3: Cross-section with gauges and flood waves

2.3. CURRENT WARNING SYSTEM

There are a number of different systems for warning of an imminent dam failure. These include video surveillance (e.g. closed-circuit television), strong motion digital accelerometer and geotechnical instrumentation with automated data acquisition [6].

Methods such as close-circuit television (CCTV) can be particularly useful where defects below water level or in inaccessible areas are suspected and an inspection is required without lowering the water levels [7]. However, these systems require site personnel to point out an anomaly.

Strong motion digital accelerometers are special required in earthquakes susceptible areas. They range from seismic alarm devices to digital accelerographs installed in the foundation. The high installation and maintaining costs make this system no reachable for all structures. Furthermore, some experts consider it only in some cases meaningful, because of the low probability of obtaining significant data. [8].

3. THE DAM CREST IN EXTREME SITUATIONS AND THE PROPOSED WARNING SYSTEM

The dam crest is a suitable indicator of the dam condition in extreme events. Particularly high water levels in impoundment (e.g. due to unexpected extreme inflow or severe problems at appurtenant structures) cause higher shear stresses which bring erosion forward. The following overtopping performance depends essentially on the embankment fill type [9]. Even after a shorter or longer time period, along with the formation of an initial breach, deformations may be registered in the dam crest.

A similar performance could be observed in cases of embankment dam failures due to internal erosion. Failures due to this mechanism involve a long process and their detection is normally very difficult. For instance, after the formation of an erosion tube, the process of the following expansion of the tube could conclude in diverse scenarios [10]. The most frequent scenario covers deformations and/or sinkholes which could be observed during the breach formation and before the overtopping of the embankment. The occurrence of a cavity which crosses the body of the embankment dam with a subsequent reservoir emptying is a less frequent scenario.

According to the previously mentioned embankment failure study, in all failure cases due overtopping and in around 84% of the failures due internal erosion, a clear change or a relevant deformation of the dam crest was evident in an early phase of the failure development -usually at the start or before of the breach formation-. Therefore, the observation of these deformations could not only extend the warning time in several cases but also

give further information about the breach development (e.g. the location and the approximate size of the anomalies respectively the significant deformations).

In conclusion, as soon as a noticeable damage at the embankment crest is identified, a major risk for the dam structure could be assumed. So, a reliable and early recognition of a problem by means of an embankment dam break warning system contributes to improve the management of the remaining risk and consequently to enhance the safety of the people living downstream.

Currently, it seems that there is no warning system for monitoring the entire embankment crest internally and permanently under operation. Therefore, this work proposes a cable-based warning system installed at the embankment dam crest.

Distributed fibre optic measurements along cables offer the option of measuring temperature and strain as a continuous profile along a single optical fibre. In other words, the distributed temperature and strain sensing (DTSS) permits monitoring of deformations lengthways the entire fibre optic cable. Compared to conventional sensing techniques, this distinctive feature made this technology interesting for monitoring of large structures such as dams, tunnels or bridges. Indeed, a remarkable advantage of this sensing system in internal parts of dams is the detection and localization of differential deformations where a single point, geodetic or visual monitoring methods are not feasible [11]. The use of cable - based systems is well known through the successful application in civil engineering [12], [11], [13], [14], [15], [16]. However, for the purpose to use this technology as an operative and reliable dam failure warning system, several adjustments are necessary and discussed in the following.

The monitoring of the dam crest integrity as an indicator of the probable condition of the embankment dam using a cable – based system for early detection of a dam failure could contribute to an increasing of the safety level of an embankment dam in extreme situations. Basically, the warning system consists of a DTSS sensor cable that is installed lengthwise in the embankment crest within the dam structure and of a measuring system which is located at a convenient and safe position [4] (see Figure 4). For this purpose, a high accuracy of the temperature and strain sensing system is not required. However, it has to be able to confirm the dam integrity through its permanent functioning (i.e. by means of continuously recurrent measurements). In addition, in the case of a significant structural change at any point of the embankment crest, the warning system has to provide an immediate detection of the position and depending on the possibility, the approximated magnitude. Then, the collected information has to be automatically and directly sent to the responsible person (e.g. operator or safety responsible person). Other requirements associated with the system and its effectiveness in several structures are great robustness, low maintenance efforts and reasonable installation costs. The idea is to implement this safety measure in newly built embankments (large and small embankment dams), but also in existing structures with a reasonable effort.

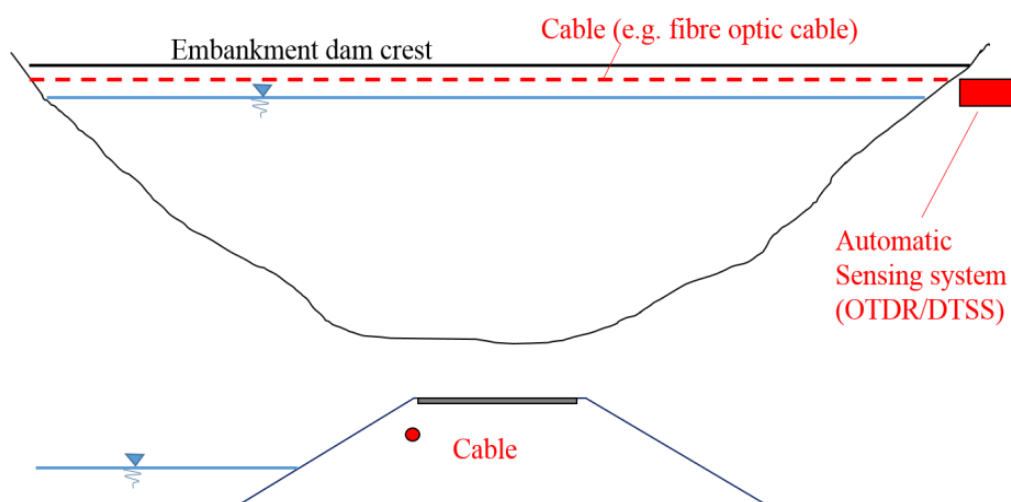


Figure 4: Cable based warning system [4]

4. CONCLUSIONS

Failure mechanism such as overtopping and internal erosion are the cause of approximately 90% of the registered embankment dam failure cases. The residual 10% of failures are attributed to problems in the foundation and sabotage actions. Despite, the continuous improvement of the construction of embankment dams,

a remaining risk of a dam failure is present. The development of dam break warning systems, which handle these outstanding threats is recommended. Furthermore, the systems should be applicable and financially reachable for small and large embankment dam projects.

Based on the analysis of the historical dam failure cases, the embankment crest could be considered as a consistent indicator of the dam structural behavior – especially during extreme situations. A suitable cable based sensing system located longitudinal in the embankment dam crest in a shallow installation depth could contribute to enhancing the dam safety (people, infrastructure and environment).

5. OUTLOOK

Although cable - based dam warning systems installed at the dam crest could provide important data about the breach formation and its development, essential issues such as the system efficacy, the scope of application, and the detailed description of the installation require further research.

Physical models and numerical simulations are suitable for studying the possible scenarios of a dam failure. A combination of both simulation methods could contribute in different ways to a further development of the cable based warning system. A physical model can provide significant information about the installation (system set-up) and the efficiency in diverse materials. In addition, the numerical simulation could investigate dam failure scenarios, and therefore, improve the data about the scope of application.

6. REFERENCES

1. López, D. (2016), “*The integrity of the dam crest as indicator of the structural behavior of an embankment dam in extreme situations*”, Master Thesis, University of Innsbruck, Faculty of Engineering Science, Unit of Hydraulic Engineering, Innsbruck, Austria. (in german).
2. Wieland, M., and Mueller, R. (2009), “*Dam safety, emergency action plans and water alarm systems*”, International water power & dam construction, **61** (1), pp.34–38.
3. DWA (2017), “*Stauanlagensicherheit und Folgen bei der Überschreitung der Bemessungsannahmen nach DIN 19700*”, Merkblatt, DWA Deutsche Vereinigung für Wasserwirtschaft, Abwasser und Abfall e.V., Hennef, Germany.
4. Aufleger, M. and López, D. (2016), “*Die Dammkrone als Indikator für die Talsperrensicherheit in Extremsituationen*”. Wasserwirtschaft, **6**, pp. 136-139.
5. U.S. Department of Homeland Security. (2011) “*Dams Sector - Estimating Loss of Life for Dam Failures Scenarios*”, Washington, USA.
6. <http://www.damsmart.com/portfolio/tuttle-creek-dam-failure-warning-system/>
7. British Dam Society and Environmental Agency (2011), “*Delivering benefits through evidence. Modes of dam failure and monitoring and measuring techniques*”, Bristol, England.
8. Erdik, M. Ö., Çelebi, M., Mihailov, V., and Apaydin, N. (2012). “*Strong motion instrumentation for civil engineering structures*”, 373, Springer Science & Business Media.
9. Powledge, G. R., Ralston, D. C., Miller, P., Chen, Y. H., Clopper, P. E., and Temple, D. M. (1989), “*Mechanics of overflow erosion on embankments. II: Hydraulic and design considerations*”, Journal of Hydraulic Engineering, **115** (8), pp. 1056-1075.
10. Huber, N. P. (2008), “*Probabilistische Modellierung von Versagensprozessen bei Staudämmen*”, Rheinisch- Westfälischen Technischen Hochschule Aachen, Lehrstuhl und Institut für Wasserbau und Wasserwirtschaft, Aachen.
11. Goltz, M. (2012) “*A Contribution to Monitoring of Embankment Dams by Means of Distributed Fibre Optic Measurements*”, Doctoral Thesis, University of Innsbruck, Faculty of Engineering Science, Unit of Hydraulic Engineering, Innsbruck, Austria.
12. Aufleger, M.; Conrad, M.; Perzlmaier, S.; Porras, P. (2005), “*Improving a fibre optics tool for monitoring leakage*”, HRW Hydro Review Worldwide, **13** (4), pp. 18 – 23.

13. Höpffner, R. (2008), “*Distributed Fiber Optic Strain Sensing in Hydraulic Concrete and Earth Structures*”, Berichte des Lehrstuhls und der Versuchsanstalt für Wasserbau und Wasserwirtschaft, Technische Universität München, Wasserbau und Wasserwirtschaft, 121, München.
14. Iten M. (2011), “*Novel Applications of Distributed Fiber-Optic Sensing in Geotechnical Engineering*”, ETH Zürich, Institute of Geotechnical Engineering, Zürich.
15. Iten, M., Ravet, F., Niklès, M., Facchini, M., Hertig, T. H., Hauswirth, D., and Puzrin, A. (2009). Soil-embedded fiber optic strain sensors for detection of differential soil displacements. *Proc. of 4th International Conference on Structural Health Monitoring on Intelligent Infrastructure (SHMII-4)*, pp. 22-24, Zürich.
16. Johansson S., Watley D (2007), “*Dam Safety- Experiences from Distributed Strain Measurements in Five Embankment Dams*”, Stockholm.

Performance and Safety Assessment of Seven Storage Dams in Khuzestan Province, Iran

Reza Esmaili¹, Morteza Rayati², Seyed Mehdi Hosseini Tehrani³, Yaghoub Arab⁴

1- PhD in Hydraulic Engineering, Tarbiat Modares University, and Project Engineer, Zistab Consulting Engineers, Tehran, Iran

2- Project Engineer, Zistab Consulting Engineers, Tehran, Iran

3- Project Manager, Zistab Consulting Engineers, Tehran, Iran

4- Director of the Operation and Monitoring of Dams Office, Khuzestan Water & Power Authority, Khuzestan, Iran

Email: reza.esmailli@gmail.com

Abstract

This study attempted to monitor the performance and assess the safety of seven storage dams in Khuzestan province, including Karkheh, Masjed Soleiman, Marun, Jarreh, Shahid Abbaspour, Dez and Karun. Moreover, a GIS database was developed for the dams to assess the structural and non-structural damages, while creating access to a wide range of descriptive information, relevant maps, guidelines and reports concerning damages and rehabilitation plans provided based on two different information levels. The level-one GIS database displays the geographical location of each dam along with layers such as rivers, cities and access roads. The level-two GIS database displays the components of each dam separately on their general plan and also provides information regarding each dam component through Identify. According to previous studies, it can be concluded that the methodology adopted in the current study is applicable to other dams to ensure proper performance and safety expected by project designers and operators.

Keywords: Performance and Safety Assessment, Storage dam, GIS Database.

1. INTRODUCTION

Nowadays, one of the major challenges in the dam construction industry is the poor consistency between modern requirements and functional characteristics of many existing dams. In practice, many dams have lost their capability to fulfill the water and energy generation requirements for various reasons. These include managerial and executive factors, which leads to failure of realization of the project objectives in the design and implementation of dams. There are several factors contributing to that trend, including failure to finance essential and timely credits, weaknesses in design and implementation, insufficient well-documented statistical information about the design of dams, utilization of inappropriate equipment, inferior construction materials and the ever-growing population. By identifying the damage factors and providing desirable solutions, it is possible to achieve the previous (or even higher) structural performance and safety at lower costs. Undoubtedly, this is not possible without proper recognition of the type of damage and its causes.

Performance monitoring and safety assessment of dams aims to ensure the acceptability of the safety and performance of dams in accordance with the expectations of designers and owners. The results will form the most important record on which performance reviews will be based [1].

In recent years, the modern technology of Geographical Information System (GIS) has initiated many developments in design, management and operation [2]. Effective planning and decision-making require access to accurate and up-to-date information. In order to adopt a concentrate data management, it is critical to import all available information into a GIS database [3].

The advantages of information integration include:

- Facilitated use of information in computers
- Facilitated integration of information
- Accelerated information updating in the integrated GIS

GIS-based projects are capable of handling a large amount of different information at minimal cost and in the shortest possible time, providing reliable forecasts for experts and users. GIS is capable of producing a variety of maps at different scales and in different image systems with a variety of colors. Also it is an analytical

tool for spatial information. The most important advantage of GIS lies in its ability to identify the spatial relationships between various geographical features on the map [3].

GIS is not merely a means of storing and maintaining a map (recording of cartographic documents), but also provides a tool to store information for specific purposes. GIS links spatial data with geographical data of a particular phenomenon on the map, while data are stored in the form of geographic features in the computer.

This study attempted to monitor the performance and assess the safety of seven storage dams in Khuzestan, including Karkheh, Masjed Soleiman, Marun, Jarreh, Shahid Abbaspour, Dez and Karun 3. At the end, a GIS database was developed for the seven Iranian dams to assess the structural and non-structural damages, while creating access to a wide range of descriptive information, relevant maps, guidelines and reports concerning damages and rehabilitation plans provided.

2. METHODOLOGY

This study was carried out on 7 storage dams in Khuzestan (Iran), including Karkheh dam over Karkheh River, Masjed Soleiman (Godar Landar) dam over Karun River, Marun dam over Marun River, Jarreh dam over Yellow River, Shahid Abbaspour (Karun 1) dam, Dez and Karun 3 dams over Karun River (Figure 1).



Figure 1- Location of storage dams

The mechanism of dealing with identified damages to the dams and providing rehabilitation plans was determined according to Table (1). Furthermore, the damages were classified into five categories based on type, severity and weakness (Table 2), while prioritizing rehabilitation studies based on severity of damages separately. This study involved the following stages:

1. Identification and investigation of damages found in dams and appurtenant facilities.
2. Identification of cause(s) of damage to predict and prevent factors leading to exacerbation of damage. It also serves to find appropriate and effective solutions to repairing and rehabilitating of the damage.
3. Overall examination of rehabilitation plans for damages or describing services for more in-depth investigation of damages and proposing comprehensive plans for rehabilitation of damages.
4. Providing appropriate solutions and procedures for improving performance and safety of dams.
5. Realizing timely essential measures to prevent or minimize any possible damages to downstream buildings and facilities surrounding the dams.

6. Compiling a GIS database where information about dams and associated facilities are accessible and new data can be added or removed.
7. Examining the quantity and quality of manpower in exploitation of storage dams and providing the employer with necessary advice in those areas.

Table 1- The mechanism of dealing with identified damages to the dams and providing rehabilitation plans [3]

Type I damages	Collecting the previous plans, reviewing and completing plans and estimating the executive operations
Type II damages	Carrying out essential studies and presenting preliminary plans to identify and estimate the project overall costs.
Type III damages	A general assessment of damages and their effects, description of services and estimation of research plans
Type IV damages	Reviewing the current instructions for operation and maintenance, completion and refinement, if necessary

Table 2- Prioritizing damages to dams and providing rehabilitation plans [3]

Priority I	Very severe damages with highly destructive aftereffects
Priority II	Severe damages with moderate destructive aftereffects
Priority III	Moderate damage with weak destructive aftereffects
Priority IV	Low damage with very weak destructive aftereffects
Priority V	Very low damage without destructive aftereffects or with long-term destructive aftereffects

In the first step, the initial information and existing records were collected by holding several meetings with the project employer, executive and stability managers of the dam as well as their proficient experts. The primarily identified damages (structural and non-structural) were listed along with their respective approach to dealing with, significance, future effects and priority. Then, the information and records about damages were requested from the employer, who made available a portion of information. The information included case reports and behavior studies, maps, published guidelines and a few photos related to dam damages and associated structures.

The next step consists of two sections of initial and specialized visits to the dam sites. In the initial visits, after negotiating and discussing issues with the employer, the details of damages to dam components and related facilities were explored. Then, any information inadequacy was resolved by the employer. Meanwhile a part of GIS database was prepared. Afterwards, the expert team did specialized visits to the dam and related structures including the body, abutment, instrumentation, hydromechanical equipment, access roads and dam site. With regard to the primarily identified damages, the expert team members included the specialty of structural, geological, geotechnical and hydraulic. After reviewing the results of visits, additional information was requested from the employer concerning the damage type and severity. The final list and location plan of damages were compiled for each dam.

At the last step, the GIS database of Khuzestan dam was developed to investigate structural and nonstructural damages, while creating access to a wide range of descriptive and spatial information. In addition to providing damage-related reports and rehabilitation plans, the database can easily load information in case an appropriate structure is developed for a web-based system. The key feature in the new GIS database is the dual information levels, each offering different capabilities separately. This database can also be loaded across intraorganizational networks in order to easily gain access to all available information with different levels of access. The new GIS system can update information in all subsequent periods, which provides access to latest information revised at any time interval.

During compilation of this GIS database, it is crucial to design an appropriate structure for implementation. In this regard, two information access levels were developed through data models representing the structure of each level. These data models provided the basis for creating a database at each level.

Furthermore, a suitable structure was developed for storing and encoding additional information concerning each layer. For instance, Figures 2 and 3 display the level-one database structure of Khuzestan dams and level-two database of Karun 3.

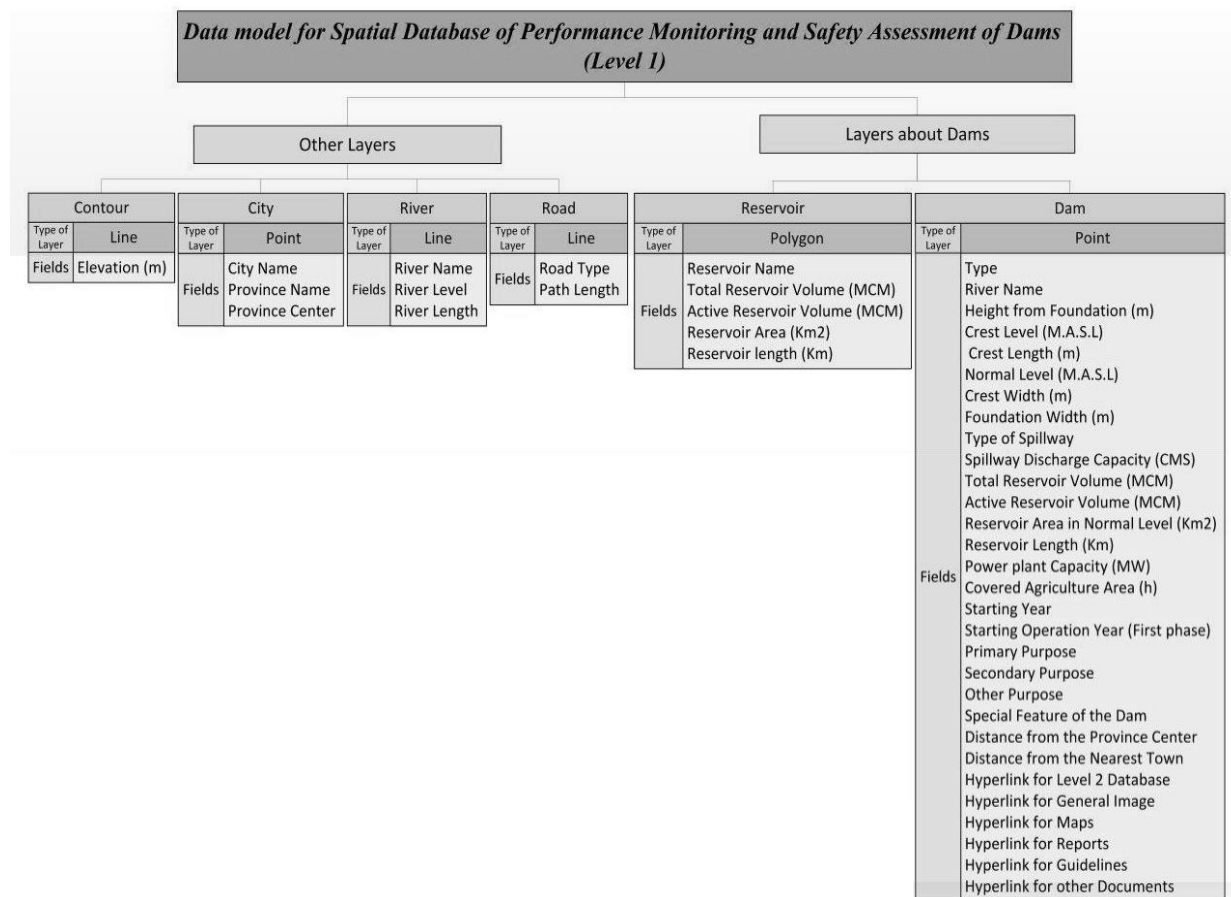


Figure 2- GIS data model (Level 1) [3]

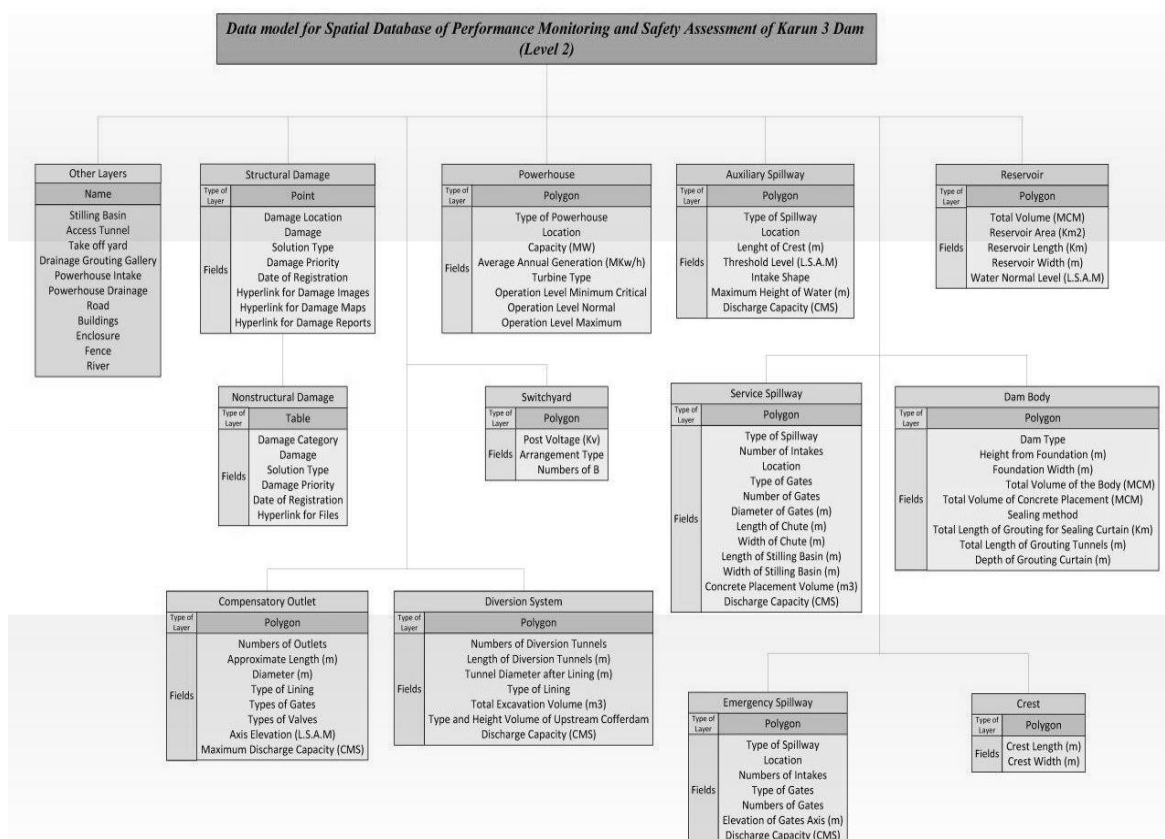


Figure 3- GIS data model (Level 2) - Karun 3 Dam [3]

Prepared on a provincial scale, the level-one GIS database displays the geographical location of each dams along with layers such as rivers, cities and access roads. This level also includes technical and general information about each dam, while all other layers provide descriptive information. In addition to displaying descriptive data of dams, the system provides access to all classified maps, relevant reports, guidelines, and other documents. It is also possible to update all information in every section. In addition, access roads to each dam from Khuzestan central city and nearest cities have been marked down. Figure 4 displays an overview of levelone database along with available access levels to each section.

The level-two GIS database displays the components of each dam separately from a plan perspective. This level also provides information regarding each dam component through Identify. The precise locations of structural damages have been located at this level. In addition to displaying the precise coordinates of each damage through access links, this level provides access to photos of each damage, maps drawn from various related sections, previously prepared damage detection reports and damage detection reports. The remarkable point about the new GIS database lies in accessibility between the two levels. In fact, users can select an option to gain access to level-two database of each dam. The communication process takes place automatically as the user switches between the two information levels. It is necessary to note that all access levels and links have been established according to structures described above. Hence, the database is absolutely dynamic, enabling users to update all information at any stage and add new information. Figure 5 illustrates the level-two database for Masjed Soleiman Dam together with accessible information.

3. RESULTS

The frequency of each damage identified in the dams has been provided by priority (Table 2) as well as the location of each damage in Figures 6a and 6b. As shown in Figure 6a, the frequency of moderate damages with 6 poor destructive aftereffects, low damages with very weak destructive aftereffects and severe damages with moderate destructive aftereffects were more abundant than other types of damages.

employ floating docks as a rehabilitation plan in dam lakes given the prevailing conditions such as high depth, water level fluctuations and location limitations. One advantage of this system is the communication from one dam point to another or even from one dam to another.

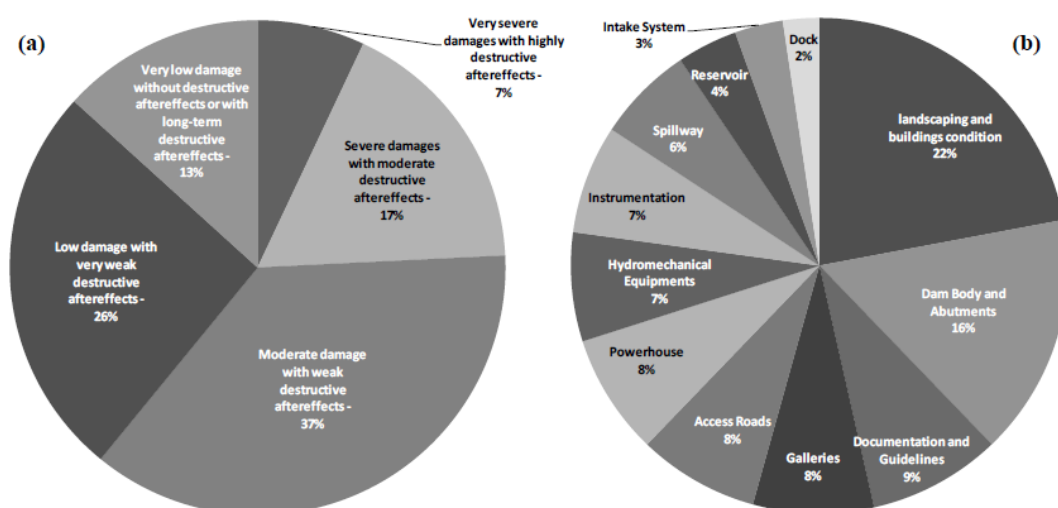


Figure 6- Damages in 7 storage dams in Khuzestan Province by: (a) priority of damages, (b) location of damages.

This type of damage also covers the failure to carry out landscaping and poor condition of buildings in charge of dam operation and maintenance. In this regard, a comprehensive description of services was provided to design dam site plans according to environmental requirements and essential access levels as well as distribution of dam operation and maintenance at different dimensions. This served to develop uniform studies on all dams through integration of spaces required for dam operation and maintenance.

One example of severe damage with moderate destructive aftereffects was instability of excavation rocks and trenches. Collapse in the vicinity of rock mass fractures is the major cause of instability observed in the dam area. Considering the suitable location of the dam with regard to instability potential associated with rock mass discontinuities, the instability near the reservoir does not significantly affect the dam and related structures.

However, it is critical to control debris flows on higher horizons in an effort to prevent damage to related facilities and structures. This partly concerns poorly developed anti-collapse protectors during the dam implementation.

As can be seen in Figure 6b, it can be stated that three major damages observed in dams involved landscaping, body and abutment as well as inadequacy of documents and operating/maintenance instructions.

4. CONCLUSIONS

This study aimed to assess the performance and safety of seven storage dams in Khuzestan (Iran) including Karkheh, Masjed Soleiman, Marun, Jereh, Shahid Abbaspour, Dez and Karun 3 dams. Several specialized field visits were completed and statistical data and behavioral reports were collected to monitor the performance of the dams and assess their safety. Then, the approach to dealing with identified damages to dams was clarified based on type, severity and weakness, while prioritizing rehabilitation studies based on severity of damages separately.

Then, a rehabilitation plan was provided for each identified damage. At the last step, the GIS database of Khuzestan dams was developed to investigate structural and non-structural damages, while creating access to a wide range of descriptive and spatial information. In addition to providing damage-related reports and rehabilitation plans, it is possible to load information easily if a proper structure is created to provide a web-based system.

It can be concluded that the frequency of moderate damages with poor destructive aftereffects, low damages with very weak destructive aftereffects and severe damages with moderate destructive aftereffects were more abundant than other types of damages. Finally, it can be stated that the methodology adopted in the current study is applicable to other dams to ensure proper performance and safety expected by project designers and owners.

5. ACKNOWLEDGMENT

This research was supported by Khuzestan Water & Power Authority, Khuzestan, Iran.

6. REFERENCES

1. “*Dam Safety Guidelines, Guidelines for Construction, Maintenance and Monitoring*,” Auckland Regional Council (2000).
2. Foote, K. E., Lynch, M. (2015) "*Geographic Information Systems as an Integrating Technology: Context, Concepts, and Definitions*", The Geographer's Craft Project, Department of Geography, The University of Colorado at Boulder.
3. “*Safety Assessment of Dams in Khuzestan Province*”, Zistab Consulting Engineers, Technical Report (2016), (in Persian).

Numerical Study on the Effect of Grout Properties On the Results of Borehole Extensometers in Earth Dams

Afshin Gholinia¹, Majid Nikkhah², Reza Naderi³

1- Msc student, Faculty of mining, petroleum and geophysics, Shahrood University of Technology

2- Assistant Professor, Faculty of mining, petroleum and geophysics, Shahrood University of Technology

3- Associate Professor, Faculty of civil engineering, Shahrood University of Technology

Email: Afshin.Gholinia@shahroodut.ac.ir

Abstract

Measurements of surface and deep soil displacements are among the best approaches for monitoring and controlling the behavior of geotechnical structures such as dams, which can be conducted by using magnetic borehole extensometers. This type of instrumentation is installed into the boreholes and the space inside the borehole is filled with a mixture of Bentonite-cement grout. Studies have shown that the mechanism of borehole extensometer measurement, the effect of the mixing design of Bentonite-cement grout to fill the gap between the borehole and the extensometer and the effect of grout properties on the measurement have not been carefully studied. In this paper, a number of laboratory tests with different grout mixing designs were performed to determine mechanical properties and geo-mechanical parameters for numerical analysis. The results of numerical analysis show that compressive strength and hardness of the sample of grout will decrease as Bentonite to cement ratio increases. Furthermore, as the hardness of the grout and soil converge, the measurement error will decrease accordingly.

Keywords: Instrumentation, Magnetic extensometer, Bentonite-Cement Mixing, Numerical Modeling.

1. INTRODUCTION

Due to the uncertainty in assumptions of the design process, problems and constraints of the construction of dams, it seems necessary to pay closer attention to the assessment of the behavior of the dams and to study the results of the analysis of the actual behavior of the dam from the start of construction to the impoundment and within the operation period.

Engineering monitoring in geotechnical projects are part of the design process. Instrumentation is a way to control the stability of structures during the time of construction and operation. [1].

One of the important steps during installation of extensometers, is filling the gap between tube and borehole internal wall. The filling material is in direct contact with rock and instrument and thus can have significant impact on the accuracy of the measurements. If the filling material does not have the proper features it will not be able to provide the proper contact and thus the stability between the extensometer tube and borehole wall will be compromised. Materials commonly used to fill the gaps include cement, granular materials such as sand and Bentonite pallets. Experience has shown that cement - Bentonite grout is the best option for a filler material in the borehole and has been widely used in many applications. In cases where grout stiffness reduction is required, fly ash can be used instead of cement [2].

The ideal type of grout should be consistent with the ground stiffness. A weaker blend of the grout does not reflect the behavior of the surrounding soil, even if the grout is properly injected into the borehole. Also, a stronger mixture may exhibit a behavior which is independent of the surrounding ground. [3]

Burland et al (1972) described the grout around access tube of the magnetic extensometer as a soft flexible material that could prevent the collapse of borehole. Also, in order to inject in soft ground after installing extensometers a thick Bentonite grout was suggested [4]. Sonebi et al (2012) performed experiments on properties of Bentonite grout for geotechnical applications and the results showed significant effect of Bentonite on fluidity, the properties of the deformation and the compressive strength of the grout. The increase in the amount of Bentonite, unlike the water / Bentonite ratio (W / B), leads to an increase in the amount of flow time, plate adhesion, plastic viscosity and yield tension, and decreases water deflation and compressive strength in 3 days, 7 days and 28 days [5].

Also, Salehi (2008) carried out experiments on different mix designs with cement, Bentonite, and fly ash. The results of these experiments show that the increase of Bentonite has the greatest impact on reducing drainage water followed by decreasing water. In the meantime, the increase in the fly ash has the least impact. The dry density of the grout samples increases with increase in the amount of fly ash, comparing that with shear stress of

interface between the grout and tube show a specific trend. It was also shown that the phenomenon of bleeding and, as a result, detachment causes significant errors in measuring the shear strength of the interface between the grout and the tube and the uniaxial compressive strength. [1]

2. GROUT MIXING DESIGN

A review of past studies shows that the mechanism of measurement in extensometers, effect of Cement-Bentonite mixing design and the effect of grout properties have not been addressed. In this study, a number of laboratory tests with grout mixing design were used to determine mechanical properties. Mikkelsen (2002) [2], Kuisi et al. (2005) [6], as well as Slope Indicator Co. [7] and Soil Instruments Ltd. [3], introduced a grout mixing design for Cement-Bentonite in the installation of soil inclinometers (Table 1).

Table-1 Mixing design for Cement-Bentonite grout

Row	(W/C)	(B/C)
1	3	0.3
2	3	0.4
3	3	0.5

Mikkelsen (2002) believed that the water-to-cement ratio should be controlled to perform field experiments [2]. For this purpose, in this mixing design, the cement was first mixed with water, which makes the ratio of water to cement constant. Furthermore, the strength and grout modulus will be more controllable. Finally, after 5 minutes, Bentonite was added to the mixture and, according to Will (1997) [8], and it took 30 minutes to hydrate Bentonite and better mixing. From each mixing design in Table (1), some examples are made in Nx standard dimensions, as shown in Fig.1



Fig. 1 - Materials and steps to prepare the sample

After performing uniaxial compressive test with self-controlling loading device in Shahrood university of Technology Laboratory on the provided samples presented in Fig.2 , the extracted results are presented in Table(2).

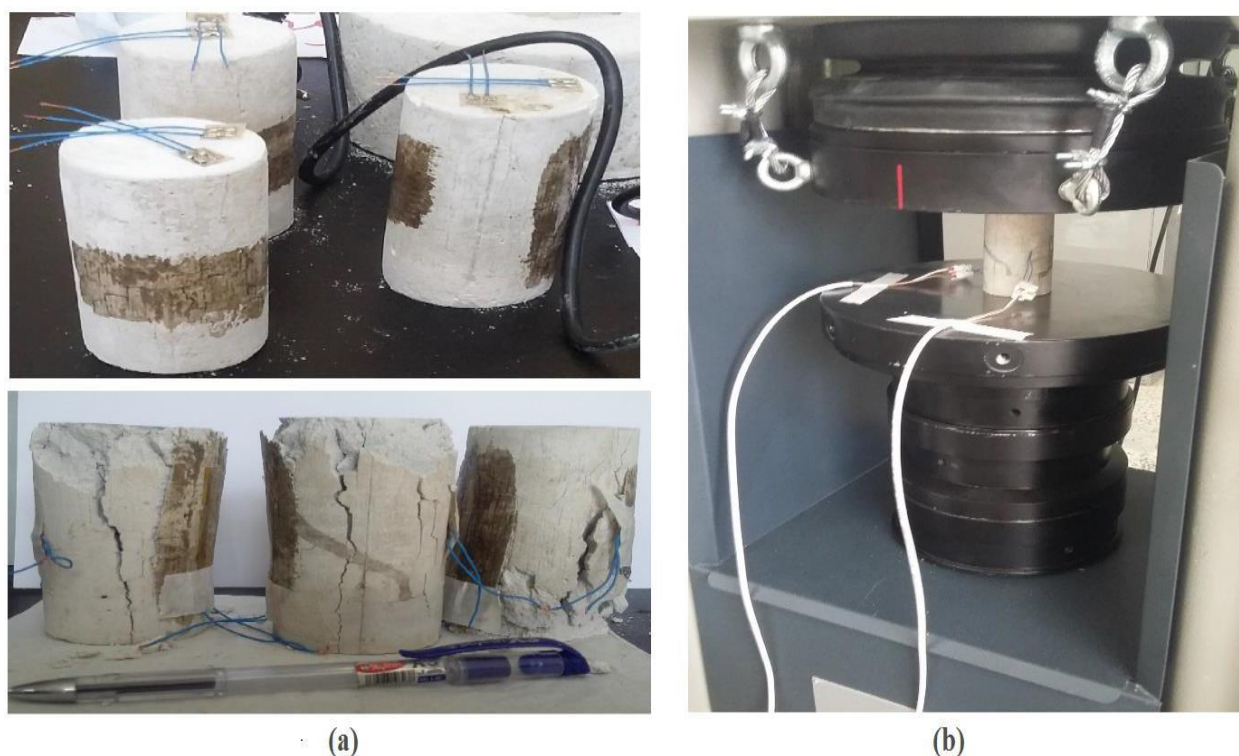


Fig.2 a) Sample before and after loading, b) Sample with strain gauge under the self-controlling loading unit

Table-2. Parameters obtained from uniaxial test

row	Ratio of (B/C) in constant ratio of (W/C=3)	Density (Kg/m ³)	Peak of strength (MPa)	Modulus of elasticity (MPa)	Poisson's ratio
1	0.3	1268	1.18	91	0.26
2	0.4	1166	0.9	79	0.27
3	0.5	1012	0.7	62	0.25

3. NUMERICAL MODELING

In order to investigate the effect of slurry properties on the results of measuring the borehole extensometer, a block was created in FLAC3D. The dimensions of the block is 8 m in length, 4 m in width and 10 m in height. Then a borehole with 0.15 m diameter was generated in the block.

A tube with 70 mm in diameter and 5 mm in thickness was modeled inside the borehole and the magnetic/spider ring is considered as a loop connected to the tube at measuring points 2 and 5 m from the surface of the model. As shown in Fig. 3, the space between the tube and borehole is filled with grout. Due to axisymmetric property of the model, half of model has been used for analysis. The surroundings of the borehole have been considered dry, and no change in volume or creep has been made in the grout.

Constitutive models provide a qualitative description of the materials behavior and other parameters of the material to determine this behavior [9]. A good constitutive model is able to predict the soil response under critical loading constituents, taking into account the actual properties under these critical loads [10]. The FLAC 3D software provides various constitutive models for the user. Among existing models, the Mohr Coulomb model

is used to simulate plastic deformations and to show shear failure in soil [11]. The used soil parameters are shown in Table (3).

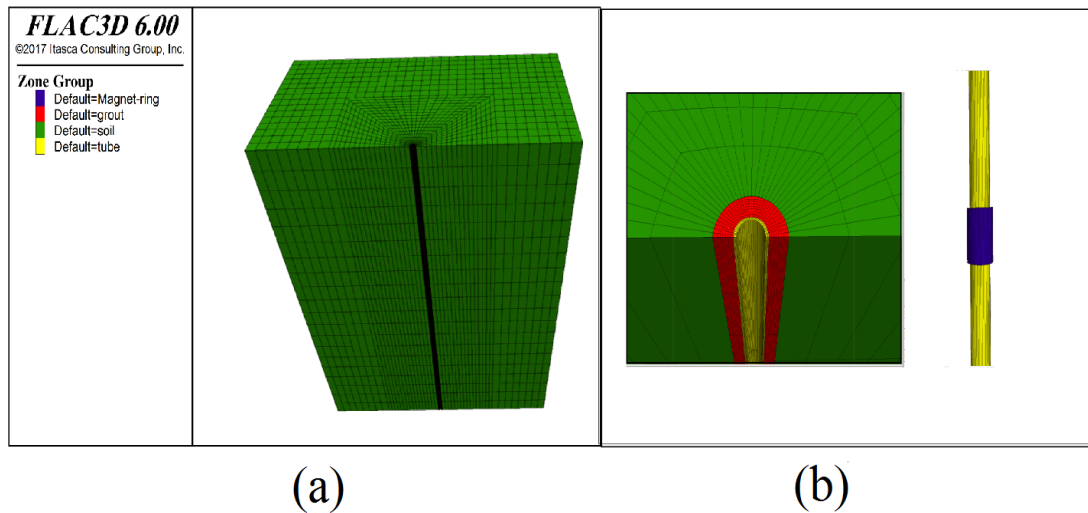


Fig 3-a) Model geometry and its meshing, b) Components of the model include grout, tube and magnetic ring

Table 3. Geomechanical Properties of Soil Types

Row	Parameter	Unit	Soft soil	Medium soil	Stiff soil
1	Density	Kg/m ³	1750	1800	2000
2	Modulus of elasticity	MPa	10	40	80
3	Poisson's ratio	-	0.35	0.3	0.35
4	Internal friction angle	Degree	25	17	38
5	Dilation angle	Degree	0	0	15
6	Cohesion	KPa	3	30	0
7	Interface friction angle	Degree	22	18	28

After applying the boundary conditions, the stress and vertical displacement contour are presented in this study for numerical model verification (Fig. 4).

To determine the error percentage of the extensometer measurement according to Fig. 4, the model is placed under an additional 10 kPa load and the points are located within the grout at a distance of 2.5 m from the borehole axis in the soil environment.

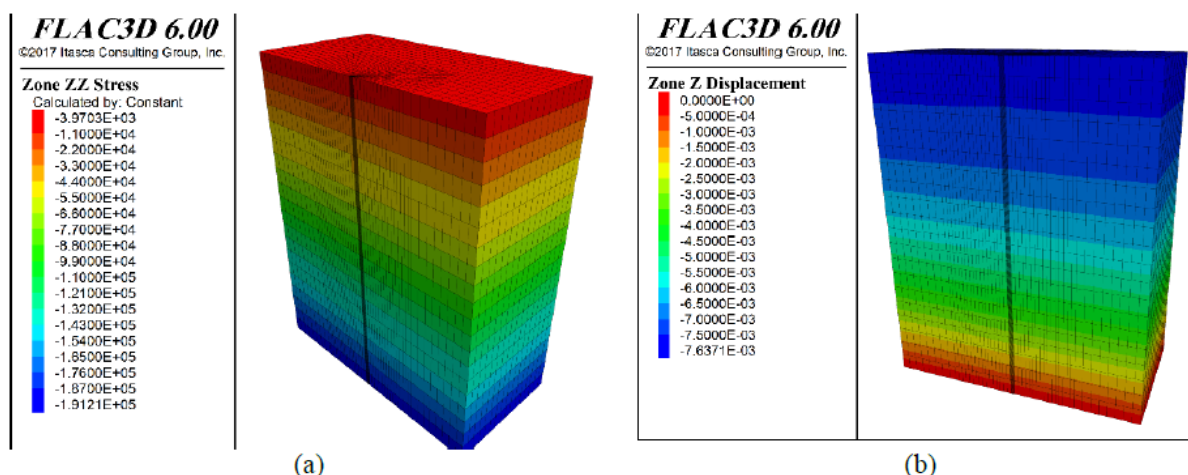


Fig 4- a) Stress contour, b) Displacement contour

The measured points are indicated by distance (d) from the model surface and the difference between the displacement obtained within the grout (y_c) and its corresponding soil (y_r) is the measurement error. In this study, the percentage of the measurement error of the settlement is obtained from equation (1).

$$\text{Measurement error (\%)} = \frac{y_c - y_r}{y_r} \times 100 \quad (1)$$

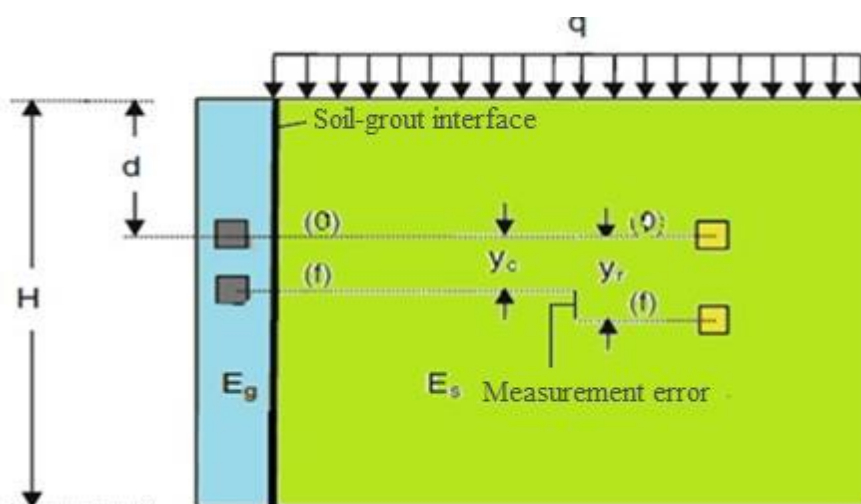


Fig 5- Determination of measurement error

Using the parameters obtained from the uniaxial compressive test presented in Table (2), for all types of soil including soft, medium, and stiff soils, the results are shown in Fig 6.

4. ANALYSIS OF THE RESULTS

Obviously, if the stiffness of grout inside the borehole is equal to the stiffness of the surrounding environment, the displacement of the environment will be transferred to the extensometer more accurately. Therefore, if the stiffness of grout to the stiffness of soil is closer to one, then less error percentage is found. It can also be found from fig (1) that with increasing the percentage of Bentonite to cement, due to reduced stiffness of grout, the measurement error percentage decreases.

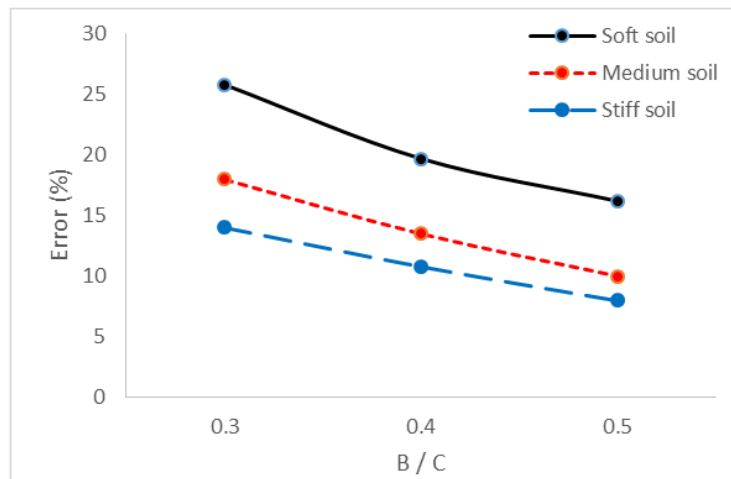


Fig 6- Error percentage of measurement for different ratios of (B / C)

Also a parametric study is carried out on different (E_g/E_s) ratios for soft, medium and stiff soils, where E_g is the elastic modulus of the grout and E_s is the elastic modulus of the soil. This study is also carried out in 3 states where the cohesion of the interface (between soil and grout) is a coefficient of the soil cohesion (1, 2/3, 1/3) and the angle of friction of the various levels has been investigated, and the results are shown in Fig (7), (8) and (9).

According to the fig (2), (3), (4), it can be seen that, the higher the ratio of E_g / E_s increases the error percentage of measurement, and if grout stiffness is less than the soil stiffness, the measurement error percentage will be lower, but there will be a borehole stability problem. Also, the closer the interface cohesion is to the soil cohesion, the lower the measurement error percentage and the internal friction angles of the interface also have no effect on the error of measurement.

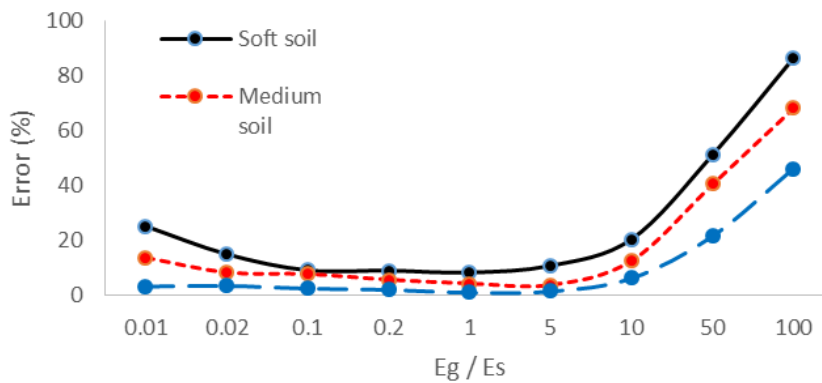
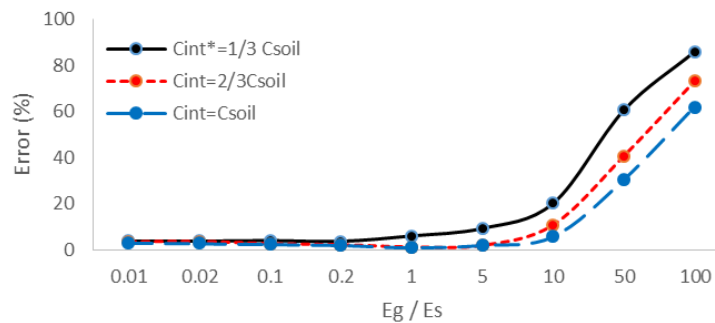


Fig 7- Error percentage of measurement for different (E_g / E_s) ratios for different soils



* Interface

Fig.8 Error percentage of measurement with different interface cohesion for different (E_g / E_s) ratios for medium soil

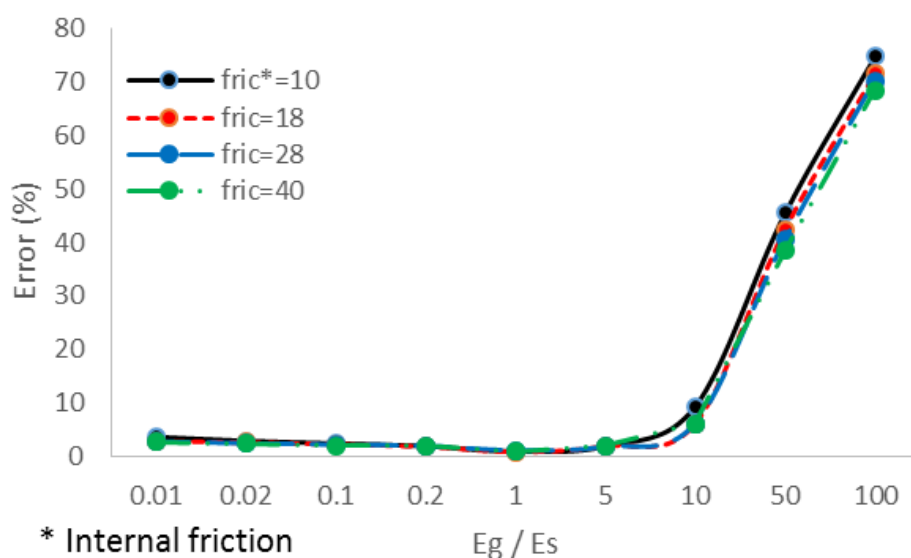


Fig.9 Percentage error of measurement with different friction angles in different ratios of E_g / E_s for medium soil

5. CONCLUSIONS

The results of laboratory studies on grout samples show that as the amount of Bentonite to cement ratio increases, the strength and grout stiffness decreases. Also, according to the numerical study, the measurement of the displacement of the extensometer in the borehole is a function of grout stiffness surrounding it. The error percentage of measurement is reduced by increasing the ratio of Bentonite to cement. This reduction in error percentage of measurement is compared in three soft, medium and stiff soil types. Comparison of these results shows that stiff soil is less affected by grout properties and less error percentage will occur. Measurement errors have been increased by increasing the modulus ratio and was not significant for rates of the elastic modulus of (E_g / E_s) more than 5% for the three different soil types (soft, medium, and stiff), and the higher error in the soft soil type is found.

It has also been shown that the grout with less stiffness than the surrounding soil has lower measurement error. The interface cohesion in different ratios of E_g/E_s less than 5, has no significant effects on the results, but when this ratio is more than 10 and the closer the interface cohesion to soil cohesion, the lower the measurement error rate, is. Also, the friction angle of the interface was studied, according to the results obtained, these angles do not affect the results of the error percentage.

6. REFERENCES

1. Salehi, M. (2008). "Interaction between soil and grout in Boreholes of extensometer in Soil Dams" M.S Thesis, Department of Civil Engineering, Iran University of Science & Technology, (in Persian).
2. Mikkelsen, P. E. (2002). Cement-Bentonite grout backfill for borehole instruments. *Geotechnical News*, 20(4), 38-42.
3. Soil Instruments Ltd. (2014). User Manual. Bentonite Pellets/Cement Grout
4. Burland, J. B., Moore, J. F., & Smith, P. D. (1972). A simple and precise borehole extensometer. *Geotechnique*, 22(1).
5. Sonebi, M., Hughes, D., Harley, R., & Lynch, K. (2012). Characterisation of the performance of sustainable grout containing Bentonite for geotechnical applications". In *The international conference on Sustainable Built Environment for Now and the Future*, Hanoi, Vietnam (pp. 1-10).
6. Al Kuisi, M., El Naqa, A., & Shaqour, F. (2005). Improvement of Dam Foundation Using Grouting Intensity Number (GIN) Technique at Tannur Dam Site, South Jordan. *Electronic Journal of Geotechnical Engineering*, 10.

7. Slope indicator website: <http://www.slopeindicator.com/>
8. Will, D., (1991) “*Cement-Bentonite Grouts Compatible with Compliant TDR Cables*”, M.S Thesis, Department of Civil and Environmental Engineering, Northwestern University, Evanston, IL, USA.
9. Brinkgreve, B. R. (2005). Selection of Soil Models and Parameters for Geotechnical Engineering Application. Geotechnical Special Publication No. 128, 69 - 98.
10. Sridhanya, K., Rajagopal, K., & Rao, L. (2008). Modelling of Degradation of Clayey Soils under Repeated Loading. The 12th International Conference of International Association for Computer Methods and Advances in Geomechanics (pp. 877 - 882). Goa, India: IACMAG.

Evaluation of Groundwater Management Techniques for the City of Mashhad

Mahdi Safdari Seh Gonbad¹, Poorya Nakhaei², Farzin Kalantary³

1- M.Sc. Student of Geotechnical Engineering at K.N. Toosi University of Technology, Tehran, Iran

2- M.Sc. Student of Water Recourses Management Engineering, Amirkabir University of Technology, Tehran, Iran

3- Assistant Professor of Civil Engineering at K.N. Toosi University of Technology, Tehran, Iran

Email: m.saffdari@gmail.com

Abstract

In recent years the rise of groundwater level in some regions of Mashhad, attributed to the water transfer from the surrounding dams has caused complications in many projects. Groundwater in Mashhad is mainly charged from Binalood Mountain in addition to absorbing wells traditionally used as an effluent disposal method. However, the balance of groundwater has been further tipped by decommissioning of upstream suburban water wells, having been replaced by the water transferred from Dousti dam. Obviously, inbound groundwater diversion methods and/or regional drainage projects are needed to compensate the extra inflow. One of the successful methods for groundwater diversion is appropriately positioned grout curtains in aquifers, acting as a subsurface dam. River and canal engineering projects aimed at prevention of surface runoff infiltration, as well as re-commissioning of wells, would also positively affect the problem. In this study, the effectiveness of the aforementioned methods for groundwater management is studied and based on the available data tentative proposals are made as to the most effective methods.

Keywords: Mashhad, groundwater management, subsurface dams.

1. INTRODUCTION

Typically, the major concern in groundwater for water resource management engineers is a decline in groundwater levels [1]. But today rise in groundwater levels has become a major concern all over the world which has been reported in most cities around the world [2, 3]. In Iran, we can mention the cities of Mashhad, Kerman, southern Tehran and Sabzevar. As direct groundwater recharge is reduced by the development of urbanization, new sources for recharging aquifers, including leakage from water pipes, sewage, absorption wells and other waterways, are created. The effects of these changes often increase groundwater recharge than pre-urbanization. The rate of increase in groundwater level in arid regions and populated cities where drinking water is usually supplied from other resources is significant [4].

If the groundwater level rising continues, it may have a geotechnical effect on the structures [5]. The rising water level causes serious problems for existing structures as well as new constructions. The problems for new constructions include water entering the construction sites, increased maintenance costs for trenches and the system supporting structure for the temporary stabilization of trenches. In the existing structures, the rise in groundwater level and an increase in the moisture content of the soil will reduce the soil's resistance, increase the liquefaction potential, increase the risk of soil compaction due to the water compression, the increase in the soil corrosivity potential and the deterioration of concrete and metal components [6]. In this study, we will show the rise in groundwater levels, describe its problems and finally, we will present solutions to deal with these problems or mitigate their effects.

2. SOIL TEXTURE OF MASHHAD CITY

In general, sediments of Mashhad city include sedimentary deposits, flood plains and conifers. The maximum thickness of sediments in the center of the Mashhad plain is more than 250 meters. The thickness of sediments is reduced to the southern and northern slopes (Fig. 1) [8].

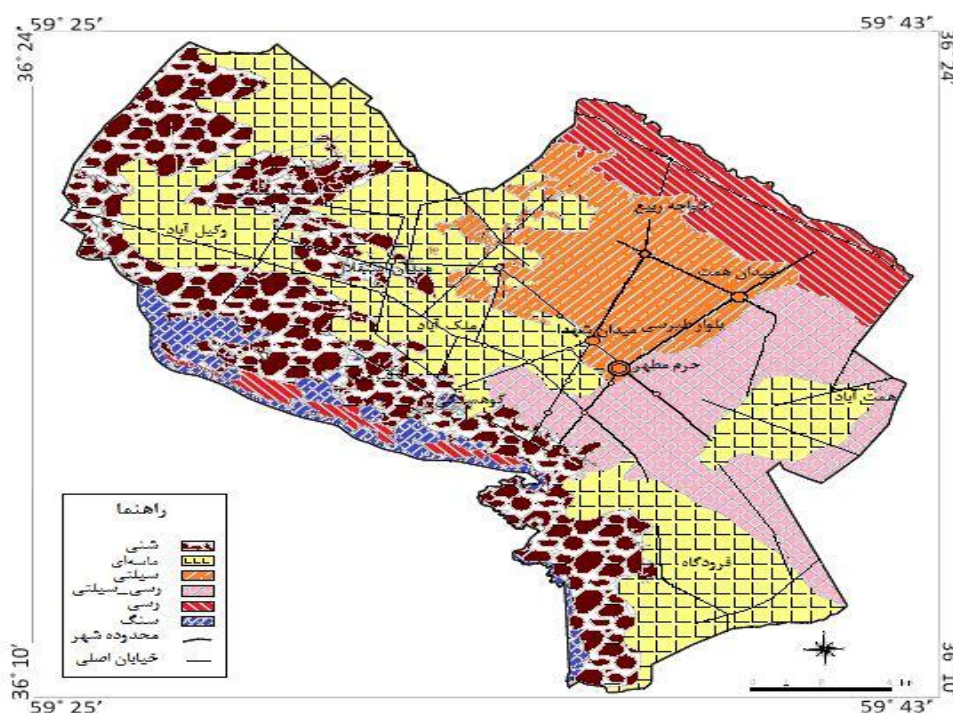


Figure1. Map of Soil texture of Mashhad city [8].

3. LOCALIZED RISING OF GROUNDWATER WATER LEVEL IN MASHHAD

In recent years, Dousti Dam has been one of the most important Mashhad’s sources of drinking water. In this way, 500 million cubic meters of the outflow of the dam enter into the Mashhad watershed. With the arrival of this volume of water, the drinking water wells in the city were turned off. On the other hand, the development of some urban infrastructures such as the sewer collecting network did not construct along with other urban developments. As a consequence, the water entering the aquifer has caused the localized water level rises, especially in the central areas of the city, which imposes some problems for other urban development [9].

Ghandahari et al. (2014), showed that there are four periods of groundwater water level changes during the period of 1985 to 2013, by drawing the hydrograph of the existing piezometers in the city center (Fig.2). In general, groundwater level decreased from 1985 to 1991, increased from 1991 to 2001 and again decreased until 2008 and then increased. From 2008 to present, despite the drought, a rise in groundwater level is observed. The groundwater level has been rise 36.23 meters in 68 months (an average monthly increase of 1.53 meters). Therefore, it can be concluded that the main factors of the rise in groundwater level are the entrance of the Dusti dam outflow into the watershed and the lack of utilization of drinking water wells [9].

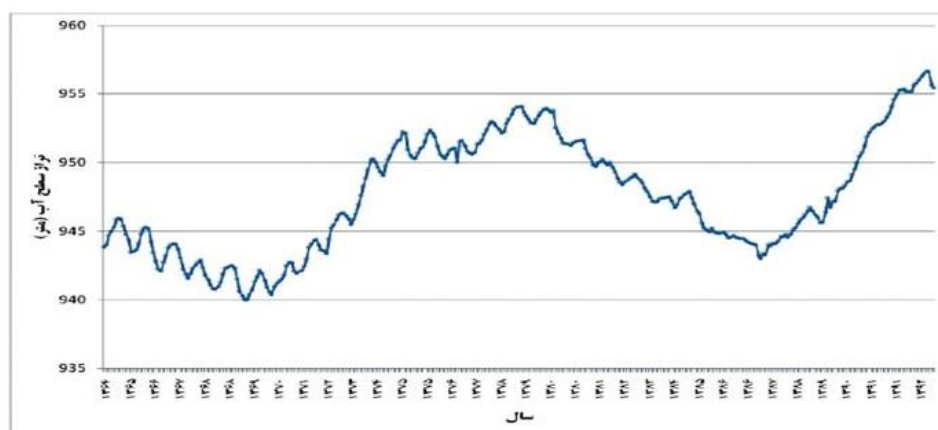


Figure 2. Hydrograph of the piezometers in the city center.

In general, the reasons for the localized rising of groundwater water level in Mashhad are:

1. Transferring more than 500 million cubic meters of water out of the basin (Dusti dam) into a small watershed for drinking water and turning off the drinking water wells in the Mashhad city, simultaneously [9].
2. Numerous Qantas that drain groundwater from different areas to the central basin of Mashhad [7].
3. The existence of Golestan artificial recharge in the upstream basin of the catchment area and on the Qantas route, hence transfer water to the central basin [12].
4. Consolidation of soil due to groundwater withdrawal, reduction of soil storage capacity, and consequently the increase in the velocity of entry water rising from absorption wells [9].
5. The existence of clay layers with a low depth (up to 40 meters) below Mashhad creates a shallow aquifer [9].

4. PROBLEMS DUE TO LOCALIZED RISING OF GROUNDWATER LEVEL IN MASHHAD

The rising water level causes serious problems for existing structures as well as new constructions. The problems for new constructions include water entering the construction sites, increased maintenance costs for trenches and the system supporting structure for the temporary stabilization of trenches (Fig. 3). In the existing structures, the rise in groundwater level and an increase in the moisture content of the soil will reduce the soil's resistance, increase the liquefaction potential, increase the risk of soil compaction due to the water compression, the increase in the soil corrosivity potential and the deterioration of concrete and metal components [10].



Figure 3. Water entering the construction sites.

- I. Reduction in bearing capacity [11]
- II. Reduction in soil stiffness and/or Collapsibility phenomenon [12]
- III. Degradation and corrosion of structures [13]
- IV. Liquefaction
- V. Sewage Infiltration to groundwater

5. SOLUTIONS FOR LOWERING GROUNDWATER LEVEL

- I. Aquifers management and prevention of excessive recharging of the aquifer, through the construction and development of sewage and surface water collection networks (completion and development of the energy tunnel in the distressed area of Mashhad city) (Fig. 4).
- II. Water supply management from the Dousti Dam and the water wells in the northwest of Mashhad (Ghasem Abad area), which is no longer withdrawn from them.
- III. Construction of underground dams in the north, northwest and southwest areas, pumping of stored water behind these dams into canals and rivers inside the city and eventually, transferring the water to the Kashafrud river as a natural drainage area.



Figure 4. Energy tunnel in the distressed area of Mashhad city.

From the above, we will explain the underground dam.

6. THE UNDERGROUND DAM

I. What is underground dam?

A facility that dams up groundwater flow, stores in the pores of the stratum and uses groundwater in a sustainable way. Furthermore, a facility for preventing saltwater intrusion is also included to definition of the underground dam. In a wide sense, it is called as underground dam including reservoir area (Fig. 5). Underground dam have no huge “Tank” under the ground, generally have a lot of porosity in the aquifer (underground). In other words, underground dam reserves the groundwater in “hard” porous sponges [14 and 15].

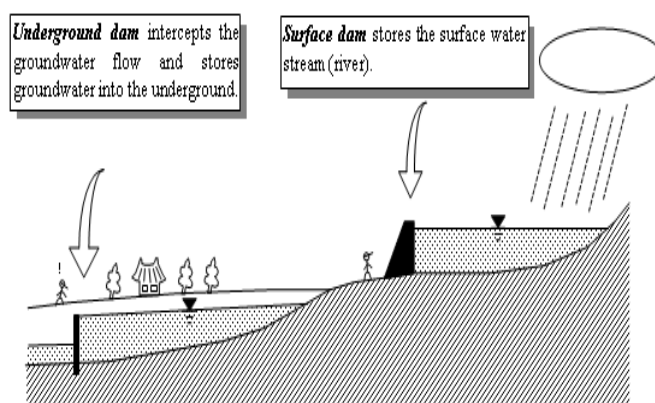


Figure 5. Scheme of surface dam and underground dam [14].

II. Types of Underground Dams

- i. Classification by dam purpose.
- ii. Classification by construction method.
- iii. Classification by the reservoir type.

i. Classification by dam purpose.

a) Dam up type (Storage type, Run-off control type): This dam type is planned to store groundwater. The reservoir, which dams up groundwater and regulates its discharge, accordingly increases the groundwater level and allows stable intake of groundwater [14 and 15] (Fig. 6).

b) Saltwater intrusion prevention type: This dam type is planned to prevent intrusion of saltwater into the groundwater and to protect available water resources. The reservoir unconditionally allows groundwater pumping and the resultant adjustment of the groundwater level [14 and 15] (Fig. 6).

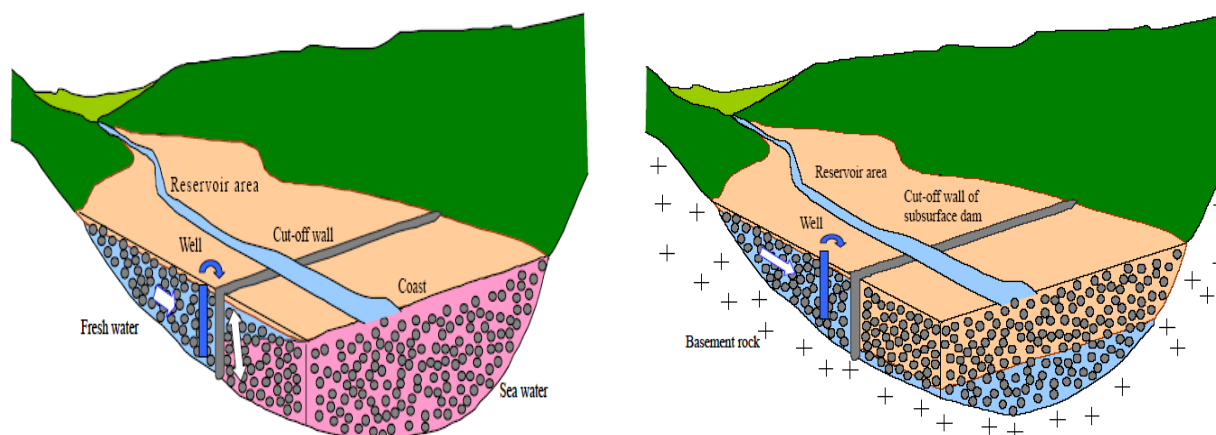


Figure 6. Dam up type (storage type), Saltwater intrusion prevention type [14].

ii. Classification by construction method.

- a) Ground improvement method (grouting method): In general, is applied by foundation improvement of the surface dam, using an injection of cement milk under the ground and hardening the milk, and so constructing the impermeable barrier (grout curtain). This method is applied to the underground dam in small scale [14 and 15].
- b) Impermeable body driving method: This method is to construct a dam body by driving steel sheet pile (or concrete sheet pile). This method is used for shallow unconsolidated layer [14 and 15].
- c) Diaphragm wall method: Diaphragm wall method is applied to the underground dam in large scale. Among of the several types of diaphragm method used for underground dam construction, (Soil Mixing Wall method) [14 and 15].

iii. Classification by the reservoir type.

- a) Fully subsurface storage type: This dam type is an ordinary case of underground dam and reservoir is not visible directly [14 and 15].
- b) Partially surface storage type: This dam type has functions not only to reserve groundwater but also to store surface water on the ground in the reservoir area [14 and 15].
- a) Surface dam hybrid type: At the surface dam, reservoir water is stored in the ground in addition to on the ground by the effectiveness of the water-tightness barrier, which is created by the foundation treatment such as grouting works [14 and 15].

7. REQUESTED NATURAL CONDITIONS FOR UNDERGROUND DAM

a) Excellent storage aquifer

An aquifer with large effective porosity and hydraulic conductivity must be available in the planned area.

a) Impermeable basement

The basement stratum forming the reservoir floor and side boundaries must be relatively watertight so as to form efficient groundwater reservoir.

a) Sufficient recharge to the reservoir area

Sufficient and appropriate groundwater recharge must be available in the reservoir area of the underground dam. Normally, high precipitation and infiltration will be required corresponding to the planned amount of storing water [14 and 15].

8. CRITERIA FOR CHOOSING DAM SITE

- Sandy soil (images of river bed and surface information).
- Less salt content.
- Large average annual flow rates (annual rainfall data is the measure).

- Land gradient <5% (Topography and DEM).
- Less drainage density (WMS calculation).
- Less evaporation rate (meteorological data).
- Bedrock not too deep (experience 20-70 m, geological maps, geophysics, etc.).
- Do not build on fractured rocks or large boulders to prevent seepage.
- Build on solid bedrocks instead or 1 meter in the solid and impermeable soil [14 and 15].

9. CONCLUSIONS

The rise of the groundwater level in some parts of the Mashhad over the past few years has caused disturbances in some construction projects. Over the past decades, factors such as water transfer from the surrounding dams, waste water disposal through absorbing wells and the decommissioning of upstream wells have led to an increase in the water balance of the region.

One of the successful methods in groundwater diversion, which can be a suitable solution for diversion of the excess inflow to the north and northwest of Mashhad is subsurface dams. also, river engineering projects in Binalood Mountain and pumping and water transfer to Kashafrud river (as natural drainage of the area) can be complementary to this action.

10. REFERENCES

1. Lashgripur, Gh., Ghafouri, M., Soveyzi, Z, and Pivandi, Z. (2005), "*Drop of Groundwater Level and Land settlement in Mashhad Plain*," Proceedings of Ninth Conference on Iranian Geological Society, Tarbiat Moallem College, Tehran, September 8th and 9th August. (in Persian)
2. Ray, A. (2005), "*Participatory Governance: Addressing the Problem of Rising Groundwater Level in Cities*," J. Hum. Ecol., 18(2): 137-147.
3. Brassington, F.C. (1990), "*Rising groundwater levels in the United Kingdom*," Proc.Instrn. Civ.Engrs.part 1,1037-1057.
4. Lerner D. N. 1990. Groundwater recharge in urban areas. Hydrological process and water management in urban areas. IAHS pub. No. 198.
5. Wilkinson, B. (1985), "*Rising groundwater levels in London and possible effects on engineering structures*," Memoirs of the 18th Congr. Int. Assoc. Hydrogeol. Cambridge, 145–157.
6. Dean, J.L. and Sholley, M.G. (2006), "*Groundwater basin recovery in urban areas and implications for engineering projects*", in Culshaw, M., Reeves, H., Spink, T. and Jefferson, I. (Eds), Engineering Geology for Tomorrow's Cities, Theme 2, The Geological Society of London, Nottingham.
7. Ghafouri, M., Lashkaripoor, Gh. R., Hafezy Moghadas, N., Salehi Moteahed, F., and Naseh, S. (2009), "Investigating the Environmental Problems Caused by Abandoned Qanats in Mashhad City. (in Persian)
8. Hafezy Moghadas, N., Qaeim magham, M. R., and Qazi, A. (2008), "*Evaluation of Alluvium Effects and Land Classification in Mashhad City Based on Seismic Wave Spectrum Ratio*", Geological Studies, Year 1, No. 1, Winter. (in Persian).
9. Kandahari, A., Geerd Noushahri, A., Barati, R., and Hosni, h., (2014), "*Local Rise of the Groundwater in Metropolitan, its Opportunities and Challenges*," Journal of Water and Sustainable Development, First Year, No. 2, 75-82. (in Persian).
10. Oyedele, K. F., et al. (2009), "*Geophysical and hydrogeological evaluation of rising groundwater level in the coastal areas of Lagos, Nigeria*" *Bulletin of engineering geology and the environment* 68.1, 137-143.
11. Khaksar Najafi, A., Islamy, A., and Chegini, A. E., (2010), "*Investigation of Damage Caused by Water and Soil Interaction on Technical Buildings and Optimum Control methods of it*," 5th National Congress of Civil Engineering, Ferdowsi University of Mashhad, Iran, May 14-16. (in Persian).

12. Hassanpour, N., Abbas Nezhad, A., Radfar, Sh., and Dad Elahi, h. (2011), "*Environmental Challenges of Kerman City regarding the rise of groundwater level and its structural damaging effects*," 5th Specialized Conference on Environmental Engineering, Tehran, Iran, 14th -16th May. (in Persian).
13. Leon, Roberto T., and Moon-Gu Jeon. "*Effect of reinforcing bar chemical composition on corrosion resistance*" (1994).
14. Onder, H., and Yilmaz, M., (2005), "*Underground Dams: A tool of Sustainable Development and Management of Groundwater Resources*", European Water, 35-45.
15. A manual on SubSurface Dams construction based on an experience of Vétérinaires Sans Frontières in Turkana District (Kenya) "*SubSurface Dams: a simple, safe and affordable technology for pastoralists*", September 2006.

The Mountain Water Reservoirs Influence on Meteorological Conditions of Coastal Area

Parviz Normatov, Bakhtiyor Markaev, Abulqosim Muminov, Inom Normatov
Institute of Water problems, Hydropower and Ecology of the Academy of Sciences of republic of
Tajikistan, 14a Ajni Street, Dushanbe, Tajikistan

Email: norparviz89@gmail.com

Abstract

Considering actuality of a problem of climatic factors influence on development of agricultural grades the results of the Nurek reservoir influence on meteorological parameters of three agricultural regions of Dangara, Fayzabad and Yavan of the Republic of Tajikistan are presented in this paper. In mountain districts, as usual because of the heights processes of reflection influence, a deviation of the directed movement of air masses are observed. Consequently, existence of the developed network of meteorological stations in mountain districts is pledge of receiving a real scenario of meteorological parameters dynamics. Timely establishment of the weather conditions variations and development of adaptation technology to the modern meteorological conditions and selection of agricultural grades steady against changes of climatic factors and stressful situations pledge of ensuring food security.

Keywords: Reservoir, Impact, Agriculture, Adaptation, Mountain.

1. INTRODUCTION

In the Aral Sea Basin, on the territory of which five states are located, water resources are used generally for an irrigation and hydropower. These water users demand the different modes of a river drain regulation. In interests of hydropower – the greatest power generation and, respectively, the use of the most part of the rivers annual drain in winter- the cold period of year. For an irrigation, the greatest volume of water is required in the summer, during the vegetative period. Regulation of a river drain thus is carried out by the large reservoirs. Thus, all largest hydroelectric power stations are constructed in the republics of a formation zone of a drain in upstream of the Amu Darya and Sir-Darya Rivers – in Kyrgyzstan and Tajikistan. The main areas of the irrigated lands are located in the republics of the rivers downstream – Kazakhstan, Turkmenistan and Uzbekistan.

The question of a river drain regulation in the region and construction of large reservoirs as Kayrakkum, Nurek (Tajikistan), Toktogul (Kyrgyzstan) and Tyuyamuyun (Uzbekistan) in Central Asia arose from the 1950th years in connection with development of the irrigated agriculture.

What are the possibilities of this problem solution? Cardinal resolution of conflict between an irrigation and hydropower is not restriction of activity some one of them or submission one another, and on the contrary, their greatest joint development by construction of new large hydroelectric power stations with reservoirs of large volume. For hydropower it means the increase in production of cheap and environmentally friendly energy, for an irrigation – the increase of depth of long-term drain regulation and water security of already developed lands.

Existence of several water-engineering systems with reservoirs will allow to resolve contradictions between hydropower and an irrigation. Today the conflict between them arises because in basins of each of two main rivers of the Region-Sir-Darya and Amu Darya the only one large water-engineering system with a reservoir is available: on Sir-Darya – Toktogul in Kyrgyzstan, on Amu Darya – Nurek in Tajikistan. The only a large water-engineering system on the river cannot carry out a drain regulation at the same time in two modes – irrigational and power.

Construction of one larger water-engineering system on each of two rivers will cardinal change a situation. In this case, the reservoir, top on a flow will be able to work in purely power mode; the lower reservoir of the same volume will be able to overregulate a drain up to restoration of its natural mode. Especially it can provide a drain regulation in interests of an irrigation. The presence of numbers of water-engineering systems with reservoirs will improve the situation even more [1].

The Republic of Tajikistan possesses 527 Billion kWt·h the general potential hydroenergy resources but now more than 5% are used [2]. Therefore, to expect that in near future not one tens averages and large hydroelectric power stations with reservoirs will be built. It means that at planning of the agriculture perspective development of coastal areas to reservoirs it is necessary to consider a factor of the water reservoirs influence in

transformations of meteorological conditions of the district and introduction of adjustments to norms of the corresponding cultures irrigation.

According to [3] direct influence of reservoirs on meteorological parameters of nearby areas is felt at distances some hundreds of meters and in the direction of a wind such influence can be registered at distances more than 10 km.

2. METODOLOGY AND BASIC DATA

The purpose of the present research is the retrospective comparative analysis of statistical parameters of 60-year temporary temperature ranks, atmospheric precipitation and humidity and monitoring of the Nurek reservoir influence on a trend of change of these parameters.

For establishment of the mountain reservoirs influence on possible changes of Agroclimatic conditions we analyzed a trend of meteorological parameters of two regions of Dangara and Fayzabad of the Republic of Tajikistan with the developed agricultural branch coastal to the Nurek reservoir. The meteorological data of the 1950-2012 period of stations located in areas of researches are used.

Construction of the Nurek reservoirs begun in 1961 and in 1979 reached water level of 890 m. The mark of NPU of equal 910 m was reached in September 1983. Therefore, it is possible to consider that of a reservoir influence on meteorological parameters of the district has to be felt after the eightieth years.

For removal of other factors, a method of the analysis of spatial differences was used. If physiographic conditions do not change strongly, spatial differences between two couple's stations are steady sizes (in a long-term section). On change of spatial differences of two couples' stations one of which is located in the sphere of a reservoir influence, it is possible to estimate the effect its influence. An indispensable condition of the analysis - duration of the meteorological parameters number before and after construction of reservoirs.

3. RESULTS AND DISCUSSION

The studied areas coastal to Nurek reservoir are located in a radius up to 35 km around of reservoirs and at various heights from sea level and altitudes: Fayzabad (1215 m a. s. l., 38°15' N, 69°32' E), Dangara (660 m a. s. l., 38°10' N, 69°32' E), Yavan (632 m a. s. l., 38° 32' N, 69°05' E).

It should be noted that for the period 1950-2012 the change of temperature in all three areas has the increasing character without manifestation of any deviations or extreme after 80-their years testifying about influence of the Nurek reservoir.

Comparison of the temperature change before construction of the Nurek reservoir shows various trends of the temperature increase for the considered districts (Fig. 1). For example, if the temperature changes in the districts of Fayzabad and Dangara up to 1980 is fluently but after 1980 increase of temperature gains abrupt character (Fig.1).

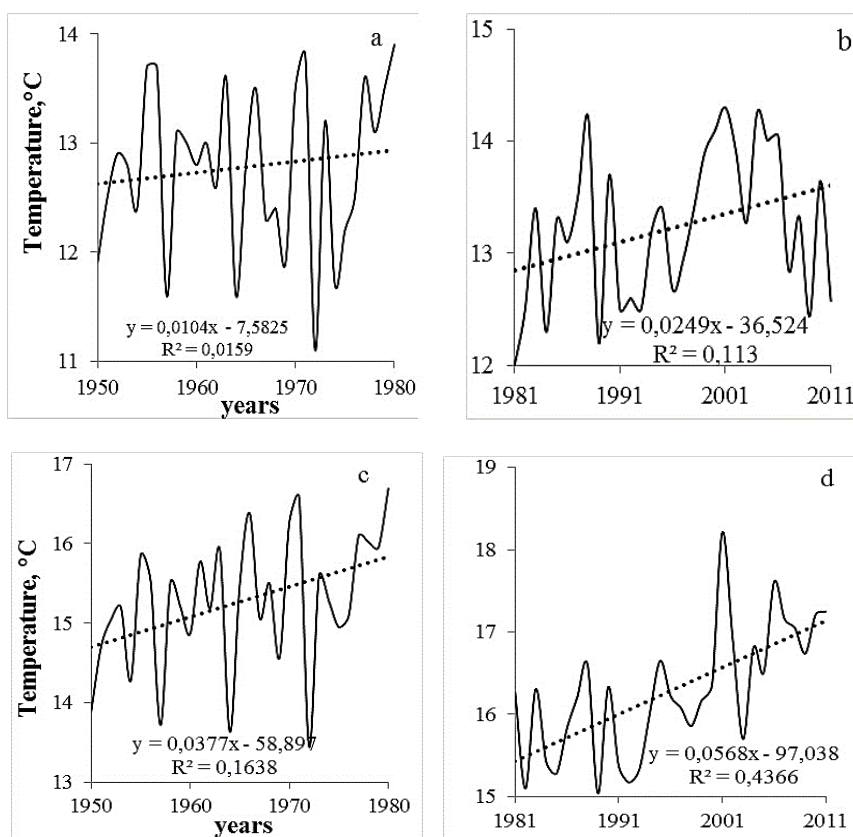


Figure 1. Trend of change of temperature of Fayzabad and Dangara districts before (a, c) and after (b, d) construction of the Nurek reservoir

Thus, exactly the opposite temperature changes are observed in Yavan district. A trend of change of average annual value of temperature before construction of a reservoir more abruptly and replaced on fluently after 1980 (Fig. 2 a, b).

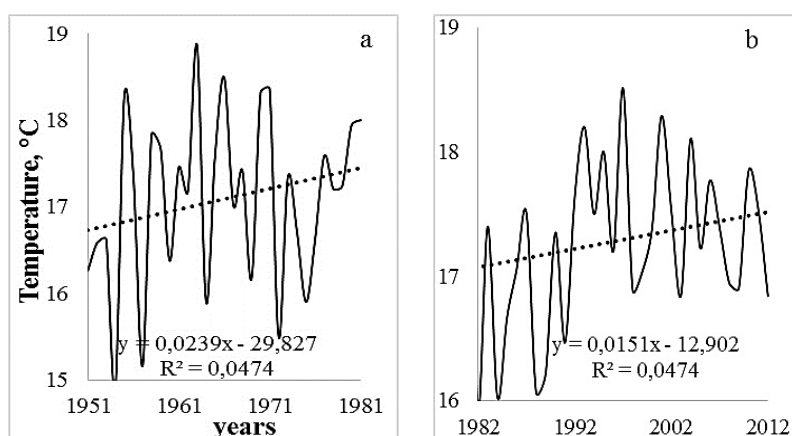


Figure 2. Trend of change of temperature of Yavan district before (a) and after (b) construction of the Nurek reservoir.

The explanation of the observed phenomena from the point of view of districts remoteness from Nurek reservoir is wrong as Fayzabad is at distance of 20 km, Dangara at distance of 35 km and Yavan on 30 km. On height of a situation of districts above sea level, Dangara (660 m) and Yavan (639 m) are closer to each other and it is logical to assume similarity of behavior of their meteorological parameters.

In addition, we carried out the monitoring spatially - temporary change of an atmospheric precipitation above the listed areas during 1950-2012 years. On the Fig. 3 (a, b) the average annual values of precipitation in Fayzabad district for the 1950-1980 periods and 1981-2011 are presented. A trend of change of an atmospheric precipitation Fayzabad both before construction of a reservoir and after it has the decreasing character. However, the change of humidity of the area for the considered periods is characterized by the increasing trend (Fig. 3 (c, d)).

Absolutely other nature of the humidity change and an atmospheric precipitation was revealed at monitoring of meteorological parameters of Dangara and Yavan. The humidity change of Dangara before construction of the Nurek reservoir is present on Fig.4. For the period after construction of a reservoir, i.e. after 1980 the humidity reduction tendency though its increasing trend up to 1980 is observed. The same transition from the increasing trend of the 1951-1979 period to the decreasing trend for the 1980-2011 period it was observed in change of precipitation also.

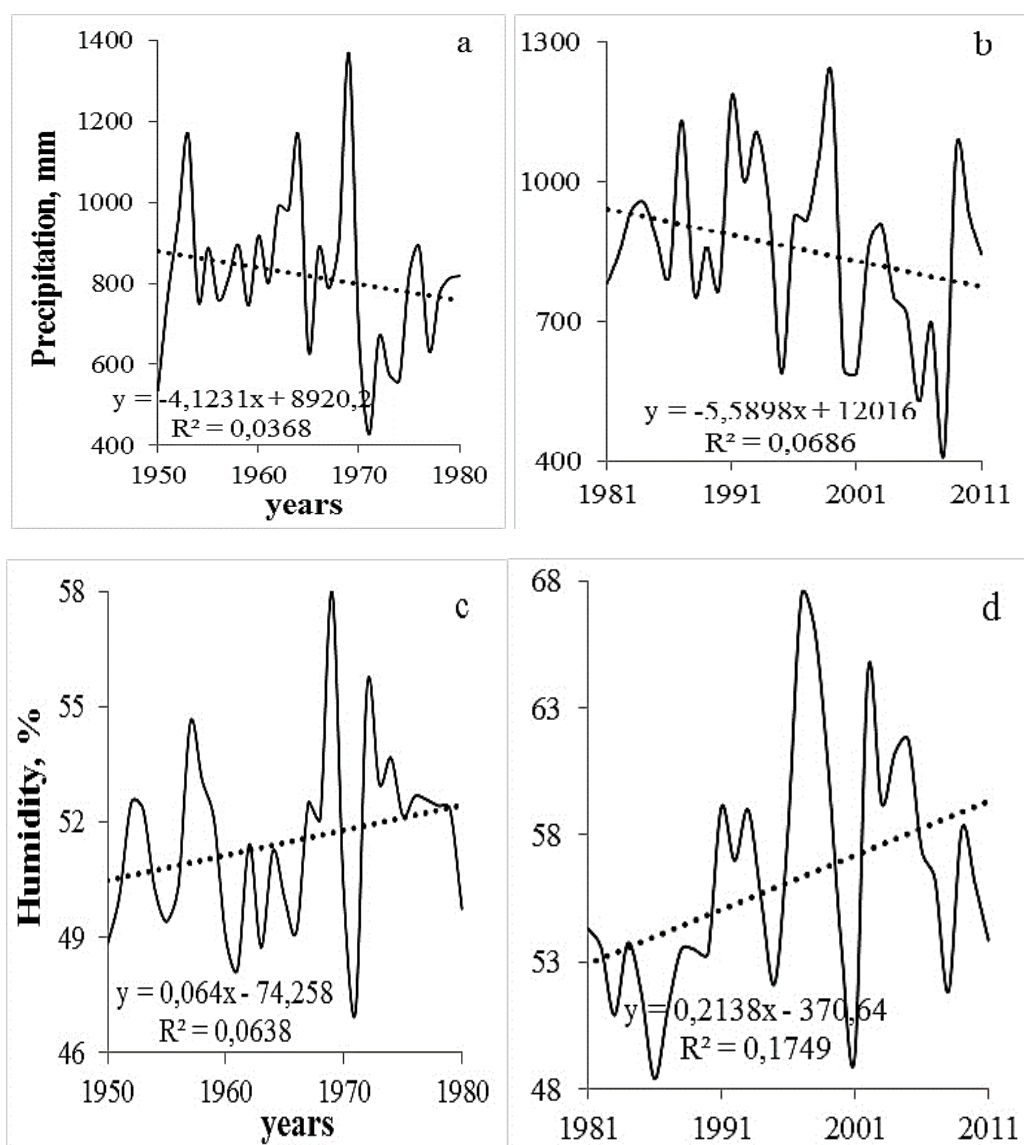


Figure 3. Trend of change of precipitation and humidity of Fayzabad district before (a, c) and after (b, d) construction of the Nurek reservoir.

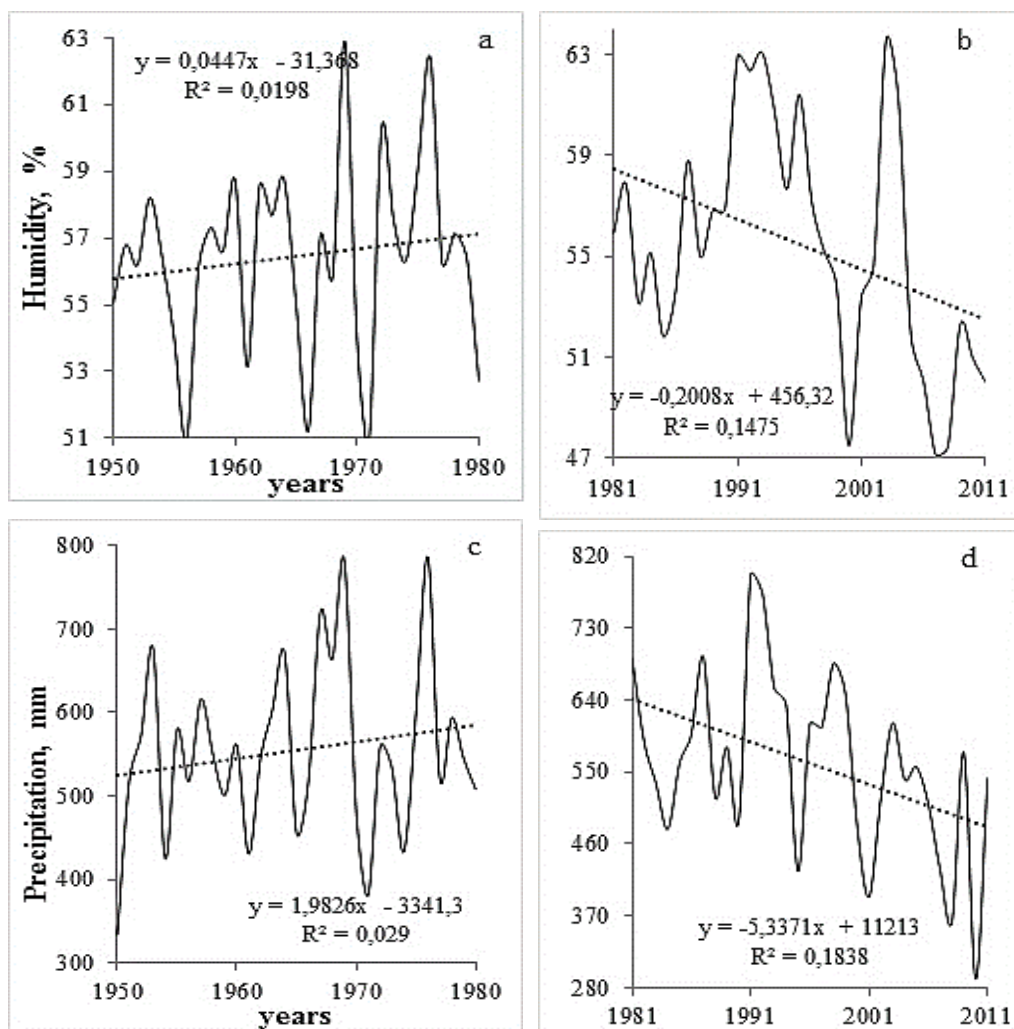


Figure 4. Trend of change of humidity and precipitation of Dangara district before (a, c) and after (b, d) construction of the Nurek reservoir.

Dynamics of the humidity change of Yavan is presented on the Fig.5 (a, b). From the Fig.5 (a, b) seems that humidity of this area had everything the reducing character up to 1980 and was characterized by moderate increase of precipitation. After 1980 sharp increase and humidity and an atmospheric precipitation is observed.

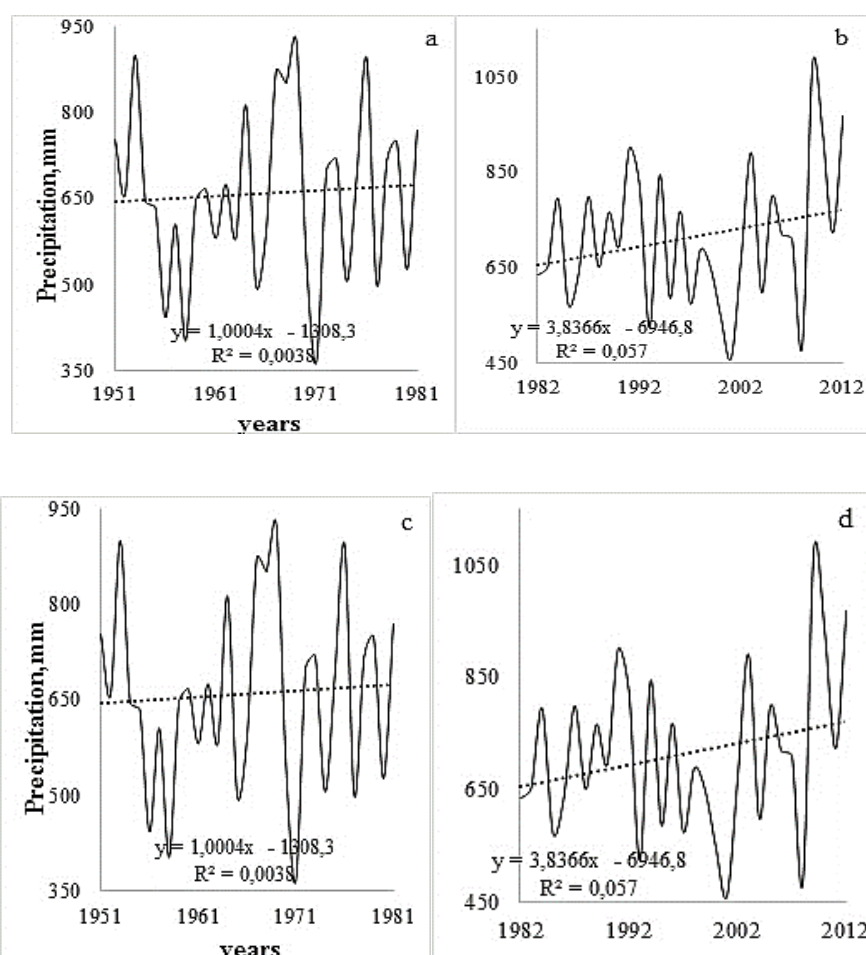


Figure 5. Trend of change of humidity and precipitation of Yavan district before (a, c) and after (b, d) construction of the Nurek reservoir.

The reduction of an atmospheric precipitation of Yavan for the periods 1950-1979 on 4.7 mm and increase for the period 1980-2011 on 443 mm is calculated (in comparison with 1979 makes about 30%). The temperature change of Yavan for the period 1980-2011 equals 1.1 C against his increase on 0.97 C for the period 1950-1979.

According to our opinion, the behavior of meteorological parameters of coastal to Nurek reservoir areas in winter and the summer periods represented a considerable interest. For example, on Fig. 6 a trend of the temperature change of Dangara in winter and the summer periods before and after construction of a reservoir is presented. Before construction of a reservoir the temperature change corresponds to the natural mode is reduction of their values in the winter and increase in the summer. After construction of a reservoir the return to the natural course of temperature the following phenomenon is observed- temperature increases in the winter. The Fig. 6 demonstrated that after construction of a reservoir on a curve of temperature change the deep minimum of the covering period 1982-2012 years testifying about influence of a reservoir on temperatures of Dangara district.

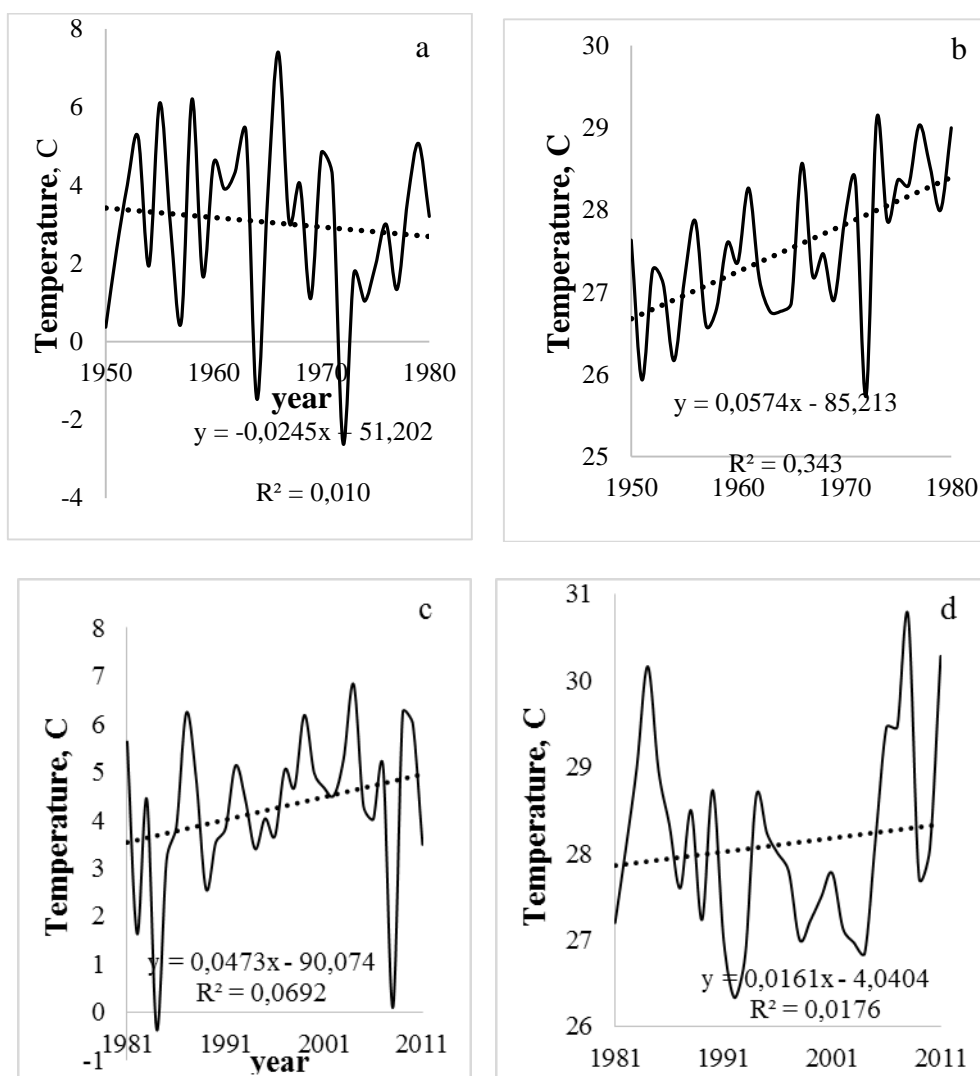


Figure 6. Change of temperature of Dangara in winter (a, c) and the summer (b, d) before and after a reservoir construction r respectively.

4. CONCLUSIONS

Thus, the analysis shows the ambiguous reservoirs influence on meteorological conditions of coastal areas. It first is caused by that the considered areas are characterized by a mountainous terrain. In mountain districts, as usual because of influence of heights processes of reflection, a deviation of the directed movement of air masses is observed. Consequently, the existence of the developed network of meteorological stations in mountain districts is pledge of receiving a real scenario of the meteorological parameters dynamics.

It should be noted that continuous monitoring of meteorological parameters of large water reservoirs is important from the point of view of agriculture development. Timely establishment of weather conditions variations and development of adaptation technology to the modern meteorological conditions and selection of agricultural grades steady against changes of climatic factors and stressful situations pledge of ensuring food security.

5. ACKNOWLEDGMENT

The authors are appreciation to USAID for funding research and support in the Framework of the PEER Project.

6. REFERENCES

1. Normatov I. Sh. and G. Petrov G.N. (2005, “*Use of Central Asia water resources in irrigation and Hydropower: conflict of interests or mutually beneficial collaboration*”, J. Water Resources, **2**, pp. 24-29.
2. Normatov I. Sh., Murtazaev U. and N. Nasirov N. (2010), “Creation of adaptation mechanisms: the key to cost-effective and environment-friendly water management”, IAHS Publ. Red Book **338**, pp. 74-76.
3. Murtazaev U, “*Evolution of natural complexes of Reservoirs of Tajikistan and their influence on adjoining Landscapes*,” Dushanbe, 2005, -322p.

Defining a Framework for Integrating Environmental and Social Aspects in Dam Rehabilitation

Sobhaniyeh Zahra¹, Sarang Amin²

1- Ph. D. Candidate, Department of Environment, University of Tehran, Tehran, Iran

2- Assistant Professor, Department of Environment, University of Tehran, Tehran, Iran

Email: zahra.sobhaniye@ut.ac.ir

Abstract

There are more than 36000 dams in the world. In 1950 there were 20000. That means there are now at least 20000 dams in the world more than 50 years old. This is the challenge we face in dealing with rehabilitation. Many of these dams were built under difficult circumstances with inadequate resources, the population in desperate need of drinking water, hydroelectric power, or flood relief. Therefore, the establishments of these dams such as Latyan and Amir Kabir dams in Iran are very old and this has created an increasing attention to the issue in recent years. In this paper we have investigated the possibility of introducing new techniques for rehabilitation and improvement of dams' behavior through a holistic viewpoint. In order to proceed with dam rehabilitation analysis, dam owners should perform a detailed incremental hazard evaluation of the dam which is the main focus of this research. The step by step approach discussed in this paper is the recommended standard protocol that will assist dam owners in performing decision analysis. An integrated environmental and social Assessment with an environmental management plan have been developed to manage risk and maximize environmental and social benefits wherever it is applicable. This will be finalized based on earlier work and experiences and consideration of improvement activities proposed by Water and Power Ministry.

Keywords: integrating, environmental, rehabilitation, framework.

1. INTRODUCTION

There are more than 36 000 dams in the world. In 1950 there were 20 000. That means there are now at least 20 000 dams in the world more than 50 years old. This is the challenge we face in dealing with rehabilitation. Many of these dams were built under difficult circumstances with inadequate resources, the population in desperate need of drinking water, hydroelectric power, or flood relief.

The world is becoming more litigious and many countries regulate dam design, construction and operation. There is therefore often a need to rehabilitate a dam following a review of the design to check that it complies with current standards.

The purpose of this article is to present an overview of the state of the art in dam rehabilitation, to highlight the major innovations and to provide sufficient references for the non-specialist to pursue areas of particular interest. Case histories are used to illustrate the methods.

2. MANAGEMENT OF REHABILITATION

2.1. MANAGEMENT OF DESIGN

Good practice in terms of monitoring the behaviour of a dam should comprise the following as a minimum:

- Sufficient monitoring equipment in good order to be provided to allow a basic understanding of the behaviour of the dam.
- Measurement data to be regularly evaluated.
- The dam should be inspected regularly and independent advice should be called for when unusual behaviour is noted.

The first step in rehabilitation is to develop an investigation programme to define the extent of rehabilitation, and the methods to be used. Operating experience should be established through structured questioning of operating personnel and reference to published work. Hydrological studies may suggest an increase in spillway capacity, power studies may recommend more hydroelectric capacity or irrigation and water supply and these possibilities should be included in the programme. It is costly to take important hydraulic structure out of operation. There may be an annual window when investigations can be made, and failing to use the window can delay the work by a year. The owner and the financing agency may have to agree urgently on the most

practicable and expeditious way forward. They may agree to single source or price enquiry contracting for specific services.

Often the problems are complex, emphasising the need for lateral thinking when devising solutions, and the foresight to know what data will be required and when. Senior experienced personnel are required. A brainstorm approach may be appropriate. A site inspection is essential.

Having examined the available data and understood the problems, the engineer undertakes a feasibility study to identify the possible solutions to each of the problems. At this level of study, the engineer identifies the options and examines them from technical and economic points of view. Comparison is usually on the basis of benefit/cost ratios. The bases of costs and benefits are kept consistent from one option to another so that meaningful comparisons between them can be made quickly and at low cost. In this way he identifies and excludes options that do not merit costly data collection.

Integral to the feasibility study is arranging the financing of the rehabilitation work. The source of funding depends on several factors. If there are definable and reliable income stream for the rehabilitated project it may be possible to arrange private funding in which an investor takes an equity share in the project for an agreed period. Where the income stream is neither well-defined nor politically reliable, grants or loans from a funding agency become relatively more likely. The financial arrangements depend on how the rehabilitation project may be structured into fundable contracts without comprising the progress of the works.

2.2. MANAGEMENT OF CONSTRUCTION

Surprises are endemic in rehabilitation. A good contract for rehabilitation work therefore requires the work to be defined accurately. The selected form of contract must be equitable for both parties, minimizing the points of conflict, and permitting the quick and fair agreement of additional work. Alternative forms of contract for rehabilitation work include: the *bill-of-quantities* format, *cost-plus*, *target cost*, and *design and construct*. Careful structuring of pre-qualification documentation ensures that the owner, his engineer, and the funding agency receive appropriate information to judge which contracting companies are to be included in the tendering list. Joint ventures between local and off-shore contractors are favoured for two principal reasons. The local contractor brings intimate knowledge of the local business environment and government procedures while the international company brings project management and technical skills. The form of joint venture can be specified in the contract.

The construction manager needs regular submissions of supporting data from the contractor and needs to generate significant records himself. Experience is needed to anticipate problems before they arise and to arrange for the necessary data to be collected in good time. The site supervisory team must be organized so that every critical piece of permanent construction is witnessed and monitored. Each position in the team carries well-defined responsibilities. The team must always be led by a person with sound technical skills and contracts administration experience.

2.3. RISK MANAGEMENT

Dam operators increasingly carry out risk management to assist in the identification and quantification of potential threats to the works, and to manage the risk effectively. This allows better decisions to be made concerning the rehabilitation of ageing structures, taking into account both the value of the asset to the business and the safety of the public. There is often inadequate operating data available to assess failure frequency, particular for remote plants, underlining the value of experience and generalized statistical data. It emphasizes too the value of a comprehensive data base of operating incidents. Whether or not they reflect well on the operating staff, they are encouraged to report them faithfully. The priority in assessing risk is to understand the consequences of a failure in terms of the business that relies on the works. The study should include assessment of the safety of the general public. Several approaches to risk analysis have been proposed to supplement the direct and effective method of inspection, analysis and reporting which suffer from the limitation that they principally identify defects that have already developed.

A technique described by Beak *et al* (1997) is known as the Failure Mode, Effect and Critically Analysis (FMECA). This is based on a British Standard (5760 part 5 1991). It involves applying simple criteria to an engineering system in order to identify the areas of greatest risk. Potential modes of failure are identified for each component of the works. For each failure mode the severity of the event is assessed, taking into account (a) the effect of failure on the operations, environment and wider community, (b) the probability of the occurrence and (c) the likelihood of the failure being detected. Each of these three circumstances is assigned a relatively coarse indicator on a rising scale, typically 1 to 5. The term *criticality* is given to the product of three indicators. The method produces a qualitative rather than a quantitative result. The actual probability of the event occurring

is not calculated but the approach identifies which elements of the works pose the greatest threat and is useful in allowing effort to be concentrated on those elements.

Several approaches to a probabilistic risk analysis have been proposed. This technique has been used for a number of years by the chemical and nuclear industries. It has been argued that in both of these industries the works are largely constructed of standard components with well-known reliability, whereas every dam is a prototype with the reliability of its components being less easy to define. It has also been asserted that the results obtained from studies of chemical or nuclear plants are less precise than has been assumed.

Typical of the probabilistic approach applied to dams is the procedure detailed by Bowles *et al* (1990) and Vick *et al* (1996). This involves developing all the possible failure scenarios that could develop as the result of a triggering event and developing them into an event tree. A probability of failure is then allocated to each component of each scenario. Thus the probability of each of the components of the tree occurring is assessed and the overall probability of each of the failure modes identified is calculated as the product of all the components in that branch of the tree.

This technique provides a quantitative risk of failure for every failure path identified and for each possible event. It is therefore possible to use this to justify whether to carry out works based on comparison of the calculated risk with a predetermined acceptable risk of loss of life or cost to the community or operator. It must however be borne in mind that the overall risk has been developed as a product of many components. A small error in each component may have a significant effect on the overall assessment. Calculation of accurate probabilities of failure for the various elements of the tree can be difficult and usually involves significant costs.

This technique has been further developed into the Portfolio Risk Assessment (PRA) approach by Bowles *et al* (1998). This is usually based primarily on available information, without performing extensive additional analyses or investigations; the steps are normally conducted at a reconnaissance level and make use of professional judgment which leads to an engineer certifying aspects of safety of the dam. Subsequent to the initial PRA, additional engineering studies will usually be necessary to verify the need for remedial work and to justify the extent of the work. As with the FMECA technique, this produces a qualitative rather than quantitative result.

Hoeg (1996) describes a simplified probabilistic risk analysis in the re-certification of existing rockfill dams that seeks to use the rigour of a logical approach via an event tree while making full use of the professional judgment of the engineers involved. The first step is a site inspection—a desk study is not an acceptable alternative. Next, all possible failure modes are visualized and defined. Those that lack technical credibility are eliminated. The third step is to construct an event tree that allows the interrelationships between events to be displayed. Only those events that lead to an uncontrolled release of water are developed at this stage. Each of these events is then reviewed to find those with greatest probability of occurrence, perhaps using a simple scale of likelihood from *virtually impossible* through *very unlikely*, *completely unknown* to *complete certainty*. The final step is to review the results from the event tree to determine the reasons for certain failure modes giving larger contributions than others.

Other methods include the production of fault trees and Hazop studies. With a fault tree the initial consideration is the failure of the element being considered and a tree is built up to establish the various means by which the failure could develop. As with the event tree the probability of each component is assessed to calculate an overall probability of failure. Hazop is a well established technique used in the chemical industry and bears many similarities to the event tree process but uses standard probabilities of failure for the components used in the construction of the plant.

None of the techniques remove all risk. The aim is to reduce the risk of failure to one that is *As Low As Reasonably Practicable* (ALARP). The basis for ALARP is that risks are acceptable only if reasonably practical measures have been taken to reduce risks. This is commonly taken to mean that the risks have been reduced to the point where it is longer cost effective to reduce them further.

With all the methods of risk assessment the procedure should involve a team including engineers with experience of design, operations and maintenance and may also require advice from specialists in hydrology, geology and seismology in order to develop a comprehensive assessment. A site visited by the team to inspect all aspects of the works is essential, as are discussions with the local operators and the study of such construction drawings and operational records as can be obtained, to enable them to produce a worthwhile assessment.

3. REHABILITATION OF FOUNDATIONS OF CONCRETE & MASONRY DAMS.

3.1. INTRODUCTION

Three important scenarios in which the foundations of masonry or concrete dams need rehabilitation are described below, together with a description of appropriate methods. Table 1 summarizes some case studies describing the methods mentioned below.

Table 1. Rehabilitation of foundations of concrete and masonry dams

Cause of rehabilitation	Dam data					Rehabilitation
	Name	Height	Type	Construction	Country	
Loss of strength under repeated loading	Albigna	115	PG		Switzerland	After 20 years, permanent displacement of the foundation noted. Successfully treated by
Loss of strength under repeated loading	Zeuzier		VA	1957	Switzerland	After 20 years, substantial foundation movements noted. A recently constructed tunnel 400m below the dam and 1400m was responsible for draining the foundation. Successful treatment of grouting the
Erosion and solution	Lister	40	PG (M)		Germany	The hydraulic gradient from the reservoir to new drainage gallery was steep enough to erode the fillings from joints in the foundation.
Erosion and solution	Henne		PGn (M)		Germany	Soluble foundation rock became so pervious that the effective solution
Ageing grout curtain	Schlegeis	131	VA	1973	Austria	Cracked grout curtain repaired with a new 5m deep cut off wall
Blocked drains	Baitings	53	PG	1958	UK	Choked foundation drains replaced.

3.2. LOSS OF STRENGTH UNDER REPEATED ACTIONS

Rehabilitation may be needed when the foundation rock is damaged by alternating stresses caused by the variation in hydraulic gradient experienced when the water level in the reservoir changes. These variations may lead to deformation, to movements on joints and to the initiation and propagation of cracks. There may be changes in the water content and pressure within joints. The rock mass is usually strong enough to adopt a new equilibrium after several years of operation. Sometimes, however, there is permanent change that may adversely affect the seepage quantity, uplift pressure and rock strength over a long time scale so that rehabilitation is needed. Such effects are usually detected through reliable and detailed monitoring. The aim of rehabilitation is usually to strengthen the foundation by grouting, improving the drainage, or by installing an impervious apron upstream of the dam.

3.3. EROSION AND SOLUTION

The flow of water through erodible or fractured rock can lead to increasing leakage from the reservoir. Large flows may be observed when the rock itself or the joint infill is soluble, resulting in karstic caverns. Detailed investigations of the foundation rock mass at the design stage is the best way of avoiding this problem. Monitoring the volume and pressure of the seepage through the foundation will be helpful in giving warning of this condition. A useful correlation of seepage quantity and pressure shows that when both are increasing, urgent rehabilitation may be necessary. When both are reducing no action is necessary to improve the foundation drainage. Rising seepage and decreasing pressure reveals the possibility of erosion within the foundation.

The aim of rehabilitation is to reduce the seepage flow through the foundation. Improved drainage to reduce the seepage pressure of the water may also be appropriate for rehabilitation, but care is needed. The case history of Eder dam, shown on Table 3, is one in which the improvement of the drainage within the foundation caused increased seepage and consequential erosion.

3.4. AGEING GROUT CURTAINS AND DRAINS

Grouting is one of the most common current methods of reducing the seepage below the dam. Older dams often were not provided with a grout curtain. Although cement is the most frequently used material for grouting, other materials are used in specific circumstances where, for example, the seepage paths to be grouted are particularly fine.

Drainage systems are designed to intercept and reduce the pressure of the water seeping below the dam. They include galleries, tunnels and bore holes. Both grouting and drainage are among the most useful measures for rehabilitating the foundations of ageing dams. When these elements deteriorate, owing to poor maintenance, or to chemical or physical attack, seepage may increase in quantity or it may begin to carry sediment. There may develop unusual readings of piezometric pressure. Rehabilitation usually consists of reconstructing the ageing component whether it is the grout curtain or a drainage system.

4. REHABILITATION OF CONCRETE AND MASONRY DAMS

4.1. INTRODUCTION

The four most common scenarios triggering the need for rehabilitation of the body of concrete and masonry dams are described below. This is followed by a brief account of rehabilitation in particular circumstances: at structural joints, in pre-stressed structures, and where the rehabilitation is required to improve the static stability of the dam. Table 2 summarizes a selection of case histories.

Table 2. Rehabilitation of concrete and masonry dams

Cause of Rehabilitation	Dam data					Rehabilitation
	Name	Height m	Type	Construction	Country	
Chemical reaction resulting in	Chambon	90	PG	1934	France	Slots cut in the concrete to relieve the stresses. Expected to be in
Shrinkage and creep leading	Olef		Buttress	1955	Germany	Detailed monitoring and analysis justified additional concrete and
Degradation at dam	La Girotte		Mult arch	1949	France	Comparison of facing repair methods show the good performance
Degradation at	Agger	45	PG	1928	Germany	New 120mm thick asphaltic concrete face has lasted 30 years.
Degradation at	Pracana	65	Buttress	1948	Portugal	Successful repair using pvc facing (Silva
Degradation at	Lost Creek	36	VA	1924	USA	Successful underwater installation of a pvc facing. (Harlan et al)
Loss of strength due to repeated actions	Zillergrund i	186	VA	1978	Austria	Locking of the joints in the dam by grouting. (Schoberl et, at
Loss of strength due to repeated actions	Ternay	41	PG	1867	France	Additional structural support through reconcreting.(Lino et al,
Loss of strength due to repeated actions	La Bourne	18	PG	1878	France	Increase of the overall level of compressive stress using post tensioned anchors.

5. REFERENCES

1. Aisiks EG, Pallares JJ, Tipping Ed & Varde OA, 1991. Special techniques for corrective treatment of right abutment at El Chocon dam. 17th ICOLD Congress, Vienna, Q65 R 65.
2. Baeker, E & Koehne, HD, 1985. Die Staumauer der Oleftalsperre; Konstruktion und Ausführung der Ertüchtigung. Deutscher Beton-Verein.
3. Beak C, Findlay JW & Alikman DI, 1997. Experience of Failure Mode, Effect and Critically Analysis on UK hydro power schemes. *Hydropower '97*, Trondheim.
4. Bister D, Bonnet P, Burdin J & Charvoz B, 1993. Maintenance des Barrages en Béton Techniques et Coûts. Colloque technique sur La Maitenance Des Vieux Barrages, Chambéry, France.
5. Bister D, Bonnet P, Denis B, De Beauchamp R, Dubois P & Goguel B, 1991. Contribution au suivi des barrages en béton Français sujets a gonflement ou retrait application a des ouvrages adultes (Chambon, Vouglans) et au béton jenne (cas de BCR) 17th ICOLD Congress Q65 R 7.
6. Bister D, Fry J-J, Costaz JJ Houis J, Degoutte G, Lino M, & Rizzoli J-L, 1994. Reassessment of earth - and - rockfill dams safety, Case Histories. 18th ICOLD Congress, Durban Q68 R43.
7. Bowles D, S, Anderson L, R, Glover T, F & Chauhan S S, 1998. Portfolio Risk Assessment: A Tool for Dam Safety Risk Management, Eighteenth USCOLD Annual Meeting and Lecutre, Buffalo, New York, 8-14 August.
8. Bowles D S, Anderson LR, Glover T F, Tarbox G, S, Waiter R B & Yin Au-Yeung P E, 1990. Evaluation of Dam safety at a series of hydropower dams including risk assessment. *The Embankment Dam*, Conference of the British Dam Society, published by Thomas Telford, London ISBN 0 7277 1647 6.
9. BRE, 1991. An Engineering Guide to Seismic Risk to Dams in the United Kingdom. Report BR 210, BRE Garston WATFORD UK, ISBN 0 85125 5108.
10. BRE, 1988. Alkali Aggregate Reactions in Concrete, Digest 330, HMSO London.
11. Brezina P, Satrapa L & Skonant T, 1998. The reconstruction of the collapsed bituminous concrete facing of the Morvka Dam, Czech Republic. Indian National Committee on Large Dams Symposium. *Rehabilitation of Dams*, 66th ICOLD Annual Meeting, New Delhi , November.
12. Brighton R & Lampa J. 1991. Ageing of B C Hydro's dams. 17th ICOLD Congress, Vienna, Q65 R 30.
13. Carlyle WJ, 1988. Wave Damage to upstream Slope Protection of Reservoirs in the UK. Proceedings of BNCOLD *Conference on Reservoir Renovation*, Manchester.
14. Cederwall K & Nilsson A, 1991. Description of three deterioration scenarios. *Hydraulic Engineering no 15.49. Royal Institute of Technology, Stockholm.*
16. Charles J A, Tedd P, Hugges A K & Lovenbury H T, 1996. Investigating embankment dams. Building Research Establishment Report, London, 82 pp.
17. Chen Z, 1993. Breaching of the Gouhou Concrete Face sand and gravel dam. International Symposium on High Earth and Rockfill Dams, Beijing.
18. Erwin E & Glenn J, 1991. Major Rehabilitation of Wister Dam. *USCOLD Newsletter* March 1991.
19. Feiner A & Zichner G, 1967. Sealing of the Agger Dam. 9th ICOLD Congress, Istanbul, Q34 R11.
20. Flemming J H & Rossington D T, 1985. Repair of Greenbooth Dam following localised settlement in the crest. 15th ICOLD Congress, Lausanne, Q59 R 55.
21. Flögl H & Stauble H, 1991. Experience with the Supplementary Installation of an Elastic Diaphragm in the Rock of Schelgeis Arch Dam. 17th ICOLD Congress, Vienna, Q66, R 41.
22. Frohnauer R & Torkhul C, 1996. New asphaltic lining for the Rabenleite Upper Reservoir. Strabag Brochure No 51, Asphaltic concrete for hydraulic structures, Cologne.
23. Gallacher D, Doake RM & Hay-Smith D, 1998. Remedial works to upstream face protection, Megget Reservoir. *The Prospect for Dams in the 21st Century*. 10th British Dam Society Conference. Thomas Telford, London.

24. Gillon M D, Everitt S & Mejia L, 1998. Rehabilitation of the Matahina Dam for foundation fault trace displacements. Symposium on Rehabilitation of Dams, 66th ICOLD Annual Meeting , New Delhi, India.
25. Harlan RC, Onken S, Scuero AM, Vaschetti GL, 1998. The underwater installation of a drained geomembrane system on Lost creek dam. Proceedings of CANCEL Conference, Nova Scotia, Canada.
26. Heitefuss C H, Kny H J & Ruhnke H, 1998. Die Sanierung des Sorpe Dammes mit einer HDIDichtwand. Wasserwirtschaft 88 (11), pp 562-565.
27. Heitfeld H, 1961. Beispiel der Verkarstung für den Talsperrenbau (am Beispiel der Hennetalsperre im Einzugsgebiet der Ruhr)- Journal Karst-und Hölenkunde, 2 iXXII, München.
28. Hewlett H WH, Boorman L A & Bramley M E, 1987. Guide to the design of reinforced grassed waterways. Construction Industry Research and Information Association Technical Note 120, London
29. Hoeg K, 1996. Performance Evaluation, Safety Assessment and Risk Analysis for Dams, Symposium Repair and upgrading of Dams, Stockholm, Sweden, June 1996.
30. Hopkins J K, Wickham D B & Stirling D M, 1990. The use of close-range photogrammetry for reservoir embankment monitoring. Proceedings of the 6th Conference of the British Dam Society *The Embankment Dam*, paper 24 published by Thomas Telford, ISBN 0 7277 1647 6.
31. ICOLD, 1983, Deterioration of Dams and Reservoirs, Report prepared by a team of Portuguese engineers of the LNEC, Lisbon.
32. ICOLD, 1994. Ageing of dams and appurtenant works. Review and Recommendations. Bulletin 93. ICOLD, 1985. Filling materials for waterlight cut-off walls. Bulletin 5.1.
33. Kollagaard EB & Chagwick WL, 1988. Development of dam engineering in the United States. Pergamon ISBN 0-08-034685-5.
34. Kovari K, 1985. Detection and Monitoring of Structural Deficiencies in the Rock Foundation of Large Dams. 15th ICOLD Congress, Lausanne, Q56 R36.
35. Kuusiniemi R, 1991. Internal Erosion of the Uljua earth dam. 17th ICOLD Congress, Vienna, Q65 Contribution no 15.
36. Lemelin D & Jobin H, 1996. Rehabilitation of a rockfilled timber crib dyke. SwedCOLD Symposium *Repair and Upgrading of Dams*, Stockholm, Sweden, June 1996.
37. Lino M, Salembier M, Antoine F, Rouas, G, Clerdouet D & Saintmarcel A, 1991. Vieillessement des quelques barrages Français très anciens. Pratique der leur rehabilitation . 17th ICOLD Congress, Vienna Q65 R1.
38. Marcuson III W F, Hadala P F & Ledbetter R H, 1993. Seismic Rehabilitation of Earth Dams. ASCE Special Publication No 35, Geotechnical Practice in Dam Rehabilitation.
39. Millmore J P, Stables J F & Shannon, F E, 1998. The Rehabilitation of Luxhay Dam, Somerset. *The Prospects for Reservoirs in the 21st Century*. 10th British Dam Society Conference. Thomas Telford, London.
40. Montfort L, Millet JC, Fabre JP, Bordes JL, Euvrard D, Ricard C & Royet P , 1991.
41. methodologie pour la detection et l'analyse du vieillissement illustres par des exemples. 17th icold
42. Congress, Vienna, Q65 R 23.
43. Mueller R & Pougatsch H, 1985. Comite National Suisse des Grands Barrages Chapter 6.2.2.-Zeuzier.
44. Nilsson A & Mikaelsson J, 1996. Groundwater Pressure Increase and Internal Erosion at Langbjorn Dam, SwedCOLD Symposium Repair and Upgrading of Dams, Stockholm pp 503-519.
45. Nilsson A & Norstedt U, 1991. Evaluation of ageing processes in two Swedish dams. 17th ICOLD Congress, Vienna, Q65 R2.
46. Obernhueber P, 1991. Remedial works for the kölnbrein Dam: Design and Analysis. 17th ICOLD Congress, Vienna, C7.
47. Rissler P, 1994. Rehabilitation of existing gravity dams in Germany with respect to safety philosophy and economy. 18th ICOLD Congress, Durban Q 68 R 5.

48. Rissler P, & Heitefuss C, 1999. Adaptation of the Ennepe dam Germany to the established technical standards. Intl journal of Hydropower and Dams vol6 no 2.
49. Schöberl P, Duber H & Döpfer H, 1993. Kraftschlüssige RiBinjektion an der Gewölbemauer Zillergründl (Force-locking Crack Injection at Zillergründl Arch Dam). *Grouting in Rock and Concrete*, Balkema, Rotterdam.
50. Schneeberger CE, Pigeon Y, Leavy J & Boncompain B, 1991. The use of slurry walls and jet grouting techniques to repair existing cofferdams at LG- 1. 17th ICOLD Congress, Vienna, Q65 R 29.
51. Scuero AM & Vaschetti G L, 1998. A drained synthetic geomembrane system for rehabilitation and
52. construction of dams. *The prospects for reservoirs in the 21st Century*. 10th British Dam Society
53. Conference. Thomas Telford, London.
54. Silva Matos D & Liberal O, 1993. Pracana powerplant refurbishment and uprating. An uncommon and challenging project. *Conference Uprating and refurbishment of hydro powerplants-IV*. Water Power & Dam Construction, Florence.
55. Sims GP, 1994. Ageing of masonry dams. Proc Instn Civ Engrs Wat, Marit & Energy 106. March, 61-70. Sims GP, 1991. Contribution 2, Section A: Alkali-aggregate reaction (AAR): reaction process; effects on the structures; interpretations of these effects; mathematical models; aggregate reactivity tests; remedial measures. 17th ICOLD Congress, Vienna Q65. Vol 5pp 193-196.
56. Taddei B & Poupart M, 1996. Reinforcement of the Chambon Dam. SwedCOLD Symposium *Repair and Upgrading of Dams*. Stockholm.
57. USCOLD, 1984. Bibliography on performance of dams during earthquakes. USCOLD, 1992. Observed performance of dams during earthquakes.
58. USCOLD, 1996. Anthology of Dam Modification Case Histories , ISBN 1-884575-09-9, April 1996. USCOLD, 1999. Observed performance of dams during earthquakes, volume II.
59. Vaughan PR, Kluth DJ, Leonard MW & Pradoura HHW, 1970. Cracking and erosion of the rolled clay core of Balderhead dam and the remedial works adopted for its repair. 10th ICOLD Congress, Montreal, Q36 R 5.
60. Vick SB G & Stewart R A, 1996. Risk analysis in dam safety practice. ASCE geotechnical speciality conference *Uncertainty in Geologic Environment: from theory to practice*.
61. Wasser Und Schifffahrts Verwaltung Der Bundesrepublik Deutschland (WSB), 1994. Edertalsperre.
62. Wittke W & Greb H 1994. Überprüfung der Standsicherheit der Urftalsperre. *Wasserwirtschaft* 84 11.
63. Biographical Sketch
64. Geoffrey P. Sims; Dr, eng. is the former chairman of the British Dam Society. He was the Chairman of the ICOLD committee on rehabilitation of dams from 1994 to 2000.
65. He has over 50 years of experience in management and execution of large civil engineering works
66. Associated with water in the UK and overseas, including design, rehabilitation, inspection and special technical advice on risk management for dams.

The Effect of Saturated Lime Solution on Increasing the Strength of Silty Sandy Soils

Forough Hassanvand¹, Mohammad Hadi Davoudi²

1- Central Branch, Islami Azad University, Tehran, Iran

2- Neishabur Islamic Azad University, Neishabur, Iran

Email: Hsn.forough@gmail.com

Abstract

Due to the increase of construction projects, we are faced with the necessity of using lands, having loose and soft soils more than before. Recently a new method for strengthening these soils has been developed, by which saturated lime is intruded into soil. As it penetrates due to the gravity, improves the soil strength through pozzolanic reactions. In this paper, the influence of two key parameters, on the improvement of unconfined strength of sandy soils is studied. Two sets of laboratory tests were conducted on silty sandy soil specimens. In the first set, the saturated lime solution (SLS) was intruded with different volumes through the specimens and then they have been used for uniaxial strength test. In the second set, after passing specific volume of SLS through the specimens, they have spent different curing times under controlled humidity and temperature conditions, then have been used for uniaxial strength test. The first set of tests indicates that the uniaxial strength increases with an increase of the volume of infiltrated solution linearly. And the second indicates, contrarily to clay soils, the curing time, cannot be a contributing factor to the improvement of the silty sandy soils.

Keywords: stabilization, the volume of infiltration, curing time, uniaxial stress, silty sandy soils.

1. INTRODUCTION

Using the Calcium cation is common in civil projects. The main method for having that is by virtue of lime. Adding lime to increase the strength parameters of fine graded soils have been used before. Alongside with environmental issues, the economy of projects should be considered as a significant factor that should be relevant to the importance of site.

Although using lime as a whitewash or dry mixture with soils have been suggested by Puppala et al., (2003) [1], Rao and Shivananda, (2005) [2], Farzaneh and Mosaddegh (2007) [3] and other researchers for fine graded soils, it is not practicable because of not being able to move the rockfill materials. As had been studied by Davoudi (2007) [4], if the lime is soluted in water and infiltrated as a saturated lime solution, the result will be the increase of the friction angle and cohesion in soils. This recently used method by researchers is known as Saturated Lime Solution (SLS).

There has been researches such as Rostami (2010) [5], "Investigation on Effects of Saturated Lime Solution on Uniaxial Compressive Strength of Clayey Soils", that has shown this method is economical comparable in stabilizing the landslides. But there has been no research for this method on silty sandy soils so far. In this research, it has been tried to study the usage of SLS method on silty sandy soils by means of investigating the volume of filtration and the curing time after that.

2. THISIS METHOD

This study has been done on silty sandy soils by virtue of laboratory tests. The soil had 7.5% clay and $PI=0$, it was categorized due to ASTM-D422 as SM. By standard proctor test, its maximum dry density was 1.92 gr/cm³ while its optimum moisture content was 12%.

A special device has been designed and made for this research including three parts: cylinder molds with 50 mm diameter and 130 mm height, cubic tank with 50*150*150 mm capacity and a big tank with 500*500*800 mm capacity. The tanks have been connected by plastic vessels and the filtration was upside down through the soil specimens. All specimens were compacted at 10% moisture content, in 10 cm height, 95% of standard compaction and with dry density of 1.80 gr/cm³. For each specimen, specific volume of saturated lime was passed in 48 hours. After filtration completed, the cylinder was separated from the cubic tank. In 7 specimens, water was penetrated for comparison purpose. In 10 specimens, different volume of saturated lime was penetrated and then they were used for uniaxial strength test. In 16 other specimens, saturated lime was passed through the soil in 48

hours, then they had curing times of 4, 8 and 28 days, then they were used for uniaxial strength test as well. The “controlled stress” uniaxial test has been held in this study.

For evaluation, the volume of penetration is presented based on their void volume (V_v). And also, to ease the comparison between results, the “relative uniaxial strength” is defined as the equation 1 below in which, q_{u0} and q_u are the strength of unreformed and reformed specimens respectively.

$$\Delta q_u = \frac{q_u - q_{u0}}{q_{u0}} \times 100 \quad (1)$$

In the equation above, q_{u0} is derived from the uniaxial strength plotted versus the specific dry density in unreformed specimens, shown in fig.1 which is presented as equation 2:

$$q_{u0} = 0.0249(\rho_d)^{15.977} \quad (2)$$

In addition, the “relative failure strain” is presented in equation 3 in which ε_u is the strain of reformed specimens and the ε_{u0} is the strain of the unreformed ones which has been derived from the failure strain plotted versus the specific dry density in unreformed specimens, shown in fig.2 which is presented as equation 4.

$$\Delta \varepsilon = \frac{\varepsilon_{u0} - \varepsilon_u}{\varepsilon_{u0}} \times 100 \quad (3)$$

$$\varepsilon_{u0} = 0.5916 - 0.984 \ln(\rho_d) \quad (4)$$

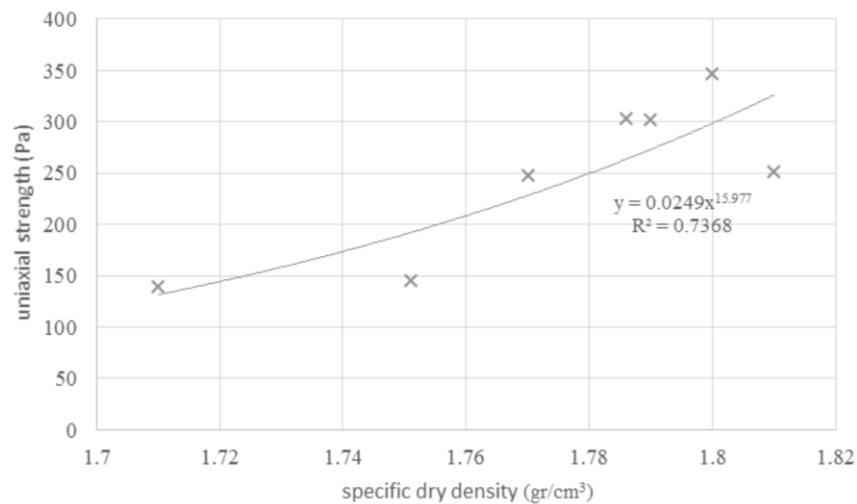


Fig 1: Uniaxial strength versus specific dry density in unreformed specimens

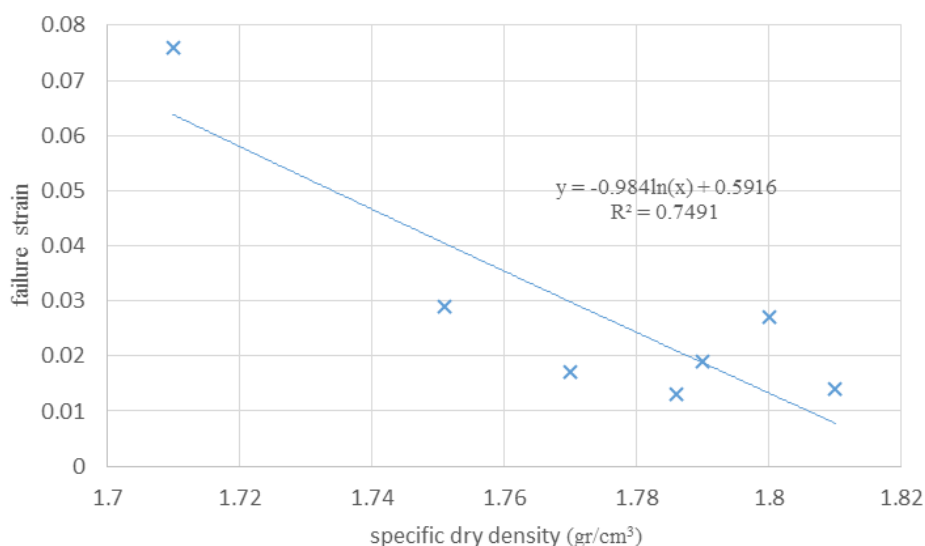


Fig. 2: Failure strain versus specific dry density in unreformed specimens

3. RESULTS AND DISCUSSION

The results of first set of tests are presented in table 1.

Table 1: Results of uniaxial strength test in first set of specimens

Volume of penetration (V _v)	Relative failure strain (%)	Relative uniaxial strength (%)	Failure strain mm/mm	Maximum uniaxial strength Pa	NO.
1.5	559.48	3.5	0.014	402.09	L-4-5-10
4.53	9.21	1.71	0.012	303.43	L-1-1-14
4.95	-12.3	45.03	0.021	395.8	L-1-12-9
6.26	-93.14	8.72	0.015	354.37	L-1-4-26
6.47	53.59	110.3	0.019	400	L-4-5-2
6.95	3.74	65.07	0.018	450.5	L-2-5-20
7.87	-111.83	15.1	0.028	343.38	L-3-5-10
7.88	16.78	0.34	0.011	299.33	L-3-4-26
9.27	36.15	76.03	0.019	401.47	L-2-4-26
10.5	54.57	82.49	0.011	455.4	L-1-4-14
11.6	2.29	78.57	0.040	339.64	L-1-5-17
13.27	34.90	184.55	0.023	592.81	L-1-5-2
16	25.66	343.32	0.018	1106.32	L-1-3-19
16.51	-15.64	75.19	0.028	437.18	L-1-5-20
21.77	49.59	275.6	0.015	856.64	L-2-4-14
24.37	15.09	179.2	0.030	581.67	L-3-5-2

The purpose of first set was identifying the effect of the volume of solution penetrated on uniaxial strength as it is shown in figure 3.

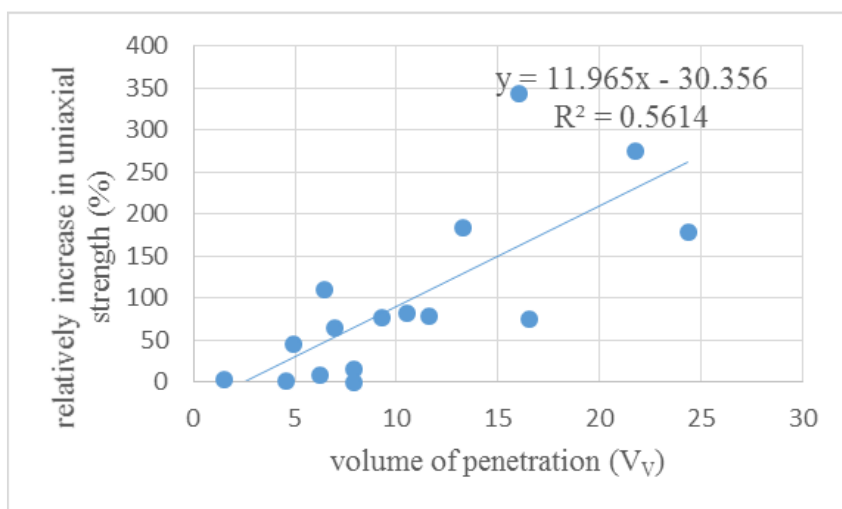


Fig 3-1: All specimens of the first set

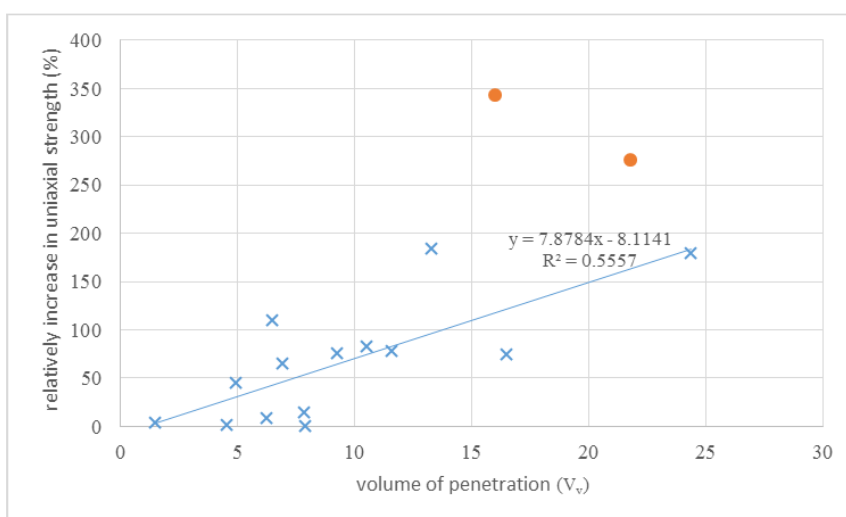


Fig. 3-2: All specimens in first set without considering L-2-4-14 and L-1-3-19

Fig 3: Relative uniaxial strength versus volume of penetration in first set without considering L-2-4-14 and L-1-3-19

Specimens L-12-4-14 and L-1-3-19 had different behavior in comparison with others. Without considering these two specimens, the correlation will not get better, but considering that, without any solution the relative uniaxial strength would be equal to zero, the graph in which the correlation is close to zero would be acceptable. Therefore, according to Fig 3-2, the equation can be derived for the “volume of penetrated solution” and the “relative uniaxial strength” as presented in equation 5.

$$\Delta q_u = 7.8784V - 8.1141 \quad (5)$$

In case of comparison between this study and the same on CL-ML soils (Rostami, 2010, [5]), figure 4 is presented.

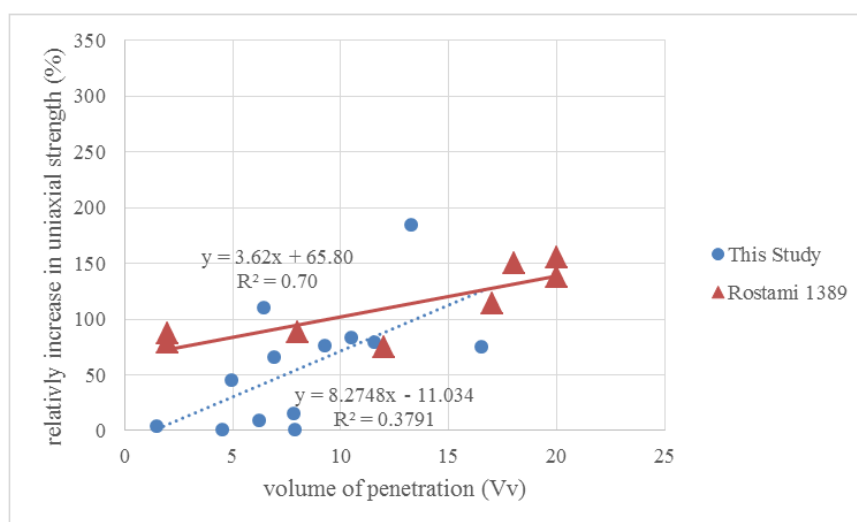


Fig. 4: Comparison in relative uniaxial strength versus volume of penetration between this study and Rostami 2010 [5]

Figure 4 illustrates that in case of less than $20V_v$ of penetrated solution, the increase in relative uniaxial strength in CL-ML is much more than in SM. This might be a reason of the soil nature that the passing of sieve NO.200 in CL-ML was around 65% while it was almost 29% in SM. The uniaxial strength between these two soil types are different as well, in CL-ML with 80% of compaction, it is around 40 kPa while in SM with 95% of compaction it is around 0.3 kPa, that might be a result of cohesion in clays. This cohesion causes chemical reaction between Ca^{++} and clay minerals. Table 2 shows the uniaxial strength after filtration of different volume of solution in specimens. Consequently, by increase of the volume of filtration in specimens, the effect of this method will be more noticeable.

Table 2: Comparison of uniaxial strength (kPa) between CL-ML and SM after filtration of different volumes of solution

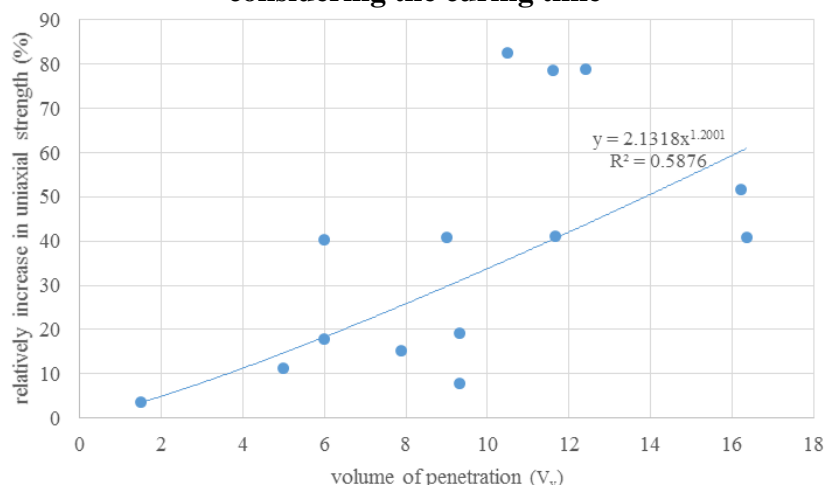
		Volume of filtration (V_v)	0	5	10	15	20
Soil Type	(This Study) SM		0.32	0.37	0.42	0.47	0.52
	(Rostami, 2010 [5]) CL-ML		41.45	46	46	55.1	59.65

The results of the second set of tests are shown in table 3. Also, in figure 5 the relative uniaxial strength versus volume of penetration without considering the curing time, is presented.

Table 3: Results of uniaxial strength test in second set of specimens

Volume of penetration (V_v)	Curing time (day)	Relative failure strain (%)	Relative uniaxial strength (%)	Failure strain mm/mm	Maximum uniaxial strength Pa	NO.
1.5	4	559.48	3.5	0.014	402.09	L-4-5-10
5	28	-1435.26	11.22	0.036	395.82	L-3-6-14
6	28	-36.18	17.83	0.018	351.50	L-4-6-14
6	8	17.40	40.26	0.020	350.03	L-2-5-27
7.87	4	-36.18	15.1	0.018	343.38	L-3-5-10
9	8	54.57	40.92	0.011	249.55	L-2-6-10
9.3	28	-144.64	7.89	0.019	351.65	L-2-5-31
9.3	28	17.40	19.25	0.020	297.59	L-1-5-31
10.5	4	54.57	82.49	0.011	455.4	L-1-4-14
11.6	4	2.29	78.57	0.040	339.64	L-1-5-17
11.65	8	33.92	41.17	0.016	352.2	L-2-5-24
12.4	28	-210.85	78.78	0.041	533.36	L-1-6-14
16.22	8	26.06	51.69	0.022	345.97	L-1-5-24
16.35	28	-27.37	40.72	0.045	293.17	L-2-6-7

Fig. 5: Relative uniaxial strength versus volume of penetration in second set without considering the curing time



The results are shown in figure 6

This figure (5) illustrates the effect of volume of filtration on increase in uniaxial strength even without considering the curing time.

To evaluate the effect of “curing time” on “uniaxial strength”, specimens are divided in two groups based on the volume of filtration:

1. first group, which less than $10V_v$ of solution is passed
2. second group, which more than $10V_v$ is passed

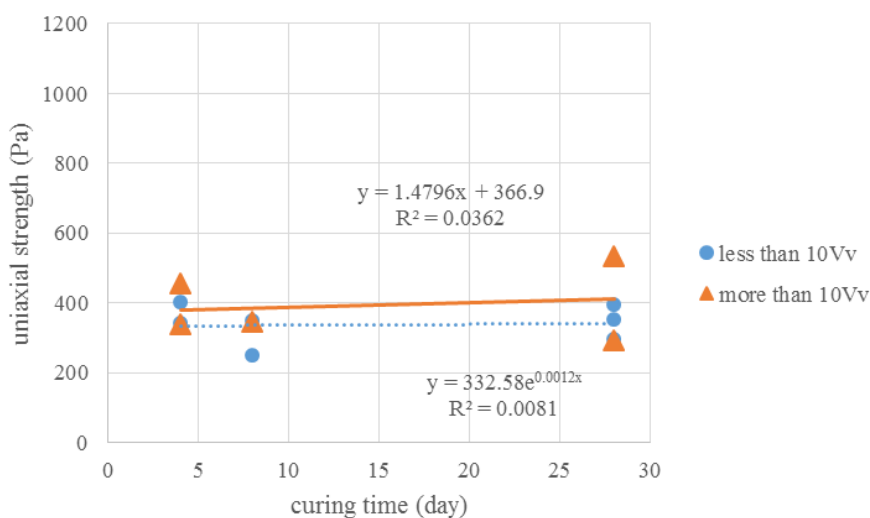


Fig. 6: Uniaxial strength versus curing time in all specimens of second set

As it can be seen, curing time does not affect uniaxial strength of specimens that might be as a result of lack of clay minerals in SM to reach the goal in this method. In other words, the access of the increase in strength in this method requires clay minerals for pozzolanic reactions which is around 7.5% in the tested soil in this study. Also, due to passing more saturated lime in second group, we can see an increase in uniaxial strength in comparison with the first group.

In the research had been done by Rostamiy (2010) [5], for three groups of $19V_v$, $28V_v$ and $40V_v$, as it is shown in figure 7, correlations between uniaxial strength versus curing time, have been found.

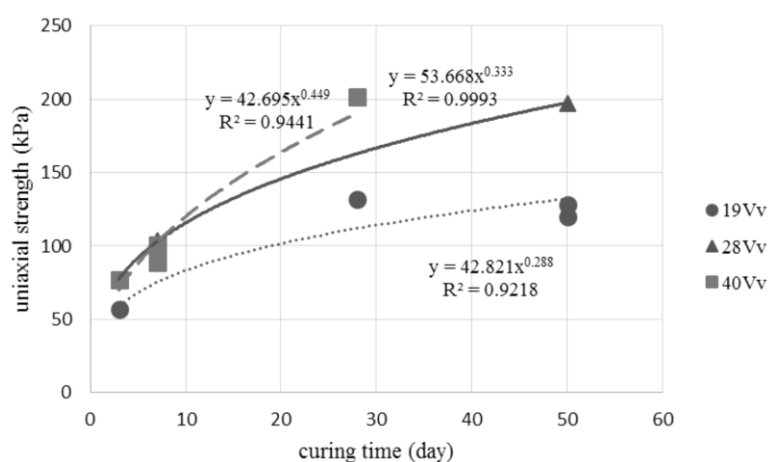


Fig. 7: Comparing the uniaxial strength of three CL-ML groups treated with different volume of solution versus curing time (Rostami, 2010 [5])

Comparing these two figures (6 and 7) illustrates that due to lack of clay minerals in SM soils, curing time is not as effective as it is in increasing the relative uniaxial strength in CL-ML soils, which has a relation with the volume of filtration, as the more volume of solution passed, the more effectiveness of this method by passing curing time can be seen.

4. CONCLUSIONS

The study has been shown that there is no correlation between the volume of filtration and failure strain in SM soils. Also because of the difference of soil natures in CL-ML and SM, in case of the volume of less than 20V_v of filtration, the relative uniaxial strength in SM is much less than it is in CL-ML due to less clay minerals in SM, that causes less cohesion. In addition, by increasing the volume of saturated lime solution passed through SM, the uniaxial strength can be more affected. The studies have been shown that in case of the 17V_v of filtration, the increase of relative uniaxial strength in both SM and CL-ML soils are the same considerable value of 129%. In CL-ML specimens due to the presence of clay minerals, noticeable increase of relative uniaxial strength can be seen after curing time.

5. REFERENCES

1. A. J. Puppala, E. Wattanasanticharoen, and K. Punthutaecha, (2003). Experimental evaluations of stabilization methods for sulphate-rich expansive soils. Department of Civil and Environmental Engineering, Box 19308. The University of Texas at Arlington, Arlington, Texas 76019, USA.
2. Rao and Shivananda (2005). Impact of Sulfate Contamination on Swelling Behavior of Lime-Stabilized Clays. Journal of ASTM International, vol.2, NO.6, 2005, pp.1-10.
3. Farzaneh and Mosaddegh (2010). Laboratory study of rockfill stabilization on Kerman- Zangi Abaad road by using of four materials, lime, RRP, ZAM I and ZAM II. Faculty of Engineering, Tehran University. Islamic Republic of Iran (in Persian).
4. Davoudi, Mohammad Hadi (2007). The Increase of Shear Strength of Landslides by means of Lime Trench. Soil Conservation and Watershed Management Research Center, Tehran, Islamic Republic of Iran (in Persian).
5. Rostami, Mehdi (2010). Thesis for Master degree. Investigation on Effects of Saturated Lime Solution on Uniaxial Compressive Strength of Clayey Soils. Faculty of Engineering, Tehran Central Branch, Islamic Azad University, Tehran, Islamic Republic of Iran (in Persian).

Strategies for Greenhouse Gases Mitigation in Hydro-Electrical Water Reservoir

Saeed Karbin¹, Hadi Karbin², Hossein Ali Alikhani¹

1- Department of soil science engineering, University College of Agriculture & Natural Resource, University of Tehran, Karaj, Iran

2- Water Research Institute, Center of Micro-hydro Power Technology Development, Tehran, Iran

Email: saeed.karbin@ut.ac.ir

Abstract

There are many uncertainties for greenhouse gases (GHG) emission in hydro-electrical water reservoirs. GHG sources and sink are different than ponds and lakes and they should be addressed specifically to understand the processes affecting GHG emissions. In many studies, only limited sources and sinks are included in models and it leads to production of unreal GHG budget for water reservoirs. In this study, we discussed different sources and sinks in water reservoirs for calculation of GHG net fluxes. Among the sources, water-level drawdown and turbine degassing effects are specifically for hydro-electrical water reservoirs and molecular diffusion, ebullition, plant-mediated transport and woody material decomposition might happen in ponds or lakes. The water-level drawdown magnitude and timing has a huge effect on ebullition events and it might be the reason for wide variation of GHG fluxes in different studies. Regarding the sinks, proper methods should be selected to measure carbon burial in sediments, net primary production in aqueous environment, vegetation in landscape of coast and CH₄ oxidation in landscape of coast precisely. Methanotrophic activity in the soils around the reservoir induced by alteration in hydrological regimes and land use changes after creation of the reservoir is not included in GHG prediction models yet. Reservoir management, improving green carbon capture in shore lines and afforestation around the reservoir are main strategies for GHG mitigation in water reservoirs.

Keywords: greenhouse gas, reservoir, sources, sinks.

1. INTRODUCTION

It has shown in recent studies that water reservoirs are sources of greenhouse gases (carbon dioxide (CO₂), methane (CH₄), and nitrous oxide (N₂O)) for the atmosphere [1, 2]. Inland waters contain large quantities of organic carbon produced by terrestrial primary production [3]. Carbon input is dominated by dissolved organic carbon (DOC) and it can increase microbial production and respiration. Gradually, this addition leads water to be CO₂ supersaturated and act as a source for greenhouse gases (GHG) fluxes [4].

In the first studies, hydroelectric power was considered as a carbon-free source of energy (i.e.[5]). Rudd *et.al.*, for the first time, concluded that the greenhouse gas production per unit of power generated is not zero [6]. Although recent development in GHG flux measurements there are uncertainties in GHG emission in water reservoirs. There are two main reasons for these uncertainties: i) GHG fluxes are measured by different methods (e.g., floating chamber, thin boundary method, eddy covariance tower, acoustic methods and funnels). CO₂ and N₂O are soluble in water (mole fraction solubility of 7.07×10^{-4} and 5.07×10^{-4} respectively at 20°C) and the dominant flux pathway is the air-water interface. In contrast, CH₄ is relatively insoluble in water and often emitted from the sediment in the form of bubbles [7, 8]. Several methods do not capture ebullition events (e.g., air-water gas exchange) or exclude ebullition due to interfere with the linear accumulation of CH₄ in the sampling chamber. ii) Temporal and spatial variation of aquatic GHG fluxes is high. For instance, CH₄ ebullition measured by funnel traps are deployed for relatively short period of time in relatively limited number of locations. However, it is not convenient to estimate both temporal and spatial variability of fluxes[8].

Investigating on GHG sources and sinks in water reservoirs facilitate the process to have a real estimation of GHG budget and manage the existing sinks and sources to mitigate GHG emissions. There are very limited studies that included all GHG sinks and sources in estimation of GHG emissions. However, a guideline for future studies to include the most affecting sources and sinks for GHG emission in water reservoirs is crucial. In below sections, we will discuss briefly GHG sources and sinks. Finally, we will focus on GHG mitigation strategies in water reservoirs for moving to carbon-neutral hydropower production.

2. GREENHOUSE GAS SOURCES

Water reservoirs around the world can affect biogeochemical cycles of elements (e.g., carbon and nitrogen). Although reservoirs are considered as a carbon-neutral sources of energy, there are many studies reported their role as GHG sources. There are very limited studies to include all possible GHG sources and pathways in their investigations. GHG sources in water reservoirs may vary than lakes and ponds and should be addressed specifically.

2.1 MOLECULAR DIFFUSION

CO₂ is highly soluble in water and therefore deep water layer depth contain higher CO₂ concentration. Photosynthesis at surface layers can deplete CO₂ in this layer and lead to an influx of atmospheric CO₂. In water reservoirs where photosynthesis rate is not high at the surface layer, water is over saturated with CO₂ and release CO₂ into the atmosphere. N₂O like CO₂ is soluble in water and diffusive loss is high. In contrast, CH₄ is insoluble in water and consequently rate of diffusive loss to the atmosphere is relatively low. Floating chambers are regularly used to measure diffusive gas flux in aquatic surfaces. Both spatial and temporal variation of gas fluxes can be measured by placing numerous chambers in different location and various time.

2.2 EBULLITION

This is the main gas transportation pathway when an insoluble gas (e.g., CH₄) produced in sediment cannot be dissolve in water and consequently produced bubbles emit into the atmosphere by ebullition[9]. Funnel trap is the most used method to capture ebullition which float beneath the surface of water. In recent years development modified funnel traps can measure bubbles in longer-term by incorporating an air tight tank equipped with a differential pressure sensors or optical bubble size sensors [10]. Acoustic techniques or an echosounder mounted with a boat or a stationary object associated with funnel traps can support higher spatial and temporal resolution for ebullition measurements [8, 11, 12].

2.3 PLANT-MEDIATED TRANSPORT

Plants can transport CH₄ produced in the rhizosphere through the *aerenchyma* tissue into the atmosphere. There are many studies showing that more than half of CH₄ emitted from wetland soils, including rice paddies, was plant-mediated transport [13, 14]. Plants growing along the shore in water reservoirs can transport considerable amount of CH₄ from the anoxic soils. In the majority of studies for water reservoirs, GHG budget measurements vegetation effects, especially for CH₄, are ignored.

2.4. WATER LEVEL DRAWDOWN

Water level management can substantially affect the magnitude and timing of CH₄ fluxes into the atmosphere. Although water-level fluctuation can clearly affect the timing and the magnitude of CH₄ fluxes in reservoirs there have been very limited of this effect in reservoirs. Harrison *et. al.*, showed that water-level fluctuations can increase drastically CH₄ fluxes to the atmosphere [15]. They examined CH₄ emission dynamic in six reservoirs varying in trophic status, morphology and management regime. They reported water-level drawdowns can increase CH₄ emission for more than 90% of annual reservoir CH₄ flux in a period of just few weeks. However, it is possible to reduce CH₄ fluxes in reservoirs by water-level management.

2.5 DEGASSING BY TURBINES

As water undergoes rapidly depressurization or aeration dissolved gases can be emitted. After water passes through the turbines GHG gases can be emitted into the atmosphere or can be absorbed by microbes (e.g., CH₄ oxidation by methanotrophic bacteria). Large degassing emission are expected when GHG content in spilled water is high. Rohem and Tremblay [16] reported that the highest quantity of degassing observed in winter and spring when water temperature and CO₂ solubility were low and the buildup of gases due to mineralization of organic matter and the influx from watershed sources due to the springtime melt were high. They concluded that depending on the effluxes occurring at the air-water interface of the main reservoir, degassing can represent a maximum equivalent 16%.

2.6 WOODY MATERIAL DECOMPOSITION

Abril, G., et al reported that standing woody material decomposition constitute a high amount (26-45% of CO₂ equivalents in a 100-year period) of total GHG emissions in tropical reservoirs [16]. This GHG source should be investigated in future studies in temperate and arid regions.

3. GREENHOUSE GAS SINKS

After creating a water reservoir carbon can be captured in several pathways. To have a real estimation for GHG budget carbon sink strengths should be investigated and included in real budget calculation. In many studies and investigations for calculation of net GHG emissions, carbon sources are included in models but the capacity of carbon sinks are underestimated or ignored. In below we present the main carbon sinks in water reservoirs.

3.1 CARBON BURIAL IN SEDIMENT

Inland water reservoirs can accumulate carbon more than natural lakes because of higher sedimentation rate (three to four times higher, [17]). The real carbon accumulation rate in water reservoirs is not well-investigated yet. The potential of water reservoirs in carbon sequestration depends on organic carbon deposition rate, efficiency of organic carbon preservation process and the life-span of system. In more productive and smaller systems organic carbon deposition rate and organic carbon burial are high. Organic carbon preservation efficiency depends on sediment source, oxygen exposure and temperature [18-20]. There are few studies on organic carbon burial assessment in artificial reservoirs and applying a precise method for estimation of sediment deposition rates, organic carbon content and sediment density measurements remain challenging. Mendonça *et al.*, (2014) determined the organic carbon burial rate and the total organic carbon stock accumulated in the sediments of a tropical reservoir by combining sediment sample analyses and a seismic survey. They estimated organic carbon burial in two tropical reservoirs was about 2.5 times lower than emission in one reservoirs and about 2.5 times higher in the other one. The main two important factor for this variations were the trophic state and the sediment load.

3.2 NET PRIMARY PRODUCTION IN AQUEOUS ENVIRONMENT

Primary production is the synthesis of organic compounds from atmospheric or aqueous CO₂. This process occurs by photosynthesis which uses the light as a source of energy. Gross primary production (GPP) is the amount of chemical energy as biomass that primary producers produce in given time. Some fraction of this energy is used by primary producers as cellular respiration and maintenance of tissue. The remaining fixed energy is referred as net primary production (NPP). The main primary producers in aquatic environments are planktonic algae (phytoplankton), periphytic algae (periphyton) and macrophytes (aquatic plants). The relative contribution of these main primary producers to total primary production depends on basin morphology, water clarity, substrate suitability and extent of water level fluctuations. Phytoplankton productivity is higher in reservoirs than natural lakes. Reservoirs are located in fertile regions and however, the natural trophic equilibrium level is higher than most of natural lakes [21]. Primary production is influenced by water size of reservoir, latitude, insolation and nutrient availability [22].

In addition, aquatic vegetation in water reservoir has the high potential to capture carbon. For example, it has been shown that over 10 years after dam construction the most rapid changes in soil cover was the area of aquatic vegetation [23]. These plants sequester atmospheric CO₂ and however act as a carbon sink in reservoir environment. Bini *et al.*, [24] showed that floating macrophyte assemblage in water reservoirs has a direct relation with nutrient concentration in both sediment and water and light penetration was the strongest predictor of submerged species occurrence. Perera *et al.*, [25] showed that vegetation in coastal water can be functionally as sink for atmospheric CO₂ and this was contrary with previous studies considering near-shore ecosystems as a source of CO₂. The key factor for determining whether or not coastal ecosystems directly decrease the concentration of atmospheric CO₂ may be net ecosystem production.

3.3 VEGETATION OF LANDSCAPES OF COASTS

Soil hydrological regime changes can affect land cover, wildlife, and micro-climatic conditions. Increased water table depth induced by water reservoir leads to changes in soil physio-chemical properties and soil cover. Creating a reservoir can change plant species richness and plant community structure in the coastal regions and the places where soil hydrological regime is affected. This effect can be more obvious in arid and semi-arid regions where water is the main limiting factor for the region.

Many studies demonstrate that, on shore of reservoirs, several years after the construction the changes in ecological conditions promote the growth of tree vegetation. The magnitude of these changes depends on geographic position of reservoir and local geological-geomorphological condition of the coast. Novikova and Nazarenko [26] reported that the soil vegetation cover and the species number tend to increase in the direction away from the coast in water reservoirs. They concluded that this is the results of diversity of conditions in the biotope and a decrease in the externality of factors. They added that the typical vegetation after creating the reservoirs for steppe zones includes 115 species of higher vascular plants from 29 families. The leading families were *Asteraceae*, *Poaceae*, *Fabaceae*, *Chenopodiaceae*, *Labiatae*, and *Polygonaceae*. Lange *et. al.*, [27] showed that in diverse plant communities soil carbon storage and soil microbial communities are higher than in soils with low species number. However, creating water reservoir can increase carbon sequestration rate by increasing vegetation growth and plant diversity in landscape of coasts.

However, creating water reservoir can change soil vegetation and through this process atmospheric CO₂ can be captured. In most of recent biogeochemical models for GHG emissions, this effect is ignored.

3.4. CH₄ UPTAKE IN LANDSCAPE OF COAST

Methanotrophic bacteria have the ability to utilize CH₄ as their energy source [28] and have been found in many terrestrial ecosystems. Soil moisture is the main driver of methanotrophic activity. In the other hand, water stress can restrict the activity of methanotrophic bacteria. The optimal range of water content depends on land use. In grassland soils, maximum CH₄ oxidation occurred in a range from 18 to 33% of gravimetric moisture content and in forest soils, optimal soil moisture was between 30 and 51% [29]. Creating water reservoir can alter soil moisture in the landscape of the coast and optimise methanotrophic activity in the oxic soils. In many studies effects of water reservoirs on methanotrophic activity in the coastal soil are ignored and it should be investigated in future studies. In addition, land use changes in the coastal landscapes can improve soil CH₄ oxidation. Karbin *et. al.*, [30] showed that CH₄ oxidation in grassland soils is less than forests and it increases as the forest stand age increases. However, the forest soils around the reservoirs has the potential to increase soil CH₄ oxidation and decrease the net CH₄ emission.

4. GHG MITIGATION STRATEGIES IN WATER RESERVOIRS

Renewable energy sources such as hydropower contribute significantly to the GHG emission reduction. Comparing with conventional coal power plants hydropower reduce CO₂ emission about 3 GT annually or about 9% global annual CO₂ emission [31]. Over last decade there has been many investigations on methodologies of GHG budget in hydropower reservoirs and in some cases, unreal data in GHG emission has challenged hydropower development. As an instance, in some studies in early 2000 estimated hydropower emissions as high as 7% of global emissions. High level of GHG emission estimations were due to studies at sites with very unfavorable conditions. In the recent synthesis by Deemer *et.al.*, [8] CO₂ and N₂O fluxes in reservoirs are lower than anthropogenic or natural sources as reported by the IPCC and CH₄ emissions are similar to rice paddies. GHG mitigation and adaptation programs in water reservoirs are important and should be considered in reservoir management. Mitigation refers to reduce the source or enhance the sinks for GHG and adaptation assign for adjustment in natural or human systems in response to actual or expected effects of global warming conditions which moderate negative effects or exploits beneficial opportunities.

Reservoir management can mitigate GHG fluxes in reservoirs by affecting CH₄ ebullition events. Demmer *et. al.*, [8] demonstrated that water level drawdown events affects timing and the magnitude of CH₄ ebullition substantially in water reservoirs. Decreasing the number and the magnitude of drawdowns could decrease CH₄ emissions but there is a potential trade-off between power generation and GHG fluxes. In addition, it is possible to reduce CH₄ emission by changing drawdown timing from the end of the stratified summer to a period when waters are better mixed. This allows rapid methanotrophy at the sediment-water interface.

Moreover, in recent studies “Blue Carbon” refers for the carbon captured by aquatic living organisms and has been recently highlighted as a new method for climate change mitigation strategy. For instance, carbon sink capacity of seagrass meadow in water reservoirs could be used to support strategies to mitigate climate change. Carbon accumulation rate for seagrass meadow is reported between 83 and 133 g C m⁻² y⁻¹ and about 50% of this organic matter is driven from seagrass tissue. However, between 41 and 66 g C m⁻² y⁻¹ of the organic matter produced by seagrasses become buried in the sediments [32].

In addition, methanotrophic bacteria in upland soils can oxidize atmospheric CH₄ and act as a sink for emitted CH₄ from reservoirs. Forest soils pose the highest ability in CH₄ oxidation comparing to other different land uses (e.g., grasslands, agricultural fields). However, afforestation and land use changes (i.e., altering rangeland to forest) rooted from microclimatic effects of water reservoirs can increase CH₄ sink strength.

5. CONCLUSIONS

There are many uncertainties in GHG flux estimation for hydro-electrical water reservoirs. Some of these uncertainties are results of selecting improper sampling methods to collect data with clear spatial and temporal resolution. Including data for all sinks and sources strengths in biogeochemical models is the next challenge for estimation of GHG budget in water reservoirs. This is due to very limited studies with proper data collection for all available sinks and sources water reservoirs. To mitigate GHG fluxes in water reservoir the strengths of the sinks and sources should be determined first and the proper method should be selected in next step. Water-level management has a huge effect on CH₄ ebullition events and should be done when water is not stratified and is better mixed. Methanotrophic activity in soils in the landscape of the coast and “Blue Carbon” capture by aquatic vegetation in the shore line are important GHG sinks and should be included in biogeochemical models for water reservoirs.

6. REFERENCES

1. St. Louis, V.L., et al., *Reservoir Surfaces as Sources of Greenhouse Gases to the Atmosphere: A Global Estimate* Reservoirs are sources of greenhouse gases to the atmosphere, and their surface areas have increased to the point where they should be included in global inventories of anthropogenic emissions of greenhouse gases. *BioScience*, 2000. 50(9): p. 766-775.
2. Rosenberg, D.M., et al., *Large-scale impacts of hydroelectric development*. *Environmental Reviews*, 1997. 5(1): p. 27-54.
3. Cole, J.J., et al., *Plumbing the global carbon cycle: integrating inland waters into the terrestrial carbon budget*. *Ecosystems*, 2007. 10(1): p. 172-185.
4. Duarte, C.M. and Y.T. Prairie, *Prevalence of heterotrophy and atmospheric CO₂ emissions from aquatic ecosystems*. *Ecosystems*, 2005. 8(7): p. 862-870.
5. Victor, D.G., *Strategies for cutting carbon*. *Nature*, 1998. 395(6705): p. 837-838.
6. Rudd, J.W., et al., *Are hydroelectric reservoirs significant sources of greenhouse gases*. *Ambio*, 1993. 22(4): p. 246-248.
7. Bastviken, D., et al., *Methane emissions from lakes: Dependence of lake characteristics, two regional assessments, and a global estimate*. *Global biogeochemical cycles*, 2004. 18(4).
8. Deemer, B.R., et al., *Greenhouse gas emissions from reservoir water surfaces: a new global synthesis*. *BioScience*, 2016. 66(11): p. 949-964.
9. Chanton, J.P., C.S. Martens, and C.A. Kelley, *Gas transport from methane-saturated, tidal freshwater and wetland sediments*. *Limnology and Oceanography*, 1989. 34(5): p. 807-819.
10. Delwiche, K., S. Senft-Grupp, and H. Hemond, *A novel optical sensor designed to measure methane bubble sizes in situ*. *Limnology and Oceanography: Methods*, 2015. 13(12): p. 712-721.

11. Ostrovsky, I., et al., *Quantifying gas ebullition with echosounder: the role of methane transport by bubbles in a medium-sized lake*. *Limnology and Oceanography: Methods*, 2008. 6(2): p. 105-118.
12. DelSontro, T., et al., *Size does matter: Importance of large bubbles and small-scale hot spots for methane transport*. *Environmental science & technology*, 2015. 49(3): p. 1268-1276.
13. Cicerone, R.J. and J.D. Shetter, *Sources of atmospheric methane: measurements in rice paddies and a discussion*. *Journal of Geophysical Research: Oceans*, 1981. 86(C8): p. 7203-7209.
14. Ding, W., Z. Cai, and H. Tsuruta, *Plant species effects on methane emissions from freshwater marshes*. *Atmospheric Environment*, 2005. 39(18): p. 3199-3207.
15. Harrison, J.A., et al., *Reservoir water-level drawdowns accelerate and amplify methane emission*. *Environmental science & technology*, 2017. 51(3): p. 1267-1277.
16. Roehm, C. and A. Tremblay, *Role of turbines in the carbon dioxide emissions from two boreal reservoirs, Québec, Canada*. *Journal of Geophysical Research: Atmospheres*, 2006. 111(D24).
17. Abril, G., et al., *Carbon dioxide and methane emissions and the carbon budget of a 10-year old tropical reservoir (Petit Saut, French Guiana)*. *Global biogeochemical cycles*, 2005. 19(4).
18. Dean, W.E. and E. Gorham, *Magnitude and significance of carbon burial in lakes, reservoirs, and peatlands*. *Geology*, 1998. 26(6): p. 535-538.
19. Sobek, S., et al., *Organic carbon burial efficiency in lake sediments controlled by oxygen exposure time and sediment source*. *Limnology and Oceanography*, 2009. 54(6): p. 2243-2254.
20. Gudasz, C., et al., *Temperature-controlled organic carbon mineralization in lake sediments*. *Nature*, 2010. 466(7305): p. 478-481.
21. Mendonça, R., et al., *Carbon Sequestration in a Large Hydroelectric Reservoir: An Integrative Seismic Approach*. *Ecosystems*, 2014. 17(3): p. 430-441.
22. Kimmel, B.L. and A.W. Groeger, *FACTORS CONTROLLING PRIMARY PRODUCTION IN LAKES AND RESERVOIRS: A PERSPECTIVE*. *Lake and Reservoir Management*, 1984. 1(1): p. 277-281.
23. Downing, J., et al., *The global abundance and size distribution of lakes, ponds, and impoundments*. *Limnology and Oceanography*, 2006. 51(5): p. 2388-2397.
24. Bogdanets, V. and A. Vlaev, *Analysis of land use changes near large water bodies in Ukraine using GIS*. *Journal of environmental biology*, 2015. 36(1): p. 37.
25. Bini, L.M., et al., *Aquatic macrophyte distribution in relation to water and sediment conditions in the Itaipu Reservoir, Brazil*, in *Biology, Ecology and Management of Aquatic Plants: Proceedings of the 10th International Symposium on Aquatic Weeds, European Weed Research Society*, J. Caffrey, et al., Editors. 1999, Springer Netherlands: Dordrecht. p. 147-154.
26. Perera, K., M. Amarasinghe, and W. Sumanadasa. *Contribution of plant species to carbon sequestration function of mangrove ecosystems in Sri Lanka*. in *Meeting on Mangrove ecology, functioning and Management (MMM3) 2-6 July 2012, Galle, Sri Lanka*. 2012.
27. Novikova, N. and O. Nazarenko, *Natural complexes of shores of artificial reservoirs in territories of southern part of European Russia*. *Arid ecosystems*, 2013. 3(3): p. 131-143.
28. Lange, M., et al., *Plant diversity increases soil microbial activity and soil carbon storage*. *Nature Communications*, 2015. 6: p. 6707.
29. Semrau, J.D., A.A. DiSpirito, and S. Yoon, *Methanotrophs and copper*. *FEMS microbiology reviews*, 2010. 34(4): p. 496-531.

30. Czepiel, P., P. Crill, and R. Harriss, *Environmental factors influencing the variability of methane oxidation in temperate zone soils*. Journal of Geophysical Research: Atmospheres, 1995. 100(D5): p. 9359-9364.
31. Karbin, S., et al., *Spatial micro-distribution of methanotrophic activity along a 120-year afforestation chronosequence*. Plant and Soil, 2017. 415(1-2): p. 13-23.
32. Berga, L., *The Role of Hydropower in Climate Change Mitigation and Adaptation: A Review*. Engineering, 2016. 2(3): p. 313-318.
33. Kennedy, H., et al., *Seagrass sediments as a global carbon sink: Isotopic constraints*. Global biogeochemical cycles, 2010. 24(4): p. n/a-n/a.

Optimizing Selective Withdrawal System in Reservoir to Manage Downstream Water Quality and Hydropower Energy Generation

Motahareh Saadatpour¹, Shima Javaheri²

1- Assistant Professor, School of Civil Engineering, Iran University of Science and Technology, Tehran, Iran

2- M. Sc. Graduated Student of Civil and Environmental Engineering, College of Environment, Karaj, Alborz, Iran

Email: msaadatpour@iust.ac.ir

Abstract

The integrated water quality and quantity management in reservoir design and operation is the key to meet sustainable development goals while maintain ecological services and economic benefits. Selective withdrawal systems (SWS) can help adapt reservoir operation to manage and enhance downstream water quality. This research develops a surrogate based simulation-optimization approach (SBSOA) to release water from different intakes in reservoir to minimize deviations from standard dissolved oxygen (DO) concentration and maximize annual hydro power peak energy generation. ANN is developed to act as surrogate of time consuming CE-QUAL-W2 model in approximation reservoir outflow DO concentration. The developed surrogate model is coupled with multi-objective particle swarm optimization (MOPSO) to derive optimal SWS (locations and withdrawal ratio) in Karkheh reservoir. Optimization results for water quality and quantity management with SWS are compared to historical release model. The results show optimal SWS can help enhance release water quality compared with historical scenario.

Keywords: ANN, CE-QUAL-W2, Karkheh reservoir, MOPSO, Selective Withdrawal System.

1. INTRODUCTION

Dams as man-made structures, whose effects, besides the obvious change from a stream to a lake environment in the reservoir itself, are related to the spatial and temporal changes of in-stream flow, downstream nutrients and sediment flow reductions, vertical and longitudinal changes of water temperatures and water quality profiles, and impeding fish and wildlife migration [1]. Historically, in many countries over the worlds, water reservoir planning, management, and designs have aimed to satisfy quantity and/or economic objectives. As a result, a lot of water-related problems have arisen. This has caused the need for better and more comprehensive viewpoints in planning and management process. Nowadays, water quality has become increasingly more important in reservoir design, planning, and management due to intense multi-objective demands on limited resources, its effects on other environmental interests, such as fish and wildlife, impact or impairing water use. Therefore, laws and regulations require consideration of water quality for new reservoir construction and structural or operational modifications of existing reservoirs [2].

Natural conditions and human interventions affect the reservoir hydrodynamic and water quality parameters. The effects of natural events (hydrological and meteorological conditions) couldn't be considered directly into the realm of reservoir design and/or management process. But human interventions can influence/enhance water quality through a) pre-treatment or control of reservoir inflows; b) in-pool management or treatment techniques; and c) management of reservoir outflows [2]. Reservoir outflow management is the most common method which affects reservoir in-pool and release water quality. Outflow management can consist of controlling the outflow rate, outlet location and timing of releases, and treating the release. In this paper, third alternative is considered on the case which the outflow is controlled through equipping the reservoir with multilevel outlets. The aforementioned selective withdrawal system (SWS) provides water releasing at different elevation with various physical, chemical, and biological characteristic [3]. In this regards, the reservoir is outfitted with SWS in order to meet downstream water quality objectives and also the quantity objective (hydropower peak energy 2 generation). The main objectives of the problem are to reduce downstream water quality deterioration and increase hydropower peak energy generation through SWS application in reservoir.

In this study simulation-optimization (SO) approach has been developed to determine optimal SWS design in hypothetical case study (Karkheh reservoir, Khuzestan, Iran) with sufficient, known, and complete hydrological, meteorological, hydraulic, and water quality data. The calibrated and verified 2D hydrodynamic and water quality simulation model of Karkheh reservoir has been applied to assist the design and evaluation process

of the outlet structures in order to predict the effects on water quality and designing water quality targeted operation in new and existing reservoirs. Due to high computational burden of numerical hydrodynamic and water quality simulation model (WQSM), CE-QUAL-W2, a surrogate model is developed to overcome the computational obstacles. The surrogate model has been coupled with Multi-objective particle swarm optimization (MOPSO) algorithm to derive optimal SWS (the outlet locations and withdrawal ratio) in reservoir.

2. METHODOLOGY

Proper SWS designing and deriving optimal reservoir operation strategies in selective withdrawal framework are efficient and effective approaches help achieve quantity objectives and also prevent and/or reduces water quality deterioration. In this point, social, economic, and environmental objectives are achievable. Coupled numerical WQSM and evolutionary algorithm (EA), as SO approach, are effective tools to solve this high complicated, inter-related, non-linear, and large scale problems. Unfortunately, EA requires plenty of numerical WQSM calls to converge near- optimal and/or optimal solutions and therefore considering water quality issues in water resources planning and management problems results in higher computational intensity. To reduce the computational burden in highly expensive SO model, approximation model is often suggested. These approximation models are initially developed as the “surrogates” of the expensive simulation models in order to improve the overall computational performance. The details about applied tools and approaches of this research are discussed below.

2.1. MODEL DEVELOPMENT

In this research, MOPSO algorithm has been developed to be coupled with CE-QUAL-W2 as 2D hydrodynamic and water quality simulation model. The applied WQSM is capable to simulate the effective factors on mass and energy circulation, transportation, and fate process in the reservoir, temporally and spatially. Due to extensive WQSM call requirement in SO approach and also expensive time and computational costs CE-QUAL-W2 model, surrogate based SO approach (SBSOA) has been applied. The proposed approximation model, as a surrogate of numerical WQSM in this research, has the ability to quickly and inexpensively respond to various SWS design in reservoir. The interaction between various applied tools in this research is presented in Figure 1.

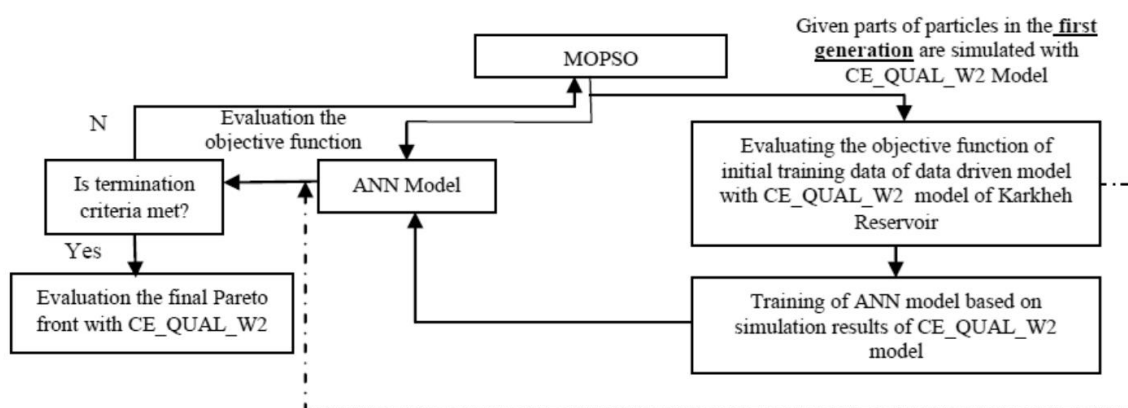


Figure 1. The structure of SBSOA in optimal SWS design in reservoir

The considered SWS in this research have been located vertically in dam structure. The intake type, elevation of location, and the corresponding layer numbers of each intake in CE-QUAL-W2 model have presented in Table 1. The last two lines present current intake elevations in Karkheh reservoir. In this study, up to five intakes could be selected in SWS design process in the reservoir in SBSOA.

Table 1- Intake elevations and locations corresponding to computational layers of CE-QUAL-W2 model

Intake Number	Intake type	Intake Elevation, masl	Intake top layer number	Intake bottom layer number
1	Point	212	7	9
2	Point	206	10	12
3	Point	200	13	15
4	Point	196	15	17
5	Point	192	17	19
6	Point	188	19	21
7	Point	182	22	24
8	Point	176	25	27
9	Point	170	28	30
10	Point	162	32	34
Main 1	Point	180	23	25
Main 2	Point	161.5	32	34

2.2. SIMULATION MODELS

Process based WQSMs are useful tools which depict the transportation and fate mechanism, physical, chemical, and biological inter-relations in water bodies explicitly, spatially and temporally. To model the complicated and inter-connected physical, chemical, and biological mechanisms, massive hydrological, meteorological, hydraulic, water quality data is required and extensive model parameters should be set. In contrast, data-driven models, discarding the aforementioned mechanisms and processes, approximate the water quality responses in water bodies quickly and inexpensively. In this study, ANN model, as data-driven model, has been trained and tested according to numerical and process based WQSM, CE-QUAL-W2 model.

2.2.1. CE-QUAL-W2 MODEL

CE-QUAL-W2 as 2D hydrodynamic and WQSM has been applied in this study. This model has the capability to simulate the spatial and temporal hydrodynamic and water quality variations in reservoirs. The reservoir geometry is gridded vertically and longitudinally as computational elements which mass and transport equations are solved in each element with finite difference method. The elements connections have been considered through settling and diffusion processes. Water surface elevation, velocity, flow rates, as important hydrodynamic variables, affect the mass transportation in water body. The 2D advection-diffusion-reaction equations have been solved to simulate water quality concentration in each computational grid. The model has the ability to simulate the mechanisms affect temperature, nitrate, phosphate, algae, dissolved oxygen, organic and inorganic matters, sediments, total dissolved solids, coliforms, and etc. in reservoir [4].

2.2.2. ANN AS SURROGATE WQSM

Surrogate models have been developed to approximate the partial behaviors of complicated, multi variant model based on limited data originated from the expensive and more fidelity simulation models [5]. Proper and correct relevance definitions between decision variables (intake elevation and outflow rate of each intake in this research; SWS) and state variables (reservoir outflow DO concentration) are main and significant step in surrogate model 4 development. ANN has been recognized as a useful and efficient tool in surrogate model development process. The mathematical function of ANN could be written as:

$$Y=f(X,W)+\varepsilon \quad (1)$$

Y, f, X, W and ε are output vector, input vector, ANN model parameter vector, connecting vector among system input and output, and ANN model error vector, respectively. Successful and proper ANN input data selection lead to increasing the accuracy of surrogate model in design and planning problem through enhancing the approximation precision. To achieve the aforementioned aims in developing ANN model as reservoir outflow DO concentration, it is required to acquire profound knowledge and understanding on the mass transport and fate mechanism, the cause and effect relations among various water quality parameters, among water quality and quantity parameters, temporal and spatial dynamics of system responses, and delays and their main reasons.

2.2.2.1. ANN MODEL DEVELOPEMENT IN DO CONCENTRATION APPROXIMATION

DO is significant water quality parameters in water-bodies and is essential element in aquatic lives. The simplification of mathematical equations describing DO fate and transport in reservoir is required in surrogate model development process. Reviewing the mathematical equations (2) shows algae growth rate (AG), phosphorous half-saturation coefficient (p_s), nitrate half-saturation coefficient (n_t), solar radiation half-saturation coefficient (I), algae respiration coefficient (k_{ra}), algae concentration (V_a), flow area ($A_{Surface}$), reaeration coefficient (K_L), DO saturated concentration (O_{sat}), DO concentration (O), nitrification coefficient (K_{NH4}), denitrification coefficient (K_{NO3}), organic matter decay rate (K_{POM}), nitrate concentration (V_{ni}), NH_4 concentration (V_{NH4}), sediment organic matter decay rate (K_s), sediment concentration (V_{sed}), bottom sediment oxygen demand (SOD), bottom sediment area (A_{sed}), required oxygen to decay organic matter (γ_{OM}), and required oxygen to decay NH_4 (γ_{NH4}) [4].

$$V \frac{\partial O}{\partial t} = (AG(T, n_t, p_s, I) - k_{ra})V_a\gamma_{OM} + A_{Surface}K_L(O_{sat} - O) + K_{NO_3}(T)V_{ni}\gamma_{NH_4} - K_{POM}(T)V_{c_{POM}}\gamma_{OM} - K_{NH_4}V_{NH_4}\gamma_{NH_4} - \gamma_{OM}K_s(T)V_{sed} - SOD(T) \times A_{sed} \quad (2)$$

Furthermore, understanding the thermal energy transportation and modeling is required due to temperature (T) effects the reservoir water quality parameters. The mathematical equations prove that inflow water temperature, the exchanged heat flux with atmosphere, inflow and outflow rates, flow area, and water body volume have more effects on water temperature in water-bodies. Meteorological parameters such as air temperature, dew point temperature, wind speed and direction, ... affect the exchanged heat fluxes with atmosphere.

Due to spatial distribution and extension of reservoir water body, various mass and energy diffusion and advection process, the role of wind speed and gravity, reservoir geometry, the withdrawal locations in reservoir, and etc. there are vertical thermal and quality gradients in deep reservoirs. Furthermore, in long reservoirs due to effective fate and transport processes, there are longitudinal thermal and quality gradient, too. In this regards, the longitudinal gradient leads to delays between outflow and inflow water temperature and quality in reservoir. Considering the above concepts and mathematical equations describing the DO concentration in water bodies, water temperature, transportation and circulation processes in reservoir, NH_4 inflow flux, NO_3 inflow flux, TSS inflow flux, BOD inflow flux, PO_4 inflow flux, DO inflow flux, algae inflow flux, thermal inflow flux, air temperature, wind speed, outflow rate, water surface elevation (WSE), and outflow ratio from each outlet (10 outlets are considered in this study) have been considered as ANN input data to model reservoir outflow DO concentration (Figure 2).

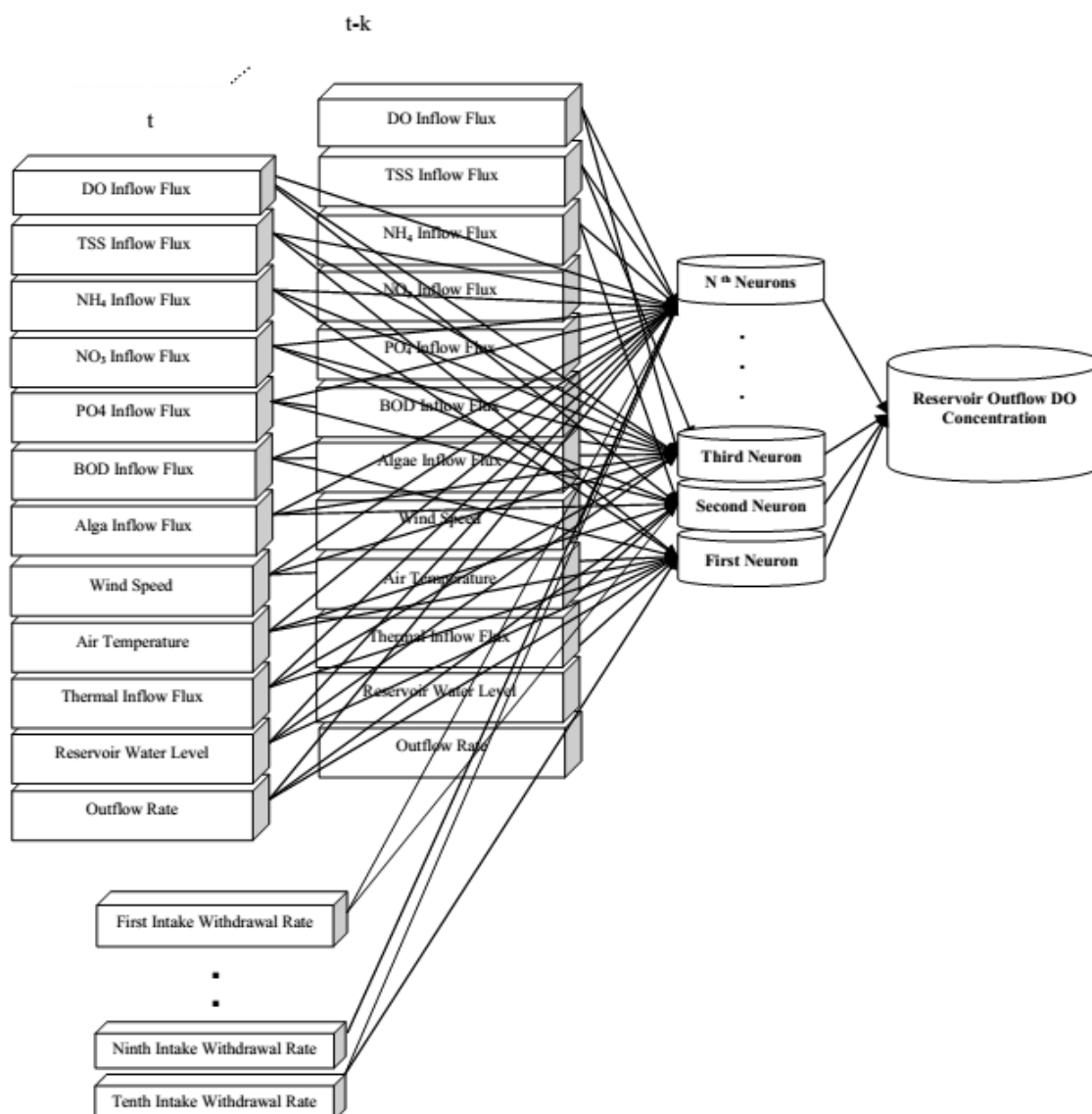


Figure 2. Input data in neural network model of reservoir outflow dissolved oxygen [6]

The studies on Karkheh reservoir show system responses in time step t are affected by meteorological, hydrological, water quality, and reservoir operation strategy in time step $t-k$. As a result, the time delays of input data except the withdrawal ratio of each outlet are considered. In this regards, various water quality inflow fluxes, thermal inflow fluxes, outflow rates, WSE, and the meteorological data are introduced with three months delays. All aforementioned data are arranged as 15-day averaging time steps. Reservoir outflow DO concentration is approximated in each 10-day time step. CE-QUAL-W2 model has been applied to train ANN DO approximation model. 20 various reservoir operation scenarios in selective withdrawal scheme during 15 years have been simulated with CE-QUAL-W2 model. 80% of scenarios have been implemented for ANN training and the remaining scenarios have been applied as ANN model test.

2.3. MODEL STRUCTURE

The developed surrogate model has been coupled with MOPSO to determine the optimal SWS (design problem). In this study, minimizing the number of DO concentration violation from standard value and maximizing the average annual peak energy generation have been considered as objective functions. ANN DO approximation model, simulate reservoir outflow DO concentration, is coupled with MOPSO. The simulation model (surrogate WQSM and hydropower simulation model) and optimization algorithm have coupled sequentially (Figure 1).

The final derived Pareto front, derived in SBSOA, have been simulated and evaluated with CE-QUAL-W2 model.

2.4. WATER QUALITY AND QUANTITY OBJECTIVE FUNCTIONS

DO as water quality index is considered in this study. Minimizing the number of DO violation from standard value in each 10-day is defined as water quality objective function in this research. In equation (3) and equation (4), $DO_{standard}$ and $DOConcentration_i$ are standard DO value (5 mg/L) and reservoir outflow DO concentration in time step i, respectively.

$$Min \quad f_{quality} == (NumberofDOViolationDay) \quad (3)$$

$$DOConcentration \begin{cases} DO_{standard} & DOConcentration \geq DO_{standard} \\ DOConcentration & else \end{cases} \quad (4)$$

Maximizing average annual hydropower peak energy generation is defined as water quantity objective in Karkheh reservoir (equation (5) to equation (7)).

$$DesignFlow = (IC \times 1000 / (9.81 \times Eff \times DesignHead)) \quad (5)$$

$$Q_{in} = Outflow_t \times (Y_{1_t} + Y_{2_t} + Y_{3_t} + Y_{4_t} + Y_{5_t} + Y_{6_t} + Y_{7_t}) \quad (6)$$

$DesignFlow$, Q_{in} , $Outflow_t$, Y_{it} , IC , Eff , $DesignHead$, $plantInflow_t$ are power plant design flow, available flow in power plant, Karkheh reservoir outflow rate in time step t, withdrawal ratio of outlet i at time step t, power plant installed capacity, and design head, respectively. In equation (7), $plantInflow_t$ and $NetHead_t$ are water inflow rate to power plant and net head water in system. $peaktime$ and $Energy$ are power plant operation in peak time (hourly) and average annual peak energy generation, respectively.

$$Energy = ((\sum_{t=1}^{TotalContolDay} 9.81 \times plantInflow_t \times NetHead_t \times Eff \times peaktime \times 10 / 1000000) / 5310) \times 365 \quad (7)$$

2.5. CASE STUDY AREA

The proposed methodology in this research has been applied in hypothetical case study with complete and comprehensive calibrated and verified 2D hydrodynamic and water quality model, Karkheh reservoir. Karkheh reservoir is constructed on Karkheh River, Khuzestan, Iran. The dam crest and maximum depth are 3030 m and 117 m, respectively. With 5346.2 MCM capacity, 162 km² surface areas, and 60 km length in normal water level, 220 masl, this reservoir is the largest reservoir in Iran. Supplying agricultural water demand for approximately 50000 km² of irrigation area, 934 GW annual hydropower energy generation, and flood control are the main objectives of this large scale hydraulic structure.

3. METHODOLOGY APPLICATION IN CASE STUDY WITH SUFFICIENT DATA; RESULTS AND DISSCUSION

The developed ANN model to approximate reservoir outflow DO concentration has been trained and tested with CE-QUAL-W2 model results. Then SBSOA has been applied to derive optimal decision variables in SWS problem. Finally, the Pareto front derived in SBSOA has been evaluated with CE-QUAL-W2 model to revise the derived Pareto front. The results are presented below.

3.1. SURROGATE MODEL DEVELOPMENT TO APPROXIMATE RESERVOIR OUTFLOW DO CONCENTRATION

The performance of ANN model in approximation reservoir outflow DO concentration has been evaluated with four various SWS. The approximated values with ANN model have been compared with CE-QUAL-W2 model results. The intensive sensitivity analysis have been done on learning and training functions and also the neuron numbers in hidden layer of ANN model. Then the network with higher performance has been

chosen to simulate system responses according to various reservoir operation strategies in selective withdrawal framework. The comparison results have been presented in Figure 3. The statistical criteria represent suitable convergences between ANN model predictions compared with CE-QUAL-W2 model.

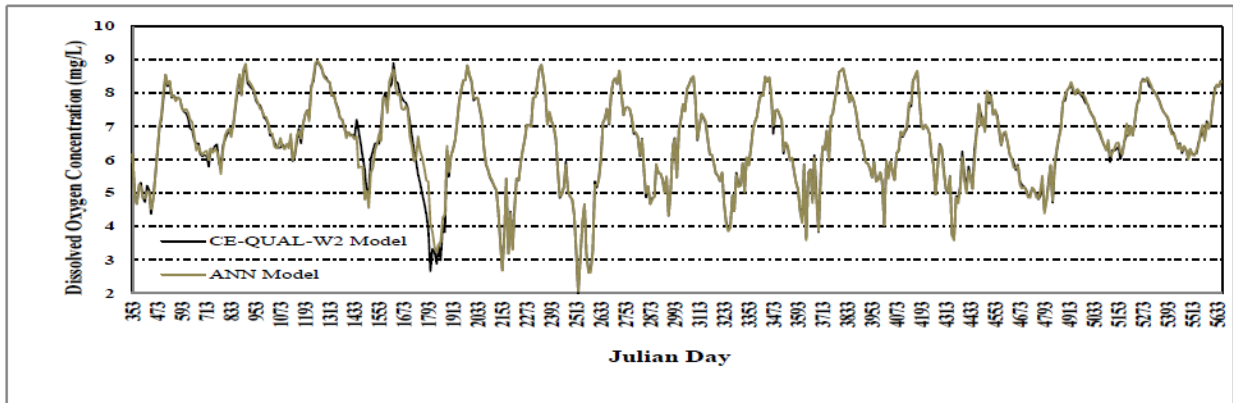


Figure 3. Comparison the performance of DO neural network model with CE-QUAL-W2

3.2. SWS Design Problem and Reservoir Operation Strategy in Selective Withdrawal Framework

Maximizing average annual peak energy generation and minimizing number of DO violation from standard value have been defined as two main objectives of this problem. The Pareto front evaluated with CE-QUAL-W2 model is presented in Table 2. The optimal outlet locations, withdrawal ratio, and the objective function values corresponding to each of Pareto front are presented. The number of DO violation from standard value in the best water quality scenario and best water quantity scenario are 16 and 52 days, respectively. The results show water quality objective conflicts with hydropower energy generation objective.

Table 2- The Final Pareto Front Evaluated with CE-QUAL-W2 Model

Pareto Front No	Scenario Characteristic	Characteristic					Water Quality Objective (day)	Water Quantity Objective (GWh)
		5	6	7	9	10		
1	Intake No.	5	6	7	9	10	52	409.19
	Withdrawal ratio	0.96	0	0.04	0	0		
2	Intake No.	1	5	7	9	10	16	405.52
	Withdrawal Ratio	0.81	0.09	0.08	0.01	0.01		

Time series of reservoir outflow DO concentration in best water quantity scenario is compared with historical operation based on one hydropower intake. The comparison results are presented in Figure 4 . The studies show the number of DO violation in historical operation scenario is 94 days which is more than the worst water quality scenario derived with SBSOA.

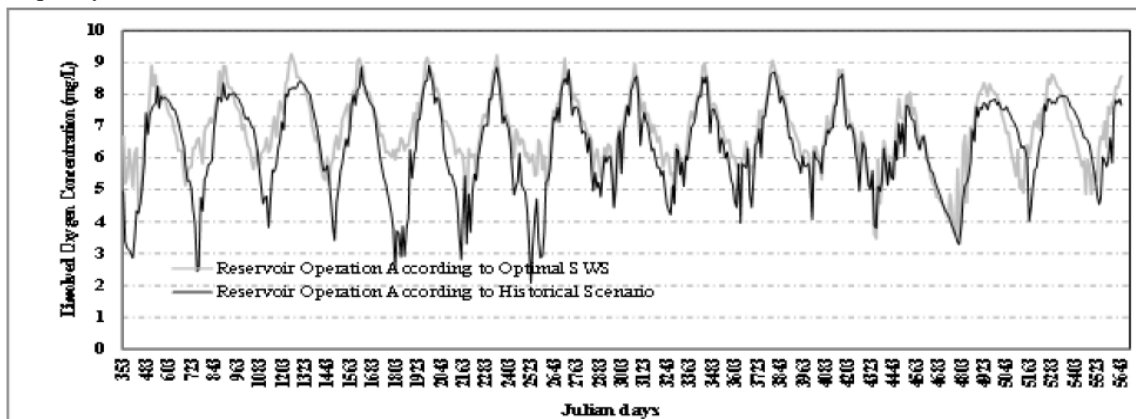


Figure 4. Comparison reservoir outflow DO concentration in optimal and current intake designing scenarios

4. CONCLUSIONS

In this study a new methodology was applied to design SWS in reservoir which could be equipped with multiple outlet release schemes. Water quantity and quality objectives (minimizing number of DO violation from standard value and maximizing average annual hydropower peak energy generation) have been considered as objective functions in this study. Static ANN model is trained and tested to approximate reservoir outflow DO concentration based on dynamic simulation results of CE-QUAL-W2 model according to various SWS. MOPSO has been coupled to ANN DO approximation model sequentially to derive optimal SWS. The derived Pareto front of SBSSA has been evaluated with CE-QUAL-W2. The comparison results show reservoir outflow DO concentration in optimal SWS is more adapted to standard value compared with historical operation system in reservoir. Future research will concentrate on deriving optimal reservoir operation rules in selective withdrawal framework considering quantity and quality issues, adaptive SBSOA, and broaden the range of quality and quantity objectives such as temperature, turbidity, salinity, environmental flow, and etc.

5. REFERENCES

1. Olivares, M. A. (2008), “*Optimal Hydropower Reservoir Operation with Environmental Requirements*,” Ph. D. Thesis, University of California, Davis.
2. Dortch, M., 1997, “*Water Quality Consideration in Reservoir Management*,” Water Resources Update, 108: 32-42.
3. Rheinheimer, D. E., Null, S. E., Lund, J. R. (2014), “*Optimizing Selective Withdrawal from Reservoirs to Manage Downstream Temperatures with Climate Warming*,” Journal of Water Resources Management (ASCE), DOI: 10.1061/(ASCE)WR.1943-5452.0000447.
4. Cole, T.M. and Wells, S.A. (2013), “*User's Guide for CE-QUAL-W2: A Two-Dimensional, Laterally Averaged, Hydrodynamic and Water Quality Model, Version 3.71*,” Washington, DC: U.S. Army Corps of Eng, Draft File report, 20314-1000.
5. Solomatine, D. (2015), “*Surrogate Modelling in Model-Based Optimization. An Introduction*,” The UNESCO-IHE Institute for Water Education, Delft, Netherland.
6. Javaheri, S. and Saadatpour, M. (2017), “*Deriving Hydropower Reservoir Operation Rules in Selective Withdrawal Framework Considering Quality and Quantity Objectives; Simulation-Optimization Approach Based on Meta-Modelling*,” Journal of Iran Water Resources Research, http://www.iwrr.ir/article_45175_0.html.

Double-stilling basin modelling, Pakistan – case study

Ubaid Ullah¹, Eric J Lesleighter², Muhammad Iqbal³

1- Principal Hydraulics Engineer, Engineering General Consultants (Pvt. Ltd.), Pakistan

2- Lesleighter Consulting Pty Ltd, Sydney, Australia

3- Principal Hydraulics Engineer, Associated Consulting Engineers (Pvt. Ltd.), Pakistan

Email: lesleighter@yahoo.com

Abstract

The Mohmand Dam is a 213m tall concrete-faced rockfill dam (CFRD) under design by a consortium of consultants in Pakistan. The consortium comprises SMEC International (Australia), Nippon Khoe (Japan), National Engineering Services (Pakistan), Associated Consulting Engineers (Pakistan), Engineering General Consultants (Pakistan), and BAK Consulting Engineers (Pakistan). The dam is for construction on the Swat River in Pakistan.

A strategic component of the hydraulics studies has been large-scale physical model studies carried out by the Irrigation Research Institute, Pakistan. The paper will discuss in detail the use of, and the hydraulic behavior of a double hydraulic jump stilling basin facility incorporated in a 600m long concrete chute. The upper basin was designed to operate with a maximum head of about 100m, and the lower basin was designed to operate with a maximum head of approximately 120m with respect to tailwater level. The studies considered discharges up to approximately 25,500 m³/s. Detailed pressure transducer measurements of transients as part of the design of the basins, and the chutes incorporated several aerators along the length of the chutes.

Keywords: Dams, spillways, hydraulic jump basins, energy dissipation, turbulence, pressure transients.

1. INTRODUCTION

The Mohmand Dam Hydropower Project (MDHP) is a large power project to be built on the Swat River approximately 200 km northwest of Islamabad. The location of the dam is illustrated in Figure 1. The project investigation and design passed through several studies with a detailed feasibility study preceding the lengthy study that derived the double-stilling basin spillway arrangement – the subject of the present paper. The work, comprising site and dam selection, detailed hydrology, reservoir sedimentation aspects, power station sizing, diversion detailing and hydraulics progressed the earlier feasibility studies and all has been carried out on behalf of the Water and Power Development Authority (WAPDA) by a consortium of consultant companies.

The diversion works comprise two 15m diameter tunnels. One is to be developed into a permanent, low level outlet facility for necessary releases to the downstream and for drawdown purposes. The power intake will direct flows into a separate tunnel leading to an 800MW power station on the right bank of the river a short distance downstream of the dam and near the spillway discharge location.

2. HYDROLOGY

In July 2010, the Swat River experienced extreme flooding with a discharge estimated as 9,909 m³/s and considered to have an Annual Exceedance Probability (AEP) of 1 in 1,000. The return periods for the Project went through a number of studies, updating and finally an accepted series of magnitudes. It was confirmed by WAPDA in January 2016 that the Project design team should adopt a panel of expert's recommendation for the Probable Maximum Flood (PMF) of 27,427 m³/s inflow discharge. The computed peak value for AEP 1 in 1,000 and 1 in 10,000 are 10,669 m³/s and 18,640 m³/s, respectively. Figure 2 presents the inflow flood hydrographs at Mohmand Dam site.

As will be described below, the energy dissipation arrangement selected a two-stilling basin arrangement. The flood routing yielded a PMF outflow discharge from the reservoir of 25,362 m³/s. For the spillway energy dissipation design the design discharge was selected as 90% of the PMF for the upper stilling basin and the AEP 1 in 10,000 discharge for the lower basin.

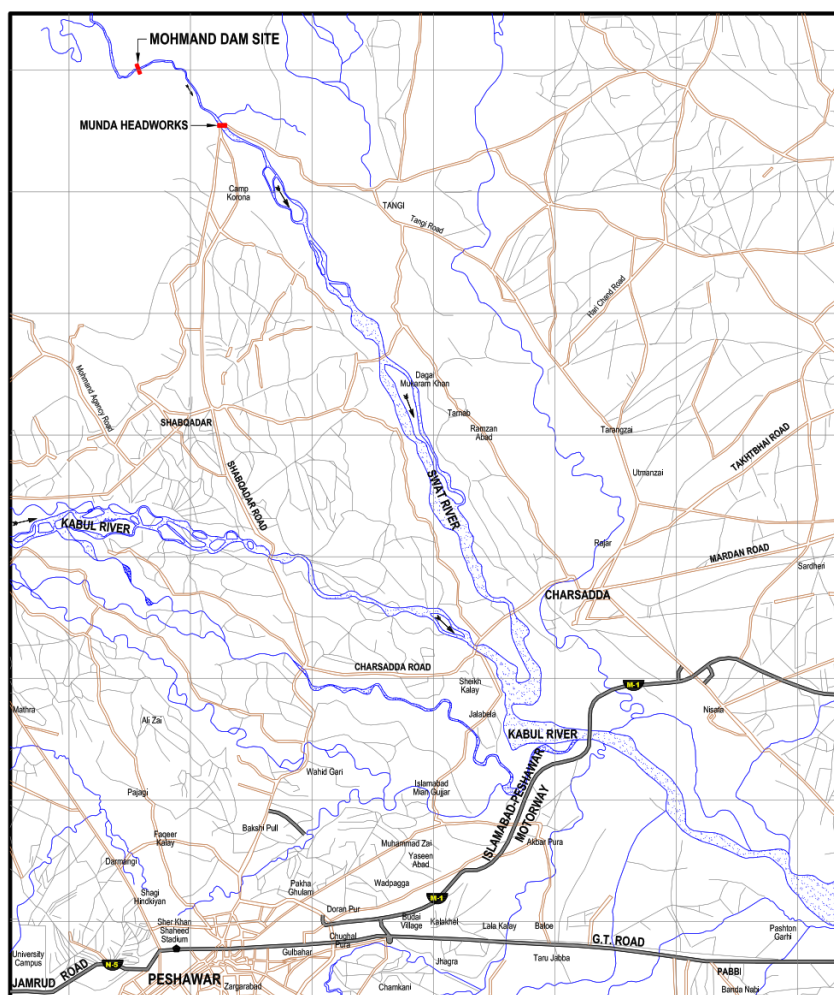


Figure 1. Location of Mohmand Dam Project, Pakistan

3. SPILLWAY TYPE AND KEY DIMENSIONS

The proposed spillway was to be located on the left abutment of the dam, following the dam-type selection of a concrete-faced rockfill dam (CFRD). The type of spillway received detailed consideration. Originally, the project commenced with the plan to use a flip bucket and plunge pool energy dissipation arrangement, for which the plunge pool pre-excitation would be a large-volume depression on the river's left and against a steep excavation of the hill on the spillway's left. Essential to the provision of an acceptable plunge pool dissipater was the consideration of rock scour and its longitudinal and lateral extent. Even the pre-excitation of the plunge pool would require a large slope excavation on the left side. The site investigations revealed rock largely classified as a foliated schist. Based on the Consultant's experience it was considered very erodible under the action of velocities around 45 m/s.

The main issue with the plunge pool erosion, apart from a likely depth to 60m below river bed level, was its lateral expansion and movement with the result that the entire left hill excavation would be undermined and be subject to collapse. Figure 3 is a portion-plan of an early plunge pool possibility; it shows the large excavation on the left side of the plunge pool. Such collapse in turn would produce a large volume of scoured and collapsed material to form a huge blockage in the river, affecting the power station, the permanent outlet works and the spillway itself.

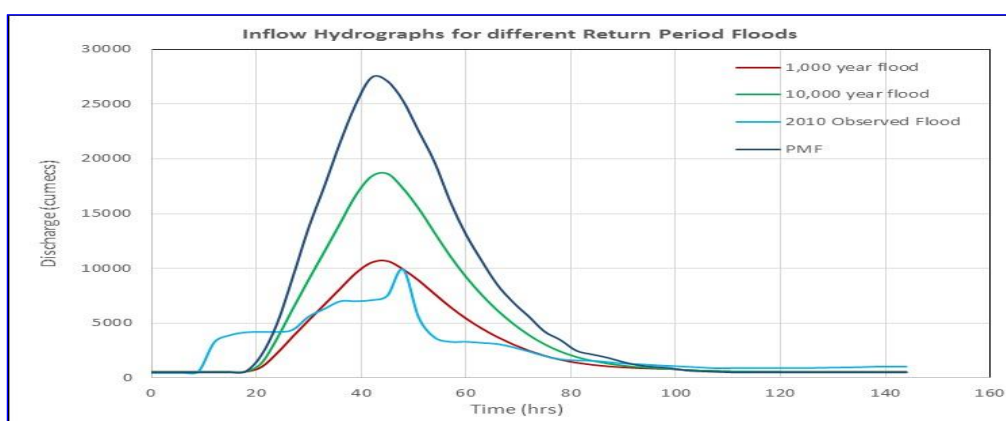


Figure 2. Inflow flood hydrographs

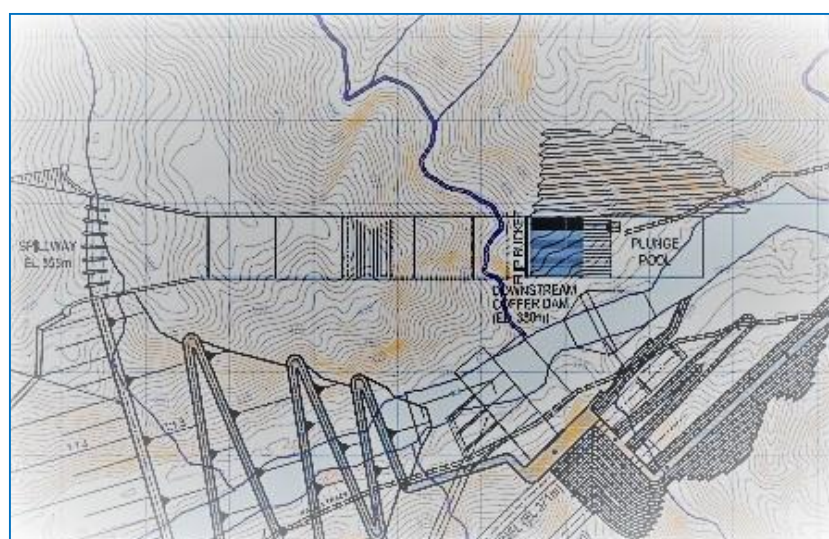


Figure 3. Early Plunge Pool arrangement

The flip bucket-plunge pool arrangement was abandoned and consideration moved to the application of a hydraulic jump stilling basin alternative as the means of dissipating the energy from the spillway. The dam with a crest level at EL 563, and a parapet wall level at EL 564.5, would provide for a reservoir with a full supply level of EL555m, and a spillway crest level of EL 539m.

Several chute and stilling basin arrangements were contemplated. The headworks also passed through several alternatives for the number of gates, and whether part of the spillway would remain ungated with the crest at FSL. The result was seven gates, each 15m wide, and piers 5.3m thick, all placed on a curved crest alignment on a 500m radius. The chute was converged from the total gross crest width of approximately 137m to a width of 100m. This led to a unit outflow discharge at PMF of approximately 255 m²/s.

With a reservoir level in the region of EL 560 and the river bed in the dissipation area at EL360, clearly the 200m head placed stringent conditions on the spillway design. Early considerations of a single stilling basin indicated basin inflow velocities around 60m/s, and in due course it was decided to investigate the use of a double stilling basin configuration, somewhat similar to the arrangement used some decades earlier on the Mangla Dam spillway, also in Pakistan. The investigation of the double basin configuration is the thrust of this paper. Detailed physical model studies were carried out at the Irrigation Research Institute (IRI), Nandipur, Pakistan.

Figure 4 shows a plan view of the spillway and Figure 5 a profile, depicting the chute from the headworks into the upper basin with an end weir and discharge into the lower basin with an invert level at EL348.

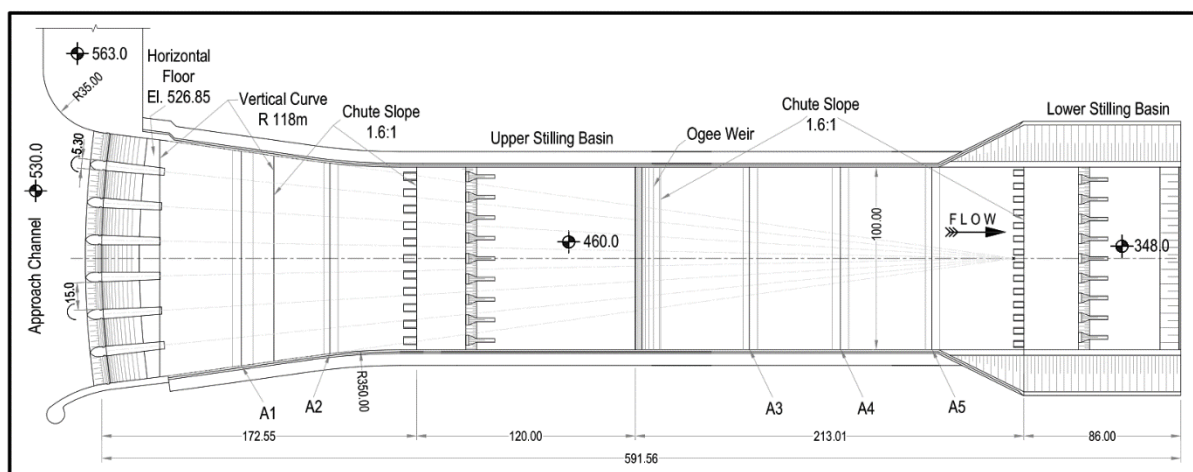


Figure 4. Plan of the double basin spillway

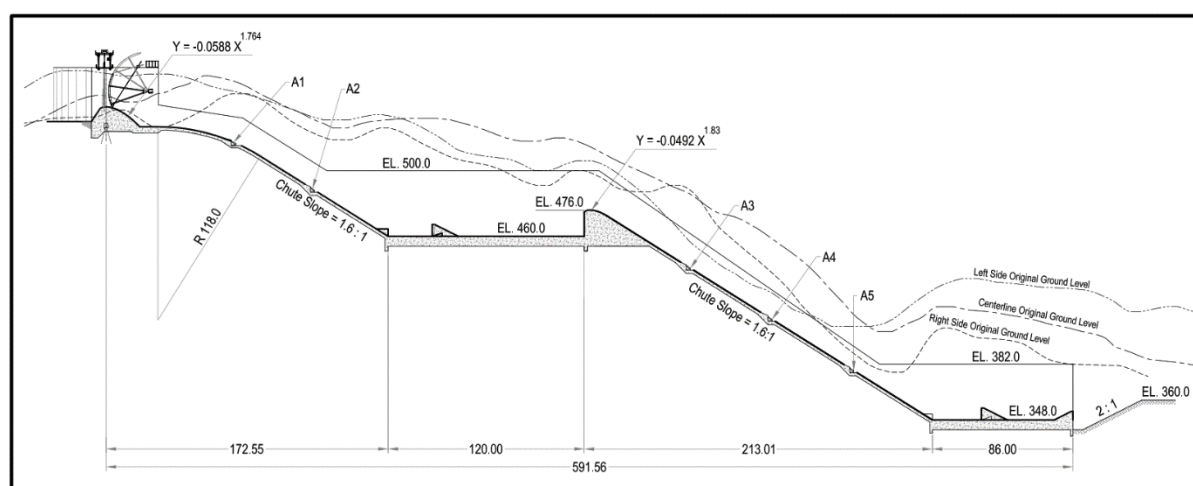


Figure 5. Profile of the spillway

The upper basin was designed to operate with a maximum head of about 100m, and the lower basin was designed to operate with a maximum head of approximately 120m. The studies considered discharges up to approximately 25,500 m³/s. Detailed pressure transducer measurements of transients in the upper basin were made as part of the design of the basins, and the chutes incorporated several aerators along the length of the chutes, the geometry of which was studied and varied on the hydraulic model.

4. HYDRAULIC MODEL DESCRIPTION

The model was built and tested with a scale of 1:60. Figure 6 shows a general arrangement plan of the model boundary. Each stilling basin was designed initially with estimation of spillway losses, and basin length and depths based on the hydraulic jump characteristics, on the basis that a USBR Type III arrangement would be used. The basins were provided with conventional chute blocks, and baffle blocks were sized according to the jump characteristics and the USBR guidelines on sizes and spacing. The model was constructed in Perspex and instrumented with many piezometers and several locations for pressure transducers. Figure 7 is a view of the model in operation with a AEP 1 in 10,000 discharge, and Figure 8 shows the lower basin at AEP 1 in 1,000 discharge.

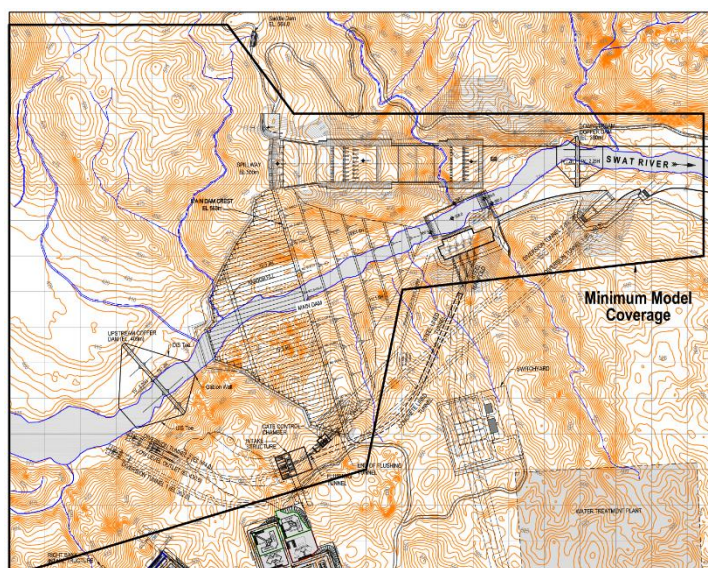


Figure 6. Coverage of the spillway model

5. THE MODEL STUDIES

Many of the key and major aspects of the hydraulics, leading to a final design arrangement, were studied. First, to obtain satisfactory retention of the hydraulic jumps, by making alterations to the basin lengths and floor levels, and numerous changes to the energy dissipation baffle blocks and aerators. A workable and safe design was achieved through the studies. The second major stage of the studies were the measurements of transient and static pressures in key locations. Several aspects of the model dimensions and details were subject to change:

- Upper basin length from 90m to 120m and end weir height from 14m to 16m
- Aerators reduced from six to five – two on the upper chute and three on the lower chute
- Aerator geometry
- Location, height and number of the baffle blocks in the upper basin, and
- Lower basin lowered from EL 355 to EL348 having regard to the tailwater rating based headworks 5 km downstream.

The baffle block utilized the shape developed by USBR studies of a “supercavitating” block during testing for the Folsom Dam auxiliary spillway (USBR, 2009). The purpose was to “push the limits” for which baffle blocks could be used in a cavitation environment, meanwhile ensuring generous aeration of the lower flow layers in the chute and into the stilling basins.

The aerators on the Mohmand model showed the nappe profiles well. The performance led to the lowering of ramp heights in some cases to reduce the length of the aerated zone as well as relocating the aerators to command the chute length sufficiently to provide assurance that the full chute flow would have adequate aeration. There is sufficient experience – model and prototype – to allow confidence in the designs, both in their location and in the air duct areas to meet the demands of the jets from the ramps. Figure 9 shows the dimensions of the five aerators. Figure 10 shows the flow profile at the two upstream aerators.

6. PRESSURE TRANSIENTS

A key consideration in stilling basin design is the amount of uplift forces due to the combination of under pressures, pressure transients and transmission of pressures through joints. The high-energy conditions in both stilling basins dictated close consideration of the pressure transients in the stilling basins for the slab and anchoring design. Pressure transducers were used on the floor of the basin both upstream and downstream of the baffle blocks, and on the sidewall of the stilling basin. Records of pressures were obtained at a sampling speed of 300Hz for generally up to 5 minutes (model).



Figure 7. View of the upper basin operation for AEP 1 in 10,000



Figure 8. Lower chute and lower basin entry Q1,000

By way of illustration, Figure 11 shows the deployment of 8 transducers on the floor of the model upper basin. Figure 12 shows a small part-sample of the 2,300s (prototype time) total capture of the transients at two of eight transducers in the upper basin. The information, together with cross correlation analysis of signals from pairs of transducers and spectra, provided information for the design of the basin floor thickness as well as anchors. A sample of the spectral density plots for two transducers for the PMF is shown in Figure 13. Clearly, the major fluctuations power is around 1 Hz or less, frequencies which are well within the “capability” of the structure floor slabs to respond and therefore relevant for any dynamic analysis of the slab/anchor system.

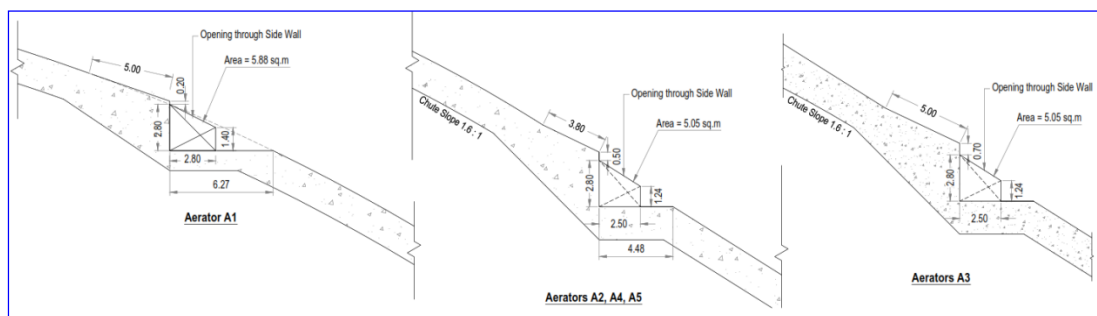


Figure 9. Final aerator geometry



Figure 10. Nappe profiles at aerators 1 & 2

7. CONCLUSIONS

The paper, describing detailed studies on a physical model, shows the value of the exercise in improving significantly on desk-type estimates. Many aspects of the hydraulic structures needed to be addressed by making modifications to the basins, the aerators, and the stilling basin appurtenances. The conditions are major by all comparisons, with high heads and large potential discharges. The double stilling basin presented a workable and desirable option to fit within a narrow corridor with a high mountain (and appreciable excavation) on one side and the dam on the other side. The model results allowed confidence in the detailed design exercise which followed.

8. ACKNOWLEDGMENTS

The authors express their appreciation to the IRI, Nandipur for its skill in building and testing the model, particularly research officers Tariq Anwar and Sana Ullah. Thanks also to Manly Hydraulics Laboratory's (Sydney) assistance in providing instrumentation and advice for the model transient work, and running the pressures analysis.

9. REFERENCES

1. USBR, Denver, Colorado, 2009, Cavitation Potential of the Folsom Auxiliary Stepped Spillway, Hydraulic Laboratory Report HL 2009-07.

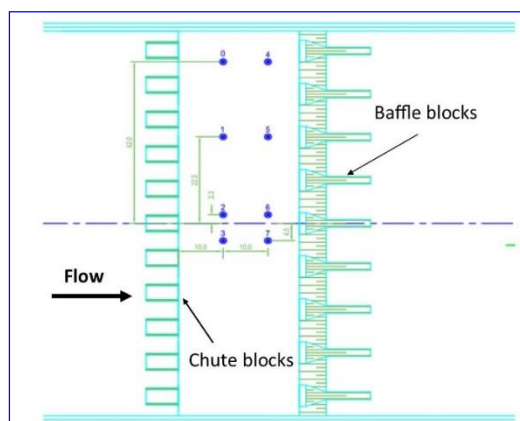


Figure 11. Transducer locations in the upper basin for one test configuration

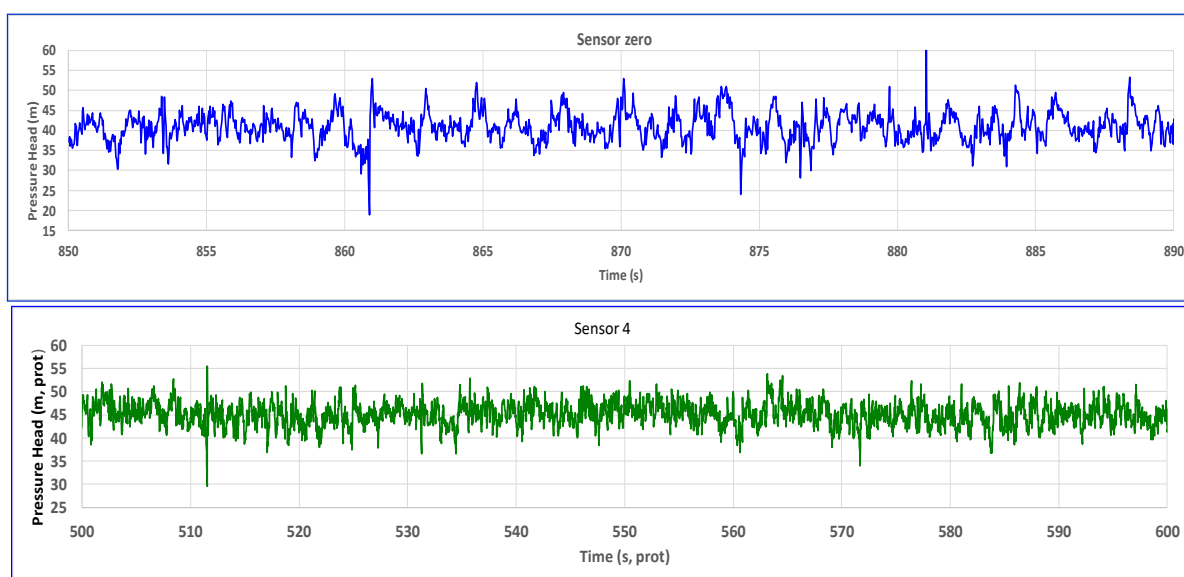


Figure 12. Sample transient pressures at two transducers, upper basin

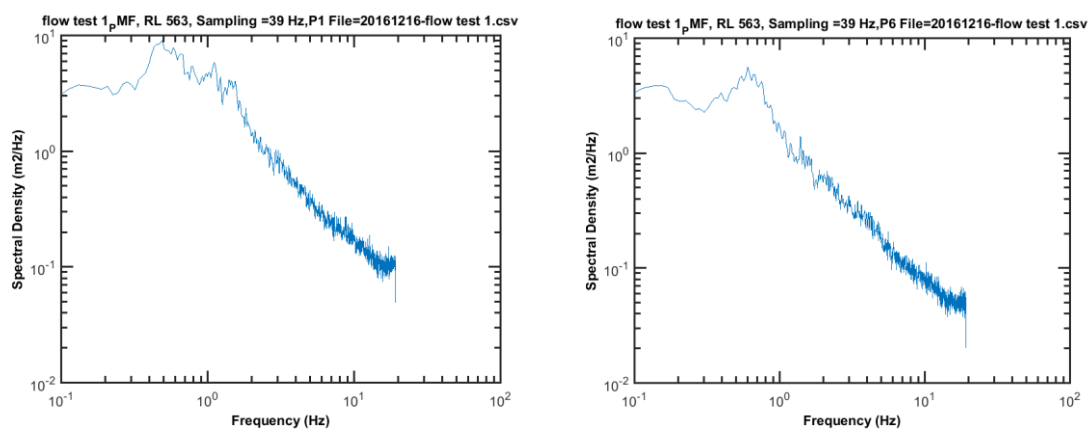


Figure 13. Sample spectral density plots for transducers 0 and 5 for the PMF

Review of reservoir water quality monitoring and modelling

**Nasser Talebbeydokhti¹, Shokoufeh Pourshahabi², Gholamreza Rakhshandehroo³,
Mohammad Reza Nikoo⁴, Mehrab Amiri⁵**

1- Professor, Department of Civil and Environmental Engineering, Head of Environmental Research and Sustainable Development Center, Shiraz University, Shiraz, Iran

2- Ph.D. Candidate, Department of Civil and Environmental Engineering, Shiraz University, Shiraz, Iran

3- Professor, Department of Civil and Environmental Engineering, Shiraz University, Shiraz, Iran

4, 5- Assistant Professor, Department of Civil and Environmental Engineering, Shiraz University, Iran

Emails: nassertaleb@gmail.com; pshahabi@shirazu.ac.ir

Abstract

Reservoir water quality assessment is important for decision makers to manage the water quality in the reservoir and downstream. Integration of reservoir water quality monitoring and modelling could provide better information for water quality assessment. The purpose of this study is to review the development of reservoir water quality models and monitoring network designs. Various mathematical models like CE-QUAL-W2, MIKE, WASP, and EFDC have been developed in the literature in order to simulate water quality in a reservoir. The capabilities and limitations of different models are presented and illustrated in this paper. Several studies may be found in the literature for selection of water quality variables, design of sampling locations to monitor reservoir water quality, and identification of sampling frequencies. Generally, the optimal design of monitoring networks would reduce the fiscal burden of long term stewardship and improve the understanding of reservoir operators on the water quality that is delivered to downstream, while allowing stakeholders to select, understand, and balance their design objectives. This research could aid the decision makers to directly select the reliable reservoir water quality models and appropriate approaches for optimal design of monitoring networks to save millions of dollars that are currently spent on sampling redundant data.

Keywords: Reservoir water quality, Monitoring network, Mathematical models, Stakeholder involvement.

1. INTRODUCTION

Designing a reservoir monitoring network is an important issue which plays a direct role in the monitoring network reliability and expenditure. Numerous aspects have to be considered in this problem such as sampling locations, sampling frequencies, and stakeholders' monitoring objectives.

Integration of reservoir water quality monitoring and modelling could provide better information for water quality assessments. Besides, modelling may be used in some situations where monitoring is not possible. Water quality modelling in reservoirs is more difficult compared to river and estuarine systems because of thermal stratification and wind mixing processes [1]. Various models have been developed to simulate the water quality in reservoirs. From the variety of mathematical models, only two and three-dimensional models which are widely used (CE-QUAL-W2, MIKE, WASP, and EFDC) are briefly discussed here. The capabilities and limitations of these models are presented and illustrated in this paper.

In order to find the best compromised monitoring plan, concerned stakeholders must be included in the decision-making process. It is an effective way to achieve a shared vision (a consensus) and lead to more sustainability for water resources system [1]. Participated stakeholders can input their expert knowledge during the design process of a reservoir monitoring network.

This study provides a review of the most challenging problems in reservoir water quality monitoring and modelling to identify the state-of-the-art in this field. The following sections condense an extensive literature on reservoir monitoring network design, reservoir water quality models, and stakeholder involvement in reservoir water quality modelling and monitoring.

2. RESERVOIR MONITORING NETWORK DESIGN

Designing a monitoring network is difficult because of complex aspects such as selecting water quality variables, identifying sampling locations and sampling frequencies as well as the duration and objectives of sampling [2].

Identifying optimal locations to monitor water quality at a reservoir reduces the cost of monitoring program considerably. Generally, the optimal locations reduce the number of trips to sample a reservoir and improve the understanding of reservoir operators on the water quality that is delivered at downstream. Lee and Kwon (2009) and Lee et al. (2011) tried to decrease redundant sampling locations in a reservoir with measuring their similarity using statistical techniques [3, 4]. Lee et al. (2014) applied entropy theory to optimize water quality monitoring stations in a reservoir and identified the relative importance of water quality variables including chemical oxygen demand, suspended solids, total nitrogen, and total phosphorus. They used the collected water quality data from nine sampling locations at depths between 5 and 6 m of Lake Yongdam in the Korean peninsula. They tested all possible combinations of the nine sampling locations to find the optimal locations and showed that the time series of each water quality variable averaged over all the nine sampling locations closely matched the time series averaged on the six optimal locations [5]. Yenilmez et al. (2015) minimized the number of monitoring stations in the Porsuk Dam Reservoir located in Turkey based on the spatial correlation structure in surface dissolved oxygen values. In their study, kernel density estimation and ordinary kriging was coupled to identify the representative monitoring stations in the reservoir [6]. Jabbari et al. (2016) obtained critical paths with maximum time variance in quality indices values for placement of monitoring stations in Karkheh Dam Reservoir using CE-QUAL-W2 model. They considered phosphate, nitrate, chlorophyll-a, and dissolved oxygen to control eutrophication in the reservoir [7]. Nikoo et al. (2017) presented a new methodology for multi-objective optimization of water quality monitoring stations of the *Karkheh Dam Reservoir* in Iran. Their proposed approach was based on NSGA-II (Non-dominating Sorting Genetic Algorithm-II), transinformation entropy and social choice methods to achieve a common option agreed upon by social stakeholders. They selected five water quality variables: phosphate (PO_4), nitrate-nitrite ($\text{NO}_3\text{-NO}_2$), electrical conductivity (EC), ammonium (NH_4), and dissolved oxygen saturation (DO_{sat}). In their study, water quality samples were taken at two stations (monthly) at 5 m depth intervals for 14 months. They simulated water quality over 40 years by a calibrated and verified CE-QUAL-W2 model. They selected 22 potential monitoring stations at different depths along the length of the reservoir. Their results showed that the number of optimized monitoring stations was 3 out of 22 potential stations across all seasons, however, the locations were different across seasons [8].

Identifying optimal sampling frequencies could decrease the corresponding expenditure. Varol et al. (2012) studied the spatial and temporal variations of water quality in Kralkızı, Dicle and Batman dam reservoirs in the Tigris River basin, in Turkey based on multivariate statistical techniques like cluster analysis, principal component analysis, factor analysis, and discriminant analysis. They showed that discriminant analysis resulted in more data reduction [9].

3. RESERVOIR WATER QUALITY MODELS

Water quality models are designed for simulation and assessment of water quality in water bodies, which may reduce the monitoring expenditure. Integration of reservoir water quality monitoring and modelling could provide better information for water quality assessment. Designing a water quality model is a difficult task because of highly non-linear and complex aspects, stochastic elements of natural systems, and limited knowledge of the events taking place in water bodies. Thus, many simplification and assumptions are considered in any model [10]. Various models have been developed to simulate the water quality in reservoirs like DYRESEM, HEC-5Q, WQRRS, CE-QUAL-W2, MIKE, WASP, and EFDC. Only two and three-dimensional models i.e. CE-QUAL-W2, MIKE, WASP, and EFDC are discussed in the following sub-sections. Capabilities and limitations of these models are presented in Table 1. The models are compared in Table 2.

3.1. CE-QUAL-W2

CE-QUAL-W2 model is a two-dimensional, hydrodynamic and water quality model, that was developed by the United States Army Corps of Engineers [11]. The CE-QUAL-W2 model has the ability to model 21 water quality state variables [12]. It is most appropriate for simulation of the water quality in narrow and deep reservoirs due to well mixing in the horizontal and lateral direction. The governing equations are the continuity, momentum and advection/diffusion equations. The hydraulic parameters and geometric, inflow/outflow and meteorological data are needed for model application [13].

A review of previous studies shows that CE-QUAL-W2 model is widely used for water quality modelling in reservoirs. Kuo et al. (2006) investigated the stratification and eutrophication problem in two reservoirs (Tseng-Wen and Te-Chi) in Taiwan using a CE-QUAL-W2 model. The simulated values of temperature, total phosphorus, ammonia, nitrite/nitrate, chlorophyll-a, and dissolved oxygen matched the field data well [14]. Ha and Lee (2007) applied a CE-QUAL-W2 model to study the eutrophication in Daechong Dam Reservoir in South Korea. They monitored dissolved oxygen, biochemical oxygen demand, chemical oxygen demand, total suspended solids, and pH [15]. Debele et al. (2008) utilized the CE-QUAL-W2 model for water quality simulation in the Cedar Creek Reservoir (long and narrow), TX, USA [12]. Liu et al. (2009), Dai et al. (2012); Huang (2014); Chang et al. (2015), and Torres et al. (2016) applied this model for reservoir water quality modelling [16, 17, 18, 19, 20]. Noori et al. (2015), Jabbari et al. (2016), and Nikoo et al. (2017) used the CE-QUAL-W2 model for simulation of water quality in the *Karkheh Dam Reservoir* in Iran [21, 7, 8].

3.2. MIKE 11- RESERVOIR

MIKE 11 is a fully dynamic model that is designed by Denmark Hydrology Institute (DHI) in 1993 for simulation of flood, sediment transport, and water quality in rivers and channels [22]. The Reservoir Module (MIKE 11-Reservoir) is developed within MIKE 11 for water quality simulation in deeper water bodies like reservoirs. The water quality model of MIKE 11-Reservoir is a two-dimensional hydrodynamic model that solves Navier Stokes equation, combined with the equation for conservation of mass, salinity and temperature [23].

Kjelds and Storm (2001) presented a comprehensive integrated modelling system including MIKE 11, MIKE 11-Reservoir, MIKE BASIN, and MIKE SHE to assess and minimize the adverse environmental impact of Wielowies Klasztorna Reservoir in Poland [24]. Rzadar et al. (2011) compared the CE-QUAL-W2, WASP5 and MIKE11 models for simulation of the water quality of Pasikhan River in Iran. They showed that the CE-QUAL-W2 model was more reliable comparing with WASP5 and MIKE11 models. They also concluded that MIKE11 model did not consider the wind effects [25]. Xin et al. (2015) applied MIKE 21 to simulate the water quality in the Danjiangkou Reservoir [26]. The MIKE 21 model is suitable for simulation of water quality, eutrophication and sediment transport in two-dimensional horizontal free surface flows [27].

3.3. WATER QUALITY ANALYSIS SIMULATION PROGRAM (WASP)

Water Quality Analysis Simulation Program (WASP) was developed by the USEPA (Di Toro et al., 1983) for water quality simulation in one, two, or three-dimensional problems (rivers, lakes, estuaries, coastal wetlands, and reservoirs) [28]. The boundary conditions, loads, mass transfer rate, kinetic rates and concentrations of organic compounds, trace elements and phytoplankton are needed for model application. The output are variable concentrations [10]. The WASP model is a time-variable model that can be coupled with hydrodynamic and sediment transport models to calculate flows, velocities, temperature, salinity and sediment fluxes [29].

The WASP model has been used in many rivers, lakes, and reservoirs. Kuo et al. (1986) investigated the vertical water quality variations in the Te-Chi Reservoir using the WASP model [30]. Kuo et al. (1994) coupled the WASP model with a two dimensional laterally averaged hydrodynamic model (LARM2) to study the eutrophication problem in Te-Chi Reservoir [31]. Debele et al. (2008) claimed that using the CE-QUAL-W2 model has more advantages than the WASP model for simulation of water quality in Cedar Creek Reservoir. Also, the CE-QUAL-W2 is suitable for modeling the changes in water levels in the reservoir [12]. Ernst and Owens (2009) combined a WASP model with a SWAT model to control eutrophication in Cedar Creek Reservoir in Texas. The nutrient loads in their study came from various sources (watershed loading, wastewater treatment plans, atmospheric loading and internal NH_4 and OPO_4 sediment flux). They claimed that the WASP model has fewer degree of freedom and consequently is less affected by errors in comparison with CE-QUAL-W2 model [32]. Narasimhan et al. (2010) applied the WASP model in combination with the watershed model SWAT to develop a comprehensive modeling approach to simulate the algal growth (chlorophyll-a) in the Cedar Creek Reservoir in Texas. They concluded that the proposed modeling approach can lead us to find out the dynamics of nutrient loading from the watershed in large reservoirs [33].

3.4. ENVIRONMENTAL FLUID DYNAMICS CODE (EFDC)

Environmental Fluid Dynamics Code (EFDC) is a three-dimensional model which includes hydrodynamic, sediment and contaminant, and water quality modules. It was developed by Hamrick (1992), Virginia Institute of Marine Science [34]. The EFDC model solves the equations of motions, transport equations for turbulent kinetic energy, salinity and temperature and Eulerian transport-transformation equations for dissolved and suspended materials [35]. This model, as noted by the United States Environmental Protection Agency (USEPA), is a tool for water quality management [36].

Literature shows that this model has been used in many rivers, lakes, and reservoirs. Li et al. (2007) applied the EFDC model for water temperature simulation in Manwan Reservoir in China. Their results showed that the simulated values of water temperature data using the EFDC model matched the observed data well [37]. Çalışkan and Elçi (2009) used the EFDC model to study the effects of selective withdrawal on hydrodynamics of Tahtali Reservoir in Turkey. The numerical model results showed the same trends as the measurements. Their results also showed that EFDC had not the capability of simulating internal waves [38]. He et al. (2011) modeled eutrophication in Beijing Guanting Reservoir in China using EFDC model to manage the reservoir's water quality and reduce the external nutrients loading. The Beijing Guanting Reservoir was shallow and wide, and they selected the EFDC model to identify the nutrients concentration in the reservoir [39].

4. STAKEHOLDER INVOLVEMENT IN RESERVOIR WATER QUALITY MODELLING AND MONITORING

Involving stakeholders in decision-making, and a shared vision, can lead to more sustainability for water resources system [1]. Integrated water resources management is based on stakeholder engagement that include policy-makers, decision-makers, water conservation organizations, universities and the general public [40].

Participated stakeholders, which often have conflicting requirements, can input their expert knowledge during the design process of a reservoir monitoring network. As we mentioned earlier, stakeholder participation was proposed by Nikoo et al. (2017) in a multi-objective optimization of water quality monitoring stations of the *Karkheh Dam Reservoir* in Iran. In their study, the involvement of the stakeholders was performed using social choice methods [8]. Social choice methods can be used to find the best solution considering conflicting objectives and disputing stakeholders [41].

Table 1- Capabilities and limitations of Reservoir water quality models

Models	Capabilities	Limitations
CE-QUAL-W2	<ul style="list-style-type: none"> • Two-Dimensional (longitudinal/vertical) • Based on continuity, momentum and advection/diffusion equations • Using a fully explicit or an explicit/implicit finite difference solution technique • Predicting water surface elevations, velocities, and temperatures, in addition to water quality computation • Ability to model rivers, lakes, reservoirs, estuaries, and combinations thereof • Ability to model multiple water bodies in the same computational grid including multiple reservoirs, steeply sloping riverine sections between reservoirs, and estuaries • Any combination of constituents can be included/excluded from a simulation • Including time-varying data input subroutine • Adjusting the time step to ensure hydrodynamic stability • Allows the model user to set dynamic parameters for the water level control over time • Calculation of ice-cover • Having numerical algorithms for pipes, weir/ spillways, gates, and multiple pumps • Having a graphical pre/postprocessor, allowing the user considerable flexibility in the type and frequency of outputs • Having multiple turbulence closure schemes including $k - \epsilon$ turbulence model • Selective withdrawal calculations and vertical port selection in a reservoir • Computation of topographic and vegetative shading • Estimating suspended solids re-suspension as a result of wind-wave action [13] 	<ul style="list-style-type: none"> • Laterally averaged • Model application is a complicated and time-consuming task • The user must decide among several vertical turbulence schemes the one that is most appropriate for the type of water body being simulated • The equations are written in the conservative form using Boussinesq and hydrostatic approximations • Since vertical momentum is not included, the model may give inaccurate results where there is significant vertical acceleration [13].
MIKE 11-Reservoir	<ul style="list-style-type: none"> • Two-Dimensional (longitudinal/vertical) • Solves Navier Stokes equation, combined with the equation for conservation of mass, salinity and temperature • Ability to simulate flows, water quality and sediment transport • Selective withdrawal (outflows) and inflows calculations • Reservoir flushing and eutrophication • Vertical oxygen profiles, i.e. oxygen conditions, in the bottom waters • The model is equipped with advanced turbulence models (e.g. $k - \epsilon$ model) • Including 12 state variables: phytoplankton (C, N, P, chlorophyll-a), zooplankton, detritus (C, N, P), inorganic nutrients (ammonia, nitrate and phosphate) and DO. • It is specifically designed to study impacts of catchment inflow and operational strategies on the physical and biological processes within the reservoir [23] 	<ul style="list-style-type: none"> • Laterally integrated Navier Stokes equation assuming hydrostatic pressure distribution • Does not consider the wind effects [25]
WASP	<ul style="list-style-type: none"> • Three-dimensional • Ability to model rivers, lakes, estuaries, coastal wetlands, and reservoirs • A time-variable model • Predicting water quality responses to natural phenomena and man-made pollution • Including variables: DO, CBOD, ammonia, NO_3, organic nitrogen, orthophosphate, organic phosphorous, algae, benthic algae, detritus, sediment, and salinity • It can be linked with hydrodynamic and sediment transport models that can provide flows, depths velocities, temperature, salinity and sediment fluxes • Ability to bring data into the model as simple as cut and paste or queried from a database [10, 28, 29] 	<ul style="list-style-type: none"> • Not capable of simulating control structures
EFDC	<ul style="list-style-type: none"> • Three-dimensional • Based on the equations of motions, transport equations for turbulent kinetic energy, salinity and temperature and Eulerian transport-transformation equations • Using a semi-implicit, conservative finite volume solution scheme • Ability to model rivers, lakes, reservoirs, estuaries, coastal regions and wetlands • Simulation of drying and wetting, representation of hydraulic control structures, vegetation resistance, wave-current boundary layers and wave induced currents • Allows the simulation of multiple size classes of cohesive and non-cohesive sediment • Can represent the transport and fate of an arbitrary number of contaminants, including metals and hydrophobic organics, sorbed to any of the sediment classes and dissolved and particulate organic carbon using a three-phase equilibrium partitioning formulation • Allows the representation of various degradation and transformation processes • Includes a variable configuration eutrophication component for simulation of aquatic carbon, nitrogen and phosphorous cycles • The full configuration of state variables based on the CE-QUAL-ICM model (The configuration can be readily reduced to WASP equivalent configurations) • Can create hydrodynamic transport files formatted for WASP and CE-QUAL-ICM • Support various graphics packages such as IDL, TECPLOT and MATLAB [34, 35, 36] 	<ul style="list-style-type: none"> • Not capable of simulating internal waves [16]

Table 2. Comparison of Reservoir water quality models

		Models			
		CE-QUAL-W2	MIKE	WASP	EFDC
Dimension	1-D	✓	✓	✓	✓
	2-D (length-width)	-	-	✓	✓
	2-D (length-depth)	✓	✓	✓	✓
	3-D	-	-	✓	✓
Hydrodynamics	inlet	✓	✓	✓	✓
	control structure	✓	✓	-	✓
Water quality processes	TDS	✓	✓	✓	✓
	temperature	✓	✓	-	✓
	bacteria	✓	-	✓	✓
	DO-BOD	✓	✓	✓	✓
	nitrogen cycle	✓	✓	✓	✓
	phosphorus cycle	✓	✓	✓	✓
	phytoplankton	✓	✓	-	-
	zooplankton	✓	✓	✓	-
	algae	✓	-	✓	✓
	SOD* simulation	✓	-	✓	✓

*Sediment Oxygen Demand

5. CONCLUSIONS

This paper addresses the three most challenging issues that face reservoir monitoring network designers: (1) optimal design of monitoring networks; (2) reliable reservoir water quality models; (3) stakeholder engagement. Optimal design of monitoring networks reduces the cost of monitoring program considerably. Different approaches for optimization of reservoir water quality monitoring stations are presented in this paper. A comparative study of different models shows that there is no general model that can be appropriate for all situations. In wide reservoirs, like the Beijing Guanting Reservoir in China, the EFDC model is appropriate for simulation of the reservoir's water quality. However, the EFDC has not the capability of simulating internal waves. The CE-QUAL-W2 model is the most appropriate for simulation of the water quality in narrow and deep reservoirs. This model has more advantages than WASP model for simulation of water quality. Also, it is suitable for modeling the changes in water levels in the reservoirs. WASP model has fewer degree of freedom and consequently is less affected by errors in comparison with CE-QUAL-W2 model. CE-QUAL-W2 model is more reliable comparing with WASP and MIKE11 models. Furthermore, MIKE11 model does not consider the wind effects. Finally, in developing long-term monitoring plans, decision makers and stakeholders must be involved to discover, understand, and balance tradeoffs among a variety of performance objectives.

6. REFERENCES

1. Loucks D.P. Beek E.V. Stedinger J.R. Dijkman J.P.M. and Villars M.T. (2005), “*Water resources systems planning and management*”. UNESCO publishing.
2. Harmancioglu N. B. Fistikoglu O. Ozkul S. D. Singh V. P. and Alpaslan N. (1999), “*Water quality monitoring network design*”, Boston: Kluwer.
3. Lee, Y. Kwon, S. (2009). “*A study on measuring the similarity among sampling sites in Lake Yongdam with water quality data using multivariate techniques*”. Environ. Impact. Assess. **18** (6), pp. 401-409.
4. Lee, Y. S. Kwon, S. H. Lee, S. U. and Ban, Y. J. (2011), “*Construction and application of network design system for optimal water quality monitoring in reservoir*”. Journal of Korea Water Resources Association, **44** (4), pp. 295-304.
5. Lee, C. Paik, K. Lee, Y. (2014), “*Optimal sampling network for monitoring the representative water quality of an entire reservoir on the basis of information theory*”, J. Water. Clim. Change. **5** (2), pp. 151-162.
6. Yenilmez, F. Düzgün, S. Aksoy, A. (2015), “*An evaluation of potential sampling locations in a reservoir with emphasis on conserved spatial correlation structure*”, Environ. Monit. Assess. 187.
7. Jabbari, E. Chavoshian, A. Boroumand, A. and Masoumi, F. (2016), “*A new approach to selecting optimum locations of sampling stations in Karkheh dam reservoir using CE-QUAL-W2 model*”, Modares Civil Engineering Journal, **15** (4), pp. 1-8 (in Persian).
8. Nikoo, M.R. Pourshahabi, S. Rezazadeh, N. **Shafiee, M.E.** (2017), “*Stakeholder engagement in multi-objective optimization of water quality monitoring network, case study: Karkheh dam reservoir*”, Water Science and Technology: Water Supply, 17 (2), ws2016196, IWA. DOI: **10.2166/ws.2016.196**.
9. Varol, M. Gökot, B. Bekleyen, A. and Şen, B. (2012), “*Spatial and temporal variations in surface water quality of the dam reservoirs in the Tigris River basin, Turkey*”. Catena, **92**, pp. 11-21.
10. Chapman, D. V. (Ed.). (1996), “*Water quality assessments: a guide to the use of biota, sediments, and water in environmental monitoring*”. Great Britain at the University Press, Cambridge.
11. Cole, T. and Buchak, E. (1995), “*CE-QUAL-W2: A Two-Dimensional, Laterally Averaged, Hydro-dynamic and Water Quality Model*”, Version 2.0, Technical Report EI-95-1, U.S. Army Engineer Waterways Experiment Station, Vicksburg, MS.
12. Debele B. Srinivasan R. and Parlange J. Y. (2008), “*Coupling upland watershed and downstream water body hydrodynamic and water quality models (SWAT and CE-QUAL-W2) for better water resources management in complex river basins*”, Environmental Monitoring and Assessment, **13**, pp. 135–153.
13. Cole, T.M. and Wells, S.A. (2013), “*CE-QUAL-W2: A two-dimensional, laterally averaged, Hydrodynamic and Water Quality Model*”, Version 3.71, Department of Civil and Environmental Engineering, Portland State University, Portland, OR.
14. Kuo, J. T. Lung, W. S. Yang, C. P. Liu, W. C. Yang, M. D. and Tang, T. S. (2006), “*Eutrophication modelling of reservoirs in Taiwan*”. Environmental Modelling and Software, **21** (6), pp. 829-844.
15. Ha, S. R. and Lee, J. Y. (2007), “*Application of CE-QUAL-W2 model to eutrophication simulation in Daecheong reservoir stratified by turbidity storms*”, In Proceedings of Taal2007: The 12th World Lake Conference (Vol. 824, p. 833).
16. Liu, W.C. Chen, W.B. Kimura, N. (2009), “*Impact of phosphorus load reduction on water quality in a stratified reservoir-eutrophication modeling study*”. Environ. Monit. Assess. **159** (1-4), pp. 393-406.
17. Dai, L. Dai, H. Jiang, D. (2012), “*Temporal and spatial variation of thermal structure in Three Gorges Reservoir: A simulation approach*”, J. Food Agri. Environ. **10** (2), pp. 1174-1178.
18. Huang, Y. (2014), “*Multi-objective calibration of a reservoir water quality model in aggregation and non-dominated sorting approaches*”, J. Hydrol. **510**, pp. 280-292.

19. Chang, C.H. Cai, L.Y. Lin, T.F. Chung, C.L. van der Linden, L. and Burch, M. (2015), “*Assessment of the impacts of climate change on the water quality of a small deep reservoir in a humid-subtropical climatic region*”. *Water* 7, pp. 1687-1711.
20. Torres, E. Galván, L. Cánovas, C. R. Soria-Píriz, S. Arbat-Bofill, M. Nardi, A. Papaspyrou, S. and Ayora, C. (2016), “*Oxycline formation induced by Fe (II) oxidation in a water reservoir affected by acid mine drainage modeled using a 2D hydrodynamic and water quality model—CE-QUAL-W2*”. *Science of the Total Environment*, **562**, pp. 1-12.
21. Noori, R. Yeh, H. D. Ashrafi, K. Rezazadeh, N. Bateni, S. M. Karbassi, A. Kachoosangi, F.T. and Moazami, S. (2015), “*A reduced-order based CE-QUAL-W2 model for simulation of nitrate concentration in dam reservoirs*”, *Journal of Hydrology*, **530**, pp. 645-656. doi:10.1016/j.jhydrol.2015.10.022.
22. Danish Hydraulic Institute (DHI). (1993), “*MIKE 11 User Guide and Reference Manual*”, Horsholm, Denmark, DHI.
23. The Modelling Tool for Optimisation of Reservoir Management, Water Quality Simulation and Impact Assessment (<http://www.ib.usp.br/limnologia/textos>)
24. Kjelds, J. and Storm, B. (2001), “*Integrated water resources modeling water use and water quality simulation*”. In *Bridging the Gap: Meeting the World's Water and Environmental Resources Challenges*, pp. 1-10.
25. Razdar, B. Mohammadi, K. Samani, J. M. V. and Pirooz, B. (2011), “*Determining the best water quality model for the rivers in north of Iran (case study: Pasikhan River)*”, *Computational Methods in Civil Engineering*, **2** (1), pp. 105-116.
26. Xin, X. K. Li, K. F. Finlayson, B. and Yin, W. (2015), “*Evaluation, prediction, and protection of water quality in Danjiangkou reservoir, China*”, *Water Science and Engineering*, **8** (1), pp. 30-39.
27. Danish Hydraulic Institute (DHI). (2001), “*MIKE 21 User Guide and Reference Manual*”. Horsholm, Denmark, DHI.
28. Di Toro, D.M. Fitzpatrick, J.J. and Thomann, R.V. (1983), “*Documentation for Water Quality Analysis Simulation Program (WASP) and Model Verification Program (MVP)*”, U.S. Environmental Protection Agency, Large Lakes Research Station, Grosse He, MI, EPA- 600/3-81-044, 158 pp.
29. <http://www.epa.gov/athens/wwqtsc/index.html>
30. Kuo, J.T. Young, D.L. Wu, W.H. Li, C.Y. and Chen, S.C. (1986), “*Water quality modeling of Te-Chi Reservoir (III)*”. Project Completion Report to Water Resource Planning Commission, Ministry of Economics Affairs, Taipei, Taiwan (in Chinese).
31. Kuo, J. T. Wu, J. H. and Chu, W. S. (1994), “*Water quality simulation of Te-Chi Reservoir using two-dimensional models*”, *Water Science and technology*, **30** (2), pp. 63-72.
32. Ernst, M. R. and Owens, J. (2009), “*Development and application of a WASP model on a large Texas reservoir to assess eutrophication control*”. *Lake and Reservoir Management*, **25** (2), 136-148.
33. Narasimhan, B. Srinivasan, R. Bednarz, S. T. Ernst, M. R. and Allen, P. M. (2010), “*A comprehensive modeling approach for reservoir water quality assessment and management due to point and nonpoint source pollution*”. *Trans. ASABE*, **53** (5), pp. 1605-1617.
34. Hamrick, J. M. (1992), “*A three-dimensional environmental fluid dynamics computer code: Theoretical and computational aspects*”, Virginia Institute of Marine Science, College of William and Mary.
35. Hamrick, J. M. (1996). “*User's manual for the environmental fluid dynamics computer code*”, Department of Physical Sciences, School of Marine Science, Virginia Institute of Marine Science, College of William and Mary.
36. Wang, Q. Li, S. Jia, P. Qi, C. and Ding, F. (2013), “*A review of surface water quality models*”. *The Scientific World Journal*.

37. Li, L. Wu, J. Wang, X. Zhou, H. L. and Fang, B. (2007), “*Application of the three-dimensional environmental fluid dynamics code model in Manwan Reservoir*”. In *New Trends in Fluid Mechanics Research*, Springer Berlin Heidelberg, pp. 414-414.
38. Çalışkan, A. and Elçi, Ş. (2009), “*Effects of selective withdrawal on hydrodynamics of a stratified reservoir*”, *Water resources management*, **23** (7), pp. 1257-1273.
39. He, G. Fang, H. Bai, S. Liu, X. Chen, M. and Bai, J. (2011). “*Application of a three-dimensional eutrophication model for the Beijing Guanting Reservoir, China*”, *Ecological Modelling*, **222** (8), pp. 1491-1501.
40. Behmel, S. Damour, M. Ludwig, R. and Rodriguez, M.J. (2016), “*Water quality monitoring strategies — A review and future perspectives*”, *Sci. Total. Environ.* doi:10.1016/j.scitotenv.2016.06.235.
41. Sheikhmohammady M. and Madani K. (2008), “*Bargaining over the Caspian Sea- the Largest Lake on the Earth*”, *World Environmental and Water Resources Congress: Ahupua'a*.

Smoothed particle hydrodynamics for morphology changes and a non-newtonian fluid

Pooyan Nikeghbali¹, Pourya Omidvar², Payam Rasooli³, S. Mehdi Mohammadizadeh⁴

1- Hydraulic Structure Engineering, Absar Fars Consulting Engineers Co., Shiraz, Iran

2- Faculty of Engineering, Yasouj University, Yasouj, Iran

3-Civil Engineering, Eastern Mediterranean University, Famagusta, North Cyprus

4- Hydraulic Structure Engineering, University of Sistan and Baluchestan, Zahedan, Iran

Email: pooyannikeghbali@gmail.com

Abstract

The interaction between bed-load sediment and water flow is an important topic of great concern which should be modeled for a wide range of hydrodynamic systems. In this paper, smoothed particle hydrodynamics (SPH) is utilized for the simulation of mudflow with non-Newtonian behavior and dam-break propagation over an erodible bed that sediment particles as weakly compressible flow is treated as a non-Newtonian fluid using Bingham-Cross model coupled with the Newtonian treat (Owen's relation) at the interface. To cope with the difficulties arisen from different densities, the continuity and momentum equations are rather modified so that the interactions between the sediment and water are accurately modeled. To validate the Bingham-Cross model, a mudflow test case is studied and compared with other experimental and numerical studies. Then, the two-phase model is used to simulate the dam-break models with PVC bed materials. Comparisons are then made with the available experimental data indicating that the defined SPH model provides the sensible prediction for a test case.

Keywords: Smoothed Particle Hydrodynamics, Dam-break problem, Non-Newtonian fluid, Mudflow, Movable bed.

1. INTRODUCTION

The study on changes in the shape of channels and river beds is necessary for understanding bed load transports. It is clear that the knowledge of random particle movement of bed material transport is also essential for understanding the river morphology, which depends on the pattern of sediment transfer along the river with the local erosion and deposition. Sediment transportation in hydrodynamics is of great industrial and environmental importance which is complicated to model due to its complex boundary conditions and random particle movements. The crucial characteristics of loose boundary problems is the interaction between the fluid and sediment, which is the erosion and sediment transport problems. This cannot be treated in an isolation from the hydrodynamics. Sediments form a passive medium that only reacts to the applied forces [1].

Dam-break with a moveable bed is a challenging problem needed to be simulated in particular when a large amount of sediments is propagated mainly due to dam failure or other defense structures. This may result in a large-scale modification of the valleys morphology along with the environmental and geological changes which significantly increases the hazardous damages to the mankind and urban infrastructures [2]. Modeling of the dam-break problem over mobile bed, based on the Eulerian methods, is rather complicated. The predicted models should be able to accurately evaluate the bed movement and the free-surface variation. Smoothed particle hydrodynamics (SPH) is a fully Lagrangian and meshless method. In this method, each particle carries an individual mass, position, velocity and other physical quantities. The Lagrangian nature of SPH is suited for simulating problems with large deformation, e.g., dam-break, as there is no special treatment needed for free surface.

In this paper, the open-source SPHysics code [3] will be modified into two phases, where the sediment phase is considered as non-Newtonian. Moreover, the viscosity of sediment in the momentum equation is simulated using Bingham fluid with Cross model. The water-sediment interface is modeled using Owen's equation, leading to precise study of the water-sediment interface. Therefore, a case of mudflow is studied to validate the SPH code on Bingham fluid behavior and is compared with the experimental study of Komatina and Jovanovic [4] and numerical studies of Shao and Lo [5] and Capone [6]. Then, the case of dam-break problem is studied and compared with the experimental results of Spinewine [2] and two numerical results of Shakibaieina and Jin [7] and also Razavitoosi *et al.* [8].

2. SPH METHOD

The SPH method generally applies an integral interpolation of a function f , defined over a domain of interest Ω , allowing f to be estimated in terms of its values in the surrounding domain. The value of f at location \mathbf{r} can be written as a convolution product of the function f [9]:

$$f(\mathbf{r}) \approx \langle f(\mathbf{r}) \rangle = \int_{\Omega} f(\mathbf{r}') W(\mathbf{r} - \mathbf{r}', h) d\mathbf{r}' \quad (1)$$

The transition to a discrete domain is obtained by approximating the integral of equation 1 by a summation. The value of quantity f relative to the particle i located at the point $\mathbf{r}_{ij} = \mathbf{r}_i - \mathbf{r}_j$ can be written as:

$$f(r_{ij}) = \sum_j \frac{m_j}{\rho_j} f_j W(r_i - r_j, h) = \sum_j \frac{m_j}{\rho_j} f_j W_{ij} \quad (2)$$

where $W(\mathbf{r}-\mathbf{r}',h)=W_{ij}$ is called the smoothing kernel and h is the smoothing length, $d\mathbf{r}$ is a differential volume element, m is the particle mass and f_j denotes the value of f at the point occupied by particle j .

The SPH continuity and momentum equations of the Lagrangian form of the Navier–Stokes equation can be obtained using the following formulations [9]:

$$\frac{d\rho_i}{dt} = \sum_j m_j u_{ij} \cdot \nabla_i W_{ij} \quad (3)$$

$$\frac{dv_i}{dt} = -\sum_j m_j \left(\frac{P_i}{\rho_i^2} + \frac{P_j}{\rho_j^2} \right) \cdot \nabla_i W_{ij} + g + \sum_j m_j \left(\frac{4\nu r_{ij} u_{ij}}{(\rho_i + \rho_j)(|r_{ij}|^2 + \iota^2)} \right) \cdot \nabla_i W_{ij} + \sum_j m_j \left(\frac{\bar{\tau}_i}{\rho_i^2} + \frac{\bar{\tau}_j}{\rho_j^2} \right) \cdot \nabla_i W_{ij} \quad (4)$$

where m_i is the mass of particle i , P_i is the pressure that particle experienced, u is the velocity vector of particle, ρ is the density, g is the gravity acceleration, ν is the kinematic viscosity, ι is a very small number avoiding the term become infinity and $\bar{\tau}$ represents the SPS stress tensor.

Due to the discontinuity in density in multi-fluid simulation, Greiner et al. [10] proposed a new method for multiphase problems. The algorithm requires sweeps over the particles to determine the volume distribution, density, rate of change of volume (continuity equation), and the acceleration. The following simple algorithm (according to Monaghan and Rafiee [11]) is capable of handling the density ratios that normally occur. The continuity and momentum equations in this algorithm are:

$$\frac{d\rho_i}{dt} = -\rho_i \sum_j \frac{m_j}{\rho_j} (u_j - u_i) \cdot \nabla_i W_{ij} \quad (5)$$

$$\frac{dv_i}{dt} = -\sum_j m_j \left(\frac{P_i + P_j}{\rho_i \rho_j} + R_{ij} \right) \cdot \nabla_i W_{ij} \quad (6)$$

The following form of R_{ij} is used according to Monaghan [12] and Grenier et al. [10]:

$$R_{ij} = K * \left(\frac{\rho_d - \rho_l}{\rho_d + \rho_l} \right) \left| \frac{P_i + P_j}{\rho_i \rho_j} \right| \quad (7)$$

where ρ_d and ρ_l are the reference density of the denser and the lighter fluid, respectively, and K is a free coefficient.

In multiphase systems viscosity, discontinuity happens when phases have different viscosities. Therefore, we use Owen's equation (see [13]) for an interface viscosity which is used in the laminar viscosity term of equation 4 instead of viscosity parameter ν .

$$\vartheta_{mix} = \frac{\vartheta_{fluid}}{1 + C \frac{\rho_s}{\rho_f}} \quad (8)$$

where ρ_s and ρ_f are the sediment and fluid density, respectively, and C is the concentration of solid particle which is defined as:

$$C = \frac{\sum_{j \neq i} \delta_{sf} W_{ij}}{\sum_{j \neq i} \delta_{sf} W_{ij} + \sum_{j \neq i} (1 - \delta_{sf}) W_{ij}} \quad \delta_{sf} = \begin{cases} 0 & \text{for fluid particle} \\ 1 & \text{for solid particle} \end{cases} \quad (9)$$

For modeling the sediment herein, the Bingham fluid assumption is used which is due to the non-Newtonian behavior of shear stress distribution for the sediment particles. Bingham model can be stated on two

different behaviors. The first is the solid behavior which is below the yield stress point and second is above this point as fluid behaves similar to the Newtonian fluid with a constant viscosity.

In this study, the numerical computation effective viscosity μ_{eff} is used to simulate the Bingham fluid behavior as:

$$\mu_{eff} = \mu_B + \frac{\tau_y}{D} \quad (10)$$

To define the effective viscosity, the general Cross model is as follows according to [5]:

$$\frac{\mu_0 - \mu_{eff}}{\mu_{eff} - \mu_\infty} = (KD)^m \quad (11)$$

where μ_B and τ_y are the Bingham viscosity and yield stress, respectively. Moreover, μ_0 and μ_∞ are viscosity at very low and very high shear rates, respectively; K and m are constant parameters. The shear rate which is simplified in 2D is defined as:

$$D = \sqrt{2 \left(\frac{\partial u}{\partial x} \right)^2 + 2 \left(\frac{\partial v}{\partial y} \right)^2 + \left(\frac{\partial u}{\partial y} + \frac{\partial v}{\partial x} \right)^2} \quad (12)$$

Considering m in equation 11 as unity, the effective viscosity in a Cross model is expressed as:

$$\mu_{eff} = \frac{\mu_0 + K\mu_\infty D}{1 + KD} \quad (13)$$

By comparing the above equation with equation 10, the other parameters under $KD \gg 1$ are defined as:

$$K = \frac{\mu_0}{\tau_y} \quad \text{and} \quad \mu_\infty = \mu_B \quad (14)$$

The remaining unknown parameter in the equation 13 is the viscosity at low shear rate (μ_0). This viscosity should have a large value to fix and freeze the particles when the shear rate is very low. So, in this study, the viscosity at low shear rate is set as $\mu_0 = 10^3 \mu_\infty$. Due to continuous variation of effective viscosity and in order to avoid the numerical instability, the Cross model (equation 13) is suggested [5].

The sediment–water mixture is the two-phase flow that sediment is treated as a non-Newtonian and water is a Newtonian fluid. In this paper, we use the effective viscosity, which is identified as Cross model, for each sediment particle, and for the interface between two phases we use equation 8.

To calculate the pressure term and to avoid solving the Poisson equation of incompressible fluids at each time step, in weakly compressible form of SPH, the Tait's equation of state is used [14]:

$$P = B \left[\left(\frac{\rho}{\rho_0} \right)^\gamma - 1 \right] + \chi \quad (15)$$

Where ρ_0 is the reference density and $B = c_s^2 \rho_0 / \gamma$ where $\gamma = 7$ is typically used to induce strong pressure response to density variations, such that the density variation remains small enough for the fluid volume to be conserved and c_s being the corresponding speed of sound.

In two-phase flows, [15] suggested additional term back pressure, X , in addition to modify the bottom phase pressure. This back-pressure term is the column of water above each SPH sediment particle which is updated at each time step. This term is added for two-phase flow to ensure that the excessive pressure of water corresponding to the column of water above the sediments is calculated for sediment, while it is zero for water [15]. This numerical simulation could be found in [16] in detail.

3. NON-NEWTONIAN FLUID

The Bingham fluid as a non-Newtonian fluid is studied by comparison of the dam-break SPH model using Cross model with the experimental [4] and numerical [5,6] models with the ISPH (Incompressible SPH) and SPH methods. In these studies, channel bed slope $S_0=0.1\%$ is considered. The density of mudflow is 1200 Kg/m^3 , the yield stress $\tau_y = 25 \text{ Pa}$ and viscosity $\mu_B = 0.07 \text{ Ns/m}^2$ are reported by [4].

Figure 1 shows the propagation of the Bingham fluid in present study in comparison with the numerical study by [5] that used ISPH method at $t=0.1, 0.3, \text{ and } 0.6\text{s}$.

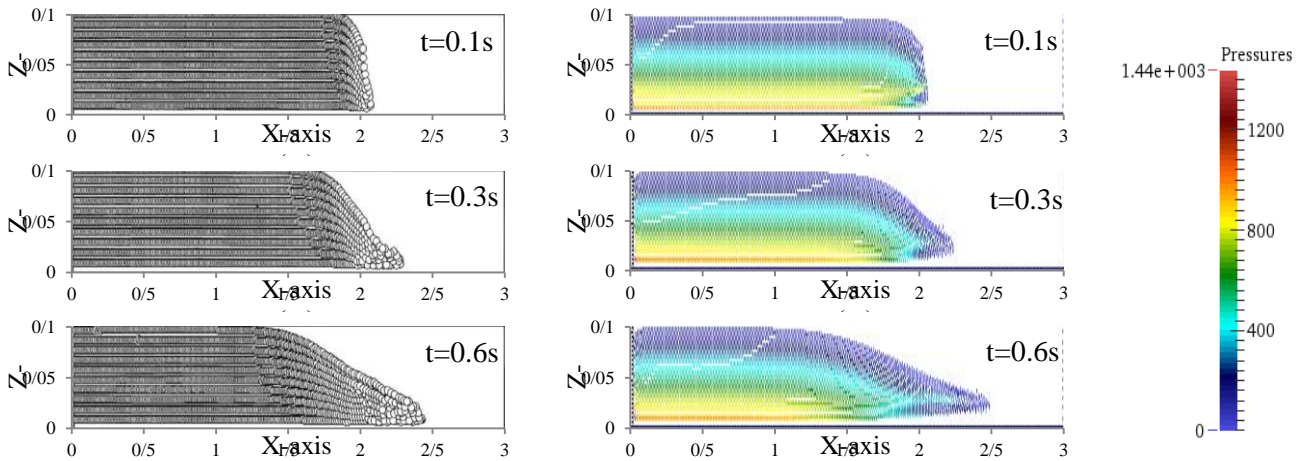


Figure 1. Mudflow profile in dam-break problem; left column is studied by [5]; right column is the present study

The dimensionless comparison on the experimental [4], Capone’s SPH numerical [6] studies and the present model illustrate in figure 2. This figure shows the present model has almost proper behavior in compare with experimental study. In this figure, H is the initial depth of fluid and x is the propagation length of fluid. T and ε are the dimensionless form of time and propagation length, respectively.

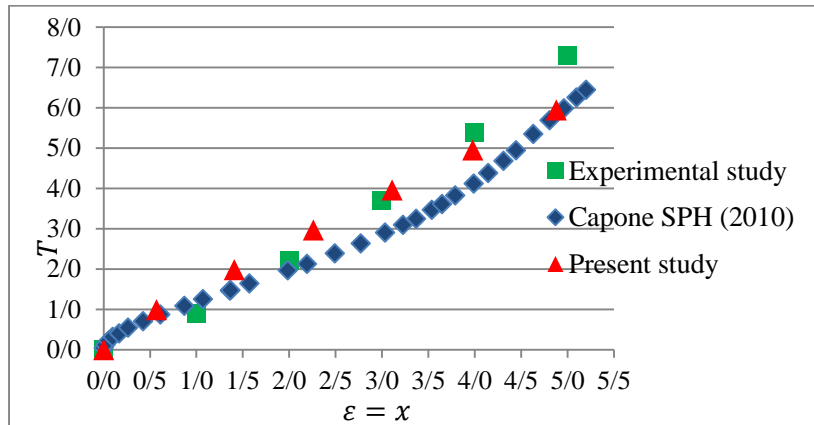


Figure 2. Propagation of mudflow in compare with other studies

4. DAM-BREAK MODEL ON THE PVC BED

The experimental model of Spinewine [2] is exerted to simulate the dam-break problem. In this experiment, a dam-break model is studied, in which the PVC materials with diameter of 3.9 mm are used for the saturated sediment of the bed. The study is considered in the flume with the length of 6m and a gate with a negligible friction factor, located at the middle of flume and separates upstream and downstream. In these models, water flows to downstream due to the gate removal, eroding the bed and subsequently changing the topography. The schematic of the problems is presented in Figure 3 and the sediment properties are summarized in Table 1. In these case studies, the particle spaces are 0.01 m and the CPU cost on a workstation, Core i7, 2.20 GHz, RAM 8.0 GB for 39,748 particles is about 5 h.

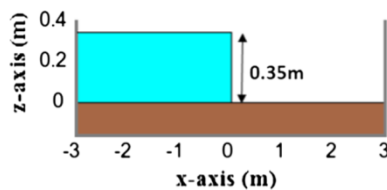


Figure 3. Scheme of dam-break model

Table 1. Properties of sediments for the bed material

Material	Mean diameter of sediment (m)	Specific density (kg/m ³)	Bulk density (kg/m ³)	Friction angle (°)
PVC	0.0039	1580	1336	38

In this test case, the flume bed is cover with the PVC pellets sediment which has a flat surface bed. Figure 4 presents the SPH dam-break of this test case at 0.25, 0.50, 0.75 and 1.0s compared with experimental studies.

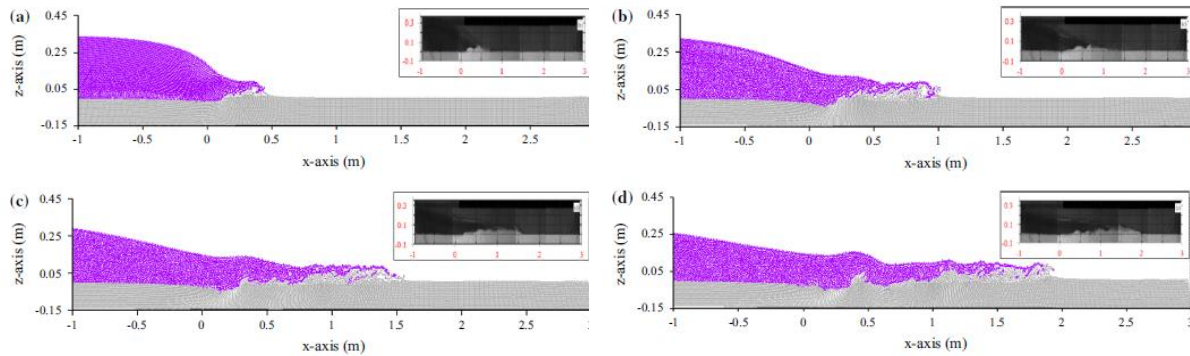


Figure 4. The snapshots of dam-break problem on PVC bed study at t=0.25, 0.50, 0.75, 1.0s (compared with [2])

As the figures show, after removing the gate, water flows to the downstream while the shear stress increases and it becomes unstable with erosion. Large erosion is happened near the gate while the sediments distribute to the downstream and deposit far from the gate. Increasing the bed elevation is occurred behind the wave front due to the erosion beneath the front. As the figure shows, the bed is not decreased monotonously but series of humps and troughs are generated due to the wave propagation.

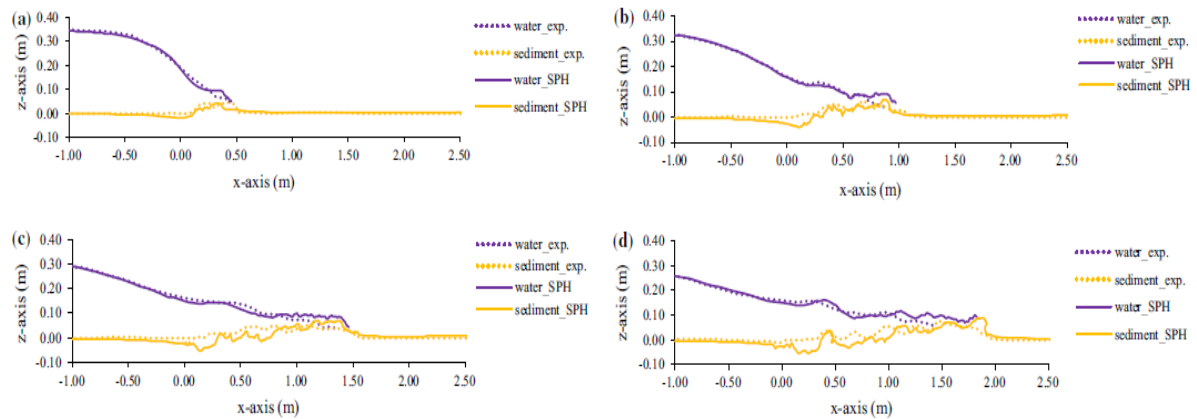


Figure 5. Free surface and bed surface changes on PVC bed study at t=0.25, 0.50, 0.75, 1.0s (compared with [2])

Here, the SPH simulation is in a good agreement with experimental studies as also shown in Figure 5. This Figure compares the SPH surface elevation with the results of [2]. As shown, the rheological model of bed is reasonably treated, and the results are in good agreement. It is worth mentioning that the snapshots of experimental model are taken from the side of flume. This may be the reason of discrepancy between SPH and experimental snapshots.

To quantify the existing error in the calculation of water and sediment surface elevation, the relative error norm (ϵ_{L2}) is defined to provide a good measureable precision. RSM error is defined as [7]:

$$\epsilon_{L2} = \left(\frac{\sum_{i=1}^N (\Delta H)_i^2}{\sum_{i=1}^N (H)_i^2} \right)^{1/2} \tag{16}$$

where ΔH is the deviation of numerical water surface/sediment bed surface elevation from the experimental values (H) and N is the number of points at which the elevations are compared. The sediment and water surfaces of numerical results are compared with their related points in a deformed area according to Shakibaeinia and Jin [7]. The errors of the free surface and bed surface SPH model according to the experimental ones are illustrated in Table 2. The results indicate the reasonable behavior of the rheological model is used in this article.

Table 2. The relative error, ε_{L2} , between experimental and numerical results

Time(s)	0.25	0.50	0.75
Error in free surface	0.046	0.034	0.045
Error in bed surface	0.057	0.096	0.105

Figure 6 presents the difference between three models of simple Newtonian Owen’s relation (Figure 6b), Bingham–Cross model (Figure 6c), and Bingham–Cross model coupled with Owen’s relation (Figure 6d).

As these figures show, the Bingham–Cross model coupled with Owen’s relation has a better result at $t=0.25s$ and correctly treated as a PVC sediment bed with time proceeding in comparison with experiments. In this model, equation 8 is used for the interface of water and sediment (Figure 6d). In this method, the sediment particles have granular behavior where sediment particles are pushed and eroded with water particles. Therefore, there are some isolated particles for fluid in sediment area and for sand in water area. Although, the behavior of sediment using equation 8 results in a noisy pressure distribution at the interface (See Figure 7) but according to Figure 6 it gives a better interface in comparison with experiment. Figures 8 and 9 present the relative errors of free surface and bed surface, respectively.

Figure 8 presents a better result of current study than the model proposed by [7]. As this figure shows, the error of both models is not significant at $t=0.25s$ but with time proceeding this error increases until $t=0.5s$ and after that the error becomes constant.

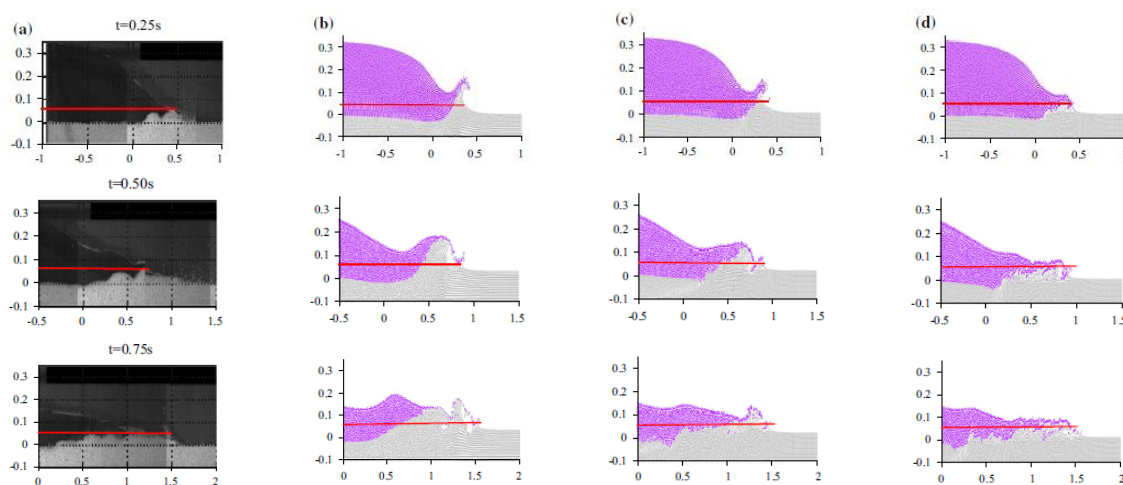


Figure 6. Dam-break problem over PVC bed; a) experiment of [2]; b) the Newtonian Owen’s relation; c) the Bingham-Cross model; d) the Bingham-Cross model coupled with Owen’s relation

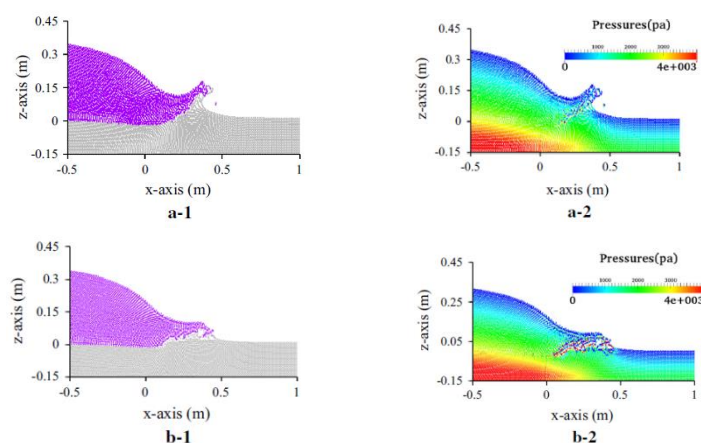


Figure 7. Particle distribution and pressure field for a) Bingham-Cross model and b) Bingham-Cross model coupled with Owen's relation at the interface

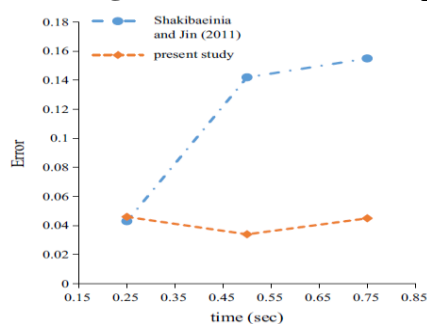


Figure 8. Comparison between the relative errors for the free surface

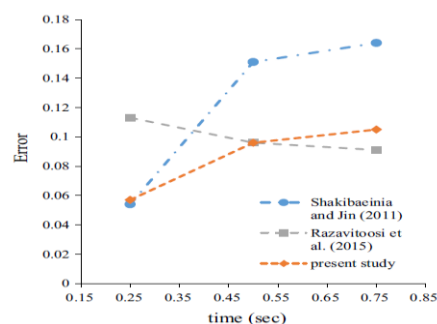


Figure 9. Comparison between the relative errors for the sediment bed surface

As Figure 9 shows, at $t=0.25s$, the error of sediment bed surface of current study is close to MPS and less than the [8] model who used only Cross model. With the time proceeding, the error of the current study increases less than the MPS model and close to the errors of [8] SPH model to $t=0.75s$. The errors of both SPH models (present and [8] studies) with the time proceeding are close to each other and less than the model of [7]. The results for $t=1.0s$ have not reported by these researchers.

5. CONCLUSIONS

Here, we used the SPH method to model violent flow over a movable bed where sediment is considered as a Bingham fluid. The study of mudflow was done and compared with the experimental and numerical studies to validate the Bingham-Cross model. The comparison was illustrated that the Bingham-Cross model has proper ability to simulate the mudflow. In the two-phase model, the Bingham-Cross model that coupled with Owen's relation is used to simulate the sediment bed with a careful study of the water-sediment interface. This study shows, in water-sediment models, sediment at the interface does not treat as the Bingham behavior exactly. We have used available experimental and numerical methods to validate our results.

6. REFERENCES

1. Raudkivi, A.J. (1998), “*Loose boundary hydraulics*”, A.A. Balkema, Rotterdam.
2. Spinewine, B. (2005), “*Two-layer flow behaviour and the effects of granular dilatancy in dam-break induced sheet-flow*” PhD thesis, Univerisite’ de Louvain, Belgium.
3. Gómez-Gesteria, M., Crespo, A.J.C., Rogers, B.D., Dalrymple, R.A., Dominguez, J.M., and Barreiro, A. (2012), “*SPHysics development of a free-surface fluid solver—part 2: efficiency and test cases*” Comput Geosci. <http://www.Sphysics.org>
4. Komatina, D. and Jovanovic, M. (1997), “*Experimental study of steady and unsteady free surface flows with water-clay mixtures,*” J Hydraul Res **35**(5), pp. 579-590.
5. Shao, S. and Lo, Y.M.E. (2003), “*Incompressible SPH method for simulating Newtonian and non-Newtonian flows with a free surface*” Adv Water Resour, 26, pp. 787–800.
6. Capone, T. (2010), “*SPH numerical modeling of impulse water waves generated by landslide*” PhD thesis, Sapienza University of Rome.
7. Shakibaenia, A. and Jin, Y.C. (2011), “*A mesh-free particle model for simulation of mobile-bed dam break*” Adv Water Resour 34. pp. 794–807.
8. Razavitoosi, S.L., Ayyoubzadeh, S.A. and Valizadeh, A. (2014), “*Two phase SPH modelling of waves caused by dam break over a movable bed*” Int J Sedim Res **29**(3), pp. 344–356.
9. Monaghan, J.J. (1992), “*Smoothed particle hydrodynamics*” Ann Rev Astron Astrophys, 30, pp. 543–574.
10. Grenier, N., Antuono, M., Colagrossi, A., Le Touze, D., Alessandrini, B. (2009) “*An Hamiltonian interface SPH formulation for multifluid and free surface flows*” J Comput Phys 228, pp. 8380–8393.
11. Monaghan, J.J. and Rafiee, A. (2013). “*A simple SPH algorithm for multifluid flow with high density ratios*” Int J Numer Meth Fluids, 71, pp. 537–561.
12. Monaghan, J.J. (2012). “*Smoothed particle hydrodynamics and its diverse applications*” Annu Rev Fluid Mech, 44, pp. 323–346.
13. Gotoh, H. and Fredsøe, J. (2000), “*Lagrangian two-phase flow model of the settling behavior of fine sediment dumped into water*” In: Proceedings of the ICCE, Australia, pp. 3906–3919.
14. Batchelor, G.K. (1967), “*An introduction to fluid dynamics*” Cambridge University Press, Cambridge
15. Colagrossi, A. and Landrini, M. (2003), “*Numerical simulation of interfacial flows by smoothed particle hydrodynamics*” J Comput Phys, 191, pp. 448–475.
16. Omidvar, P. and Nikeghbali, P. (2016), “*Simulation of violent water flows over a movable bed using smoothed particle hydrodynamics,*” J Mar Sci Technol, DOI: 10.1007/s00773-016-0409-7.
17. Chang, H.Y., Simons D.B. and Brooks R.H. (1967), “*The Effect of Water Detention Structures On River and Delta Morphology,*” Symp. On River Morphology, General Assembly Iugo, Bern, Switzerland.
18. Sugio, S. (1972), “*Laboratory study of degradation and aggradation a discussion,*” Proc. ASCE, Vol. 98, No. WW4.
19. Fan, J. and Morris, G. (1992), “*Reservoir sedimentation. I: delta and density current deposits,*” Journal of Hydraulic Engineering, Vol. 118, pp. 354-369.
20. Morris, G. and Fan, J. (1998), “*Reservoir Sedimentation Handbook, Design And Management Of Dams, Reservoirs, And Watersheds For Sustainable Use,*” McGraw- Hill companies, Washington. 1800p.
21. Shieh, C., Tseng, C., and Hsu, M. (2001), “*Effect Of Sediment Gradation On The Geometry Of River Deltas,*” International Journal of Sediment Research, vol.16, pp. 45-59.
22. Kostic, S. and Parker, G. (2003), “*Progradational Sand-Mud Deltas in Lakes and Reservoirs, Part 2, Experimental and Numerical Simulation,*” Journal Of Hydraulic Research, Vol.4, No.2, P.P. 127-140.
23. Lai, S. Y. J. and Capart, H. (2007), “*Two-Diffusion Description of Hyperpycnal Deltas,*” J. Geophys. Res., 112, F03005.

24. Lai, S. Y. J. and Capart, H. (2008), “*Response of Hyperpycnal Deltas to A Steady Rise in Base Level,*” 5th IAHR Symposium on River, Coastal and Estuarine Morphodynamics.
25. Lai, S. Y. J. and Capart, H. (2009), “*Reservoir Infill by Hyperpycnal Deltas Over Bedrock,*” J. Geophys. Res. Lett., 36, L08402.
26. Dewals, B.J., Kantoush, S.A., Erpicum, S., Piroton, M. and Schleiss, A.J. (2008), “*Experimental and numerical analysis of flow instabilities in rectangular shallow basins,*” Environ Fluid Mech. 8:31–54.
27. Dufresne, M., Vazquez, J., Terfous, A., Ghenaim A., Poulet, J.B. (2009), “*Experimental investigation and CFD modelling of flow, sedimentation, and solids separation in a combined sewer detention tank,*” Computers & Fluids, Vol. 38, pp. 1042–1049.
28. Dufresne, M., Dewals, B.J., Erpicum, S., Archambeau, P. and Piroton, M. (2010), “*Experimental investigation of flow pattern and sediment deposition in rectangular shallow reservoirs,*” International Journal of Sediment Research, Vol. 25, No. 3, pp. 258–270.
29. Dufresne, M., Dewals, B.J., Erpicum, S., Archambeau, P. and Piroton, M. (2010), “*Classification of flow patterns in rectangular shallow reservoirs,*” Journal of Hydraulic Research, Vol. 48, No. 2, pp. 197–204.
30. Dufresne, M., Dewals, B.J., Erpicum, S., Archambeau, P. and Piroton, M. (2011), “*Numerical Investigation of Flow Patterns in Rectangular Shallow Reservoirs,*” Engineering Applications of Computational Fluid Mechanics, Vol. 5, No. 2, pp. 247–258.
31. Camnasio, E., Orsi, E. and Schleiss, A.J. (2011), “*Experimental study of velocity fields in rectangular shallow reservoirs,*” Journal of Hydraulic Research, Vol. 49, No. 3, pp. 352–358.
32. Camnasio, E., Erpicum, S., Orsi, E., Piroton, M., Schleiss, J. and Dewals, B. (2013), “*Coupling between flow and sediment deposition in rectangular shallow reservoirs,*” Journal of hydraulic research, Vol. 51, No. 5, pp. 535–547.
33. Mamizadeh, J., Ayyoubzadeh, S.A. and Banihashemi, M.A. (2012), “*Experimental study of hydraulic-sediment properties on deltaic sedimentation in reservoirs,*” International Research Journal of Applied and Basic Sciences, Vol., 3 (4), 810-816.
34. Sediqkia, M. (2011), “*Experimental study on the Effect of Inflow Hydrograph and Non-uniform Graded Sediment Particles on the Rate of Progression and Delta Pattern in Reservoir,*” MSc Thesis, Tarbiat Modares University (in Persian).
35. Heydari, M. (2013), “*Experimental study of the effect of internal flood hydrograph and non-uniform graded sediment particles on the rate of progression and delta pattern,*” MSc Thesis, Tarbiat Modares University (in Persian).
36. Cherdron, W., Durst, F. and Whitelaw, J.H. (1978), “*Asymmetric flows and instabilities in symmetric ducts with sudden expansions,*” Journal of Fluid Mech., 84(1), 13-31.
37. Durst, F., Melling A. and Whitelaw J. H. (1974), “*Low Reynolds number flow over a plane symmetric sudden expansion,*” J. Fluid Mech., Vol. 64, part 1, pp. 111-128.
38. Sobey, I. J. (1985), “*Observation of waves during oscillatory channel flow,*” J. Fluid Mech. 151,395-426.
39. Fearn, R. M., Mullin, T. and Cliffe, K.A. (1990), “*Nonlinear flow phenomena in a symmetric sudden expansion,*” J. Fluid Mech., 211, 595-608.
40. Shapira, M., Degani, D. and Weihs D. (1990), “*Stability and existence of multiple solutions for viscous flow in suddenly enlarged channels,*” Computers & fluids, 18, 3,239-258.
41. Chiang, T.P., Sheu, W.H. and Wang, S.K. (2000), “*Side wall effects on the structure of laminar flow over a plane-symmetric sudden expansion,*” Computers & Fluids, 29, 467-492.
42. Stovin, V. R. and Saul, A. J. (1994), “*Sedimentation in Storage Tank Structures,*” Water Science and Technology, Vol. 29. No. 1-2. pp. 363-372.
43. Stovin, V. R. and Saul, A. J. (2000), “*Computational Fluid Dynamics and the Design of Sewage Storage Chambers,*” Water and Environment Journal, Vol. 14, pp.103–110.

Rockfall hazard assessment in the right abutment of sefidrud dam, Gilan (Iran)

Mahnaz Firuzi¹, Ali Noorzad², Mohammad Hossein Ghobadi¹

1- Department of Geology, Bu-Ali Sina University, Hamadan, IRAN

2- Faculty of Civil, Water and Environmental Engineering, Shahid Beheshti University, Tehran, IRAN

Email: Firuzi.mahnaz@yahoo.com

Abstract

Sefidrud dam is one of the four largest dams of Gilan Province, Iran. The height and crest length of the dam are 106 and 425 m, respectively. In the right abutment, the intersection of bedding plane with four joint sets has initiated wedge and toppling failures and falling blocks with the potential southwest trends. In the present research, rockfall modeling (at four seeders) was performed to assess the hazards related to these falling blocks. The obtained results indicate that the maximum run-out distance for seeders 3 and 4 are 230.1 and 230.7 m, respectively. These values present that dam is not affected by the coverage distance and block amplitude. In comparison, for seeders 1 and 2 all blocks pass over the Qazvin-Rasht freeway and fall down into the dam. The maximum bounce height, maximum velocity, and maximum kinetic energy at seeder 2 are 12 m, 13.7 m/s, and 15,000 kJ, respectively. Therefore, rockfall occurrence may pose some safety risks to the cars in the freeway and also the dam itself. As some remedies to deal with this situation, it is suggested removing loose blocks and installing rockfall-retaining structures such as protection barrier at the elevation 245 m.

Keywords: Sefidrud Dam, Joints, RocFall Modeling, Coverage Distance, Barrier.

1. INTRODUCTION

Rockfall mainly occurs when the downward forces acting on rock mass changes probably due to the morphological changes in rock slope face caused by natural or anthropogenic factors [1]. These events occur due to various reasons. In the study area, rockfall is probably triggered due to the presence of discontinuities, topography, lithology of the rock, slope angle size/shape of the falling blocks, and the slope surface parameters. There are some simulation tools developed and tested to simulate rockfall and also to compute the trajectory of falling blocks [2, 3, and 4]. The present study was conducted to investigate the rockfall hazard of the right abutment of the Sefidrud dam using RocFall software [5]. An extensive fieldwork was performed to identify and to record the vulnerable locations and dimensions of overhanging rock blocks to analyze the possibility of rockfall at four locations and its damage extent. Discontinuity survey was performed to record the joint and bedding parameters.

2. DESCRIPTION OF THE STUDY AREA

Sefidrud dam (originally named Manjil dam) is a buttress dam on the Sefidrud river in the Alborz mountain range, located near Manjil city in Gilan Province, Iran. It was constructed to store water for irrigation and produce hydroelectric power. The dam is 106m height and forms a reservoir with a capacity of 1.82 km³. The situation and aerial photograph of the study area are displayed in Fig. 1.

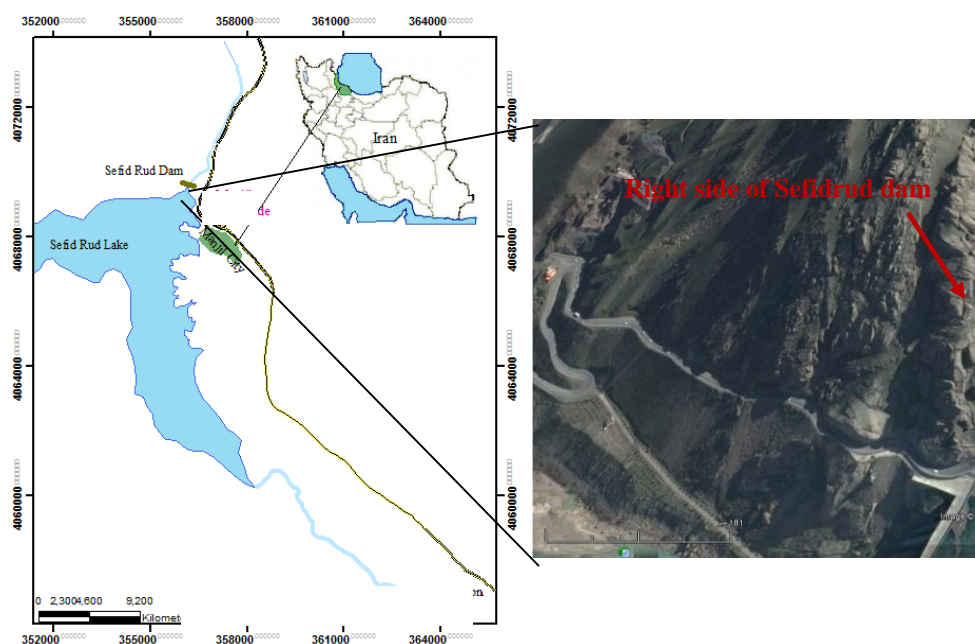


Fig. 1: Location and an aerial photograph of the right abutment dam

3. GEOLOGICAL AND STRUCTURAL SETTING

The Sefidrud dam was constructed in a deep valley. The dip and direction of the right abutment are about $40\text{-}45^\circ$ and 255° , respectively. The abutment is approximately perpendicular to the freeway and dam axis (N70E). The geological units and structure of study area were analyzed based on information obtained from field investigations and 1:25,000 geological map of Rudbar (Khalil Abad) [6]. The geological map and cross-section of the study area are depicted in Fig. 2. As shown in this figure, the rockfall in this area mainly occurs in the middle Eocene Karaj Formation. Outcrops of this formation consist of massive light gray to cream andesite tuffs. The trend and dip/dip direction of these layers are NW-SE and $70\text{-}75^\circ$ -SW, respectively. Fig. 3a–b represents typical photomicrographs of this rock. The petrographic studies show that the rock is andesite. The rock type was characterized by rectangular plagioclase feldspar, rock fragments, and quartz with porphyroid texture (Fig. 2). These samples have a stream microlites matrix composed mainly of feldspar and quartz with curved grain boundaries. The main minor minerals include bent biotites, which represent applied pressures. The compositions of the fragments are granites, chert, diorite containing biotites and pyroxenes with angular grain boundaries, indicating that the temperature of the magma has not high enough to melt it. Moreover, their burnt margins suggest the presence of high oxygen content. The coarse grains existing in these rocks illustrate some imbalance evidence including gluten, skeletal, zoning, and segment zoning (Figs. 3 and 4). The rock units of the region have a slight to moderate alteration. Sericitization and chloritization of biotite and plagioclase, and identification olivine and pyroxene have also occurred in these rocks.

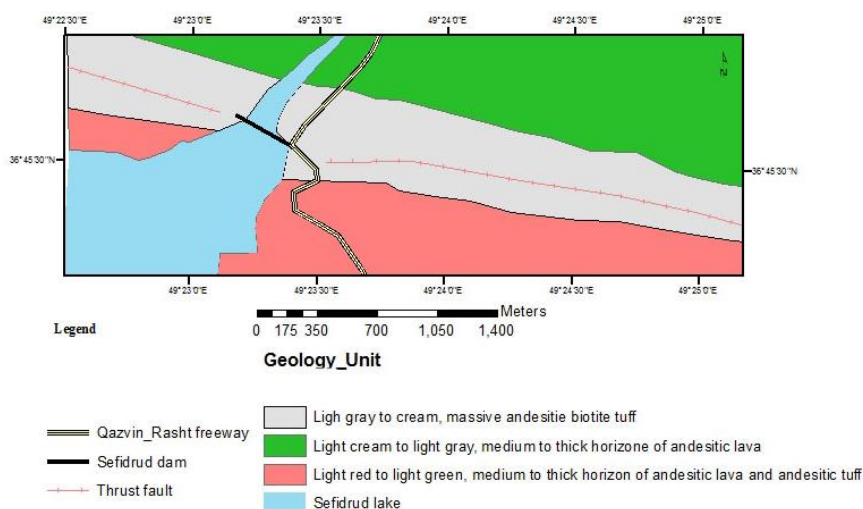


Fig. 2: Geological setting of the study area

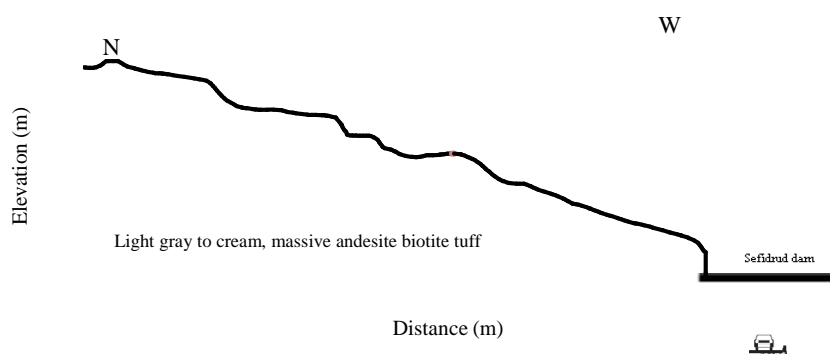


Fig. 3: Cross sections of the right abutment and the dam axis and the freeway under rockfall risk

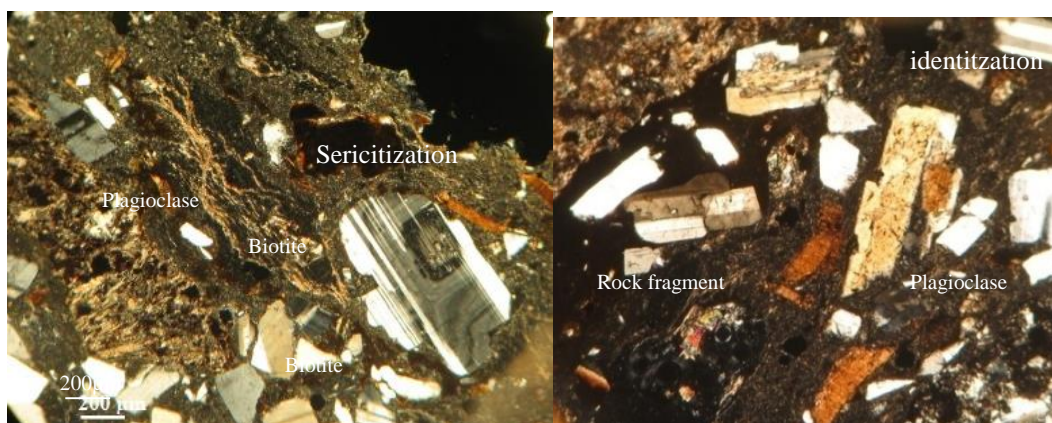


Fig. 4: Microscopic images of andesite outcrops in the right abutment dam

4. KINEMATIC ANALYSIS

Through a field survey, scanline recording was carried out to determine discontinuity parameters such as spacing, orientation, continuity, roughness, and aperture. Scanline locations were at least 10 m long in the horizontal and were chosen as being the best representatives of the rock mass and discontinuity properties. The dip/dip direction measurements were plotted on stereonet using dips V.5.1 software [7]. Stereonets and spacing of the discontinuities obtained from scanline surveys are given in Fig. 5. The friction angles were calculated from direct shear tests for the rock to determine the potential types of failure. As can be seen in the figure, slope face

dips at an angle of 45° toward the azimuth 255°. Also, the measured friction angle of the slope is 35°. Four discontinuity sets were used in this analysis. One set dips about 45° in the direction 75°, the second one dips about 50° in the direction 245°, the third one dips 40° in the direction 254°, and the fourth one (bedding) dips 73° in the direction 183° (Fig. 5). Some large wedges with potential sliding trends can be formed by the intersection of existing joints. As shown in Fig. 5, the wedges resulted from the intersection of bedding plane with joint set 1 and joint set 2 are unstable and has sliding potential along the trend calculated at 50°/245° and 37°/255° (dip/dip direction). Moreover, the stereonet plots and related analysis show that there is a potential for planar and toppling sliding/failure in the abutments owing to the following reasons: 1) the dip direction of joint set 3 is the opposite to that of the slope and 2) dip direction of joint set 2 is in line with the slope. It is noteworthy that due to the low dip of J2 compared to slope dip, there is a chance of planar failure.

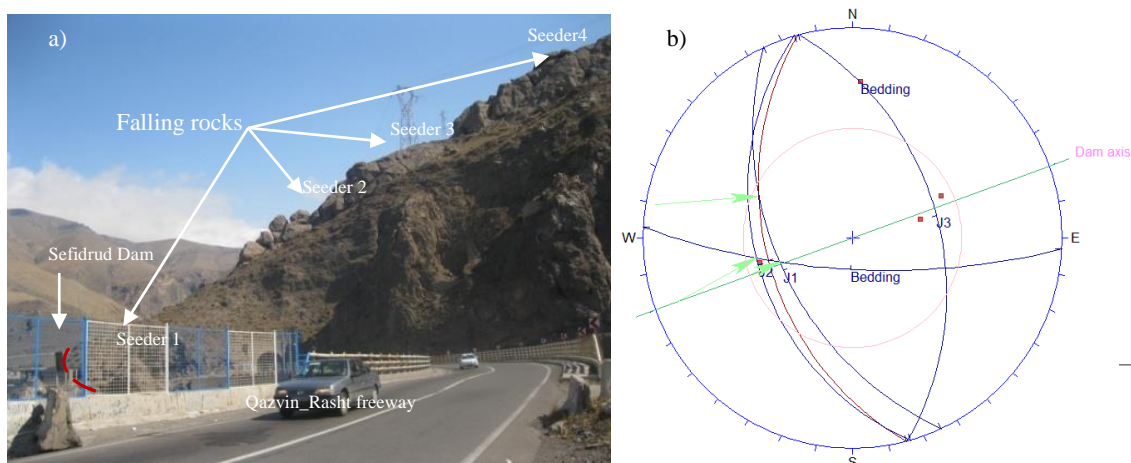


Fig. 5: a) A field photograph of right abutment dam showing the falling rock at the four locations toward the dam and road (view toward the northwest) and b) A stereonet showing the main sets, friction angle, and slope face plotted in dips V.5.1

5. ROCKFALL ASSESSMENTS

Rockfall assessments were carried out in four seeders using RocFall program [6]. Table 1 shows the values of the parameters used in rockfall simulations. Some of the crucial parameters required to design block trajectories and rockfall simulations are slope geometry, surface roughness, and coefficient of restitution. The size of the falling blocks has been determined directly from the field. Different rock masses with 200 kg and of 150,000 kg at different elevations were considered in the analysis. Accordingly, four seeders were chosen for the ultimate analysis performed in this work. The specifications of these seeds are as follows: seeder 1: (elevation = 263.5, weight = 200kg), seeder 2: (elevation = 304.1, weight = 150,000 kg), seeder 3: (elevation = 336.4, weight = 150,000kg), and seeder4: (Elevation = 338.1, weight = 150,000kg). The bounce height, total kinetic energy, and translational velocity were also calculated in this work. The unit weight of falling rocks was measured to be $\gamma = 22.3$ kN/m³ through the laboratory tests. The results of a typical rockfall analysis and variation of the run-out distance are shown in Fig. 6.

Table 1: Parameters used in rockfall analysis

Parameters		Values
Rock	Number of rockfalls	10
	Min. velocity cutoff (m/s)	0.1
	Initial velocity (m/s)	0
	Coefficient of normal restitution	0.48±0.05
	Coefficient of tangential restitution	0.89±0.05
	Friction angle (°)	35±2
	Slope roughness	2±0.5
Asphalt	Coefficient of normal restitution	0.4±0.04
	Coefficient of tangential restitution	0.9±0.04
	Friction angle (°)	30±2
	Slope roughness	0

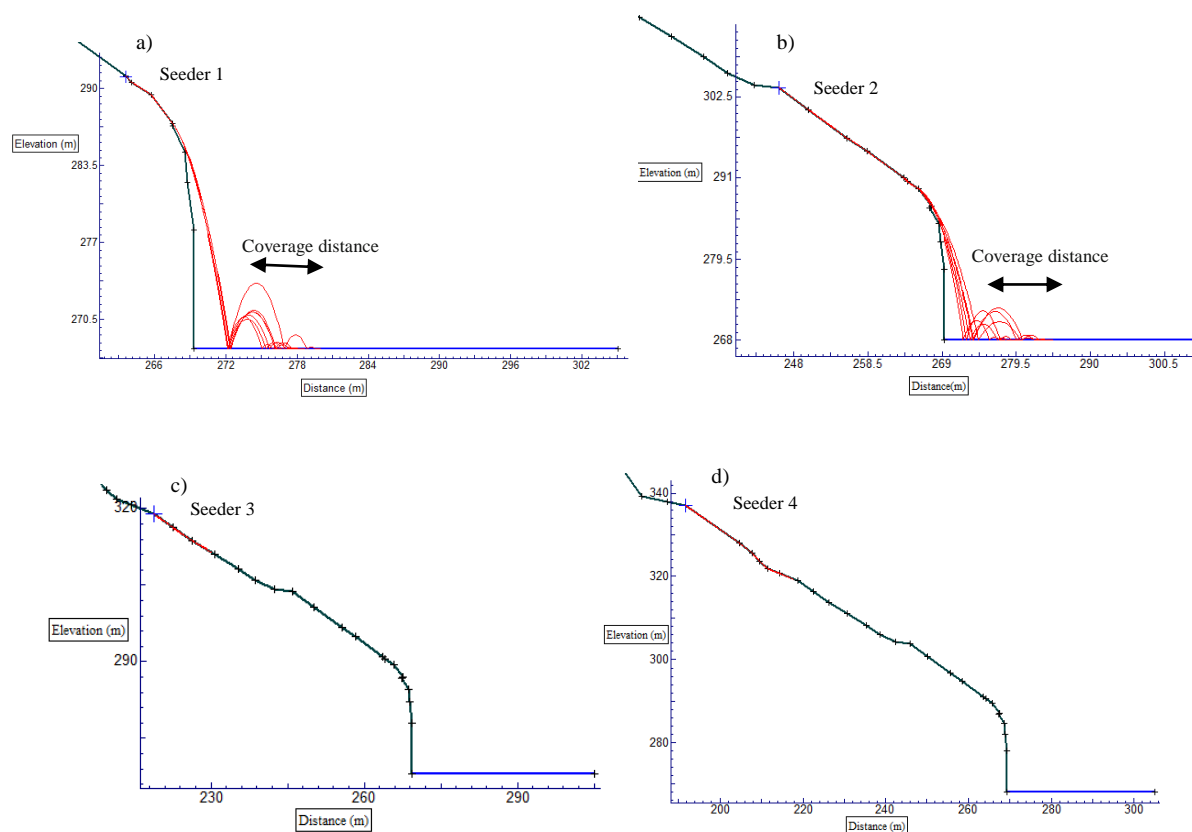


Fig. 6: Potential trajectories of falling boulders for different seeders at the right abutment of the Sefidrud dam

6. RESULTS AND DISCUSSIONS

As presented in Figs. 6c and d, the maximum run-out distances for seeders 3 and 4 are 230.1 and 230.7m, respectively, suggesting that the dam is not affected by the coverage distance and block amplitude. In comparison, for seeders 1 and 2 all blocks pass the freeway and fall down into the dam. Therefore, if rockfall happens, the safety of the cars at the freeway will be under question. Total kinetic energy, translational velocities, and bounce height for the 200 kg at elevation 290 and 150000 kg at elevation 304.1 m are shown in Figs. 7a, b, c, and d, respectively. The maximum total kinetic energy varies from 15.9 kJ to 15,000kJ for 200kg to 150,000 kg mass, respectively. Also, the maximum translational velocities range from 12.5 to 13.7 m/s, which indicate that an increase in the masses of the falling blocks does not have much effect on the translational velocity. Bounce height reached the maximum value of 12.7 and 3.8 m for fallen blocks with the masses of 200 kg and 150,000 kg, respectively (Fig. 7a). In order to prevent further damages, it is suggested to utilize some remedies such as protective barriers to overcome the future problems caused (Fig. 8). Rockfall barriers are key protection systems in mountainous regions worldwide. They are designed to intercept and capture falling rocks. Most systems are composed of flexible steel wire-nets connected to wire-rope cables, which are in turn attached to steel posts and anchored to the ground.

7. CONCLUSIONS

Based on simulation results, it is observed that the dam and the Qazvin-Rasht freeway are exposed to the risk of damage induced by the probable future rockfall. Hence, the proper protective measures are required to minimize the risk of the damage to the dam and the life of the passengers in the Qazvin-Rasht freeway. The extensive usage of the Manjil city for tourism, infrastructure, and residential areas results in an increasing need for protecting the civil installations against natural hazards. Removal of loose blocks and also installation of the rockfall retaining structures such as protection barrier at the elevation 245m of the dam are suggested as some remedies for dealing with this situation. Moreover, barriers provide rockfall protection by stopping falling rock blocks and also absorbing the kinetic energy of the falling blocks.

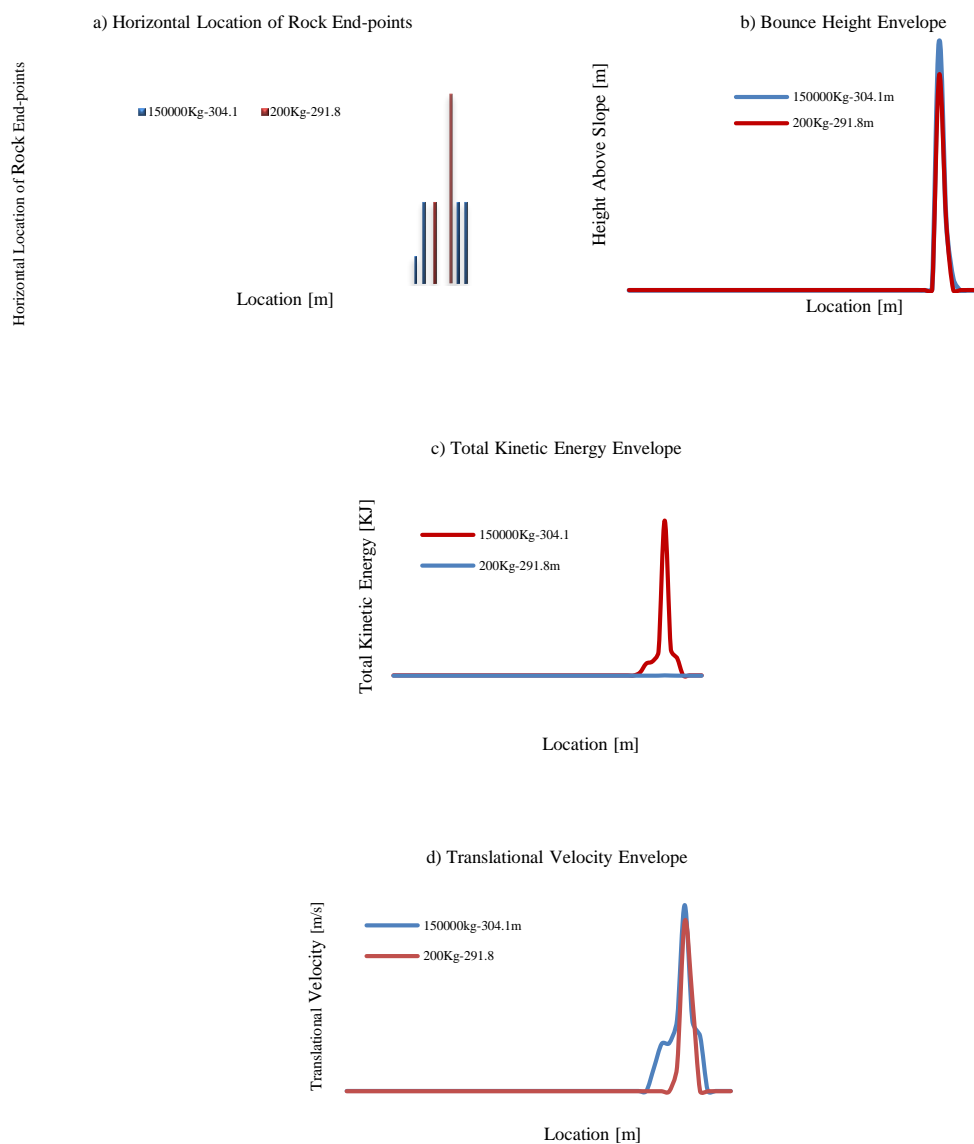


Fig. 7: a) Rockfall simulation outputs an end-point, b) Bounce heights, c) Total kinetic energies, and d) Translational velocities of the falling blocks

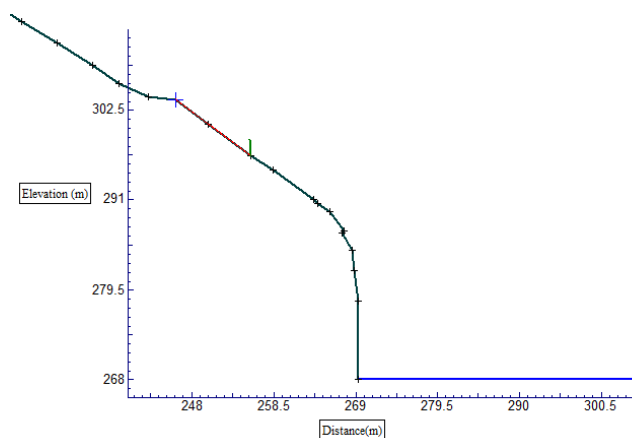


Fig. 8 Critical location of the protection barrier

8. REFERENCES

1. Ahmad, M. Umrao, R.K. Ansari, M.K, Singh, R. and Singh, T.N. (2013), “*Assessment of rockfall hazard along the road cut slopes of State, Highway-72, Maharashtra, India,*” *Geomaterials*, 3(1), pp. 15–23.
2. Singh, P.K. Kainthola, A. Panthee, S and Singh, T.N. (2016), “*Rockfall Analysis along Transportation Corridors in High Hill Slopes,*” *Environmental Earth Science*, 75, pp. 1–11.
3. Sun, S.Q. Li, L.P. Li, S.C. Zhang, Q.Q. and Hu, C. (2017), “*Rockfall Hazard Assessment on Wangxia Rock Mass in Wushan (Chongqing, China),*” *Geotechnical and Geology Engineering*, 35(4), pp.1895-1905.
4. Vishal, V. Siddique, T. Purohit, R. Phophliya, M.K. Pradhan, S.P. (2017), “*Hazard Assessment in Rockfall-Prone Himalayan Slopes along National Highway-58, India: Rating and Simulation,*” *Natural Hazards*, 85(1), pp.487-503.
5. Geological Survey of Iran. (2016), “*1: 25,000 Geology Map of Rudbar (Khalil Abad),*” Geological Survey of Tehran, Iran
6. Rocscience. (2004), “*RocFall Software for Risk Analysis of Falling Rock on Steep Slope*”, Rocscience User’s Guide, www.rocscience.com
7. Rocscience. (2004), “*DPS 5.0 software for graphical and statistical analysis of orientation based geological data*”, Rocscience User’s Guide, www.rocscience.com

Positive and negative effects of damming industry

Mohammad Ali Jaberi¹, Ghasem Shahparifar²

1- Iran Water and Power Company, Tehran, Iran

2- Graduated at geological engineering, department of geology, university of Isfahan, Isfahan, Iran

Email: m.jaberi@iwpc.ir

Abstract

Dam construction, like other industries, can cause environmental and social losses in a region. The greatest damage is caused by ponds of dams. Although these ponds reduce a few opportunities, they bring with it more opportunities for the development of society. Regardless of all positive effects such as clean energy production, job creation, increasing the reliability of power plants during a crisis, and increasing the credibility of the executives and advisers, it is easy to say that the created reservoirs can be used in such a way by increasing the capacity created; the profits generated could be more than damaging. Firstly, the advantages of this industry are mentioned in this study. Then, the possibility of reducing the adverse effects with the mention of successful experiments is studied. In the end, it came to the conclusion that if these projects were correctly implemented and replaced by hydroelectric power plants, instead of the pollutants that produce environmental pollution, green growth could be improved. Damage can also be justified by proper utilization of water resources behind the dams.

Keywords: Dam, Greenhouse gases, Global warming, Hydropower, Water per capita.

1. INTRODUCTION

The development and improvement of human societies after the Industrial Revolution of Europe is by no means without changes in the environment. During each of the activities, it has always been tried to reduce the adverse effects of various industries, such as dam construction. To this end, many of sciences have been used together to the extent that the high profitability of these structures and their lower complications are assured nowadays. Advances in agriculture, industry, mining, and so on were not possible without the construction of a large dam. So far, 50,000 dams 800 of which are in Iran have been built around the world and advanced society such as Canada and USA have many of them. Below is a summary of advantages and disadvantages of this industry.

2. POSITIVE EFFECTS OF DAMMING

The following are the most significant positive impacts of dams: electricity generation, recreation and tourism, water and water sports, moderating greenhouse gas emission, fish caught and fish farming, water supply, flood control, job creation and foreign exchange entry into the country and high safety factor in times of crisis has been investigated.

2.1. ELECTRICITY GENERATION

Hydroelectricity power plants are considered as the third source of power generation and also the most important renewable energy producer in the world. Currently, these types of powerhouses are the cheapest and most cost-effective power plants in prone countries that are capable of generating electricity. In addition, other renewable energy generating plants can be efficient and helpful, but due to their big problems, they are not economical in the absence of hydroelectric power plants or cannot be effective in meeting the needs of the community.

According to the latest studies, about 19 percent of the world's electricity is supplied from hydroelectric power [1]. China, Brazil, the United States and Canada have 27, 8.5, 7.5, and 7.3 percent of the world's hydroelectric power respectively. This owns more than 90 percent of electricity of 24 countries and as well as more than 50 percent of electricity of 63 countries [2]. While today, due to the destruction of a few old dams in the United States at various assemblies dealing with the destruction of dams in the country, it produces a high percentage of its electricity from the industry and is one of the developed countries in this field by having more than 9000 dams. Population growth and the advancement of energy consuming industries will double the needing

of development of this kind of power plants. According to the statistics the production of power plants in 2014, it was 10778 MW [3]. If we reach the maximum capacity of the country, this figure will be almost a little more than double. Despite problems such as the water crisis in the country and its impact on the performance of hydroelectric power stations, the Ministry of Water and Energy has several plans with the capacity of 22.7 GW in exploitation, implementation and investigation. Yet, the country's capacity is lower than many other countries in the world, such as Tajikistan and Paraguay, which produce more than 98% of their electricity by hydroelectric power plants, also Iran is behind advancing countries such as Japan and Turkey. These countries, despite the damming effects on the perimeter environment, are working seriously to reduce the possible complications of developing this industry with more capacity than Iran. Since per capita energy consumption in Iran is 1.61 times the global per capita and 0.73 times per capita in OECD countries; comprehensive planning in this field will be helpful to development.

2.2. RECREATION AND TOURISM, SHIPPING AND WATER SPORTS

Iran is one of the first five countries in the world in terms of climate diversity and one of the top ten in terms of culture and history. This is while only 0.7% of the world's tourism revenue is devoted to Iran. According to forecasts by the World Tourism Organization in 2020, about one billion and five hundred and sixty million people will go to tourism, and revenues from it will reach \$ 1.5 trillion [4]. This issue has been studied in various researches, but due to various shortcomings in this regard, Iran has not yet achieved its main position in this field. Dams and power plants, in addition to being one of the most important sources of water and electricity supply, have created great potential for the development of the tourism industry by creating their own special sights. In many countries, dams and reservoirs are considered to be the most important tourist hubs, attracting thousands of travelers annually. For example, the Grand Dixence Dam in Switzerland is one of them, which capabilities of this dam and its planning have made it one of the largest tourist attractions. The Moiry dam in Switzerland, Navajo in Mexico, and Hoover in the United States are examples of major dams in attracting tourists. Statistics of visiting for the Hoover Dam with a capacity for spectacular sights, boating and water sports is nine million people annually, as well as a visit statistic to the Three Gorges Dam in China with more than one million people sailing and doing water sports [5]. Considering the success of these countries and the capacity to create a dam in the beautiful areas of different province, as well as the successes achieved in some Iranian dams such as Zayandehrood, tourism can be considered the most important horizons of the country's development.

2.3. PREVENTING GREENHOUSE GAS EMISSIONS

Greenhouse gases are toxic to humans, animals and even plants, are the main cause of air pollution, acid rain, climate change, droughts and environmental degradation, and today it is a serious threat to human health and, if not controlled in time, there will be irreparable consequences for all the people of the world and the planet. According to Table 1, a high share of greenhouse gas emissions is generated in the power plant. According to studies, less than 1 percent of the country's power plants are due to hydroelectric power plants. And this low percentage also includes carbon production and can be compensated by planting trees and creating green spaces. This is one of the most important reasons for the development of these types of power plants globally.

Table 1: The share of each energy consumer in poisonous and greenhouse gases emissions in 2014(%) [3]

N ₂ O	CH ₄	CO ₂	SPM	CO	SO ₃	SO ₂	NO _x	Gas/part
4.55	6.94	22.79	2.71	0.52	2.64	2.53	5.84	Final energy consumption Domestic, commercial and public
2.43	3.56	16.67	4.30	0.24	16.85	11.65	8.77	Industry
54.84	80.68	24.93	79.76	97.20	47.68	39.72	49.64	Transportation
32.01	0.98	2.07	5.71	0.13	2.27	3.74	2.74	Agriculture
								Consume energy
0.48	0.79	4.02	*	*	*	*	*	Refinery
5.70	7.06	29.51	7.52	1.91	30.55	42.35	33.01	Power plant
100.00	100.00	100.00	100.00	100.00	100.00	100.00	100.00	SUM

* Values are not available

¹. Organisation for Economic Co-operation and Development

Greenhouse gasses cause greenhouse phenomena and therefore global warming. Today, the phenomenon of global warming is one of the problems that various national and international institutions are struggling to resolve. In addition to increase the efficiency of pollutant generating plants, replacing hydropower plants, it is being tried to solve the problem of environmental pollution and global warming. In this regard regional and international meetings are held annually. The most important meeting was held in Paris in 2015. During this conference, Iran pledged to reduce the production of these gases by 8% until 2030, if the international sanctions were lifted, and to put 7.500 MW of clean energy into the electricity distribution network. It should be noted that the domestic institutions have implemented effective and efficient programs to reduce greenhouse gases in different sectors, so that according to the data of Power and Energy in 2009, many damages caused by the gases from transportation, power plants, agriculture and other sectors were reduced. According to the World Bank and World Environment Organization data in Table 2 and the greenhouse gas emission index in the country's power plants, in a calculation in general, it can be concluded that in case of full exploitation of the country's hydroelectric power, it can save 52 million tons of greenhouse gas annually, equivalent to \$330 million. This figure is equivalent to 30 percent of greenhouse gases from power plans and 9 percent of total greenhouse gases in Iran according to the data of Power and Energy in 2016.

Table 2: The amount of savings from non-polluting gases in 2013

N ₂ O	CH ₄	CO ₂	SPM	CO	SO ₃	SO ₂	NO _x	
*	60	3	123	53	*	521	171	Saving cost (Dollar/Ton) [3]
654	4243	177744913	31105	177660	6586	627934	651610	Total annually gas emission(Ton) [3]
*	0.1	170	13	3	*	110	37	Amount of annually saving by total hydropower capacity(million dollar)

*unknown

2.4. FISHING AND BREEDING FISH

One of the most important benefits of this industry is the creation of fishing opportunities. Of course, the aquatic ecosystem created is greater than that of before damming. Therefore, the opportunity to increase the population of aquatic animals, especially with the special support of the new methods, is provided. The quiet environment of the ponds behind the dams is more susceptible to current rivers for catching fish. Developing dams in cold regions such as Chaharmahal and Bakhtiari, with less water BOD, can provide more opportunities to breeding fish in cages. According to the report released by the Department of fisheries of Chahar Mahal and Bakhtiari, the Karoon IV Dam reservoir has the capacity to raise 3000 tons of salmon trout, which is equivalent to about 30 percent of cold blooded fish from Chaharmahal and Bakhtiari province, the largest producer in the country. It is also equivalent to 2 percent of cold-blooded fish produced in the country in 2014, and 30 percent of the fishery products exported to foreign countries in the year 2016 [6].

The Karoon IV Dam basin, with a volume of 2190 million cubic meters, forms only a small fraction of the total dams in the province. Behesht Abad, KaroonV, KhersanI, KhersanII, KhersanIII, Bazoft and several other dams, such as the Karoon IV dam, can contribute to fish farming potential and increase the province's income. If the fish farming capacity in the dams of this province is increased in the same way, after the exploitation of these dams, this figure will increase to 14,000 tons per year (equivalent to \$50 million gross). And if this action is taken in other provinces, Iran can be one of the largest exporters of cold-blooded fish. According to the data of Iran Water Resources Management Company, the capacity of the study, implementation, and exploitation dams of the country is 50000, 24500 and 48500 million cubic meters respectively, which in case of fish farming in 25% of these waters, 40,000 tons of fish can be produced annually. It is almost equivalent to \$130 million of gross domestic product (this figure can be increased by processing and canning and exports to other countries). Obviously, investing in cage breeding is one of the low-cost schemes, which gathering of more production units in one area, the costs of breeding are reduced, as well as in the production and marketing of products and the processing of products, a lot of help is given to it.

Dam construction is different in various parts of the country. According the table 3, the volume of water in reservoirs of Khoozestan dams is much higher than adjacent provinces, while using the existing plans and studies of Chahar Mahal and Bakhtiari and Lorestan provinces; it is possible to create 23573 million freshwater pond cubic meters for various uses. These statistics, as well as similar statistics, indicate that there are still areas of the country that despite adequate capacity, have not been given priority to the development, and damming industry has still not reached the final capacity of 10 percent.

Table 3: Comparison of Dam Development in Khoozestan with other provinces

Religion	Number of Dam				Volume of reservoir (million cubic meter)			
	Study phase	Implementation	Exploitation	Sum	Study phase	Implementation	Exploitation	Sum
Khoozestan	22	5	20	47	7647	379	21711	29739
Chaharmahal and Bakhtiari	19	7	8	34	6675	1576	2290	10541
Lorestan	31	12	3	46	5701	6299	22	12022

2.5. WATER SUPPLY FOR AGRICULTURE, DRINKING AND INDUSTRY

According to the 2015 United Nation Organization Water Report, the world's renewable freshwater per capita in 2013 is about 1700 cubic meters, on the verge of tension [7]. In recent years, a large part of Iran has faced tensions due to insignificant rainfall despite a large population. According to the World Heritage List, in 2014, among the 182 countries, there are 58th in renewable water sources. Brazil holds 8647 billion cubic meters per year and Russia, the United States, Canada and China are ranked after Brazil which is the first [8]. But it's important to note that Iran has less renewable water per capita than the first 10 countries in the world [7 and 9]. Table 4 shows the renewable water per capita of the top ten dam building countries in the world. Iran's renewable water per capita and GDP per capita are less than the world's 10 most dam building countries, with the exception of India. Similarly, the per capita water behind the dams of Iran is much lower than that of those countries, which if the dam construction continues, this figure will reach from 423 to about 1500 cubic meters. This figure is almost equivalent to the renewable freshwater per capita, which is very easy to achieve at low cost, and can increase the country's resistance to the drought phenomenon and facilitate the development of agriculture and industry. Water as a source of life is one of the most important sources of development in industry, agriculture, and, consequently, for the improvement of economic indicators and the lack of dependence on oil.

Table4: Comparison of Iran with developed and developing countries [8 and 9]

Country	GDP per capita (2014)	Dam capacity per capita (2010) (M ³ /year)	Total renewable water resources per capita(2014)(M ³ /year)	Total renewable water resources(2014) (billion cubic meter)	Dams number
China	7390	589(2013)	2018	28040	23842
USA	54075	2304	9538	3069	9261
India	1579	189(2005)	1458	1911	5102
Japan	36343		3397	430	3112
Brazil	11306	3460	41603	8647	1411
Canada	49805	24134	80746	2902	1170
South Africa	6423	577	942	51.35	1114
Spain	30354	1149	2418	111.5	1063
Turkey	10170	2102(2012)	2690	211.6	972
Iran	5246	423	1732	137	802

According to the International Committee of the Great Dams in 2000, India, China, Turkey, South Korea, Japan and Iran, are in the process of studying and developing the largest dams in the developing world. According to Table 4, Iran has a lower per capita water capacity and water per capita behind the dam reservoir is less than some of these countries. These countries, despite the capacity of the dam's ponds more than in Iran, are developing this industry, or they have already had a very high record in this regard.

2.6. FLOOD CONTROL

Flood event is one of the three major natural disasters in Iran. There is a destructive flood at least at a point in this land. Several people every year die due to rivers flooding, or their homes and agricultural lands destroy. The most important impacts of dams, especially large dams, on rivers such as Karoon, Dez, Bazoft, Khersan and Beheshtabad is flood control. The statistics of the country's floods from 1951 to 1990 are presented in the table below.

Table5: Distribution of events and flood damage during 1951-1991 [10]

Period	Cities		Events	
	Percent	Number	Percent	Number
1951-1960	16	101	10.1	191
1961-1970	21	131	13.3	251
1971-1980	25	154	23.3	440
1981-1991	38	239	53.3	1008
SUM	100	625	100	1890

During this period, approximately 48 incidents occurred annually throughout the country, with 75 deaths. Although the flood damage in Iran is not comparable to some countries, the likelihood of a devastating flood must not be ignored. The 1932 floods, with more than 10,000 casualties in the Netherlands, occurred at a time when there were no such measures as flood control such as damming. At the same time, due to the flooding of the Anwar River in Italy, damage to the country's historical monuments was irreparable. The most severe flood caused by cyclone rains occurred in Canada in 1954. In October of this year, the outbreak of the Alliance, the Canadian state of Ontario and New York, flooded the United States into a catastrophe. The 1954 flood of India occurred as a result of rainfall of 250 to 500 mm of rainfall at 67,000 km in the northeast of the country, and about 9.5 million people were injured and 247 people were killed. The estimated area of the damaged agricultural land in the flood is estimated at 5.5 million hectares [10]. The financial losses caused by the flood are not accurately quantifiable, but more accurate new estimates show that countries such as Korea and Russia are losing \$ 500 and \$ 380 billion annually, respectively. United Nations statistics show that over the course of a 25-year period (1991-1996) there were 1358 floods in the whole world, with flood events accounting for 13.5% of the world's total risk of occurrence. The same reference has mentioned the number as 305,000 dead and more than 266,000 people injured. Meanwhile, 1.06 billion people are estimated to have suffered from flood damage.

The number of floods in the future is anticipated to increase due to global climate change. During the period from 1952 to 1991, floods with the severity of 2016 flood of Khoozestan hasn't been occurred. However, the likelihood of similar floods in the country's management should be taken into account. It was one of the most unprecedented floods in the country, which threatened to destroy the cities of Khoozestan including Dezful, Ahvaz and Abadan and a large number of villages and fields of Khoozestan. The entrance flow to the Dez dam was 80,000 cubic meters per second, however, with the Dam the flow reaching 5,000 cubic meters per second. It is obvious to anyone that the damage caused to the province in the absence of dams could have been hundreds of times higher. In the absence of the dam, the metropolis of Ahvaz would have been devastated, which, like the earthquake-stricken city of Bam, had to be used for several years by the country's large budgets to reconstruct it, but with the cost of building the Dam and several other dams this damage was heavily controlled and diminished. It is safe to say that, even if all of the revenue and effects of the dam were ignored, most and perhaps all of the cost of making the dam was justified and compensated only by controlling the flood of 2016. Of course, this flood did not only affect Khoozestan, but also affected the provinces of Ilam and Lorestan. Previously, a flood happened in 2005, which, fortunately, was controlled by the dams of the province. In fact, the existence of dams in flood-prone areas of the country can turn the natural threats of the region into opportunities by storing water and sediments, generating electricity, exploiting clean water in other industries and other positive effects.

But the question is, whereas dam construction projects in the similar provinces have been sufficiently developed and capable of controlling possible floods? The comparison of dam construction in Khoozestan province with Lorestan and Chaharmahal and Bakhtiari in the Karoon area and its branches (Table 3) shows the number of dams and the small volume of reservoirs in these provinces, indicating the weakness of these provinces against floods. In the event of a similar or even weaker flood occurrence in Lorestan and Chaharmahal and Bakhtiari, there will certainly be significant losses in the absence of dams and the damage caused would be more than thousands.

2.7. THE OPPORTUNITY TO WORK IN THE COUNTRY AND FOREIGN COUNTRIES, AND THE ENTRY OF FOREIGN CURRENCY

In addition to creating employment, this industry can help the country to enter currency. According to Tavanir's statistics in 2016, more than 1,500 people across the country are engaged in permanent employment at hydroelectric plants [11]. From the time of the initial studies to exploitation, after which several thousand people are employed in the construction of a dam and power plant. This can be the solution for the high unemployment rate in the country. Neighboring countries, such as Iraq, Afghanistan, Pakistan, etc., are one of the opportunities that can only be exploited by the proper planning of the capacity of natural resources and their growing industries to enter the currency and adjust the unemployment problems in the country. Today, according to the brilliant

records of domestic companies in this field, one of the sources of currency entry to the country with a high degree of reliability is the implementation of hydroelectric projects in foreign countries. The success of private and public companies in hydropower projects in Tajikistan, Pakistan and etc. are due to the fact that for the past thirty years, various projects have been implemented at the domestic low expense level. It is safe to say that the casualties caused by the destruction of dams in Iran are zero. In the case of European and American countries, several destructions of soil and even concrete dams occurred, for example, the demolition of the Malasso dam in France killed more than 500 people. Therefore, the development of this industry, in addition to direct revenues, will be effective in building credibility and attracting the trust of other countries and will result in the assignment of important and expeditious tasks abroad.

2.8. CREATING A HIGH SAFETY FACTOR IN TIMES OF CRISIS (WAR, EARTHQUAKE, ETC.)

Nonproliferation measures are called non-combatant measures that increase deterrence, reduce vulnerability, sustain the necessary activities, promote national sustainability and facilitate crisis management against all types of threats and military actions of the enemy. The dispersal of hydroelectric power plants, their excessive distance to the country's boundaries and the deployment of these power stations deep underground ensures that, in the event of war and earthquake crises, the overall vulnerability of the power grid is very low and the compensation will be possible more quickly. The fuel consumed by the thermal power plants is provided through pipelines from areas with high oil and gas supply, which during the wartime is likely to target pumping stations and even pipelines. Obviously, in the event of damage to the facility, it can cause irreparable damage to the restoration and repair of the power plant in the densely populated cities of the country. Hydraulic power plants in such cases can help a lot and provide emergency power to units such as hospitals, industrial centers, and so on.

3. NEGATIVE EFFECTS OF DAMMING

3.1. DESTROYING THE TREES

Destruction of trees in the pond and at the site of the construction and access roads is one of the damages that could be a hindrance to the development of this industry if modern technology is not used to mitigate the effects. Of course, this is not the only industry that is destroying trees. Road construction, railways, petrochemicals, etc. cause damage to the wild animals and plants environment. In such cases, the continuation of the development process is subject to proof of moderation and compensation. One of the industries that can easily compensate bio-plant damage is damming because of the high water availability of dams with high volumes, which can be exploited by using its insignificant amount in creating vast parks and green spaces. Obviously, the created parks in addition to the compensation can be very effective in attracting tourists.

3.2. DESTROYING ANIMAL SPECIES

Although the reservoir is damaging the animal environment, creating a relatively large reservoir can provide water for drinking animals, birds, the amphibian, fish and migratory birds. The natural breeding of different species of amphibians and fish with the transmission of baby fish and marine animals increases the population of fish species and birds. Reviving the species of animals, birds and fish is more complicated than being included in an article. But given the fact that water is available in these projects as a source of life, today's technology can be used to compensate for and create new opportunities.

3.3. DESTRUCTION OF RESIDENTIAL HOUSES

The adverse effects of drowning dwelling houses in reservoir can be reduced by creating settlements in the right place. In various levels of the study, the construction of a dam will be considered and estimated for damages to villages close to the project. If possible, it will be effective in locating the dam, even in the event of pond damage to the villages nearby, the residents of the region will be re-evaluated in the implementation of the project. In cases where we are forced to move the people of the region, by creating a town in the best place and developing it with proper management, we can manage water resources, waste, energy, and even create affordable amenities.

3.4. DESTRUCTION OF BRIDGES, RAILS, TUNNELS AND OTHER STRUCTURES

Laying damages to road, tunnel, bridge and other facilities has been partially decreased in comparison to the profits from the production of clean energy and various facilities for exploiting the reservoir. In some cases, to modify the damages, it is necessary to move the location of the site, change the height or displacement of the structures. In any case, the damage to the facility is much easier and can easily be estimated during phase one of evaluation.

3.5. DESTROYING THE FOUNTAINS AND THE AQUEDUCTS

Applying the various abilities of the consulting engineers and contractors of this industry can lead to the registration of global records and the creation of international credentials for them. The rescue of Bel fountain, by utilizing the special abilities of domestic specialists, indicates their high ability in this field. Bel fountain with 3000 liters per second flow in the Darian Basin was saved by the efforts of domestic researchers from drowning in the pond. In addition, the displacement of religious constructions in the KaroonIII Dam reservoir using special methods to their appearance, they are unique measures that can be used to save other old structures from dangers such as dipping in ponds, floods and earthquakes.

4. CONCLUSIONS AND SUGGESTIONS

The dam construction industry, like any other development project, has many benefits and damages. Social damages, destruction of nature and structures are some of the main damages. Of course, under the pretext of development, there cannot be much damage to society and nature. On the contrary, it is not possible to comment on the precision of an industry with losses and burdens. In all survey phases, which usually take several years, they try to investigate damages and ways to reduce them. Therefore, nowadays, the advantages and disadvantages of each industry are measured by different researchers and ultimately the development methods are communicated to the relevant executives. Sometimes, despite the losses of the industry, even if other options are available, it is also possible to make the losses incurred justifiable. Some of the most important factors influencing the development of a country are climate, population, distribution of resources and the level of native technology. The possibility of reducing damages and increasing the profits from current and future dam construction for each region should be investigated separately and especially. From the benefits that can be gained over time, the use of water resources in reservoirs as fishing, reforestation of forests and animal species, tourist attraction, drinking water and agriculture can be mentioned. Using the accumulated water can further increase the dam benefits. Today, efforts have been made to reduce the damage to society and nature by many researchers. The results of their studies show that only scientific methods and the use of incident technologies can be taken to this goal.

The high capacity for damaging in Iran and future needs for clean water and energy, as well as the insignificant development of Iran compared with countries such as the United States, China and Canada, and the need to create jobs are some of the reasons that will reveal the need for development in this field. In addition to flood control and energy production during a crisis with high reliability are some other goals that can only be achieved through the development of damming. In addition, the ability of domestic specialists in this field is logical justification to continue damming in large areas of the country.

5. REFERENCES

1. Ren21 R. (2010). “*Global status report. Renewable Energy Policy Network for the 21st Century*”, Paris.
2. Avami, A. (2016), “*Dams and development, New Framework for Decision Making*”, Quarterly Journal of Strategic Policy Studies, 20,p.1-10. (in Persian).
3. Power and Energy Office, (2016) “*Energy balance sheet 2014*”, 556p. (in Persian).
4. Shoaii, Sh. (2015), “*Tourism in the Zagros region*”, Maaref, p.10-15. (in Persian).
5. Hooshmand aiini, A. and Rezaei, P. (2012),” *Investigation of the Sefidrud Dam Tourism Abilities* “, The first national tourism and nature gathering conference of Iran, p.1-8. (in Persian).
6. Deputy Director of Management of the Planning and Budget, (2015), “*Statistical Yearbook*”, pp. 1-7. (in Persian).
7. Connor, R. (2015). “*The United Nations world water development report 2015: water for a sustainable world*”, (Vol. 1). UNESCO Publishing.
8. Food and Agriculture Organization: <https://knoema.com/FAOAQST2015R/fao-aquastat-2015>
9. International Commission on Large Dams:
http://www.icold-cigb.org/GB/World_register/general_synthesis.asp
10. Ministry of Power. (2016), *Investigation of flood damage, Journal161*”. pp.12-15. (in Persian).
11. Tavanir company, Human Resources and Research, Office of Information Technology and Statistics - Deputy of Statistics and Information (2016), “*Statistics and detail of Iranian power industry, Power generation in 2015*”, 141p. (in Persian)

Environmental impact assessment of dams at construction and operation phases

Abdolhosein Haddad¹, Maryam Naeimi², Ghasem Mohammadi³

1- Associate Professor, Dept. of Civil Engineering, Semnan University, Iran

2-Postdoctoral Research Fellow, Research Institute of Petroleum Industry, Iran

3- Ph.D. Candidate, Dept. of Civil Engineering, Semnan University, Iran

Email: Gm.mohammadi@gmail.com

Abstract

Environmental impact assessment (EIA) in the projects of civil engineering, was not being considered by many countries until recent years. However, in recent decades of 20th century and after observing environmental impacts of some of the projects, it was stated that the environmental factors played a noticeable role in speeding and directing of projects. Dam construction as one of the important civil and developing projects have positive and negative effects on environment. The environmental impacts can be categorized based on different criteria e.g. short and long term, impacts on surface and the ecosystem of the region, upstream and downstream side of dam, and social and economic impacts. Whereas dams have positive effects, it is necessary to minimize the negative impacts of dams toward stable development. At the same time, it is known that the consequences and impacts are different during construction and operation period in terms of intensity, importance and extent. In this paper, at first, the effectible geophysical factors related to river and reservoir water, vegetation and animal, social, economic and cultural factors are studied. Then, as a case study, Gotvand dam for quantifying the environmental impacts using the Iranian matrix are presented.

Keywords: Environmental impact assessment, Earth dams, Environmental factors.

1. INTRODUCTION

The environmental considerations in the civil and developing projects were not taken in to account by most of the countries until recent years. The environmental consequences of some projects raised notices that environmental factors played an important role in the direction and speed of development in the last decades of 20th century. Nevertheless, development is not in contradiction to environment; but, exceeding extraction of natural resources leads to disturbance and contamination of environment. Development is stable and persistent when it is appropriate from environmental point of view in addition to technical, social and economic justification [1].

At the same time, it is known that the consequences and impacts during construction and operation period in term of intensity, importance and extent are different. In advance of any environmental impact assessment of the project, all other effects should be evaluated. It should be noted that environmental impact assessment depends on many factors e.g. existing records, collected data interpretation, statistics, sampling, and finally analysis of these subjects.

The environmental impacts of dam construction are shown in Fig.1 [1]. Also, the impacts of different environmental factors of dam construction is presented in following.

2. STUDY ON THE EFFECTIVE GEOPHYSICAL FACTORS

2.1. THE IMPACT OF TOPOGRAPHY

During construction period, the topography is subject to significant change due to rock and soil excavation, backfilling, road construction, temporary and permanent camps, borrow area excavation and etc. [10]. This impact is considered as a negative impact while it changes the region from its intact and natural condition. It would be intense, permanent and unavoidable. However, the impact would be on the ground shape and general view of the region during operation period.

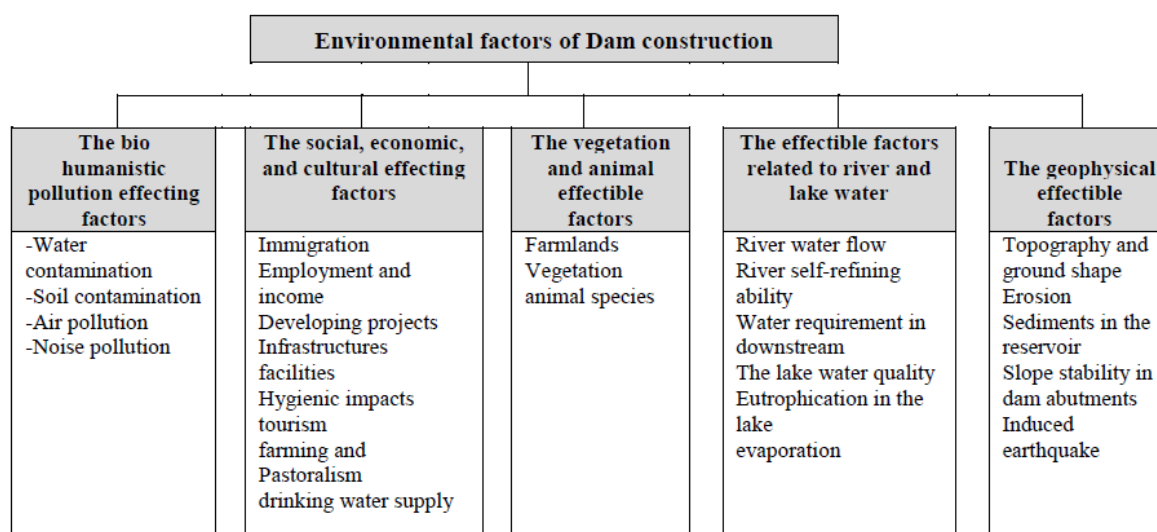


Fig.1- EIA diagram for dams

2.2. IMPACT ON SOIL EROSION

River diversion system, excavation and backfilling, removal of vegetation at the construction area, borrow area extraction and deposition, road and structures construction and machinery travelling are the factors that have intense effect on erosion during construction works.

During operation, it is possible that people, especially in the upstream side of dam, try to expand their farmlands due to providing the water supply. This can lead to increased soil erosion and sediment in dam reservoir. The soil erosion is very important because of sediment and suspended solids loading. Therefore, it is predicted that the project impact on the soil erosion during construction and operation periods is exposed in medium to high intensity.

2.3. SEDIMENTATION IMPACT ON THE RESERVOIR

One of the main issues in dam construction is sediment and deposition. When a dam is constructed, whether small or large, reservoir or regulatory, the river sediments are collected in the dam reservoir [2]. The impacts of deposition in the reservoir are reviewed from different aspects:

1. Reduction of dam service life: accumulation and combination of sedimentary materials lead to rapid increase of reservoir dead volume and thus, reduction of dam service life. This has a direct impact on economic of the project in form of losing national capital and social problems.
2. Reduction of the nutrients in the downstream side of dam: the river flow transmits a lot of amount of nutrients e.g. nitrogen, phosphorus and other required substances for plants to downstream. These materials divert to the farmlands, enrich the soil and so, the nutrient taken by plants from the soil would be compensated. Dam construction and water controlling change the natural pattern of deposition in the downstream side of the dam and reduction of suspended loads in the river leads to deposition decreasing in the farmlands located in the river trusses and the farmlands in the plains.

According to statistics, 50 billion cubic meters (1% of world reservoir capacity) accumulate in dams at all around the world each year. Sanmenxia dam on the Yellow river stored 50 billion tones sediment after dam impounding. The dam made 66000 hectare of the most fertile farmlands of the world went under the water. Kulekhani dam in Nepal was filled by sediment to 0.9 of its volume 12 years after construction. So, operation of the 114 m dam with predicted 100-year service life was finished. [3]

2.4. THE IMPACT ON INDUCED EARTHQUAKE

Dam construction and making a big reservoir of water, several millions or even billions of new load impose on the dam and foundation where haven't been experienced such a load at the area. There are lots of evidences of earthquake due to dam impounding [2]. The research has done on the 20 big dams of the world about induced earthquake and the results show that induced earthquake with different intensities while impounding has occurred. Based on past experiences, after dam impounding some induced earthquakes with low or micro

intensities occur and their frequencies and intensities increase by water depth till it reaches a fixed amount. Water impact on the lake base or the connate water weight in the reservoir make the fault movement that causes earthquake. When the water height is above 100 meters or the reservoir volume is about 1 billion cubic meter, a more intense earthquake occurs with 3-5 Richter magnitude or rarely more than 5 Richter. Then, less intense earthquakes occur till it ended.

Today, the relation between earthquakes and dam reservoirs has been proved in more than 70 dams. For example, Koyna dam with 103 m height caused a 6.3 Richter earthquake and Koynangar village in Maharashtra state was destroyed on 1967, Dec.11 [4]. Vaiont dam in Italy with 261 m height was constructed in 1960 and the earthquakes occurred immediately after impounding [5]. In 19663, when the dam height reached to 180 m, 60 shakings were recorded and on October 9th the Longarone city destroyed and all people were killed.

2.5. THE IMPACT ON FLOOD AND SLOPE STABILITY OF THE RESERVOIR ABUTMENTS

Flood control is one of the side purposes of dam construction due to damaging impact of river floods [6]. One of the natural processes after dam construction is water penetration in to the surrounded ground layers of the dam. In case of inappropriate bedding e.g. Marnstone, Conglomerate, limestone and etc. and when the bedding has the steep slope toward the reservoir, water penetration causes less friction between rock layers and the natural slope stability ruined and landslide of soil and rocks happens. Inappropriate extraction of borrow areas near to the reservoir and making slopes of abutment steeper can cause the slope instability.

In some valleys of Iran, especially north parts due to bedding, landslide makes limitations. In general, instability of abutments can cause potential dangers in dams and bring important issues. Like:

- The long waves on the reservoir surface, make the risk of overtopping and high pressure to dam body that cause dam failure and destroying all the facilities and therefore, lots of human and financial damages.
- Reduction of dam useful volume due to soil and rock failure in to dam causes water resources management and investment get ruined. So, social, political and economic damages will happen.
- The intake systems, gates and trash racks will be broken and cause the operational system to be out of function.

3. THE EFFECTIBLE FACTORS RELATED TO RIVER AND RESERVOIR WATER

3.1. THERMAL STRATIFICATION IN DAM RESERVOIR

In general, the quality of the reservoir water alters each season. Usually, lake in mild regions have 2 yearly turnovers in spring and fall. They have thermal layering in summers and reverse thermal layering in winters. Most of lakes in the world have this situation that is very important for gas exchanges and nutrient distribution. According to these studies it could be known the elevation of gates installation. [6]

Stratification is a thermal process and is a function of different factors like reservoir volume, morphology and depth, geographic conditions of the environment, the ratio of inflow to reservoir and the ratio of reservoir depth to length. It is because of layering and making two or three layers of water that the conditions of above layer and under layer are different. It is possible that the dissolve oxygen reduces or even anaerobes conditions happen. This may lead to gas production and the organic matters of dam bed float on the reservoir surface. The layering phenomena is one of the most common in the lakes and reservoirs and makes the most important impact on the hydraulic and thermal features of the dam. It is layers of fluid that are created due to differences in density or temperature or dissolve or suspended substances.

3.2. STUDY THE PROBABILITY OF EUTROPHICATION IN THE RESERVOIR

The base of eutrophication phenomena in dam reservoir, is accumulation of organic matters and sediments in the reservoir. Therefore, the phenomena mean enrichment of water with nutrients e.g. Nitrogen, phosphorus and consequently, algae and other aquatic plants will grow more in the reservoir. Increasing and accumulation of the materials in dam reservoir may lead to eutrophication in lake and reduction of the quality of water. Considering the effectible factors for the phenomena in the catchment area, it is expected that this happens after impounding.

The other factor for this phenomena is still water. The more time, the algae grow more. For reducing the eutrophication, considering the above mentioned issues, some treatments would be done during the dam and related structures operation period.

3.3. THE IMPACT ON EVAPORATION

Evaporation of the lakes depends on some factors e.g. lake surface, its depth, region's climate, wind. Evaporation of the lake has a direct relation with area of the lake and reverse relation with its depth. In other word, if the lake surface expands the yearly evaporation will increase accordingly.

In dry and semi-dry climate, the evaporation increases and in humid climate it decreases. Therefore, the most evaporation happens in dry regions when the wind takes away the vapor and the lake surface would expose to evaporation again.

It should be noted evaporation from natural and artificial lakes is complicated and billions cubic meters of fresh water that are collected and stored with high costs will return to atmosphere due to this process.

The evaporation from the lakes are much larger than rivers and the dam reservoir water would be salted consequently. For example, Colorado salted water made farming and crops less efficient.

In addition to the above mentioned effects, other important impacts as following should be considered in environmental assessment impact:

The impact on surface water quality (river)

The river self-refining

The impact on quality and quantity of underground water

4. THE VEGETATION AND ANIMAL EFFECTIBLE FACTORS

This includes the impact on plants species that are near to extinction and on vegetation inside dam reservoir. The impact on animal species divides to aquatic and terrestrial animal categories. With dam water supply, the wild animal would have access to water during summers and this could lead to their population growth. For aquatic animals, dam lakes could lead to more fishing.

5. THE SOCIAL, ECONOMIC, AND CULTURAL EFFECTING FACTORS

The social, economic and cultural effects of dam construction include knowledge, employment and income, houses and resettlement, hygiene and diseases, and tourism [2] and [7]. All these effects would be positive. During dam construction, the employment makes the immigration less and population of the area more. During dam operation, the tourism and increased value of the properties makes long term positive effects.

6. THE EFFECTING FACTORS DUE TO POLLUTION MADE BY HUMAN

6.1. WATER QUALITY

The environmental consequences may happen by not considering water quality until the investment will rather or completely ruins and reaching to dam goals would be impossible [6]. One important factor on water quality is the organic matters. The allowable limits of organic matters differ with the kind of water usage (farming, drinking etc.). In addition, if the reservoir gets empty and full yearly and water would be just for farming, the environmental impacts are low and even the sediments of water would help to the soil to get fertile. But, if the water is for drinking or industrial usage, the high and out of standard organic matters make the project out of function. The sources of organic matters in dam reservoir are: jungles and grasslands, Manure, waste water of factories, animal trapping production, organic fertilizers etc.

6.2. SOIL POLLUTION

As agricultural works develops and farmers use fertilizers and pest repellent poisons for gaining more corps, the penetration of chemical substances to soil and water resources due to farming drainages is possible in long term. This issue makes soil pollution in areas with high underground water level because one of factors of soil pollution (except rare factors due to radioactivity and oil pollution) is losing soil substances due to going underwater. Therefore, the project impact on soil pollution as a negative factor, is considerable with average intensity.

The other issue related to soil pollution is tourism or other industries in the region that can make more trashes and this is the secondary and indirect impact of the project.

6.3. AIR AND NOISE POLLUTION

The different preparation and construction works e.g. rock and soil excavation, road construction, blasting, exploration drill holes, upstream and downstream cofferdams, temporary and permanent camps, equipment transportation, borrow area extraction and machineries make dust, particulates, smoke from heavy machineries and therefore, this lead to air and noise pollution [5]. Some treatments could make the negative impacts less however, this phenomenon is an unavoidable impact that is temporary in construction site and around of it.

During operation period, and after this works have done, no air and noise pollution is expectable.

7. CASE STUDY: GOTVAND DAM

In this part, Gotvand dam with considerable environmental impacts are reviewed Based on above mentioned impacts. The upper Gotvand Dam is the highest earth dam in Iran which is located on Karoon River about 10 km from Gotvand city. Regarding to the geology, it was investigated that Gachsaran salted formation in the reservoir made the reservoir water and consequently Karoon River salty [8]. According to studies, the nearby salt mine and salty Gachsaran formation weren't considered in study phase of the dam. The mine with 5 km distance from the dam made it (with hundreds of millions of tones reserves) completely drowned in the water after dam impounding and therefore the salt amount of Karoon River reaches to the highest level [9]. After dam construction, and before impounding, a clay blanket was constructed on the formation, but only 3 days after impounding the clay was cracked and it didn't work and not prevented salting the water.

Therefore, the quality reduction of water in the reservoir due to salt dome dissolving lead to huge environmental damage in the downstream. The Iranian matrix is used for indicating the impacts of the project works on environmental parameters and quantity studying. In this method, the impacts of a work are studied based on intensity, importance, amount and weight.). The sum of these factors will define the general impact of the project. When an impact is helping to balance the environment it is positive otherwise negative.

Considering the effective factors mentioned in parts 2-6, the environmental impact assessment (EIA) of Gotvand dam during construction and operation phases was done as a case study. The results are presented in table (1).

Table 1- EIA of Gotvand dam

Activities		Construction Period Major Activities								Operation Period Major Activities				Algebraic Sum of Construction Period	Algebraic Sum of Operation Period	Algebraic Sum of Total Activities
		Diversion System Cons.	Excavation & Embankment	Access Road	Dam & Relevant structures	Powerhouse cavern & Tunneling	Equipment Transport	Borrow Area Excavation	Blasting	Reservoir Impounding	Hydropower Energy	Installations Operation	Environmentally Water need			
Geophysical factors	topography and ground shape	-2	-3	-3	-5	-1	-1	-2	0	0	0	0	0	-17	0	-17
	sedimentation in reservoir	-1	-2	0	0	0	0	-1	0	-3	0	0	0	-8	-3	-7
	stability of the reservoir abutment	-1	-1	-1	2	-1	0	0	-2	-4	0	0	0	-6	-4	-8
	flood impact	-2	0	0	0	0	0	0	0	5	0	0	2	-10	7	5
river and reservoir impacts	water river quality	-1	-2	0	-1	-2	0	-1	-1	-5	-2	0	1	-11	-6	-14
	reservoir water quality	-1	-1	0	0	0	-1	0	0	-5	1	0	3	-3	-1	-4
	Eutrophication	0	0	0	-1	0	0	0	0	-4	0	0	0	-2	-4	-5
	evaporation	-1	0	0	0	0	0	0	0	-5	1	0	2	-4	-2	-3
vegetation and animal factors	agricultural land	0	-1	0	0	0	-1	-1	0	-4	0	0	1	-3	-3	-6
	plants species & land	0	0	-1	-1	-1	0	-2	-1	-2	0	0	-1	-17	-3	-9
	animal species	-1	-1	0	-2	0	-1	-2	-4	2	0	0	-1	-11	1	-10
social, economic & cultural factors	employment and income	2	1	1	3	2	3	3	0	-2	2	1	0	18	1	16
	development planings	0	0	0	1	1	1	0	0	1	4	0	0	5	5	8
	infrastructures	0	0	0	2	0	0	0	0	2	3	1	0	2	6	8
	tourism	0	0	0	-2	-2	0	0	-1	4	4	0	1	-5	9	4
	drinking water secure	0	-1	0	-1	0	0	0	0	-5	0	0	1	-9	-4	-6
bio-humanistic pollution factors	water quality	-1	-1	0	-2	-1	0	0	-2	-3	1	0	1	-27	-1	-8
	noise pollution	-2	-2	-1	-3	-4	-1	-2	-5	0	0	0	0	-22	0	-20
	soil pollution	0	0	0	0	0	0	0	-2	-2	0	0	0	-13	-2	-4
	Air pollution	-1	-2	-1	-2	-1	-1	-2	-1	1	0	0	0	11	1	-10
Algebraic Sum of positive impacts		2	1	1	8	3	4	3	0	15	16	2	12	51	30	41
Algebraic Sum of negative impacts		-14	-17	-7	-20	-13	-6	-13	-19	-44	-2	0	-2	-186	-33	-131
Algebraic Sum of impacts		-12	-16	-6	-12	-10	-2	-10	-19	-29	14	2	10	-135	-3	-90

8. SUMMERY AND CONCLUSIONS

According to this study, the general conclusions about EIA are as following:

- The experience from construction and impounding of Gotvand dam and other dams in Iran demonstrates that environmental impact assessment (EIA) prior to dam construction could prevent the environmental hazardous consequences.
- The positive impacts of dam construction projects are more than negative impacts considering social, economic and cultural parameters. For negative impacts, whereas they are long-term, the suitable environmental treatments should be planned and make it minimum (environmental management planning).
- Dams have hazardous and positive impacts. The negative impacts of construction period due to improper geophysical, biological and hygienic changes are much more than operational period. However, this is unavoidable considering the civil projects nature.
- The undesirable consequences of dam construction are as: reducing bio diversity in downstream, destroying the farmlands, gardens, grasslands near to river after impounding, destroying the houses and residential areas near the river, resettlement of people in the neighborhood and etc. therefore, the environmental management program is necessary for dam study and construction.
- The environmental management program (EMP) includes solutions for reducing important negative environmental impacts and also, make positive effects of the project more. This program has the stable development goal and considers solution for controlling the negative impact of environment and plans are made to reduce hazardous environmental impacts, supervise the treatments and reduce the negative impacts by survey and test the environment.
- In dams located south of Iran, thermal layering exists due to low elevation above the sea, rather high evaporation of the lake, organic matters, rural wastewater and chemical fertilizers and this lead to decreasing lake water quality. In dam reservoirs salted water collects in lower layers because of more weights and they mix very slowly with the reservoir water. Therefore, the salted water, made from dissolution, influences lower layers. The amount

of EC starts from less than 1000 μ mho in the above layers and reaches to more than 1800 μ mho (4 times more salted than Persian Gulf) in the lower layers.

The lower bottom outlet can be used to take out this improper water and also, water intakes in different levels can be utilized for the better quality water.

9. REFERENCES

1. Environmental protect organization, the environmental impact assessment of civil projects, No.9, 1378.
2. Shabankari M., Halabian A., the environmental impact assessment of Zayande-Rud dam reservoir, Human and Environment magazine, 1389.
3. K.M. Sthapit, Sedimentation of Lakes and Reservoirs with Special Reference to the Kulekhani Reservoir. Department of soil concervation, Kathmandu, Nepal.
4. Harsh Gupta, Reservoir Triggered Seimicity at Koyna, India, National Geophysical Research Institute, 2009.
5. Patrick McCully, Dam-Induced Seismicity, International Rivers, London, 1996.
6. Water Resources Management Company, technical standards and criteria office, the instruction for environmental impact assessment of dam projects (detail design), No.250-A publication, 1384.
7. Khazraie M., Dam and the hazardous impacts on environment, 1386.
8. The Investigation of Negative Effects of Salt Dome on the Quality of Water in Gotvand Olya Dam and the Use of Cut-off Wall as Treatment, Mahmood Mansournejad, Behzad.
9. Upper Gotvand Dam and Hydro Power Plant Dealing with Salinity in Reservoir Challenges, Remedies and Evaluations, D. Mahjoob Farshchi & A. Sadatifard, International Syposium on Dams in a global environmental challenges, bali, Indonesia, 2014. [10] Monavari M., guideline for environmental impact assessment of dams, Environmental protect organization, 1380.
10. Pirestani M., Shafeghati M., Environmental review of Dam construction, Human Geographic research magazine, year.1, No.3, 1388.
11. Sabetraftari A., Mostafapour S., Review of challenges and difficulties of dam environmental impacts, First dam and environment workshop, 1386.
12. Amar T., Parvizi R., Tahvildari M., Analysis of economic, social and environmental consequences of Shafarud dam construction, Talesh-shenasi national conference, 1394.
13. Jahanshahi N., Shabani S., Samandani M., Review of value engineering function in dam projects with case study of Gegin dam, the 5th conference of water and soil resources management, 1390.
14. A handbook on environmental impact assessment, 4th Edition, 2013, Scottish Natural Heritage
15. Environmental Geotechnics, Second edition 2013, Robert W. Sarsby.
16. Kalantari, Mehdi Mahdavi Adeli, American Journal of Civil Engineering, 2015 [17] Numerical simulation of wave generated by landslide incidents in dam reservoirs, Behzad Ataie-Ashtiani, Saeedeh Yavari-Ramshe.
17. Craig L. Westenburg, Guy A. DeMeo, and Daron J. Tanko, Visitor Serv. Evaporation from Lake Mead, Arizona and Nevada, 1997-99.

Aerobiology, biophysical studies through integration of zigbee communication protocols in fixed wing air vehicle for dam regions

Syed Mohammed Shoaib¹, Shaik Abdul Khader Jilani²

1-Engineering Physics Lab, MANUU Poly DBG Off Campus, School of Sciences, Maulana Azad National Urdu University, Gachibowli, Hyderabad-500032, Telangana State., India

2-Department of Electronics & Communication Engineering, Madanapalli Institute of Technology and Sciences Madanapalli-517325, Chittoor District, A.P., India

E-mail: dr.smdshoaib@manuu.ac.in

Abstract

Aerobiological sampling using unmanned Micro Air Vehicles (MAVs) on Long-Term Behaviour and Environmentally Friendly Rehabilitation Technologies of Dams is an exciting research field blending various scientific and engineering disciplines. The biological data collected surrounding the Dams using MAVs helps to better understand the atmospheric transport of microorganisms. Aerobiological research aims to improve our understanding of these aerial organisms to ensure human health and to help sustain and safely manage terrestrial ecosystems, including important food resources. Airborne bacteria, fungi, viruses and pollen are responsible for many human respiratory diseases and allergies. Autopilot-equipped MAVs can accurately sample along pre-defined flight plans and precisely regulated altitudes with help of GPS (Global Position System). They can provide even greater utility when they are networked together in coordinated sampling missions: such measurements can yield further information about the aerial transport process quickly and efficiently. Accordingly, the problem of coordinating multiple autonomous vehicles to address scientific and other missions has enjoyed increased attention from researchers.

Keywords: Communications Engineering, Aerobiology Instrumentation, Biophysics Engineering and LTBD.

1. INTRODUCTION

In this present investigation, flight vehicle path planning, real-time sample analysis, control and coordination strategies are considered for unmanned autonomous aerial vehicles with the help of Zigbee protocols. A time-optimal path planning algorithm, that is simple enough to be solved in real time, is derived based on geometric concepts. The work is part of a larger effort that focuses on the validation of atmospheric dispersion models of Dams developed to predict the spread of bacteria and plant diseases in the lower atmosphere. The use of Zigbee protocols allows us to control MAV and monitor various sensors in real-time with distributed control. Low power, long distant and authentic data communications features of Zigbee are fully utilized in the present LTBD work. The present novel method would be a significant improvement upon the existing system due to the presence of an Zigbee based control and monitoring system.

The objective of the present investigation is to implement advanced communication Zigbee protocol, which provide most reliable and secure data transfer for guided unmanned aerial platforms along with GPS technology which can locate the MAV with considerable accuracy and collect Aerobiological sample from pre- determined geographical Dam locations at accurate altitudes.

In this work path planning and control strategies will be focused that are to be used in aerobiological sampling field experiments surrounding the Dams. The area surrounding the dam is very important for aerobiological study as this area harbor new and artificial ecosystem compared to other area. Artificial water level control at the Dam also influence the ecosystem of the surrounding area. Aerobiology is a branch of science that studies the processes and factors that influence the motion of aero biota in the atmosphere. Aero biota may include plant and animal pathogens, insects, seeds and pollen, or other living organisms that use the air to change habitat. The atmosphere of the Earth is primarily composed of the mixture of two gases, nitrogen (78%) and oxygen (21%), commonly known as air. Other than gases, air also contains small particles, like dust, and it may also host microscopically living organisms. Although many of these aerial living organisms have a significant impact on humans, little is known about the processes and mechanisms that affect their motion. One may face numerous fascinating questions when dealing with aerial life forms: In addition to questions regarding their role, and interaction with other living organisms, for example, one is concerned with the aerial transport mechanisms that transfer them from one location to another. Aerobiological research near the Dams aims to improve our understanding of these aerial organisms to ensure human health and to help sustain and safely manage terrestrial ecosystems, including important food resources.

2. EXPERIMENT

Airborne bacteria, fungi, viruses and pollen are responsible for many human respiratory diseases and allergies. Pulmonary tuberculosis, Diphtheria, or Influenza an indirect impact on humans of these living aerial organisms is the devastating effect of plant diseases.

A risk management system is needed that would help growers make informed decisions about fungicide use, or sanitation. In order to accurately assess the risk of an infection at some location spreading to other areas, especially in Dam located regions, mathematical models of varying complexity may be employed to predict the trajectories of the sporangia, given ambient wind and other environmental conditions. It is understood that long-distance aerial transport plays an important role in the evolution of plant disease epidemics. This research investigation also aims to inspire other research teams to continue venturing into the MAVs with an increased concentration in the applicability aspects using latest communications and global position systems on Long-Term Behaviour and Environmentally Friendly Rehabilitation Technologies of Dams (LTBD).

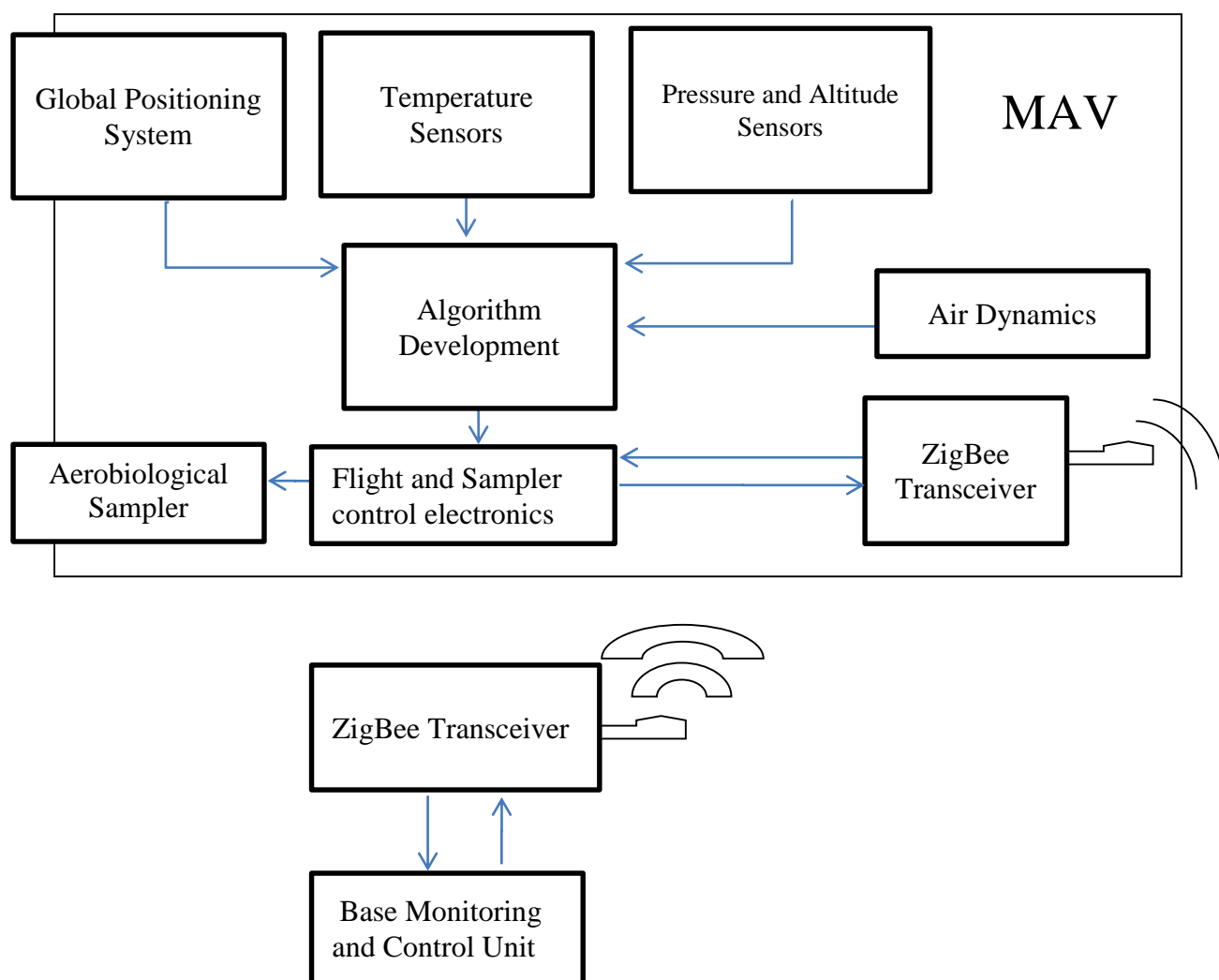


Figure 1: Flowchart depicting the various stages of the investigation

The development of a novel setup for this purpose would aid the research in various applications and industries like LTBD, agriculture, disaster affected areas, identification epidemic affected areas, air pollution control and monitoring etc. thereby opening up research options for faculty and students. Various workshops and seminars would also be conducted across Universities in order to ensure the dissemination of all knowledge gained during the investigation among University students.



Figure 2: Unmanned Micro Air Vehicle (MAVs)

3. RESULT

The studies indicate that micro-organisms vary in abundance, distribution and diversity in the atmosphere. Yet, the air remains the least understood environment from a biogeography perspective. Patterns in the variation of micro-organisms in the atmosphere have not been well documented, nor have the processes that underlie these patterns been identified. Here, we consider defining attributes of land, water and air environments, and how these attributes may contribute to similar and different biogeography patterns across these domains. Building on a rich history of research in terrestrial and aquatic systems, we explore two patterns that are likely to play an important role in shaping the emerging field of air biogeography: environmental diversity gradients and the existence of biogeographic Dam regions. Ultimately, a more unified understanding of the biosphere will entail comparing and contrasting these patterns across the lithosphere, hydrosphere and atmosphere.

A few different papers comprising of a few different approaches have been published on the use of the algorithms that are the topic of this research. Background information from a variety of sources has been studied to augment our knowledge and understanding of the technologies. In this present investigation we aim to draw from the substantial applied research available in this area to develop a novel application for MAV for the purposes of aerobiology studies in LTBD regions.

4. DISCUSSION

Our country is very active in aerobiology studies for the last six decades and contributing effectively to the world. The pioneer Aerobiologist from North East India was H.K. Baruah, Ph.D. (Cantab., 1942) and is now regarded as the Father of Aerobiology in the region. He started his aerobiological research works in the region after visiting Imperial College of Science and Technology, London where he worked with P.H. Gregory, F.R.S. under Colombo plan fellowship (1955-56).

"THE INDIAN AEROBIOLOGICAL SOCIETY" (IAS) is established in 1961 and is located at the Division of Palynology and Environmental Biology, Bose Institute, Calcutta. The society is affiliated with the International Association for Aerobiology. It is responsible for publishing research papers in Indian Journal of Aerobiology which is noted Indian Journal for Aerobiology. This society conducts various workshops and conferences in the field of Aerobiology.

Recently we entered in to development of MAVs, currently various organizations and research institutes like, SBMJCE NAL, IITs, IISc, MSRSAS etc. are undertaking research in the field of MAVs. A research work by a group from IIT, Kanpur focuses on Feature Based Object Tracking Using PTZ Camera. But our present work is very innovative and we wish to extend the scope and applicability of this by fitting GPS on MAV and enabling the MAV to locate exactly on required location and altitude for the study of Dams. However, many International Research workers utilized this MAV for different studies.

5. CONCLUSIONS

An MAV system with the present Zigbee control can patented upon maturation of the results obtained through different funding agencies. Once a patent is secured, the technology could be used to estimate pollens distribution on crop fields, Ariel bacteria / virus estimation over Dams atmosphere, epidemic plant virus estimation in crops etc. The potential uses with respect to agriculture and epidemic virus distribution studies make it ideally suited for various environmentally socially beneficial activities. Various technical experts are being consulted for the development of the algorithms and the MAV. Technical consultancy to various Central Universities, State Universities, various colleges and industries like town planning, DRDO, Armed Forces, Large Dams, Private Security Agencies etc. would be provided after the investigation results reaches a

certain degree of completion and robustness. The system once developed can be commercialized due to applicability in various environmental, agricultural and health related activities. Revenue generation could be expected to begin shortly after the successful demonstration of the systems capabilities through proper channel.

6. ACKNOWLEDGMENT

The Author is thankful to **Dr. Mohammad Aslam Parvaiz** Sir Honorable Vice Chancellor MANUU and **Dr. Shakeel Ahmad** Sir Joint Secretary UGC, Govt. of India, New Delhi presently deputed as Pro Vice Chancellor for our MANUU Central University, Hyderabad for their encouragement to do Research Activities for the overall development of Students and Faculties in our University.

7. REFERENCES

1. D. E. Aylor, M. T. Boehm, and E. J. Shields. Quantifying aerial concentrations of maize pollen in the atmospheric surface layer using remote-piloted airplanes and Lagrangian stochastic modeling. *Agricultural and Forest Meteorology*, 45:1003–1015, 2006.
2. J. N. Bakambu and V. Polotski. Autonomous system for navigation and surveying in underground mines: Field reports. *J. Field Robot.*, 24(10):829–847, 2007.
3. D. G. Schmale III, B. R. Dingus, and C. Reinholtz. Development and application of an autonomous unmanned aerial vehicle for precise aerobiological sampling above agricultural fields. *Journal of Field Robotics*, 25(3):133 – 147, 2008.
4. S. A. Isard and S. H. Gage. *Flow of Life in the Atmosphere*. Michigan State University Press, East Lansing, MI, 2001
5. R. M Baxter, Environmental effects of Dams and Impoundments, *Annual Review of Ecology and Systematics*, Vol .8, 255-283, 1977.
6. Marcus W. Beck, Andrea H. Claassen & Peter J. Hundt, Environmental and livelihood impacts of dams: common lessons across development gradients that challenge sustainability, *IJRBM, iFirst*, 1-20, 2012.

Assessment of hydrologic alternation of flow due to dam construction in an arid basin (the case of the gadar river in Urmia basin)

Somayeh Sima¹, Behdad Saed²

1- Assistant Professor, Faculty of Civil & Environmental Engineering, Tarbiat Modares University, Tehran, Iran

2- Graduated Student, Department of Civil Engineering, Iran University of Science and Technology, Tehran, Iran

E-mail: s.sima@modares.ac.ir

Abstract

Gadar River located at the south part of the Urmia Basin is one of the imperative source of water for Urmia Lake and its satellite wetlands. It has been regulated since 2000 by diversion of its flow to the Hasanlu dam for supplying irrigation water. This study was aimed at investigating hydrologic alternation of the river flow during the post-dam period compared to the natural reference condition using the RVA and Eco-deficit methods. Results show that simultaneous with decreased base flow index, occurrence of zero flows has been increased as well as the duration of low flow events. Furthermore, considerable decreases in the frequency and duration of the high flows were detected. Analysis of eco-deficit/surplus curve also indicated that not only the reservoir operation has created no eco-surplus but also it has produced an average eco-deficit of 218 MCM/y. To improve the hydrologic condition of the river through conserving low flow and peak flow components of its natural regime, the acceptable range for the regulated flow was calculated using the RVA method and recommended to be considered by implementing active and restrictive management policies in the reservoir and river, respectively.

Keywords: Hydrologic alteration, Eco-deficit, Range of Variability Approach (RVA), Environmental Flows.

1. INTRODUCTION

The World Resources Institute (WRI) found that at least one large dam modifies 46% of the world's 106 primary watersheds. In addition, more than 60% of the rivers worldwide have been regulated by dam construction. Among the many factors leading to the degradation of watershed ecosystems, dams are the main physical threat, fragmenting and transforming aquatic and terrestrial ecosystems with a range of effects that vary in duration, scale and degree of reversibility. Allocation and supplying environmental flows (EFs) of rivers are the most effective strategies to move toward the sustainable management of the river ecosystems (WCD, 2000). The foremost step to determine EFs is to assess the changes in the flow regime after regulation and then try to redesign modified flow pattern so that to preserve the main components of the flow which have critical ecological functions.

A number of hydrological methods have been developed to assess the variation in the regulated flow of the dammed river and to determine ecologically-sound environmental flow strategies (see review by Poff and Zimmerman, 2010). The Range of Variability Approach (RVA), developed by Richter et al. (1996), is among the most comprehensive techniques which employs a subset of 33 ecologically-important hydrological variables, called Indicators of Hydrologic Alteration (IHA), to evaluate variability of the annual flow regime in terms of magnitude (size), frequency, timing, duration, and rate of change/ the IHA variables can be used for long-term trend analysis or for comparative statistical analysis to quantify change pre- versus post-activity, e.g. dam construction or water abstraction flashiness (Olden and Poff, 2003). The RVA identifies flow targets as ranges for each of the IHA variables (Richter et al. 1997).

In an effort to develop an overall measure of habitat alteration based on streamflow data, the concept of "eco-deficit" and "eco-surplus" were first introduced by Homa et al. (2005) and Vogel et al. (2007). These two eco-flow metrics provide an overall numerical and graphical representation of the tradeoff between human and ecological needs for available water. Later, Gao et al. (2009) found that the eco-deficit and the eco-surplus statistics can provide good overall measures of hydrologic alteration in a river. The annual eco-deficit appears to be the best generalized index among all the indices in the simulated data set.

GadarChay is one of the main rivers of the Urmia Basin, located at the south part of Urmia Lake (Fig.1). Based on the hydrometric records at the most downstream station of the river, Bahramlu Station, the river provides about 9 percent of Urmia Lake inflows between 1980-2013 water years (Fig.2).

The Hasanlu dam was constructed on the Shore of Gadar River near the Naghadeh city. It has been operated since 2000, for the aim of providing irrigation water for more than 12000 ha of downstream agricultural lands, which currently about 5000 ha are irrigated. It has a volume about 93 MCM and is fed through a diversion canal from Gadar River with a capacity of 15 m³/s. Before construction of the dam, there was a seasonal brackish wetland at the site of reservoir having an area of 1100 ha, called Shurgol. There are also several wetlands near the reservoir including Dorgehsangi, GordehGhit and Solduz which are fed by the Gadar River, groundwater discharge as well as the flows from agricultural drainages. Therefore, the river not only plays an important role in supplying part of Urmia Lake environmental water requirements, but also it is of high importance for delivering water requirements of its downstream wetlands. Figure 3 shows the variation in the river’s inflow into Urmia Lake. It is obvious that between 1998 and 2002, both the volume of inflow and the share of river compared to other surface runoffs to Urmia Lake were dramatically decreased due to impoundment of the Hasanlu dam.

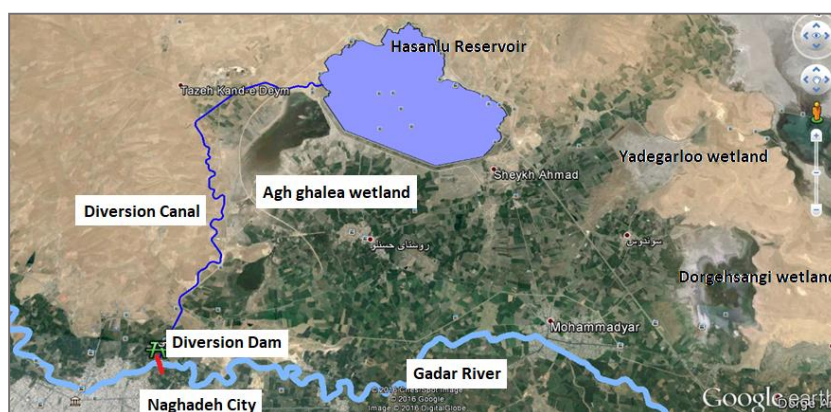


Figure 1. Study Area

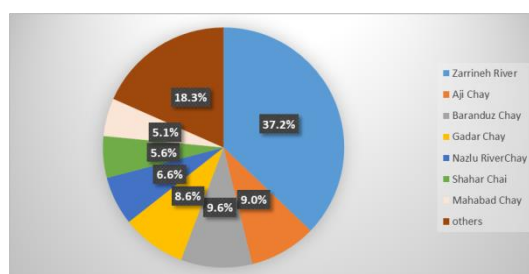


Figure 2. Portions of main rivers inflows into Urmia Lake based on the mean annual runoff from 1982 to 2012.

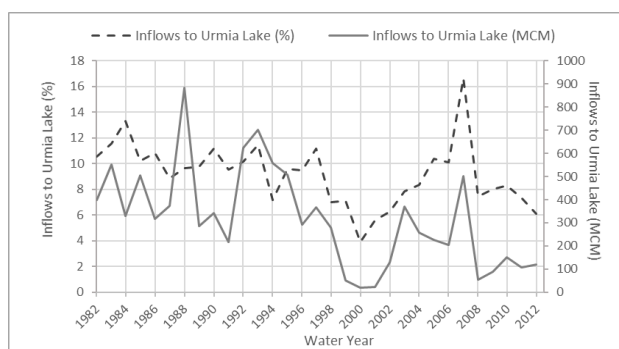


Figure 3. Variation in the volume and share of inflow from the Gadar River to Urmia Lake.

This study focuses on assessing the hydrologic alteration of the Gadar River after operation of the Hasanlu dam. To do this task first, the RVA and Eco-deficit methods were used to quantitatively describe changes in the frequency, duration, timing and magnitude of post-dammed period. Second, an appropriate range is determined for regulated flow to conserve the key component of flow regime within an ecologically acceptable range. Finally, several recommendations are provided to be taken into account as management strategies to improve hydrologic condition the river which in turn highly affects its ecological sustainability.

2. METHODOLOGY

To assess the variation of the flow regime of the Gadar River, a 20-year period before diversion of the river flow to the Hasanlu dam and 12 years after the dam operation were considered. Daily hydrometric data of the river at Bahramlu station, the most downstream station on the river, from 1981 to 2012 was acquired from Iran Water Resources Management Company (IWRMC). Then, the hydrological methods of RVA and Eco-deficit which are commonly used to determine EFs of rivers were used. However, the primary objective here, was not to determine the river's EF, rather was to investigate the hydrologic changes between pre and post-dam periods. To conduct the RVA method, the IHA software was used. This program was developed by researchers at The Nature Conservancy to facilitate hydrologic analysis in an ecologically-meaningful manner.

IHA parameters can be calculated using parametric (mean/standard deviation) or nonparametric (percentile) statistics. As recommended in the manual of the software for most situations, since the skewed (non-normal) nature of many hydrologic datasets violates the normality assumption required for non-parametric statistics, the former method is preferred in most cases. Then, the variation in the IHA parameters from the pre-impact period (reference scenario) to the variation in the post-impact period is compared to determine the extent of the changes. Each IHA parameter is analyzed to determine the frequency with which it falls into one of three RVA categories (Low, Middle, High), as defined by the RVA Category Boundaries. Hydrologic Alteration (HA) for each parameter is defined as the change in frequency from pre-impact to post-impact of that parameter in each of the three RVA categories (Eq.1).

$$HA = (\text{observed frequency} - \text{expected frequency}) / \text{expected frequency} \quad (1)$$

Where "expected frequency" is the frequency expected in the post-impact period if it followed the same pattern as the pre-impact period, and "observed frequency" is the frequency actually observed in the post-impact period. A positive HA indicates increased frequency (from pre- to post-dam period), whereas a negative HA factor corresponds to decreased frequency.

As described in the previous section, the concepts of eco-deficit and eco-surplus, are metrics to evaluate the volumetric environmental flows of a river based on flow duration curves (FDCs) (Vogel et al. (2007)). Flow duration curves provide a graphical illustration of the overall hydrologic state of a river system and is commonly used in a variety of hydrological studies (Vogel and Fennessey, 1995; Acreman, 2004). FDCs are constructed from daily streamflow data over a time interval of interest and provide a measure of the percentage of time duration that streamflow equals or exceeds a given value (Gao et al. 2009). Two different types of FDCs are possible: (1) period-of-record FDCs and (2) a median annual or seasonal FDC (see Vogel and Fennessey, 1994). Based on FDCs, the eco-deficit and eco-surplus can be computed over any time period of interest (month, season, or year) and reflect the overall loss or gain, respectively, in streamflow during that period that results from flow regulation (Fig.4). In this study we employed median annual FDCs for the purpose of eco-deficit/Eco surplus calculation.

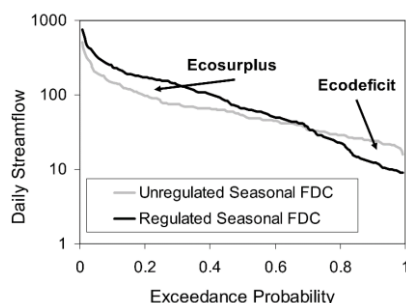


Figure 4. Schematic graph showing the eco-deficit and eco-surplus concepts corresponding to areas between regulated and unregulated (FDCs) of a river.

3. RESULTS & DISCUSSION

When the RVA and Eco-deficit techniques were applied the main outcomes including graphs and statistics were used for interpretation. In applying RVA, first the three categories of high, middle and low boundaries of HA, were determined to be more than 68%, 34-68% and less than 33%. Those parameters which showed high HA are base flows, mean monthly flows from June to September and from December to February and low flows with the duration of 1, 3 and 7 days as well (Fig.5). Other words, the highest impact of the river flow diversion has been on the low flow components of the hydrograph.

Fig.6 compares the mean monthly flow alteration in the regulated period versus natural reference condition of the river flow. The maximum reduction in the river flow has been occurred in April and May, while the expected variation from July to October is minimal. Moreover, ranges of the flow variation both in pre and post dam periods are wider in flood seasons (April, May, June), compared to other months. The amount of 7-days minimum flow has been also declined from 0.2 m³/s in natural condition to about zero after the Hasanlu Dam operation. This condition has been repeated in almost all years from 2001 to 2012, except the year of 2008 (see Fig.7).

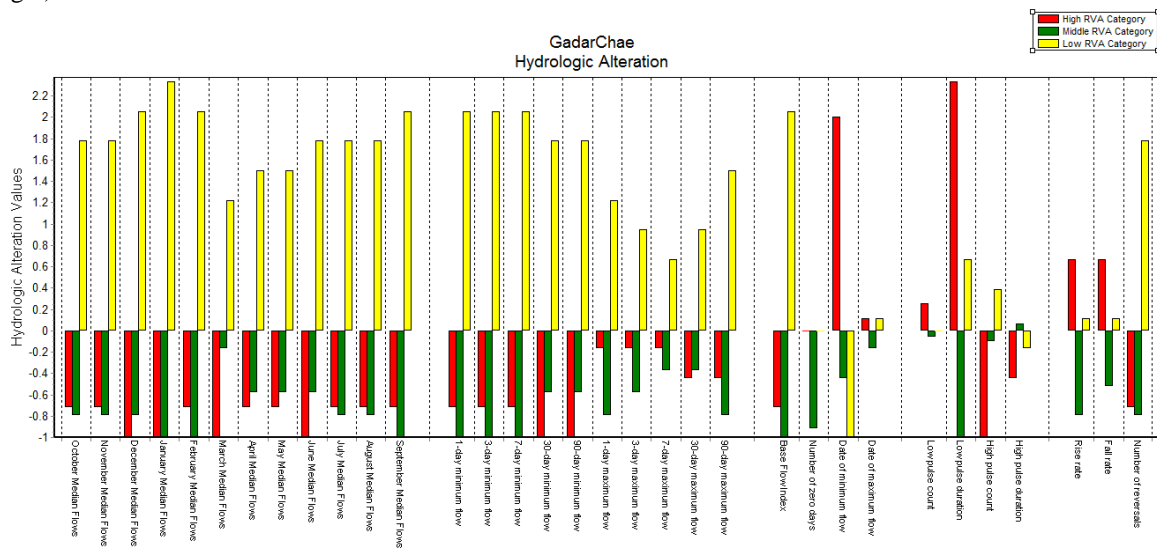


Figure 5. Hydrologic Alteration of various Hydrologic parameters in the Gadar River.

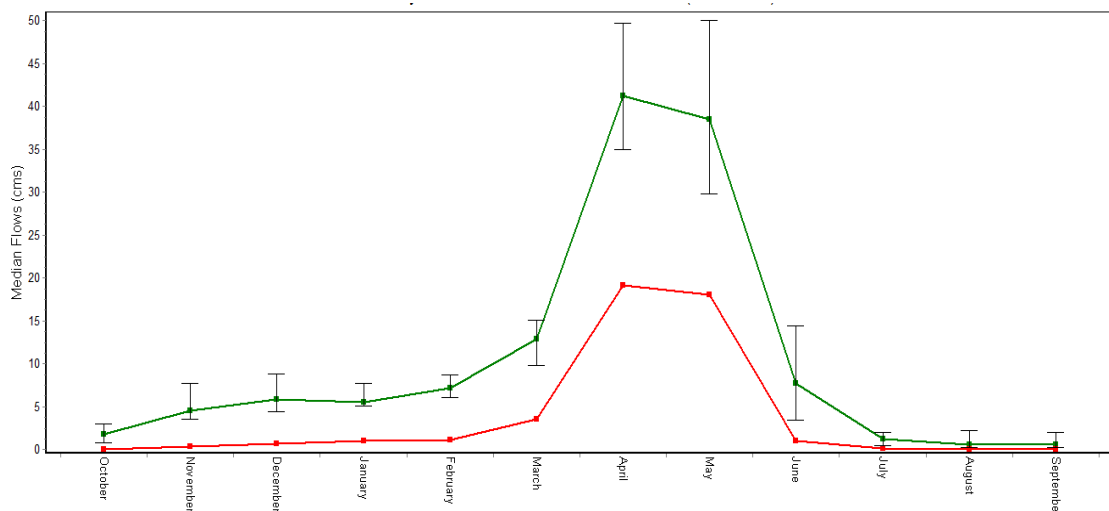


Figure 6. Mean Monthly Flow of the Gadar River during pre (green) and post-dam period (red line).

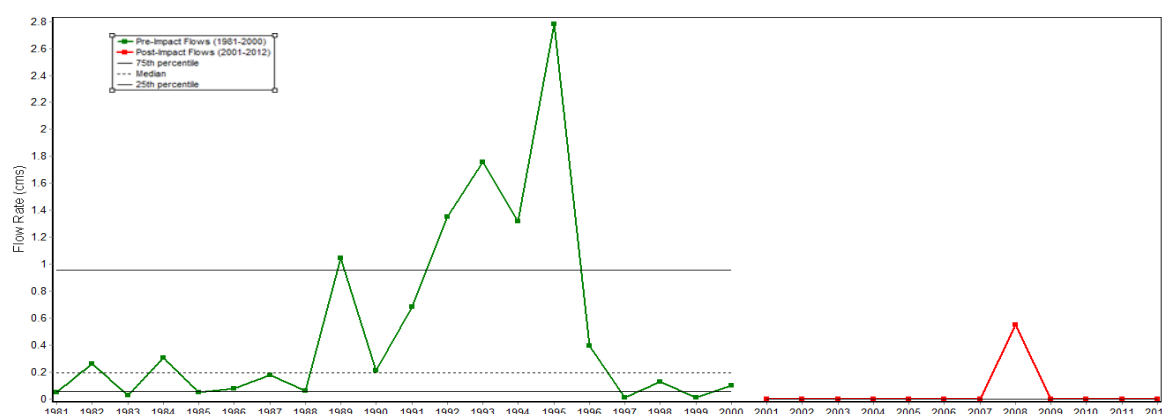


Figure 7. Comparison of the 7-days Minimum flows before (green line) and after (red line) the dam operation.

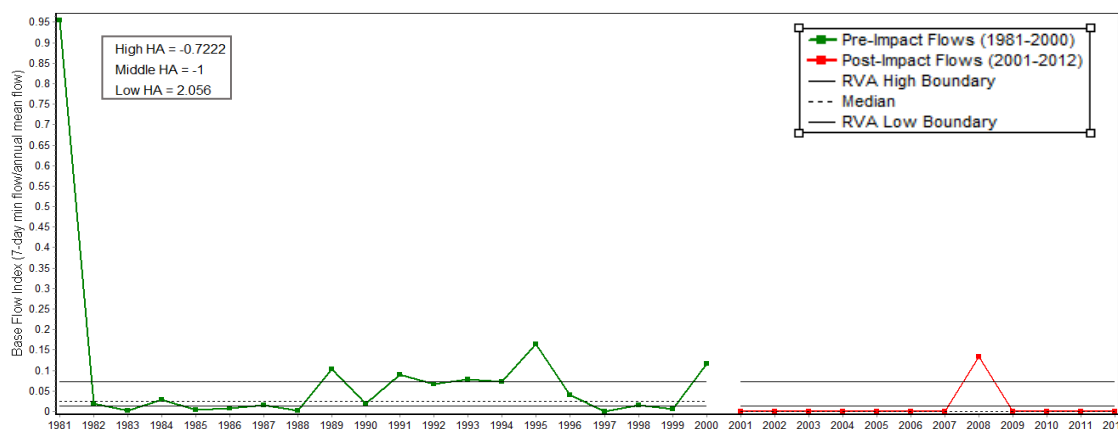


Figure 8. Comparison of the base-flow Index before (green line) and after (red line) the dam operation.

Base flow which is an important component of the streamflow especially in arid basins. Base flow Index (BFI), is defined as the ratio of annual base flow to the total annual run-off that and can be interpreted as contribution of ground-water discharge into a river. In general, the low BFI of the Gadar River shows the little dependency of the river flow to groundwater compared to the high runoffs, which usually occurs in early spring as a result of snow melt.

Decrease in BFI of the Gadar River from 2001 to 2012 as a result of water diversion to the Hasanlu Dam, reveals the fact that not only the mean annual runoff of the river has been declined after flow diversion (as displayed in fig.3), but also the minor inflows from ground water into the river has been approached zero in the last decade. The zero base flow of the Gadar River was reported in more than 90 percent of the post-dam period, whereas in the natural flow condition only in 3 out of 20 years such a situation had been observed (Fig.8).

As depicted in Fig. 9, before operation of the Hasanlu dam extreme low flows lasted typically less than 120 days, but since then it has been increased to more than 180 days a year. Obviously, extended period of extreme low flows can significantly change biodiversity of the rivers flora and fauna in an unpredictable way. The amount of extreme low flows has been also decreased by almost 90 percent (from 2.25 m³/s to 0.25 m³/s) after operation of the Hasanlu dam (Fig. 9). However, the average frequency of extreme low flows has been remained quite unchanged after regulation of the river.

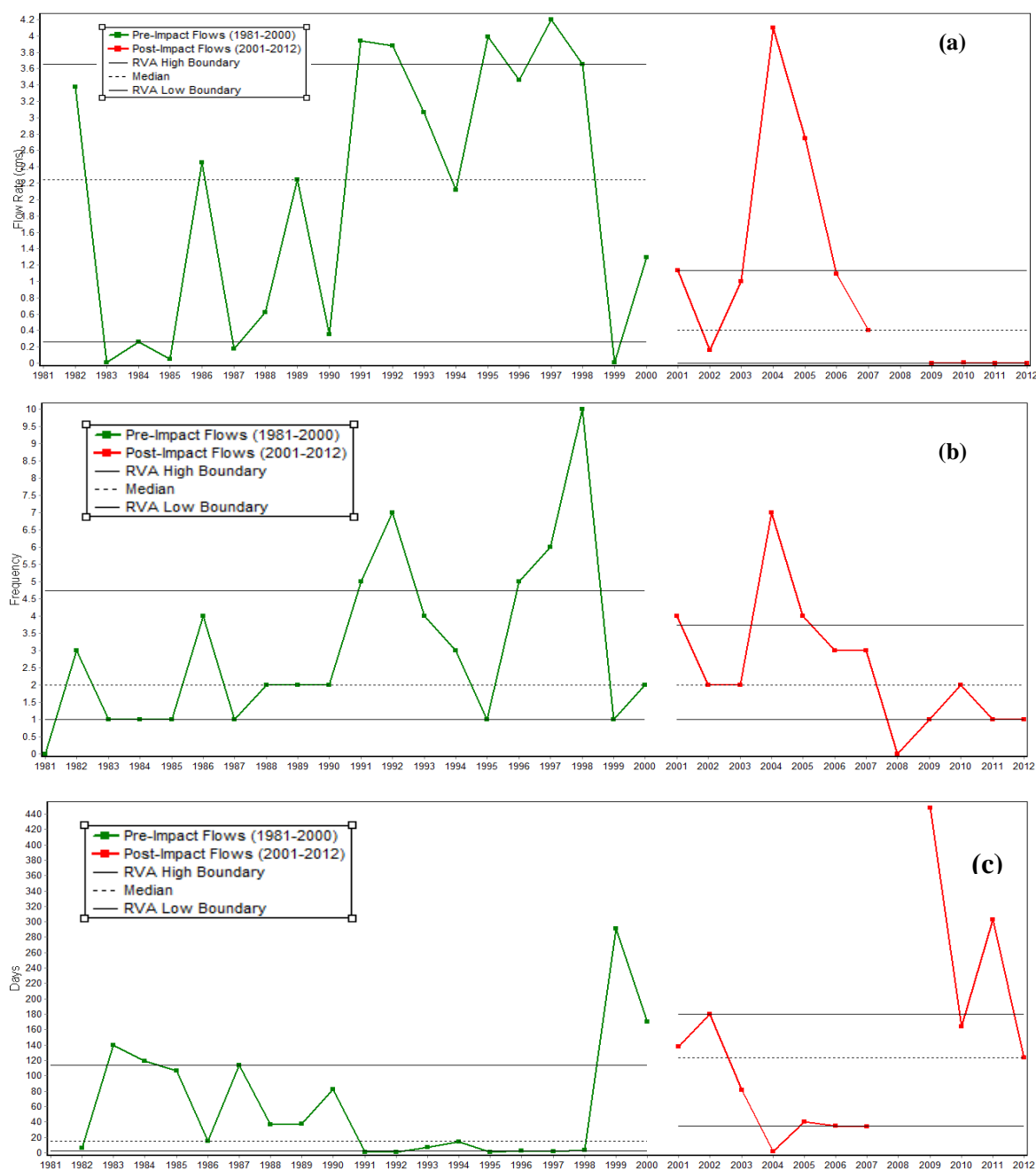


Figure 9 . Comparison of the (a) Mmagnitude, (b) Frequency, and (c) Duration of extreme low flows before (green line) and after (red line) operation of the Hasanlu reservoir.

When analyzing changes in the amount of high flow pulses, a slight decrease can be detected (Fig 10.a). However, both the frequency and the duration of high flows has been considerably influenced by the dam operation in 2000 and have been reduced in the post-dam period (Figs 10.b, c). Flood flows was occurred with the frequency of occurrence between 1 to 5 times per year (with an average of 3 times per year), whereas in the regulated flow period it has limited to 2 times per year in average. Furthermore, while peak flows lasted between 3 to 75 days before operation of the dam, their duration has been never exceeded more than 10 days, in the past decade. Peak flows provide variety of ecological functions which are vital for river, floodplain, riparian ecosystems including protection of plant habitats in the riparian zone and floodplain, improve connectivity between upstream and downstream habitats, providing suitable habitats for spawning and rearing of fish species, refreshing water quality conditions and helping transfer nutrients (e.g. Poff et al., 1997, Mathews and Richter,

2007). Reduction of flood flows, whether in their amount, frequency or duration, degrades or eliminates many of these functions. Moreover, such modifications in river systems can alter ecological communities and facilitate invasion of non-native species (Poff et al., 1997), and lead to a variety of negative geomorphological consequences (Magilligan et al., 2003). Flood flows are particularly important for the downstream wetlands which are highly dependent on such flows for flushing.

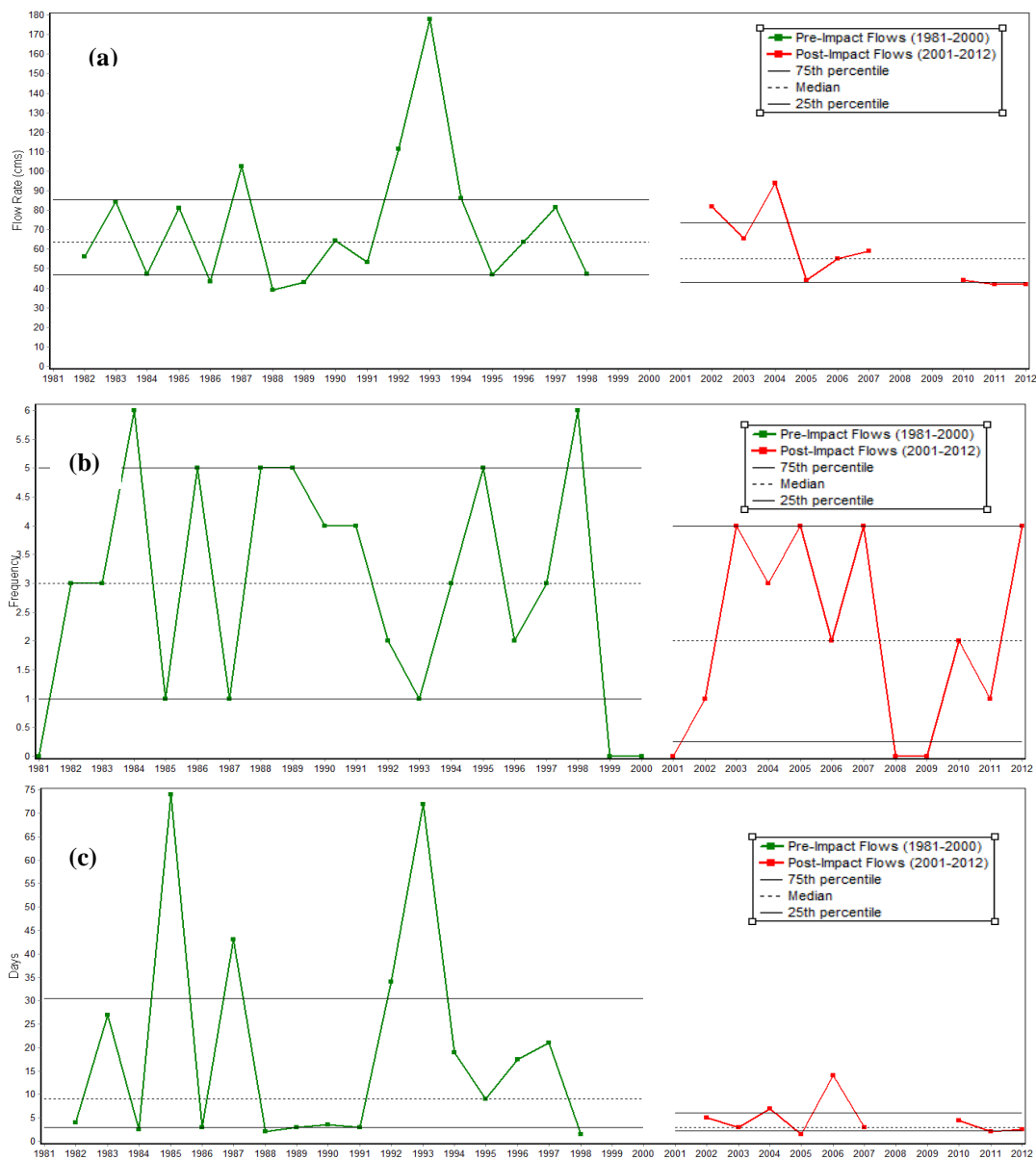


Figure 10. Comparison of the (a) magnitude, (b) Frequency, and (c) Duration of high flow pulses before (green line) and after (red line) operation of the Hasanlu reservoir.

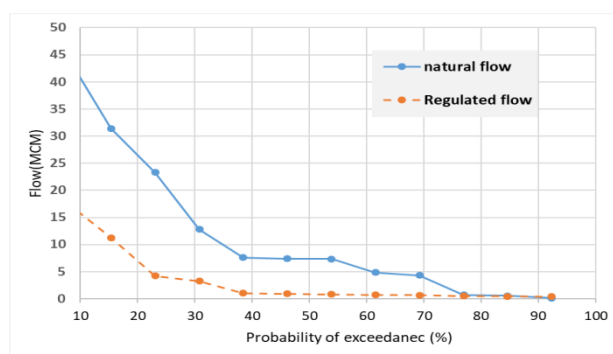


Figure 1. Comparison of Natural (Solid line) and Regulated (dash line) Mean Annual Flow Duration Curve (FDC) of the Gadar River.

As illustrated in Fig.11, The FDCs of the pre and post-regulation period are cross each other at about 85% exceedance probability, which causes near-zero eco-surplus volume. This means that after operation of the Hasanlu reservoirs, the volume of the river has been significantly decreased. It is usually expected that reservoir construction lead to an increase in the low flows (having high exceedance probability) of a river. However, in the case of the Gadar River, because of the concurrent development of the irrigated agriculture and the Hasanlu drain, dramatic diversion of water from the river channel has been occurred. This overexploitation of the water makes the river totally dried up in dry seasons. The amount of eco-deficit is about 218 MCM which can be interpreted as the total deficit in the volume of river compared to its natural ecological regime during the 11 years.

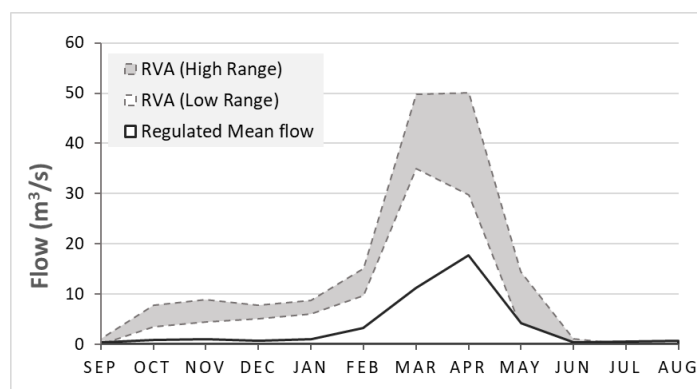


Figure 2. Comparison of the mean flow of Gadar River after operation of the Hasanlu Dam to the flow range proposed by the RVA method as environmental flows of the river.

When analysis of the hydrologic alternation was completed trough the RVA method, there is possibility to calculate the proper flow range for the sake of preserving the sustainability of the river environment. The recommended range for the river flow is depicted by a gray bound in Fig.12 and are supposed to be considered in the reservoir operation or flow diversion. Although keeping flow in this range does not guarantee the entire ecological health of the river and its relevant ecosystems, it can improve at least hydrologic condition of the river through the fulfilment of RVA criteria. The hydrograph of the average flow of the Gadar River during the post-dam period indicates that it is far beyond the proposed range. Therefore, there is an urgent need to revise the operation rules of the dam and adapt the flow diversion from the river so that the ultimate flow of the river after abstractions remain within the RVA suggested range.

4. CONCLUSIONS

Like many watersheds in the world, water resources of the Urmia Basin has been under extreme pressure during the past decades by the compound effect of increased water demands and arid climate. Almost all permanent rivers in the basin have been regulated by dams to supply water for agriculture. the Gadar River in the south part of Urmia Lake supplies about 9% of the lake and is an important source of water for the satellite wetlands at the region. Dramatic changes has been occurred in the natural flow regime of the river, since the

operation of the Hasanlu dam in 2000. In this study the hydrologic alternation of the river flow in the post-dam period were investigated using the RVA and Eco-deficit methods. Main changes observed in the flow pattern include occurrence of more frequent zero flows, increase in the duration of low flows, considerable decrease in the frequency and duration of the high flows, and the decreased base flow index. Moreover, results of eco-deficit/surplus curve indicated that not only the reservoir operation has been no eco-surplus but also it causes an average eco-deficit of 218 MCM/y.

To modify some of these changes it is required to revise both the flow diversion volume from the Gadar River and the rule curve of the reservoir for the sake of the river ecosystem sustainability through considering environmental flows of the river and its relevant ecosystem. Beside active management action, implementing environmental flows also required restrictive flow management strategies for example through reducing the abstractions for irrigation. Application of active management will help to preserve the key components of flow regime, including low flows and floods. On the other hand, restrictive flow management policies can ensure that enough water is left in the river, particularly during dry periods, by controlling abstractions and diversions. Both types of interventions depend on people changing their behavior, and should be based on an informed decision that has broad societal support.

5. REFERENCES

1. Acreman, M., and M.J. Dunbar. (2004). "Defining environmental river flow requirements: a review". *Hydrology and Earth System Sciences*, 8, pp. 861-876.
2. Gao Y, Vogel RM, Kroll CN, Poff NL, Olden JD. (2009). "Development of representative indicators of hydrologic alteration". *Journal of Hydrology*. 374(1), pp.136–147.
3. Homa, E., Vogel, R.M., Smith, M.P., Apse, C.D., Huber-Lee, A. (2005). "An Optimization Approach for Balancing Human and Ecological Flow Needs", EWRI 2005 World Water and Environmental Resources Congress. Anchorage, Alaska.
4. Magilligan, F.J., Nislow, K.H. (2005). "Changes in hydrologic regime by dams". *Geomorphology* (71), pp. 61–78.
5. Mathews, R., Richter, B.D. (2007). "Application of the indicators of hydrologic alteration software in environmental flow setting". *Journal of the American Water Resources Association* 43, 1400–1413.
6. Olden, J.D., and Poff. N.L. (2003). "Redundancy and the choice of hydrologic indices for characterizing streamflow regimes". *River Research Application*. 19: 101-121.
7. Poff, N.L., Allan, J.D., Bain, M.B., Karr, J.R., Prestegard, K.L., Richter, B.D., Sparks, R.E., Stromberg, J.C. (1997). "The natural flow regime: a paradigm for river conservation and restoration". *Bioscience*, 47 (11), pp.769–784.
8. Poff, N.L., and Zimmerman, J.K.H. (2010). "Ecological responses to altered flow regimes: a literature review to inform environmental flows science and management". *Fresh Water Biology*. 55, pp. 194-205.
9. Richter, B.D., Baumgartner, J.V., Powell, J., Braun, D.P. (1996). "A method for assessing hydrologic alteration within ecosystems" *Conservation Biology* 10, pp. 1163–1174.
10. Vogel, R. M., J. Sieber, S. A. Archfield, M. P. Smith, C. D. Apse, and A. Huber-Lee. (2007). "Relations among storage, yield, and instream flow". *Water Resources Research*. 43, W05403.
11. Vogel, R.M., Fennessey, N.M. (1994). "Flow duration curves I: a new interpretation and confidence intervals", *ASCE Journal of Water Resources Planning and Management* 120 (4).
12. Vogel, R.M., Fennessey, N.M. (1995). "Flow duration curves II: a review of applications in water resources planning". *Water Resources Bulletin* 31 (6), pp. 1029–1039.
13. WCD - World Commission on Dams, (2000). "Dams and Development: A New Framework for Decision-Making", Earthscan, London.

Parametric investigation of valley shape effects on seismic response of concrete gravity dams

Behzad Nikkhakian¹, Mohammad Alembagheri²

1- M.Sc. Student of Hydraulic Structures, Tarbiat Modares University

2- Faculty of Civil and Environmental Engineering, Tarbiat Modares University

Email: behzadnikkhakian@modares.ac.ir

Abstract

The seismic failure of concrete dams is possible in earthquake-prone areas. Their failure can put high risks to life and property. Furthermore, any structural damage to dams will cause negative economic effects. This fact has led to increased attention in dynamic behavior of dams during the last decades. The aim of this study is comparing two and three dimensional seismic response of concrete gravity dams and also necessity of providing more realistic models for considering the effects of cross-stream motions. The effects of dam-reservoir-foundation interaction, nonlinear behavior of mass concrete, the effect different shapes of valley are studied and their effect on nonlinear response and seismic stability of concrete gravity dams are evaluated under two and three-component earthquake records.

Keywords: concrete gravity dam, seismic response, three-dimensional behavior, dam-reservoir-foundation interaction, nonlinear behavior.

1. INTRODUCTION

During last decades, the growing demand for green energy has led to the construction of high concrete dams, which may be located in seismic areas. Seismic safety of concrete dams is one of the most important issues in the field of hydraulic structures, which may disrupt the normal operation of these infrastructures during the seismic event and cause a catastrophic failure that results in loss of life and human property.

Since 1928, after collapse of St. Francis Dam in California, failure of large dams have attracted a lot of attention which have led to extensive research in this field. The investigation of incidents that have occurred since then for various types of dams, emphasizes the importance of this issue. Among the damaged concrete dams during seismic events, the following cases can be mentioned: the Koyna gravity dam with a height of 103 meters in India (1967), the Hsingfengkinag buttress dam with a height of 105 meters in China (1962), the Pacoima arch dam with a height of 113 meters in the United States (1971, 1944), and also the Sefid Rud buttress dam with a height of 106 meters in Iran (1990) [1]. In the past, the seismic analysis of concrete gravity dams was often considered ideally using two-dimensional monoliths and earthquake effects were usually applied by defining a simple seismic coefficient. However, in recent years, attentions have been paid to analyzing of failure of concrete dams in three-dimensional space.

In 1972, Chopra and Chakrabarti conducted the two-dimensional monolith linear analysis of the Koyna dam under the 1967 earthquake [2]. Chopra in 1988 did comprehensive studies on the Pine Flat Dam. In this study, he considered the effects of the reservoir and analyzed the dam under harmonic loading and different earthquake types [3]. In 1985, A.Rashed and Iwan mentioned the necessity of 3D analysis for the dams seismic design in narrow valleys [4]. In 1997 Paultre and Proulx put the Outardes 3 dam under a forced vibration test. They showed that a three-dimensional model for the dam-reservoir-foundation system, could produce more accurate behavior with consideration of the water compressibility effects. It was also shown that two-dimensional approach can only predict the main frequency of system resonant. According to finite element simulation results, it was found that the 3D behavior of dam is significantly different from ideal two-dimensional behavior of monoliths [5]. Paultre and Azmi in 2002, using the ADAP88 software a finite element computer program, investigated joints behavior and their effect on stability and dynamic response of the Big Tujunga Dam and Outardes 3 Dam [6]. Berets et al. (2012) investigated 3D stability of concrete gravity dams on steep cliff, using finite equilibrium method [7]. Arici et al. in 2014 studied the 3D seismic dam-reservoir-foundation interaction of Andiraz RCC Dam [8]. Wang et al. (2017) studied the Guandi concrete gravity Dam, emphasized on importance of 3D analysis, especially in the presence of transverse earthquake component [9].

The valley shape is one of the important geometric parameters in choosing dam type and determining the ratio of length to height of the dam, this parameter has a significant effect on seismic excitation and its results. The issue that is studied in this paper is the effect of valley shape on seismic stimulation of concrete gravity dams,

which is carried out by using dynamic analysis of dam-reservoir- foundation system in frequency domain and time . In the present study, the finite element 3D model of Pine Flat gravity dam has been prepared along with the nonlinear behavior of dam body material, without considering contraction joint. Regarding importance of valley shape, the valley width variations and dam response to all three components of the ground motion is being discussed, and effect of valley width to height ratio are examined as well as the importance of ground motion transverse component along with the horizontal and vertical components. The dam-reservoir-foundation interaction effects are considered in the analysis, and ultimately compared with the results of the 2D model.

2. NUMERICAL MODELING

Numerical modeling of large structures such as dams is a suitable means for performing seismic analysis and evaluating their performance. Solid and fluid interaction is one of the important issues in seismic analysis of structures in the vicinity of liquids such as water reservoirs and concrete dams. Solving the problem of dam interaction with reservoir and foundation is more complicated than other structures due to the behavioral differences between the reservoir water (the fluid) and the constituent materials of the dam body and the foundation (structure) [10]. Assuming the inviscid linear compressible behavior of low-amplitude irrotational motion, the governing equation for the large dam reservoir is explained as follows (wave equation):

$$\nabla^2 P(x, y, z) = \frac{1}{c^2} \cdot \ddot{P}(x, y, z) \quad (1)$$

In which c is the velocity of the compressive wave in water, $P(x,y,z)$ is the hydrodynamic pressure in addition to the hydrostatic pressure and ∇^2 is the Laplacian operator. In the problem of the dam-reservoir interaction, there is no flow across the interfaces. This assumption is based on the fact that the face of concrete dam is (impervious). This assumption leads to the condition that there is no relative velocity in the direction perpendicular to the (shared) boundary.

The boundary condition of the reservoir bottom divides the hydrodynamic pressure into the vertical acceleration and the acceleration resulting from the interaction between the stored water and the reservoir floor materials. In this modeling, only the interaction will be considered in the vertical direction, this condition is similar to the previous condition, although the coefficient of absorption of the bottom can be considered. At the free surface of the reservoir, the hydrodynamic pressure is zero. In other words, for all nodes located on the reservoir surface, zero pressure is defined as the boundary condition. This assumption also states that there is no surface waves in the reservoir and surface waves are not considered in the modeling.

The far-end boundary at the end of the reservoir in the finite element model of reservoirs with infinite length has been investigated by numerous researchers. Sommerfeld's boundary condition is one of the most common ones, which is based on the assumption of the propagation of plane waves in the fluid at far distance from the dam. This (assumption) is expressed mathematically as follows:

$$\frac{\partial P}{\partial n} = -\frac{1}{c} \cdot \frac{\partial P}{\partial t} \quad (2)$$

Where n is perpendicular direction to the far-end boundary. This condition introduces a damping to the system, which models the loss of energy from outgoing waves. At the boundaries of the foundation, based on a simplistic assumption, if the propagation effect of the waves is ignored, it is not necessary to define a specific boundary condition for absorption of waves.

3. FINITE ELEMENT FORMULATION OF DAM-RESERVOIR-FOUNDATION SYSTEM

The relationship between hydrodynamic pressure within the reservoir [10], and the vector of applied forces to the dam-reservoir intersection $\{f\}$, is made by a coupling matrix $[Q]$

$$[Q] \cdot \{P\} = \{f\} \quad (3)$$

Using the discretization of reservoir and also considering solids finite element equations, the dam-reservoir interaction is a classical problem involving a second-order differential equation. These equations for dam structure and reservoir are as follows:

$$[M]\{\ddot{U}\} + [C]\{\dot{U}\} + [K]\{U\} = \{f_1\} - [M]\{\ddot{U}_g\} + [Q]\{P\} = \{F_1\} + [Q]\{P\} \quad (4)$$

$$[G]\{\ddot{P}\} + [C']\{\dot{P}\} + [K']\{P\} = \{F\} - \rho[Q]^T (\{\ddot{U}\} + \{\ddot{U}_g\}) = \{F_2\} - \rho[Q]^T \{\ddot{U}\} \quad (5)$$

Where $[M]$, $[C]$, and $[K]$ respectively are the mass, damping and dam structure stiffness matrices, and $[G]$, $[C']$ and $[K']$, respectively are the mass, damping and reservoir stiffness matrices. $\{f_1\}$ is body forces and hydrostatic vector, $\{6\}$ and $\{2\}$, respectively are the displacements vector and hydrodynamic pressures vector. $\{\ddot{U}_g\}$ is the ground motion acceleration vector and ρ is the fluid density. The dot represents the variable time derivative. In formulation of the dam-reservoir-foundation finite element system, with the assumption of massless foundation, $[K]$, $[M]$ and $[C]$ matrices comprise the subset of matrixes that is composed of the dam and the foundation structures. In this case, the dam and foundation are considered as a unit, interacting with the water of the reservoir.

4. CASE STUDY

The case study in this is Pine Flat gravity dam. The dam consists of 36 monoliths with the width of 15 m and a 12-m width monolith. The crest length is 550 m and the highest monolith is 122 m. The geometric characteristics of 2D section of the dam with its foundation and the reservoir are shown in Fig. 1. The downstream 3D view of the dam and the main geometric parameters are shown in Fig. 2. As it can be seen, the valley lateral sides (θ) are considered at angle of 45° and the main parameter studied is the width of the valley at the river level (B). H represents the highest dam monolith height with the value of 122m.

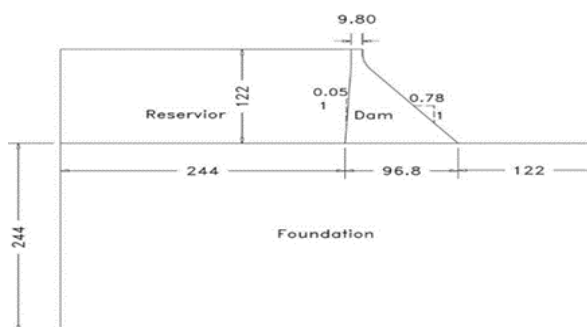


Figure 1. geometric characteristics of 2D Pine Flat dam section

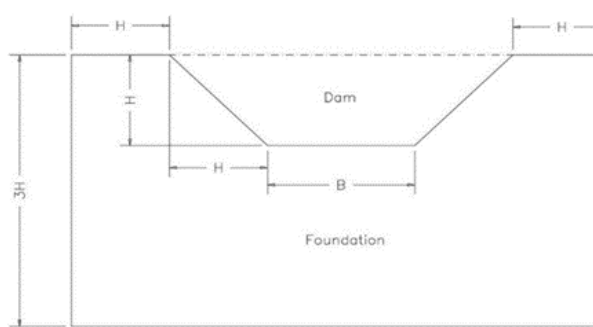


Figure 2. The downstream view of the dam

The concrete material of the dam body with nonlinear behavior has been modeled by using concrete damage plasticity approach. The elastic behavior of concrete is: density of 2400 Kg/m^3 , initial Young's modulus of 30 GPa and Poisson's Ratio of 0.2. For nonlinear behavior of concrete, only tensile failure is considered and the behavior of the concrete has been assumed linear in compression. Concrete stress-strain behavior in nonlinear state with the corresponding values of tensile failure has been shown in Fig. 3 [11].

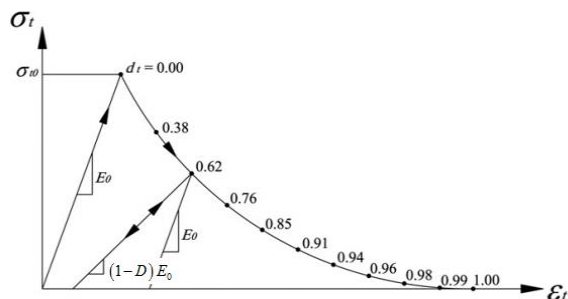


Figure 3. stress-strain relation for the nonlinear concrete

The post-yielding behavior is modeled in a softening form by decreasing the concrete elasticity modulus with a tensile load failure variable dt . The tensile failure variable is a function of nonlinear strains and its variation is shown in Fig. 3. The tensile yield of concrete is assumed as 2.9 Mpa. The reservoir water is considered as full and has been modeled by the density of 1000 Kg/m^3 and the bulk modulus of 2.07 GPa. In the case of gravity dams which are constructed on competent abutments, the finite element model of mass-less foundation can adequately/ model the rock. In this study, massless foundation with Young's modulus of 30 GPa and Poisson's

Ratio of 0.33 has been used. In this research, six 3D finite element models of the dam-reservoir-foundation with the ratio of valley width (B) to dam height (H) are investigated as follows: $\frac{B}{H} = \frac{1}{3}, \frac{2}{3}, 1, \frac{4}{3}, \frac{5}{3}, 2$

Fig. 4 shows the finite element model of the dam-reservoir-foundation system in 2D mode and Fig. 5 shows 3D model with B / H ratio of 1. It should be noted that Pine Flat dam is actually located in valley with B / H ratio of 2.5. It has been tried to use approximately same mesh density in all models. The finite element mesh has been sufficiently refined to simulate the nonlinear behavior of the dam body.

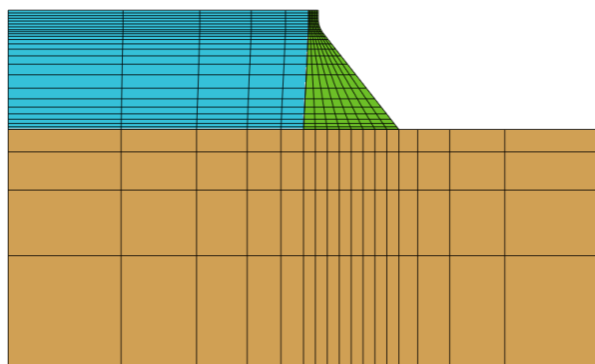


Figure 4. 2D Finite element model

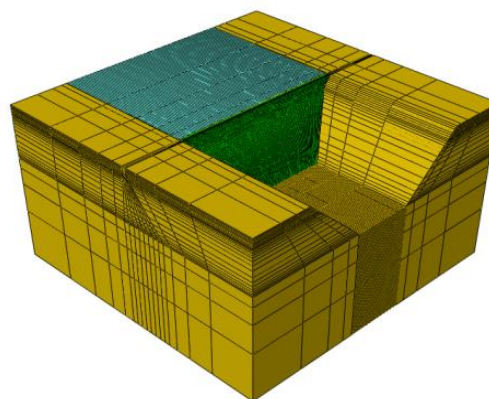


Figure 5. 3D Finite element model

4.1. SEISMIC LOADING

The loading consists of two static and dynamic steps. In this modeling, static loading includes the dam body weight and the full reservoir hydrostatic load. Typical foundation weight is not applied during static analyses, after the static loading, the seismic loading of the model begins. This seismic loading is the recorded accelerogram during the Kern County earthquake at Taft Station on July 21, 1952. Dynamic analysis of the Pine Flat dam is done by considering the separate and also simultaneous influence of horizontal components (in the stream direction), vertical and transverse (perpendicular to the stream). In Fig. 6, horizontal, vertical, and transverse records are shown, respectively.

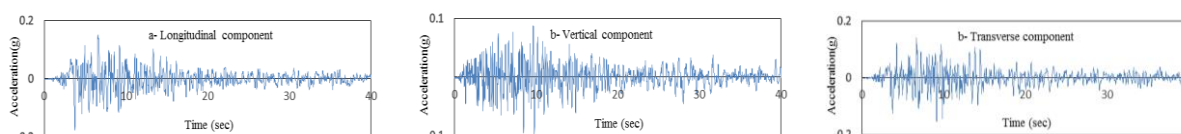


Figure 6. Kern County earthquake record

4.2. DAMAGE INDEX

In order to show damaged areas in the models, and to compare the imposed damages, a failure index is defined as follows:

$$DI = \frac{\sum D_e \cdot V_e}{\sum V_e} \tag{6}$$

in which D_e is the tensile damage of the element e and V_e is the element volume. This index, which is the weighted average of the damage imposed to the dam body, can be calculated on the entire dam body or locally on damage prone areas such as neck of the dam, its heel or lateral abutment areas. The locations for computing this index have been shown in Figs.7, 8 and are explained as follows:

- 1- Right abutment in 3D models
- 2- Left abutment in 3D models
- 3- The neck of the dam from 102-meter level (downstream kink) to 114-meter level (curved end in upstream).
- 4- Dam heel, in 2D and 3D models

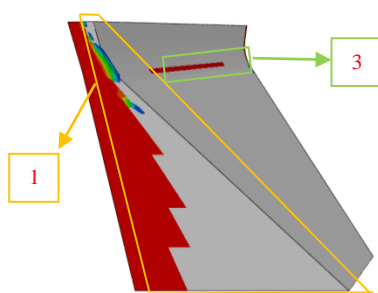


Figure 7. Downstream view

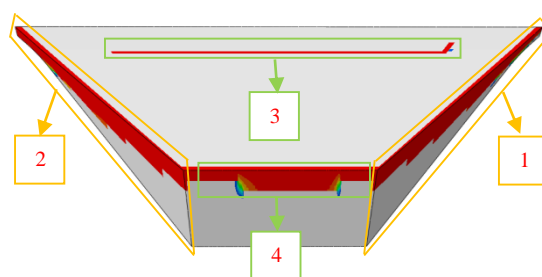


Figure 8. Upstream view

5. RESULTS AND DISCUSSION

5.1. DAM'S CREST DISPLACEMENT

The maximum relative absolute displacement of the dam crest middle point under three components of the earthquake has been shown separately and simultaneously for all 3D and 2D models in Fig. 9. x , y , and z is respectively horizontal, vertical, and transverse records.

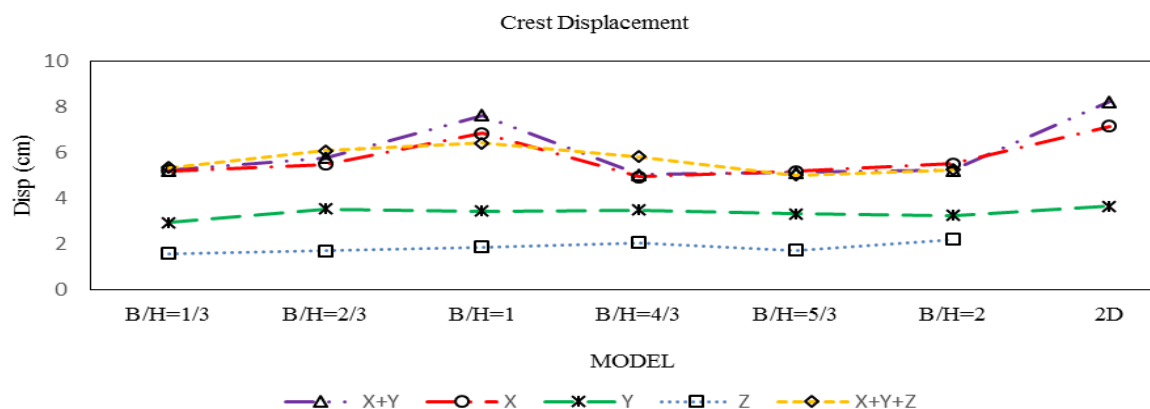


Figure 9. Crest Displacement

It should be noted that in the 2D model only two longitudinal and vertical earthquake components are applied. The minimum displacement is observed in applying transverse component, and the application of vertical component only causes the least relative displacement. As shown in Fig. 9, the greatest relative displacement of the crest is related to the records containing horizontal component, although the addition of transverse and vertical components may sometimes reduce the relative displacement. The two-dimensional model shows more displacements in comparison with most 3D models. In general, there is no definite conclusion of (B / H) ratio effect on the dam seismic response due to the natural frequencies change of system and, consequently, the amounts of spectral intensity (according to the earthquake record) by changing the (B / H) ratio.

5.2. DAMAGE INDEX

The calculated damage index in the highest monolith of the 3D models, which is located in the middle of the model, is compared with the 2D model in two areas of the neck and heel of the dam in Figs. 8, 9. The index has been calculated separately and the results of applying the three earthquake components is shown simultaneously and separately in Fig. 10. Final tensile damage at the middle monolith for three models of $(B / H) = 1/3, 1, 2$ and the 2D model under the Kern County earthquake record is compared in Fig. 11. As can be seen, the lowest damage value is for the model $(B / H) = 2$. By increasing the (B / H) ratio, the amount of damage in the dam neck region decreases. This damage, especially under the longitudinal component, can only reach over 20%. In general, there is no damage in the neck region of the 2D model. About the dam heel, the addition of transverse and vertical components to the longitudinal component sometimes increases and (sometimes) reduces the imposed damage. But in contrast to the dam neck, the damage which is applied to the dam heel in the two-

dimensional model is more than the 3D model. Therefore, it can be concluded that considering the 2D model results in far-fetched and non-conservative results, especially in the case of damage in dam neck region

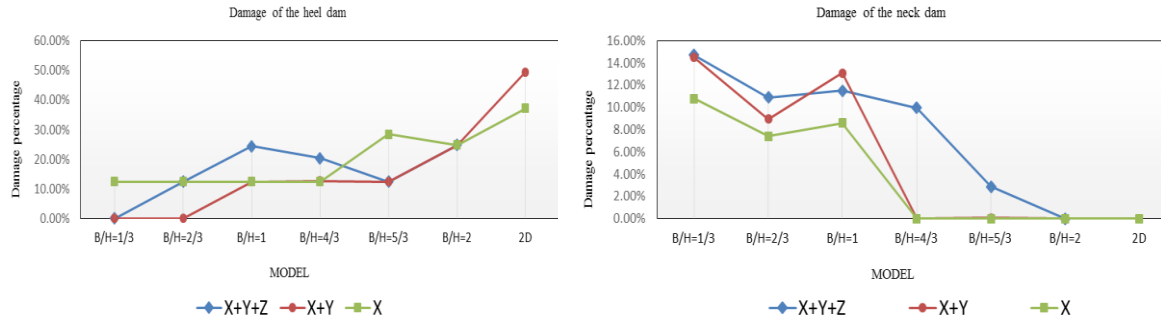


Figure 10. Comparison of the damage in the 2D and 3D models

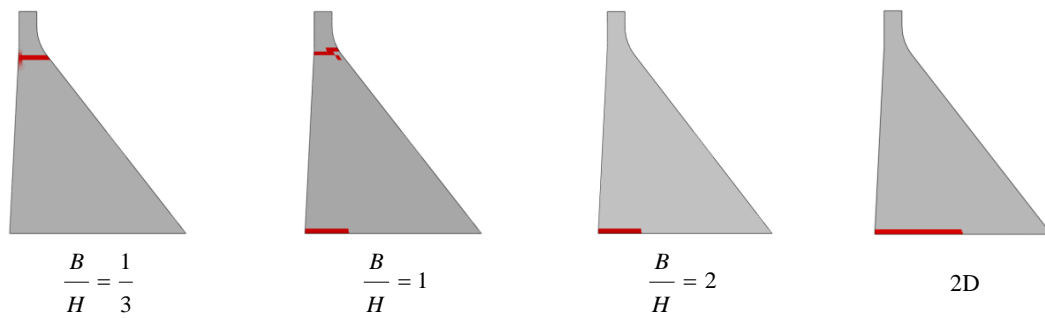


Figure 11. Tensile damage in the highest monolith of 3D and 2D models

In the following, we investigate the damage index in four areas shown in Fig. 8, in which only the 3D models were compared and the results has been presented in Fig. 12. As can be seen, the earthquake transverse component that is ignored in the 2D analysis, causes increase in the applied damage to the right and left lateral supports and also the dam neck in all 3D model. However, the damages that are applied to the dam heel are more likely to be governed by the earthquake longitudinal component.

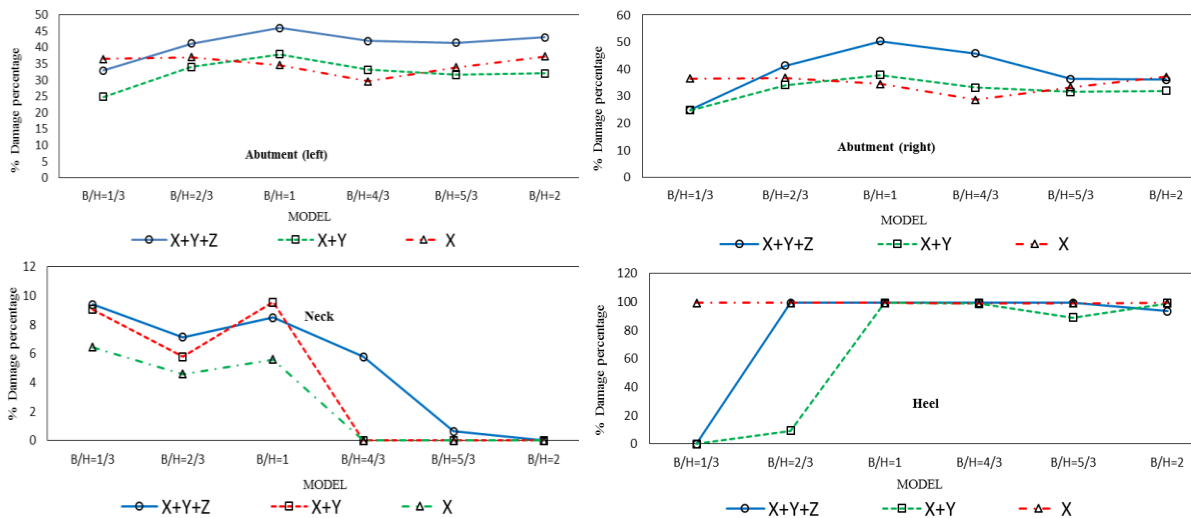


Figure 12. Comparison of the damage in 3D model

6. CONCLUSIONS

This study shows that increasing the width of valley at the river level and, consequently, increasing the length of dam cause:

1. The lowest relative absolute displacement of the dam crest middle point is related to the only application of the transverse component and then only with the application of the vertical component.
2. The maximum crest relative displacement is related to the records, containing the horizontal component, although the addition of lateral and vertical components may sometimes reduce the relative displacement of the dam crest.
3. In comparison with the most of 3D models, the 2D models concluded more relative crest displacement which indicates that the 2D model results are unrealistic.
4. Evaluation of ultimate tensile damage in the highest monolith of 3D models for comparison with the two-dimensional model under the Kern County earthquake record indicates reduction in the dam neck region damage by increasing valley width to model B/H= 2 and by further increase in valley width, the damage amount has remarkable increase, specially under longitudinal component. In two-dimensional model, the damage is only related to dam heel and generally is more than the three-dimensional models.
5. Comparison of just three-dimensional models shows that the earthquake transversal component is ignored in the 2D analysis and leads to increase of applied damage to the right and left side supports and also the dam neck in all 3D models, and applied damage to the dam heel is governed by the longitudinal component of the earthquake.
6. Totally, in comparison of 3D models, the maximum amount of tensile damage is concentrated in the abutments, and by increasing the valley width, the dam neck damage decreased.

7. REFERENCES

1. Hinks, J. and E. Gosschalk, Dams and Earthquakes—a Review. *Dam Engineering*, 1993. 4(1): p. 234-240.
2. Chopra, A.K. and P. Chakrabarti, The earthquake experience at Koyna dam and stresses in concrete gravity dams. *Earthquake Engineering & Structural Dynamics*, 1972. 1(2): p. 151-164.
3. Chopra, A.K., Earthquake response analysis of concrete dams. *Advanced dam engineering for design, construction, and rehabilitation*, 1988: p. 416-465.
4. Rashed, A.A. and W.D. Iwan, Dynamic analysis of short-length gravity dams. *Journal of engineering mechanics*, 1985. 111(8): p. 1067-1083.
5. Proulx, J. and P. Paultre, Experimental and numerical investigation of dam reservoir foundation interaction for a large gravity dam. *Canadian Journal of Civil Engineering*, 1997. 24(1): p. 90-105.
6. Azmi, M. and P. Paultre, Three-dimensional analysis of concrete dams including contraction joint non-linearity. *Engineering Structures*, 2002. 24(6): p. 757-771.
7. Bretas, E.M., P. Léger, and J.V. Lemos, 3D stability analysis of gravity dams on sloped rock foundations using the limit equilibrium method. *Computers and Geotechnics*, 2012. 44: p. 147-156.
8. Arici, Y., B. Binici, and A. Aldemir, Comparison of the expected damage patterns from two-and three-dimensional nonlinear dynamic analyses of a roller compacted concrete dam. *Structure and Infrastructure Engineering*, 2014. 10(3): p. 305-315.
9. Wang, G., et al., Deterministic 3D seismic damage analysis of Guandi concrete gravity dam: A case study. *Engineering Structures*, 2017. 148: p. 263-276.
10. Alembagheri, M. and M.Seyedkazemi, Numerical Modeling of Concrete Gravity Dams by ABAQUS 2014, Iran. 320.
11. Alembagheri, M. and M. Ghaemian, Seismic assessment of concrete gravity dams using capacity estimation and damage indexes. *Earthquake Engineering & Structural Dynamics*, 2013. 42(1): p. 123-144.

Dynamic analysis of dam-reservoir-intake tower considering sediments absorption

Ali Mahdian Khalili¹, Bahram Navayi Neya², Leila Kalani Sarokolayi³

1- MSc of Water Engineering and Hydraulic Structures, Babol Noshirvani University of Technology, Babol, Iran

2- Associate Professor, Faculty of Civil Engineering, Babol Noshirvani University of Technology, Babol, Iran

3- Assistant Professor, Tabari University of Babol, Babol, Iran

Email: Ali.Mahdian@stu.nit.ac.ir

Abstract

In this paper, dam-reservoir-intake tower system with interior water of tower are analyzed using finite element method considering sediments absorption. Reservoir is modeled by Lagrangian approach and effect of sediments absorption on responses of dam-reservoir-intake tower is considered. Three types of sediments and also distance between dam and tower are determined for parameter study. Dynamic analysis has been performed under horizontal and vertical excitation of Northridge and Tabas earthquakes. Results show that increasing distance between dam and tower, can increase frequencies of dam-reservoir-intake tower system. Also in models with rigid sediments, the frequencies of system are a little more than model with two other kind of sediments. Dynamic responses show that increasing the distance between dam and tower reduce the effects of sediments on the dam and tower responses. It is concluded that the maximum displacements of dam crest and principal stresses of dam heel increase by increasing distance between them. In time domain responses, displacements of dam crest and principal stresses of dam heel increase in rigid sediments but sediment type has fewer effects on tower responses specially on displacements.

Keywords: intake towers, lagrangian approach, sediments absorption, vertical excitation, reservoir.

1. INTRODUCTION

Seismic analysis of concrete dams and connected hydraulic structures like intake towers were studied by researchers because they are related to water supply systems and may influence human necessities in life. In primitive researchs basically solid-fluid interaction was study parameter where defined useful equations but in recent decades due to the computerized modeling, systems have been modeled and analyzed in three directions. Although presence of dam has been considered in new models but sediments in reservoir bottom didn't investigate as a parameter study. Because important role of reservoir interaction in analysis of dam-reservoir-intake tower system, in this paper reservoir bottom sediments are modeled for three absorption conditions and for three distance between dam and tower. In the following some important articles and their results about dynamic analyses of intake towers will express.

During 1974 to 1975 Liaw and Chopra [1,2] started extensive researchs on reservoir-intake tower interaction problems and studied surrounding water interaction by hydrodynamic added mass method on dynamic behavior of cantilever intake tower. They obtained dynamic responses of reservoir and tower by ignoring surface waves and compressibility of water in the hydrodynamic solutions. In 1989 Goyal and Chopra [3-5] by adding foundation to previous model, analyzed foundation-water-intake tower system under harmonic loading using hydrodynamic added mass method. They presented total system as four substructures: tower, surrounding water, contained water, and the foundation supported on flexible soil and defined frequency domain equations for these four substructures and foundation-water-intake tower system by analytical method. Daniell and Taylor [6] in 1993 conducted dynamic tests on a 50 meter high intake tower at Wimbleball dam in England and compared results of these tests with predictions from a corresponding numerical model. Their aim was to affirm the assumption that the compressibility of reservoir water is not important parameter in seismic analysis of intake towers. In the year 2009 for first time Millán and co-workers[7] added dam to reservoir-intake tower model and investigated dam effects on seismic responses of tower. They understood locating dam in proximity to the tower leads to a new resonance mode near the tower's second resonance frequency due to the dam-reservoir excitations. Alembagheri [8] in 2016 studied numerically dynamics of a coupled concrete gravity dam-foundation-reservoir-intake tower considering two hollow slender towers submerged in reservoir of gravity dam. He represented that presence of the dam significantly influence the seismic responses of the towers under both horizontal and vertical excitations;

however the dam didn't affected by the towers. It was concluded that when the dam was present in the model, the water contained inside the towers had different effects if the foundation was rigid, but it decreased the towers motion if the foundation was flexible.

2. GOVERNING EQUATIONS AND BOUNDARY CONDITIONS OF SYSTEM

In this paper Lagrangian-Lagrangian formulation used for analyzing dam-reservoir-intake tower system with interior water of tower. Equilibrium dynamic motion equation for this system underground acceleration in terms of nodal displacements in finite element meshing is[9,10]:

$$Ma + Cv + Ku = P(s) \quad (1)$$

Where M , C and K are mass, damping and stiffness matrixes and a , v and u are nodal dynamic acceleration, velocity and displacement vectors of finite element meshing respectively and $P(s)$ is nodal external forces vector. The total stiffness matrix of system has been obtained by assembling stiffness matrix of dam, reservoir, tower and interface elements, like this[11]:

$$K = K_D + K_R + K_T + K_{INT} \quad (2)$$

Where K_D , K_R and K_T are stiffness matrix of dam, reservoir, tower respectively. K_{INT} is the stiffness matrix of interface elements which applied between solid and fluid leads to freedom sliding and water from dam and tower dor t separate in connected boundaries. Stiffness matrix of dam and tower depends on D : elasticity matrix, B : shape function matrix, B^T : transposed of B and V_S : volume of integral range for each part of dam and tower[12].

$$K_D = K_T = \int_{V_S} B^T . D . B . dv \quad (3)$$

The total stiffness matrix of reservoir elements is achived by summation of S_f : stiffness matrix of surface waves and K_W : stiffness matrix of reservoir elements. In equation (4) ρ_w is water density, g is gravity acceleration, s is range area of reservoir, V_R is range volume of reservoir elements, N is shape function of fluid nodes and N^T is transposed of N [11]. In ANSYS software which we used in this article, by modeling surface of reservoir S_f creates and it is not need to apply boundary condition in that border.

$$K_R = K_W + S_f = \int_{V_R} B^T . C_f . B . dv + \rho_w . g \int_s N^T . N . ds \quad (4)$$

The total damping matrix of system is achived by summation of C_I : internal viscose damping matrix, C_R : damping matrix caused by wave propagation and C_{abs} : damping matrix of absorbing waves by reservoir bottom sediments[12]:

$$C = C_I + C_R + C_{abs} \quad (5)$$

In equilibrium dynamic equation, internal viscose damping matrix is combination of mass matrix and stiffness matrix of system like this[11]:

$$C_I = \alpha M + \beta K \quad (6)$$

Where α is mass matrix coefficient and β is stiffness matrix coefficient which computed by equations (7,8):

$$\alpha = 2\omega_1 \xi_1 - \omega_1^2 \quad (7)$$

$$\beta = 2(\omega_1 \xi_1 - \omega_2 \xi_2) / (\omega_1^2 - \omega_2^2) \quad (8)$$

in these two equations number of 1 and 2 are related to first and second structural modes, ω is angular frequency of system and ξ is damping ratio which considered 0.05 for dam and intake tower.

Because sediments and masses of rock and soil in reservoir bottom have varied flexibility, they have different absorption capability but rigid sediments in reservoir bottom can absorp all of the waves energy arrive them. In Table 1- bottom absorption coefficients of a_1 and b_1 for different kinds of reservoir bottom sediments define. For providing this condition we used equivalent dampers in three direction for 3D finite element model with this damping matrix [13]:

$$C_{abs} = b_1 . \rho_w . C_W \int_s N^T . N . ds \quad (9)$$

Where C_w is water wave velocity and relates to ρ_w and K_w : bulk modulus of water in this formulation:

$$C_w = (K_w/\rho_w)^{0.5} \tag{10}$$

Table 1- Values of coefficients a_1 and b_1 for different reservoir bottom sediments

Kinds of reservoir bottom sediments	a_1	b_1	Result on waves
Rigid	1	∞	Waves completely come back
Stiff	0.6-0.8	4-9	Waves partially come back
Soft	0.5	3	Waves partially come back
Water	0	1	Waves propagate
Air	-1	0	Waves come back with reverse amplitude

3. NUMERICAL MODELING OF SYSTEM

For determining dam-reservoir-intake tower interaction on dynamic responses of dam and tower, we modeled concrete gravity dam 21 meter high with 0.05 and 0.75 slope in upstream and downstream face of it, tower 20 meter high with length and width of 4 and 5 meters in plan and inside water and surrounding reservoir have 20 meter height. Longitudinal distance between tower and free upstream face of reservoir is 60 meter and lateral distance of them is 20 meter in each side. Dam-reservoir-intake tower system with interior water of tower has been modeled by considering three types of sediments with different absorption and distance between dam and tower are determined 10, 20 and 30 meters so we analyze 9 models. Figure 1. represent geometry of dam-reservoir-intake tower system with interior water of tower.

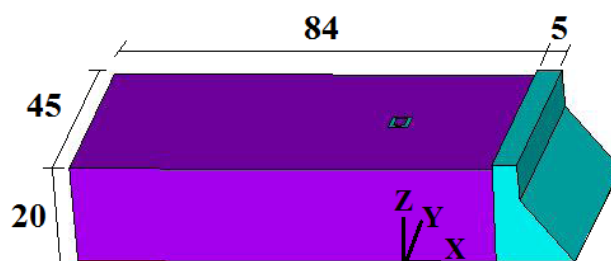


Figure 1. Geometry of dam-reservoir-intake tower system with interior water of tower

Mechanical properties of materials applied in modeling are defined in Table 2- where E is elasticity modulus, ν is poisson coefficient and ρ is density. Volumetric percents of reinforcement bars applied in finite element model are 0.0213 in X axis, 0.0223 in Y axis and 0.573 in Z axis.

Table 2- Mechanical properties of materials applied in finite element model

Materials applied	E , N/m ²	ν	ρ , Kg/m ³
Concrete of dam and tower	2.5×10^{10}	0.17	2400
Water	2×10^9	0	1000
Reinforcement bars	2.1×10^{11}	0.3	7800

ANSYS was used for modeling dam-reservoir-intake tower system and 3D eight nodes elements Solid65 for concrete and Lagrangian 3D eight nodes elements Fluid80 for water were applied in finite element model of system. Solid-fluid interaction faces are coupled in contact direction and in free faces of reservoir linear elements Combination14 with distinct damping and stiffness were used in finite element model and also in reservoir bottom these elements applied with distinct damping and stiffness for each kind of sediments as an equivalent dampers in three directions.

4. RESULTS OF MODAL ANALYSES

For obtaining angular frequencies of system ω , modal analyses performed on finite element models and their values for first and second structural modes are represented in Table 3- also α as mass matrix coefficient and β as stiffness matrix coefficient which computed by equations (7) and (8) are defined in this table. Table 3- represent that by increasing distance between dam and tower, frequencies of this system become greater. Also, in models with rigid sediments, the frequencies are a little more than model with two other kind of sediments, which can be due to greater stiffness.

Table 3- Results of modal analyses for different types of sediments and distance between dam and tower

Types of sediments		Soft			Stiff			Rigid		
Distance between dam and tower , m		10	20	30	10	20	30	10	20	30
ω , rad/s	First mode	36.72	39.26	39.36	37.37	39.14	40.09	37.61	39.86	40.36
	Second mode	47.31	42.97	46.41	47.77	46.84	50.01	47.93	48.30	50.89
α		2.07	2.05	2.13	2.10	2.15	2.23	2.11	2.18	2.25
β		0.00119	0.00122	0.00117	0.00117	0.00116	0.00111	0.00117	0.00113	0.00110

5. RESULTS OF DYNAMIC ANALYSES

Dynamic analyses has been performed under horizontal, lateral and vertical excitations of Northridge and Tabas earthquakes which their properties are showed in Table 4-.

Table 4- Properties of earthquakes used for dynamic analysis

Earthquake	Time occurred	Station	Magnitude	Distance from epicenter , Km	Recorded component	PGA (g)
Northridge	1994/1/17	Arleta CDMG Station 24087	6.9	11.79	Horizontal	0.308
					Lateral	0.344
					Vertical	0.438
Tabas	1978/9/16	Tabas	7.4	74.8	Horizontal	0.852
					Lateral	0.868
					Vertical	0.702

After analyzing system, displacements of dam and tower crest and principal stresses of dam heel and tower bottom have been extracted for each model and their maximum positive and negative values define in Table 5,6- for Northridge and in Table 7,8- for Tabas earthquakes. Where u_x is horizontal displacement, u_y is lateral displacement, u_z is vertical displacement and σ is principal stress.

Table 5- Maximum positive values of dam and tower Dynamic responses under Northridge earthquake for different models

Structure	Distance between dam and tower , m	Types of sediments	u_x , m	u_y , m	u_z , m	σ , N/m ²
Dam	10	Soft	0.00087	0.00025	0.00020	6.6×10^5
		Stiff	0.00089	0.00025	0.00020	6.7×10^5
		Rigid	0.00091	0.00026	0.00021	6.8×10^5
	20	Soft	0.00103	0.00028	0.00029	7.2×10^5
		Stiff	0.00104	0.00028	0.00029	7.3×10^5
		Rigid	0.00106	0.00028	0.00030	7.4×10^5
	30	Soft	0.00108	0.00033	0.00029	7.6×10^5
		Stiff	0.00109	0.00033	0.00029	7.7×10^5
		Rigid	0.00110	0.00034	0.00030	7.8×10^5
Tower	10	Soft	0.00530	0.00356	0.00091	2.24×10^6
		Stiff	0.00537	0.00354	0.00092	2.26×10^6
		Rigid	0.00548	0.00350	0.00093	2.31×10^6
	20	Soft	0.00699	0.00361	0.00086	2.38×10^6
		Stiff	0.00706	0.00359	0.00087	2.41×10^6
		Rigid	0.00713	0.00355	0.00088	2.46×10^6
	30	Soft	0.00704	0.00405	0.00112	2.66×10^6
		Stiff	0.00708	0.00403	0.00112	2.67×10^6
		Rigid	0.00713	0.00401	0.00113	2.69×10^6

Table 6- Maximum negative values of dam and tower Dynamic responses under Northridge earthquake for different models

Structure	Distance between dam and tower , m	Types of sediments	u_x , m	u_y , m	u_z , m	σ , N/m ²
Dam	10	Soft	0.00089	0.00033	0.00019	5.9×10^5
		Stiff	0.00090	0.00033	0.00019	6×10^5
		Rigid	0.00092	0.00034	0.00020	6.1×10^5
	20	Soft	0.00091	0.00035	0.00023	6.2×10^5
		Stiff	0.00092	0.00035	0.00023	6.2×10^5
		Rigid	0.00094	0.00036	0.00023	6.3×10^5
	30	Soft	0.00104	0.00042	0.00026	6.6×10^5
		Stiff	0.00104	0.00042	0.00026	6.6×10^5
		Rigid	0.00105	0.00043	0.00026	6.7×10^5
Tower	10	Soft	0.00558	0.00403	0.00080	3.7×10^5
		Stiff	0.00565	0.00400	0.00081	3.7×10^5
		Rigid	0.00577	0.00396	0.00082	3.8×10^5
	20	Soft	0.00569	0.00492	0.00101	5.1×10^5
		Stiff	0.00575	0.00490	0.00102	5.2×10^5
		Rigid	0.00581	0.00485	0.00103	5.3×10^5
	30	Soft	0.00658	0.00498	0.00106	5×10^5
		Stiff	0.00662	0.00495	0.00107	5×10^5
		Rigid	0.00667	0.00493	0.00107	5.1×10^5

Table 7- Maximum positive values of dam and tower Dynamic responses under Tabas earthquake for different models

Structure	Distance between dam and tower , m	Types of sediments	u_x , m	u_y , m	u_z , m	σ , N/m ²
Dam	10	Soft	0.00168	0.00052	0.00032	2.08×10^6
		Stiff	0.00172	0.00053	0.00033	2.12×10^6
		Rigid	0.00179	0.00055	0.00034	2.17×10^6
	20	Soft	0.00192	0.00055	0.00034	2.21×10^6
		Stiff	0.00198	0.00056	0.00034	2.24×10^6
		Rigid	0.00224	0.00058	0.00035	2.29×10^6
	30	Soft	0.00219	0.00067	0.00041	2.33×10^6
		Stiff	0.00222	0.00067	0.00041	2.34×10^6
		Rigid	0.00234	0.00067	0.00042	2.36×10^6
Tower	10	Soft	0.01116	0.01303	0.00110	3.92×10^6
		Stiff	0.01123	0.01293	0.00110	4.26×10^6
		Rigid	0.01134	0.01279	0.00111	4.45×10^6
	20	Soft	0.01121	0.01524	0.00122	4.01×10^6
		Stiff	0.01147	0.01510	0.00121	4.28×10^6
		Rigid	0.01168	0.01480	0.00122	4.51×10^6
	30	Soft	0.01317	0.01506	0.00162	4.32×10^6
		Stiff	0.01323	0.01505	0.00163	4.42×10^6
		Rigid	0.01337	0.01502	0.00164	4.80×10^6

Table 8- Maximum negative values of dam and tower Dynamic responses under Tabas earthquake for different models

Structure	Distance between dam and tower , m	Types of sediments	u_x , m	u_y , m	u_z , m	σ , N/m ²
Dam	10	Soft	0.00189	0.00061	0.00029	2.7×10^5
		Stiff	0.00193	0.00062	0.00029	2.8×10^5
		Rigid	0.00201	0.00065	0.00030	2.9×10^5
	20	Soft	0.00217	0.00066	0.00037	2.9×10^5
		Stiff	0.00224	0.00068	0.00037	2.9×10^5
		Rigid	0.00231	0.00070	0.00038	3×10^5
	30	Soft	0.00226	0.00073	0.00040	3×10^5
		Stiff	0.00229	0.00073	0.00040	3×10^5
		Rigid	0.00231	0.00074	0.00041	3.1×10^5
Tower	10	Soft	0.00965	0.01303	0.00096	6.5×10^5
		Stiff	0.00971	0.01293	0.00097	7.1×10^5
		Rigid	0.00977	0.01281	0.00098	7.4×10^5
	20	Soft	0.01096	0.01339	0.00124	7×10^5
		Stiff	0.01117	0.01326	0.00128	7.5×10^5
		Rigid	0.01142	0.01301	0.00134	7.9×10^5
	30	Soft	0.01303	0.01793	0.00136	7×10^5
		Stiff	0.01309	0.01791	0.00137	7.1×10^5
		Rigid	0.01322	0.01788	0.00138	7.7×10^5

As it is seen from the above tables, due to the hardness and thickness of dam and the enclosure of the tower with the reservoir, the dam responses are far less than the tower's response. Dynamic responses in the above tables show that increasing the distance between dam and tower can disorder the ascending procedure of maximum dynamic responses of dam and tower in the more difficult reservoir sediments. This means that increasing this distance can reduce the effects of sediments on the dam and tower responses. On the other hand, the maximum responses of dam and tower increase by increasing distance between them. This ascending procedure by changing the dam and tower distance from 10 meters to 20 meters is more tangible than the change from 20 meters to 30 meters. Also, changes of the tower responses are more obvious than the dam responses for increasing the dam and tower distance. It is concluded from above tables that stresses increase in dam and tower in reservoirs with more stiff sediments. Displacements of dam crest and principal stresses of dam heel increase in rigid sediments because reflective waves are more and they influence dam in one face but sediment type has fewer effects on tower responses specially on displacements it can be because tower is embedded in reservoir.

For distinguishing difference between effects of sediments types in time history responses, horizontal displacement of tower crest under Tabas earthquake compare for rigid and soft sediments in the model that distance between dam and tower is 20 meter, see Figures 2. It is included that the aggregation of sediments in reservoir bottom may amplify dam and tower responses.

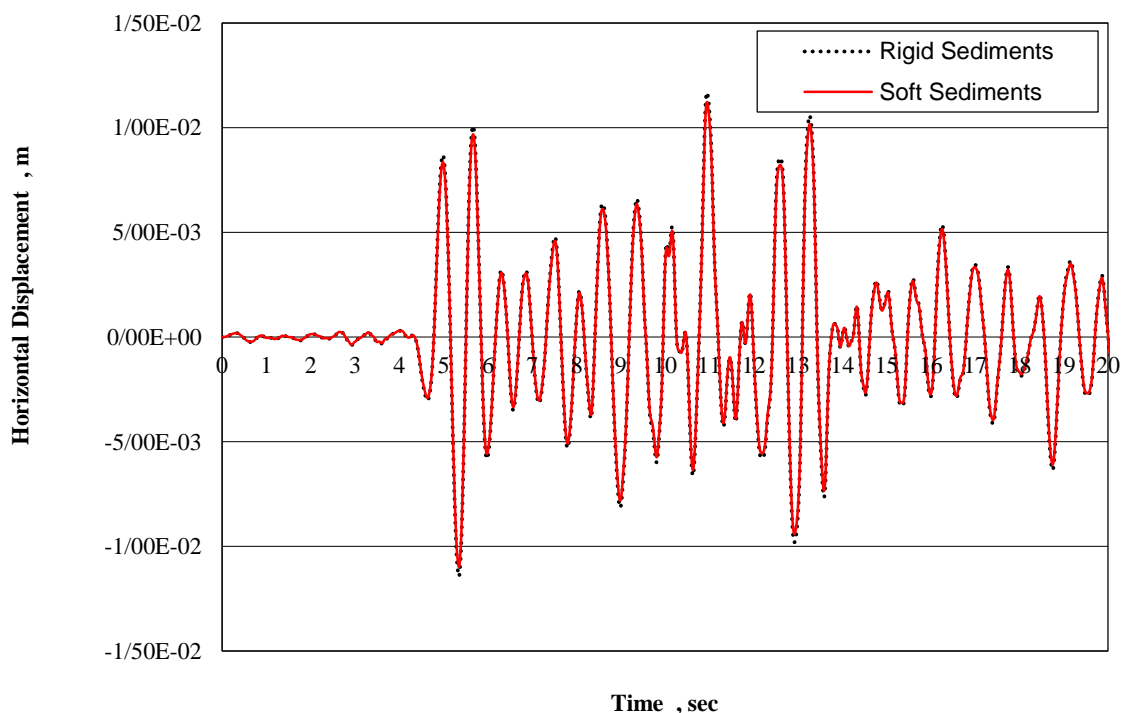


Figure 2. Horizontal displacement of tower crest under Tabas earthquake

6. CONCLUSIONS

Dam-reservoir-intake tower system with interior water of tower are analyzed using finite element method considering sediments absorption and distance between dam and tower as a parameter study. Displacements of dam and tower crest and principal stresses of dam heel and tower bottom have been extracted and results define in the following:

1. Increasing distance between dam and tower, can increase frequencies of dam-reservoir-intake tower system with interior water of tower. Also, in models with rigid sediments, the frequencies are a little more than model with two other kind of sediments, which can be due to greater stiffness.
2. Results show that the dam responses are far less than the tower's response, it can because hardness and thickness of dam and the enclosure of the tower with the reservoir.
3. Dynamic responses show that increasing the distance between dam and tower can disorder the ascending procedure of maximum dynamic responses of dam and tower in the more difficult reservoir sediments. This means that increasing this distance can reduce the effects of sediments on the dam and tower responses.
4. It is concluded that the maximum displacements of dam crest and principal stresses of dam heel increase by increasing distance between them. This ascending procedure by changing the dam and tower distance from 10 meters to 20 meters is more obvious than the change from 20 meters to 30 meters.
5. In time domain responses, displacements of dam crest and principal stresses of dam heel increase in rigid sediments because reflective waves are more and they influence dam in one face but sediment type has fewer effects on tower responses specially on it's displacements it can be because tower is embedded in reservoir.

7. REFERENCES

1. Liaw, C.Y. and Chopra, A.K. (1974),“*Dynamics of Towers Surrounded by Water*,”*Earthquake Engineering and Structural Dynamics*, 3 (1), pp. 33–49.
2. Liaw, C.Y. and Chopra, A.K. (1975),“*Earthquake Analysis of Axisymmetric Towers Partially Submerged in Water*,”*Earthquake Engineering and Structural Dynamics*, 3 (3), pp. 233–248.
3. Goyal, A. and Chopra, A.K. (1989),“*Earthquake Analysis of Intake-Outlet Towers Including Tower–Water–Foundation–Soil Interaction*,”*Earthquake Engineering and Structural Dynamics*, 18 (3), pp. 325–344.
4. Goyal, A. and Chopra, A.K. (1989),“*Simplified Evaluation of Added Hydrodynamic Mass for Intake Towers*,”*Journal of Structural Engineering*, 115 (7), pp. 1393–1412.
5. Goyal, A. and Chopra, A.K. (1991),“*Simplified Earthquake Analysis of Intake–Outlet Towers*,”*Journal of Structural Engineering*, 117 (3), pp. 767–788.
6. Daniell, W.E. and Taylor, C.A. (1994),“*Simplified Full–Scale Dynamic Testing and Analysis of a Reservoir Intake Tower*,”*Earthquake Engineering and Structural Dynamics*, 23 (11), pp. 1219–1237.
7. Millán, M.A., Young, Y.L. and Prévost, J.H. (2009),“*Seismic Response of Intake Towers Including Dam–Tower Interaction*,”*Earthquake Engineering and Structural Dynamics*, 38 (3), pp. 307–329.
8. Alembagheri, M. (2016),“*Dynamics of Submerged Intake Towers Including Interaction with Dam and Foundation*,”*Soil Dynamics and Earthquake Engineering*, 84, pp. 108–119.
9. El-Aidi, B., Hall, J.F. (1989),“*Non–Linear Earthquake Response of Concrete Gravity Dam Part 1: Modelling*,”*Earthquake Engineering and Structural Dynamics*, 18 (6), pp. 837–852.
10. El-Aidi, B., Hall, J.F. (1989),“*Non–Linear Earthquake Response of Concrete Gravity Dam Part 1: Behaviour*,”*Earthquake Engineering and Structural Dynamics*, 18 (6), pp. 853–865.
11. Kalani Sarokolayi, L., Navayi Neyaa, B., Vaseghi Amiri, J., and Tavakoli, H.R. (2014),“*Effect of Rotational Components of Earthquakes on Dynamic Response of Concrete Gravity Dams Considering Reservoir Interaction*,”*Sharif Journal of Civil Engineering*, 30 (2), pp. 81–93‘(in Persian)’.
12. Kalani Sarokolayi, L., (2013),“*Nonlinear Dynamic Analysis of Concrete Gravity Dams under Spatially Varing Translational and Rotational Earthquakes*,”*A Thesis for the Degree of Doctor of Philosophy*, Babol Noshirvani University of Technology, Faculty of Civil Engineering‘(in Persian)’.
13. Ali Jamshidi, D., Navayi Neyaa, B. and Vaseghi Amiri, J. (2007),“*Dynamic Analysis of Concrete Gravity Dams with Modeling Reservoir by Lagrangian and Eulerian Methods*,”*Modares Civil Engineering Journal*, 41 (6), pp. 709–724‘(in Persian)’.

Design and performance of drainage systems for long term stability

W. Riemer¹, F. B. Samani²

1- Consultant, Trier, Germany

2- Tamavan Consulting Engineering, Tehran, Iran

Email: samanifer@gmail.com

Abstract

Drainage systems serve many tasks related to the performance of dams, auxiliary structures and reservoirs. But for developing an appropriate design, which efficiently handles the prevailing tasks, comprehensive information on hydrogeological parameters, hydrogeological regime and geological setting must be elaborated. The contribution points out pitfalls experienced in this context, their potential consequences and mentions practical precautions. Several case histories illustrate the performance of drainage systems, successfully coping with complex conditions. But drainage systems are not only demanding in design, they also need sustained monitoring and maintenance to assure the safety of the projects on the long term.

Keywords: Drainage, Foundation and Slope Stability, Design and Maintenance.

1. INTRODUCTION

The earliest design of gravity dams did not consider the effect of uplift pressures on their stability. However, some masonry dams constructed at the beginning of the 20th century incorporated drains arranged behind the upstream facing (e. g. Lister dam, Germany, 1907), similar to arrangements actually found in RCC structures. Eventually, Casagrande (1961) stressed the importance of drainage for the stability of concrete dams and its function in conjunction with the geology of the foundation rock. De Mello (1977, 1984) elaborated on the subject of drainage, included embankment dams in his discussion and pointed out the relation between grout curtain and foundation drainage. With these publications, the drainage has developed into a standard component for all types of dams. It has proven to offer an efficient, economic and versatile tool for a wide range of purposes as there are mainly:

- control of uplift in the foundation of dams for stability against sliding and toppling
- control of internal pore pressures in dams
- stability of the abutments of dams, especially for concrete dams
- safe handling of seepage water inside embankment dams
- assistance to consolidation of foundations of dams as well as of the body of an embankment dam itself
- control of uplift downstream of dams
- stability of appurtenant structures (spillway, power plant, etc.) downstream of dams
- control of seepage gradients in foundations and managing the hazards of internal erosion and piping
- preventing deterioration of foundations by hydrochemical effects in relation with seepage
- stabilizing reservoir slopes and slopes downstream of dams
- preventing waterlogging downstream of dams.

Although much experience has accumulated in the application of drainage for the various purposes listed above, the authors see the need to emphasize the importance of geological and hydrogeological investigation and analysis to provide the basis for designing an effective and reliable system. Many geological features, geotechnical and hydrogeological parameters are to be determined and a geotechnical-hydrogeological model must be established. The following paragraphs, mainly from a geological point of view, discuss the methods for obtaining the basic input, the identification of design requirements and the adjustment of designs to cope with specific site conditions. Finally, considerations in respect of operation and maintenance of drainage systems are addressed.

2. BASIC PARAMETERS

2.1. GENERAL REQUIREMENTS

The permeability of soil or rock mass of foundation and abutments as well as of embankment materials constitutes the most important parameter. Common practice in the investigation of dam sites estimates the permeability from point tests: Lugeon or permeameter tests. These tests have limitations in accuracy, suffer from random errors and may be misleading if statistics of the mean are applied to cases where extreme values are decisive. The tests do not provide reliable information on the anisotropy of permeability (as for instance frequently applies to varved soils). These conditions call for judgement in the selection of design parameters, and for cross checking.

Permeability determined in the course of project studies will not necessarily apply to the performance of the dam and its foundation because:

- mechanical stresses exerted by the structures can raise or decrease the permeability
- hydrojacking caused with the rising reservoir level can increase the permeability
- internal erosion can raise the permeability of foundation soils, colmatation by sediments can create seepage barriers
- leaching of grout, of concrete and of soluble minerals from the foundation may raise the permeability.

Other aspects to be studied in relation with the design of a drainage system are:

- the grainsize distribution of the foundation soils (for hydraulic efficiency of the drains, for finding admissible gradients, for design of filters)
- hydrochemical parameters (related to incrustation or corrosion).

Casagrande (1961) encourages application of flow nets in the design of drainage system and de Mello points out that the foundation may have to be homogenized by grouting in order to meet the conditions, which allow tracing of a flow net.

2.2. CASE HISTORIES

Low permeability of foundation will obstruct drainage and, accordingly, be more demanding for the design of the system, even if little seepage water is captured. In this regard, the Tavera spillway (Dominican Republic) suffered from an erroneous concept. A massive conglomerate with a tight argillaceous matrix forms the foundation. During construction, the originally designed drainage system was eliminated because little seepage was expected. Upon reservoir filling, on occasion of the inauguration ceremony, the uplift destroyed the chute.

For the Karkheh project (Iran), the assessment of the rock mass permeability posed a difficult task. Very early in the project study, the geological investigations identified a potential problem with uplift in the alternating horizons of conglomerate and mudstone. Lugeon tests indicated a moderate permeability for the conglomerate but pumping tests arrived at $k \approx 10^{-3} \text{ m/s}$, which is far out of scale of the Lugeon values. Experts consulted by the engineer questioned the representativity of the high values. In view of the uncertainty, the engineer adopted an observational approach, providing load berms and relief wells to cope with moderate permeability and allowing the option of substantially strengthening the defenses against high uplift pressures. Observations during reservoir filling eventually confirmed the high permeability for the conglomerate and required remedial action.

At the Colbún project (Chile), a heterogeneous sequence of soils formed part of the reservoir rim. The low groundwater level in the reservoir rim left a substantial part of the sequence in dry, a condition which further complicated the determination of the permeability. The design anticipated a permeability of 10^{-4} m/s and a seepage of $0.3 \text{ m}^3/\text{s}$ (Noguera et al, 1988). With rising reservoir, the seepage increased drastically and emergency measures had to be taken to prevent hydraulic failure of the reservoir rim. At full reservoir, with the strengthened drainage system, underseepage approaches $10 \text{ m}^3/\text{s}$, about 30 times of the initially expected value. In another case, permeameter tests in the soil deposits forming the foundation for part of the Middle Marsyangdi dam (Nepal) suggested the existence of highly permeable layers and raised the call for the construction of a diaphragm. But the high permeability was incompatible with conditions established by geological field surveys, the diaphragm was rejected and observations during reservoir filling and operation justified the decision (Rissler et al., 2015). Finely stratified sediments can be notably anisotropic in permeability, a condition which common permeability tests cannot quantify accurately and reliably. But the anisotropy significantly affects uplift and seepage gradients in such type of foundation and, accordingly, has to be considered in the design of the foundation and its drainage system. The study of the Naga Hammadi barrage on the Nile in Egypt encountered typical problems in the determination of hydrogeological parameters: permeameter tests indicated $k = 5 \times 10^{-5} \text{ m/s}$, estimates based on grain size distribution rendered an average of $6 \times 10^{-4} \text{ m/s}$ and interference pumping tests found $k = 10^{-3} \text{ m/s}$ for the sand

and a ratio horizontal/vertical permeability ≥ 10 (Guth et al., 1988). Figure 1 demonstrates the important effect of the anisotropy on the flow net. Mitigating the risk of hydraulic failure downstream of the barrage, the design provided a diaphragm on the upstream side and a downstream apron with sheetpiles on the downstream side.

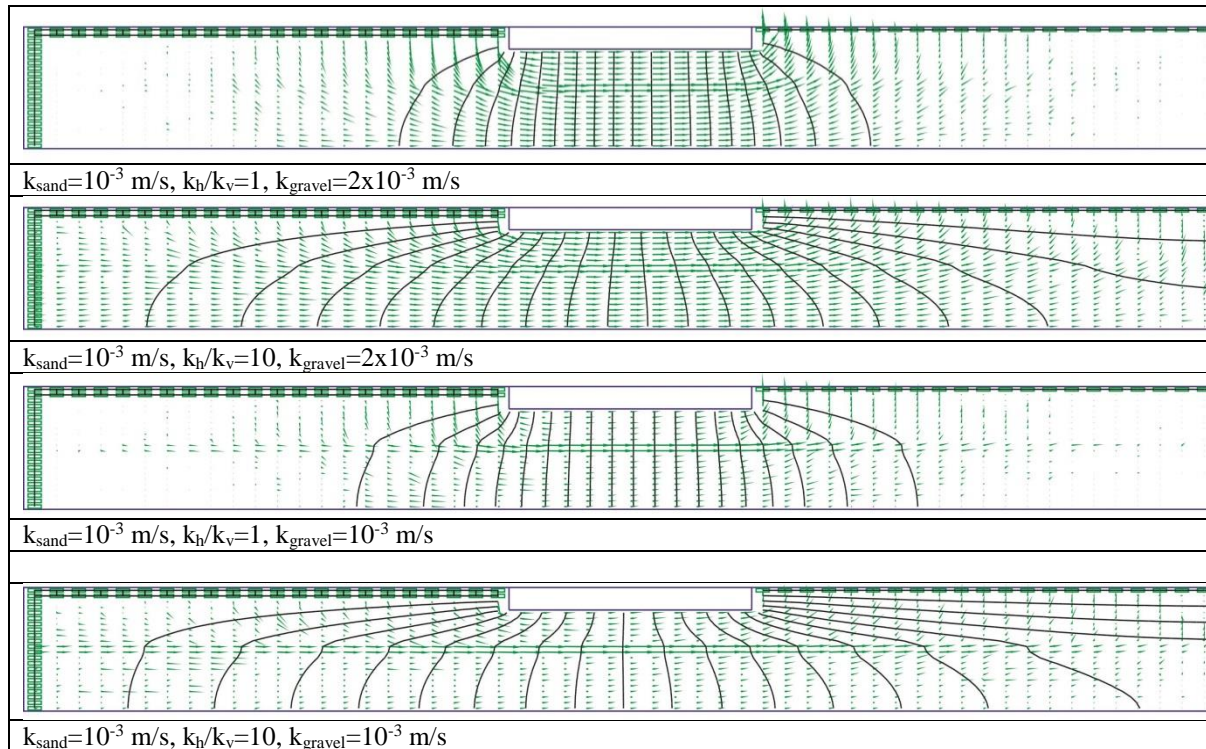


Figure 1: Hydrogeological FE model, probing the effect of input parameters on uplift and seepage gradients. Foundation slab in the center, equipotential contours spaced 0.4m. A gravel layer is intercalated in the sand.

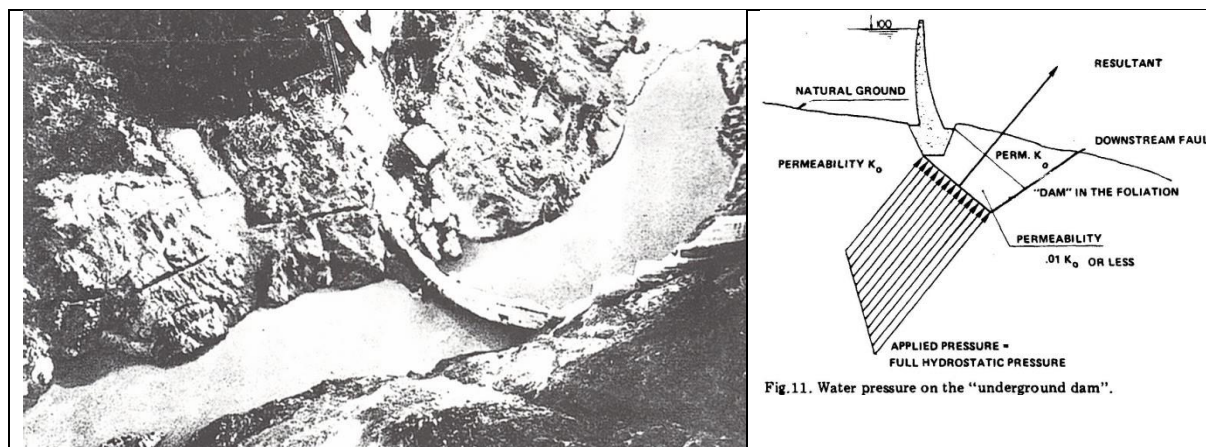


Figure 2: Failure of Malpasset arch dam foundation, attributed to uplift pressure (Londe, 1987)

A prism of rock broke out of the foundation on the left abutment of Malpasset dam, causing the disastrous failure of the dam. Londe (1987) attributes the failure to changes in the permeability of the rock mass, caused by the stresses imposed by the dam – tension opening a discontinuity at the upstream heel of the dam with subsequent jacking by the infiltrating reservoir water and compression in the direction of the thrust of the dam, reducing rock permeability to form an “underground dam” preventing pore pressure relief (Figure 2, right).

3. DRAINAGE IN THE BODY OF DAMS

3.1. EMBANKMENT DAMS

Drainage layers constitute a standard element in homogeneous and zoned embankments. But there are also cases with less common design features. For instance, impervious upstream facing allows adopting steep slopes, under condition that the body of the dam drains freely. Drains will have to be provided, if this condition is not granted. For instance, the compaction test of basalt for the Mohale dam produced fines potentially obstructing drainage. Therefore, a drainage layer with dolerite was placed in the valley floor, which proved useful when the concrete face cracked, drastically increasing the seepage. Foreclosing even more serious cracking at the Paute Mazar dam (Ecuador), 175 m high in a narrow valley, required intensive compaction of the rockfill, which left a layer of low permeability fines on the top of each lift. A central chimney drain was added to the design and proved useful when seepage developed. A similar drain in the Porce III CFRD (Columbia) permitted steep slopes constructed with problematic schist. If gravel with a notable proportion of fines supplies the fill for a concrete face dam, the incorporation of a drainage system acquires particular importance. The internal drainage performed satisfactorily on the Caracoles dam (Argentina) and was also incorporated into the body of the Misicuni dam (Bolivia). The Bigge dam (Germany) displays a special design. With the experience of the catastrophic damage during World War 2 of the Möhne masonry dam, an embankment with an internal reinforcement of the crest and with an inner buffer zone was adopted. The buffer zone serves to contain excessive seepage in the event that the upstream facing would be damaged. However, drains in the valley floor will relieve internal pressure against the facing when the lake is drained.

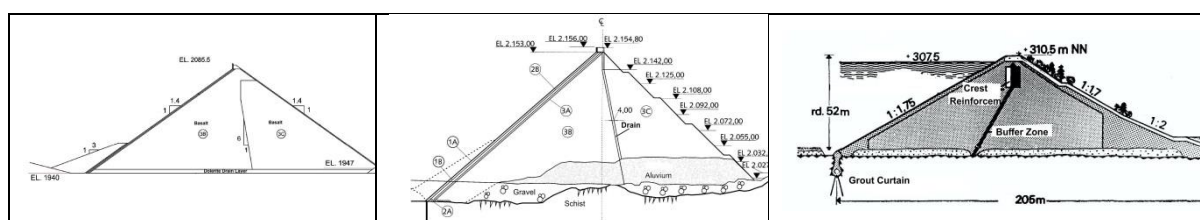


Figure 3: Drains in dams with upstream facing, Mohale (ICOLD, 2009), Paute Mazar (Cruz et al., 2009), Bigge (Heitfeld, 1973)

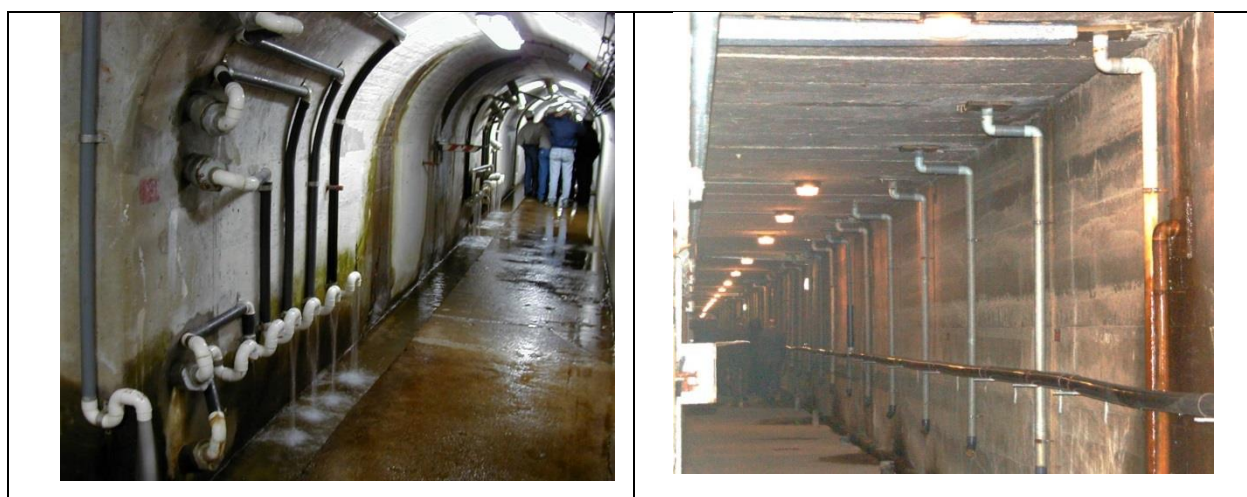


Figure 4 Left: drains relieving pressure in cracks of the Piedra del Aguila gravity dam (Hidroeléctrica Piedra del Águila, Argentina). Note goose necks on drains. Right: vertical drains in Platanovrissi RCC intercepting lift joints

3.2. CONCRETE DAMS

It is common practice to provide drains in concrete dams to collect seepage from block joints and in RCC also from lift joints (Figure 4). But there is an apparently paradoxical application of drains to reduce seepage from cracks in the concrete. Thermal shrinkage is a frequent cause of such cracks. When the reservoir rises, the

hydraulic pressure jacks the cracks open and seepage increases with the third power of the crack width. If this happens, drains drilled into the crack will relieve the jacking pressure and reduce the seepage (Figure 4).

4. DRAINS FOR FOUNDATIONS, ABUTMENTS AND APPURTENANT STRUCTURES

The hydrogeological parameters are to be introduced into a model which also reflects the engineering geology and geotechnical conditions. Several publications (Terzaghi, 1929, Casagrande 1961, de Mello 1977, 1984) emphasize the importance of geological conditions, specifically also of geological details for the appropriate design and satisfactory performance of drainage systems (samples see Fig. 5).

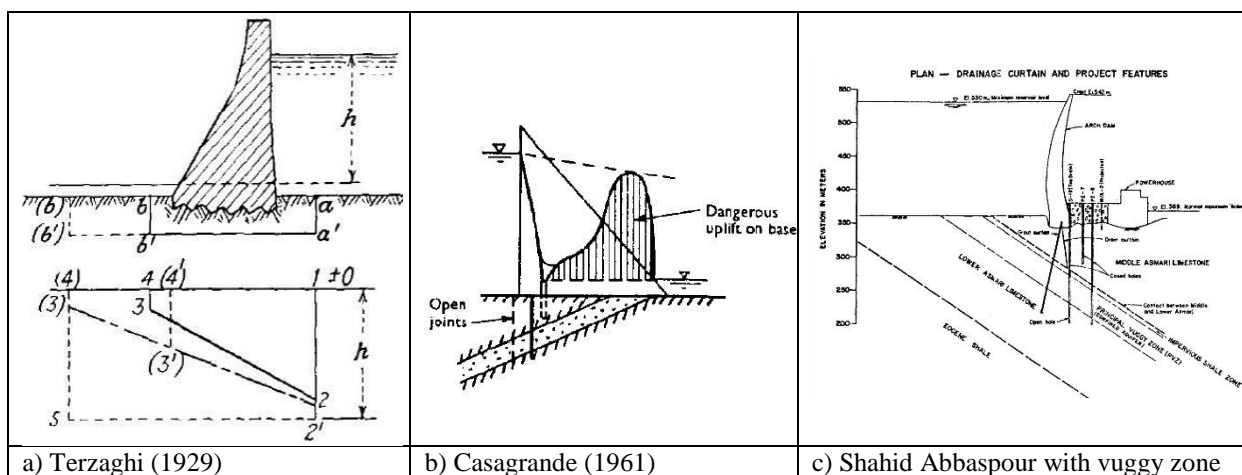


Figure 5: Geological conditions in the foundation of concrete dams and their effect on uplift and the arrangement of drainage systems

4.1. CASE HISTORIES – HYDROGEOLOGICAL/GEOTECHNICAL MODEL

The design of the drainage system requires hydrogeological parameters, geotechnical characteristics and a hydrogeological model. Developing the model may need exploratory works covering an area substantially extending beyond the foundation area of the dam. For the Karkheh dam, early stages of geological explorations had correctly defined the hydrogeological model, indicating the risk of uplift. But with the uncertainty regarding the permeability, the final requirements for drainage and buttress fills were quantified concurrent with reservoir impounding. At the Colbún dam, in addition to the uncertainty in respect of the permeability, an unforeseen geological feature aggravated the problem. A lateral moraine, buried by fluvial and volcanoclastic soils, formed a hydrogeological barrier downstream of the dam, creating dangerous upward gradients (see Figure 6). An emergency action, constructing counterweight berms, 8 km of drainage ditches and 150 relief wells prevented the failure of the dam and the reservoir rim (Noguera, 1988).

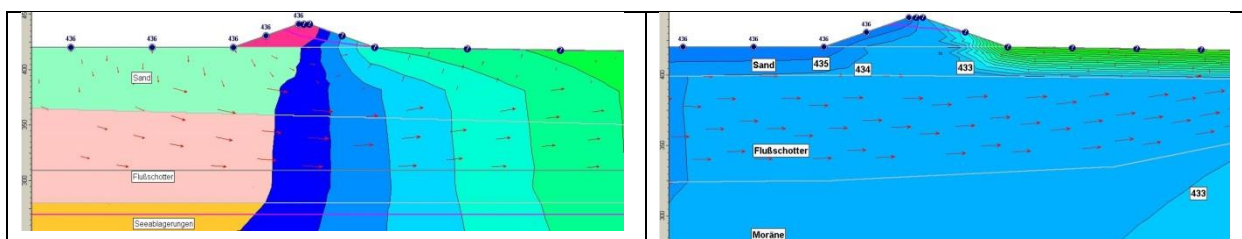


Figure 6: Seepage model for the drainage divide dam of Colbún reservoir, left expected flow pattern, right with flow forced upward by low permeability moraine

On the contrary, for the Middle Marsyangdi project, a hydrogeological model indicated high seepage gradients, implying a risk of erosion and suffusion in the soil foundation of the dam, and the contractor claimed the need for a diaphragm and drainage system. However, the critically high exit gradients were an artefact, due to incorrect placement of a barrier boundary in the FE model shortly downstream of the toe of the dam, which does not exist in reality, as meanwhile confirmed in nearly 10 years of operation.

4.3. CASE HISTORIES – DRAINS FOR FOUNDATION STABILITY

A complex geological structure of the foundation rock frequently also produces intricate hydrogeological conditions, difficult to unravel and requiring extensive treatment. The Thissavros dam, Greece, illustrates such setting (Anastassopoulos et al., 2004). Faults in the metamorphic rock create compartments differing in hydrogeological regime and requiring individual treatment. Although the dam partially rests on a slide mass, the drainage system has secured the stability of the abutments. Budget limitations prevented the downstream extension of the drainage system in the right valley flank and eventually a voluminous rockslide occurred there (communication O. Papageorgiou).

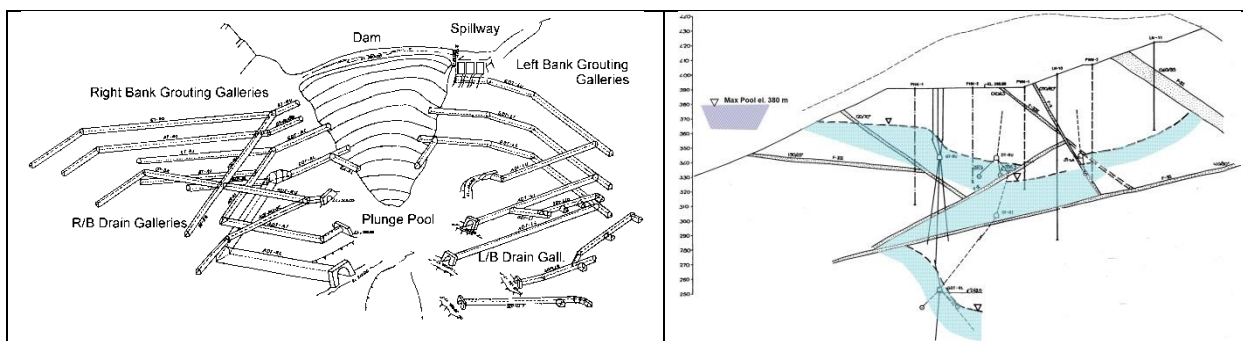


Figure 7: Thissavros dam, arrangement of drainage and grouting galleries and hydrogeological section of right abutment. Hatching represents groundwater.

A karstic foundation of a high arch dam assigns particular importance to the drainage system. In this regard, Shahid Abbaspour dam forms a successful example. The drainage system is more comprehensive on the right side of the valley where the structure of the rock mass is more critical for slope stability. The response diagram demonstrates stable performance over a period of 10 years (Figure 8, right). When the reservoir level exceeds el. 530m the seepage increases abruptly, indicating the need for a complement to the grout curtain.

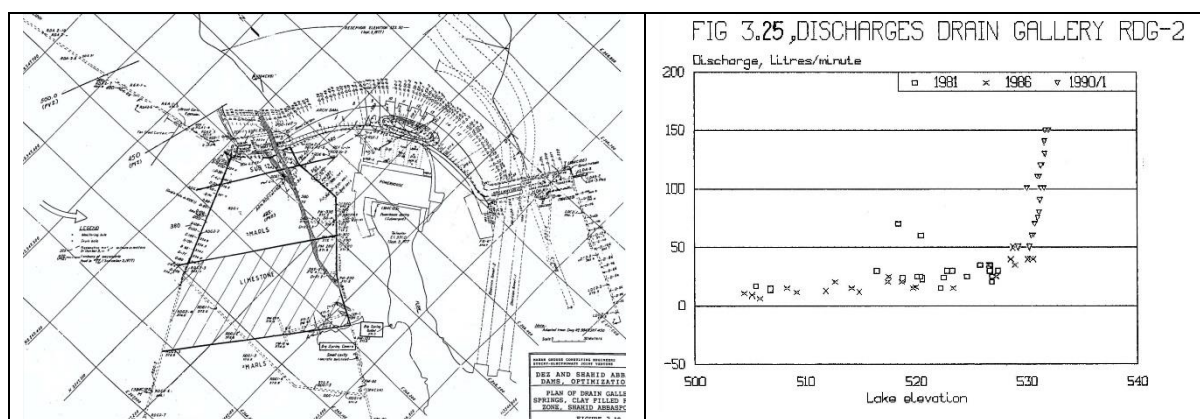


Figure 8: Shahid Abbaspour dam, arrangement of drainage and grouting galleries, sample of discharge response diagram (Mahab Ghodss – Stucky – Electrowatt Optimization Study)

4.4. CASE HISTORIES – DRAINS PREVENTING EROSION AND DETERIORATION OF FOUNDATIONS

If the foundation is capable of developing erosion, piping, suffusion or leaching, the seepage gradients and percolation velocities must be kept at safe limits and the drainage systems must retain soil particles. Already in 1910, Bligh formulated relevant criteria, recently ICOLD (2015) treated the subject comprehensively.

The Casa de Piedra dam, Argentina, rests on a layer of shale, expected to act as blanket obstructing seepage. However, a layer of vuggy limestone below the shale transfers high pressure from the reservoir to the shale blanket. The shale is gypsiferous and smectite forms a proportion of the clay fraction. According to a hydrochemical evaluation, the reservoir seepage would attack the gypsum and substitute the Ca-content in the

shale by Na. The process constitutes a double hazard: increasing permeability by dissolution and activating the dispersivity of the smectite by exchanging Ca for Na. In fact, boils appeared downstream of the dam and seepage water left efflorescence of minerals leached from the shale (Figure 9). To halt the deterioration of the shale layer, a line of relief wells was proposed, dropping the head in the vuggy limestone just enough to keep the piezometric level below the ground surface.

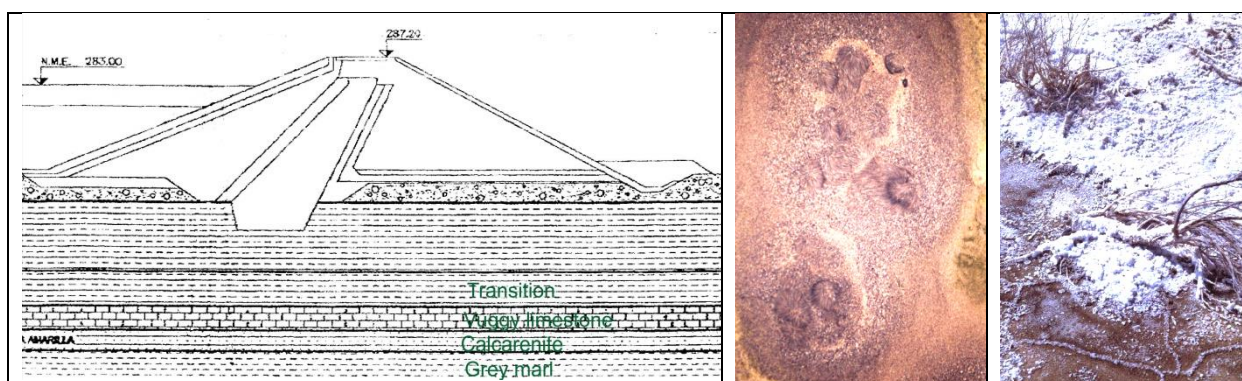


Figure 9: Casa de Piedra Dam, geological section of foundation, boils, efflorescence



Figure 10: Daule Peripa reservoir rim dike, relief wells showing erosion and settlement cracks.

An 18 km long auxiliary dam was constructed on the reservoir rim of the Daule Peripa reservoir. It rests on a complex series of volcanoclastic and fluvial soils. At depressions in the reservoir rim, drainage wells are arranged, intended to relieve potentially hazardous uplift pressures. With a few exceptions, the drainage system has performed satisfactorily for more than 20 years. Very few wells have indications of erosion and/or settlements (Figure 10). In these places remedial measures will have to be taken.

5. DRAINS FOR AUXILIARY STRUCTURES

Uplift related with reservoir seepage can affect the stability of structures downstream of a dam. This conditions may apply to spillways and powerhouses. The destruction of the Tavera spillway by uplift was mentioned above. For Karkheh, the design provided ample drainage systems for the spillway chute and the powerhouse. With reservoir filling, further measures were taken for reduction of uplift pressures at the powerhouse.

In view of the notable karstification at the Ataturk dam site, the design provided a combination of a grouted box with external and internal drains for the powerhouse (Figure 11, Riemer et al., 1991). After reservoir filling, the drainage system was further strengthened, extending a gallery upstream of the plant. It is now in operation for more than 25 years.

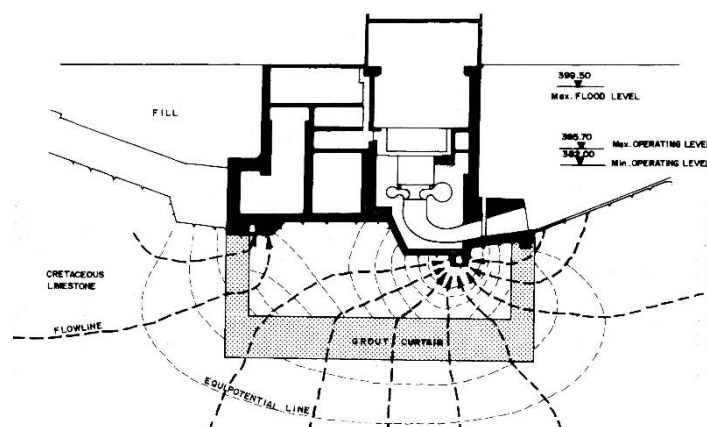


Figure 11: Management of uplift pressure at Ataturk powerhouse. Hatching represents grouted rock.

6. DRAINS FOR RESERVOIR SLOPE STABILITY

ICOLD Bulletin 124 mentions several case histories where drainage offered a reliable and economic solution for problems of reservoir slope stability, including such monumental tasks as Dutchmans Ridge at Mica Dam and the Cromwell Gorge in New Zealand. Along the Cromwell Gorge, 11 large landslides had to be stabilized before impounding of Lake Dunstan could start. The task was accomplished within 2.5 years and at a cost of 250 million US\$, mainly by drainage measures. The economical and technical success was achieved by a well-organized team of 50 dedicated professionals. The team managed to unravel the complex geological and hydrogeological conditions of the landslides (see sample in Figure 12) and found efficient solutions for the stability problems. Impounding started in 1992 and the reservoir slopes have performed fully satisfactorily.

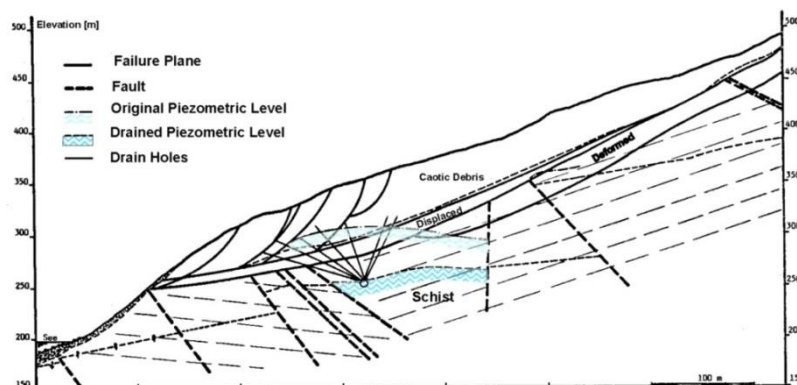


Figure 12: Geological and hydrogeological conditions at Cairnmuir Slide. Mainly the drainage of the sub-basal confined aquifer stabilized the slide. Hatching marks groundwater below main failure plane.

7. OPERATION AND MAINTENANCE OF DRAINAGE SYSTEMS

Frequently applied design criteria for the stability of dams require a safety factor equal to 1 with the drainage system not functioning. However, there are cases where this condition is not viable and which, accordingly, call for circumspect measures to either guarantee the efficiency of the drainage system or, alternatively, manage the risks potentially associated with a failure of the drainage system. Two case histories illustrate this condition:

Lake Dunstan in New Zealand and Piedra del Aguila in Argentina.

Hydrogeological instrumentation of the Lake Dunstan Landslides comprises: 63 discharge gauges, 733 piezometers, 22 multi-position Westbay piezometers.

Data from primary instruments are transmitted in real time, introduced into a data base, automatically checked for consistency, checked against alarm criteria and, if exceeding alarm or alert level thresholds, immediately communicated to the operating staff. Assisted by various modules connected to the data base – e. g. location maps, diagrams – operating staff takes remedial measures or initiates pre-defined emergency action.

Routine checks verify the efficiency of the drain holes to determine the need for flushing or replacement. An independent panel periodically reviews the conditions of the monitoring system and the performance of the landslides.

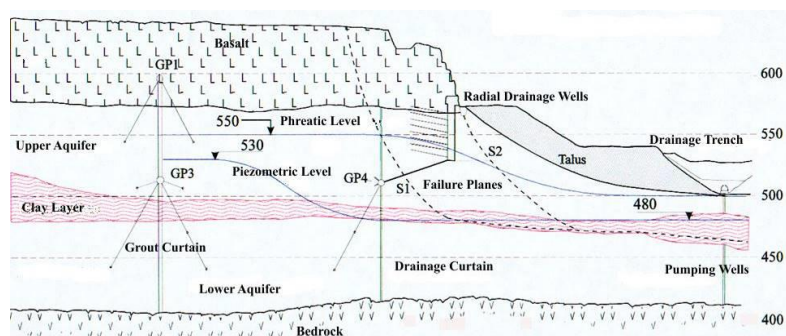


Figure 13: Drainage system in buried valley under left abutment of Piedra del Águila Dam

On the left abutment of Piedra del Águila Dam, Argentina, the stabilization measures include drainage by gravity as well as by pumped tube wells (Figure 13). The area is controlled by video, instrumentation data are automatically transmitted to the operation center of the powerplant (with two independent lines), the well field has a multiple of the normally required capacity, there are two lines of power supply and additional emergency power supply. ORSEP, the Argentinian authority in charge of dam safety, has developed plans for emergency action and imposes periodic safety inspection by independent engineers.

Also drainage systems less complex than the above mentioned two cases should be monitored and checked for need of maintenance. Common problems are incrustation of drain holes, typically by calcium carbonate or by oxides of iron and manganese, due to loss of dissolved gases, to oxidation, sometimes assisted by biological processes. Goose necks on drain pipes (Figure 4) help prevent incrustation. Alternatively, corrosion may attack the installations. H_2S , which forms with eutrophication, acts particularly aggressive.



Figure 14: Device for collecting sediments from drainage water (design A. Pujol), severe corrosion of piezometer panel by aggressive water, incrustation with carbonate and manganese precipitate.

8. CONCLUSIONS

Properly designed drainage systems efficiently cope with many tasks related to the stability of dams, their foundations, associated structures and reservoir slopes. Drainage also serves for preventing damage to foundations by erosion or leaching. However, developing the appropriate design, requires information on hydrogeological and geological conditions, which in turn calls for specific geological and hydrogeological explorations and studies, sometimes covering areas substantially extending beyond the foundation of a dam. Reliance on conventional point permeability tests has led to mistakes.

If the safety of a dam depends on the correct functioning of the drainage system, sustained monitoring and capacity for maintenance have to be provided and plans for emergency action must exist.

Ample experience evidences the satisfactory performance of drainage system even under highly complex geological and hydrogeological conditions and high risk settings. On the other hand, disregard in the design or neglect in operation have caused incidents.

9. ACKNOWLEDGMENT

The authors wish to express their gratitude to the many professionals with whom they had the privilege of working on hydro projects.

10. REFERENCES

1. Anastassopoulos, K., Hoek, E., Milligan, V., Riemer, W. (2004), "*Thissavros hydropower plant. Managing geotechnical problems in the construction*," Proc. 5th Int. Conf. Case Histories in Geotech. Eng., paper 2-63
2. Bligh, W. G. (1910), "*Practical design of irrigation works*", Second edition, Constable, Edinburgh
3. Brown, R., Gillon, M., Riemer, W. (1993), "*Sanierung von Rutschungen am Dunstan Stausee, Clyde Wasserkraftwerk, Neuseeland*", Ber. 9. Nationale Tagung für Ingenieurgeologie, Garmisch Partenkirchen, 1993, Geotechnik, Sonderheft, pp 93-102.
4. Casagrande, A. (1961), "*Control of seepage through foundations and abutments of dams*" 1rst Rankine Lecture, Geotechnique 11,3, p 161-181
5. Casagrande, A. (1965). "*Role of calculated risk in earthwork and foundation engineering*", Jnl ASCE 91, SM4, Part 1, 1-40.
6. Cruz, P. T., Materón, B., Freitas, M., (2009), "*Concrete face rockfill dams*", 448 p
7. Guth, W., Riemer, W. (1998) "*Geotechnical and hydrogeological site characterization for the Naga Hammadi barrage on the river Nile*", International conference IAEG 1998, pp 3275-3286
8. Heitfeld, K. H. (1991), "*Talsperren*" Lehrbuch der Hydrogeologie Band 5, Bornträger, 468 p
9. ICOLD (2000), "*Reservoir landslides, investigation and management*", Bulletin 124
10. ICOLD (2009), "*10th benchmark workshop on numerical analysis of dams*"
11. ICOLD (2015), "*Erosion, Processes and Engineering Assessment*", Bulletin 164 Volume 1,
12. Londe, P. (1987), "*The Malpasset dam failure*", Eng. Geol. 24, pp 295-329
13. de Mello, V.F.B. (1977), "*Reflecting on design decisions of practical significance to embankment dams*" 17th Rankine Lecture, Geotechnique 27, 3, p 279-355
14. de Mello, V.F.B. (1984), "*Concrete gravity dam foundations: an open case of geomechanical interaction, structure-foundation and theory-practice*" 4th Australia-New Zealand Conf. Geomech.
15. Noguera, G., Garcés, E. (1988) "*Colbún reservoir seepage*", Proc. 16th Congr. ICOLD, C18, Vol III, pp 1223-1235
16. Riemer, W., Andrey, J. D. (1991) "*Baugrundbehandlung am Atatürk Damm*", Ber. 8. Nationale Tagung für Ingenieurgeologie, Berlin, 1991, pp 167-174
17. Rissler, P., Riemer, W. (2015): "*Handling a complex foundation below the rockfill dam at the Middle Marsyangdi Hydroelectric Scheme, Nepal*", Proc. 25th Congr. ICOLD, Q.98-R.26
18. Terzaghi, K. 1929. "*Effect of minor geological details on the safety of dams*", American Institute of Mining and Metallurgical Engineers. Technical Publication 215, p. 30.

Impact of mining waste effluents on the shear strength of compacted lateritic soils used in waste containment dikes (DRC)

Gustave Mukoko Kalenda^{1,2}, Gabriel Lile Amisi¹, Yannick Kiyukeno Kitwanyoka¹, Elie Musoya Kyulu¹, Ramiro Daniel Verastegui Flores², Jean-François Thimus², Kelly Guerrier³

1-Department of Civil Engineering, University of Lubumbashi, Lubumbashi, Democratic Republic of Congo

2-Department of Civil Engineering, Louvain School of Engineering, Catholic University of Louvain, Louvain-la-Neuve, Belgium

3-Department of Geological Engineering, State University of Haiti, Port-au-Prince, Haiti

Email: mukoko.kalenda@polyechunilu.ac.cd

Abstract

Hydraulic fracturing is the evoked main cause of dikes failure. Several authors analyzed the soils properties under mechanic and hydraulic solicitation. However, these analyses don't take into account the chemical influence of liquid percolating the matrix of soil. This article analyzes the impact of liquid effluents emanating from ore concentrators on compacted lateritic soils behavior in waste containment dikes. It emphasizes shear strength parameters of compacted laterite and percolated by liquid effluents with different chemical nature. The tests include the shear strength measurements when the specimens were imbibed with different fluids. The results show that acid and basic liquid effluents affect shear strength parameters and the strain modules are modified. The effect of the initial suctions and the density before the imbibition was also investigated, which reveals that structural changes caused by initial saturation and density of specimens seem to be more important for explaining strength behavior than chemical interaction.

Keywords: Waste, Effluent, Shear, Lateritic, Dikes.

1. INTRODUCTION

Chemical effects of percolating fluid on shear strength parameters and strain modulus of compacted lateritic soils, used in waste containment dikes in Katanga (DR Congo), are investigated in this paper. Consolidated drained and undrained shear strength were determined using distilled water, acid and basic effluents from ore concentrators. Strength behavior was investigated by studying triaxial shear tests after imbibition with demineralized water as reference and imbibition in acid or basic liquid effluents, which led to the full saturation of the samples. Initial suction before wetting revealed to have significant impact on the behavior observed. The interaction of the clay soil with ions in the percolating fluid is an aspect related with osmotic suction (Cardoso et al. 2012), difficult to be interpreted in conventional saturated soil testing. This interaction explains the change of shear behavior observed when replacing the distilled water by liquid effluents acid or basic.

2. EQUIPMENTS AND MATERIALS USED IN THIS STUDY

For the physical characterization, we conducted a sieve dry and wet analysis according to CME 01.01 standard. The water content was determined by the oven method according to the standards NF P94-050 and NBN 589-203 respectively for laterites of Kakanda, Kipushi and laterite quarries. The determination of particle density was done in accordance with the pycnometer procedure: N03-09. Atterberg limits were obtained according to standard NF P94-051 and shrinkage limits following the procedure Peltier 108. The maximum dry weight density and the optimum water content was obtained by Standard Proctor test according to NF P 94-093. The materials used are conventional laboratory equipment that require no particular description. The studied soil is laterite used in the construction of road embankments and tailings dams of dikes from mining companies and civil engineering earthworks in Katanga, D. R. Congo. The average density of the solid particles is of $G_s = 2.77$. Samples were taken at Kakanda on the big dam of Kakanda, at Kipushi on the dike of Kipushi and in quarries where road fill materials are extracted from.

The weight proportions on the extracted soil (Fig. 1a) and the fraction less than 2 mm (Fig. 1b) give us about 31 and 19%; 71 and 41% respectively for the clay laterite of Kakanda and Kipushi. Mineralogical composition of the laterites samples is given in table 1.

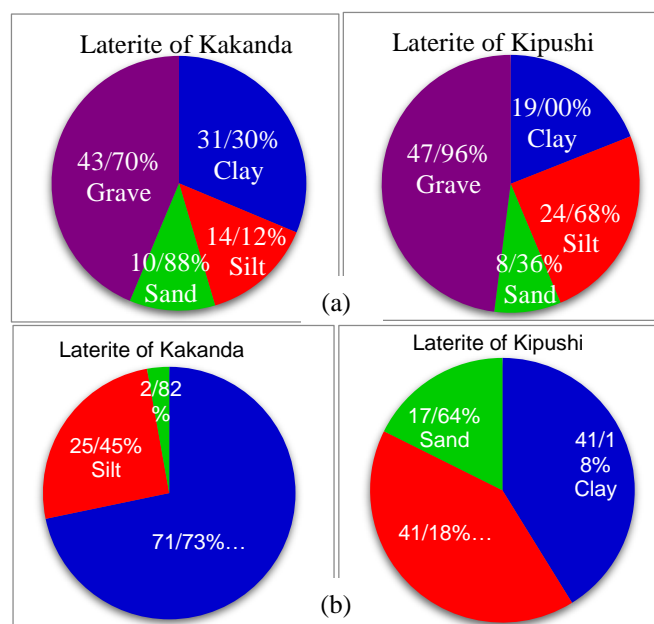


Figure 1. Grain size fractions of laterite on the raw sample (a) and on sieved to 2 mm (b)

Table 1- Mineral composition of the samples of laterite and oxides contained in the soil

Soil	Kda	Kshi	Oxydes	Kda	Kshi
minerals	[%]	[%]		[%]	[%]
Quartz	32,90	45,70	SiO ₂	56,27	66,34
Kaolinite and Halloysite	34,87	19,77	TiO ₂	1,10	1,06
Illite	11,64	16,24	Al ₂ O ₃	16,31	15,62
Muscovite or feldspar	2,23	4,93	Fe ₂ O ₃	15,29	8,78
Hematite	-	8,78	MgO	0,38	0,53
Goethite	17,02	-	MnO	0,02	0,01
Corundum	-	3,02	CaO	0,08	0,06
Anatase	1,10	1,06	K ₂ O	1,15	1,82
Calcite	0,18	0,14	Na ₂ O	0,29	0,59
Pyrolusite	0,02	0,01	LI*	8,83	5,01
Total	99,96	99,65	Total	99,72	99,82

* Loss on Ignition

Liquid effluents used come from retention ponds of the dikes of Kakanda and Kipushi. They have a weakly basic pH being situated between 7.5 and 8.7 for Kakanda and weakly acid for Kipushi with values between 5.9 and 6.5 (Baize & Girard 2008). These liquid effluents were sampled in the various ponds of retention in the range of 3 years over various periods of the year. The values of the pH measures are averages of around thirty measurements made for the pH. The chemical composition of the liquid effluents used in this study is presented in the table 2 that shows the concentration in polluting elements, these elements which pollute the water of the ponds of dikes are not in weak quantity with regard to the legislation in force in DRC (Cabinet du Président de la RDC 2003)

Table 2: Chemical composition of the liquid effluents

Chemical elements [ppm]							
Soil	Al	Ca	K	Mg	Mn	Na	P
Kakanda	3	11,9	68	58	0,313	274	2,4
Kipushi	200	328	22	1058	130	405	1,6
Chemical elements [ppm]							
Soil	S	Iron	Co	Cu	Zn	Ni	
Kakanda	290	65,4	6,87	5,9	0,09	0,03	
Kipushi	2693	70	81	350	35	1	

The dosage of the chemical elements (total chemistry) was made by fusion at the metaborate and tetraborate of Lithium followed by putting in solution and an analysis of elements by spectrometry of atomic emission ICP AES (Inductively Coupled Plasma Absorption Emission Spectral), model ICAP on 2500. The values of the measures presented in the table 1 are averages of about ten measurements made for the chemical composition. These ions contained in the liquid effluents have an influence on the properties of the clayey fraction of the laterite.

A usual classification of pollutants is presented by Delage P. and Schrefler B. (Bouazza et al. 2005), it includes: soluble chemical pollutants; heavy metals; and the hydrocarbon compounds derived of some crude oil. The same source indicates three pollutant categories namely: metal (heavy metal), minerals (Ca, Mg, Na, K, Fe, Si, Sr, Ti, Al, N, Cl, F, P, S and cyanides) and organic (including, among other hydrocarbons, alcohols, phenols, esters, sulfides, pesticides ...).

3. IMPACT OF LIQUID WASTE ON THE SHEAR STRENGTH PARAMETERS OF COMPACTED LATERITIC SOIL

In order to analyze the strength behavior of the soil in a favorable ion exchange environment, the specimens were made with the same initial parameters and saturated with the polluted water of the retention basins or the distilled water. The triaxial apparatus used during our works consists of a triaxial cell of type Bishop and Wesley (Mukoko 2014). The whole is connected to a system of acquisition. The specimen of cylindrical shape is placed in a sealed chamber which is connected to the various systems of pressure application and measurement. The cell is filled with liquid (distilled water or liquid effluents), which allows to apply to the specimen a field of isotropic stress during consolidation and anisotropic during shearing. These triaxial tests have been controlled in constant strain rate (0.2062 [mm/ min]), under confining pressures σ_3 of 100, 150, 200 and 300 kPa.

When a sample is taken, it has an initial moisture and thus an initial suction that can be inferred from the retention curve. Similarly, when samples are reconstituted, we submit them to a certain suction and by shearing them directly, we can have an idea of the effect of the initial suction on soil strength characteristics. But a disadvantage is that the state of the sample is neither on the drying path nor on the moisturizing path of the retention curve.

- Effect of waste effluents of retention basins on the shear parameters.

The influence of the pollution on the response of lateritic soil at the undrained monotonous triaxial loading is described in the following figures (Figs 2-4, 5, 6) under the same initial state ($\gamma_d = 17.31 \text{ kN/m}^3$ et $w = 14.95\%$), the figure 2 presents the failure envelopes of Mohr-Coulomb and the shearing parameters relative to that. It appears that the acid pollution decreases the cohesion, with a light increase of the internal friction. This observation is made on about fifteen tests of which the repeatability seems uniform.

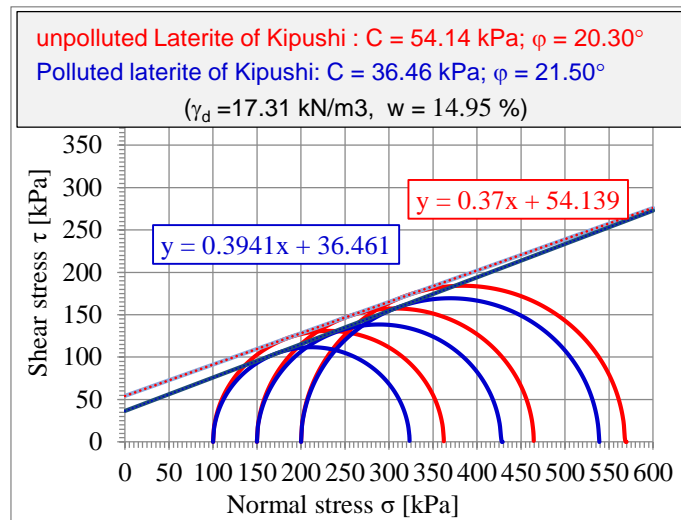
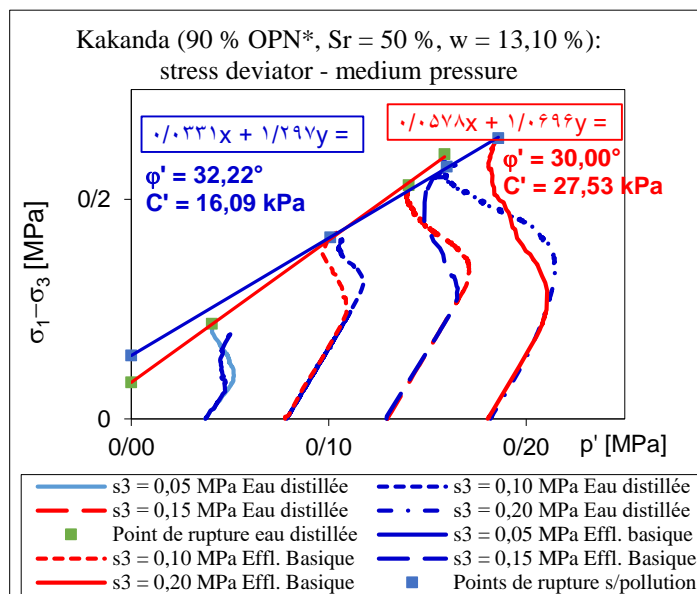


Figure 2. Circle of Mohr and intrinsic right for the soil of Kipushi

On the other hand, there is an increase of more or less 42 % of the effective cohesion and a decrease in the angle of friction as a result of the contamination by the basic liquid effluent for specimens tested at 90 % of the dry density for the soil of Kakanda (figure 3).



OPN* Optimum Proctor Normal

Figure 3. Effective stress path and critical state lines for the soil of Kakanda

This increase of the cohesion could be attributed to the contribution of the exchangeable cations by the basic liquid effluent in the ligands of the lateritic soil after interaction with the effluent.

On figures 5 and 6 we compare the variations of the deviator stress and the pore pressure in function of the axial deformation (in CU) respectively in the case of the soil of Kakanda (Fig. 5a) and of Kipushi (Fig. 5b) uncontaminated and polluted by the liquid effluents of retention basins.

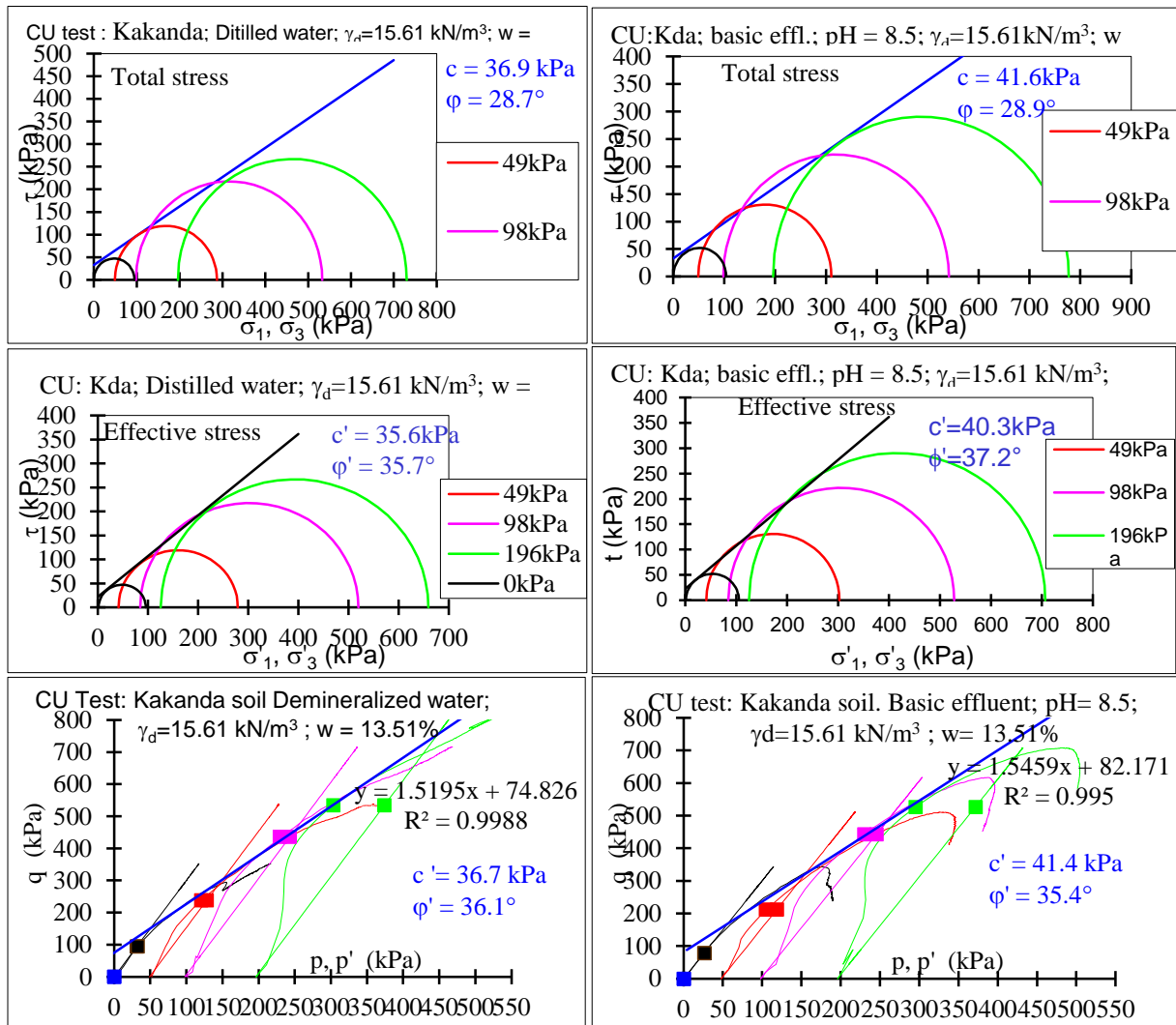


Figure 4. Circle of Mohr, intrinsic right, and critical state line for the soil of Kakanda.

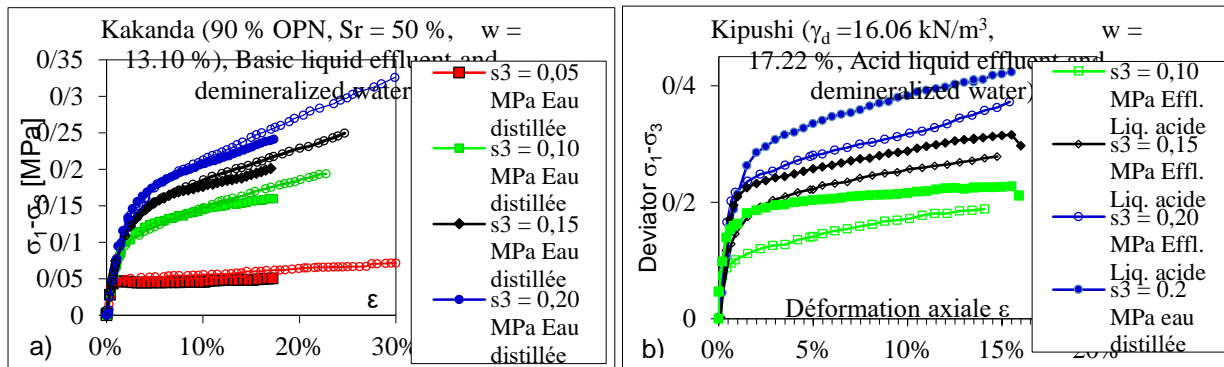


Figure 5. Diagram deviator - axial deformation in CU

We observe no influence of the soil pollution in the elastic domain where curves superpose (Figs 5a, 5b). On the other hand, in the plastic domain, the deviator stress for the soil saturated with the basic liquid effluent is slightly higher than its equivalent saturated with demineralized water, whereas it is widely lower for the soil saturated with acid liquid effluent compared to the soil saturated in distilled water.

As for the excess of pore pressure, the behavior is completely inverse, the strong increase of the pore pressure in the case of the saturated soil with acid liquid effluent (Fig. 7b) goes hand in hand with the hydraulic conductivity brought up under acid pollution (Mukoko et al. 2015). Available results in the literature (Spagnoli et al. 2010), (Spagnoli et al. 2011) attribute this behavior to the decrease of the pH in acid medium.

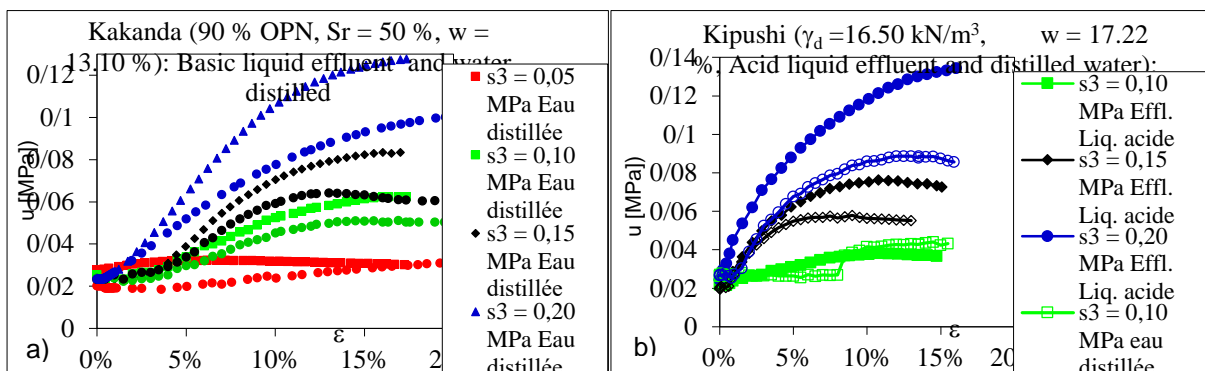


Figure 7. Diagram pore pressure – axial deformation in CU

Figures 7a and 7b present some UU testing results and show the impact of the initial suction of the specimens on the deviator stress at failure. In these figures we compare the results in unconsolidated and undrained compression. The behavior remains the same that is to say a reduction of deviator under acid contamination (Fig. 7a) and a slight increase in basic middle (Fig. 7b).

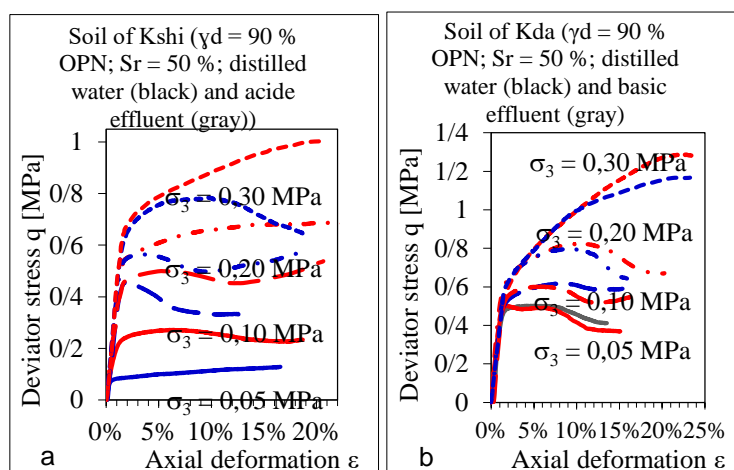


Figure 7. Diagram deviator stress - axial deformation (UU test)

- Effect of waste effluents of retention basins on the deformation modulus.

The experimental laboratory studies on different soils showed that the modulus of deformation depends on numerous factors, in particular on the size grading of soil, the density, the confining stress, the loading history, the specimens preparation method (Hardin & Richart 1963; Boelle 1983; Hicher 1985; Presti 1987) quoted by (Nguyen 2008).

These various factors are known and have been broadly studied. If we take into account the influence of the particle grading and the type of the soil, the void ratio (or compactness) and the confining stress, the deformation modulus can be written as:

- $Module = A(material) \times B(compactness) \times C (pressure)$

where: A (material): is a parameter that translates the influence of the nature of the material,

B (compactness): is a function that takes into account the compactness of the soil,

C (pressure): is a function related to the influence of the confinement.

For soil used in waste containment dikes, the influence of the pollution (by acid or basic liquid effluents) is not negligible, the module of deformation decreases for acid liquid effluent and increases for basic one, at least for the lateritic soil analyzed as showed in figure 8.

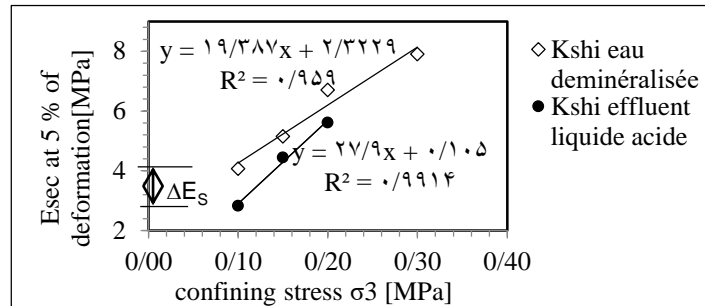


Figure 8. Variation of the secant modulus as a function of lateral stress

In this case, the modulus of deformation can be written:

- $Module = A(material) \times B(compactness) \times C (pressure) \times D (chemistry\ of\ percolating\ fluid)$

With: D (percolating fluid): a parameter that reflects the influence of the pH of the liquid percolating the chemisorbed soil matrix.

Figure 8 shows the variation of deformation modulus as a function of the confining pressure and indicates the fall of the modulus in acid medium.

- Influence of the initial saturation of specimens on the deviator and the secant module of rigidity.

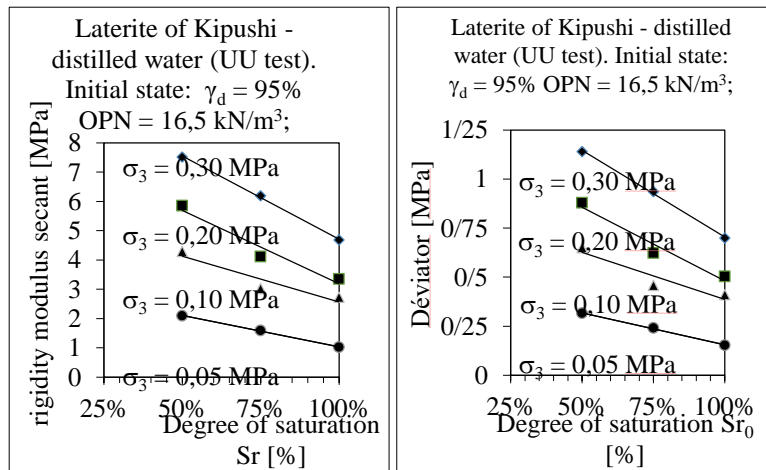


Figure 9. Influence of the initial saturation of the specimens on the deviator and the secant modulus of rigidity

The deviator stress at failure decreases significantly in the partially saturated soil with increasing saturation degree under the same level of compaction. As for the secant modulus at 15% of strain, shown in Figure 9 above, it increases with the confining pressure and decreases with saturation.

4. CONCLUSIONS

It appears that acid pollution decreases the shear strength parameters of laterite by increasing its deformability, while in basic pollution, that is to say by saturating specimens in basic liquid effluent, a tendency to oppose soil deformation is observed.

The deformation modulus not only depends on a parameter which translates the influence of the nature of the material such as its granularity, a parameter that takes into account the compactness of the soil such as its

porosity and a parameter which translates the influence of the confinement, but also a parameter which reflects the influence of the pH of liquid percolating the chemisorbed soil matrix.

5. REFERENCES

1. Baize, D. & Girard, M.C. 2008. *Référentiel Pédologique*, Collection savoir-faire, Afes, (ed.), Quae ISBN : 978-2-7592-0186-0.
2. Bouazza, A. Delage, P. & Wojnarowicz. M. 2005. Nature et reconnaissance de la pollution des sols. Dans *Géomécanique environnementale sols pollués et déchets*. Sous la direction de Delage. P. & Schrefler, B. (ed.), Hermès-Science Publication, Lavoisier. Chap. 1, p 17- 45. Paris.
3. Cabinet du Président de la RDC. 2003. Décret n°038/2003 du 26 mars 2003 portant règlement minier. Journal officiel de la RDC. Nu-méro Spécial, 44ème Année.
4. Cardoso, R. Barbedo, D. & Ribeiro, D. 2012. Hydro-Mechanical Behavior of Compacted Kaolin Considering Percolating Fluids with Different Chemical Nature. In *Unsaturated soil: Research and application*. (ed.) Springer: volume 2. ISBN 978-3-642-31342-4 e-ISBN 978-3-642-31343-1, p439-446.
5. Mukoko, G. 2014. Comportement des sols latéritiques compactés dans les remblais et digues de retenue des rejets miniers du Katanga (R.D.C). Thèse de doctorat. (ed.), Presse universitaire de Louvain. Dépôt légal D/2014/9964/30. ISBN 978-287558-314-7. www.i6doc.com. Belgique.
6. Mukoko Kalenda, G., Thimus, J.F. & Ngoie Nsenga, D. 2015. Interaction lateritic soil –concentrators’ discharges: what impact(s)? In *Proceedings of the 16th African Regional Conference on Soil Mechanics and Geotechnical Engineering, Innovative geotechnics for africa tunisia 27-30 april, 2015* © ISBN: 978-9938-12-936-6, p 587 – 594.
7. Nguyen Pham Ph. Th. 2008. Etude en place et au laboratoire du comportement en petites déformations des sols argileux naturels. Thèse de doctorat. Ecole Nationale des Ponts et Chaussées.
8. Pialy. P. 2009. Étude de quelques matériaux argileux du site de Lembo (Cameroun): minéralogie, comportement au frittage et analyse des propriétés d’élasticité. Thèse. Université de Limoges.
9. Spagnoli, G., Azzam, R. Feinendegen, M. 2010. Relevance of pore fluid composition for the drained strength of clays. In *General Assembly of the European Geosciences Union 2010*. Vienna (Austria). Vol. 12 (EGU2010-8535-1).
10. Spagnoli, G., Rubinos, D., Stanjek, H., Fernandez-Steeger, T.M., Feinendegen, M. & Azzam, R. 2011. Undrained shear strength of clays as modified by pH variations. In *Bulletin of Engineering Geology and Environment*. DOI: 10.1007/s10064-011-0372-9..

Climate Change Adaptation in Multi-Reservoir Systems through Revising Operation Policies

Banafsheh Zahraie¹, Hamed Poorsepahy-Samian², Saeed Jamali³, Bahareh Noroozi⁴, Mohsen Nasser⁵

1- Associate Professor, Center of Excellence for Infrastructure Engineering and Management, School of Civil Engineering, College of Engineering, University of Tehran, Iran

2- Ph.D. Candidate, School of Civil Engineering, College of Engineering, University of Tehran, Iran

3- Iran Water and Power Resources Development Company, Iran

4- Water Institute, University of Tehran, Tehran, Iran

5- Assistant Professor, School of Civil Engineering, College of Engineering, University of Tehran, Iran

Email: bzahraie@ut.ac.ir

Abstract

Many river-reservoir systems have been significantly affected by climate change. Karun and Dez multi-reservoir system is the largest reservoir system in Iran, which has experienced significant decline of surface runoffs in the past 10 years. Currently, the system contains six multi-purpose hydropower reservoirs and 8 more dams have been studied to be built on these two rivers. In this study, potential impacts of climate change on the optimal operation policies of the reservoirs were assessed. For this purpose, time series of reservoir inflows under A2, B1 and A1B emission scenarios were projected using outputs of HadCM3, CGCM3 and ECHAM5 Atmosphere-Ocean General Circulation Models (AOGCM). In order to formulate the optimal operation policies for the Karun-Dez multi-reservoir system, a stochastic optimization model, namely Stochastic Dual Dynamic Programming (SDDP), was utilized. Comparison between the simulation of operation policies proposed based on the historical and projected inflows, showed that by considering the climate change projections, the performance of the policies could be improved by up to 30%. The results also showed that a relatively important share of negative impacts of climate change on Karun and Dez multi-reservoir system can be mitigated by utilizing the operation policies derived based on the climate change projections.

Keywords: Climate change, optimal operation, hydropower, Karun and Dez reservoir system, Stochastic Dual Dynamic Programming.

1. INTRODUCTION

Climate change has affected the hydrologic conditions of the water systems throughout the world. Adapting to the changing hydrologic conditions is essential to mitigate the negative impacts of the climate change. In particular, hydropower generation has been significantly impacted by change in the hydrologic conditions [1]. Adaptation to climate change, to some extent can be achieved by taking into account the changing conditions in the process of developing operation policies for hydropower systems.

Optimization methods are common tools for developing optimal operation policies for multi-reservoir systems. Stochastic Dynamic Programming (SDP) is one of the most commonly used methods for developing optimal operation policies in reservoir systems. However, the curse of dimensionality, which is the exponential increase in runtime needed with the increase in the dimensions of the optimization problem, restricts the application of SDP to systems with 3-4 reservoirs [2]. Different approaches have been proposed to circumvent the curse of dimensionality, with Stochastic Dual Dynamic Programming (SDDP) [3] being supposedly the most successful of these approaches.

SDDP is one of the most commonly used approaches for the problem of optimal operation of multireservoir systems. Pereira and Pinto [3] developed SDDP for the problem of hydrothermal scheduling. SDDP uses the dual information of one-stage optimization to approximate the expected cost-to-go function in each stage of the problem. In this sense, SDDP could be regarded as an extension of Benders decomposition, and each approximation of the cost-to-go function, is a Benders cut. The accuracy of this approximation is increased through an iterative simulation-optimization process. Philpott and Guan [4] has given a mathematical proof of convergence for SDDP.

SDDP has been largely used in hydrothermal scheduling [5, 6]. Tilmant and Kelman [7] utilized SDDP in order to analyze trade-offs between agricultural development scenarios and hydropower benefits in a big water resources system. Tilmant et al. [18] proposed a method for incorporating irrigation benefits in the objective function of SDDP in order to assess the marginal value of water. Goor et al. [9] proposed a method based on the convex hull approximation of the true hydropower function in order to take into account the variable productivity of hydropower plants. Rouge and Tilmant [10] provided a discussion on the existence of multiple near-optimal solutions in SDDP and proposed a periodic reoptimization algorithm to stabilize the policies developed from SDDP. Poorsepahy-Samian et al. [11] proposed a method for incorporating box-cox transformation in the inflow modelling of SDDP. The results showed that inflow modelling significantly affects the quality of the policies from SDDP.

This paper studies the potential impacts of climate change on operation policies developed by SDDP for Karun-Dez hydropower multi-reservoir system in Iran. The remaining of this paper is organized as follows. Section 2 presents a brief description of the stochastic dual dynamic programming and the one-stage problem. Karun-Dez Multireservoir system is introduced in Section 3 followed by a summary of the results from inflow projections in climate change scenarios. Section 3 finishes by presenting and comparing the results from the simulation of optimal policies. Finally, Section 4 presents the concluding remarks.

2. STOCHASTIC DUAL DYNAMIC PROGRAMMING

In SDDP, the multistage optimization problem is decomposed into a set of one-stage optimization sub-problems. Then starting from the last one-stage sub-problem, the sub-problems are solved and the value of the objective function for each time stage is approximated using a linear approximation. As the number of these linear approximations increases, the accuracy of the approximation improves and algorithm reaches the convergence when the approximation is a good representation of the real objective function. In a reservoir operation optimization problem, taking the reservoir storages and the inflow to the reservoirs in the last p time stages as the state variables, in a system with J reservoirs, each linear approximation has the following form:

$$F_t^* \leq \sum_{j=1}^J \alpha_{t,j} s_{t,j} + \sum_{j=1}^J \sum_{i=1}^p \beta_{t,j}^i q_{t-i,j} + \delta_t \quad (1)$$

Where $\alpha_{t,j}$ is the approximation parameter associated to the water storage in reservoir j in the beginning of the time stage t , $\beta_{t,j}^i$ is the approximation parameter associated to the inflow to reservoir j in the time stage $t-i$ and δ_t is the approximation offset. Therefore, the one-stage optimization sub-problem in SDDP has the following general form:

$$\text{minimize} \quad F_t = f_t + F_{t+1}^* \quad (2)$$

$$\text{Subject to: } \mathbf{s}_{t+1} - \mathbf{C}^R (\mathbf{r}_t + \mathbf{r}_t^{spill}) - \mathbf{C}^I \mathbf{w}_t = \mathbf{s}_t + \mathbf{q}_t \quad (3)$$

$$\underline{\mathbf{s}}_{t+1} \leq \mathbf{s}_{t+1} \leq \bar{\mathbf{s}}_{t+1} \quad (4)$$

$$\mathbf{r}_t \leq \mathbf{rmax} \quad (5)$$

$$\begin{cases} F_{t+1}^* \leq \sum_{j=1}^J \alpha_{t,j}^1 s_{t,j} + \sum_{j=1}^J \sum_{i=1}^p \beta_{t+1,j}^{1,i} q_{t-i,j} + \delta_{t+1}^1 \\ \vdots \\ F_{t+1}^* \leq \sum_{j=1}^J \alpha_{t,j}^L s_{t,j} + \sum_{j=1}^J \sum_{i=1}^p \beta_{t+1,j}^{L,i} q_{t-i,j} + \delta_{t+1}^L \end{cases} \quad (6)$$

$$\mathbf{o}_t + p_t^{ins} \geq \mathbf{Ins}_t \quad (7)$$

$$\mathbf{w}_t + p_t^{consumptive} = \mathbf{demand}_t \quad (8)$$

$$G_{j,t} + p_t^{power} \geq pf_j \times pmax_j \quad \forall j = 1, \dots, J \quad (9)$$

$$f_t = z_{ins} p_t^{ins} + z_{consumptive} p_t^{consumptive} + z_{power} p_t^{power} \quad (10)$$

Where F_t is the total expected penalty from the beginning of the stage t to the end of planning horizon; f_t is the penalty at the stage t ; \mathbf{w}_t is the $(D \times 1)$ matrix of the allocations to different consumptive demands in the stage t (m^3); \mathbf{r}_t is the matrix of the reservoir releases in the stage t (m^3); \mathbf{q}_t is the matrix of the reservoir inflows in stage t (m^3); \mathbf{r}_t^{spill} is the matrix of the spills in the stage t (m^3); \mathbf{rmax} is the upper bound of reservoir releases in the stage t (m^3); $\bar{\mathbf{s}}_{t+1}$ and $\underline{\mathbf{s}}_{t+1}$ are the upper and lower bound matrixes of reservoir storages at the end of stage t , respectively; pf_j is the plant factor for the reservoir j ; $G_{j,t}$ is the amount of power generated in reservoir j (MWh); \mathbf{o}_t is the matrix of discharges from the point of instream flow demands in the stage t ; \mathbf{Ins}_t is the matrix of instream flow demands; \mathbf{demand}_t is the amount of consumptive demands; p_t^{power} is the amount of reliable energy production deficit in the stage t (MWh); $p_t^{consumptive}$ is the matrix of the consumptive demand deficit; p_t^{ins} is the matrix of the instream flow demand deficit in the stage t ; z_{power} is the penalty factor for deficit in supplying hydropower demand; $z_{consumptive}$ is the matrix of the penalty factors for deficit in supplying the consumptive demands and p_t^{ins} is the matrix of penalty factors for deficit in supplying instream flow demands.

The approximation parameters for each time stage are calculated by exploiting the dual variables associated to the constraints. The solution algorithm in SDDP involves two main phases: (1) Backward recursion and (2) Forward simulation. In backward recursion, starting from the last stage, the one-stage optimization sub-problem is solved by assuming a trial value for the state variables and then an approximation is built for that trial value. The backward recursion is followed until the first stage and then the forward simulation phase is executed where starting from the first stage, the optimization sub-problems are solved. The value of state variables from the forward simulation are then fed into the next backward recursion as the new trial values. The algorithm is repeated until reaching convergence. For more information about the solution algorithm, see [7] and [11].

The inflow uncertainty in SDDP is generally handled by fitting an Autoregressive or Periodic Autoregressive model to the inflow time series. The fitted inflow model is used to generate inflow scenarios for both backward recursion and forward simulation phases. Gjelsvik et al. [12] proposed that an Autoregressive model of order one (i.e. AR(1)) is a good trade-off between speed and accuracy.

3. CASE STUDY AND RESULTS

Karun-Dez Multireservoir system is located southwest Iran. Six hydropower reservoirs, namely Karun4, Karun3, Karun1, Godarlandar, Gotvand and Dez are under operation in the system, and eight more dams are planned to be built in the near future. The location map and the schematic of the system are shown in Figure 1.

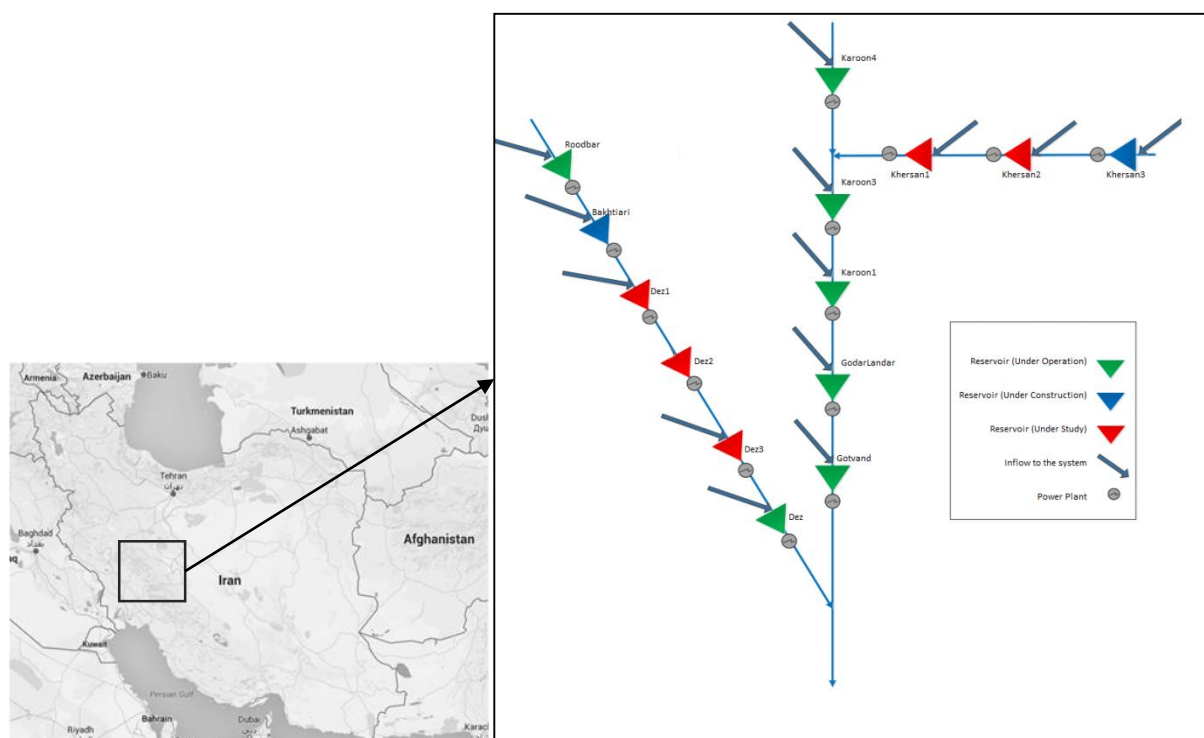


Figure 1. Location map and Schematic of the Karun-Dez Multireservoir system

The system has experienced a significant decline in the amount of inflows in the past 10-15 years period compared with the long-term mean and part of this decline is identified as a consequence of climate change. More specifically, the total inflow to the Karun and Dez river basins have declined by 24% and 30% respectively, in the 2001-2010 period compared with the long-term 1975-2000 period.

In order to assess the impact of the climate change on the optimal operation policies in the system, time series of the inflows to the system in the 2000-2050 were projected under A2, B1 and A1B emission scenarios using the outputs of HadCM3, CGCM3 and ECHAM5 Atmosphere-Ocean General Circulation Models. Figure 2 presents the comparison between the mean annual inflows to the Karun and Dez basins in the historical period with the climate change projections [13].

Figure 2 reveals that the annual inflow to the system is expected to decline in the future compared with the 1975-2000, in both basins. However, in Karun basin it could be expected that the future inflows will increase compared with the inflow of 2001-2010 period. Furthermore, HadCM3 AOGCM model has resulted in higher inflow projections compared with the ECHAM5 and CGCM3 Models. Based on the observed patterns in the system, it could be deduced that HadCM3 model results in implausible inflow projections. Therefore, HadCM3 model is omitted from the subsequent analysis.

Based on the historical inflow of the 1975-2000 period and the inflow projections under the different climate scenarios, seven different sets of optimal operation models were developed in this study utilizing SDDP algorithm, one of which was developed based on the historical inflows of the 1975-2000 period and the six others were developed based on the climate change projections. Following suggestions in [12], the inflow time series for the climate change projections and the historical time series were modelled using AR(1) model.

Afterwards, the extracted operation policies were simulated based on the inflows of the 2001-2010 period and the results were compared. More specifically, the performance of the operation policies derived for the inflow data of 1975-2000 period were compared with the policies derived for the inflow projections based on climate change scenarios. The results are presented in Table 1. The reliability, resiliency and vulnerability indexes proposed by Hashimoto et al. [12] were utilized to quantify the efficiency of the operation policies.

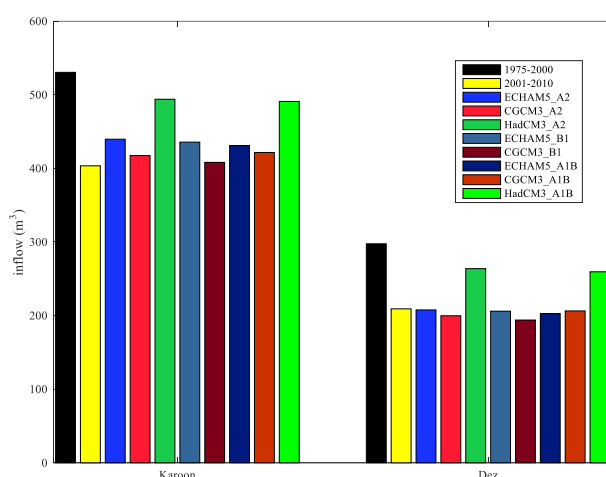


Figure 2. Comparison of the mean total inflows to the Karun and Dez River basins in the historical period with the climate change projections

Table 1. Comparison between the performances of different operation policies based on the simulation of 2001-2010 period

Policy	Total Penalty	Total Power Generation (GWh)	Reliability			Resiliency			Vulnerability		
			Reliable Energy	Consumptive demand	Instream Flow	Reliable Energy	Consumptive demand	Instream Flow	Reliable Energy	Consumptive demand	Instream Flow
Historical	10.02×10^7	232180	47.0	81.6	98.9	27.5	62.9	97.2	1427	852	39
CGCM3-A2	9.08×10^7	238400	63.3	83.3	94.5	32.4	63.3	81.2	1123	775	43
CGCM3-B1	7.50×10^7	238670	63.4	83.4	94.3	32.6	66.5	85.2	980	771	74
CGCM3-A1B	8.92×10^7	235380	63.9	83.0	94.2	32.1	68.9	86.4	1183	812	18
ECHAM5-A2	7.70×10^7	237580	63.2	84.1	95.7	35.0	65.8	88.5	892	802	24
ECHAM5-B1	7.23×10^7	235640	61.1	83.7	96.0	29.8	65.9	88.3	975	878	4
ECHAM5-A1B	7.70×10^7	243190	65.3	84.8	94.7	32.0	70.7	87.8	889	740	20

The results indicate that by considering the climate change projections, the total simulated penalty (which is the main performance index as it is the objective function of the optimization to derive the optimal operation policies), has improved by 10% to 30% compared with the policies developed using historical inflows. The reliability of supplying reliable energy and consumptive demands have also increased 34% and 2.5%, respectively. Meanwhile, the reliability of supplying instream flow demand has decreased by 4% when using the policies derived for climate change projections. The better instream flow demand supply reliability based on the historical optimal operation policy is due to the overestimation of the inflow in this policy. In other words, this policy over-predicts inflows to the system and as a result, reservoirs released more water downstream in order to supply instream flow demand. However, by doing so, the reliability of supplying other demands, in particular energy demand, decreased significantly.

The resiliency and vulnerability indexes, also reveal that by using the policies derived based on the climate change projections, the performance could be improved significantly. Furthermore, the policies derived based on the projections of ECHAM5 AOGCM model performed better when compared with the policies derived based on the CGCM3 model projections. The operation policies for B1 scenario performed better in the period of 2001-2010 in comparison to A2 and A1B scenarios. Hence, it can be concluded that the ECHAM5-B1 projections provided best operation policies for the period of 2001-2010 and performed better in capturing the inflow decrease in this period.

4. CONCLUSIONS

In this paper, the potential impacts of the climate changes on the optimal operation policies in Karun-Dez multireservoir system were analyzed. The mean annual inflow to the system was decreased by 27% in the 2001-2010 period compared with the long-term 1975-2010 period. The optimal policies derived for 1975-2010

period were compared with the optimal policies derived based on the inflow projections of A2, B1 and A1B emission scenarios and ECHAM5, CGCM3 AOGCM models.

Based on the results, it was shown that by considering the inflow projections based on climate change scenarios, the reliability of supplying reliable energy and consumptive demands in the dry period of 2001-2010 could be improved by 34% and 2.5%, respectively. However, this was accompanied by a 4% decrease in the reliability of supplying the instream flow demand. The main performance index, namely the total penalty (which have been the objective function in the optimal operation models), could be improved by up to 30% when utilizing the policies derived for the climate change scenarios.

Also based on the results, it could be concluded that projections of the ECHAM5 AOGCM model for B1 emission scenario provides a better understanding of the behavior of the system in the 2001-2010 period, compared with the projections of CGCM3 and HadCM3 models for A2, B1, and A1B scenarios.

5. ACKNOWLEDGEMENT

This study has been supported by a grant from Iran Water and Power Resources Development Company (IWPCO). The technical contributions of the staff of Technical and Research Division of IWPCO is hereby acknowledged.

6. REFERENCES

1. National Energy Education Development Project (2007), *Hydropower*, in Secondary Info Book, pp. 24 – 27, Need Project, Manassas, Va.
2. Bellman, R. (1961), “*Adaptive Control Processes, A Guided Tour*”, Princeton University Press, Princeton.
3. Pereira, M. V. F. and Pinto, L. M. V. G. (1991), “*Multi-stage Stochastic Optimization Applied to Energy Planning*”, *Mathematical Programming*, 52, pp. 359-375.
4. Philpott, A. B. and Guan, Z., (2008), “*On the Convergence of Stochastic Dual Dynamic Programming and Related Methods*”, *Operation Research Letters*, 36 (4), pp. 450-455.
5. Homem-de-Mello, T., de Matos, V. L. and Finardi, E. C. (2011), “*Strategies and Stopping Criteria for Stochastic Dual Dynamic Programming: A Case Study in Long-term Hydrothermal Scheduling*”, *Energy Systems*, 2 (1), pp. 1-31.
6. Rebennack, S., Flach, B., Pereira, M. V. and Pardalos, P. M. (2012), “*Stochastic Hydro-Thermal Scheduling Under Emissions Constraints*”, *Power Systems, IEE Transactions on*, 27 (1), pp. 58-68.
7. Tilmant, A. and Kelman, R. (2007), “*A Stochastic Approach to Analyze Trade-offs and Risks Associated with Large-Scale Water Resources Systems*”, *Water Resources Research*, 43 (6), W06425.
8. Tilmant, A., Pinte, D. and Goor, Q. (2008), “*Assessing Marginal Water Values in Multipurpose Multireservoir Systems via Stochastic Programming*”, *Water Resources Research*, 44 (12), W12431.
9. Goor, Q., Kelman, R. and Tilmant, A. (2011), “*Optimal Multipurpose-Multireservoir Operation Model with Variable Productivity of Hydropower Plants*”, *Journal of Water Resources Planning and Management*, 137 (3), pp. 258-267.
10. Rouge, C. and Tilmant, A. (2016), “*Using Stochastic Dual Dynamic Programming in Problems with Multiple Near-Optimal Solutions*”, *Water Resources Research*, 52, pp. 4151-4163, doi:10.1002/2016WR018608.
11. Poorsepahy-Samian, H., Espanmanesh, V. and Zahraie, B. (2016), “*Improved Inflow Modeling in Stochastic Dual Dynamic Programming*”, *ASCE Journal of Water Resources Planning and Management*, 142 (12): 04016065.
12. Gjelsvik, A., Mo, B. and Haugstad, A. (2010), “*Long- and Medium-Term Operations Planning and Stochastic Modeling in Hydro-Dominated Power Systems Based on Stochastic Dynamic Programming*”, in: *Handbook of Power Systems I. Energy Systems*, pp. 33-55, Springer, Berlin.
13. Water Research Institute (2017), *Analysis of Climate Change Impacts on Water Resources Development Projects in Karun-Dez and Karkheh Systems*, Final Report, University of Tehran, Iran.
14. Hashimoto, T., Stedinger, J.R. and Loucks, D.P. (1982), “*Reliability, Resiliency, and Vulnerability Criteria for Water Resources System Performance Evaluation*”, *Water Resources Research*, 18 (1), pp. 14–20, doi:10.1029/WR018i001p00014.

Laouzas dam: behavior of a thin concrete arch dam located in a wide valley and foundation stability improvement

Emmanuel Robbe¹, François Morel¹

1- Electricité de France - Hydro Engineering Center – Le Bourget du Lac

Email: emmanuel.robbe@edf.fr

Abstract

Through the example of Laouzas dam owned by Electricité de France, this paper presents the mechanical behavior of a thin concrete arch dam located in a wide valley. From the first impoundment of the reservoir, this dam was affected by an opening of the rock-concrete interface near the central cantilevers. The reinforcement of the monitoring system, in particular the installation of piezometers at the downstream part of the dam-foundation contact, enhanced the progression of pore pressure in this zone beyond the generally admitted hypotheses. In order to explain such situation and to evaluate the consequences, finite-element analyses taking into account hydro-mechanical modeling were performed. They helped in understanding the observed phenomena and described the conditions of the dam-foundation thrust transmission towards downstream in the central part of the foundation. On Laouzas dam, after study of different solutions of reinforcement, local foundation reinforcement downstream of the central blocks was decided and implemented.

Keywords: Arch, Concrete, Reinforcement, Finite-element.

1. INTRODUCTION

Through the example of Laouzas dam owned by Electricité de France, this paper presents the mechanical behavior of a thin concrete arch dam located in a wide valley. From the first impoundment of the reservoir, this dam was affected by an opening of the rock-concrete interface near the central cantilevers. The reinforcement of the monitoring system, in particular the installation of piezometers at the downstream part of the dam-foundation contact, enhanced the progression of pore pressure in this zone beyond the generally admitted hypotheses. In order to explain such situation and to evaluate the consequences, finite-element analyses taking into account hydro-mechanical modeling were performed. They helped in understanding the observed phenomena and described the conditions of the dam-foundation thrust transmission towards downstream in the central part of the foundation. On Laouzas dam, after study of different solutions of reinforcement, local foundation reinforcement downstream of the central blocks was decided and implemented.

2. PRESENTATION OF LAOUZAS ARCH DAM, DESIGN AND OBSERVED BEHAVIOR

Laouzas dam, part of Montahut Hydraulic Scheme, is a 52 m high concrete arch dam built on the Vèbre River, in the south-east of France (Figure 1). This scheme is currently owned and operated by Electricité de France (EDF). The dam, whose construction was achieved in 1965, is located in a wide valley: [Width of the valley]/[Height of the dam] ratio close to 5,5.

The dam is founded on sound granite affected by a low density of cracks. In the central part of the valley, the dam is embedded in 4 to 5 meters of sound rock.

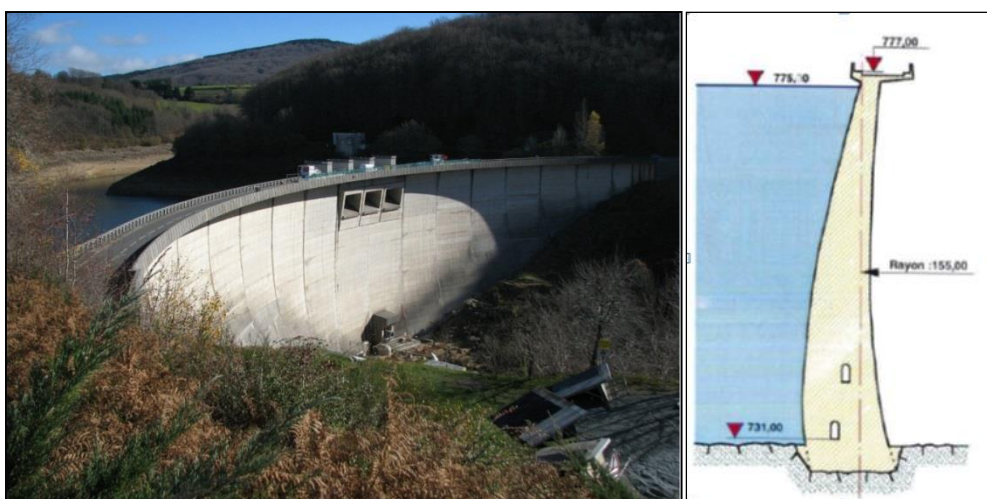


Figure 1. downstream view of the Laouzas dam and central cantilever design.

Considering that vertical tensile stresses would occur at the upstream toe of the dam, the design of the dam included a horizontal joint located close to the toe of the upstream face of the 4 central cantilevers. This joint runs from the upstream face of the dam to the upstream face of the lower drainage gallery. To avoid initiation of cracks in the concrete, the base of the central blocks is densely reinforced by rebars. The joint has proved to be inefficient and a fissure has progressively developed at the interface between concrete and foundation of the central blocks.

Since the first impounding of the reservoir, significant drain discharge was observed in the lower drainage gallery (up to 410 l/min in 1969), on the downstream face of the dam, and immediately downstream, mainly due to the opening of the rock-concrete interface in the central part of the dam. Irreversible displacements of the structure were recorded by the monitoring system, namely at the base of the central blocks. Joint re-grouting was performed during the period end 1969 - end 1971 along with sealing of some cold concrete joint on the upstream face of the dam, leading to temporary positive effects on the behavior of the dam. In 1982 and 1983, in order to reduce the drain water discharge in the lower gallery, a new drainage system was bored immediately downstream of the dam and the existing drains in the lower drainage gallery were plugged. During the 1990', the dam was placed under close supervision, due to the progression of irreversible displacement, and additional monitoring system and drainage were installed.

At the end of winter 2005/2006, the combination of cold weather conditions and high reservoir level leads to the highest displacement and leakage rate ever observed by the monitoring system equipping the dam. Following this event, a limitation of the reservoir level in winter (5 m under the normal water level) was decided. Meanwhile, studies required to fully understand the behavior of the dam and assess its safety were performed [1].

In 2007, the installation of additional interstitial pressure cells at different locations in the vicinity of the concrete/foundation contact enhanced the progression of the rock/concrete interface opening and the diffusion of the interstitial pressure towards downstream beyond the generally admitted hypotheses. In parallel, complementary geological & geotechnical investigations and 3D finite-element analyses of the dam & foundation were performed by the Hydro Engineering Center of EDF.

3. FINITE-ELEMENT ANALYSIS OF THE DAM

In order to represent the observed behavior of the arch dam, a 3D nonlinear finite-element (FE) model using joint-elements at the dam-foundation interface and able to take into account the hydro-mechanical linkage was developed, first, using the FE software Gefdyn, and then with the open-source FE software Code_Aster (developed by EDF). Only the analyses performed with Code_Aster are presented in this paper.

The non-linear model computes crack openings and its propagation, uplift pressure and its diffusion which leads to extend the initial crack. For this purpose, joint elements are implemented, in the numerical model (Error! Reference source not found.). At the dam/foundation and abutment/foundation interface, these zero-thickness elements behave mechanically with high stiffness in compression and zero stiffness in tension. The tangential stiffness at the dam/foundation interface becomes equal to zero once the joint opens. The mechanical behavior of the dam-abutment interface follows a Mohr-Coulomb law.

In the joint-elements, effective state of stresses is considered. The propagation of the uplift pressure is modeled according to the Poiseuille law (or cubic law), considering that the flow increases with the cube of the crack opening.

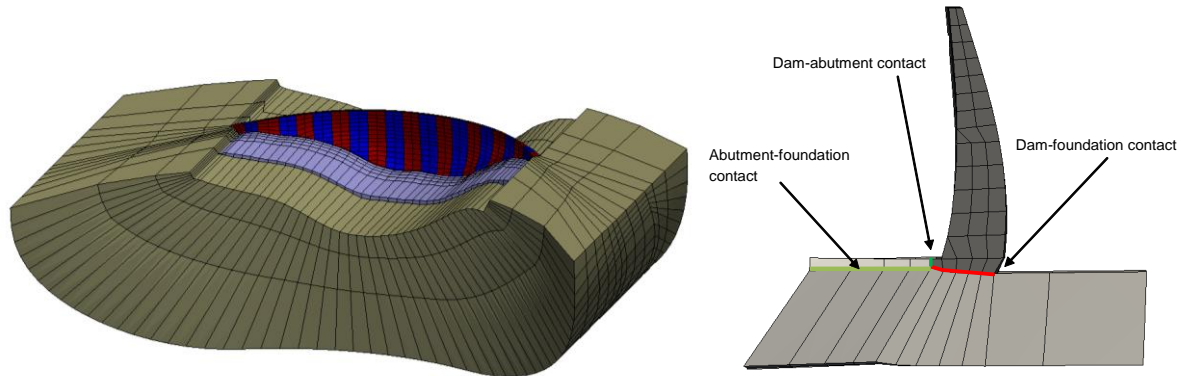


Figure 2 mesh of the dam, foundation and abutments and introduction of joint-element.

The FE model is calibrated from statistical analysis of the measured dam's displacement by adjustment of the elastic properties of the concrete and the foundation. Creep of the concrete is also taken into account in the study due to its contribution to the irreversible downstream displacement of the crest of the dam.

The FE analyses confirm that the hydrostatic load is responsible for the opening of the rock-concrete interface and the diffusion of the uplift pressure in the downstream direction. This behavior is enhanced by the increase of the dam's displacement toward downstream due to creep and to winter thermal conditions. Error! Reference source not found. shows the opening computed by the FE model at the dam/foundation interface due the normal hydrostatic load, under winter thermal conditions and creep: in that situation, with an opening of about 16 mm at the upstream toe of the dam, the full uplift pressure expands under the central cantilevers of the dam and the thrust can no more be transferred from the cantilevers to the foundation by the horizontal interface. The embedment of the structure in the sound rock foundation plays then a major role for stability.

The FE analyses compute the thrust from each cantilever to the underlying and downstream foundation. As shown in Error! Reference source not found., the thrust from the cantilevers is distributed between the underlying foundation (in red) and the downstream abutment (in blue). For the central cantilevers, due to the uplift pressure expansion and the model's assumption that no tangential forces are transmitted when the joint is open (which is probably slightly overestimated considering the irregular shape of the dam/foundation interface), all the thrust is transmitted through the downstream abutment (around 700 t/m for the 3 central cantilevers).

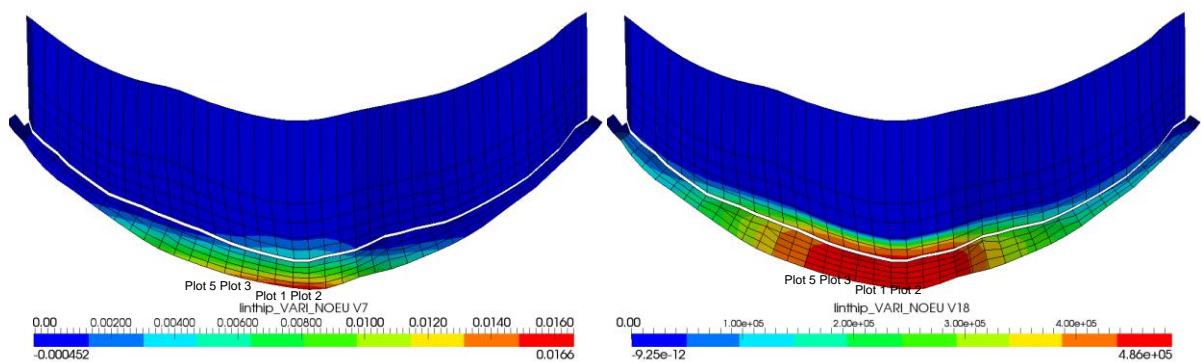


Figure 3 opening of the joint elements (left) and uplift propagation (right) on the dam/foundation and abutment/foundation interface (view from the top).

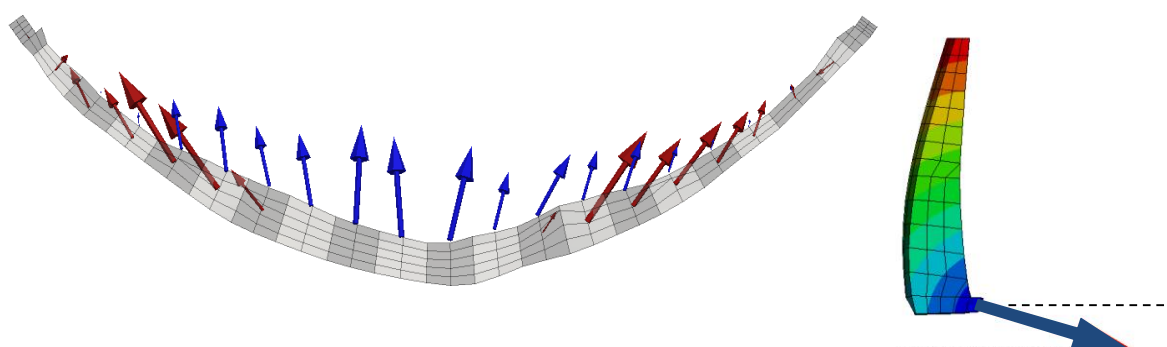


Figure 4 thrust from cantilever to foundation (underlying in red, downstream in blue) on the dam-foundation interface mesh (left) and view from the side of the central cantilever.

4. STUDIES OF REINFORCEMENT OF THE DAM AND FOUNDATION

In parallel with the analyses of the behavior of the dam and foundation, various solutions of reinforcement or treatment of the dam and foundation were studied in order to restore the normal operation of the scheme (suppression of the reservoir level limitation during winter).

4.1. SEALING WORKS OF THE DAM/FOUNDATION CONTACT AT THE UPSTREAM TOE OF THE DAM

The construction of an anchored plinth at the upstream toe of the dam associated with a new grout curtain and a membrane on the upstream face of the dam was studied. This solution is proven to be very effective to reduce the opening of the dam-foundation contact and maintain the thrust through the underlying foundation of the structure, and therefore limit the diffusion of uplift.

This technical option was not implemented, mainly due to risks and uncertainties which might affect the construction works, among which:

- Flood management during the time allocated to the works in the vicinity of the upstream toe of the dam,
- Uncertainties related to the depth of the fractured rock at the upstream toe of the dam, particularly on the left bank which affect the determination of the volume of excavations, the volume of grout to be injected, the efficiency of the grout curtain, and, as a corollary, the duration allocated to the works,
- Full emptying of the reservoir required to perform the works has great environmental, societal and operational impacts considering that the works would be planned over 2 years,
- Uncertainties related to the impoundment of the reservoir at the end of the works which may lead to a low water level on the edge of winter.

4.2. INSTALLATION OF ACTIVE ROCK ANCHORS

Bringing an additional vertical stress to reduce the opening of the dam/foundation contact, by using high capacity active rock anchors was studied. These anchors could be installed from the crest of the dam or from the lower drainage gallery.

The emptying of the reservoir is not required to perform the works; therefore this option would reduce environmental and societal impacts and impose lower constraints on the scheme management.

However, finite-element analyses show that, to have a significant positive impact on the dam's behavior, the required density and capacity of rock anchors is beyond which can realistically be installed.

This technical option was therefore abandoned.

4.3. STABILIZATION OF THE DAM WITH DOWNSTREAM CONCRETE BLOCK

Stabilization of Laouzias dam by concrete blocks in contact with the downstream face of the dam was studied. Lateral or central reinforcement options were considered (Figure 5).

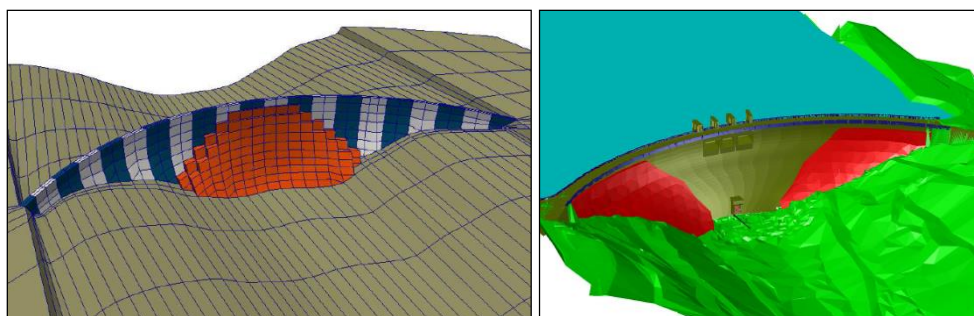


Figure 5 central and lateral downstream reinforcement of the dam.

Both solutions lead to favorable results relating to the reduction of the opening of dam/foundation contact and improve the transmission of the thrust on the foundation.

For the lateral block option, the depth of the fractured rock on the left abutment requires to perform deep excavations whose execution has an impact on the scheme management (significant lowering of the water level in reservoir during excavation works).

The central block reinforcement requires less excavation but interacts with the surface gated spillway and the bottom outlet.

The link between the existing arch dam and the new structure downstream has to be carefully designed in order to prevent any deterioration of the dam itself whose behavior is considered satisfactory to date.

For the central reinforcement: an adjustable device between the dam and the downstream reinforcement has to be designed to avoid any hard points which would crack the arch dam. In addition, a procedure has to be defined for reservoir impounding and progressive load transfer to the downstream structures.

The central reinforcement presented some interest but was judged somewhat risky with respect to the potential alteration of the arch dam behavior. In addition, the works has an incidence on the scheme management: temporary lowering of the water level in the reservoir, period of time allotted to the calibration of the device transferring the load thrust...

3.4. REINFORCEMENT OF THE DOWNSTREAM CENTRAL ROCK ABUTMENT

Considering that the concrete arch dam itself behaves perfectly well under loading (finite-element analyses show an acceptable state of stress in the concrete, visual inspections of the dam do not bring to light any non-conformity) and that every attempt to adapt the existing structure by adding concrete blocks or rock anchors can potentially modify the behavior or deteriorate the existing structure, the study focuses on the assessment of the capacity of the central rock abutment to sustain the thrust from the existing arch, especially as the quality of the rock in the center of the valley is extremely good.

This technical option, which is the one implemented, is described in the following chapter.

4. CONTAINMENT AND DRAINAGE OF THE DOWNSTREAM CENTRAL ROCK ABUTMENT

Following the event of 2006 (combination of a high water level in the reservoir and winter condition leading to the highest opening of the dam/foundation contact and therefore additional downstream displacements of the central blocks (which were totally reversible) & high drainage discharge) and the first finite-element analysis that highlights the near-horizontal thrust on the central rock abutment, a structure dedicated to containment and drainage of the rock located immediately downstream of the 2 central cantilevers was constructed in 2008-2009: two reinforced concrete beams housing, each, 5 pre-stressed anchors and a dense drainage network (Error! Reference source not found.). The anchors are 3 m spaced and are designed for a nominal tension close to 4000 kN. The aim of this reinforcement is to prevent the decontainment of the upper edge of the rock and the spreading of the uplift pressure.

The structure designed is evolutionary. It allows the installation of additional rock anchors and the densification of the drainage network. The structure hosts instrumentation devices: leveling points, rock extensometers, interstitial pressure cells, and gauges measuring the residual tension in the rock anchors.

2D finite-element analyses were performed to assess the stability of the rock abutment based on the thrust estimated by the 3D finite-element analyses of the dam and taking into account the rock fracturing and the topography.



Figure 6 view of the downstream beam and of the installation of the anchors.

Additional refined finite-element analyses performed in 2013-2014 show that the downstream reinforcement of the foundation needs to be extended to the adjacent cantilevers (each side of the two central ones), which also transfer a significant thrust to the rock abutment. This work has begun during summer 2016 and will be achieved in mid-2017.

Simultaneously a densification of the monitoring network is carried out. Additional direct and inverted pendula, and rock extensometers, tele-operated, are currently installed.

A test rise of the reservoir water level up to Normal Water Level took place at the end of winter 2017. The analysis of data collected by the monitoring system and the comparison to the predictions of numerical modeling assessed the satisfactory behavior of the dam.

5. CONCLUSIONS

In February 2006, the combination of cold winter condition and high water level in the reservoir have led monitoring devices to record historical maxima in terms of displacement of the central cantilevers of Laouzas dam and drainage discharge, and have raised questions regarding the behavior of this thin arch dam located in a wide valley.

After the decision taken, in 2006, to limit the water level of the reservoir during winter, and the construction, in 2008-2009, of the first phase of the reinforcement of the downstream rock abutment facing the two central cantilevers, almost 10 years were required, through the installation of additional monitoring devices,

additional geological and geotechnical surveys, observational method and complex non-linear finite-element analyses, to collect the data and fully understand the mechanism driving the behavior of Laouzas dam and its foundation.

In this case, the analyses show that the hydro-mechanical coupling and the downstream central rock abutment play a major role in the diffusion of the forces from the arch to the foundation. The detailed surveys carried out confirm the pertinence of the foundation reinforcement constructed in 2008-2009 downstream of the central cantilevers and highlights the necessity to extend this structure to the adjacent blocks.

The understanding of the behavior of the dam and its foundation allowed the design of the best reinforcement solution, suitable for the specificities of the site and taking into account environmental, societal and operational requirements.

6. REFERENCES

1. Bourdarot, E. and Hoonakker, M., “*Le comportement des barrages-voûtes en vallée large expérience tirée des barrages de Laouzas et Vouglans*”, 24th International Conference on Large Dams, Kyoto, 2012.

Risk assessment of earth dam overtopping using system dynamics and monte carlo simulation (case study: hajilarchay dam)

Ali Ebrahimzadeh¹, Mahdi Zarghami², Vahid Nourani²

1- Ph.D. Candidate, Faculty of Civil Engineering, University of Tabriz, Tabriz, Iran

2- Professor, Faculty of Civil Engineering, University of Tabriz, Tabriz, Iran

Email: a_ebrahimzadeh_a@yahoo.com

Abstract

Risk assessment of the hydraulic structures is one of the serious concerns of researchers especially in earth dams. Using uncertainty and risk analysis, it is possible to use uncertain parameters in mathematical equations for designing. This paper considers the different uncertainties related to flood and wind with various return periods and uses system dynamics to evaluate overtopping risk on earth dams in order to mitigate this risk and then increase the earth dam's operational life. In order to evaluate risk in proposed model, we use Monte-Carlo simulation (MCS) method with different iterations. In this research, system dynamics is used as a simulation OF overtopping risk in the Hajilarchay dam, Northwestern Iran. The results show the effectiveness of system dynamics in earth dams overtopping risk assessment with different parameters effecting the overtopping risk. Moreover, opening the bottom outlet of the Hajilarchay dam could cause 12 percent reduction in overtopping risk. Also overtopping risk obtained from the Monte-Carlo simulation is one to two percent greater than Latin hypercube sampling and with less simulation running time. It can be concluded that system dynamic is very effective tool for evaluation and calculation of overtopping risk of dams and is easier and faster than other common numerical methods like Programming.

Keywords: Earth dam, Overtopping risk, System dynamics, Uncertainty, Return period.

1. INTRODUCTION

Although dams have a lot of benefits, their failure can create many dangers and problems for life and property of human beings. Among all the factors that cause the failure of dams, overtopping is considered as one of the most important factors. In designing and performance of engineering systems there are always uncertainties. Calculating the risk of failure with these uncertainties will be necessary. With the help of reliability and risk theory, all uncertainties of random nature of parameters can be formed as mathematical equations, and safety and performance considerations are quantitatively enter the process of designing (Mays, 2000).

Because of the importance of dam in terms of economic, efficiency, failure and destruction, safety and risk of dams' destruction have always been of interest to researchers and engineers. Hsu et al. (2011) examined uncertainty parameters caused by two effective phenomena that is wind and flood on dam overtopping. They compared the probability of overtopping based on two models of maximum monthly and annual data. Goodarzi et al. (2012) examined dam overtopping risk by univariate and bivariate flood frequency analyses and stated that in assessing the dangers of dam two mathematical analyzes of uncertainty and risk are taken into consideration. In their studies, five univariate and bivariate flood frequencies by applying Gumbel logistic distribution for Doroudzan dam has been evaluated. Mansouri and Kabiri (2012) examined the risk of Vanak dam overtopping using the Monte Carlo method. The results of their research indicated that the initial water level of reservoir does not have much effect on the overtopping risk of this dam and the important factor in this regard is water flow entering dam reservoir. Gebregiorgis and Hossain (2012) evaluated hydrological risk of the old Wilson dam. These researchers reassessed dam risk analysis by flow data, in which old peak-flow data is considered instead of distribution of values. They also used L-moment method for maximum annual volume of reservoir. Mollahosseini et al. (2012) evaluated the effect of creating reservoir capacity in reducing flood damage using a simulation – optimization model based on the systems dynamics. In the aforementioned study, PSO-Vensim simulation – optimization model has been developed to optimize exploitation from reservoir during the flood and allocation of optimal initial control volume of reservoirs. The results showed that improving the conditions of exploitation in terms of flood peak reduction optimal criterion and distribution of initial control volume between the reservoirs of river basin are advantage of constructing Garsha dam. Goodarzi et al. (2012) investigated the possible dam overtopping risks in the case of Mijran dam and stated that hydrological risk assessment and uncertainty analysis by mathematical and statistical methods provides useful information for decision makers. Sharafati and

Zahabiyou (2014) analyzed dam overtopping analysis by using Monte Carlo simulation. The results of this research show that the average changes of Jamishan dam failure per unit, spillway width variation, normal level and dam crown level is 0.03, 3.1 and 1.56 percent respectively. Goodarzi et al. (2014) in another study examined overtopping risk of Doroudzan dam with Monte Carlo and latin hypercube methods and indicated that increasing the initial level of reservoir water of dam increases the risk of overtopping. Vali Samani et al. (2015) examined uncertainties and evaluation of Maroon dam overtopping risk. In their research, they used Monte Carlo and latin hypercube methods in analyzing overtopping risks and by comparing these two methods they showed that an increase in the input flow is more effective compared to the return period in overtopping risk changes of this dam. In another research, Sharafati (2015) examined overtopping risk of Jamishan dam. In this research by using precipitation threshold theory and combining it with the conditional Monte Carlo method, he reduced the simulation time.

Risk management of earth dams due to various failure modes is one of great importance. Dam overtopping risk contains large number of uncertainty factors, parameters and effective modes. Since these modes have feedback and system dynamics perspective can serve as a simulation tool for managers in risk management. By using system dynamics perspective and modelling the interactions and feedbacks inside the system along with imposing different scenarios to the system, an approximation of what actually happens will be presented which will enable stakeholders to make proper decisions in relation to safety and economic issues.

In this paper by using system dynamics simulation and using Monte Carlo simulation method, we tried to examine and calculate Hajilarchay earth dam and in order to calculate overtopping risk, in addition to flood and wind return period as effective parameters on overtopping of dam and considering their integrative effect, initial height of water in dam reservoir and also dam height itself are considered as uncertainty parameters. The risk by using above methods is calculated and the obtain results are compared with each other. These cases can be stated as innovation in this research.

2. MATERIALS AND METHODS

2.1. MONTE CARLO SIMULATION METHOD (MCS)

Monte Carlo analysis is one of the strongest engineering tools that is able to statistically analyze uncertainties in engineering issues. This method is useful especially in complex issues in which many random variables are connected by nonlinear equations. The basis of this method is producing a set of random numbers that are mechanically or electronically generated. First n random numbers are generated for each of the available random parameters. After that, with regard to an appropriate probability distribution, n random number with certain probability density is obtained and finally we will have n value for performance function (Z), and by using statistical information and frequency histogram for obtained results, the probability of failure and reliability of system can be evaluated (Ghias, 2014).

2.2. THE EFFECT OF FLOOD ON OVERTOPPING PHENOMENON

In this paper flood hydrograph with different return periods is taken into consideration and then overtopping risk is calculated after flood routing in reservoir using Vensim software and calculation of water height in reservoir.

2.3. THE EFFECT OF WIN ON OVERTOPPING PHENOMENON

The speed of wind and the length of river that is exposed to severe wind blows are among the most important factors affecting the occurrence of the overtopping phenomenon. Overtopping phenomenon of wind is defined as the following equation in which overtopping happens when increase in the height of lake water due to wind blow exceeds dam height (Khakbaz et al, 2001).

$$P_f = P(h_w > H_{dam} - H_0) \quad (1)$$

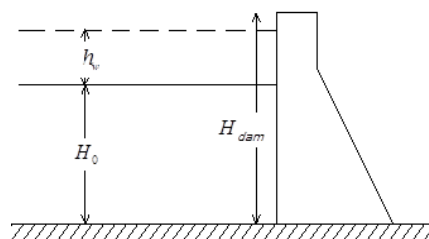


Figure 1. A view of dam height, initial height of water in dam reservoir and increasing water height due to the wind

In figure 1, H_{dam} is dam height, H_0 is initial level of water and h_w is increased water level due to the wind. Increased water level due to the wind h_w is normally divided into the following factors:

a. Wave height due to wind in reservoir level (h_s)

The height of biggest waves due to prevailing winds of the area is called wave height. To calculate wave height due to the wind, USBR (1992) presented the following equation:

$$h_s = 0.00237V^{1.23}F^{0.5} \quad (2)$$

In which h_s is wave height (m), F is flux wavelength (km) and V is the velocity of wind blow (km/hr).

b. Wave flux height due to the wind (h_t)

Because of continuous wind blowing to the surface of dam lake water, water level rises. The amount of this rise is a function of wavelength, wind speed and average depth of water along with the flux wavelength and is calculated based on equation USBR (1992) as follows:

$$h_t = \frac{V^2 F}{62772D} \quad (3)$$

In which h_t is flux height due to wind (m), F is flux wavelength (km), V is the speed of wind (km/hr) and D is the average depth of water in flux wavelength (m).

c. The height of wave flux on the upper roof of dam

When a wave collides with the body of dam, part of energy is wasted due to porosity and roughness of dam roof and the remainder of the energy causes the wave to rise on the upper roof of dam. Hugh presented the following equation to calculate this parameter (Hugh, 2004).

$$\frac{h_r}{h} = 3.84 \times \tan \theta \left(\frac{M_F}{\rho g h^2} \right)^{\frac{1}{2}} \quad (4)$$

In which h_r is the height of wave rise on the roof (m), h is the depth of water (m), ρ is density of water and M_F is instantaneous movement of wave in width unit which can be calculated from the following equation:

$$\left(\frac{M_F}{\rho g h^2} \right)_{Max} = A_0 \left(\frac{h}{g T^2} \right)^{-A_2} \quad (5)$$

Where

$$A_0 = 0.6392 \times \left(\frac{h_s}{h} \right)^{2.0256} \quad (6)$$

And

$$A_1 = 0.1804 \times \left(\frac{h_s}{h} \right)^{-0.391} \quad (7)$$

And h_s is the height of dam wave (m) (Wang and Bowles, 2005). Finally the height of water rise due to the wind is calculated as follows:

$$h_w = h_s + h_t + h_r \quad (8)$$

2.4. ANALYSIS OF OVERTOPPING RISK AND DAM FAILURE

The failure of a system occurs when the system does not have an acceptable performance against the loads. In other words, failure of a system occurs when the load on the system (L_F) exceeds system capacity (R). In analyzing overtopping phenomenon and water spillway of dam, water height in dam reservoir (H_{dam}) and dam height (H_{dam}) are considered as load and resistance of system.

Overtopping risk of input flood to the dam reservoir and wind speed can be explained by the following functions:

$$Z_{Flood} = \ln \frac{H_{dam}}{H_{max}} \quad (9)$$

$$Z_{Flood\&Wind} = \ln \frac{H_{dam}}{H_{max}+h_w} \quad (10)$$

In the above equations, Z is performance function and h_w is the height of water rise due to the wind. Finally, dam overtopping risk is calculated as follows:

$$Risk = 1 - \varphi\left(\frac{\mu_Z}{\sigma_Z}\right) = 1 - \varphi(\beta) \quad (11)$$

In which μ_Z and σ_Z are the average and variation coefficient Z . $\beta = \frac{\mu_Z}{\sigma_Z}$ is reliability index and $\varphi(\beta)$ is normal cumulative probability of β (Kwon and Moon, 2005).

3. SYSTEM DYNAMICS MODEL

System Dynamics is able to make long term decisions by setting feedback relationship between phenomena and simulation of these relationships. This methodology in first time was used by Forster in 1961 and it was modified over the past decades. It was originally used for business and resource management. Dynamics simulation allows us to observe the behavior of modeled system and its response while interacting with external factors and changes over time. In system dynamics analysis four tools of storage, flow, interfaces, and converters are used to transform system characteristics into flow and chart. Storages represent accumulation and they are considered as the source. Flow is a component of storages that one does not exist without another (Sterman, 2000). If something accumulates (like water in reservoir), this accumulation must lead to an activity (input flow to reservoir). Storages and flows form the minimum structure for defining a dynamics. Converters convert inputs to outputs. They can be the representative of values or information. Connection connects storages to converters, storages to regulator flows and converters to other converters. They do not take numerical values but they transfer information (Simonovic and Ahmad, 2000).

Generally, storages accumulate input and output differences and we have the following formula:

$$Stock(t) = \int_{t_0}^{t_n} [Inflow(t) - Outflow(t)]. dt + Stock(t_0) \quad (12)$$

In which $Stock(t)$, $Inflow(t)$ and $Outflow(t)$ are value storage, input and output value respectively. In this research Vensim DSS software has been used for systems dynamics simulation by Monte Carlo method in earth dam overtopping issue.

4. THE DAM UNDER STUDY

The Hajilar River basin is one of the tributaries of Aras river basin and is located in eastern Azarbaijan, Iran. The Hajilarchay dam is located two kilometers north of Garagayeh village, 50 km south-east of Varzaghan and 135 km south of Tabriz (Figure 2). Hajilarchay dam is planned for irrigating nearly 2000 hectares of current low efficiency farmlands and about 40 million cubic meters of water for domestic and industrial use and totally it will prevent 65 million cubic meters water loss of river (Bandab, 2013).

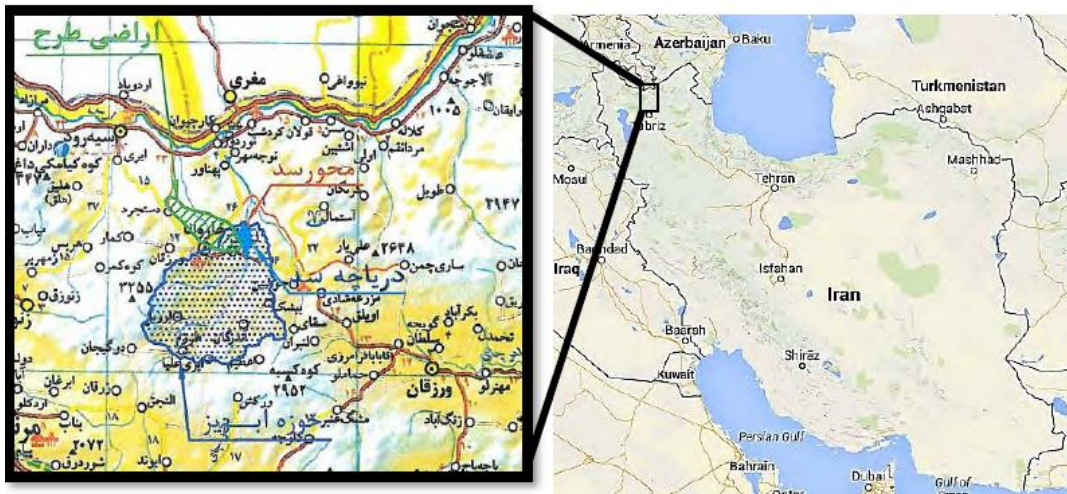


Figure 2. The scope of location of Hajilarchay dam. (Bandab, 2013)

The characteristics of Hajilarchay reservoir dam is presented in table 1.

Table 1. Hajilarchay dam information and dependent structures

Type of spillway	Useful volume (MCM)	Reservoir volume in normal level (MCM)	Height from bed (m)	Height from foundation (m)	Crest width (m)	Crest length (m)	Dam type
Morning glory spillway	47.30	48.90	71	95	10	265	Earth dam with clay core

Figures 3 and 4 shows the Vensim model of Hajilarchay reservoir to simulate water level changes and evaluates dam overtopping risk.

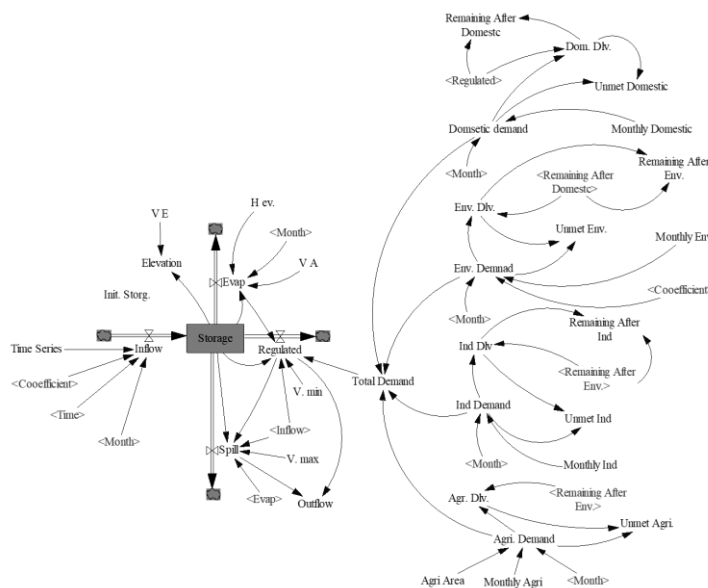


Figure 3. A view of system dynamics model made for simulating water changes in reservoir

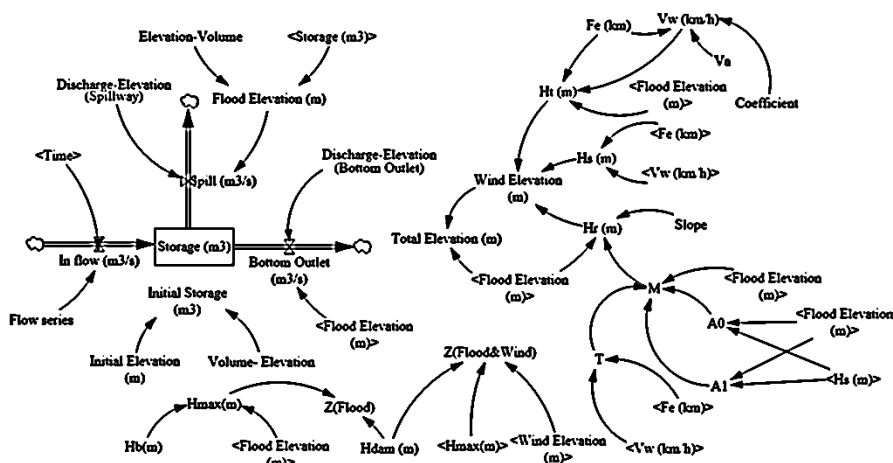


Figure 4. A view of system dynamics model made for simulation of water level and calculating performance function (Z) in Vensim environment.

5. RESULTS AND DISCUSSION

In this study parameters of initial level of water and dam height were considered as uncertainty factors along with the speed of wind with different return periods. and flood with different return periods with maximum probability. Also we assumed that dam bottom outlet is closed within the occurrence of the flood and probable overtopping. Regarding the model of the reservoir, the minimum and maximum initial water level of dam before the flood is 1005 and 1047 meters respectively. Also according to dam characteristics reported by Bandab consulting Engineers Company, dam height was 71.00 meters and the maximum long-term settlement of dam in 50 years is 1.48 meters. Therefore the minimum and maximum dam height is 69.52 meters and 71.00 meters.

5.1. THE EFFECT OF WIND AND FLOOD RETURN PERIOD ON OVERTOPPING RISK

In this part of study, effects of wind and flood return period on overtopping risk are investigated and in the first mode, the uncertainty of initial level changes of water reservoir is from 1005 to 1047 meters and in the second mode in addition to initial level changes of the reservoir, the uncertainty of dam height changes is from 69.52 and 71.00 m. simulation numbers in Monte Carlo method for these modes is 200000 and by considering these change, the overtopping risk of wind and flood effect was calculated simultaneously. The results show that maximum value of overtopping risk was for probable maximum flood (PMF) and wind with 100-year return period and its value is 0.101702 for uncertainty of initial height changes of dam reservoir water and it is 0.115223 for uncertainty of initial height changes of dam reservoir water and dam height itself. Also the results show that by considering uncertainty of dam height changes in addition to initial level changes of dam reservoir water, the amount of overtopping risk will increase averagely about 8.8 percent. The results are presented in figures 5 and 6.

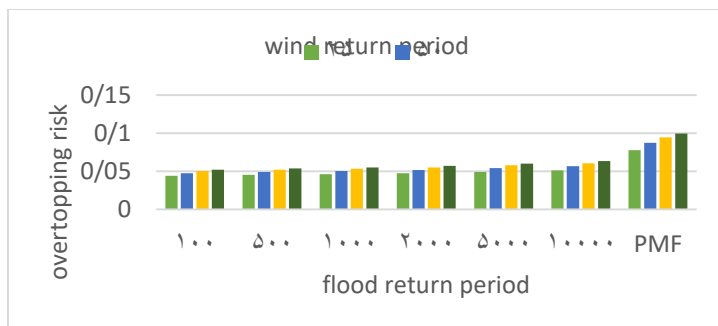


Figure 5. The effect of wind and flood return period changed on overtopping risk by considering uncertainty of water initial level

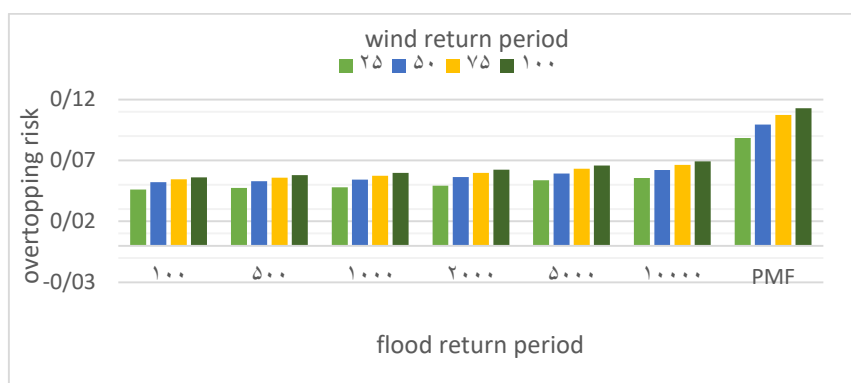


Figure 6. The effect of wind and flood return period changes on overtopping risk by considering uncertainty of water initial level and dam height

5.2. THE EFFECT OF THE NUMBER OF SIMULATION WITH MONTE CARLO METHOD ON OVERTOPPING RISK VALUE

In this part of study effect of the number of simulation repetitions on overtopping risk due to flood and wind is investigated. In this part to calculate overtopping risk calculations, probable maximum flood (PMF) and also wind with 100-year return period has been used. The obtained results of these calculations are presented in figure 7.

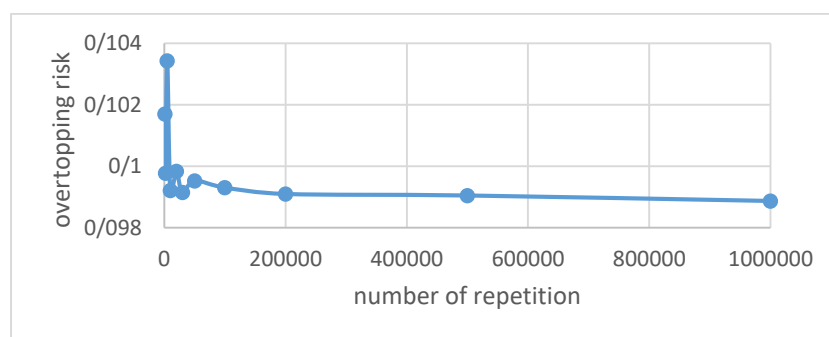


Figure 7. The effect of simulation repetitions of dam reservoir on overtopping risk due to simultaneous effect of wind and flood

With regard to the above graphs, it is clear that in both cases after 200000 simulation repetition, overtopping risk will have the same value.

5.3. THE EFFECT OF OPENING BOTTOM OUTLET GATE ON OVERTOPPING RISK AMOUNT

In order to examine the effect of opening bottom outlet on overtopping risk amount, in first time dam reservoir l was simulated in close bottom outlet gate and overtopping risk amount was calculated and another time in addition to simulating dam reservoir in open bottom outlet gate, the overtopping risk amount was calculated and the results are presented in figure 8. It should be noted that in both modes initial level of dam reservoir water was considered with the minimum and maximum amount of 1005 and 1047 meters respectively and also dam height with the minimum and maximum amount of 69.52 and 71 meters respectively as uncertainty parameters and in both modes Monte Carlo simulation with 200000 repetitions was performed.

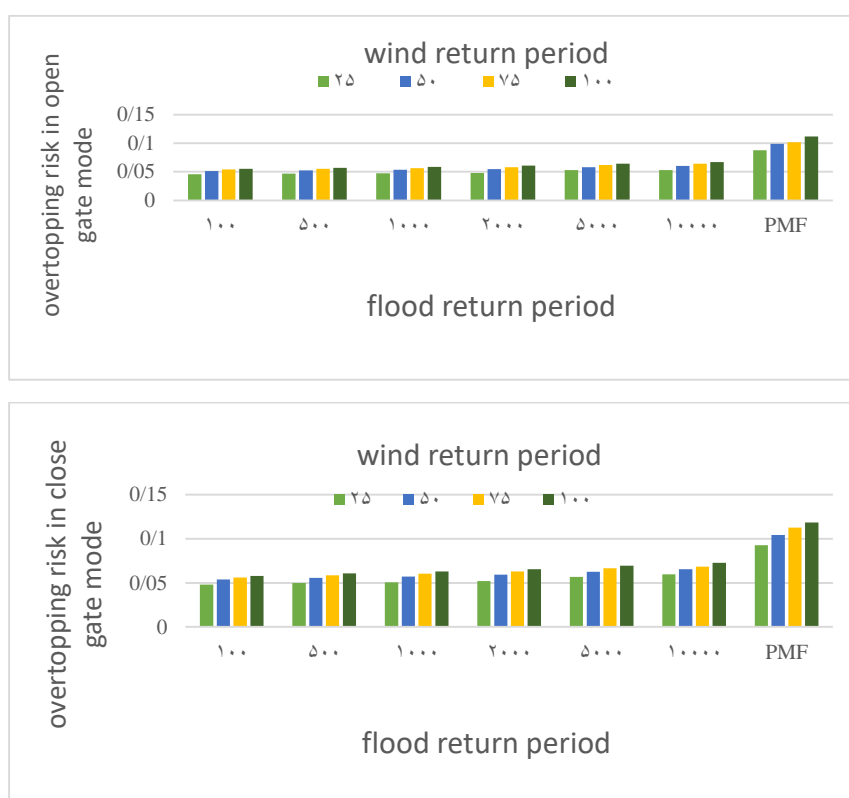


Figure 8. The comparison of overtopping risk due to flood and wind for close and open bottom outlet mode

With regard to figure 8 in which overtopping risk which is under the influence of wind and flood for a condition that bottom outlet gate is closed it is compared to open mode of gate, we can see that in this mode by opening bottom outlet gate the overtopping risk value reduces averagely 7.2 percent.

6. CONCLUSIONS

In this paper Hajilarchay overtopping risk was calculated for different return periods of flood and wind using dam reservoir modeling through system dynamics method in uncertainty condition. For this purpose, by considering initial level uncertainties of dam reservoir water and dam height and using Monte Carlo simulation methods in system dynamics model made for dam reservoir, the overtopping risk value in the mode of flood and wind combination was calculated. The obtained results of simulation show that adding the effect of wind considerably increases overtopping risk value compared to the effect of flood alone. Furthermore, considering both the effect of dam height along with initial water level uncertainty, causes a considerable increase in the amount of calculated overtopping risk compared to the condition in which the only uncertainty is initial water level of dam reservoir is. Also the obtained results of reservoir simulation indicate that when bottom outlet gate is open the overtopping risk reduces 12 percent due to flood and 7.2 percent due to flood and wind respectively. With regard to the obtained result, systems dynamics method with Monte Carlo can be considered as a useful tool to evaluate and calculate dam overtopping risk.

7. ACKNOWLEDGMENTS

The authors acknowledge and appreciate the input data and helps of East Azarbayjan Regional Water Authority and Bandab Consulting Engineers and they are grateful for the helps of the Mahmoud Rashidi and Esmaeil Babazadeh.

8. REFERENCES

1. Bandab Consulting Engineers (2013) Hajilarchay storage dam project report volumes 1 to 9. East Azerbaijan Regional Water Management Company, Iran (In Persian)
2. Gebregiorgis A, Hossain F (2012) Hydrological risk assessment of old dams: case study on Wilson dam of Tennessee River basin. *Journal of Hydrologic Engineering* 17(1):201-212
3. Ghias M (2014) an introduction to the Monte Carlo simulation methods. *Journal of Polymerization* 4(1):67-77 (In Persian)
4. Goodarzi E, Mirzaei M, Ziaei M, (2012) Evaluation of dam overtopping risk based on univariate and bivariate flood frequency analyses. *Canadian Journal of Civil Engineering* 39(4):374–387
5. Goodarzi E, Shui L T, Ziaei M (2014) Risk and uncertainty analysis for dam overtopping- case study: the Doroudzan dam, Iran. *Journal of Hydro-Environment Research* 8(1):50-61
6. Goodarzi, E.; Shui, L. T. and Ziaei, M.; “*Dam Overtopping Risk Using Probabilistic Concepts-case Study: The Meijaran Dam, Iran,*” *Ain Shams Engineering Journal*, Vol. 4, No. 2, pp. 185–197, 2013.
7. Hsu Y C, Tung Y K, Kuo J T (2011) Evaluation of dam overtopping probability induced by flood and wind. *Journal of Stochastic Environmental Research and Risk Assessment* 25(1): 35–49.
8. Hughes S A (2004) Estimation of wave run-up on smooth, impermeable slopes using the wave momentum flux parameter. *Journal of Coastal Engineering* 51(11):1085-1104
9. Khakbaz B, Tajrishi M, Abrishamchi A (2001) Risk and reliability analysis of dam overtopping due to wind. *Proceedings of the 3rd Iranian Hydraulic Conference*, 6-8 November 2001, Tehran University, Iran, 445-453 (In Persian)
10. Kwon H, Moon Y (2005) Improvement of overtopping risk evaluations using probabilistic concepts for existing dams. *Journal of Stochastic Environmental Research and Risk Assessment* 20(4):223-237
11. Mansouri N, Kabiri Samani A (2012) Risk based analysis of earth dam overtopping (Vanak Dam as a case study). *Proceedings of the 9th International Congress on Civil Engineering*, 8-10 May 2012, Isfahan University of Technology, Iran, 324-333 (In Persian)
12. Mays LW (2000) The role of risk analysis in water resources engineering. *Journal of Contemporary Water Research and Education* 103(1):8-12
13. Mollahosseini M, Mousavi S J, Salavitabar A (2012) Evaluation the effect of storage capacity creation to reduce flood damage using optimization-simulation system dynamics based model. *Proceedings of the 9th International Congress on Civil Engineering*, 8-10 May 2012, Isfahan University of Technology, Iran, 237-245 (In Persian)
14. Sharafati A, Zahabiyoun B (2014) Dam overtopping risk analysis considering hydrologic and hydraulic uncertainties. *Journal of Hydraulics* 8(1):1-18 (In Persian)
15. Sharafati A (2015) Jamyshan dam overtopping risk analysis using Monte Carlo simulation and precipitation threshold curve. *Journal of Hydraulics* 10(3):15-26 (In Persian)
16. Simonovic S P, Ahmad S (2000) System dynamics modeling of reservoir operations for flood management. *Journal of Computing in Civil Engineering* 14 (3):190-198
17. Sterman J D (2000) *Business dynamics System thinking and modeling for complex world*. Irwin, McGraw-Hill, MA, 982p
18. USBR (1992) *Freeboard criteria and guidelines for computing freeboard allowance for storage dams*. U.S. Department of the Interior, Bureau of Reclamation, 47p
19. Vali Samani JM, Radmehr H, Delavar M (2015) Uncertainty analysis and overtopping risk evaluation of Maroon dam with Monte Carlo and latin hypercube methods. *Journal of Water and Soil* 29(3):517-527 (In Persian)
20. Wang Z, Bowles D S, (2005) Dam breach simulations with multiple breach locations under wind and wave actions. *Journal of Advances in Water Resources* 29:1222-1237

Optimum characteristic compressive strength for cmds (case study: dasht-e-palang dam)

Ahmad Ghezel Ayagh¹, Abbas Mohammadian²

1- Managing Director, Abfan Consulting Engineers, Tehran, Iran

2- Project Manager, Abfan Consulting Engineers, Tehran, Iran

Email: absmmt@gmail.com

Abstract

Using Cemented Material Dams (CMD) is advantageous in a prospect that it allows construction of concrete dams on almost every foundation rocks including weak ones. For a successful design of this type of dams on weak rocks, more consideration is needed. Since stresses in dam body are proportional to modulus of rock and dam body, determining an optimum compressive strength (f_c) for material of dam body (named hardfill) is a major concern. Choosing low f_c means inadequate safety factor for stresses while choosing high f_c means high cost and thermal challenges for dam body. Stresses are dependent on dam and foundation's modulus of deformations and modulus of deformation itself depends on compressive strength of material, which in turn produces a loop that should be solved correctly in an optimum way. In this paper, a probabilistic approach to determine optimum and safe f_c is proposed. Hardfill material of Dasht-e-Palang dam is chosen as a case study and analyzed by this method to obtain an optimum compressive strength of hardfill. An applicable graph for CMD design with arbitrary height and symmetrical slopes is presented in this paper.

Keywords: CMD, Hardfill, FSHD, Optimum Cement, Probabilistic.

1. INTRODUCTION

Cemented Material Dam (CMD) is a type of Gravity Dam which includes Faced Symmetrical Hardfill Dam (FSHD), Cemented Sand and Gravel (CSG), Rockfill Concrete (RFC), Cemented Soil Dam (CSD) etc. A main branch of CMD is FSHD/CSG/CSGR. Western countries hardfill, Japanese CSG and Chinese CSGR are variations of the same basic concept. Dam body material of these three types is called "Hardfill". FSHD and CSG are very similar to each other. All mentioned types have been constructed and widely welcomed by the engineers all over the world. For the first time in IRAN, some CMD's are under construction, which are designed, and now are under supervision of construction by ABFAN Consulting Engineers Co.

As ICOLD anticipated in bulletin No. 117 dated 2000, this generation of Gravity dams are "the future dams" especially in under-developed countries. In IRAN, suitable dam sites with good foundation rock and good borrow materials have been selected for the previous hundreds of dams, and now the country faces severe conditions for selecting dam sites. CMD design concept, allows having a rigid (or gravity) dam body on almost every rock foundation even on very weak rocks and with low specific aggregates used in the dam.

Nowadays there is common understanding on how to distinguish hardfill from lean RCC. In CMD committee meeting at Johannesburg 2016, the main features of hardfill dams agreed as: "No tension governing in design, Quasi symmetrical shape, Range of UCS from 3 to 10 MPa, Sum of slope greater than one and Watertight upstream facing".

It is noted frequently that these kind of dams (in comparison with conventional RCC dams) have less challenges in design and construction, but "CMD on weak foundation" still needs more considerations for a successful design. For example, the "variations" of compressive strength of hardfill is more than RCC projects because the aggregates are not processed like RCC projects. It results in various and unknown value of modulus of elasticity of hardfill which results in unknown stress generation in structure. Determining characteristic compressive strength for hardfill dams is very important because it plays the main role in total cement usage. In this paper, a probabilistic approach to determine optimum compressive strength (and in other words, it may be used to calculate the optimum cement usage) for this type of dam is proposed.

2. STRESS ANALYSIS

At the first step of designing a gravity dam, stability is checked and the optimum geometry of dam is determined. Stress analysis is conducted in the second step. All stresses in dam body, considering various load

combinations, should be compared to allowable stresses. For each value of E_c or $E_{hardfill}$ (modulus of deformation for the dam body), a new stress distribution with respect to the load combination is obtained (figure 1.a). Note that stress values depend on ratio of $E_{hardfill}$ to E_{rock} foundation, but for simplicity we will consider E_{rock} foundation values equal to 1 GPa.

By performing finite element analysis for different values of $E_{hardfill}$ and finding the highest compressive stress generated in the structure (or transformed tensile stress to compressive stress) a fitted curve for input $E_{hardfill}$ against maximum compressive strengths can plotted (figure 1.b).

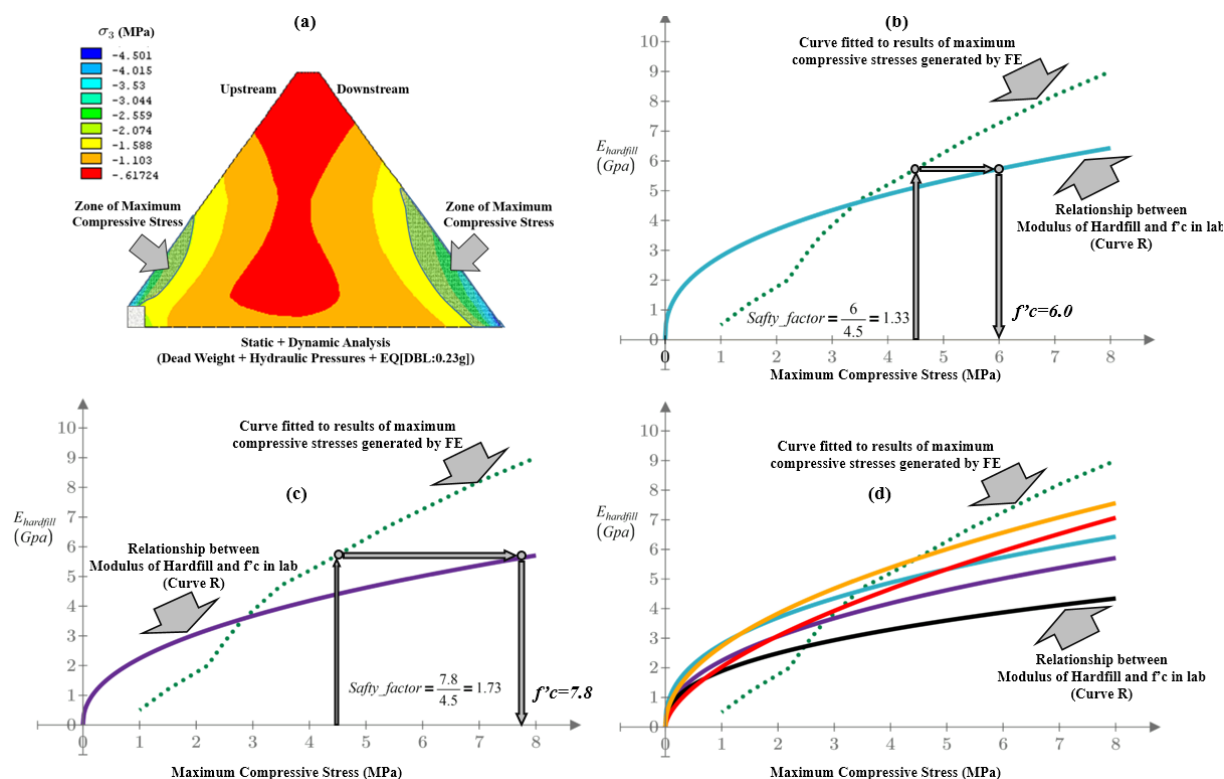


Figure 1. Modulus of deformation vs. compressive strength

Maximum required strength is the higher value between f'_t and f'_c where:

f'_t : Maximum required hardfill strength to withstand the tensile stress

f'_c : Maximum required hardfill strength to withstand the compressive stress

So it is needed to find the relationship between f'_t and f'_c of the hardfill material. Comparison between USBR formula and other practical references (Conrad 2006 [1]) shows a meaningful correlation between f'_t and f'_c which is: $f'_t = 0.2 \cdot f'_c^{0.8}$ (units in Mpa) (1)

On the other hand, each f'_c of hardfill material will produce an initially unknown $E_{hardfill}$. Assuming that this relationship is known as curve R in the figure 1. b, it is clear that intersection of these two curves may be the desired f'_c . Strengths lower than this value are not permitted and strengths higher than this value are uneconomical and will produce more heat and thus to increase potential for cracks in the structure. In addition, it should be noted that safety factors should be considered for stresses. For example, to determine the characteristic strength of hardfill, if a dynamic analysis is performed (using an unusual earthquake load), maximum compression stresses should be multiplied by a factor of 1.54. In this manner, a non-linear equation should be solved to find the optimum f'_c (figures 1.b and 1.c) that meets all the requirements for allowable stresses. For example, as shown in figure 1, when there is no fixed approved curve for relationship between E_c and f'_c of hardfill, each sample of hardfill material may generate a different curve, which in turn yields a different stress safety factor. The curve shown in figure 1.b has a safety factor of 1.33 which is lower than allowable safety factor (1.54) and the curve shown in figure 1.c has a safety factor of 1.73 which is upper than allowable safety factor. The challenge is how to find a minimum f'_c for hardfill that satisfies allowable safety factors?

3. PROBABILISTIC APPROACH

In this paper, it will be shown that, probabilistic approach is a proper way to find a minimum f'_c that satisfies allowable stresses for hardfill materials. Followings are considered to be affecting the results of this analysis:

- Relationship between f'_c and E_c in Lab tests
- Estimating modulus of “hardfill mass” of dam body
- Probabilistic parameters of rock foundation (mainly E of rock)

The formulation of probabilistic functions are as follows:

$$E_{mass} = f^* \left(f'_c, E_{rock}, \frac{E_m}{E_i} \right) \quad (2)$$

$$\sigma_{max} = g^* (E_{mass}) = g^* \left(f^* \left(f'_c, E_{rock}, \frac{E_m}{E_i} \right) \right) \quad (3)$$

$$\frac{f'_c}{\sigma_{max_i}} = Safety_factor_i \quad (4)$$

Further explanation on each item is presented in next sections.

4. RELATIONSHIP BETWEEN (f'_c) AND (E_c) IN LAB TESTS

Using Schrader’s [2] data (figure 2 right) for f'_c lower than 10 MPa, following relation to obtain the stress-strain curve for the hardfill material can drive:

$$E_c = 2700 \cdot f'_c{}^{0.5} \quad (\text{units in Mpa}) \quad (5)$$

Strain and creep properties of some laboratory RCC mixtures

Dam/project	Cement, lb-yd ³ (kg/m ³)	Pozzolan, lb-yd ³ (kg/m ³)	w/cm	Loading age, days	Creep coefficients		Compressive strength, psi (MPa)	Modulus of elasticity, 10 ⁶ psi (GPa)
					i/E	/iK		
Concepcion	152 (90)	0	1.20	7	1.14 (0.20)	0.12	640 (3)	1.40 (10)
	152 (90)	0	1.20	28	0.73 (0.11)	0.08	980 (7)	2.10 (14)
	182 (108)	210 (125)	0.47	28	1.05 (0.15)	0.11	2150 (15)	1.03 (7)
Upper Stillwater	129 (77)	286 (170)	0.43	28	0.66 (0.10)	0.04	2030 (14)	1.49 (10)
	129 (77)	286 (170)	0.43	180	0.57 (0.08)	0.01	4170 (29)	1.69 (12)
	121 (72)	269 (160)	0.45	180	0.62 (0.09)	0.02	3230 (22)	1.24 (9)
	182 (108)	210 (125)	0.47	365	0.57 (0.08)	0.02	4990 (34)	1.75 (12)
	121 (72)	269 (160)	0.45	365	0.57 (0.08)	0.01	4870 (34)	1.43 (11)
	182 (108)	210 (125)	0.47	90	0.84 (0.12)	0.06	3410 (24)	1.32 (9)
Willow Creek	129 (77)	286 (170)	0.43	365	0.53 (0.08)	0.02	5140 (35)	1.82 (13)
	182 (108)	210 (125)	0.47	180	0.67 (0.10)	0.05	4120 (28)	1.58 (11)
	80 (47)	32 (19)	1.81	7	1.97 (0.29)	0.20	580 (4)	1.20 (8)
	175 (104)	80 (47)	0.73	7	0.58 (0.08)	0.08	1150 (8)	2.40 (17)
	80 (47)	32 (19)	1.81	28	1.09 (0.16)	0.11	1170 (8)	1.59 (11)
	80 (47)	32 (19)	1.81	90	0.52 (0.08)	—	1730 (12)	1.91 (13)
Zantei Canyon	175 (104)	0	1.06	7	0.48 (0.07)	0.08	1000 (7)	2.20 (15)
	175 (104)	0	1.06	28	0.34 (0.05)	0.05	1850 (13)	2.67 (18)
	100 (59)	0	2.00	28	0.76 (0.11)	0.08	830 (4)	1.54 (11)
	100 (59)	0	2.00	90	0.47 (0.07)	—	1090 (8)	2.15 (15)
	100 (59)	0	2.00	365	0.39 (0.06)	—	1550 (11)	2.37 (18)
	200 (119)	0	1.00	7	0.76 (0.11)	0.05	990 (7)	1.54 (11)
200 (119)	0	1.00	28	0.45 (0.07)	0.03	1620 (11)	2.39 (16)	
200 (119)	0	1.00	90	0.40 (0.06)	—	2130 (15)	2.47 (17)	
200 (119)	0	1.00	365	0.30 (0.04)	—	3100 (21)	3.28 (23)	
100 (59)	0	2.00	7	1.43 (0.21)	0.09	280 (2)	0.68 (5)	

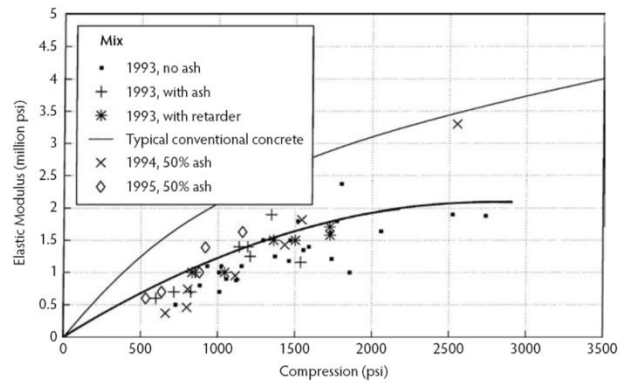


Figure 2. Elastic modulus at 25% of ultimate load vs. compression (left : ACI207 , right : Schrader [2])

It can be seen from figure 2 (right side) that conformity is poor. In addition, some samples of Kahir dam (the first CMD in Iran) have been used. The Kahir relationship is in the form of power regression but with low regression coefficient.

Using ACI records [3] gives higher amount of modulus, which could be stated by:

$$E_c = 4700 \cdot f'_c{}^{0.5} \quad (\text{units in Mpa}) \quad (6)$$

Therefore, probabilistic formulation can be assumed in the form of the following:

$$E_c := a \cdot f'_c{}^b \quad (7)$$

If there were enough tests that relates E to f^c , we could establish a probabilistic formula instead of fitting curve with low coefficient. Otherwise we may assume “a” as a random normal distribution with mean value equal to 3.5 and standard deviation value equal to 0.5 and “b” as a random normal distribution with mean value equal to 0.5 and standard deviation value equal to 0.05. These assumptions may cover the ACI and the Schrader formula with a probability of 95 percent.

5. PROPOSING A NEW METHOD FOR ESTIMATING MODULUS OF HARDFILL MASS

In hardfill dams, the modulus of mass body is lower than intact sample and it plays the main role in calculation of stress and its distribution. The authors of this paper propose to use rock mechanics approach for estimating modulus of hardfill bodies. In rock mechanics, there is a wide range of studies on how to relate intact modulus to mass modulus [4]. The basic theory is illustrated in figure 3. Most of the methods, apply a reduction factor to E_i (intact modulus) to obtain the E_m (mass modulus).

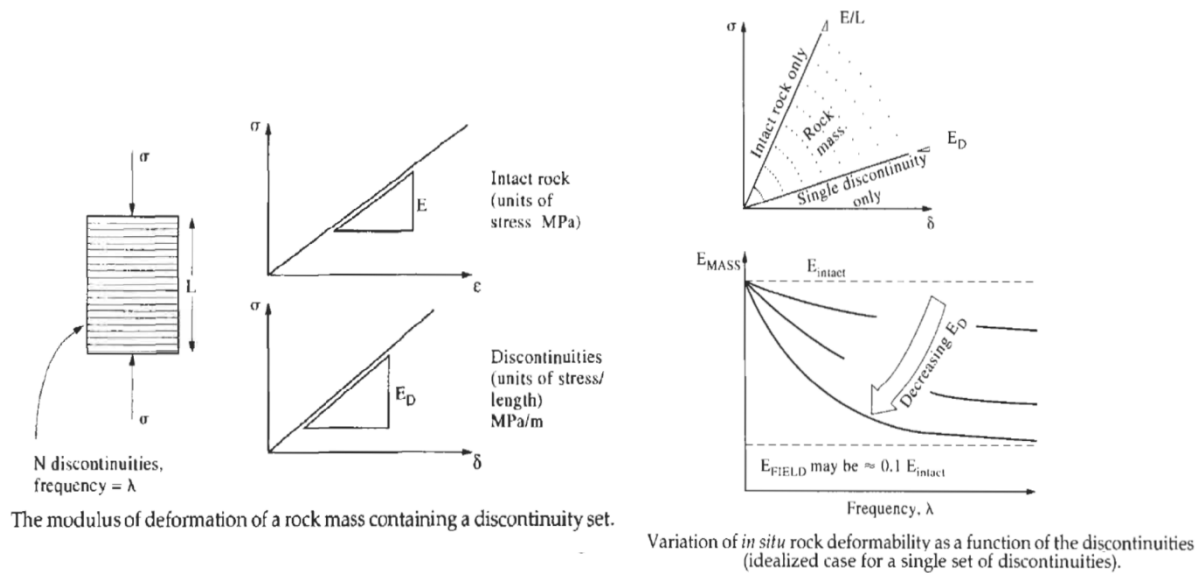


Figure 3. Variation of in situ deformability as a function of discontinuities

A simple relation, proposed by Bieniawski [5], relates the two moduli using RQD as follows:

$$E_m := E_i \cdot (10^{0.186 \cdot RQD - 1.91}) \tag{8}$$



Figure 4. Core samples of Kahir dam

Horizontal joints between layers of CMD are very weak (because we have no bedding mortar) and therefore RQD values are below 100%. For Kahir project, RQD of cores has a mean value of 85% (see figure 4

as an example). In this paper, a uniform random distribution of RQD between 70% to 100% for hardfill is assumed (see figure 5) and CQD term is used instead of RQD. Another method is relating the reduction factor to RMR, which in layered dam bodies relates it to RQD again.

$$\frac{E_m}{E_i} = \frac{1}{100} \cdot \left(0.0028 \cdot RMR^2 + 0.9 \frac{RMR}{22.82} \right) \quad (9)$$

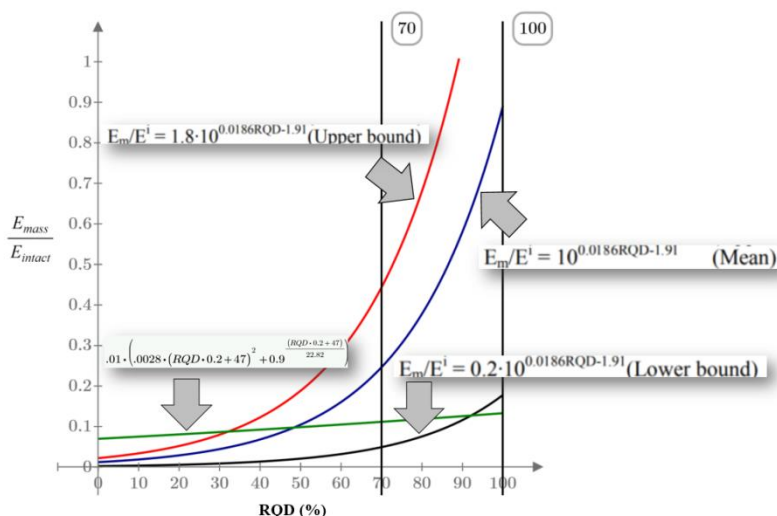


Figure 5. Upper bound, mead and lower bound of Bieniawski reallionship

6. USING MATHCAD TO PERFORM PROBABILISTIC ANALYSIS

Mathcad is an engineering math software that allows user to perform, analyze, and share mathematical calculations. Using Mathcad software for solving probabilistic equation, a simple written code should solve (a sample code is shown in figure 6). In this figure, “e” is the iteration, “af” and “bf” are the factors for fitted line in figure 1.a, which is derived from FEM analyses. The output of this code is density distribution of stress safety factors. To find the optimum f_c , we should change f_c as an input to find such a distribution of stress safety factors that has only 20% failures (accepted for many gravity dams). For example, if the minimum stress safety factor is 1.54 (for unusual earthquake load), we should change f_c as an input until the integral of distribution of stress safety factor curve is less than 20% (or any other value that is acceptable by designer).

```

stress :=
  for j ∈ 0 .. e
    CQD ← mean (runif (1, RQDmin + j · ε, 100 + j · ε))
    FBieniusky ← 10 · 0186 · CQD - 1.91
    q1 ← mean (rnorm (1, 0.5 · (maxErock + minErock) + j · ε,  $\frac{(maxE_{rock} + minE_{rock})}{2} \div (-2) + maxE_{rock} \cdot .5 + j \cdot \epsilon$ ))
    if q1 ≤ 0
      Erock ← 0.1
    else
      Erock ← q1
    q3 ← mean (rnorm (1, μa + j · ε, σa + j · ε))
    if q3 ≤ 0
      a ← 0.1
    else
      a ← q3
    for y ∈ 0 .. e2
      q2 ← mean (rnorm (1, μ + y · j · ε, σ + y · j · ε))
      if q2 ≤ 0
        Fcdesign ← 0.1
      else
        Fcdesign ← q2
      ffy ← Fcdesign
      Emassy ← ((a · Fcdesignb) ÷ Erock) · FBieniusky
    ffj ← mean (ff)
    Ej ← mean (Emass)
    stressj ← (af - bf) ·  $\frac{E_j - 6}{4}$  + bf
    SPj ← ffj ÷ stressj
  stress
  
```

Figure 6. A sample code to solving the probabilistic equation

7. CASE STUDY: DASHT-E-PALANG DAM

Dasht-e-Palang dam is under construction in Bushehr province on a river with the same name. Project objectives are providing drinking, industrial and agriculture water. The dam is a combination of gravity and earthfill dam (which the main part is CMD) with following specifications [6]:

- Maximum height: 56m
- CMD part crest length: 350m Earthfill crest length: 680m
- CMD part crest width: 4m Earthfill crest width: 8m
- Upstream and downstream slope of dam body: 0.7 h/ 1.0 v
- Hardfill volume: 540,000m³ CVC volume: 150,000m³
- Earthfill volume: 1,000,000m³

Design parameters of DASHT-E-PALANG dam are as follows:

Foundation rock modulus: 0.5-1.0 GPa (a normal probabilistic distribution for this parameter is used in the analysis)

Shear strength parameters of foundation: Ø=29°, C=0.14 MPa

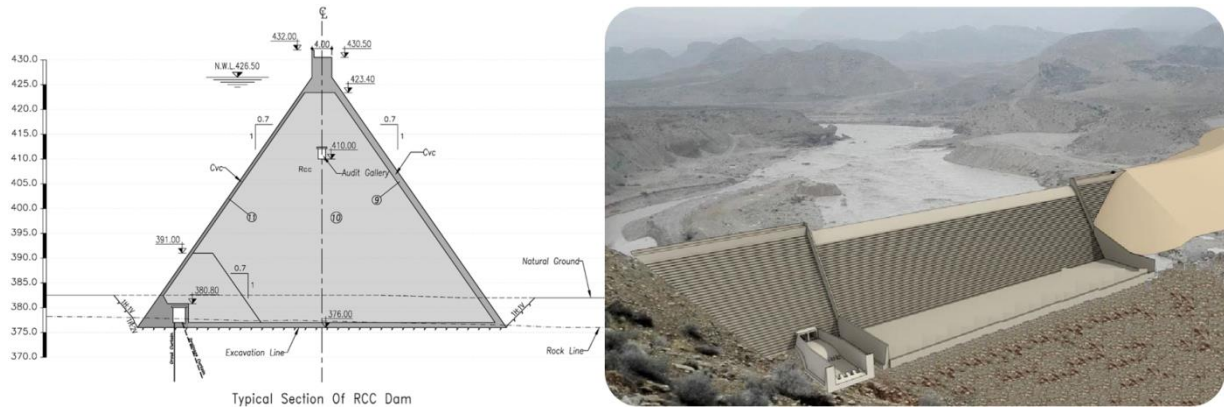


Figure 7. Dasht-e-Palang Dam (a combination of CMD & Earthfill)

Analysis, using probabilistic assumed and real data, will give us the following graphs (Figure 8). By trial and error, we will find that assuming a normal distribution for f'_c of samples in Dasht-e-Palang dam, with a mean of 7 MPa (known as f_{cr}) and a coefficient of variations of 30% (which means a standard deviation of 2.1 MPa) we will have a f'_c equal to $7 - 0.824 * 2.1 = 5.2$ MPa. After performing tests (to determining E in the lab), it is possible to estimate f'_c better. Note that after construction of dam body, it is possible to use the real distribution of compressive strengths to evaluate the safety of structure.

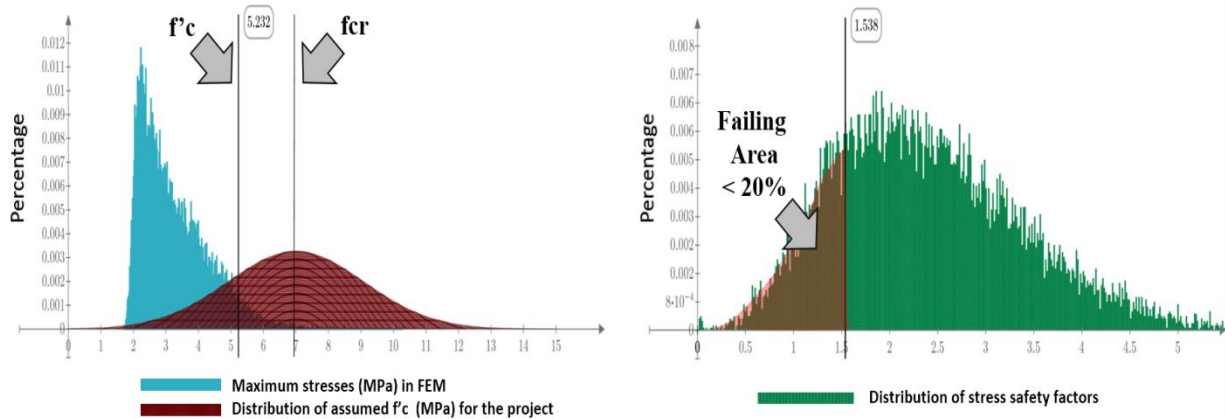


Figure 8. Dasht-e-Palang dam probabilistic analysis results

8. APPLICABLE GRAPHS

Using the method described here, a probabilistic relation between modulus of foundation and optimum f'_c can be acquired for each shape of the dam and following graphs (Figure 9) may produce.

On how to use the graphs, consider Dasht-e-Palang dam for example. If modulus of foundation rock is 0.8 GPa with dam slopes equal to 0.7h:1.0v, a characteristic compressive strength not less than 5.5 MPa must be selected.

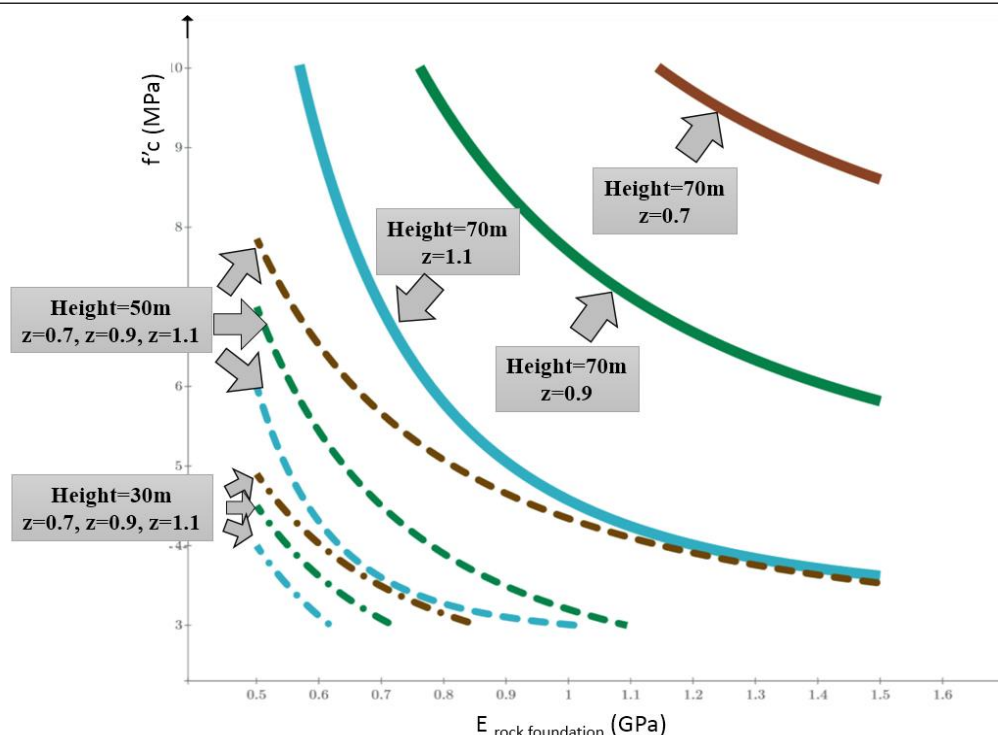


Figure 9. Relationship between modulus of foundation and optimum f'_c of Hardfill

9. CONCLUSIONS

There is not a reliable deterministic relationship between modulus of hardfill and f'_c . This relationship has an immense role in determining optimum f'_c for each project. Using probabilistic method on estimating modulus of samples with various f'_c , and estimating the “mass modulus” of dam body by methods proposed in rock mechanics and establishing a probabilistic distribution on rock modulus of deformation (if needed) a probabilistic distribution graph of stress safety factors can be produced. Using said graph, calculating the characteristic compressive strength of hardfill material with a desired reliability is possible. An applicable graph for designers, which shows the relationship between E_{rock} (modulus of deformation of foundation) and optimum f'_c (of hardfill of many CMD geometries), is presented in this paper.

10. ACKNOWLEDGMENT

We would like to give special thanks to Dr. M. Ghaemian for his excellent comments and Bushehr/S&B Regional Water Authorities (as the client of these projects) for their contributions.

11. REFERENCES

1. Conrad, M. (2006). "A contribution to the thermal stress behavior of Roller-Compacted-Concrete (RCC) gravity dams-field and numerical investigations." Techn. Univ., LWWII.
2. Schrader, E. (2008). "Roller-compacted Concrete." In E.G.Nawy, "Concrete Construction Engineering Handbook", CRC press.
3. ACI 207.5R-99, "Roller-Compacted Mass Concrete"
4. Hudson, J. A. (2008). "Engineering Rock Mechanics, an introduction to the principals", Pergamon.
5. Bieniawsky Z. T. (1989) "Engineering Rock Mass Classifications" John Wiley, New York.
6. Abfan Co. (2013). "Dasht-e-Palang storage dam", dam body report

Design experience on slope stability for rockfill dams, Turkey

Hasan Tosun

Professor, Eskisehir Osmangazi University, Turkey

Email: hasantosun26@gmail.com

Abstract

Turkey has a good practice in construction of embankment dams. Up-to now, 95 percent of all dams, which have been constructed by various organizations, are categorized into earthfill or rockfill dams. In this study, slope stability of seventeen large rockfill dams having a height of 70 m to 169 m from river bed were re-analyzed by means of software as based on material properties given in their planning reports. In the context of this study, there are large dams located on very active seismic regions as well as large dams on the sites having low seismic activity. Analyses includes end-of-construction stage for downstream and upstream slopes, rapid drawdown stage from maximum water level and gate level, operation stage for partly and fully storage, and earthquake stage for end-of-construction and operation stages. This study indicates that deviation on safety factors increases for the cases located on site having low seismic activity. For the area having low seismic activity, rapid drawdown case is more critical when considered upstream slope stability. In Turkish design practice, downstream slope is selected as little steeper than upstream slope for rockfill dams for usual cases.

Keywords: Dam, pseudo-static analysis, seismic coefficient and slope stability.

1. INTRODUCTION

Dams with large reservoirs pose a high risk for downstream life and property when they are built near urbanized area. Therefore, dams are considered as critical structures for public safety, designed, constructed and operated due to specific requirements. These structures must have design and construction measures for both static and dynamic loading conditions. Damages and failures resulted by recent earthquakes indicate that more conservative requirement should be considered for dams during design stage.

For an embankment dam, conventional slope stability analyses, which compare the forces and moments tending to cause instability of the mass with those tending to resist instability, are commonly used. Most procedures consider a two-dimensional (2-D) cross section and plane strain conditions for analysis. Successive assumptions are made regarding the potential slip surface until the most critical surface (lowest factor of safety) is found. All of the methods used for computing slope stability are termed "limit equilibrium" methods. In these methods, the factor of safety is calculated using one or more of the equations of static equilibrium applied to the soil mass bounded by an assumed, potential slip surface and the surface of the slope.

This study introduces design experience on slope stability of 17 rockfill dams constructed in Turkey. Seventeen large rockfill dams are considered and each of them was analysed by the Simplified Bishop method with considering actual soil properties and local conditions. Table 1 gives the list of dams and their physical properties. Dams considered for this study were selected from different regions of Turkey and their heights from river basin range from 70 m to 169 m. Their construction was completed and they were designed for different purposes such as irrigation, energy, flood control, domestic water and industrial use. Their total reservoir capacity changes within a wide range of 31 hm³ to 47 800 hm³. A general view from Akkopru dam considered for this study is given figure 1.

Table 1. The dams considered for this study and their typical properties.

Dam		River	Height from river bed (m)	Purpose (*)	Completed year	Embankment volume (hm ³)	Maximum reservoir volume (hm ³)
#	Name						
1	Adıguzel	B.Menderes	144	I+E+F	1990	7.13	1 076
2	Akkopru	Dalaman	113	I+E+F	2011	12.99	385
3	Akyar	Bulak	71	D	1999	2.93	56
4	Altunkaya	Kızılırmak	137	E	1988	16.00	5 763
5	Ataturk	Fırat	169	I+E+D	1992	84.50	48 700
6	Batman	Batman	73	I+E+F	2003	7.18	1 250
7	Derinoz	Derinoz	74	I	2003	3.25	19
8	Dicle	Maden	75	I+E+D	2001	3.10	595
9	Ikizdere	Ikizdere	101	I+D	2010	7.10	196
10	Kavsakkaya	Ovacayı	71	D	2007	4.70	90
11	Kığı	Peri	146	E	2017	23.00	1 200
12	Koprubasi	Mengen	108	E+F	2011	9.01	199
13	Kralkızı	Maden	113	I+E	1988	15.17	1 919
14	Ozluce	Peri	124	E	2000	2.14	1 120
15	Nilufer	Nilufer	74	D	2007	3.70	31
16	Uzunçayır	Munzur	70	E	2010	2.25	308
17	Vezirkopru	İstavloz	74	I	2005	2.57	52

(*) I:Irrigation E: Energy Production F:Flood Control D:Domestic Water

2. MATERIAL AND METHODS

The various limit equilibrium methods can be used for slope stability analysis of embankment dams [1, 2, 3, 4, 5]. They consider different assumptions to make the number of equations equal to the number of unknowns and also differ with regard to which equilibrium equations are satisfied. According to U.S. Army Corps of Engineers [6] the Ordinary Method of Slices, the Simplified Bishop Method, and the Modified Swedish Methods do not satisfy all the conditions of static equilibrium while methods such as the Morgenstern and Price's and Spencer's do satisfy all static equilibrium conditions [6]. Methods that satisfy static equilibrium fully are referred to as "complete" equilibrium methods. The slope stability analysis methods have been compared in detail in literature [7, 8, 9, 10].

Three main loading conditions are defined for static stability analyses of embankments dams. These are (1) construction conditions, (2) Steady-state seepage conditions and (3) Operational conditions. In the first stage, the end-of-construction condition is analyzed for a new dam. It can also be necessary to analyze stability for partial completion of fill conditions. According to USBR manual [11] the stability of the downstream slope is analyzed at the reservoir level that will control the development of the steady-state seepage surface in the embankment for steady-state seepage conditions. For operational conditions, the stability of downstream slope is analyzed under maximum reservoir loading while the upstream slope is analyzed for rapid drawdown conditions.



Figure 1. A general view from Akkopru dam considered for this study.

Slope stability analyses are made in terms of total and effective stresses. The USBR Manual states that the end-of-construction condition can be examined either by effective stress concepts or by undrained shear strength concepts [11]. The effective shear strength value is needed for the stability analysis for operational conditions. Author and his co-workers evaluate the shear strength of materials and their tests in detail and summarize the country design practice for embankment dam [12, 13, 14].

In slope stability analysis, the factor of safety is defined as the ratio of total available shear strength of the soil to shear stress required to maintain equilibrium along a potential surface of sliding. The factor of safety indicates a relative measure of stability for various conditions, but does not precisely indicate actual margin of safety [11]. Table 2 summarizes the minimum factor of safety (F_s) for each loading condition [6].

Table 2. The required safety factors for different loading conditions

Case	Description	Slope	Required Factor of Safety
I	End-of Construction	Downstream Upstream	1.3
II	Rapid drawdown	Upstream	1.1-1.3*
III	Operation	Downstream Upstream	1.4-1.5**
IV	Earthquake	For end-of Construction Downstream Upstream For operation Downstream Upstream	1.0

(*) $F_s = 1.1$ applies to drawdown from maximum surcharge pool

$F_s = 1.3$ applies to drawdown from maximum storage pool.

(**) $F_s = 1.4$ applies to operation from maximum surcharge pool

$F_s = 1.5$ applies to operation from maximum storage pool.

For the end-of-construction loading condition, a minimum factor of safety of 1.3 is adequate when the analysis is carried out in terms of total shear strength for both slopes. For rapid drawdown condition, a minimum factor of safety of 1.3 should be obtained when used minimal shear strength envelope. It is recommended for downstream slope that the minimum factor of safety should be 1.4 for maximum surcharge loading and 1.5 for condition having maximum water level. For earthquake loading condition a minimum factor of safety of 1.0 is

adequate according to Corps of Army Manual [6]. USBR Manual recommends a minimum factor of safety of 1.1 for earthquake loading conditions [11]. Tosun and Batmaz [12] evaluates the factor of safety concept and mentions the critical issues for stability analyses of embankment dams. In this study seventeen existing dams are considered and the slope stability analysis was performed for each dam by simplified Bishop Method for different loading conditions by means of professional software. For each loading condition a factor of safety is calculated. The minimum value of safety factor obtained from analysis was compared to obtain exceedance ratio for each dam.

3. ANALYSES

Evaluation of slope stability of dams was performed for four design conditions such as the end of construction, steady state seepage, sudden drawdown and earthquake loading. The first three conditions are static; the fourth involves dynamic loading. Summaries concerning the analysis of slope stability for the loading conditions are given in Table 3. In this table, I-U and I-D represents end-of construction conditions, while IV-D and V-U mean the operational stage conditions. II-U is the analysis for rapid drawdown conditions of upstream slope. Pseudo-static analyses were represented by four cases (I-DE, I-UE, IV-DE and V-UD). This table also introduces the seismic coefficient (k-value) for each dam.

The end-of-construction condition was examined by undrained shear strength concepts for all dams. For operational conditions the stability of the downstream slope was analyzed at the reservoir level that will control the development of the steady-state seepage surface in the embankment. However, the stability of the upstream slope was analyzed under partial reservoir loading condition. Effective shear strength parameters were considered for both slopes under operational conditions. For sudden drawdown, the effective shear strength parameters were considered at minimum case. For upstream and downstream slopes, pseudo-static analyses were performed for end-of construction and operational stages by considering a seismic coefficient. Seismic coefficient (k-value) was selected according the simplified method as based on the national earthquake map used before 2012.

The factor of safety values for end-of condition are too much greater than the required values. This study indicates that the values belonging to upstream slope are generally higher than those of downstream slope in Turkish design practice. Same evaluation can be made for operational conditions. For rapid drawdown conditions the calculated factors of safety provide safely the required value given in the specifications. Minimum factors of safety were obtained for all dams under earthquake loading conditions of operational stage (case of IV-DE and V-UD). The values of factor of safety range from 1.00 to 1.75 for downstream slope, while those are between 1.03 and 1.65 for upstream slope, as based on slope inclination and other physical conditions.

4. RESULTS AND DISCUSSION

This study indicates that most critical case is earthquake loading condition for rockfill dam with central core in Turkey. Table 4 shows the slope inclinations, which were considered in design stage for all dams, and the minimum values of safety factors, which were calculated throughout this study. This table also introduce exceedance ratio for each dam. The exceedance ratio means comparison between the actual and the required value given in the specification ($F_S = 1.1$). Its negative (-) value shows the calculated factor of safety which is less than that of required value.

Table 3. Safety factors of four loading conditions for each dam considered throughout the study

Dam		Güvenlik Sayısı*									Seismic coefficient,k
No	Name	I-U	I-D	II-U	IV-D	V-U	I-DE	I-UE	IV-DE	V-UD	
1	Adıguzel	2.50	2.29	2.01	2.14	2.05	1.54	1.70	1.41	1.16	0.15
2	Akkopru	2.46	2.06	2.23	1.70	2.24	1.39	1.69	1.0	1.25	0.17
3	Akyar	2.22	2.10	1.61	2.10	1.79	1.44	1.45	1.07	1.03	0.15
4	Altınkaya	1.71	1.62	1.52	1.55	1.52	1.47	1.55	1.40	1.31	0.04
5	Ataturk	1.94	2.01	1.78	2.00	1.88	1.66	1.61	1.65	1.39	0.07
6	Batman	2.83	1.66	2.25	2.32	1.69	1.59	2.13	1.57	1.40	0.04
7	Derinoz	2.40	2.82	2.22	2.38	2.00	1.71	1.47	1.42	1.31	0.17
8	Dicle	1.59	1.45	1.51	1.45	1.45	1.38	1.50	1.38	1.36	0.02
9	Ikizdere	2.60	1.57	2.37	1.53	2.38	1.23	1.47	1.02	1.26	0.20
10	Kavsakkaya	1.74	2.08	1.61	1.68	1.76	1.31	1.56	1.28	1.22	0.12
11	Kığı	2.19	2.08	2.01	2.09	1.98	1.39	1.44	1.00	1.20	0.15
12	Koprubasi	2.90	2.64	2.58	2.64	2.74	1.84	1.97	1.75	1.65	0.13
13	Kıralkızı	1.97	1.83	1.76	1.81	1.78	1.54	1.65	1.51	1.48	0.05
14	Ozluce	1.77	1.71	1.65	1.69	1.70	1.24	1.27	1.22	1.04	0.14
15	Nilüfer	2.12	2.41	1.83	2.49	1.88	1.63	1.36	1.32	1.11	0.20
16	Uzunçayır	2.63	2.15	1.60	1.64	1.68	1.51	1.76	1.15	1.07	0.13
17	Vezirkopru	2.09	2.00	1.76	1.86	2.26	1.56	1.65	1.20	1.43	0.10

- (*) I-U: End-of construction for upstream slope
I-D: End-of construction for downstream slope
II-D: Rapid drawdown for upstream slope
IV-D: Operation stage for downstream slope
V-U: Operation stage for upstream slope
I-DE: End-of construction for downstream slope with earthquake
I-UE: End-of construction for upstream slope with earthquake
IV-DE: Operation stage for downstream slope with earthquake
IV-UE: Operation stage for upstream slope with earthquake

In Turkish design practice, upstream slope has an inclination (Horizontal/ Vertical) of 1 /2.0 and 1 /2.5 for rockfill dam. Similar inclinations are considered for downstream slope. However, the inclination of downstream slope is little steeper than that of upstream for most of rockfill dams. It is not acceptable for the dams located on very active seismic region. Minimal values of safety factor were generally obtained for upstream slope of the rockfill dams considered for this study. The 65 percent of values for safety factor belongs to upstream slope, while others for downstream slope. The values of factor of safety take place within a wide range (1.04-1.65) for upstream slope, whereas the related values range from 1.00 to 1.20 for downstream slope. The variation for the values of upstream slope is very small. The exceedance ratio ranges from -9.1 to 50.0 percent for both slope. The negative values of exceedance ratio generally belong to downstream slope (% 67.7). It means that the downstream slope is more critical when considered earthquake loading conditions.

Table 4. Slope inclinations, minimum values for factor of safety and exceedance ratio for all dams considered throughout this study

Dam		Slope		Minimum value for factor of safety (calculated)		Exceedance ratio (%)
No	Name	Upstream (V/H) *	Downstream (V/H) *	Upstream slope	Downstream slope	
1	Adiguzel	1/ 2.25	1/ 2.0	1.16	-	5.5
2	Akkopru	1/ 2.5	1/ 2.0	-	1.0	-9.1
3	Akyar	1/3.0	1/ 2.5	1.03	-	-6.4
4	Altinkaya	1/ 2.2	1/ 1.9	1.31	-	19.1
5	Ataturk	1/ 2.2	1/ 2.2	1.39	-	26.4
6	Batman	1/ 2.5	1/ 2.0	1.40	-	27.3
7	Derinoz	1/ 3.0	1/ 2.5	1.31	-	19.1
8	Dicle	1/ 2.5	1/ 2.0	1.36	-	23.6
9	Ikizdere	1/ 3.25	1/ 2.0	-	1.02	-7.0
10	Kavsakkaya	1/ 2.25	1/ 2.0	1.22	-	10.9
11	Kigi	1/ 2.75	1/ 2.5	-	1.00	-9.1
12	Koprubasi	1/ 3.0	1/ 2.5	1.65	-	50.0
13	Kiralkizi	1/ 2.75	1/ 2.5	1.48	-	34.5
14	Ozluce	1/ 2.25	1/ 1.50	1.04	-	-5.5
15	Nilufer	1/ 2.0	1/ 2.0	-	1.11	0.9
16	Uzuncayir	1/ 2.75	1/ 2.5	-	1.07	-2.7

Table 5 summaries some physical properties and slope of impervious core materials for all dams throughout this study. In the table, group symbol and name of impervious material of each rockfill dam is given as based on the Unified Soil Classification. Author thinks that there is no a clear correlation between types of impervious core material and their slope. It can be stated that the inclination ratio of low plasticity clay and sand with low plasticity clay or silt is taken within a range of 0.33 to 0.50. However, it should be confirmed using by much data.

Table 5. Some physical properties and slope of impervious core material for dams considered for this study.

Dam		Height from river bed (m)	Impervious material used		Slope for impervious core	
#	Name		Group Symbol *	Group name	(H/V) **	Ratio (H/V)
1	Adiguzel	144	CL	Low plasticity clay	1 /2.15	0.47
2	Akkopru	113	SM-MH	Silty sand (high plasticity)	1 /4.0	0.25
3	Akyar	71	SC-CL	Clayey sand (low plasticity)	1 /2.0	0.50
4	Altinkaya	137	CL	Low plasticity clay	1 /2.0	0.50
5	Ataturk	169	CH-MH	High plasticity silt-clay	1 /2.5	0.40
6	Batman	73	CL	Low plasticity clay	1 /2.0	0.40
7	Derinoz	75	CH	High plasticity clay	1/0.66	0.67
8	Dicle	75	CL	Low plasticity clay	1 /2.0	0.50
9	Ikizdere	101	SC-CL	Clayey sand (low plasticity)	1 /2.0	0.50
10	Kavsakkaya	71	CL-CH	Low-high plasticity clay	1 /2.0	0.50
11	Kigi	146	CL	Low plasticity clay	1 /3.0	0.33
12	Koprubasi	108	CL-ML	Low plasticity silt-clay	1 /2.5	0.40
13	Kiralkizi	113	CH	High plasticity clay	1 /4.0	0.25
14	Ozluce	124	CL	Low plasticity clay	1 /3.0	0.33
15	Nilufer	74	CL	Low plasticity clay	1 /3.0	0.33
16	Uzuncayir	70	CL-CH	Low-high plasticity clay	1/3.0	0.33
17	Vezirkopru	75	CL-CH	Low-high plasticity clay	1 /2.0	0.50

(*) Unified Soil Classification System

(**) V:Vertical H:Horizontal

5. CONCLUSIONS

Turkey has at least 1250 large dams with different types. The ninety-five percent of them are constructed in embankment type. More than half of embankment dams has been designed in rockfill dams. Therefore, there is a good experience in designing and construction of this dam type in Turkey. This study concludes as follows:

- It seems that upstream and downstream slopes have an inclination (Vertical/Horizontal) of 1 /2.0 and 1 /2.5 for rockfill dam throughout country. However, the inclination of downstream is little steeper than that of upstream for most of rockfill dams. Author states that it is not acceptable for the dams located on very active seismic region.
- Designers consider more flat inclination for the rockfill dams located on seismologically active region or dams having high risk potential for downstream life and properties. Sometime, these unusual cases cannot be technically explained.
- There is no good experience on selecting the slopes of impervious core material as based on material type. It seems that the inclination ratio of low plasticity clay and sand with low plasticity clay or silt is taken within a range of 0.33 to 0.50. However, it should be confirmed using by much data
- The pseudo- static analyses of large dams considered for this study were performed as considering k-values based the simplified chart of National Map of Earthquake Regions. However, these dams should

be analyzed by considering actual seismic hazard analyses used updated seismo-tectonic data, under the context of National Dam Safety Program.

6. ACKNOWLEDGMENT

Author would like to thank former and actual authorities of General Directorate of State Hydraulic Works for their sincere supports.

7. REFERENCES

1. Bishop, A.W., (1955), “*The Use of the Slip Circle in the Stability Analysis of Slopes*” Geotechnique, V.5, No.1, 7-17.
2. Morgenstern, N.R. and Price, V.E., (1965), “*The Analysis of Stability of General Slip Surfaces*” Geotechnique, Vol.15.N0.1.
3. Spencer, E., (1966), “*A method of Analysis Assuming Parallel Interslices Technique*” Geotechnique, 17 (1), 11-26.
4. Janbu, N., (1973), “*Slope Stability Computation*” in Embankment Dam Engineering, Casagrande Memorial Volume, Wiley, New York, 47-86.
5. Lowe, J, (1988), “*Stability Analysis*” in Advanced Dam Engineering for Design, Construction and Rehabilitation (edited by R.B. Jansen), Van Nostrand Reinhold, New York, 275-285.
6. EM 1110-2-1902, (2003), “*Slope Stability*” Engineering and Design Manual, US Army Corps of Engineers.
7. Whitman, R. V., and Bailey, W. A. (1967), “*Use of Computers for Slope Stability Analysis,*” *Journal of the Soil Mechanics and Foundations Division, ASCE*, Vol 93, No. SM4, pp 475-498.
8. Wright, S. G. (1969), “*A Study of Slope Stability and the Undrained Shear Strength of Clay Shales,*” Thesis presented to the University of California at Berkeley, California, in partial fulfillment of requirements for degree of Doctor of Philosophy.
9. Duncan, J. M., and Wright, S. G. (1980), “*The Accuracy of Equilibrium Methods of Slope Stability Analysis,*” *Engineering Geology*, Vol 16, No. 1/2, pp 5-17.
10. Fredlund, D. G., and Krahn, J. (1977) “*Comparison of Slope Stability Methods of Analysis,*” *Canadian Geotechnical Journal*, Vol 14, No. 3, pp 429-439.
11. USBR, (1987), “*Static Stability Analysis*”, Design Standards No.13-Embankment Dams. US Bureau of Reclamation, Denver.
12. Tosun, H. ve Batmaz, S., (2007) “*Slope Stability Analysis for Embankment Dams and Critical Issues*” I. National Dam Safety with International Participation and Exposition, May 28-30, 191-202, Ankara,
13. Tosun, H., (2009) Lesson Notes for Earth Structures, Osmangazi University Civil Engineering Department, Master Science Level, Eskişehir, (unpublished).
14. Tosun, H., Karadag, A. ve Topçu, S. (2014), “*Main Requirements for Slope Stability of Embankment Dams and Turkish Practice*” IV. National Dam Safety with International Participation and Exposition, May 28-30, Oct. 9-13, Elazığ, 335-344.

Investigation of the leakage and maximum stress in plastic concrete cut- off wall with 100 centimeter width instead of clay core in static state on embankment dam's raz & jargalan

Ahmad Sedighian¹, Abbas Ali Ghezel Sooflo²

1- Civil Engineering Department, Faculty of Engineering, Khavaran Institute of Higher Education, Mashhad, Iran

2- Assistant Professor's, Civil Engineering Department, Faculty of Engineering, Azad Islamic University, Mashhad, Iran

Email: Ahmad.sedighian@yahoo.com

Abstract

The clay core rock fill dams have such a special place in the world. In this kind of dams, the implementation of their core and adjacent filters are placed in the critical path of dam construction. While the coarse grain shells are performable easy and quickly. Considering this fact, the possibility of replacing the clay core with other appropriate sealing material, has been studied. following the sealing plastic concrete dams has been widely used in the world if the use it as sealing element is less considered. Leakage has been the main reason failure in body and foundation and solution is cut-off wall. In this research plastic concrete seal's wall with 100 centimeter widths will be compered by clay core earth dam. Modeling Raz & Jargalan dam was conducted by ABAQUS software in north Khorasan. The result show the maximum stress value reduce in sealing cut-off wall and the stress values of authorized dam are lower and The use of proposed sealing cut-off wall reduce the amount of leakage by 66.6 percent which is significant.

Keywords: Clay core, ABAQUS, Plastic concrete, The maximum stress, Seepage.

1. INTRODUCTION

Storage dam was made for save and regulation of river run off in Raz & jargalan. Dam axis is located at the distance of about two kilo meter north of it. This river is permanent and the run off is 11.2 million cubic meters yearly. The fertile coast of shootout incurred huge losses from floods in Raz & jargalan yearly. [1]

So proper control of considered the agriculture and animal husbandry development, drinking water supply in it and addition to the control the destruction of river too. Technical specifications Raz & jargalan dam has been show in table 1.

Table 1- Technical specifications design dam Raz & jargalan [1].

Soil with clay core	Type of dam
920 m	Length of crest dam
8 m	Width of crest dam
1.1 million square meter	The total volume of body dam
23.5 m	Height of dam from river bed
30 m	Maximum thickness of alluvial river
1214 m	Balance of floor river
1233 m	Normal balance water surface of the lake
1237.5 m	Dam crest balance
263.5 m	Catchment domain space
74.8 kilo meter	Catchment domain environment

And the section of the dam is showing in figure.1

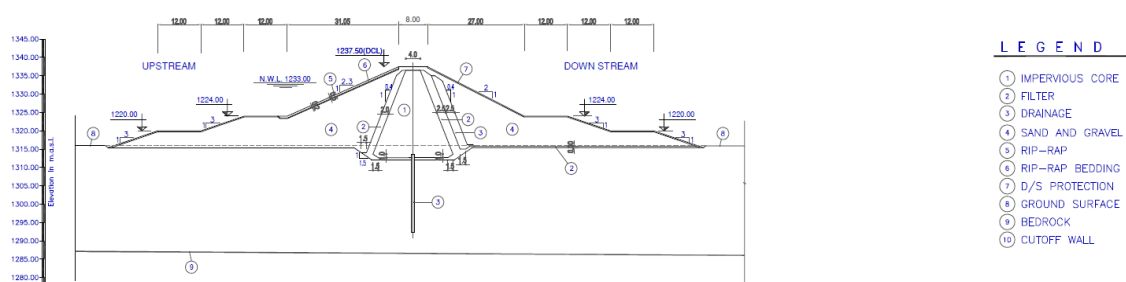


Figure 1. section of body type of the dam Raz & jargalan.[1]

2. SOFTWARE ABAQUS

This software by DASSULT-SYSTEMS American company was built as one the pioneers of finite elements software and researchers put it for took advantage fit and one of the first software that puts the non-linear analysis, fracture mechanics, reservoir and other analysis in its package. Powerful solvers and intelligent software, application has promoted research into industrial applications. Modeling and networking in this application is very simple, yet powerful simplicity the rational software. In Abaqus software, the graphical relationship between software and user is access and work with them is very simple. [2]

3. HOW MODELING ABAQUS SOFTWARE

Software on a regular foundation and dam with mesh and improved element is used modeling of this element is very simple. In this section to become familiar with the capabilities of the software and how can model to explain. It should be noted that all parts of the back wall of the dam because of the soil, with the logo that is hardly saturated soil behind the wall we modeling.

Building the dam wall is the same characteristics apply in both sealing and without it.

Material of dam: specification for various materials, including unclear dam, layouts, filters, gutters and wall of sealing are as shown in table 2.

Table 2- Elastic properties of dam's material. [3]

Vertical permeability (cms^{-1})	Horizontal permeability (cms^{-1})	Passion's ratio	Modulus of elasticity (kpa)	Density tm^{-3}	
10^{-6}	5^{-7}	0.48	22900	2	Clay core
4.62^{-2}	4.62^{-2}	0.2	40000	2.2	Crust
4.62^{-2}	4.62^{-2}	0.2	40000	2	Filter
4.62^{-2}	4.62^{-2}	0.2	40000	2	Drain
10^{-6}	10^{-6}	0.2	600000	2.1	Plastic concrete

4. BOUNDARY CONDITIONS

In Abaqus finite element mesh nodes boundary condition instead of applying to apply to the geometry of the assembly. The relationship between the assembly geometry, boundary conditions and the possibility of changing the mesh without the need to the re-define and extend the boundary conditions provides. After all nodes of the mesh model boundary conditions that apply geometric area. In the analysis of Raz & jargalan dam without cut-off wall proposed conditions for foundation bed is rigid. Boundary condition of bed foundation is encaster. The means that all degrees of freedom to apply for a place, pick a lock that is meant to be completely rigid. [2]

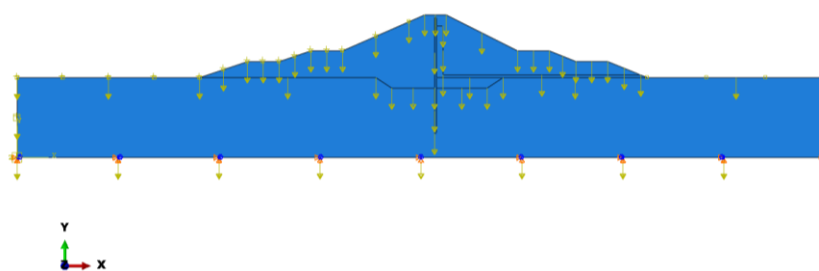


Figure 2. boundary condition on embankment dam without cut-off wall proposed 100 centimeter

In modeling, housing and dam foundation is modeled as two-dimensional as well as water level upstream dam wall is included in the model also. The four node element of CPE4P (fluid/stress) is used for modeling upstream and downstream shell, clay core, upstream and downstream filter and drain CPE4R (plain stress) the four-node element is used for modeling plastic concrete seal's wall. Embankment dam's mesh come by applying the seal's wall proposed and exterior f mesh on the seal's wall proposed respectively in figure 3 and 4. [4]

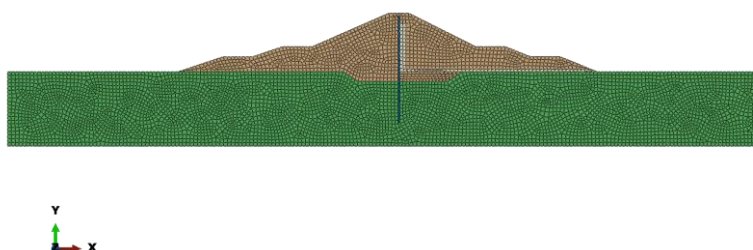


Figure 3. mesh finite element Raz & jargalan dam by method applied seal's wall 100 centimeter proposed

5. LEAKAGE ANALYSIS

The general equation of flow in a non-homogeneous soil masses in the absence of any power supply and discharge is as follow. This equation is known as the Richards equation.[5]

$$\frac{\partial \theta}{\partial t} = \frac{\partial}{\partial x} \left(k_x \frac{\partial h}{\partial x} \right) + \frac{\partial}{\partial y} \left(k_y \frac{\partial h}{\partial y} \right) + \frac{\partial}{\partial z} \left(k_z \frac{\partial h}{\partial z} \right) \quad (1)$$

Where H is water head and K_z , k_y , k_x are electrical conductivity of soil in direction z, y, x respectively, θ is moisture content of soil mass.

In steady-state condition, and for a state in which saturated soil masses change volumetric moisture content over time zero. Therefore, the above equation for a two- dimensional stream is summarized as follows:[6]

$$\frac{\partial}{\partial x} \left(k_x \frac{\partial h}{\partial x} \right) + \frac{\partial}{\partial y} \left(k_y \frac{\partial h}{\partial y} \right) = 0 \quad (2)$$

Where h is peysometric height. K_x permeability coefficient in direct x and k_y permeability coefficient in direct y.

The equation of intersection for a homogeneous environment is used by the equation above as the Laplace equation. Now we use Green's theorem: [7]

$$\int_{\Omega}^0 \nabla \cdot A \cdot d\Omega = \oint_{\Gamma}^0 A \cdot n \cdot d\Gamma \quad (3)$$

A: Unit vector Ω : Field of interest Γ : Boundary field n: Vertical unit perpendicular to the boundary.

By dividing the desired field. The problem is achieved by a set of polygonal elements using the Gales Keynes method.[7]

$$\int_{\Omega} \left(\frac{\partial h}{\partial x} \cdot \frac{\partial N_i}{\partial x} + \frac{\partial h}{\partial y} \cdot \frac{\partial N_i}{\partial y} \right) \cdot d\Omega = \oint_{\Gamma} \frac{\partial h}{\partial n} \cdot N_i \cdot d\Gamma \quad (4)$$

Whereas h in each element, the function is as follows:[8]

$$h = N_j \cdot h_j \quad (5)$$

The above relationship is as follows: [8]

$$\left\{ \int_{\Omega} \left(\frac{\partial N_i}{\partial x} \cdot \frac{\partial N_j}{\partial x} + \frac{\partial N_i}{\partial y} \cdot \frac{\partial N_j}{\partial y} \right) \cdot d\Omega \right\} h_j = \oint_{\Gamma} \frac{\partial h}{\partial n} \cdot N_i \cdot d\Gamma \quad (6)$$

In which according to Darcy low $\frac{\partial h}{\partial x} \frac{-v_n}{k_n}$ is the speed of perpendicular to boundary.

The above equation forms the basic of the finite element method in the leakage. This equation applies to each element, and then the relation of the final matrix of the assembly with the solution of the Laplace equation can be obtained by obtaining theoretical flow of water from the earth's dam under two-dimensional conditions.[9]

$$k_x \frac{\partial^2 h}{\partial x^2} + k_z \frac{\partial^2 h}{\partial z^2} = 0 \quad (7)$$

6. INVESTIGATION OF THE LEAKAGE IN PROPOSED SEALING CUT-OFF WALL INSTEAD OF CLAY CORE

In finite element method the geometry of the model is dividing into several elements connected to the nodes. The total fields within the flow region are approximated using the interpolation functions within each element. These functions intercept the amount of head in the nodes of the element. By solving an equation, we can calculate the flow through the body of the earth and dam. The accuracy of the answers depends on the number of elements used to approximate the continuous flow field.

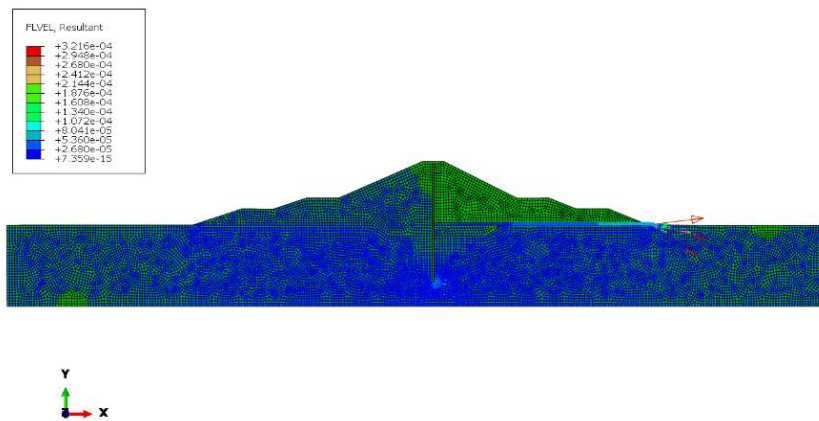


Figure 4. Distribution of water flow rate in the dam by applying sealing cut-off wall

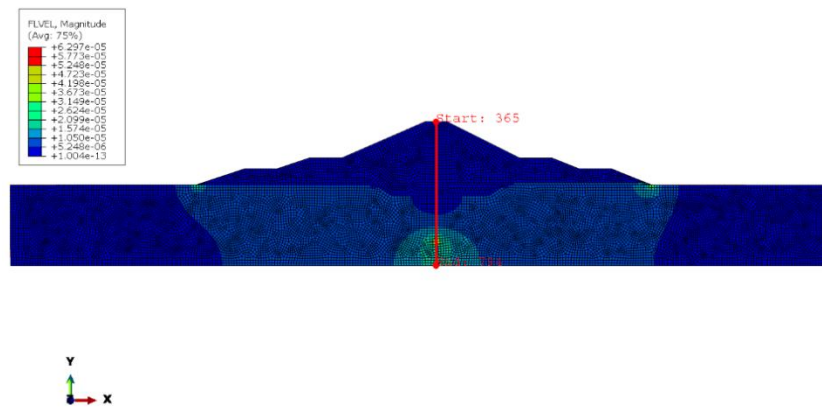


Figure 5. Selection section for calculating leakage value

As you can see in the figure above the amount of discharge with no action recommended cut off wall was 45000 cubic meter per year and by applying the proposed sealing cut-off wall this amount is reduced to 15000 cubic meter per year. The use of proposed sealing cut-off wall reduces the amount of leakage by 66.6 percent which is significant.

7. INVESTIGATE THE MAXIMUM PRINCIPLE CAUSED BY THE PROPOSED DAM ON THE WALL 100 CM

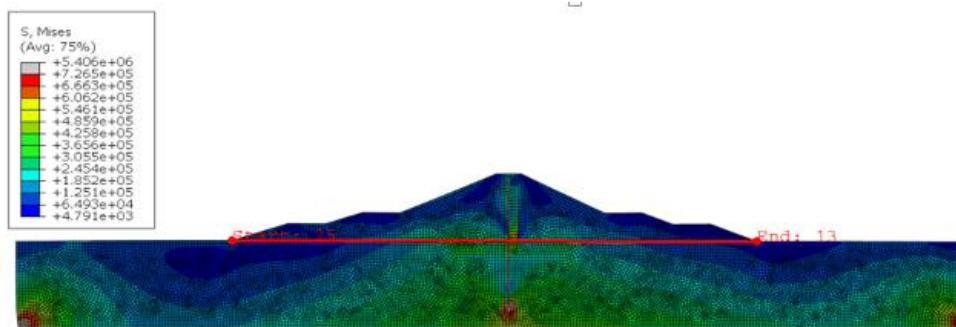


Figure 6. select section for check the maximum stress in the cut-off wall proposed 100 cm

The result show that the tension in the core of dam is more than of upstream and downstream shells. Because upstream of the dewatering tank that the shell is immersed.

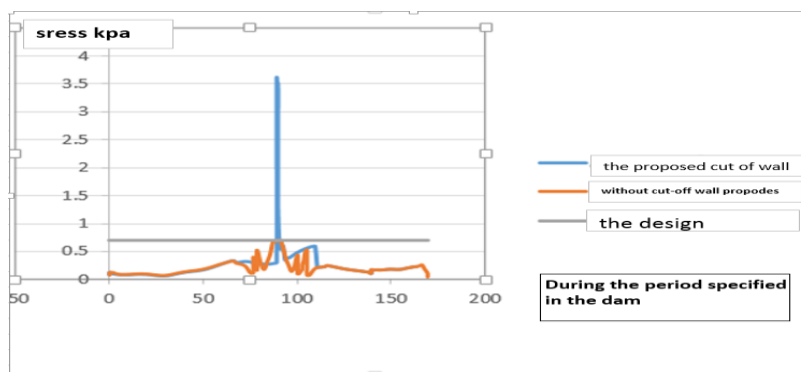


Figure 7. selectsection for check the maximum stress in the cut-off wall proposed 100 cm

As can be seen in figure 7, amount of the tension on the dam wall proposed is (3.7 M pa). that the amount is much higher than its actual value (0.7 M pa). so the dam wall proposed is not tolerated forces and defeat is inevitable.

9. DISPLACEMENTS

The vertical and horizontal displacements in this analysis are illustrated in figures 8 and 9. As you can see, upstream and downstream displacements of the dam are almost symmetrical. Maximum horizontal displacements in upstream are calculated as 12 centimeters and in downstream are calculated as 14 centimeters. The reason of this little difference in the horizontal displacements in downstream and upstream of the dam is the slope angle difference between the upstream and downstream shells. The vertical displacement in the center of dam reaches to maximum 75 centimeters. Stress-Deformation Modeling with Abaqus (2007)

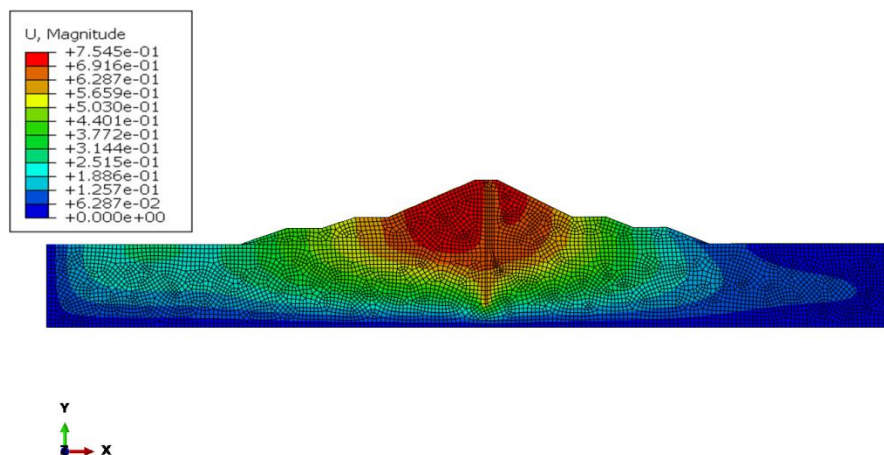


Figure 8. Total Vertical Displacements at the End of Construction Stage Considering the Sealing Wall Implementation up to the Crest Level

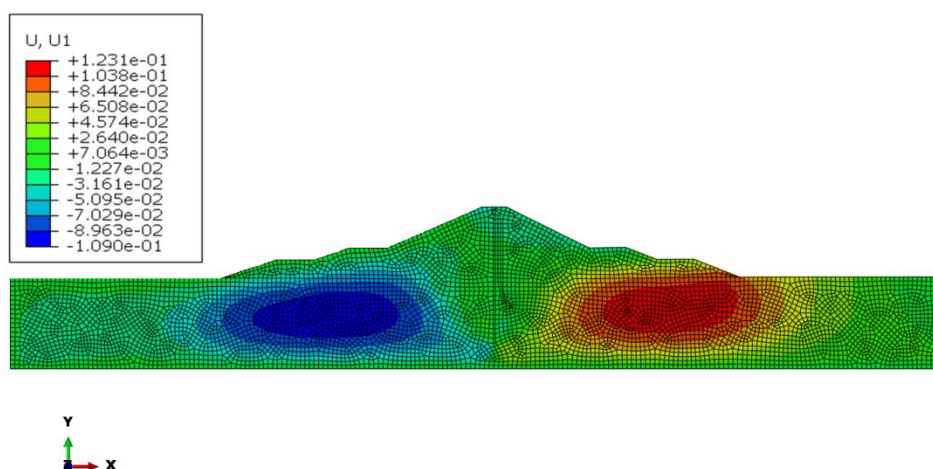


Figure 9. Total Horizontal Displacements at the End of Construction Stage Considering the Sealing Wall Implementation up to the Crest Level

10. CONCLUSIONS

The clay core rock fill dams have such a special place in the world. In this kind of dams, following the sealing plastic concrete dams has been widely used in the world if the use it as sealing element is less considered. Leakage has been the main reason failure in body and foundation and solution is cut-off wall. Performance of the plastic concrete seal's wall instead of clay core dam with 100 centimeter widths checked out by the finite element analysis of static load. The result show that the maximum stress value reduce in sealing cut-off wall and the stress values of authorized dam are lower.

The use of proposed sealing cut-off wall reduces the amount of leakage by 66.6 percent which is significant.

The replacement of the clay core with the plastic concrete sealing wall for the constructed dams on the subsiding alluvial foundation is not advised. The replacement of the clay core with the plastic concrete sealing wall for the constructed dams on the subsiding alluvial foundation is not advised.

11. REFERENCES

1. Maharab Consulting Engineers, (2007),” *Soombar Reservoir Dam, Technical report on Dam Body.*” Mashhad, Iran.
2. Abaqus Technical Brief. (2007),” *Construction Rapid Drawdown, and Earthquake Simulation of an Earthen Dam*”, TB-03-DAM-1.
3. Maharab Consulting Engineers, (2007),” *Soombar Reservoir Dam, Technical Report on alluvium Foundation.*”, Mashhad, Iran.
4. Stress-Deformation Modeling with Abaqus (2007). An Engineering Methodology, Third Edition.
5. Shivakumar, S. (2015),” *Seepage and Stability Analyses of Earth Dam Using Finite Element Method.*” International Conference on Water Resources, Coastal and Ocean Engineering. Aquatic Procedia 4, 876 – 883.2015.
6. Liu, Lie. Lie. and cheng, yung. meng, (2017),” *Effect of spatial autocorrelation structure of permeability on seepage through an embankment on a soil foundation.*” computer and Geotechnics 87, pp.62-75.
7. Kanchana, H.J. and Prasanna H.S, (2015),” *Adequacy of seepage analysis in core section of earth dam with different mix propprties.*” Aquatic procedia 4. 868-875
8. Owaga, Masaya. and kanie, shunji, (2017),” *Analysis of the seepage due to the thawing of permafrost, considering the gradient of the impermeable layer.*” procedia engineering 171, pp.469-475.
9. Carastoian, Andreea. (2016). “*Unsaturated Slope Stability and seepage analysis of a dam.*” Energy procedia 85, pp. 93-98

Evaluation of long-term settlement of ghoocham dam by numerical analysis

Hooman Rezaee¹, Hamidreza Hajihassani², Shahram Mahzarnia³

1- Rock mechanics engineer of Tahkimkav Consulting Engineers Company, Iran

2- Project Manager of Tahkimkav Consulting Engineers Company, Iran

3- Project Manager of Iran Water and Power Development Company, Iran

Email: Hooman.rezaee@mi.iut.ac.ir

Abstract

Ghoocham dam is 45 m height ECRFD type with a vertical clay core and soft alluvial and rock foundation under construction in west of Iran. To obtain the settlement distribution in dam body and foundation during different stages of construction, end of construction, first impounding and steady state, numerical analysis was conducted using a material behavior model including a combination of non-linear elastic Duncan and Chang model and elastic- perfectly plastic Mohr-coulomb. Numerical analysis was carried out by FLAC^{2D} which is explicit finite difference software. The material behavior model is implemented in numerical finite difference code, FLAC^{2D}, using its built-in fish language and plane strain analysis carried out to obtain deformations and stresses within dam body and foundation. The results show that the distribution of settlements of dam body and foundation are in acceptable ranges.

Keywords: rockfill dam, hyperbolic model, non-linear behavior, soft foundation, numerical analysis.

1. INTRODUCTION

Dams play a significant role in fulfilling the increasing demand of water for municipal and agricultural purposes. Embankment dams have become very popular among dam engineers since available materials of different types at the site could be used in appropriate zones of dam. Safety of rockfill dams depends on the proper analysis, design, construction and monitoring of actual behavior during the construction and the operation of the structure. The deformations in dam body and foundation are a crucial consideration in the design and construction of earth dams. Geotechnical analysis using numerical methods requires the implementation of material non-linear models for better prediction of structure behavior. In numerical analysis constitutive modeling of soil and rock mass is an essential component. Elastic- perfect plastic Mohr-coulomb and hyperbolic model are the most common constitutive models for predicting the behavior of foundation and dam body. Ghoocham dam is an ECRFD type which is under construction in west of Iran. In this paper, to obtain the deformation in dam body and foundation, numerical analysis was conducted by a combination of non-linear elastic Duncan and Chang model and elastic-perfectly plastic Mohr-coulomb constitutive model.

2. GEOMETRY

Ghoocham dam is an ECRD with vertical clay core material with 45 m height. The length of dam crest is 1820 m at the elevation 1856 m.a.s.l. The slopes of both dam abutments are gentle, around 12%-15% and 600 m of the central part of dam foundation is almost flat. Upstream and downstream slopes of rockfill shell are 1:1.7 and 1:1.5 (V:H), respectively. The slope of central core is 1:0.35(V:H).

Due to weak rock foundation, two stabilizing berms at upstream and downstream of dam with 70 m width have been designed in central part of dam. At maximum height section of dam, two 3 m and 2 m width fine filter and transition zone are considered at both upstream and downstream of core with the same slope of central core. Figure 1 shows the typical cross section of Ghoocham dam. Shell materials are obtained from two limestone and andesite-bazalt quarries close to the dam site. Materials for zones 4, 5A, filter and transition are obtained from limestone quarry and material for zones 4A and 4B are from andesite-bazalt quarry. Zone 7 material is from mandatory excavation of fine alluvial and rock foundation of dam body. Foundation of dam consists of 4-14 m thickness alluvial material and weak rock of tertiary quaternary unit of sanandaj-sirjan zone underneath. Fig. 1 shows the typical cross section of Ghoocham dam.

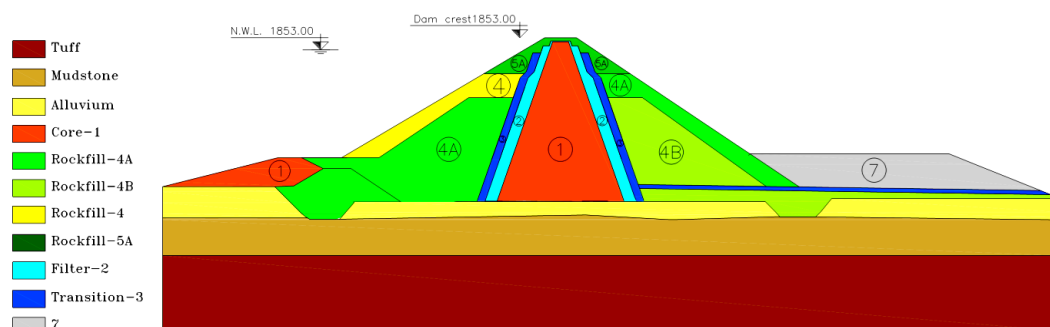


Fig 1. Typical cross section of Ghoocham dam

3. FOUNDATION AND DAM BODY MATERIAL

3.1. OVERBURDEN AND FOUNDATION

The overburden of Ghoocham site with 4-14 m thickness consists of alluvial, slopewash and residual soils. The type of soil is majority silt, clay with thin layer of sand and gravel. The Consistency of overburden is classified as stiff to hard based on standard penetration test (SPT). A complete set of site and laboratory tests have been performed on these materials. Summary of overburden material parameters is shown in table 1.

Table 1. Geomechanical parameters of overburden.

Materials	γ_d (kg/m ³)	E (MPa)	ν	C (KPa)	ϕ	k (cm/sec)
Alluvium	1800	10 – 40	0.25	34	19	3×10^{-7}

Rock types of foundation at Ghoocham dam site are mudstone, tuff and weak conglomerate. The average of rock quality designation (RQD) of rock is 81. The different types of foundation rock parameters are shown in table 2. Based on this table, the cohesion of rock is 40-50 KPa, internal friction angle is 22-25 degree and deformation modulus ranges between 470-800 MPa. The permeability of rock is around 3×10^{-7} cm/s.

Table 2. Geomechanical parameters of dam foundation.

Materials	γ_d (kg/m ³)	E (MPa)	ν	C (KPa)	ϕ	k (cm/sec)
Tuff	2400	470	0.3	40	22	3×10^{-7}
Mudstone	2180	800	0.3	50	25	3×10^{-7}

3.2. DAM BODY MATERIAL

Clay material of central core has been obtained from 0.5-1.5 Km upstream borrow areas in dam reservoir. The Core material is classified as CL based on unified classification, average PI of material is 22 and compacted with 2-3 percent moisture more than optimum water content. The maximum size of core material aggregates is 25 mm. fine and coarse filters at both upstream and downstream of core zone are processed from limestone quarry. D_{15} of fine filter is 0.45 mm with 10 mm maximum size aggregate (MSA). The MSA of coarse filter is 50 mm. The upstream outer shell zone (zone 4) and upper elevation shell (5A) are from limestone quarry. The other shell zones (4A & 4B) are andesite-bazalt type rock from basalt quarry. The layer thickness of zones 4, 4A and 4B is 60 cm. The maximum percent of passing sieve no.200 for zones 4 and 4A materials is 5 percent and for zone 4B material is 15 percent. The filling of shell zones has been done with wet procedure. A complete series of laboratory tests including large scale triaxial, shear and index tests performed on shell materials.

4. NUMERICAL ANALYSIS

The numerical analysis for different stages of during construction, end of construction, first impounding and steady state were carried out through the finite difference code FLAC^{2D}. The ratio of crest length to dam height is high enough to permit a two dimensional plane strain analysis. The analysis is performed in a layer by layer construction in effective stress condition. The seepage analysis in parallel to deformation analysis simulates the real condition of saturated soil materials behavior and consolidation process. Many researchers have proposed various constitutive models to simulate the behavior of rock and soil [1-5]. The Studies have shown that most of soil materials show non-linear behavior under different stages of loading [3,6-9]. Regarding the non-linear behavior of soil material, it's necessary to use a non-linear constitutive model in numerical analysis. One of the most prevalent non-linear constitutive models is Duncan & Chang. The hyperbolic model proposed by Duncan & Chang (1970), has been vastly used to predict non-linear behavior of soil materials [3]. In a hyperbolic constitutive model, the elastic modulus (E) changes relates to confining pressure and has an increasing trend with increasing confining pressure. The relationship between the deviatoric stress and axial strain for a constant confining pressure is described as:

$$\sigma_1 - \sigma_3 = \frac{\varepsilon}{\frac{1}{E_i} + \frac{\varepsilon}{(\sigma_1 - \sigma_3)_{ult}}} \quad (1)$$

E_i = initial tangent modulus, ε = axial strain, $(\sigma_1 - \sigma_3)_{ult}$ = ultimate deviatoric stress at large strain. σ_1 and σ_3 are the maximum and minimum principal stresses, respectively. Based on above equation, the young modulus (E) is defined as non-linear function of stress level and confining pressure. Therefore, the tangential Young modulus of elasticity (E_t) can be determined as:

$$E_t = [1 - R_f S_1]^2 K_{pl} P_a \left(\frac{\sigma_3}{P_a}\right)^n \quad (2)$$

Where R_f , S_1 , P_a , σ_3 are failure ratio, stress level, atmospheric pressure (Kpa), confining pressure and K_{pl} , n are non-dimensional parameters.

Stress level (S_1) is a ratio between the deviatoric stress level and the failure stress level. The failure ratio and the stress level are defined as:

$$S_1 = \frac{\sigma_1 - \sigma_3}{(\sigma_1 - \sigma_3)_f} \quad (3)$$

$$R_f = \frac{(\sigma_1 - \sigma_3)_f}{(\sigma_1 - \sigma_3)_{ult}} \quad (4)$$

Where $(\sigma_1 - \sigma_3)_f$ is deviatoric failure and it is expressed by the Mohr-Coulomb failure envelope as function of the friction angle (ϕ) and the cohesion (C).

$$(\sigma_1 - \sigma_3)_f = \sigma_3 (N_\phi - 1) - 2c \sqrt{N_\phi} \quad (5)$$

$$N_\phi = (1 + \sin \phi) / (1 - \sin \phi) \quad (6)$$

$$\phi = \phi_0 - \Delta\phi \cdot \text{Log} \left(\frac{\sigma_3}{P_a}\right) \quad (7)$$

Where ϕ is the friction angle and ϕ_0 is the friction angle of soil at atmospheric pressure [3,10,11].

The Duncan & Chang hyperbolic model couldn't predict elasto-Plastic behavior of soil [10], therefore the Mohr-Coulomb constitutive model is implemented to predict plastic behavior of soil and calculate plastic strains. Thus, the constant elastic modulus in the Mohr-Coulomb model is modified based on hyperbolic model and is replaced with the tangential modulus presented in Duncan & Chang model. Equations of the proposed model have been implemented in the numerical finite difference code FLAC^{2D} using its built-in FISH language for the constitutive model. Then the model used for soil materials behavior of the dam body to calculate the deformation during different stages of loading. Due to stress distribution, the dimension of geometrical model has been considered 320×82 m (L×H). Construction stage analysis was conducted layer by layer with a thickness around 2 meters for each layer. Aanalysis was performed based on effective stress approach along with water flow analysis to determine pore pressure within core and foundation zones. The analysis duration for each layer is set according to the dam construction time schedule.

In the analysis, the parameters of constitutive model have been assumed as table 1 to 3. These parameters have been obtained by in-situ and laboratory tests. The constitutive models of dam body and foundation are the combination model and the Elasto-plastic Mohr coulomb model, respectively.

Table 3. Material parameters of dam body for the analysis

Material/Zone	γ_d (kg/m ³)	K_p	N	R_f	ν	C (KPa)	ϕ	K(cm/sec)
Core	1650	125	0.56	0.87	0.35	41	28.8	$7 \cdot 10 \times 4$
Filter	1900	250	0.7	0.8	0.25	0	38	$3 \cdot 10 \times 1$
Rockfill (4)	2150	147	0.88	0.83	0.25	38	43	$5 \cdot 10 \times 1$
Rockfill (4A)	2150	631	0.4	0.86	0.25	0	43.2	$5 \cdot 10 \times 1$
Rockfill (4B)	2150	891	0.73	0.81	0.25	0	43.2	$5 \cdot 10 \times 1$
Rockfill (5A)	2150	147	0.88	0.83	0.25	38	43	$5 \cdot 10 \times 1$
Zone 7	1900	170	0.8	0.7	0.25	30	30	$5 \cdot 10 \times 1$

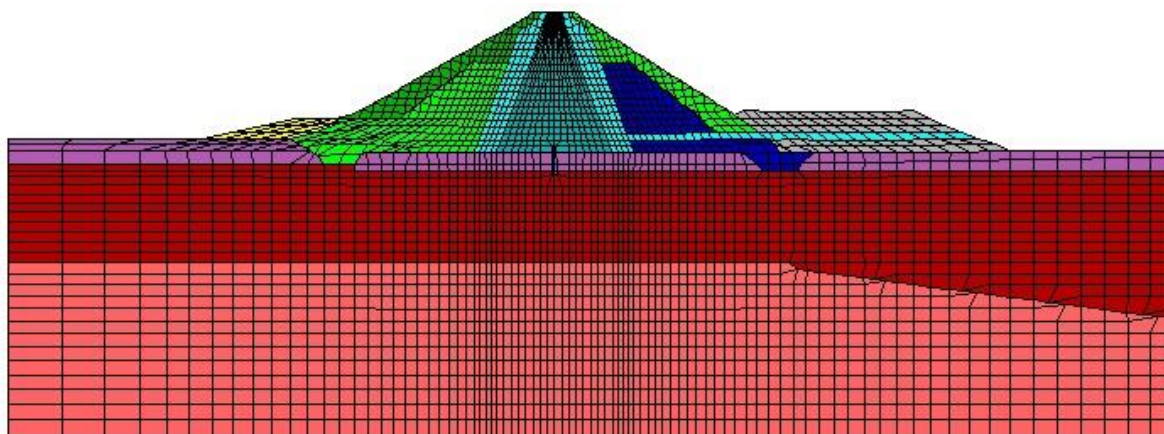


Fig 2. Finite difference mesh of Ghoocham dam body and foundation

4.1. CONSTRUCTION STAGE ANALYSIS

At first stage, the stress- deformation analysis has been conducted up to elevation 1849 (m.a.s.l.). By comparison the measured settlement and instrumentation data with analysis results, the numerical model has been calibrated. To verify the calibrated model, the settlement of diversion system under the dam body has been measured at different time intervals and compared with the numerical results. The maximum settlement has been reported 40 cm at embankment elevation of 1849 (m.a.s.l.) equal to 38 m dam height. At next step, the stress- deformation analysis for end of construction stage has been done up to dam crest elevation (1856 m.a.s.l.), then the first impounding and steady state analysis have been carried out and stress and settlement distribution have been computed.

The vertical and horizontal displacements are illustrated in Fig. 1 and Fig. 2. The maximum settlement and horizontal displacement in dam body are 73 cm and 17 cm. Fig. 6 shows foundation settlements profile along pipes of diversion system, in the vicinity of pipes the maximum settlement happened in upstream and it's equal to 41 cm. Compared the numerical results with reported settlements shows the suitability of calibrated model to predict dam body and foundation deformations. Due to the cut off wall the settlement in the axial of dam is lower than another area.

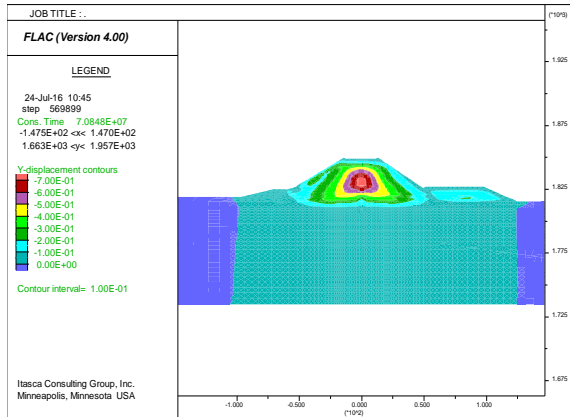


Fig 3. Vertical displacement contours (m)

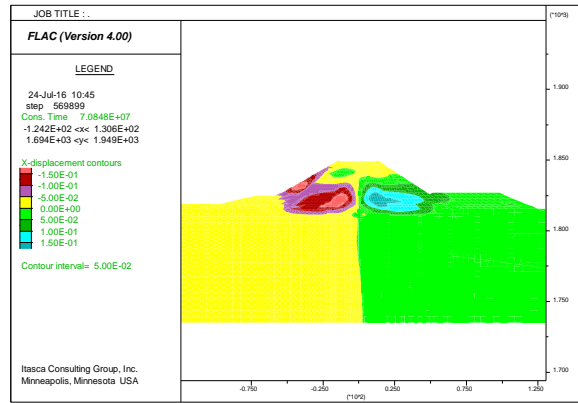


Fig 4. Horizontal displacement contours (m)

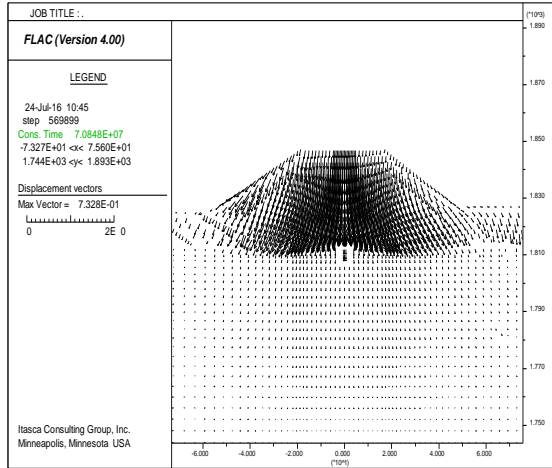


Fig 5. Displacements vectors (m)

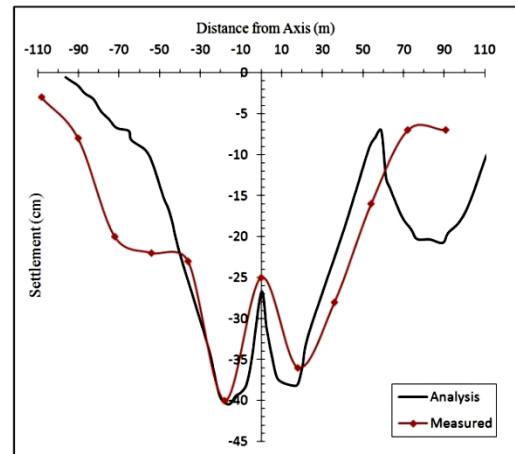


Fig 6. Settlements profile along pipes of diversion system (cm)

4.2. END OF CONSTRUCTION ANALYSIS

Construction stage analysis was conducted layer by layer. The settlement and the horizontal deformation contours and vector are presented in Fig. 7 and Fig. 8, respectively. It can be seen that the maximum settlement in dam body is 97.5 cm occurs in middle height of core zone and maximum horizontal displacement is 22 cm. Fig. 9 shows the displacement vectors, as shown with increase embankment elevation the shells moved toward upstream and downstream. Fig. 10 shows foundation settlements profile along pipes of diversion system. As shown, the maximum settlement of foundation along the pipes is equal to 45 cm at end of construction stage.

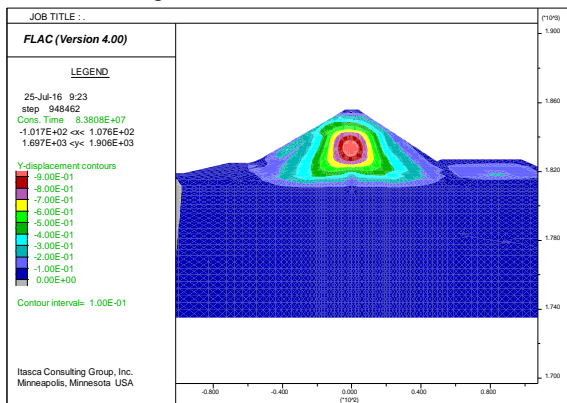


Fig 7. Vertical displacement contours (m)

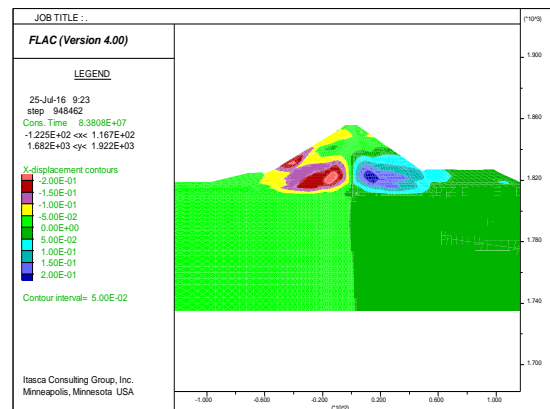


Fig 8. Horizontal displacement contours (m)

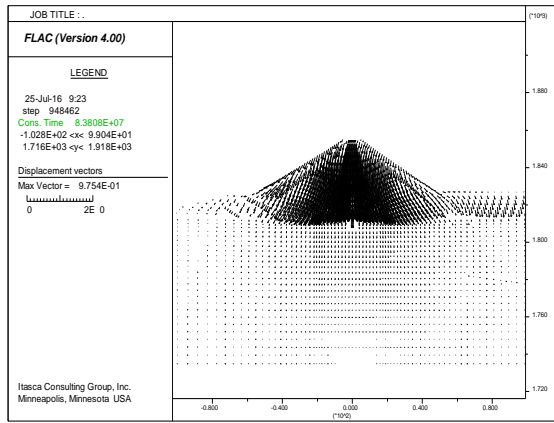


Fig 9. Displacements vectors (m)

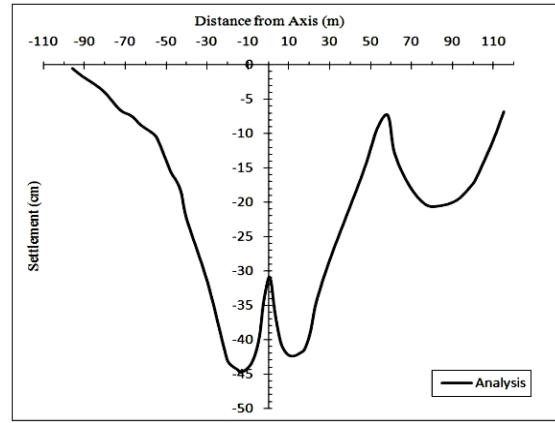


Fig 10. Settlements profile along pipes of diversion system (cm)

4.3. FIRST IMPOUNDING STAGE

The first impounding and steady state are the most important stages of dam construction. Increasing the water elevation in reservoir leads to horizontal and vertical displacements in dam body and foundation. In order to predict the dam behavior, the numerical analysis has been conducted using the parameters same as construction stage. Impounding duration up to normal water elevation (1853 m.a.s.l.) has been assumed 2 months. The vertical and horizontal displacements contours are illustrated in Fig. 11 and Fig. 12. The maximum settlement and horizontal deformation of dam body at this stage are 108 cm and 46 cm respectively. As shown in Fig. 13 the reservoir water pressure leads to horizontal deformation toward the downstream and settlement in dam body and foundation. Fig. 14 shows the foundation settlements profile along pipes of diversion system. The maximum settlement along the diversion system is 52 cm.

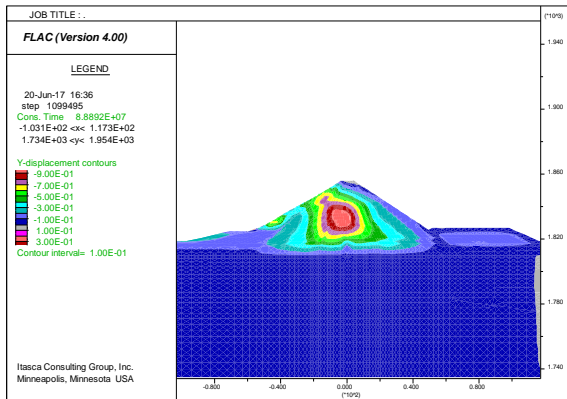


Fig 11. Vertical displacement contours (m)

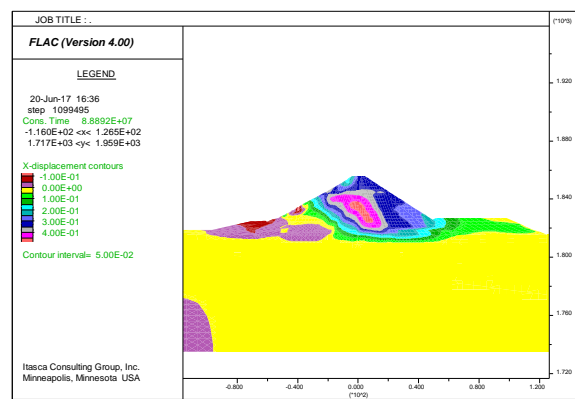


Fig 12. Horizontal displacement contours (m)

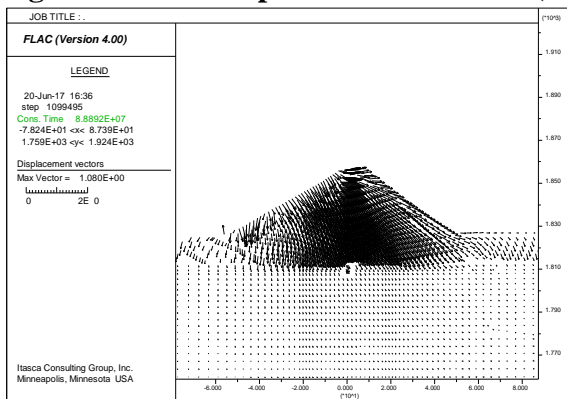


Fig 13. Displacements vectors (m)

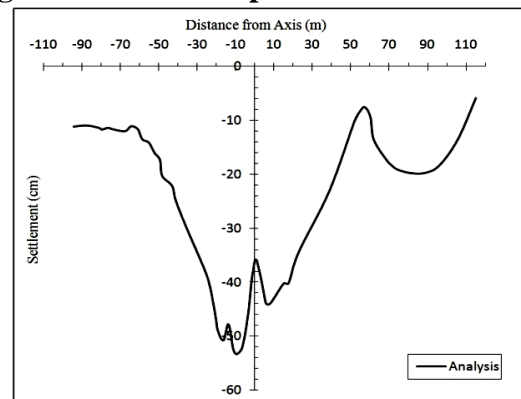


Fig 14. Settlements profile along pipes of diversion system (cm)

4.4. STEADY STATE STAGE

At the steady state stage, the pore pressure in low permeability zones begins to dissipate and long term deformations and consolidation settlements occur. The duration of this stage in numerical analysis assumed 180 months. The vertical and horizontal displacements are illustrated in Fig. 15 and 16. The displacement vectors of dam body s illustrated in Fig. 17. The maximum settlement and horizontal displacement include immediate and consolidation settlements in dam body are 110 cm and 49 cm, respectively. Fig. 18 shows the foundation settlements profile along pipes of diversion system. The maximum settlement in foundation along the diversion system is 52 cm.

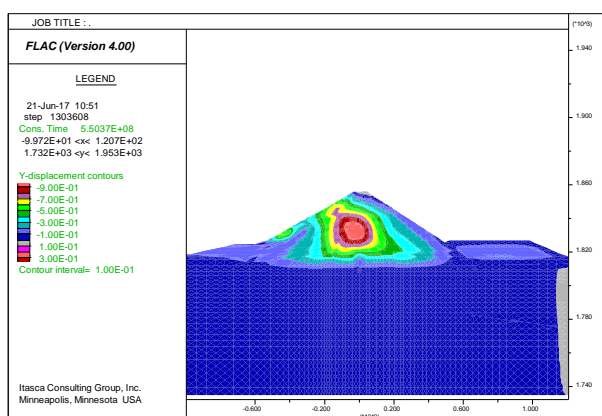


Fig 15. Vertical displacement contours (m)

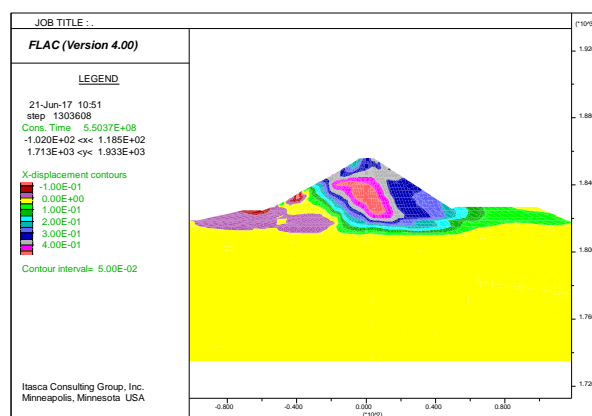


Fig16. Horizontal displacement contours (m)

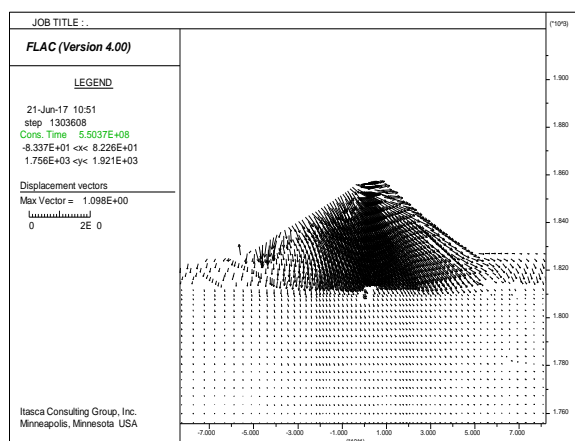


Fig 17. Displacements vectors (m)

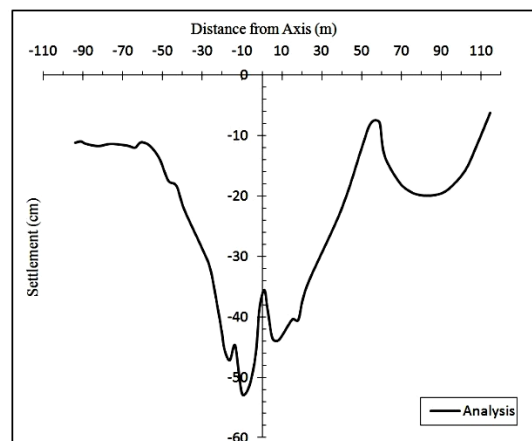


Fig 18. Settlements profile along pipes of diversion system (cm)

5. CONCLUSIONS

To obtain the long term settlements of dam and foundation, numerical analysis has been conducted. Based on experience and laboratory test results, a combination of non-linear elastic Duncan and Chang model and elastic perfectly plastic Mohr-coulomb model was used in the analysis. The model is implemented in numerical finite difference code FLAC2D using its built in FISH language and then used to analyze dam. The results show the maximum settlement of dam body and diversion system up to elevation 1849 (m.a.s.l.) that is equal 37 m height of embankment is 73 cm and 41 cm, respectively. The last measured settlement of diversion system is 40 cm, the comparison between measured settlements and numerical results confirm the suitability of assumed constitutive model and parameters to predict the dam behavior. The numerical results show the maximum settlement of dam body and diversion system at end of construction are 97.5 cm and 45 cm. Also, the maximum settlements of dam body at first impounding and steady state are 108 cm and 110 cm and the maximum settlements of diversion system are 46 and 49 cm, respectively. Based on some engineering codes such as ICOLD, USBR and USSD which have suggested allowable deformation of dam body and foundation can be said, the distribution of settlements is acceptable.

6. REFERENCES

1. Drucker, D. C., and Prager, W, (1952), “*Soil mechanics and plastic analysis in limit design*,” Quarterly of Applied Mathematics, Vol. 10,PP. 157-165.
2. Burland, J. B,(1965),“*The yielding and dilation of clay*,” Geotechnique, Vol. 15, PP. 211-214.
3. Duncan,J.M., and Chang,C. Y., (1970),“*Nonlinear analysis of stress and strain in soil*,” Journal of the Soil Mechanics and Foundation Division, ASCE, Vol. 96. No. SM5,PP. 1629-1653.
4. Schanz, T., Vermeer, P. A., Bonnier, P. G.,(1999),“*The hardening soil model: Formulation and verification*,” Beyond 2000 in Computational Geotechnics, Balkema, Rotterdam.
5. Clausen, J., and Damkilde, L., (2008),“*An exact implementation of the Hoek–Brown criterion for elasto-plastic finite element calculations*,” International Journal of Rock Mechanics and Mining Sciences, Vol. 45,PP. 831-847.
6. Mahin Roosta, R., and Alizade, A., (2012),“*Simulation of collapse settlement in rockfill material due to saturation*,” International Journal of Civil Engineering, Vol. 10,No. 2,pp. 93-99.
7. Janbu, N.,(1963),“*Soil Compressibility as Determined by Oedometer and Triaxial tests*,” Proceedings, European Conference on Soil Mechanics and Foundation Engineering, Wiesbaden, West Germany, Vol. 1, pp. 19-25.
8. Burland, J.B., (1989),“Ninth Laurits Bjerrum Memorial Lecture: “*Small is beautiful*” - the stiffness of soils at small strains,” Canadian Geotechnical Journal, Vol. 26, No. 4, PP. 499-516.
9. Jardine, R.J., Potts, D.M., Fourie, A.B. and Burland, J.B., (1986),“*Studies of the influence of non-linear stress strain characteristics in soil structure interaction*,” Géotechnique, Vol. 36, No. 3, PP. 377-396.
10. Smith, I. M., (1994), “*Validation of finite element solutions*,” Proceedings of the 13th International conference on Soil Mechanics and Foundation Engineering, New Delhi, Vol. 5, PP. 229-231.
11. Davis, R.O and Selvadurai, A. P. S, (2002),*Plasticity and Geomechanics*, Cambridge University Press, New York.

Safety evaluation of concrete gravity dams founded on inhomogeneous rock media due to static loads

Hamid Taghavi Ganji¹, Mohammad Alembagheri²

1- Department of Civil and Environmental Engineering, Amirkabir University of Technology, Tehran, Iran

2- Department of Civil and Environmental Engineering, Tarbiat Modares University, Tehran, Iran

Email: h.taghavi.g@gmail.com

Abstract

Dams are mega structures which their safety is of great importance. One of the vague points for engineers during design process is the uncertainty in mechanical and geological form of their massive foundation which inhomogeneity is an inevitable part of them. Large fissures and joints in this media are one of the reasons that would lead to inhomogeneity. Therefore, rock foundation would be divided into many parts which can have different mechanical properties. In this study, static performance of Pine Flat dam is studied by modeling more than 1000 different FE models with different mechanical and geological situations. In specific, the effect of seepage loading is studied in all models. By looking to the results, it has been demonstrated that geological figure in many cases is more important than mechanical properties. In addition, existence of joints in some specific points of foundation would lead to critical responses, the mechanical properties be that as it may.

Keywords: Concrete Gravity Dams, Inhomogeneous Rock Foundation, Static Loading, Safety Indices, Seepage.

1. INTRODUCTION

Large concrete gravity dams are among the most important national infrastructures playing key role in world's economy. Due to catastrophic consequences of failure of concrete dams, their structural stability is of great concern. The structure of gravity dams mostly performs very well, but there is always doubt and uncertainty in rock mass foundation [1]. A rock mass is a set of individual integral rock blocks, which are separated by systems of differently oriented joints. The foundation situation can significantly affect the safety and stability of gravity dams; one of the most prone areas is the dam-foundation interface plane. The foundation failure has been the case of significant catastrophes such as experiences at St. Francis, Malpasset and Vajont Dams. Geological conditions of concrete dams' foundation are usually complicated due to: (1) variety of rock materials which leads to different mechanical properties from one place to another, and (2) presence of discontinuities such as faults, joints and fissures. These discontinuities can be assumed to be tied to each other or they can slide against each other. They may be parallel or interrupt each other in any depth of foundation [2]. Although the foundation is often assumed to be a homogeneous unbounded medium, critical situations of concrete dams founded on inhomogeneous multi-layered rocks have forced researchers to study the foundation's inhomogeneity [3-5]. Almost these studies dealt with a real project along with its specific foundation's geometry and geological conditions [6-8].

The history has taught engineers that concrete dams often fail under the action of static loads such as the gravity, hydrostatic and uplift forces [9]. The tragic events have forced designers to make accurate model of seepage regime and the static performance of concrete dams and their rock beds. Hence, a variety of researches have been carried out in this field which led to this conclusion that two most probable failure modes, which should be considered in stability analysis and safety evaluation of each gravity dam, are [10]: (a) overstressing in tension or compression as well as (b) sliding of the monolith along the dam-foundation interface, or with part of foundation, along a failure surface within the foundation. Another potential failure mode is overturning; however, in the usual operating conditions, it is not as possible as the two above-mentioned failure modes [10].

In this paper, the safety of gravity dams located on heterogeneous rock foundations is evaluated under the static loads. For this goal, tallest monolith of Pine Flat dam is utilized for a case study. In addition, the configuration of foundation would change by considering a single large joint within it. The effects of the position of foundation joint, mechanical properties of the rock, and presence of uplift forces are assessed on the safety and stability of the dam through a detailed parametric study.

2. INHOMOGENEITY OF GRAVITY DAMS' FOUNDATION

Typically, there are many geological structures in massive rock foundations. The rock masses inevitably include various kinds of discontinuities, so the geological conditions of dam-sites are complicated and determined by the geometry of their structure and the properties of the blocks and discontinuities [2]. The mechanical properties of the rock masses are the basic input for analysis of dam-foundation systems [8].

It is practically impossible to model all discontinuities of a rock foundation. Therefore, only the major ones can be taken into account for mechanical analysis. The ratio of the elastic modulus of the dam and various parts of the foundation represents the impedance contrast between them. This ratio along with their Poisson's ratios can considerably affect the response of the dam-foundation system [11]. For the seepage analysis, in spite of complicated shapes and different directions of small discontinuities, their effects can be simply considered by changing the rock material behavior [12]. This assumption is valid for large dam foundations [2]. The seepage pattern and the pore pressures within the foundation depend on its stress-strain state. The distribution of pore pressures determines, in turn, the magnitude of seepage forces which affect the stress-strain state of the foundation. Therefore, the coupled problem of stress-seepage analysis requires iterative solution.

3. STABILITY ANALYSIS AND SAFETY EVALUATION

A gravity dam maintains its stability relying on its large weight. There are two risky potential failure modes which may jeopardize the stability of gravity dams. The first one is the tensile or compressive overstressing. Because the tensile strength of brittle materials like mass concrete or rock is lower than 10% of their compressive strength [13], the tensile failure is more probable. The safety factor against overstressing can be defined as:

$$SF_{\sigma,i} = \frac{\sigma_{S,i}}{\sigma_{P,i}}, \quad i = T \text{ or } C \quad (1)$$

Where σ_P is the peak principal stress within the considered domain, and σ_S is the material uniaxial strength. Subscripts T and C represent the tension and compression conditions, respectively.

The second failure mode is sliding along the dam base or a potential failure surface within the foundation. The sliding stability can be studied by numerical methods such as limit equilibrium method and finite element method [6, 7]. However, this study concerns the sliding mechanism along predefined planes considering motion in the upstream-downstream direction. For the dam-foundation interface plane, considering the equilibrium of forces shown in Figure 1. (a), the global safety factor against sliding for entire dam's body is defined by utilizing the Mohr-Coulomb criterion as:

$$SF_{GS} = \frac{F_R}{F_S} = \frac{\mu_s F_n + cA}{F_s} = \frac{\mu_s(W + H_{Uy} - U) + cA}{H_{Ux} - H_D} \quad (2)$$

Where F_R , F_S and F_n are the resisting, shear and normal forces, respectively. W and U are dam weight and uplift force, c and μ_s are the cohesion and the friction coefficient of the dam-foundation interface, A is the base length (area), H_U and H_D are the hydrostatic forces acting on dam's upstream and downstream faces, respectively. The global dominant forces (i.e. F_R and F_S) and hence the global safety factor, will not considerably change due to inhomogeneity of the foundation, if the shear resistance parameters c and μ_s are assumed to be constant. But the distribution of the normal and shear stresses on the base interface plane may locally change significantly. Therefore, it is better to compute local safety factors against sliding (SF_{LS}) in the sliding-prone regions along the dam base using the local normal and shear forces.

4. NUMERICAL EXAMPLE

The tallest monolith of Pine Flat dam is selected for the purpose of analysis as it is shown in Figure 1. (b). The inhomogeneity of rock foundation is considered by changing the properties of the rock through major discontinuities of the foundation. In this paper, these discontinuities are assumed as one single large joint/fault plane with varying position within the foundation (Figure 2). This joint/fault is assumed to behave linear, and there is no sliding or opening across its interfaces. Therefore, the foundation is a continuous and heterogeneous medium. As it is illustrated in Figure 2, joint/fault orientation is fully defined by two parameters: l which is measured from the foundation domain corner, and α which measures the dip angle of the fault. In all models,

based on the previous practical observations, the main geometric parameters of the foundation discontinuities independently vary in the following ranges: $1B \leq l \leq 4B$, and $30^\circ \leq \alpha \leq 150^\circ$.

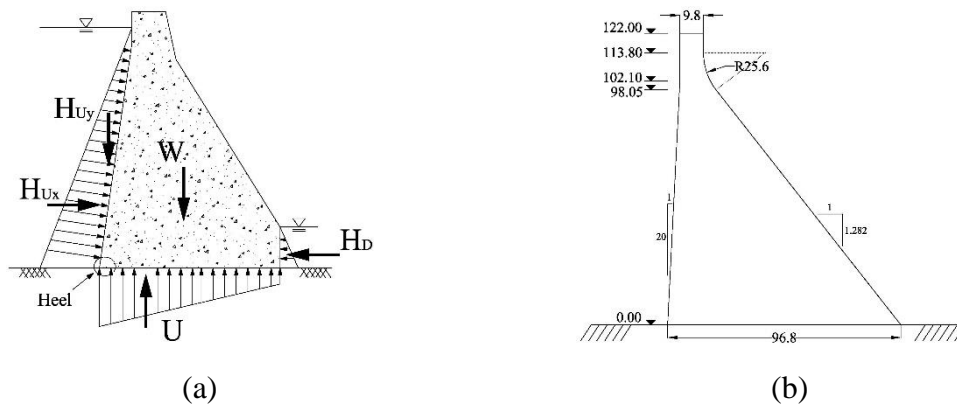


Figure 1. (a) Schematic representation of dominant static loadings applied on a gravity dam's section; (b) the tallest non-over-flow monolith of Pine Flat dam (all dimensions are in meter).

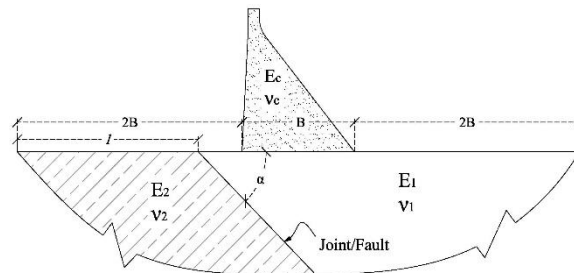


Figure 2. Inhomogeneity of the foundation

The concrete's behavior is assumed to be isotropic linear elastic with the Young's modulus of 27.58 GPa, Poisson's ratio is 0.2, and density is considered to be 2400 kg/m³. The foundation rock behavior is also linear elastic, but with various stiffness through the joint/fault to investigate the effects of foundation inhomogeneity. Seeking this goal, in all models, it is assumed that $E_1 = E_c$, $\nu_1 = \nu_2 = 0.33$, and \bar{E} which denotes the ratio of E_2/E_1 is 0.25, 0.33, 0.5, 1.5, and 2. The case in which $\bar{E} = 1$, represents the homogenous foundation which is named as the base-case model.

Two loading combinations are studied: LC1 and LC2. The LC1 consists of the dead weight of the dam and the hydrostatic force of the full reservoir on the upstream face of the dam. In addition to these forces, the seepage load through the foundation is also added in the LC2. The dam body is assumed to be impermeable. The steady-state seepage in the foundation follows the Darcy's law assuming isotropic permeability (i.e. the same permeability coefficient in any direction). Moreover, the foundation is assumed to be fully saturated with the permeability coefficient of $k = 4 \cdot 10^{-7}$ m/s for all of the models. The same permeability coefficient is assumed across the joint/fault. The full reservoir and zero head are assigned to the upstream (US) and downstream (DS) horizontal surfaces of the foundation, respectively. No grout curtain or drainage system is modelled in the analysis. The in-situ stresses of the rock mass are neglected.

A potential sliding path along the dam-foundation interface plane is assumed in all models to assess the local sliding stability of the entire dam body using equation (2). For this aim, zero cohesion and unit friction coefficient are assumed for shear resistance parameters (i.e. $c = 0$ and $\mu_s = 1$). The effects of the foundation inhomogeneity including various geometries and stiffness as well as the effects of the seepage within the foundation are studied by generating and analyzing more than 1000 models. The results are presented in the next section.

5. RESULTS AND DISCUSSION

The analysis results of various geometries and mechanical properties which are made up due to existence of a discontinuity in the foundation are presented in this section. The results include the relative displacement of the dam crest with respect to the base (i.e. U_{rel}), which is always into the DS direction; the peak minimum (compressive) principal stress of the dam's body (i.e. PS_{CD}), which is always at the dam's toe; and the peak maximum (tensile) principal stress of the dam's heel (i.e. PS_{TD}). The stresses are positive in tension. It is observed from results for base-case model under the load combination LC1 that U_{rel} , PS_{CD} and PS_{TD} would be respectively 1.57cm, -3.37MPa and -0.33MPa. Moreover, under hydrostatic loading, the dam heel is the most prone location to slide, so the local sliding safety factor (i.e. SF_{LS}) is computed for this area. It is illustrated that this parameter around the heel area of base-case model is 2.84 and 1.20 under the load combinations LC1 and LC2, respectively. The global safety factor (i.e. SF_{GS}), is approximately the same for all models along the dam-foundation interface plane. This parameter for all models is almost 1.9 and 1.2 under the load combinations LC1 and LC2, respectively. Figure 3 represents U_{rel} , PS_{TD} , and PS_{CD} in terms of l/B , α , and \bar{E} . The ratio of l/B between 2 and 3 represents the fault intersecting with the dam base. As it is observed in Figure 3, reducing \bar{E} ratio, i.e. the softer foundation, increases the variation of the results and also increases the difference between results of similar models while seepage is included or excluded. The results of the models with $\bar{E} < 1$ oppose to the models with $\bar{E} > 1$, as it was expected.

In the models without seepage (i.e. under the load combination LC1), if $\bar{E} < 1$, minimum and maximum values of U_{rel} will be observed when the fault respectively passes through the dam base and the DS side. It would be opposite for the models with $\bar{E} > 1$, where maximum U_{rel} is obtained when the fault intersects with the dam base. The highest value of U_{rel} is 2.7cm which occurs for the most flexible foundation, i.e. $\bar{E} = 0.25$, $\alpha = 30^\circ$, and $l/B = 4$. The lowest value of U_{rel} belongs to the model with $\bar{E} = 0.25$, $\alpha = 90^\circ$, $l/B = 2.75$ with the value of 0.4cm. The lowest value of U_{rel} when seepage is included in the models is 1.6cm for the model with the most stiff foundation, i.e. $\bar{E} = 2$, $\alpha = 30^\circ$, and $l/B = 4$. The highest value of U_{rel} occurs again for the most flexible foundation with the value of 4.1cm.

About PS_{TD} , when seepage is excluded and $\bar{E} < 1$, whole dam body is in compression, so it is negative. Increasing the \bar{E} ratio, i.e. the stiffer foundation, increases the tension within the dam body. In the models with $\bar{E} > 1$, if the fault intersects with the dam base while it is oriented into the DS side ($\alpha < 90^\circ$), then the dam heel would be in tension. If the fault does not pass through the dam base, the heel would be in compression specifically when it is oriented into the US side ($\alpha > 90^\circ$). The highest value of PS_{TD} belongs to the model with $\bar{E} = 2$, $l/B = 2.5$ (fault passing middle of the dam base), $\alpha = 60^\circ$ with the value of 0.26MPa. By considering seepage and in the cases which $\bar{E} < 1$, the minimum tension in the dam heel will be observed when the fault passes near it. The models with $l/B = 4$, exposes the maximum value of PS_{TD} . For the stiffer foundations with $\bar{E} > 1$, the heel is completely in tension. The maximum tension is observed when the fault passes near the heel, and the peak PS_{TD} belongs to the model with $\bar{E} = 2$ and $\alpha = 120^\circ$, with the value of 0.71MPa, however, most of the dam body undergoes compression again.

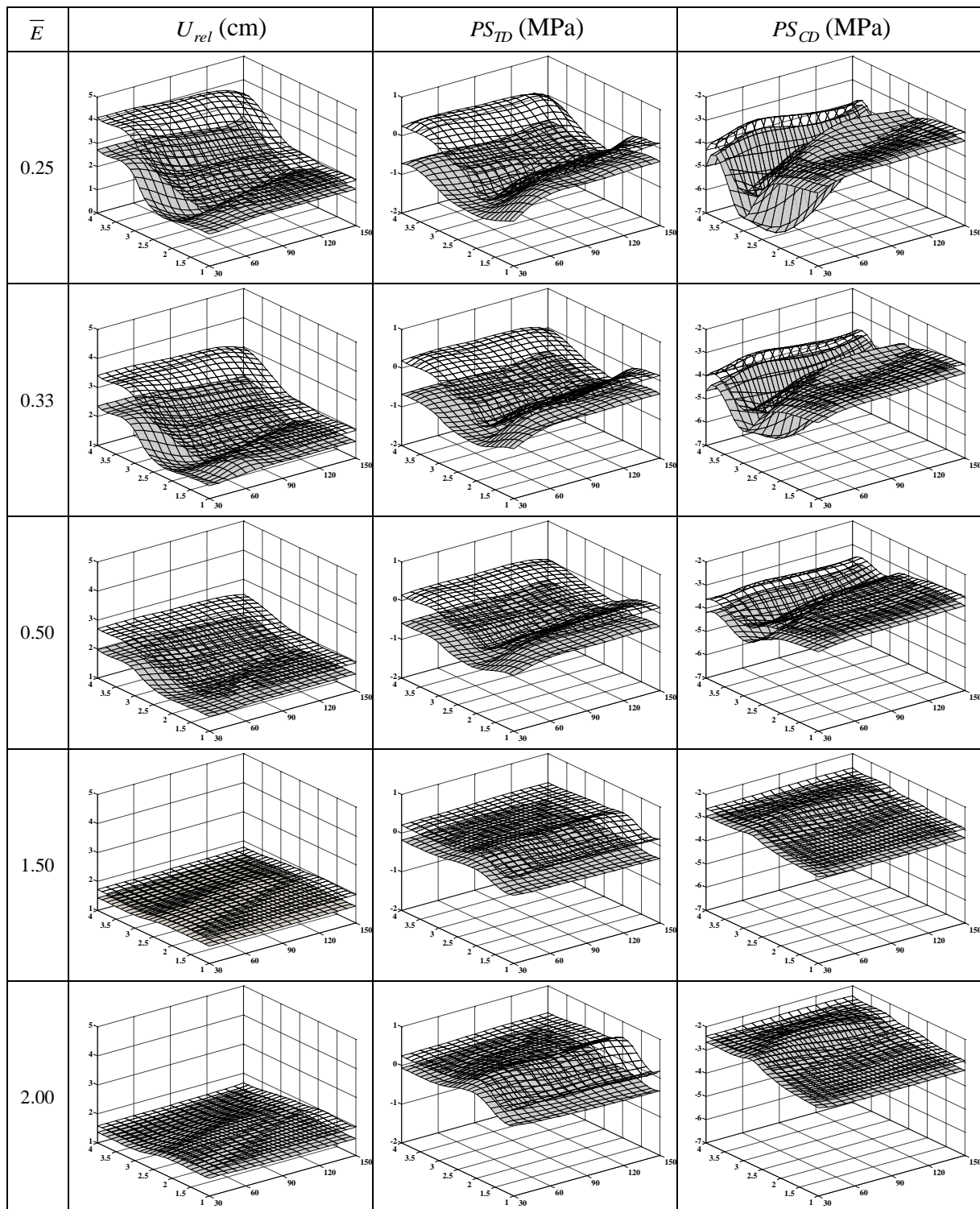


Figure 3. The results of the one-fault models. The second, third and fourth column respectively show the U_{rel} , PS_{TD} and PS_{CD} for the dam body in terms of l/B (left horizontal axis), α (right horizontal axis) and \bar{E} . The filled and un-filled curves are representing the models under the loading combination LC1 and the LC2, respectively.

Increasing the \bar{E} ratio totally decreases the value of compressive stresses in the dam body. With and without seepage, if $\bar{E} < 1$, the maximum and minimum compression in the dam toe will occur when the fault passes through the toe and US side, respectively. Opposite trend is observed for the models with $\bar{E} > 1$. The

PS_{CD} in the dam toe is almost the same when the fault passes the US side. The peak value of PS_{CD} , which is -7.25 MPa, belongs to the model with flexible foundation of $\bar{E}=0.25$, fault passing the dam toe ($l/B=3$) and orienting into the DS direction ($\alpha=45^\circ$). When seepage is included in loading, the maximum PS_{CD} again belongs to the above-mentioned model with the value of -6.044 MPa. The peak compressive stress of the dam body is totally lower than the common compressive strength of concrete, say 30 MPa, so, the dam remains in the elastic mode. Furthermore, $SF_{\sigma C}$ is higher than 4 and 4.9 for the models without and with seepage, respectively.

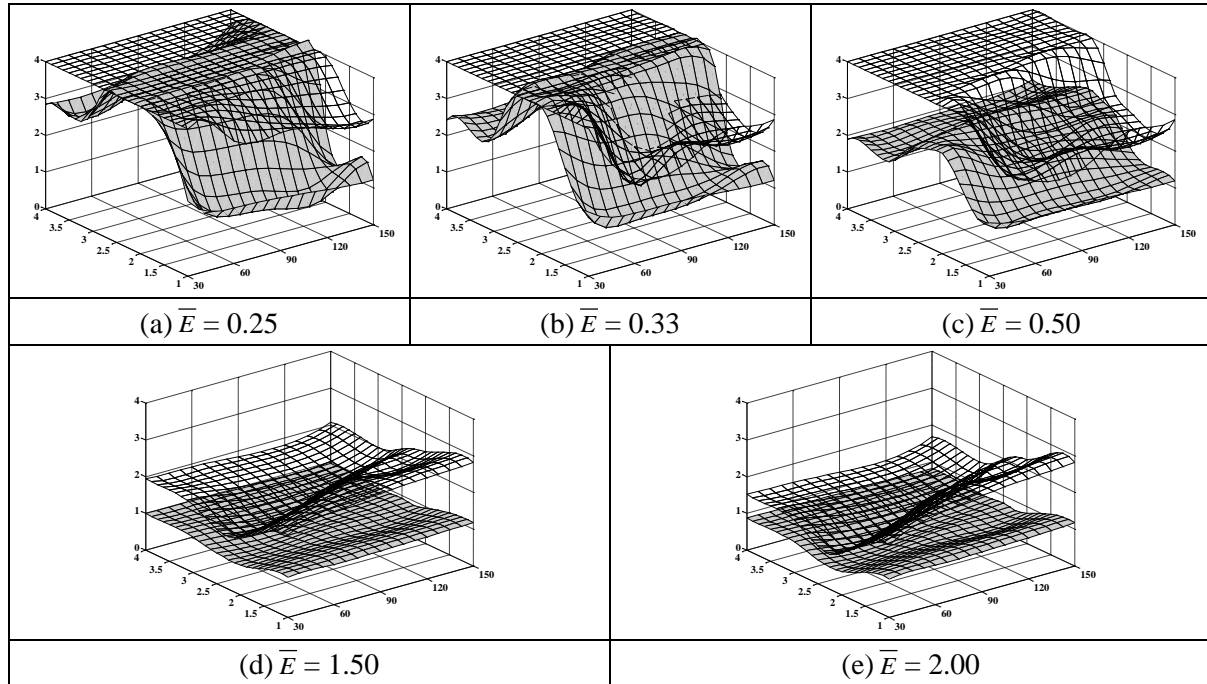


Figure 4. The local sliding safety factor at the dam heel in terms of l/B (left horizontal axis), α (right horizontal axis) and \bar{E} ratio. The filled and un-filled curves are representing the models under the loading combination LC2 and the LC1, respectively.

As it was explained, the local sliding safety factor (i.e. SF_{LS}), is computed for the dam heel region and is presented in Figure 4. To better plot the obtained results, the local safety factors more than 4 are constantly shown as four. Increasing the \bar{E} ratio, i.e. the stiffer foundation, generally leads to decrease of SF_{LS} . Without seepage, if $\bar{E} < 1$, then generally $SF_{LS} > 2.0$. If the fault passes the DS side, i.e. the foundation beneath the dam is softer than the dam concrete, then $SF_{LS} > 4$. For the models with $\bar{E}=0.25$ or 0.33 , if the fault intersects with the dam base oriented into the US side ($\alpha \leq 90^\circ$), then the horizontal force in the heel region may be into the US direction. In the models of $\bar{E} > 1$, minimum SF_{LS} is observed when the fault passes exactly through middle of the dam base. If $\bar{E}=2$ (Figure 4.(e)), then $SF_{LS} < 1$ when the fault passes through the dam base oriented into the DS side ($\alpha < 90^\circ$). The lowest SF_{LS} value occurs for the model with $l/B=2.5$ and $\alpha=60^\circ$ which is 0.823.

The seepage reduces SF_{LS} . Again, the stiffer foundation shows lower SF_{LS} values. If $\bar{E} < 1$, then the horizontal forces in the dam heel region are totally into the DS direction. In general $SF_{LS} > 1.2$, but if the fault passes through the dam base or DS side, this parameter will be greater than 1.6. The minimum values of SF_{LS} are observed when the fault intersects with the dam base for the models with $\bar{E} > 1$. In general in this situation, totally $SF_{LS} < 1.2$; in particular if the fault passes through the dam base or DS side, then $SF_{LS} < 1.0$. The lowest SF_{LS} is observed in the model with $l/B=2.5$ and $\alpha=60^\circ$ with the value of 0.749 and 0.547 for $\bar{E}=1.5$ and 2, respectively. For these two critical cases, the local sliding safety factors are also computed along the dam base to locally investigate the possibility of base sliding. As it is shown in Figure 5, the local sliding safety factor

becomes more than one immediately after the heel region. It is more than 2.5 for the range of 0.3 to 0.7 of the base and reduces to 1.4 at the dam toe.

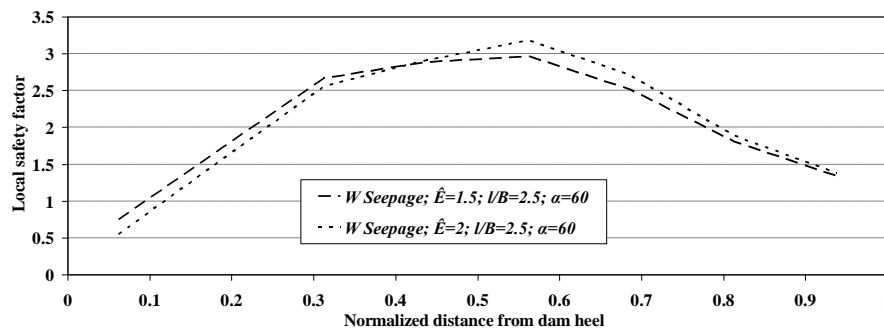


Figure 5. Local sliding safety factor along the dam base for the critical models while seepage is included.

6. SUMMARY AND CONCLUSIONS

In this paper, the structural stability and safety of gravity dams located on inhomogeneous rock foundations is evaluated under dominant static loads by measuring overstressing and sliding safety factor indices. For this purpose, Pine Flat gravity dam is considered as a case study. The spatial configuration of the foundation is changed by inserting one single large joint/fault plane within it. The effects of the position of the foundation joint/fault, mechanical properties of the rock, and presence of the uplift forces on the safety and stability of the dam are assessed through a detailed parametric study using more than 1000 finite element models. It is found that the foundation inhomogeneity may increase or decrease the response results. Therefore, it should be taken into account for the safety assessment of concrete gravity dams. The conclusions of results are presented as follow:

- The presence of softer foundation increases the variation of the results and also increases the difference between results of similar models while seepage is included or excluded.
- The results of the models with weaker foundation oppose to the models with stiffer foundation, as it was expected.
- When the fault passes with a distance of more than $0.5B$ through DS or US sides of the dam, the trends of responses are smoother. To put it another word, it has been demonstrated that only if the fault passes through a close distant of $0.5B$ from dam's body, they will influence in dam's responses.
- The local sliding at the dam heel is more perilous than the dam body's overstressing in all models.
- The seepage increases the peak relative displacement and tensile stress of the dam body but decreases the peak compressive stress and local safety factor.
- By comparing responses of the cases which seepage is included with the cases which seepage is excluded, similar trends would be observed.
- The stiffer foundation increases the tension within the dam body but generally decreases local safety factor.

7. REFERENCES

1. Zhang L, Wang D, Zhang H, Wang W. (2008), “*Stability analysis of gravity dams on sloping layered rock foundation against deep slide*”, 11th Biennial ASCE Aerospace Division International Conference on Engineering, Science, Construction and Operations in Challenging Environments.
2. Hosseinzadeh A, Nobarinasab M, Soroush A, & Lotfi V. (2013), “*Coupled stress–seepage analysis of Karun III concretes arch dam*”, *Geotechnical Engineering*, **166** (5), pp. 483-501.
3. Ukhov S.B, & Semenov V.V. (1973), “*Calculation of displacements and stresses in anisotropic rocks by the finite element method*”, *Hydrotechnical Construction*, **7** (2), pp. 146-154.
4. Kotov P.B. (1975), “*Stressed state and Bearing capacity of anchors embedded in rocks*”, *Hydrotechnical Construction*, **9** (12), pp. 1167-1170.
5. Semenov V.V, & Shevarina N.N. (1976), “*Application of the finite element method in calculating seepage in the foundations of hydraulic structures*”, *Hydrotechnical Construction*, **10** (4), pp. 326-331.
6. Chen Y, Zhang L, Yang G, Dong J, & Chen J. (2012), “*Anti-sliding stability of a gravity dam on complicated foundation with multiple structural planes*”, *International Journal of Rock Mechanics & Mining Sciences*, **55** (1), pp. 151-156.
7. Chen S, Qiang S, Shahrour I, & Egger P. (2008), “*Composite element analysis of gravity dam on a complicated rock foundation*”, *International Journal of Geomechanics*, **8** (5), pp. 275-284.
8. Pausz S, Nowotny H, & Jung G. (2015), “*Rock mass classification and geotechnical model for the foundation of a RCC gravity dam*”, *Geomechanics and Tunneling*, **8** (5), pp. 436-440.
9. Sun G.H, Zheng H, & Liu, D.F. (2011), “*A three-dimensional procedure for evaluating the stability of gravity dams against deep slide in the foundation*”, *International Journal of Rock Mechanics & Mining Sciences*, **48** (3), pp. 421-426.
10. USACE 1995. Gravity dam design. US Army Corps of Engineers. EM 1110-2-2200. Washington DC.
11. Lin G, Du J, & Hu Z. (2007), “*Earthquake analysis of arch and gravity dams including the effects of foundation inhomogeneity*”, *Frontiers of Architecture and Civil Engineering in China*, **1** (1), pp. 41-50.
12. Hasani H, Arshadnejad S, Khodadadi H, & Goodarzi N. (2008), “*3D numerical modeling of a couple of power intake shafts and head race tunnels at vicinity of a rock slope in Siah Bishe pumped storage dam, north of Iran*”, *Journal of Applied Sciences*, **8** (23), pp. 4294-4302.
13. Alembagheri M, & Ghaemian M. (2013), “*Incremental dynamic analysis of concrete gravity dams including base and lift joints*”, *Earthquake Engineering and Engineering Vibration*, **12** (1), pp. 119-134.

Behavior analysis of ghale chay earth fill dam using instruments data

Mohammad Manafpour¹, Mojtaba Ghahremannezhad²

1- Assistant professor, Department of Civil Engineering, Urmia University, Urmia, Iran

2- M.Sc. student of civil Engineering, Urmia University, Urmia, Iran

Email: m.gahraman1992@gmail.com

Abstract

The Analysis of earth fill dam behavior during construction first impounding and operation periods. May help to recognize any possible destructive phenomena such as high water pore pressure, non-uniform settlements, excessive leakage, piping, and arching etc. In this research, the behavior components of Ghale Chay earth fill dam are investigated using instrumentation data. These components are: water pore pressure, total soil pressure, settlement in foundation and dam body. Various instruments installed in four different section of dam including: piezometers, settlement gages, inclinometers, total pressure cells and stand pipes. The research results indicate that the water pore pressure in the clayey core reduces in flow direction. For different reservoir water level pore pressure is nearly constant downstream of cut-off wall located in dam foundation (changes less than 10%). Maximum settlement occur at cross section No.2 of dam is equal to 816 mm (equal to 1% of dams' height) is seen at 43.7% of dam height.

Keywords: Earth fill Dam, Behavior Analysis, Instrumentation, Settlement, Pore pressure.

1. INTRODUCTION

The safety of embankment dams depends on accurate designing, construction and monitoring the real behavior of dam during the periods of construction and exploitation . recognition of design parameters are needed for accurate and stable designing in the future of which the geotechnical parameters are the most important ones [1]. Scouring, high pore pressure and hydraulic gradient in foundation and body of dam are the most recognized factors in dam's failure [2,3]. In this study, Ghale Chay earth fill dam with vertical and oblique clayey core and 85m height from rocky foundation was evaluated as a case study. In order to investigate the dam's behavior during the construction period, the first impoundment and exploitation time, the settlements, pore water pressure, total pressure and horizontal displacements were studied.

2. PORE WATER PRESSURE

The pore water pressure development in embankment dam's core is one of the main factors which has an important role in stability of dam and soil mechanics. Increasing the pore water pressure can decrease the effective stress resulting in lower shear strength -that has a direct relation with effective stress, and consequently the stability of dam is reduced. Due to the high importance of this subject, the reasons of development of pore water pressure in embankment dams and effective factors on it are mentioned as below (13):

1. The type of materials of dam's core: The type of soil can have effect on pore water pressure from two points of view including compressibility and permeability of soil. These two factors have opposite effects. Compaction of soil causes reduction in void ratio and permeability. Soil compaction that occurs through increasing the water content and pummeling the soil, affects the pore water pressure during dam's construction. According to USBR recommendation, if the core's materials are compacted with a water content between 1% and 3% under optimum water content, the pore water pressure will change in an acceptable range.
2. The drainage condition of soil: Existence of drainage around core causes dissipation of pore water pressure. This causes an appropriate water flow and decrease the pore water pressure.
3. The filling speed: Increased overburden is caused due to increased height of filling which can cause development of pore water pressure in embankment dam's core. Increment of overburden causes lower soil porosity and higher saturation of soil and because of fully saturation of materials the pore water pressure

- develops. So by controlling the filling speed in a way that the pore water pressure in core can be dissipated, the increment of pore water pressure will be controlled in order not to exceed the confidence interval.
- The saturation degree of materials: Saturation degree has a direct relation with developing and increasing the pore water pressure and as mentioned before, by fully saturation of the materials the pore water pressure develops and before fully saturation increment of overburden leads to higher saturation degree.
 - The impoundment velocity of dam's cistern: The impoundment increases the pore water pressure and decreases the effective stress in dam's core and the probability of sliding or piping in core's upstream increases.

3. SETTLEMENT

Deformations of an embankment dam start occurring during the construction of the dam. These deformations are caused by the increase of effective stresses during the construction by the consecutive layers of earth material and also by effects of creep of material. Later, the rate of deformations decreases generally in time, with the exception of variations associated to the periodic variations of the level of the reservoir and, in seismic zones, to the earthquakes. Intensity, rate and direction of movements, in a specific point of the body of the dam or its crest, can vary during the various phases of the construction and the operation of the reservoir. [4]

At the different elevations and in different zone types may occur the variations of stresses what can be caused by differential settlements between the core and the upstream and downstream filter zones. If the core is more compressible than the upstream and downstream filter zones, it settles more under its weight than the filter zone and, by the effect of arching, core mass leans on stiffer filter zones. This causes the reduction of vertical stresses and consequently the lateral stresses develop towards the base of the core. This phenomenon can cause a hydraulic fracturing and a risk of erosion of the fine particles of the core. [4]

The maximum settlement frequently occurs in 1/3 – 1/5 of dam's height [10]. According to reliable references, the value of acceptable settlement of a typical dam is 1% -2% of the dam's height [11,12]

4. RESEARCH METHODOLOGY

Ghale Chay embankment dam is located in the city Ajabshir, Iran, and its construction process was started on July 31st in 2004 and was ended on April 23rd in 2008. The dam is zoned into two parts, with clayey vertical core until the level of 1670 and with oblique part toward the downstream to the level of 1680.4. The drainage blanket at downstream is used with vertical drainage for safe discharge of leakage water. Also, three horizontal drainage layers are located in upstream shell in order to facilitate quick discharge of water of shell and speeding up the saturation of upstream shell during impoundment. The materials of clayey core and body materials are in GC and GP classification, respectively. The other part of the dam is the cut off wall that is built in order to control the pore water pressure in dam's foundation and water flow from it in dam's foundation and sides. The length of crown, the height of dam from alluvial bed and from bedrock and volume of cistern in normal water level (1676m from sea level) are 336 m, 77 m, 85 m and 40 mm³, respectively.

5. INSTRUMENT OF DAM

As can be seen from the plan in Figure 1, four sections were instrumented along the dam's axis. Also two sections in the middle part of the valley and in the maximum section and the other two sections were located on abutments and around the average height of the dam. The middle sections 2 and 3 were located in 0+207 and 0+260 kms, respectively and side sections were located in 0+160 and 0+320 kms from the left side.

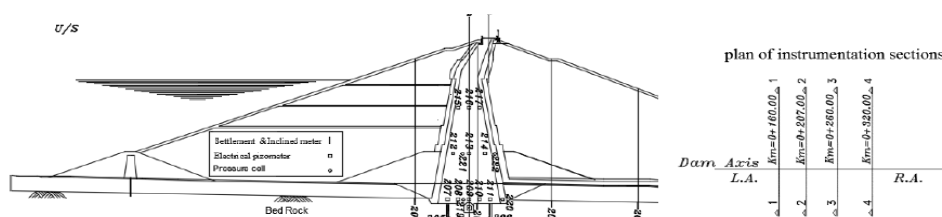


Fig1. Installed instrument in body and foundation in cross section of dam and plan of instrumented sections.

Table 1. number of installed instruments in different sections

total	Section 4		Section 3		Section 2		Section 1		
	Rocky foundation	body							
14	-	3	-	4	-	4	-	3	Settlement/deviation gauge
45	-	6	6	11	6	11	-	6	Electrical pisometer
12	-	2	-	4	-	4	-	2	Total pressure cell

Considering the point that in the present article four parameters of pore water pressure, total pressure and horizontal and vertical displacements were studied, so just the location and number of electrical piezometers, total pressure measurement cells, settlement and deviation gauges have been mentioned. In order to control the condition of pore water pressure during the period of dam's construction and control the depression amount of water energy from core in seepage time, in the sections with maximum dimensions (sections 2 and 3) three rows of electrical piezometers were considered in core. The first row was located in a little distance from the contact surface of core and rocky foundation (level of 1600m) including 5 piezometers, and the second and third rows including 3 electrical piezometers were embedded in the middle level of stable seepage line (1621 m level) and in the level that the stable seepage line meets the core (level of 1644 – 1645 m), respectively. In order to control the piezometric pressure in bedrock, 12 electrical piezometers in sections 2 and 3 were installed. In section 2, three rows of electrical piezometers in the levels of 1569.5, 1570.5 and 1587 were installed. In section 3, for controlling the efficiency of cut off wall in dissipation of piezometric pressures three rows of electrical piezometers in levels of 1568.5, 1578.5 and 1586 were embedded. Four strings of deviation gauges were installed for measuring the settlement and horizontal displacements from which two strings in downstream were in distances of 40 and 77.5 m, one string in core in a distance of 4 m and one string in a distance of 25 m from axis were considered in downstream and upstream, respectively. In the instrumentation plan, all the deviation gauges with magnetic plates were used for measuring the settlements. Two total pressure measurement cells were embedded that one of them was in the core and along the axis (level of 1598 – 1600 m) and one of them was installed in the same level into the downstream filter. Two pressure cells were installed at the level of 1621 m near the dam axis and the downstream filter.

In the sections that were on the abutments (sections 1 and 4), two rows of electrical piezometers were considered in the core. The first row consisting of 3 piezometers was located in the level of 1621 – 1625 m with a short distance from the contact surface of the core and rocky foundation and the second row consisting of three piezometers was located in the level of 1643 – 1644 m. Two pressure cells were installed at the level of 1620 – 1624 m near the dam's axis and downstream filter. In each section there were three deviations – settlement gauges that one of them was in the distance of 20 m from the upstream, and another one was in the distance of 4 m from the downstream and the other was in the distance of 40 m from the downstream.

6. ANALYSIS INSTRUMENT DATA

6.1 PORE WATER PRESSURE

In the modified soils the pore water pressure develops due to material's weight and other factors. Under several conditions, the safety of slopes of embankment dams is considerably affected by distribution of pore water pressure [6, 7, 8 9]. In this section, because of the similar results, pore water pressure of instrumented sections of cross section 2 are considered. As can be clearly seen in Figure 1, total of 17 electrical piezometers were installed in that section.

According to figure 2, by increasing the filling level, the values of pore pressure increased by increasing the overburden due to the weight of materials. While at the beginning of earthworks the soil had the optimum water content, but by continuing the filling and compacting it, the voids between soil particles decreased and due to water content the soil became saturated. By resuming the filling process and by considering the low permeability of clayey core, the water in the soil did not have any time for drainage and it caused development of pore water pressure.

In order to dissipate the pore water pressure, water should have adequate for drainage that is done through stopping the filling process. As it can be seen until the 16th of May in 2006 that the water level of cistern was higher than the installation level of piezometers, due to cut off wall and upstream berm the dam's body did not affected by the water level of cistern, so it did not have any impact on pore water pressures and their values decreased during filling was stopped. After May 16th in 2006, because of the water flow from

upstream berm and saturation of dam's body, the higher water level of cistern compared to increment in filling level, the pore water pressure was affected more.

The piezometer Number 207 that was located at upstream of clayey core, was highly influenced by change of the water level of cistern and by movement toward the downstream its effect on piezometer's results reduced where it had the lowest effect on the piezometer number 211 while for different levels of cistern it had a constant value of 1608.

Figure 3 shows the changes of pore water pressure for second level of piezometers and it can be seen that in the early installation of piezometers they had almost fixed values because of their higher levels in comparison with the cistern's water level and lower overburden compared with the first level piezometers.

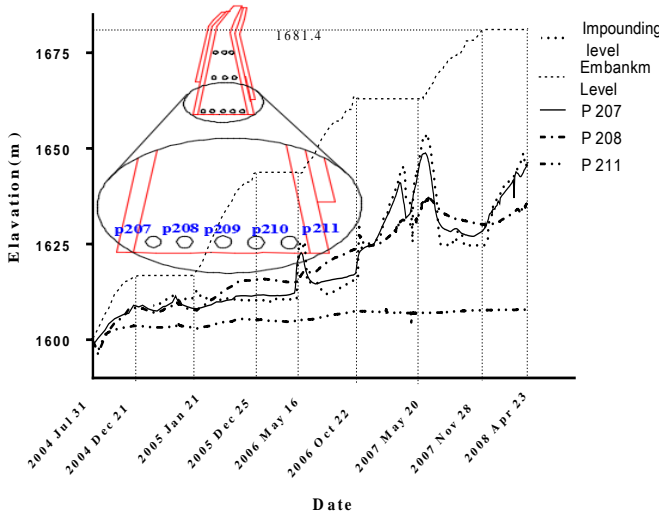


Fig2. Second level piezometric pressure results from piezometers of cross section 2

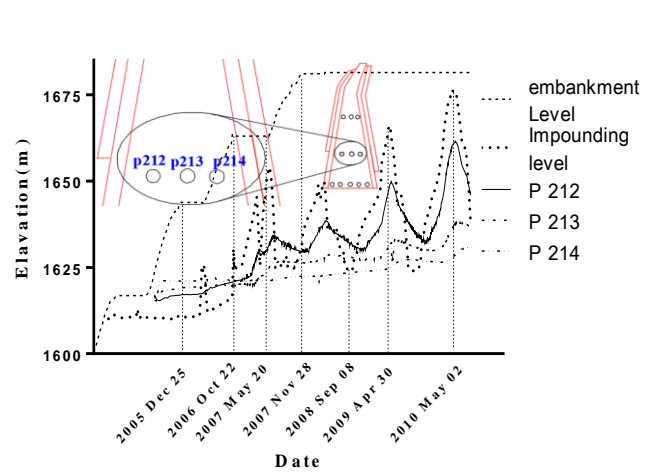


Fig 3 . Second level piezometric pressure results from piezometers of cross section 2

The cut off wall was built under the dam's body in order to avoid scouring and high flow of water. It is able to reduce the water flow by increasing the flow path and decreasing the hydraulic gradient. Figure 4 illustrates the changes of cistern water level versus piezometric pressure of the installed piezometer at the upstream and downstream of cut off wall. It is clear from Figure 4 that increment in water level of cistern increased the ability of cut off wall in dissipating the pore water pressures. The data of installed piezometers at the upstream and downstream of cut off wall are available from April 30th, 2009 and according to Figure 5, the piezometer number 203 that was installed at the upstream of cut off wall had a greater effect due to the short path compared to the piezometer number 204 that was installed at the downstream.

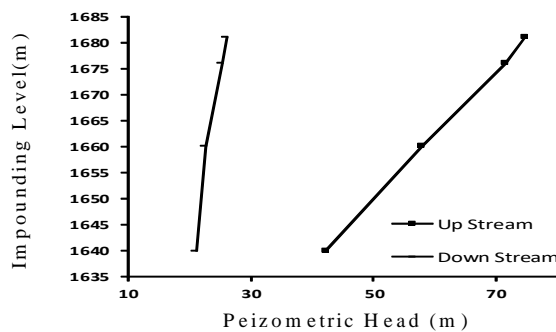


Fig4. The effect of cut off wall in dissipating the piezometric pressure

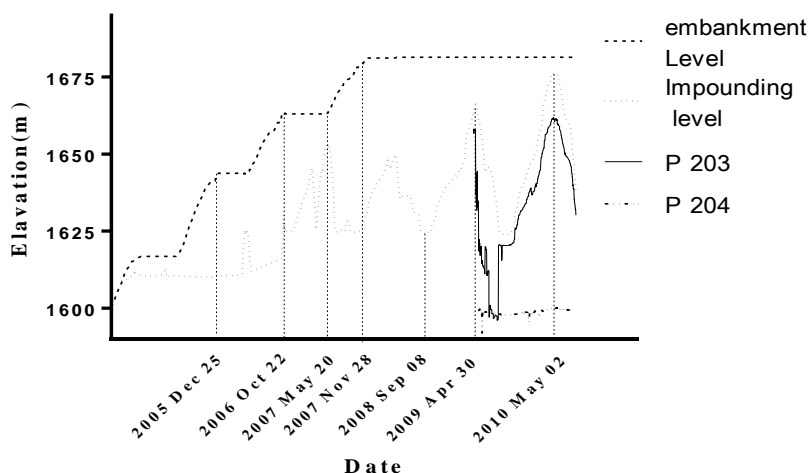
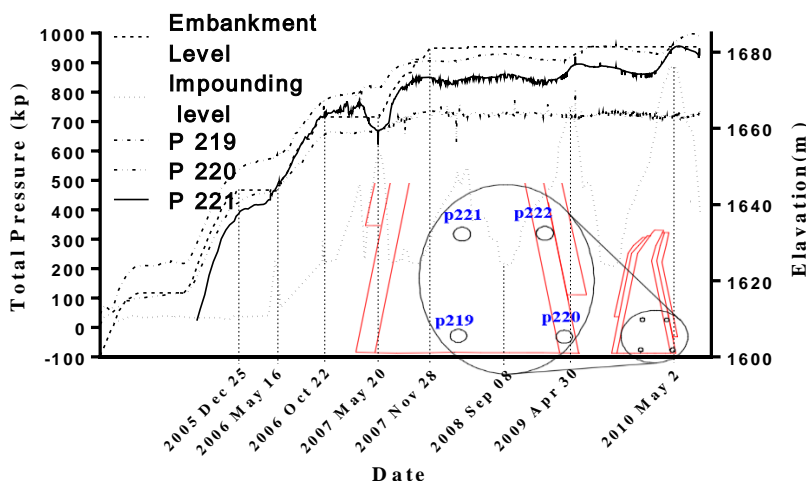


Fig5. The results of piezometric pressure at upstream and downstream of cut off wall

7. TOTAL PRESSURE

In order to measure the total pressure in core at section 2, four pressure measurement cells were installed that the location of each cell and their results are illustrated in Figure 6 as a graph. The graph of number the total pressure measurement cell of 222 was omitted due to the illogical data. During the filling process the total pressure graphs were affected by the changes in filling volume and cistern's water level, but by ending the filling process and fixing the pressure due to the weight of materials the total pressure changes were affected by cistern's water level and other parameters. The total pressure measurement cell of 219 had the higher value than the other cells during the dam's lifetime because of the highest pressure of water head and material's weight.



8. SETTLEMENTS

In order to evaluate the displacements of dam, the data of settlement and deviation gauges in the instrumented section were extracted until the first spillway of the dam on May 2nd, 2010 and were drawn as counters of cross section 2, settlement counter of longitudinal sections and direction of horizontal displacements in longitudinal sections of the dam. Due to the defectiveness of settlement and deviation gauges of number 3001 and 2003, their data weren't applied. Due to the zero height of filling and because there was not any measurement instrument on the left and right sides and in the farthest part of the upstream and downstream the values of settlements were considered equal to zero.

According to Figure 7, maximum amount of the settlement in clayey core until the exploitation time (May 2nd of 2010) at section 2 that was located in a distance of 260 m from the left side, was 816 mm that was equal to 1% of dam's height that was located at 43.7% of dam's height and it was in an acceptable range. Since

the settlement gauge number 2003 was defective, the settlement counters of cross section 2 were drawn without considering its data. If its data were available, the settlement counters would be drawn in a pattern of dashed line as it is illustrated in Figure 8.

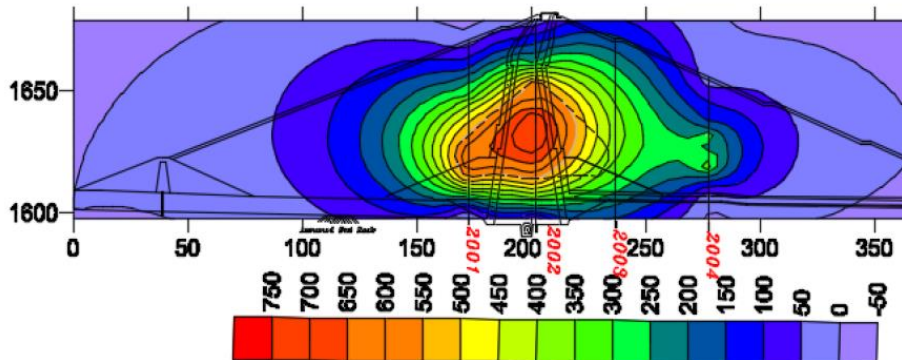


Fig7. Settlement counters of cross section 2 in service time

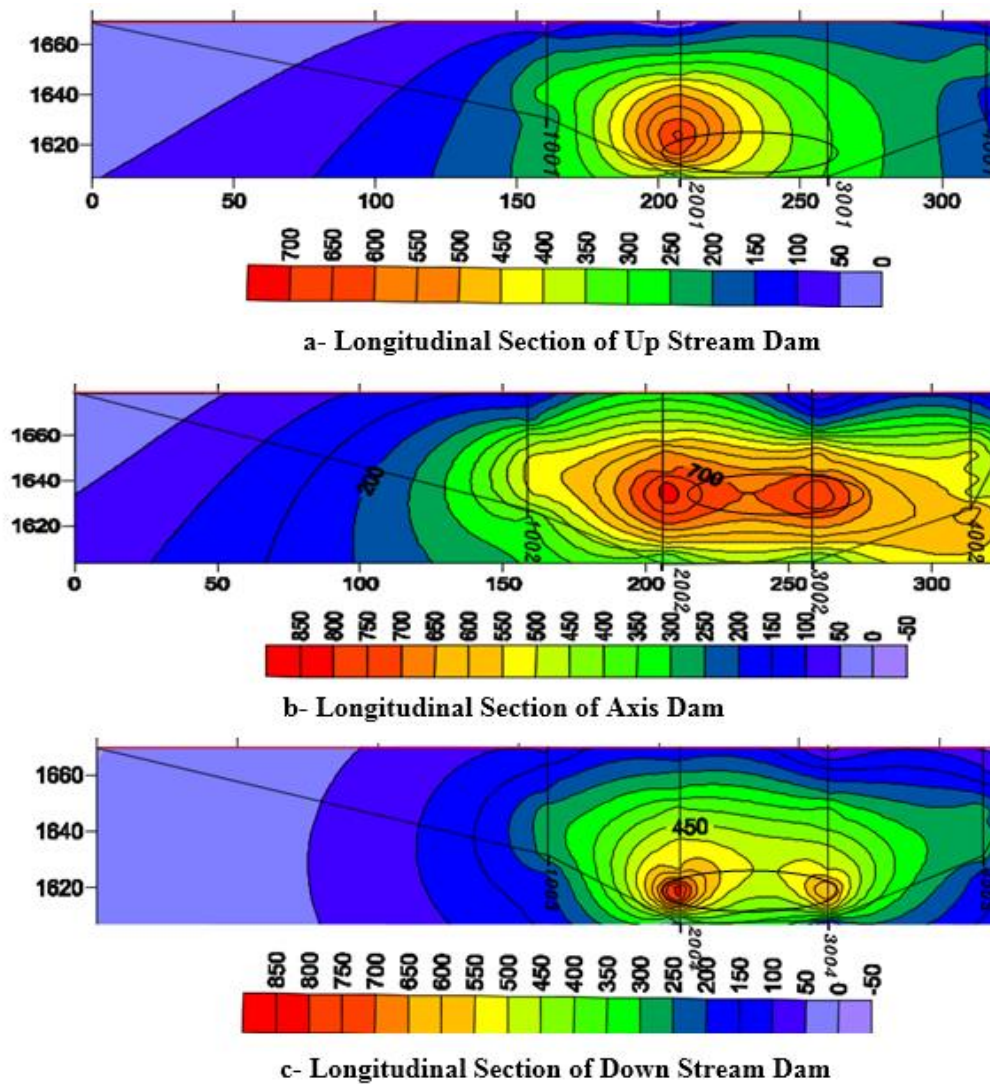


Fig 8. Settlement counters of longitudinal sections of dam at service time

The result of the research is summarized as follows:

- 1- The assessment of instrumentation data shows that the dam behaviors are normal and similar to those was predicted during the dam design period.
- 2- The increasing rate of water pore pressure inside dam core is close to the rise rate of reservoir water level for first impounding condition.
- 3- The dam clayey core is appropriately performed in reduction of pore pressure in seepage flow direction.
- 4- The cut-off wall was built in dam foundation behave properly as the pore pressure is sharply reduced following passing through the wall.
- 5- The maximum settlement value of 816 mm equal to 1% of dam height is observed in core at about 43.7% of dam height.

10. REFERENCES

1. Sozostak-Chrzanowski, A., Chrzanowski, A. and Massiera, M. (2003), “*Use of Geodetic Monitoring Measurements in Solving Geomechanical Problems in Structural and Mining Engineering*,” Proceedings, FIG 11-th International Symposium on Deformation Measurements, Santorini Island, Greece
2. Sowers G, Sally H. (1962), “*Earth and rockfill dam engineering*”. London (UK): Asia Publishing House.
3. Szostak-Chrzanowski, A. and Massiera, M. (2004), “Modelling of deformations during construction of a large earth dam in the La Grande complex, Canada. Technical Sciences Journal, University of Warmia and Mazury, Olsztyn, 109-122.
4. Derakhshandi, M., Pourbagherian, H. R., Baziar, M. H., Shariatmadari, N. and Sadeghpour, A. H. (2014), “*Numerical analysis and monitoring of a rockfill dam at the end of construction (case study: Vanyar dam)*”. International Journal of Civil Engineering, 12(4), 326-337.
5. Pagano, L., Picarelli, L., Rianna, G. and Urciuoli, G. (2010a), “*A simple numerical procedure for timely prediction of precipitation-induced landslides in unsaturated pyroclastic soils*”, Landslide Vol.7, N. 3, pp 273-289, doi: 10.1007/s10346-010-0216-x
6. Pagano, L., Zingariello, M.C. and Vinale, F. (2008), “*A large physical model to simulate flowslides in pyroclastic soils*”, Proceedings of the 1st European Conference on Unsaturated Soils, E-UNSAT 2008: Unsaturated soils- advances in geo-engineering, Durham, UK, pp. 111-115.
7. Toll D.G., Lorenzo S.D.N., Mendes J., Gallipoli D., Evans F.D., Augarde C.E., Cui Y.J., Tang A.M., Rojas Vidovic J.C., Pagano L., Mancuso C., Zingariello C. and Tarantino A. (2011), “*Soil Suction Monitoring for Landslides and Slopes*”, Quarterly Journal of Engineering Geology and Hydrogeology, vol. 44, N.1., pp. 23-33, doi: 10.1144/1470-9236/09-010
8. Rojas J.C., Pagano L., Zingariello M.C., Mancuso C., Giordano G. and Passeggio G. (2008), “*A new high capacity tensiometer: first results*” Proceedings of the 1st European Conference on Unsaturated Soils, E-UNSAT 2008: Unsaturated soils- advances in geo engineering, Durham, UK, pp. 205-211, London: CRC Press - Taylor & Francis Group
9. Sadrekarimi, J. and Kia, M. (2005), “*Performance of a large dam, field measurements and analytical approach*” 16th Int. Conf. Soil Mechanics and Geotechnical Engineering, Osaka, Japan, PP. 1115-1116
10. Fell, R., Mas Gregor, P. and Stapledon, D. (1992), “*Geotechnical engineering of embankment dams*” Publication, A.A, Balkema.
11. Sherard, J.L., Woodward, R.J., Gizienski, S.F. and Clevenger, W.A. (1976), “*Earth and earth-rock dams*”, Publication, Wiley & Sons.
12. Niromand, H. (2000), “*Analisis behavior of Karkheh earth fill dam during construction using instrument data*” thesis of msc degree (in Persian)

Effective parameters for calculating the discharge of spillway with radial gates at large dams

Hossein Khalili Shayan¹, Javad Farhoudi², Younes Aminpoor³, Amin Seyedzadeh⁴
Reza Roshan⁵, Alireza Vatankhah⁶

1, 3- Ph.D. Student in Hydraulic Structures, Irrigation and Reclamation Engineering Dept., University of Tehran, Tehran, Iran

2- Professor, Irrigation and Reclamation Engineering Dept., University of Tehran, Tehran, Iran

4- MSc. Student in Hydraulic Structures, Irrigation and Reclamation Engineering Dept., University of Tehran, Tehran, Iran

5-Academic Member, Hydraulic Structures Division, Water Research Institute, Tehran, Iran

6- Associate Professor, Irrigation and Reclamation Engineering Dept., University of Tehran, Tehran, Iran

Email: h_kh_shayan@ut.ac.ir

Abstract

In addition to the use of spillways with radial gate with a short height at regulating dams, they are used in the body of large reservoir dams and at the lower levels for flushing the sediments or regulating the flow at the outlet. At the earth and rockfill dams, the spillway is not a part of the dam and it is provided on either of the banks of the river which results in an oblique approach flow to the spillway that likely to affect the discharge capacity of the spillway. Accordingly, in each case, the parameters affecting the discharge of gated spillway are different. Studies on the determination of the discharge of spillways with radial gates are limited to three categories: USACE (1977), USBR (1973) and Sinniger and Hager (1989). There are some complexities for estimation the discharge of spillways with radial gates, which need further studies in this field (The difference in base form of the variation of the discharge with upstream head, providing the earlier methods based on limited experimental and field verifications, the complexity of determining the required parameters for estimation the discharge in USACE (1977), ignoring the effect of gate seat location on the discharge of gated spillways in USBR (1973) and Sinniger and Hager (1989), ambiguity in accuracy of the proposed method for estimating the discharge of gated spillway for its application as the flood discharge systems in large dams). Also, there is insufficient information about the capability of proposed equations under transition flow between orifice and non-orifice conditions. This paper presents an investigation about the ability of different methods in estimating the discharge of the spillway with radial gates. For this goal, 912 data series were collected from some experimental observations on the physical models which constructed from seventeen flood discharge systems in Iranian large dams. In addition to dimensional analysis of effective parameters on the discharge of gated spillway, new relations were established for the simple determination of gate opening and gate lip angle, in contrast to the sophisticated approach used in the USACE (1977) method. In addition to assessing the effects of different parameters on the discharge of gated spillways based on F-test, a new dimensional equation was proposed for estimating the discharge of gated spillways in relation to the most important parameters. Based on all experimental data, the Mean Absolute Relative Errors (MARE) for discharge estimation from USACE (1977), USBR (1973), Sinniger and Hager (1989) and new proposed equation are 6.9%, 9.1%, 5.1% and 3.9%, respectively. Under transitional flow condition, MARE from the above methods are 13.9%, 5.4%, 22.2% and 4%, respectively. This result shows that the unanimous performance of the new proposed method under all flow conditions. Also, it is significant the accuracy of USBR (1973)'s method for discharge estimation under transitional flow condition. The results show that the difference in the shape of the downstream shape of spillway compared to the standard ogee shape, lead to MARE up to 11.8% in the earlier methods. However, the new proposed method is suitable for application in the presence of different downstream shapes of spillway. In similar conditions, the MARE for discharge estimation has decreased to 4.4% by using the new proposed method. The results show that under the simultaneous operating conditions of eight radial gates over the spillway, MARE from the previous proposed methods increased to 22.3%. In this condition, MARE from the new proposed method was about 2.9%. Experimental observations also show an increase in the MARE for discharge estimation of gated spillway up to 11% in operating conditions of only one gate from the several gates. This is due to the effect of the fatigue flow lines behind of the closed gates on the pattern of open-gate flow lines.

Keywords: Discharge, Flood Discharge System, Gated Spillway, Large Dams, Physical Modelling.

1. INTRODUCTION

The application of gates, including sluice and radial (or Tainter) gates in combination with overflow structures, would result in better management of the reservoir of the dam compared to the design of the free overflow design. The use of radial gates is more common than sluice gates, especially in the large dam, but to the ease operation and need less force for operation.

Radial gates are designed on an ogee spillway to achieve a variety of goals. In regulating dams, gated spillways with short height, are used to regulate the flow according the downstream water need or to stabilize the upstream water depth for passing the constant discharge from the upstream intakes. Also, ogee spillways with radial gates can be used in the body of large reservoir dams and at the lower levels for flushing the sediments or regulating the flow at the outlet. Figure 1 shows the use of gated spillways with radial gates as a flood discharge system at the sideway of Karkheh dam in Khuzestan province in Iran.



Figure 1- An example of the use of gated spillways with radial gates as a flood discharge system at the sideway of Karkheh dam in Khuzestan province in Iran.

By using the stage-discharge relationship, it is possible to measure the flow discharge from the reservoir. On the other hand, by using this relationship, the operator can regulate the desired gate opening to release the discharge according the downstream water needs. In spite of the extensive use of gated spillways, there are only some limited works for discharge estimation of these structures. United States Bureau of Reclamation (USBR, 1973), developed the following equation for discharge estimation of an ogee spillway with radial gate [1]:

$$Q = \frac{2}{3} C_d L \sqrt{2g} \left(H_1^{\frac{3}{2}} - H_2^{\frac{3}{2}} \right) \quad (1)$$

in which, Q =the discharge, C_d =the discharge coefficient, L =effective length of the spillway, g =acceleration due to the gravity, H_1 =upstream water head over the crest, and H_2 =upstream water head over the bottom of the gate ($H_2=H_1-y_L$, where y_L is the vertical opening of the gate against to the crest). The discharge coefficient (C_d) from this method can be determined as a function of the ratio of y_L/H_1 . It should be noted that this method is developed for situations where the gate seat designed at the weir crest. Figure 2 shows the geometric parameters which affect the discharge of spillways with radial gate.

United States Army Corps of Engineers (USACE, 1977), proposed the following formula for discharge estimation of spillways with radial gates [2]:

$$Q = C_d L w \sqrt{2gH} \quad (2)$$

where w = net gate opening (the distance between the bottom edge of the gate from the crest) and H =head to center of gate opening (Figure 2). C_d is the discharge coefficient, which can be determined as a function of β and the ratio of X_s/H_d from Hydraulic Design Chart 311-1 (X_s is the distance of gate seat to the crest and H_d is the design head of the spillway) According to Figure 2, the angle (β) formed by the tangent to the gate lip and the tangent to the crest curve at the nearest point of the crest curve. The net gate opening is considered to be the shortest distance from the gate lip to the crest curve.

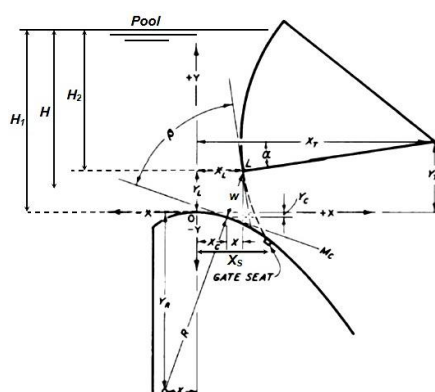


Figure 2- Defination sketch of geometric parameters for discharge estimation of spillways with radial gates

USACE (1977)'s method was developed based on limited experimental data from the three physical models and some data about field operation of three spillways with a radial gate in the United States. This relation is also based on a limited some observation in which at least three gates have been operated simultaneously on the same gate openings. Discharge coefficients for a single bay would be lower because of side contractions. In this method, it is necessary to use three Hydraulic Design Charts named as Chart 311-2, 311-3, 311-4 to determine β and w . It is noteworthy to mention that USACE (1977)'s method for Tainter gates mounted on spillway crests shaped to $X^{1.85} = -2H_d^{0.85} \times Y$. It is believed that this method is accurate to within $\pm 2\%$, for gate opening-head ratios (w/H_0) less than 0.5.

To find out the discharge coefficient of gated spillways in Equation (2), Sinniger and Hager (1989) proposed the following formula [3]:

$$C_d = 0.908 \left[1 - \frac{\beta}{277^\circ} \right] \left(\frac{H}{H_d} \right)^{0.12} \quad (3)$$

Due to the difference in the level of gate seat point compared to the downstream channel, Gated spillways only operated under free flow condition, especially for its application as a flood discharge system in the vicinity of large dams. However, there are some complexities in the discharge estimation of gates spillways for above mentioned applications. Depending on the level of the edge of the gate in the opening position and upstream water level, there are three flow conditions from the gated spillways: (a) Free Non-Orifice flow, (b) Free Orifice flow and (c) Transition zone between the orifice and non-orifice flow. Hussain et al. (2014), indicated that the orifice flow condition requires head over the crest exceeds from (1.5-1.7) w [4]. Also, Hager and Bremen (1988) found that the flow from the spillways with sluice gate changes to non-orifice condition for $y_1/H_1 > 0.77$ [5]. Under orifice and non- orifice flow conditions, the discharge of gated spillways, varies with half and three second

power of upstream head, respectively. However, there has not yet been a general study about the variation of the discharge of gated spillways with upstream head under a transition between orifice and non-orifice flow conditions. Under transition zone, the flow condition is unstable and it seems that the discharge variation with upstream head is different under falling with rising. Consequently, the discharge estimation under transition zone requires further sensitivity and precision.

Due to the curvilinearity of the flow, a suction effect predominates and the flow increases for the same gate opening and reservoir level. It is economical to provide a gate slightly below crest as it reduces the cost of the spillway structures which has to conform to the shape of the jet for the orifice flow. The Ogee profile, determined for free flow condition, may be subjected to cavitation damage for orifice flow, especially for small gate opening. When the gate seat is provided slightly downstream of the crest, the cavitation problem is also reduced. Among of the previous studies for discharge estimation of gated spillways, the proposed method by USBR (1973) is presented for the design of gate seat on the crest which is not applicable in practical cases. Consequently, further studies are required for about the effect of gate seat position on the discharge estimation of gated spillways.

In the earthen and rockfill dams, the spillway is not a part of the dam and it is provided on either of the banks of the river. Thus approach flow to the spillway is oblique and that will affect the discharge capacity of the spillway. However, the effect of presence of guide walls and the curvature effect of the flow lines on the

discharge coefficient of gated spillways has not been studied with the above mentioned methods and requires further study.

Due to executive considerations such as the easy operation of the gates, reduction in the required force for gate displacement, a defect in the operation system of the gate, the designers are more likely to set up a set of multiple gates. In this case, some gates may be open and some others closed. The dead zone behind the closed gates, can affect the pattern of flow lines near the open gates. This could affect the discharge estimation of gated spillways using above mentioned equations.

The previous methods only can be used for discharge estimation of gated spillways where the downstream face of the spillways follows from the ogee standard shape. Deviation from ogee standard shape can be affect the application of the previous methods for calculation of β and w . Consequently, some general methods are needed for the different geometrical characteristics of the spillway.

On the other hand, differences in the form of the stage-discharge relationships from Equations (1) and (2), necessitate the evaluation of the efficiency of various proposed methods for discharge estimation of gated spillways under orifice and transition flow conditions.

Table (1) shows a series of effective parameters for calculating the discharge of spillways with radial gates and its application as a flood discharge system at the vicinity of large dams.

Table 1- Effective Parameters for Calculating the Dicharge of Spillways with Radial Gates at Large Dams

Series	Parameter	Symbol	Series	Parameter	Symbol
1	Gate lip angle	β	11	Width of approach channel	B
2	Upstream weir slope	m	12	Width of gate	b
3	Upstream weir depth	H	13	Pier width	b_p
4	Discharge of each gate	Q_i	14	Pier shape	-
5	Opening of each gate	$y_{Li} (i=1-N)$	15	Radial distance of each gate	r
6	Viscosity	ν	16	Weir height	P
7	Surface tension	σ	17	Gate radius	R
8	Design head	H_D	18	Gate seat situation	X_S
9	Downstream weir face	-	19	Turnnion	X_T
10	Mass density	ρ	20	Turnnion height	Y_T

In this paper, totally 912 data series was used to evaluate the performance of different methods for estimating the discharge of gated spillways. The data was derived from some experimental observations on the physical models which constructed from seventeen flood discharge systems in Iranian large dams. Based on the Pi-Buckingham theory, it was presented some non-dimensional parameters which affected the discharge of gated spillways and the corresponding relationship was deduced. The capability of different methods for discharge estimation was compared under orifice and transitional flow conditions. Also, a set of theoretical equations was derived for explicit and simple determination of β and w . Based on F-test, a new dimensional equation was proposed for estimating the discharge of gated spillways in relation with the most important parameters.

2. MATERIALS AND METHODS

In this study, an extensive set of laboratory data was used to investigate the applicability of the different previous proposed relationships and to propose a new relationship to determine the discharge of spillways with radial gate. For this purpose, the results of studies on the physical models made from the flood discharge systems as a part of the Iranian reservoir dams were used. Totally, 17 models were studied. From this set of physical models, 16 dams were constructed in Iran during the years 1992 to 2014 at the Hydraulic Laboratory of the Iranian Water Research Institute. Also, the results of a physical model of the Ostor dam have been used in the EPFL hydraulic laboratory in Switzerland. Figure 3 shows the images of a set of physical models of the 17 flood discharge systems. Also, in Table 2, the range of non-dimensional parameters in the experimental collection data is mentioned. In most of the models, such as the Kheyraabad, Jareh, Azad, Doosti,

Gotvand Olya, Siazakh, Seymareh, Karun 3, Raeesali Delvari, Mamloo, Nyan, Mansion, Chamyshir, Karkheh, Karun 4 and Ostor dams, the spillway is not a part of the dam body, and the flow passes through the guide walls (Figure 3). However, eight gates were designed in the dam body of Salman Farsi according to Figure 3.

The number of radial gates on the crest varies from 2 to 8 in the models studied. In most physical models, the downstream weir face forms follow from the form of $y/H_D = -K (x/H_D)^n$. However, in the physical model of the Ssiazakh dam, the weir face is completely different from the standard Ogee spillway. Accordingly, the differences in K and n and the form of downstream weir face in the set of studied models can be used to examine the applicability of the previous proposed methods for estimating the discharge of gated spillways.

Also in the physical models of Salman Farsi and Siazakh dams, arched spillway could affect errors in estimating the discharge of gated spillways by the previous methods.

In most laboratory experiments, all designed gates have the same openings. However, in the findings of the physical models of the Ostor and Salman Farsi flood discharge systems, a number of experiments relate to the operation of one or more gates from a set of the gates.

In the data collection, the relative position of the gate seat is located at $0.1 \leq X_g/H_D \leq 0.4$, which provides an appropriate examination of the effect of the gate seat on the discharge estimation.

Another advantage of the data is the existence of 31 data series related to the transitional flow range ($y_L/H_1 > 0.77$), which is mainly related to the physical model of the Mamlou flood discharge system.

Table 1- Range of effective non-dimensional parameters in the present experimental observations.

Non-Dimensional Parameters	K	n	m	R/H _d	Y _T /H _d	P/H _d	X _g /H _d	b _p /b
Range	0.24-0.70	1.00-1.85	0-1.03	0.68-1.97	0.25-0.66	0.15-2.25	0.10-0.40	0.20-0.57
Non-Dimensional Parameters	N	We	Re	β*	H ₂ /H _D	w/H _D	C _{dexp}	Q* _{exp}
Range	2-8	(2.9-349) ×10 ⁵	(4-65)×10 ⁶	52.2-98.2	0.01-1.27	0.07-0.79	0.39-0.92	0.57-3.99



Figure 3- Images from hydraulic models of flood discharge systems in the present study

3. Results and Discussions

Dimensional Analysis

From Table (1), the discharge of the spillways with radial gate is a function of different parameters which can be defined as follows:

$$F \left(b_p, b, R, Y_T, X_T, X_S, P, m, \left\{ \begin{matrix} H_1 \\ H_2 \\ H \end{matrix} \right\}, r, H_D, y_{L(i)}, k, n, v, \sigma, g, \rho, Q_i \right) = 0 \quad (4)$$

On the other hand, it can be shown:

$$x_{c(i)} = f_2(k, n, y_{L(i)}, X_T, R, Y_T) \quad (5)$$

$$\beta_i = f_3(k, n, x_{c(i)}, y_{L(i)}, Y_T, R) \quad (6)$$

As a result of Equations (5) and (6), it can be shown that,

$$\beta_i = F_1(k, n, y_{L(i)}, X_T, R, Y_T) \tag{7}$$

The functional relation (4) will be obtained as follows:

$$F(b_p, b, X_S, P, m, r, H_2, H_D, y_{Li}, \nu, \sigma, g, \rho, \beta_i, Q_i) = 0 \tag{8}$$

in which β_i and m are non-dimensional parameters. From Equation (8), the total number of dimensional variables is $n=13$ and from all three geometric, kinematic, and dynamic parameters there is at least one parameter in the set of parameters. As a result, 10 non-dimensional parameters need to be as follows:

$$\begin{aligned} \pi_1 &= \frac{X_S}{H_D}, \pi_2 = \frac{P}{H_D}, \pi_3 = R_e, \pi_4 = We, \pi_5 = \frac{b}{H_D}, \pi_6 = \frac{b_p}{H_D}, \pi_7 = \frac{r}{H_D}, \pi_8 = \frac{H_2}{H_D}, \\ \pi_9 &= \frac{y_{Li}}{H_D}, \pi_{10} = \frac{Q_i}{\sqrt{gH_D^5}} \end{aligned} \tag{9}$$

Due to the combination of non-dimensional parameters, and ignoring from Reynolds and Webber Numbers due to their significant amounts within the scope of the present research (Table 2), the following dimensional relationship is achievable:

$$Q_i^* = \frac{Q_i}{b\sqrt{gw_i^3}} = f\left(\beta_i, m, \frac{X_S}{H_D}, \frac{P}{H_D}, \frac{b_p}{b}, \frac{b}{H_D}, \frac{r}{H_D}, \frac{H_2}{y_{L(i)}}, \frac{y_{L(i)}}{H_D}\right) \tag{10}$$

Derivation of Geometric Relations for Explicit Estimation of β and w :

Discharge estimation of the spillway with radial gate using USACE (1977)’s method needs to calculate β and w . As mentioned above, determining these parameters in USACE (1977)’s method requires several steps and the use of three hydraulic design charts. Also, this method is limited to the standard ogee spillways and a different shape lead to an error in the calculation β and w . Generally, gate lip and weir crest levels (E.L.L and E.L.o, respectively) are known. As a result, the vertical opening of the gate will be known ($y_L=E.L.L-E.L.o$). Taking into account the general form ($y/H_D=-K(x/H_D)^n$) for the downstream face of a gated spillway and knowing y_L, H_D, Y_T, R, K, n , reservoir level (E.L.R) and gate seat level (E.L.s), it can be shown that,

$$\frac{x_T}{H_D} = \frac{x_S}{H_D} - \sqrt{\left(\frac{R}{H_D}\right)^2 - \left(\frac{Y_T}{H_D} - \frac{y_S}{H_D}\right)^2} \tag{11}$$

$$\frac{x_L}{H_D} = \frac{x_T}{H_D} - \sqrt{\left(\frac{R}{H_D}\right)^2 - \left(\frac{Y_T}{H_D} - \frac{y_L}{H_D}\right)^2} \tag{12}$$

As shown in Figure (2), point C has the smallest distance from the downstream edge of the gate. This point is over the weir. Consequently,

$$\frac{y_c}{H_D} = -k\left(\frac{x_c}{H_D}\right)^n \tag{13}$$

On the other hand, the passage line from points L and C is perpendicular to the weir face at C and therefore it can be shown:

$$\frac{\frac{y_L}{H_D} + k\left(\frac{x_c}{H_D}\right)^n}{\frac{x_L}{H_D} - \frac{x_c}{H_D}} \times kn\left(\frac{x_c}{H_D}\right)^{n-1} = 1 \tag{14}$$

Thus, by knowing x_L/H_D and x_C/H_D from Equations (12) and (14), y_C/H_D is determined from Equation (13). Also, the distance of point L from the MC line is equal to the gate opening (w) (Figure 2):

$$\frac{w}{H_D} = \frac{\left| \frac{y_L}{H_D} + kn \left(\frac{x_C}{H_D} \right)^{n-1} \frac{x_L}{H_D} + k(1-n) \left(\frac{x_C}{H_D} \right)^n \right|}{\sqrt{1 + \left[kn \left(\frac{x_C}{H_D} \right)^{n-1} \right]^2}} \quad (15)$$

The angle of tangent tangency on the weir at point C, along the horizon, is:

$$\theta = \tan^{-1} \left| -kn \left(\frac{x_C}{H_D} \right)^{n-1} \right| \quad (16)$$

Also, the gate lip angle can be found from the following equation:

$$\alpha = \sin^{-1} \left[\frac{\frac{Y_T}{H_D} - \frac{y_L}{H_D}}{\frac{R}{H_D}} \right] \quad (17)$$

Finally, the angle β can be obtained from the following equation:

$$\beta = \frac{\pi}{2} - \theta - \alpha \quad (18)$$

Table (3), shows some examples for calculating β and w which presented by USACE (1977)'s method from the Hydraulic Design Chart 311-2. These examples were defined for a standard ogee spillway with radial gate ($y/H_D = -0.5(x/H_D)^{1.85}$, $X_S = 0.1 \times H_D$, $R = 0.831 \times H_D$, $X_T = 0.907 \times H_D$, $Y_T = 0.324 \times H_D$, $H_D = 37$ ft). Tale (3) also compares the results of USACE (1977)'s method with the new method in the present study for calculating β . It can be seen that the present study accurately estimate β and w without the need for a set of graphs as mentioned in USACE (1977)'s method.

Table (3)- comparison between USACE (1977) and present study for calculating β and w [Hydraulic Design Chart 311-2]

y_L (ft)	x_L (ft)	x_C (ft)	y_C (ft)	w (ft)	w/H_D	α°	$ m $	θ°	β° Present Study	β° USACE (1977)
3.700	3.950	3.464	-0.231	3.936	0.106	15.638	0.124	7.043	67.319	67.200
7.400	3.156	2.461	-0.123	7.438	0.201	8.582	0.092	5.279	76.140	76.080
11.100	2.825	1.970	-0.081	11.062	0.299	1.655	0.076	4.372	83.973	83.980
14.800	2.941	1.859	-0.073	14.753	0.399	-5.247	0.073	4.162	91.085	91.200

The new proposed method also can be used for gated spillways with the different downstream weir face in comparison with the standard ogee spillways. For example, the downstream weir face at the gated spillway at Apalachia dam follows from the different shape ($y = -x^3/27000 + x^2/68 + x/15$). Figure (3) compares the variation of β , x_C/H_D , x_L/H_D , y_C/H_D , w/H_D , α , $|\theta|$, $|m|$ with y_L/H_D using the new proposed method and for three gated spillways with the different downstream faces (Ogee standard spillway, Kheirabad dam in Iran and Apalachia dam in USA).

For an ogee standard spillway with radial gate ($y/H_D = -0.5(x/H_D)^{1.85}$, $X_S = 0.1 \times H_D$, $R = 0.831 \times H_D$, $X_T = 0.907 \times H_D$, $Y_T = 0.324 \times H_D$), the following equations can be used for explicit estimation of β and w :

$$\beta = \begin{cases} \frac{57.2+207.94\left(\frac{y_L}{H_D}\right)}{1+1.58\left(\frac{y_L}{H_D}\right)-0.55\left(\frac{y_L}{H_D}\right)^2}, \frac{y_L}{H_D} \geq 0 \\ 57.2+109.683\left(\frac{y_L}{H_D}\right), \frac{y_L}{H_D} \leq 0 \end{cases} \quad (19)$$

$$\frac{w}{H_D} = \begin{cases} \frac{0.013+0.933\left(\frac{y_L}{H_D}\right)}{1-0.1\left(\frac{y_L}{H_D}\right)+0.013\left(\frac{y_L}{H_D}\right)^2}, \frac{y_L}{H_D} \geq 0 \\ 0.013+0.908\left(\frac{y_L}{H_D}\right), \frac{y_L}{H_D} \leq 0 \end{cases} \quad (20)$$

Evaluation of Different Methods for the Discharge Estimation of Spillways with Radial Gate:

Based on the 912 series of experimental data collected in the present study, it is possible to evaluate and compare the capability of different methods for the discharge estimation of gated spillways as a part of the flood discharge system in large dams. Table (4) shows the specification of gated spillways studied in this research. Also, Table (4) and Figure (5) present the values of Mean Absolute Relative Error (MARE) for discharge estimation of gated spillways by the different methods.

Based on all experimental data, the Mean Absolute Relative Errors (MARE) for discharge estimation from USACE (1977), USBR (1973) and Sinniger and Hager (1989) are 6.9%, 9.1%, and 5.1%, respectively. The range of variation in the average values of the relative errors in discharge estimation of gated spillways using above mentioned equations is (2.48%-10.69%), (2.01%-22.28%) and (1.86%-11.86%), respectively (Table 4). Consequently, Sinniger and Hager (1989) has improved the accuracy of the discharge estimation of spillways with radial gate, significantly. The limited range of variation in the Sinniger and Hager (1989) method indicates that the dominant parameters (β and w) have been considered in this method. Also, the discharge estimation of gated spillways using the based form according Equation (2) is more accurately compared to Equation (1).

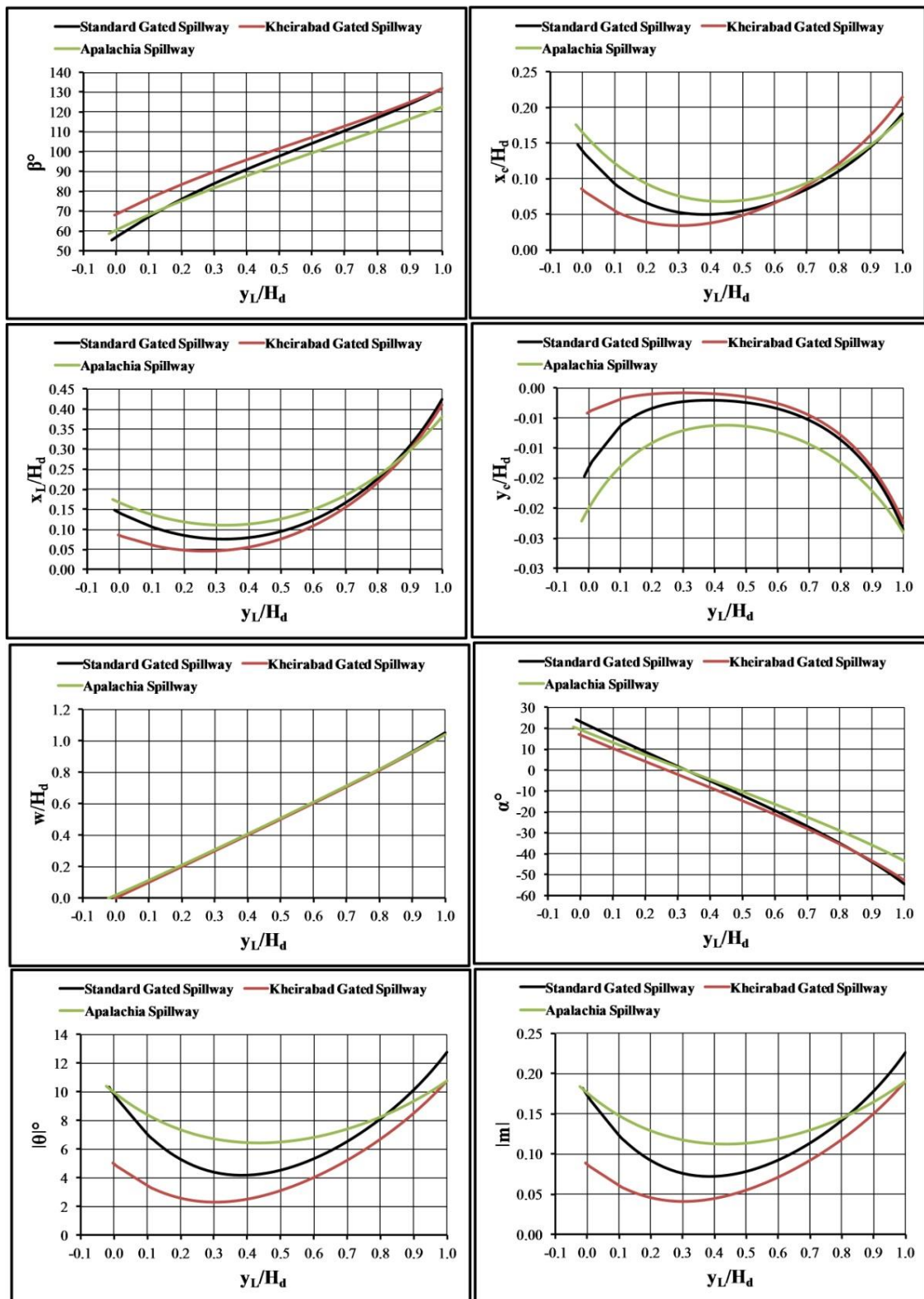


Figure (3)- Variation of β , x_c/H_d , x_L/H_d , y_c/H_d , w/H_d , α , $|\theta|$, $|m|$ with y_L/H_d using the new proposed method and for three gated spillways with the different downstream face

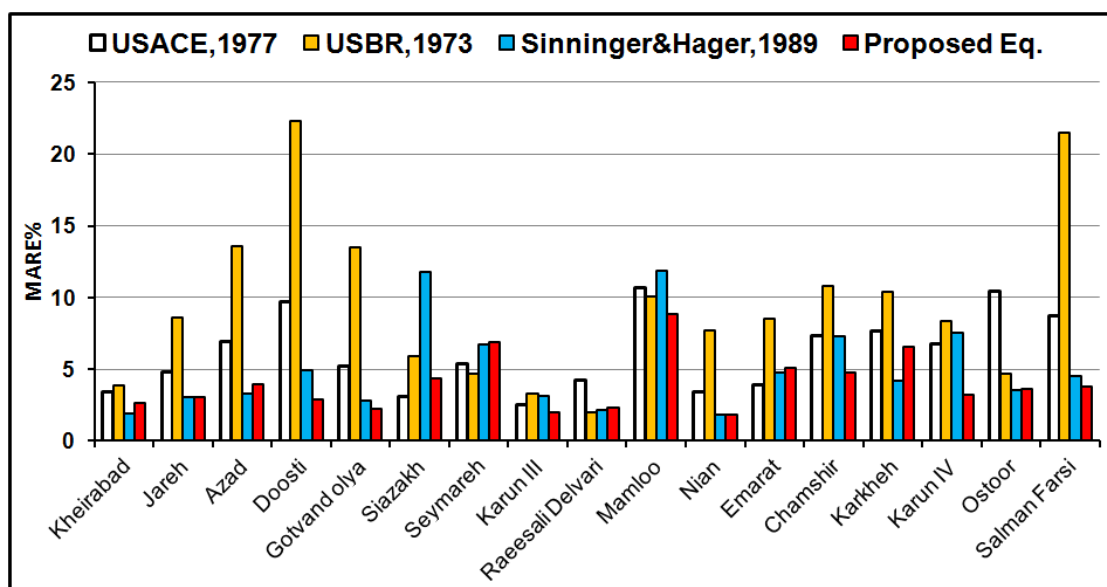


Figure (5)- Evaluation of different methods for the discharge estimation of spillways with radial gate

In the present study, especially for experimental observation of the hydraulic model of Mamloo dam, a part of experimental data related to the operation of gated spillway under transition zone between orifice and non-orifice flow conditions. Figure (6) shows the discharge values from USACE (1977)’s method and the corresponding values from experimental observations on the hydraulic model of Mamloo dam. In the present study, based of the proposed criterion by Hager and Bermen (1988), the range of $0.77 < y_L/H_1 < 1$ is considered as a transition zone. It can be seen that using USACE (1977)’s method gives the mean absolute relative error about 25.7% and 11.6% for the discharge estimation under non-orifice and transition flow conditions, respectively.

For passing the low discharge from the gated spillways, it is necessary to adjust the gates with a small opening. In these conditions, the gate may be operated under transition zone. One solution to prevent the operation of the gate under transition zone is setting one or more gates with the greater openings and closing the others. However, this solution is not very desirable due to the effects of supercritical flow extracting from the one gate over the downstream of chute spillway.

Figure (7) compares the capability of different methods for the discharge estimation of the spillway with radial gate using collected data under the gated and transition flow conditions. The MARE% for the orifice flow condition from USACE (1977), USBR (1973) and Sinniger and Hager (1989) are 6.7%, 9.2% and 4.5%, respectively. Consequently, Equation (2) is more applicable for discharge estimation under orifice flow conditions. It can be shown that Equation (1) changes to Equation (2) for the ratio of w/H_1 lower that a certain value.

The MARE% for the transition flow condition from USACE (1977), USBR (1973) and Sinniger and Hager (1989) are 13.9%, 5.4% and 22.2%, respectively. Consequently, the accuracy of USACE (1977) and Sinniger and Hager (1989) methods considerably decrease under transition flow condition. On the other hand, due to the general form of Equation (1) USBR (1973)’s method, this method is much more efficient than the two other methods for the discharge estimation in the transition zone. Consequently, it is necessary to provide some methods for accurate flow estimation of the gated spillways continuously from non-orifice to orifice flow conditions.

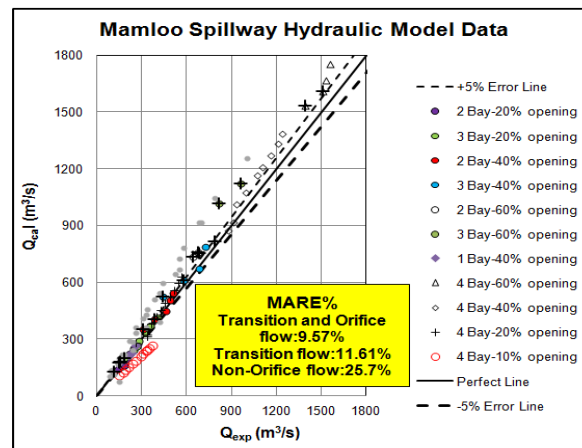


Figure (6)- Evaluation of USACE (1977)’s method for the discharge estimation under transition zone (Mamloo spillway)

Figure (8) shows the capability of USACE (1977)’s method for the discharge calculating based on the data from hydraulic models of Doosti, Karkheh and Salman Farsi spillways. It was obviously that the values of MARE for the three above models are greater than the correspond value which computed based on all experimental data. In all three models, all gates have the same opening and have been operated in gated flow condition. on the other hand, the downstream face of spillway follows from the standard ogee shape. It seems that the main reason for the increase of the error of estimating the discharge in these three models is increasing the number of gates over the spillway. It can be seen from Figure 8 In most cases, the actual flow rate is greater than the calculated values using the USACE (1977)’s method. In the presence of multi gates over the spillway, flow pattern behind of each gate affected by adjacent gates. In these cases, the discharge of gated spillways is different from the provided value based on equations which have been developed for operation of one or limited gate. As a result, it is necessary to take more precaution regarding the application of USACE (1977)’s method in terms of the designation a lot of the gates over the spillway.

From Table (4) and Figure 9(a), It can be seen that the Mean Absolute Relative Error for discharge estimation using Sinniger and Hager (1989) method (as the best method which mentioned above) considerably increases to about 11.68% based on the data from the Siazakh hydraulic model. The reason is that the proposed equation by Sinniger and Hager (1989) for calculation β and w is only valid for an ogee standard spillway. While, the crest of Siazakh spillway is a part of an arch and the downstream face of the weir is different from the ogee shape (Figure 9b, c). In this case, the proposed relation by Sinniger and Hager (1989) has an error in the determination of β and w . However, the proposed method in the present study can be used to determine the above parameters and for all downstream faces of gated spillways in general.

Figures (10) and (11) shows increasing the error of discharge estimation affected by operating one gate from the several gates. It can be seen from Figure (10) that the MARE% increases to 10.3%, 9.9% and 11.1%, respectively, when the left gate, central gate and right gate operated uniquely in the Ostoor spillway. Also, the data from the hydraulic model of Salman Farsi spillway shows that the MARE values for only operating the central gates, the pair of right gates and the pair of left gates are about 9.3%, 10.6% and 9.8%, respectively (Figure 11). It is interesting that the MARE for discharge estimation by USACE (1977)’s method considerably decreases to 6.4% when all gates are operated with the same openings. This is due to the effect of the fatigue flow lines behind of the closed gates on the pattern of open-gate flow lines. On the other hands, USACE (1977)’s method was developed based on a limited observation in which at least three gates have been operated simultaneously on the same gate openings. Consequently, it is expected that for these conditions, the actual values of the discharge will be reduced to the corresponding values from the USACE (1977)’s method. This result is in agreement with Figures (10) and (11).

There are some other uncertainties in the discharge estimation of gated spillways as a flood discharge system in large dams. For example, the presence of guide walls, the distance of the gate from the center, affected the discharge of each gate. It seems that the discharge increases by increasing the distance of the gate from the center of guide wall. This requires more experimental observations.

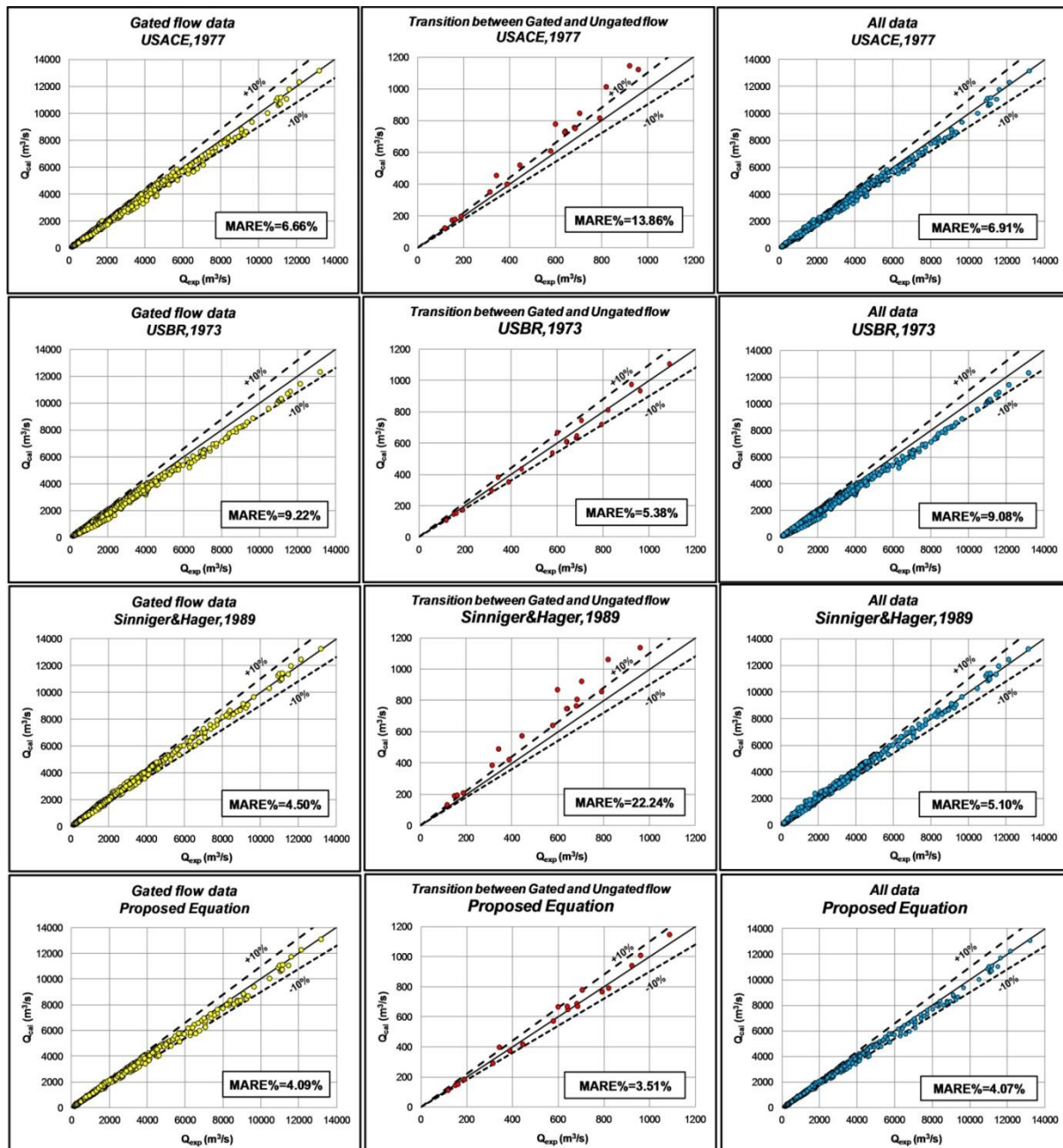


Figure (7)- Evaluation of different methods for the discharge estimation of gated spillways using Gated and Transition flow data

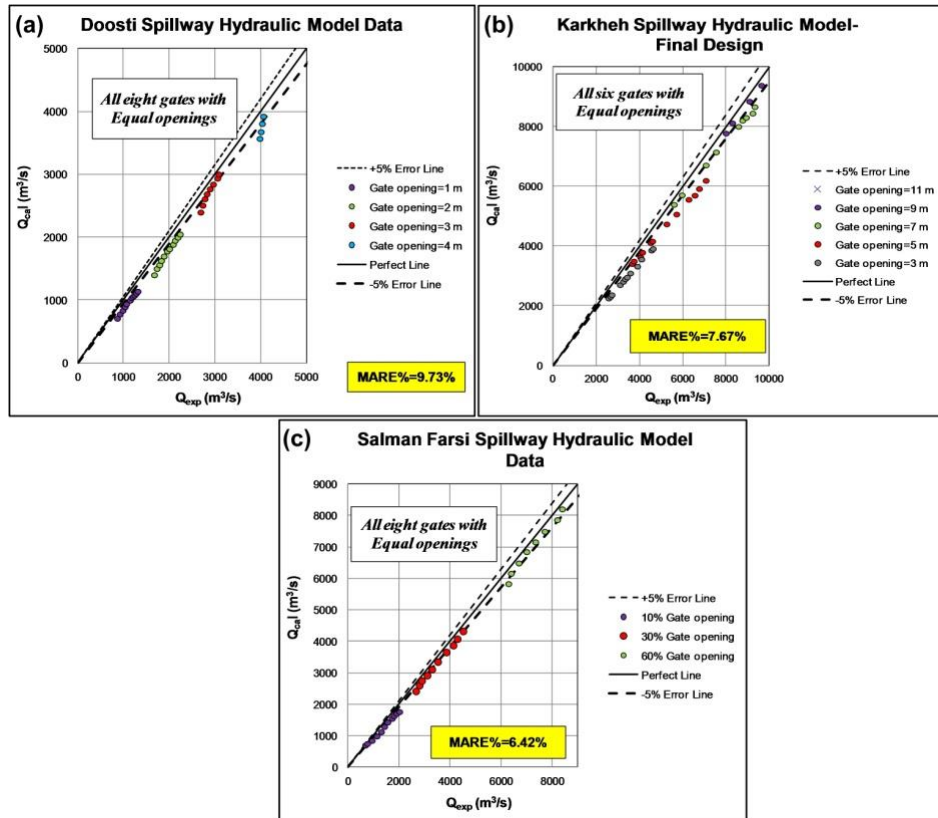


Figure (8)- Effect of downstream weir face on the discharge estimation of gated spillway using USACE (1977)'s method

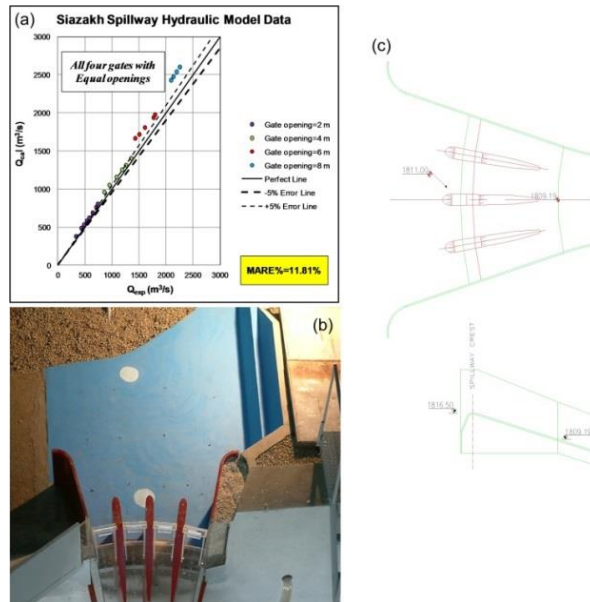


Figure (9)- Siazakh Hydraulic Model (a) Discharge values from Sinniger and Hager (1989) against observation data (b), (c) Image and asbuilt map

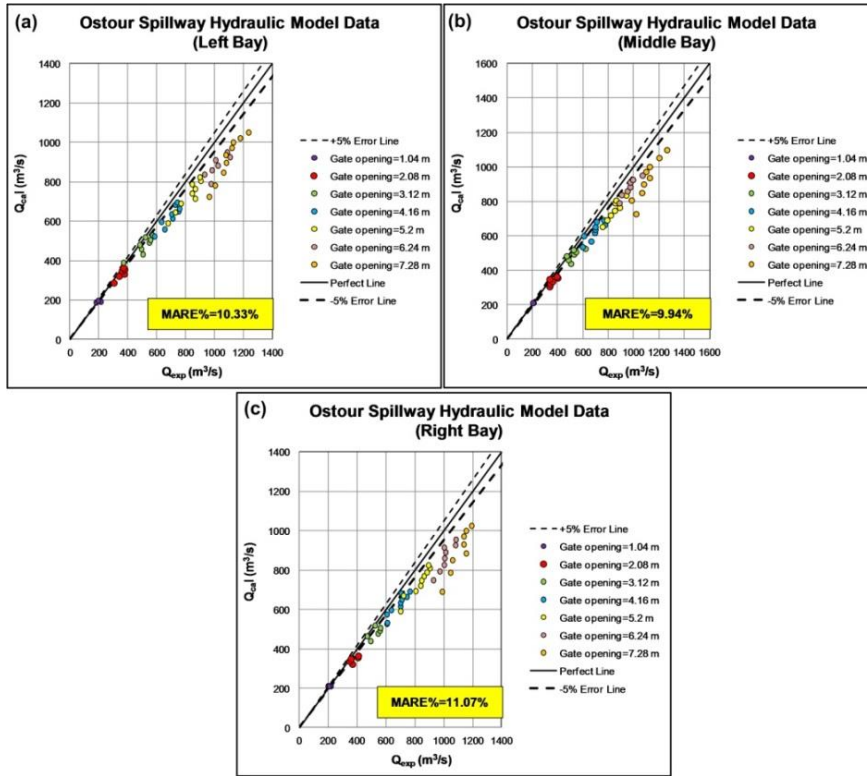


Figure (10)- Effect of the operation of one gate from several gates on the rising of the error in discharge estimation (Ostoor Spillway)

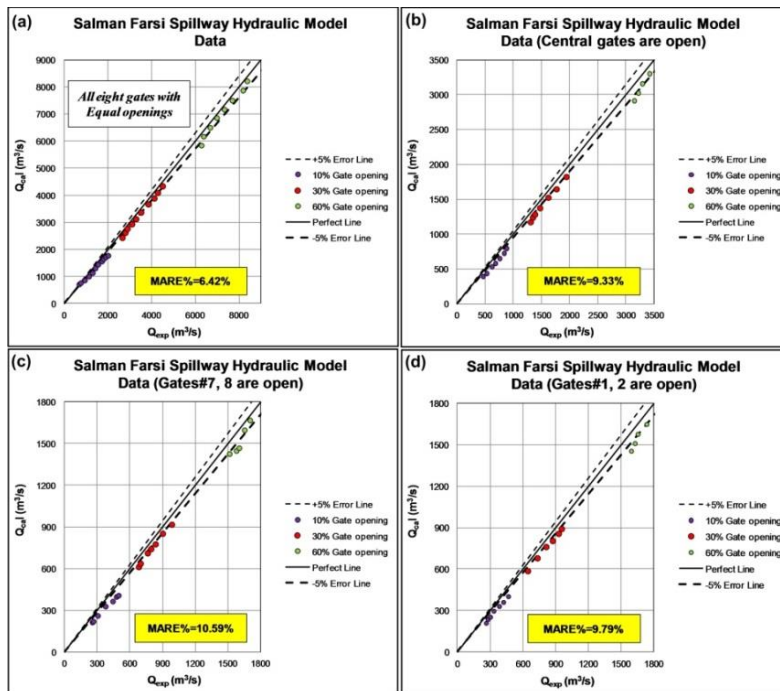


Figure (11)- Effect of the operation of one gate from several gates on the rising of the error in discharge estimation (Salman Farsi Spillway)

Development a New Equation for Discharge Estimation of Spillways with Radial Gate:

Figure (12) shows the variation of C_d with β from the USACE (1977)'s method using the data series from 17 hydraulic models. It can be seen that the discharge coefficient depends on other parameters in addition to β and X_s/H_D . Equation (10) presents non-dimensional parameters which affected the discharge of gated spillways as a part of the flood discharge system in large dams. Based on Table (2), the effects of Reynolds and Webber Numbers have been ignored.

In large dams, the discharge of gated spillways is influenced by the guide walls. Accordingly, the discharge changes with the radial distance. For this reason, the ratio of r/H_D is considered in Equation (10). Unfortunately, most of the experiments in this study were performed when the all gates operated with the same opening. Consequently, the data series at the present study is not sufficient to evaluate the effect of r/H_D . Accordingly, the ratio of r/H_D is ignored in Equation (10).

To find out the importance of various independent variables in predicting $Q^*=Q/(N.b.\sqrt{(g.w^3)})$ (Q is the total discharge), feature selection and variable screening have been carried out using F -Test. A F -Test is any statistical test in which the test statistic has an F - distribution under the null hypothesis (F = explained variance/unexplained variance).

The least F -value parameter is dropped because this parameter is considered as not affecting the whole value of the equation. As shown in Figure (13), H_2/y_L , β and y_L/H_D have the greatest effect on the Q^* . Other parameters show the least importance and are, therefore, dropped while deriving the relationship for Q^* .

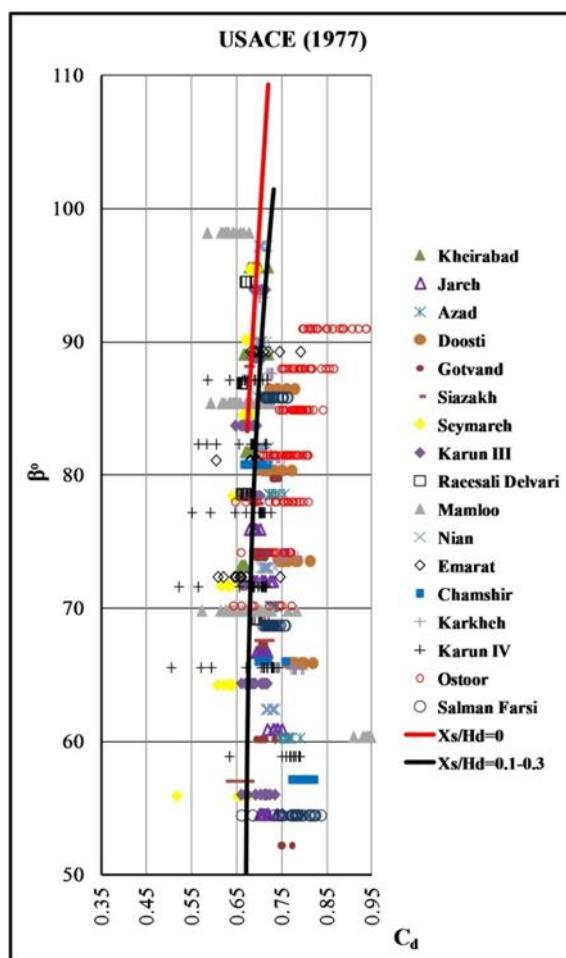


Figure (12)- variation of C_d with β and X_s/H_D based on hydraulic model data

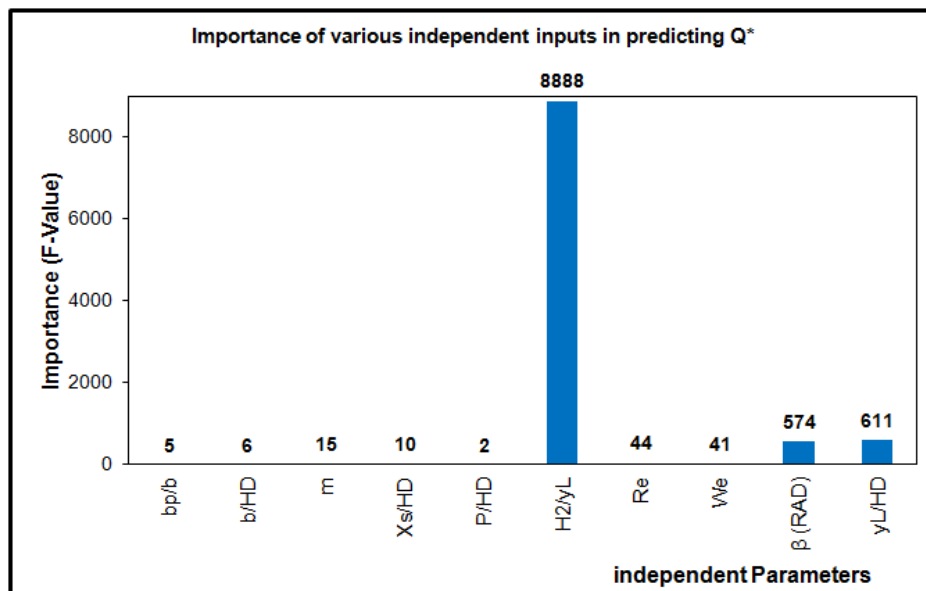


Figure (13)- Importance of various independent inputs in predicting Q*

Finally, the following equation was proposed for estimating the discharge of gated spillways in relation with the most effective parameters:

$$Q^* = a \left(\frac{H_2}{y_L} \right)^{[b + c \times \beta]} + d \left(\frac{y_L}{H_D} \right)^e + f \tag{21}$$

where a , b , c , d , e and f are constant parameters which can be found from the experimental data. In Equation (21), the angle of β is in radians. Using 912 data series from the 17 hydraulic models, the values of above mentioned parameters are 0.752, 0.633, -0.060, 0.323, 0.162 and 0.174, respectively.

Table (4) presents a comparison for the accuracy of Equation (21) with other methods in discharge estimation of gated spillways based on the data from 17 hydraulic models. Also, Figure (7) shows the capability of Equation (21) for discharge estimation under the different flow conditions. The following results were obtained:

- 1- Based on all experimental data, the MARE% from the Equation (21) was obtained about 4.07%. Accordingly, the new proposed method has increased the precision of discharge estimation in comparison with the previous equations.
- 2- Under orifice flow (Gate flow) condition, the MARE% from the Equation (21) was obtained 4.9% which is more accurate than the other methods.
- 3- Under transition zone, Equation (21) calculates the discharge of gated spillways with MARE% about 3.5%. Interestingly, Equation (21) is more accurate for discharge estimation under transition flow condition. As a result, the new proposed method, unlike other previous methods, can be used for accurate discharge estimation of gated spillways with radial gate under orifice and transition flow conditions.
- 4- Based on data series of the hydraulic models of Doosti and Salman Farsi spillways, the MARE%, considerably decreases to 2.9 and 3.8% respectively. Consequently, Equation (21) can be used for accurate discharge estimation in the presence a large number of radial gates over the spillways.
- 5- Based on data series of the hydraulic models of Siazakh spillway, the MARE% considerably decreases to 4.38. Consequently, Equation (21) can be used for accurate discharge estimation of gated spillways with non-ogee shape of the downstream face.
- 6- The data from the hydraulic model of Ostor dam have been collected where only one gate was operated from the several gates. In this condition, the MARE% from Equation (21) considerably decreases to about 3.58%. However, the assurance about the capability of new proposed equation in this case, requires more experimental observations under operation of one gate from the several gates.

The experimental data in this research were collected when the all gates have the same opening. As a result, it is suggested the development of new equations for operating multi gates with the different opening. It is also necessary to investigate the effect of oblique approach flow over the discharge passing of gated spillway.

4. CONCLUSIONS

This paper presents to evaluate the capability of different methods for discharge estimation of spillways with radial gate as a part of the flood discharge system in large dams. For this, the data from 17 hydraulic models of the Iranian large reservoir dams was used. Based on the Pi-Buckingham theory, effective non-dimensional parameters were determined. Based on the F-Test and using of a set of experimental data, the effect of different parameters on the discharge estimation was compared. Also, a new relationship was developed to estimate the discharge of gated spillways in relation with the most important parameters and its constants was calibrated based on experimental data. Based on geometric analyses, some relations were presented for simple estimation of the parameters β and w . This method can be used for the different shapes of downstream weir faces. Based on experimental data, Equation (21) can be used for accurate discharge estimation of spillways with radial gate under orifice and transition flow conditions. However, it is necessary to develop new relationships to estimate the discharge of spillway with multi gates when the gates have the different openings. Also, it is recommended to study the effect of oblique approach flow over the discharge of gated spillway.

5. ACKNOWLEDGMENT

The work performed here would never have been possible without the extensive data sets provided by the Water Research Institute (WRI) in Iran. The completion of this work was greatly aided by these data set from the 17 Hydraulic models which constructed in WRI. Also, the support provided by the Center of Excellence for Evaluation and Rehabilitation of Irrigation and Drainage Networks, University of Tehran, is gratefully acknowledged.

6. REFERENCES

1. U.S. Bureau of Reclamation (USBR). (1973). Design of small dams, U.S. Government Printing Office, Washington, D.C.
2. U. S. Army Engineer Waterways Experiment Station, CE, Discharge Rating Curves for Vertical Lift Gates on Spillway Crests, by R. H. Multer. Miscellaneous Paper No. 2-606, Vicksburg, Miss., October 1977.
3. Sinniger R. O. and Hager W. H. (1989). Constructions Hydrauliques, Presses Polytechnique Romanades, pp 197-201.
4. Hussain, S., Hussain, A. And Ahmad, Z. (2014). Discharge characteristics of orifice spillway under oblique approach flow. Vol (39). pp. 9-18
5. Hager, W. and Bremen, R. (1988). Plan Gate on Standard Spillway. J. Hydraul. Eng., 114(11), pp. 1390-1397.

Numerical simulation of post-construction deformation of a concrete face rockfill dam

Mohammadkeya Khosravi¹, Linke Li¹, Erich Bauer¹

Institute of Applied Mechanics, Graz University of Technology, 8010 Graz, Austria

E-mail: kh.mkia@gmail.com

Abstract

In this paper a novel hypoplastic constitutive model is used to investigate post-construction deformations of a concrete face rockfill dam caused by water impounding and creep. Creep deformations are related to the time dependent process of degradation of the solid hardness of the weathered rockfill material, in which the solid hardness and its rate is introduced into the constitutive model in the sense of a continuum description. The hypoplastic model captures the influence of pressure, density and state of the solid hardness on the incremental stiffness, the peak friction angle and the volume strain behaviour as well as the influence of a degradation of the solid hardness on creep and stress relaxation in a unified manner. The material parameters considered in the present study are relevant for weathered broken granite. The results obtained from the finite element simulations are compared with monitoring data of four different concrete face rockfill dams. It is demonstrated that the solid hardness and its degradation velocity are key parameters for modelling long-term deformations. For the constitutive parameters assumed long-term deformations after 15 years are more pronounced than the instantaneous deformation caused by the first water impounding.

Keywords: Concrete Face Rockfill Dam, Solid Hardness, Creep, Hypoplasticity.

1. INTRODUCTION

Post-construction deformations of concrete face rockfill dams (CFRDs) can be caused by various events such as among others repeated changes of the water table in the reservoir, seepage-driving internal erosion processes, earthquake, and the progressive mechanical and hydro-chemical weathering of the rockfill material. The latter leads to a degradation of the solid hardness and as a consequence to grain fragmentation and rheological deformations [1-3]. The process of weathering can be initiated in a complex manner by different environmental conditions and has a strong influence on long-term deformations. For moisture sensitive rockfill materials a change of the moisture content can lead to an acceleration of degradation of the solid hardness. Rheological deformations are related mainly to the state of weathering of the rockfill material, the degree of compaction, the geological conditions of the dam foundation, the seepage behaviour, local defects of the sealing and other construction details of the individual CFRD.

The prediction of long-term deformations of CFRDs is a challenging task. In this context the selection of an appropriate constitutive model and the accurate calibration of the constants involved are of great importance for the quality of the calculated results. Depending on the type of the rockfill material various constitutive concepts for the numerical modelling of the rheological behaviour are proposed in the literature, e.g. [4-8].

The focus of this paper is on numerical simulation of post-construction deformations of a CFRD caused by water impounding and creep of the rockfill material. To this end, an artificial CFRD with a height of 100 m is considered. The slope ratio of upstream and downstream slope of the dam is for both 1:1.5. The upstream water level is 94 m after water impounding. As illustrated in Figure 1, the dam body is decomposed of the main rockfill, the transition layer, the concrete slab and the concrete toe slab. The thickness of the concrete slab is 0.3 m at the top and 1.1 m at the bottom.

For numerical simulations of long term deformations of the rockfill material the version of the hypoplastic constitutive model proposed by Bauer in 2009 is used [8]. In this model the solid hardness is introduced to reflect the state of weathering of the material on its stiffness. This state parameter does not mean the hardness of a single grain, but it is related to the stiffness of the grain skeleton in the sense of a continuum description. In the proposed model long-term deformations are related to the degradation of the solid hardness. Thus, in addition to the hypoplastic constitutive equation an additional evolution equation for modelling the degradation of the solid hardness is needed.

The paper is organised as follows. In Section 2 the main constitutive relations for modelling the mechanical properties of rockfill materials are summarized. The model captures the influence of pressure and density on the incremental stiffness, the peak friction angle and the volume strain behaviour as well as the influence of a degradation of the solid hardness on creep and stress relaxation in a unified manner. The numerical model and the constitutive parameters used are outlined in Section 3. In particular, finite element calculations are carried out to investigate the deformations after water impounding and the evolution of creep within a period of 15 years after finishing the construction of the dam. The results of the numerical simulations are discussed and compared with monitoring data in Section 4.

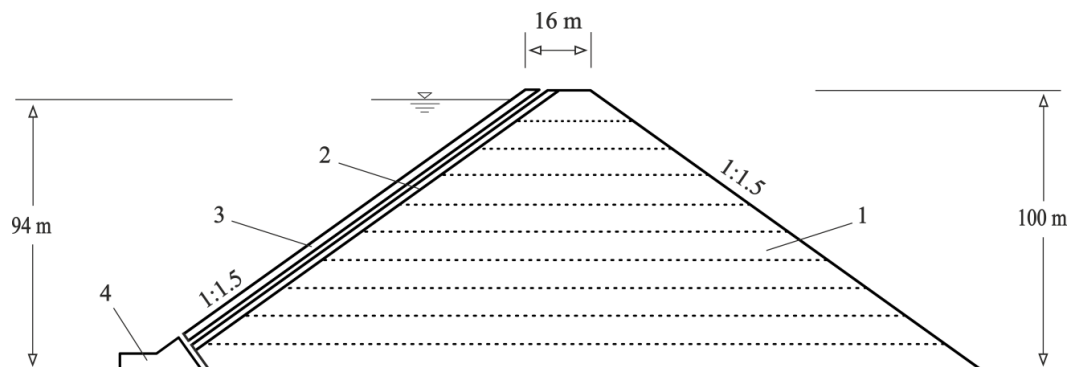


Figure 1. Sketch of the cross section of the CFRD: <1> main rockfill; <2> transition layer <3> concrete slab layer; <4> concrete toe slab.

2. HYPOPLASTIC MODEL FOR CREEP SENSITIVE ROCKFILL MATERIALS

In hypoplasticity, the constitutive equation is of the rate type, where the objective stress rate, ${}^{\circ}\sigma$, is expressed by an incrementally non-linear isotropic tensor-valued function that depends in the simplest case on the current effective Cauchy stress tensor, σ , and the strain rate tensor, $\dot{\epsilon}$, i.e. [9]:

$${}^{\circ}\sigma = ({}^{\circ}\sigma, \dot{\epsilon}). \quad (1)$$

To model the influence of the degree of compaction of the material on the peak friction angle and dilatancy behaviour, the hypoplastic concept was extended with the current void ratio e , i.e.:

$${}^{\circ}\sigma = (e, \sigma, \dot{\epsilon}). \quad (2)$$

In the particular models by Wu and Bauer [10], Gudehus [11] and Bauer [12-14] the current void ratio was related to the pressure dependent critical void ratio, e_c , and for simulating of the influence of grain damage on the incremental stiffness, the so-called solid hardness, h_{s0} , was introduced in the sense of a continuum description [13]. These models are based on the concept of Critical State Soil Mechanics [15] and applicable for modelling rate independent material properties of granular materials like sand.

In order to take into account time-dependent effects like creep and stress relaxation of rockfill materials, the constant solid hardness, h_{s0} , was replaced by a solid hardness, h_{st} , depending on the state of weathering. Taking into account a time dependent process of degradation of the solid hardness, the rate of the solid hardness, \dot{h}_{s0} , is also included as an additional quantity in the model, i.e. [8]:

$${}^{\circ}\sigma = (e, h_{st}, \dot{h}_{st}, \sigma, \dot{\epsilon}). \quad (3)$$

The specific hypoplastic version by Bauer [8] for modelling creep sensitive rockfill materials can be represented in index notation as follows:

$$\dot{\sigma}_{ij} = f_s \left[\hat{a}^2 \dot{\epsilon}_{ij} + (\hat{\sigma}_{kl} \dot{\epsilon}_{kl}) \hat{\sigma}_{ij} + f_d \hat{a} (\hat{\sigma}_{ij} + \hat{\sigma}_{ij}^*) \sqrt{\dot{\epsilon}_{kl} \dot{\epsilon}_{kl}} \right] + \left(\frac{\dot{h}_{st}}{h_{st}} \right) \left[\frac{1}{3} \sigma_{kk} \delta_{ij} + \kappa \sigma_{ij}^* \right], \quad (4)$$

$$\dot{e} = (1 + e) \dot{\epsilon}_v, \quad (5)$$

$$\dot{h}_{st} = - \frac{(h_{st} - h_{sw})}{c}. \quad (6)$$

In equation (4) $\hat{\sigma}_{ij} = \sigma_{ij}/\sigma_{kk}$ and $\hat{\sigma}_{ij}^* = \hat{\sigma}_{ij} - \delta_{ij}/3$ are the normalized components of the stress tensor and of its deviatoric part, respectively. δ_{ij} is the Kronecker delta and function \hat{a} is related to the critical friction angle, φ_c , and to the stress limit condition by Masuoka and Nakai [16] as illustrated in Figure 2(b). More details about function \hat{a} are outlined in [13]. The influence of the current void ratio, e , and the mean pressure, $p = -\sigma_{ii}/3$, on the incremental stiffness is taken into account with the stiffness factor, f_s , and the density factor, f_d . In these factors the current void ratio is related to the maximum void ratio, e_i , the minimum void ratio, e_d , and the critical void ratio, e_c , according to:

$$f_d = \left(\frac{e - e_d}{e_c - e_d} \right)^\alpha, \quad (7)$$

and

$$f_s = \left(\frac{e_i}{e} \right)^\beta \frac{1}{\hat{\sigma}_{kl} \hat{\sigma}_{kl}} \frac{(1 + e_i) h_{st}}{n h_i e_i} \left(\frac{3p}{h_{st}} \right)^{(1-n)}. \quad (8)$$

Herein α and β are material constants and h_i can be derived from a consistency condition [8]. According to the postulate by Gudehus [11] the pressure dependency of e_i , e_c and e_d are related to the compression law by Bauer [12], i.e.:

$$\frac{e_i}{e_{i0}} = \frac{e_c}{e_{c0}} = \frac{e_d}{e_{d0}} = \exp \left[- \left(\frac{3p}{h_{st}} \right)^n \right]. \quad (9)$$

As illustrated in Figure 2(a) in the phase diagram of void ratios the range of possible void ratios is bounded by the pressure dependent maximum void ratio e_i and minimum void ratio e_d . The upper bound, e_i , is related to an isotropic compression starting from the loosest possible skeleton with grain contacts [12]. The curve e_c represents the pressured dependent critical void ratio. In equation (9) the quantities e_{i0} , e_{c0} and e_{d0} are the corresponding void ratios for $p \approx 0$. The dimensionless exponent n is a material parameter.

Investigations by Bauer et al. [17] show that the deviatoric stress has a significant influence on the amount of rheological deformation. For a refined modelling, the deviatoric stress in the second term on the right hand side of the constitutive Equation (4) is therefore scaled by factor κ . It can be noted that with this term creep and stress relaxation are modelled in a unified manner. Equation (5) describes the relationship between the rate of the void ratio, \dot{e} , and the volume strain rate, $\dot{\epsilon}_v$, which is obtained from the balance equation of mass. Equation (6) represents the evolution equation for the solid hardness. With respect to the initial state, i.e. at time $t=0$, $h_{st} = h_{s0}$ and the final state, i.e. $t = \infty$, $h_{st} = h_{sw}$, the integration of equation (6) yields for the solid hardness as a function of the degradation time t :

$$h_{st} = h_{sw} + (h_{s0} - h_{sw}) \exp \left\{ - \frac{t}{c} \right\}, \quad (10)$$

where parameter c controls the velocity of degradation. Experiments indicate that the delayed deformation of stressed rockfills, i.e. the progressive particle breakage and contact plastification, is mainly influenced in a relatively complex manner by an interaction between the state of weathering, the humidity, the local stress state and the pre-compaction of the material, e.g. [4, 5, 18]. In the present paper parameter c is assumed to be a constant for the sake of simplicity. The applicability of this model to rockfill materials was demonstrated by comparison of the numerical simulations with data from laboratory tests for instance in [7, 8, 17].

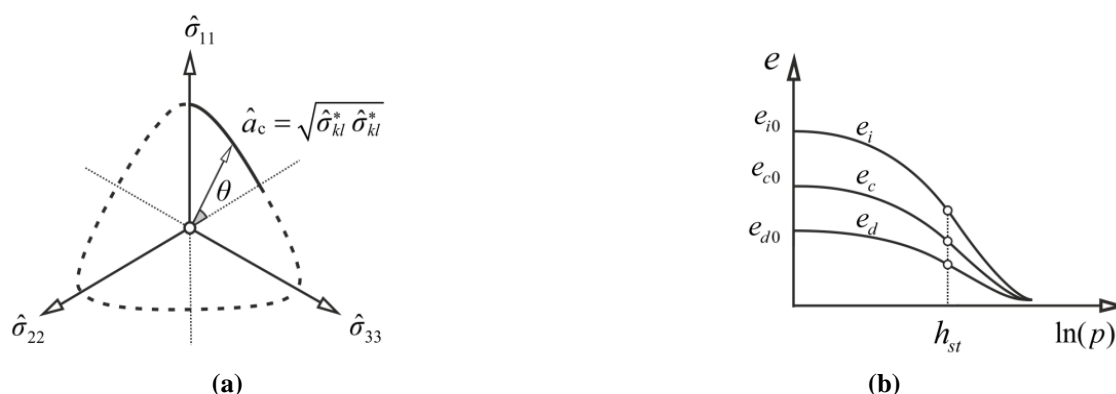


Figure 2. (a) Trace of the critical stress surface in the π plan; (b) Illustration of the pressure dependent maximum void ratio e_i , minimum void ratio e_d and critical void ratio e_c .

3. NUMERICAL MODEL AND CONSTITUTIVE PARAMETERS

The commercial program Abaqus [19] is used for finite element simulation. The idealised CFRD shown in Figure 1 is discretised by 4841 four-node bilinear quadrilateral elements for plane strain condition. The foundation of the dam is assumed to be rigid and immovable, thus the element nodes along the bottom surface of the dam are fixed. The interface behaviour between concrete slab and the transition layer, as well as between the concrete toe slab (plinth), the concrete slab, transition layer and rockfill material is simulated using the concept of contact pairs provided by Abaqus. For simulating of post-construction deformations, the following steps are considered:

Step 1: The initial stress distribution in the rockfill material as a result of gravity load is obtained by simulation of the influence of the construction of the rockfill dam in 10 layers with same heights. In this step only the main rockfill material <1> and plinth <4> are activated;

Step 2: The concrete slab <3> and transition layer <2> are activated with respect to the interface between these two materials and the plinth. In order to investigate the post-construction behaviour the deformation induced by the construction of the CFRD is set to zero;

Step 3: Calculation of the deformation caused by water impounding;

Step 4: Simulation of long-term deformation as a result of stiffness degradation of the main rockfill material <1> and of the transition layer <2>.

The material behaviour of the concrete slab and the plinth are described as linear elastic material with an elastic modulus of $E=20$ GPa, a Poisson ratio of $\nu=0.17$ and a density as $\rho=2400$ kg/m³. The hypoplastic constitutive model for the rockfill material and the transition layer presented in Section 2 is implemented into a user defined material subroutine. The constitutive model includes 11 parameters which are tabulated into Table 1. Parameters h_{s0} , n , φ , e_{d0} , e_{c0} , e_{i0} , α and β are calibrated based on experimental results obtained for weathered granite [6]. For the parameters h_{sw} , c and κ three different sets are considered to simulate the influence of this parameter on the long-term behaviour. For the compacted rockfill material an initial void ratio of $e_0=0.33$, and a density of $\rho=2200$ kg/m³ is considered in all calculations.

Table 1. Constitutive parameters for three different rockfill materials

Parameter	h_{s0} [MPa]	n	h_{sw} [MPa]	c [years]	κ	φ_c [°]	e_{d0}	e_{c0}	e_{i0}	α	β
Set A	75	0.6	68.4	0.91	1.0	42.0	0.2	0.39	0.85	0.125	1.05
Set B	75	0.6	68.8	2.0	1.0	42.0	0.2	0.39	0.85	0.125	1.05
Set C	75	0.6	70.7	3.3	1.0	42.0	0.2	0.39	0.85	0.125	1.05

4. INTERPRETATION OF THE NUMERICAL RESULTS

The numerical results obtained with the constitutive parameter Set A are shown in Figures 3-5. In particular, the contours of vertical displacements after water impounding and the corresponding change of the void ratio is shown in Figure 3(a) and Figure 4(a), respectively. While additional compaction is mainly concentrated in the upstream part of the dam, the deformation in the downstream part is almost zero. In particular, the vertical displacement is extremal approximately at the half height of the concrete slab, and the maximum compaction occurs in the vicinity of the dam toe. As a results of degradation of the solid hardness creep settlements occur in the whole rockfill dam. The additional compaction can be explained by grain fragmentation and reorientation of the particles into a denser state. Figure 3(b) and Figure 4(b) show the resulting quantities caused by water impounding and the degradation of the solid hardness after 15 years. It is evident that with the assumed parameters for degradation of the solid hardness the corresponding long-term deformation is more pronounced than the deformation caused by water impounding.

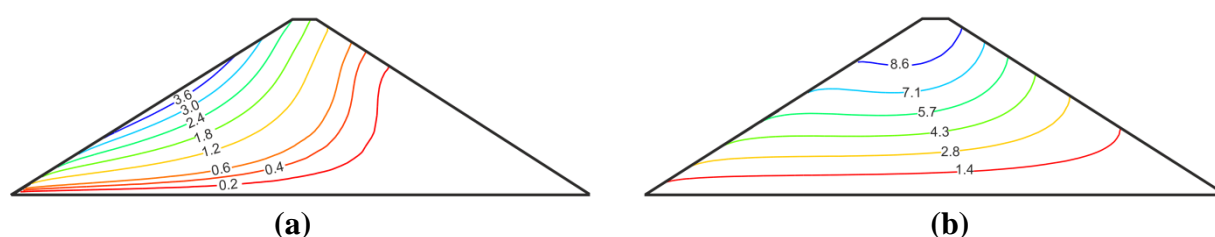


Figure 3. Contour of vertical displacement (unit: cm):
(a) After reservoir filling; (b) After 15 years.

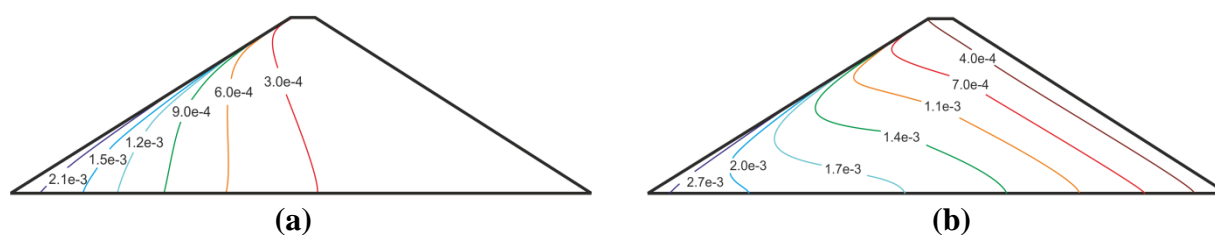


Figure 4. Contour of reduction of the void ratio:
(a) After reservoir filling; (b) After 15 years.

Figure 5 shows the normal deflection of the concrete slab after reservoir filling (curve 2), at the end of the first year (curve 3), after 7 years (curve 4) and after 15 years (curve 5). Although the water pressure increases with the depth, the deflection of the concrete slab is nearly the same at the top and bottom after water impounding. The maximum deflection occurs close to the centre which is similar to the distribution of the vertical displacements of the rockfill material shown in Figure 3(a). The long-term deformation, however, leads to a monotonic increase of the deflection of the concrete slab at the top.

The evolution of crest settlements within a 15-year period after water impounding is shown in Figure 6 for three different sets of the constitutive parameters h_{sw} and c . The numerical simulations are compared with monitoring data of four CFRDs. It is evident that with the present model the amount of creep deformation mainly depends on the difference between the final, asymptotical value of the solid hardness and the initial value, i.e. $h_{sw} - h_{s0}$, while the velocity of creep deformation is related to the rate of the solid hardness which is scaled by the parameter c . As experimental data of the material behaviour are not available, the parameters h_{sw} and c are.

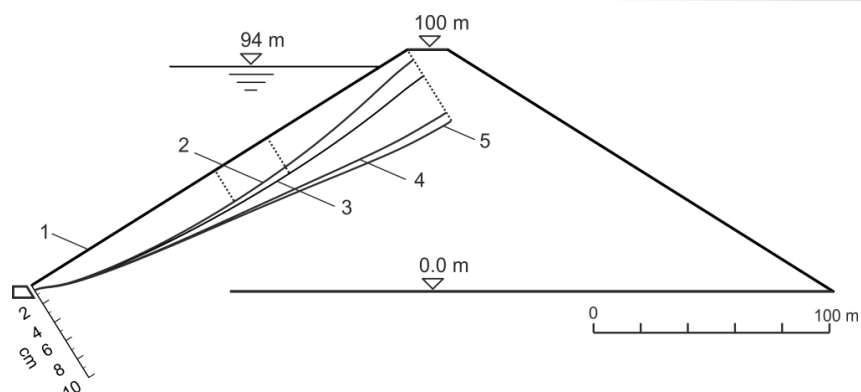


Figure 5. Normal deflection of the concrete slab: <1> at the end of construction; <2> after reservoir filling; <3> at the end of the first year; <4> after 7 years; <5> after 15 years.

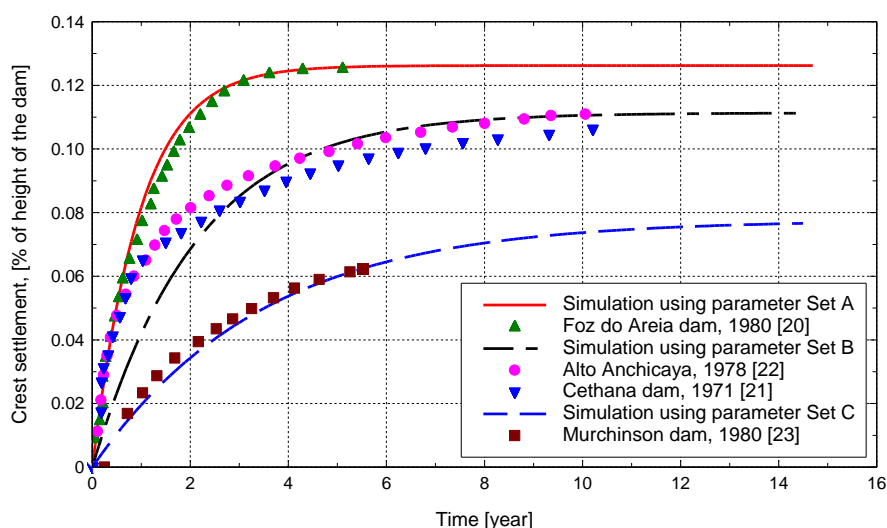


Figure 6. Evolution of crest settlements within a 15 year period after water impounding: numerical simulations (solid and dashed curves); monitoring data (markers).

calculated by back analysis to obtain the best agreement with the monitoring data. In this context it should be noted that neither the influence of the relevant 3-D geometries nor the individual properties of the different rockfill types and grain size distributions are taken into account, which of course would be necessary for an accurate calibration. The present study should therefore only demonstrate the capability of the current hypoplastic constitutive model to simulate long-term deformations. The comparison of the simulation with the monitoring data shows, that the parameter Set A and Set C fit well with the monitoring data of the Foz do Areia CFRD [20] and of the Murchison CFRD [23], respectively. On the other hand, the adaptation of the constitutive parameters to the crest settlements of the Alto Anchicaya CFRD [22] and the Cethana CFRD [21] is less satisfactory for the first three years. It can be noted that this imperfection was the motivation to develop a more sophisticated evolution equation for the degradation of the solid hardness shown in the paper by Bauer [24].

4. CONCLUSIONS

A hypoplastic constitutive model is used for investigating post-construction deformations of a concrete face rockfill dam (CFRD), which is suitable for describing the rheological properties of rockfill materials. The key parameters for modelling rheological properties such as creep and stress relaxation are the state of the solid hardness and its rate. These quantities are introduced into the constitutive model in the sense of a continuum description. A change of the solid hardness leads to creep deformations and/or stress relaxation. For numerical

simulations of the rockfill material the constitutive parameters used are relevant for a weathered granite. The numerical results show that the instantaneous normal deflection at the top of the concrete slab is small compared to the long-term deformations after 15 years. The same can be concluded for the computed crest settlements. The comparison of the calculated crest settlements with monitoring data of four CFRDs shows that the amount of the crest settlement depends on the difference between the final, asymptotical value of the solid hardness, while the velocity of creep deformation is related to the rate of the solid hardness.

5. ACKNOWLEDGMENT

The authors wish to thank Dr. A. Niemunis from the Institute of Soil Mechanics and Rock Mechanics at Karlsruhe Institute of Technology, and Dr. Z. Fu from the Nanjing Hydraulic Research Institute in China for helpful remarks. The second author wishes to thank the Chinese Scholarship Council for the financial support.

6. REFERENCES

1. Maranha, E. (1990), "*Advances in Rockfill Structures*", NATO ASI Series, Series E: Applied Science, Vol. 200, Kluwer academic publisher, Netherlands.
2. Cook, J.B. and Sherard, J.L. (1985), "*Proceedings of concrete face rockfill dams-design, construction and performance*", American Society of Civil Engineers, New York, United States.
3. Fell, R., MacGregor, P. and Stapledon, D. and Bell, G. and Foste, D. (2015), "*Geotechnical Engineering of Dams*", 2nd Edition, CRC Press, Netherlands, pp. 845-846.
4. Oldecop, L.A. and Alonso, E.E. (2007), "Theoretical investigation of the time-dependent behaviour of rockfill, *Geotechnique*, Vol. 57, Issue 3, pp. 289-301.
5. Alonso, E.E. and Cardoso, R. (2009), "*Behaviour of Materials for Earth and Rockfill Dams Perspective from Unsaturated Soil Mechanics*", In Proceedings of the 2nd Int. Conf. on Long-term Behaviour of Dams, Bauer, E., Semprich, S., and Zenz, G. (eds), Publisher Graz University of Technology, pp. 1-38.
6. Oldecop, L.A. and Alonso, E.E. (2001), "*A model for rockfill compressibility*", *Géotechnique*, Vol. 51, Issue 2, pp. 127-139.
7. Li, L., Wang, Z., Liu, S.H. and Bauer, E. (2016), "*Calibration and performance of two different constitutive models for rockfill materials*", *Water Science and Engineering*, Vol. 9, Issue 3, pp. 227-239.
8. Bauer E. (2009), "*Hypoplastic modelling of moisture-sensitive weathered rockfill material*", *Acta Geotechnica*, pp. 261-272.
9. Kolymbas, D. (1991), "*An outline of hypoplasticity*", *Archive of Applied Mechanics*, Vol. 63, Issue 3, pp. 143-151.
10. Wu, W. and Bauer, E. (1993), "A hypoplastic model for barotropy and pyknotropy of granular soils", *Proc. Int. Workshop on Modern Approaches to Plasticity*, Kolymbas, D. (ed), Elsevier, pp. 225-245.
11. Gudehus, G. (1996), "*A Comprehensive constitutive equation for granular materials*", *Soils and Foundation*, Volume 36, Issue 1, pp. 1-12.
12. Bauer, E. (1995), "*Constitutive modelling of critical states in hypoplasticity*", *Proc. of the 5th International Symposium on Numerical Models in Geomechanics*, Pande, N., and Pietruszczak, S. (eds), Balkema press, pp. 15-20.
13. Bauer, E. (1996), "*Calibration of a comprehensive hypoplastic model for granular materials*", *Soils and Foundations*, Vol. 36, Issue 1, pp. 13-26.
14. Bauer, E. (2000), "*Conditions for embedding Casagrande's critical states into hypoplasticity*", *Mechanics of Cohesive-Frictional Materials*, 5, pp. 125-148.
15. Schofield, A.N. and Wroth, C.P. (1968), "*Critical State Soil Mechanics*", McGraw-Hill.
16. Matsuoka, H. and Nakai, T. (1997), "*Stress-strain relationship of soil based on 'SMP'*", In: Proceedings of Specialty Session 9, IX Int. Conf. on Soil Mech. and Foundation Engineering, Tokyo, pp. 153-162.

17. Bauer, E., Fu, Z.Z. and Liu, S.H. (2010), “*Hypoplastic constitutive modelling of wetting deformation of weathered rockfill materials*”, *Frontiers of Architecture and Civil Engineering in China*, Vol. 4, Issue 1, pp. 78–91.
18. Alonso, E.E. and Oldecop, L.A. (2000), “*Fundamentals of rockfill collapse*”, In: Rahardjo H., Toll D.G., Leong E.C. (eds) *Proceedings of the 1st Asian Conference on Unsaturated Soils*, Rahardjo, Toll and Leong (eds), Balkema Press, Rotterdam, pp. 3-13.
19. Abaqus, Version 6.13, Complete Abaqus Environment, Dassault Systèmes Simulia Corp, United States of America.
20. Pinto, N., Filho, P. and Maurer, E. (1985), “*Foz Do Areia Dam-Design, Construction, and Behaviour*”, *Proceedings of the concrete face rockfill dams-design, construction and performance*, Cook, J. B. and Sherard, J.L. (eds), pp. 173-191.
21. Fitzpatrick, M.D. and Barnett, R.H.W. (1982), “*Instrumenting Australia's Cethana dam*”, *Water. Power and Dam Construction*, Vol. 34, (11), pp. 26-30.
22. Bayardo, M. (1985), “*Alto Anchicaya dam-Ten years performance*”, In *proceedings of concrete face rockfill dams-design, construction and performance*, Cook. J. B. and Sherard. J. L (eds), pp. 73-82.
23. Sherard, J.L. and Cook, J.B. (1987), “*Concrete face rockfill dams,*” I. Assessment, *ASCE Journal of Geotechnical Engineering*, Vol. 113, (10), pp. 1096-1112.
24. Bauer, E. (2017), “*Constitutive modelling of wetting deformation of rockfill materials*”, *Proceedings of the 4th International Conference on Long-term Behaviour and Environmentally Friendly Rehabilitation Technology of Dams (LTBD2017)*, Noorzad, A., Bauer, E., Ghaemian, M. and Ebrahimian, B. (eds), Teheran, Iran.

Numerical investigation of the flow characteristics in the vicinity of pressure conduit's gates

Mohammad Manafpour¹, Tohid Jamali Rovesht²

1- Assistant professor, Department of Civil Engineering, Urmia University, Urmia, Iran

2- M. Sc. Student of Civil Engineering, Urmia University, Urmia, Iran

Email: mo.manafpour@gmail.com

Abstract

Bottom outlet is one of the related hydraulic structures of dams used to control initial water volume in reservoir and to help the spillways discharge capacity in floodwaters. Designed elements of bottom outlet such as control gates must be able to properly act to regulate downstream flow in entirely closed and semi-open situation. Bottom outlets which work with high heads, may create intense change in velocity and pressure field near the control systems (gates) by high velocity that probably causes cavitation phenomenon and unusual vibration on the structure's wall and conduit to happen. In the present research, characteristics of the flow, such as momentary and average flow's pressure and velocity near the service gate, cavitation index and gate vibration frequency in reservoir normal head (100 m) at various service gate openings were extracted and analyzed using numerical model of Seymareh dam's bottom outlet with FLOW 3D software and RNG(K- ϵ) turbulence model. The results of this research will help to appropriately understand the hydraulic phenomena occurred around outlet gates.

Keywords: Control Gate, Flow Characteristics, FLOW 3D, Seymareh Dam.

1. INTRODUCTION

Dams are used to provide water for industry, drinking and agriculture needs, also to regulate the river excessive flow and flood control. Generally, dams are divided into two categories, earth fill dams and concrete dams which have different related hydraulic structures. Bottom outlet is one of them, which is used to control initial water volume in the reservoir and to help the spillway discharge capacity in floodwaters [1]. After studying the cause for failure of bottom outlets in damaged dams, it has been obvious that cavitation phenomenon and gate vibration are known as the main problems [2].

According to intense flow's sensitivity on geometric parameters of the outlet conduit, any changes in these parameters will cause fluctuation in velocity and pressure fields. Due to high-velocity flow and existence of irregularities in the conduit surface, separation of the flow from the conduit bed may occur, and the pressure will reduce locally. If the flow's pressure becomes less than the water vapor pressure, the state of the water will change from liquid to gas and vapor cavity bubbles will be formed. The vapor cavities may move into a zone of higher pressure with the flow, so they collapse and send out high pressure shock waves; if the cavities collapse near the conduit surface, there the materials will be damaged at the boundary and this will cause an unusual vibration in the control structures such as control gates in bottom outlet. The downstream of the service gate, the area between the emergency and the service gate (in the case of operating the gates together), and also in gate slots, where an unusual surface stands against the flow, are the most potential areas of damage [3].

So in this research characteristics of the flow, such as momentary and average flow's pressure and velocity near the service gate, cavitation index and gate vibration frequency in reservoir normal head (100 m) at various service gate openings were analyzed using numerical model of Seymareh dam's bottom outlet with FLOW 3D software and RNG (K- ϵ) turbulence model to assess the probability of damage.

Roun shi et al. (2005) experimentally studied the aerators' hydraulic performance used on the floor of Goupitan dam's bottom outlet. Their results showed that the rate of entranced air increases with a decrease in aerator's downstream bed slope which has an effective role to protect the bottom outlet conduit against cavitation damage [4].

Daneshman et al. (2007) experimentally analyzed the hydraulic flow characteristics through a Sivand dam's bottom outlet conduit at various service gate openings. The results of their research indicated that, for service gate openings which are more than 85%, the amount of turbulence in emergency gate slots increases. To overcome this problem, it is recommended to reduce the emergency gate slot's width and the cavitation index should be more than the critical amount (0.2) at all openings [5].

Daneshman et al. (2014) experimentally and numerically studied the hydraulic flow parameters and forces effecting the gate in the various service gate openings using Finite Element method in Shahryar dam's bottom outlet. Their results showed that the cavitation index was proper and the service gate vibration frequencies were not close to critical value at all openings. They also found that the minimum amount of discharge coefficient occurs at 20% gate openings [6].

2. BASIC EQUATIONS OF FLOW FIELD

The basic equations of fluid motion are the continuity and momentum equations which are expressed as equation (3), (4) for incompressible and turbulent flow with constant viscosity and density [7].

$$\frac{\partial U_i}{\partial x_i} = 0 \quad (3)$$

$$\frac{\partial U_i}{\partial t} + U_j \frac{\partial U_i}{\partial x_j} = -\frac{1}{\rho} \frac{\partial \bar{P}}{\partial x_i} + \frac{\partial}{\partial x_j} \left(\nu \frac{\partial U_i}{\partial x_j} - u_i' u_j' \right) \quad (4)$$

Where x_i shows Cartesian system, t is time, ρ is fluid density and \bar{P} , U_i , u_i' , u_j' are average pressure, velocity and Reynolds stress tensor, respectively.

Free water surface is defined by means of volume of fluid (VOF) and computing the function, $F(x, y, z, t)$. This function represents the volume of fluid #1 per unit volume and satisfies the equation.

$$\frac{\partial F}{\partial t} + \frac{1}{V_F} \left[\frac{\partial}{\partial x} (F A_x u) + R \frac{\partial}{\partial y} (F A_y v) \right] + \frac{1}{V_F} \left[\frac{\partial}{\partial z} (F A_z w) + \xi \frac{F A_x u}{x} \right] = F_{DIF} + F_{SOR} \quad (5)$$

$$FDIF = \frac{1}{V_F} \left[\frac{\partial}{\partial x} \left(v_F A_x \frac{\partial F}{\partial x} + R \frac{\partial}{\partial x} \left(v_F A_y R \frac{\partial F}{\partial y} \right) \right) \right] + \frac{1}{V_F} \left[\frac{\partial}{\partial z} \left(v_F A_z \frac{\partial F}{\partial z} \right) + \xi \left(\frac{v_F A_x F}{X} \right) \right] \quad (6)$$

Where V_F is the fractional volume of flow, (u, v, w) , A_x, A_y, A_z are velocity and fractional area of flow components in the coordinate directions (x, y, z) , Respectively. When Cartesian coordinates are to be used, R is set to 1 and ξ is set to 0. The term F_{SOR} corresponds to the density source R_{SOR} in Eq (5); F_{SOR} is the time rate of change of the volume fraction of fluid #1 associated with the mass source for fluid #1.

The interpretation of F depends on the type of problem being solved. Incompressible problems must involve either a single fluid with a free surface or two fluids and no free surfaces. For a single fluid, F represents the volume fraction occupied by the fluid. Thus, fluid exists where $F=1$, and void regions correspond to locations where $F=0$. "Voids" are regions without fluid mass those have a uniform pressure assigned to them. Physically, they represent regions filled with vapor or gas whose density is insignificant with respect to the fluid density [8].

3. GENERAL CHARACTERISTICS OF SEYMAREH DAM AND RELATED FACILITIES

Seymareh dam, as a concrete double - arch dam (fig (1)), has two bottom outlets, their entrances are 620 and 640 m above the sea level respectively, therefore, they are 20 and 40 m above the river bed. Due to the plan and longitudinal profile number (1), the entrance bottom outlet shown in fig (2) and (3), is bell shape and it is 17.85 * 9.56 m (height * width). To prevent entering large objects, a concrete rack is used at the entrance of the conduit. The emergence and service gate are slider and radial, respectively. In this research characteristics of flow have been investigated in No. 1 bottom outlet which has 45.4 m length. Note that on 100% service gate opening the length of pipe flow is 36.5 m and free flow is 8.9 m. This bottom outlet has been designed for maximum discharge 654 (m^3/s) at 111/5 m upstream water head [9].



Figure 1. Location of Seymareh dam and its related structures (Seymareh Dam and Power Plant Website)

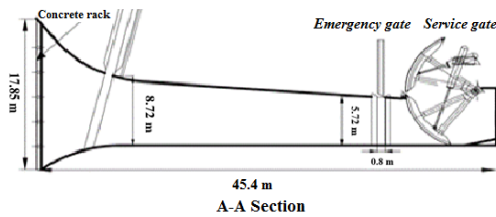


Figure 2. Longitudinal section of No. (1) Seymareh Dam's bottom outlet

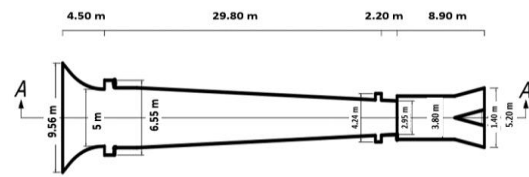


Figure 3. Plan of No. (1) Seymareh Dam's bottom outlet

4. NUMERICAL MODEL

The three-dimensional model is prepared in actual size using the plan and longitudinal bottom outlet's maps via AutoCAD 3D software, then it has been exported to FLOW 3D software with Stl format. According to the essence of basic equations, flow analysis starts with fixed boundary condition, and as time passes, the process reaches the steady state. The fluid is considered as a compressible and single phase fluid, the time of analysis assumed to be 30s. K- ϵ (RNG) is chosen as the turbulent model due to the advantage of Renormalization Group Instead of constant factors. To calculate the free surface profile, VOF model is used [10].

One of the effective issues for the accuracy of calculation in numerical models is the appropriate definition of boundary condition. In figure (4) and table (1), boundary condition of the model is shown. The wall and outflow boundary condition are set to wall and outlet flow and inlet boundary condition whose head equals to reservoir's head is set to specified pressure.

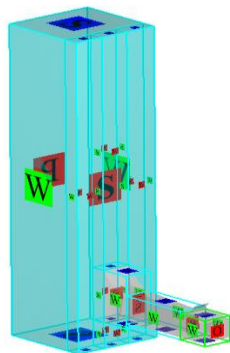


Figure 4. the blocks have been used in numerical mode

Table 1. The boundary condition of numerical model

Specified pressure	Model input
Outflow	Model output
wall	walls
Symmetry	The border of the between blocks
1.503.019	The total number of computational mesh

To identify the appropriate upstream reservoir dimension (length, width), the model is performed with different dimensions which are shown in the table (2). Due to the calculated flow velocity profiles at the different sections of bottom outlet conduit, it is observed that the flow velocity profiles have adopted on each other after the No.3. Reservoir dimension and increasing of dimension had not affected the velocity. So the size of 30 * 29.53 m is selected as upstream reservoir dimension.

Table 2. The boundary condition of numerical model

number of computational mesh	The reservoir dimensions, respectively: (width, length)	number of reservoir
50,592	9.53×10	1
219,443	19.53×20	2
507,500	29.53×30	3
884,268	39.53×40	4
1,126,650	44.53×45	5

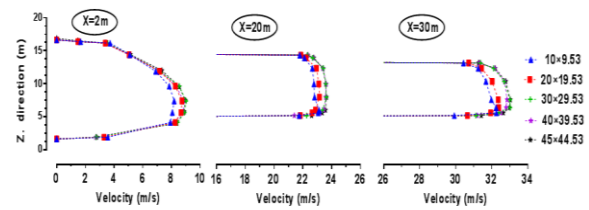


Figure 5. The velocity profiles for different reservoir dimension at the section of 2 , 20 , 30 m from the conduit entrance

5. NUMERICAL MODEL VERIFICATION

In this research to verify the results of the numerical model, the average pressure value on the bed of the conduit and outlet discharge parameters in the normal head (100 m) of bottom outlet’s hydraulic model are used. Verification is done at 30, 70, 100 and 10, 20, 30, 40, 50, 60, 70, 80, 90, 100 service gate openings.

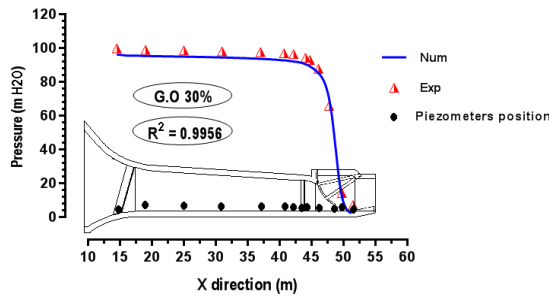


Figure 6. Average pressure variation along the conduit on the floor at 30% gate opening

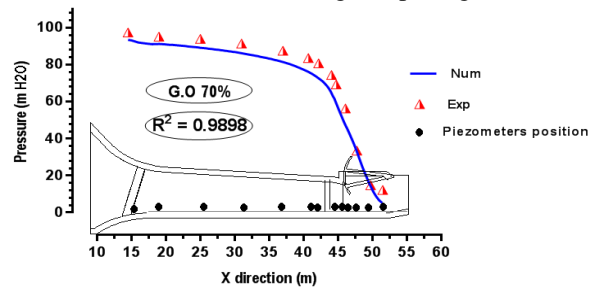


Figure 7. Average pressure variation along the conduit on the floor at 70% gate opening

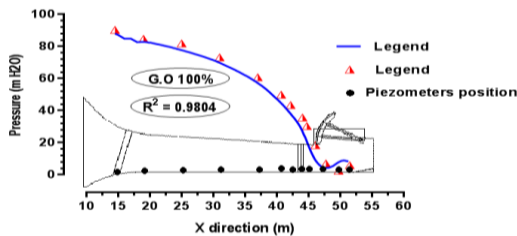


Figure 8. Average pressure variation along the conduit on the floor at 100% gate opening

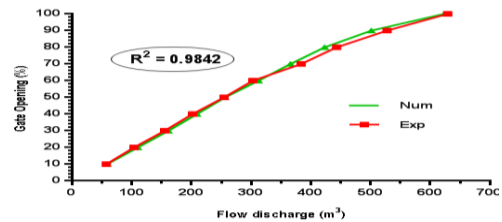


Figure 9. Outlet discharge variation at the different service gate opening

The results of figures 6 to 8 show that the most difference of average pressure value in the conduit bed happens at the downstream of service gate caused by intense turbulent flows at these areas, and resulted in an error by reading the pressure in the laboratory or exact calculation of the numerical model.

The obtained values for the correlation coefficient (R^2) in figures 6 to 9 show good agreement between the experiment and numerical results and confirm the numerical model results.

6. ANALYZE OF RESEARCH RESULTS

Velocity and pressure of the flow are two important parameters which have a basic role to identify the flow pattern at the downstream gate and anticipating the problems in bottom outlet conduit. Because of high velocity and pressure drop at the vicinity of control systems (gates) in the bottom outlets which work with high heads, the occurrence of cavitation damage is expected [11]. The improper design of bottom outlets geometry may cause negative pressure on the conduit walls and gate vicinity, therefore, gate structures encounter unusual vibrations. So studying these phenomena has an important role in designing safe hydraulic structures [12].

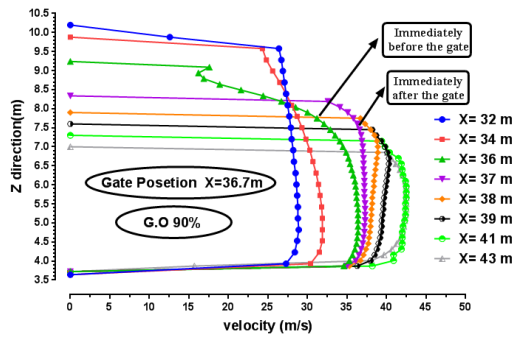


Figure 14. The profile of flow velocity distribution in vertical sections of outlet conduit in vicinity of service gate for 90% gate opening

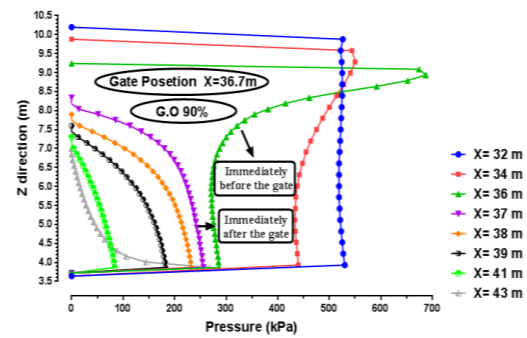


Figure 15. The profile of flow pressure distribution in vertical sections of outlet conduit in vicinity of service gate for 30% gate opening

As a result of the flow's velocity and pressure values in the vicinity of the service gate for 30% and 90% gate openings (figures 12 to 15), the large service gate openings influence the profiles of velocity and pressure further than the upstream of the gate; so that the changes of flow velocity and pressure profiles for the 30% and 90% service gate openings occur at 36m and 34m sections, respectively. By approaching the flow to the service gate, unlike the pressure in front of gate opening, the flow velocity increases in bottom levels, and by passing through the gate, it distributes fairly in a uniform manner.

6. 2. INVESTIGATION OF CAVITATION INDEX IN VICINITY OF SERVICE GATE

6. 2. 1. CAVITATION INDEX ON THE CONDUIT FLOOR

The cavitation index relationship representing the relation of hydraulic pressure energy to dynamic pressure would be reduced by the reduction of pressure and increasing of flow velocity. Consequently, the flow velocity and pressure investigation in figures of 10 to 15 show the increased intensity of velocity and decreased pressure more occur for the small gate openings. So the occurrence of cavitation phenomenon will be possible in this condition.

In figure18, by investigation the cavitation index variations at the bed of the conduit for various service gate openings, it is observed that the cavitation index is less than the critical value (0.2) for the 10, 20, 30, 40 and 80% of service gate openings from the 41m section to the end and for the 50 and 70% of gate openings from the 41m to 43m section, therefore, the occurrence of cavitation damage is possible. However, there is no probability of damage due to high cavitation index for 60, 90 and 100% of gate openings.

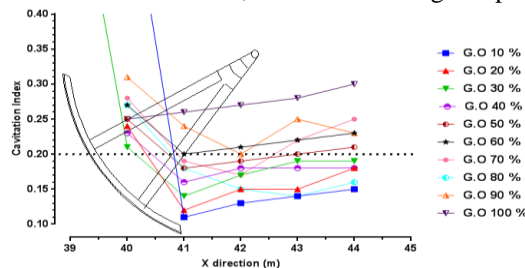


Figure 16. Cavitation index variation on the floor of conduit for the different service gate opening from the 40m to 45m of conduit entrance

6. 2. 1. CAVITATION INDEX ON THE CONDUIT WALLS AND CEILING

Figures NO. 17 and 18 show the cavitation index value at various sections of the wall for different service gate openings. The obtained results indicate that the cavitation index value is less than the critical value (0.2) for all the gate openings. For small gate openings, cavitation starts from the bottom of the gate and the damage will continue to the end of the conduit; and for most gate openings, cavitation occurs at the end of the conduit.

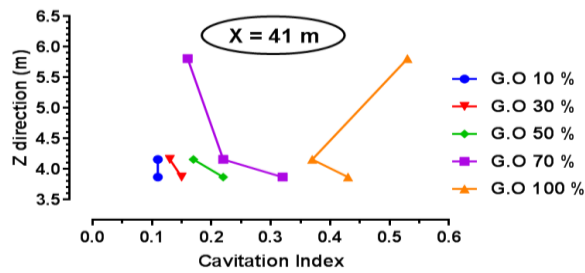


Figure 17. Cavitation index variation on the conduit wall for the different service gate opening at section of 41m from the conduit entrance

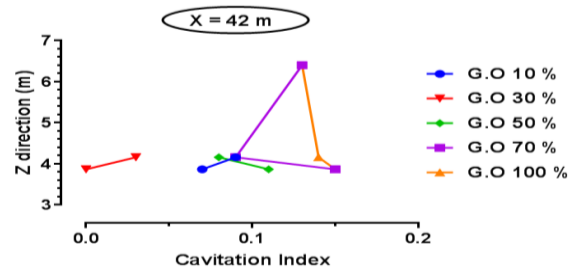


Figure 18. Cavitation index variation on the conduit wall for different service gate opening at the section of 42m from the conduit entrance

The value of this parameter for the conduit's ceiling is more than the critical value and the minimum obtained value equals to 0.46 which occurs in the section of 36m from the conduit entrance.

6. 2. FREQUENCY IDENTIFICATION OF HYDRODYNAMIC PRESSURE

Hydrodynamic pressure fluctuations could cause significant effects on gate structure, so the magnitude and frequency contents of the pressure fluctuations should be accurately investigated. In this section, hydrodynamic pressure time history for two gate openings analyzed. 20% and 40% gate openings have been selected to frequency identification analysis. In figure 19, power spectrum of hydrodynamic pressure in the condition of 20% opening for 5 different points is presented. As shown, all these points have similar spectrum and similar frequencies.

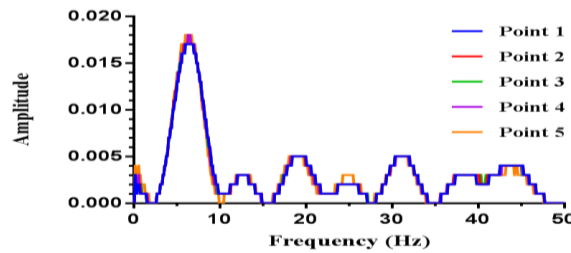


Figure 19. hydrodynamic pressure power spectrum for 20% gate opening

In the case of 40% gate opening condition, again 5 different points have been considered on the gate structure. In contrast to the previous case, here, the first point has a completely different spectrum. Figure 20 and figure 30 show point1 and four other points' power spectrum, respectively.

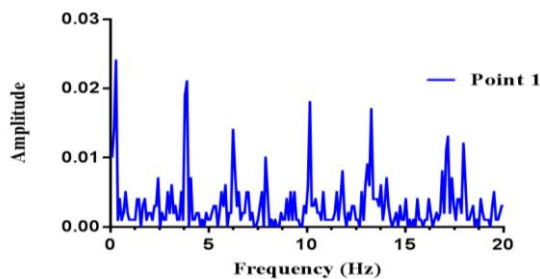


Figure 20. hydrodynamic pressure power spectrum for point1 in case of 40% gate opening

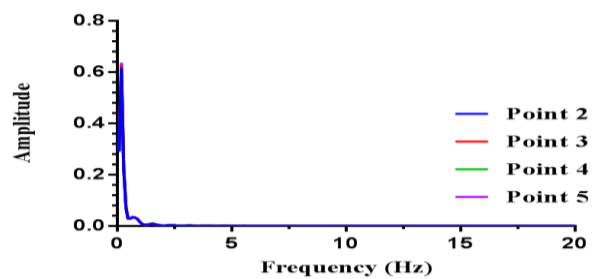


Figure 21. hydrodynamic pressure power spectrum for 40% gate opening except point1

Point 1 shows more frequency contents because it is located just in the edge of the gate, so pressure in this point has more fluctuations.

7. CONCLUSIONS

In the present research, the Flow Characteristics were investigated in the vicinity of Seymareh dam's bottom outlet service gate at various gate openings. The results of the study showed:

1. By moving towards the downstream conduit, due to the reduction of cross section to the service gate, the flow velocity increases and the pressure reduces, and for less gate openings, velocity of the flow at the upstream of service gate gradually increases, but in gate location, it has a sudden increase.
2. The large service gate openings influence the profiles of velocity and pressure more than the upstream of the gate.
3. The cavitation index at the bed of the conduit for the 10, 20, 30, 40 and 80% of service gate from the 41m section to the end and for the 50 and 70% of gate openings from the 41m to 43m section is less than the critical value (0.2).
4. On the wall of the conduit, cavitation starts from the bottom of the gate and the damage continues to the end of the conduit; and for more gate openings, cavitation occurs at the end of the conduit. And also, for the conduit's ceiling the amount of this phenomenon is not closed to the critical value.
5. The frequency of 20% gate opening shows that the power of hydrodynamic pressure for 5 different points have similar frequencies; and for the 40% gate opening point 1 since it has located at the edge of the gate, it has more frequency contents than the other 4 points.

8. REFERENCES

1. Toombes, L. Chanson, H. (2005), "*Air entrainment and velocity redistribution in a bottom outlet jet flow*", 31th IAHR World Congress., 11-16 September, Seoul, Korea, Water Engineering for the Future-Choices and Challenges.
2. Dong, Z. Chen, L and Ju wen, J. (2006), "*Hydraulic characteristics of partial opening of the working gate for a discharge tunnel*", Journal of Hydrodynamics., Ser. B, 19(4):488-493.
3. Wang, H. (2014), "*Turbulence and Air Entrainment in Hydraulic Jumps*", A thesis submitted for the degree of Doctor of Philosophy at The University of Queensland.
4. Ruan shi, P. Wu jian, H and Wu wei, W. (2005), "*Hydraulic research of aerators on tunnel spillways*", Journal of Hydrodynamics. Ser. B. 19(3):330-334.
5. Daneshmand, F. Adamowski, J and Liaghat, T (2007), "*Hydraulic model test of the bottom outlet of Sivand dam*", Proceedings of the 5th ISME/WSEAS International Conference on Fluid Mechanics and Aerodynamics. 25-27 August, Athens. Greece.
6. Daneshmand, F. Adamowski, J and Liaghat, T (2014), "*Bottom outlet dam flow: physical and numerical modelling*", Proceedings of the Institution of Civil Engineers Water Management. Pages 176-184.
7. Ferziger, J. and Peric, M. (1996), "*Computational methods for fluid dynamics*", springer verlag. New York. ISBN 3-540-59434-5.
8. Hirt, C. Nichols, B. (1981), "*Volume of fluid (VOF) method for the dynamics of free boundaries*", Journal of Computational Physics. (39): 201-225.
9. The final report of Seymareh dam's bottom outlet hydraulic model, Water Research Institute, 2005, Tehran.
10. Wilcox, D. C. (2006), "*Turbulence Modeling for CFD*", (Third Edition). Pages 84-90.
11. Kramer, K. Hager, W. H and Minor, H. E. (2006), "*Development of air concentration on chute spillways*" Journal of Hydraulic Engineering. 132 (9): 908-915.
12. Hua, G. Genhua, Y. (2011), "*Analysis of vibration mode of hydraulic gate structure*". Advanced Materials Research. ISSN: 1662-8985. Vols. 199-200. Pages 966-972.

The Multiphase Capability of Openfoam CFD Toolbox in Solving Flow Field in Hydraulic Structure

Mohammad Manafpour¹, Hamzeh Ebrahimnezhadian²

1- Assistance Prof. in Civil Eng., Water & Hydraulic Structures, Dept. of Civil Eng., Faculty of Eng., Urmia University, Urmia, Iran. Email: m.manafpour@urmia.ac.ir

2- Ph.D. Candidate in Water & Hydraulic Structures, Dept. of Civil Eng., Faculty of Eng., Urmia University, Urmia, Iran. Corresponding Author

Email: h.ebrahimnezhadian@gmail.com

Abstract

The widely known CFD-toolbox “OpenFOAM” is a well-designed C++ library that allows the numerical simulation of various Engineering problems. Owing to its object-orientated structure and the open source code concept, it is very flexible and can be adjusted to very specific problems. Therefore, the code analysis and its manipulation are possible. In general, the library is designed for tackling complex physical problems which can be described with the means of Partial Differential Equations (PDEs). These PDEs are then discretized on the basis of the Finite Volume Method (FVM) in space and with a Finite Differences Scheme in time. However, inappropriate documentation and the lack of a graphical user interface make the usage in the beginning more difficult than most commercial software. The aim of this study is to show the functionalities and capabilities of the toolbox for hydraulic engineering applications, including a short description of the meshing process, boundary condition and the numeric of the solvers. Therefore, a short overview of the applicability and the limitations of the solver “TwoPhaseEulerFoam and InterFoam” which is most commonly used in hydraulic Engineering are presented.

Keywords: OpenFOAM, InterFoam, TwoPhaseEulerFoam, Multiphase, Hydraulic Engineering.

1. INTRODUCTION

Computational Fluid Dynamics is essentially a method for solving a set of partial differential equations that represent a fluid system. These typically include equations representing the principles of conservation of mass, momentum and energy, as well as auxiliary equations to represent other physical phenomena or sources e.g. porous medium, heat exchangers, actuator discs, magnetic fields, etc. Additional transport equations can also be included within a CFD solution to model the transport of a given property such as species concentration in the case of combustion modelling, or turbulent quantities such as the turbulent kinetic energy k and its dissipation rate ε when modelling turbulence using the standard k - ε model.

The three most common methods for numerically solving partial differential equations are the Finite Difference (FDM), Finite Element (FEM) and Finite Volume (FVM) Methods. Common to all of these is that the computational domain is divided into smaller regions with a computational grid, and the differential equations are approximated at discrete points using algebraic equations. Different schemes can be used for approximation and interpolation, usually trading complexity and computational costs for accuracy. For CFD the standard method is FVM, which is rarely used for other purposes. In FVM the domain is divided into control volumes (CV) and the integral form of the conservation equations are applied to each of them. The variables are defined at the centres of the CVs and are interpolated to the CV boundaries. Importantly for CFD, conservation is built into the method. Other reasons for its popularity are that it can be applied to any kind of computational mesh, as the mesh only defines the boundaries of the CVs – instead of the computational nodes as in FDM – and all the variables have a clear physical meaning (Ferziger and Peric, 2002). Open source software is an attractive CFD tool for academic and research purposes. Unrestricted access allows detailed insight into the algorithms used and limitless customization for specific purposes. In CFD applications, the lack of licensing fees makes massively parallel computations economically feasible, provided that the parallelization of the solver is efficient. The widely known CFD-toolbox “OpenFOAM” (Open Field Operation and Manipulation) is a well designed C++ library that allows the numerical simulation of various engineering applications. Through its object-orientated structure it is very flexible and can be adjusted to very specific problems. Since the code is open source, code analysis and manipulation are possible. In general, the library is designed for tackling complex physical problems, which can be described with the means of partial differential equations (PDEs). These PDEs are then discretized on the basis of the Finite-Volume-Method (FVM) in space and with a Finite-

Differences-Scheme in time. With its specific data types for describing the PDEs and the usage of operator overloading, OpenFOAM allows formulating the equations in a way that resembles the mathematical formulation (Weller et al. 1998). Thus, operators like divergence, gradient or laplacian can be simply written as `div1`, `grad` and `laplacian`. A Message-Passing-Interface based parallelization concept is embedded seamlessly which enables highly effective massive parallel computing. As the code is open source, parallel computing with OpenFOAM is limited by the hardware resources available and not by the number of licenses available. But, as the parallelization is based on a domain decomposition approach, the efficiency of parallelization is only given, if the problem size is large enough (Hinkelmann 2003). The class based structure divides the software into the smallest possible units, where each is designed for performing one specific task. Through the object orientated structure the maintenance of the code and development of extensions are generally made easier, as it is possible to add functionality at the outer layers of the code without the necessity to know everything about the inner layers of the libraries. Furthermore, code duplication is avoided, since all parts of the library can be used at multiple positions. With its ingenious concept for the discretization, which is described below, the software allows the usage of arbitrarily shaped cells in the mesh. Besides the official release some forks and adaptations are available. One noteworthy release is the community-driven distribution by the “extend- project”, which aims to “open the OpenFOAM CFD toolbox to community contributed extensions in the spirit of the Open Source development” (www.extend-project.de). Containing various valuable user-developed extensions, it is widely used by many researchers. With the ongoing developments the differences between the two main release branches are growing, therefore switching between different versions is not recommended. The following description refers to the official version 2.2.2. The program package can be installed or compiled for most Linux distributions; versions for Mac OS are available. Running OpenFOAM on Windows is possible but entails several restraints. For post-processing results of OpenFOAM simulations, the open source software ParaView or other common post-processing tools like Tecplot or Gnuplot can be used. With ParaView, even domain decomposed cases (that were calculated in parallel on several CPUs and are stored in separate directories for each domain), can be post-processed without reconstructing the case. In contrary to most CFD programs, OpenFOAM is not delivered with a graphical user interface for performing the pre- and post-processing of the simulations. Settings and data are saved in ASCII text files, where the names of the files and folders have to correspond to a predefined structure. Simulation results are saved in folders named according to the time-step or iteration (Schulze & Thorenz.,2014).

2. FINITE VOLUME DISCRETION IN OPEN FOAM

Since an analytical solution of the PDEs is rarely possible, the solution has to be approximated. For this, the FVM is used here. The discretization process can be done as follows:

2.1. EQUATION DISCRETIZATION

To solve the equations that describe the flow transport, a transformation from partial differential equation to linearized algebraic equation is to be performed. For a generic transport equation this can be done as follows (Jasak 1996).

The generic transport equation for the field variable ϕ in integral form can be formulated as:

$$\frac{\partial \rho \phi}{\partial t} + \nabla \cdot (\rho U \phi) - \nabla \cdot (\rho \Gamma \nabla \phi) = S_\phi(\phi) \quad (1)$$

All terms are integrated over the time step ranging from t to $t + \Delta t$ and the control volume v_p :

$$\int_t^{t+\Delta t} \left[\frac{\partial}{\partial t} \int_{v_p} \rho \phi dV + \int_{v_p} \nabla \cdot (\rho U \phi) dV - \int_{v_p} \nabla \cdot (\rho \Gamma \nabla \phi) dV \right] dt = \int_t^{t+\Delta t} \left[\int_{v_p} S(\phi) dV \right] dt \quad (2)$$

By using the Gauss theorem, volume integrals can be converted into surface integrals, which can then be written as sums over the regarded control volume:

$$\int_t^{t+\Delta t} \left[\left(\frac{\partial \rho \phi}{\partial t} \right)_p + \sum F \phi_f - \sum (\rho \Gamma_\phi)_f S \cdot (\nabla \phi)_f \right] dt = \int_t^{t+\Delta t} [S_u v_p + S_p v \phi_p] dt \quad (3)$$

ρ represents the density, U is the velocity field, through which the variable ϕ is transported through the domain, Γ describes the diffusion coefficient and S includes all source terms. Index P denotes the midpoint of the control volume, index f indicates the value at the surface of the control volume.

The first term accounts for the temporal variation of the generic variable ϕ , the second term describes the convective transport, the third term quantifies the diffusive transport and the right hand side in the equations specifies sources and sinks. The exact way of discretization is defined through the chosen discretization scheme. Since the discretization in OpenFOAM works on a “per operator basis”, different schemes (e.g. upwind or different TVD schemes are available) for each operator can be chosen during runtime. As described below, this choice has a large influence on the accuracy of the results and must therefore be handled with care.

The order of accuracy is also of first order, but the time-step restrictions are much less severe. For achieving second order accuracy, the discretization can be blended between the implicit and the explicit scheme. In standard literature an equally weighted blending between implicit and explicit calculation is labelled as Crank Nicolson Method (Ferziger und Perić 2002), however in Open- FOAM the user can blend between a 50:50-weighting and the fully implicit method. That means, the entry `ddtSchemes {default CrankNicolson 0;}` refers to a fully implicit temporal discretization, whereas `ddtSchemes {default CrankNicolson 1;}` implies the standard Crank Nicolson scheme with 50 % implicit and 50 % explicit discretization (Schulze & Thorenz., 2014).

3. MESHING

Mesh generation is a mandatory process phase in typical CFD, structural and acoustic simulations and analyses. Although being just requirement for performing calculation it has an important impact on efficiency and accuracy of computation; element or cell shape and size does matter on both computation speed and numerical accuracy.

The mesh is an integral part of the numerical solution and must satisfy certain criteria to ensure a valid, and hence accurate, solution. During any run, OpenFOAM checks that the mesh satisfies a fairly stringent set of validity constraints and will cease running if the constraints are not satisfied. By default OpenFOAM defines a mesh of arbitrary polyhedral cells in 3-D, bounded by arbitrary polygonal faces, i.e. the cells can have an unlimited number of faces where, for each face, there is no limit on the number of edges nor any restriction on its alignment. A mesh with this general structure is known in OpenFOAM as a polyMesh. This type of mesh offers great freedom in mesh generation and manipulation in particular when the geometry of the domain is complex or changes over time. The OpenFOAM toolbox includes a meshing toolbox that allows the generation and manipulation of structured and unstructured meshes. The meshing generation is performed with two main utilities: `blockMesh` and `snappyHexMesh`. `blockMesh` allows the generation of block structured, bodyfitted meshes. On the basis of coordinates, the boundaries of the domain are defined. In the further settings, the names of the boundaries and the size of the cells can be specified. In general, all meshes are created in three dimensions. For a two-dimensional mesh, the mesh gets only one cell in the third dimension and the faces normal to the third dimension get a specific boundary condition (“empty”). With the `snappyHexMesh` utility the mesh can be adapted to complex external geometries. The mesh generation is based on a `blockMesh` grid and consists of three successive steps (see Figure 1):

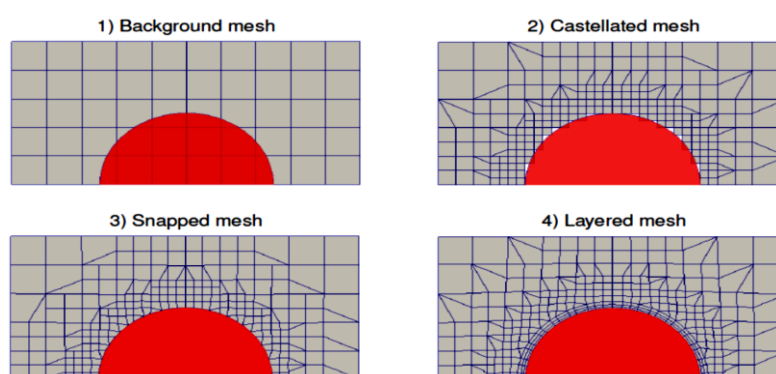


Figure 1. Grid generation steps with the native OpenFOAM meshing tools: a) `blockMesh` grid, b) `snappyHexMesh` castellated, c) `snappyHexMesh` snapped, d) `snappyHexMesh` `addLayers`

Castellated mesh generation: In the first step, the input mesh is locally refined according to the predefined settings. Cells close to the surface of the external geometries and cells in predefined regions are refined by orthogonal division of the block structured cells. Afterwards, all cells that overlap the external geometry are deleted from the mesh. This results in the so called castellated mesh.

Snapping: In the second step, cells that are intersecting with the geometry surface are deformed such that the mesh fits the external geometry. This process is performed in an iterative manner to assure that the shape of the surface resembles the external geometry's surface and fulfills the required mesh quality parameters. Cells on the inside are deformed, too, in order to avoid too distorted cells.

Addition of boundary layers: The third step adds boundary layers to the mesh. This is done by first shrinking the existing mesh and then inserting stretched block structured cells at the surface of the external geometry. These layers have the purpose of improving the modelling of boundary layer flow. If local head losses are dominating the flow and friction losses can be neglected, the creation of boundary layers can be avoided. As the creation of boundary layers in snappyHexMesh often results in a decreased mesh quality, the necessity of boundary layers is to be thought over before the simulation setup. The snappyHexMesh grid generation can be performed in parallel. This is advantageous, if large meshes are to be created. With OpenFOAM it is also possible to use meshes that are not created with the native tools. For the conversion of these meshes, several tools are available (e.g. fluentToFoam, starToFoam etc. (Schulze & Thorenz.,2014).

4. CASE SETUP

After the meshing, solver settings, calculation settings and boundary conditions have to be defined. For that, a case must contain at least the following subfolders: 0, constant, system. In the 0 folder, files with the boundary and initial conditions of all primary variables are stored. The constant folder contains all constant parameters like gravity, surface tension and the mesh data. In the system folder, the chosen discretization schemes, iterative solving methods and parameters that control the solution process like the time-step size or the maximum Courant number are defined. The system folder will be read during runtime, which means that a change of settings in this folder is immediately effective. Since appropriate choice of boundary conditions and discretization schemes are crucial for a successful simulation setup, more details on these topics are given below.

4.1. BOUNDARY CONDITIONS

In OpenFOAM boundary conditions are defined per variable at each boundary patch. It is possible to define generic type boundary conditions like fixed values (Dirichlet) or fixed normal gradients (Neumann), additionally derived boundary condition types are available that combine several generic conditions with additional restrictions. It is necessary that the conditions for various variables at one patch match, so that the boundary conditions result in a physically sound combination.

4.2. DISCRETIZATION SCHEME AND ITERATIVE SOLVERS

In the fvSchemes file the user has to define, which discretization schemes are to be used. As explained before, the discretization of the equation is based on a per operator basis. This means that one discretization scheme can be chosen for each operator. With the choice of the schemes, stability and accuracy of the calculation are strongly influenced. Therefore, a lot of effort should be put into the choice of the schemes. The chosen schemes in the official tutorials of the toolbox are mostly chosen such that the simulation runs fast and stable (i.e. using upwind schemes) whereas for real world applications higher accuracy (higher order schemes) is needed in most cases.

The fvSolution file specifies the iterative solvers and limiters that should be used for solving the PDE systems. The choice for the iterative solvers strongly affects the simulation time but only has small influence on the actual results, if the error tolerances of the different solvers are set to the same order.

5. MULTIPHASE SOLVERS

In OpenFOAM, multiple multiphase solvers are available. These are namely:

- InterFoam, LTSinterFoam InterDyMFoam: Solvers that are based on the Volume-of-Fluid Method (as explained below). These are useful for simulations, where a sharp and well-defined interface between the fluid phases exists.

- TwoPhaseEulerFoam, multiphaseEulerFoam, and multiphaseInterFoam: Solvers that are based on the Eulerian-Eulerian approach (for detailed information refers to Rusche, 2002).

For hydraulic engineering applications, the first three are of most relevance, whereas the last three are rather used for applications where small-scale flow regions (i.e. as in chemical engineering) are considered. In the following the interFoam and TwoPhaseEulerFoam solver is analysed in detail. The interFoam solver is made for

simulating flow of two immiscible fluids, which share an interface that is significantly larger than the cell size. The continuous fluid regions should contain a multitude of cells. In this approach, only one mass and one momentum conservation equation is solved for both fluids. For that, density and viscosity of both fluids are averaged according to the volume fractions in the cell. Mass and momentum transfer between the phases is neglected (Schulze & Thorenz., 2014). On the other hand, two incompressible fluid phases with one phase dispersed are solved using TwoPhaseEulerFoam solver. Both the phases are described using the Eulerian conservation equations and thus it is referred as Euler-Euler model. Each of the phases is treated as a continuum in this approach.

5.1. INTERFOAM SOLVER BASIC EQUATIONS

The Volume of Fluid (VoF) method is used for tracking the position and shape of the interface through solving an additional advection equation for the volume fraction in each cell. Together with the Navier- Stokes equations this results in the following set of equations that has to be solved for each cell during each time step:

$$\nabla \cdot U = 0 \tag{4}$$

$$\frac{\partial \rho U}{\partial t} + \nabla \cdot (\rho U U) = -\nabla p_{-rgh} + [\nabla \cdot (\mu \nabla U) + \nabla U \cdot \nabla \mu] + \rho \cdot g + \int_s \sigma k \delta(x - x_s) n dS(x_s) \tag{5}$$

$$\frac{\partial \alpha}{\partial t} + \nabla \cdot (U \alpha) + \nabla \cdot (U_r \alpha (1 - \alpha)) = 0 \tag{6}$$

With ρ = density; U = velocity; t = time; $p_{-rgh} = p - \rho g \cdot x$ = modified pressure, obtained by subtraction of the hydrostatic pressure from the pressure; x = special position vector ; μ = dynamic viscosity; g =gravity; S = interface between the phases; σ = surface tension coefficient; k = curvature of the surface; δ = dirac delta; $(x - x_s)$ = distance from the considered point to the surface; n = normal vector on the interface; α = volume fraction of the first phase (water); U_r = compressive velocity counteracting numerical diffusion. The first equation accounts for the conservation of mass, the second represents the momentum Conservation equation and the third describe the transport of the volume fraction α . For counteracting numerical diffusion in the VoF equation, an artificial compression velocity U_r is introduced. This term creates a flux in the direction of the gradient of the volume fraction $\nabla \alpha$, e. g. the smeared interface is artificially compressed. It only acts within the zone of the interface as it becomes 0 where $\alpha = 0$ or $\alpha = 1$.

5.2. TWOPHASEEULERFOAM SOLVER BASIC EQUATIONS

TwoPhaseEulerFoam is a two-fluid, Euler-Euler method solver for incompressible two- phase turbulent flows. It has been included in OpenFOAM releases since version 1.3 with small variations. The twoPhaseEulerFoam is based on a solver called bubbleFoam, which is a result of Henrik Rusche’s work for his PhD thesis “Computational Fluid Dynamics of Dispersed Two-Phase Flows at High Phase Fractions” (2002) and on further development (Weller, 2002, 2005) of the algorithm developed for the BRITE II project at Imperial College. TwoPhaseEulerFoam differs from bubbleFoam by the addition of models for particle- particle interaction. Two alternative approaches are included. Firstly, with a particle normal force, i.e. a powder modulus model as suggested by Gidaspow et al. (1983; 1985) and Bouillard et al. (1989) and secondly, using the kinetic theory for granular flow (KTGF) model.

Two incompressible fluid phases with one phase dispersed are solved using this solver. Both the phases are described using the Eulerian conservation equations and thus it is referred as Euler-Euler model. Each of the phases is treated as a continuum in this approach.

The Eulerian conservation equations are used to describe both the phases in the two-fluid model. Each of the phase is treated as continuum and inter-penetrating each other and is represented by averaged equations. The equations implemented in OpenFOAM solver are given here. The equations for two fluid modeling approaches in OpenFOAM are implemented from “Computational Fluid Dynamics of Dispersed Two-Phase flows at high phase fractions” by Henrik Rusche. The averaged inter-phase momentum transfers term accounts for the transfer of momentum between the two phases. The averaged momentum and continuity equations for each phase ϕ can be written as:

$$\frac{\partial \alpha_\varphi \bar{U}_\varphi}{\partial t} + \nabla \cdot (\alpha_\varphi \bar{U}_\varphi \bar{U}_\varphi) + \nabla \cdot (\alpha_\varphi \bar{R}_\varphi^{-eff}) = -\frac{\alpha_\varphi}{\rho_\varphi} \nabla \bar{p} + \alpha_\varphi g + \frac{\bar{M}_\varphi}{\rho_\varphi} \quad (7)$$

$$\frac{\partial \alpha_\varphi}{\partial t} + \nabla \cdot (\alpha_\varphi \bar{U}_\varphi) = 0 \quad (8)$$

Where the subscript φ denotes the phase, α is the phase fraction, \bar{R}_φ^{-eff} the combined Reynolds (turbulent) and viscous stress, \bar{M}_φ is the averaged inter-phase momentum transfer term. Combining the second equation for the two phases when $\varphi = a$ and $\varphi = b$ yields the volumetric continuity equation and can be formulated as an implicit equation for pressure.

The inter-phase momentum transfer can be calculated by adding the forces acting on the Dispersed Phase particles. The drag, lift and the virtual mass forces are considered as the main contribution. The other forces such as Basset or history forces are neglected.

The volumetric continuity equation is:

$$\nabla \cdot \bar{U} = 0 \quad \text{Where: } \bar{U} = \alpha_a \bar{U}_a + \alpha_b \bar{U}_b \quad (9)$$

This equation is recast into a pressure equation:

$$\bar{U} = \alpha_a \bar{U}_a + \alpha_b \bar{U}_b \left[\nabla \cdot \left(\left(\alpha_{af} \left(\frac{1}{\rho_a (A_a)_D} \right)_f + \alpha_{bf} \left(\frac{1}{\rho_b (A_b)_D} \right)_f \right) \nabla [\bar{p}] \right) \right] = \nabla \cdot (\alpha_{af} \varphi_a^* + \alpha_{bf} \varphi_b^*) \quad (10)$$

The phase continuity equation solved is:

$$\frac{\partial \alpha_\varphi}{\partial t} + \nabla \cdot (\alpha_\varphi \bar{U}) + \nabla \cdot (\bar{U}_r \alpha_\varphi (1 - \alpha_\varphi)) = 0 \quad (11)$$

where \bar{U} is as given above and \bar{U}_r is the relative velocity between the phases.

5.3. DISCRETIZATION WITH APPROPRIATE SCHEMES

Since the numerical solution of advection equations tends to produce numerical diffusion and thereby smear discontinuities, a special solution technique for the VoF equation is available in OpenFOAM. To guarantee a bounded solution with sharp interface between the phases, the total variation diminishing scheme “interGamma” (Jasak 1996) is, used mostly in combination with the flux corrected transport approach “MULES” (MULTidimensional Limiter for Explicit Solutions) (Damian 2013). However, other advection schemes for the flux calculation can also be used. The experience showed that for free-surface hydraulic engineering simulations, the choice of the divergence schemes for the VoF equation has significant impact on the quality of the results. In particular, the usage of the Minmod scheme for the discretization on the convection term $\text{div}(\alpha, \phi)$ and the interface Compression for the artificial compression term $\text{div}(\alpha, \phi_{int})$ showed good results. For the discretization of the momentum transport $\text{div}(\bar{U}, \rho)$ it is absolutely necessary to use discretization schemes of higher order, as first order upwind discretization smears the results (Schulze & Thorenz., 2014).

5.4. PRESSURE-VELOCITY COUPLING

For the mass and the momentum conservation equation incompressibility is assumed, therefore the densities of the phases do not change over time. The equations of the system are strongly coupled; therefore, a special solution algorithm is needed. In the interFoam solver, a segregated approach is adopted for the pressure velocity coupling. For this, the PISO (Pressure Implicit Splitting of Operators (Issa 1986)) algorithm is applied. To avoid the “checkerboarding” phenomena, an interpolation method “in the spirit of the Rhie Chow method” is used (Peng Kärholm 2006). In particular, the complete solution procedure of the interFoam solver consists of the following steps (Damian 2013), when the standard PISO algorithm is set: 1 Solve VoF equation on basis of the old velocity field from the previous time step. This gives new values for the volumetric phase fraction and the dependent density in each cell. 2 Perform the momentum predictor step, where the new momentum is calculated on basis of the previous velocities which are interpolated as fluxes from the cell midpoints to the cell faces, the old pressure values and the new density distribution from step 1. 3 The predicted (2.) or the old velocities from the previous timestep are used to set up a linear equation system for solving the new pressure values. 4 The new pressure is calculated. 5 In the last step the predicted velocities are corrected, so that continuity is fulfilled. The momentum predictor step (2.) is not mandatory, but it can reduce the calculation time

in some cases. The last two steps are performed several times within one time-step; the number of cycles is user-defined and can be set in the fvSolution file for each case. The fact, that the volume fraction is solved on the basis of the old velocity field, results in a solution where the variables are “temporally staggered”. This could be avoided when an additional correction of the volume fraction variable would be performed after the PISO algorithm. Since the PISO algorithm is based on the assumption, that the time-step size is small ($Co < 1$) (Jasak 2006), the temporal offset can be neglected. Alternatively, the SIMPLE or PIMPLE algorithm can be selected instead. PIMPLE (in other software this is called SIMPISO) is an extension of the SIMPLE algorithm which performs only one momentum corrector step but applies a more detailed treatment for the pressure gradient arising from non-orthogonality similar to the PISO algorithm (Aguerre et al. 2013). When the non-orthogonal correctors are set to unity, PIMPLE reduces to the PISO algorithm.

5.5. BOUNDARY CONDITIONS FOR HYDRAULIC ENGINEERING APPLICATIONS

In the standard toolbox of OpenFOAM, the available generic boundary conditions are often not practical for hydraulic engineering investigations. Only with some work around it is possible to set a fixed water level or a specific water inflow condition, when simulating with the VoF-solver `interFoam` and Eulerian-Eulerian solver `TwoPhaseEulerFoam`. This was the motivation to develop a set of boundary conditions for hydraulic engineering purposes. In particular, a boundary condition for a fixed water level (to be used primarily at the downstream side of a model) and one for a fixed flow rate of water independent from the water level (to be used at the upstream side) were developed amongst others at the Federal Institute for Waterway Engineering and Research. A more detailed description of this code extension can be found in Thorenz und Strybny (2012). A release of the code to the public is planned in the near future.

6. APPLICABILITY AND LIMITATIONS OF INTERFOAM AND TWOPHASEEULERFOAM

As with every CFD simulation, the accuracy and credibility of the results is highly dependent on the grid resolution. With a too coarse grid important effects of the flow can get lost. For some aspects, models can be applied, which compensate the lost information. In hydraulic engineering turbulence and free-surface modelling is essential. Due to the program structure of OpenFOAM, all available turbulence modeling approaches can be combined with almost every solver. OpenFOAM's VoF-solver `interFoam` is a valuable tool for many hydraulic engineering investigations. Through the volume of fluid approach it is suitable, when the free surface between water and air is of interest. However, the user must be aware, that the interface between the fluids can only be represented with a limited accuracy that is mainly dependent on the size of the cells. Bubbles or droplets, which are smaller than the control volumes, cannot be represented appropriately. Therefore, air entrainment or bubble transport and detrainment cannot be modelled in most hydraulic engineering simulations (Schulze & Thorenz.,2014).

`TwoPhaseEulerFoam` is Solver for a system of 2 incompressible fluid phases with one phase dispersed, e.g. gas bubbles in a liquid including heat-transfer. Therefore, air entrainment or bubble transport and detrainment can be modelled in most hydraulic engineering simulations. In general, the computation time and the stability of the `interFoam` and `TwoPhaseEulerFoam` simulations are strongly dependent on the mesh size and quality, the chosen numerical schemes and matrix solvers.

7. CONCLUSIONS

In this paper, the CFD software OpenFOAM is introduced. It has been highlighted that OpenFOAM is a powerful tool which offers an extensive range of features to model fluid flow, from incompressible to compressible flows, as well as multi-phase flows. OpenFOAM is distributed with a large number of models, including laminar and turbulence models within the RANS, LES and DNS simulation/modelling frameworks.

The included meshing tool and the solvers allow the modelling of complex systems, which can be post processed with tools like ParaView, Gnuplot or similar software. Due to the sophisticated structure of the library massive parallel computing is possible, which is almost only limited to the available hardware resources. The experience shows, that the above described `interFoam` solver is a suitable tool for typical hydraulic engineering questions based on the investigation of water levels, velocities, pressures etc. The named solver is capable of simulating turbulent two-phase flow, with long, stretched water-air interfaces. On the other hand, `TwoPhaseEulerFoam` solver is a suitable for a system of two incompressible fluid phases with one phase dispersed; therefore, air entrainment or bubble transport and detrainment can be modelled in most hydraulic engineering simulations. The quality of the results is mainly dependent on the grid quality and the chosen discretization schemes. In comparison to many commercial CFD software packages OpenFOAM is very

sensitive concerning the grid quality; it is therefore advisable to put effort into the grid generation. Further, the user should be aware, that the chosen discretization schemes have a great influence on the stability of the calculation and the quality of the results. As usual in numerical simulations, the definition of the domain extent, the definition of the boundary condition as well as the adjustment of all other settings is also crucial for getting plausible results. As only little user-friendly documentation and no graphical user interface exist, the start with Open-FOAM might be not as easy as with commercial CFD software.

8. REFERENCES

1. Aguerre, H. J.; Damián, S. M.; Gimenez, J. M.; Nigro, N. M. (2013): Modelling of compressible fluid problems with Open- FOAM using dynamic mesh technology XXXII, pp. 995–1011. Available online at <http://www.cimec.org.ar/ojs/index.php/mc/article/viewFile/4404/>, checked on 5/29/2014
2. Damian, S. M. (2013): An Extended Mixture Model for the Simultaneous Treatment of Short and Long Scale Interfaces. Doctoral Thesis. Universidad Nacional del Litoral, Santa Fe, Argentina. Facultad de Ingeniería y Ciencias Hídricas. Available online at <https://docs.google.com/file/d/0B21pdhG-Zh05Y0ZzOHVlb3lGekk/edit?pli=1>, checked on 5/22/2014.
3. Ferziger, J. H.; Perić, M. (2002): Computational methods for fluid dynamics. 3rd, rev. ed. Berlin, New York: Springer.
4. Gisen, D. (2014): Generation of 3D mesh using snappyHexMesh featuring anisotropic refinement and near-wall layers for hydro power dam tailwater. In: Proceedings of the 11th International Conference on Hydroscience & Engineering (ICHE) 2014. Hamburg.
5. Hinkelmann, R.-P. (2003): Efficient Numerical Methods and Information-Processing Techniques in Environment Water. Habilitation. University of Stuttgart, Stuttgart. Institute of Hydraulic Engineering.
6. Issa, R.I (1986): Solution of the implicitly discretised fluid flow equations by operator-splitting. In Journal of Computational Physics 62 (1), pp. 40–65. DOI: 10.1016/0021-9991(86)90099-9.
7. Jasak, H. (1996): Error Analysis and Estimation for the Finite Volume Method with Applications to Fluid Flows. Doctoral Thesis. Imperial College of Science, Technology and Medicine, London, Great Britain. Department of Mechanical Engineering. Available online at <http://powerlab.fsb.hr/ped/kturbo/OpenFOAM/docs/HrvojeJasakPhD.pdf>, checked on 5/22/2014.
8. Jasak, H. (2006): Numerical Solution Algorithms for Compressible Flows. Lecture Notes. Zagreb.
9. Peng Kärrholm, F. (2006): Rhie-Chow interpolation in OpenFOAM. Chalmers University of Technology. Available online at http://www.tfd.chalmers.se/hani/kurser/OS_CFD_2007/rhiechow.pdf, checked on 5/22/2014.
10. Rusche, H. (2002): Computational fluid dynamics of dispersed two-phase flows at high phase fractions. Doctoral Thesis. Imperial College of Science, Technology and Medicine, London, Great Britain. Department of Mechanical Engineering. Available online at <http://powerlab.fsb.hr/ped/kturbo/OpenFOAM/docs/HenrikRuschePhD2002.pdf>, checked on 5/22/2014.
11. Saad, Y. (2003): Iterative methods for sparse linear systems. 2nd ed. Philadelphia: SIAM.
12. Thorenz, C.; Strybny, J. (2012): On the numerical modelling of filling-emptying systems for locks. In Hinkelmann R.-P, Liang,
13. Schulze, L; Thorenz, C.(2014): The Multiphase Capabilities of the CFD Toolbox OpenFOAM for Hydraulic Engineering Applications. ICHE Conference, , Hamburg , Lehfeldt & Kopmann
14. Y. Savic, D., Nasermoaddeli, M., Daemrich, K.-F., Fröhle, P., Jacob, D. (Eds.): Proceedings, 10th International Conference on Hydroinformatics HIC 2012. International Conference on Hydroinformatics. Hamburg, July 14-18 2012. Hamburg: TuTech Innovation.
15. Weller, H. G.; Jasak, H.; Fureby, C. (1998): A tensorial approach to computational continuum mechanics using object-oriented techniques. In Journal of Computational Physics 12 (6), pp. 620–631. Available online at
16. <http://www.foamcfp.org/Nabla/main/PDFdocs/CompInPhys98.pdf>, checked on 5/22/2014.

Design of neural networks by using genetic algorithm for the prediction of immersed CBR index

Mohammed el Amin Bourouis¹, Abdeldjalil Zadjaoui¹, Abdelkader Djedid¹,
Abderrahmen Bensenouci²

1- Aboubekr Belkaid University, BP 230 - 13000 Chetouane Tlemcen, Algeria

2- Laboratory of public works of the west, BP 164 Abou Tachefine Tlemcen, Algeria

Email: medamin_bourouis@yahoo.fr

Abstract

The most important parameter of soil for the conception of flexible pavements is the California Bearing Ratio after immersion (CBR_{imm}). This parameter is determined from laboratory testing, which requires skilled workforce and time. Based on parameters simply measured like Maximum Dry Density (MDD), Optimum Moisture Content (OMC), Liquid Limit (LL), Plastic Limit (PL) and the fine fraction passing at 0.08 mm and 2 mm ($F_{0.08\text{ mm}}$, $F_{2\text{ mm}}$) we proposed a neuro-genetic model to predict the index CBR_{imm} . The aim to use the genetic algorithm is to evolve at the same time: The determination of the artificial neural network architecture, transfer function and the optimization of synaptic weights. Using a neuro-genetic approach helps to increase neural network performance and it gave us a minimal average absolute error.

Keywords: CBR_{imm} , Compacting, Prediction, Artificial neural network, Genetic algorithm.

1. INTRODUCTION

During the work of excavation of earth dams, road embankments and slopes of the airport it is necessary to compact mechanically the material to increase its shear strength and reduce its permeability. To simulate the compacting procedure to be adopted which ensures a certain level of compactness on site, laboratory tests have been developed for many years; they differ only in the level of energy applied to the soil sample. The CBR California Bearing Ratio test takes a lot of time and requires skilled labor. For this reason, several correlations by various researchers have been developed to estimate this fundamental parameter. In this study we proposed a hybrid model between the artificial neural network and the genetic algorithms in order to predict this index accurately. The role of the genetic algorithm in this work is to optimize the structure of the network and to determine its synaptic weights. The input variables of our model are simply measured parameters such that Optimum moisture content (OMC), maximum dry density (MDD), liquid limit (LL), The fine fraction passing at 0.08 mm ($F_{0.08\text{ mm}}$), and the fraction passing at 2 mm ($F_{2\text{ mm}}$).

2. LITERATURE REVIEW

Geotechnical properties of soils are controlled by factors such as mineralogy, fabric, and pore water, and the interactions of these factors are difficult to establish solely by traditional statistical methods due to their interdependence. Shahin et al (2008) showed that despite soil variability and complex behavior, artificial neural networks (ANN) can be used to predict the geotechnical and geological model of soils with a good approximation [1]. Ripley (1996) indicate that the use of more than one layer hidden in ANN methodology provides the flexibility needed to model complex phenomena [2]. Patel and Desai (2010) proposed a correlation between the plasticity index, the optimum dry density, the optimum Proctor water content and the CBR_{imm} of the alluvial soils [3]. Roy et al. (2007) has developed a multiple regression model. He chose MDD and OMC as input parameters because they have a strong correlation with CBR_{imm} . The model gave satisfactory results with a coefficient of determination equal to 0.982 [4]. Rakaraddi and Gomarsi (2015) proposed a multiple linear regression model to predict the CBR from the liquid limit, plastic limit, percentage of fines and soil density. Bad result for a coarse soil because of the ignorance of the percentage of sand and gravel in the model [5]. Tang et al. (1991) found that when the number of input variables increases the predictive capacity of the neural network improves [6]. The same authors also suggested that even with little data, the neural network can perform reasonably if the input parameters are significant [6]. Pradeep Kumar and Harish Patel (2016) proposed models based on the neural and statistical approach, the neural network model with five input parameters; MDD, OMC, LL, PL and PI gave the best result with an average square error equal to 0.13 [7]. The modeling power of the

artificial neural network relies on the transfer functions used. Several works have studied the effects of transfer functions on the performance of neural models, such as Falode and Udombosoot (2016) which used the symmetric saturated linear function; this saturation effect will severely limit the possibility of the network to capture The Input-Output relationship when the problem is complex [8]. The derivation and the simplicity of the sigmoid function calculation logically led Philip et al. (2011) And Bourouis et al. (2015) to use [9-10]. Smith (1986) stated that if $|R| > 0.8$ implies the existence of a strong correlation, if $0.2 < |R| < 0.8$, this means the occurrence of a correlation and if $|R| < 0.2$, a weak existing correlation [11]. Willmott and Matsuura examined relative RMSE and Mean Absolute Error (MAE) to describe the average error in model performance. The results indicate that MAE is a measure of the actual average error trend (unlike RMSE). Our contribution is intended in this sense and exploits the works cited above [12].

3. DESCRIPTION OF THE APPROACHES USED

3.1. GENETIC ALGORITHM (GA)

Genetic algorithms are a family of heuristic algorithms for finding the optimum or near-optimum of any functions, called objective basis on which it is necessary to make any particular hypothesis as decent gradient algorithms regarding their derivability. Genetic algorithms manipulate a population of individuals of constant size, this population of constant size is subject to competition between individuals. Each individual is given as a single string of characters called a chromosome and represents a point in the search space [13]. Using selection, crossing and mutation operators based on natural phenomena, the genetic algorithm evolves this population of individuals over generations (Figure 1).

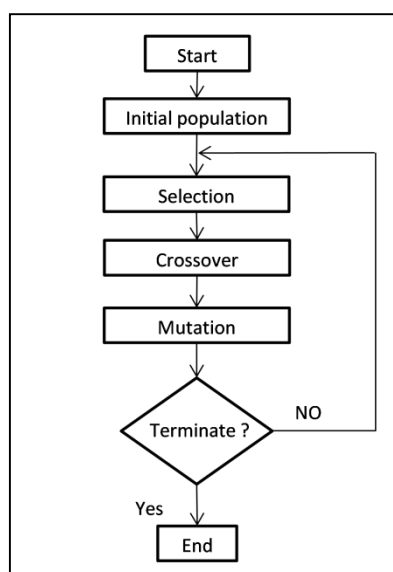


Figure 1: Flow Chart of the genetic algorithm

Crossing and mutation are responsible for exploring the research space by building new individuals from the previous generation, while selection favors individuals who have a high adaptation. Genetic algorithms offer the possibility of finding solutions to very varied problems when it is possible to express these problems in terms of objective function optimization.

3.2. ARTIFICIAL NEURAL NETWORK

Neural networks are a real way to solve several problems where classical methods have shown their limitations. Neural networks, with their classification, memory, filtering and approximation skills, have become a very effective way. The gradient propagation (BP) is a learning algorithm, the problem of this algorithm that it converges very difficult in the case of complex neural networks and the error function is minimized with several local optima because the error surface of a complex network includes many maxima and minima (Figure 2). This means that the gradient algorithm can converge to a minimum which is not the global optimum. The researchers know well that the choice of network architecture can lead to the success or failure of an application,

in order to ensure a good performance. We used intelligent search methods namely genetic algorithms where optimization of these parameters is done in an automatic way. The application of genetic algorithms to determine an optimal network structure will be the subject of our study.

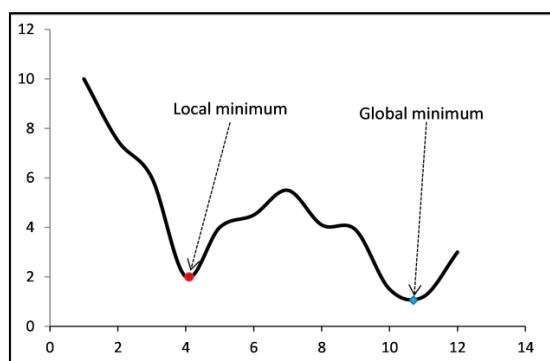


Figure 2: Minimum local and total of the solution

4. PREDICTION OF CBR_{imm} OF SOILS USING NEURO GENETIC (NG)

In this work we used a database of 220 measurements collected from the laboratory of public works of the west (LTPO - Unit of Tlemcen). Content of optimal Proctor (OMC), dry density (MDD), liquidity limit (LL), the fine fraction passing at 0.08 mm ($F_{0.08\text{ mm}}$) and the fraction passing at 2 mm ($F_{2\text{ mm}}$) are used as input variables in the model developed for the CBR_{imm} index. The characteristics of the samples used in this study are defined in the Table 1.

Table 1: The characteristics of the samples used

Type of data	Symbol	Range
Input	$F_{0.08\text{ mm}}$	5.0-79
	$F_{2\text{ mm}}$	12.0-99
	LL	13-65
	OMC	3.0-18
	MDD	1.65-2.35
Output	CBR_{imm}	1.9-100

4.1. METHODOLOGY

The strategy for obtaining RNA optimized by genetic algorithms is based on the development of a program on Matlab, comprising two parts; in a first step, we start by choosing the transfer functions summarized in the Table 2 and find the number of neurons in each hidden layer. In a second time we fix the network parameters (number hidden layers, the number of neurons in each layer, type of the neuron activation function) and optimize the synaptic weights to minimize the error function.

Table 2: The functions of transfer

Name of the function	Relation Input /Output	Symbol
Threshold	$a = 0$ si $n < 0$ $a = 1$ si $n \geq 0$	
Symmetric threshold	$a = -1$ si $n < 0$ $a = 1$ si $n \geq 0$	
Linear	$a = n$	
Linear saturated	$a = 0$ si $n < 0$ $a = n$ si $0 \leq n \leq 1$ $a = 1$ si $n > 1$	
Symmetric saturated linear	$a = -1$ si $n < -1$ $a = n$ si $-1 \leq n \leq 1$ $a = 1$ si $n > 1$	
Positive Linear	$a = 0$ si $n < 0$ $a = n$ si $n \geq 0$	
Sigmoid	$a = \frac{1}{1 + e^{-n}}$	
Hyperbolic tangent	$a = \frac{e^n - e^{-n}}{e^n + e^{-n}}$	
Competitive	$a = 1$ if n maximum $a = 0$ if other	

We adopted two layers hidden because it is considered suitable and adequate for good performance [2]. Performances were evaluated using the mean absolute error (MAE) and the correlation coefficient (R)

4.2. ANALYSIS BY THE SIMPLE REGRESSION

A simple regression analysis was performed to identify useful input parameters that they have a good correlation with the CBR_{imm} index. The aim of this step is to reduce the risk that neural networks will remain in local minima. The results of this analysis are presented in Figure 3 for the five parameters $F_{0.08\text{ mm}}$ (Figure 3.a), $F_{2\text{ mm}}$ (Figure 3.b), LL (Figure 3.c), OMC (Figure 3.d) and MDD (Figure 3.e).

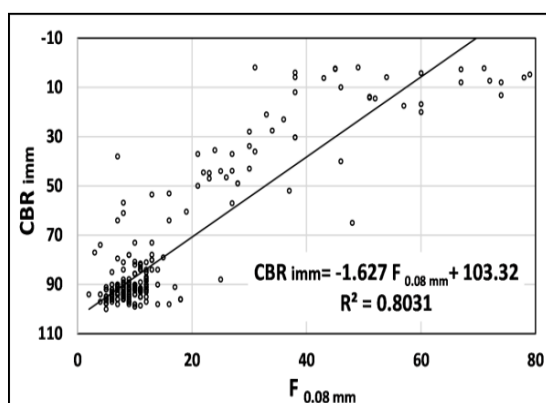


Figure 3.a: Simple regression for the parameter $F_{0.08\text{ mm}}$

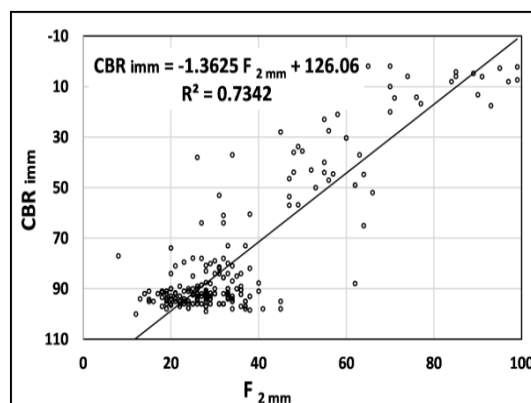


Figure 3.b: Simple regression for the parameter $F_{2\text{ mm}}$

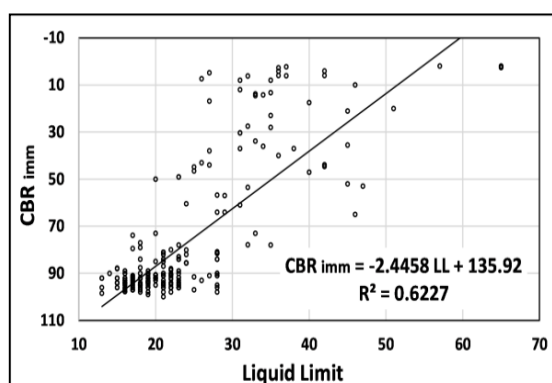


Figure 3.c: Simple regression for the parameter LL

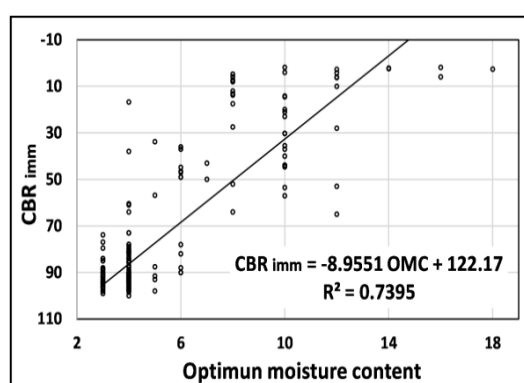


Figure 3.d: Simple regression for the parameter OMC

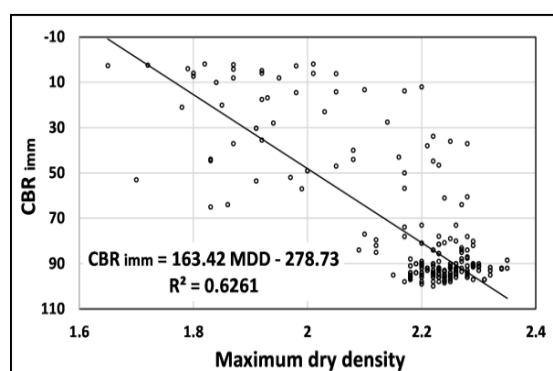


Figure 3.e: Simple regression for the parameter MDD

As shown: The input parameters have a linear relationship with the CBR_{imm} index and they bear a better correlation with the output with a coefficient of determination between 0.62 and 0.81.

4.3. ANALYSIS BY PROPOSED MODEL

For the prediction of the CBR_{imm} index using the proposed model, the five input variables used are the MDD, OMC, LL, $F_{0.08\text{ mm}}$ and $F_{2\text{ mm}}$. The input and output data were normalized by the logarithmic function to obtain good network behavior. The set of data used to develop the model is divided into two parts: one for learning and the other for testing. The training set is used to determine the values of significant network weights. The work of the proposed model gets started with the creation of a random generation composed of a chromosome collection. The size of initial population was considered to be 100. This particular population was then subjected to the genetic operators of selection, crossover, and mutation to produce a new evolved generation. The roulette wheel method was used for the selection operator, whereas for crossover and mutation, probabilities of 0.9 and 0.01 were applied, respectively. A final verification of network performance is made by using the test set. Moreover, the mean absolute error (MAE) is used as a measure of network performance. Four models were developed to predict the CBR_{imm} index. Two hidden layers are considered suitable for good performance. The optimal number of neurons in hidden layers and activation functions is determined using genetic algorithms. The model parameters are summarized in Table 3

Table 3: The parameters of the models developed

Model	Inputs	Topology	Synaptic weights
Model 1	OMC, MDD	2-53-11-1	765
Model 2	LL, OMC, MDD	3-18-44-1	953
Model 3	$F_{0.08\text{ mm}}$, $F_{2\text{ mm}}$, LL, MDD	4-15-12-1	280
Model 4	$F_{0.08\text{ mm}}$, $F_{2\text{ mm}}$, LL, OMC, MDD	5-46-39-1	2149

For all proposed models the genetic algorithm was selected "satlins" as a function of activation of two hidden layers and a linear output. The output of the "satlins" function is obtained as numerical values between -1 and 1. The study shows that the neuro genetic analysis gives a faster convergence compared to the algorithms descended gradient used in a previous work [14]. The correlation coefficient is all in the vicinity of 1 but it does not necessarily mean that the model deduced is adequate because the regression function is an average line linking the output with the input and does not pass through the origin.

Table 4: Comparison between predicted and measured

Measured	Predicted: Model 1	Predicted : Model 2	Predicted : Model 3	Predicted : Model 4
94.20	93.77	97.71	94.61	95.77
94.70	93.77	92.73	92.78	95.40
23.00	17.39	19.52	20.01	23.37
96.50	93.77	95.26	94.91	96.39
90.70	89.87	90.94	93.76	91.64
93.10	93.77	95.71	94.80	94.44
10.00	6.88	13.36	13.25	9.12
90.50	93.77	86.36	89.69	89.71
92.50	93.77	91.31	89.65	93.00
96.00	93.77	92.42	96.30	95.78
5.90	3.87	5.84	11.94	5.91
87.00	93.77	90.40	87.05	88.65
6.00	12.59	11.79	8.71	4.96
R	0.9910	0.9938	0.9963	0.9996
MAE	2.807	2.659	2.130	0.779
MSE	12.431	9.575	6.991	0.869
RMSE	3.526	3.094	2.644	0.932
MAPE	16.989	13.071	15.906	2.797

The mean absolute error of model 4 which contains five input variable is decreased by 15% compared to model 1 which contains only two inputs which means that using more input parameters in neuro genetic models ensures predictive reliability of the CBR_{imm} index (Table 4).

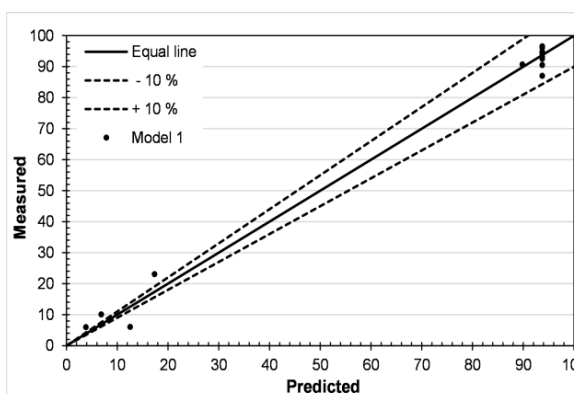


Figure 4.a: Comparison between predicted and measured of model 1

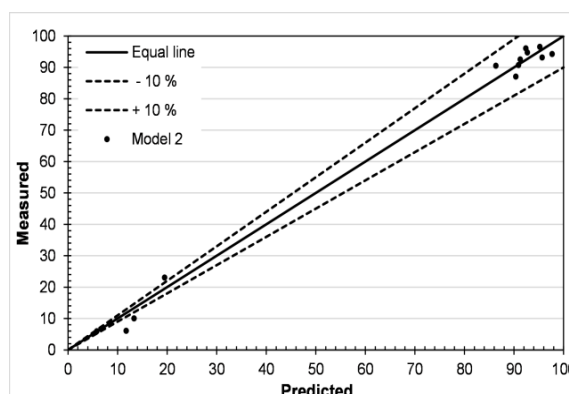


Figure 4.b: Comparison between predicted and measured of model 2

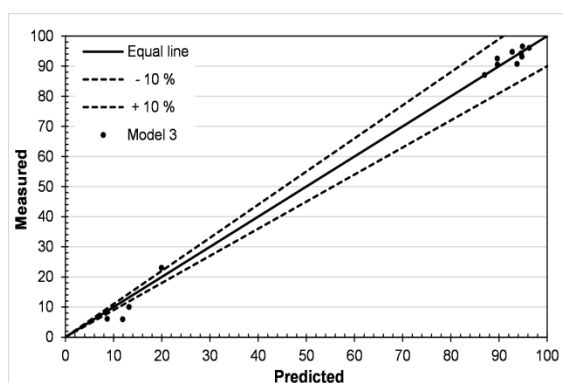


Figure 4.c: Comparison between predicted and measured of model 3

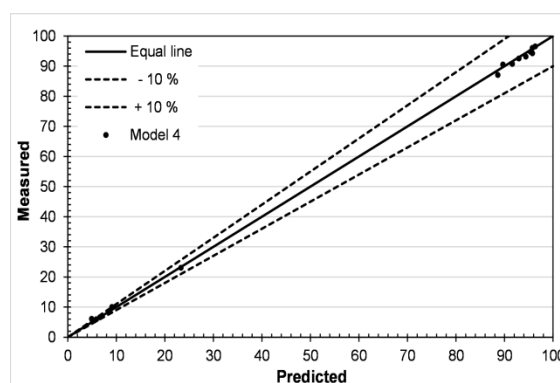


Figure 4.d: Comparison between predicted and measured of model 4

As shown in Figure. 4, model 4 has increased its prediction efficiency with an average absolute error equal to 0.779, all predicted values are included in the error range -10%, + 10%, in contrast to the others models that failed to predict CBR_{imm} index values below 20.

5. CONCLUSIONS

This study was carried out to develop the models of prediction of the CBR index after immersion by exploitation of a database enriched with easily measurable geotechnical parameters. The main conclusions drawn from this study are:

- The choice of two layers hide gave flexibility to our network as it was recommended by Ripley [2].
- The choice of the "stalins" function as an activation function has improved the performance of our network.
- Despite the importance of the number of unknown presented in Table 2 the genetic algorithm has successfully optimized it accurately.
- The use of a large number of parameters makes learning more correct and consequently increases the information available for the networks.
- It is known that the behavior of soils presents a spatial variability, for this it is always preferable to increase the number of influential parameters in the models, which ensures predictive safety.

6. REFERENCES

1. Shahin, M. Jaksa, M. and Maier, H. (2008), "*State of the Art of Artificial Neural Networks in Geotechnical Engineering*," *Journal of Geotechnical Engineering*, **8**, pp. 1-26.
2. Ripley, B. (1996), "*Pattern Recognition and Neural Network*," Cambridge, Cambridge University Press.
3. Patel, R. Desai, M. (2010), "*CBR Predicted by Index Properties of Soil for Alluvial Soils of South Gujarat*," *Proceedings of the Indian Geotechnical conference Indian Geotechnical Conference, Mumbai*, pp. 79-82.
4. Roy, T. Chattopadhyay, B. and Roy, S. (2007), "*Prediction of CBR for Subgrade of Different Materials From Simple Test*," *Proceedings of the International Conference on Civil Engineering in the new millennium :opportunities and challenges, West Bengal*, pp. 2091-2098.
5. Rakaraddi, P.K. and Gomarsi, V. (2015), "*Establishing Relationship Between CBR With Different Soil Properties*," *International journal of research in engineering and technology* **4**, pp. 182-188.
6. Tang, Z. Almeida, C. and Fishwick, P. (1991), "*Time Series Forecasting Using Neural Networks Versus Box-Jenkins Methodology*," *Simulation*, **57** (5), pp. 303–310.
7. Pradeep Kumar K.J. and Harish Patel, Y.M. (2016), "*Soft Computing Technique for Prediction of CBR from Index Properties of Subgrade Soil*," *International Journal of Innovative Research in Science, Engineering and Technology*, **5** (7), pp. 853-860.
8. Falode, O. and Udomboso, C. (2016), *Predictive Modeling of Gas Production, Utilization and Flaring in Nigeria Using TSRM and TSNN: A Comparative Approach*, *Open Journal of Statistics*, **6** (1), 194-207.
9. Philip, A.A. Taofiki, A.A. and Bidemi, A.A. (2011), "*Artificial Neural Network Model for Forecasting Foreign Exchange Rate*," *World of Computer Science and Information Technology Journal*, **1** (3), pp. 110-118.
10. Bourouis, M.A. Zadjajoui, A. and Djedid, A. (2015), *Prediction of the CBR Index by a Neuronal Approach. University Meetings of Civil Engineering, Bayonne, France.*
11. Smith, G. (1986), "*Probability and Statistics in Civil Engineering: An Introduction*," London.
12. Willmott, C. and Matsuura, K. (2005), "*Advantages of the Mean Absolute Error (MAE) Over the Root Mean Square Error (RMSE) in Assessing Average Model Performance*", *climate research*, **30** (1), pp. 79-82.
13. Goldberg, D. (1989), "*Genetic Algorithms in Search, Optimization and Machine Learning*," Addison Wesley Longman Publishing.
14. Bourouis, M.A. Zadjajoui, A. and Djedid, A. (2016). *Neuro-Genetic Approach for Immersed CBR Index Prediction*, *Proceedings of the First Southern African Geotechnical Conference, CRC Press, Sun City*, pp. 143-148

Long-term behavior of kinevars embankment dam using numerical model and compare it with the instrumentation results

Ahmad Ghezelayagh¹, Mansour Fadaei², Amin Bolouri³

1- M.S. in Civil Engineering, University of Tehran, Abfan Consultant Engineering, Iran

2- M.S. in Geotechnical Engineering, Sharif University of Technology, Abfan Consultant Engineering, Iran

3- M.S. in Geotechnical Engineering, Khaje Nasire Tousi University, Abfan Consultant Engineering, Iran

Email: mansour_fadaee@yahoo.com

Abstract

During the construction and operation of an embankment dam, various parameters, such as total stress, settlement, and most importantly pore pressure in the core affect the dam stability. To study these parameters, numerical modeling of dam behavior in drained or undrained loading and unloading is essential. In this study, the result of instruments in the construction and operation of the Kinevars dam, which include the actual values of stress and settlement is compared with the values obtained from the analysis of stress-settlement achieved from numerical modeling. According to the results, it was found that Geostudio software and Duncan nonlinear elastic model are suitable for analyzing the behavior of an embankment dam. Additionally, our results revealed that the use of simplified common methods for stress-settlement-leakage modeling in dams is reliable. Also, in the construction filling time, the results of numerical modeling and instrumentation for the parameters of pore water pressure and total stress in core are close. Considering the results of this study, it was concluded that the behavior of an embankment dam during construction and operation with acceptable accuracy is predictable by using Geostudio software.

Keywords: Long-Term Behavior, Embankment Dam, Numerical Modeling, Instrumentation.

1. INTRODUCTION

During the construction and operation of an embankment dam, various parameters, such as total stress, pore pressure and settlement affect the stability of dam. The most important parameters among these is the pore pressure in the core during construction and operation. To study of these parameters, numerical modeling of dam behavior in drained or undrained loading and unloading using is essential. In this study, the result of instruments in the construction and operation of the Kinevars dam, which include the actual values of stress and settlement is compared with the values obtained from the analysis of stress-settlement that obtained from numerical modeling.

Kinevars dam is located in Zanjan province, about 14 km southwest of Abhar city. This dam is built on Abhar-rud River. Supplying drinking water demand of Abhar city and Khorramdarrah city is an important objective of this dam [1]. In the following figure, Kinevars dam and its structure are shown.

The dam specification is presented as following [1]:

- Dam Type: earth-rock fill dam with Vertical Clay Core
- Maximum dam height from the bottom: 45 meters
- Crest length: 374 meters
- Crest width: 8 meters
- The total volume of the reservoir in the normal elevation: 16 million cubic meters
- Type overflow: free overflow ogee
- Type water tightening system: two parallel cement slurry wall with grout curtain

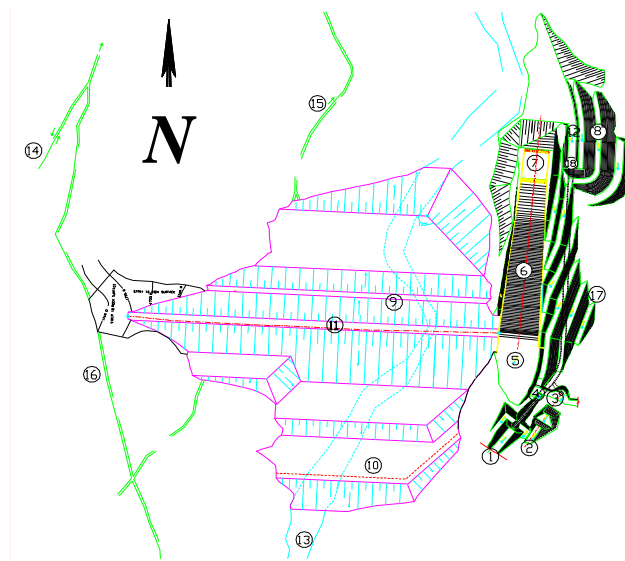


Figure 1. Kinevars dam and its structure

In order to investigate the behavior of the dam, the instrumentation are designed as described in Table 1 for 5 sections in the dam [2].

Table 1- Instrument list of Kinevars dam

Instrument	Number of Installed
stand pipe Piezometer	21
vibrating wire Piezometer	43
Total pressure cell	8
Observing well	6
leakage Measurement device	1
Reservoir water level meter	1
Inclinometer-settlement	9
Benchmark	27
Total	116

In figure 2 and figure 3, instrument in sections 8 and 11 are shown [2].

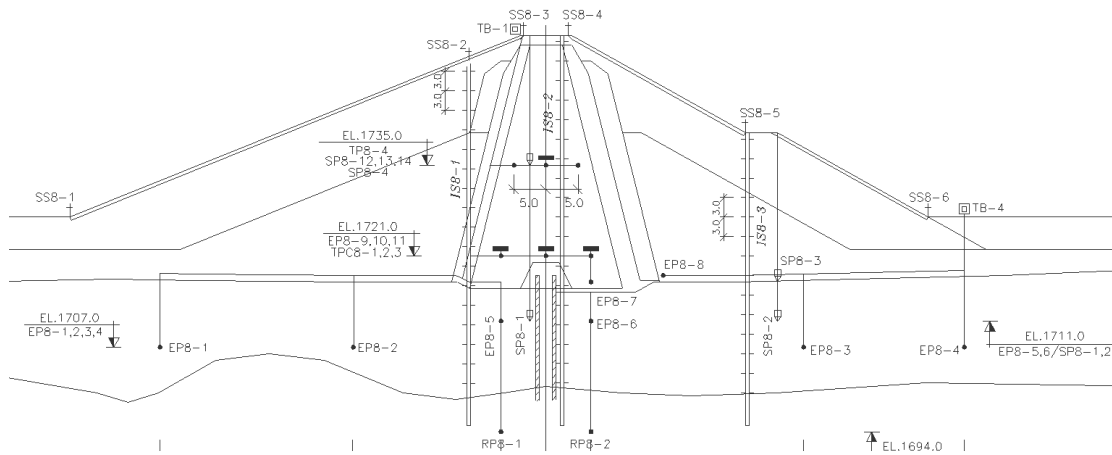


Figure 2. instrument in Section 8

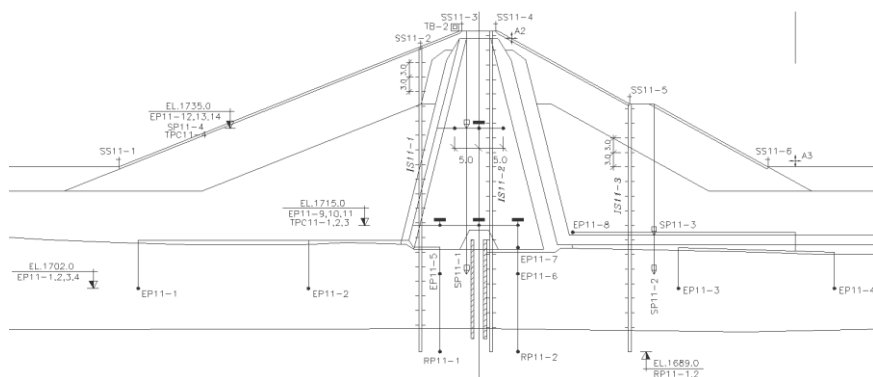


Figure 3. instrument in section 11

2. NUMERICAL MODELING

In this paper, for numerical modelling, boundary condition and loading for construction and impounding were used based on the actual data of construction and impounding.

The results of numerical modeling was compared with the results of instrumentation for core. The studied parameters are:

- Pore water pressure
- Total pressure
- Settlement

In Figure 4, 5 and 6 the geometry for sections 11, the modelled mesh with boundary conditions for stress-strain finite element analysis and finite element mesh with boundary conditions for seepage analysis are shown, respectively.

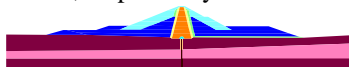


Figure 4. Geometric model for section 11



Figure 5. Finite element mesh and boundary conditions for stress-strain analysis

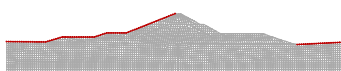


Figure 6. Finite element mesh and boundary conditions for seepage analysis

In Table 2, the parameters used in the analysis is presented. These parameters are the result of tests conducted on materials and designed Dam reports.

Table 2- The parameters used in the analysis

Ky/Kx	Kx (cm/s)	C' (Kpa)	ϕ' (degree)	ν	Rf	n	K	E (Mpa)	γ (KN/m3)	Material
0.1	4.0E-08	17	29	0.4	0.75	0.4	130	-	20.5	Core
1	1.0E-02	5	36	0.3	0.70	0.4	200	-	19	Filter
1	1.0E+01	5	38	0.3	0.70	0.4	200	-	19	Drain
1	1.0E-03	5	40	0.3	0.62	0.5	350	-	21	Alluvial Shell
1	1.0E-03	5	44	0.3	0.62	0.5	500	-	22	Rockfill Sell
1	1.0E-03	-	-	0.3	-	-	-	300	22	Alluvial Foundation
1	1.0E-05	-	-	0.3	-	-	-	1000	24	Rock foundation
1	1.0E-06	-	-	0.3	-	-	-	1200	23	Cutoff Wall

Because of the nonlinear nature of the soil materials, it is recommended to use the nonlinear behavior for material. In this analysis, the hyperbolic models (Duncan And Chang 1970) [3] is used. The foundation and Cutoff wall is modeled as a linear elastic (because of these materials are linear in low stresses)[4]. The process of building the dam structure is modeled in eight steps close to reality, as shown in Figure 7. The actual process of dam embankment and loading process are shown in the model. After the completion of each step and zeroing up the created shapes (due to their compensation during the construction stages), the next stage is modeled. Then, the reservoir is impounded according to the actual conditions after the completion of the simulated dam construction, which is presented in Figure 8 of the impounding process in reality and in the modeling.

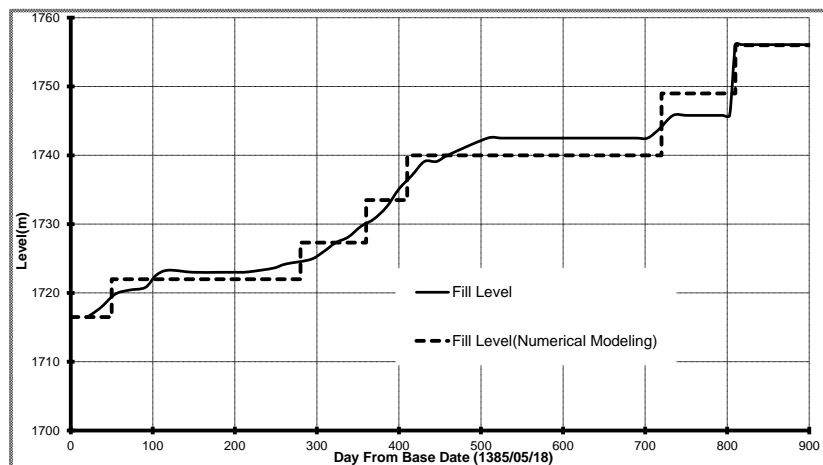


Figure 7. Compare the Real embankment filling with the model

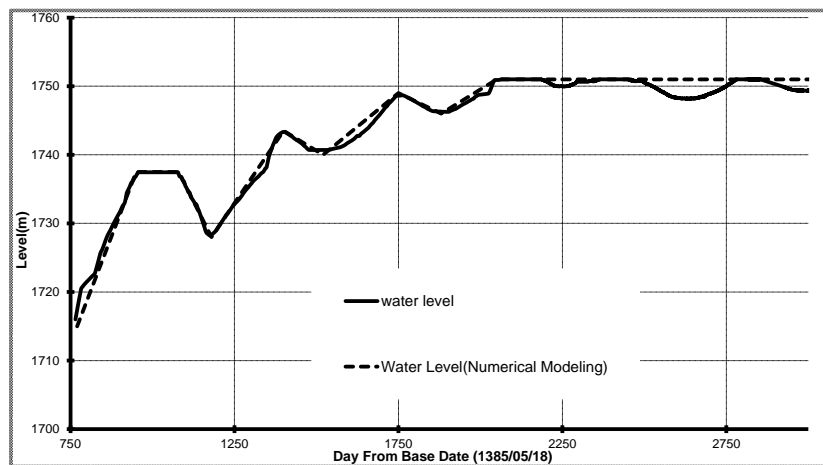


Figure 8. Compare actual impounding trend with model

3. PORE WATER PRESSURE IN CORE

The results of modeling and instrumentation for the pore water pressure in the core are shown in Figures 9 and 10.

As it is known during the construction period, the general trend of the results of the instrumentation and the modeling is coincide, but because of the limitation in the number of loading steps in the modeling, the water pressure fluctuations is a function of the loading, but in reality, this loading is gradual and the pressure of generation and dissipation is gradual either.

But the remarkable thing is that overall, after the end of each stage, the end result is very close.

After impounding, the results are very close to each other and the results are coincide. Thus, according to the results, the water surface line is forming in the core.

The difference in results of the two instruments (EP 11-12 and EP 11-13) is due to the excess pore water pressure that is not yet dissipated and after impounding (and always) shows a pressure above the reservoir water level.

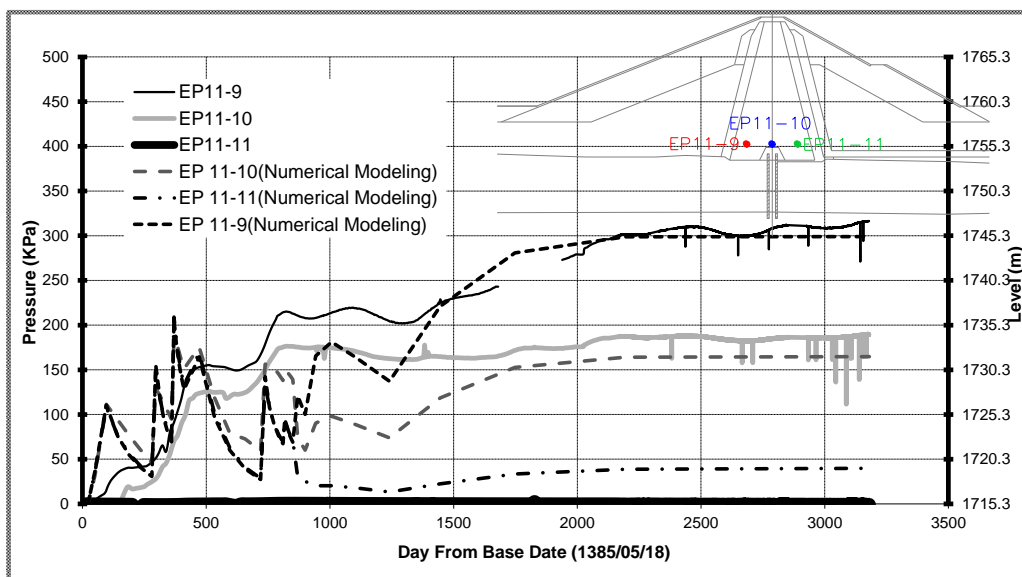


Figure 9. Comparison of pore water pressure in the core at the level 1715

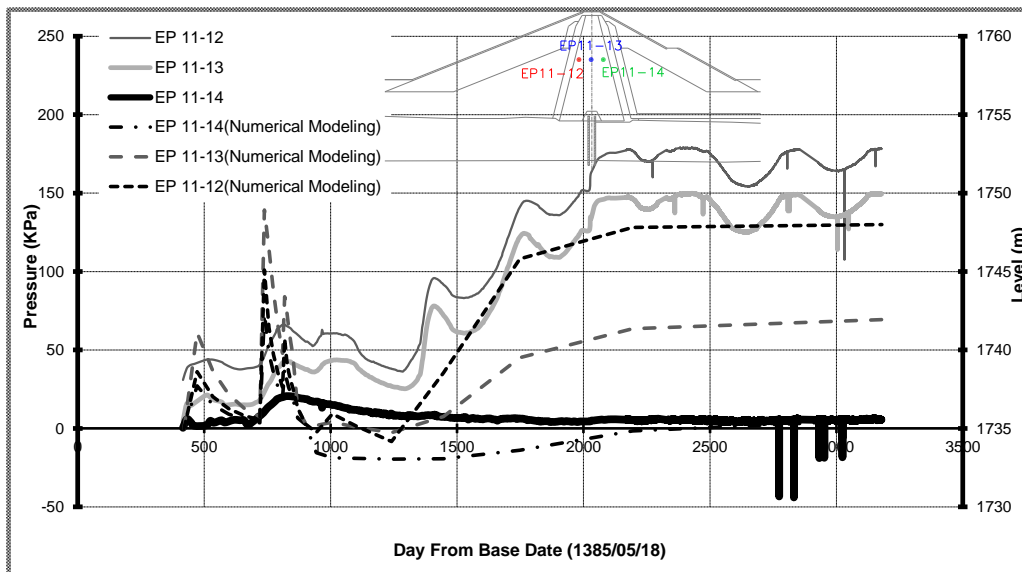


Figure 10. Comparison of pore water pressure in the core at the level 1730

4. TOTAL STRESS IN THE CORE

The results of modeling and instrumentation for total stress changes in the core are shown in Figures 11 and 12.

As it is known during the construction, the results of the instrument and the modeling are completely overlapping, but there are very few fluctuations due to the limited number of loading steps in the modeling.

After impounding, the results are very close together and the results are coincide.

The difference in results of TPC 11-4, as mentioned earlier, is due to the localized arching at the instrument location and the results of the modeling seem to be more realistic.

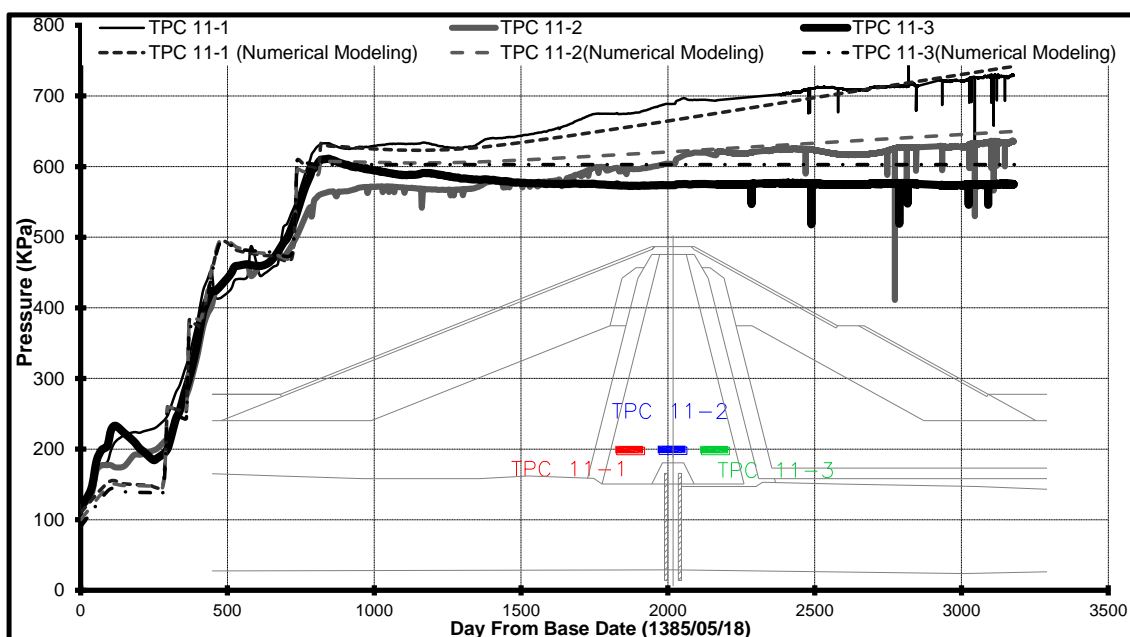


Figure 11. Compare the results of the total stress at the level of 1715

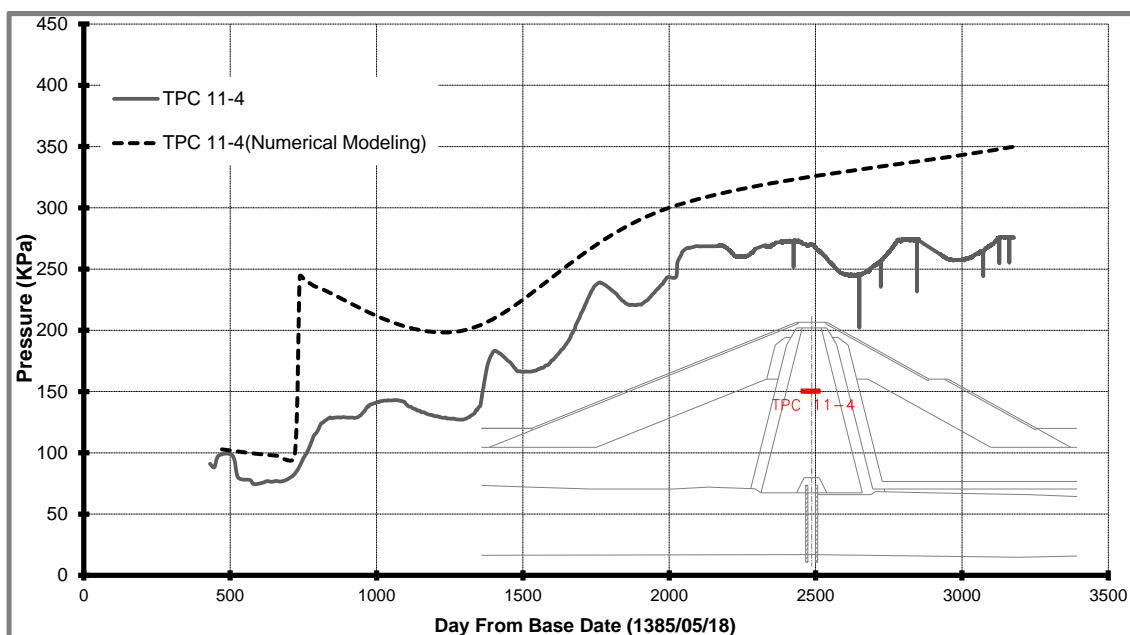


Figure 12. Compare the results of the total stress at the level of 1735

5. SETTLEMENT AT THE CORE

The results of modeling and instrumentation for settlement changes in the core of dam are presented in figures 14 and 15.

As it is known during the construction and impounding process, the general trend of the instrument results and numerical modeling is coincide.

The results show that the assumed parameters are very close to reality.

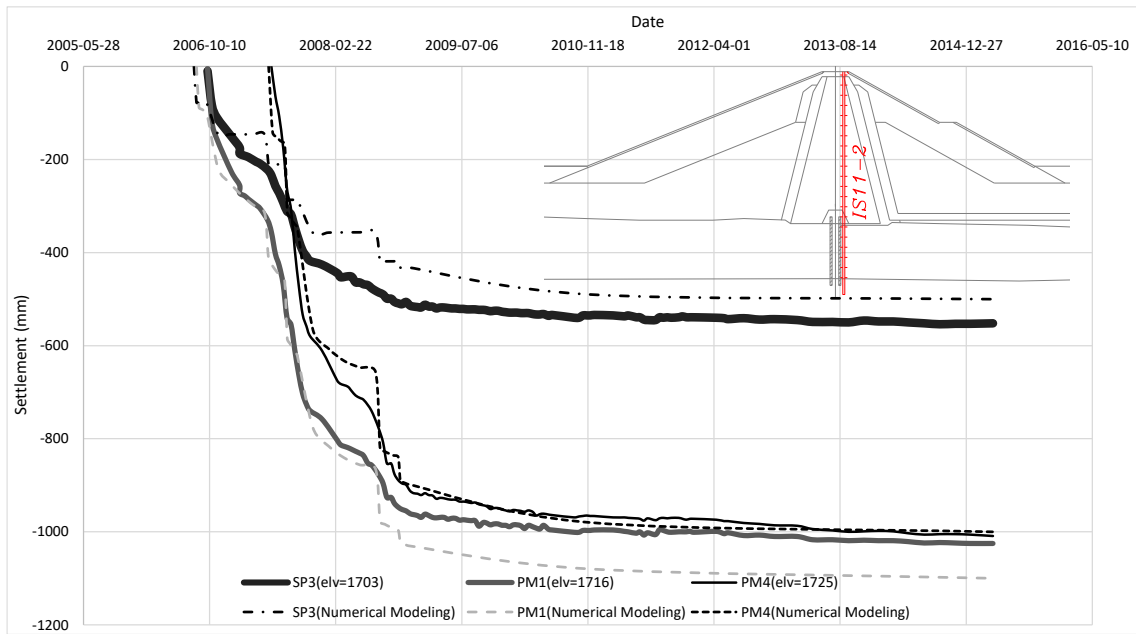


Figure 13. Compare the results of the settlement in core at levels 1703, 1716 and 1725

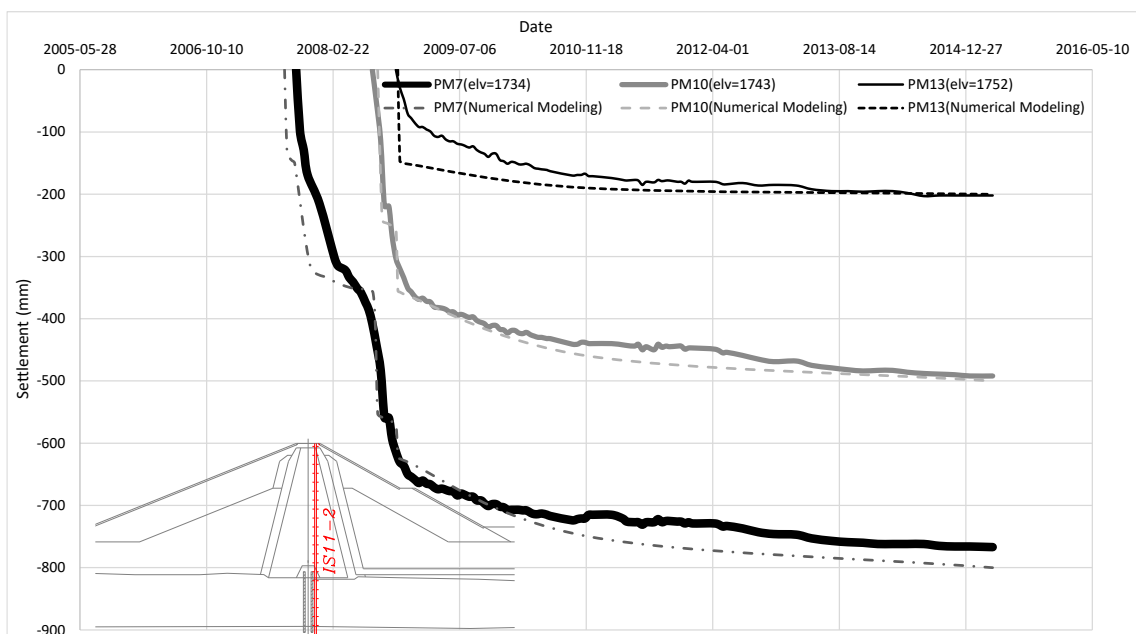


Figure 14. Comparison of the results of settlement in core at the levels of 1734, 1743, and 1752

6. CONCLUSIONS

The results of the numerical modeling presented in this paper are summarized as follows:

- Common methods for embankment dams modeling are reliable.
- Duncan's nonlinear elastoplastic behavioral model is suited for modeling the behavior of the core of the earth's dam.
 - During the construction period, the modeling process results and the model for the pore water pressure parameter and total stress are completely overlapping, but there are very few fluctuations due to the limited number of loading steps in the modeling.
 - After impounding, the results of pore water pressure and total stress are very close to each other and the results are coincide.
 - In examining the results of the total stress calculated from the instrumentation results, due to the localized arching on the instrument location, these results should be carefully considered.
 - As the results of the instrument showed, during the construction and impounding period, the general trend of the settlement in instrument and numerical modeling is coincide.
 - The results obtained from this paper indicate that the assumed parameters are very close to reality.

7. ACKNOWLEDGMENT

We would like to give special thanks to Iran water resources management company, Tehran and Zanjan Regional Water Authorities (as the client of this projects) for their contributions.

8. REFERENCES

1. Abfan Co. (2005). “*Kinevars storage dam, dam body report*” (in Persian).
2. Abfan Co. (2015). “*Kinevars storage dam, instruments report*” (in Persian).
3. Duncan, J. M., & Chang, C. Y. (1970). Nonlinear analysis of stress and strain in soils. *Journal of Soil Mechanics & Foundations Div.*
4. Rashidi, M., & Haeri, S. M. (2017). Evaluation of behaviors of earth and rockfill dams during construction and initial impounding using instrumentation data and numerical modeling. *Journal of Rock Mechanics and Geotechnical Engineering*, 9(4), 709-725.
5. Wen, L., Chai, J., Xu, Z., Qin, Y., & Li, Y. (2017). Monitoring and numerical analysis of behavior of Miaojiaba concrete-face rockfill dam built on river gravel foundation in China. *Computers and Geotechnics*, 85, 230-248.

Determination of Optimum Cross Section of Earth Dams by Using Artificial Intelligence

Mohammad Davoodi¹, Mohammad Kazem Jafari², Amin Rezaeeian³

1- Assistant Prof, IIEES, Tehran, Iran

2- Prof, IIEES, Tehran, Iran

3- Department of Civil Engineering, Science and Research Branch, Islamic Azad University, Tehran, Iran

Email: m-davood@iiees.ac.ir

Abstract

Earth Dams are one of the most important and expensive civil engineering structures. Cost of construction of these structures directly depends on the needed volume of embankments which in turn depends on their cross section area. Reduction in the cross section area of earth dam causes decreasing in the embankment volume and leads to a significant reduction in the construction cost of these structures. Obtaining optimum cross section for earth dams including traditional design method utilizations in addition to stability and construction aspects, is too time-consuming and almost impossible. In this paper, an Artificial Neural Network and ant colony optimization algorithm have been used to solve this complicated problem which is known as one of the most important problems in geotechnical engineering.

Keywords: Earth dams, Slope stability, Artificial intelligence, Artificial neural network, Ant colony optimization algorithm.

1. INTRODUCTION

The purpose of this paper is finding the cross section of earth dam which attains satisfying slope stability conditions and accounting for construction aspects and furthermore reaches a minimum volume of earth works. This purpose is gained by creating some berms with various widths and heights in the body of an earth dam, as shown in Figure. 1.

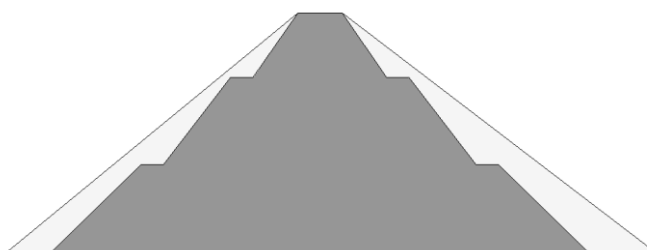


Figure.1. Employing berms in order to reduce fill volume in earth dams

In traditional methods of designing earth dams, obtaining the optimum cross section with suitable configuration of berms is rigorous and time consuming. Optimization methods are required for solving this problem and finding the optimum section for earth dams. Since there are many variables of the problem, employing the classic optimization methods is difficult. Therefore, it is advantageous to use heuristic methods for solving such problems. Although finding the global optimum solution in heuristic methods is not granted, but with optimum solution. These methods are being used for solving the combinational optimization problems, especially in engineering optimization problems. Despite their success in various fields of engineering, however, these methods have not been applied significantly in geotechnical problems. In this paper, the ant colony optimization algorithm tool was used for finding the optimum section for an earth dam. The ant colony algorithm (ACO) was originally inspired by the behavior of real ants. Dorigo [1] first developed ant ACO and successfully applied it to the traveling salesman problem (TSP). Several variations of the original ACA including ant system (AS) [1], elitist ant system (ASelite) [1], max-min ant system (MMAS) [2-4] and ranked ant system (ASrank) [5, 6] have been introduced recently. ACO has enjoyed important success in various fields of engineering. Despite its success, however, the method has found little success in geotechnical engineering

applications. As a frontier in application of modern metaheuristic optimization algorithms to slope stability analysis, Cheng et al. [7] have evaluated the performance of six heuristic global optimization methods in the location of critical slip surface in slope stability analysis, including ACO.

The problem under consideration is one conditional optimization problem and its object is minimization; namely, finding a section with minimum cross section area. The program includes the following steps:

First of all, a connected graph is created by problem variables, as shown in Figure. 2. This graph provides a searching space for artificial ants for finding the shorter path, and it is combined by some decision points which are variables of the problem. Each decision point is constituted by decision components created from discrete variables. At second step, artificial ants are directed to this graph. after preparing the connected graph. They find solutions by randomized walk across the connected graph. They choose some paths on this graph which each of them presents a cross section of an earth dam. Once all the ants survey their path and touch to the destination node, they will go back to the initial point after obtaining a solution. At third step, pheromone trail is deposited on the nodes of every path. Pouring pheromone trail on every path depends on quality of the path (cross section area of earth dam section). Paths with higher quality (or with lower cross section area) are smeared with more pheromone trial. Therefore, these paths have more chance for selecting in next iterations. Also, paths that cannot satisfy conditions of the problem are called impossible solutions. These paths are then forgotten by applying heavy penalties to them through attributing high safety factors.

At second iteration, once again artificial ants are directed to the graph and they build solutions by performing randomized walk on the graph. Thus, new paths are chosen in this graph, and paths with higher quality at first iteration have more chance of being chosen in the second iteration. This process was continued until more ants tended to more optimum path (shorter path). Finally, the shorter path is found. In this problem the shorter path is the optimum cross section for certain earth dam.

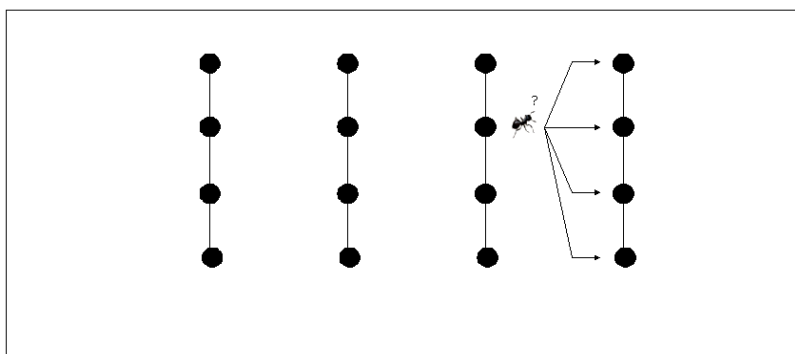


Figure.2. Graphical representation of the optimization problem in ACO

2. CHARACTERISTIC OF DETERMINING OPTIMUM CROSS SECTION MODEL

The optimization problem of finding optimum cross section is represented by Eq.1:

$$C = \min A(x) \tag{1}$$

Where C is the objective function of the problem, $A(x)$ is the cross section area for a certain section of the earth dam, x parameter is a set of variables of this problem which are defined subsequently.

In determining optimum cross section problem, the objective function is the cross section area for certain section which should be minimized. It means that the objective is finding one cross section with minimum area and thereupon minimum volume of earth works for certain earth dam. The variables of determining optimum cross section problem consist of n , n' , b_{1i} , b_{2i} , h_{1i} , h_{2i} , I_{1i} and I_{2i} , where are defined in Figure.3. As shown in Figure.3, n and n' are the number of berms at upstream and downstream of earth dam. b_{1i} and b_{2i} are the width of berm i -th at upstream and downstream of the earth dam. h_{1i} and h_{2i} are the height of berm i -th at upstream and downstream of the earth dam from foundation level. I_{1i} and I_{2i} are the slope of zone i -th at upstream and downstream of the earth dam. Also at Figure.3, B , H and H_f are constant parameters of cross section of the earth dam which are respectively, the width of crest of earth dam, the height of the dam and the foundation depth.

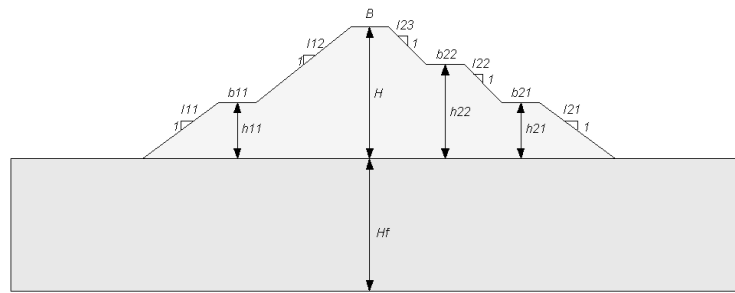


Figure.3. optimization of cross section of an earth dam

The mentioned variables are represented in a graph, as shown in Figure.4, which involves finding the optimum values of cross section with n berm at upstream and n' berm at downstream variables by passing the artificial ants on this graph and deposit pheromone trail on the nodes of every path.

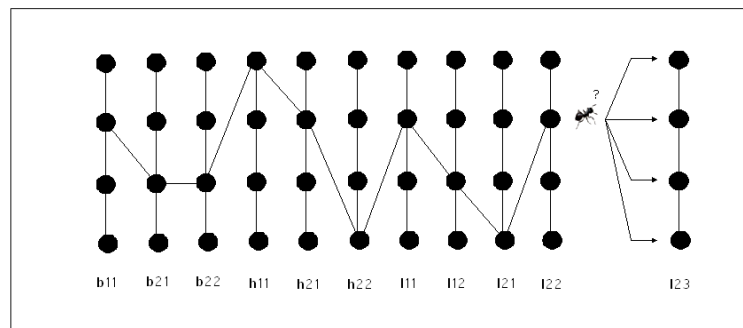


Figure.4. Graph of the optimization problem involving minimization of the cross section of an earth dam.

There are two group of independent constraints in this problem. First group includes constraints which define the boundary of ants search space. These constraints are provided the search space which includes the possible solutions (possible paths). It should be avoided of zones which include the impossible solutions to determine the search space. In the problem, $b1_i$ and $b2_i$ were chosen among 4 meter up to 10 meter randomly. Minimum value of $b1_i$ and $b2_i$ was determined due to practical conditions and the maximum value was determined due to maximum value of normal berms width. Also the values of $h1_i$ and $h2_i$ are chosen among 10 meter and H minus 10 meter randomly. $I1_i$ and $I2_i$ are randomly selected through a reasonable range which is between response angle of soil material and 5:1 slope.

Second group of constraints includes conditional constraints. They separate possible solution from impossible solutions that are not satisfied. A method for applying impossibility of these solutions and inattention at these decisions is fining these paths (solutions) in order to offend of conditional constraints. Thus, instead of pheromone trial depositing as many as the value of their objective function on these paths, pheromone trail depositing is avoided by applying a penalty. This problem subjected the conditional constraints which are presented at Eq.2 to Eq.4.

$$h1_{i+1} - h1_i \geq a \quad (2)$$

$$h2_{i+1} - h2_i \geq a \quad (3)$$

$$Fs \geq Fs_{allow} \quad (4)$$

Eq.2 and Eq.3 suggest that the height of each berm must be more than height of previous berm. Also, height difference of each berm with the previous berm must be more than, or equal to a . Moreover, minimum height of first berm (lower berm) must be greater than or equal the foundation level a . Unless, this section is forgotten with applying penalty, because it can not satisfy geometrical conditions. Eq.4 also indicates that each

section of earth dam must satisfy slope stability conditions for all load cases of earth dam. These load cases, include the end of construction step, steady state seepage of mid level step, steady state seepage of maximum level step and rapid drawdown of normal level step. For all the load cases, minimum factor of safety of certain cross section must be more than allowable factor of safety for this load case. If the certain section factor of safety, even at one of load cases, was below the allowable factor of safety, it would be forgotten by applying penalty. The penalty for sections which are offensive of the conditional constraints is applying value of cross section area equal a large number as $10^{10} m^2$. This large value led to less than zero pouring pheromone deposit trail on unsuitable paths. So, impossible paths (solutions) were forgotten, and they could not be effective in attracting artificial ants' selection at future iterations. Figure.5 show flowchart for the ant colony algorithm.

3. REVIEW OF ANT COLONY OPTIMIZATION ALGORITHMS

The basic idea of ant colony optimization (ACO), inspired by the behavior of real ants, is to use artificial ants to search for *good solutions* of a combinatorial optimization problem. ACO is therefore a metaheuristic in the sense that the absolute optimum solution is not found, but *good solutions* practically close enough to the optimum are found. Real ants coordinate their activities through stigmergy, which is a form of indirect communication [8]. Specifically, in the search for food, ants deposit chemicals along the path they travel which is recognized by other ants, and will increase the probability of the path being travelled by other ants of the colony. The chemical is called *Pheromone* [8].

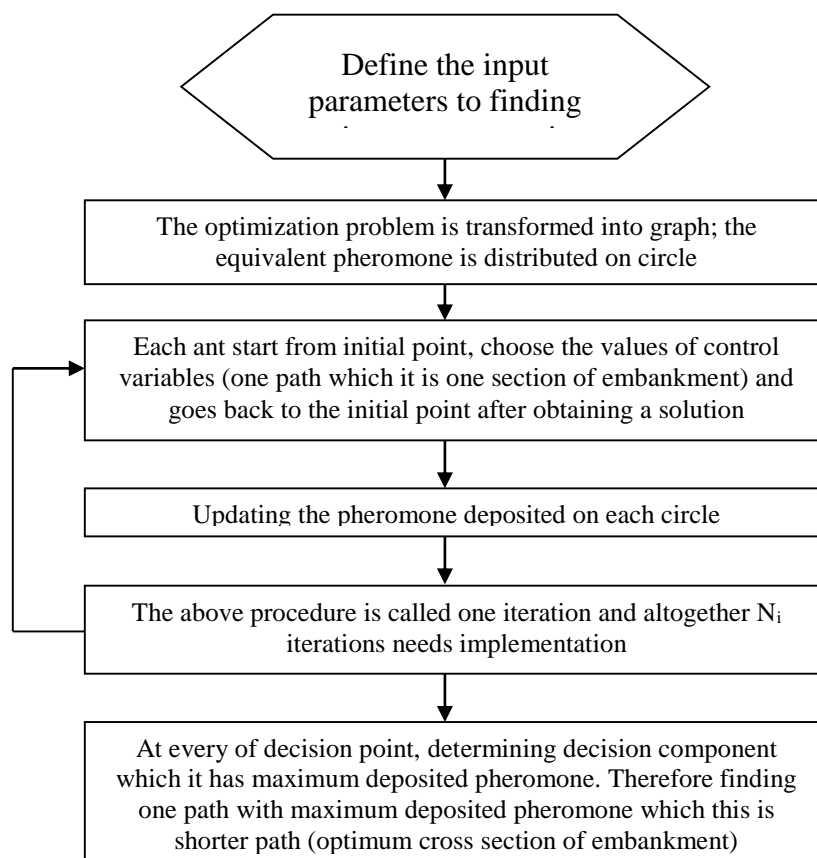


Figure.5. Flowchart of ant colony optimization algorithm

The fundamental components of ACO can be briefly categorized as:

I- Construct a graph of the problem: In the case of finding the optimum cross section, this step involves dividing the two dimensions in the x and y direction into m and n discrete subdivisions, respectively. The resulting graph will have m columns, and each column has n nodes.

II- Define the objective function and the restraints: When finding the optimum cross section, the objective function is the cross section area, i.e. the function to be optimized. Also, some restraints are

placed on the variables in this stage. The number of ants and the number of attempts for solving the problem are also specified in this step.

III- Move artificial ants on the graph in order to construct admissible solutions to the problem: In this step, artificial ants placed on the initial point start moving on the grid from left to right, randomly selecting a node on each consecutive column in order to build incremental solutions to the problem under consideration. In finding the optimum cross section, ants move from the start point of the graph towards the end point, following the rule described in section 2 above. Every time an ant reaches the end point of the graph, a cross section is formed. The more ants placed on the graph, the more cross sections produced, and the higher the chances are that the best solution is approached. In selecting the nodes of a column to move to, the probability of an ant selecting the j -th node of the i -th column is described by the following relation:

$$P_{i,j} = \frac{\tau_{i,j}}{\sum \tau_{i,j}} \quad (5)$$

In Eq.5, $\tau_{i,j}$ is the sum of the pheromone placed on node (i,j) from previous attempts. In the first attempt, all nodes have an equal pheromone of τ_0 , and therefore in the first attempt, all nodes have an equal chance of being selected by the ants.

IV- Evaluate the solutions obtained by each ant in the first attempt: Once all the ants complete the first attempt, the objective function f is calculated for each ant. The objective function here, as mentioned previously, is the cross section area. Next, pheromone is deposited along the trail which each ant has chosen in forming an incremental solution. The amount of pheromone deposited on each node is reversely related to the objective function of the path being considered, i.e., $\tau = \frac{1}{f}$. As the rule states, the lower the objective function (cross section area) of a path (cross section), the more pheromone will be deposited on the components of the path.

V- Update the pheromone value of each node in the graph: After calculating the pheromone value of every node for the present attempt, the updated pheromone value of each node is obtained through the following relation:

$$\tau_{i,j}(t+1) = (1-\rho)\tau_{i,j}(t) + \Delta\tau_{i,j}(t) \quad (6)$$

In Eq.6, $\Delta\tau_{i,j}$ is the difference between the deposited pheromone in the present attempt and the previous attempt, $\tau_{i,j}^*$ is the updated pheromone value, and ρ is the evaporation index which takes a value between zero and one. Pheromone evaporation is a useful form of forgetting, preventing the algorithm from rapidly converging towards local optima. The term $(1-\rho)$ thus determines how much of the pheromone accumulated from previous attempts is evaporated.

VI- Repeat steps III through IV in the next attempts in order to reach the optimum solution: in the next attempts, the decision making process of the artificial ants is no longer completely random; as stated by Eq. 5, nodes with more pheromone have a higher chance of being selected by the ants. After each attempt, pheromone values are updated and some pheromone is evaporated. The combined action of pheromone deposit and evaporation enables a constant exploration of the search space towards a global optimum in ACO.

The above mentioned steps form the fundamental framework of the ACO algorithm. Various improvements have been introduced to the original algorithm in recent years, aiming to make the search algorithm both more effective and more efficient. Accordingly, in addition to the ants system (AS) algorithm discussed above, three other algorithms have been more successful, and have been used in the present study: ranked ant system (AS_{rank}), elite ant system (AS_{elite}), maximum-minimum ant system (MMAS). The principle features of these algorithms are briefly discussed herein.

Ants System (AS): This is the simplest form of ACO first introduced by Dorigo et al. [1]. In AS, artificial ants choose their path according to the following probabilistic relation:

$$\rho_{i,j}(k,t) = \frac{[\tau_{i,j}(k,t)]^\alpha [\eta_{i,j}(k,t)]^\beta}{\sum_{j=1}^j [\tau_{i,j}(k,t)]^\alpha [\eta_{i,j}(k,t)]^\beta} \quad (7)$$

in which $\rho_{i,j}(k,t)$ is the probability of selecting i -th node of the j -th column, by the k -th ant in the t -th attempt. $\eta_{i,j}(k,t)$ in Eq.7 represents the heuristic information and the determination of its value is problem-specific. In some problems, the value of $\eta_{i,j}(k,t)$ is hard to determine, and is therefore omitted from equation. α and β in Eq.7 are constants which determine the role of pheromone and heuristic information in the artificial ants' decision making process. If $\alpha \gg \beta$, the role of pheromone is emphasized and heuristic information has less effect on the decision of the ants. Adversely, $\beta \gg \alpha$ means that the ants decide which node to move to based on the heuristic information, paying less attention to the pheromone deposited from previous attempts.

Another important characteristic of ant colony algorithms is the way that pheromone update is defined in these algorithms. AS defines pheromone using Eq.6. $\Delta\tau_{i,j}$ is determined as:

$$\Delta\tau_{i,j}(t) = \sum_{k=1}^m \frac{Q}{f(S_k(t))} I_{S_k(t)} \{(i,j)\} \quad (8)$$

in which m is the number of artificial ants, or the number of solutions produced; Q is a constant named the pheromone return index and its value depends on the amount of pheromone deposited; $S_k(t)$ represents all the nodes which the k -th ant has chosen on the t -th attempt; $I_{S_k(t)} \{(i,j)\}$ is a coefficient which is either zero or one, depending respectively on whether the k -th ant has chosen the node (i,j) or not. In other words, $I_{S_k(t)}$ ensures that only the nodes on which the k -th ant has moved to will be considered in depositing pheromone. It can be deduced from Eq.8 that in AS, solutions with a lower objective function will have more pheromone deposited, and vice versa.

Elitist Ants System (AS_{elite}): In this algorithm, more attention is focused on the elite ant of the colony. The elite ant is the one which has produced the best answer in all previous attempts. Specifically, in AS_{elite} extra pheromone is deposited on the path which the elite ant has produced. The ants decide which node to move to using Eq.7. The pheromone update rule in AS_{elite} is

$$\tau_{i,j}(t+1) = (1-\rho)\tau_{i,j}(t) + \Delta\tau_{i,j}(t) + \sigma\Delta\tau_{i,j}^{gb}(t) \quad (9)$$

Where $\sigma\Delta\tau_{i,j}^{gb}(t)$ is the extra pheromone deposited by the elite ant, and σ is the weight of the extra pheromone. AS_{elite} is an attempt to balance between exploration and exploitation in the algorithm.

Ranked Ants System (AS_{rank}): The ranked ants system was first introduced by Bullnheimer et al [5, 6] as an extension of the elitist ants system. In this algorithm, unlike the AS_{elite} in which all ants participate in the pheromone update process, only $\sigma-1$ elite ants which have created better solutions are chosen to update the pheromone of the paths they have chosen. In AS_{rank}, following each attempt, the ants are lined up according to the solutions they have obtained, and pheromone update values are assigned to each ant, the most pheromone being assigned to the best solution and decreasing thereafter to the last ant in the line. Thus, the pheromone update rule in AS_{rank} can be stated as

$$\Delta\tau_{i,j}^{rank}(t) = \sum_{k=1}^{\sigma-1} (\sigma-k) \frac{Q}{f(S_k(t))} I_{S_k(t)} \{(i,j)\} \quad (10)$$

Minimum-Maximum Ants System (MMAS): Stutzle and Hoos [2-4] first reported the MMAS algorithm in a successful attempt to improve the efficiency of AS. The general structure of MMAS is similar to AS. However, only the path with the best solution in each attempt is chosen to deposit pheromone on its trail. In this way, the solution rapidly converges to the optimum. The danger always exists that the ants quickly move towards the first optimum solution achieved, before having the chance to explore other possibly better solutions in the search space. In order to prevent this from occurring, a restriction is placed on the minimum and maximum allowable net pheromone deposit on the trails, i.e., the deposited pheromone value is limited to $[\tau_{min}, \tau_{max}]$. Following each pheromone deposition step, all pheromone values are controlled to fit within the mentioned limit, and any node for which the pheromone value exceeds the limits is adjusted to the allowable limit. This is a way to promote the ants

to explore new solutions in the search space. The maximum and minimum allowable pheromone values of the t -th attempt is calculated as

$$\left\{ \begin{aligned} \tau_{\max}(t) &= \frac{1}{1 - \rho} \frac{Q}{f(s^{gb}(t))} & (11) \\ \tau_{\min}(t) &= \frac{\tau_{\max}(t)(1 - \sqrt[n]{P_{best}})}{(NO_{avg} - 1)\sqrt[n]{P_{best}}} & (12) \end{aligned} \right.$$

where $f(s^{gb}(t))$ is the value of the objective function up to the t -th attempt, P_{best} is the probability of the ants choosing the best solution once again, NO_{avg} is the average of the number of decision choices in the decision points. It is noteworthy to mention that the initial pheromone value associated with the nodes, τ_0 is $\tau_{\max}(t)$.

The above discussed four algorithms were employed in the present study in searching for the critical failure surface in slope stability analysis. The implementation procedure is described in the next section.

4. IMPLEMENTATION OF ACO IN OPTIMIZATION OF EARTH DAM AND NUMERICAL EXAMPLES

The basic components of ACO applied to the problem of optimization the earth dam is shown as a flowchart in Figure.5. The aim of the present study was to assess the ability of four aforementioned ACOs in finding the optimum cross section of earth dam.

The first example represents the homogeneous earth dams composed of coarse soils with different heights. The soil parameters are: unit weight 19.0 kN/m³, cohesion 15.0 kpa and effective friction angle 20°. The results obtained by this example show the effect of berms on earth dams which decrease the volume of the earth dams. In this example it was assumed the earth dam is founded on bedrock. Figure.6 shows the layout of the embankments. The upstream shape of embankments is similar to downstream. In the example, different height was considered for earth dams and the effect of different number of berms was considered for each earth dams. Thus not only effect of berms at decreasing in embankment volume was considered, but also the optimum number of berms for each specific dam height was determined. Furthermore, four different ant colony algorithms namely the ant system, elite ant system, ranked ant system and maximum-minimum ants system were employed for studying the efficiency of ant colony optimization algorithms in the finding optimum cross section problem. For different earth dams, the cross section areas obtained by each algorithm are tabulated in Table 1 to 7. In comparison to the cases which there are no berms, when there are berms, the percentage of volume reduction for different height earth dams is presented in Table 8.

According to table 8, for homogeneous earth dam, if height of earth dam is less than 40m, using of berms with suitable number, level and width in body of earth dam will reduce embankment volume more than 10 percent in contrast to an earth dam section without berms. Moreover, if height of earth dam exceeds 40m, in case of increasing in height of earth dam, the effect of berms will reduce. Also, according to Tables 1 to 7, there is an optimum number of berms that can be considered in maximum reduction of fill volume in the earth dam. This number is three berms for 80m height earth dam and is one berm for 40m, 30m, 20m, 10m and 5m earth dams.

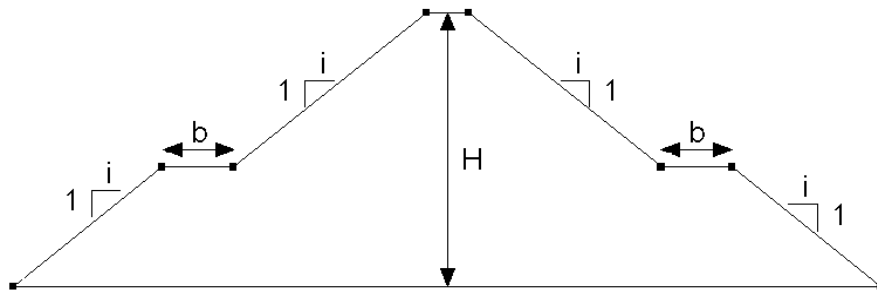


Figure.6. configuration of variables controlling the section fill volume.

Table 1. Results of ACO calculations for minimum fill volume for 160m earth dam

	<i>six</i>	<i>five</i>	<i>four</i>	<i>three</i>	<i>Fill volume</i> <i>two</i>	<i>one</i>	<i>zero</i>	<i>Number of</i> <i>berms</i>
	68340	52745	49278	43592	45339	43499	63840	<i>Algorithm</i> AS
	43456	43444	43118	44236	42602	43971	43360	AS _{elite}
	42135	43523	43227	42316	42317	44336	43360	AS _{rank}
	42638	42877	42616	43071	42834	42306	43360	MMAS

Table 2. Results of ACO calculations for minimum fill volume for 80m earth dam

	<i>Four</i>	<i>three</i>	<i>two</i>	<i>one</i>	<i>zero</i>	<i>Number of</i> <i>berms</i>
	12314	12163	11135	11596	12080	<i>Algorithm</i> AS
	11007	11112	10960	11580	11440	AS _{elite}
	11363	10842	11316	11121	11440	AS _{rank}
	11731	11426	11177	11213	11440	MMAS

Table 3. Results of ACO calculations for minimum fill volume for 40m earth dam

	<i>two</i>	<i>one</i>	<i>zero</i>	<i>Number of</i> <i>berms</i>
	2737	2739	2960	<i>Algorithm</i> AS
	2775	2593	2800	AS _{elite}
	2681	2723	2800	AS _{rank}
	2636	2507	2800	MMAS

Table 4. Results of ACO calculations for minimum fill volume for 30m earth dam

	<i>two</i>	<i>one</i>	<i>zero</i>	<i>Number of berms</i> <i>Algorithm</i>
	1437	1501	1740	AS
	1488	1382	1560	AS _{elite}
	1492	1350	1560	AS _{rank}
	1550	1390	1560	MMAS

Table 5. Results of ACO calculations for minimum fill volume for 20m earth dam

	<i>two</i>	<i>one</i>	<i>zero</i>	<i>Number of berms</i> <i>Algorithm</i>
	697	656	760	AS
	686	672	760	AS _{elite}
	787	728	760	AS _{rank}
	740	710	760	MMAS

Table 6. Results of ACO calculations for minimum fill volume for 10m earth dam

<i>two</i>	<i>one</i>	<i>zero</i>	<i>Number of berms</i>
			<i>Algorithm</i>
243	170	200	AS
220	157	200	AS _{elite}
182	166	190	AS _{rank}
212	164	190	MMAS

Table 7. Results of ACO calculations for minimum fill volume for 5m earth dam

<i>two</i>	<i>one</i>	<i>zero</i>	<i>Number of berms</i>
			<i>Algorithm</i>
59	50.5	55	AS
52	51.5	55	AS _{elite}
54.25	47.5	55	AS _{rank}
54	50	55	MMAS

Table 8. Percentage of reduction of fill volume for various earth dam heights

<i>Reduction of embankment volume than without berm cross sections (%)</i>	<i>Height of earth dam (m)</i>
14	5
17	10
13.7	20
13.5	30
10.6	40
5	80
3	160

5. CONCLUSIONS

This paper dealt with the evaluation of the effectiveness and accuracy of ant colony optimization (ACO) algorithms in finding optimum cross section of earth dams. Four ant colony algorithms were studied, such as ants system (AS), elite ants system (AS_{elite}), ranked ants system (AS_{rank}) and maximum-minimum ants system (MMAS). In order to evaluate the performance of the four mentioned algorithms, two illustrative examples were considered. The following conclusions were drawn from the results of this study:

- (1) For homogeneous earth dams with height of 40m, on resistant foundation, suitable number could decrease embankment volume more of 10 percent in contrast of cross section which has not berm. But for earth dam than 40m, when the height increase then the rate of reduction of embankment volume with berms will decrease. In this case, using of berms at body of earth dams usually due to construction aspects.
- (2) In earth dams, for each height there are the optimum number of berms which if it uses further or lesser number of berms then it will increase embankment volume.
- (3) For determining optimum cross section of earth dams, MMAS, AS_{rank} and AS_{elite} are more efficiency than AS which is weakest and initial algorithm of ant colony optimization algorithms. Also in this

problem weak efficiency of AS algorithm has shown. It is due to low support of this algorithm from surveying optimum paths.

- (4) Comparing various height homogeneous earth dam shows whatever the berms located in lower levels of the body, more optimum cross sections will be created. The wider the bottom of the berms, the more effective decreasing volume will be at top levels.

6. REFERENCES

1. Dorigo M. Optimization, learning and natural algorithms (in Italian). PhD Thesis, Politecnica di Milano, Milan, Italy, 1992.
2. Stutzle T, Hoos HH. Improving the ant system: a detailed report on the MAX-MIN ant system. Technical report AIDA-96-12, Intellektik, FB Informatik, TU Darmstadt, Germany, 1996.
3. Stutzle T, Hoos HH. MAX-MIN ant system. *Future Generation Comput Sys* 2000; 16:889-914.
4. Stutzle T. Local search algorithms for combinatorial problems: analysis, improvements and new applications, Vol. 220 of DISKI, Sankt Augustin, Germany, Infix, 1999.
5. Bullenheimer B, Hartl RF, Strauss C. A new rank base version of the ant system – a computational study. Technical report, Institute of Management Science, University of Vienna, Austria, 1997.
6. Bullenheimer B, Hartl RF, Strauss C. A new rank-based version of the ant system: a combinatorial study. *Central European Journal for Operations Research and Economics* 1999; 7:25-38.
7. Cheng YM, Li L, Chi SC. Performance studies on six heuristic global optimization methods in the location of critical slip surface. *Comput Geotechnics* 2007; 34:462-84.
8. Dorigo M, Stutzle T. *Ant colony optimization*. MIT Press, 2004.

Numerical Investigation of Damage Types Through Concrete Dam by Multi-Laminate Model upon Instrumentation Data

Seyaed Amirodin Sadrnejad

**Department of Civil Engineering, K. N. Toosi University of Technology
P. O. Bax15875-4416, Tehran, Iran**

Email: sadrnejad@kntu.ac.ir

Abstract

In maintenance of concrete made dam, damages and their type's outcome internally after strong earthquake are generally judged upon engineering experience and guess which mostly may be not logical and even not true. A meso-scale multi-laminate based damage model has been developed and employed to simulate the location, orientation and type of internal damages due to any change at boundaries such as earthquake. The proposed model can rationally describe the semi-macroscopic behavior of quasi-brittle materials, and especially concrete, under the effects of any change sensed by overall instrumentation data outcome with regards to the pre-existing values before damage. The capability of proposed model was investigated through modeling the interaction of meso-scale heterogeneities and formulating the damage constitutive law governing on predefined sampling planes interactions. Accordingly, any compressive/tensile/shearing on plane conditions created upon experimental tests (under both quasi-static and dynamic conditions) can be numerically simulated. The analysis will include discussion of failure/post failure pattern as well as fragment distribution. The capability of proposed model in crack progression and fragmentation is investigated through the analysis of any plain and reinforced concrete dam to show the ideal damages across dam body.

Keywords: instrumentation data analysis, internal damage, crack type, damage orientation.

1. INTRODUCTION

Concrete infrastructures such as dam require regular control by instrument data acquisition and assessment to ensure safety for maintenance practice. These assessments effort can verify and confirm in place, position and geometry of any internal damages such as crack propagation or crack extended continuity which may decrease strength and increase seepage through vein. The proposed Model has been developed upon multi-laminate framework which defines the small continuum structural units as an assemblage of particles and voids that fill infinite spaces between the sampling planes. This model has appropriately justified material particles and voids interactions as the contribution of interconnection forces in overall macro-mechanics internal deformation mechanism. Upon these assumptions, nonlinear deformations are to occur due to sliding, separation/closing of the boundaries and elastic deformations are the overall responses of structural unit bodies. Therefore, the overall deformation of any small part of the medium is composed of total elastic response and an appropriate summation of sliding, widening/closing phenomenon under the current effective normal and shear stress/strains on predefined random sampling planes. Representation of the overall stress/strain/compliance tensor in terms of semi-micro or micro level stresses and the condition, number and magnitude of contact forces has long been the aim of numerous researchers (Christofferson, et. al., (1981) [1], Nemat-Nasser, et. al., (1983) [2]. The multi-laminate developed by Sadrnejad, et al., (1992, 2017) [3, 4], is capable of predicting the behaviour of geo-materials, such as rock/concrete, on the basis of sliding mechanisms, elastic behaviour of intact parts and possibilities to see different plasticity models for the most possible sliding orientations. To overcome limitations exceeding continuum mechanic limits, certain calibration parameters can be obtained with regards to the concrete type and a linear isotropic medium with no remaining porosity is assumed by means of polyhedron bodies [5,6]. The artificial polyhedrons are assumed in between 17 sliding planes, passing through each point in medium. The location of tip heads of normal to the planes defining corresponding direction cosines are shown on the surface of unit radius sphere. In ideal case, the normal integration is considered as summing up the individual micro effects correspond to infinite number of micro sampling planes [7].

2. MULTI-LAMINATE CONCEPT

A multi-laminate model incorporating a mixture of the kinematic and static constraints should be physically more realistic than simply is supported by continuum mechanics law. Figure 1 shows Real aggregation of particles and 2D representation of artificial polyhedron. Figure 2 shows the geometry and orientation of 17 sampling planes tangent on sphere surface and in cubes. The values of weighted coefficients of 17 independent planes are shown in Table 1.

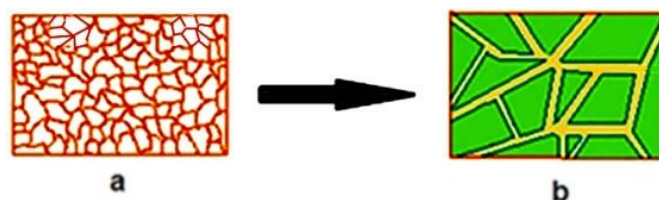


Figure 1 (a) Real aggregation of particles; (b) 2D representation of aggregation of artificial polyhedron

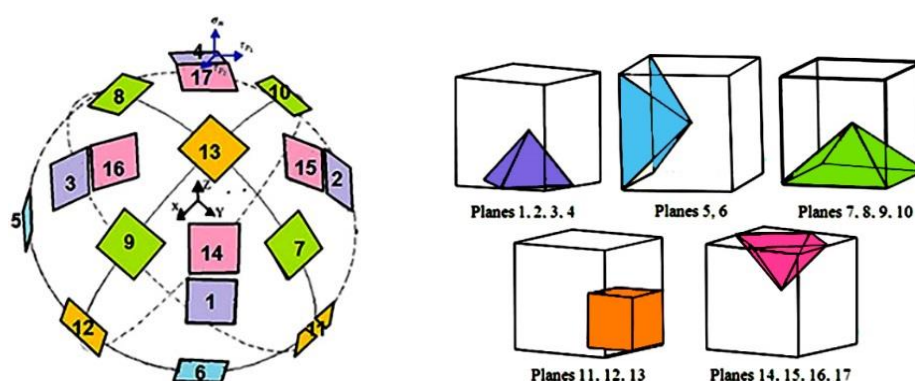


Figure 2 direction of 17 sampling planes on the surface of sphere and in cubes

Table 1: direction cosines and weighted coefficients for 17 planes

Plane No	normal axis			w_i					
	n_1	n_2	n_3						
1	$\frac{\sqrt{3}}{3}$	$\frac{\sqrt{3}}{3}$	$\frac{\sqrt{3}}{3}$.020277985	9	0	$-\frac{\sqrt{2}}{2}$	$\frac{\sqrt{2}}{2}$.030091134
2	$\frac{\sqrt{3}}{3}$	$-\frac{\sqrt{3}}{3}$	$\frac{\sqrt{3}}{3}$.020277985	10	0	$\frac{\sqrt{2}}{2}$	$\frac{\sqrt{2}}{2}$.030091134
3	$-\frac{\sqrt{3}}{3}$	$\frac{\sqrt{3}}{3}$	$\frac{\sqrt{3}}{3}$.020277985	11	1	0	0	.038296881
4	$-\frac{\sqrt{3}}{3}$	$-\frac{\sqrt{3}}{3}$	$\frac{\sqrt{3}}{3}$.020277985	12	0	1	0	.038296881
5	$\frac{\sqrt{2}}{2}$	$\frac{\sqrt{2}}{2}$	0	.058130468	13	0	0	1	.029390060
6	$-\frac{\sqrt{2}}{2}$	$\frac{\sqrt{2}}{2}$	0	.058130468	14	$\frac{\sqrt{6}}{6}$	$\frac{\sqrt{6}}{6}$	$\frac{\sqrt{2}}{\sqrt{3}}$.019070616
7	$\frac{\sqrt{2}}{2}$	0	$\frac{\sqrt{2}}{2}$.030091134	15	$\frac{\sqrt{6}}{6}$	$-\frac{\sqrt{6}}{6}$	$\frac{\sqrt{2}}{\sqrt{3}}$.019070616
8	$-\frac{\sqrt{2}}{2}$	0	$\frac{\sqrt{2}}{2}$.030091134	16	$-\frac{\sqrt{6}}{6}$	$\frac{\sqrt{6}}{6}$	$\frac{\sqrt{2}}{\sqrt{3}}$.019070616
					17	$-\frac{\sqrt{6}}{6}$	$-\frac{\sqrt{6}}{6}$	$\frac{\sqrt{2}}{\sqrt{3}}$.019070616

The spaces between 17 sliding planes, passing through each point in medium divide three dimension domains in several polyhedrons. The choice of 17 planes for the solution of any three dimensional problems is a fair number that can comply compatibility condition as well as equilibrium through the use of numerical integration.

Any set of six or nine strain components apply to $dx dy dz$ element sides can be transferred to a new coordinate built on a sampling plane where, one coordinate axis is normal to plane surface. According the use of 17 planes in multi-laminate numerical integration (sadnejad, (2017)) [4], the strain tensor at any point with 6 or 9 components is equal to numerically integrated weighted 17 on plane, 3 components strain tensor.

Consequentially, gradual application of abnormal differences of instrument recorded values converted to equivalent stress/strain increments and solving to satisfy minimum energy level on any of $dx dy dz$ element leads to carry out internal sampling plane deformations which can introduce damaged widened/slides on plane cracks. This analytical method is to be used to detect internal damages through concrete dam body.

3. PORE PRESSURE AND DEFORMATION EFFECTS

Under an externally applied stress, quick acceleration, deformation or crack progressions are forced into more intimate concrete limit strength destroying cementation, and the mass volume changes associated with vein production. If drainage is prevented or impeded, stress will develop in the pore water opposing the externally applied stress increase associated with crack propagation. Therefore, pore water pressures are a controlling factor on stability or local/global failure during construction. Measurement of movements and deformations is as important to assess internal damages as the measurement of pore pressures. Generally, piping must particularly be guarded against because it occurs gradually through seepage and is often not apparent until either crack path remediation or the structure’s failure is imminent. Seepage and erosion along the lines of vein, continuous crack or local poor compaction and through cracks in foundations and concrete mass may specially be indicated by such measurements.

In this research, numerical analysis of concrete dams are based on radical simplifications of the on plane stress or strain patterns defining internal mechanism and the shape of the rupture planes. However, accurate measurement of stress/strain/pore pressure is sometimes difficult and distribution of stress/strain in concrete dams is complex. Strains may be calculated either from displacements, mechanical constitutive equations or be measured directly which may not be conformed to due to several known or unknown reasons.

4. DAMAGE EFFECTS ON MODULUS MATRIX

The proposed damage model constitutive modulus matrix is computed from superposition of its counterparts on the multi-laminate that such counterparts in turn, are calculated based on the plasticity and damage occurred on each sampling plane during deformation depending on its specific loading conditions and crack growth [8,9]. The on plane dislocations are evaluated according to the combination of two proposed functions; each of them is due to strain exceeding the particular on plane damage limit. This two loading conditions are as follows:

I. axial, w_{axial} : $w_{ax}(x(\epsilon_{ax})) = [1 - e^{-a_{ax} \times x(\epsilon_{ax})}] \cdot H(x(\epsilon_{ax}))$ (1-a)

II. Shear, w_{shear} : $w_{sh}(x(\epsilon_{sh})) = [1 - e^{-a_{sh} \times x(\epsilon_{sh})}] \cdot H(x(\epsilon_{sh}))$ (1-b)

a_{ax} and a_{sh} are two material constant, ϵ_{ax} and ϵ_{sh} are on plane axial and shear strain. Therefore, function $x(\epsilon)$ is written as follows:

$$\epsilon_{ax} = \epsilon_N, \quad \epsilon_{sh} = \sqrt{\epsilon_M^2 + \epsilon_L^2}, \quad x(\epsilon) = (\epsilon - \epsilon_0) / \epsilon_0 \tag{2}$$

ϵ_0 stands for starting damage dislocation strain. Also, Heaviside function is introduced as follows:

$$H(x(\epsilon)) = \begin{cases} 0 & : x(\epsilon) \leq 0 \\ 1 & : x(\epsilon) > 0 \end{cases} \tag{3}$$

The calculation of damage plane modulus matrix and on plane stress components are as follows:

$$\begin{Bmatrix} \sigma_{Ni} \\ \sigma_{Mi} \\ \sigma_{Li} \end{Bmatrix} = [D_i] \begin{Bmatrix} \epsilon_{Ni} \\ \epsilon_{Mi} \\ \epsilon_{Li} \end{Bmatrix}, \quad [D_i] = \begin{bmatrix} 1-w_{axial} & 0 & 0 \\ 0 & 1-w_{shear} & 0 \\ 0 & 0 & 1-w_{shear} \end{bmatrix} \begin{bmatrix} E_N & 0 & 0 \\ 0 & E_T & 0 \\ 0 & 0 & E_T \end{bmatrix}, \quad \begin{matrix} E_N = E / (1-2\theta) \\ E_T = E_N \cdot (1-4\theta) / (1+\theta) \end{matrix} \tag{4}$$

To transfer the on plane stress matrix (size: 3x1) to global coordinate (6x1) and summing them up upon numerical integration equation can be written as follows:

$$\sigma_{ij} = 6 \sum_{i=1}^{17} w_i [L_i]^T \{ \sigma_{Ni} \quad \sigma_{Mi} \quad \sigma_{Li} \}^T \tag{5}$$

L_i^T is transformation matrix (3x6). The on plane compliance matrices (3x3) are found by the following equation to be summed up to obtain main compliance matrix C (6x6) as follows:

$$[C_i] = [D_i]^{-1} \quad [C] = 6 \sum_{i=1}^{17} w_i [L_i]^T [C_i] [L_i] \tag{6}$$

Also, the variation of strength due to damage can be obtained by two strength functions as follows:

$$R(x(\varepsilon_{eq})) = \begin{cases} c.e^{d.x(\varepsilon_{eq})} & x(\varepsilon_{eq}) \leq b \\ g.e^{f.x(\varepsilon_{eq})} & x(\varepsilon_{eq}) \geq b \end{cases}, \quad \varepsilon_{eq} = \sqrt{\varepsilon_N^2 + \varepsilon_M^2 + \varepsilon_L^2} \tag{7}$$

where b, c, d, f and g are material properties. The value of g is found upon continuity of function $R(x(\varepsilon_{eq}))$ at the location $x(\varepsilon_{eq}) = b$. ε_{eq} is on plane equivalent strain. To ease the analogy of projections of stress and strain tensors on sampling planes, the behavior of material can be divided into two distinct parts as on plane normal (volumetric) and shear (deviatoric). Consequently, modulus matrix at the center of unit sphere is obtained by integration its variation over sphere surface. This integration can be calculated numerically through sampling points correspond to sampling planes. As a result, the point modulus matrix after some manipulations is written as follows:

$$D_{ijkl} = \frac{3}{4\pi} \int_{\Omega} \left(\frac{E}{1+\nu} \right) \left[\left(N_{ij} - \frac{\delta_{ij}}{3} \right) \left(N_{kl} - \frac{\delta_{kl}}{3} \right) + M_{ij} M_{kl} + L_{ij} L_{kl} \right] d\Omega + \frac{E}{1-2\nu} \frac{\delta_{kl}}{3} \delta_{ij} \tag{8}$$

M_{ij}, N_{ij} and L_{ij} are components of transformation matrix.

5. ON PLANE STRAIN EFFECTS ON PERMEABILITY

According to *Choinska et al. (2007-b)* [10], the general permeability changes versus the strain ratio defining damage function for different types of concrete has been presented as shown in Figure 3-a. The permeability ellipsoid is shown in Figure 3-b. A cracked sampling upon corresponding on plane strain ratio as a damaged plane makes a local jumped value on permeability ellipsoid of Gauss point to evaluate the crack effects of hydraulic conductivity. This local jump can be assumed belong to a new higher level similar permeability ellipsoid that its diameters multiplied by $\sqrt{\omega}$ ($\omega = \frac{k_{ni(new)}}{k_{ni}}$) that can be accounted as follows:

$$k_{ni(new)} = \frac{\sqrt{\omega} A \cdot \sqrt{\omega} B}{\sqrt{(\ell_i^2 + m_i^2)(\sqrt{\omega} A)^2 + n_i^2(\sqrt{\omega} B)^2}} = \sqrt{\omega} k_{ni} \tag{9}$$

With this regards, calculating the i^{th} plane strain ratio, damaged permeability matrix is provided and the new permeability matrix of i^{th} plane has been replaced to obtain the corresponding Gauss point permeability matrix in FEM solution. The strain components and damage function for 17 planes can be computed upon multi-laminate damage model, (Labibzadeh, M., Sadrnejad, S. A., 2006) [11, 12], Sadrnejad, S. A., et al., 2002) [13].

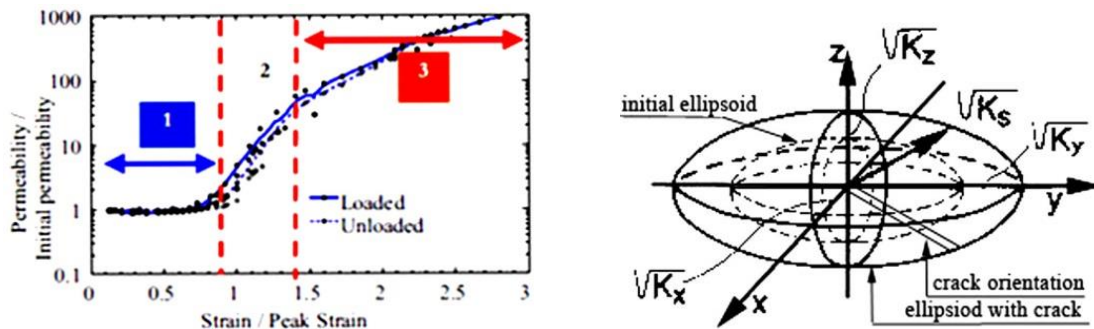


Figure 3 a) Permeability changes vs. the strain ratio [13], b) Initial, cracked affected ellipsoids

The governing equations for single phase flow and transport in a saturated aquifer are the continuity equation combined with Darcy's law as follows:

$$S_0 \frac{\partial h}{\partial t} + \text{div}[(8\pi \sum_{i=1}^n w_i T_i^T K_i^D T_i) \text{grad}(h)] = q \quad (10)$$

Therefore, the advection–dispersion transport–equation employed is as follows:

$$\frac{\partial c}{\partial t} + \text{div}(cv) - \text{div}[(8\pi \sum_{i=1}^n w_i T_i^T K_i^D T_i) \text{grad} c] = r \quad (11)$$

where S_0 represents the specific storage coefficient, h the piezometric head, t the time, K_i^D the hydraulic conductivity tensor for i^{th} plane, c the solute concentration, v the seepage velocity, q flow flux, r externally applied source and sink terms, T_i is transformation matrix for i^{th} plane and n is number of sampling planes.

The permeability matrix K_i^D for i^{th} plane is a 3×3 matrix in Cartesian coordinate built on i^{th} plane, including the effects of strain tensor variations of corresponding plane. The transformation matrix is defined for three perpendicular planes at global Cartesian coordinate of each Gauss points; therefore, T_i for each set of three planes corresponding to i^{th} plane. Summing up the permeability matrices of all sampling planes, a numerical integration rule and corresponding transformed weighted matrix of all planes must be employed as follows:

$$K_{Gauss}^D = 8\pi \sum_{i=1}^n w_i T_i^T K_i^D T_i \quad (12)$$

6. DAMAGE DETECTION METHOD

The existing safe condition solution of a concrete dam with a certain water level must be ready as initial conditions for any damage computation. A numerical analysis of current condition must be conducted to provide a complete evaluation of different current variables such as stress, strain, deformations, and excess pore water pressure as nonconformity or disorder in records. Therefore, any unexpected non-conformed values measured by right instrument reading presented through stress or strain meters, piezometer or other instruments is known as a signal for the occurrence of a damage. A difference vector as the net disorder values is defined by jump values with regards to initial normal values as lack of conformity components. These vector components must be converted to a loading vector composed of equivalent nodal forces that can be incrementally and carefully applied to nodes in vicinity of instrument sensors. The aim of this gradual numerical back analysis is to find any abnormal condition as on plane stress/strain disorders which may be created by satisfying gradually equilibrium, compatibility and on plane undamaged/damaged constitutive equations. The maximum care must be employed checking any condition that exceeds limitations or may break assumption of continuity through materials. Therefore, any sharp hydraulic gradient, quick seepage flows through the vein, stress component reductions, strain component increase or sever deformations effects on plane widening/closing/sliding lead to create heave as local void ratio increase, appearing veins and unexpected seepage, local different types of crack. Such a control can be numerically carried out up to local or even global failure that may happen.

7. RESULTS OF CRACKS IN SEFID-ROOD BUTTRESSED DAM

This dam height is 106 m. with 417 m. of crest length that was built in between 1956 to 1963 in Gilan state at north of Iran. The dam downstream view is shown in Figure 4-a. Due to earthquake magnitude 7.3 Richter 1990, rib base no.18 of this dam cracked and some seepage started at the shown located in Figure 4-b that later on, it was amended by resin injection. This rib base was modeled through FE developed computer program and the internal damages and permeability changes predicted. Figure 5-a and 5-b show the combined stress distribution before and after earthquake, respectively. The concrete mechanical properties are shown in Table 2.

Table 2: Concrete properties

Dynamic Young Modulus E_d (MPa)	Elastic Young Modulus E (MPa)	Poisson' ratio ν	Density (kg/m^3)	Compressive strength f'_c (MPa)
29000	20000	0.17	2250	16.9

The FE mapped mesh of rib number 18 including first cracked locations are shown in Figure 6. The first failed plane number 8 at node 85, as combined stress and normal strain time histories are presented in Figure 7-a and 7-b. The plane no. 8 of node 85 normal stress vs. strain and its time history and also its stress path plus the orientation of this failed plane are presented in Figure 8.

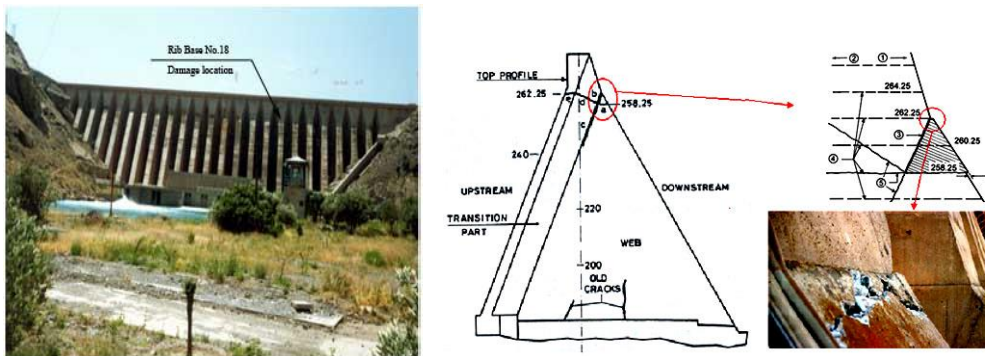


Figure 4-a) Sefid-Rood dam down stream view, b) downstream cracks view of rib number 18 and cracks location

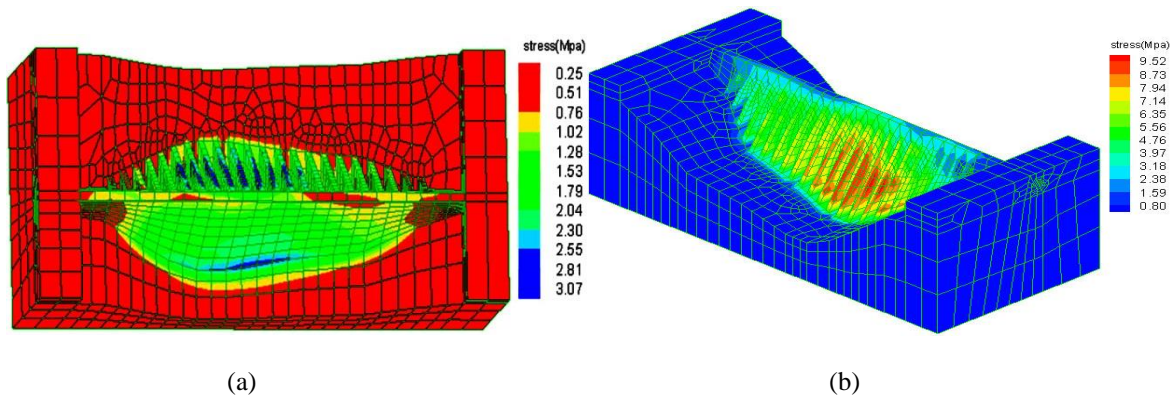


Figure 5 Dam combined stress analysis, a) before and b) after earthquake

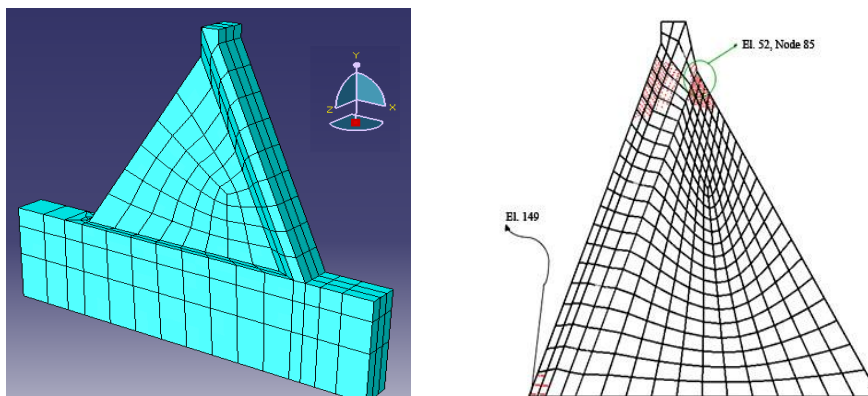


Figure 6 a) Mapped elements and b) damaged locations

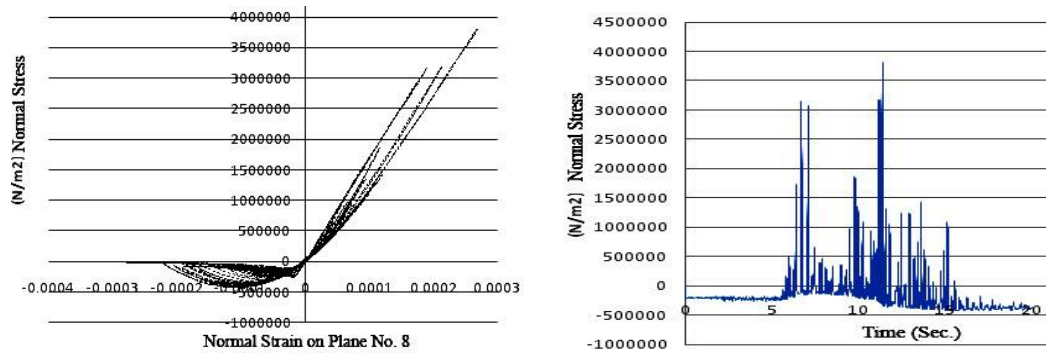


Figure 7 a) normal stress vs. strain, b) time history of Normal stress on plane no. 8 of Node 85

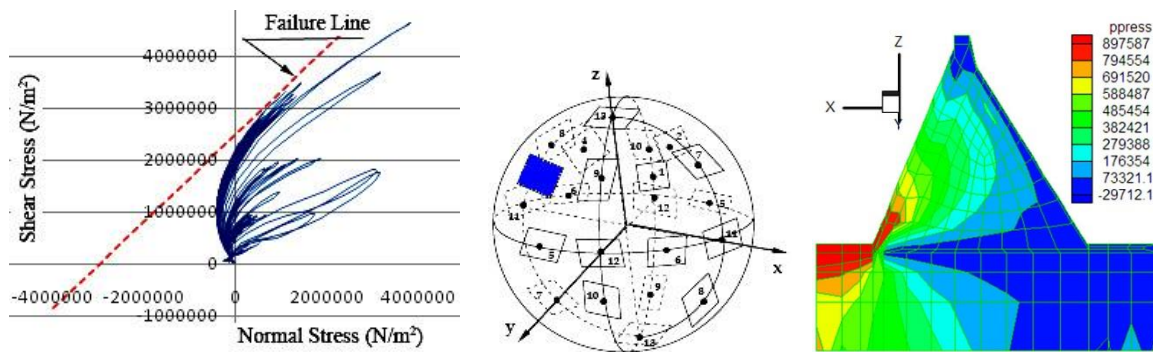


Figure 8 a) stress path on plane no. 8, b) its direction on sphere, and c) initial P.W.P.

Figure 9 show pore water pressure (P.W.P.) contours and the comparison of measured hydrostatic pore water pressure at the piezometer locations after 4 seconds since the start of earthquake with model results. To show the capability of proposed model, the two measured pore water pressure histories at piezometer no. 139 and 435 during earthquake are compared with model results in Figure 9-a and -b respectively. This comparison reveals that the proposed model is quite capable of predicting such a dynamic damage history after earthquake.

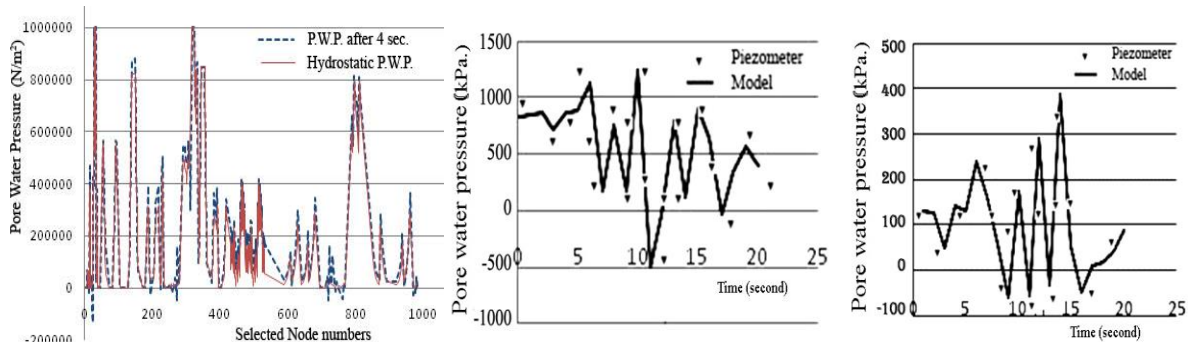


Figure 9 a) comparing pore water pressure after 4 seconds with hydrostatic P.W.P., b) P.W.P. at piezometer No. 139 and 435 during earthquake

8. CONCLUSIONS

A certain accurate program is required to record and data acquisition of any concrete structure instruments usage. Current trends in the field of instrumentation emphasize the search for higher resolution and precision, providing more accurate measurements and permitting rapid detection of any behavioral anomalies

through structure. A damage permeability tensor containing crack orientation effects associated with fracture generation in multi-laminate framework has been developed and employed to examine the influence of fracture–matrix interaction on flow and transport processes. The proposed model results on concrete dam have shown that, the presence of a fractured matrix in a fractured system leads to a considerable conductivity matrix change affecting pore water pressure, and the flow and transport conditions through a cracked concrete medium. A simple multi-laminate technique has been able to evaluate different damages as crack opening displacement/sliding and permeability tensor change based on orientation damage, led to failure mechanism analyses.

A certain flow gradient approach which is equivalent to a non-local average with a sharper distribution, lending less weight to neighboring points compared to the non-uniform Gaussian distribution in the classical integral approach. Therefore, this gradient approach provides better limit values of the quality for a formed crack than with the integral model.

In closing, it should be recalled that dam monitoring is a key component of dam safety. Because the failure of a dam can lead to human as well as economic disaster, no compromise in regards to instrumentation quality or reliability should be made.

9. REFERENCES

1. Christofferson, Mehrabadi M. M. and NematNasser, S., A micromechanical description of granular behavior, *J. Appl. Mech.*, 48, 339344 (1981),
2. NematNasser, S. and Mehrabadi M. M., Stress and fabric in granular masses, *Mechanics of granular Materials: New Models and Constitutive Relations* (Eds. J.T. Jenkins and M. Satake), pp. 18, Elsevier Sci. Pub., 1983.
3. Sadrnejad S. A., (1992) Multilaminar elastoplastic model for granular media. *International Journal of Engineering* 5: 11.
4. Sadrnejad S.A., Shakeri, S., (2017), Multi-laminate non-coaxial modelling of anisotropic sand behavior through damage formulation, *Computers and Geotechnics* 88 (2017) 18–31
5. Sadrnejad, S, A., Labibzadeh, M., "A *Continuum/ Discontinuum Micro Plane Damage Model for Concrete*", *International Journal of Civil Engineering*, Vol. 4, pp. 296-313, 2006.
6. Sadrnejad S.A., (2006), Numerical Evaluation of Non-homogeneity and Anisotropy due to Joints in Rock Media, *International Journal of Civil Engineering*. Vol.4, No. 2.
7. Sadrnejad S.A. and Karimpour H., (2011), Drained and Undrained Sand Behaviour by Multilaminar Bounding Surface Model, *International Journal of Civil Engineering*, vol.9, No.2
8. Sadrnejad S.A., Hoseinzadeh, H.R., (2017), Multi-Laminar Rate-Dependent Modelling of Static and Dynamic Concrete Behavior through Damage Formulation, *Scientia Iranica, Transaction A, Civil Engineering*, (accepted to be published).
9. Sadrnejad S.A., Multi-laminar elasto-plastic model for granular media, *Journal of Engineering, Islamic Republic of Iran*, vol.5, Nos.1&2, May 1992-11.
10. Choinska, M., Gilles Pijaudier-Cabot, Frédéric Dufour, 2007-b, Permeability due to the Increase of Damage in Concrete: From Diffuse to Localized Damage Distributions, *Journal of Engineering Mechanics* Sep 2009, Vol. 135, No. 9, pp. 1022-1028, Online Publication Date: 6 Mar 2009, [http://ascelibrary.org/doi/abs/10.1061/\(ASCE\)EM.1943-7889.0000016](http://ascelibrary.org/doi/abs/10.1061/(ASCE)EM.1943-7889.0000016)
11. LABIBZADEH, M., SADRNEJAD, S. A., Mesoscopic Damage Based Model for Plane Concrete under Static and Dynamic Loadings. *American Journal of Applied Sciences*, 3(9): 2011-2019, 2006.
12. LABIBZADEH, M., SADRNEJAD, S. A., Dynamic Solution Code for Structural Analysis upon Joint Element. *Journal of Computer Science*, 2(5): 401-409, 2006.
13. Sadrnejad S.A., "A *sub-loading surface multi-laminar model for elastic plastic porous media*", *IJE*, Vol. 15, No.4, Nov. 2002.

Non-Destructive Numerical Investigation of Local Heave/Liquefaction through Rock-Fill Dam upon Instrumentation Data

Seyaed Amirodin Sadrnejad

**Department of Civil Engineering, K. N. Toosi University of Technology
P. O. Bax15875-4416, Tehran, Iran**

Email: sadrnejad@kntu.ac.ir

Abstract

In maintenance of rock-fill dam, internal damages as any local heave or liquefaction/hydro-fracture outcome after strong earthquake shaking are detected numerically. The proposed model can rationally describe the semi-macroscopic behavior of geo-materials under the effects of any change sensed by overall instrumentation data outcome with regards to the pre-existing values before damages. The solution method is based on satisfying equilibrium, compatibility and minimum energy level as three main nature laws for any porous medium during elastic, plastic, softening, and hardening regimes. Accordingly, any compressive, tensile, shearing on plane conditions created upon experimental tests (under both quasi-static and dynamic conditions) can be numerically simulated. Any changes of displacements, stresses, strains, and even inclinations, excess pore water pressure at measuring points are converted to equivalent nodal effects and are applied to affected nodes to contribute in the solved equations. Therefore, various boundary conditions are applied to corresponding nodes creating damages or cracks as opening/widening/closing/sliding at predefined sampling planes to change strength/permeability as the effects due to damages. The capability of proposed model in damage progression and fragmentation is investigated through the analysis of any earth structure and rock-fill dam to show the ideal damages across dam body.

Keywords: instrumentation data, shear banding, liquefaction, hydraulic fracture, damage orientation.

1. INTRODUCTION

The instrumentation of dam body and foundation plays a vital role as though any change in the structural behavior such as plastic heave, shear banding, seepage vein, etc., can be established in time based on the data observed by the instruments [1,2]. Accordingly, any remedial action and out coming measures can be taken up so as to avoid failure of the structure. Adequate instrumentation in earth fills and their foundations provide significant quantitative data indicating the magnitude and distribution of stress/strain, inclination, displacement, acceleration, pore pressures and their variations with time and other patterns of seepage, zones of potential piping, proper functioning of the filter media and effectiveness of under seepage control measures.

On the other hands, numerical analysis of the behavior of dam under any load application such as earthquake shaking and effects of existing boundary conditions, clearly, is expected to show stability through equilibrium, compatibility and under limit material behavior within continuum mechanic laws. However, any deficiency makes exceeding the limits creating abnormal differences and transferred to the location of measuring instruments. There are evidences too that exceptionally strong earthquakes have produced remarkable damages, thus showing that the actual seismic behavior of these structures is not yet fully understood, because damages are mostly internal, therefore, not directly checkable [3].

Upon an advanced model being able to present deformability orientation, failure mechanisms require applying the effects of measured quantities by instruments as equivalent nodal forces producing equal energies to abnormal difference values as mechanical load, starting with changing of stress, deformations and pore pressure at different locations in the embankments and the foundation. The limited instrument location values and impossibility of measuring continuous pressure at every point means limiting the number of measurements along certain profiles upstream and downstream from needs special cares to judge about probable damages which could occur between measuring points. Generally, pressure should be measured at any point where a variation could indicate a potential disorder. For each type of earth/rock-fill dam, design principles and modes of potential of different damage/failure are to be detailed and damage correlation to different instrument measured quantities must be investigated and clarified through the use of a capable constitutive model.

The paper concludes with the general case of dam foundation related to monitoring for any embankment dams and stresses the importance of automatic data acquisition and processing as a complement to modern dam instrumentation programs leads to the proposed damage detecting method.

2. MULTI-LAMINATE CONCEPT

For a multi-phase material such as soil that supports the overall applied loads through contact cohesion/friction, the overall mechanical response ideally may be described on the basis of micro-mechanical behaviour of grains interconnections. Naturally, this requires the description of overall stress/strain, characterization of fabric, representation of kinematics, development of local rate constitutive relations and evaluation of the overall differential constitutive relations in terms of the local quantities. Representation the overall stress/strain/compliance tensor in terms of micro level stresses and the condition, number and magnitude of contact forces has long been the aim of numerous researchers (Nemat-Nasser, et. al., (1983) [4]. The multi-laminate developed by Sadrnejad, et al., (1992, 2017) [5, 6], is capable of predicting the behaviour of geo-materials, such as rock, on the basis of sliding mechanisms, elastic behaviour of intact parts and possibilities to see different plasticity models for the most possible sliding orientations.

A multi-laminate model incorporating a mixture of the kinematic and static constraints should be physically more realistic that simply is supported by continuum mechanics law. Figure 1 shows Real aggregation of particles and 2D representation of artificial polyhedron, orientation of 17 sampling planes tangent on sphere surface and in cubes. The values of weighted coefficients of 17 independent planes are shown in Table 1.

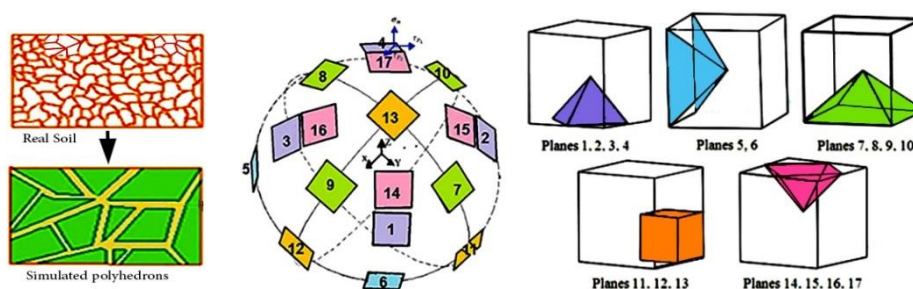


Figure 1 (a) Real aggregation of particles and simulated polyhedrons view; (b) direction of 17 sampling planes on the surface of sphere and, c) in cubes

Table 1: direction cosines and weighted coefficients for 17 planes

Plane No	normal axis			w_i
	n_1	n_2	n_3	
1	$\frac{\sqrt{3}}{3}$	$\frac{\sqrt{3}}{3}$	$\frac{\sqrt{3}}{3}$.020277985
2	$\frac{\sqrt{3}}{3}$	$-\frac{\sqrt{3}}{3}$	$\frac{\sqrt{3}}{3}$.020277985
3	$-\frac{\sqrt{3}}{3}$	$\frac{\sqrt{3}}{3}$	$\frac{\sqrt{3}}{3}$.020277985
4	$-\frac{\sqrt{3}}{3}$	$-\frac{\sqrt{3}}{3}$	$\frac{\sqrt{3}}{3}$.020277985
5	$\frac{\sqrt{2}}{2}$	$\frac{\sqrt{2}}{2}$	0	.058130468
6	$-\frac{\sqrt{2}}{2}$	$\frac{\sqrt{2}}{2}$	0	.058130468
7	$\frac{\sqrt{2}}{2}$	0	$\frac{\sqrt{2}}{2}$.030091134
8	$-\frac{\sqrt{2}}{2}$	0	$\frac{\sqrt{2}}{2}$.030091134
9	0	$-\frac{\sqrt{2}}{2}$	$\frac{\sqrt{2}}{2}$.030091134
10	0	$\frac{\sqrt{2}}{2}$	$\frac{\sqrt{2}}{2}$.030091134
11	1	0	0	.038296881
12	0	1	0	.038296881
13	0	0	1	.029390060
14	$\frac{\sqrt{6}}{6}$	$\frac{\sqrt{6}}{6}$	$\frac{\sqrt{2}}{\sqrt{3}}$.019070616
15	$\frac{\sqrt{6}}{6}$	$-\frac{\sqrt{6}}{6}$	$\frac{\sqrt{2}}{\sqrt{3}}$.019070616
16	$-\frac{\sqrt{6}}{6}$	$\frac{\sqrt{6}}{6}$	$\frac{\sqrt{2}}{\sqrt{3}}$.019070616
17	$-\frac{\sqrt{6}}{6}$	$-\frac{\sqrt{6}}{6}$	$\frac{\sqrt{2}}{\sqrt{3}}$.019070616

The created polyhedrons are roughly by 17 sliding planes, passing through each point in medium. The location of tip heads of normal to the planes defining corresponding direction cosines are shown on the surface of unit radius sphere. In ideal case, the normal integration is considered as summing up the individual micro effects correspond to infinite number of micro sampling planes. Any set of six or nine strain components apply

to $dxdydz$ element sides can be transferred to a new coordinate built on a sampling plane where, one coordinate axis is normal to plane surface. According the use of 17 planes in multi-laminate numerical integration (sadrnejad, (2017)) [6], the strain tensor at any point with 6 or 9 components is equal to numerically integrated weighted 17 on plane, 3 components strain tensor. Consequentially, gradual application of abnormal differences of instrument recorded values converted to equivalent stress/strain increments and solving to satisfy minimum energy level on any of $dxdydz$ element leads to carry out internal sampling plane deformations which can introduce damaged widened/slides on plane cracks. This analytical method is to be used to detect internal damages through concrete dam body. According to continuum mechanics law, any set of six or nine strain components apply to an element can be transferred to a new coordinate built on a sampling plane where, one coordinate axis is normal to plane surface. In multi-laminate frame work, the on plane micro-strain components were calculated and finally the macro-strain tensor was identified by superimposition of on-plane micro-strain components of sampling plane transformed matrix obtained through direction cosines of sampling points on the surface of a unit sphere. The basic numerical integration equation of function $f(x,y,z)$, distributed over the surface of sphere element and replacing that by strain distribution over the element surface as that function are written as follows:

$$\int_{\Omega} f(x,y,z) d\Omega = 4\pi \sum_p W_p f(\alpha_p, \gamma_p, z_p) \Rightarrow \int_S \varepsilon(x,y,z) dS = 4\pi \sum_p W_p \varepsilon(\alpha_p, \gamma_p, z_p) \quad (1)$$

Furthermore, it is worth noting that to relate global stress and strain relation to this micro-level upon equation 1, it is written as follows:

$$\varepsilon_{spherurface} = \int_S \varepsilon(x,y,z) dS = \int_S D^{-1} \sigma(x,y,z) dS = 4\pi \sum_p W_p D^{-1} \sigma(\alpha_p, \gamma_p, z_p) \quad (2)$$

D^{-1} is material compliance matrix. According to equilibrium of forces of corresponding stresses in continuum law, the integration of stress distribution on the sphere surface is equal to the summation of on plane stresses that can be omitted from both sides of equation. Then a new integrand equation based on material compliance matrix is obtained as follows:

$$D^{-1}_{spherurface} = \int_S D^{-1}(x,y,z) dS = 4\pi \sum_p W_p D_p^{-1}(\alpha_p, \gamma_p, z_p) \quad (3)$$

Regarding the equilibrium of the forces to find three stress components on an oblique plane through element, equilibrium is satisfied. On the other hand, transferring six or nine stress components of three faces of element to new coordinate system that the oblique plane is normal to one axis of that, the same results as equilibrium will be obtained [6].

3. DAMAGE EFFECTS ON MODULUS MATRIX

In order to attain to the double constraint aspect, after analogy of the projections of stress and strain tensors on the multi-laminates, it was certain that it is possible to separate the behavior of material into two distinct parts as deviatoric and volumetric. So if we discrete the strain tensor as the volumetric and deviatoric parts firstly and then project each of them on the multi-laminates separately, we may try to obtain the deviatoric part of the modulus matrix from the behaviors which are taking place on the multi-laminates and the volumetric one which is not affected by the direction characteristics and essentially is isotropic, obtained in the ordinary coordinate system and summed up to the deviatoric part at the end of each step of loading. Therefore, modulus matrix is written as follows:

$$D_{ijkl} = \frac{3}{4\pi} \int_{\Omega} \left(\frac{E}{1+\nu} \right) \left[\left(N_{ij} - \frac{\delta_{ij}}{3} \right) \left(N_{kl} - \frac{\delta_{kl}}{3} \right) + M_{ij} M_{kl} + L_{ij} L_{kl} \right] d\Omega + \frac{E}{1-2\nu} \frac{\delta_{kl}}{3} \delta_{ij} \quad (4)$$

Total deviatoric part of constitutive matrix is computed from superposition of its counterparts in turn, are calculated based on the damage occurred on each plane depending on its specific loading conditions. This

damage is evaluated according to the five separate damage functions; each of them belongs to the particular loading states. This five loading conditions are as follows:

I. Hydrostatic Compression; II. Hydrostatic Tension; III. Pure Shear; IV. Shear + Compression; V. Shear + Tension

On each multi-laminate at each time of loading history, there exists one specific loading situation that it may be in one of the five mentioned basic loading conditions. For every five moods, a specific damage function according to the authoritative laboratory test results available in the literature is assigned. Then, for each state of on plane loading, one of the five introduced damage functions will be computed with respect to the history of micro-stress and strain components. These five damage functions are as follows:

$$I) \text{ hydrostatic compression: } \omega_{HC} = 0.0 \quad (5)$$

$$II) \text{ hydrostatic tension: } \omega_{HT} = 0.0 \quad \text{if } \varepsilon_{eq} \leq \sqrt{3}a$$

$$\omega_{HT} = 1.0 - \left(\frac{\sqrt{3}a}{\varepsilon_{eq}} \right) \times \exp \left[- \left(\frac{\varepsilon_{eq} - \sqrt{3}a}{b - \sqrt{3}a} \right) \right] \quad \text{if } \varepsilon_{eq} > \sqrt{3}a \quad (6)$$

$$III) \text{ pure shear: } \omega_{SH} = 0.5 \times (\omega_C + \omega_T) \quad (7)$$

$$IV) \text{ shear + compression: } \omega_C = d \times \varepsilon_{eq} \quad \text{if } \varepsilon_{eq} \leq e$$

$$\omega_C = f \left(\varepsilon_{eq} - e \right)^2 + g \left(\varepsilon_{eq} - e \right) + h \quad \text{if } e < \varepsilon_{eq} \leq i$$

$$\omega_C = 1.0 - \left(\frac{j}{\varepsilon_{eq}} \right) \times \exp \left[- \left(\frac{\varepsilon_{eq} - i}{k - i} \right) \right] \quad \text{if } \varepsilon_{eq} > i \quad (8)$$

$$V) \text{ shear + tension: } \omega_T = 0.0 \quad \text{if } \varepsilon_{eq} \leq a$$

$$\omega_T = 1.0 - \left(\frac{a}{\varepsilon_{eq}} \right) \times \exp \left[- \left(\frac{\varepsilon_{eq} - a}{c - a} \right) \right] \quad \text{if } \varepsilon_{eq} > a \quad (9)$$

Parameters a to k in the above relations are computed according to laboratory results obtained for each specific concrete. ε_{eq} in equations (5) to (9), is equivalent or combined average strain and in the other relations stands for the magnitude of projected deviatoric strain vector on each sampling plane. Linear elastic intact behavior of concrete adopted upon two parameters for ease as elasticity and Poisson's coefficients [7].

4. EQUIVALENT NODAL FORCES TO DISORDERS

Any excess disorder values of displacements, stresses and pore water pressures are balanced to equivalent nodal forces and apply to corresponding elements in whole structure with initial normal condition. Assuming large deformation u recorded, the equivalent nodal forces are calculated as follows:

$$\int B_{nl} D \delta \varepsilon dV = f \Rightarrow (B_0 + \delta B_{nl}) D (B_0 + \delta B_{nl}) \delta u dV = f \Rightarrow f_{eq} = \int (2B_0 D \delta B_{nl} + \delta B_{nl} D \delta B_{nl}) \delta u dV \quad (10)$$

Assuming excess stresses $\delta \sigma$ recorded, the equivalent nodal forces are calculated as follows:

$$\int B_{nl} \delta \sigma dV = f \Rightarrow (B_0 + \delta B_{nl}) \delta \sigma dV = f \Rightarrow f_{eq} = \int \delta B_{nl} \delta \sigma dV \quad (11)$$

Assuming excess pore water pressure δp recorded, the equivalent nodal forces are calculated as follows:

$$\int B_{nl} \delta p dV = f \Rightarrow (B_0 + \delta B_{nl}) \delta p dV = f \Rightarrow f_{eq} = \int \delta B_{nl} \delta p dV \quad (12)$$

Assuming excess strain $\delta \varepsilon$ recorded, the equivalent nodal forces are calculated as follows:

$$\int B_{nl} D \delta \varepsilon dV = f \Rightarrow (B_0 + \delta B_{nl}) D \delta \varepsilon dV = f \Rightarrow f_{eq} = \int \delta B_{nl} D \delta \varepsilon dV \quad (13)$$

Adding incrementally these equivalent forces and corresponding strains, damage functions approach to one and stiffness matrices start decreasing. Therefore, more volumetric strains increase with on plane normal

strains are created and permeability coefficients increase lead to less pore water pressure and more seepage flows.

5. ZIPINGPU CFRD AND WENCHUAN EARTHQUAKE

The strong ground motion ($M_s = 8.0$) of the 2008 Wenchuan earthquake in Sichuan Province of China caused severe damage to the Zipingpu concrete face rock-fill dam (CFRD) [1, 8, 9]. The maximum crest settlement was approximately 1.0 m, and several local failure and joint dislocations were observed in the reinforced concrete face slabs. Figure 2 shows cross section geometry and three-dimension FEM mesh of dam employed in numerical analysis. The three components of acceleration time history of earthquake and global/local damages as face slab sheared line [10, 11, 12] are shown in Figure 3-a, b, c and d, respectively. The site measuring analysis represented that the rupture process of the earthquake has extended along the fault from south to north east up to more than 300km. The represented seismic source time function displays a sequence of rupture cause a quite long duration with a total interval of about 120 s as shown in Figure 4. However, the conducted calculation showed that the only the first 16 seconds, particularly the last 6 seconds (i.e. since 10th to 16th seconds) of this time history was enough to create some on plane failure (as a set of initial damages) in face slabs at elevation 850 m.a.s.l. Exceeding the stated failure condition (till 16th second), the calculation was stopped.

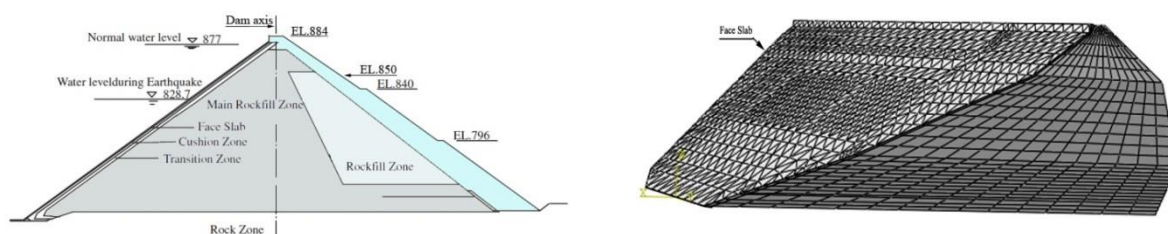


Figure 2 a) Dam cross section geometry [11], b) 3D FEM mesh

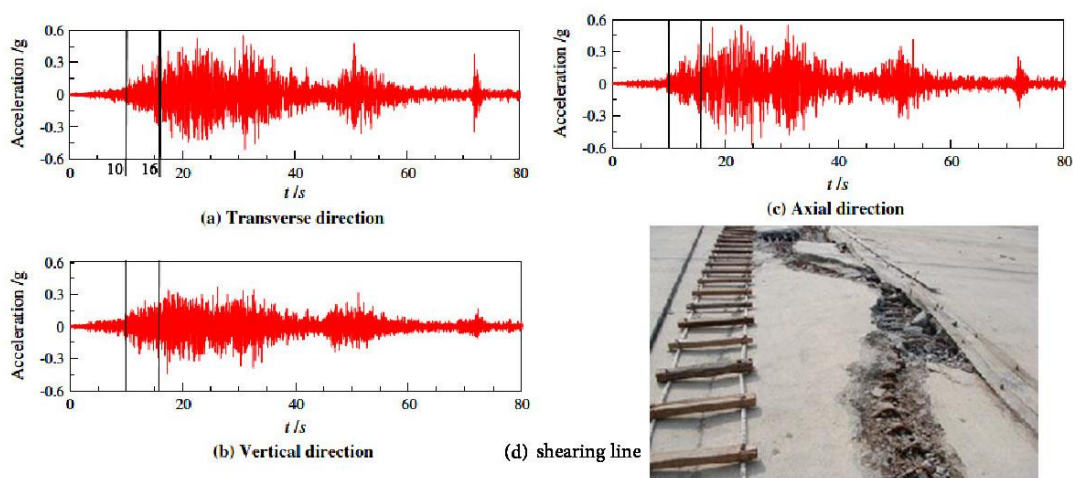


Figure 3 a, b, and c) three components of acceleration time histories, and d) global and local damages in dam concrete face [10].

The most critical point close to the selected position at elevation 850 has been supervised during the stated time period. The on plane normal and shear stress time histories of 17 planes are recorded and presented to control and compared with each other to check the priority. Figure 4-a to -c shows on plane normal stress during 6 seconds. Also, Figure 5-a to -c shows on plane shear stress during the same period. It must be noted that all 17 planes were active during earthquake shaking, however, planes number 2, 5, 6, and 11 met failure showing damage coefficient equal to 1. Figure 5-d shows the orientation of failed planes. The final stress components values on plane number 5, 6, and 11 reveal that there are a few shear stresses, however, tensile stress caused tensile failure. The final stress condition on plane number 2 is not tensile; however, before this stage its damage coefficient reached 1 and failed due to high shear stress in combination with tension.

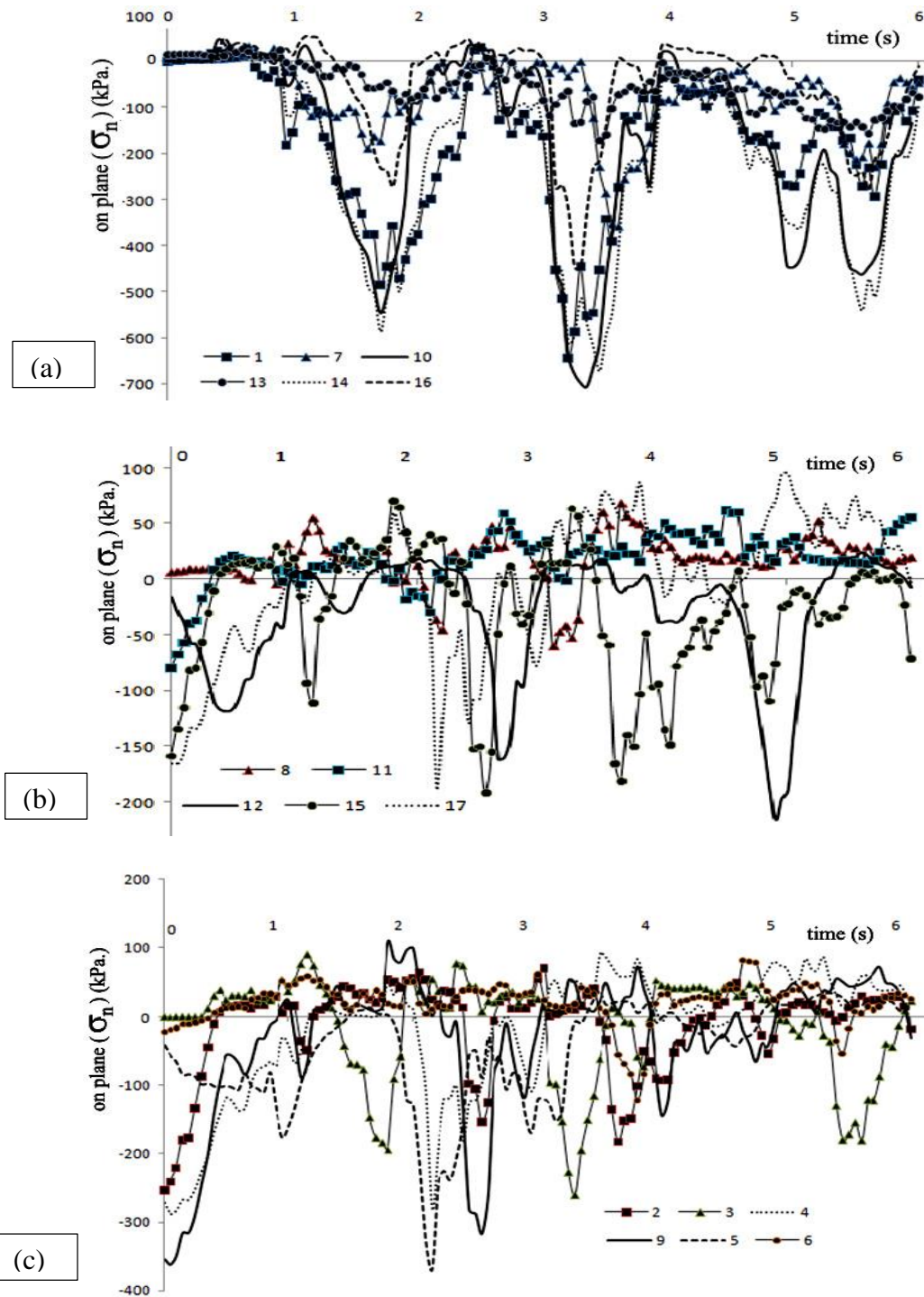


Figure 4-a to -c shows on plane normal stress during 6 seconds

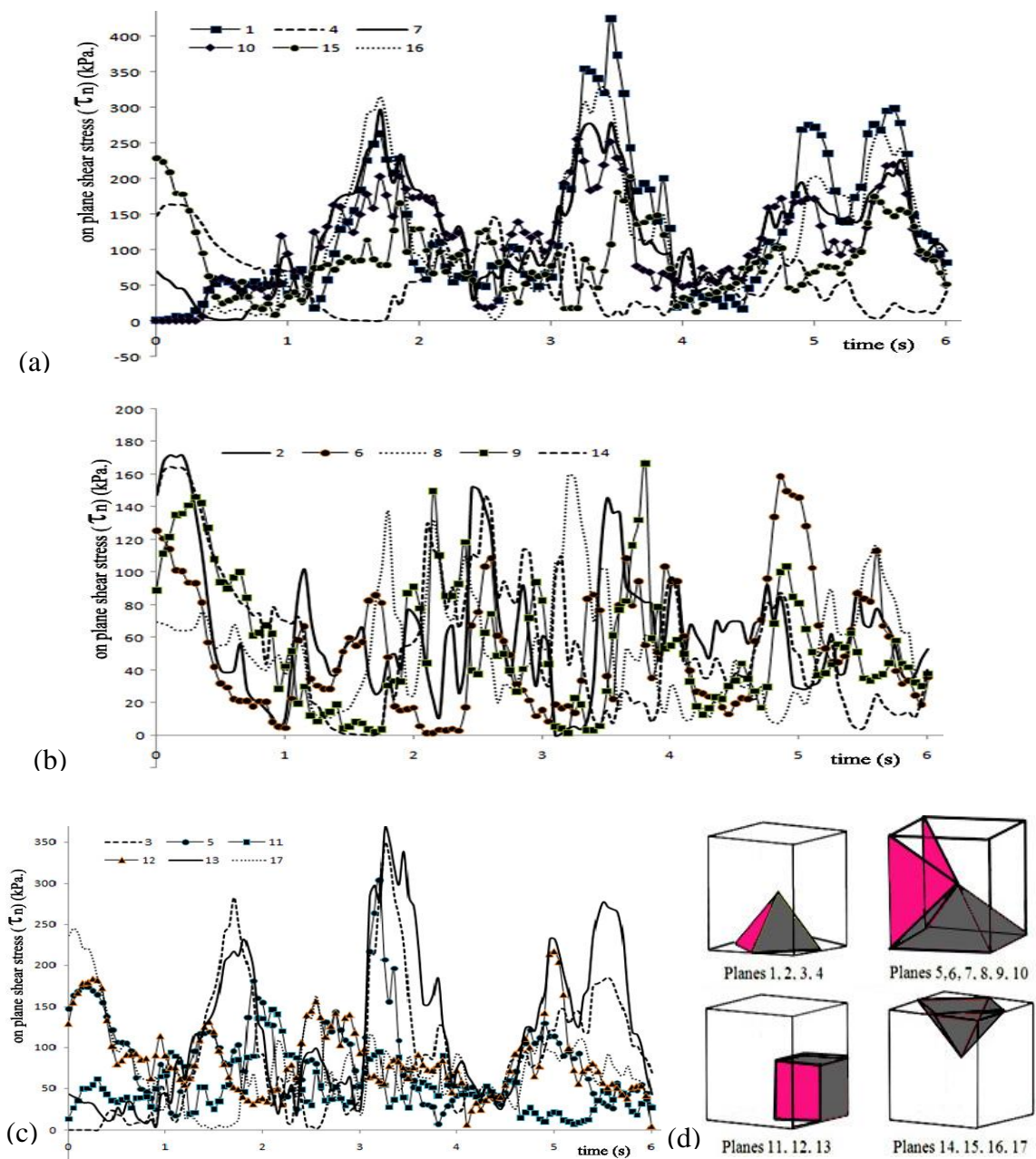


Figure 5-a to -c shows on plane shear stress during 6 seconds, d) the failed planes

To configure a continuous failure surface, a push over all failed planes in different gauss points must be plotted. However, the activity and damage progressions of gauss points located along and across sheared zone reveal a physical crushed fissured in concrete face slab and also in supporting rock fill zone shear bands. Although, only a short period of 6 seconds duration of 120 seconds earthquake time history is considered in this example, severe damaged zones including very many damaged points including several failed planes detected that show a huge crushed zone in both concrete face and supporting rock fill.

6. CONCLUSIONS

This article sets out to present the main points of how to employ instrumentation recording data to analyze numerically detecting damaged zone and types in dam static/dynamic mode. Also, it has been revealed that since each dam and its foundations represent an individual case, it is essential that a dialogue be established between the designers of the structures and the instrumentation specialists, before a site's instrumentation is determined for possibility of accurate damage detection by the proposed model.

As a result of the considerable capability of the proposed damage detecting model, the equipment recording data involved undergoes constant study designed to improve its performance and improvements can be especially notable not only in the area of improved instruments but also in automatic data acquisition and related software. Current trends in the field of instrumentation and numerical modeling emphasize the search for higher resolution and precision, providing more accurate measurements and permitting rapid detection of any behavioral anomalies. Increasing the life of these instruments as well as dam safety through strict quality control is a constant concern, moreover, with special attention paid to protection against recording accuracy due to resolution and proper location of instruments. Finally, virtually no instrumentation and corresponding location is considered complete without automatic data acquisition and processing, which increases the reliability of the results, yields more detailed analyses, with alarm thresholds, and unquestionably enhances dam safety.

In closing, it should be recalled that dam monitoring and this kind of numerical analysis is a key component of dam safety. Because the failure of a dam can lead to human as well as economic disaster, no compromise in regards to instrumentation quality or reliability should be made.

7. REFERENCES

1. Chen Houqun, (2008), CONSIDERATION OF DAM SAFETY AFTER WENCHUAN EARTHQUAKE IN CHINA, 14th World Conference on Earthquake Engineering October 12-17, 2008, Beijing, China, China Institute of Water Resources and Hydropower Research, 20, West Chegongzhuang Rd., 100044 Beijing, China
2. ICOLD Committee on Seismic Aspects of Dam Design, (2006). Reservoir Triggered Seismicity-State of knowledge, ICOLD Bulletin, Paris.
3. Chinnarasri, T. T. (2001). Numerical modelling of dam failure due to flow overtopping. *Hydrological Sciences-Journal—des Sciences Hydrologiques*, 46(1) February.
4. Nemat-Nasser S and Mehrabadi M. (1983) Stress and fabric in granular masses, *Mechanics of granular Materials. New Models and Constitutive Relations* (Eds. JT Jenkins and M. Satake), 1-8. Elsevier Sci. Pub.
5. Sadrnejad S. A., (1992) Multilaminate elastoplastic model for granular media. *International Journal of Engineering* 5: 11.
6. Sadrnejad S.A., Shakeri, S., (2017), Multi-laminate non-coaxial modelling of anisotropic sand behavior through damage formulation, *Computers and Geotechnics* 88 (2017) 18–31
7. Sadrnejad S.A. and Labibzadeh M. (2006) A continuum/discontinuum micro plane damage model for concrete. *International Journal of Civil Engineering* 4: 296-313.
8. Vncold. (2008). Guidelines for Design High Concrete Face Rockfill Dam.
9. Zeping, X. (2009). Performance of Zipingpu CFRD during the strong earthquake. Retrieved 05 07, 2010, from Chinese national committee of large dams: <http://www.chincold.org.cn/newsview.asp?s=3226>
10. Zhang, B., Wang, J., & Shi, R. (2004). Time-dependent deformation in high concrete-faced rockfill dam.
11. Wieland, M., & Houqun, C. (2009). Lessons learnt from the Wenchuan earthquake. Retrieved June 26, 2011, from: <http://www.waterpowermagazine.com/graphic.asp?sc=2054099&seq=11>
12. Yang, H., Haynes, M., Winzenread, S., & Okada, K. The history of dams. Retrieved May 7, 2011, from: http://cee.engr.ucdavis.edu/faculty/lund/dams/Dam_History_Page/History.htm

Evaluation of Collapse Deformation Behavior of a Rockfill Material Using Large Scale Triaxial Tests

Ahmadreza Tabibnejad

Mahab Ghodss Consulting Engineering Co., Tehran 1918781185, Iran

Email: artabib@yahoo.com

Abstract

An experimental program including dry-saturated large-scale triaxial tests was conducted in order to investigate the effects of gradation curve and dry density on the saturation-induced collapse deformation behavior of a rockfill material. Two large scale triaxial equipments with three different sample diameters of 20, 30 and 80cm were employed and a set of dry-saturated tests were conducted. Specimens with different gradation curves and various initial dry densities were tested. The results indicate that in all of the dry-saturated tests, sudden reductions in the shear strengths and volumes of the specimens were observed during the submerging process. The effects of material maximum particle size, fines content and initial dry density on the value of sudden shear strength reduction, internal friction angle reduction caused by saturation ($\Delta\phi_c$), the change in elasticity modulus of the material due to submerging, i.e., (E_{wet}/E_{dry}), and also the saturation-induced sudden volumetric strain (Δv_c) were evaluated and discussed. Based on the results of dry-saturated tests, the intensity of collapse deformation behavior of the rockfill material increases as the material maximum particle size and fines content increases. However, increasing the initial dry density of the material decreases the intensity of collapse deformation phenomenon.

Keywords: Rockfill, Collapse Deformation, Large Scale Triaxial Test.

1. INTRODUCTION

The extensive application of rockfill materials in geotechnical structures, specially in rockfill dams during recent decades, makes the precise recognition of different aspects of the behavior of these materials ineluctable. Rockfill material such as other coarse grained materials undergoes rapid or sudden settlements, that could have relatively large values, without any changes in the applied loads and only because of submerging (or wetting) ([1],[2],[3],[4],[5],[6]). This phenomenon is called collapse deformation ([2],[7]). Intensification of particle breakage and crack propagation, particles rearrangement and facilitation of particles displacement because of lubrication effects of water are among major events that were found responsible for this phenomenon ([8],[9],[10]).

Rapid settlements caused by saturation that are reported in the literature for different rockfill dams and also for other rockfill embankments (such as railway embankments), are the main examples of this phenomenon ([2],[7],[11]). This event is frequently reported in the upstream shell of rockfill dams during first impounding of the reservoir or in other rockfill structures because of heavy rains ([12],[13],[14]). Although some valuable investigations have been carried out to recognize the principles and mechanism of collapse deformation, some aspects of this phenomenon are still unknown.

Because of the large size of the particles, testing of the prototype rockfill materials is almost impossible and the grain sizes are usually scaled down for laboratory testing. However, since the scaled materials are still relatively coarse grained, large scale laboratory tests such as triaxial, direct shear and odometer tests have been employed for studying the behavior of rockfill materials ([15],[16],[17],[18],[19]). However because the large scale laboratory tests are usually expensive and difficult to perform the number of these researches are relatively limited.

Due to the quarry properties and the mineralogy of the rockfill materials and also because of technical considerations, the materials could have different gradation curve envelopes. In addition, various rockfill structures were constructed with different dry densities of rockfill materials. therefore, evaluation of the effects of grain size distribution curve and the initial dry density of the rockfill materials on the pattern and intensity of the saturation-induced collapse deformations could be useful.

The main purpose of this study is to evaluate the effects of gradation curve and initial dry density on the collapse settlement behavior of rockfill materials and to determine the changes in the strength and deformability parameters of this material caused by submerging. To this end, two large scale triaxial equipments with different sample diameters were employed and a set of dry-saturated tests were conducted on

the specimens of a rockfill material. In these dry-saturated tests, the specimens were first sheared (in dry conditions) up to a specified shear stress level; then the axial loading was stopped, the specimen was gradually and fully submerged with de-aired water and then axial loading was continued until the failure of the specimen. The effect of materials gradation curve was evaluated by testing specimens with three different material fines contents (percent passing #200 sieve) and three maximum particle sizes. Testing materials with different maximum particle sizes could be helpful in exploring the effects of unavoidable scaling down of the particle sizes that should be performed when the laboratory tests are used to estimate the behavior of prototype rockfill materials. Moreover, three different initial dry densities were used for reconstitution of the specimens in order to probe the influence of the materials dry density. Finally the results of the tests were analyzed and interpreted to study the effects of these factors on the collapse settlement behavior of the rockfill materials.

2. EXPERIMENTAL PROGRAM

Two large scale triaxial apparatuses with maximum sample diameters of 800mm and 300mm were used in this study. The smaller equipment was used for testing specimens with diameters of 200mm and 300mm. The samples were sheared strain-controlled by the moving down of the top cap at a constant rate. LVDT sensors were used to measure the vertical displacement of the samples. Vertical load was also measured by means of sensors installed inside and outside the cell.

In this study rockfill material were obtained from the shell borrow area of a rockfill dam. Characteristics of the material along with the standards employed for their determination are presented in table 1.

Table 1: Rockfill Material Characteristics

Mineralogy	Shape	Water Absorption	Gs	Los Angeles Abrasion (500 cycles)
Limestone	Subrounded to Subangular	1% ASTM (C127-128)	2.7 ASTM (C127-128)	28% ASTM (C131)

The prototype rockfill material has a maximum particle size of 700 mm. It is obvious that testing the prototype material was almost impossible because of its coarseness and the limitations of the triaxial cell dimensions. Therefore, the material particle sizes for laboratory test specimens were scaled down by some degrees. The ratio of specimen diameter to material maximum particle size was selected to be about six or less. Specimens with three diameters of 200mm, 300mm and 800mm were used and the maximum particle sizes of the testing materials were selected equal to 19.1mm, 50mm and 150mm respectively. Gradation curves of these materials are shown in figure 1a; these materials have a fine content (percent passing #200 sieve) of 8%. Materials with three fines contents of 2, 8 and 15% were also tested. Fines content is defined as the percent (by weight) of the material passing sieve # 200. Gradation curves of these materials are illustrated in figure 1b; these materials have a maximum particle size of 50mm.

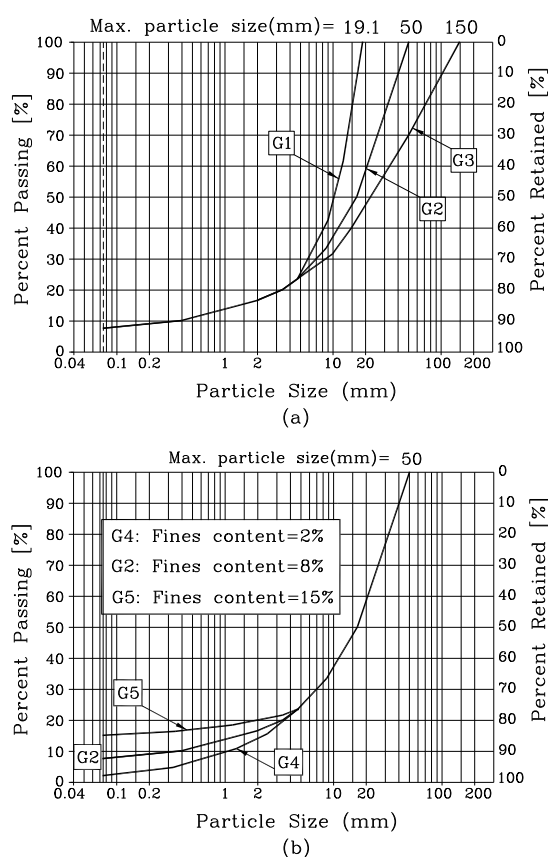


Figure 1. Gradation curve of testing materials a) Different maximum particle sizes b) Different fines contents

3. TESTING PROCEDURE

In order to prepare specimens with specified dry densities and gradation curves, the quantity of various sizes of the material was determined by weight. The individual fractions were mixed thoroughly in order to achieve a more homogenous sample. The produced material was compacted in six layers in accordance with the ASTM D7181 proposed "tamping method" to achieve the required density. The strain-controlled axial loading of the specimens was applied with a rate of 1mm/min based on the method proposed by the same standard (ASTM D7181) because of the relatively high permeability of the tested material.

The experimental program consisted of twenty-four large scale strain-controlled triaxial tests that were conducted on the specimens with diameters of 200, 300 and 800mm in three confining pressures of 100, 500 and 1000 kPa. In the dry-saturated tests, the specimens were first sheared (in dry condition) up to a specified shear stress level, then the axial loading (monotonic movement of the top cap) was stopped, the specimen was gradually and fully submerged from bottom to the top under very low head of de-aired water and then axial loading was continued.

Shear stress level (SSL) is defined by the ratio of shear stress at the moment of saturation to the maximum shear strength of the specimen in dry condition. According to the current design criteria of rockfill embankments, the minimum allowable safety factor for long-term stability of rockfill slopes in static loading conditions is around 1.5. Therefore the shear stress level that regarding to its definition could be considered as the inverse of the safety factor (at the moment of saturation) was selected equal to 0.7 ($\cong 1/1.5$). This shear stress level could represent the static stability conditions of properly designed slopes before getting submerged. Each specimen was first sheared in dry condition to determine its maximum shear strength required for performing tests in SSL of 0.7. As mentioned before, two series of tests were conducted in order to explore the effects of fines content and dry density. In these two series, the specimens were submerged in two shear stress levels (SSL) of 0.7 and 1.0. Table 2 shows the experimental program of this study.

Table 2- Experimental program

Test series name & purposes	Name of Gradation curve	Specimen Diameter (mm)	Max. Particle Size (mm)	Dry Density (gr/cm ³)	Fines Content (%)	Confining Pressure (kPa)	SSL	Test Name	
Series A: Effect of maximum particle size	G1	200	19.1	2.15	8	100	Dry	100D-DI200	
							0.7	100D0.7S-DI200	
							1000	Dry	1000D-DI200
								0.7	1000D0.7S-DI200
							100	Dry	100D-DI300
								0.7	100D0.7S-DI300
	G2	300	50			100	Dry	100D-DI300	
							0.7	100D0.7S-DI300	
						1000	Dry	1000D-DI300	
							0.7	1000D0.7S-DI300	
						100	Dry	100D-DI800	
							0.7	100D0.7S-DI800	
1000	Dry	1000D-DI800							
	0.7	1000D0.7S-DI800							
Series B: Effect of fines content	G4	300	50	2.15	500	500	1.0	500D1.0S-F2	
							0.7	500D0.7S-F2	
	G2						1.0	500D1.0S-F8	
							0.7	500D0.7S-F8	
	G5						1.0	500D1.0S-F15	
							0.7	500D0.7S-F15	
Series C: Effect of dry density	G2	300	50	2.15	8	500	1.0	500D1.0S-DD1.7	
							0.7	500D0.7S-DD1.7	
							1.0	500D1.0S-DD1.9	
							0.7	500D0.7S-DD1.9	
							1.0	500D1.0S-DD2.15	
							0.7	500D0.7S-DD2.15	

4. RESULTS

4.1. STRESS-STRAIN BEHAVIOR

Figures 2 and 3 present the axial stress-axial strain and the volumetric strain-axial strain behavior of the tests of series A. Figures 4 and 5 indicates the axial stress-axial strain and the volumetric strain-axial strain behavior of the tests of series B and C respectively. In these figures the first number (three to four digits) represents the confining pressure value in kPa, “D” stands for dry condition, “S” refers to saturated condition and the number between “D” and “S” represents the shear stress level in which the specimen was submerged. The last part coming after “S” in series A is the specimen diameter in millimeters (that comes along with DI), in series B it is the material fines content in percent (coming along with F) and in series C it is the dry density in gr/cm³ (that comes along with DD). In these figures the dilation is considered positive.

For each confining pressure first the maximum shear strength of the material (in dry condition) was identified by performing tests in dry condition or by conducting dry-saturated tests at the shear stress level (SSL) of 1.0. Then the other d-s tests were conducted at the shear stress level of 0.7, i.e., specimens were submerged in 70% of their identified maximum dry shear strength.

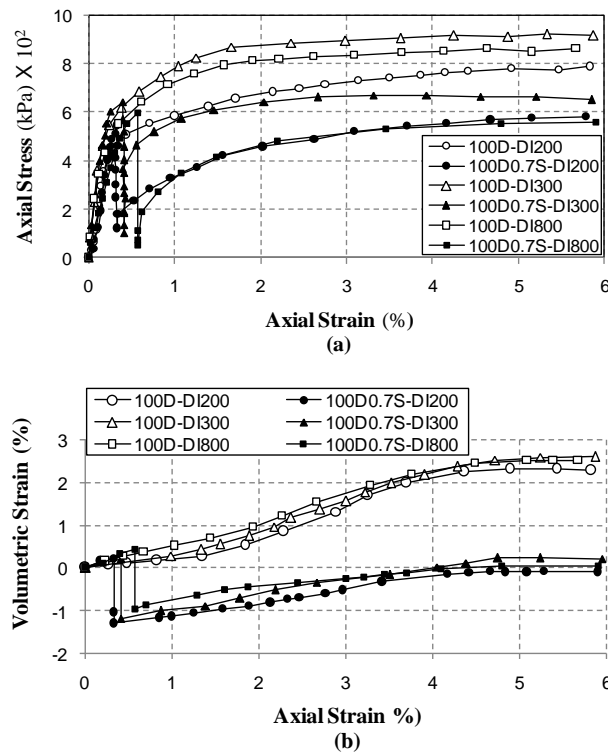


Figure 2. a) Axial stress-axial strain b) volumetric strain-axial strain behavior of series A tests performed in confining pressure of 100 kPa, Effect of materials maximum particle size

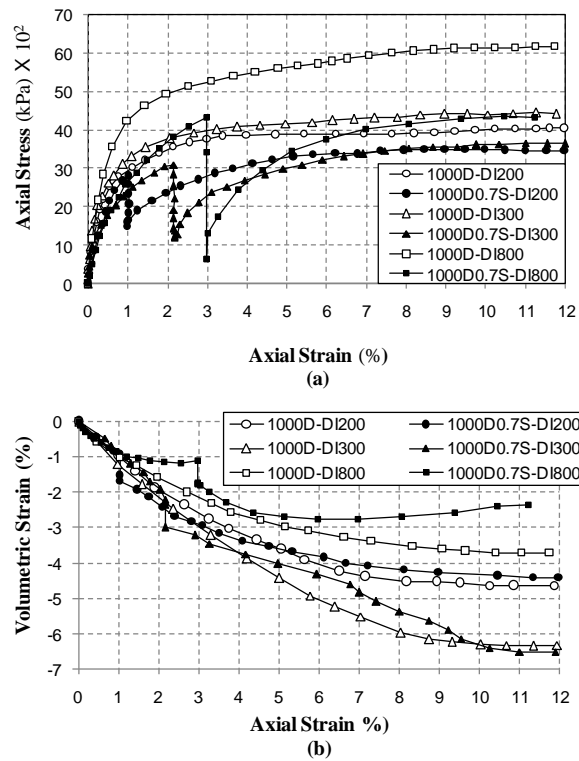


Figure 3. a) Axial stress-axial strain b) volumetric strain-axial strain behavior of series A tests performed in confining pressure of 1000 kPa, Effect of materials maximum particle size

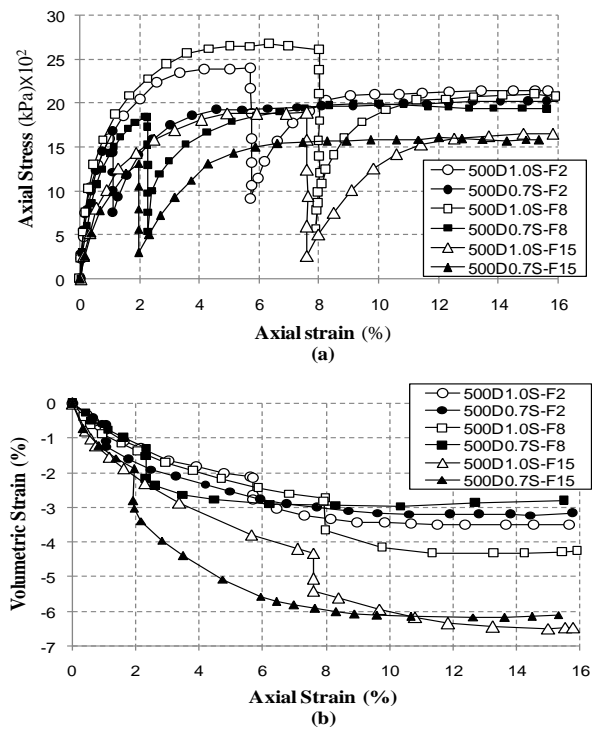


Figure 4. a) Axial stress-axial strain b) volumetric strain-axial strain behavior of series B tests, Effect of materials fines content

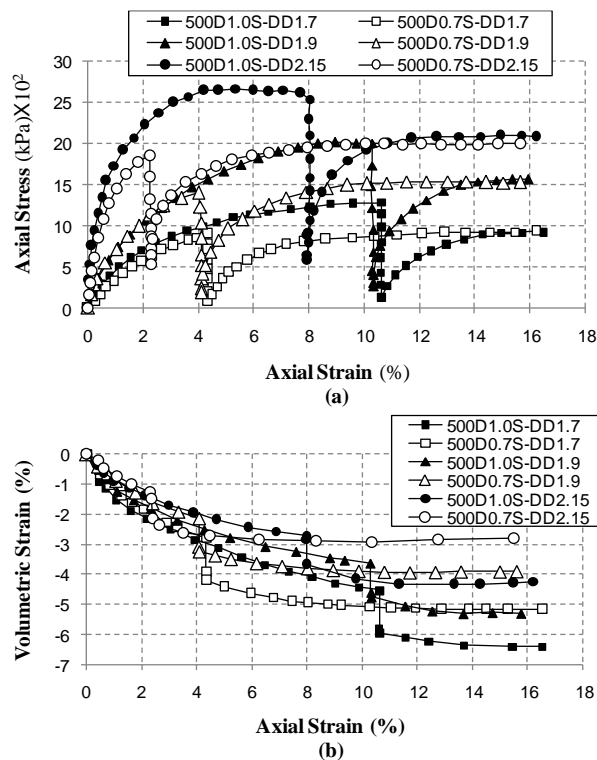


Figure 5. a) Axial stress-axial strain b) volumetric strain-axial strain behavior of series C tests, Effect of initial dry density

As seen in figures 2 to 5, in all of the dry-saturated tests saturation caused a sudden reduction of axial stress (representing shear strength of the specimens) in a constant axial strain. These behaviors were expected ([20], [21]); however, one of the purposes of this study was to estimate the value of this reduction and to find

out its dependence (if any) to the fines content, maximum particle size and initial dry density of the material. When the specimens were completely submerged with water, the axial stress reached its minimum value and remained constant. Then the monotonic movement of the top cap restarted and the axial stress increased to a maximum value and stayed approximately constant to the end of the test.

The ratio of the minimum axial strength (deviatoric stress) of a submerged specimen at the end of the saturation process to the shear strength of the specimen before saturation is defined as the coefficient of stress recovery, C_{sr} and referring to figure 6, could be calculated by the following equation.

$$C_{sr} = \frac{\sigma_{d2}}{\sigma_{d1}} \tag{1}$$

Where σ_{d1} and σ_{d2} represent the deviatoric stresses before saturation and at the end of saturation process, respectively.

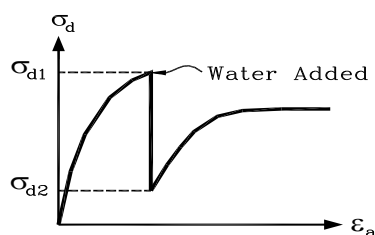


Figure 6. Typical behavior of dry-saturated specimens

The values of C_{sr} were calculated for all of the dry-saturated tests by applying equation 1. Figure 7 presents the variation of C_{sr} values versus materials maximum particle size (obtained from series A tests).

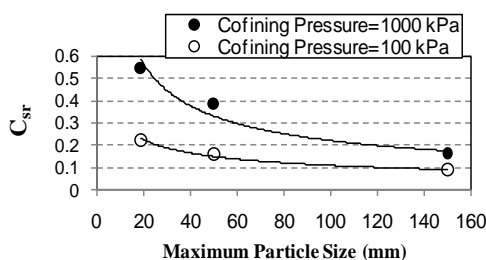


Fig 7. Coefficient of stress recovery (C_{sr}) versus materials maximum particle size

Figure 7 shows that by increasing materials maximum particle size the coefficient of stress recovery (C_{sr}) decreases by a decreasing rate. This evidences that performing laboratory tests on the materials with limited particle sizes may underestimate the intensity of saturation-induced stress relaxation of the prototype materials. However greater accuracy may be achieved by employing large scale equipments with larger sample diameters (bigger maximum particle sizes). In the tests performed on the initially dry specimens in a specific dry density (and therefore in a constant void ratio), when the maximum particle size of the material increases or, in the other words, as the gravelly part of the material becomes coarser, the sizes of the solid particles and also the sizes of the voids increase. Therefore, the number of the contact points between rockfill particles per unit area decreases and accordingly the stress values at these contact points increase. This stress concentration could intensify the above-mentioned events that were found responsible for the collapse deformation phenomenon. Also according to figure 7, in a specified maximum particle size the tests performed in confining pressure of 1000 kPa show higher values of C_{sr} compared to the tests conducted in the confining pressure of 100 kPa. This was expected since the materials that experienced higher confining pressures become denser and more compressed before wetting. Therefore, during submerging the specimens tested in higher confining pressures will undergo smaller values of deformation and so their stress relaxation will be smaller.

The variation of C_{sr} values against materials fines content (obtained from series B tests) is presented in figure 8. Here increasing materials fines content decreases the coefficient of stress recovery (C_{sr}) at a decreasing rate. Also it could be seen that the value of shear stress level (SSL) in the moment of saturation does not have a significant effect on the variation of (C_{sr}).

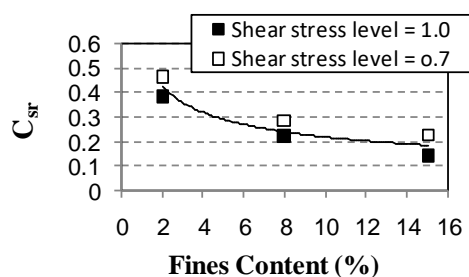


Figure 8. Coefficient of stress recovery (C_{sr}) versus materials fines content

Plots of C_{sr} values versus initial dry density of the material (obtained from series C tests) are shown in figure 9. The coefficient of stress recovery (C_{sr}) increases as the initial dry density of the material increases. This could be explained considering the fact that the materials with higher values of dry density are denser, less deformable and therefore will undergo smaller values of strength sudden reduction caused by saturation. Figure 9 also indicates that the value of shear stress level (SSL) in the moment of saturation does not have a meaningful effect on the values of (C_{sr}) and the results obtained for two shear stress levels of 1.0 and 0.7 are pretty close to each other.

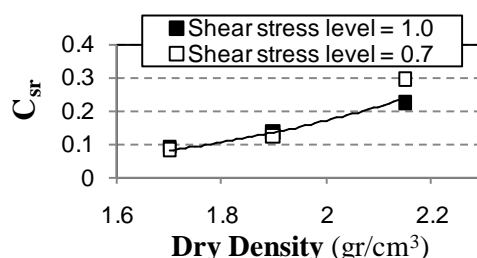


Figure 9. Coefficient of stress recovery (C_{sr}) versus initial dry density

Making acceptable estimations of the values of collapse deformation of rockfill materials requires the development of a precise numerical modeling of this phenomenon ([22], [23]). Since the explained results were obtained using a limited number of tests for specific materials and for particular stress range applied in this study, therefore no equations are presented for the variations of C_{sr} against the aforementioned parameters. Nevertheless, finding out and using the C_{sr} coefficient could be an applicable approach to estimating the post saturation shear stresses, *e.g.* in a numerical analysis to specify the values of shear stresses in the elements one cycle after submerging.

4.2. INTERNAL FRICTION ANGLE

According to the literature saturation degrades the strength parameters of rockfill materials ([1],[4],[24],[25]). The results of dry-saturated tests were analyzed to probe the effects of materials maximum particle size, fines content and initial dry density on the intensity of this degradation. Figure 11 shows that the internal friction angles of the specimens in dry condition decrease when the materials become saturated.

Based on the results (figures 2a to 5a) for each specimen values of the maximum principle stresses, *i.e.* σ_1 , could be obtained in dry condition. Therefore, considering no cohesion for the rockfill material the values of internal friction angles of the specimens in dry condition for each confining pressure are calculated. On the other hand, in dry-saturated tests and after submerging, for each confining pressure the final maximum shear strengths, the related values of σ_1 and therefore the internal friction angles of the specimens in saturated condition could be specified. Then the values of the reductions of the internal friction angles ($\Delta\phi_c$) due to saturation could be calculated for each specimen. Variation of these reductions (values of $\Delta\phi_c$) versus materials maximum particle size, fines content and initial dry density are presented in figures 10a to 10c, respectively.

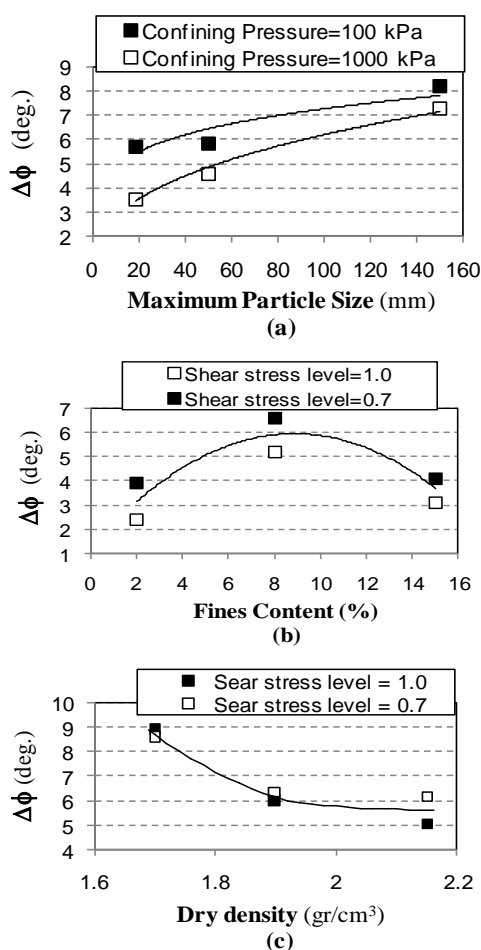


Figure 10. Reduction of internal friction angle due to saturation ($\square\square_c$), a) versus material maximum particle size, b) versus fines content, c) versus initial dry density

Figure 10a indicates that the values of $\square\square_c$ (reduction of the internal friction angle caused by saturation) increase as the material maximum particle size increases. The explanation for the variation of C_{sr} against maximum particle size offered above could also be applied here. It is also clear that the values of $\square\square_c$ for tests performed in confining pressure of 1000 kPa are smaller than those obtained from tests carried out in confining pressure of 100 kPa. However, the values of $\square\square_c$ obtained from tests performed in confining pressures of 100 kPa and 1000 kPa get closer to each other as the material maximum particle size increases.

According to figure 10b, increasing the material fines content from 2% to 8% increases the value of $\square\square_c$ however more increase of the fines content from 8% to 15% decreases the value of $\square\square_c$. therefore the values of $\square\square_c$ for fines contents of 2% and 15% are pretty close to each other. Meanwhile the value of shear stress level (SSL) in the moment of saturation does not have a significant effect on the value of $\square\square_c$.

Figure 10c indicates that increasing the initial dry density of the materials decreases the values of $\square\square_c$ by a decreasing rate. This was expected because the materials with smaller initial dry densities are looser and will undergo more degradation of strength parameters due to submerging. However, the value of shear stress level (SSL) does not have a meaningful effect on the value of $\square\square_c$.

4.3. DEFORMATION BEHAVIOR AND PARAMETERS

Turning to figures 2b to 5b, it can be seen that in comparatively low confining pressure of 100 kPa (related to series A tests with initial dry density of 2.15 gr/cm³) dilation governs the deformation behavior of the material and a general trend of volume increase (positive values of volumetric strain) is observed during deviatoric loading due to relatively high dry density of the specimens. As confining pressure increases to higher values (*i.e.* 500 and 1000 kPa) the volume of the specimens decreases during deviatoric loading and the effect of dilation is not considerable. Figures 2b to 5b also shows that during the submerging process a sudden reduction in the volume of the specimens was observed in all of the dry-saturated tests (in a constant axial strain). This

observation is compatible with the saturation-induced sudden settlements reported in the literature for odometer or direct shear tests on rockfill materials ([1], [3], [26]).

In order to evaluate the changes in the deformation parameters of the materials due to saturation, elasticity modulus of the specimens in dry condition and after submerging are specified. The initial elasticity modulus of the specimens in dry condition (E_{dry}) and the elasticity modulus of the material after submerging (E_{wet}) are calculated considering the axial stress-axial strain curves ($\sigma_a-\epsilon_a$) obtained from the triaxial tests ([27]). The ratios of the elasticity modulus of the material after saturation to their elasticity modulus in dry condition, *i.e.*, (E_{wet}/E_{dry}), are calculated and the variation of this ratio (E_{wet}/E_{dry}) versus materials maximum particle size, fines content and initial dry density are illustrated in figures 11a to 11c, respectively.

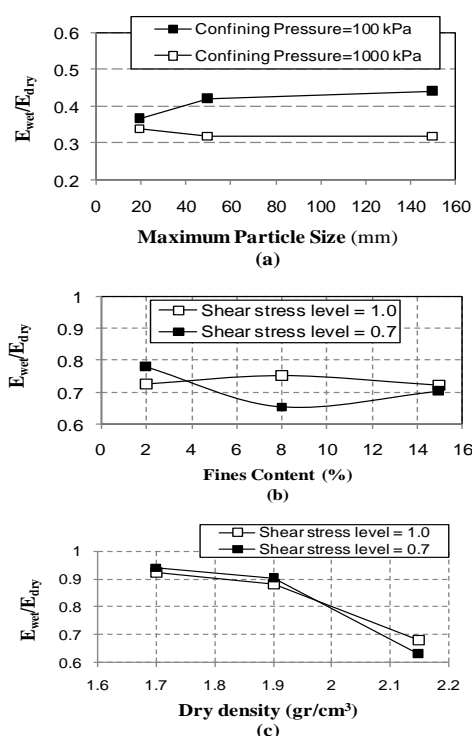


Fig. 11 Ratio of the saturated to dry elasticity modulus of the material (E_{wet}/E_{dry}), a) versus material maximum particle size, b) versus fines content, c) versus initial dry density

These figures show that the ratio of E_{wet}/E_{dry} is not affected by the material fines content and there is also no clear trend for the variation of this ratio (E_{wet}/E_{dry}) against material maximum particle size. However, the ratio of E_{wet}/E_{dry} decreases as the initial dry density increases. For the specimens with relatively low dry densities the material is initially loose and it has a relatively low value of elasticity modulus before submerging. Therefore, saturation could not cause a major reduction on its initially low elasticity modulus. So that the ratio of E_{wet}/E_{dry} increases to more than 0.9 for the materials with the dry density of 1.7 gr/cm³ (figure 11c of series C tests).

5. CONCLUSIONS

A set of large-scale triaxial tests have been conducted to investigate the saturation-induced collapse settlement behavior of a rockfill material. Specimens were tested in dry-saturated conditions with three different material fines contents (percent passing #200 sieve), three maximum particle sizes and three different initial dry densities. The effects of gradation curve and initial dry density on the collapse settlement behavior of rockfill material were explored and the changes in the strength and deformability parameters of these materials caused by submerging were evaluated.

According to the results of all of the dry-saturated tests a sudden reduction of axial stress (representing shear strength of the specimens) in a constant axial strain was observed due to saturation.

The ratio of the minimum axial strength (deviatoric stress) of a submerged specimen (at the end of the saturation process) to the shear strength of the specimen before saturation is defined as coefficient of stress

recovery, C_{sr} . Results of dry-saturated tests showed that increasing materials maximum particle size decreases the coefficient of stress recovery (C_{sr}) by a decreasing rate. This evidences that performing laboratory tests on the materials with limited particle sizes may underestimate the intensity of saturation induced stress relaxation of the prototype materials. However, the value of this underestimation will reduce when large scale equipments with larger sample diameters (bigger maximum particle sizes) are employed. Based on the results, as the materials fines content increases, the coefficient of stress recovery (C_{sr}) decreases by a decreasing rate. In addition, the coefficient of stress recovery (C_{sr}) increases as the initial dry density of the material increases. Also it is obvious that the value of shear stress level (SSL) in the moment of saturation does not have a considerable effect on the variation of C_{sr} .

The results indicated that saturation degrades the strength and deformability parameters of the rockfill material. Results of dry-saturated tests showed that the values of internal friction angle reduction caused by saturation (ϕ_c) increase as the material maximum particle size increases. Furthermore, increasing the material fines content from 2% to 8% increases the values of ϕ_c however then decreases as the material fines content increases from 8 to 15%. In addition, as the initial dry density of the material increases, the values of ϕ_c decrease by a decreasing rate.

The results indicated that the ratios of the elasticity modulus of the material after saturation to their elasticity modulus in dry condition, *i.e.*, E_{wet}/E_{dry} , decreases as the initial dry density increases; however, the values of this ratio are not affected by the material fines content and there is also no clear trend for variation of this ratio (E_{wet}/E_{dry}) against material maximum particle size.

In all of the dry-saturated tests a sudden reduction in the volume of the specimens was observed during the submerging process (in a constant axial strain). This observation is compatible with the saturation induced sudden settlements reported in the literature for oedometer or direct shear tests on rockfill materials.

6. ACKNOWLEDGMENT

The tests with sample diameter of 80 cm were conducted in the Soil and Rock Mechanics Institute of the University of Karlsruhe, Germany. The authors are thankful to the Institute staff. The rest of the tests were performed at the laboratory of the geotechnical department of Road, Housing & Urban Development Research Center of Iran. The authors are grateful to Dr. A. Aghaee and Mr. H. Hasani (the laboratory staff) for their useful comments and help in conducting the tests.

7. REFERENCES

1. Alonso E., (2003), "*Exploring the limits of unsaturated soil mechanics: The behavior of coarse granular soil and rockfill*", The 11th Spencer J. Buchanan lecture, College station Hilton.
2. Alonso E., Cardoso R., (2009), "*Behavior of materials for earth and rockfill dams: Perspective from unsaturated soil mechanics*", The 2nd International Conference of long term behavior of dams, Austria.
3. Alonso E., Oldecop L. A., (2000), "*Fundamentals of rockfill collapse*", Unsaturated soils for Asia, (Toll & Leong, Eds), Balkema, Rotterdam, 3-12.
4. Soroush A., Aghaei Araei A., (2006), "*Analysis of behavior of a high rockfill dam*", Proceeding of the institution of civil engineering , Geotechnical engineering, 159(GEI), pp. 49-59.
5. Charles J. A., (2008), "*The engineering behavior of fill materials: the use, misuse and disuse of case histories*", *Geotechnique* 58, No. 7, pp. 541-570, DOI:10.1680/geot.2008.58.7.541.
6. Xu M., Song E. and Cao G. (2009), "*Compressibility of broken rock-fine grain soil mixture*", *Geomechanics and Engineering*, 1(2), 169-178.
7. Oldecop L. A., Alonso E., (2007), "*Theoretical investigation of the time-dependent behavior of rockfill*", *Geotechnique* 57, No. 3, pp. 289-301, DOI:10.1680/geot.2007.57.3.289.
8. Soroush A., Aghaei Araei A., (2005), "*Uncertainties in mechanical behavior of rockfills during first impounding of rockfill dams*", The 73rd Annual meeting of ICLOD, Teheran, Iran, Paper No. 186-S5.
9. Silvani C., Bonelli S., Philippe P., Desoyer T., (2008), "*Buoyancy and local friction effects on rockfill settlement: A discrete modeling*", *Journal of computers and mathematics with applications*, 55, pp. 208-217, DIO:10.1016/j.camwa.2007.04.011.

10. Houston S. L., Houston W. N., Zapata C. E., Lawrence C., (2001), "*Geotechnical engineering practice for collapsible soils*", Journal of Geotechnical and Geological Engineering, 19, pp. 333-355, DOI: 10.1023/A:1013178226615.
11. Tabibnejad A.R., Mahin Roosta R., (2011), "*Evaluation of Marun Rockfill dam behavior during the construction and operation period using instrumentation system data*", Modares Civil Engineering Journal (M.C.E.L), Vol.11, No.1, pp. 99-115.
12. Ohta H., Ishiguro T., Mori Y., Uchita Y., Tsuruta S., Takahashi A., (2005), "*Uncertainties in safety evaluation of large rockfill dams during first filling*", The 73rd Annual meeting of ICLOD, Tehan, Iran, Paper No. 082-S5.
13. Touileb B. N., Bonelli S., Anthiniac P., Carrere A., Debordes O., LA Berbera G., Bani a. and Mazza G., (2000), "*Settlement by wetting of the upstream rockfills of large dams*", Proc. Of the 53rd Canadian Geotechnical Conf., Montreal, pp. 263-270.
14. Soriano A. and Sanchez F. J. (1999), "*Settlement of railroad high embankment*" Proc. 12th Eur. Conf. Soil Meck. Geotech. Engng., Amsterdam, pp. 1885-1890.
15. Varadarajan, A., Sharma, K., Venkatachalam, K. and Gupta, A. (2003), "*Testing and Modeling Two Rockfill Materials*" J. Geotech. Geoenviron. Eng., 129(3), 206–218, DOI:10.1061/(ASCE)1090-0241(2003)129:3(206).
16. Eshtaghi V., Mahin roosta R., (2010), "*Changes in the stress and strain conditions of dry gravelly material caused by saturation*", Proc., 4th Int. Conference of Soil Mechanics and Geotechnical Engineering of Iran, Tehran, Iran, Paper No. & Code: 190-TVTMAH.
17. Indraratna B., Ionescu D. and Christie H. D., "*Shear behavior of railway ballast based on large-scale triaxial tests*", Journal of Geotechnical and Geoenvironmental Engineering., 124(5)(1998), pp. 439-449, DOI:10.1061/(ASCE)1090-0241(1998)124:5(439).
18. Aghaei Araei, A., Razeghi, H., Ghalandarzadeh, A., and Hashemi Tabatabaei, S. (2012). "*Effects of loading rate and initial stress state on stress–strain behavior of rock fill materials under monotonic and cyclic loading conditions*" Scientia Iranica, 19(5), 1220-1235. DOI:10.1016/j.scient.2012.08.002.
19. Aghamajidi M., (2004), "*Laboratory investigation of creep in rockfill Material*", MSc thesis, Tarbiat Modarres University, Tehran, Iran, (in Persian).
20. Naylor D. J., Maranha Das Neves E., Mattar D., Veiga Pinto A. A., (1986), "*Prediction of construction performance of Beliche dam*", *Geotechnique* 36, No. 3, pp. 359-376, DOI:10.1680/geot.1986.36.3.359.
21. Pourjafar A., Mahin roosta R., (2011), "*Evaluation of the collapse settlement behavior of sandy material using triaxial shear tests*", Proc., 6th National Congress of Civil Engineering, Semnan, Iran.
22. Naylor D. J., Maranha Das Neves E., Veiga Pinto A. A., (1997), "*A back analysis of Beliche dam*", *Geotechnique* 47, No. 2, 221-233, DOI:10.1680/geot.1997.47.2.221.
23. Escuder I., Andreu J., Rechea M., (2005), "*An analysis of stress-strain behaviour and wetting effects on quarried rock shells*", Canadian Geotechnical Journal, 42, pp. 51-60, DOI:10.1139/t04-071.
24. Salehi D., Tabibnejad A.R., Feizi Khankandi S., (2008), "*Evaluation of strength and deformability parameters of the rockfill shell material of Gotvand dam*", Proc., 2nd National Conference on Dam and Hydropower (NCDH), Tehan, Iran, pp. 77-86.
25. Xu M., Song, E. and Chen J. (2012), "*A large triaxial investigation of the stress-path-dependent behavior of compacted rockfill*" Acta Geotechnica, 7(3), 167-175, DOI:10.1007/s11440-012-0160-0.
26. Asadzadeh M., Soroush A., (2009), "*Direct shear testing on a rockfill material*", The Arabian Journal for Science and Engineering, Vol. 34, Number 2B, pp. 379-396.
27. Duncan J. M., Chang C-Y., (1970), "*Nonlinear Analysis of stress and strain in soils*", Journal of the soil mechanics and foundations division, ASCE, Vol. 96, No. SM5, Proc. Paper 7513, September, 1970, pp. 1629-1653.

Study of Hydraulic Characteristics of Large Dam's Spillway (Case Study: Zola Dam Spillway)

Mohammad Manafpour¹, Sevda Kafshdooz Salimy²

1- Assistant Professor of Civil Engineering Department, Urmia University, Urmia, Iran

2- Ph.D. Student of Civil Engineering- Hydraulic Structures, Urmia University, Urmia, Iran

Email: Sevda.salimy@yahoo.com

Abstract

In the past century, various types of the large dams were built on rivers in order to control the water surface flows and supply water needed for domestic, agriculture, industrial sectors, hydroelectric power plants and also for flood control purposes. One of the important hydraulic structures related to this type dam is spillway which plays a key role to discharge safely the flood flow to the downstream of dam without causing any damage to the dam structure; therefore, in large dam's spillway considering the formation of turbulent flow, assessing the pressure and velocity is important. In order to optimize the geometry of spillways, the study of hydraulic performance and pattern of flow past spillways, longitudinal water surface profile is necessary. In the present research, the pattern and characteristics of flow over Zola Dam spillway as a case study are numerically investigated using FLUENT software k-epsilon RNG turbulent model and multi-phase. The VOF method is applied to simulate the free surface flow. The numerical model was verified using physical model results. Comparison of the results of the numerical model with those of the physical model indicates that the numerical model is able to appropriately predict the air-water flow pattern as well as velocity and pressure fields.

Keywords: Spillway, Hydraulic Behavior, Two Phase Flow, Numerical Model, FLUENT.

1. INTRODUCTION

A study on the flow through the hydraulic structures is usually conducted using physical modeling. Physical modeling is based on the basic fluid mechanic equations. Physical modeling of hydraulic structures means that a scaled laboratory model of the prototype is constructed. This approach is a safe way to analyze the flow through or over the hydraulic structures [1]. The spillway is one of the most important hydraulic structures in the hydropower project to ensure the safety of hydraulic structures during the flood. Spillways is a structure which discharges excess water form maximum water level avoiding damage to the dam and its facilities. So the spillway must be carefully designed to verify the flow characteristics [2]. To better understand the flow characteristic, it is recommended to study the pressure and velocity pattern of the flow.

Study of the flow pattern by means of physical models needs time and expense. In recent years due to the development of advanced techniques and accurate software, it is desirable to reduce the cost via numerical models.

Many researches have studied the flow pattern of different types of spillways, for example Zhan et al., Kositgittiwong et al. and Xiangju et al. studied the characteristics of flow over stepped spillways by numerical models [3, 4, 5]. Dargahi investigated flow field over an over-flow spillway and simulated the flow by a three-dimensional (3D) numerical model [6]. Varjavand studied flow pattern over a side spillway.

There are few articles about flow patterns in the ogee and chute spillway. The main purpose of this study was to justify the methodology adopted in ANSYS FLUENT via comparing water surface elevation in physical and simulated model, and also to assess the pressure and velocity in two phase air-water flow.

2. METHODOLOGY

Computational fluid dynamic (CFD) is an advanced numerical approach used along the physical modeling for modeling the hydraulic phenomena. Advances in high-performance computations and the development of computational fluid dynamics general-purpose software have made it possible to investigate the physical reliability of simulations of complex flows measured in reduced-scale models and prototype spillways [7]. The geometry of the spillway was built based on the original layout provided by Iran Water Research Institute. An appropriate meshing will be inserted to match the geometry and the simulation will be initialized

with experimental data. Accuracy and validation of the simulations will be carried out using the flow data received from physical model by Iran Water Research Institute.

2.1. CASE STUDY

Zola Dam located at 17 kilometers to Salmas in West Azarbayjan province. It is built on Zola Chay and supplies water needed for domestic, agriculture, industrial sectors, hydroelectric power plants and also for flood control purposes. Zola water basin area is about 945 square kilometers. It is an earthfill reservoir dam and its spillway includes an ogee and a chute. Characteristics of Zola dam are shown in Table 1.

Table 1 : Introduction to Zola Dam

Dam	River	Type	Latitude	Longitude	Width of ogee(m)	Effective storage volume (MCM)	Length of spillway (m)
Zola Dam	Zola Chay	Earthfill with clay core	59.99 '05 38°	00.01 '39 44°	40	72	225.2

2.2. PHYSICAL MODEL

Zola Hydraulic model of spillway is constructed in 1:25 scale. Most parts of the spillway including ogee, chute and stilling basin are made by Plexiglas. Guidance walls are made of wood. There are 183 piezometers in the bottom of the ogee, chute and stilling basin in three axes (center and side walls) to measure the pressure. Also 32 piezometers are located in the side walls of stilling basin to measure the static and dynamic pressure. Physical model of Zola dam is constructed by Iran Water Research Institute and is shown in Figure 1.



Figure 1: Physical Model Of Zola Dam

2.3. DESCRIPTION OF CFD MODEL

Geometric model is simulated by Gambit according to the data collected from West Azarbayjan Regional Water Authority, then the model was exported to Ansys Fluent 16.0 to model the hydraulic flow over the spillway.

In the present study, the diffusion terms are discretized using a second-order accurate central scheme, while the convective terms are discretized using the second-order upwind scheme. The momentum equation is

discretized with second order upwind method. Through turbulence closure models available in Fluent, the $k-\epsilon$ model was chosen because it was found to be the most robust model for different initial conditions [9].

The VOF model was chosen to model the free-surface water-air interface boundary. The VOF is a surface-capturing algorithm in which the interface between water and air is determined by solving an additional water volume fraction transport equation [10]. The model's upstream boundary was set on approach channel in relatively straight channel reaches about 40 m from the spillway ogee to ensure that the flow was not influenced by increasing the bed level. Similarly, the outlet boundary section was located at stilling basin to reduce the effect of omitting the rest of spillway.

The no-slip boundary condition is used. The type of inlet is set on Velocity Inlet boundary condition. The free surface boundary condition is specified as pressure inlet condition. The outlet condition is the pressure outlet condition, with the pressure set equal to atmospheric pressure.

Depending on the position of the cell, Quad meshes were used. The size of 0.15 m was used for the entire ogee and Pave meshes with different sizes (according to the turbulence of flow) in the rest of the spillway, approach channel and stilling basin. The calculation domain and boundary conditions are shown in Figure 2.

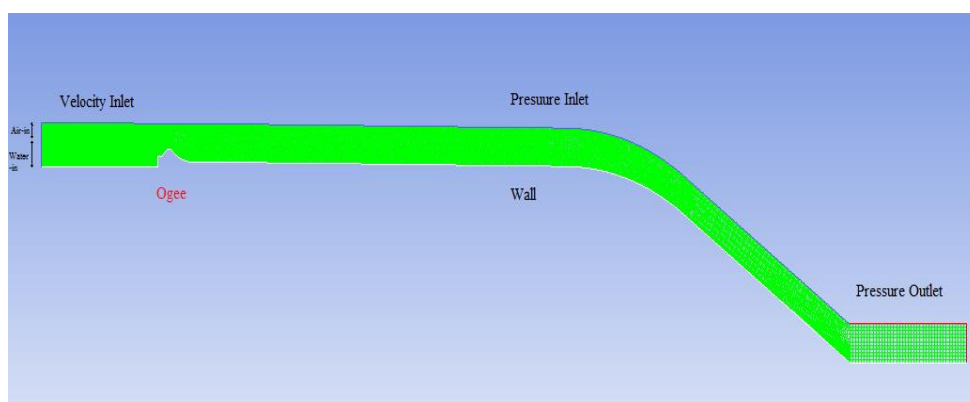


Figure 2: The calculation domain and boundary conditions.

3. VERIFICATION OF NUMERICAL MODEL

The numerical model was verified using the results of the physical model. Comparison of the results obtained of the numerical model with those of the physical model indicates that the numerical model is able to appropriately predict the air-water flow pattern as well as velocity and pressure fields. Depth measurements provided by Iran Water Research Institute using the physical model are applied to validate the accuracy of results. In the case of $Q=501.5$ m³/s Regression equals to 0.98 and in the case of $Q=1006$ m³/s Regression equals to 0.95, so the validity of the results is acceptable. Comparison of observed and simulated surface water elevation is shown in Figure 3 and 4. The difference in PMF discharge ($Q=1006$ m³/s) may have been caused by excessive turbulence.

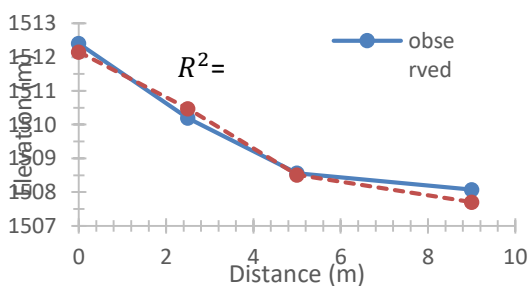


Figure 3: Comparison of observed and simulated surface water elevation for $Q=501.5$ m³/s

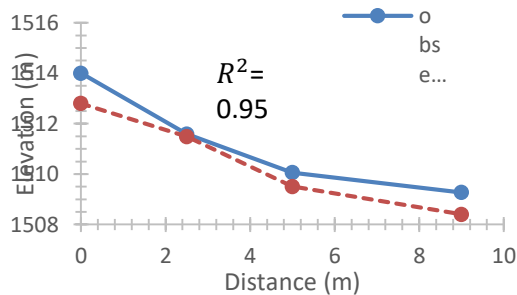


Figure 4: Comparison of observed and simulated surface water elevation for $Q=1006$ m³/s

4. SIMULATION RESULTS AND ANALYSIS

Pressure and velocity is one of the main characteristics of the flow. To understand the flow pattern and to design safe hydraulic structures, it is necessary to study the pressure and velocity. Here, this goal is achieved by means of Ansys Fluent on the base of CFD. After simulation of geometric model and running the calculation, pressure and velocity are exported in six sections $x=0, 2.5, 5, 7, 9$ and 10 meters (where $(x, y) = (0, 0)$ shows the ax of ogee) for two discharges $Q=501.5$ and $Q=1006$ cubic meter per second which is shown in

Figure 5 and

Figure 6. Also flow pattern is computed as below for two discharges (Figure 7 and 8).

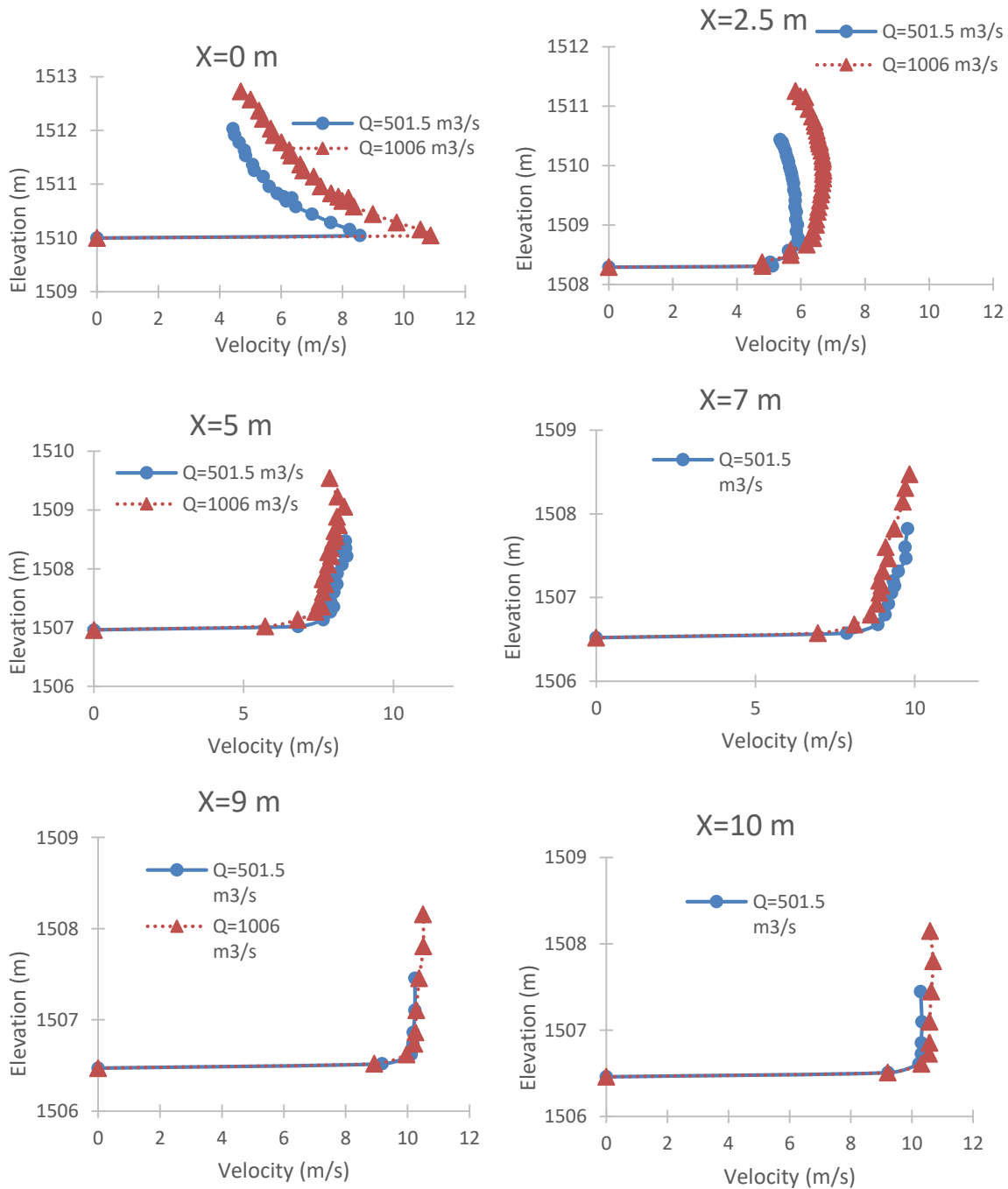


Figure 5: Comparison of velocity profile between discharges of 501.5 m³/s and 1006 m³/s in six sections (x=0, 2.5, 5, 7, 9 10)

According to

Figure 5, at x=0 section, the velocity profile is not fored yet and this may be caused by turbulence of water passing the head of ogee. After X=2.5m, the expected velocity profile is showing off. Comparison of velocity in different sections also clearly reflects the tendency of the flow's velocity to gradually increase.

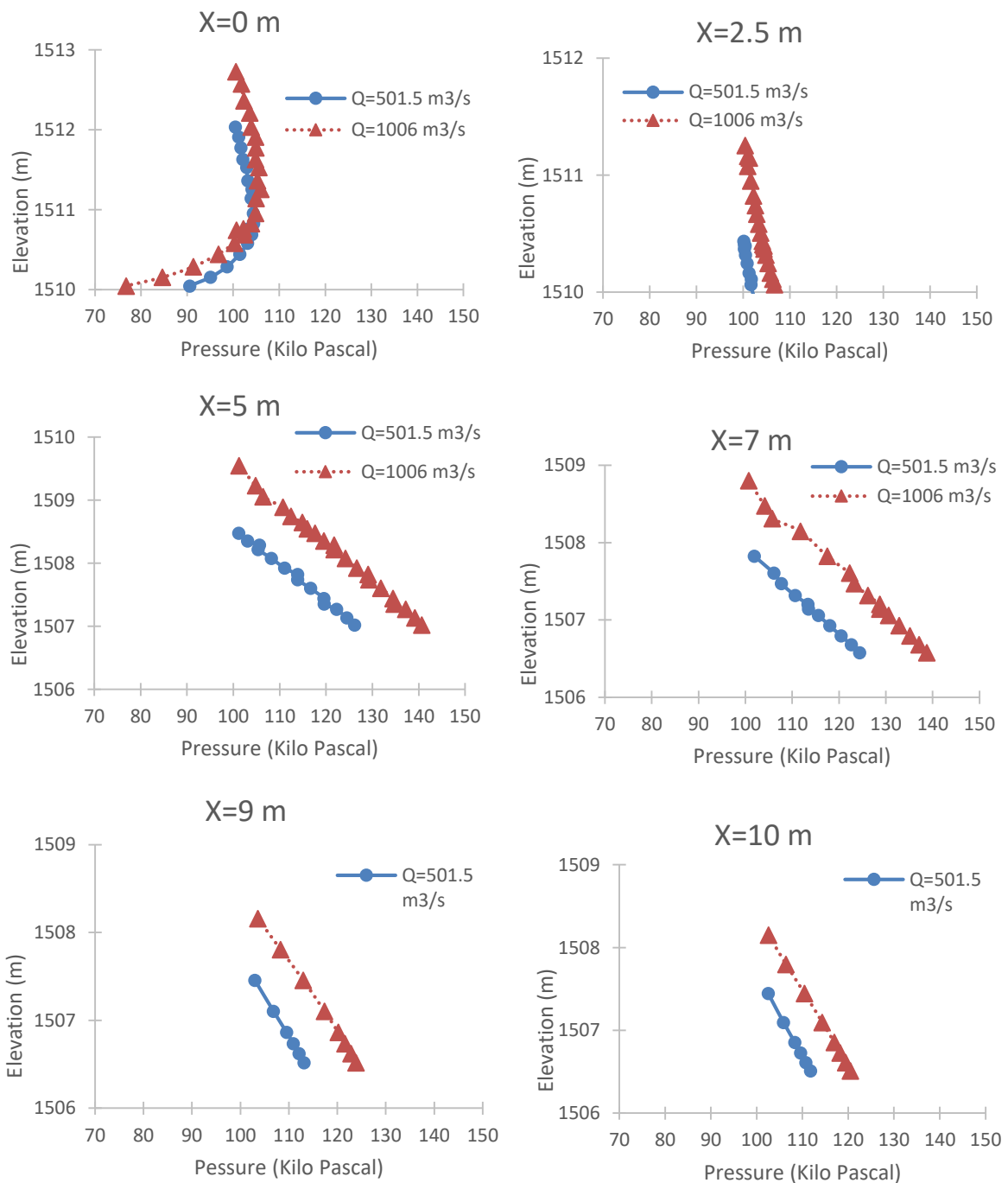


Figure 6: Comparison of static pressure profile between discharges of 501.5 m³/s and 1006 m³/s in six sections (x=0, 2.5, 5, 7, 9 10)

Static pressure is influenced by the hydraulic head of water. According to Figure 6, it is obvious that the static pressure profile is linear which provides the linear relation between depth of water and static pressure. There is a non-linear pressure profile at section $x=0$ m which may be caused by turbulence.

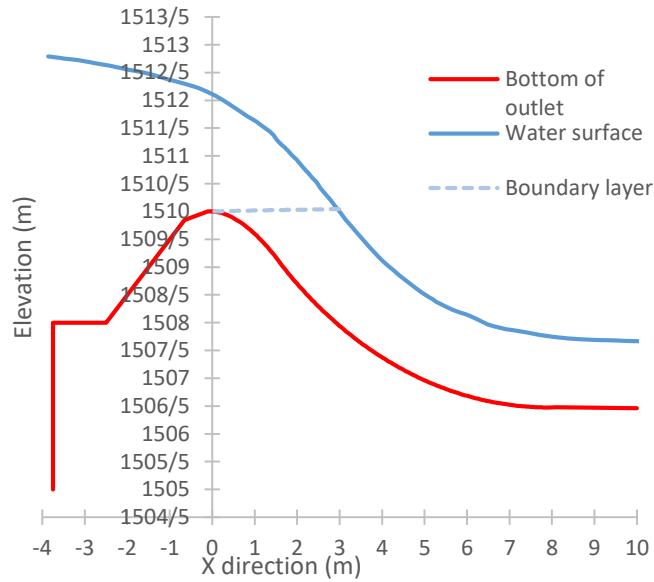


Figure 7: Flow pattern for $Q=501.5$ m³/s

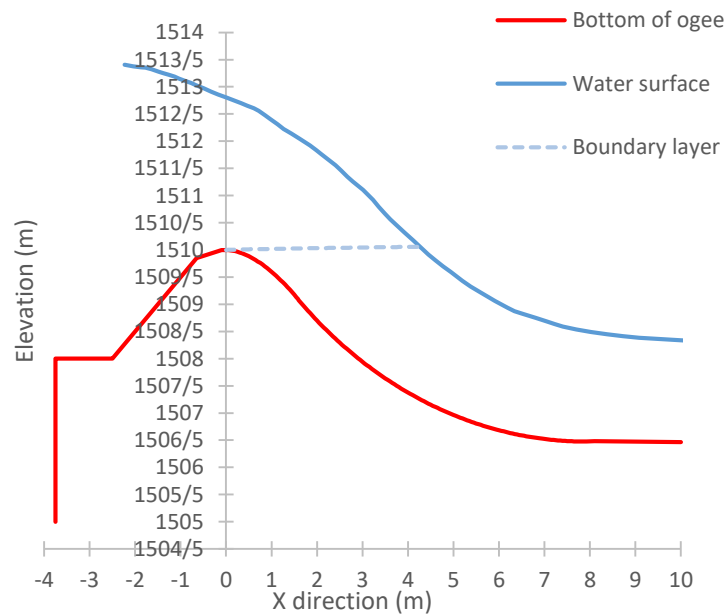


Figure 8: Flow pattern for $Q=1006$ m³/s

One of the important topics in hydraulic is the distribution of the boundary layer passing through the crest of the ogee. Distribution of boundary layer is highly influenced by the roughness of surface [12]. The process of air entrainment begins where the outer limit of the boundary layer meets the flow surface. Boundary layer reaches the surface of flow at $x=3\text{m}$ for $Q=510.5\text{ m}^3/\text{s}$ and at $x=4.2\text{ m}$ for $Q=1006\text{ m}^3/\text{s}$ which is shown in Figure 7 and Figure 8. This is calculated by Davis Formula which is shown below.

$$\frac{\gamma}{L} = 0.08 \left(\frac{L}{k}\right)^{-0.233}$$

Where

γ =	Boundary layer thickness, meter
L =	Surface distance from upstream end of the ogee crest, meter
k =	Absolute concrete-surface roughness (ranges from 0.0006 to 0.002 meter)

5. CONCLUSIONS

A numerical model using multiphase flow, VOF is used to study and compare the flow over an ogee spillway with two different discharges. In the current study, the VOF model for air-water two-phase flow and RNG k - ϵ turbulence model are combined to successfully simulate the flow characteristics over ogee spillways. The simulated pressure profiles on the ogee surfaces provide the theoretical foundation for assessing the cavitation risk. Moreover, the numerical method in this paper is an essential tool for designing a safe hydraulic structure. The main goal of this study was to justify the methodology adopted herein for CFD model setup, as well as the reliability of k - ϵ turbulence closure and VOF method to simulate complex 2D flow fields in open channels and hydraulic structures by means of ANSYS FLUENT. This goal is achieved by negligible difference in comparing the water surface level in the physical and simulated model.

6. REFERENCES

1. Dehdar-Behbahani, S., & Parsaie, A. (2016). Numerical modeling of flow pattern in dam spillway's guide wall. Case study: Balaroud dam, Iran. *Alexandria Engineering Journal*, 55(1), 467-473.
2. Zhenwei, M. U., Zhiyan, Z., & Tao, Z. H. A. O. (2012). Numerical simulation of 3-D flow field of spillway based on VOF method. *Procedia Engineering*, 28, 808-812.
3. Zhan, J., Zhang, J., & Gong, Y. (2016). Numerical investigation of air-entrainment in skimming flow over stepped spillways. *Theoretical and Applied Mechanics Letters*, 6(3), 139-142.
4. Kositgittiwong, D., Chinnarasri, C., Julien, P. Y., Ruff, J. F., & Meroney, R. N. (2010, May). Multiphase Flow Models for 2D Numerical Modeling of Flows over Spillways. In *The Third International Junior Researcher and Engineer Workshop on Hydraulic Structures, IJREWHS-10*, Edinburgh, Scotland, UK.
5. Cheng, X., Chen, Y., & Luo, L. (2006). Numerical simulation of air-water two-phase flow over stepped spillways. *Science in China Series E: Technological Sciences*, 49(6), 674-684.
6. Dargahi, B. (2006). Experimental study and 3D numerical simulations for a free-overflow spillway. *Journal of Hydraulic Engineering*, 132(9), 899-907.
7. Zeng, J., Zhang, L., Ansar, M., Damisse, E., & González-Castro, J. A. (2016). Applications of computational fluid dynamics to flow ratings at prototype spillways and weirs. I: Data generation and validation. *Journal of Irrigation and Drainage Engineering*, 143(1), 04016072.
8. Varjavand, P., Farsadizade, D., Hosseinzadeh, A., Sadraddini, A. (2009). 3D Simulation of Flow in Side Spillway with k-ε Turbulence Model and Comparing the Results with Physical Model. *Journal of water and soil science (in Persian)*.
9. Wolfgang, R. Shamloo, H. (2009). *Turbulence models and their application in hydraulics*. Tehran: Khaje Nassir Tousi University (in Persian).
10. Hirt, C. W., and Nichols, B. D. (1981). "Volume of fluid (VOF) method for the dynamics of free boundaries." *J. Comput. Phys.*, 39(1), 201-225.
11. Zipparro, V. J., & Hasen, H. (Eds.). (1993). *Davis' handbook of applied hydraulics*. McGraw-Hill Companies.
12. Manafpour, M., Mirizadeh, N., (2016). Distribution of boundary layers on stepped spillways. *Fifteenth Hydraulic Conference of Iran, Imam Khomeini University of Qazvin (in Persian)*.
13. Davis, C. V., & Sorensen, K. E. (1969). *Handbook of applied hydraulics*. In *Handbook of applied hydraulics*. McGraw-Hill.

On the Slices-based Limit Equilibrium Method for the Active Earth Pressure Applied by Soils with Nonlinear Strength Behavior

Zhongzhi Fu¹, Shengshui Chen², Guoying Li³

1-Senior Engineer, Geotechnical Engineering Department, Nanjing Hydraulic Research Institute, Nanjing 210024, China

2- Professor, Key Laboratory of Failure Mechanism and Safety Control Techniques of Earth- Rock Dams, Ministry of Water Resource, Nanjing 210029, China

3-Professor, Geotechnical Engineering Department, Nanjing Hydraulic Research Institute, Nanjing 210024, China

Email: fu_zhongzhi@yahoo.com

Abstract

The slices-based limit equilibrium method was used to study the active earth pressure applied by soils with nonlinear strength behavior. An iterative scheme and a local minimization process were employed to consider the dependence of the peak friction angle on the normal effective stress and the mathematical nature of the active earth pressure, respectively. The preference of iterative variable for local minimization processes as well as the influence of the distribution of interslice force angles on the active earth pressure and its points of application were discussed. Numerical examples show that the slices-based limit equilibrium method is reliable in predicting static and dynamic active earth pressures upon vertical or sloping retaining walls for soils with both linear and nonlinear failure criteria. The use of nonlinear strength parameters in the slices-based method was also discussed.

Keywords: Active Earth Pressure, Retaining Wall, Limit Equilibrium, Generalized Slice Method.

1. INTRODUCTION

The active earth pressure problem is an important and classical issue in soil mechanics that deals with the stability of a retaining structure and the backfilled soils. The two major early theories to estimate the active (and passive) earth pressure values are those by Coulomb (1776) and by Rankine (1857) as summarized in standard textbooks (e.g. Smith and Smith 1998). Both theories are recommended in designing specifications for retaining structures and are very much in use in geotechnical engineering. Other theories for earth pressure problems include the slices-based limit equilibrium method (Rahardjo and Fredlund 1984; Chen and Li 1998), the limit analysis method (Chen 1975; Yang 2007) and the slip line method (Liu and Wang 2008; Peng and Chen 2013) as summarized by Sun and Song (2016). In most of these works, the peak shear stress that a surface can sustain is assumed linearly dependent upon the normal effective stress applied, which makes them inapplicable to earth pressure problems where the retained soils exhibit strong nonlinear strength behavior.

The above situation is often encountered in rockfill dams. Fig.1 (a) depicts a retaining wall truncating the downstream slope of a rockfill dam built on a sloping mountain for a pumped storage station, so as to considerably reduce the amount of rockfill materials needed (Liu et al. 2008). A retaining wall is also used sometimes to truncate the upstream slope so as to avoid building the toe plinth on an unsatisfactory foundation such as a fault as shown in Fig. 1(b) (Fu et al. 2014). Designing such retaining structures needs the information about the active earth pressure exerted by the backfilled rockfill materials. It is well known that the strength of coarse granular materials, like gravels and rockfills, depends on the normal stress or the confining pressure (Leps 1970; Maksimovic 1989; Xiao et al. 2014). For instance, the peak friction angle (φ) of a stressed rockfill in triaxial compression can be well approximated by the following equation (Liu et al. 2008):

$$\varphi = \varphi_0 - \Delta\varphi \lg \left(\frac{\sigma_3}{p_a} \right) \quad (1)$$

In which $\varphi = \sin^{-1}[(\sigma_1 - \sigma_3)/(\sigma_1 + \sigma_3)]$, and σ_1 and σ_3 are the maximum principal stress and the minimum one, respectively. φ_0 and $\Delta\varphi$ are two parameters, and p_a denotes the atmospheric pressure ($p_a = 101325$ Pa). Because the peak friction angle of the retained soils along a given failure surface is not known a priori, the widely used Rankine theory and Coulomb theory as well as other analytical approaches cannot be directly used in most circumstances.

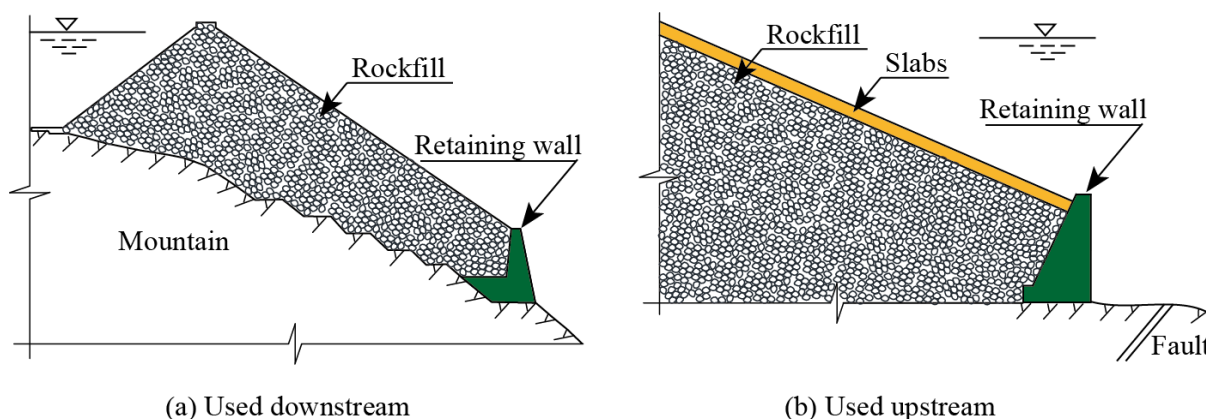


Fig. 1. Use of retaining walls in concrete face rockfill dams

Multilayered soil strata and complex topography as well as variable loading conditions sometimes result in extra difficulty in using classical earth pressure theories, and therefore numerical methods exemplified by the finite element method and the finite difference method have been increasingly used in solving earth pressure problems (Potts and Fourie 1986; Bhatia and Bakeer 1989; Benmeddour et al. 2012; Worden and Achmus 2013). Certain constitutive models were required to represent the stress ~ strain behavior of the retained soils and therefore much more parameters were inevitably needed, obtaining more information but meanwhile adding expense and uncertainty to such numerical analyses. Early endeavor was also exercised in predicting the active earth pressure using the slices-based limit equilibrium analysis (Rahardjo and Fredlund 1984; Chen and Li 1998; Zakerzadeh et al. 1999). However, the nonlinear strength behavior of the retained soils was seldom considered in earth pressure problems, despite of their wide consideration in slope stability analysis (Collins et al. 1988; Zhang and Chen 1987; Jiang et al. 2003).

Recently, the nonlinear strength behavior of soils was considered in using the upper bound limit analysis method (Yang 2007) and the slip line method (Sun and Song 2016) for active earth pressure problems. A common advantage of both methods is the unnecessary of introducing any assumption for the interslice forces as in those slices-based limit equilibrium methods (Rahardjo and Fredlund 1984; Chen and Li 1998; Zakerzadeh et al. 1999). However, in the method by Yang (2007), the nonlinear strength of soils is only reflected in an average manner since a single and constant apparent friction angle (φ_i) is used along the failure surface in evaluating the internal energy dissipation. The method by Sun and Song (2016) can consider the variation of the shear strength along the failure surface. However, it cannot reflect the influence of the flexibility of retaining structures upon the active earth pressure, since for each failure surface a single and unique active earth pressure can be obtained.

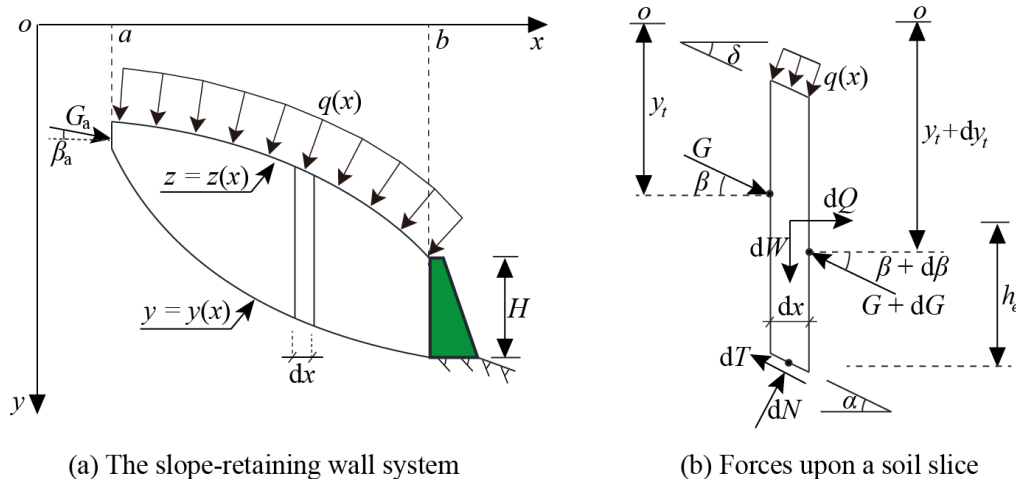
Since the slices-based limit equilibrium analysis is among the most widely used methods in geotechnical engineering, and its ability in seeking the active earth pressure applied by soils with linear strength behavior has already been demonstrated by several authors (Rahardjo and Fredlund 1984; Chen and Li 1998; Zakerzadeh et al. 1999), it is natural to extend this popular method for soils with nonlinear shear strength. In this paper, the generalized method of slices (Chen and Morgenstern 1983; Chen and Li 1998) was extended for this particular aim. The equilibrium equations derived by Chen and Morgenstern (1983) were used. An iterative cycle was incorporated so as to obtain the mobilized strength of soils that is compatible with the normal stress along the failure surface. In addition, a local minimization process was performed to seek the minimum active earth pressure for each possible failure surface. Some cases were studied and the results were compared with those obtained by other methods. The selection of the iterative variable for the local minimization processes was discussed, and the influence of the interslice force angle as well as the type of failure surfaces on the solutions were studied. Nonlinear strength parameters used for the slices-based limit equilibrium analysis were also discussed.

2. LIMIT EQUILIBRIUM EQUATIONS AND THE SOLUTION STRATEGY

For the sake of integrity and familiarity of notations, the equilibrium equations of the retained soil mass were simply presented in this part. The slope-retaining wall system was shown in Fig. 2, in which the retaining surface of the wall was assumed vertical tentatively. The active earth pressure applied upon a sloping surface can also be calculated using the vertical slices-based method as will be shown later. Before introducing the force and moment equilibrium equations, the forces that a typical soil slice (width = dx) bears were summarized as follows:

1. vertical body force, dW , and horizontal body force, dQ ;
2. surcharge perpendicular to the free surface, $q(x)$;
3. normal force, dN , and shear force, dT , upon the bottom failure surface;
4. interslice forces, G and $G+dG$, exerted by the neighboring slices.

Other symbols in Fig. 2 include the height of the retaining wall, H ; the inclination of the failure surface measured from the horizontal plane, α ; the inclination of the action line of G denoted by β ; the inclination of the free surface, δ , the vertical coordinate of the application point of G denoted by y_t , and the vertical distance between the action line of dQ and the bottom of the slice denoted by h_e . The elevation of the failure surface and that of the free surface were represented by the function $y = y(x)$ and $z = z(x)$, respectively.



(a) The slope-retaining wall system

(b) Forces upon a soil slice

Fig. 2. The slope-retaining wall system and forces upon a soil slice

2.1. FORCE AND MOMENT EQUILIBRIUM EQUATIONS

The horizontal and vertical force equilibrium conditions of the soil slice read:

$$\left. \begin{aligned} dN \sin \alpha - dT \cos \alpha + G \cos \beta - (G + dG) \cos (\beta + d\beta) + dQ - q \tan \delta dx &= 0 \\ -dN \cos \alpha - dT \sin \alpha + G \sin \beta - (G + dG) \sin (\beta + d\beta) + dW + q dx &= 0 \end{aligned} \right\} \quad (2)$$

For the sake of universality, the following failure criterion was used to describe the stress state of soils along the failure surface $y = y(x)$:

$$dT = (dN - u \cdot dx \sec \alpha) \tan \varphi + c \cdot dx \sec \alpha \quad (3)$$

In which c and φ are the cohesion and the friction angle of the soil, respectively. u is the pore pressure along the failure surface. For most coarse granular materials, $c = 0$ and φ is a nonlinear function of the normal effective stress. Solving dN and dT from Eq. (2) and substituting them into Eq. (3) yield the following differential equation for the interslice force, G (Chen 2003):

$$\cos(\varphi - \alpha + \beta) \frac{dG}{dx} - G \sin(\varphi - \alpha + \beta) \frac{d\beta}{dx} = -p(x) \quad (4)$$

in which

$$p(x) = \left(\frac{dW}{dx} + q \right) \sin(\varphi - \alpha) - \left(\frac{dQ}{dx} - q \tan \delta \right) \cos(\varphi - \alpha) - u \cdot \sin \varphi \sec \alpha + c \cdot \cos \varphi \sec \alpha \quad (5)$$

The moment equilibrium equation of the soil slice that around the center of the failure surface can also be derived (Chen 2003), that is

$$G \sin \beta = \frac{d}{dx} (y_t \cdot G \cos \beta) - y \frac{d}{dx} (G \cos \beta) + \frac{dQ}{dx} h_e - q \tan \delta (y - z) \quad (6)$$

Eqs. (4) and (6) govern the equilibrium of the differential soil slice, which, combined with certain boundary conditions, can be solved analytically or numerically. For the active earth pressure problem depicted in Fig. 1, the following boundary conditions can be introduced:

$$\left. \begin{aligned} y(x=a) &= Y_a; & \beta(x=a) &= \beta_a; & G(x=a) &= G_a; & y_t(x=a) &= T_a \\ y(x=b) &= Y_b; & \beta(x=b) &= \beta_b \end{aligned} \right\} \quad (7)$$

The unknown variables to be sought are the force acted at the right boundary ($x=b$) and its point of application denoted by the following notations:

$$G(x=b) = G_b; \quad y_t(x=b) = T_b \quad (8)$$

The force applied at the left boundary, G_a , is considered herein for generality. In addition, β_b depends on the roughness of the wall and is generally set to the friction angle between the soil and the retaining wall under an active condition.

2.2. THE SOLUTION STRATEGY

Eq. (4) is a linear nonhomogeneous first-order ordinary differential equation (Kreyszig 2010), the solution of which can be derived following a standard procedure (Chen 2003):

$$G(x) = \exp \left[\int_a^x \tan(\varphi - \alpha + \beta) d\beta \right] \cdot \left[G_a - \int_a^x p(\xi) s(\xi) d\xi \right] \quad (9)$$

in which

$$s(x) = \sec(\varphi - \alpha + \beta) \exp \left[- \int_a^x \tan(\varphi - \alpha + \beta) d\beta \right] \quad (10)$$

Therefore, it is easy to obtain the explicit expression for the earth pressure at the right boundary, G_b :

$$G_b = \exp \left[\int_a^b \tan(\varphi - \alpha + \beta) d\beta \right] \cdot \left[G_a - \int_a^b p(x) s(x) dx \right] \quad (11)$$

As can be seen from Eq. (11) and expressions of the functions $p(x)$ and $s(x)$, the active earth pressure depends on the location of the failure surface (via the functions $\alpha(x)$ and $y(x)$) and the interslice force angle function $\beta(x)$. Mathematically, this is a problem of seeking an extreme of the functional, and the standard approach is to apply the so-called Euler-Lagrange condition (Andrews and Phillips 2004). However, such an analytical approach generally leads to some highly nonlinear ordinary differential equations of $\alpha(x)$ and $\beta(x)$, which are almost unsolvable. In addition, it will be shown later that for practical problems the extreme of Eq. (11) can be achieved often at places other than the stationary points due to the constraints of some boundary conditions. Therefore, the extreme of Eq. (11) was obtained numerically in this study.

Eq. (6) can also be integrated as follows (Chen 2003):

$$\begin{aligned} & (y_t - y) \cdot G \cos \beta - (T_a - Y_a) \cdot G_a \cos \beta_a \\ & = \int_a^x \left[G (\sin \beta - \tan \alpha \cos \beta) - \frac{dQ}{dx} h_e + q \tan \delta (y - z) \right] d\xi \end{aligned} \quad (12)$$

which, by introducing the boundary conditions given in Eqs. (7) and (8), can be rewritten as follows:

$$G_b t_b \exp \left[- \int_a^b \tan(\varphi_e - \alpha + \beta) d\beta \right] + \int_a^b p(x) s(x) t(x) dx - M_e = 0 \quad (13)$$

in which

$$t(x) = \int_a^x (\sin \beta - \tan \alpha \cos \beta) \exp \left[\int_a^\xi \tan(\varphi_e - \alpha + \beta) d\beta \right] d\xi \quad (14)$$

and

$$M_e = (T_b - Y_b) \cdot G_b \cos \beta_b - (T_a - Y_a) \cdot G_a \cos \beta_a + \int_a^b \left[\frac{dQ}{dx} h_e - q \tan \delta (y - z) \right] dx \quad (15)$$

The concept of seeking an extreme of the active earth pressure is similar to that in safety factor evaluation in slope stability problems. Assume that the location of the failure surface is known so that the functions $y(x)$ and $\alpha(x)$ are determined, varying the function $\beta(x)$ within the valid range will yield a local minimum of G_b , which can be further substituted into Eq. (13) to get its point of application (T_b). Traversing all the possible locations of the failure surfaces and repeatedly implementing the optimization processes, we can obtain a series of local minimums of G_b . The physically meaningful active earth pressure will be the maximal one of those local minimums. Therefore, the cornerstone here is to select the function $\beta(x)$ that minimizes the earth pressure for a given failure surface.

The influence of the interslice force angle function $\beta(x)$ was studied by a few authors (Chen 2003; Zakerzadeh et al. 1999). Zakerzadeh et al. (1999) suggested that a reasonable active earth pressure could be obtained when using an interslice force function that varies linearly from the starting point of the failure surface (a in Fig. 2) to the end point of the failure surface (b in Fig. 2). Chen and Morgenstern (1983) and Chen (2003) suggested a more general form as follows:

$$\tan \beta = f_0(x) + \lambda \cdot f(x) \quad (16)$$

herein λ is a scalar, and $f_0(x)$ and $f(x)$ are two independent functions. A reasonable choice of the functions that satisfies the boundary conditions strictly was given by Chen (2003), that is

$$f_0(x) = \frac{\tan \beta_b - \tan \beta_a}{b-a} (x-a); \quad f(x) = \sin \frac{\pi}{b-a} (x-a) \quad (17)$$

It is clear that the use of Eq. (16) largely reduces the possibility of the function $\beta(x)$, and the active earth pressure is now simply dependent on the factor λ . For a given failure surface, this coefficient could be increased gradually within its possible range to yield the minimum earth pressure and its point of application. Note only those physically reasonable results, which satisfy the condition $0 < (Y_b - T_b) < H$, or an even narrower one based on physical considerations, can be accepted.

It is also feasible to assume an acceptable range for the point of application of the active earth pressure and seek the value of λ that is consistent with the given T_b by solving Eq. (13). Then the obtained λ can be used further in Eq. (11) to calculate the corresponding G_b . This approach was used by Chen and Li (1998) and Chen (2003), however, without finding the local minimum earth pressure for a given failure surface. For this alternative strategy, Eqs. (11) and (15) can be substituted into Eq. (13) to yield the following nonlinear equation without the presence of G_b :

$$\begin{aligned} M_u = & \left[G_a - \int_a^b p(x) s(x) dx \right] t_b + \int_a^b p(x) s(x) t(x) dx \\ & - (T_b - Y_b) \cdot \exp \left[\int_a^b \tan(\varphi - \alpha + \beta) d\beta \right] \cdot \left[G_a - \int_a^b p(x) s(x) dx \right] \cos \beta_b \\ & + (T_a - Y_a) \cdot G_a \cos \beta_a - \int_a^b \frac{dQ}{dx} h_e - q \tan \delta (y - z) dx = 0 \end{aligned} \quad (18)$$

in which M_u denotes the unbalanced moment. It will be shown later that the use of a nonlinear failure criterion for the retained soil may result in a non-monotonic function of $M_u(\lambda)$ for a given T_b , which may makes the second approach not effective.

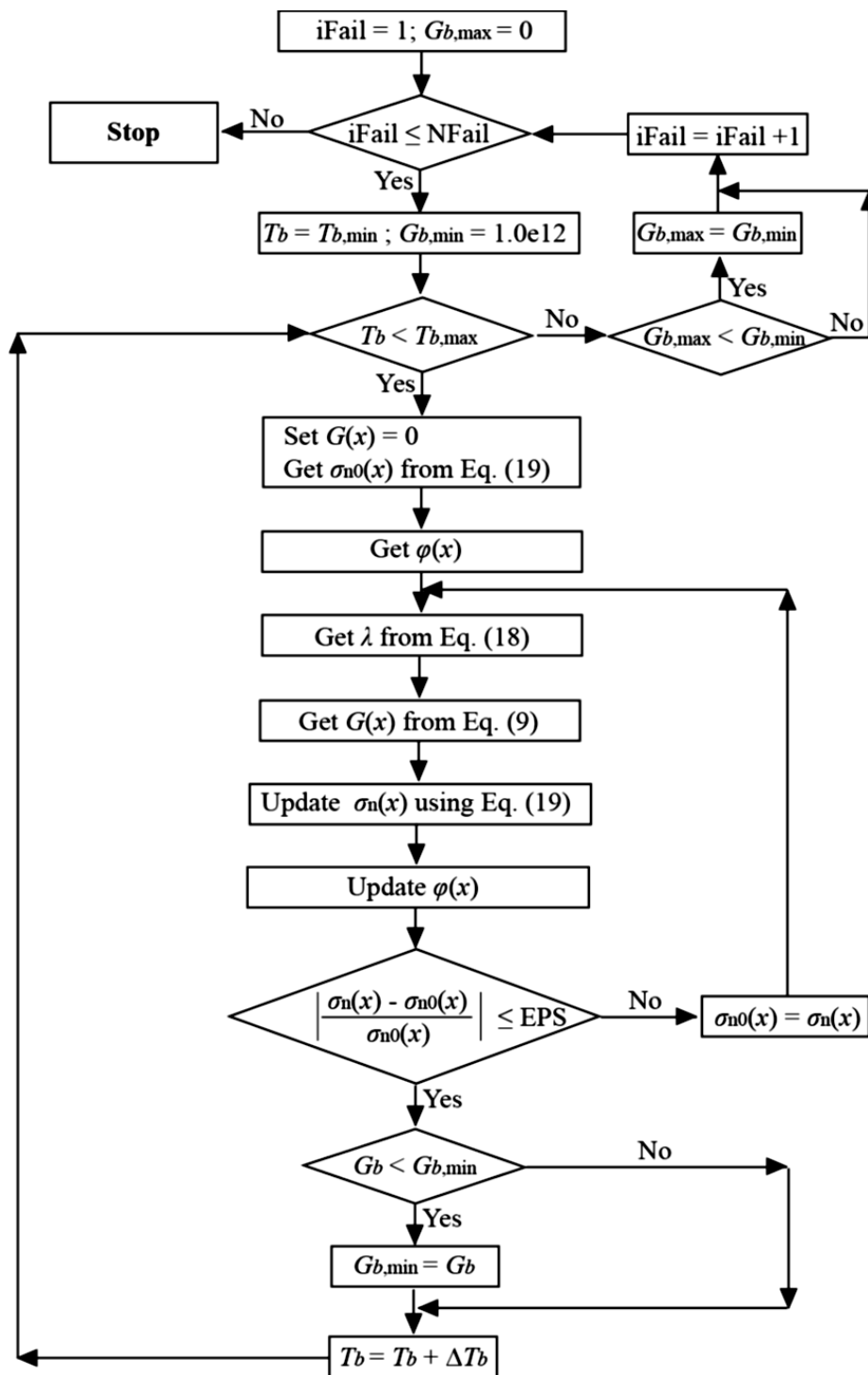
2.3. USE OF A NONLINEAR FAILURE CRITERION

For materials with a nonlinear failure criterion, the friction angle mobilized along the failure surface should also be determined during the solution. An extra iteration should be added for this purpose. Once the force angle function $\beta(x)$ is determined, the inter-slice forces, $G(x)$, can be integrated slice by slice using Eq. (9), and the normal effective stress on each soil slice can be calculated as follows:

$$\sigma_n = \frac{dN}{dx \cdot \sec \alpha} \quad (19)$$

in which the effective normal force, dN , can be obtained by using the vertical force equilibrium equation and the failure criterion as given in Eqs. (2) and (3), that is

$$dN = \frac{G_L \sin \beta_L - G_R \sin \beta_R + dW + qdx + u \cdot dx \tan \alpha \tan \varphi - c \cdot dx \tan \alpha}{(\cos \alpha + \tan \varphi \sin \alpha)} \quad (20)$$



NFail: number of failure surfaces considered; $T_{b,min}$ & $T_{b,max}$: lower and upper bounds of T_b ;
 iFail: the counter of failure surfaces; ΔT_b : increment of T_b adopted;
 $G_{b,max}$: global maximum active earth pressure; σ_n & σ_{n0} : normal effective stress;
 $G_{b,min}$: local minimum active earth pressure; EPS: convergency criteria for iteration.

Fig. 3. Flowchart for seeking the active earth pressure on retaining structures

in which the variables with subscripts L and R denote the interslice forces and their angles applied at the left and right sides of the concerned soil slice. Fig. 3 describes the flowchart of the numerical algorithm for the solution of the active earth pressure. A possible range was prescribed for the point of application (T_b) of the active earth

pressure herein. However, it is sometimes better to set an upper bound and a lower bound for λ and let it be the iterative variable instead of T_b . In the latter case, there is no need to solve the nonlinear equation, i.e. Eq. (18). However, the resultant point of application should be verified.

3. VERIFICATION

The algorithm described above was incorporated into a limit equilibrium analysis program LEAPERS (Limit Equilibrium Analysis Program for Earth and Rockfill Structures) developed initially for slope stability problems in earth and rockfill dams (Fu & Chen 2013) based on the generalized method of slices by Chen and Morgenstern (1985) and Chen (2003). Both λ and T_b could be used as the iterative variable during the local minimization process. In this part, same examples were studied to verify and demonstrate the capability of the method and the program.

3.1. SOIL WITH A LINEAR STRENGTH BEHAVIOR

The active earth pressure exerted by a cohesionless soil upon a concrete wall ($H=20$ m) with a sloping surface was considered first. The unit weight of the soil and its strength parameters as well as the friction angle between the soil and the retaining wall were given in Fig. 4(a). The simplest way to use the vertical soil slices based method for such a sloping retaining structure is to rotate the coordinates so as to keep the retaining surface vertical as shown in Fig. 4(b). Meanwhile, the gravity (g) of each soil slice should be decomposed into a horizontal component, g_x , and a vertical component, g_y , in the rotated system, that is

$$g_x = g \sin \varepsilon; \quad g_y = g \cos \varepsilon \quad (21)$$

in which ε is the angle between the retaining surface and the vertical axis in the original system.

By doing this, the vertical and horizontal components of the gravity can be considered in dW and dQ related terms in Eq. (5), respectively. It should be noted that the boundary conditions for $\beta(x)$ should also be modified accordingly.

The active earth pressure was determined using LEAPERS with plane failure surfaces, and the resultant pressure coefficient ($K_a = G_b/(\gamma H^2/2)$) was plotted against the inclination angle of the failure surface, α , and the coefficient λ in Fig. 5(a). The variations of K_a and the corresponding point of application ($(Y_b-T_b)/H$) with λ for the critical (most dangerous) failure surface were also plotted in Fig. 5(b). Both the critical failure surface and the corresponding active earth pressure obtained herein coincide exactly with Coulomb's theoretical solutions. In addition, it is interesting to note that K_a was not influenced by λ for a given α in this particular case. This feature can be explained by simplifying Eq. (10) with a constant φ and α , that is

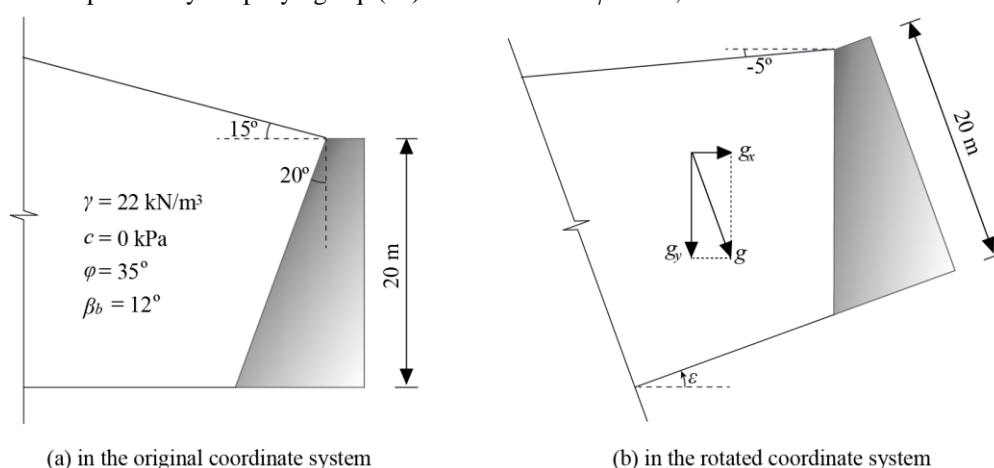


Fig. 4. The active earth pressure problem on a sloping retaining surface

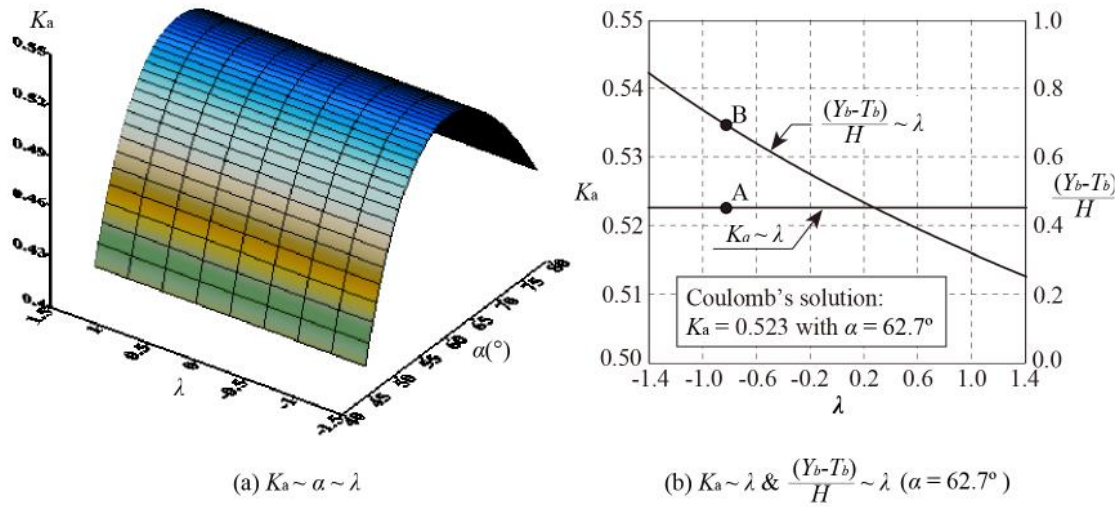


Fig. 5. The variation of the active earth pressure and its application point with α and λ (based on linear strength parameters: $c = 0$ and $\varphi = 35^\circ$)

$$s(x) = \sec(\varphi - \alpha + \beta_a) \tag{22}$$

Therefore, Eq. (11) can be reduced to the following form:

$$G_b = \frac{\cos(\varphi - \alpha + \beta_a)}{\cos(\varphi - \alpha + \beta_b)} \cdot \left[G_a - \sec(\varphi - \alpha + \beta_a) \int_a^b p(x) dx \right] \tag{23}$$

which is a function depends only on the loads and the friction angle between the wall and the soil (β_b), but not influenced by the $\beta(x)$ distribution within the soil mass. This conclusion, however, is valid only for a plane failure surface in a single soil stratum. Even in such a simple condition, the strength mobilized along the vertical sides of the soil slices does affect the application point of the earth pressure. For instance, if the wall cannot sustain the pressure indicated by A that applied at a point indicated by B as shown in Fig. 5(b), then it will deform away from the retained soil, which in turn results in a downward movement of the point of application, but preserving the amount of active earth pressure.

Since the change of the point of application does not alter the amount of active earth pressure for a given plane failure surface, the point of application cannot be determined in this method. This conclusion is exactly like the fact that Coulomb's earth pressure theory in itself cannot predict the point of application of the active earth pressure (Fu et al. 2014; Sun and Song 2016).

3.2. SOIL WITH A NONLINEAR STRENGTH BEHAVIOR

The previous problem shown in Fig. 4 was used as the first example in this subsection. Eq. (1) was employed for the retained soil so as to reflect the nonlinear strength behavior. However, the confining pressure σ_3 in Eq. (1) was replaced tentatively by the normal effective stress, σ_n , along the failure surface. Use of the nonlinear strength parameters was discussed later. Herein, the two parameters for the peak friction angle were $\varphi_0 = 45^\circ$ and $\Delta\varphi = 8^\circ$. Other parameters were the same as those in Fig. 4. In order to compare with the results in Fig. 5, only plane failure surfaces were considered in this case.

Fig. 6(a) shows the variation of K_a with α and λ , and Fig. 6(b) plots the particular results for the critical failure surface ($\alpha = 69.3^\circ$). Differently from the results shown in Fig. 5, K_a is evidently influenced by the value of λ and hence the point of application for any given failure surface. In addition, for each failure surface there is a clear local minimum of K_a that could be attained when λ approaches a certain value as illustrated in Fig. 5(b), either an increase or a decrease of λ from this stationary point will result in an increase of the active earth pressure.

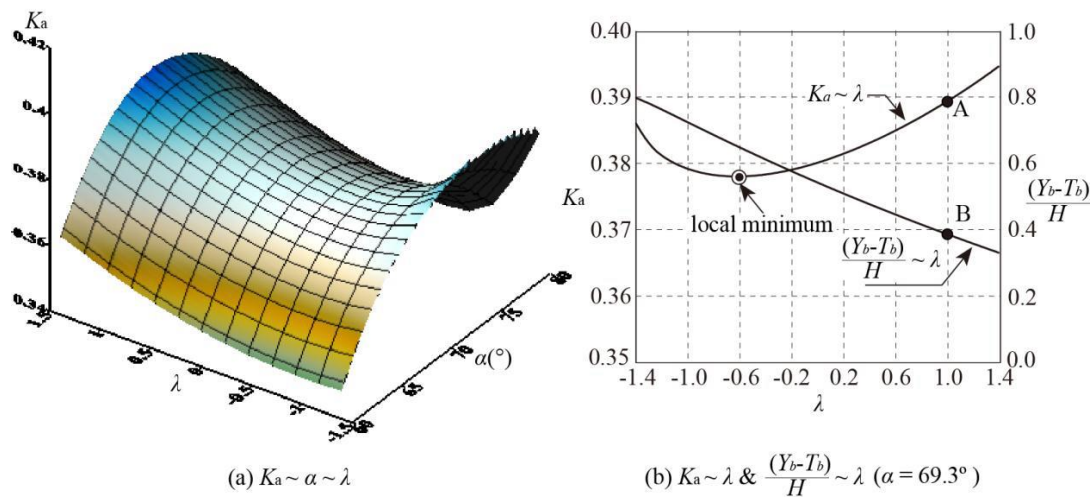


Fig. 6. The variation of the active earth pressure and its application point with α and λ (based on nonlinear strength parameters: $\varphi_0 = 45^\circ$ and $\Delta\varphi = 8^\circ$)

Variation of the active earth pressure and its point of application with the interslice force angles reflects the fact that the soil-retaining wall system has a flexibility to adjust the internal forces so as to sustain an overall stability. For instance, if the interslice forces initially follow a distribution corresponding to $\lambda = 1.0$, then, to keep the soil mass stable, the retaining wall should provide a force, the amount and application point of which were denoted by A and B in Fig. 5(b). However, the retaining wall itself may not be able to keep stable under such a high earth pressure, and it tends to displace or deform away from the retained soil. Such a tendency will result in a change of the earth pressure and an adjustment of the application point. The soil, on the hand, should also adjust the internal forces to keep itself stable. Such a mutual adjustment of earth pressure and soil strength mobilization will cease if and only if the retaining wall can sustain the minimal earth pressure without losing stability. This is the reason why for a given failure surface the minimal earth pressure is meaningful but not the maximum. However, for all the possible failure surfaces, the retaining wall can keep stable if and only if it can sustain the maximum of those minimal earth pressures. Therefore, the active earth pressure problem is mathematically finding the so-called saddle point on a surface demonstrated in Fig. 6 (a).

The second example demonstrated in this subsection is the active earth pressure problem studied by both Yang (2007) and Sun and Song (2016) based on the limit analysis method and the slip line method, respectively. The retaining wall was assumed smooth and vertical, and the following nonlinear failure criterion was used for the retained soil:

$$\tau = c_0 \left(1 + \frac{\sigma_n}{\sigma_t} \right)^{\frac{1}{m}} \tag{24}$$

in which σ_n and τ are the normal and the shear stresses on the failure surface, c_0 , σ_n and m are three parameters. The surface of the soil was horizontal and no surcharge was applied.

Table 1 and Table 2 compares the results obtained using different methods. Note that an additional horizontal acceleration ($a_h = 0.98\text{m/s}^2$) was considered in the cases listed in Table 2. In most of the cases, the results obtained by the present method agree well with those by Sun and Song (2016), and are slight higher than the ones by Yang (2007). These minor deviations may be caused by different shapes used for the failure surfaces. Herein, circular failure surfaces were used, while quadratic and log-spiral surfaces were assumed in Sun and Song (2016) and Yang (2007), respectively.

Table 1 Comparison of static active earth pressures acting on a smooth and vertical wall

Active earth pressure (kN/m)	Coefficient m				
	1.2	1.4	1.6	1.8	2.0
Present method	25.56	32.19	37.56	41.79	45.30
Sun and Song (2016)	23.30	31.16	37.29	41.28	43.88
Yang (2007)	22.53	28.87	34.01	38.41	41.98

$H = 4.0\text{m}$, $c_0 = 9\text{ kPa}$, $\sigma_t = 20\text{ kPa}$, $\gamma = 18\text{ kN/m}^3$.

Table 2 Comparison of dynamic active earth pressures acting on a smooth and vertical wall

Active earth pressure (kN/m)	Coefficient m				
	1.2	1.4	1.6	1.8	2.0
Present method	36.19	43.83	49.86	54.63	58.46
Sun and Song (2016)	34.35	42.04	49.32	55.13	59.96
Yang (2007)	32.66	39.78	45.61	50.39	54.32

$H = 4.0\text{m}$, $c_0 = 9\text{ kPa}$, $\sigma_t = 20\text{ kPa}$, $\gamma = 18\text{ kN/m}^3$, $\sigma_h = 0.98\text{m/s}^2$.

The satisfactory solutions obtained for the above examples prove that the slices-based limit equilibrium method is reliable in evaluating the static and dynamic active earth pressure exerted upon vertical or sloping retaining walls by soils with either linear or nonlinear failure strength behavior. In the following part, some topics related to the slices-based limit equilibrium method were discussed further.

4. DISCUSSIONS ON THE SLICES-BASED METHOD

All the examples demonstrated previously were studied using the assumption in Eqs. (16) and (17). In this part, another two continuous $f(x)$ functions were used for the construction of $\beta(x)$, i.e.

$$f(x) = \begin{cases} \sin \frac{2\pi}{b-a}(x-a) & \frac{x-a}{b-a} \leq \frac{1}{4} \\ \sin \left[\frac{\pi}{3} + \frac{2\pi}{3(b-a)}(x-a) \right] & \frac{x-a}{b-a} > \frac{1}{4} \end{cases} \quad (25)$$

and

$$f(x) = \begin{cases} \sin \frac{2\pi}{3(b-a)}(x-a) & \frac{x-a}{b-a} \leq \frac{3}{4} \\ \sin \left[\frac{2\pi}{(b-a)}(x-a) - \pi \right] & \frac{x-a}{b-a} > \frac{3}{4} \end{cases} \quad (26)$$

Both functions were shown in Fig. 7 together with the one given in Eq. (17). Eq. (25) shifts the peak to the coordinate $x = a + (b-a)/4$, while Eq. (26) moves it to $x = a + 3(b-a)/4$.

4.1. PREFERENCE OF THE ITERATIVE VARIABLE FOR LOCAL MINIMIZATION PROCESSES

As was pointed out previously, both the coefficient λ and the point of application T_b could be used as the iterative variable for the local minimization processes. Herein, it will be shown that for soils with linear strength behavior the minimization process is not necessary essentially. However, some subtle difference may exist when a nonlinear failure criterion was used for the retained soil, and there would be a preference for different problems.

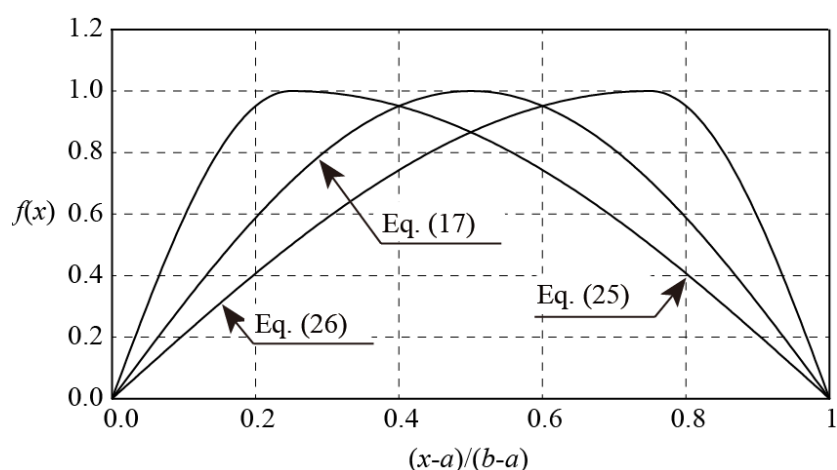


Fig. 7. The $f(x)$ functions given by Eqs. (17), (25) and (26)

The example shown in Fig. 4 was studied again here to clarify the above argument. First, the linear failure criterion was used ($\varphi = 35^\circ$). Fig. 8(a) shows the variation of the unbalanced moment M_u with the coefficient λ for a particular failure surface (the critical circular one based on Eq. (17) and a given point of application, i.e., $(Y_b - T_b)/H = 0.5$). No matter which function was used for $f(x)$, the unbalanced moment increases monotonically with λ , and there is only one particular λ that makes the unbalanced moment vanishing ($M_u = 0$). This characteristic is quite beneficial for solving Eq. (18). Fig. 8(b) ~ (d) plots the mutual relationships between the coefficient λ , the active earth pressure coefficient and the point of application for this critical failure surface. A continuous increase of λ results in a monotonic decrease of the active earth pressure and meanwhile a continuous descending of the point of application as shown in Fig. 8(b) and Fig. 8(c).

Furthermore, it is interesting to note that for a given point of application, the resultant active earth pressures predicted with three $f(x)$ functions are almost the same as shown in Fig. 8(d). This finding can be explained by the fact that the critical circular failure surface is steep and very close to a plane one and therefore the active earth pressure is almost not influenced by $\beta(x)$ as verified in Section 3.1.

It also deserves to point out that no stationary points exist on the curves plotted in Fig. 8(b) and Fig. 8(d), and the local minimum active earth pressure can only be attained at the specified upper bound of λ or the lower bound of $(Y_b - T_b)/H$. The local minimization process, therefore, is in fact not necessary for soils with linear strength behavior. Instead, the upper bound of λ or the lower bound of $(Y_b - T_b)/H$ could be specified directly. Since the point of application has a clearer physical meaning and the bound of which can be judged more easily according to the flexibility of the retaining structures (Chen 2003), we suggest using the lower bound of the latter for the evaluation of the active earth pressure. The fact that given a point of application the active earth pressure is almost independent of the selection of $f(x)$ (Fig. 8(d)) serves as an additional reason for this suggestion.

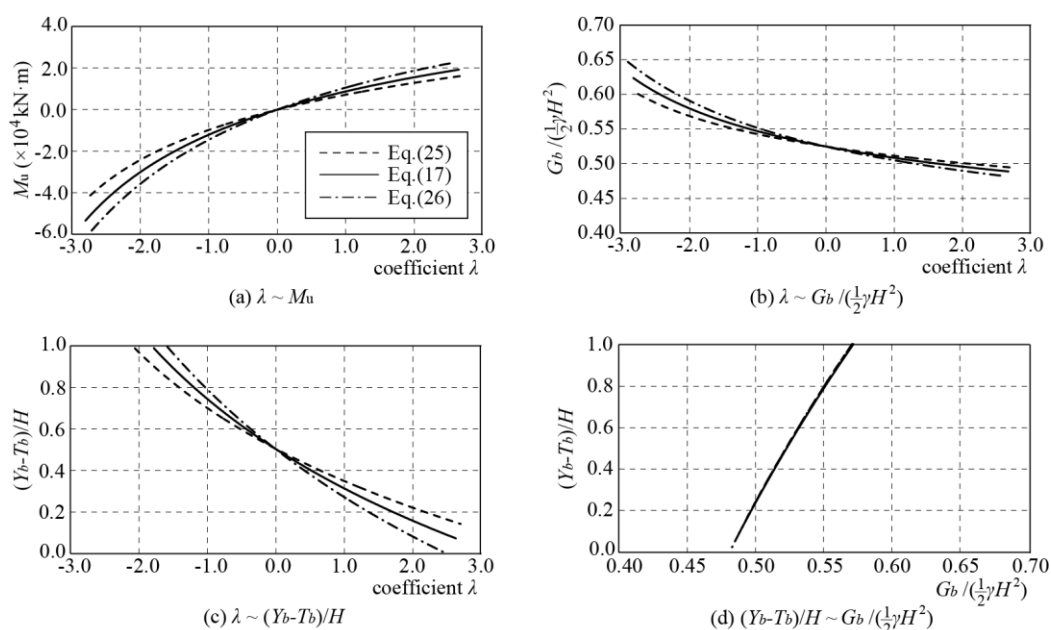


Fig. 8. The influences of λ on the unbalanced moment and the active earth pressure as well as its point of application for a given circular failure surface ($c = 0$, $\phi = 35^\circ$)

To study the counterparts of the curves plotted in Fig. 8 for soils obeying a nonlinear failure criterion. Eq. (1) was used again with σ_3 replaced by σ_n . ϕ_0 and $\Delta\phi$ were set to 54.0° and 11.6° , respectively, which were among the typical ranges of rockfill materials. The failure surface used was the critical one corresponding to $(Y_b - T_b)/H = 0.66$ without local minimization processes. Fig. 9(a) plots the unbalanced moment M_u against the coefficient λ . Only the M_u predicted with Eq. (25) increases monotonically with λ while the M_u predicted with Eq. (17) and Eq. (26) experienced an initial decrease and a subsequent increase when λ was increased continuously. In particular, the $M_u \sim \lambda$ curve predicted with Eq. (17) has two points satisfying $M_u = 0$ while the one by Eq. (26) has no solution for this nonlinear equation. These characteristics can result in numerical difficulty in obtaining converged or reliable solutions for some given T_b . Although such numerical difficulty may not always present for all failure surfaces, it cannot be judged in advance.

The curves plotted in Fig. 9(b) demonstrate again the existence of local minimum active earth pressures and therefore the necessity of performing local minimization processes, when the retained soil exhibits a nonlinear strength behavior. As the solution of Eq. (18) may not be unique for a given T_b , it is possible to obtain an unreliable active earth pressure if no local minimization was employed. Take the curves corresponding to Eq. (26) as an example, there are two possible values of λ that satisfy the condition $(Y_b - T_b)/H = 0.6$ for the current failure surface, as indicated by A and B in Fig. 9(c). It is very possible that the solution denoted by B be obtained due to the selection of the initial guess of λ , and hence the high active earth pressure denoted by B in Fig. 9(d) be recorded. Because the global maximization process is to seek the maximal value of G_b , it is very likely that the active earth pressure indicated by point B be finally picked, which, of course, overestimates the real active earth pressure. Selecting other $f(x)$ functions makes no guarantee to avoid such a possible dilemma. Therefore, for soils with nonlinear strength behavior, we suggest using the coefficient λ as the iterative variable and always performing a local minimization process for each possible failure surface, so that the unreasonable solutions such as the one denoted by point B can be discarded.

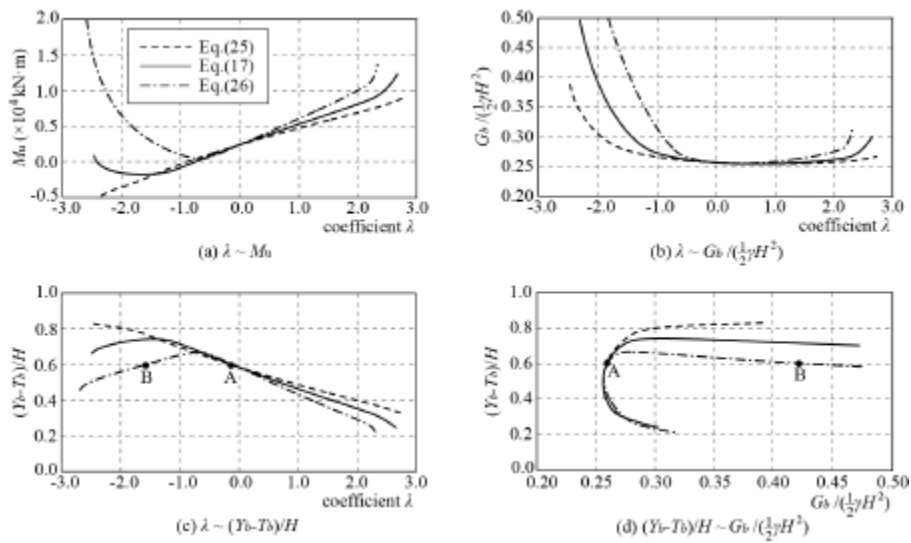


Fig. 9. The influences of λ on the unbalanced moment and the active earth pressure as well as its point of application for a given circular failure surface ($\varphi_0 = 54^\circ, \Delta\varphi = 11.6^\circ$)

The possible range of λ can be obtained by specifying the maximum interslice force angle according to the shear strength of the retained soils. It is also necessary to provide an allowable range for the point of application of the active earth pressure based on the flexibility of the retaining structures.

4.2. INFLUENCE OF $\beta(x)$ ON THE ACTIVE EARTH PRESSURE

To clarify the influence of the interslice force angle function $\beta(x)$ on the active earth pressure further, Eqs. (17), (25) and (26) were used in conjunction with Eq. (16) to study the problem stated in Fig. 6 again. Both plane failure surfaces and circular failure surfaces were used herein. Fig. 10 shows the locations of the critical failure surfaces ($y=y(x)$) and the lines of thrust ($y=yt(x)$), lines formed by connecting the points of application of $G(x)$ as well as the values of the active earth pressure predicted.

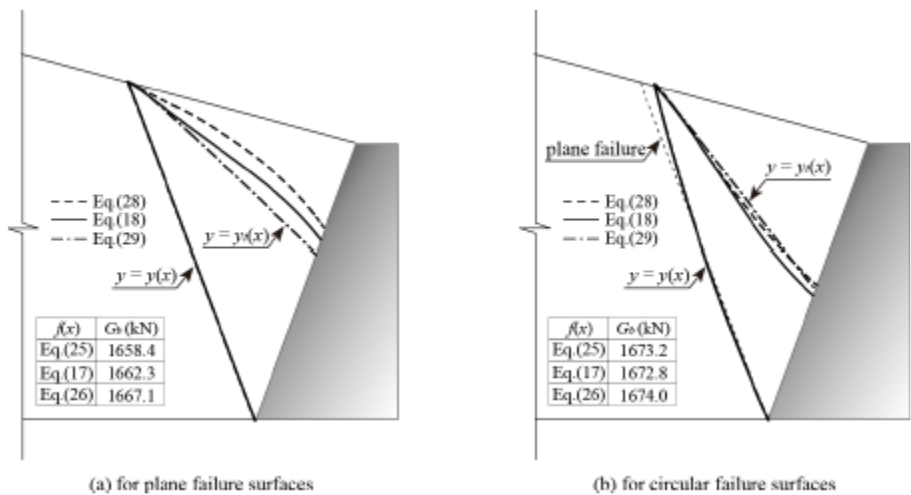


Fig. 10. The failure surfaces ($y=y(x)$), lines of thrust ($y=yt(x)$) and the active earth pressures predicted using Eqs. (17), (25) and (26)

The locations of the critical failure surfaces, either the plane ones or those circular ones, are almost the same regardless of the $f(x)$ functions used in Eq. (16). For both types of surfaces, the differences between the active earth pressures predicted with different $f(x)$ functions are negligible, with the maximum deviations not exceeding 1%. This is an evidence that the active earth pressure is almost not influenced by the interslice force angles. Furthermore, the circular critical failure surface as well as the magnitude of the active earth pressure are also very close to those of the plane one as shown in Fig. 10. That is to say a plane failure surface is acceptable in

evaluating the active earth pressure exerted by soils with a nonlinear failure criterion, at least for a first approximation. However, it should be noted that the lines of thrust and the point of application of the active earth pressure are clearly influenced by the selection of $f(x)$ functions and the type of failure surfaces. A circular failure surface generally results in a lower line of thrust and also a lower point of application compared with those for plane failure surfaces. In addition, the influence of the $f(x)$ function on the lines of thrust is more evident for plane failure surfaces than that for circular ones.

The detailed distributions of $G(x)$, $\sigma_n(x)$, $\beta(x)$ and $\varphi(x)$ corresponding to the results shown in Fig. 10 were plotted in Fig. 11 and Fig. 12, respectively. The abscissa in these figures is the relative distance of the concerned point measured from the left boundary ($x=a$) towards the retaining surface ($x=b$). For both types of failure surfaces, the interslice force, $G(x)$, increases monotonically from the left boundary to the retaining surface, with the influence of function $f(x)$ more evident near the center of the sliding mass than that near the both boundaries, as shown in Fig. 11(a) and Fig. 12(a). Despite of the small difference between the active earth pressures predicted for plane and circular failure surfaces, the distributions of normal stress, $\sigma_n(x)$, exhibit more considerable deviations. In Fig. 11(b) the normal stress σ_n increases initially with the relative distance until a peak is attained. After that point the normal stress σ_n decreases gradually until the retaining surface is reached. This particular distribution results in an initial decrease and a subsequent increase of the mobilized friction angle along the failure surface as shown in Fig. 11(d). Differently, the normal stress σ_n along the circular failure surface increases monotonically from the left boundary to the retaining wall, yielding a continuous decrease of the mobilize friction angle along the failure surface as shown in Fig. 12 (b) and (d).

Although the values of the active earth pressure predicted with different $f(x)$ functions are very close to each other for a given failure surface, the interslice force angles along the sides of soil slices, $\beta(x)$, may show considerable difference, as demonstrated in Fig. 11(c) and Fig. 12(c). As a result, the normal stress and the mobilized friction angle along the failure surface also differ from each other as shown in Fig. 11 and Fig. 12. It is the versatility of the backfilled soil in adjusting the interslice forces and the stresses along the failure surface according to the interslice force angle distributions that makes the minimum force required to keep the sliding mass stable almost not changed by $\beta(x)$. Examples studied herein also demonstrate the applicability of Eqs. (16) and (17) in earth pressure problems, even if the retained soil obeys a nonlinear failure criterion.

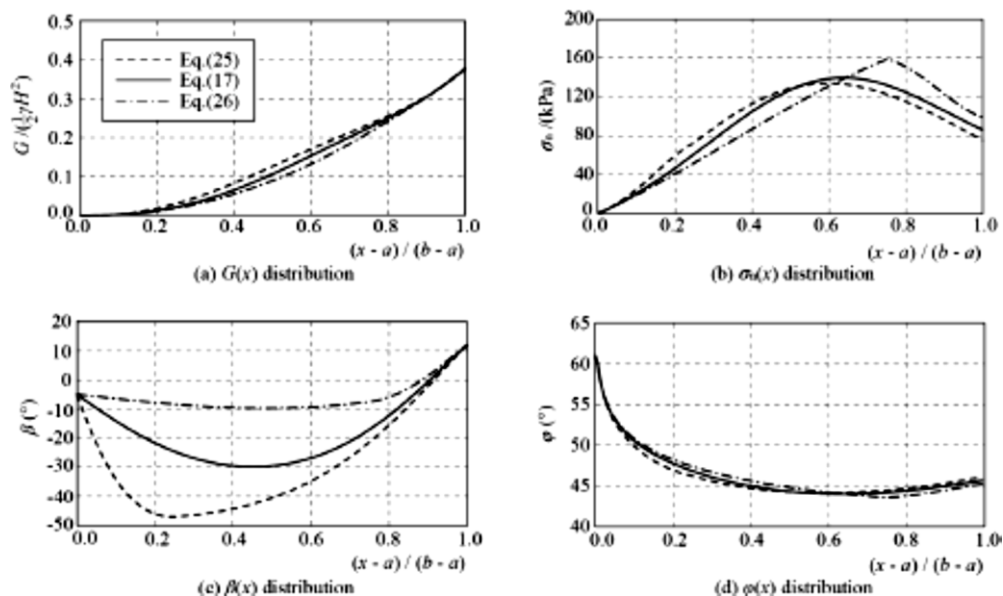


Fig. 11. The distributions of $G(x)$, $\sigma_n(x)$, $\beta(x)$ and $\varphi(x)$ (using a plane failure surface)

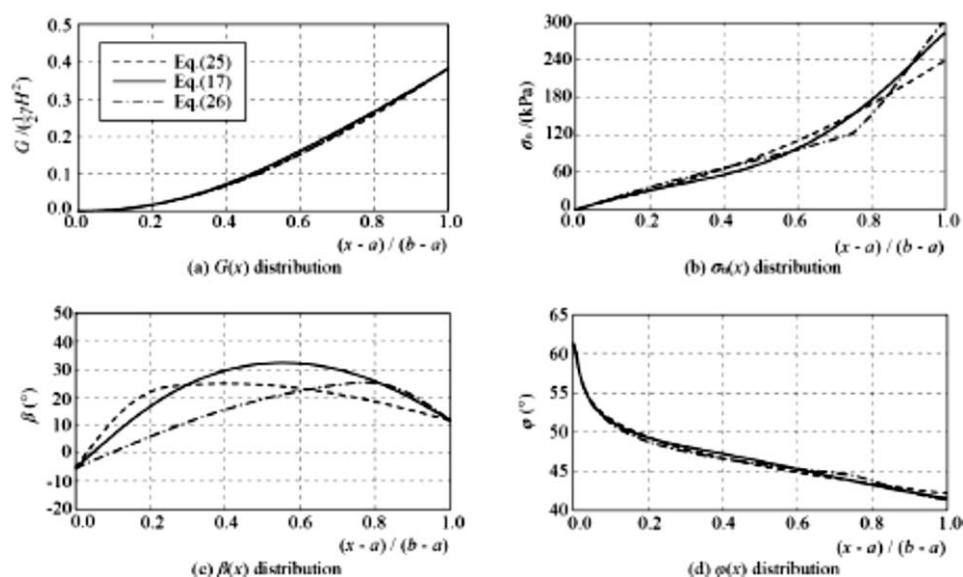


Fig. 12. The distributions of $G(x)$, $\sigma_n(x)$, $\beta(x)$ and $\varphi(x)$ (using a circular failure surface)

4.3. DETERMINATION OF NONLINEAR STRENGTH PARAMETERS

In geotechnical practice, two types of experiments are most widely used in determining the strength of soils, i.e. direct shear experiments and triaxial compression experiments (Smith and Smith 1998). Definitions of the friction angle in both experiments are not the same. In direct shear experiments, the friction angle is defined as $\varphi = \tan^{-1}(\tau/\sigma_n)$, and it is evaluated in triaxial experiments by $\varphi = \sin^{-1}[(\sigma_1 - \sigma_3)/(\sigma_1 + \sigma_3)]$. Note cohesionless soils are considered here. It can be seen from Eq. (3) that in the slices-based limit equilibrium method, the definition used in direct shear experiments is inherently used. However, for soils with linear strength behavior, the friction angles obtained by triaxial compression experiments can be used equivalently because $\tan^{-1}(\tau/\sigma_n) = \sin^{-1}[(\sigma_1 - \sigma_3)/(\sigma_1 + \sigma_3)]$.

For soils with nonlinear strength behavior, cautions should be exercised on the experiments and the way to establish the failure envelope. Take the one given in Eq. (24) as an example, if it was based on direct shear experiments, then the relevant parameters can be used directly. However, if triaxial experiments were conducted to determine the parameters, attentions should be paid. It is a common practice in geotechnical engineering that the common tangent of a series of Mohr circles be defined as the strength envelope as illustrated by the solid curve in Fig. 12. The points sampled in this way do not coincide with those where the shear stress ratio (τ/σ_n) achieves a maximum. For instance, point A on the largest Mohr circle is sampled to construct the strength envelope, however, the shear stress ratio achieves a maximum at point B, which is not the same as point A. To be consistent with the strength definition in slices-based limit equilibrium method, point B should be sampled from this particular Mohr circle, instead of point A. The final strength envelope thus obtained will be slightly lower than the common tangent as shown in Fig. 12 (the dashed curve). For soils with a linear strength envelope, the points on the common tangent always coincide with those points where the shear stress ratio achieves a maximum, therefore the parameters can be used directly.

Based on the above considerations, the easiest way to obtain a nonlinear strength envelope and the relevant parameters for active earth pressure problems using the current method is to conduct direct shear experiments (Matsuoka and Liu 1998; Oyangurena et al. 2008; Liu 2009;) and plot the peak friction angle or the peak shear stress against the vertical normal stress. On the other hand, if triaxial compression experiments were performed and a series of Mohr circles were at hand, it is also simple to convert them to the normal stress ~ maximum shear stress pairs. To this end, the equation for the Mohr circle is used, i.e.

$$\tau = \sqrt{(\sigma_1 - \sigma)(\sigma - \sigma_3)} \tag{27}$$

Therefore, the shear stress ratio could be expressed as follows:

$$\frac{\tau}{\sigma} = \sqrt{\left(\frac{\sigma_1}{\sigma} - 1\right)\left(1 - \frac{\sigma_3}{\sigma}\right)} \tag{28}$$

At the maximum shear stress ratio point, the following stationary condition should be fulfilled:

$$\frac{d(\tau/\sigma)}{d\sigma} = 0 \tag{29}$$

from which the normal stress can be obtained, i.e.

$$\sigma_n = \frac{2\sigma_1\sigma_3}{\sigma_1 + \sigma_3} \tag{30}$$

Substituting the normal stress obtained into Eq. (27) yields the corresponding shear stress τ_n , and then a failure envelope can be constructed based on these (σ_n, τ_n) pairs.

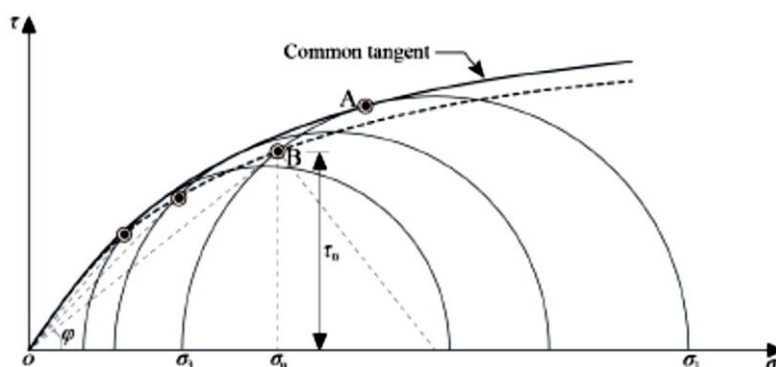


Fig. 12. The strength envelope based on triaxial experiments

5. CONCLUSIONS

In this paper, we demonstrated the applicability of the slices-based limit equilibrium method in evaluating the active earth pressure applied by soils with nonlinear strength behavior. Two extensions to the original method for soils with linear strength behavior were made. First, an iterative process was performed for the normal effective stress along the failure surface, so that the peak friction angle mobilized is consistent with the normal effect stress. Second, a local minimization process was employed for each possible failure surface, so that the unreasonable results can be discarded. The following conclusions can be summarized based on the current research:

(1) The active earth pressure is a functional depends on the location of the failure surface and the distribution of interslice force angles. Mathematically, solving an active earth pressure problem is seeking the saddle point of a surface. At this particular point, a maximum active earth pressure of a series of minimum ones is achieved. The local minimums can be obtained by varying the distribution of interslice force angles, and the global maximum is the one corresponding to the critical failure surface.

(2) Introducing an assumption (Eq. (16)) for the interslice force angle distribution largely simplifies the processes of seeking a maximum from minimums. The variational problem in the function space is simplified into an extreme problem in the real space. In addition, for soils with linear strength behavior, the active earth pressure for a given failure surface decreases continuously as the point of application is lowered. Therefore, the local minimums can only be achieved at the lower boundary of the application point and the minimization process is actually not needed. However, for soils with nonlinear strength behavior, local minimums do exist and the nonlinear equation for moment equilibrium may become non-monotonic and ill-shaped, which adds difficulty in obtaining a converged and reliable solution. Therefore, the coefficient λ in Eq. (16) is suggested to be used for the local minimization processes.

(3) The distribution of interslice force angle, $\beta(x)$, influences the normal stress distribution and the mobilized friction angle along the failure surface. However, the resultant active earth pressure applied on the retaining surface is almost not influenced. In particular, for soils obeying a linear failure criterion, the active earth

pressures predicted with different $f(x)$ functions are almost the same for a given point of application. For soils with nonlinear strength behavior, however, the lines of thrust and the application points of the active earth pressure are clearly influenced by $f(x)$ and $\beta(x)$, particularly when plane failure surfaces were used. The lines of thrust and the points of application predicted for circular failure surfaces are generally lower than those for plane failure surfaces. However, the critical failure surface and the corresponding active earth pressure are very close to each other, indicating the feasibility of using plane failure surfaces for the evaluation of the active earth pressure by soils with nonlinear strength behavior.

(4) In the slices based limit equilibrium method, the peak friction angle is defined using the normal and shear stresses along the maximum shear stress ratio plane, which is consistent with the direct shear experiments. When the nonlinear strength envelope is constructed using triaxial compression experiments, cautions should be exercised. If the common tangent of a series of Mohr circles is drawn to represent the strength envelope, then the parameters cannot be used directly. Conversion of the experimental data ((σ_1, σ_3) pairs) to the normal and shear stresses pairs ((σ_n, τ_n)) is required.

It deserves to point out finally that the assumption used for the interslice force angles evidently reduced the possibility of the distribution of interslice force angles. Exclusion of other possible distributions means the local minimum active earth pressure obtained may not be the real minimum one. That is to say the local minimum active earth pressure obtained with a given distribution of the interslice force angles is always a conservative one, the maximum of which may lead to a conservative design in engineering practice.

6. ACKNOWLEDGEMENT

This work was supported by the national Natural Science Foundation of China (NSFC, Grant Nos. 51539006 & 51379130). The financial support from the Ministry of Water Resource (MWR, Grant No. 201501035) was also greatly appreciated.

7. REFERENCES

1. Andrews L C, Phillips R L. *Mathematical Techniques for Engineers and Scientists*. SPIE Press, Washington, 2004.
2. Benmeddour D, Mellas M, Frank R, Mabrouki A. Numerical study of passive and active earth pressures of sands. *Computers and Geotechnics*, 2012, 40: 34-44.
3. Bhatia S K, Bakeer R M. Use of the finite element method in modelling a static earth pressure problem. *International Journal for Numerical and Analytical Methods in Geomechanics*, 1989, 13(2): 207-213.
4. Chen W F. *Limit Analysis and Soil Plasticity*. Elsevier, Amsterdam, 1975.
5. Chen Z Y, Li S M. Evaluation of active earth pressure by the generalized method of slices. *Canadian Geotechnical Journal*, 1998, 35(4): 591-599.
6. Chen Z Y, Morgenstern N R. Extensions to the generalized method of slices for stability analysis. *Canadian Geotechnical Journal*, 1983, 20(1): 104-119.
7. Chen Z Y. *Soil Slope Stability Analysis, Theory, Methods and Programs*. China Water & Power Press. Beijing, 2003.
8. Collins I F, Gunn C I M, Pender M J, Yan W. Slope stability analyses for materials with a non-linear failure envelope. *International Journal for Numerical and Analytical Methods in Geomechanics*, 1988, 12(5): 535-550.
9. Fu Z Z, Chen S S. *Limit Equilibrium Analysis Program for Earth and Rockfill Structures (LEAPERS)*. Theory and Manual. Report of Nanjing Hydraulic Research Institute. Nanjing, 2013
10. Fu Z Z, Li G Y. *Three-Dimensional Finite Element Analysis of the Behavior of the Jiayan Concrete Face Rockfill Dam in Yunnan Province, China*. Scientific Report of Nanjing Hydraulic Research Institute (No. HJ312029), Nanjing, 2012.
11. Fu Z Z, Wang Z J, Chen S S. Calculation method for earth pressure and stability of high submerged toe walls of concrete faced rockfill dams. *Hydro-Science and Engineering*, 2014, 3: 1-8.
12. Jiang J C, Baker R, Yamagami T. The effect of strength envelope nonlinearity on slope stability computations. *Canadian Geotechnical Journal*, 2003, 40(2): 308-325.
13. Kreyszig E. *Advanced Engineering Mathematics (Tenth Edition)*. John Wiley & Sons. Jefferson City, Missouri, 2010.

14. Leps T M. Review of shearing strength of rockfill. *Journal of the Soil Mechanics and Foundation Division*, 1970, 96(4): 1159-1170.
15. Liu F Q, Wang J H. A generalized slip line solution to the active earth pressure on circular retaining walls. *Computers and Geotechnics*, 2008, 35(2): 155-164.
16. Liu S H, Fu Z Z, Yang J Z. Back analysis of deformation parameters of rockfills in a pumped storage station project. In: *Proceedings of the 1st International Conference on Long Term Effects and Seepage Behavior of Dams* (eds. Zhu Y M & Liu S H). pp. 23-30, 2008.
17. Liu S H. Application of in situ direct shear device to shear strength measurement of rockfill materials. *Water Science and Engineering*, 2009, 2(3): 48-57.
18. Maksimovic M. Nonlinear failure envelope for soils. *Journal of Geotechnical Engineering*, 1989, 115(4): 581-586.
19. Matsuoka H, Liu S H. Simplified direct box shear test on granular materials and its application to rockfill materials. *Soils and Foundations*, 1998, 38(4): 275-284.
20. Oyangurena P R, Niciezab C G, Fernándezb M I, Palaciob C G. Stability analysis of Llerin dam: an in situ direct shear test. *Engineering Geology*, 2008, 100(3-4): 120-130.
21. Peng M X, Chen J. Slip-line solution to active earth pressure on retaining walls. *Géotechnique*, 2013, 63(12): 1008-1019.
22. Potts D M, Fourie A B. A numerical study of the effects of wall deformation on earth pressures. *International Journal for Numerical and Analytical Methods in Geomechanics*, 1986, 10(4): 383-405.
23. Rahardjo H, Fredlund D G. General limit equilibrium method for lateral earth force. *Canadian Geotechnical Journal*, 1984, 21(1): 166-175.
24. Smith G N, Smith I G N. *Elements of Soil Mechanics* (7th Edition). Blackwell Science, London, 1998.
25. Sun Y J, Song E X. Active earth pressure analysis based on normal stress distribution function along failure surface in soil obeying nonlinear failure criterion. *Acta Geotechnica*, 2016, 11(2): 255-268.
26. Worden F T, Achmus M. Numerical modeling of three-dimensional active earth pressure acting on rigid walls. *Computers and Geotechnics*, 2013, 51: 83-90.
27. Xiao Y, Liu H L, Chen Y M, Jiang J S. Strength and deformation of rockfill material based on large-scale triaxial compression tests. I: Influence of density and pressure. *Journal of Geotechnical and Geoenvironmental Engineering*, 2014, 140(12): 10.1061/(ASCE)GT.1943-5606.0001176, 04014070.
28. Yang X L. Upper bound limit analysis of active earth pressure with different fracture surface and nonlinear yield criterion. *Theoretical and Applied Fracture Mechanics*, 2007, 47(1): 46-56.
29. Zakerzadeh N, Fredlund D G, Pufahl D E. Interslice force functions for computing active and passive earth force. *Canadian Geotechnical Journal*, 1999, 36(6): 1015-1029.
30. Zhang X J, Chen W F. Stability analysis of slopes with general nonlinear failure criterion. *International Journal for Numerical and Analytical Methods in Geomechanics*, 1987, 11(1): 33-50.

The Effect of Grout Curtain Efficiency on Abutments Stability of an Arch Dam

H. Mostafaei¹, M. Sohrabi Gilani², M. Ghaemian³

1- Civil Engineering Department, Isfahan University of Technology, Isfahan, Iran

2- Engineering Faculty, The University of Guilan, Rasht, Iran

3- Civil Engineering Department, Sharif University of Technology, Tehran, Iran

Email: m.sohrabi@guilan.ac.ir

Abstract

Abutment stability analysis of arch dams is one of the most challenging aspects in dam stability field of study. Generally, the rigid block model which has been presented by Londe is used to evaluate the stability of foundation wedges. In this paper the rock wedge in the left abutment of Luzzone dam has been studied. For this purpose, three components of unit-g acceleration are applied to the dam-reservoir-foundation finite element model. The safety factors are calculated due to different distribution of uplift pressure on the planes based on the extent of damages presumed for the grout curtain. The obtained results indicate that the uplift pressure can strongly affect the foundation stability and may lead to the wedge movement.

Keywords: Abutment Stability Analysis, Wedge, Arch Dams, Uplift Pressure.

1. INTRODUCTION

The safety of concrete dams is a major challenge for the owners due to their possible failure consequences when subjected to severe earthquake ground motions. One of the most important aspects in the stability of arch dams which have been encountered is the abutment stability. Failure of concrete arch dams showed that the main cause of the destruction of concrete arch dams is due to the rock mass instability in the abutments. In this regard, it is completely necessary to have proper and thorough analysis in order to evaluate stability of abutments for the purpose of dam safety. Yet it is not exclusively academic, as amply evidenced by disasters such as the Malapasset dam abutment failure and the Vajont rock slide [1, 2]. Because of scale effect, stability of the abutment varies generally with the wedge size and laws governing this variation are unknown. The rock slopes usually consists of discontinuities such as faults, joints and layering that must be considered in the abutment analysis.

Stability analysis of arch dam abutments was the topic of many studies. U.S. Army Corps of Engineering emphasize that the analysis of abutment stability requires very careful application of both engineering geology and rock mechanics and analytical techniques. The corresponding stability criteria have been recommended for different load case. Sohrabi et al. studied the stability of dam abutment including seismic loading. Time histories of safety factors as well as corresponding wedge displacement have been presented in their study[3]. Zenz et al. investigated seismic abutment stability of concrete arch dams. Accordingly they found that more sophisticated, realistic models show higher margins to entire system failure, which anticipates, that the existing model assumptions are conservative – as it is assumed[4]. In this paper, the abutment stability of Luzzone arch dam due to static and seismic loadings has been investigated. In order to calculate the thrust forces, a three dimensional finite element model of dam-foundation-reservoir has been developed and all three components of Kobe earthquake ground motions are applied to the model simultaneously. The safety factors are obtained for different scenarios of uplift pressure.

2. STABILITY ANALYSIS

In order to assess the stability of rock wedges, Londe method has been used by many researchers. In this method the wedges are defined by three probable sliding planes which have been shown by P1 (O, B, C), P2 (O, A, C) and P3 (O, A, B) in figure 1.

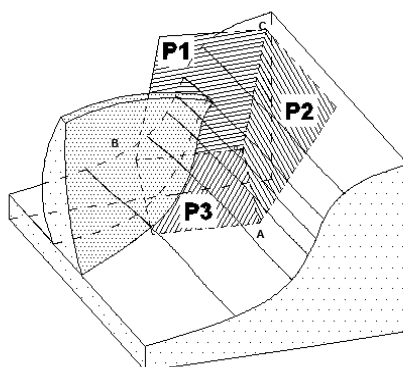


Figure 1. The geometry of plane

The geometry of each plane is characterized by its area and orientations (Dip and Dip direction). In this method the wedge is considered to be rigid and tensile strength on contact surfaces of the wedge are neglected. The cohesion and friction angle of each plane have profound effects on the wedge stability and should be estimated by the geology and rock mechanics studies. The moments of the forces are assumed negligible and their corresponding effects on the equilibrium equations are ignored. The wedge failure occurs only in the case of its movement on one or two of its supporting surfaces in the direction opposite to the wedge corner[3].

3. APPLIED FORCES

The dead load is encapsulated in the weight of the wedge. The weight of the wedge as a dead load can be calculated by the wedge volume time the specific weight of the rock. The uplift pressure on each plane can be determined due to the water level, geometry and area of the plane and the performance of grout curtain. In spite of these two forces which are constant during the analysis, the inertia and thrust forces are time dependent and their magnitudes and directions will change during earthquakes. It should be mentioned that the thrust forces which are applied by the dam to the wedge include the weight of the dam, hydrostatic, hydrodynamic and seismic loads based on the considered load combinations. The resultant of the applied forces can be calculated as:

$$F_{Res}^W = F_W^W + F_{Up}^W + F_{EQ}^W + F_{TH}^D \quad (1)$$

Where F_W^W , F_{Up}^W , F_{EQ}^W and F_{TH}^D are weight of the wedge, total uplift forces on planes, inertia force on wedge and the thrust force of the dam, respectively. Considering coordinate system that z-component corresponds to the vertical direction, the applied forces are represented in vector notation as follow:

$$F_W^W = \begin{bmatrix} 0 \\ 0 \\ -m^W \times g \end{bmatrix} \quad (2)$$

$$F_{UP}^W = \begin{bmatrix} U_X^1 \\ U_Y^1 \\ U_Z^1 \end{bmatrix} + \begin{bmatrix} U_X^2 \\ U_Y^2 \\ U_Z^2 \end{bmatrix} + \begin{bmatrix} U_X^3 \\ U_Y^3 \\ U_Z^3 \end{bmatrix} \quad (3)$$

$$F_{EQ}^W = (-m^W) \times \begin{bmatrix} \ddot{u}_x \\ \ddot{u}_y \\ \ddot{u}_z \end{bmatrix} \quad (4)$$

$$F_{EQ}^W = \begin{bmatrix} F_{TH-x}^D \\ F_{TH-y}^D \\ F_{TH-z}^D \end{bmatrix} \tag{5}$$

Where m^W , U^1 , U^2 and U^3 are mass of the wedge and the uplift forces on planes P_1 , P_2 and P_3 respectively.

Also \ddot{u}_x , \ddot{u}_y , \ddot{u}_z and F_{TH}^D are three components of ground acceleration time histories and the thrust force due to static and seismic loadings.

4. EQUILIBRIUM EQUATION AND SLIDING

Equilibrium equations are used to obtain three corresponding reaction forces on the planes (N_1 , N_2 and N_3). Due to the fact that planes are sole compressive, tensile normal forces mean that the planes are opened. When a plane is open it conclude that the considered sliding mode is not appropriate and will lead to the other different sliding modes excluding this plane. Eight possible separations or sliding modes which are likely to happen are listed in Table 1.

Table 1- Possible separation or sliding modes

<i>Separation or Sliding Index</i>	<i>Definition</i>	<i>Nature of Sliding Vector</i>
1	All the plane are compressive	Stable
2	N1 is compressive	Sliding on Plane P1
3	N2 is compressive	Sliding on Plane P2
4	N3 is compressive	Sliding on Plane P3
5	N1 and N2 are compressive	Sliding on intersection P1,P2
6	N1 and N3 are compressive	Sliding on intersection P1,P3
7	N2 and N3 are compressive	Sliding on intersection P2,P3
8	All the plane reactions are tensile	Unstable

The sliding modes are described briefly in the following:

- ❖ Case 1: The planes normal reaction forces are compressive which means that all planes are in contact. So, the wedge is perfectly stable.
- ❖ Case 2: The normal force on plane P1 is compressive but, the reactions of planes P2 and P3 are in tension. By ignoring the planes P2 and P3 and solving the equilibrium equations the normal and shear forces on plane P1 are obtained. If the obtained normal force on P1 is compressive it means that the assumption is verified and sliding occurs on plane 1. The safety factor is obtained as follow:

$$SF = \frac{N_1 \times \tan(\varphi_1) + c_1 \times A_1}{\text{Shear force on plane P1}} \tag{6}$$

- ❖ Case 3: The reaction of plane P2 is compressive and reactions of planes P1 and P3 are in tension. This case is similar to case 2.
- ❖ Case 4: The reaction of plane P3 is compressive and reactions of plane P1 and P2 are in tension. This case is similar to case 2.
- ❖ Case 5: The normal forces on planes P1 and P2 are compressive and the reaction of plane P3 is in tension. In other word plane P3 is open and planes P1 and P2 are still in contact. To check the movement along the intersection line of planes P1 and P2, the force in this direction should be calculated. By solving the equilibrium equation and ignoring the plane P3, the values of normal forces on planes P1 and P2 and the corresponding shear force are obtained. The safety factor is calculated as follow:

$$SF = \frac{N_1 \times \tan(\varphi_1) + c_1 \times A_1 + N_2 \times \tan(\varphi_2) + c_2 \times A_2}{\text{Shear force in direction of inter section P1 P2}} \quad (7)$$

- ❖ Case 6: The reactions of planes P1 and P3 are compressive and normal force of plane P2 is in tension. This case is similar to case 5.
- ❖ Case 7: The reactions of planes P2 and P3 are compressive and normal force of plane P1 is in tension. This case is similar to case 5.
- ❖ Case 8: All the reactions are in tension and the wedge is detached from all its three supporting planes. In this case, the other sliding modes should be checked and if the assumption that all planes are in tension has been verified it means that the wedge is completely unstable.

4. CASE STUDY

This study is aimed to investigate the abutment stability of an arch dams due to seismic loading. For this purpose, Luzzone dam is selected. The Luzzone dam is a double curved concrete dam completed in 1963. The dam elevation heightened 17m between 1997 and 1998 and so the total height of dam is receipted 225m (Sohrabi Gilani, et al., 2009). Figure 2 shows a view of Luzzone dam [5].

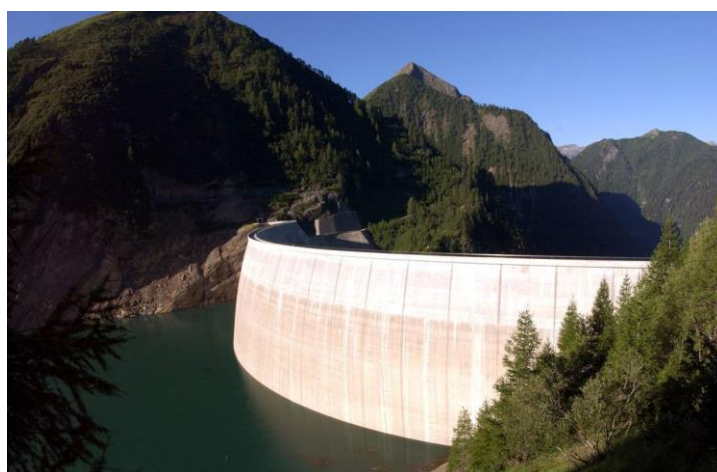


Figure 2. Luzzone dam

5. FINITE ELEMENT MODEL

Figures 3 and 4 shows the provided finite element model of Luzzone dam. 332 and 2984 eight nodes brick elements including 249 and 3797 nodes are used to model the dam body and foundation, respectively. For modeling the reservoir 1080 eight nodes fluid elements are used. The reservoir is truncated at a distance from the upstream face which is about two times of the dam height.

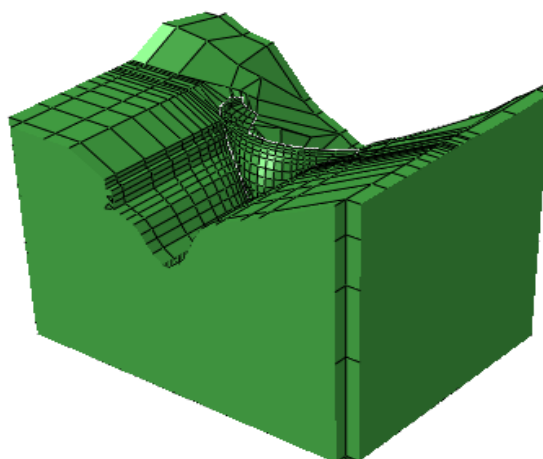


Figure 3. Finite element model of Luzzone dam

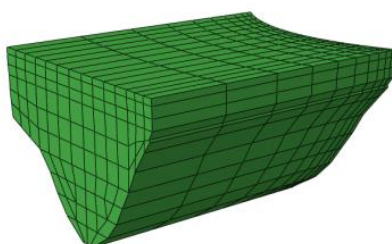


Figure 4. Reservoir finite element model

The material properties of the concrete and rock foundation are presented in table 2. The damping of the material considered to be five percent.

Table 2- Material properties of the dam concrete and the foundation rock

Materials	Elastic modulus (GPa)	Poisson's ratio	Density ($\frac{\text{kg}}{\text{m}^3}$)
Concrete	27	0.167	2400
Foundation rock	25	0.2	2600

6. WEDGE DEFINITION

A unit-g acceleration is excited in each of three global directions for the purpose of seismic analysis. The accelerations are scaled according to the peak ground acceleration to 0.30g.

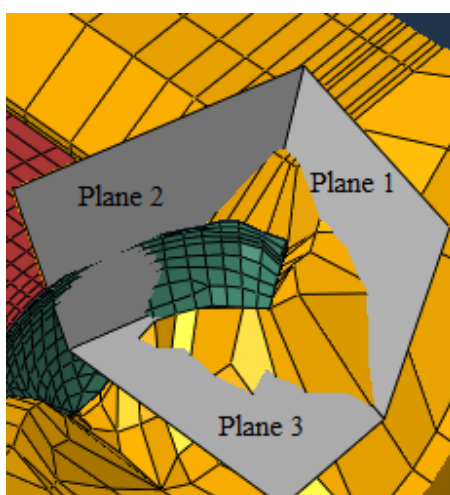


Figure 5. Geometry of the wedge

Table 3- Characteristic of the wedge

Plane	Friction degree	Cohesion	Area (m ²)	Dip Angle	Dip Direction
Plane1	35	-	23300	65	5
Plane2	35	-	7200	76	280
Plane3	35	-	28650	0	0

7. SEISMIC LOADS

The ground acceleration time history of the Kobe earthquake is considered for the purpose of seismic analysis. The accelerations are scaled according to the peak ground acceleration to 0.40g. The ground acceleration earthquakes are applied in stream (x-direction), cross-stream (y-direction) and vertically upward (z-direction) directions, simultaneously.

8. UPLIFT PRESSURE EFFECTS

In order to investigate the uplift pressure effects on the wedge stability, as indicated in table 4, six load combinations were considered based on damage of the grout curtain.

Table 4- Load combination

Combination	Load			
	Weight	Uplift	EQ	Thrust Force
Combo1	<input type="checkbox"/>	0%	<input type="checkbox"/>	<input type="checkbox"/>
Combo2	<input type="checkbox"/>	20%	<input type="checkbox"/>	<input type="checkbox"/>
Combo3	<input type="checkbox"/>	40%	<input type="checkbox"/>	<input type="checkbox"/>
Combo4	<input type="checkbox"/>	60%	<input type="checkbox"/>	<input type="checkbox"/>
Combo5	<input type="checkbox"/>	80%	<input type="checkbox"/>	<input type="checkbox"/>
Combo6	<input type="checkbox"/>	100%	<input type="checkbox"/>	<input type="checkbox"/>

By rotating the applied horizontal acceleration, the safety factor varies from 0.98($\theta=320$) to 1.49($\theta=170$). Figure 6 indicate the minimum safety factors for all load combinations. The obtained results show that when the uplift forces increase, the safety factors significantly decrease and even for the full uplift condition, the safety factor is less than one. This means that the wedge moves and seriously jeopardize the dam safety[6].

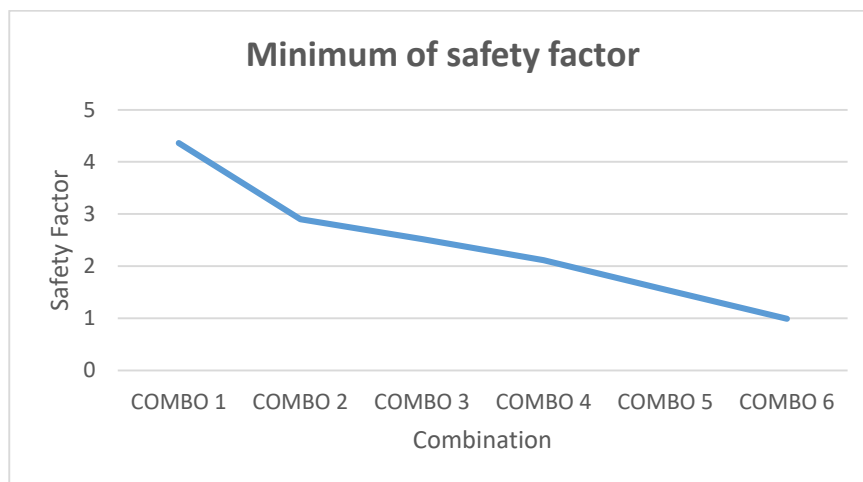


Figure 6. The minimum of safety factor of wedge for different load combination

9. CONCLUSIONS

The stability analysis of the left abutment of Luzzone dam was carried out to investigate the effect of uplift pressure on the wedge stability. In this study the Londe method is used and the safety factors are calculated for different distribution of uplift pressure based on the extent of damages of the grout curtain. The obtained results indicate that the uplift pressure can strongly affect the foundation stability and may even lead to wedge movement. So, the probability of the grout curtain failure during severe ground motions should be considered as a post-earthquake load combination. The monitoring of drainage system can play a significant role to assure the owner of the dam safety and help them to take the proper measures in critical conditions.

10. REFERENCES

1. P. Londe, "Analysis of the stability of rock slopes," *Quarterly Journal of Engineering Geology and Hydrogeology*, vol. 1, pp. 93-127, 1973.
2. P. Londe, "The Malpasset dam failure," presented at the The International Workshop on dam Failure, Indiana, 1987.
3. M. Sohrabi Gilani, R. Feldbacher, and G. Zenz, "Stability of dam abutment including seismic loading," presented at the 10th ICOLD Benchmark Workshop, Paris, 2009.
4. G. Zenz, M. Goldgruber, and R. Feldbacher, "Seismic stability of a rock wedge in the abutment of an arch dam," *Geomechanics and Tunneling*, vol. 5, pp. 186-194, 2012.
5. H. Mirzabozorg, M. Varmazyari, M. Hoseini, and A. Gharebaghi, S. , "A comparative study of rock wedge stability of an arch dam abutment subjected to static and seismic loading," *Soil mechanics and Foundation Engineering*, vol. 52, 2015.
6. H. Mostafaei, M. Sohrabi Gilani, and M. Ghaemian, "Stability analysis of arch dam abutments due to seismic loading," *Scientia Iranica A*, vol. 24, pp. 467-475, 2017.

Effect of Fine Content on Lateral Wall Movement of Bearing Reinforcement Earth (BRE) Walls

K. Sukmak¹, S. Horpibulsuk², P. Sukmak³

1-School of Engineering and Resources, Walailak University, k.sukmak_ce@hotmail.com

2- School of Civil Engineering, Suranaree University of Technology, suksun@g.sut.ac.th

3-School of Engineering and Resources, Walailak University, patimapon.su@wu.ac.th

Email: suksun@g.sut.ac.th

Abstract

This paper presents a numerical parametric study on lateral movement of bearing reinforcement earth (BRE) walls with different backfill properties using the finite element method software PLAXIS 2D. The backfill materials consisted of four types of soils, which were mixtures of silty clay and sand at different fine contents of 2, 20, 40, and 80% by dry weight. The model parameters for the numerical simulation were obtained from the conventional laboratory tests and back-calculated from the laboratory pullout tests of the bearing reinforcement. The geotextile elements were used to model the bearing reinforcements by converting the contribution of friction and bearing resistances to the equivalent friction resistance, which was represented by the soil-bearing reinforcement interaction ratio, R_{inter} . The relationship between the maximum horizontal wall movement and the fine content can be expressed by a polynomial function. The maximum horizontal wall movement significantly increased as the fine content increased. The excessive movement was realized when the fine content was greater than 45%. The increase of the fine content moved the location of the maximum wall movement higher up from the mid to the top of the wall.

Keywords: Bearing reinforcement, Fine content, Lateral movement, Bearing reinforcement earth wall.

1. INTRODUCTION

The bearing reinforcement system was initially developed as an inextensible reinforcement in Thailand by Horpibulsuk and Niramitkornburee (2010) [1]. It is a relatively cost-effective reinforcement system whose advantages include: availability of raw materials, simple and fast installation, convenient transportation, and high pullout and rupture resistances with a less required steel volume. The configuration of the bearing reinforcement is shown in Figure 1. It is composed of a combination of a longitudinal member and several transverse (bearing) members. The longitudinal member comprises a deformed steel bar while the transverse members are a set of equal steel angles, which produce high pullout bearing resistance. This reinforcement has been introduced into industry practice in Thailand since 2008. Several BRE walls have been constructed in several different regions of Thailand; namely in the north, northeast, and south of the country. The BRE wall design method with coarse-grained fill materials (<15% fine content) has been developed based on laboratory and full-scale tests [2,3,4,5].

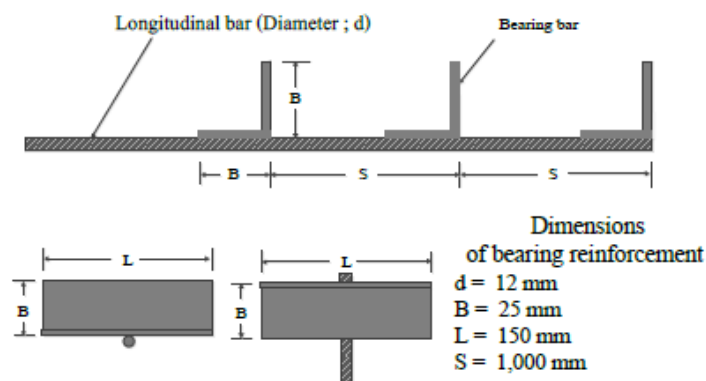


Figure 1 (a) Typical configuration of the bearing reinforcement

Coarse-grained soil is often required as a backfill material. When coarse-grained soils are not locally available within a construction site, the construction cost is largely dependent on haulage cost. The haulage cost

between a borrow source and the construction site is often exorbitant. A potential means to reduce the construction cost is to use locally available soils as backfill materials. The use of locally available marginal soils (e.g. low-quality soils with more than 15% fine content) as a backfill could reduce the cost of fill material by as much as 60% compared to the use of high-quality offside soils and reduce the air pollution from the transportation [6,7]. However, due to the low shear strength of fine-grained soil, internal stability against pullout failure is questionable. To ensure the use of fine-grained soil as a backfill material, [8,9] investigated the pullout mechanisms of the bearing reinforcements embedded in cohesive-frictional soils at various fine and water contents. The bearing pullout mechanism was found to be dominant by the fine content.

According to many researchers [10,11,12,13,14], numerical methods (i.e. finite difference and finite element methods) have been widely used for design and analysis of MSE structures. Numerical methods can model structural components, material properties, construction sequence and compute deformations, forces, strains, and stress distribution at any location of interest in a reinforced soil structure [15]. In addition, they can be used for design, parametric studies, and simulation of the behavior of the earth structures [16]. However, the suitability of a numerical method for modeling MSE structures requires calibration and validation between calculated and observed behavior of laboratory and full-scale tests in order to produce convincing results. The PLAXIS program has been proved as a powerful and accurate tool to predict the performance of the MSE wall and pullout test results [3,17,18].

The finite element code incorporated in PLAXIS 2D was used in this study. The finite element models with material properties were first calibrated according to laboratory large-scale pullout test reported by Horpibulsuk and Niramitkornburee (2010) [1] and Sukmak et al. (2015) [8] and the full-scale bearing reinforced earth wall reported by Horpibulsuk et al. (2011) [2]. The objective of this paper was to evaluate the effect of fine content on the lateral wall movement of BRE wall. The knowledge gained from this study provides useful information for further analysis and design of other BRE walls with different types of backfills, ground conditions, and features of bearing reinforcement.

2. FULL-SCALE TEST OF BRE WALL FOR REFERENCE NUMERICAL MODEL

The construction of a bearing reinforcement earth (BRE) wall was completed on the campus of the Suranaree University of Technology (SUT) in Thailand on 20 July 2009. The foundation consisted of a 1.5-m thick weathered crust layer of silty sand, which was underlain by a medium dense silty sand layer down to about 6 m deep and then a very dense silty sand layer. Soil samples were obtained from a borehole at the construction site down to 8 m deep. The ground water was not detected during boring. The backfill for the earth wall was clean sand, which is classified as poorly-graded sand (SP), according to the Unified Soil Classification System (USCS). The details of the foundation and the backfill can be found in Horpibulsuk et al. (2011) [2]. The backfill was compacted in layers of about 0.15 m lift thickness to a density of higher than 90% the standard Proctor maximum density. The total time spent for the construction of the wall was 20 days. The details of the staged construction the test can be referenced to Horpibulsuk et al. (2011) [2].

The test wall was 6 m high, 9 m wide, 6 m long at the top, and 21 m wide at the base, as illustrated in Figure 2. The side and back slopes were 1:1. The wall facing panels made of segmental concrete panels (1.50 x 1.50 x 0.14) were placed on a lean concrete leveling pad (0.15 m wide and 0.15 thick) at two days after curing. During the construction, four facing panels were installed in the middle portion of the wall width (9 x 6 x 6) with eight reinforcement levels. The details of the bearing reinforcement for each layer are summarized in Table 1.

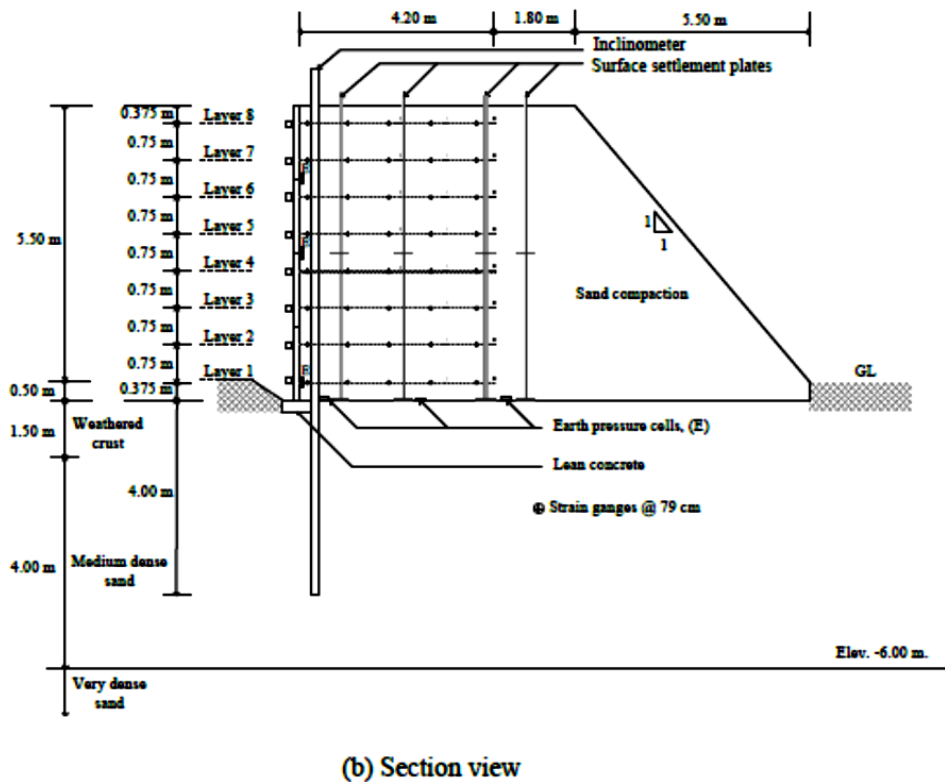
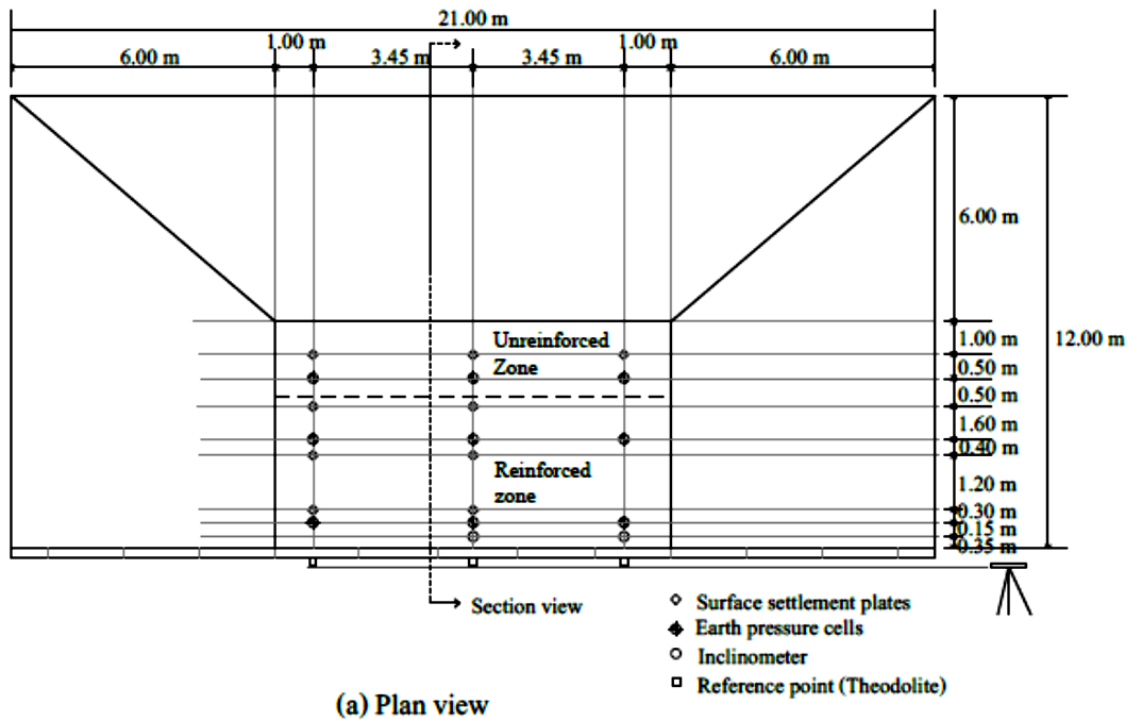


Figure 2. Schematic diagram of the test wall instrumentation

Table 1-Reinforcement details for the test wall (Horpibulsuk and Niramitkornburee, 2010)

Facing panel	Reinforcement layer	Spacing between longitudinal members (mm)	Number
1	1 (bottom)	500	2
	2	500	2
2	3	500	2
	4	750	3
3	5	750	3
	6	750	3
4	7	750	3
	8 (Top)	750	3

3. CALIBRATION OF BRE WALL FOR REFERENCE NUMERICAL MODEL

The 2D Plaxis Finite Element (FE) program was used to simulate the construction of the wall. The BRE wall was modeled as a plane strain problem. The FE mesh and boundary condition are shown in Figure 3. The nodal points at the bottom boundary were fixed in both directions and those on the side boundaries were fixed only in the horizontal direction. The simulation was performed under a drained condition because the ground water was not detected during the test. Properties of the compacted soil were determined from conventional laboratory tests that did not consider the time-dependent behavior, such as creep of soil. The creep model is beyond the scope of this study because it aimed to simulate the wall behavior with simple and well-known soil models for practical design.

The backfill materials used in this study consisted of four types of soils, which were mixtures of silty clay and sand at different fine contents. The four backfill materials were poorly-graded sand (F:S=2:98), clayey sand (F:S=20:80), clayey sand (F:S=40:60), and high-plasticity clay (F:S=80:20), in which F stands for percentage of fines and S stands for percentage of sand. The material properties used for simulation were determined according to the laboratory large-scale direct shear tests reported by Horpibulsuk and Niramitkornburee (2010) [1] and Sukmak et al. (2015) [8]. As such, all backfill materials and all foundation soils were modeled as linearly elastic-perfectly plastic materials with the Mohr-Coulomb (MC) failure criteria, which had five input parameters: elasticity modulus (E), Poisson's ratio (ν), cohesion (c), internal friction angle (ϕ), and dilatancy angle (ψ). The material properties of the backfill used for the FE simulation are shown in Table 2.

The facing panel was modeled as beam (plate) elements. The input parameters for strength and modulus of elasticity are shown in Table 3. Linearly elastic material was used to simulate behavior of wall facing. AASHTO (1992) recommended that the soil-facing panel interface coefficient, R should be 0.75-1.0, which has been used in the numerical studies by Suksiripattanapong et al. (2012) [3]. Since the variation of this interface coefficient is not large, the effect of interface coefficient was not investigated in this research and it was assumed to be 0.90 for all simulations.

The bearing reinforcement (3-D material) was modeled as 2-D continuous sheet elements (called geotextile elements) in the Plaxis manual with a linear elastic material. The required equivalent parameters for 2-D geotextile elements were soil-reinforcement interaction ratio, R_{inter} and axial stiffness per meter, EA, which is the product of the elastic modulus (E) of reinforcement ($= 20$ GPa) and its cross-sectional area per unit width (A). The linearly elastic-perfectly plastic model was used to simulate the interaction between soil and bearing reinforcement. The input parameters of reinforcement are shown in Table 3, where $EA = 4.5 \times 10^4$ kN/m.

The soil-reinforcement interaction ratio, R_{inter} is defined as the ratio of the shear strength of soil-reinforcement interface to the shear strength of the surrounding soil [19]. R_{inter} in the numerical model was determined by simulating large-scale laboratory pullout test results. The equivalent frictional resistance is represented by the soil-structure interaction ratio, R_{inter} . The linearly elastic-perfectly plastic model was used to simulate the interaction between soil and bearing reinforcement.

25.00 m 12.00 m 28.00 m Weathered crust Medium dense sand Very dense sand 1.5 m 4.5 m 1

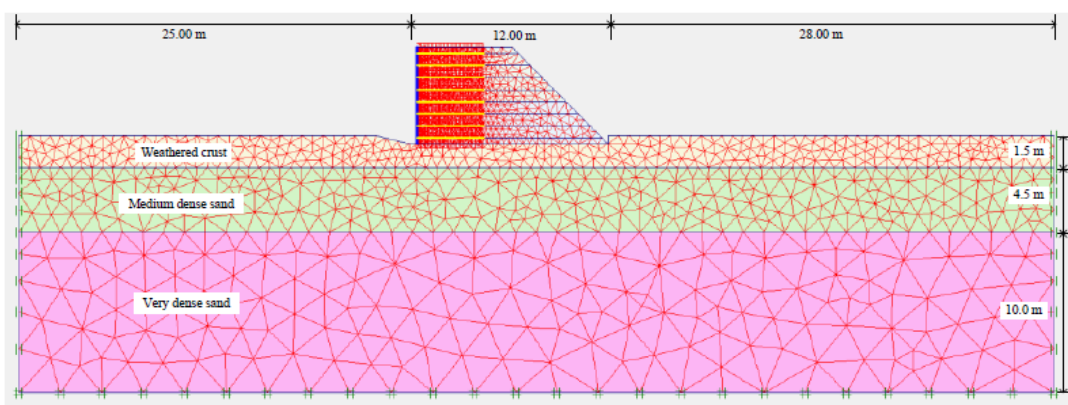


Figure 3 Numerical model and mesh details for 2D FE model simulation of BRE wall

4. FINITE ELEMENT ANALYSIS

4.1. SOIL-STRUCTURE INTERACTION RATIO, R_{inter}

Several laboratory pullout tests were carried out in a metallic box of 2.6 m x 0.6 m x 0.6 m high. The details and sketch of the pullout apparatus are referenced to Horpibulsuk and Niramitkornburee (2010) [1]. The longitudinal member of the reinforcement was 12 mm in diameter and 2.6 m long. The width of the transverse member was 150 mm. The number of transverse members, n used in this study were $n = 2$ and 3. The laboratory pullout test was modeled as a plane strain problem. The nodal points at the bottom boundary were fixed in both directions and those on the side boundaries were only fixed in the horizontal direction. The detail of simulated pullout apparatus model can be reference to Sukmak et al. (2016) [20]. The soil-bearing reinforcement interaction ratio for a specific number of transverse members was back-calculated from the laboratory pullout tests by Horpibulsuk and Niramitkornburee (2010) [1] for poorly-graded sand (F:S = 2:98) and by Sukmak et al. (2015) [8] for clayey sands (F:S = 20:80), clayey sand (F:S = 40:60), and high-plasticity clay (F:S = 80:20). The R_{inter} value is dependent on the number of transverse members and soil properties.

Several pullout tests at different applied normal stresses were modeled ($\sigma_n = 30, 50, \text{ and } 90 \text{ kPa}$) in order to simulate the reinforcement at different depths in the wall. In the back-calculation, the input parameter for the geogrid element is the equivalent axial stiffness. The input parameters for soils and reinforcement were provided in Tables 2 and 3.

Table 2-Model parameters for backfills and foundations

Types of soil	Backfill				Foundation		
	Poorly-graded sand	Clayey sand (F:S =20:80)	Clayey sand (F:S =40:60)	High plasticity clay (F:S =80:20)	Weathered crust	Medium dense sand	Very dense sand
Material model	Mohr Coulomb	Mohr Coulomb	Mohr Coulomb	Mohr Coulomb	Mohr Coulomb	Mohr Coulomb	Mohr Coulomb
$\gamma_{dry} (kN/m^3)$	17.0	20.1	18.9	16.1	17.0	17.15	18
$\gamma_{sat} (kN/m^3)$	18.15	22.0	20.8	18	18.0	18.15	19.0
$E (kN/m^2)$	35,000	10,000	5,000	1,500	6,250	40,000	50,000
ν	0.33	0.40	0.40	0.40	0.30	0.25	0.25
c (kPa)	3	20	25	38	20	1	1
ϕ (degrees)	40	35	32	14	26	35	38
δ (degrees)	8	0	0	0	0	3	8

Table 3-Model parameters for reinforcement and concrete facing

	Bearing reinforcement (Geotextile)		Concrete facing (Plate element)		
Material model	Elastic		Elastic		
EA (kN / m)	4.5 E+4		3.556 E+6		
Longitudinal member (SD40)	Tensile strength	560	EI (kN.m ² / m)	5,808	
	Elongation (%)	15			
Transverse member (Fe24)	Tensile strength	402	w (kN / m / m)	3.36	
	Elongation (%)	21			
<i>Rinter</i>	Poorly-graded sand	n=2	0.65	v	0.15
		n=3	0.75		
	Clayey sand (F:S =20:80)	n=2	0.60		
		n=3	0.70		
	Clayey sand (F:S =40:60)	n=2	0.55		
		n=3	0.65		
High plasticity clay (F:S =80:20)	n=2	0.38			
	n=3	0.40			

4.2. LATERAL WALL MOVEMENT

The simulated and measured horizontal wall movements with different backfills are compared and shown in Figure 4. The simulated result of the wall with the fill of F:S = 80:20 is not included because of its excessive horizontal wall movement. The comparison between the measured and simulated horizontal wall movements with the backfill of F:S = 2:98 is considered to be reasonable. The horizontal wall movements were the sum of the horizontal movement during construction (caused by the lateral movement of reinforced and unreinforced soil zones) and the foundation wall movement and settlement. The horizontal wall movements increased as the fine content increased due to the decrease in shear strengths of the backfills. The increase of the fine content changed the location of the maximum wall movement higher up from 2.0 m for F:S = 2:98 to 6.0 m (the top of the wall) for F:S = 80:20. In addition, the maximum horizontal movement occurred at the top of the wall (6 m high). This characteristic implies that the BRE wall tends to rotate around the toe

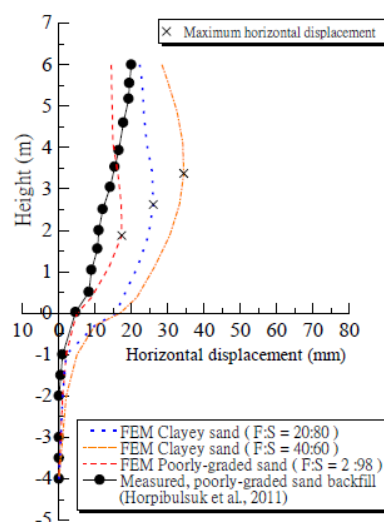


Figure 4. Comparison between the measured and simulated horizontal wall movement for different soil embankments

Figure 5 shows the relationship between the ratios of maximum lateral wall movement to wall height (δ_{max}/H) and the fine content. This relationship can be expressed by a polynomial function. The ratio of maximum lateral wall movement significantly increased with the fine content especially for $F > 45\%$, which δ_{max}/H is higher than the allowable value of 0.40% for inextensible reinforcement suggested by Berg et al. (2009) [21] Thus, based

on this specific BRE wall feature and the constitutive models, the selected soil that can minimize horizontal movement should not contain fine contents higher than 45%. The large horizontal displacement for F:S = 80:20 may result from the low shear strength of the backfill and the low bearing resistance due to the failure mode approaching to the punching shear [8].

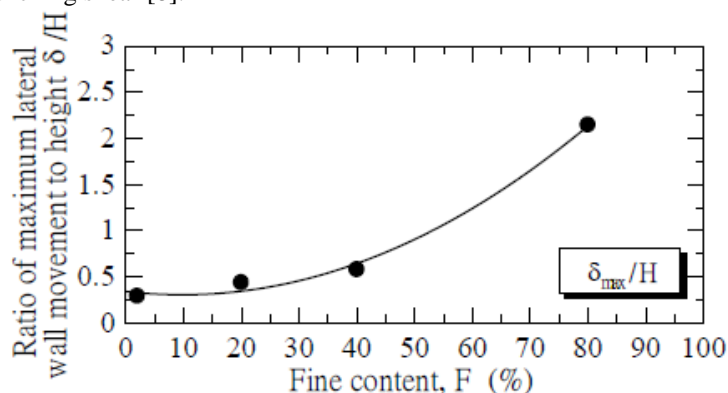


Figure 5. Relationship between maximum horizontal wall movement and fine content

5. CONCLUSIONS

This paper presents a numerical parametric study on behavior of bearing reinforcement earth (BRE) walls with different backfill properties using the numerical software PLAXIS 2D. The backfill materials consisted of four types of soils, which were mixtures of silty clay and sand at different fine contents of 2, 20, 40, and 80% by dry weight. The results from the numerical analysis in this study can provide an understanding of the influence of fine content on the behavior of BRE walls. The following conclusions can be drawn from this study:

1. The geotextile elements were used to model the bearing reinforcements by converting the contribution of friction and bearing resistances to the equivalent friction resistance. The equivalent friction resistance was represented by the soil-bearing reinforcement interaction ratio, R_{inter} , which was back-calculated from the laboratory pullout test. The R_{inter} values decreased following a polynomial function with an increase in the fine content. The soil-structure interactions varied as an increase of the fine content in the ranges of 0.65-0.38 and 0.75-0.40 for $n=2$ and 3, respectively.

2. The behavior of lateral wall movement of the BRE wall with different backfill materials during and at the end of construction was simulated. The relationship between the maximum horizontal wall movement and the fine content can be expressed by a polynomial function. The maximum horizontal wall movement significantly increased as the fine content was more than 45% ($F > 45\%$). The increase of the fine content changed the location of the maximum wall movement higher up from the mid to top of the wall.

6. REFERENCES

1. Horpibulsuk, S., Niramitkornburee, A., 2010. Pullout resistance of bearing reinforcement embedded in sand. *Soils Found* 50, 215-226.
2. Horpibulsuk, S., Suksiripattanapong, C., Niramitkornburee, A., Chinkulkijniwat, A., Tangsutthinon, T., 2011. Performance of anearth wallstabilizedwith bearing reinforcements. *Geotextiles and Geomembranes* 29, 514-524.8
3. Suksiripattanapong, C., Chinkulkijniwat, A., Horpibulsuk, S., Rujikiatkamjorn, C., Tanhsutthinon, T., 2012. Numerical analysis of bearing reinforcement earth (BRE) wall. *Geotextiles and Geomembranes* 32, 28-37.
4. Suksiripattanapong, C., Horpibulsuk, S., Chinkulkijniwat, A., Chai, J.C., 2013. Pullout resistance of bearing reinforcement embedded in coarse-grained soils. *Geotextiles and Geomembranes* 36, 44-54.
5. Suksiripattanapong, C., Suksun, H., Chinkulkijniwat, A., Chai, J., Shen, S.L., Arulrajah, A., Suddeepong, A., 2016. Numerical and Sensitivity Analysis of Bearing Reinforcement Earth (BRE) Wall. *KSCE Journal of Civil Engineering*, Accepted February, 14, 2016, Published Online.
6. Esmaili, D., Hatami, K., Miller, G.A., 2014. Influence of matric suction on geotextile reinforcement-marginal soil interface strength. *Geotextiles and Geomembranes* 42, 139-153.

7. Keller, G.R., 1995. Experiences with mechanically stabilized structures and native soil backfill. *Transportation Research Record* 1474, 30-38.
8. Sukmak, K., Sukmak, P., Horpibulsuk, S., Han, J., Shen, S.-L., Arulrajah, A., 2015. Effect of fine content on the pullout resistance mechanism of bearing reinforcement embedded in cohesive–frictional soils. *Geotextiles and Geomembranes* 43, 107-117.
9. Sukmak, K., Sukmak, P., Horpibulsuk, S., Chinkulkijniwat, A., Arulrajah, A., Shen, S.-L., 2016. Pullout resistance of bearing reinforcement embedded in marginal lateritic soil at molding water contents. *Geotextiles and Geomembranes* 44, 475-483.
10. Abdelouhab, A., Dias, D., Freitag, N., 2011. Numerical analysis of the behaviour of mechanically stabilized earth walls reinforced with different types of strips. *Geotextiles and Geomembranes* 29, 116-129.
11. Bergado, D.T., Teerawattanasuk, C., 2008. 2D and 3D numerical simulations of reinforced embankments on soft ground. *Geotextiles and Geomembranes* 26, 39-55.
12. Ho, S.K., Rowe, R.K., 1994. Predicted Behavior of Two Centrifugal Model Soil Walls. *Journal of Geotechnical Engineering* 120, 1845-1873.
13. Wang, Z., Jacobs, F., Ziegler, M., 2014. Visualization of load transfer behaviour between geogrid and sand using PFC2D. *Geotextiles and Geomembranes* 42, 83-90.
14. Youwai, S., Bergado, D.T., 2004. Numerical analysis of reinforced wall using rubber tire chips–sand mixtures as backfill material. *Computers and Geotechnics* 31, 103-114.
15. Mohamed, S.B.A., Yang, K.-H., Hung, W.-Y., 2014. Finite element analyses of two-tier geosynthetic-reinforced soil walls: Comparison involving centrifuge tests and limit equilibrium results. *Computers and Geotechnics* 61, 67-84.
16. Collin, J.G., 1986. Earth wall design. Ph.D. dissertation, Univ. California, Berkeley, CA.
17. Bergado, D.T., Youwai, S., Teerawattanasuk, C., Visudmedanukul, P., 2003. The interaction mechanism and behavior of hexagonal wire mesh reinforced embankment with silty sand backfill on soft clay. *Computers and Geotechnics* 30, 517-534.
18. Khedkar, M.S., Mandal, J.N., 2009. Pullout behaviour of cellular reinforcements. *Geotextiles and Geomembranes* 27, 262-271.
19. Vermeer, P.A., Brinkgreve, R.B.J., 1995 *Finite Element Code for soil and rock analysis*. A.A. Balkema, Rotterdam (Netherlands).
20. Sukmak, K., Han, J., Sukmak, P., Horpibulsuk, S., 2016b. Numerical parametric study on behavior of bearing reinforcement earth (BRE) walls with different backfill material properties. *Geosynth. Int.* <http://dx.doi.org/10.1680/jgein.1600008>.
21. Berg, R.R., Christopher, B.R., Samtani, N.C., 2009. *Design of Mechanically Stabilized Earth Walls and Reinforced Soils Slopes*, vol. II. Publication No. FHWA-NHI- 10e025, Federal Highway Administration Report.

Effect of Hydraulic Properties of Fill and Geocomposite Drainage Materials on Seepage Response in Reinforced Earth Walls

Avirut Chinkulkijniwat¹, Suksun Horpibulsuk², Duc Bui Van³, Somjai Yubonchit⁴,
Thanakorn Rakkob³

1-Associate Professor, Center of Excellence in Civil Engineering, School of Civil Engineering, Suranaree University of Technology, 111 University Avenue, Muang District, Nakhon Ratchasima 30000 Thailand

2- Professor and Director, Center of Excellence in Innovation for Sustainable Infrastructure Development, Chair of School of Civil Engineering, Suranaree University of Technology, 111 University Avenue, Muang District, Nakhon Ratchasima 30000 Thailand

3-Ph. D scholar, School of Civil Engineering, Suranaree University of Technology, 111 University Avenue, Muang District, Nakhon Ratchasima 30000 Thailand

4-Research fellowship, School of Civil Engineering, Suranaree University of Technology, 111 University Avenue, Muang District, Nakhon Ratchasima 30000 Thailand

Email: avirut@sut.ac.th

Abstract

This research aims to investigate the effect of water retention characteristic of the fill soil and drainage material (geocomposite) on seepage responses in mechanical stabilized earth walls using geocomposite as an alternative drainage system. A set of experiments on physical models was conducted such that the dataset obtained from the tests were used to calibrate the numerical models. Obtained calibrated numerical models were then used to perform a series of parametric calculation. The studied parameters were van Genuchten parameters (g_a and g_n) and coefficient of permeability (k) of the relevant materials. Results from the parametric study indicate that the water retention characteristic of the soil outside the reinforced zone plays little role to the hydraulic response of the soil inside the reinforced zone. However, the coefficient of permeability of the soil outside the reinforced zone plays important role to the level of the phreatic surface inside the reinforced zone. Hence, the coefficient of permeability of the soil outside the reinforced zone must be taken into account as designing drainage system.

Keywords: Mechanical Stabilized Earth Wall, Geocomposite, Drainage System, Numerical Modeling.

1. INTRODUCTION

Instability of mechanical stabilised earth (MSE) walls in mountainous areas, where seasonally heavy rainfall is encountered, is often attributed to ineffective drainage systems (Koerner and Soong 2001, Shibuya et al. 2007). Shibuya et al. (2007) reported an investigated results from a catastrophic failure of a reinforced earth wall occurred in Yabu, Japan, in 2004, after a typhoon. Although the design codes were used to design and build the reinforced earth wall, in which the drainage was positioned at the bottom of the wall from drainage pipes but the area behind the wall was not fully covered; hence, there was an insufficient capacity in the drainage system installed. It was concluded that conventional drainage systems were not applicable in mountainous areas where there was a large amount and/or high level of groundwater.

The material conventionally used as the drainage medium for MSE walls is well-graded gravel. This is becoming increasingly expensive, and effective installation of this material as a vertical drainage layer is difficult in the field (Koerner and Soong 2001; Shibuya et al. 2007). An alternative to the use of well-graded gravel is to provide drainage through the use of geocomposites (Koerner and Soong 2000; Koerner 2005; Chen et al. 2007) which comprise a core material with a large flow channel (e.g., geonet) covered by two nonwoven geotextile layers. Geocomposites provide a hydraulic conductivity approximately 10 to 100 times higher than that of compacted backfills. Geocomposites offer numerous advantages over the conventional method of drainages such as ease of transportation and installation; the use of geocomposites does not add significantly to the weight of the soil in the backfill due to its light weight; construction time is significantly reduced as geocomposites is used, hence economic benefit. McKean and Inouye (2001) reported a successful field case study using geocomposites to prevent water flowing behind a retaining wall. This MSE wall was reported successfully performed for period of around of 14 years.

Although there have been many reported case studies on the successful implementation of geocomposites as alternative drainage systems, there is no known work that incorporates the water retention characteristic (WRC)

of geotextiles in these reported numerical simulations. Previous studies indicate that geotextiles' water retention characteristics are similar to those of coarse-grained soils such as gravels and sands (Stormont et al. 1997; Lafleur et al. 2000; Morris 2000; Stormont and Morris 2000; Knight and Kotha 2001; Iryo and Rowe 2003, 2004; Bouazza et al. 2006; Bathurst et al. 2007, 2009; Nahlawi et al. 2007). Therefore, an insight into the influences of WRC of geotextiles on flow response is necessary to allow for a more effective and appropriate use of geocomposites in MSE walls.

This research was conducted using a large-scale flow test through an MSE wall in which an L-shape geocomposite drain was installed. A set of needed instrumentations were positioned in the physical models to assess the flow and deformation responses during the tests, they were four standpipe piezometers, 10-time domain reflectometer (TDR) probes and 10 surface settlement plates. Numerical analyses were subsequently conducted using the Plaxis-2D finite element modelling software to investigate the effect of the hydraulic properties on the water flow taking place in the MSE wall. The numerical computation of flow results was mainly presented in terms of phreatic surface and effective saturation profiles.

2. THEORETICAL BACKGROUND

The governing equation for transient water flow in a two dimensional homogeneous anisotropic material within an unsaturated porous medium is as follows

$$k_x \frac{\partial^2 h}{\partial x^2} + k_y \frac{\partial^2 h}{\partial y^2} = \frac{\partial \theta}{\partial t}$$

where θ is the volumetric water content, h is the total head, k_x and k_y are the unsaturated coefficients of permeability in the x - and y -directions, and t is time. To solve Equation 1, constitutive equations related to θ , k_x and k_y to h are required. Iryo and Rowe (2003, 2004) concluded that there is considerable evidence to suggest that van Geuchten (VG) (van Genuchten, 1980) and van Genuchten-Mualem (VGM) models, which combine the van Genuchten and Mualem hypotheses (Mualem 1976), are applicable to nonwoven geotextiles. Thus, both of these constitutive equations were employed to approximate WRC and permeability functions for both the soil and the nonwoven geotextile.

$$S_e = \frac{S - S_{res}}{S_{sat} - S_{res}} = \left[1 + (g_a |h_p|)^{g_n} \right]^{g_c} \quad (1)$$

$$k_r(S_e) = S_e^{0.5} \left[1 - (1 - S_e^{-1/g_c})^{-g_c} \right]^2 \quad (2)$$

where S_e is the effective degree of saturation, S is the degree of saturation, S_{res} is the residual saturation at a very high value of suction, S_{sat} is the saturation of saturated soil, h_p is the matric suction head, k_r is the relative permeability coefficient. g_a [m^{-1}], g_c and g_n are fitting parameters, and according to the Mualem hypothesis (Mualem 1976), g_c is assigned a value of $1/g_n - 1$.

3. PHYSICAL EXPERIMENTS

Figure 1 shows large-scale physical experiments of MSE wall model conducted to simulate a practical scenario, in which MSE wall undergoes a leveling of groundwater table. The bottom, left and right sides of the physical model were established as impervious boundaries. Four standpipe piezometers, 10 surface settlement plates and 10 TDR probes were installed to measure water level, settlement and volumetric water contents during seepage flow, respectively. During the test, groundwater flows were controlled by observing the change in water level in the upstream and downstream water tanks. The water level in the downstream water tank was kept constant at the toe of the wall (+0.0 m) using a control weir. The water level in the upstream tank was increased stepwise from heights of +0.0 m, +0.4 m, +0.7 m, and +1.0 m, respectively. The upstream water level was continuously increased after a steady state was gained, in which there was no change in the water content values, read from the TDR probes, for a period equal to or greater than 24 h. This scenario was established to simulate the most severe situation, at which the groundwater level behind an MSE wall was very high, similar to the situation that may occur in mountainous areas during heavy rainfalls. The shallow soil layer was assumed to be underlain by a bedrock layer, such that inundation might be occurred during a heavy rainstorm (Figure 1b).

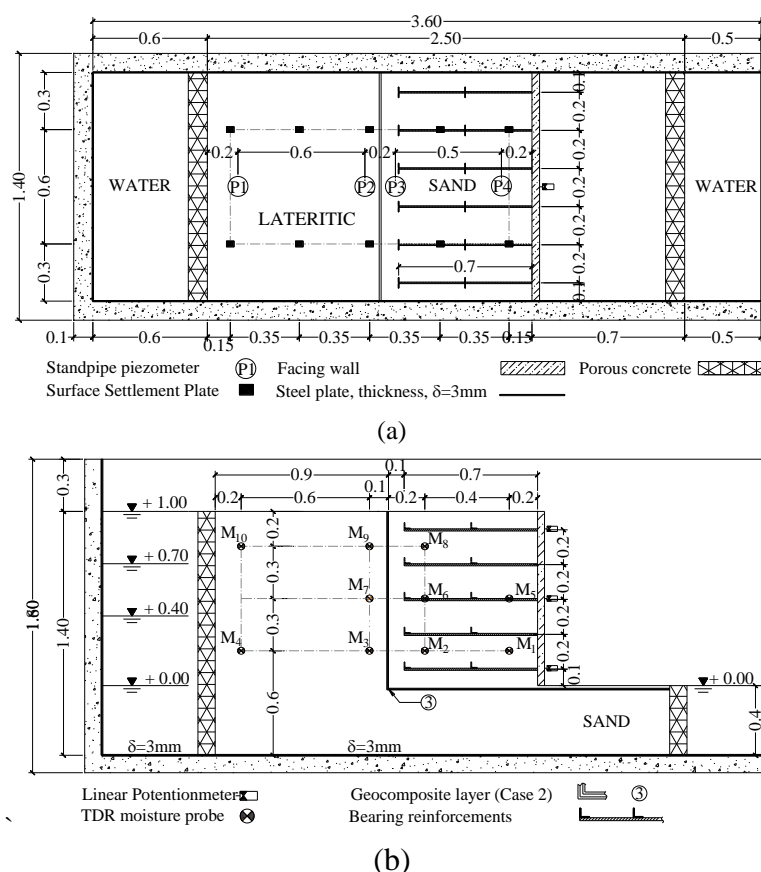


Figure 1 Sketch of the physical test and its instrumentation: (a) plan view and (b) side view of the model

4. NUMERICAL EXPERIMENTS

A series of numerical experiments was subsequently conducted to investigate the effect of the relevant material properties on the flow response through the MSE wall, with a geocomposite drain installed, using the finite element code Plaxis 2D. The discretised plane strain finite element mesh is shown in Figures 2a and 2b for the MSE wall without and with geocomposite drain installation, respectively. A triangular mesh was used in the numerical model. Although a rectangular mesh is commonly adopted in water flow models, it has been reported that the calculated results do not depend on the type of mesh because the interpolation function in flow problems is linear (Potts and Zdravković 2001).

In Plaxis, there are two well-known types of triangular elements: 6-node triangles and 15-node triangles. In this study, 15-node triangles were assigned to the models. The use of 15-node triangles yields more accurate calculation results than that of 6-node triangles. A fine mesh with an average element size of 0.033 m was assigned. A finer mesh was also assigned to the geotextile and the geonet. The initial conditions of the model were defined based on the controlled density and water content during the placement of compacted soil in the physical box. Dirichlet boundary conditions with prescribed pressures were imposed on the left, right, and upper boundaries of the model. The bottom boundary of the model was defined as impermeable. In Plaxis, the time steps were assigned automatically for steady-state calculation. At each time step, a modified Newton-Raphson model was used to solve the relevant equations iteratively. In each iteration, increments of the groundwater head were calculated from the imbalance in the nodal discharges and added to the active head. This process was continued until the norm of the unbalance vector, i.e., the error in the nodal discharges, was smaller than that of the tolerated error of 0.01 (or 1%).

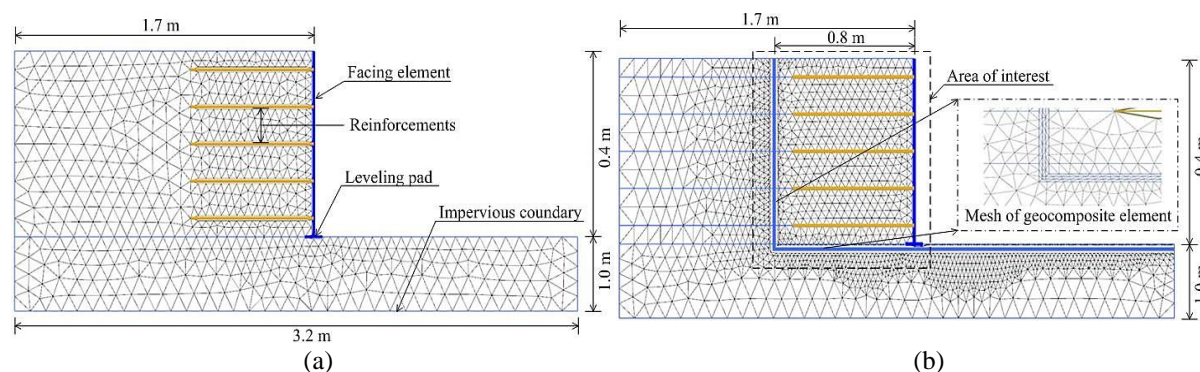


Figure 2 Mesh discretisation of the models (a) without and (b) with geocomposite installation

5. MATERIALS

The soils used in this investigation were a sandy soil and a lateritic soil. The sandy soil was classified as poorly graded sand (SP), according to the Unified Soil Classification System (USCS), with its specific gravity of 2.74. The compaction characteristics under standard Proctor energy were optimum water content (OWC) of 5.7% and maximum dry unit weight $\gamma_{d,max}$ of 16.7 kN/m³. The saturated hydraulic conductivity of the soil was k_{sat} = 17 m/day. For the lateritic soil, it was classified as SM-SC, with the specific gravity of 2.75. The compaction characteristics of the lateritic soil were 5.7% of optimum water content and 16.7 kN/m³ of maximum dry unit weight. The saturated hydraulic conductivity of the soil was k_{sat} = 0.3456 m/day.

Determinations of the WRC of the soil were conducted along the drying and wetting paths. The drying phase WRC was obtained using a pressure plate apparatus and the wetting phase WRC was obtained from the double-walled triaxial cell. The relationships between volumetric water content and matric suction of the sandy soil, lateritic soil and geotextile are presented in Figure 3.

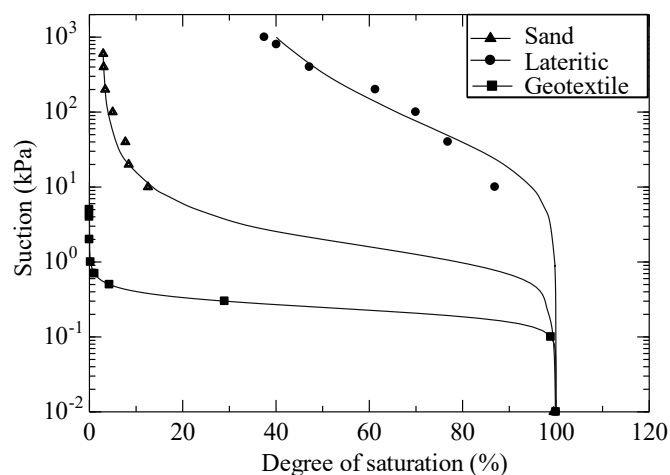


Figure 3 WRC curves of the materials used in this study

6. MODEL CALIBRATION

Figure 4 presents the measured (with symbols) and calculated (with lines) water levels and volumetric water contents for the various upstream water levels for tests without (Figure 4a) and with (Figure 4b) geocomposite installation. The water levels and the volumetric water contents presented in Figure 5 were those measured at 18 days, 21 days, and 23 days, which represent the end times of upstream water levels of +0.4 m, +0.7 m, and +1.0 m, respectively. At any upstream water level height, the water level decreases through the wall face. The measured water level data for case I (no geocomposite) were compared to those for case II (with geocomposite). The comparisons show that the highly permeable geocomposite can effectively prevent water flow to the reinforced zone (or protected zone), as it collects the water in the unreinforced zone and drains it out at the wall face.

Figures 4 also compares the measured and calculated phreatic surface, distribution of volumetric water content at various heights of the upstream water level. The numerical model yields a variation in the phreatic surface similar to that measured in the tests. Fair agreement between the measurements and the corresponding calculations for the two cases was found.

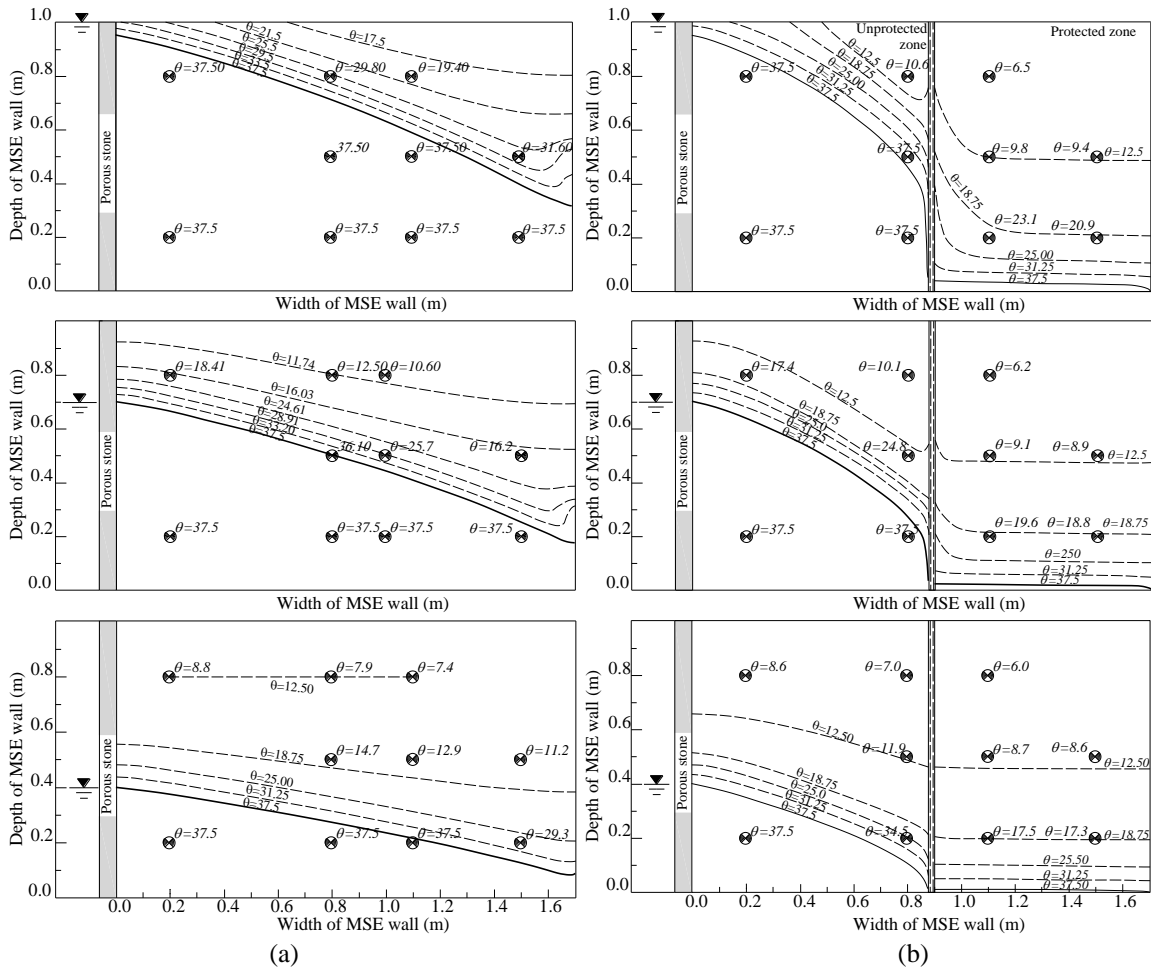


Figure 4 Measured and calculated phreatic surfaces and water contents for MSE wall
(a) case I (without geocomposite drain installed) and
(b) case II (with geocomposite drain installed)

7. PARAMETRIC STUDY

The hydraulic responses represent the effective saturation and phreatic surface, determined from numerical experiments are presented and discussed within this section. The effect of the hydrological properties of the soil and the geotextile on the hydraulic response was evaluated using (1) van Genuchten parameters (g_a and g_n) and (2) the corresponding saturated permeability. For the hydrological properties of the geonet, only the saturated hydraulic conductivity of the geonet was evaluated.

In general, it was found that the phreatic surface outside the protected zone was not notably changed within the range of considered parameters indicated in Table 1. The phreatic surface in the protected zone and the distribution of effective saturation were affected by some of the considered parameters, as discussed in this section.

Table 1 VG and VGM model parameters and saturated hydraulic conductivity of the materials used in this study

Parameter	Lateritic soil (unprotected zone)	Sandy soil (protected zone)	Geotextile	Geonet
K_{lat} [m/day]	0.00346-300	17	17-4000	2000-100000
K_{long} [m/day]	0.00346-300	17	50-2000	2000-100000
g_a [m^{-1}]	0.5-5	20	2.5	600
g_n [-]	1.1-1.5	1.5	20	40
S_{res} [-]	0.2	0.03	0.03	0
S_{sat} [-]	1.0	1.0	0.8	1

7.1. EFFECTS OF THE VAN GENUCHTEN PARAMETERS OF FILL MATERIAL

7.1.1. THE VAN GENUCHTEN PARAMETER g_a

Figures 5a and 5b present the effective saturation profiles along sections a-a and b-b, respectively, for various magnitudes of g_a . The alignment of these sections (a-a) and (b-b) are vertical and located at 0.05 m to the left and right from the geocomposite drainage. At a certain depth above the phreatic surface, the soil with a low g_a value exhibits high saturation inside the unprotected zone. The degree of saturation was found to decrease when the magnitude of g_a decreases. In short, the wet zone spreads more widely for the low g_a soil than for the high g_a soil. However, Figure 5b clearly shows that the variation of g_a parameter of outer soil slightly affect the effective saturation profiles in the reinforced zone.

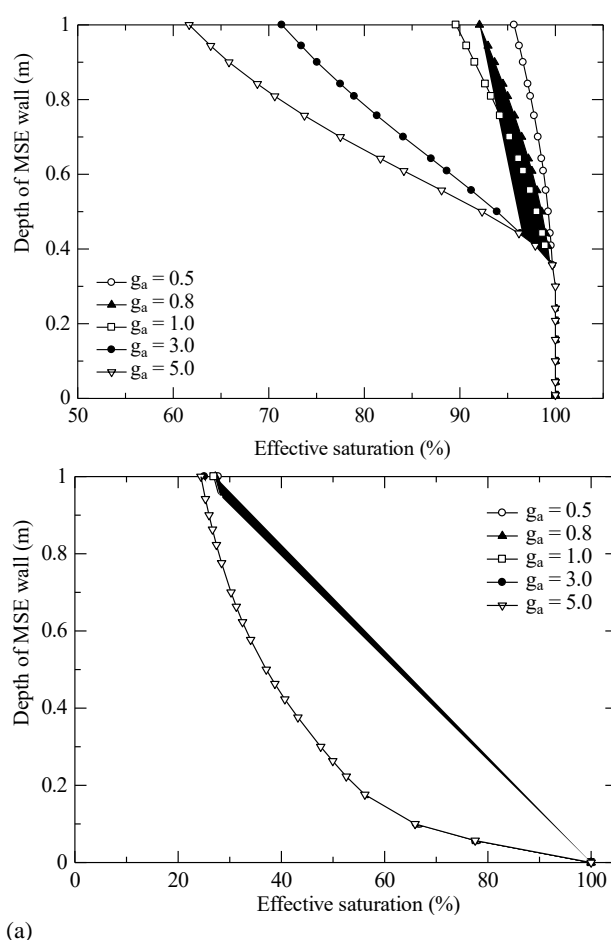


Figure 5 : Effective saturation profile along vertical sections located (a) 5 cm left and (b) 5 cm right of the geocomposite for various magnitudes of g_a of outer soil

7.1.2. THE VAN GENUCHTEN PARAMETER g_n

Figure 6 presents phreatic surface and effective saturation contour lines in the MSE wall model calculated at various magnitudes of g_n of the outer soil. The results show that effective saturation (outside the protected zone) clearly depends on the magnitude of g_n the wider distribution of effective saturation was found with a lower g_n . However, figure 6 indicates that the variation of g_n of outer soil slightly affect the effective saturation inside the reinforced zone.

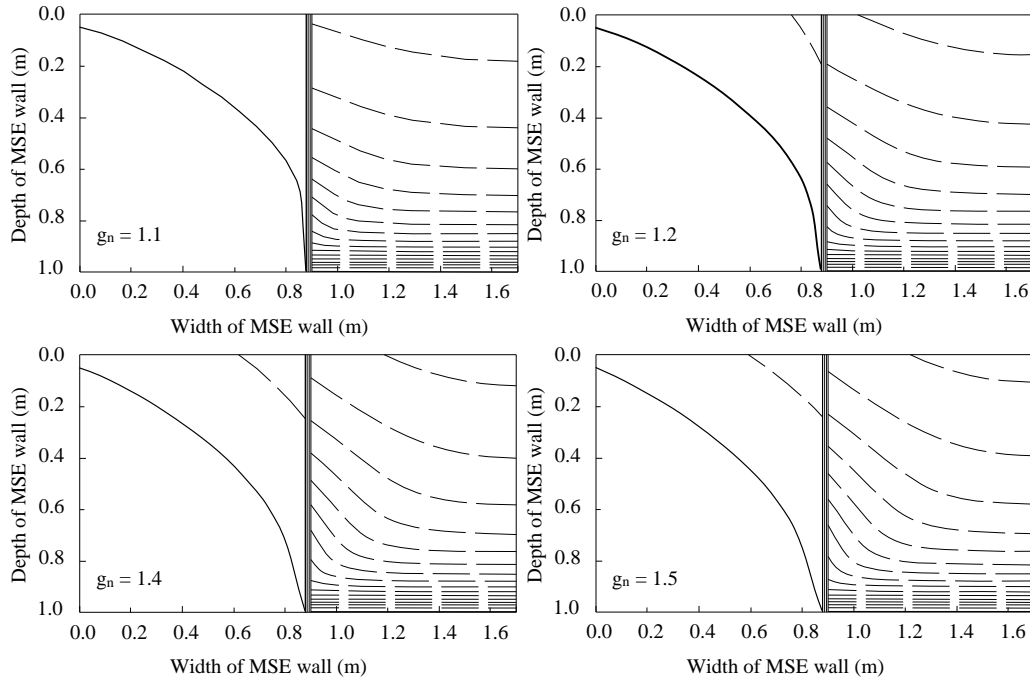


Figure 6 Phreatic surface (solid line) and effective saturation contour lines (dash line) in the MSE model for various magnitudes of g_n of soil

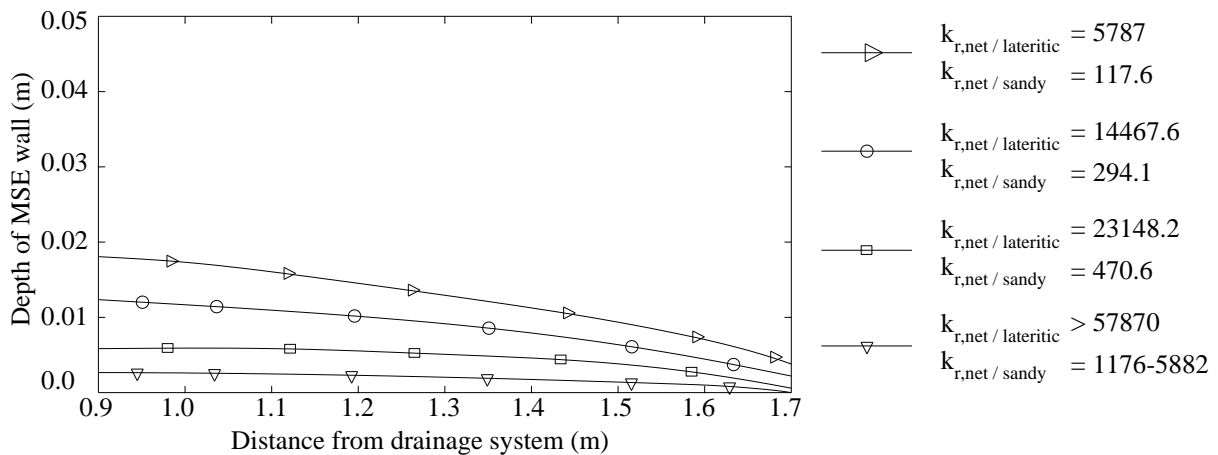


Figure 7 Variation in phreatic surface in the protected zone for various ratios between the hydraulic conductivity of the geonet and that of soil

7.2. EFFECT OF HYDRAULIC CONDUCTIVITY RATIO

The level of the phreatic surface inside the protected zone is vital to the stability of the MSE wall. The lower phreatic surface level results in a lower water content inside the protected zone, and hence a higher stability for the wall might be gained. Chinkulkijniwat et al. (2016) presented the effect of the ratio between the hydraulic conductivity of the geonet and that of sandy soil ($K_{r,net/sandy}$) on the phreatic surface in the protected zone. A large $K_{r,net}$ value was found at the lower phreatic surface level in the protected zone. Further reduction of the phreatic surface level was not observed when the magnitude of $K_{r,net}$ was greater than 1765. From these results, they concluded that the phreatic surface level in the protected zone was mainly governed by the magnitude of $K_{r,net}$. Figure 7 shows the variation of phreatic surface level at various magnitudes of the ratio between the hydraulic conductivity of the geonet and that of lateritic soil ($K_{r,net/lateritic}$) ranged from 5787 to 289351. It clearly shows that the $K_{r,net/lateritic}$ in protected zone does not affect phreatic surface level inside the reinforced zone within the range of the studied $K_{r,net/lateritic}$. Therefore, the result in this study is confirmed by the finding from Chinkulkijniwat et al. (2016).

8. CONCLUSIONS

The drainage ability of geocomposites which consists of a core material with a large flow channel (geonet) sandwiched by two nonwoven geotextile layers, was investigated through large-scale MSE wall model tests. The experimental results indicate that the geocomposite studied effectively prevents the flow of water into the reinforced zone by collecting water in the unreinforced zone and draining it in front of the wall face. Comparisons between the deformations of the MSE wall models with and without geocomposite installation indicate that the MSE wall with a geocomposite is far superior to that without a geocomposite. Numerical models were established to conduct parametric studies. The following conclusions can be drawn as a result of this research.

- (1) The WRC parameters of the soil do not reflect the distribution of effective saturation in the soil both inside reinforced zone.
- (2) The ratio between the hydraulic conductivity of the geonet and that of lateritic soil the ($K_{r,net/lateritic}$) in protected zone does not affect phreatic surface level inside the reinforced zone.

9. REFERENCES

1. Koerner, R.M., Soong, T-Y. (2000), "Stability assessment of ten large landfill failures." *Geotechnical*. Vol.103: 1-38.
2. Shibuya, S., Saito, M., Torii, N., and Hara, K. (2009), "*Mitigating embankment failure due to heavy rainfall using L-shaped geosynthetic drain*", Proceedings of the International Symposium on Prediction and Simulation Methods for Geohazard Mitigation, Kyoto, Japan, (229-306).
3. Koerner, R.M., (2005). *Designing with Geosynthetics*. 5th Edition. Englewood Cliffs, New Jersey : Prentice Hall Publ. Co.
4. Yoo, C., & Jung, H. Y. (2006), "*Case history of geosynthetic reinforced segmental retaining wall failure*" *Journal of Geotechnical and Geoenvironmental Engineering*. Vol.132 No.12 : 1538-1548.
5. Stormont, J. C., Morris, C. E. (2000), "*Characterization of unsaturated nonwoven geotextiles*" *Advances in unsaturated geotechnics*, ASCE. (153-164)
6. Lafleur, J., Lebeau, M., Faure, Y. Savard, Y., Kehila, Y. (2000), "*Influence of matric suction on the drainage performance of polyester geotextiles*" The 53rd annual conference of Canadian Geotechnical Society, Motreal, Canada. Vol.2 : 1115-1122.
7. Ho, A.F. (2000), "*Experimental and numerical investigation of infiltration ponding in one-dimensional sand-geotextile columns*". M.Sc. Thesis, Queen's University, Kingston, Ont., Canada.
8. Knight, M.A., Kotha, S.M. (2001), "*Measurement of geotextile-water characteristic curves using a controlled outflow capillary pressure cell*" *Geosynthetics International*. Vol.8 No.3 : 271-282.
9. Iryo, T., Rowe, R.K. (2003), "*On the hydraulic behavior of unsaturated nonwoven geotextiles*" *Geotextiles and Geomembranes*. Vol.21 : 381-404.
10. Iryo, T., Rowe, R.K. (2004), "*Numerical study of infiltration into a soil-geotextile column*" *Geosynthetics International*. Vol.11 No.5 : 377-389.
11. Bouazza, A., Freund, M., Nahlawi, H. (2006b), "*Water retention of nonwoven polyester geotextiles*" *Polymer Testing*. Vol.25 No.8 : 1038-1043.
12. Nahlawi, H., Bouazza, A., & Kodikara J. (2007), "*Characterisation of geotextiles water retention using a modified capillary pressure cell*" *Geotextiles and Geomembranes*. Vol.25 No.3 : 186-193.
13. Van Genuchten, M. Th. (1980), "*A closed-form equation for predicting the hydraulic conductivity of unsaturated of soil*" *Soil Science Society of America Journal*. Vol.44 No.5 : 892-898.
14. Mualem, Y. (1976), "*A new model for predicting the hydraulic conductivity of unsaturated porous media*" *Water Resources Research*. Vol.12 No.3 : 513-522.
15. Chinkulkijniwat, A., Horpibulsuk, S., Bui Van, D., Udomchai, A., Goodary, R., & Arulrajah, A. (2016), "*Influential factors affecting drainage design considerations for mechanical stabilised earth walls using geocomposites*". *Geosynthetics International*. (1-18).

Numerical simulation of sharp crested arced weir

S. Azizi ¹, M. Mehraein ²

1- Msc student of water and hydraulic structure engineering, Faculty of engineering, Kharazmi University, Tehran, Iran.

2- Assistant Professor, Faculty of engineering, Kharazmi University, Tehran, Iran.

Email: mehraein@khu.ac.ir

Abstract

Weirs have been used as many shapes in plan; (trapezoid, triangle, arc). Nowadays using numerical approaches and ease of access to personal computers and expensive laboratory researches made these approaches reasonable. Arced weir is analyzed in this research numerically. In this research k-ε model were used, this model is one of the widely used model in turbulence simulations. The k-ε model made a good approximation in many types of flows. Higher discharge coefficient is achieved by increasing the length of this type of weir. In this research the results of head and downstream mound are presented using numerical simulation. In all models weir height and vertex angle were 10 cm and 180° respectively. The discharge range was 0.16 to 0.015 m³/s. Absolute average errors of total heads over the weir and mound was 3% and 4% percent respectively. Hence, all results indicated a good agreement between numerical simulation and laboratory experiments. Numerical simulation can be used as an appropriate approach to estimate the discharge coefficients of arced weirs.

Keywords: Numerical Simulation, Arced Weir, Discharge Coefficients.

1. INTRODUCTION

Weirs are used as a part of deviation systems or flood control, by controlling the height of the flow in canals and reservoirs. By increasing the water level in the reservoir, the amount of water that is higher than the top of the weir crest is directed outward. Weirs have different shapes in plan; (triangles, trapezoidal, rectangular, and semicircular). Another category of weirs is based on the type of edges and the height of water on the crown, which is divided into two groups of sharp, broad edges. Based on this classification, if the depth of water on the crown exceeds 5 times the thickness of the crest in the direction of flow, the weir classified as sharp edge [1] & [2]. In this research weir is sharp edge. One of the few studies on arced weirs in the plan was done by Kumar et al. [3]. they introduced arced weirs as a convenient tool for easy and accurate measurement of discharge also they considered the vortex of 90 degrees as the optimum option in arced weirs. Arced shape in other kinds of weirs studied, for example discharge of arced labyrinth weirs as much as twice as classical labyrinth weirs [4].

Another study showed that when weirs inclined in to reservoir, it had twice larger discharge than classical one in channel [5]. Another aspect in weirs that was interested was Discharge efficiency. Discharge efficiency of arc labyrinth weirs were higher than conventional ones located in channels [6]. Variation in discharge coefficient in frontal weirs represented based on Reynolds numbers [7].

Based on researches, if the downstream level of fluid is higher than upstream level, submergence occurred and this phenomenon made less discharge coefficient in weir. According to this subject, an equation for discharge coefficient with respect to submergence ratio was presented [8].

Some researches focused on computing techniques to evaluating hydraulic of labyrinth weirs [9] & [10]. By increasing the length of the arced weir, the discharge increased when other effective parameters were kept constant [11].

The aeration of nape was investigated by some researchers. As the air pressure decreases, the flow curvature increases and the discharge coefficient increase. In this context, Bos, represents an equation for aeration of the weir [12]. The aeration of the arced labyrinth weir better than the normal weirs. (normal weir with equal length) Especially in triangular labyrinth weir by increasing sill slope, aeration will increase [13]. Flow over the weir based on general head-discharge equation could be calculated as below [14]:

$$Q = \frac{2}{3} \times C_d \times L \times (H_T)^{3/2} \times \sqrt{2g} \quad (1)$$

At the above equation, H_T is total head over the crest of weir, g is gravity, L is weir's length and C_d is discharge coefficient. Flow characteristics and geometry of the weir have effects on C_d [15]. It can be seen Cleary few investigations have been done on curved weirs so far. The lack of researches on estimating the discharge coefficients of arced weirs and high expense of laboratory tests made us to investigate the numerical simulation of arced weirs.

2. AVAILABLE EXPERIMENTAL DATA

The research carried out involves numerical analysis of the flow over the arced weir and its verification using laboratory data. Sangafsi et. al.'s [11] data were used for verification. The reservoir model has two approaches with 10 m length, 2 m width, 0.9 m depth and weir height is 0.10 m (Figure 1). Discharges range was 0.016-0.15 m³/s.

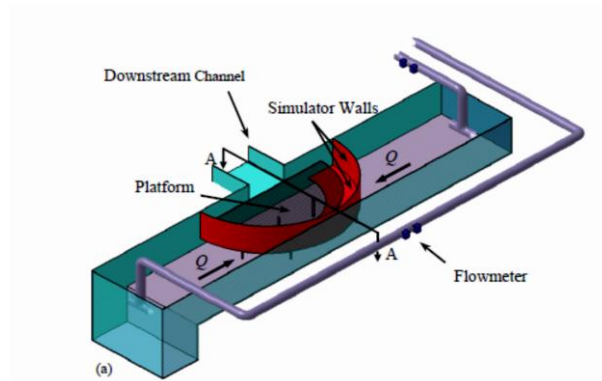


Figure 1. complete set up of reservoir [7]

In addition data measurements were done under natural aeration and steady state condition. In this study, two groups of laboratory results were focused first H_0/p and k/p . Here, H_0 is the upstream head, k is the height of downstream mound and p is the weir height. (figure 2).

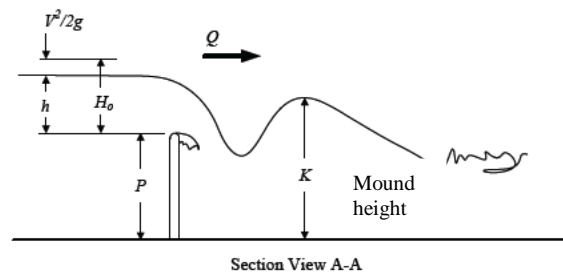


Figure 2. upstream total head (H_0) and downstream mound (k)

3. NUMERICAL SIMULATION

3.1. GOVERNING EQUATION

In this research, FLOW 3D software was used for numerical simulation. This software is widely used today to solve the problems of hydraulic structures. This software is specially developed to solve fluid motion problems. Some of the governing equations are introduced briefly. The mass continuity equations and momentum equations are among the most important of these. The general mass continuity equation is [16]:

$$V_F \frac{\partial \rho}{\partial t} + \frac{\partial}{\partial x} (\rho u A_x) + R \frac{\partial}{\partial y} (\rho v A_y) + \frac{\partial}{\partial z} (\rho w A_z) + \xi \frac{\rho u A_x}{x} = R_{DIF} + R_{SOR} \quad (2)$$

In this equation V_f is the fractional volume open to flow, ρ is fluid density, R_{DIF} is turbulent diffusion term and R_{SOR} is a mass source. The relations (3), (4) and (5) of the motion equations are about the velocity of the fluid in the directions (u, v, w) and are expressed in three main directions. These relations are the same Navier-Stokes equations with a few variations.

$$\begin{aligned} \frac{\partial u}{\partial t} + \frac{1}{V_F} \left\{ u A_x \frac{\partial u}{\partial x} + v A_y R \frac{\partial u}{\partial y} + w A_z \frac{\partial u}{\partial z} \right\} - \xi \frac{A_y v^2}{x V_F} \\ = -\frac{1}{\rho} \frac{\partial p}{\partial x} + G_x + f_x - b_x - \frac{R_{SOR}}{\rho V_F} (u - u_w - \delta u_s) \end{aligned} \quad (3)$$

$$\begin{aligned} \frac{\partial v}{\partial t} + \frac{1}{V_F} \left\{ u A_x \frac{\partial v}{\partial x} + v A_y R \frac{\partial v}{\partial y} + w A_z \frac{\partial v}{\partial z} \right\} + \xi \frac{A_y v u}{x V_F} \\ = -\frac{1}{\rho} \left(R \frac{\partial p}{\partial y} \right) + G_y + f_y - b_y - \frac{R_{SOR}}{\rho V_F} (v - v_w - \delta v_s) \end{aligned} \quad (4)$$

$$\begin{aligned} \frac{\partial w}{\partial t} + \frac{1}{V_F} \left\{ u A_x \frac{\partial w}{\partial x} + v A_y R \frac{\partial w}{\partial y} + w A_z \frac{\partial w}{\partial z} \right\} \\ = -\frac{1}{\rho} \left(\frac{\partial p}{\partial z} \right) + G_z + f_z - b_z - \frac{R_{SOR}}{\rho V_F} (w - w_w - \delta w_s) \end{aligned} \quad (5)$$

In these equations (G_x, G_y, G_z), are the accelerations, (f_x, f_y, f_z), are viscous accelerations and (b_x, b_y, b_z) are the amount of flow losses in the porous medium or porous plates defined by the user, and finally the last sentence is defined for entering the mass into geometry [16].

3.2. TURBULENCE MODEL

A sophisticated and widely used model consists of two transport equations for the turbulent kinetic energy k_T and its dissipation ε_T , the so-called k- ε model [17] has been used in this paper. An additional transport equations are solved for the turbulent dissipation, ε_T and turbulent kinetic energy k_T [16]:

$$\frac{\partial \varepsilon_T}{\partial t} + \frac{1}{V_F} \left\{ u A_x \frac{\partial \varepsilon_T}{\partial x} + v A_y R \frac{\partial \varepsilon_T}{\partial y} + \omega A_z \frac{\partial \varepsilon_T}{\partial z} \right\} = \frac{CDIS1 \cdot \varepsilon_T}{k_T} (P_T + CDIS3 \times G_T) + DIFF_\varepsilon - CDIS2 \frac{\varepsilon_T^2}{k_T} \quad (6)$$

$$k_T = \frac{1}{2} (\overline{u'^2} + \overline{v'^2} + \overline{w'^2}) \quad (7)$$

Where u', v', w' are the x, y and z components of the fluid velocity associated with chaotic turbulent fluctuations, k_T is the specific kinetic energy and u, v, w are the x, y and z components of the fluid velocity, $DIFF_\varepsilon$ is the diffusion of dissipation, V_F, A_x, A_y, A_z are FLOW3D's FAVOR functions, $CDIS1, CDIS2,$ and $CDIS3$ are all dimensionless user-adjustable parameters, G_T is The buoyancy production term, R is related to the cylindrical coordinate system (in this research Cartesian coordinate used) and P_T is the turbulent kinetic energy production [16]:

$$\begin{aligned} P_T = CSPRO \left(\frac{\mu}{\rho V_F} \right) \left\{ 2A_x \left(\frac{\partial u}{\partial x} \right)^2 + 2A_y \left(R \frac{\partial u}{\partial y} + \xi \frac{u}{x} \right)^2 + 2A_z \left(\frac{\partial w}{\partial z} \right)^2 \right. \\ \left. + \left(\frac{\partial v}{\partial x} + R \frac{\partial u}{\partial y} + \xi \frac{v}{x} \right) \left[A_x \frac{\partial v}{\partial x} + A_y \left(R \frac{\partial u}{\partial y} - \xi \frac{v}{x} \right) \right] \right. \\ \left. + \left(\frac{\partial u}{\partial z} + \frac{\partial w}{\partial x} \right) \left(A_z \frac{\partial u}{\partial z} + A_x \frac{\partial w}{\partial x} \right) + \left(\frac{\partial v}{\partial z} + R \frac{\partial w}{\partial y} \right) \left(A_z \frac{\partial v}{\partial z} + A_y R \frac{\partial w}{\partial y} \right) \right\} \end{aligned} \quad (8)$$

$CSPRO$ is a turbulence parameter, whose default value is 1.0, μ is the molecular dynamic viscosity, ρ is the fluid density and R and ξ are related to the cylindrical coordinate system.

The diffusion of dissipation, $Diff_\epsilon$, is [16]:

$$Diff_\epsilon = \frac{1}{V_F} \left\{ \frac{\partial}{\partial x} (v_\epsilon A_x \frac{\partial \epsilon_T}{\partial x}) + \frac{\partial}{\partial y} (v_\epsilon A_y R \frac{\partial \epsilon_T}{\partial y}) + \frac{\partial}{\partial z} (v_\epsilon A_z \frac{\partial \epsilon_T}{\partial z}) + \xi \frac{v_\epsilon A_x \epsilon_T}{x} \right\} \quad (9)$$

3.3. NUMERICAL SPECIFICATIONS

The models were created using Auto CAD software and were exported to FLOW 3D. Cartesian coordinate and hexahedral elements were used to represent fluid and solid geometries. Hence, six boundaries have to be defined for each model (figure (4)). In this research time-step was controlled by stability and convergence. In FLOW3D time step calculate automatically (in the range of 0.000025-0.0152 s). Upstream total head was measured at 4p from the crest of the weir to avoid the water surface curvature, [6]. The numerical model specifications are presented at table 1.

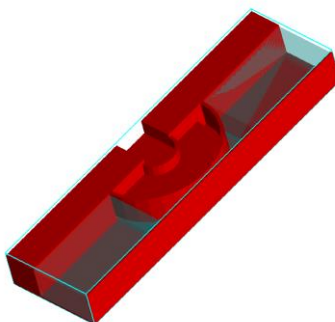


Figure 3. geometry of the model and initial condition

The upstream boundary is defined as volume flow rate, downstream end of model is represented as outflow and other boundaries are presented in table 1 and figure 4.

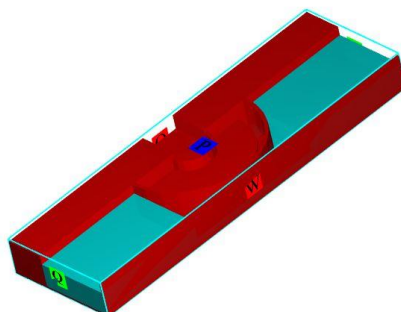


Figure 4. Boundary conditions

In figure 4: Q is volume flow rate, W is wall, p is pressure, O is outflow.

Table 1. meshing and boundary conditions

mesh	Computational block	1
	Total number of meshes	800000-1000000
Boundary conditions	Downstream	Outflow
	Left boundary	Volume flow rate
	Right boundary	Volume flow rate
	Free surface model	VOF
Equations	Turbulence model	k-ε
	Time interval	0.01

4. RESULTS AND VERIFICATION

4.1. MOUND HEIGHTS

Figure 5 and 6 show the numerical simulation of water surface profile at the downstream of arced weir. The mound height of the experimental report is also added for comparison (mound configuration illustrated in figure- 2). It is clear, that the crest of the mound simulated with acceptable accuracy.

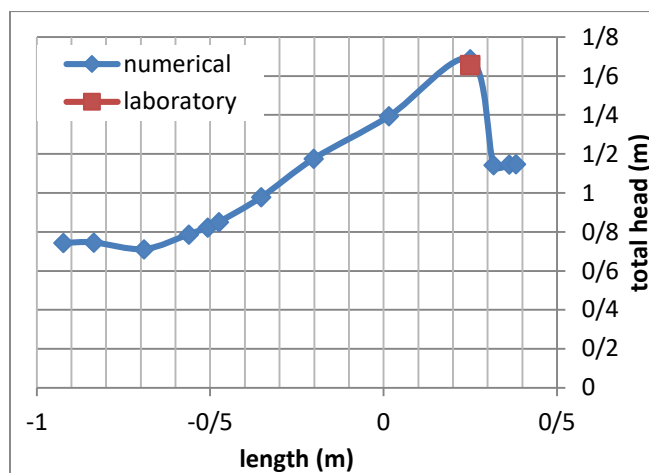


Figure 5. Numerical & Laboratory mound at Q=0.091 cmfs

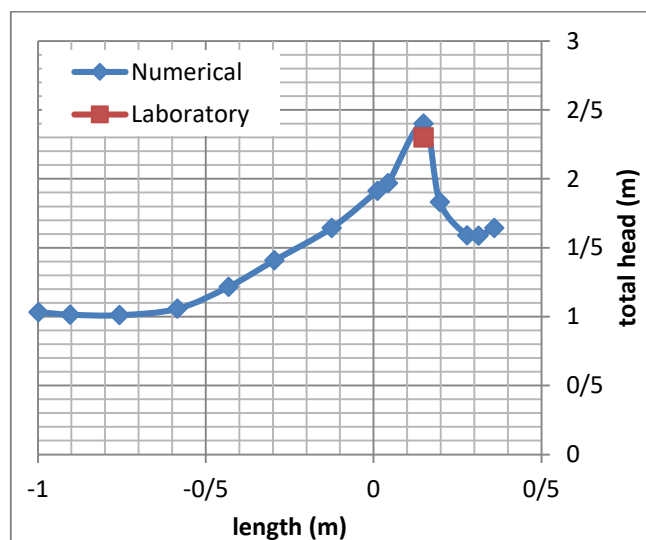


Figure 6. Numerical & Laboratory mound at Q=0.156 cmfs

Figure 7 showed simulated and experimental results for the mound height in dimensionless manner. All numerical data have A.A.E (Absolute average error) and RSQ. equal to 4.47 percent and 0.993, respectively. Hence one can concluded that the downstream height of the mound can be simulated numerically with acceptable accuracy. As the mound height has significant effect on discharge coefficient of the weir in the submerged condition, flow- 3D software can be used as an appropriate tool to find the discharge coefficient of the arced weirs.

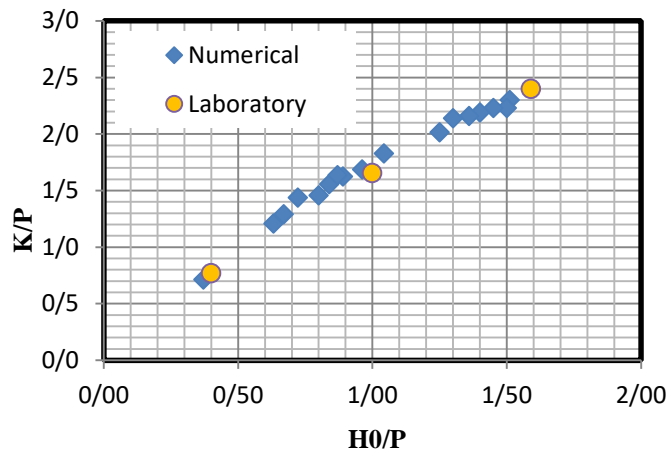


Figure 7. all results from numerical and laboratory tests

4.2. UPSTREAM TOTAL FLOW HEAD

Figure (8) showed the total head of of weir for $Q= 0.091 \text{ m}^3/\text{s}$. The error of the numerical simulation is 3%.

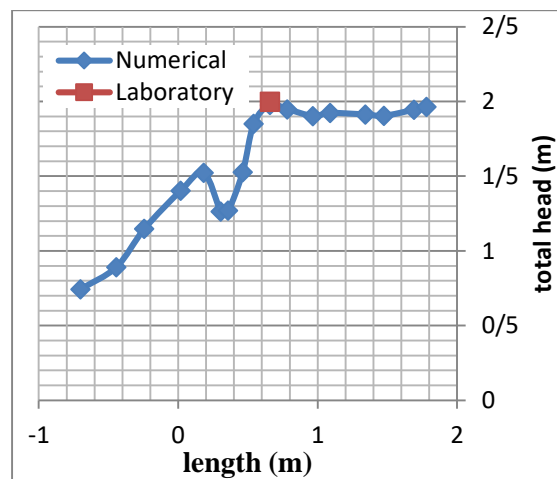


Figure 8. Total head against length (all dimension in meter)

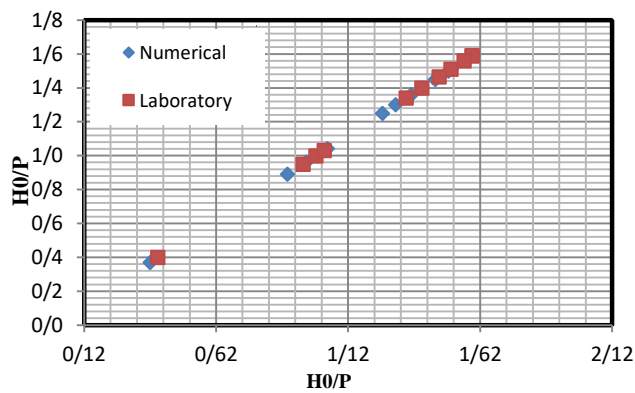


Figure 9. comparing between upstream heads of numerical simulation and laboratory tests

It should be mention that for all numerical simulation, A.A.E (absolute average error) is less than 3 % (Figure 9).

5. CONCLUSIONS

Arched weirs could be used as measuring device. In numerical simulation all results indicated that mound height had less than 5% differences from laboratory runs and total upstream head had 3% error. Finally by comparing results between laboratory and numerical simulation, good agreement was seen and because of time consuming and higher price of laboratory runs, we suggest that numerical simulation could be the sufficient substitution.

6. REFERENCES

1. Vischer, D; “*Recent developments in spillway design*”. Journal of Water Power and Dam Construction, Vol.40, No. 1, 1988, pp: 10-15.
2. Hanger, W. H; and Schwalt, “*Broad-crested weir*”. American Society of Civil Engineering, Journal of the Hydraulics Division, Vol. 120, No. 2, 1994, pp:13-27.
3. Kumar S., Ahmad Z., Mansoor T. and Himanshu S.K. (2012),“*Discharge Characteristics of Sharp Crested Weir of Curved Plan-form,*”Research Journal of Engineering Sciences ISSN 2278 – 9472 Vol. 1(4), pp: 16-20.
4. Yildiz, D. and Uzecek, E. (1996). “*Modeling the performance of labyrinth spillways*” Hydropower & Dams. Aqua-Media Int. Ltd., Surrey, UK. 3:71-76.
5. Houston, K. (1983). “*Hydraulic model study of Hyrum Dam auxiliary labyrinth spillway*” U.S. Bureau of Reclamations, Denver, Colo., # GR 82-13, pp: 9-10.
6. Crookston, B. M; and Tullis, B. P (2012). “*Discharge Efficiency of Reservoir-Application-Specific Labyrinth Weirs*”. ASCE , Vol. 138, No. 6, pp: 564-568.
7. Aydin, I. “*Flow Measurement and Instruction*”. Journal of Hydraulic Research, 2011, pp: 144-151.
8. Villemonte J. R; “*Submerged weir discharge studies*”. Engineering News Record, Vol. 139, No. 26, 1947, pp: 54-56.
9. Emiroglu M.E., Kisi O. and Bilhan O. (2010), “*Predicting discharge capacity of triangular labyrinth side weir located on a straight channel by using an adaptive neurofuzzy technique,*” Adv Eng Softw, 41(2), pp: 54–160.
10. Bilhan O., Emiroglu M.E. and Kisi O. (2010), “*Application of two different neural network techniques to lateral outflow over rectangular side weirs located on a straight channel,*” Adv Eng Softw., 41(6), 831–7.
11. Sangsefidi Y., Mehraein M., Ghodsian M. and Motalebizadeh M. (2017) “*Evaluation and analysis of flow over arched weirs using traditional and response surface methodologies,*” J. Hydraul. Eng., (Accepted for publication).
12. Bos, M. G (1976) “*Discharge measurement structures*”. International Institute For Land Reclamation and Improvement, Wageningen, the Netherlands,.
13. Emiroglu M.E. and Baylar A. (2005), “*Influence of included angle and sill slope on air entrainment of triangular planform labyrinth weirs,*” ASCE J Hyd Eng; 131(3),pp: 184–9
14. Henderson, F. (1966). “*Channel controls*”Open channel flow. MacMillan, New York, 174-176.
15. Bagheri S. and Heidarpour M. (2010), “*Application of free vortex theory to estimate discharge coefficient for sharp-crested weirs,*” Biosystems Engg., 105 (3), 423–7.
16. Flow-3D, User Manual Version 11.2, Flow Science, Inc., Santa Fe (2016).
17. Francis H. Harlow and P. I. Nakayama. (1967) “*Turbulence transport equations,*” Physics of Fluids, 10(11):2323–2332.
18. Rodi. W. (1980) “*Turbulence models and their application in hydraulics: a state of the art review.*” International Association for Hydraulic Research (IAHR), Delft, The Netherlands.

History and Overview of Self Compacting Grout and Concrete: Properties and Applications

Hakim S. Abdelgader¹, Ali S. El-Baden², Hamdi A. Abdurrahman³

- 1- Professor, University of Tripoli, Faculty of Engineering, Civil Eng. Dept., Tripoli, Libya.
2- Associate Professor, University of Tripoli, Faculty of Engineering, Civil Eng. Dept., Tripoli, Libya.
3- PhD Candidate, Florida Institute of Technology, Melbourne, FL 32901, USA.

Email: hakimsa@poczta.onet.pl

Abstract

Two-stage concrete (TSC) is a simple concept; it is made using the same basic constituents as traditional concrete: cement, coarse aggregate, sand and water as well as mineral and chemical admixtures. The main benefits of the method are widely appreciated as Low heats of hydration, high compressive strengths and density, economic savings, practically no mass shrinkage, low coefficient of thermal expansion, excellent bond to existing structures. As the name would suggest it is produced through a two-stage process. Firstly, washed coarse aggregate is placed into the formwork in-situ. Later a specifically designed grout is introduced into the form from the lowest point under gravity pressure to fill the voids, cementing the aggregate into a monolith. TSC is particularly useful for underwater construction, placement in areas with closely spaced reinforcement and in cavities where overhead contact is necessary, repairs to concrete and masonry where the replacement is to participate in stress distribution, heavyweight (high-density) concrete, high-lift monolithic sections, and in general, where concrete of low volume change is required. This paper presents some implementations of using such concrete in repair works, some formulae and guide lines which describe the mechanical parameters of this concrete such as modulus of elasticity, tensile strength and drying shrinkage.

Keywords: Modulus of elasticity, Compressive-strength, Tensile-strength, Aggregate, Drying shrinkage.

1. INTRODUCTION

Placing concrete in general is a challenging task for construction engineering, due to the risk of segregation and bleeding or washout of concrete constituents specially, when placement occurs in difficult places such as: concrete repairing or underwater applications. Thus, the quality of concrete produced is highly influenced by its placement technique during manufacturing and casting [1, 2]. Placement techniques involve free-fall gravitational placement, pumping, belt conveyors, tremie, and preplaced aggregate concreteetc. The goal when applying any of these techniques is to place concrete into the formwork with minimum segregation, minimum honeycombing and maximum possible homogeneity of the concrete constituents [3]. Concrete shrinkage and consequently shrinkage cracking has been a growing concern. Minimizing shrinkage can take place by adequate mix proportions, thorough curing and the use of shrinkage compensating cement [4, 5]. It was approved that using non-traditional concrete in engineering applications has been considered as an efficient solution to overcome challenges of limitations of the use of normal conventional concrete. Such new types of concretes which have been developed and produced are completely dissimilar from the conventional concrete in the method of mixing, handling, pouring, consolidation, behaviours, cost... etc. Based on the technology of ready-mixed self-compacting concrete (SCC), a type of non-conventional concrete has been introduced and named as: two-stage concrete (TSC) [6 to 8]. Two-stage (pre-placed aggregate) concrete (TSC), unlike normal concrete (NC), is made by first placing the coarse aggregate in the formwork and then injecting a grout consisting of sand, cement and water to fill the voids between the aggregate particles (see Figure 1). The most significant difference of TSC from conventional concrete is that TSC contains a higher percentage of coarse aggregate compared to conventional concrete; because TSC is produced by depositing coarse aggregate directly into the forms, where there is a point-to-point contact, instead of being contained in a flow-able plastic mixture as in conventional concrete. Because of this, the properties of TSC depend on the coarse aggregate, more than its other constituents. As a result of this, the modulus of elasticity of TSC is found to be slightly higher, and its drying shrinkage is less than half that of conventional concrete [4]. Investigations on some properties of TSC will demonstrated and discussed through this paper in the next subtitles.

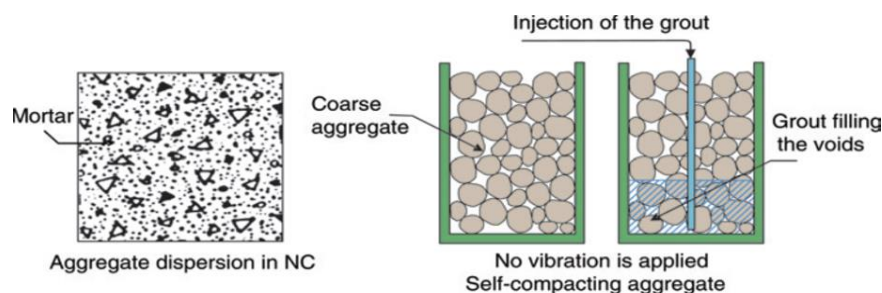


Figure 1. Theory of concreting

2. PREPARATION OF EXISTING CONCRETE SURFACES

If the TSC is used to repair surface defects, or cast as an addition to an existing concrete structure, in order to establish a good bond between the new TSC and the existing old concrete, the surface of the existing concrete must be cleaned very carefully by removing all deteriorated concrete till the sound concrete is reached, and a space which is at least four times the maximum coarse aggregate size should be provided behind the existing reinforcement, or the new reinforcing to be added [4]. One of the other special properties of TSC is its excellent bonding ability when it is added to an existing roughened concrete. This ability of TSC comes from two reasons:

1. The grout can penetrate through the surface irregularities and pores on the existing concrete surface, and establish an initial bond.
2. The low drying shrinkage of TSC minimizes the interfacial stresses taking place upon drying.

3. EXPERIMENTAL PROGRAM–PART (I)

3.1. MATERIALS

The cement used was ordinary Portland cement Type I with 28-days compressive strength of 41 MPa and Blaine fineness of approximately 3500 cm²/g. Cement properties confirmed with ASTM standards [9]. The fine aggregate used was natural beach sand of specific gravity 2.63 and maximum size of 1.18. Coarse aggregate used was angular basalt of specific gravity 2.69, crushing value of 20.74%, abrasion value of 23.81%, and absorption value of 1.96 %. Both fine and coarse aggregate properties checked in accordance with ASTM standards [10]. The super plasticizer used in the grout was a naphthalene- formaldehyde derivative, trade name ‘SikaMent-163’ and was mixed at the rate of 2% by weight of cement. The expanding agent, trade name ‘Intraplast-Z’ was an aluminium powder-based admixture; this was also used at the rate of 2% by weight of cement.

3.2. MIXTURE PROPORTIONS AND SAMPLE PREPARATION

Three different proportions of c/s, 0.5: 1, 1: 1 and 1.5: 1, with varying ratios of w/c, 0.38, 0.55 and 0.80, as shown in Table 1. A total of 360 standard concrete cylinders (150 mmx300 mm) were tested in unconfined compression and tensile strength at 28 days.

Table 1- Grout mix proportions

Water : Cement Ratio (W/C)	Cement : Sand Ratio (C/S)	Cement	Sand
		Kg/m ³	
0.38	0.5	295	590
	1	421	421
	1.5	525	350
0.55	0.5	282	564
	1	407	407
	1.5	507	338
0.80	0.5	265	530
	1	396	396
	1.5	489	326

3.3. CONSISTENCY OBSERVATIONS AND DISCUSSION

To measure consistency both a flow cone and flow table tests were conducted [11,12] as shown in Figure 2. Fluidity results are presented in Figure 3 and 4.



Figure 2. Flow cone and flow meter setup

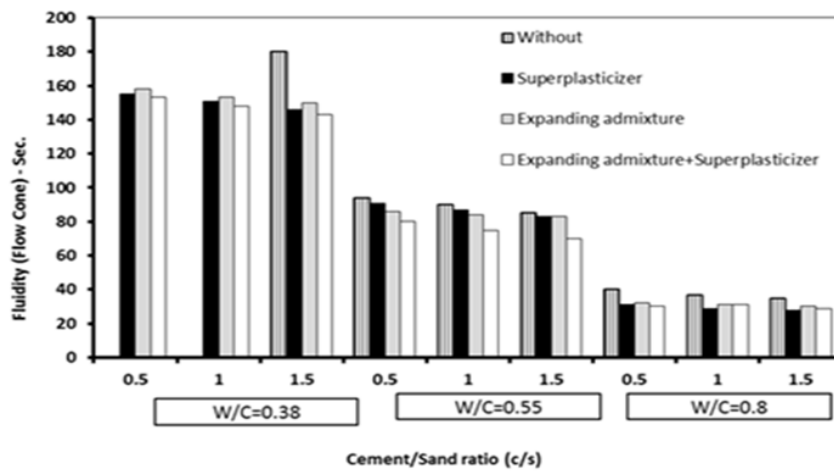


Figure 3. Flow cone test results

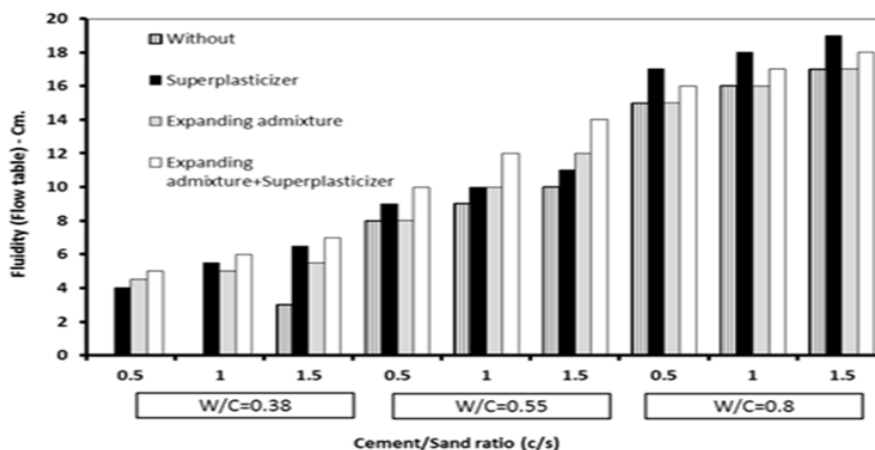


Figure 4. Flow table test results

Tests on consistency demonstrated that the higher c/s ratio of 1.5 required much more water, where the flow cone depends on the time of flow while the flow table depends on the propagation of flow [11]. For example, the w/c ratio 0.38 in the plain grout and expanding admixture at all c/s ratios is the minimum ratio to obtain grout; it was not possible to penetrate all voids in the aggregate skeleton.

3.4 COMPRESSIVE STRENGTH OBSERVATIONS AND DISCUSSION

The compressive strength f_c' of TSC was tested with and without admixture at 28 days. Sample of results is shown in Table 2. Based on the results, a relation for f_c' has been assumed, according to the design algorithm presented in reference [13]. Equation (1) is an empirical equation derived from the experimental data for prediction of compressive strength of TSC (f_c') in (MPa) as the following:

$$f_c' = a + (b) \times w/c + (c) \times (w/c)^d + (e) \times (c/s) \tag{1}$$

Where: f_c' represents the estimated compressive strength of TSC, w/c is the water-to-cement ratio and c/s is the cement-to-sand ratio. Table 3 shows the values of the regression coefficients. Compressive strength without admixture was found to be lower than compressive strength with admixture (super plasticiser). The possible reason for this decrease in strength was the low fluidity of the grout. When high fluidity of grout was used (achieved by using super plasticiser at high w/c ratios), the compressive strength of TSC did not increase. The quality of TSC depends not only on the strength of grout but on its ability to expand while fluid and remove the traces of bleed water that collect under aggregate particles [12]. With this idea of an expanding admixture, a blend of special metallic aluminium powder expansion agent was used in the grout. The strength data shows that when using the expanding admixture the compressive strength of TSC was significantly increased. Super plasticiser and expanding admixture were used together among the four types of grouts. The compressive strength was found to have the highest strength. This could be attributed to the following: (a) higher fluidity of grout using super plasticiser (which enables the grout to fill all the voids between aggregate particles) (b) expansion effect of grouts using expansion admixture to minimise bleeding and settlement of grout.

Table 2- Average compressive strength results

W/C Ratio	C/S Ratio	Average Compressive Strength (MPa)			
		Without	Super plasticizer	Expanding Admixture	Expanding and Super plasticizer
0.38	0.5	-----	15.59	15.26	18.68
	1.0	-----	17.39	16.54	18.96
	1.5	-----	18.53	18.01	19.47
0.55	0.5	15.65	18.19	16.56	19.06
	1.0	17.57	19.49	18.01	19.75
	1.5	20.49	20.59	19.67	22.72
0.80	0.5	13.69	14.39	17.06	18.16
	1.0	15.07	15.79	16.08	18.75
	1.5	16.01	16.31	19.10	19.37

Table 3- Regression results for equation (1)

Type of Grout	Regression Coefficients					Correlation Coefficients
	a	b	c	d	e	
Without Admixture*	-3.67	11.20	3.96	-1.79	3.70	0.833
Super plasticizer	43.90	-32.55	-3.27	-1.68	2.24	0.944
Expanding Admixture	-14.31	-39.38	68.45	0.47	2.63	0.891
Expanding and Super plasticizer	-25.70	-87.70	126.75	0.52	1.88	0.660

*Does not include water-cement ratio=0.38 at all cement sand ratios

3.5. TENSILE STRENGTH OBSERVATIONS AND DISCUSSION

The tensile strength of TSC was investigated at 28 days. Table 4 shows the values of experimental tensile strength. Equation (2) is an empirical equation derived from the experimental data for prediction of tensile strength of TSC (f_t) in (MPa). Table 5 shows the values of the regression coefficients.

$$f_t = A + (B) \times (w/c) + (C) \times (w/c)^D + (E) \times (c/s) \tag{2}$$

Table 4- Average tensile strength results

W/C Ratio	C/S Ratio	Average Tensile Strength (MPa)			
		Without	Super plasticizer	Expanding Admixture	Expanding and Super plasticizer
0.38	0.5	-----	1.74	1.62	1.84
	1.0	-----	1.98	1.86	2.06
	1.5	-----	2.38	2.16	2.54
0.55	0.5	2.18	2.42	2.36	2.78
	1.0	2.44	2.66	2.58	2.88
	1.5	2.61	2.84	2.82	3.36
0.80	0.5	1.80	2.20	2.26	2.38
	1.0	2.30	2.42	2.58	2.56
	1.5	2.40	2.32	2.70	3.36

Table 5- Regression results for equation (2)

Type of Grout	Regression Coefficients					Correlation Coefficients
	A	B	C	D	E	
Without Admixture*	-0.25	1.26	0.67	-1.29	0.51	0.833
Super plasticizer	-12.75	-25.27	39.03	0.50	0.39	0.860
Expanding Admixture	-11.54	-23.20	36.12	0.52	0.48	0.960
Expanding and Super plasticizer	9.82	-7.41	-1.37	-1.39	0.42	0.855

*Does not include water-cement ratio=0.38 at all cement sand ratios

3.6. DRYING SHRINKAGE OBSERVATION AND DISCUSSION

Because of the point-to-point contact of the coarse aggregate, drying shrinkage of TSC is about one-half that of conventional concrete [4]. In TSC the grout fills only the cavities, and the basic mass of concrete is the stone skeleton only. The drying shrinkage can practically occur in the vicinity of cavities. Less drying shrinkage may result in reduced cracking repair overlays. TSC shows good stability of volume and low calorific value, which is of great importance in massive structures. Some results for drying shrinkage of NC and TSC are presented in Table 6. The small values of contraction can be explained by the continuity of skeleton, individual grains of stone filling are in close contact with one another, which results in their small negative deformation.

Table 6- Drying shrinkage of TSC and NC

Age (days)	Type of Concrete	Shrinkage (10^{-5})	Temperature in Mass Concrete (+ °C)
7	NC	5	38
	TSC	2.5	20
28	NC	2.5	32
	TSC	8	25
56	NC	-2	23
	TSC	17	18
80	NC	-8	17
	TSC	8	15
100	NC	-15	15
	TSC	2.5	15

4. EXPERIMENTAL PROGRAM – PART (II)

This part of the paper presents the results of some experimental tests conducted by the author and others [13] to study the behavior of TSC under loading and derive relation between elastic modulus and the compressive strength.

4.1. STRESS-STRAIN PROCEDURE, OBSERVATIONS AND DISCUSSION

Stress-strain tests conducted using cylinder specimens (196 mm in diameter and 392 mm in length) of the same nine different grout proportions and types of aggregate. There were prepared 81 specimens in total (three

cylinders per composition). During the loading procedure, the vertical deformations were measured on three sides of the specimen versus the axial force increment. On the basis of these results, the stress and appropriate strain values were calculated. The results obtained from the cylinder specimens were used to derive the stress-strain relations and the modulus of elasticity for the two-stage concrete. As the linear part of the stress-strain curves obtained for each type of the two-stage concrete reached at least 40% of its compressive strength, the initial tangent modulus of elasticity was derived. The tangent line is drawn along the stress-strain curve at its starting point (see some examples presented in Figure 5).

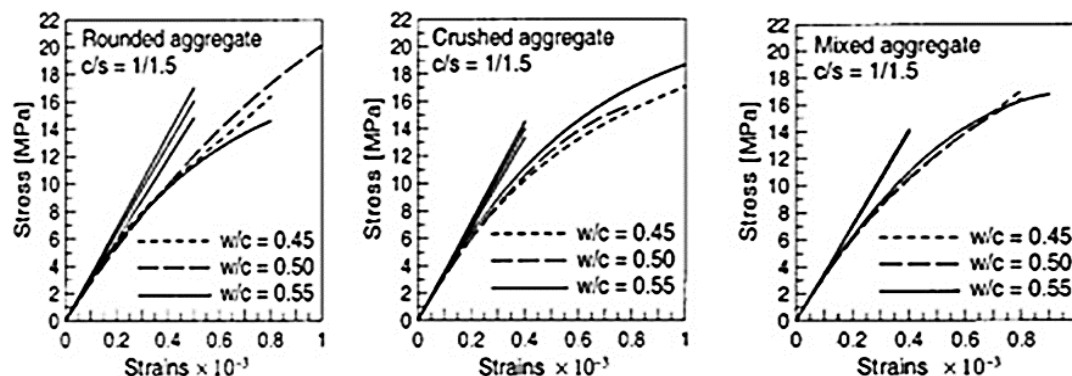


Figure 5. TSC estimated modulus of elasticity for round aggregate

The values of the module are computed from stress-strain curves for the examined cases of aggregate types and grout mixes, and are given in Table 8. From the other hand, the experimental data analysis and the statistically obtained stress-strain relations allow for formulating the relationship between the static modulus of elasticity and the compressive strength of the two-stage concrete (f_c') at 28 days as shown in Table 8. The compressive strength limit values are between 22 MPa and 32 MPa.

Table 8- Computed modulus of elasticity (Using formulas and stress-strain curves)

W/C	C/S	Modulus of elasticity (GPa)			Derived formulas for modulus of elasticity (GPa)	
		Round aggregate	Crushed aggregate	Mixed aggregate		
0.45	1/1.5	34.0	34.9	35.4	Round aggregate	$E_{TSC}=28.7+0.080* f_c'$
0.50		28.5	33.3	34.8		
0.55		32.1	36.2	35.2		
0.45	1/1.0	33.7	32.9	33.0	Crushed aggregate	$E_{TSC}=33.9+0.049* f_c'$
0.50		29.4	30.9	32.0		
0.55		30.4	31.7	32.6		
0.45	1/0.8	27.1	29.8	27.2	Mixed aggregate	$E_{TSC}=34.9+0.090* f_c'$
0.50		31.6	-	32.2		
0.55		-	30.9	29.5		

5. CONCLUSIONS

- ❑ As the method of placement in TSC is entirely different from that of NC, a suitable admixture is necessary to satisfy the requirement for the pumping ability of grout. The expanding admixture was found to be the most suitable admixture as it provided higher fluidity with minimum bleeding.
- ❑ The compressive strength and tensile strength of TSC was tested with and without admixture at 28 days for all grout proportions. On the basis of the results, a correlation between the strength and grout proportions was statistically derived.
- ❑ The stress-strain relationships for different grout mixes (water/cement ratios and cement/sand ratios) do not show a big difference. Linear relations can estimate the initial stress-strain curves. This may result from the stresses distributed mainly by the particles of stone aggregate (skeleton of stones). The specific way of stress transmission may also contribute to the initiation and propagation of cracks.

- The modulus of elasticity as a function of compressive strength of the two-stage concrete is elaborated. The modulus values for specific types of aggregate can be described by linear constant functions. The obtained equations can help engineers to design the two-stage concrete.
- It is proved that the crushed aggregate is better than the rounded aggregate for designing the two-stage concrete. The crushed aggregate makes it possible for a better contact between the grains of the aggregates than the rounded stones.
- The authors believe that there are many aspects of TSC that require clarification through further theoretical and experimental studies such as: energy dissipation, failure mechanism and cracking, shrinkage, creep and other time dependent deformations.

6. REFERENCES

1. Abdelgader, H. S., Górski, J., Khatib, Jamal., M. and El-baden, A. S (2016)., “*Two-stage concrete: effect of silica fume and superplasticizers on strength*” BFT INTERNATIONAL Concrete Plant + Precast Technology, (Concrete Technology), (03), pp. 30-36.
2. Abdelgader, H. S., Khatib, J., M. and El-baden, A.S. (2015), “*Self-compacting grout to produce two-stage concrete*”, Proceeding of The 2nd International Sustainable Buildings Symposium (ISBS), Gazi University, Ankara, Turkey.
3. ACI Committee 318 (2008), “*Building code requirements for reinforced concrete*” American Concrete Institute, Detroit, Michigan, USA.
4. ACI Committee 304, (2005), “*Guide for the use of preplaced aggregate concrete for structural and mass concrete applications*” American Concrete Institute, Farmington Hills, Michigan, USA, pp. 21 – 24.
5. Abdelgader, H.S and Górski, J., (2015), “*Concrete repair using two-stage concrete method*”. Materiały Budowlane, (in Polish), Vol. 8, pp.66-68, <http://www.materiałybudowlane.info.pl/>
6. Abdelgader H. S. “*How to design concrete produced by a two-stage concreting method*” Cement and Concrete Research, 1999, Vol.3, No. 29, pp. 331 - 337.
7. Najjar M., Soliman A., and Nehdi M., (2014), “*Critical overview of two-stage concrete: properties and application*”. Journal of Construction and Building Materials, Vol. 62(3), pp. 47-58.
8. Najjar M., Soliman A., and Nehdi M., (2014), “*Two-stage concrete made with single, binary and ternary binders*”. Journal of Materials and Structural, RILEM, December, 1-11.
9. ASTM-C150 (1994) “*Specification for Portland Cement*” American Society for Testing and Materials, Philadelphia, Pennsylvania.
10. ASTM C33 (1997), “*Specification for Concrete Aggregates*” Philadelphia, Pennsylvania.
11. ASTM C230 (2001), “*Standard specification for flow table for use in tests of hydraulic cement*” American Society for Testing and Materials, Philadelphia, Pennsylvania, pp. 129-133
12. ASTM C939 (2010), “*Standard Test Method for flow of Grout for Preplaced Aggregate Concrete (Flow Cone Method)*” American Society for Testing and Materials, Philadelphia, Pennsylvania, pp. 134-136.
13. Abdelgader, H. and Elgalhud, A. (2008), “*Effect of grout proportion on strength of two-stage concrete*” Structural Concrete Journal, vol.3, pp. 163-170.
14. King J (1959), “*Concrete by intrusion grouting*” Handbook of heavy construction” 2nd.Edition, McGraw-Hill, New York.
15. Abdelgader H. and Górski J., (2003), “*Stress-strain relations and modulus of elasticity of two-stage concrete*” ASCE Journal of Materials in Civil Engineering, Vol.4, pp. 251-255.
16. ASTM-C494 (2004), “*Standard Specification for Chemical Admixtures for Concrete*” American Society for Testing and Materials, Philadelphia, Pennsylvania.

Numerical study of the passing flow over spillway with emphasis on the potential of cavitation occurrence

Hamzeh Ebrahimnezhadian¹, MirAli Mohammadi², Ramin Abdullah Kookhi³ Ako Seyedi⁴

1- Ph.D. Candidate in Water & Hydraulic Structures, Dept. of Civil Eng., Faculty of Eng., Urmia University, Urmia, Iran

2- Associate Prof. in Civil Eng., Water & Hydraulic Structures, Dept. of Civil Eng., Faculty of Eng., Urmia University, Urmia, Iran

3- Ph. D. Candidate in Water & Hydraulic Structures, Dept. of Civil Eng., Faculty of Eng., Islamic Azad University, Arak, Iran

4- MSc in Civil Engineering-Water, Islamic Azad University, Maragheh, Iran

Email: H.ebrahimnezhadian@gmail.com

Abstract

Water has high velocity passing through spillways or bottom channels of dams. Under this condition, it would have a great deal of kinetic energy; therefore, energy dissipater structures must be used in order to dissipate such destructive energies. Analyzing the flow passing through spillways is typically done by analytical relations and physical models. However, nowadays thanks to advances in computer sciences, using numerical models has grown noticeably, because of using less time and cost compared to physical models. In this study, flow characteristics, including pressure distribution and average flow velocity, were studied in different points of flood evacuation system, and were compared with the results of physical model. Then, using the results of pressure and velocity, potential occurrence of destructive cavitation was studied on chute of spillway. The results indicated acceptable compatibility between the results of numerical model and those of experimental model; therefore, it can be argued that this software has an acceptable ability in simulating free surface flows, particularly in velocity and pressure field. RNG K- ϵ turbulence model, among other turbulence models, has the highest compatibility in simulating flow characteristics. The study of results showed that at a certain span in the length of spillway, cavitation index is set lower than the critical point, and the occurrence of cavitation is strengthened from this point onwards and the risk of cavitation occurrence increases. This necessitates the use of aeration equipment in such areas in order to prevent the occurrence of cavitation.

Keywords: Ogee spillway, velocity and pressure distribution, cavitation indicator, Flow-3D software.

1. INTRODUCTION

Spillways are one the most important components of dams, and at times when dam's reservoir cannot hold flood water due to its limited capacity, spillways move the flood water to downstream in a safe way. The reason of failure in most of the dams around the world is because of inadequate designing of spillways. Spillway geometry depends on many factors including topography, shape of valley, bedrock, type of dam, and etc. The process of flow passing over spillways typically causes remarkable destructive energy at the downstream of spillways by transformation of upstream sub-critical flow to downstream supercritical flow. One of the issues that happens in high spillways is cavitation. There are typically uneven surfaces on spillways that when water flows on them and with the increase in flow velocity (more than 10 m³/s), the flow is separated from spillway, which causes localized pressure reduction and results in cavitation and erosion in concrete surface, and finally ends in destruction of the structure. This destructive phenomenon has caused heavy losses in many dams in different parts of the world. In Iran, several times it destroyed Shahid Abbaspour Dam's spillway, whose reconstruction and repair cost was enormous. There are several ways to control cavitation. Cavitation control by changing the geometry of spillway and using concrete spillway surface is a primary corrective action. The most effective way in controlling cavitation is artificial aeration in the flow. This is accomplished by embedding aeration in spillway. Hence, checking the passing flow over the spillway has always been one of the most important steps in designing dams, but unfortunately, in most dam projects, investigating the passing flow over the spillway is not achieved, due to high costs and time-consuming physical models. Replacing hydraulic models with numerical models has always been one of the points which has progressed substantially in analyzing hydraulic issues, thanks to the advances of computer science and development of computational fluid dynamics (CFD). Using physical models,

despite a way of analyzing the passing flow over the spillway, is costly and time-consuming. However, using mathematical models that simulate hydraulic phenomena could help make more converged results, without consuming lots of time or money. Thus, one of the best tools for the analysis of the passing flow over the spillways is using mathematical models. Obviously, the use of numerical models has its own specific problems including calibration, having powerful hardware for simulation, and choosing the appropriate methods for better convergence of the results. Nevertheless, due to savings in costs and time, using the appropriate numerical model can always help. [1]

Using numerical model in simulating the passing flow over spillways was done two dimensionally for the first time in 1965 by Cassidy to determine the pressure on the spillway crest based on the potential flow theory. The results of this study indicate that first, there is a good match between experimental and numerical model data. Second, the viscosity does not affect the determination of free surface. Hu et al. (2003), examined pressure changes on spillway crest, and hydraulic conductivity of ogee spillway in the upstream head using Flow-3D two-dimensionally and three-dimensionally, and compared the results with the results obtained from the USACE. The results corresponded with USACE data. However, in both two-dimensional and three-dimensional models, numerical model predicts slightly more negative pressure on the spillway crest. In Iran, Kavianpoor et al. examined the process of static pressure changes along stepped spillway of Siah Bishe Dam using Fluent software. Experimental model was used to verify numerical model results, and the results indicated acceptable convergence. [2]

2. GEOMETRY AND HYDRAULIC CHARACTERISTICS OF FLOW FIELD

Azad dam is a rockfill dam with clay core. The height of the dam from its foundation is 125 meters and the length of the dam crest is 600 meters. It has a body capacity of 85,000,000 m³ and reservoir capacity of 300,000,000 m³. The dam's catchment area is 1007 km². Catchment gradient is 20%, the average gradient of river is 81%, and the main river length is 69 km. The purpose of this dam is to transfer 250,000,000 m³ per year to the plains of Qorveh and Dehghan in East Kurdistan. A further objective of this dam is to release 50,000,000 m³ of water per year for environmental water rights and agricultural raffle. Azad River is one of the main branches of Sirvan River. The average annual input of this river at the dam axis is 376,000,000 m³. Hydraulic model of flood discharge in Azad dam with a scale of 1 to 33 was built and installed by the Water Research Institute. Azad dam's flood evacuation system includes: 1- input channel 2- valved ogee spillway 3- chute 4- flip 5- riffle flip, which are built on the left side of the dam. Three discharges of 1226, 1545, and 2990 m³/s (flood discharge with 1000-year and 10000-year return and probable maximum flood respectively) were measured.

3. NUMERICAL SOLUTION OF THE FLOW FIELD

3.1. PREVAILING EQUATIONS IN FLOW FILED BY FLOW-3D NUMERICAL MODEL

Flow-3D is a powerful software specified for computational fluid dynamics which has been designed by Flow Science Company. Solving equations in this application is based on the finite volume method. One of the major features of this software for hydraulic analysis, is the ability to model the flows with free surface. The interface between gas and liquid, is the flow with free surface. In this software, the free surface is modeled by VOF technique that was developed in 1981 by Hirt and Nichols. Also in this software, all equations are formulated with space and volume of penetration rate functions. This formulization is called FAVOR technique which was presented in 1985 by Hirt and Lysylyan.

The prevailing equations in fluid flow include the continuity equation and the momentum equation for incompressible turbulent flow with constant density and viscosity as expressed in equations (1) and (2) [4].

$$V_F \frac{\partial \rho}{\partial t} + \frac{\partial}{\partial x}(\rho u A_x) + R \frac{\partial}{\partial y}(\rho v A_y) + \frac{\partial}{\partial z}(\rho w A_z) + \xi \frac{\rho u A_x}{x} = RDIF + RSOR \quad (1)$$

Where V_F is fractional volume of fluid, ρ is fluid density, RDIF is permeability turbulence, RSOR is mass source, u , v , and w are velocity components in Cartesian coordinates (x , y , z) or cylindrical coordinates (z , θ , r) respectively. A_x , A_y , and A_z are respectively the space of element in vertical direction to x , y , and z . ξ and R coefficient are related to system coordinates and their value in Cartesian coordinates are: $R=1$ and $\xi = 0$

$$\frac{\partial u}{\partial t} + \frac{1}{V_F} \left[u A_x \frac{\partial u}{\partial x} + v A_y R \frac{\partial u}{\partial y} + w A_z \frac{\partial u}{\partial z} \right] - \xi \frac{A_y v^2}{x V_F} = -\frac{1}{\rho} \frac{\partial P}{\partial x} + G_x + f_x - \frac{RSOR}{\rho V_F} u$$

$$\frac{\partial v}{\partial t} + \frac{1}{V_F} \left[uA_x \frac{\partial v}{\partial x} + vA_y R \frac{\partial v}{\partial y} + wA_z \frac{\partial v}{\partial z} \right] - \xi \frac{A_y v u}{xV_F} = -\frac{1}{\rho} \left(R \frac{\partial P}{\partial y} \right) + G_y + f_y - \frac{RSOR}{\rho V_F} v$$

$$\frac{\partial w}{\partial t} + \frac{1}{V_F} \left[uA_x \frac{\partial w}{\partial x} + vA_y R \frac{\partial w}{\partial y} + wA_z \frac{\partial w}{\partial z} \right] = -\frac{1}{\rho} \frac{\partial P}{\partial z} + G_z + f_z - \frac{RSOR}{\rho V_F} w$$
(2)

In these equations G_x , G_y , and G_z are mass acceleration in the direction of x , y , and z , and f_x , f_y , and f_z are accelerations of gravity in the direction of x , y , and z , and the last term in the right side is related to the injection of mass at zero velocity.

3.2. DEFINITION OF SOLID BORDERS GEOMETRY

The present numerical study simulated Azad dam’s spillway (which is a type of ogee spillway with flip bucket) using Flow-3D. To create a geometric model and define the geometry of solid boundaries, three-dimensional Auto CAD software was used. For a suitable convergence of the solution field, 1500000 computational volumes of rectangular adaptive type were used. Because of the turbulence of the discharge passing over the spillway, three-dimensional flow field has been solved by RNG turbulence model. Apparently, the right number of computational volumes of the issue, was viewed and chosen after performing various models in the software. Furthermore, in ‘Boundaries’, the boundary conditions of the issue were determined, and volume flow rate was chosen as the input border. In this section, input flow discharge was set and defined for the software, and outflow was chosen as the output border. Wall was chosen as the bottom border and the side borders. Wall boundary conditions or wall are used to separate liquids from solid border. In this boundary condition, the vertical and tangent velocity on the boundary wall is considered zero. Symmetry was chosen for the upper part that is in connection with the atmosphere, and in fact the flow has free surface. Figure (1) shows the flow geometric model and boundary conditions. [5]

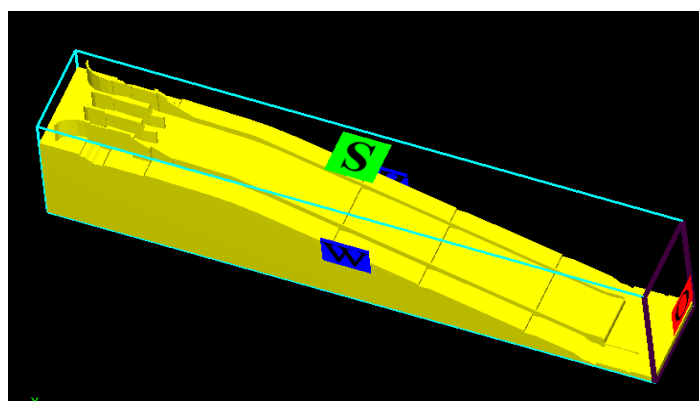


Figure 1 - View of the three-dimensional geometry and boundary conditions used by the numerical model of Azad dam’s spillway

Table 1 – Specifications of numerical model of Azad dam’s spillway

Meshing	Type of Model	VOF
	Type of Mesh	Adaptive Rectangular
	Number of computational volume	1500000
Boundary condition	Body of spillway	Solid
	Side boundaries	Wall
	Input	Volume Flow Rate
	Output	Outlet
Equation	Turbulence	<i>RNG K – ε</i>
	The Algorithm of Solving Pressure Equations	GMRES
	Free surface Model	Fluid Volume Pattern

4. ANALYSIS OF THE RESULTS

4.1. CHANGING THE FROUDE NUMBER

One of the most important parameters in studying the pattern of passing flow over spillways is Froude number. Froude number is important because the process of passing flow over spillways is accompanied by transformation of subcritical flow at upstream to supercritical flow at downstream. In this section, using Flow-3D numerical model, the Froude number of passing flow over the spillway of Azad dam was studied.

In figure (3) it can be seen that the regime of passing flow over ogee spillway, has a suitable pattern in accordance with the process of passing flow over the spillways. According to the values of the Froude number, initially the flow regime was subcritical, and with increasing distance from the flow and chute, the flow regime goes toward supercritical. It is obvious that with the flow passing over the spillway and increase in discharge, velocity is always increased. Similarly, the changes in the Froude number significantly increase, like the speed along the flow on chute. The difference between the changes in Froude number and the changes in velocity is that as the discharge increases, flow velocity is also increased. However, as it can be seen in the graph, the increase in discharge, does not necessarily result in the increase in Froude number.

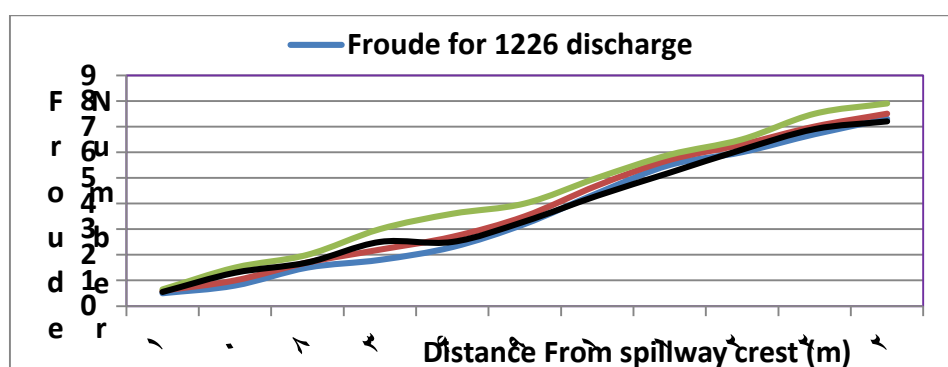
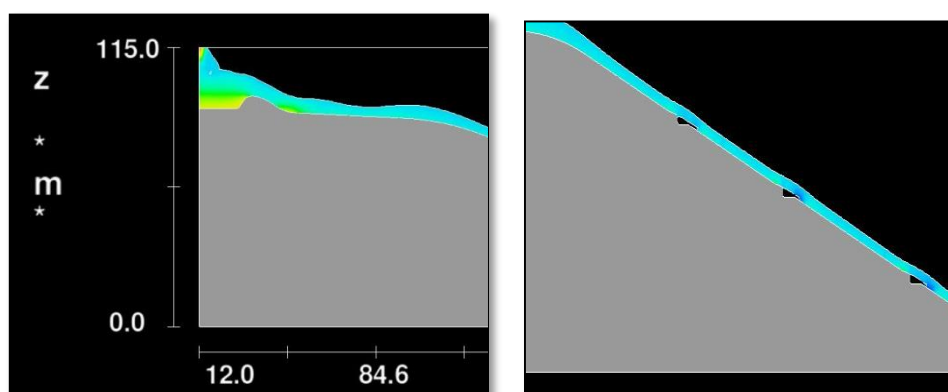


Figure 3- The comparison of Froude number changes over the spillway of Azad dam for critical discharges

4.2. THE MANNER OF CHANGES IN STATIC PRESSURE AND AVERAGE VELOCITY

The results of this study include the average static pressures and flow velocity in mentioned sections along the spillway of Azad dam. For three discharges of 1226, 1545, 2290 m³/s (flood discharge with 1000-year and 10000-year return and probable maximum flood discharge respectively) static pressure and flow velocity were measured. Similarly, the static pressure and flow velocity in the numerical model at specific points of the mentioned discharges were measured by the software.

As shown in Figure 4, the pattern of passing flow over the spillway for the largest discharge has a good match with the natural mode, so that in upper depths of the passing flow, the static pressure increases. Due to the increasing depth of flow and pressure distribution in the areas before the ogee spillway, the pressure in this area is higher compared to other areas, while on the chute, what happens is the reduction of flow depth, followed by reduction of the pressure. This reduction is normal up to this point and happens in passing of the flow over all ogee spillways, and the reason is that, by increase in velocity, the flow depth is reduced and the pressure decreases. However, the most critical pressure happens when flow pressure has a tendency toward negative pressure. This mode that is commonly called suction, increases the likelihood of cavitation occurrence in the spillway structure. Figure 4 (b) shows the reduction of pressure on the chute and the possibility of formation of negative pressure in this range. [6]



a) Pressure changes near aeration chute b) Pressure changes on ogee spillway crest
Figure 4- The manner of changes in the static pressure on the spillway and chute of Azad dam (for maximum discharge)

According to the pattern of the passing flow over Azad dam’s spillway, the changes of flow velocity are in way that at the beginning of input channel, because of the depth of the water in the input channel, the flow velocity is much lower than the other parts of the spillway. The reason for this drop in velocity is that the input flow of the spillway encounters the lump of ogee spillway. The flow at the beginning of flood evacuation system in input channel is quiet and dominant to the spillway. As it can be seen from the changes of Froude number, the flow is almost subcritical, and with passing over the spillway and with gradual increase in velocity, it changes to supercritical. Figure (5).

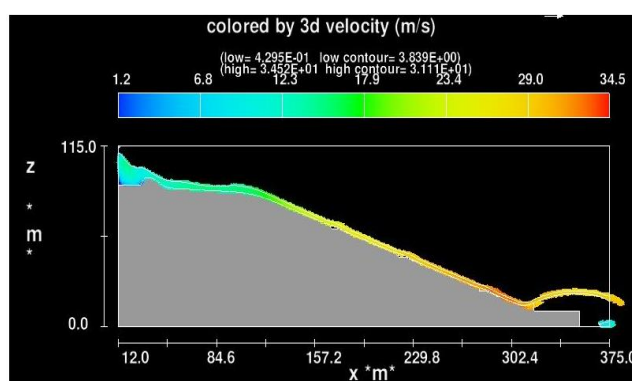


Figure 5- The changes of average velocity over the spillway for discharge of 2290 (maximum probable flood) by Flow-3D model

4.2. EVALUATION OF THE RESULTS OF THE NUMERICAL MODEL

To verify the results of the numerical model, the results of experimental model were used. The choice of three discharges was to verify the effects of the results of maximum, minimum and intermediate discharges. Therefore, the numerical static pressure, and experimental static pressure, and experimental and numerical velocity were calculated, and the graphs of velocity and pressure changes for three above mentioned discharges were drawn.

4.2.1. THE PRESSURE OVER SPILLWAY

According to evaluation of the charts, it can be said that there is a good match between experimental data and numerical data. At the beginning, the static pressure is high, and near the chute, the pressure is reduced,

and finally, reaches its peak in flip bucket. It must be pointed out that, for larger discharges, the pressure increased. In aerator positions, the pressure increased and then decreased.

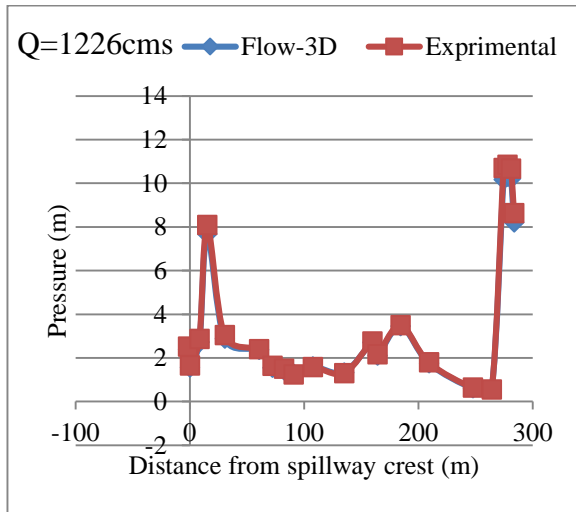


Figure 4-a) The comparison between numerical and experimental static pressure for discharge (1226 m³/s)

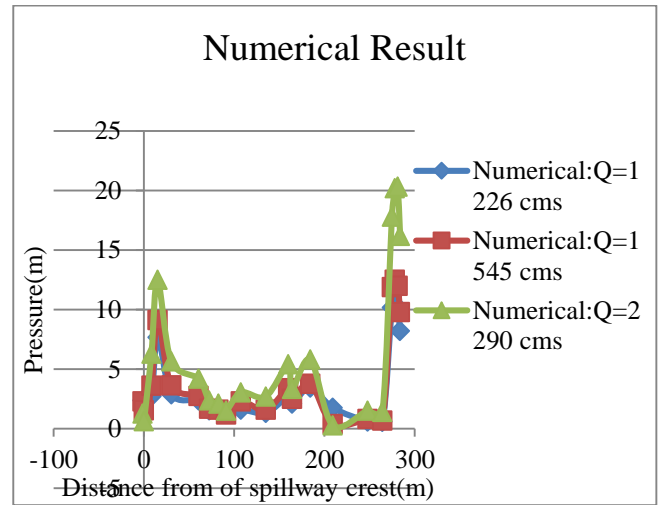


Figure 4-b) The comparison between numerical static pressure for three discharges (1226, 1545, 2290 m³/s)

4.2.2. FLOW VELOCITY OVER THE SPILLWAY

The evaluation of the results of velocity over the spillway indicates that with increasing distance from the spillway crest, flow velocity increased and reached its peak in flip bucket. The study of the results showed that with increasing discharge, flow velocity also increased.

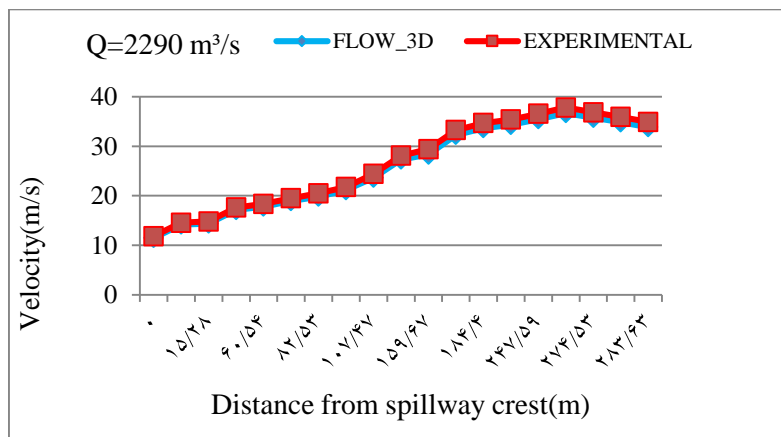


Figure 5- The comparison between numerical and experimental velocity for (2290 m³/s)

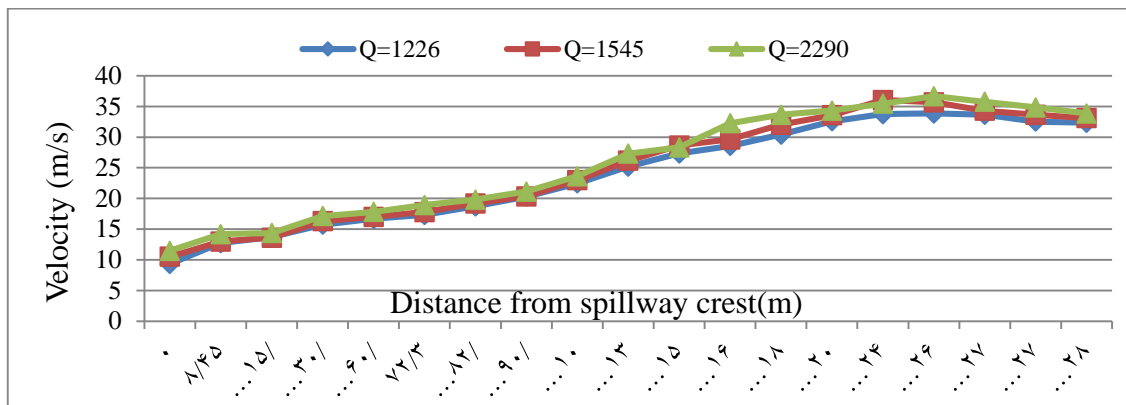


Figure 6- The comparison between numerical velocity for three discharges (1226, 1545, 2290 m³/s)

4.2.3. THE STUDY OF CAVITATION CHARACTERISTIC OVER THE SPILLWAY

4.2.3.1. CAVITATION INDEX

The main parameter for describing cavitation, is cavitation index, which is in fact a special form of Euler number.

$$\delta = \frac{(P_0 - P_v)}{\frac{1}{2} \rho u^2} \tag{3}$$

Where P_0 is a characteristic pressure of the flow, u is a characteristic velocity of the flow, ρ is the density, and P_v is the vapor pressure of the fluid.

Using velocity and static pressure measurement results, in 12 cross sections along the chute for three discharges, (from 1226 to 1800 m³/s), cavitation coefficient was calculated. The results and change curves of cavitation coefficient are indicated in Figure (7). Using the results, test parameters (static pressure and velocity) of the chute cavitation coefficient along the chute were calculated. From the beginning of the chute, to a distance of 160 meters from the threshold of the spillway, cavitation coefficient ($\delta \geq 0.25$) is above critical line.

At a distance of about 115 meters from the chute ramp leading to the flip bucket, corrosion coefficient ($\delta \leq 0.25$) is below the critical line. In order to calculate corrosion coefficient (cavitation index) using numerical models over the chute of Azad dam's spillway, for three critical discharges, velocity and average pressure in 12 cross sections were calculated.

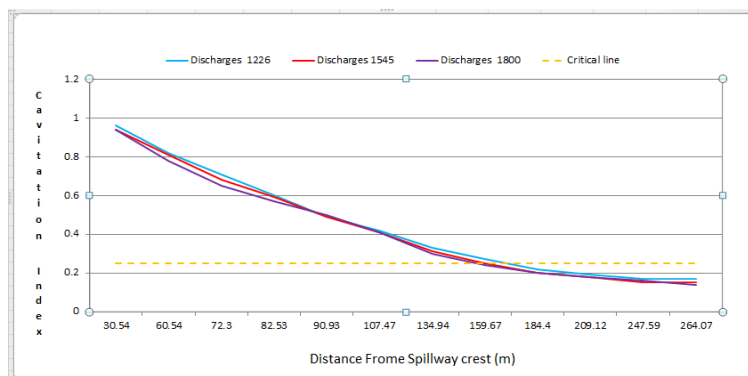


Figure 7- The comparison of curves of cavitation coefficient of Flow-3D model along the chute for three critical discharges

The important point is that in studying the cavitation coefficient over the chute for the discharge of maximum probable flood (2290 m³/s), because of the conditions of the passing flow, in experimental model, 1800 m³/s was used.

As it can be seen, cavitation coefficient acts contrary to the manner of velocity and pressure changes. The notable point is that with distancing from the spillway over the chute, cavitation coefficient has decreased. Like the changes in cavitation coefficient in physical model, in numerical models likewise, at a distance of approximately 160 meters from the threshold of the spillway, the corrosion coefficient is below the critical line, thus the occurrence of cavitation from this point onwards gains strength and the risk of cavitation occurrence increases. Therefore, in order to remove the corrosion on the surface of the chute, two aeration systems were designed and performed, one at a distance of 165 meters from the threshold of the spillways, and the other at a distance of 210 meters from the spillway.

5. CONCLUSIONS

In general, the results of this research can be summarized as follows: Flow-3D as an analytical model, due to the use of VOF method, has an appropriate capability in modeling free surface flows. RNG turbulence model, due to having additional term in the epsilon equation, compared to other turbulence models, is much more appropriate in analyzing quickly strained flows and the flows on surfaces with large curves. This model also has high potential to simulate transient flows.

1. In studying changes in static pressure of Azad dam's spillway, between the experimental and numerical data, there was little difference ranging from 3 to 5 percent. However, the greatest pressure difference was seen on the flip bucket, because due to high velocity in this point, there was turbulent flow.
2. Along the chute, due to significant reduction of pressure, there is the possibility of negative pressure and cavitation. Therefore, in order to the lower the risk of cavitation over the chute, at distances of 135, 185 and 245 meters from the threshold of the spillway, three aeration systems are recommended.
3. At a distance of 209.12 meters from the ogee spillway, maximum pressure reduction occurs. The reason for this reduction in pressure is that this point is the edge of the ramp in aeration system. However, the pressure is not in the range of negative pressure; therefore, at the presence of aeration systems, the likelihood of cavitation occurrence is reduced.
4. Pressure changes over the spillway of Azad dam are by and large affected by depth and velocity of the flow. With the increase in the flow depth, the pressure increased, and with the increase in velocity, the pressure reduced.
5. With the increase in discharge, flow velocity over the spillway increased.

6. REFERENCES

1. Abdullah Kookhi, R. (2015), "*Numerical Study of Hydraulic Performance of the Spillway and Flip Bucket of Azad Dam,*" Master's thesis, Islamic Azad University, Maragheh (in Persian).
2. Babazadeh, V, Manafipoor, M. and Mohammadi, M.A. (2012), "*Numerical Investigation of the Pattern of Flow over the Spillway and Flip Bucket of Gavshan Dam,*" Ninth International Congress of Civil Engineering, Isfahan, Isfahan University of Technology.
3. Water Research Institute (Affiliated to the Ministry of Energy). (2010), "*Final Report of Hydraulic Model of Azad Dam's Spillway,*" September 2008.
4. Husseini Sahi, S.M. (2005), "*Hydraulic Simulation of Flow in Stilling Basin Using Flow-3D,*" Master's thesis, Tarbiat Modarres University, Tehran (in Persian).
5. Ghasemzadeh, F. (2013), "*Simulation of Hydraulic Issues in Flow-3D,*" Noavar Publications, Tehran, First Edition (in Persian).
6. FLOW 3D user manual, ver .9.3

Numerical Investigation of Flow over Rectangular Side Weir in a Circular Channel

Sanaz Shoaie¹, Mojtaba Mehraein²

1- M. Sc student, Kharazmi University, Tehran, Iran

2- Assistant Prof. Department of Civil Engineering, Kharazmi University, Tehran, Iran

Email: sanaz.shoaie@gmail.com

Abstract

Side weir is one of most important structures in drainage system, irrigation, flood protection, and urban sewage systems. Therefore, the hydraulic behavior of side weirs received a level of interest by many researchers. The water surface profiles over rectangular side weirs in circular channel were investigated experimentally by many researchers in past. In present study, hydraulic behavior of a side weir is simulated by FLOW-3D software. RNG model for turbulence simulation and VOF model for water surface simulation were applied. At first, the water surface profiles and the discharges performances from CFD analyses were validated with the experimental results. The results show good agreements between CFD and experimental results in the subcritical regime. Then free surface flow and flow pattern over a side weir is simulated and effects of upstream Froude number on them are investigated. Various turbulence models were tested to determine the sensitivity of the free surface over a rectangular side weir. The results showed, RNG k- ϵ turbulence model can be used to predict the various characteristics of the side weir flow and give close results compared to other turbulence models.

Keywords: Side weir, CFD analysis, Free surface flow, Turbulence model, Circular channel.

1. INTRODUCTION

Side weirs are the hydraulic structures that have been used in drainage system, irrigation, flood protection, and urban sewage systems. A side weir is installed on the side wall of main channel to divert the flow. Flow over side weir is a typical case of spatially varied flow. The importance of channels with side weir and the passing flow over side weir were investigated experimentally and numerical by many researchers. There are several studies on side weirs, most important experimental studies in a sharp-crested rectangular side weir in rectangular channels are as follows:

De Marchi (1934), was one of the earliest investigators who gave equations for flow over side weirs and developed an equation for the water profile across a side weir on the assumption that total energy along the side weir is constant [1]. Then several researchers have developed an equation for the discharge coefficient of De Marchi until today; For instance Frazer (1954), Collinge (1957), Chow (1959), Subramanya and Awasthy (1972), El-kashab (1975), Ranga Raju et al. (1979), Ramamurthy et al. (1980), Hager (1987), Uyumaz and Smith (1991), Singh et al. (1994), Swamee et al. (1994), Swamee et al. (1995), Jalili and Borghei (1996), Vatankhah and Bijankhan (2009), Emiroglu et al. (2010), Emiroglu et al. (2011), Bagheri and Heidarpour (2012), Novak et al. (2013), Bagheri et al. (2014), Emiroglu et al. (2016), [1-21].

Although the behavior of side weir received the level of interest for many decades, there are few contributions aimed to study the hydraulic characteristics of the flow along side weirs in circular channels. Allen (1957) was the first one who conducted a laboratory study on the passing discharge over a rectangular side weir on a circular channel [22]. Uyumaz and Muslu (1985) investigated some experimental and analytical methods on the passing flow over side weirs on circular channels in both supercritical and subcritical flow conditions. Some discharge coefficient relationships were presented for supercritical and subcritical regimes [23]. Hager (1994) determined the flow features of a side weir in a circular channel in supercritical flow conditions and hydraulic jump was studied with a modified momentum approach [24]. Oliveto et al. (2001) obtained the results from theoretical and experimental study conducted along the side weir located in a circular channel when the flow along the weir is supercritical while upstream flow is subcritical and theoretical relations derived for the average lateral outflow velocity along a side weir [25]. Vatankhah (2012) using computational tool for the evolution and design of rectangular side weirs in open circular channels and introduced an analytical solution for flow profile computation over the side weir on a circular channel [26]. Granata et al. (2016) an experimental study of the flow field in a circular channel along a side weir using a Particle Image Velocimetry (PIV) system. In this research only the components of the velocity in planes parallel to the axis of the channel were measured [27].

Today, numerical methods (Computational Fluid Dynamics, CFD) with their advantages of lower cost and greater flexibility can reasonably predict the mean flow characteristics such as velocity distributions, pressure distributions, and water surface profiles of complex problems in hydraulic engineering; For instance, Aydin (2012) used VOF model to describe the free surface flow over the triangular labyrinth side weir for different Froude numbers [28]. Aydin and Emiroglu (2013) used CFD to analyze the discharge capacity labyrinth side weir for various Froude number, dimensionless nappe height, dimensionless weir width, and weir included angle [29]. Azimi et al. (2014) simulated the flow free surface and the passing flow through a rectangular side weir in circular channel in supercritical conditions by commercial software [30]. Aydin (2015) determined hydrodynamics properties of flow on the sill and effects on the discharge. It was seen that the using a sill located in a suitable place considerably increases outflow discharge of the side weir [31]. Aydin et al. (2016) investigated to determine hydrodynamic characteristics experimentally, theoretically and numerically of siphon in subcritical flow condition [32]. Aydin and Emiroglu (2016) used CFD to determine the discharge capacity of two-cycle trapezoidal labyrinth side weir. The results indicated that the discharge coefficient decreased with an increase in Froude number and the best performances were obtained with side weir angle, $\alpha=30^\circ$ and weir height, $p=20$ cm among tested values [33].

In this paper, the free surface flow and the flow pattern over a rectangular side weir in a circular channel is simulated by using FLOW-3D software. The influences of the upstream Froude number on subcritical flow conditions are investigated. The knowledge of the above characteristics expanded the knowledge on the operation of side weir in a circular channel.

2. GOVERNING EQUATIONS

A High Performance Computer (HPC) was used to simulate the CFD models in FLOW-3D software. Flow field of a non-compressible fluid solved in the continuity equation and Reynolds-averaged Navier–Stokes equations are used as follows:

$$\frac{\partial(\rho u_j)}{\partial t} + \frac{\partial(\rho u_i u_j)}{\partial x_i} = -\frac{\partial p_s}{\partial x_j} + \frac{\partial}{\partial x_i} \mu \left(\frac{\partial u_i}{\partial x_j} + \frac{\partial u_j}{\partial x_i} \right) + \rho g_j + F_j \quad (1)$$

Where ρ is fluid density, μ is dynamic viscosity of fluid, u is velocity vectors, P_s is pressure, g is gravitational acceleration and F is body force.

$$\frac{1}{\rho_q} \left[\frac{\partial}{\partial t} (\alpha_q \rho_q) + \nabla \cdot (\alpha_q \rho_q \bar{v}_q) \right] = S_{aq} + \sum_{p=1}^n (m_{pq} - m_{qp}) \quad (2)$$

In which m_{qp} and m_{pq} is mass transfers between phases, α_q is volume fraction of fluid in a cell, and S_{aq} is source term, which is by default zero. The value of α_q depends on whether the cell is empty or full, If $\alpha_q = 0$, the cell is empty, if $\alpha_q = 1$, the cell is full, and if $0 < \alpha_q < 1$, the cell contains the interface between two fluid phases [33].

3. NUMERICAL MODEL

The Uyumaz and Muslu's (1985) experimental data were used in this study to validate the numerical models [23]. The Laboratory model of the rectangular side weir in circular channels are also illustrated in Fig.1. The laboratory model is composed of a circular main channel 0.25 m wide and 10.9 m long, with a discharge collection channel 0.85 m wide and 0.30 m deep perpendicular to the main channel. A sluice gate was fitted at the end of the main channel to control flow depth. A sharp side weir is installed at the middle section of the main channel side wall.

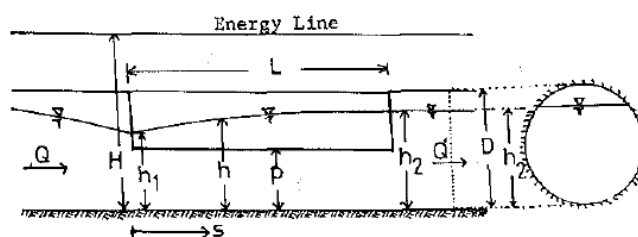


Figure 1. Geometry and characters of rectangular side weir in circular channel (Uyumaz and Muslu, 1985)

4. BOUNDARY CONDITIONS AND GRID LAYOUT IN NUMERICAL MODEL

The boundary conditions are provided to analyse the flow characteristics consist of, the inlet boundary at the inlet section with a known volume flow rate; the outlet boundary was defined as the out flow used at the side weir boundary and at the end of channels and a sluice gate was fitted at the end of the main channel to control flow depth. The symmetry was applied at the boundaries above of main channel. The wall boundary condition presents an option which ensures to easily describe the bottom and the surface levels of the main channel. The typical view of 3D model and boundary conditions are given in Fig. 2 and Fig. 3.

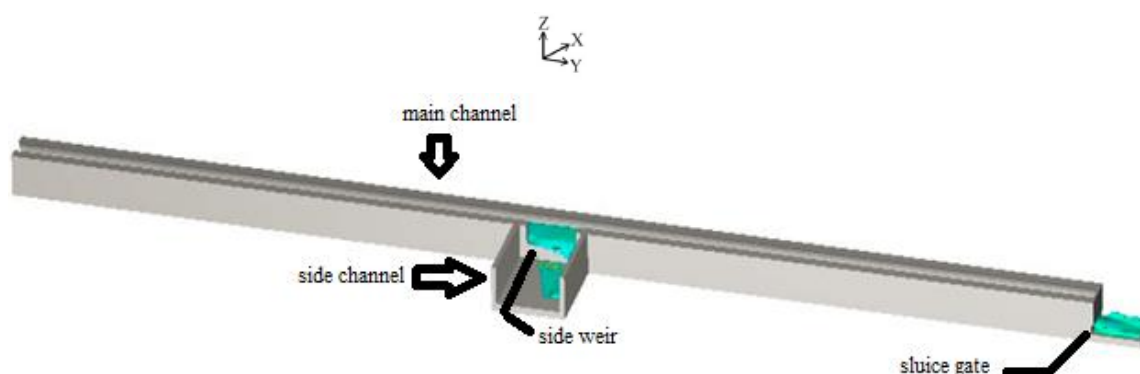


Figure 2. 3D view of rectangular side weir in circular channel in numerical model

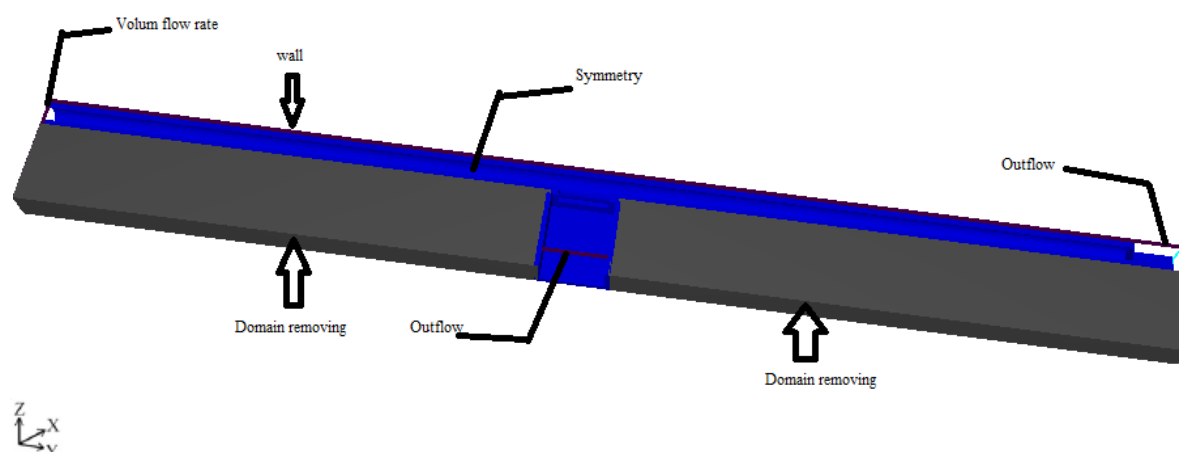


Figure 3. Boundary conditions of rectangular side weir in circular channel in numerical model

Generation of a good quality grid is one of the basic part of the numerical modeling and the greater the number of cells in the mesh grid, the more accurate will be the modelling results. The region of the side weir and some part of the downstream channel were made finer to accommodate dividing streamline, stagnation point and flow separation zone with acceptable accuracy. Grid independence study was done initially for the coarse mesh size. However, the computing time increases with mesh density. Hence we tried to find a balance between quality of results and computation time, settling on 685 000 computational cells and for reduce of time used doming remove. The grid of CFD model is depicted in Fig.4.

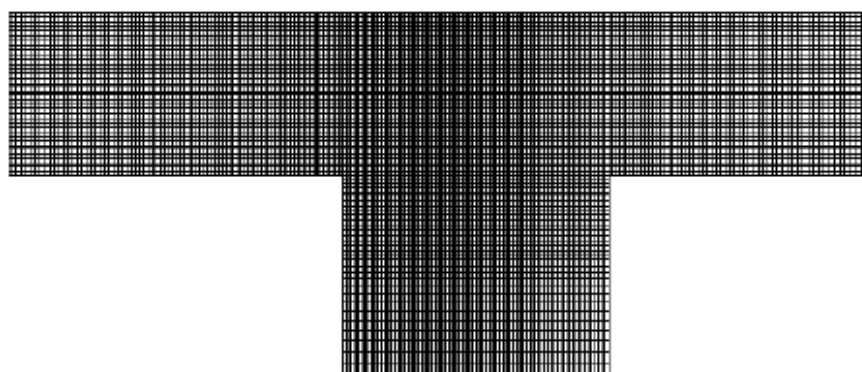


Figure 4. numerical mesh structure in the main channel and side channel

5. RESULTS AND DISCUSSION

5.1. EFFECT OF TURBULENCE

In this study, similar free surface over a rectangular side weir are used for verification of the numerical model. Whereas, turbulence models may also have effects the results of CFD simulations. Various turbulence models were tested to determine sensitivity of the free surface over a rectangular side weir to turbulence. RNG $k-\epsilon$ turbulence model can be used to predict the various characteristics of the side weir flow and give close results besides other models (Fig.5). Very good agreement is achieved between the CFD and experimental results. These results all show that the numerical simulation can be considerable to be reliable.

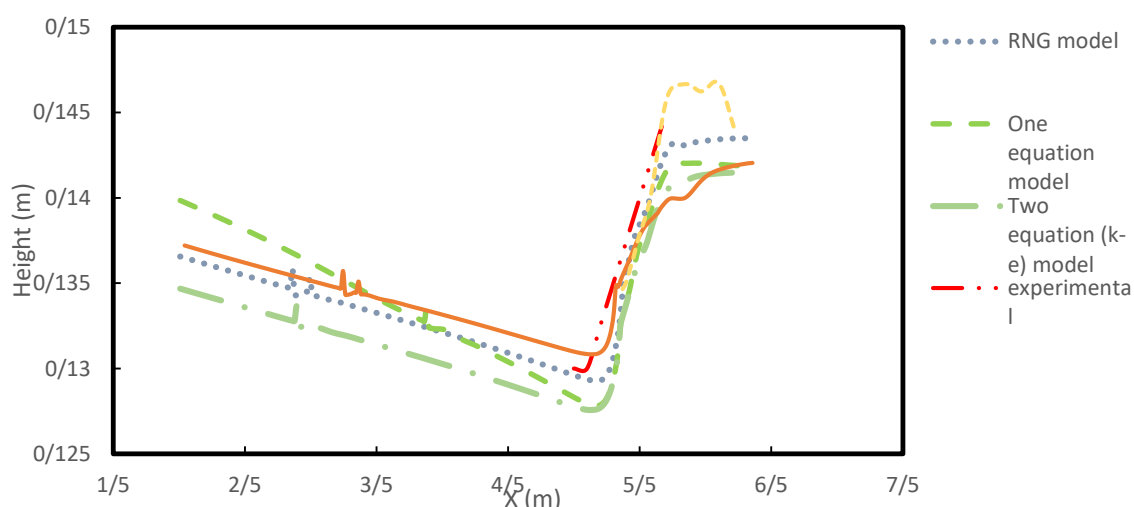


Figure 5. Free surface profiles provided from CFD simulations for $p = 0.1$ m, $L = 0.5$ m, $Fr = 0.42$

5.2. VELOCITY PROFILES

Inside the main channel and at the downstream end of the side weir, there is a stagnation zone. Stagnation point has the highest water surface elevations. Due to the collision of the flow with the wall of the downstream of the channel and assuming a constant specific energy at this zone, the minimum longitudinal velocity appears with the highest water surface elevations. Therefore, a stagnation point is formed and the amount of shear stress near the bed of the main channel is zero. If the sediment is carried by flow, the sediment particles are trapped and, due to the absence of shear stress and low velocity of the flow, the sediment particles are deposited.

The velocity contours on the free surface are specified in Fig.7. The stagnation points in downstream edge of side weir, vortices, stagnation zone near to the left side wall of the main channel downstream were apparent. On the other hand, Fig.7 shows that velocity head decreases 10 mm from the upstream toward down-

stream. The maximum velocities along main channel on the surface occur in the part between centerline and the opposite side wall.

Emiroglu et al. (2011), the primary reason for this may be the intensity of secondary flow created by lateral flow turbulence and velocity streamlines that is oriented toward the side weir. By the orientation of the velocity streamlines toward side weir, the occurrence of the stagnation zone plays an important role in flow interactions. As mentioned above, the strength of the secondary flow created by the lateral flow was affected by the length of the side weir crest height of the side weir and the Froude number. An increase in the secondary flow causes the growth of the deviation angle and kinetic energy toward the side weir when the relative length of the side weir increases [17].

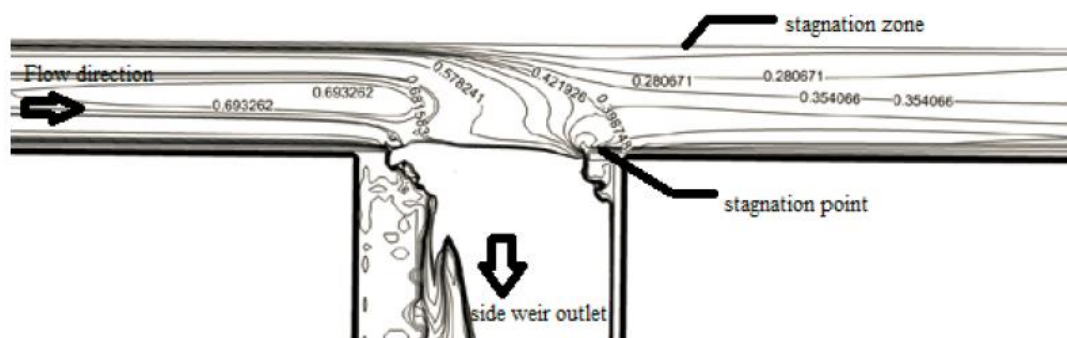


Figure 7. Velocity contours on the free surface for $p = 0.1$ m, $L = 0.5$ m, $Fr = 0.42$

5.3. Free surface profiles

Water surface profiles were obtained computationally along side-weir in the centerline of main channel in Fig.6. As shown in these figures, the water level along the side weir drops slightly at the upstream end of side weir, then rise quickly toward the downstream end of the weir. The drop of water level is probably because of the side weir entrance effect at the upstream end. Additionally, besides side weirs, a vortex or circular motion occurrence in the circular channel can also causes a drop of water level at the upstream of weir.

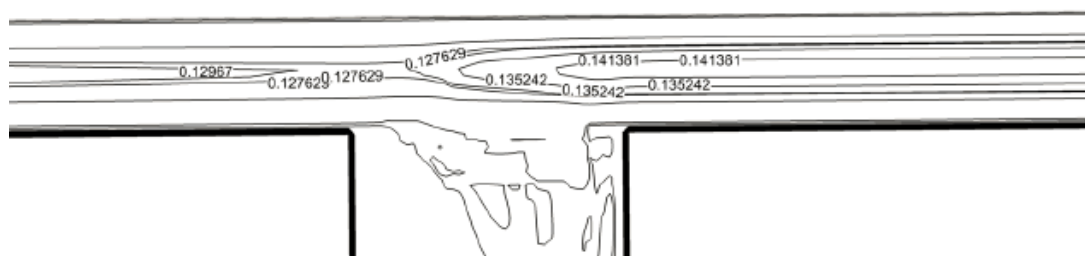


Figure 6. The contours of free surfaces for $p = 0.1$ m, $L = 0.5$ m, $Fr = 0.42$

6. CONCLUSIONS

In the present study, the CFD analyses of rectangular side weir on a circular channel were simulated by Flow-3D. The simulation results agree reasonably with experimental data. The sensitivity of turbulence models were checked with different turbulence models. The RNG recommended in literature were selected as the turbulence model because the RNG $k-\epsilon$ turbulence model can be used to predict the various characteristics of the side weir flow and give close results compared to other turbulence models. The results in this study showed that the CFD simulations can help to determine the flow characteristics such as free surface flow, stagnation point, vortex region.

7. REFERENCES

1. De Marchi, G. (1934), "Essay on the performance of side weirs," L'EnergiaElectr Milan, 11(11), pp. 849–60.
2. Frazer, W. (1954), "The behavior of side weirs in prismatic rectangular channels," [Ph.D. thesis], Glasgow (UK): Glasgow University.
3. Collinge, V.K. (1957), "The discharge capacity of side weirs," ICE Proc, 6(2), pp. 288–304.
4. Chow, V.T. (1959), "Open channel hydraulics," Berlin, Springer, pp. 349–460.
5. Subramanya, K. (1972), "Awasthy SC. Spatially varied flow over side-weirs," Journal HydraulicDiv. 98(1), pp.1–10.
6. El-Khashab, A.M.M. (1975), "Hydraulics of flow over side weirs," [Ph.D. thesis]. England: University of Southampton.
7. Ranga Raju, K.G. (1979), "Prasad B, Gupta SK. Side weir in rectangular channel," Journal HydraulicDiv, 105(5), pp. 547–54.
8. Ramamurthy, A.S. and Subramanya, K. and Carballada, L. (1980), "Side weir flow model," Journal IrrigDrain Eng, ASCE. 106(IR1), pp. 9–25.
9. Hager, W.H. (1987), "Lateral outflow over side-weirs," Journal Hydraulic Eng, 12(4), pp. 491–504.
10. Uyumaz, A. and Smith, R.H. (1991), "Design procedure for flow over side weirs," Journal Irrig DrainEng, 117(1), pp. 79–90.
11. Singh, R. and Manivannan, D. and Satyanarayana, T. (1994), "Discharge coefficient of rectangular sideweirs," Journal Irrig Drain Eng, 120(4), pp. 814–9.
12. Swamee, P.K. and Pathak, S.K. and Mohan, M. and Agrawal, S.K. and Ali, M.S. (1994), "Subcritical flow over rectangular side weir," Journal Irrig Drain Eng, 120(1), pp. 212–7.
13. Swamee, P.K. and Pathak, S.K. and Mohan, M. and Agrawal, S.K. and Ali, M.S. (1995), "Closer to subcritical flow over rectangular side weir," Journal Hydraul Eng ASCE, 121(7), pp. 309–10.
14. Jalili, M. and Borghei, S. (1996), "Discussion discharge coefficient of rectangular side weirs," Journal Irrig Drain Eng ASCE, 122(4), pp.132.
15. Vatankhah, A.R. and Bijankhan, M. (2009), "Discussion of method of solution of non-uniform flow with the presence of rectangular side weir," Journal Irrig Drain Eng, 135 (6), pp. 812–4.
16. Emiroglu, M.E. and Kaya, N. (2010), "Agaccioglu H. Discharge capacity of labyrinth side weir located on a straight channel," ASCE Journal Irrig Drain Eng, 136(1), pp. 37–46.
17. Emiroglu, M.E. and Agaccioglu, H. and Kaya, N. (2011), "Discharging capacity of rectangular side weirs in straight open channels," Flow Meas Instrum, 22(4), pp. 319–30.
18. Bagheri, S. and Heidarpour, M. (2012), "Characteristics of flow over rectangular sharp-crested side weirs," J Irrig Drain Eng, 138(6), pp. 541–7.
19. Novak, G. and Kozelj, D. and Steinman, F. and Bajcar, T. (2013), "Study of flow at side weir in narrow flume using visualization techniques," Flow Meas Instrum, 29, pp. 45–51.
20. Bagheri, S. and Kabiri-Samani, A.R. and Heidarpour, M. (2014), "Discharge coefficient of rec-tangular sharp-crested side weirs," Flow Meas Instrum, 35, pp. 116–121.
21. Emin Emiroglu, M. and Ikinciogullari, E. (2016), "Determination of discharge capacity of rectangular side weirs using Schmidt approach," Flow Measurement and Instrumentation, 50, pp. 158–168.
22. Allen, J.W. (1957), "The discharge of water over side weirs in circular pipes," ICE Proc, 6(2), pp. 270–87.
23. Uyumaz, A. and Muslu, Y. (1985), "Flow over side weirs in circular channels," Journal Hydraul Eng, 111(1), pp. 144–60.
24. Hager, W.H. (1994), "Supercritical flow in circular-shaped side weir," Journal Hydraul Eng, 120(1), pp.1–12.

25. Oliveto, G. and Biggiero, V. (2001), "*Fiorentino M. Hydraulic features of supercritical flow along prismatic side weirs,*" Journal Hydraul Res, 39(1), pp. 73–82.
26. Vatankhah, A.R. (2012), "*New solution method for water surface profile along a side weir in a circular channel,*" Journal Irrig Drain Eng, 138(10), pp. 948–54.
27. Granataa, F. and Garganob, R. and Santopietroc, S. (2016), "*A flow field characterization in a Circular channel along a Side weir,*" Journal Flow Measurement and Instrumentation, S0955-5986(16), pp. 30177-7
28. Aydin, M.C. (2012), "*CFD simulation of free-surface flow over triangular labyrinth side weir,*" Adv Eng Softw, 45, pp. 159–66.
29. Aydin, M.C. and Emiroglu, M.E. (2013), "*Determination of capacity of labyrinth side weir by CFD,*" Flow Measurement and Instrumentation, 29, pp. 1–8.
30. Azimi, H. and Shabanlou, S. and Salimi, M. (2014), "*Free surface and velocity field in a circular channel along the side weir in supercritical flow conditions,*" Flow Measurement and Instrumentation, 38, pp. 108-115.
31. Aydin, M.C. (2015), "*Investigation of a Sill Effect on Rectangular Side-Weir Flow by Using CFD,*" Journal of Irrigation and Drainage Engineering, 142(2), 04015043.
32. Aydin, M.C Mualla Öztürk, A.N Ahmet Yücel, B. (2015), "*Experimental and numerical investigation of self-priming siphon side weir on a straight open channel,*" Flow Measurement and Instrumentation, 45, pp. 140–150.
33. Aydin, M.C. and Emiroglu, M.E. (2016), "*Numerical analysis of subcritical flow over two-cycle trapezoidal labyrinth side weir,*" Flow Measurement and Instrumentation, 48, pp. 20–28

An Investigation of The Effects of Explosive Charge in Different Levels on the Dynamic Response of Concrete Arch Dams

Mirali Mohammadi¹, Mohammad Manafpour², Hesane Ghanbari³

1- Associated Professor in Civil Eng. (Hydraulic Structures & River Mechanics), Faculty of Eng, Urmia University, Iran

2- Assistant Professor in Civil Eng, Hydraulic Structures, Faculty of Eng., Urmia University, Iran

3- PhD Candidate in Civil Engineering Hydraulics, Faculty of Eng., Urmia University, Iran

Email: m.mohammadi@urmia.ac.ir

Abstract

Today, by increasing of the possibility of terrorist attacks, more studies of the behavior of structures, especially dams as massive structures, against explosive charges are needed. Arch dams should be safe against different conditions. Analysis and design of dams not only for conventional loads but also for blast loads could be futuristic. In this paper, 3D numerical model of Karun IV arch dam was modeled using ABAQUS software and dam responses for different levels of explosive masses were investigated. The results for different cases with different levels of explosion show that maximum principal stress and maximum displacement in all cases occurs in front of explosive mass and dam crest, respectively. Analysis showed that in case of explosive mass near to the dam crest, maximum calculated displacement of the crest reaches to 3.12mm.

Keywords: Concrete Arch Dam, Explosive Charge, Air Blast, Dam-reservoir-foundation Interaction.

1. INTRODUCTION

Considering the importance of the explosion on structures, especially dam structures as massive structures, in recent years, attempts have been made to study the issues in this regard comprehensively. For the phenomenon of explosion and its effect on the structure, various analytical and laboratory works have been done, pointed out: Woyak in 2002 investigated under water explosion and its effect on submerged structures. In this research, a cylinder was located at a depth of 40 meters, and 60 lb of explosives were located 7.62 meters far from the cylinder [1]. By the year 2006, Sprague et al. studied ship structure exposed to underwater explosion by spectral element-finite element method. They investigated transient response of the finite element model of the ship with 31,000 degrees of freedom [2]. Lai et al. (2007), investigated transient response of spherical shell subjected to underwater explosion. In this paper, the dynamic responses under the submarine explosive charge in sea and air were compared and the effects of the distance on the shell stress time history were presented [3]. Guzas et al. in 2010 studied simulation of structure response due to air blast. In this paper, a steel plate under the 1.36 Kg TNT which was located on 1.52 meters far from the center of the plate was investigated, and the results of the explosion-induced pressure were compared with the equations of the Bulmash and Hopkinson [4]. Zhang et al. in 2014 investigated numerical simulation of damage modes of concrete gravity dam subjected to underwater explosion. In this paper, dynamic response due to underwater explosion at different heights of the dam, from 30 meters to 142 meters were analyzed. The results indicate that increase in explosive height reduces displacement magnitude. On the other hand, the size of the mesh has a significant impact on analysis results [5]. Wang et al. in 2014 studied shock wave scattering and cavitation effects due to underwater explosion near to water free surface [6]. Also, Wang et al. in 2014 investigated damage prediction of Koyna concrete gravity dam (in India) subjected to explosion. The results indicate that because of underwater explosion, 4 types of damage can be resulted: no damage, low damage, moderate damage and high damage. The damage to the dam structure begins from the upstream face and the cavitation effects are observed in the free surface of the reservoir [7].

In this study, according to the studies carried out on the explosion, which most of them was underwater explosion, air blast was applied on a concrete arch dam.

2. EXPLOSION PARAMETERS

An explosion occurs when a large amount of energy is released quickly and suddenly in form of heat and pressure. When an explosion occurs, energy is suddenly released. This release of energy can be divided into two

sections of thermal radiation and the emission of waves in the ground and air. The waves that are released in the air are the main reason of destruction of a structure. These waves move faster than the sound speed and hit the structure [8]. Explosion in the air means that the rapid release of gases in the air creates a shock wave. The shock wave propagates radially from the explosion center. In this case, the wave due to the explosion and the reflection waves are in one environment. As shown in Figure 1, the explosion-induced wave is usually exposed to the structure earlier [9].

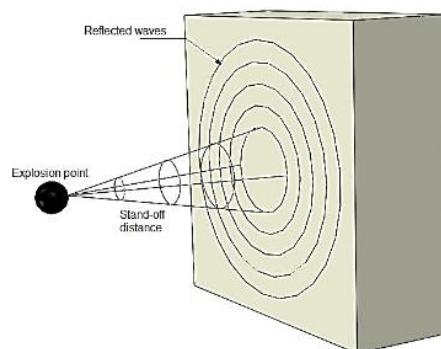


Figure 1- Schematic of air blast

Figure 2 shows the explosion pressure profile in the air, which contains positive and negative phases. As can be seen, within a few milliseconds, atmospheric pressure (P_0) reaches maximum pressure (P_{s0}^+) and returns to atmospheric pressure for several hundredths of a second, which is defined as the positive phase of the pressure impact. After this phase, a negative phase (P_{s0}^-) occurs that generates negative pressure over a few hundredths of a second. The negative phase in the design is not very important and is usually neglected [10].

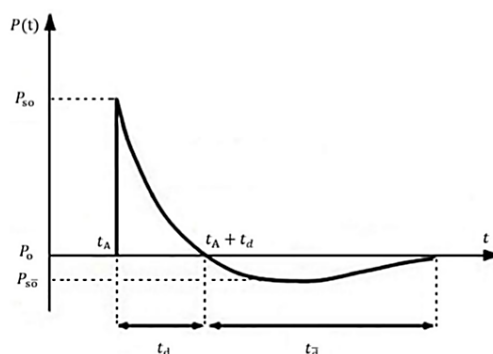


Figure 2- Time history of air blast pressure [11]

Based on the Hopkinson scale, when two explosives with identical materials and identical atmospheric conditions explode, the shock wave effects are expressed as Z:

$$Z = \frac{R}{W^{\frac{1}{3}}} \tag{1}$$

Where, R, is the distance to explosion center and W, is the explosive mass. The equation is for 1 kg or 1 lb of TNT [4]. The duration of the explosive charge is calculated directly from Kinney and Graham's relation [4]:

$$\frac{t_d}{W^{\frac{1}{3}}} = \frac{980 \left[1 + \left(\frac{Z}{0.54} \right)^{10} \right]}{\left[1 + \left(\frac{Z}{0.02} \right)^3 \right] \left[1 + \left(\frac{Z}{0.74} \right)^6 \right] \sqrt{1 + \left(\frac{Z}{6.9} \right)^2}}$$

In this equation t_d is the duration of the positive phase of the blast profile in a second. P_s , Maximum compression applied directly to the structure due to the explosion, is calculated according to the following equation [4]:

$$P_s = 808P_{atm} \frac{\left[1 + \left(\frac{Z}{4.5}\right)^2\right]}{\sqrt{\left[1 + \left(\frac{Z}{0.048}\right)^2\right] \left[1 + \left(\frac{Z}{0.32}\right)^2\right] \left[1 + \left(\frac{Z}{1.35}\right)^2\right]}} \quad (3)$$

Where P_s is equal to the load applied to the structure in bar and P_{atm} , the atmospheric pressure in bar. Calculating P_s is much easier than P_r . Brode states the relationship between P_s and P_r as follow [4].

$$P_r = P_s \left(2 + \frac{6P_s}{P_s + 7P_{atm}}\right) \quad P_s < 6.9 \text{ bar} \quad (4)$$

In equation (4) P_r , is the maximum excess reflected pressure, P_s is excess pressure and P_{atm} is the air pressure. When the excess pressure exceeds 6.9 bar, the air molecules begin to interact with each other and the assumption of ideal gas is not valid. In this case, Brode offered the following relationship [4]:

$$P_r = P_s \left[\frac{0.03851 P_s}{1 + 0.0025061 P_s + 4.041 \times 10^{-7} P_s^2} + 2 + \frac{0.004218 + 0.7011 P_s + 0.001442 P_s^2}{1 + 0.1160 P_s + 8.086 \times 10^{-4} P_s^2} \right] \quad (5)$$

3. FINITE ELEMENT MODEL

Finite element model of dam-reservoir-foundation of Karun IV was modeled using ABAQUS software. In modeling process, some assumptions were made such as: foundation modeled as a semi-sphere with radius as three times as dam height and reservoir modeled as a prismatic volume with length as three times as dam height. Finite element models of Karun IV are presented in figures 3 to 6. Because three different levels (225m, 115m and 5m from dam base) for explosion materials were considered, three different meshes were used.

In each case, area in front of the explosion point has finer mesh. For the case of explosion near to dam crest (225m from dam base), 45592 hexahedral elements were used. For the cases of explosion near to mid height of the dam (115m from dam base) and near to dam base (5m from dam base), 156706 and 63984 hexahedral elements were used respectively. Foundation and reservoir contains 41131 tetrahedral elements and 258977 tetrahedral acoustic elements.

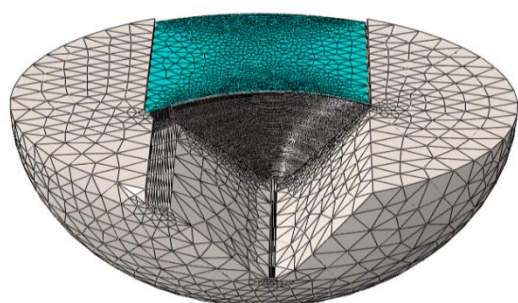


Figure3-finite element model of dam-reservoir-foundation of Karun IV



Figure4-finite element model of Karun IV dam for the case of explosion near to dam crest

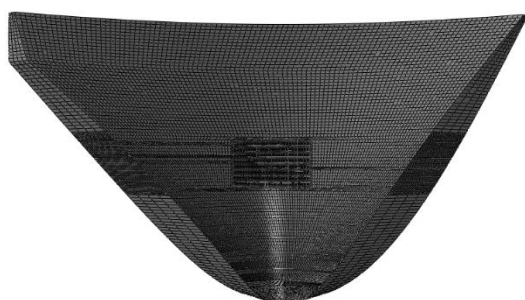


Figure5- finite element model of Karun IV dam for the case of explosion at mid height of the dam

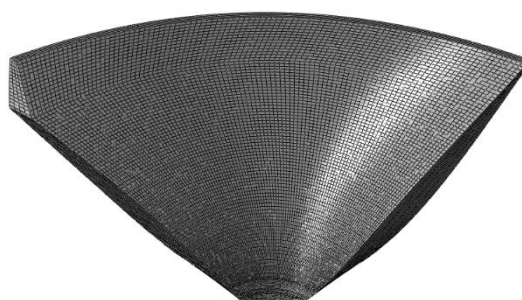


Figure6- finite element model of Karun IV dam for the case of explosion near to dam base

3.1. MATERIAL PROPERTIES

Material properties of Karun IV finite element model are shown in table1. Concrete Damage Plasticity (CDP) model was used for plastic behavior of concrete and damage modeling.

Table1-material properties

Concrete	Static elasticity modulus	24 GPa
	Dynamic elasticity modulus	30 GPa
	Poisson ratio	0.2
	Density	2400 Kg/cm ³
Foundation rock	Elasticity modulus	10 GPa
	Poisson ratio	0.3
	Density	2600 kg/cm ³
Water	Density	1000 kg/cm ³
	Bulk modulus	2.13 GPa

4. RESULTS

In this section, the results of analysis with different explosion levels are presented and compared. The effects of explosions in three different levels (225m, 115m and 5m) are investigated separately. At first, minimum explosive masses which cause damage on dam body for all three levels were calculated. These explosive masses are 1500 kg TNT 2000 kg TNT and 1800 kg TNT for explosion near to dam crest, mid height of the dam and dam base respectively. For all these cases, explosive masses were located at 10 m distance from dam body.

4.1. DISPLACEMENT

Displacement time history for dam crest and the point in front of the explosive mass for all three explosion levels are presented in Figures 7 - 9. As shown in Figure 7 and because in this case the explosive mass is near to the dam crest, displacements for two described points are almost similar and maximum displacement occurs at the same time. The calculated displacement for dam crest and the point in front of the explosive mass, are shown in Figure 8 for the case of explosion in mid height of the dam. Because there is about 115m distance between these two points, 0.44 Sec. time delay between maximum displacements is expectable. Figure 9 illustrates when an explosive mass is near to the dam base, the calculated displacements in dam crest differ significantly with base displacements. In this case, maximum displacement in front of explosive mass occurs at initial time steps but maximum displacement in dam crest occurs after 0.73 s. This time delay is the time which is needed for the explosion wave to transfer to dam crest. In the following time steps, calculated displacements for dam crest show much more magnitudes just because of cantilever behavior of arch dams. Figures represent that maximum displacement for the case of explosive mass near to dam crest occurs and the displacement decreases with lowering the explosion level.

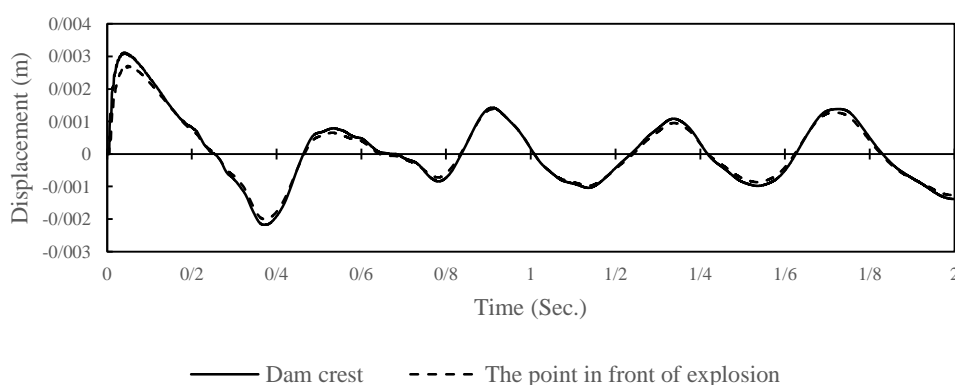


Figure7-time history of displacement for the case of explosion near to dam crest

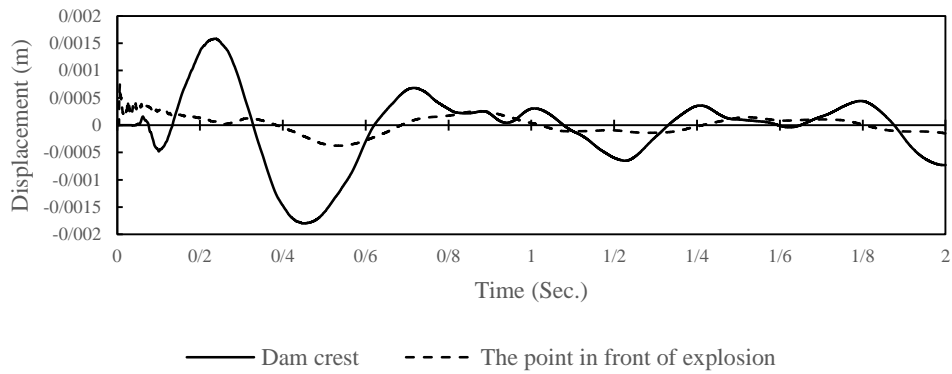


Figure 8-time history of displacement for the case of explosion near to mid height of the dam

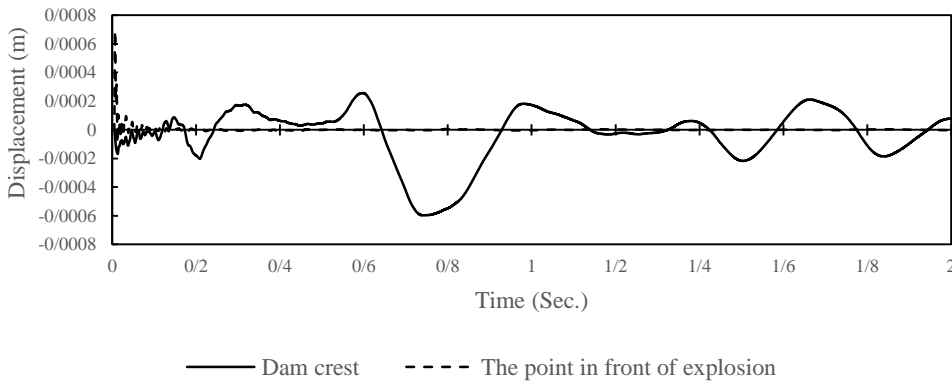
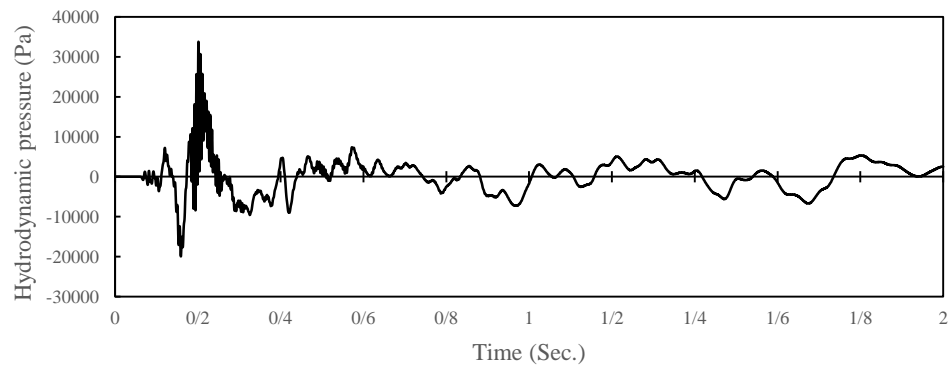


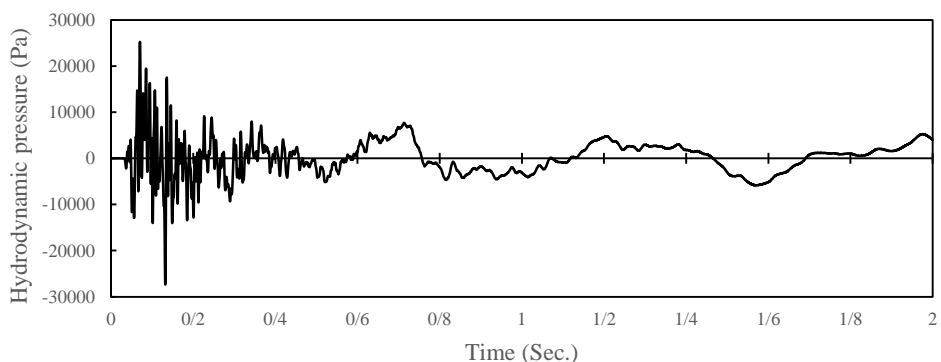
Figure 9-time history of displacement for the case of explosion near to dam base

4.2. HYDRODYNAMIC PRESSURE

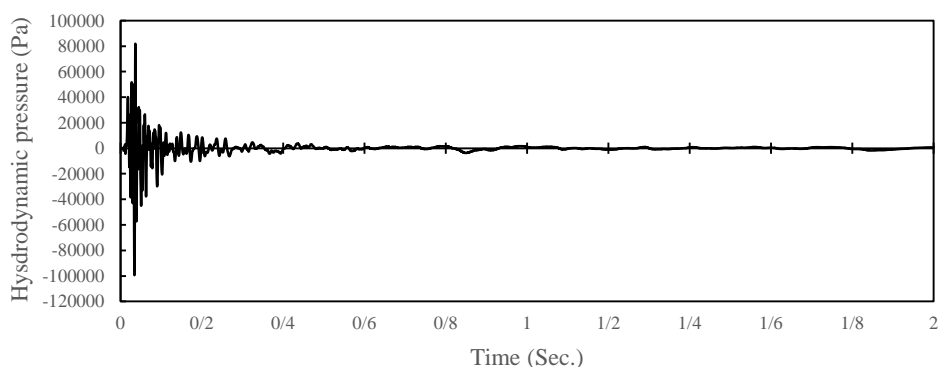
Hydrodynamic pressure time history in dam heel for all three cases (225m, 115m and 5m) are presented in figure 10. As shown in figures, maximum hydrodynamic pressure occurs when explosive mass is near to dam base.



(a)



(b)



(c)

Figure 10-time histories of hydrodynamic pressure in dam heel. A) Explosion near to dam crest. B) Explosion at the

4.3. STRESS DISTRIBUTION

Stress distribution contours for three different level of explosive mass at maximum displacement time are presented in figure 11. Maximum stress in the case of explosion near to dam crest is 0.73 MPa and occurs near to dam crest. Maximum stress in the case of explosion at mid height of the dam and near to dam base are 0.18 MPa and 0.038MPa respectively while location of maximum stress in both two cases is in front of explosive mass.

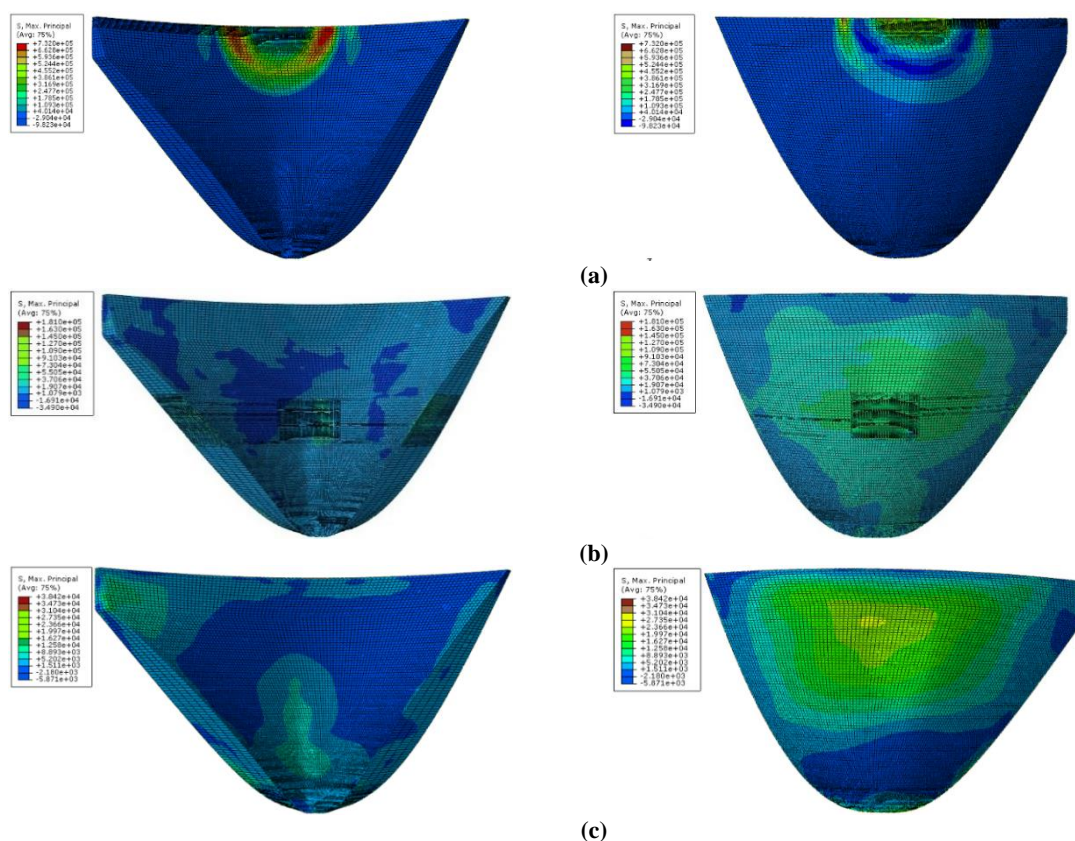


Figure11-stress contours of upstream and downstream of the dam in maximum displacement time. a) Explosion near to dam crest. b) Explosion at the mid height of the dam. c) Explosion near to dam base.

5. CONCLUSIONS

In this paper, 3D nonlinear dam-reservoir-foundation finite element model of Karun IV under air blast in three different levels analyzed using ABAQUS software. Analysis of dam-reservoir-foundation interaction system under blast loading is highly dependent on the mesh sizes. Because finer mesh needs more analysis time, only for areas near to explosive mass finer mesh was chosen. The mesh sensitivity analysis also shows good convergence.

Displacement time history of dam crest and the point in front of explosive mass in all three cases demonstrate that maximum displacement occurs when explosive mass is near to dam crest. It is because of the structural behavior of arch dams. In the case of explosive mass near to the dam crest, the maximum displacement of the crest is 3.12 mm.

Maximum principal stress on dam body locates in the closest point to the explosive mass while maximum displacement locates on the dam crest.

Maximum hydrodynamic pressure in the dam heel occurs in the case of near to dam base explosive mass. In addition, by increasing the level of explosive mass, the occurrence time of the maximum hydrodynamic pressure is postponed more.

6. ACKNOWLEDGMENT

Iran Water and Power resources development Co. (IWPCO) thanked for providing databases for this project.

7. REFERENCES

1. Woyak, D. (2002), “*Modeling submerged structures loaded by underwater Explosions with Abaqus explicit*” Abaqus Users Conference.
2. Sprague, M.A. and Geers, T.L. (2006), “*A spectral-element/finite-element analysis of a ship-like structure subjected to an underwater explosion,*” *Computer methods in applied mechanics and engineering*, pp. 2149-2167.
3. Lai, W.H. (2007), “*Transient dynamic response of submerged sphere shell with an opening subjected to underwater explosion,*” *Ocean Engineering*, pp. 653-664.
4. Guzas, E. L. and Earls, C. J. (2010), “*Air blast load generation for simulating structural response,*” *Steel and Composite Structures*, pp. 429-455.
5. Zhang, S. and Wang, G. and Wang, C. and Pang, B. and Du, C. (2014), “*Numerical simulation of failure modes of concrete gravity dams subjected to underwater explosion,*” *Engineering Failure Analysis*, pp. 49-64.
6. Wang, G. and Zhang, S. and Yu, M. and Li, H. and Kong, Y. (2014), “*Investigation of the shock wave propagation characteristics and cavitation effects of underwater explosion near boundaries,*” *Applied Ocean Research*, pp. 40-53.
7. Wang, G. and Zhang, S. (2014), “*Damage prediction of concrete gravity dams subjected to underwater explosion shock loading,*” *Engineering Failure Analysis*, pp. 72-91.
8. Mohtashami, E. and Sinayi, S. and Shushtari, A. (2010), “*evaluating steel frames behavior under blast loading,*” 5th national congress on civil engineering, Ferdowsi university, Mashhad, (in Persian).
9. Ngo, T. and Mendis, P. and Gupta, A. and Ramsay, J. (2007), “*Blast loading and blast effects on structures an overview,*” *Electronic Journal of Structural Engineering*, pp. 76-91.
10. Shiravand, M. and Shabani, M. (2013), “*behavior of the special moment frames and braced frames in steel structures under blast loadings*” *Advanced Defense Science and Technology*, pp. 109-114 (in Persian).
11. Goudarzi, M. and Zamani, J. (2014), “*Experimental and numerical investigation of the maximum deflection of circular aluminum plate subjected to free air explosion*” *Modares Mechanical Engineering*, pp. 219-226 (in Persian).

Analysis and Design of Ferrocement Cut Off Trench in Earthen Dam: A Case Study of Bham Dam

Sunil Kute¹, Patil N. P.², Ebrahim Farajpour Bonab³, Susmit Kute⁴

1- Professor, Department of Civil Engineering, K.K.W. Institute of Engg. Edu. and Res. Nashik, India

2- Assistant Professor, S.N.D.T. College of Engg. Yeola, Dist. Nashik, Maharashtra, India

3- Road and Building Expert, East Azerbaijan State, Bonab City, Governor-ate, Iran

4-Student, K.B.T. College of Engg., Nashik, Maharashtra, India

Email: sykute@kkwagh.edu.in.

Abstract

Cut off trench (COT) in the section of earthen dam is made up with impervious layer of black cotton soil. Large amount of fertile land is invested to maintain the impervious layer in cut off zone. This paper presents analysis and design of ferrocement cut off trench. Geo Studio 2012 software is used for analytical studies of cut off trench and various soil investigations are done with experimental investigation. A case study of Bham Dam located in Igatpuri, Nashik (India) is analyzed for investigations and design of ferrocement cut off trench. By designing the cutoff trench with ferrocement, thousands of tons of black cotton soil can be saved. It takes thousands of years to form the black cotton soil. The result shows that in case of Bham Dam, approximately 2.78 lakh ton of fertile soil can be saved by adopting ferrocement COT in earthen dam.

Keywords: Cut off Trench, Earthen Dam, Seepage Analysis, Geostudio.

1. INTRODUCTION

Cut off trench which is an underground seepage barrier is a conventional method for reducing the seepage through earthen dam foundation. The selection of material of COT is based impervious properties and black cotton soil is preferred as most suitable material since it has very low permeability. Black cotton soil is the earth's fragile skin that anchors all life on Earth. It is comprised of countless species that create a dynamic and complex ecosystem and is among the most precious resources to humans. Half of the topsoil on the planet has been lost in the last 150 years. To serve the agriculture needs, solution on the loss of fertile land has to find out.

Approximately 2.78 lakh ton of fertile soil is required for Bham Dam located in Igatpuri, Nashik (India) only in cut off trench zone. The solution of this problem can be explored by using the innovative technology. To have the impervious layer in foundation of the earthen dam cut off trench, Ferrocement technology is tried. Ferrocement is a composite of rich cement mortar and mesh reinforcement. Since the wire mesh is stronger in tension and makes the matrix of mortar as perfectly homogenous, the cut off trench with ferrocement is best solution to make the impervious layer in dam foundation.

In present study, the case of Bham dam is considered. It is an earthen dam and is under construction. It is situated in the catchment of *Bham river* located in Kaluste village of Igatpuri in Nasik district (India). The dam is 1500 m in the length and 31.78 m in height with average depth 13 m of cut off trench in dam foundation.

The hydraulic study of Bham dam at Chainage of 700 m along the length of dam is carried out, which includes soil studies and permeability studies for hearting and casing of the dam. This chainage is approximate mid chainage of the dam in the length of 1500 m. With the input of experimental works, detailed study of seepage analysis is carried out in GeoStudio 2012 software to get various pressure heads and total head for knowing the behavior of phreatic line.

2. SOIL INVESTIGATION

For the detailed study of seepage analysis and to know the behavior of phreatic line in the GeoStudio 2012 software, inputs of coefficient of permeability and Grain size analysis (D60 and D10) are required. Hence, in this study coefficient of permeability and Grain size analysis are calculated at CH700 m by constant head test and sieve analysis, respectively. The coefficient of permeability and grain size are calculated for both casing and hearting zone. For this experimental investigation, the different soil samples

are taken from CH700 m in the casing and hearting zone of Bham Dam. The coefficients of permeability for these samples are 6.145×10^{-3} and 3.781×10^{-4} for casing and hearting, respectively. The grain size analysis shows that the Particle size in mm for Casing and Hearting are 0.55(D10), 4.15(D60), 0.4(D10) and 5.5(D60), respectively. Moisture content of soil samples is also calculated in soil investigation. The samples were taken from actual Dam site. The moisture content was used as one of the input parameters for the Geo Studio 2012 software to perform seepage analysis. The moisture content for samples at Chainage700 m was 36.76 % for casing and that of for hearting was 14.45%.

3. HYDRAULIC ANALYSIS BY GEOSTUDIO 2012

GeoStudio 2012 is the analysis software used to perform various analyses related to earthen dam like seepage analysis, stability analysis, stress and deformation analysis, earthquake analysis, thermal analysis, contaminant analysis and air flow analysis. GeoStudio SEEP/W 2012 is used for the seepage analysis of Bham dam. The cross-section of dam at Chainage 700 m is considered for the analysis and soil properties at this Chainage are provided as input to the software. Parameters of Bham Dam used for the analysis are as follows:

- Type of Dam: Earthen
- Height: 31.78 m Width: 263.16 m
- Length: 1500 m Free board: 2.55 m
- Average depth of Foundation: 6.65m
- Average depth of Cut off Trench: 6 m

The cross-sectional profile of Bham Dam modeled in Geo Studio software at CH700, is shown in Figure 1

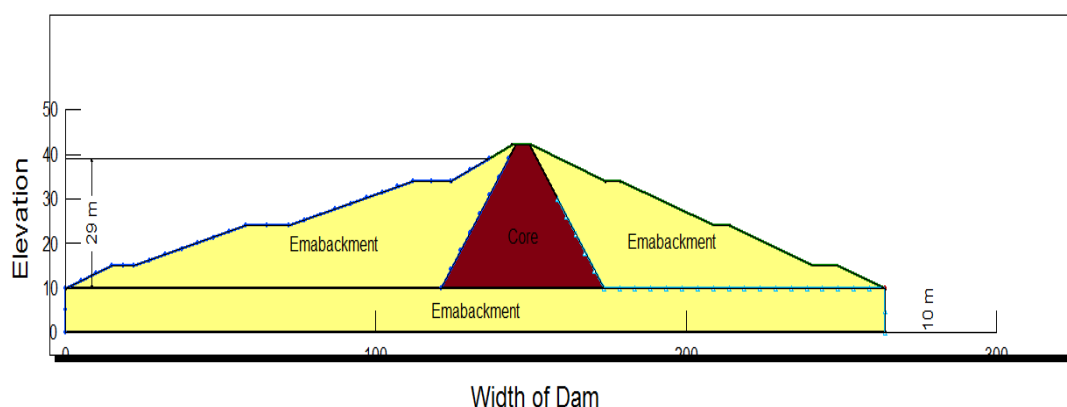


Figure 1: Total Head variation at CH130 (Total Head: 29m)

From this modeling of Bham dam in GeoStudio 2012, various results are obtained which include the Total Head, Pressure Head and Hydraulic conductivity through earthen dam. Table1 given below shows the various results of Bham dam at CH700 m.

Table 1 Results of seepage analysis at Ch.700 m

Sr. No.	Parameters	Results from GeoStudio
1	Water Flux (m ³ /sec)	9.561341e-005
2	X-Velocity Magnitude (m/sec)	1.4628577e-007
3	Y-Velocity Magnitude (m/sec)	1.4349074e-007
4	Total Head (m)	39
5	Pore-Water Pressure (kPa)	284.403
6	Pressure Head (m)	29

Figures 2, 3, and 4 show Total Head, Pressure Head and Hydraulic conductivity, respectively.

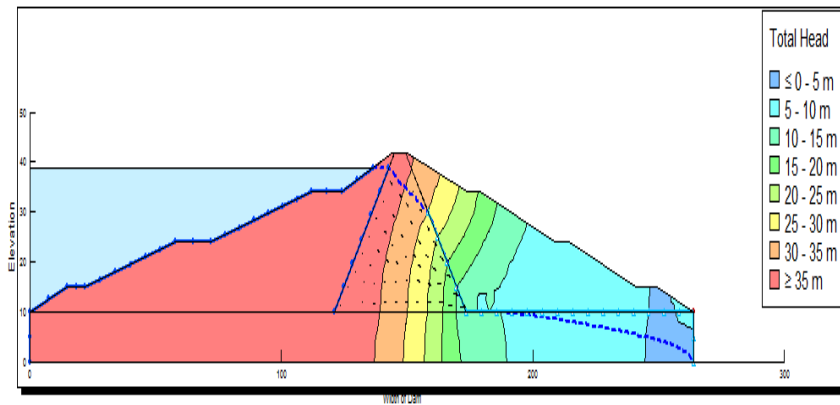


Figure 2: Total head variation at Ch.700 m (Total head :39m)

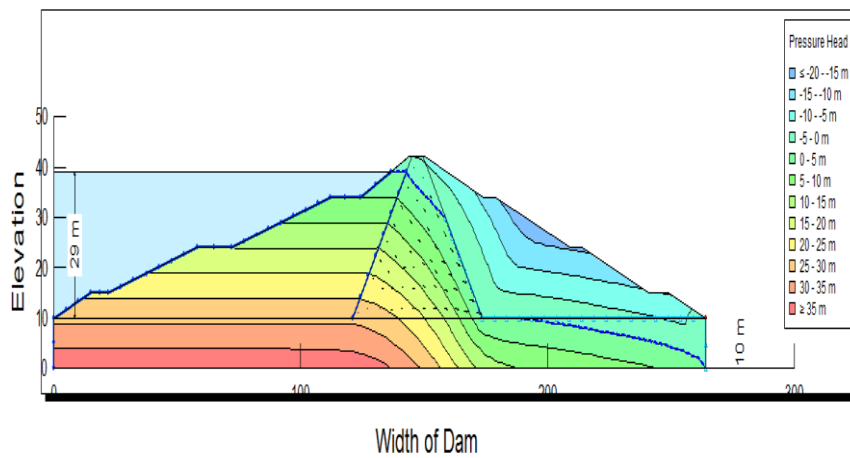


Figure 3: Pressure head variation at Ch.700 m (Total head :29m)

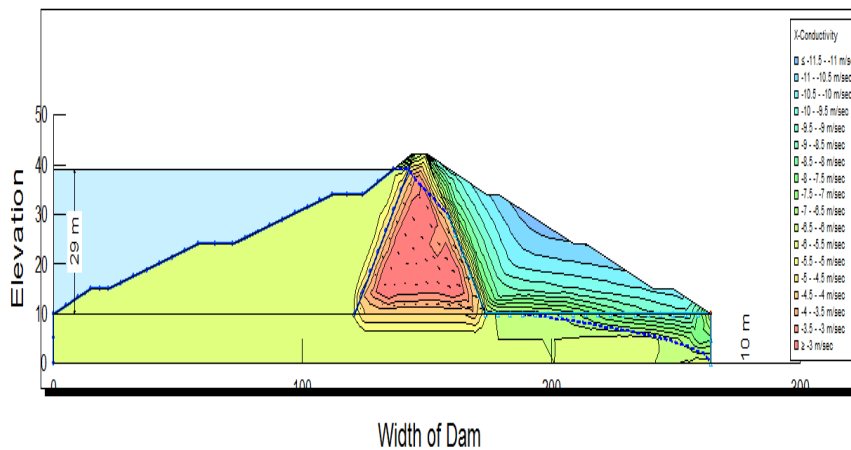


Figure 4: Hydraulic Conductivity at CH700 (Conductivity: 1.4628577e-007)

From the seepage analysis, the worst pressure conditions were determined. The results of pressures are 29 m total head of water and 6.112 kg/cm² as saturated soil pressure.

4. FERROCEMENT PANELCASTING

Ferrocement cut off trench panels were cast using the matrix of 1: 2 cement mortar and welded and chicken mesh reinforcement. The number of mesh layers were calculated using ACI Code of ferrocement, ACI 549R. The details of design data of ferrocement COT panels is shown in Table 2.

Table 2: Design data of ferrocement COT panels.

Sr. No.	Parameters	Specification
1.	Cut-off trench panels size	1 m x 1 m
2	Skeletal steel	8 mm @ 300 mm c/c
3	Type of Wire mesh	Welded mesh and Chicken mesh
4	Mortar proportions	1:2
5	Water to cement ratio	0.5
6	Thickness of panels	25 mm
7	No of wire mesh layers	2 (min.)
8	No. of panels	6 no's

The panels were cast, cured and tested in loading frame for the flexural loading. Table 3 shows the results of flexural test.

It is clearly seen from the results of flexural strength test results that, the average flexural strength of cut off trench panels with welded mesh have more strength than that of panels with the chicken mesh. But results can be carefully noted as both of panels have flexural strength more than the total pressure obtained from the analytical calculations and worst loading cases. The average flexural strength of both of the panels is compared with the total pressure of 0.6 N/mm² which is obtained from analytical solution of case II. Total pressure of second worst loading case is calculated by considering saturated unit weight of soil for the overall depth of 32 m from the foundation of the dam. The obtained flexural strength of the welded mesh panels is more than the chicken mesh wire because the strength of the ferrocement material depends on the specific surface area of the wire mesh and welded wire mesh provides more specific surface area than the chicken wire mesh.

Table 3: Flexural tests results of ferrocement cut off trench panels

Sr. No.	Sample Designation	Maximum pressure from worst loading cases	Flexural strength (N/mm ²)	Avg. flexural strength (N/mm ²)
1	Panel 1 (Chicken mesh)	Total pressure = 0.6 N/mm² (Case II: Saturated soil pressure for depth of 32 m)	1.47	1.28
2	Panel 2 (Chicken mesh)		0.92	
3	Panel 3 (Chicken mesh)		1.45	
4	Panel 4 (Welded mesh)		1.90	1.68
5	Panel 5 (Welded mesh)		1.45	
6	Panel 6 (Welded mesh)		1.71	

5. COEFFICIENT OF PERMEABILITY:

The coefficient of permeability for ferrocement cutoff trench panel core for welded mesh core and chicken mesh core is determined by falling head test. Coefficient of permeability of the ferrocement panel core is calculated by measuring the discharge per unit time. The homogenous nature of mortar and wire mesh together is not allowing any flow of water to seep through it. Hence no flow of water is obtained in the 24 hours.

6. CONCLUSIONS

From the obtained results it is clear that the ferrocement cut off trench is the possible solution for the cut off trench in earthen dam. Ferrocement cut off trench panels can be provided instead of traditional cut off trenches, as it has passed for flexural as well as permeability test. This will facilitate to avoid the use of black cotton soil in COT portion of an earthen dam in the quest of preserving the natural resources for sustainable development.

7. REFERENCES

1. B. Shadravan, A. A. Miraghasemi, M. Pakzad, Karkhek Storage Dam Cutoff Wall Analysis and Design, Fifth International Conference on Case Histories in Geotechnical Engineering, New York, April 2004, pp. 1-10.
2. B. Mansuri, F. Salmasi, Effect of Horizontal Drain Length and Cutoff Wall on Seepage and Uplift Pressure in.
3. Heterogenous Earth Dam with Numerical Simulation, Journal of Civil Engineering and Urban, pp 114-121.
4. Kute, S. Y., et.al., "An investigation for scope of fly as in dam construction for sustainable development of natural resources" 4th International R&D conference of CBIP, Aurangabad, 2003, pp. CP-36.
5. I.S.8417-2007: Guidelines for Design of Under-Seepage Control Measures for Earth and Rockfill Dams.
6. IS 8826-1978 (Reaffirmed 2002). "Guidelines for Design of Large Earth and rockfill dams" BIS, New Delhi.
7. ACI 549R-97," State-of-the-Art Report on Ferrocement" 1997
8. ACI 549R1-93, "Guide for the Design, Construction, and Repair of Ferrocement" 1993
9. IS 2720 (Part 4) -1985 (Reaffirmed 2006), "Method of test for soils - Grain size analysis" BIS, New Delhi
10. IS 2720 (Part 17) - 1986 (Reaffirmed 2002), "Method of test for soils - Laboratory determination of permeability"
11. BIS, New Delhi.
12. IS 2720 (Part 7) - 1980 (Reaffirmed 2011), "Method of test for soils - Determination of water content - dry density relation using light compaction" BIS, New Delhi.
13. IS 2720 (Part 2) - 1973 (Reaffirmed 2010), "Method of test for soils - Determination of water content" BIS, New Delhi
14. Divekar, B. N., (2012), "Ferrocement technology - A construction manual"
15. Garg, S. K., (2014), "Irrigation Engineering and Hydraulic Structures" Khanna publishers, New Delhi

Laboratory Study of the Effect of Recycled Fillers from Coking and Iron Concentrates Factories on the Roller Compacted Concrete Properties in Dams (RCC Dams)

Jaber Mahmoudi¹, Kouros Qaderi², Mohammad Zounemat Kermani³, Faeze Yazdi⁴

1- MSc of Water structures engineering

2- Member of faculty of water engineering, Shahid Bahonar University of Kerman

3- Member of faculty of water engineering, Shahid Bahonar University of Kerman

4- MSc of civil engineering, Supervisor of Civil and Chief Technical Officer of Barsoo Engineering Co.

Email: Mahmoudi.inbox@gmail.com

Abstract

This study presents mechanical and durability aspects of using different waste fillers including Iron powder, Iron concentrate, Coal Powder and Coke, which cannot be reused at industry process (samples from different parts of the Jalalabad Iron Ore Concentrate Plant and Zarand Coking Plant, Kerman, Iran) as well as mineral powder filler as a control sample to replace 3% and 6% of coarse and fine natural aggregate content in RCC. The concretes were investigated for absorption, compressive strength, workability and non-segregation of grains. The experimental results showed that RCCs of iron ore powder filler contents with 6% of the weight of coarse and fine natural aggregates had higher values of 28 days compressive strength and minimum 24-hour water absorption about 2.22%. In addition to that, using this type of waste in concrete may be more environmentally efficient, because this helps to remove some parts of wastes and protects the environment.

Keywords: Roller Compacted Concrete (RCC), Slump, Mix design, Compression strength, Water absorption.

1. INTRODUCTION

In order to achieve economic self-sufficiency, It is especially important to control the floods and surface water through the construction of dams witch considered essential and infrastructural. Since water supply has always been a fundamental human need for agriculture, industry and drinking water.

In the early 1980s, conventional concrete dam construction methods were replaced by the roller compacted concrete method. RCC dams use embankment dams construction's method, which is based on using heavy equipment machinery. Usage of heavy equipment machinery for constructing concrete dams, leads to development of RCC dams which despite the short construction time, they have the reliability of conventional concrete dams. Also, RCC dams are an economical competitive choice over embankment dams. Construction cost of RCC dams is less than conventional concrete dams as well as embankment dams. It is because of material saving, fast construction, less costly spillway, less risk of coffer dam overtopping and shorter and smaller size of diversion conduit [1].

In addition to economic benefits, the RCC is considered as a "green" concrete because the cement consumption in the RCC is lower as the RCC mixtures are normally designed with leaner binder content. Mineral admixtures are used extensively in RCC mixtures. The use of large amounts of mineral admixtures improves durability, reduce adiabatic temperature rise of concrete, construction costs, and gas emission accompanied with the manufacturing of cement clinker. Class F and Class C fly ashes, slag, and natural pozzolan have been used as mineral admixtures in the RCC [2].

Coarse aggregate size has a significant influence on the degree of RCC compaction in small layers and less effect in relatively thicker layers especially when large vibratory rollers are employed. The coarse aggregates with maximum-size diameter greater than 76 mm are seldom used in the RCC manufacturing because they cause problems in the layers spreading and compaction. However, the use of coarse aggregates with maximum-size diameter finer than 75 mm reduces the volume of voids and produces more cohesive mixture [3].

Waste coking and iron ore concentrates plants, which cannot be reused, is normally deposit causing obvious environmental problems. So use of these materials effectively in concrete, make them valorized. A mass of small particles is also produced due to the process of iron ore concentrate production, which usually

does not have the ability to become concentrate, and is deposit. The waste Coke, consisting of non-consumable materials commonly used in particles smaller than 1 cm in diameter, are discharged as waste and disposed of in garbage dumps. This waste can be called coal in input materials, and called coke in exhaust materials. Applying the aggregates smaller than 75 microns (sieve NO. #200), if not plastic, can be a useful solution for reducing the free space among fine-aggregates. Typically, the use of about 2 to 8 percent of aggregates smaller than 75 microns in pavement roller concrete is common (ACI 325.9 R) [4].

This study is included of three consecutive parts. In the first part, materials and instruments were prepared and initial tests were performed to establish material properties. In the second part, material properties were checked with codes and proper mix design were defined by testing several initial mix designs. In the last part, main specimens were prepared and tests were conducted on 7, 14, 28, 42 and 90 days specimens. In this research, we used 9 mix designs based on 140 kg/m³ cement - II and Iron ore powder, Iron ore concentrate, Coal Powder and Coke as filler materials passing sieve no. #100 (0.15>) by replacing 3% and 6% of coarse and fine-aggregate content. Finally, the results were compared with mineral powder filler as control sample. In order to study the durability and mechanical properties of concrete, maximum density, VB time, compressive strength on 7, 14, 28, 42 and 90 days and 28-hour absorption of specimens were investigated.

2. EXPERIMENTAL PROGRAM

The material properties of the concrete mixture used in this experimental study are given in the following.

2.1. MATERIALS

2.1.1. AGGREGATE

Of 0–6, 6–12 and 12–25 mm grain size aggregate used in this study have been widely used in the most civil projects in Kerman for years, provided from Gloomak Region. The aggregate grade was designed as existing between the curves of 2-4-3-A and 2-4-3-B defined in journal No. 55 Iran Standards [5]. The properties of these aggregates are presented in Table 1 and Figure 1, 2. The gradation curves of mixing the aggregate consisted of coarse-aggregates (12-25 mm) (33%), fine-aggregates (6-12 mm) (22%) and fine-aggregates passing sieve No. 4 (4.75mm) (45%) and compared with the limits set by ACI 207-5R standard is presented in Figure 3 [6].

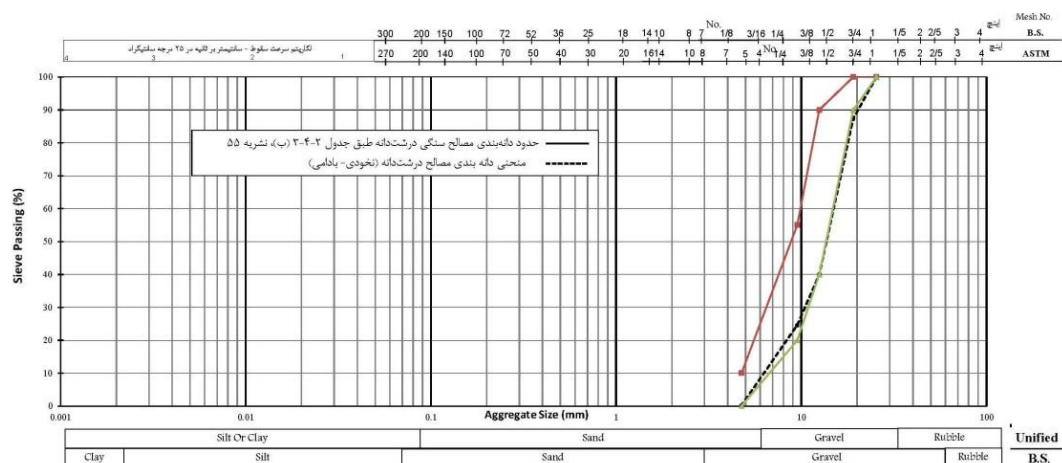


Figure 1. Particle-Size Analysis of Coarse-aggregates (6-25 mm)

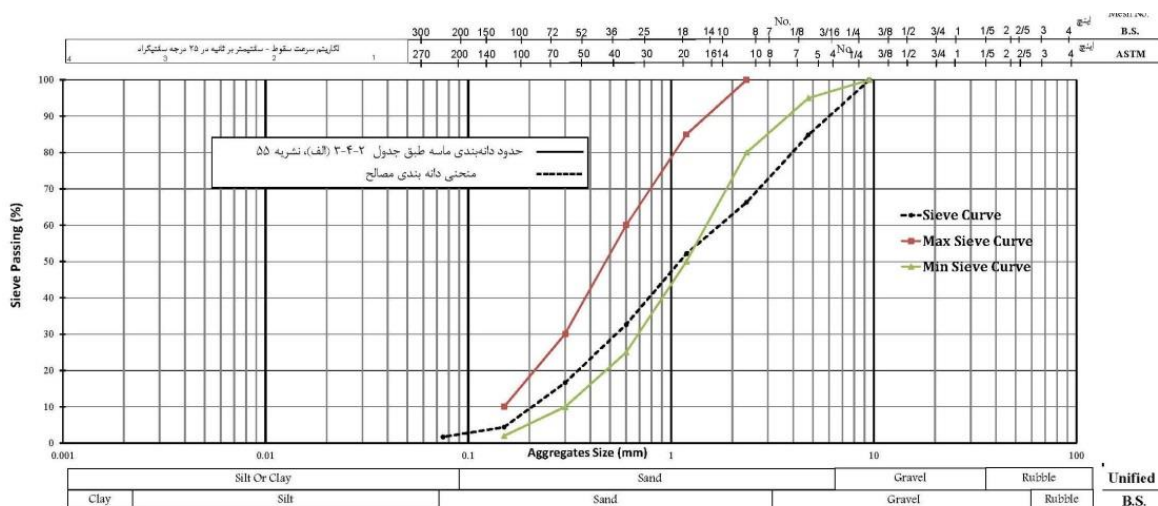


Figure 2. Particle-Size Analysis of Fine-aggregates (0-6 mm)

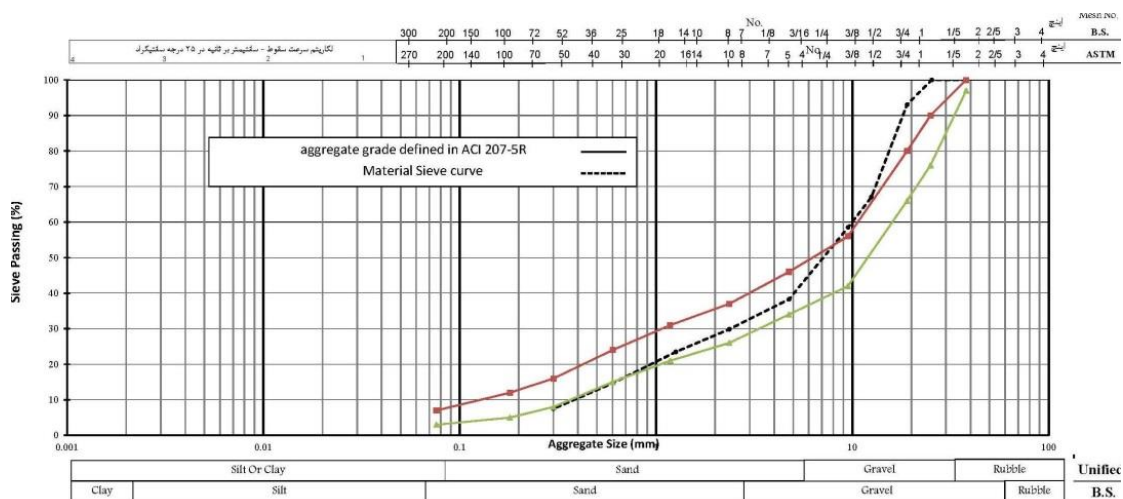


Figure 3. Particle-Size Analysis of aggregates in Mix Design (0-25 mm)

Table 1. Physical Test results of aggregates

Density & Water absorption			fractions of aggregate	Ductility of aggregate	Prolongation Of aggregate	Lose weight of aggregates by Los Angeles Test			fineness Modulus	Materials
Water absorption %	Real Density (Kg/m ³)	Bulk Density (Kg/m ³)				abrasion%	RPM	Type		
0.8	2654	2703	51	10	18	23	500	B	-	Coarse Aggregates (10-25 mm)
1.1	2641	2712	66	18	12				-	Coarse Aggregates (5-10 mm)
2.0	2580	2720	-	-	-	-	-	-	3.43	Fine Aggregates (0-6 mm)

2.1.2. CEMENT

CEM – II type of cement in appropriate to Iran Standards was used to prepare the concrete mixtures, whose physical and chemical characteristics are given in Table 2 [7, 8].

Table 2. Chemical characteristic of cement

Physical characteristics	Value
Water Concentrate %	25
Autoclave %	0.01>
Specific gravity (gr/Cm ³)	3.16
Specific area (m ² /Kg)	316
Setting period (Minutes)	Initial setting: 170
	Final setting: 215
Compressive strength (Lb./in ²)	1 days: 1370
	3 days: 2210
	7 days: 2900
	28 days: 3530

Table 3. Physical characteristic of cement

Chemical characteristics	Value (%)
CaO	62.71
SO ₃	3.06
Cl ⁻	-
C ₃ S	51
C ₂ S	21
C ₃ A	5
Ignition Loss	1.92
Remaining Desolved	0.42

2.1.3. WATER

The water used for mixing the concrete mixtures of the experimental studies was potable and appropriate to the Iran Standards [9]. Analysis results of the water used in test mixtures are given in Table 4.

Table 4. Analysis results of the water used in test mixtures

Num	Examined Factors		Results		Concrete Standard*
1	PH	Acidity	7.9	-	7
2	EC	Electro Conductivity	1.28 (ds/m)	-	-
3	S.A.R.	Sodium Absorption Ratio	2.32	-	-
			Concentration as ppm	Concentration as meq/L	Concentration as ppm
4	Na ⁺	Sodium	108.1	4.7	-
5	Ca ²⁺	Calcium	96	4.8	-
6	Mg ²⁺	Magnesium	40.8	3.4	200
7	K ⁺	Potassium	0	0	-
8	Cl ⁻	Chloride	287.5	8.1	1000
9	HCO ₃ ⁻	Bi-carbonate	292.8	4.8	-
10	CO ₃ ²⁻	Carbonate	0	0	-
11	SO ₄ ²⁻	Soleplate	0	0	1000
12	TDS	Total dissolved solids	819.2	-	1000
13	TSS	Total Suspended solids	0	-	-
14	THD	Total Hardness	-	410	-
15	Na ₂ O+0.658 K ₂ O	Alkalinity	145.7	-	600

Description: Section 9 "national building laws" by considering the medium environmental conditions

2.1.4. FILLER

Typically, the number of aggregates passing through the sieve #100 called the filler. The filler used in this research is the waste of coke factories and iron ore concentrates with various percentages whose chemical characteristics are given in Table 5.

Table 5. Chemical characteristic of fillers %

	Iron ore Concentrate	Iron ore powder	Coke	Coal
C _{Fixed}	-	-	68.78	47.93
Volatile substances	-	-	9.26	32.65
Moisture	-	-	1.90	0.39
Ash	-	-	20.06	19.04
L.O.I	0.0	4.24	80.39	80.19
K ₂ O	01	0.47	0.85	0.91
SiO ₂	5.69	36.10	7.69	10.21
Fe ₂ O ₃	90.27	35.5	4.80	1.68
Cl	-	0.27	0.30	0.20
Al ₂ O ₃	0.69	5.02	3.77	4.78
TiO ₂	0.13	0.38	0.1	0.17
SO ₃	0.02	0.67	0.51	0.36
MgO	1.46	11.3	0.29	0.30
La&Lu	1>	1>	1>	1>
CaO	1.10	4.9	0.79	0.92
P ₂ O ₅	0.008	0.17	0.02	0.02
Na ₂ O	0.36	0.82	0.49	0.26

Waste Coal is one of the products of Zarand Coal Factory that is obtained during the process of coal processing for the production of coke and consumption in iron melting furnaces.

3. IDENTIFICATION AND FORMULATION OF THE RCC MIXTURES

3.1. DETERMINE THE OPTIMUM WATER-CEMENT RATIO

A modified Vebe apparatus which is described in CRD-C 53 [10] was used for determining the consistency of RCC. Since RCC mixture with Vebe time between 15 and 20 s has a sufficient workability [11]. The results are shown in table 6.

Table 6. Water-cement ratio Results

Specific gravity of fresh concrete	Slump	Concrete Temp.	Lab. Temp.	VB time	$\frac{W}{C}$
gr/Cm ³	mm	° C	° C	S	
2.097	None	15.1	19.6	120<	0.35
2.154	None	18.0	19.8	120<	0.45
2.171	None	18.4	19.8	120<	0.55
2.395	•	17.7	19.5	15	0.80
2.237	•	18.0	20.4	34	0.7
2.349	•	18.4	20.8	18	0.75
2.365	•	23.2	21.9	18	0.80
2.375	•	20.5	19.6	22	0.75

3.2. SPECIMENS

In total, nine different concrete mixtures given in Table 7 were prepared. Cylindrical samples were used with height of 30 cm (12 in.) and diameter of 15.2 cm (6 in.). Samples were casted in three layers by vibrating method with Vebe table following the USBR 4906 [12]. Totally 72 specimens were made with 140 kg cement materials per cubic meter. Amount of 3% and 6% of total coarse and fine-aggregate materials were replaced by fillers in different mix design to investigate the effects of different amount of fillers. The results are shown in table 7.

Table 7. Mixing ratio (kg/m³)

$\frac{W}{C}$	Weight of water	Weight of fine-aggr.	Weight of coarse-aggr.	Weight of coarse-aggr.	Type of filler	Weight of filler	Weight of Cement	Specimens No.
0.8	112+34	945	460	690	6% mineral powder	130	140	RCC-1
0.8	112+34	945	460	690	6% iron concentrate	130	140	RCC-2
0.8	112+34	945	460	690	6% coke	130	140	RCC-3
0.8	112+34	945	460	690	3% mineral powder+3% iron concentrate	65 + 65	140	RCC-4
0.8	112+34	945	460	690	3% mineral powder+3% iron powder	65 + 65	140	RCC-5
0.8	112+34	945	460	690	6% iron powder	130	140	RCC-6
0.8	112+34	945	460	690	6% coal powder	130	140	RCC-7
0.8	112+34	945	460	690	3% mineral powder+3% coal	65 + 65	140	RCC-8
0.8	112+34	945	460	690	3% mineral powder+3% coke	65 + 65	140	RCC-9

Compressive strength test, workability test by VB time, water absorption test and compacted concrete density tests were conducted at the ages of 7, 14, 28, 42 and 90 days.

4. EXPERIMENTAL

4.1. VB TIME

A modified Vebe apparatus was used to determine the workability of mix designs. The results are shown in table 8.

Table 8. Workability Results

Specific gravity of fresh concrete (gr/Cm ³)	VB Time (sec)	Specimens No.
2.298	18	RCC-1
2.336	18	RCC-2
2.191	105	RCC-3
2.395	15	RCC-4
2.326	16	RCC-5
2.361	38	RCC-6
2.205	40	RCC-7
2.251	36	RCC-8
2.229	36	RCC-9

4.2. 24-HOUR WATER ABSORPTION

24-hour Water absorption test on concrete specimens was performed according to ASTM C642 standard. The results are shown in figure 4.

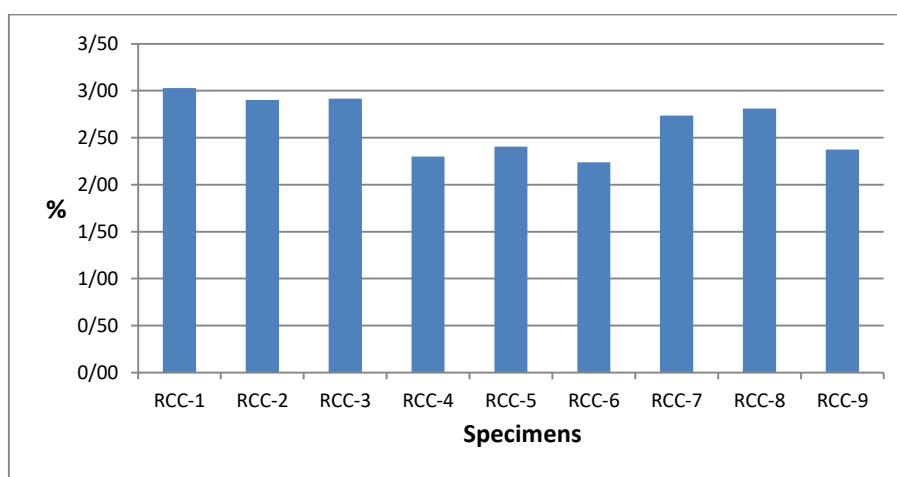


Figure 4. 24-houre water absorption

4.3. WEIGHT OF MASS

The specific density of concrete depends on the specific weight of the sand and the porosity of the roller concrete mass. There are a few air vents in roller concrete, varying between 0.5 and 5%, which reduces the action of compacting. The results are shown in figure 5.

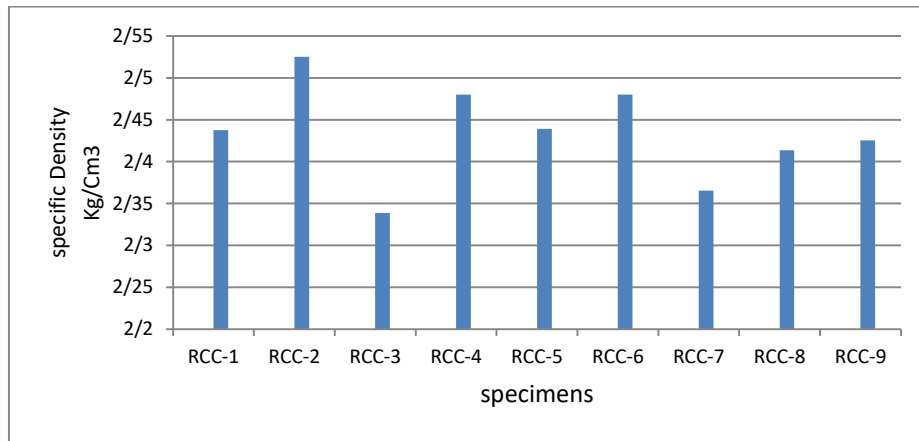


Figure 5. Specific density of specimens

4.4. CONCRETE COMPRESSIVE STRENGTH

Compressive strengths results of the various mixes are presented in Fig. 6 to fig. 8 for ages of 7, 14, 28, 42 and 90 days. Comparatively to the reference concrete, at twenty days old, the increase in compressive strength was in the mix design for RCC6 with 6% iron ore powder filler. In a study, Friedin (2005) proved that the high levels of CaO and SO₃ in the ash of wind makes the wind ash have a good cement property and therefore gradually increases the compressive strength [13].

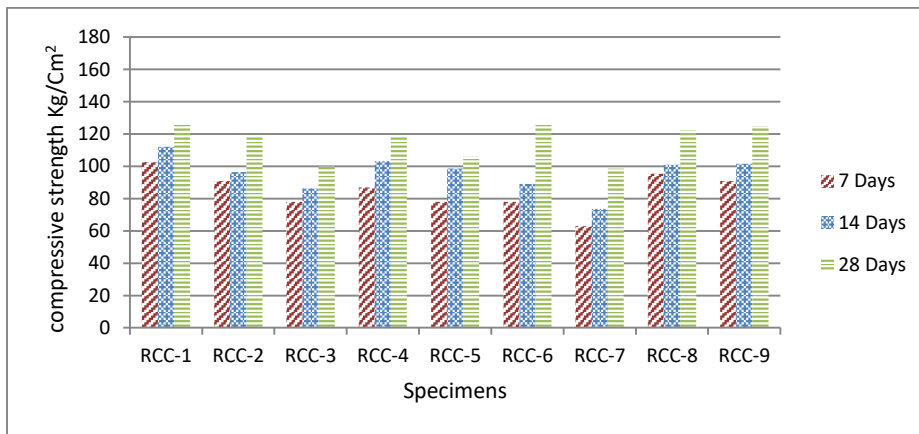


Figure 6. 7, 14, 28-days compressive strength results

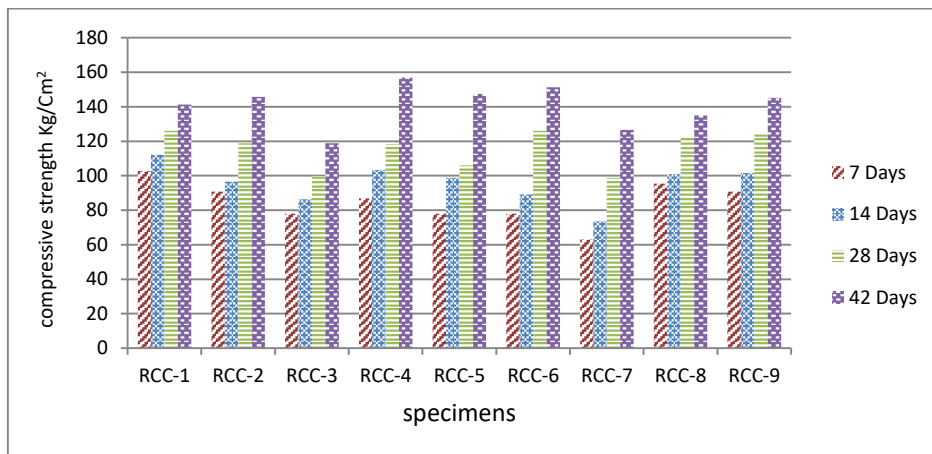


Figure 7. 7, 14, 28, 42-days compressive strength

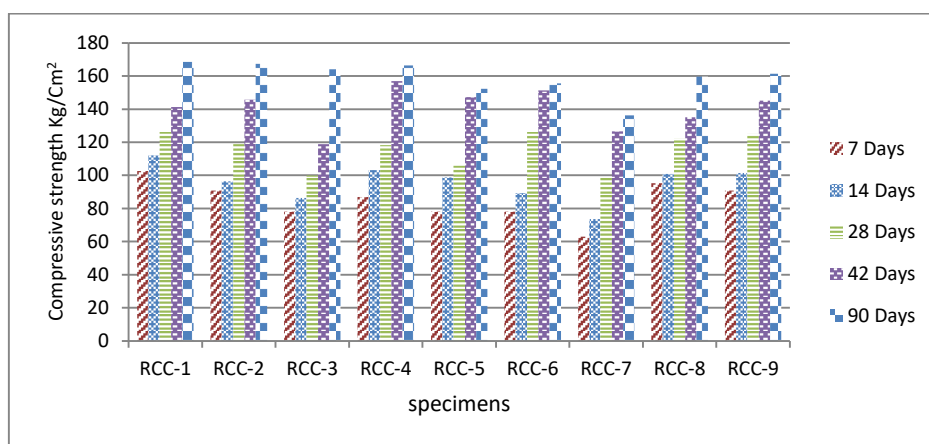


Figure 8. 7, 14, 28, 42, 90-days compressive strength

5. CONCLUSIONS

In this research, different fillers from coking and iron concentrate plants (passing sieve No. #100) made up 6% of the coarse and fine-aggregates weight, and also 3% of the filler along with 3% of the mineral powder filler has been used and investigated. The purpose of this study was to analyze the effect of various fillers on the roller concrete properties, mechanical properties of concrete and its permeability. The tests results indicated a significant change in the mechanical properties and durability of the roller compacted concrete.

1. Using a high water percentage caused the segregation, which prevented by use of fillers to some extent. According to the design and time of VB, the optimal water-cement ratio was obtained amount of 0.8
2. The highest 7-days compressive strength of concrete is related to the RCC1 mixing design with the mineral powder filler, indicating increased compressive strength at the early ages.
3. The highest 28-days concrete compressive strength is related to the RCC6 mixing design with Iron Ore Powder Filler, indicating an increase in the final strength of the concrete at an advanced age by the filler.
4. The lowest compressive strength growth over time (90 days) is observed in RCC1 and RCC3 mixing designs made with 6% mineral powder filler and 6% coke filler, which to some extent indicates that these fillers are not very effective in the cement hydration.
5. The best performance of compressive strength up to 28 days is related to the RCC6 mixing design containing 6% Iron Ore Powder Filler, which at the ages has more compressive strength and performance similar to that expected from Pozzolans.
6. The results of 24-hour water absorption of specimens showed that the minimum water absorption was related to the RCC6 mixing design with iron ore powder filler, with amount of 2.24%, which is acceptable and ideal for dam construction projects.
7. The lowest VB time measured in the study was related to the RCC4 mixing design with 3% mineral powder filler and 3% iron ore concentrate with amount of 15 seconds.
8. By studying the results of the fillers chemical tests, iron ore powder was known to be close to the pozzolan group type F.

6. ACKNOWLEDGMENT

Funding for this study was provided by MANA construction company.

7. REFERENCES

1. USBR 4913. Procedure for water permeability of concrete.
2. J.F. Lamond, Significance of Tests and Properties of Concrete and Concrete-Making Materials, 2006, ISBN 0-8031-3367-7, pp. 595–601.
3. P.K. Mehta, P.J.M. Monteiro (Concrete: Microstructure, Properties, and Materials), fourth ed., 2014, ISBN 9780071797870.
4. American concrete Institute Committee 325.9R. Guide for construction of concrete pavements. ACI Materials Journal 2015.
5. M. Dehqani pour, 1389, Instructions for implementation of general technical projects on construction works based on the publication No. 55
6. American concrete Institute Committee 207. Roller Compacted Concrete. 207.5R. ACI Materials Journal 1998.
7. ASTM C114 - 15 Standard Test Methods for Chemical Analysis of Hydraulic Cement
8. Iran national standard, 392, standard methods for physical Analysis of Hydraulic Cement
9. Development and Promotion of National Building Regulations Office, ninth topic, 1392
10. CRD-C 53. Test method for consistency of no-slump concrete using the modified Vebe apparatus
11. USBR. Roller compacted concrete, design and construction consideration for hydraulic structures. Technical Service Center; 2005.
12. USBR 4906. Casting no-slump concrete in cylinder molds using vibratory table
13. Freidin C. Influence of variability of oil shale fly ash on compressive strength of cementless building compounds. Constr Build Mater 2005;19:127–33.

Chambon Dam Reinforcement Works

Olivier Chulliat¹, Etienne Grimal², Emmanuel Robbe³

1, 2, 3 – EDF – Hydro Engineering Center – Savoie Technolac – 73373 Le Bourget du Lac – France

Email: olivier.chulliat@edf.fr

Abstract

Chambon, a 137 m high concrete gravity dam completed in 1935, is affected by severe alkali-aggregate reaction, causing several types of pathologies as a result of the concrete expansion. They mainly result in important vertical cracking of the structure, likely to affect its integrity under earthquake, important shear stresses in the structure and deformation of the crest. Reinforcement works were performed from 1991 to 1997 to guarantee the safe operation of the dam: mainly a series of slot cutting, and a drained PVC sealing geomembrane system, installed to provide waterproofing protection at the upstream face. These measures allowed an extension of service of 20 years.

New reinforcement works were performed in 2013-2014, in the continuity of those already performed in the 1990's: (i) installation of 415 prestressed tendons crossing the structure from upstream to downstream, supplemented with a carbon fiber composite net on the upstream face, (ii) realization of 7 vertical diamond wire slot cuts and (iii) replacement of the existing sealing geomembrane to allow the works.

This paper explains the approach that led to the choice of technologies based on the results of investigations and finite elements modeling.

Keywords: AAR, Modeling, Tendons, Cuttings, Membrane.

1. INTRODUCTION

Chambon dam is a 137 m high cyclopean concrete gravity dam, located on the Romanche river in the french Alps at elevation of 1,000 m. The crest length is about 300 m and the dam is curved in the left bank zone. It has been built from 1929 to 1935 and creates a 50 million m³ reservoir, which supplies a 116 MW power plant operated by EDF since 1946.

Chambon dam suffers Alkali-Aggregate Reaction. This has been discovered in 1958, when unexplained cracks and deformations were noticed. Then, the central section moved 1 mm/year downstream, while the curved left wing moved 5 mm/year upstream. The crest rose 3.6 mm/year. A horizontal crack opened between the drainage gallery of the spillway and the downstream face. A leakage flow increased yearly by 3 l/min in the downstream left bank rock abutment.

Since then, numerous investigations and laboratory tests were implemented. Alkali-Aggregate Reaction has been formally identified in the late 70's. The aggregates, considered as the main cause, came from the local quarry of gneiss with numerous layers of black micaschists.

2. THE FIRST REINFORCEMENT WORKS CAMPAIGN (1991-1997)

In 1991, a working group gathering the owner EDF, the designer Coyne et Bellier and the Public Authorities proposed an alternative to the construction of a new dam. Since the longitudinal compression stress measured varied from 2 to 6 MPa, the first idea was to separate the spillway from the dam, in view of eliminating the risk of gates blocking or piles shearing. A new underground spillway was built in the left rock abutment to provide full safety during the reinforcement works.

The second aim was to relieve the swelling stresses by innovative slot cutting through the upper part of the dam (Chambon dam was the second dam in the world to experiment this type of works). An isotropic temperature rise-swelling law was implemented in a no-tension model by Coyne et Bellier in an attempt to predict the effect of slot cutting on the dam swelling. The qualitative dam behavior was well described; however, longitudinal compressive stresses were two or three times higher than the measured ones. In such conditions, the stresses calculated by the model were unacceptable after 10 to 30 years at the top of the left bank. The role of the slot cutting was also to relieve such unacceptable stresses. However, the model showed that the effects of this stress relief should not last over 20 years and that other works should be required in the future.

Before cutting, the significant open lift joints spotted in the upper part of the downstream face (5 to 20 m below the crest, 2 to 3 m deep over a 200 m length) were grouted (Figure 1 – a). This process was necessary to

ensure static and seismic stability of blocks separated by horizontal lift joints and vertical saw cuts. Also all cracks were filled and sealed with several grouts ($0.5 < W/C < 2$) at a maximum pressure of 0.2 MPa in two seasons: 1992 and 1993. 20 m³ of grout were used. Quantities grouted in the curved area were twice those in the central section.

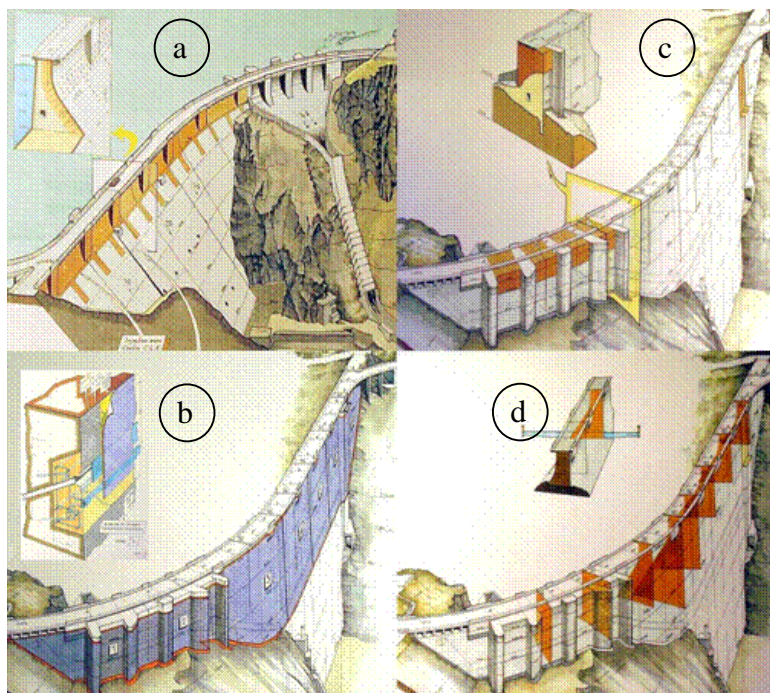


Figure 1. 1990's main works in relation with AAR
a: crack grouting, b: upstream sealing, c: old spillway concrete, d: slot cuts

From 1991 to 1997, 9000 m² of Carpi PVC sealing geomembrane were installed on the top 40 m of the upstream face in order to remove the uplift in the upper part of the dam, due to cracks opening, and to solve the question of the slot watertightness (Figure 1 – b). The upstream face was smoothed with sprayed mortar in advance. A reinforced beam was concreted at the base of the geomembrane. The drainage and puncture protection was ensured by a geogrid. The geomembrane was tightened between vertical profiles 1.85 m apart. The drainage system was divided into 9 isolated compartments with their own leakage monitoring. In such manner the localization of the entry point of any leak was facilitated. Thanks to the complementary foundation grouting works and the concrete shell added at the spillway toe, the left abutment leakage dropped from 50 l/min in 1994 to 22 l/min in 1995 and up to 17 l/min in 1997.

Before starting the slot-cutting works, the initial spillway was decommissioned. The gates were removed and the openings were filled with 4,000 m³ of concrete (Figure 1 – c).

Three campaigns of slot-cutting were required from 1995 to 1997: 2 slots in 1995, 3 in 1996 and 3 in 1997 were completed with 11 mm diamond wire from 18 to 32 m in depth below the crest (Figure 1 – d). The main effects of slot cuts on the dam were: 1) the return of the curved part toward downstream, and 2) the return of the bank side blocks toward the center of the dam. During the last campaign, the 3 slots did not close and surrounding slots and joints opened, this was the sign of the effectiveness of the stress relief.

3. THE NEW DIAGNOSIS (2007-2010)

Fifteen years after the first reinforcement works, the slots closure monitoring showed a slow crest recompression and the pendulums exhibited the restart of the curved left wing movements toward upstream. Following this movement, the horizontal crack below the spillway reopened.

According to those observations, an extensive investigation campaign was launched between 2007 and 2010. The aim was the diagnosis of the dam condition and the definition of the next works to continue the operation of the dam in safe conditions. These investigations included drill holes in the dam body to identify the extent of crack networks, detailed inspection of the concrete-rock interface by digital borehole logging inside drill holes, identification and characterization of swelling laboratory tests on samples representative of the different

areas of the dam, on-site stress measurement with flat jack devices inside the galleries and from the downstream face. Overcoring in-situ tests were also performed in order to get the three dimensional stress tensors, leading to more relevant results of the compressive stresses. Foundation modulus measurements by dilatometer tests were also carried out.

This extensive campaign showed the almost systematic presence of a vertical cracking along the elevation drainage curtain in the upper part of the dam, which led to the conclusion that it was not possible to exclude some upstream concrete blocks instability in earthquake conditions. They might be pre-cut by the elevation drainage curtain and extended horizontal or vertical discontinuities. The presence of these cracks was then explained by several factors: (i) vertical drains of diameter 800 mm (in red and green on Figure 2) and 300 mm (in blue on Figure 2) are separated by an average distance of 3.20 m; they could work as a “precut line” along the axis of the dam, (ii) the differential expansion rate between the upstream concrete containing 250 kg/m³ of cement and the downstream one containing 150 kg/m³ could create shear stresses along the same surface (Figure 2), (iii) the geometry of the dam, curved in its left bank side. Most of these cracks are observed in drilling holes through the curved zone and are several millimeters to more than 1 centimeter open. As the different cracks are most of time not linked inside the dam body, the presence of a continuous upstream slab can likely be excluded, but potentially unstable blocks under earthquake loading may exist. These virtual blocks are delimited: in the vertical longitudinal direction by the vertical longitudinal cracking and the upstream face (2.50 to 4.10 m), in the vertical transversal direction by dilatation joints and saw cuts (5.30 to 16.30 m) and by cracks potentially linking existing drains (singular points with an average distance of about 3 m) and in the horizontal direction by the construction joints (2.40 to 2.90 m).

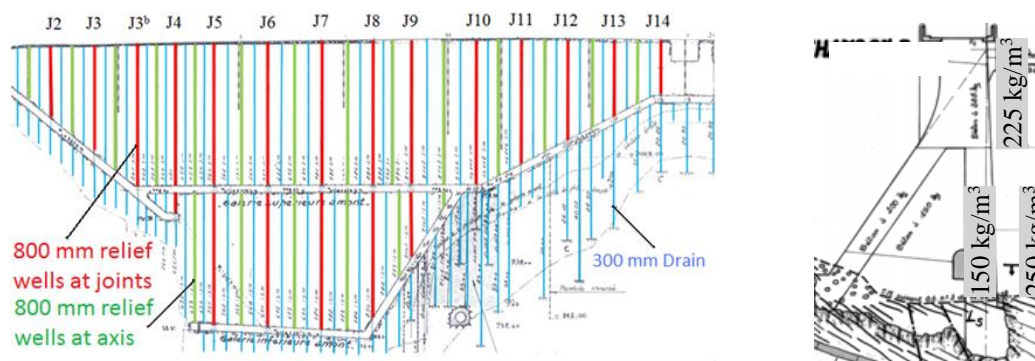


Figure 2. The vertical drainage curtain seen from downstream and cross section

Between structural cracks, the concrete displays good mechanical properties: compressive strength greater than 20 MPa, modulus of instantaneous deformation greater than 20 GPa. Moreover, the contact between limestone (Trias) and igneous rock (gneiss) in the left bank abutment is not disturbed by the thrust of the dam: it is closed and of good quality (with deformation moduli varying between 6 and 14 GPa) excluding any risk of shearing surface development inside the left bank abutment under the stresses developed by the dam swelling.

The swelling laboratory tests showed that the expansion of concrete should continue with a relatively constant rate for several decades, even if a gradual slowing is not excluded (Figure 3).

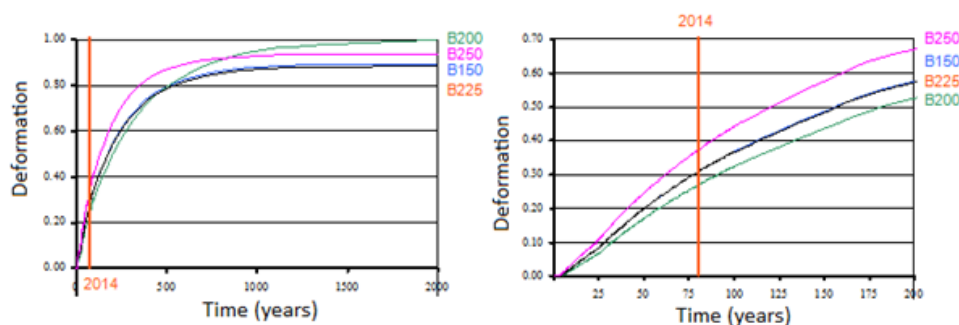


Figure 3. The predicted swelling in the future at Chambon dam

A new multi-scales swelling law for concrete implemented in ASTER computer code developed at EDF was used at this occasion (reference: Grimal E. & al. (2017), “AAR and DEF structural effects modeling”, Swelling Concrete in Dams and Hydraulic Structures, iSTE/Wiley, pp. 203–217). It provided a very good fitting

with the monitored dam behavior (Figure 4). The FEM calculations showed that the benefits of the slot cuts done in the 1990's still remained in the upper part of the structure, confirmed by the monitoring of the deformations in the curved left wing.

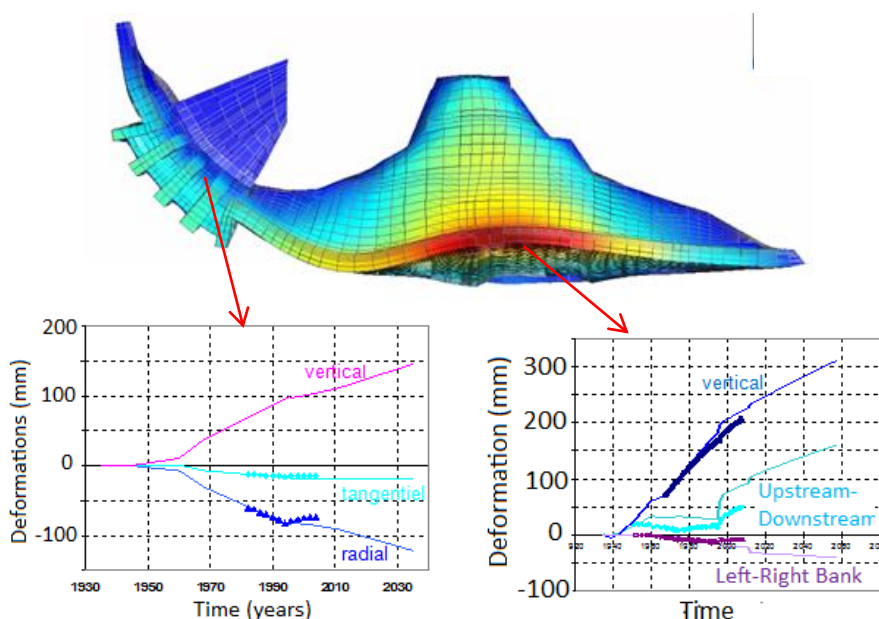


Figure 4. Comparison of measured and computed deformations in 3D modeling

They nevertheless displayed noticeable stresses parallel to the abutments, with the risk of shearing the rock/dam interface in a medium term (Figure 5).

Based on that diagnosis, a new reinforcement campaign was decided and received in 2010 the agreement from the Permanent Technical Committee on Dams and Hydraulic Structures (commissioned by the French Ministry of Industry).

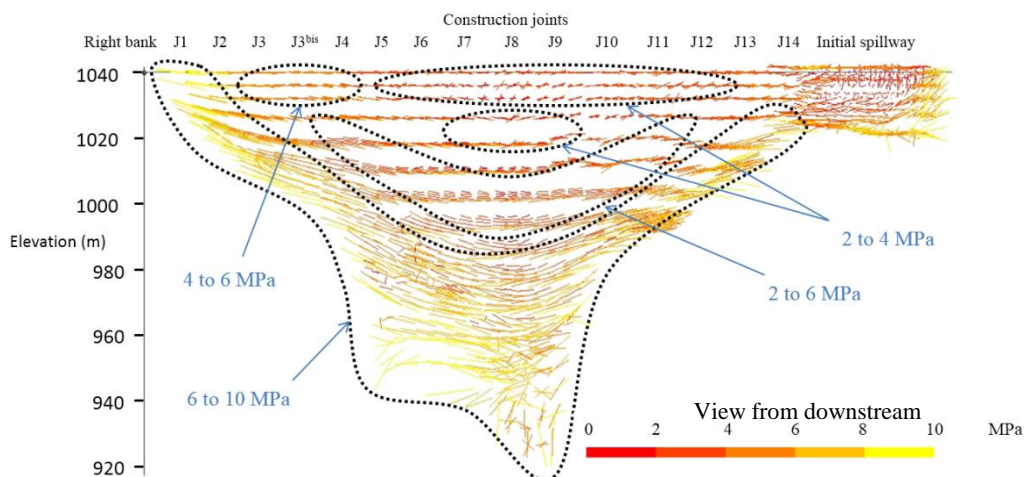


Figure 5. The maximal principal compressive stresses calculated in the dam

4. THE SECOND REINFORCEMENT WORKS CAMPAIGN (20013-2014)

The main objectives of the second campaign were to reinforce the integrity of the upper part of the dam and to prevent any upstream block from falling that could lead to destabilization of the dam. The upper part confinement was obtained by the installation of 415 tendons (Figure 6).

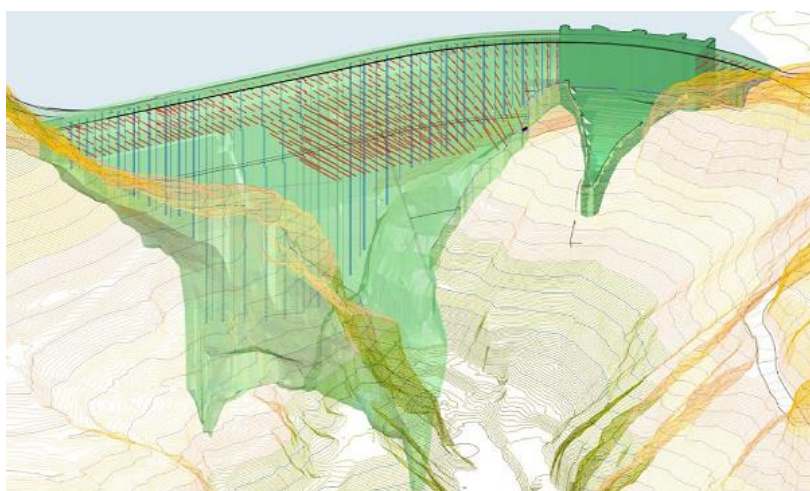


Figure 6. The tendons pattern (red) and drainage curtain (blue) seen from downstream

Consisting of horizontal cables, with greased sheathed strands type T15, crossing the structure from upstream to downstream, they were pre-tensioned and non-grouted on the outer side of the general sheath, as the successful completion of the work could be impaired due to the presence of cracks. They are 3.70 m (horizontal) and 4 m (vertical) spaced, with about one tendon for 15 m². The obtained mesh fits the most likely size of the blocks, delimited by vertical cracks parallel to the axis and the upstream face, vertical joints or former slot cuts parallel to the stream direction and the lift joints in the horizontal direction. Upstream and downstream cable heads are fully embedded in reservations drilled in the dam, with diameter ranging between 500 and 700 mm. The corrosion protection is enhanced on the upstream side by concreting the reservations and by the presence of the sealing membrane. As progressive tension increase due to concrete expansion remains possible, the downstream heads were designed to be adjustable and detensioning operations could be necessary in order to fit the required tension.

The tension of 66 tendons is monitored during dam operation. They are instrumented with sensors, each containing three vibrating wires, connected to the existing remote monitoring system of the dam. Punctual in-situ weighing of each tendon is also possible at any time. Downstream cable heads were designed to maintain their tension within specified adequate limits in any circumstances:

- a lower limit equal to the pulling force due to earthquake, thus preventing any block movement,
- an upper limit of 80% of the tendon yield stress (including earthquake forces, additional tension due to concrete swelling, differential thermal expansion between steel and concrete, as well as measurement uncertainties).

The reinforcement project was designed for a 50 years duration, with a theoretical tendons detensioning every 20 years (representing a theoretical elongation of 24 mm for the longest tendons). Tension design includes the following stresses:

- the pull forces due to earthquake: horizontal acceleration (0.18 g peak ground acceleration) combined with a maximal amplification at crest of about 7 and the thickness of the blocks to confine,
- further swelling concrete, considering isotropic rate of 50 µm/m/year.

The implemented tendons type varies from 3T15 in the lower part (length: 24 m, 369 kN ≤ T ≤ 595 kN), to 7T15 in the upper part (length: 5 m, 1,060 ≤ T ≤ 1,388 kN), locally 10T15. The 4180 m drill holes necessary for the tendons were cored from upstream, with a tolerance of 1% deflection. They were systematically inspected by logging digital in order to map the cracks network and to represent them in a 3D digital model.

In addition to tendons, a carbon fiber composite net has been set up on the upstream face. It consisted in the sticking of 6,000 m carbon fiberstrips. The 20 to 30 cm wide strips link the tendon heads, along vertical, horizontal and diagonal lines (Figure 7).

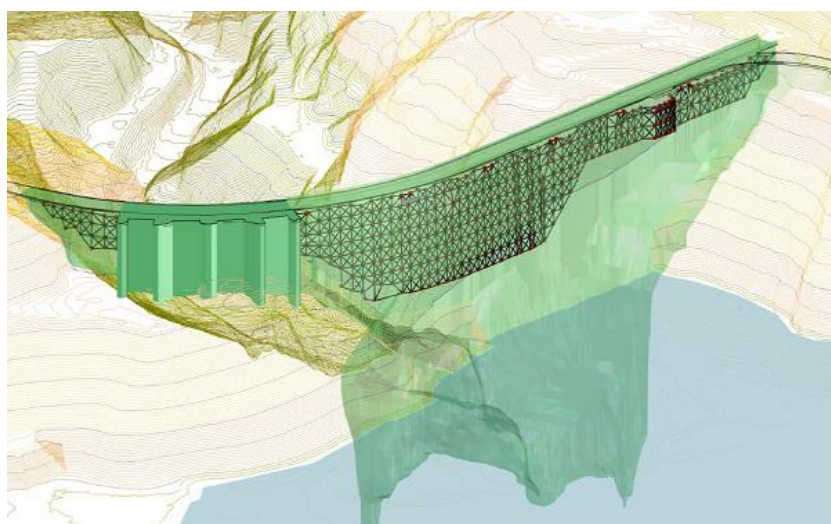


Figure 7. The carbon fiber net seen from upstream

The carbon fiber net serves confinement of small blocks that could escape the tendons action. Strips composite material (carbon strips glued with epoxy resin), composed of 1 to 8 layers glued to the surface previously sand blasted, were designed to form a “chainstitch” and to resist tensile stress due to earthquake and further swelling. An anchoring device, designed after laboratory tests and inserted into the upstream reservation, allows the connection between the carbon fiber strips and the tendon upstream heads (Figure 8). It is composed of an upstream plate maintaining the bands and a downstream plate transmitting the efforts to the tendon head, linked by eight rods (type M24 to M40 according to the efforts to be transmitted). Bands are continuous in current zone and re-curved over the anchoring devices located on the periphery of the reinforced zone.

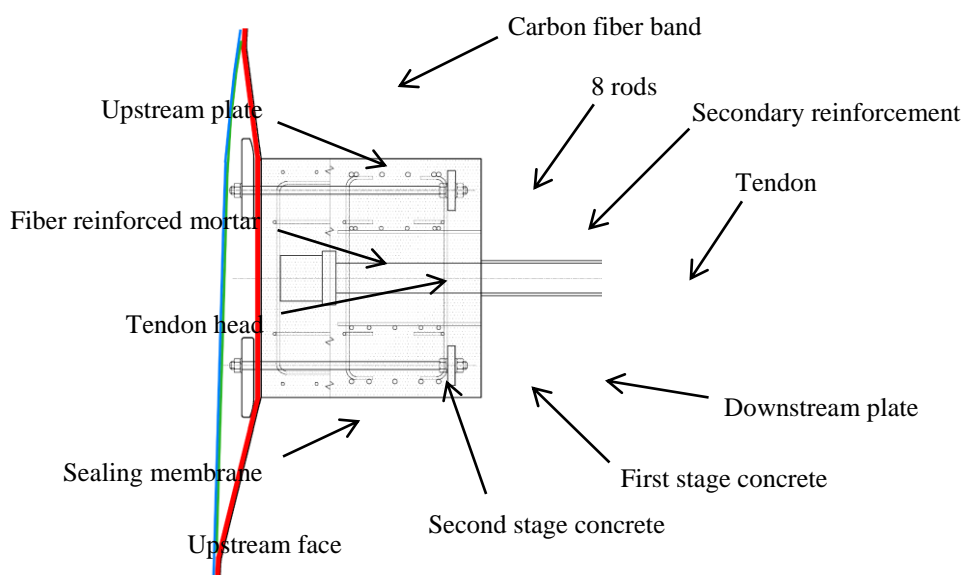


Figure 8. Carbon fiber net anchoring device

While carbon fiber composite is a material commonly used in civil engineering, its implementation as an anti-seismic net is relatively innovative and requested qualification tests in laboratory. The test device was composed of ten concrete blocks simulating tendon head hooped recesses at scale 1 and defining the average mesh (3.70 m x 4 m), connected two-by-two by the test composite bands in different configurations encountered. The tests consisted in applying a force perpendicular to the carbon fiber band. The resistance values from the trials were then included in the whole design and taken into account in a calculation model to determine the number of layers required for each band.

The new campaign by diamond wire sawing was defined using the numerical model (i) to avoid the re-compression of the upper part of the structure and (ii) to decompress the stress paths parallel to the abutments (Figure 9).

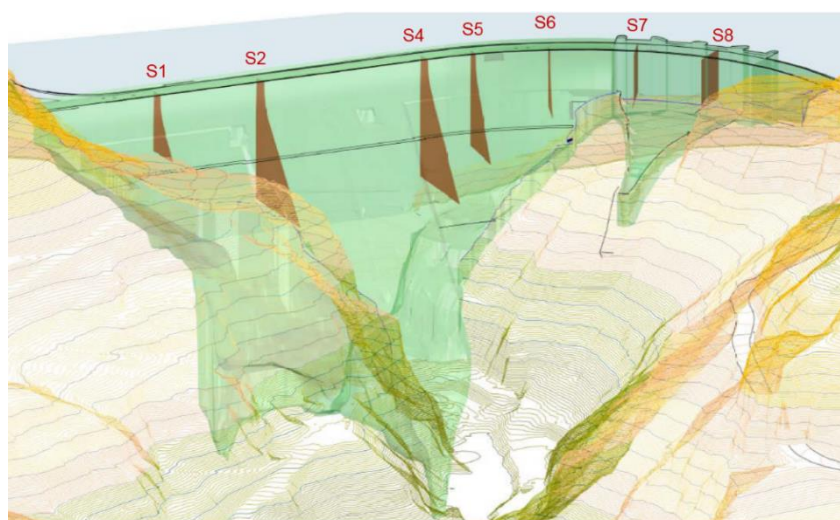


Figure 9. The design of the new campaign of slot cutting

Slot cuts mostly followed the same tracks than in the 1990's, with the following exceptions:

- slot cut S3 in the central part of the dam was not sawn again, due the presence of a cable stuck during the previous campaign,

- both slot cuts flanking S3 (S2 and S4) were deepened to 42 m, leading to an area of 650 m² each, in order to compensate the non-resawing of S3, but mainly to increase the stress reduction efficiency along the concrete/rock interface,

- the diamond wire was 16 mm wide (against 11 previously) to take advantage of technological progress made since the 1990's and avoid any risk of jamming in the event of non-fully closed former slot cuts,

- progresses in slot cutting technology allow nowadays far greater rates of cutting and made possible the 2,500 m² total cut in six months, with two equipments.

About 4 years after the works, it is now possible to estimate the influence of the slot cuts on the behavior of the dam. In the upper part of the dam, the effects were very similar to those observed after the first campaign: repositioning of the curved zone toward upstream, acceleration of the central zone and right bank side deformation toward downstream, reopening of the former construction joints and the slot cuts, return of the side blocks toward the center of the dam. In the lower part of the dam, the repositioning of the side blocks toward the center of the dam was significantly greater following the new campaign, confirming the effectiveness of S2 and S4 deepening on the stresses along the abutments.

Regarding the conditions for carrying out the works, several main on-site constraints have conditioned the procedures and the project schedule (presence of an important roadway on the dam's crest, altitude: over 1,000 m, situation in an environmentally sensitive area, ongoing operation of the hydraulic power plant, tight schedule with many interfaces between different types of works).

Access to the work sites were performed thanks to scaffolding of the entire surface concerned by the works on both upstream and downstream faces of the dam, representing a decking total length of more than 8,000 m. Two 75 m jib tower cranes were the main lifting equipments for moving up to 3 tons loads over the entire site.

The works lasted from January 2013 to December 2014. The schedule fit the reservoir low water supply, situated in winter, as the river's regime depends mainly on the snowmelt in spring. The first winter was devoted to the removal of 8,700 m² of the existing upstream sealing membrane. The second winter was dedicated to treating lower areas, by taking advantage of the natural seasonal lowering of the reservoir, limiting the energy losses. During the works and the requalification of the dam, the reservoir was lowered by 30 m. A preventive volume for storing a 10 years flood was also maintained under the lowest point of the works.

The new waterproofing membrane is conceptually identical to the one completed in 1995, with a few small modifications and improvements. It is tensioned by vertical fixings spaced 1.85 m apart, drained and divided into 12 independent compartments. The behavior of the previous geomembrane remained satisfactory after nearly twenty years of operation and gave the opportunity to re-use a large part of the stainless steel components.

Works were implemented by Bouygues-VSL company, France (tendons, carbon fiber, civil engineering and facilities), Marietta spa, Italy (slot cutting) and Carpi Tech BV, Switzerland (sealing membrane).

5. CONCLUSIONS

The slot cutting works, the installation of tendons and carbon bands, the removal and re-installation of the waterproofing system lasted two years, from January 2013 to December 2014. The good planning, strict coordination of the different tasks, that made these works so unusual, the good cooperation between EDF and the various contractors involved, allowed the works completion successfully and within the deadline.

Reservoir impounding was successfully operated during 2016 spring period, with one year of delay due to the reactivation of a landslide overlooking the reservoir. This event had nothing to do with the remedial works. The extended monitoring system enables to follow precisely the dam behavior and confirms that the effects of the slot cuttings are in line with the model predictions. Regular diagnostics will continue to be carried out in order to ensure that the dam operation continues under optimal safety conditions.

Lessons Learnt - Raising an Earthfill Dam: from the Initial Design to the Dam-Raising Works - Ganguise Dam (France)

Dr. Eric Vuillermet

BRL ingénierie, 1105 Avenue Pierre Mendès France- BP94001 – F-30001 Nîmes Cedex 5

Email: eric.vuillermet@brl.fr

Abstract

Economic reasons or evolving use of water resources may call for an earthfill storage dam to be built in two separate stages. In such cases, the idea is to design the dam structure so that can be raised during a second phase of construction with the least possible impact on its operation.

A look at the Ganguise Dam (a zoned earth fill dam in the South of France) reveals the initial design that paved the way for the two phases of construction, the design of the dam raising works 20 years later, and the unanticipated issues encountered during the implementation phase.

The first phase included certain technical choices to allow the future raising of the dam without emptying the reservoir: appropriate core and drainage device inclines.

After operating the dam for an initial phase of 20 years, the dam-raising design studies were carried out; its height was to be increased by 6 meters to provide 20 Mm³ additional storage. It thus became obvious from the analysis of the initial dam's behaviour that it was necessary to adjust the raising works design. Considering the lessons learnt when the dam was initially built, it was therefore necessary to modify the downstream structures as well as to impose certain limits during the construction works: a maximum speed for building up the earthfill and special monitoring to check dam safety.

Keywords: Upraising, Works, Behaviour, Earth Dam, Monitoring.

1. INTRODUCTION

The Ganguise Dam in the South of France is a regionally important dam for the purposes of storage and providing a steady source of water in the quantities necessary for irrigation, inland navigation on Canal du Midi and protecting natural low flows.

Right from the outset, for economic reasons, it was planned to build the Ganguise dam in two stages. During the first phase, starting in early summer 1977, a 27m dam was built. The works lasted 27 months and it was first filled in November 1979.

When the next stage consisting of raising the dam began, it became obvious that, due to the clayey materials used and the geomechanical and hydraulic behaviour of the downstream shoulder that was intended to support additional earthfill, the construction works would have to address a number of limiting factors.

The design studies, documented by special field investigations to gain insight into the supporting ground for the dam-raising earthfill, led to a series of construction and behavioural monitoring recommendations.

2. DAM DESCRIPTION

2.1. INITIAL DAM CROSS SECTION

The initial dam profile was based on the following standard cross-section (figure 1):

- Upstream shoulder composed of the most permeable materials (sand / sandstone);
- A clayey loam core and a sand filter. It is unusual because of its upstream incline. This choice made it possible to extend it during the fill works carried out from the downstream end;
- Downstream shoulder composed of marl / sandstone materials;
- A three-layered drainage blanket (sand - gravel - sand) connected to the inclined filter. The top layer of sand was entirely or partially replaced by Bidim U64 geotextile.

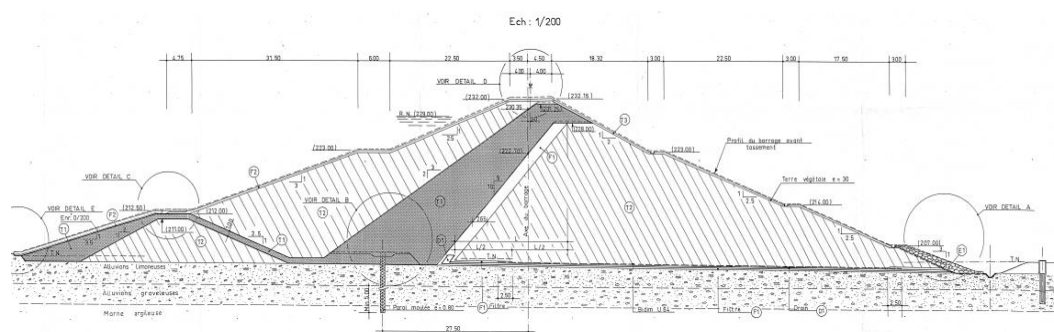


Figure 1: Cross section of initial dam

The aspects of the design selected during the first phase to allow the future raising of the dam, were paramount, especially as they allowed the works to take place without interrupting dam operation. The main aspects were:

- Inclination of the core and its filter in a downstream direction so that the shoulder could be raised without emptying the reservoir, therefore with uninterrupted dam operation;
- Integration of the additional load due to the raising of the shoulder in the overall structural design calculations.

2.2. INITIAL DAM BEHAVIOUR

After observing its behaviour by means of dam monitoring, which revealed the presence of residual pore pressure and movement in the downstream earthfill, it became clear that there was a need for more insight into the nature of the materials in the downstream shoulder. A special series of investigations was therefore carried out on the initial dam structure.

2.2.1. SCHEDULE OF INVESTIGATIONS

The whole programme [figure 2] scheduled in several interventions included:

- 10 core drillings to extract 33 undisturbed samples;
- 13 *piezocone* test (CPTU) (a cone penetration test (CPT) with additional measurement of the porewater pressure) stopping just above the drainage blanket, grid 25 x 50m;
- Controlled pumping tests in each of the existing piezometers in the earthfill;
- Laboratory tests: Identification testing, Oedometer test, Drained and undrained triaxial tests, Testing \bar{B} in a triaxial load cell.

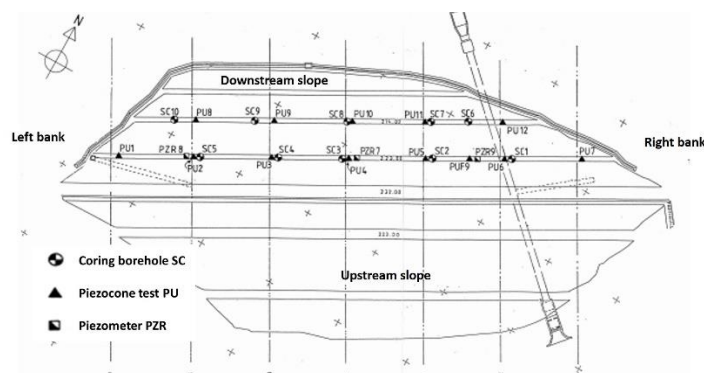


Figure 2: Location of the investigations on the downstream shoulder

2.2.2. TYPE OF MATERIALS

The features of the dam to be raised are:

- The downstream shoulder earthfill materials tend to be “marl” rather than “sandstone” (mainly clayey and gravel-type “marls”), therefore not very permeable;

- The downstream shoulder materials are moderately compressible, slightly overconsolidated, and some parts were found to be insufficiently compacted;
- Insufficient thermal and hydromechanical protection of the downstream earthfill, hence the possibility of infiltration of meteoric water through desiccation cracks;
- Decompression of the upper part of the “marly” earthfill since runoff and infiltration naturally decompress such insufficiently protected materials;
- Heterogeneous but high degrees of saturation in the downstream shoulder [figure 3].

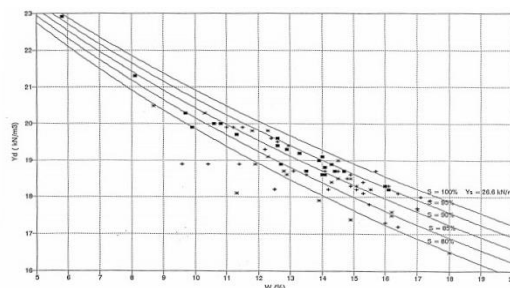


Figure 3: Degree of saturation in samples taken from the existing dam

2.2.3. MAIN OBSERVATIONS FROM SPECIFIC INVESTIGATIONS

The main results from the Piezocone tests are as follows:

- Medium to poor compactness at shallow depths,
- Rapid variation in peak strength, probably due to the great heterogeneity of the materials,
- Mostly negative pore pressure due to the “dilation” of the earthfill.
- Relaxation test results indicating:
 - Presence of decompressed materials down to a depth of 3 to 5m in the downstream slope,
 - Localised pore pressure the same as hydrostatic pressure indicating local saturation due to infiltration from the surface, facilitated by the presence of shrinkage cracks or construction defects: compacting defects, works performed during wet periods.

The conclusion was that the presence of saturated or near-saturated zones would be conducive to the development of pore pressure with the additional load of the dam-raising earthfill. To assess the parameters characterizing the development of pore pressure under the effect of the additional load, triaxial cell tests \bar{B} were carried out.

3. UPRAISING DAM

3.1. UPRAISING PROJECT DESIGN

The general design of the dam-raising project is based on putting in place the additional earthfill from the downstream side until it raises and crowns the embankment at a height of 238 NGF, in other words making the dam 6m higher. At the same time, along the banks, special watertightness mechanisms are introduced; at the downstream toe, the drainage network is consolidated, and the upstream facing protection is completed.

Materials of the same kind as those already in place are used to raise the dam by building on top of the initial structure after capping off the crown, stripping off the top layer and preparing the subformation level in the valley, along the banks and on the downstream facing.

The technical characteristics of the new dam and its reservoir are shown in [Figure 4]:

	Initial dam	Upraised dam
Dam	Zoned earthfill dam	
Height above ground level	27 m	33 m
Crest length	410 m	614 m
Crest width	7 m	10 m
Maximal length upstream/downstream	180 m	235 m
upstream slope	3,5/1 – 3/1 – 2,5/1	3,5/1 – 3/1 – 2,5/1
Downstream slope	2,5/1 – 2/1	3,5/1 – 3/1 – 2,5/1
Volume of embankment	690 000 m ³	1 270 000 m ³
Reservoir capacity	21 Mm ³	42 Mm ³
Uprasing works	27 months	24 months
Filling of reservoir	2 years	6 years

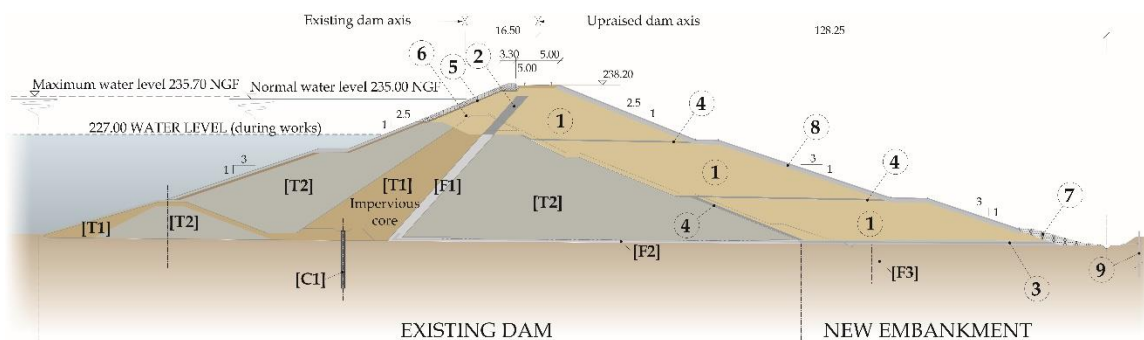


Figure 4: Upraising dam cross section

[T1]: silt / [T2]: / [T4]: impervious core / [F1]: chimney drain / [F2]: drainage blanket / [C1]: diaphragm wall / [F3]: relief wells /

1 : Fill (mixture of clay and sil) / 2 : Inclined chimney drain (sand) / 3: drainage blanket (gravel and sand layers) / 4: sand blanket / 5: geotextile filter / 6: riprap / 7: Toe protection (small riprap) / 8: slope revetment (mixture of sand and gravel) / 9: relief wells

3.2. THE MAIN RESULTS OF THE TECHNICAL STUDIES ON THE RAISING OF THE DAM

3.2.1. INFLUENCE OF THE RU COEFFICIENT – $RU = \Delta u / \Delta \sigma$

For a dam made of uniform clayey materials with conventionally designed slopes, there is a risk of failure as soon as the coefficient ru exceeds 0.4; pore pressure is therefore a primary concern in its design. Generally speaking, the factor of safety is 1 for ru values between 0.4 and 0.7. But it is important to remember that it can be very ambiguous to apply the same ru coefficient to an entire earthfill component [2]. In this case, the ru values used are by zone.

The ratio u/σ also undergoes a rapid increase from degree of saturation $S_r = 96\%$ upwards [2].

3.2.2. CALCULATION OF STABILITY AFTER COMPLETION

The investigations carried out on the downstream shoulder (Piezocone tests and undisturbed core samples) during the dam-raising studies, the results of the geotechnical tests and those of the dam monitoring piezometer measurements imply that locally, certain parts of the downstream shoulder can be subject to pore pressure due in particular to the presence of non-dissipated meteoric water.

This is why cautious values for the ru coefficients were used in the stability calculations for the downstream slope taking mean ranges of ru and looking for a 1.3 factor of safety, and a “maximum” range of ru to make sure that the stability was always verified ($FS > 1$).

The stability calculations [figure 5] on the central section P10 located in the bottom of the valley were carried out. For the various assumptions of mechanical characteristics and ru values, the overall stability coefficients range from 1.54 to 1.20.

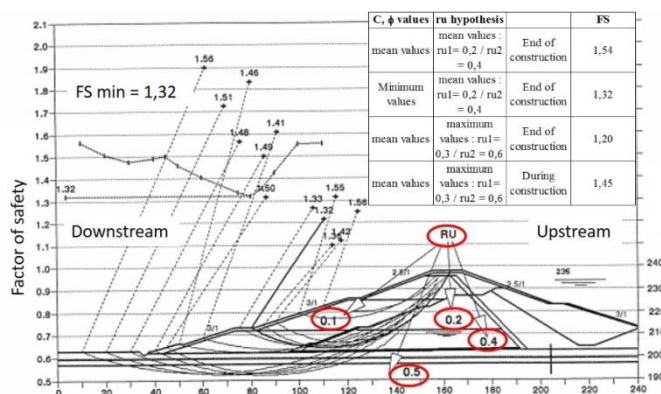


Figure 5: Results of downstream slope stability computing based on minimum mechanical characteristics and mean ru values

It can be seen that the most critical case is at the end of the construction works. The construction of the end part of the earthfill zone, a predominant threat to stability, can be steered according to the results of the pore pressure monitoring.

3.2.3. ASSESSMENT OF PORE PRESSURE DEVELOPMENT

To assess settlement, a finite element approach (Plaxis) was used to understand the earthfill construction phases divided into undrained loading stages and a consolidation phase. For each stage of construction [figure 6], the zones in which pore pressure had developed were identified and the magnitude of the parameter $\frac{\Delta u}{\Delta \sigma_1}$ was assessed.

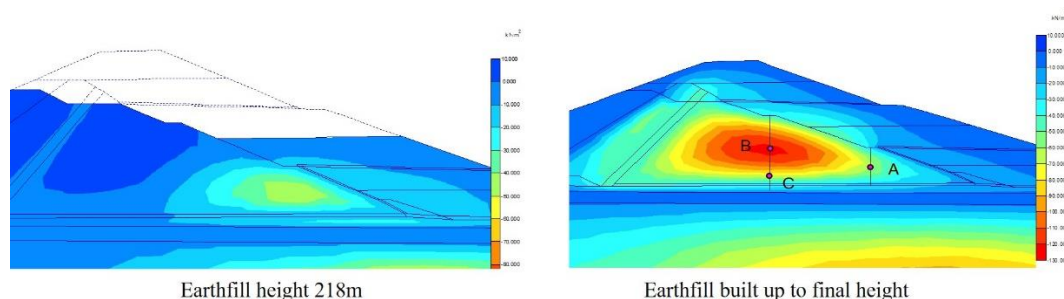


Figure 6: Example of estimated pore pressure during the construction phase

3.3. SPECIFIC DESIGN FOR NEW EMBANKMENT

- Specific design features drawn from 20 years of operating and monitoring feedback on the initial dam:
 - o The working constraints for building the new earthfill:
 - Use of materials for the new downstream shoulder with a water content between $W_{opt} - 1\%$ and $W_{opt} + 2\%$;
 - Real-time checking of pore pressure in the existing embankment thanks to a network of 9 vibrating wire load cells;
 - Limiting the earthfill construction speed as follows:

per day	per week	per month
2 layers	3.00 m	8 m

- Technical choices:
 - o Use of layers of sand in contact with the two shoulders to dissipate pore pressure due to the clayey nature of the initial downstream shoulder;
 - o Use of a shrink-prevention layer on the downstream slope to prevent cracking in the clayey materials subject to seasonal wetting and drying cycles;
 - o Diaphragm walls instead of grout curtains for watertightness on the banks (figure 4) after proof of the limits of the grout curtain in the foundation layers with alternating little-permeable marly layers and permeable sandstone layers. In places, sandstone facies imposed additional injections;
 - o Building an absorbing well and a riprap drainage blanket covering the slopes on the right bank to attenuate internal erosion risk in a sandstone facies.
 - o Regarding filling, the CTPB-OH (French Technical Committee for Dams) requested gradual filling over a 3-year period.

3.4. MONITORING AND BEHAVIOUR

3.4.1. MONITORING SYSTEM

The different behavioural analyses of the dam during the raising works revealed strong presumptions of pore pressure forming within the basic structure due to the clayey nature of the materials and their water content, and thus threatening its stability, especially towards the end of the dam-raising works. This is why a pore pressure sensor network was installed beforehand (figures 7 & 8).

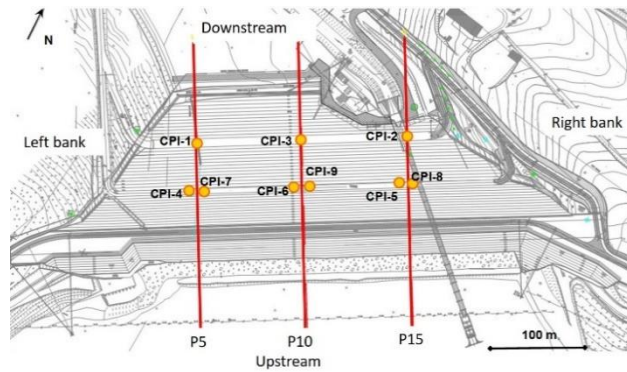


Figure 7: Location map of monitoring points

To maintain a fast response time, the sensors were installed in chambers 0.50m high with a 3m swelling clay plug and the wells filled with grout.

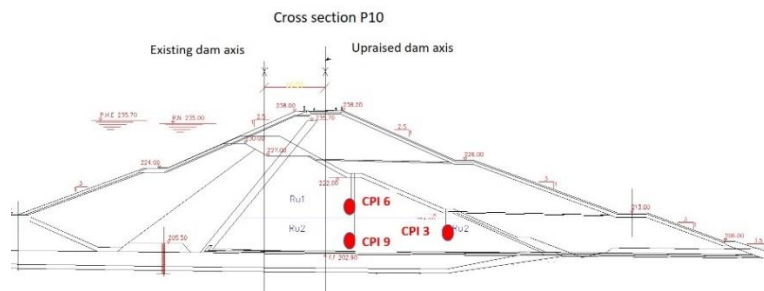


Figure 8: Location cross section of monitoring points

3.4.2. DAM BEHAVIOUR

Most of the sensors showed that pressure developed very quickly if the sensors were in the area affected by the loading.

Monitoring included:

- the evolution of pore pressure values and the rise in the earthfill;
- the estimation of the respective *ru* coefficients and comparison with those used in the calculation assumptions

Here is the first $u = f(t)$ graph for the height of the added earthfill, where u is the pressure recording [figure 9].

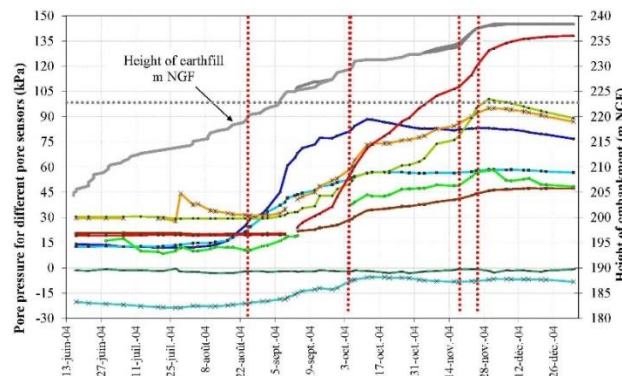


Figure 9: Evolution of pore pressure over time - Indication of the height reached during construction of the downstream shoulder

It shows a more or less pronounced rising trend in pore pressure as the height of the earthfill increases. At some of the sensors, this evolution is due to increased sensitivity to the speed at which the fill embankment rises resulting in a drop or an evening off in the pressure when the fill works are interrupted.

Pore pressure development depends on the degree of saturation, S_r , and the position in the zone under strain considering the elements that facilitate dissipation: the sandy interface layer. [2] indicates that the initial water content plays a decisive part in the development of pore pressure. Above $S_r = 96\%$, there is a rapid increase in pore pressure.

In order to analyse the development of pore pressure and to monitor dam safety, the graph $ru = f(t)$ was plotted, where $ru = \Delta u / \gamma \cdot h$ [figure 10] where Δu is the pressure variation since the beginning of the fill works, $\gamma \cdot h$ is the overloading due to the raised earthfill, where $\gamma = 21.5 \text{ kN/m}^3$ (value obtained when testing the dam-raising earthfill materials).

Considering the ru values used for the stability calculations (case of the average values: $ru_{inf} = 0.4$ and $ru_{sup} = 0.2$), the observed values are below the mean values used in the assumptions for the stability calculations. Nevertheless, due to the sensitivity of the response to strain, the building speed for the earthfill specified in the contract was made more stringent in order to anticipate potential problems.

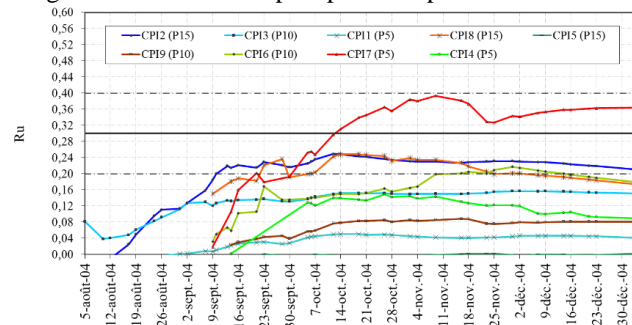


Figure 10: Evolution of the ru coefficient over time

If we refer to literature-based analyses [figure 12] regarding the influence of the initial degree of saturation on the evolution of pore pressure under loading, the unusual variations in the measurements at CPI7 (red line) can be explained by the initially high level of saturation (figure 11). This confirms the importance of respecting the speed at which the dam-raising earthfill is put in place, specified at the design stage.

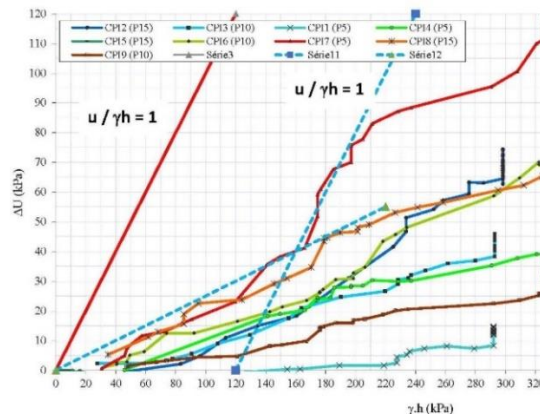


Figure 11: Evolution of pore pressure according to overloading

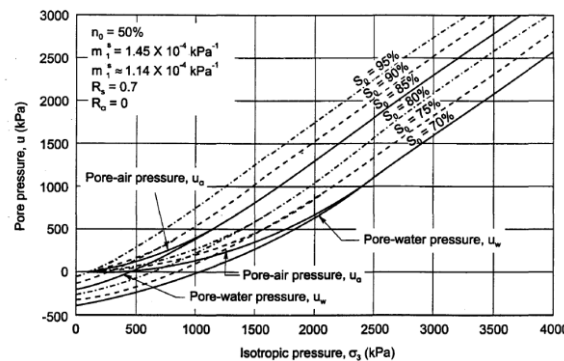


Figure 12: Variation in pore pressure for different initial degrees of saturation, S_o , using the Hill method [3]

4. POST-CONSTRUCTION BEHAVIOUR

After a period during which there was an increase in pressure due to the overloading caused by the earthfill put in place, all the pressure cells recorded a slow decline resulting from gradual and continuous dissipation of the pressure inside the earthfill zone. So far, none of the measurements indicate that the upstream water level has had any effect on pore pressure.

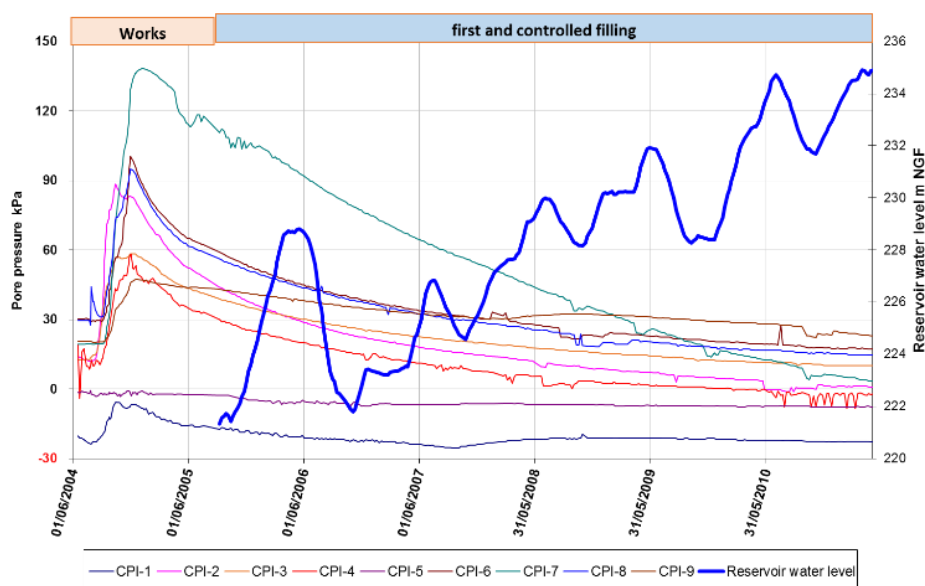


Figure 13: Pore pressure after works and during first and controlled filling

5. CONCLUSIONS

This project is a reminder of the undeniable benefit of knowing the behaviour of the existing earth dam structure that was to become the foundations of dam-raising works. It is important to know not only the type of materials used but also the parameters interacting with the development of pore pressure: the compactness of the earthfill, the water content influencing its response to strain and the estimation of specific parameters such as \bar{B} .

In the case of the Ganguise Dam, the studies heightened our awareness of the safety issues that arise when pore pressure develops, thanks to insight from laboratory tests and finite element modelling. It was thus possible to determine limitations to be observed during construction and a monitoring system allowing the works to be performed while the dam was still in operation.

Although the monitoring carried out during the construction works showed that the safety and stability of the dam were not affected, the choices made definitely proved to be appropriate. Caution in the design approach is a must, especially when confronted with heterogeneous materials and high initial degrees of saturation.

6. REFERENCES:

1. Gisele Suhett Helmer, Katia Vanessa Bicalho & Eric Vuillermet (2010). Análise e Modelização do Comportamento de Pressões Intersticiais em Barragens de Terra - COBRAMSEG 2010 congresso brasileiro de mecânica dos solos e engenharia geotécnica - Gramado (RS- Brazil) 17 a 22 de agosto de 2010
2. Daniel POULAIN (1993). Pressions interstitielles de construction dans les barrages homogènes en matériaux argileux humides – Thèse Université de Bordeaux
3. D.G. Fredlund , H.Rahardjo & T. Ng. (1999). Effect of pore-air and negative pore-water pressures on stability at the end-of-construction from the Proceedings, International Conference on Dam Engineering, Johor Bahru, Malaysia, January 12-13, 1993 pp 43-51 in The emergence of unsaturated soil mechanics, Fredlund volume, NRC RESEARCH PRESS.

The Use of Geomembranes in Dams

Alberto Scuero¹, Gabriella Vaschetti¹, Marco Bacchelli¹

1- Carpi Tech, Via Passeggiata 1, 6828 Balerna, Switzerland

Email: gabriella.vaschetti@carpitech.com

Abstract

Geomembranes, and particularly Polyvinylchloride (PVC) geomembranes, used since more than half a century to control seepage in dams, are environmentally friendly rehabilitation technologies. In rehabilitation, geomembrane systems have been applied on all types of dams, to line the entire upstream face of the dam, or only the area/s causing most seepage, or only cracks/failing joints. The geomembrane is placed in exposed position, and is drained behind. In new construction, geomembrane systems have been applied to provide the water barrier in embankment dams and RCC dams, and as external waterstop for joints in CFRDs and for joints between monolith blocks in RCC dams. In RCC dams and fill dams, the geomembrane can be at the upstream face, in exposed or covered position, in fill dams also as a geomembrane core. The paper discusses the available options for rehabilitation and gives some information on new construction, addressing case histories in the dry and underwater. The paper introduces an innovative underwater waterproofing technology, already successfully installed on two canals, which permits repairing embankment dams and canals without impacting on operation: no dewatering, no reduction of water speed. This technology can be considered also for new construction of embankment dams and canals.

Keywords: Geomembrane, Geocomposite, Waterproofing, Dams, Drainage.

1. INTRODUCTION

Geomembrane systems are the most environmentally friendly rehabilitation technologies for dams. They do not require heavy installation equipment or large excavations and processing plants for materials, the components of the system have small volume and light weight, so that transport by helicopter to remote sites not accessible by vehicles is feasible at reasonable costs; environmental impact is very limited, since large areas for site organization and plants are not needed, and there is no heavy transport affecting the environment and the communities; installation is quick and can be carried out in almost any weather condition. Different from technologies using sprayed or in-situ made products, geomembrane systems are installed also underwater and in flowing water, with practically no impact on the operation of the structure, be it a dam or a reservoir or a canal.

Geomembranes are a mature technology: they have been used to control seepage in hydraulic structures starting after World War II in canals, and at the end of the 1950ies in dams, where the first projects aimed to provide a water barrier to the pervious body of new embankment dams. Gradually, different systems were developed to rehabilitate all types of dams, and to waterproof new Roller Compacted Concrete (RCC) dams. The most recent and thorough ICOLD Bulletin dedicated to geomembrane systems [1] discusses materials, anchorage systems, installation, and makes recommendations for specifications and contracts. According to the database created during preparation of the Bulletin, Polyvinylchloride (PVC) geomembranes are by far the material with the oldest and widest experience in rehabilitation as well as in new construction, in exposed as well as in covered position. Table 1 that follows, and excerpt of the Bulletin, summarises the use of different types of geomembranes based on the data available in 2007. An updating of the database in 2009 indicated that the number of dams using a PVC geomembrane system had increased from 153 to 181, and continues increasing, while the number of dams using other types of geomembranes has had a very small increment.

The advantages of PVC geomembranes, and of the numerous systems that have been developed using them for rehabilitation of dams and other hydraulic structures, and for construction of new embankment dams and new RCC dams, have been widely discussed in international literature [respectively 2, 3, 4 for recent references]. Aspects such as performance of PVC geomembrane systems in respect to differential movements, seismic events, thermal cracking, seeping lift joints, uplift, swelling processes, and construction times and costs, were discussed in Tehran by the same authors in 2005 [5].

Table 1. Geomembranes in dams (excerpt of ICOLD Bulletin 135)

Type	Basic material	Abbreviation	Total exposed	Total covered	Total	Oldest exposed	Oldest covered
Polymeric	Polyvinylchloride	PVC-P Plasticised	80	73	153	1974	1960
Polymeric	Polyolefin	LLDPE	0	29	29	-	1970
Polymeric	Polyolefin	HDPE	3	12	15	1994	1978
Polymeric	Elastomeric	Polyisobutylene IIR (Butyl Rubber), EPDM	5	4	9	1982	1959
Polymeric	Chlorosulfonated polyethylene	CSPE	3	5	8	1981	1986
Polymeric	Polyolefin	PP	3	3	6	1995	2000
Polymeric	Chlorinated polyethylene	CPE	0	3	3	-	1970
Bituminous	Oxidized bitumen	Prefabricated GM	7	10	17	1973	1978
Bituminous	Polymeric	SBS, bitumen ethylene, ECB	0	3	3	-	1996

2. PVC GEOMEMBRANE SYSTEMS IN REHABILITATION

In rehabilitation, the geomembrane liner is placed on the upstream face of the dam, generally in exposed position, and with a drainage system behind, to allow discharge of possible backpressure, and monitoring of the performance. PVC geomembrane systems are used for full-face rehabilitation, performed in one or more campaigns, or to waterproof only the area/s causing most seepage, or only cracks/failing joints. The face anchorage and peripheral anchorage of the geomembrane are calculated to resist acting loads such as uplift by wind and waves. Face anchorage on a solid subgrade is generally linear, with a tensioning system, while on a granular subgrade it is made at points, with deep anchors. Ballast anchorage is rarely used. Where needed, additional geosynthetic layers are used to provide anti-puncture protection, or support over cavities in the subgrade, or enhanced drainage capacity. The geomembrane system can be installed in the dry, and underwater when total or partial dewatering of the impounded reservoir is not possible.

All types of dams can be waterproofed, and all types of subgrades accommodated. The chapters that follow give a range of different applications, addressing full-face and partial rehabilitation. In all cases, the waterproofing liner is SIBELON® CNT, a PVC geomembrane heat-bonded during fabrication to a nonwoven geotextile, to form a composite geomembrane, also known as “geocomposite”. The flexible elastic PVC geomembrane provides the water barrier, and the geotextile has several functions, the most important ones being enhancing the mechanical properties of the liner, and providing anti-puncture protection.

2.1. FULL-FACE REHABILITATION ON CONCRETE AND ASPHALT CONCRETE SUBGRADES: CHAMBON, PECINEAGU AND MORÁVKA

Dams having a hard subgrade, such as concrete dams and Concrete Face Rockfill Dams (CFRDs), allow using a tensioning assembly anchored to the concrete with stainless steel anchor rods embedded in chemical phials. The assembly consists of two stainless-steel profiles: the first profile, U-shaped, is anchored to the concrete, the PVC geocomposite sheets are placed overlapping on it, and are then covered by the second profile, Omega-shaped, which is fastened the first one achieving fixation and tensioning of the geocomposite, as outlined in the conceptual scheme of Figure 1 - an excerpt of ICOLD Bulletin 135. The profiles, besides providing a pre-tensioning effect avoiding formation of slack areas and folds, allow a drainage gap behind the waterproofing liner, and construct vertical channels acting as vertical drains conveying water that should be present behind the liner to a bottom collection and discharge system.

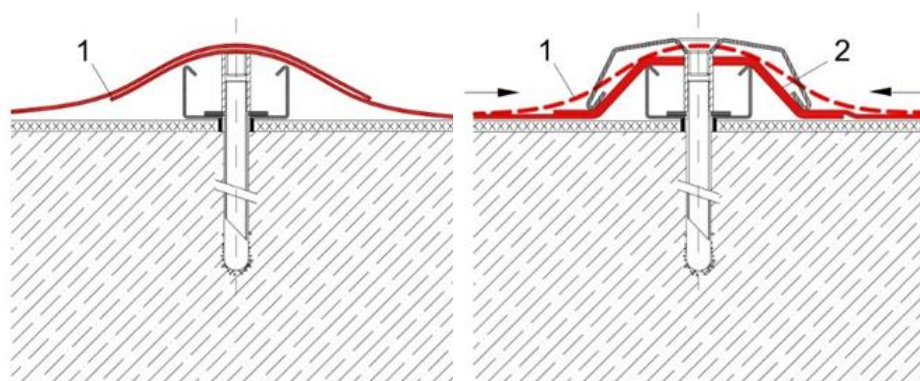


Figure 1. On the left, adjacent PVC geocomposite sheets (continuous red line, 1) overlap on the U profile secured to the dam. On the right, the Omega profile placed on the PVC geocomposite sheets compresses and forces them to change from the previous loose configuration (dotted red line, 1) into a new pre-tensioned configuration (continuous red line, 2). Fig. 85 of ICOLD Bulletin 135: Pretensioning effect of the two profiles (patented)

In concrete dams, typically there is a drainage layer (the gap allowed by the tensioning system described, or a dedicated synthetic layer of high transmissivity) between the concrete and the geocomposite. This configuration was adopted for example at Chambon 137 m high gravity dam in France, one of the most well-known and discussed case of alkali-aggregate reaction. The SIBELON[®] geocomposite system, installed in 1993/1995 (in separate summer campaigns to minimise outage), was deemed the most adequate because in the event of an earthquake the deformable and elastic geocomposite would bridge the cracks already existing and new cracks that should form due to the seismic stresses, maintaining watertightness and reducing the risk of hydro-jacking, it would stop water infiltrating into the dam body and feeding the AAR, it would avoid the risk of uplift, thus maintaining the stability of the top part of the dam, and it would easily restore watertightness after slot cutting, providing reliable protection of the slots against the risk of leakage. The geocomposite lies on a high in-plane transmissivity drainage geonet, doubled along the bottom periphery to form a longitudinal collector that conveys water to nine transverse pipes discharging into the gallery and allowing separately monitoring the nine drainage compartments. The geocomposite is anchored to the concrete face by the tensioning system discussed above, and at peripheries by seals of the tie-down type, consisting of flat stainless-steel batten strips compressing the geocomposite on the concrete, with suitable gaskets and regularisation layers, and with dimensions and anchors designed in function of the water head acting at each location.

Chambon is an outstanding example of how geomembrane systems can give a major contribution in extending the life of a dam: the system performed successfully for 18 years, and in 2013, when major structural measures were undertaken to further extend the life of the dam, the owner EDF – Electricité de France - selected the same identical system to waterproof again the dam after remedial measures (Figure 2 at left). The old geocomposite, a 2.5 mm thick PVC geomembrane laminated during fabrication to a 200 g/m² anti-puncture geotextile, was removed, structural measures were carried out and at the same time a new geocomposite was installed, with mass per unit area of the geotextile increased to 500 g/m², to provide higher anti-puncture protection. A large part of the components that were already in place since almost 20 years before were re-used. This is the only known case of a geomembrane system removed to allow performing civil works, and reinstated with the same design, due to its previous successful performance [6].

Pecineagu in Romania is an example of rehabilitation of a CFRD. The dam is 105 m high, with 1V: 1.717H upstream face inclination, slabs' thickness varying between 1.20 m (lower area) and 0.30 m (upper area), and with PVC waterstops and copper waterstops or elasto-plastic bituminous mastic poured in place. The dam is in a difficult environment with temperatures from -21.5°C and +42°C, maximum snow thickness of 100 cm, and approximately 50 cm of ice cover for minimum 4 months/year. Over time, due to settlements of the dam body, the peripheral slabs were subject to significant rotation, joints opened exceeding the elongation capacity of the waterstops, which were locally destroyed, and environmental aggression caused cracking and deterioration of the slabs, increasing leakage and requiring repeated repairs over the years. Due to importance of the dam, which ranks 12th by height and 34th by reservoir working volume, and to the importance of the reservoir that provides drinking water to the capital, Bucharest, as well as flood attenuation and power generation, the owner decided to perform

repair works, among which the most important one was to restore watertightness at the concrete slabs.

At Pecineagu, upstream rehabilitation was carried out in stages: in 2011 the reservoir was totally dewatered and the waterproofing geomembrane system was installed on the slabs from the bottom of the dam to elevation 1060 m; in 2012 the reservoir was lowered and the geomembrane system was installed at partially impounded reservoir, from elevation 1060 m to elevation 1095 m, with crews working from travelling platforms or harnessed to the face of the dam (Figure 2 at right). The waterproofing system uses a SIBELON® geocomposite of different thickness depending on the water head: from elevation 1095 m to elevation 1060 m the geocomposite consists of a 2.5 mm thick PVC geomembrane laminated during fabrication to a 500 g/m² anti-puncture geotextile, and from elevation 1060 m to bottom the thickness of the PVC geomembrane is increased to 3.0 mm. The geocomposites are anchored to the face of the dam with the same patented anchorage system shown in Figure 1, and with the peripheral seals already discussed. Due to the roughness, deterioration, and rotation of the concrete slabs, instead of a drainage geonet a 2000 g/m² anti-puncture geotextile is placed on the slabs, under the PVC geocomposite.



Figure 2. At left, PVC geocomposite sheets under installation on drainage geonet (the black material on top of the tendons and carbon bands mesh used for structural reinforcement) at Chambon dam in France in 2014. At right, PVC geocomposite sheets under installation on anti-puncture geotextile (the white material) in stage 2 at Pecineagu CFRD in Romania in 2012

The use of anti-puncture geotextiles is frequent also in rehabilitation of masonry dams, to protect the waterproofing liner against the roughness of such a type of subgrade. The mass per unit area of the geotextile is selected in function of the aggressiveness of the masonry.

When the subgrade is asphalt concrete, in rockfill dams (ACFRDs) or in earthfill dams, the same tensioning system is used for face anchorage and, if the pull-out strength of the asphalt facing so allows, anchorage of the tensioning profiles is made by chemical phials as it is done in concrete subgrades. In case the pull-out strength is not sufficient, chemical phials may need to be substituted by deep anchors, described in the next chapters. In regards to perimeter seals, if they are made on concrete they are of the tie-down type already mentioned, otherwise the insert-type seal is used, as done at several dams of this type, including Morávka dam in the Czech Republic, a 39 m high earthfill dam with a multi-layer asphalt concrete facing, built in the 1960ies and with 1V:1.75H upstream inclination. Morávka experienced leakage since the first uncontrolled filling in 1965; the reservoir was drawn-down, mastics cover and two new bituminous concrete layers were added to the original ones. At first seepage was reduced, but over time it increased again and despite several repairs defects and seepage continued until in 1997, when the biggest flood in the century caused the water level in the Morávka reservoir to rise to the maximum level. Evaluation of the data collected in that occasion showed that the main cause of the failure of the asphalt sealing had been the long-term erosion of the subgrade at the left bank of the valley, caused by the subsurface water percolating from the left bank and resulting in progressive enlargement of caverns near the surface asphalt sealing.

The owner of the dam decided to perform a total rehabilitation of the dam including also the facing. The technical requirements for the new upstream sealing were resistance to deformations and depressions in the subgrade, proven long-term resistance to changeable weather conditions, frequent freeze/thaw cycles, ice formation, high temperature excursions, and the possibility of monitoring the performance on a continuous basis. The cost-benefit analysis lead to considering as only solutions a new asphalt concrete facing, and a geomembrane facing. The technology of removing the old and placing a new asphalt concrete facing was time consuming, riskier from the point of view of protection of the dam body during the flood, and more expensive. The time allotted for

installation in summer 1999 was 90 calendar days, which included 15 days estimated for stoppage due to floods and bad weather. A PVC exposed geomembrane sealing system was deemed the only waterproof facing that could meet the technical requirements and the time constraints. The waterproofing liner is SIBELON® CNT 3750, the same adopted at Chambon in 2014 and at Pecineagu above elevation 1060 m. The asphalt concrete layer provided sufficient pull-out strength for the chemical anchors of the tensioning profiles that constitute the face anchorage of the waterproofing liner.

At Morávka there is a primary perimeter seal placed at the bottom of the asphalt concrete facing, and a secondary perimeter seal placed on the concrete plinth. The primary seal on asphalt concrete is of the insert type: a slot is made in the asphalt concrete, a PVC geocomposite strip is inserted in the slot that is then filled with watertight resin, and the PVC geocomposite waterproofing the upstream face is watertight seamed to the PVC strip. This type of seal has given excellent performance in dams with high water heads. The secondary seal on concrete is of the tie-down type, and has the function of reducing the head on the primary seal and of creating a drainage compartment to intercept water seeping from foundation.

The drainage system consists of the gap created by the anchorage system between the existing asphalt concrete face and the new PVC geocomposite liner. Drained water travels by gravity in this gap to reach a drainage collector consisting of a band of geonet with high in-plane transmissivity placed along the bottom periphery and along the compluvium between the left bank and the straight part of the dam. The drainage system is divided into 11 compartments, and each section is further divided into a primary compartment draining water from the upstream face, and a secondary compartment draining water coming from foundation, thanks to the presence of two bottom perimeter seals. Each compartment has an individual drainage discharge pipe, placed in a hole drilled to reach the inspection gallery, and equipped with a monitoring system.

When the 10-year guarantee was going to the end, the owner of the dam decided to make a final test of the sealing system. The reservoir was filled up to the emergency spillway during snow melting in spring 2009. The owner [7] reports “After the stabilization of the measured values it was proved that the function of the upstream geomembrane sealing system is excellent. The value of seepage was under guarantee limits for water level on the spillway and attained a maximum value of 0.15 l/s from one section and 1.0 l/s in total, well below the minimum acceptable contract leakage of 2.0 l/s for the entire face”.

2.2. FULL-FACE REHABILITATION ON GRANULAR SUBGRADES: VAITÉ

If the characteristics of the subgrade (granular materials, hardfill, asphalt facings with low pull-out strength) do not allow using chemical anchors, deep anchors can be used. Deep anchors can be of the “duckbill” type, as adopted at Vaité dam, or of the grouted type, as adopted in hardfill dams and at several hydropower canals. Vaité is a 23 m high earthfill dam in the island of Tahiti, in French Polynesia, used for hydropower. In 1987, the upstream face of the dam was lined with a 1 mm thick PVC geomembrane placed on an anti-puncture geotextile, and anchored at top to the parapet wall, and at the abutments in a trench. The geomembrane was extended on the bottom of the reservoir for about 50 m, and on the abutments, so to provide some waterproofing of the foundations too. In the years 2010-2011 this geomembrane was no longer functional and the owner of the dam decided to perform rehabilitation works. A requirement to the new geomembrane system was to resist 204 km/h winds (hurricane conditions) in the top 1/5 of the section, and 100 km/h winds in the remaining 4/5. The waterproofing liner, SIBELON® CNT 3750, was fastened to the dam face and at the abutments with duckbill anchors placed at depth, pattern and spacing designed to resist the design winds with the required safety factors. The system (patent pending) exploits the technology of deep anchors designed for anchorage in gravel soil, and consists of a stainless-steel tendon and of a rotating duckbill, covered by a suitable capping that guarantees that no water infiltration occurs where the anchor crosses the geocomposite, and that the forces at each anchor are adequately distributed so as to not overstress the geocomposite. The tendon and duckbill are driven into the ground and after the duckbill is in place, an upward pull on the tendon rotates it into a perpendicular “anchor lock” position in the soil that mobilises the resistance of the soil itself.



Figure 3. At left, Morávka dam at wintertime. At right, duckbill anchors being driven into the granular subgrade at Vaité earthfill dam

2.3. REHABILITATION OF FAILING JOINTS/CRACKS

The deformation that a traditional embedded waterstop can sustain is based essentially on the dimensions of the central portion of the bulb, therefore the maximum elongations that it can attain are in the order of a few centimetres. If the opening of the joint exceeds this elongation capability, traditional embedded waterstops fail (Figure 4 at left). Carpi patented external waterstop, conceived to accept much larger openings, is used to provide watertightness on failing joints or cracks. This waterstop is a multi-layered system installed over the joint/crack, exposed to the water of the reservoir, and sealed along the perimeter by a watertight mechanical seal. The various layers, which are site-specific, depend on the type of dam, on the expected opening of the joint, on the water head, and on the conditions of the subgrade. The layers solve different functions:

- a) Anti-puncture/sacrifice, to protect against aggressive subgrade - generally, a nonwoven geotextile or a geocomposite
- b) Support, to impede that the waterproofing liner intrudes in the active joint and, in case of very large openings and high water head, that it bursts - generally, this function is solved by one or more layers of flexible material, with lower or higher modulus depending on the needs, seldom by a rigid support
- c) Anti-friction: to avoid the waterproofing liner being affected by the movements of the under-layers - generally, a flexible layer
- d) Waterproofing: a geocomposite SIBELON® CNT.

The waterproofing geocomposite, typically 40 to 70 cm wide, is anchored so that it can elongate over its entire width (Figure 4 at middle). The geotextile having an elongation at break exceeding 250%, joint openings with order of magnitude of tens of centimetres/exceeding one metre are required before respectively the geotextile and then the geomembrane break. Concrete dams, CFRDs, RCC dams, and intake structures of ACFRDs and reservoirs, have been rehabilitated with this external waterstop. The same system has been adopted for new construction, on contraction joints of RCC dams and on peripheral+vertical joints of CFRDs, where it was designed for openings up to 30 cm.

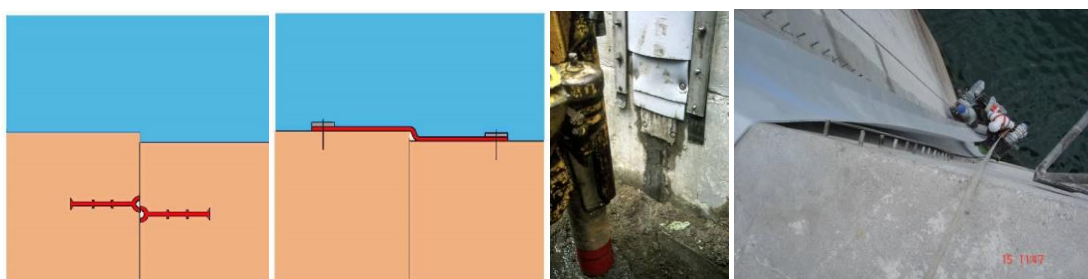


Figure 4. From left to right, conceptual behaviour of embedded waterstop and of Carpi external waterstop, typical layering (Platanovryssi 95 m high RCC dam, Greece 1998), and installation of the sacrificial and waterproofing layers at Usina da Pedra buttress dam, Brazil 2009

3. UNDERWATER INSTALLATION

All rehabilitation systems described above have been installed also in underwater conditions, adapting some anchorage components to the wet environment, for full-face rehabilitation (e.g. Lost Creek dam, USA 1997), for rehabilitation of large leaking areas (e.g. Turimiquire, Venezuela 2010/2011/2017), for repair of joints and cracks (e.g. Olai, Italy 2013, Lom Pangar, Cameroon 2017). At Olai gravity dam, underwater installation of the external water stop on three failing joints reduced seepage from 65 l/s to 0.3333 l/s (Figure 5).

In the last few years, a totally innovative underwater waterproofing technology, SIBELONMAT[®], has been developed to restore watertightness in embankment dams and canals without impacting on operation. The system consists of two watertight geomembranes connected to form a mattress. The connection of the geomembranes is designed to allow injecting between the two a ballasting filling material such as inexpensive cement grout. The lower geomembrane provides water tightness, the grout provides the ballast to anchor the mattress, and the upper geomembrane provides containment of the grout, protects the ballast during operation, and in canals improves hydraulic efficiency. SIBELONMAT[®] is prefabricated in 10 m wide mattresses having custom-made length to minimise junctions and facilitate placement. Adjoining mattresses are joined by watertight heavy-duty zippers pre-attached to each mattress during fabrication. Installation can be performed totally underwater and without stopping operation or reducing water speed.

This new technology has already been successfully installed on two canals with no reduction of water speed (Figure 5 at right). SIBELONMAT[®] can be considered also for new construction of embankment dams, to provide an impermeable upstream facing or an impermeable blanket even on very aggressive irregular subgrade, and of canals.



Figure 5. From left to right, joint 4-5 at Olai dam before and after underwater installation of Carpi external waterstop, and SIBELONMAT[®] installed underwater at Ismailia canal, Egypt 2016

4. PVC GEOMEMBRANE SYSTEMS IN NEW CONSTRUCTION

In new construction, PVC geomembranes are used to provide the water barrier in embankment dams and RCC dams, and as external waterstop for peripheral and vertical joints in CFRDs, and contraction joints in RCC dams. The geomembrane can be in exposed or covered upstream position, or as a geomembrane core in fill dams. In new embankment dams, the concept is to avoid the rigid upstream water barrier of CFRDs, and substitute it with a highly deformable exposed PVC geocomposite system, to construct a Geomembrane Facing Rockfill Dam (GFRD) designed to accommodate settlements and differential movements that can occur in the dam and between the deformable dam body and the concrete appurtenances. The upstream SIBELON[®] geocomposite allows adopting a very simple layering for the dam: zoning is not strictly required, a single fill material can be used, the drainage layer's thickness can generally be reduced, and depending of the design of the dam it can act also as base/anchorage layer for the waterproofing geocomposite.

The face anchorage can have different configurations. If the upstream base layer is made by extruded porous concrete curbs, the anchorage system consists of PVC anchor strips embedded in the extruded porous concrete curbs, to which the waterproofing geocomposite is heat-seamed, as shown in Figure 6.

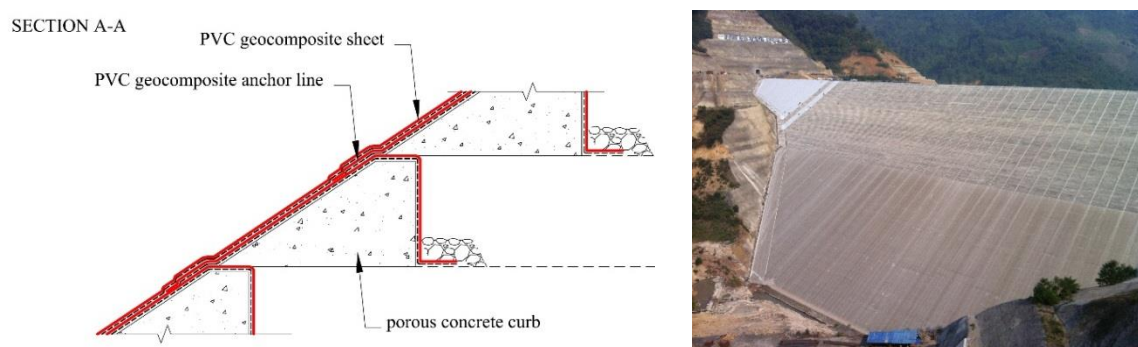


Figure 6. Face anchorage with PVC anchor strips embedded in curbs: concept and staged installation at Nam Ou VI 88 m high rockfill dam in Lao PDR

If curbs are not used, the PVC anchor strips are embedded in trenches excavated in the base layer, as shown in Figure 7. In alternative, anchorage can be made at points, by duckbill anchors or by deep grouted anchors as installed in hardfill dams and for rehabilitation of canals. Anchorage systems with deep anchors can be installed in any kind of subgrade, quickly and without any inconvenience.

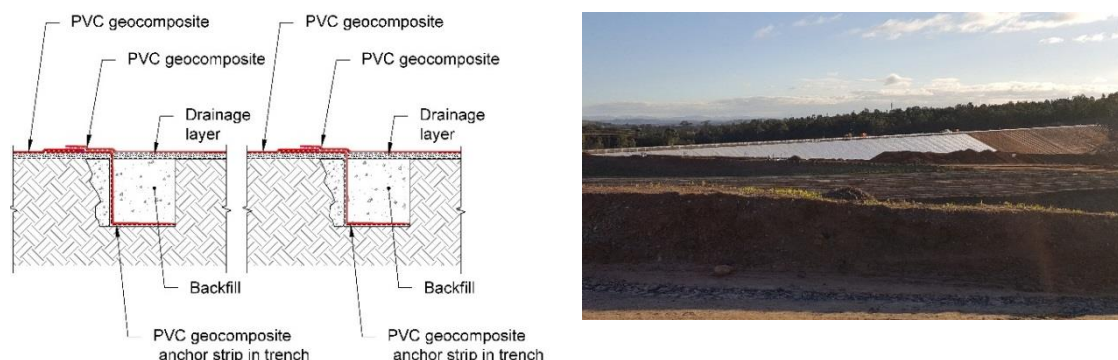


Figure 5. Face anchorage with PVC anchor strips embedded in trenches: concept and installation at Bulga new earthfill dam, Australia

All these methods have been successfully applied in several dams, allowing constructing very quickly, and at low cost, impervious dams consisting of compacted fill providing stability, and of a flexible upstream liner providing imperviousness, and capable of accommodating settlements and differential movements. In new RCC dams, the full-face waterproofing system is like the one described in rehabilitation of concrete dams; a covered option with concrete panels embedding the waterproofing geocomposite has also been adopted in several dams.

5. CONCLUSIONS

PVC geomembrane systems effectively restore watertightness in all types of leaking dams and joints, with little or no impact on operation of the dam, resisting demanding environmental conditions. They provide water barriers in new embankment dams and RCC dams. Their elongation capabilities allow resisting movements that would destroy other types of water barriers.

6. REFERENCES

1. ICOLD Bulletin 135 (2010), “*Geomembrane Sealing Systems for Dams - Design principles and review of experience*”, ICOLD, France.
2. Scuero, A., Vaschetti, G. and Subramanian, V. (2017), “*Geomembranes for long-term rehabilitation of dams*”, Proc. of Workshop on Latest Repair & Rehabilitation Technologies for Dams, Colombo.
3. Wilkes, J., Scuero, A. and Vaschetti, G. (2017), “*Geomembranes to Waterproof Embankment Dams*”, Proc. of USSD Annual Meeting and Conference, Anaheim.
4. Scuero, A. M., and Vaschetti, G.L. (2017), “*Three recent geomembrane projects on new RCC dams*”, Proc. of the 6th International Symposium on RCC dams, Zaragoza.
5. Scuero, A. M., and Vaschetti, G. L. (2005), “*Tackling uncertainties with geomembranes*”, Proc. of the 73rd Annual Meeting of ICOLD, Tehran.
6. Scuero, A., Vaschetti, G. and Machado do Vale, J. (2016). “*A unique case: new works at Chambon dam*”, Proc. of the 84th ICOLD Annual Meeting Symposium, Johannesburg.
7. Kratochvil, D., et al. (2011). “*Exposed geomembrane system at Moravka dam: 10 years performance*”, Proc. of Hydro 2011: Practical Solutions for a Sustainable Future, Prague.1

Water-filled Bladders, an Innovative Bearing Interface for Arch Dam Bracing

Alexandre Lochu¹, Thomas Pinchard¹

1- EDF-CIH (Hydro Engineering Center) – Technolac – 73373 Le Bourget du Lac - France

Email: alexandre.lochu@edf.fr

Abstract

Some existing arch dams can require the construction of a supporting downstream structure to improve their behavior. The bracing structure is generally rigidly connected to the dam, but in some cases the designer can seek a flexible connection that can adapt to the deformation mode of each structure and avoid hard points emergence and stress concentration. This has already been done at Kölnbrein dam in Austria, by the use of rubber pads. The paper presents a new solution to realize a flexible connection, allowing an excellent control of the forces transferred from the dam to its bracing structure. The solution relies on large inflatable jacks hydraulically connected to the reservoir. This EDF-patented solution also affords the distinct advantage of not requiring unloading the dam in order to load the bearings. This solution, based on the use of water-filled bladders, is under development at detailed design stage for a 50 m high arch dam. Some tests will be conducted at the end of 2017 on full scale prototypes (4 m x 11 m x 0,8 m), with a dedicated vertical test bench, in order to qualify bladders' suppliers and check the installation and filling process of the bladders.

Keywords: Arch dam, Support, Bearing, Inflatable, Rubber.

1. INTRODUCTION

Because of their original design – for example arch dams in large valleys – dams are sometimes affected by non-typical behavior, such as unstabilised irreversible displacements. In some cases, these troubles **can necessitate bracing of the dam**. The regulatory evolution, in terms of flood control or seismic protection, can also lead to a need for reinforcement.

A typical solution for bracing an existing concrete dam consists of building a **downstream concrete structure** to help support the dam, which will reduce its displacements as well as the stress applied to its foundation surface. This solution has already been used on dams such as Kölnbrein dam in Austria or Les Toules dam in Switzerland.

In this kind of project, **the control of the load that is transferred from the existing dam to the downstream bracing structure is critical**. Some reinforcement designs, such as Les Toules, require a fully rigid connection between the dam and its reinforcement, in order to make both structures behave as a monolith. In some other cases, such as for Kölnbrein dam where the massive reinforcement structure buttresses the lower section of the existing dam, the connection must be flexible in order to adapt to the deformation mode of each structure, namely the existing dam and the downstream bracing, avoiding hard points emergence and stress concentration. Consequently, the designer of the **Kölnbrein bracing used more than 600 neoprene pads** in order to bear the dam on its reinforcement structure [1]. These pads are mounted on adjustable steel wedges which allow control of the thickness of the bearings before their loading. The bearings developed for Kölnbrein have proved to be effective, but some disadvantages can be highlighted:

- the loads transferred by the neoprene pads depend on their shim adjustment, whose determining requires very accurate modelling. Moreover, the transferrable load is quite limited in the lower part of the dam because of the limited displacements at its toe;
- the loading of the reinforcement, and every modification of the shim adjustment of the pads, necessitate the unloading of the dam by emptying it;
- the monitoring of the actual transferred loads is arduous.

EDF has patented a new concept invented by A. Lochu, which avoids these disadvantages and offers some distinct advantages. The solution allows:

- **an excellent control of the loads applied** between both structures, whatever their relative displacements are;
- **an automatic and passive adaptation of the transferred loads** to the level of the reservoir;

- the loading of the reinforcement structure irrespective of the thermo-mechanical stress state of the dam during its commissioning, which **allows the scheme to continue operating without being dewatered and avoids all the associated costs and environmental impact related thereto.**

2. THE CONCEPT

The main idea is to use big **inflatable bladders filled with water** as interface elements between the downstream face of the dam and the upstream face of the reinforcement structure. As shown in Figure 1., the bladders act as jacks, applying opposite forces which only depend on the surfaces and pressures, but not (at first order) on the distance between the bearing surfaces. With this solution, the action of the reinforcement upon a dam is directly controlled in terms of load, and not in terms of displacement, unlike with elastic bearings. This aspect considerably facilitates the numerical modelling of the behaviour of both structures, which can be decoupled (for static loads).

The second point of the concept is that by hydraulically connecting the inflatable bladders to the upstream reservoir, the pressure profiles on the upstream face of the dam and inside the bearing devices are the same (according to the communicating vessels principle, and whatever the fitting level), as shown in Figure 2. The load transfer is thus proportional to the level of the reservoir, and adapts totally passively to the hydraulic upstream load on the dam.

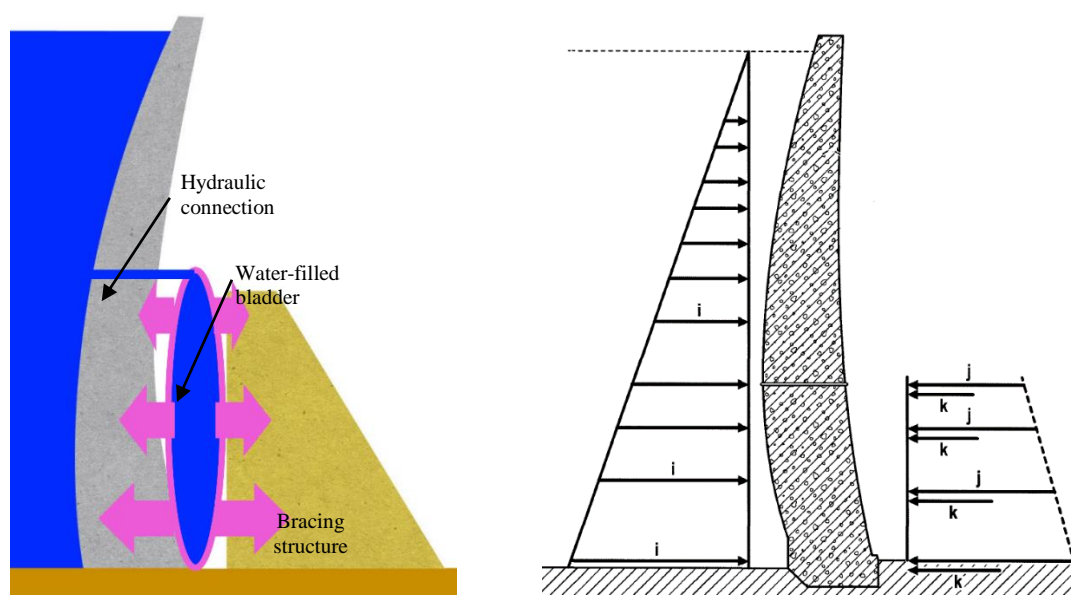


Figure 1 (left). Schematic cut-away drawing illustrating the concept.
Figure 2 (right). Pressure profiles applied on the upstream face (i) and on the downstream face of the existing arch dam (j = pressure in the bladders, k = mean pressure on the face, depending on the bladder's surface).

Moreover, if the hydraulic connection is permanent, then the system operates fully automatically. This also allows for compensation of the potential leaks of the bladders in order to avoid (or limit) pressure drops.

3. FROM CONCEPT TO DETAILED DESIGN

Based on this concept, EDF's Hydro Engineering Centre is currently developing a detailed design to reinforce a 57 m high arch dam with a 25 m high downstream structure. The name of the dam is not reported in the paper for confidentiality reasons, the owner awaiting the administration's authorization to carry out the project before communicating further.

The major questions to be solved by the design studies are discussed in the following sections.

3.1. GENERAL LAYOUT AND SIZING OF THE BLADDERS

The bladders could theoretically be made-up with any shape, and be laid out with any geometry, but regarding manufacturing rationalization and installation aspects, the best solution appears to be a layout with vertical strips.

The actual sizes of the bladders are also limited on the one hand by manufacturing and handling issues, and on the other hand by strength reasons.

The most critical aspect of the bladders is their thickness, which is actually the distance between the bearing surfaces of the dam and of its reinforcement structure (see Figure 3.). This distance corresponds to the diameter \emptyset of the free edges of the bladders, and the tension T in the membrane is directly proportional to it and to the internal water pressure p , according to the well-known formula (1):

$$T = p\emptyset/2 \quad (1)$$

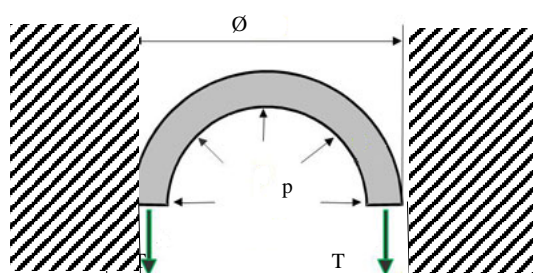


Figure 3. Typical cross section (not to scale) illustrating forces applying on free edges of the bladders.

An 80 cm thickness seems to us the minimum acceptable size in order to allow access to the inner space between the bearing surfaces, for exceptional maintenance purposes. Under a 5 bars working pressure (corresponding to the 50 m water height in the reservoir), the tension in the membrane is hence 200 daN/cm.

From our point of view, the most appropriate technology to fabricate the membrane is using rubber coated fabrics. This technology is already used for rubber dams, which are in some aspects quite similar to the bearing bladders. The usual global safety factor for the sizing of rubber dams' membranes is between 8 and 9. This factor takes into account concentration factor, creep, weathering and the chemical aggressiveness of the environment. The adaptation of the partial safety factors to the bladders' actual environment is aiming at this stage at a 5-6 global safety factor in order to maintain a safety factor of 3 at the end of the 20 years design lifetime. Therefore the initial strength of the coated fabric should be 1 000 -1 200 daN/cm for our project. Despite the fact that design tensions in rubber dams are usually lower than this, some references such as Ramspol barrier in the Netherlands prove that this strength is attainable. Indeed the initial strength of Ramspol coated polyamid fabric was ca. 2 000 daN/m [2].

It is also to be noted that the thicker the bladders are, the more space is wasted between them because of their free edges. A given mean pressure and a given thickness involve thus a minimum width of the bladders. In our case the aimed mean pressure goal is 70 % of the upstream pressure, which means the bladders must cover 70 % of the downstream face of the dam (along the height of the reinforcement structure).

In the light of the previous considerations, the following layout has been adopted for the project: 3.3 m wide bladders arranged along a vertical axis, the total height being divided into 2 rows in order to limit the length of the bladders to 11 m. This layout, illustrated by Figures. 4 and 5., allows the transfer onto the downstream reinforcement structure of approximately 50 % of the total hydraulic load applied on the arch.

Figures. 4 and 5 also show that the bladders will bear on the downstream face of the dam through concrete beams (drawn in green). These beams will be built in order to verticalize and offset the bearing surfaces. Indeed the double curvature of the dam, which makes the crest overhang the face, and which is different for each radial cross section, would make the construction of the reinforcement structure and the installation of the bladders much more complicated without these concrete beams. The same provision is also retained for the bearing surfaces onto the reinforcement structure, in order to create vertical access wells between each couple of bladders.

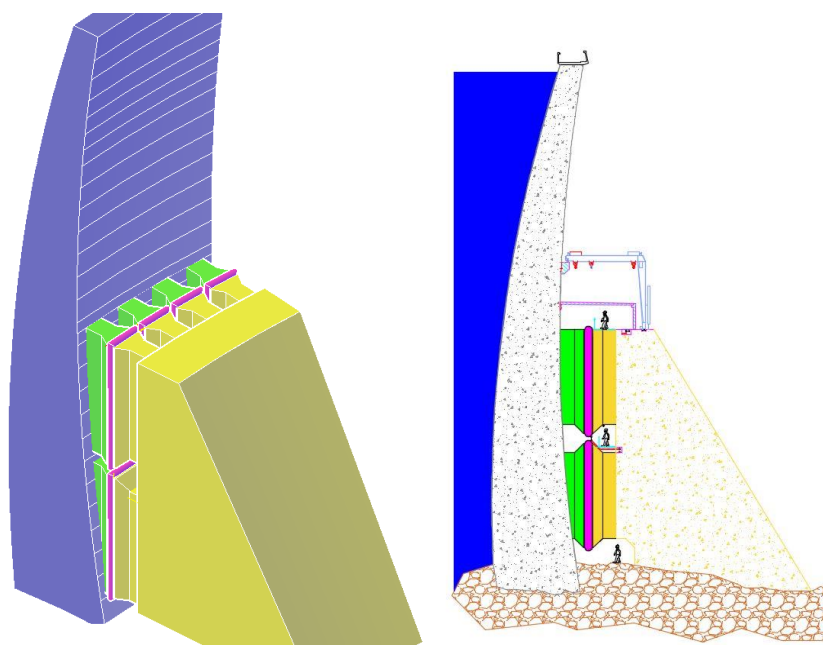


Figure 4 (left). 3D view of the layout of the bladders (drawn in magenta) for one block.
Figure 5 (right). Cross section of the layout of the bladders.

3.2. WATER SUPPLY NETWORK

Pressurizing of each bladder will be ensured by a fitting placed on top of it. Pressurizing only requires that the bladder be connected to the reservoir through one small hose, as demonstrated by Pascal's barrel experiment. The design of the network is in fact based on reliability considerations. The first retained principle is to dispatch the bladders between several independent networks, and to connect adjacent bladders to different networks in order to avoid a total loss of pressure on several blocks in case of failure of one network, as illustrated in Figure. 6.

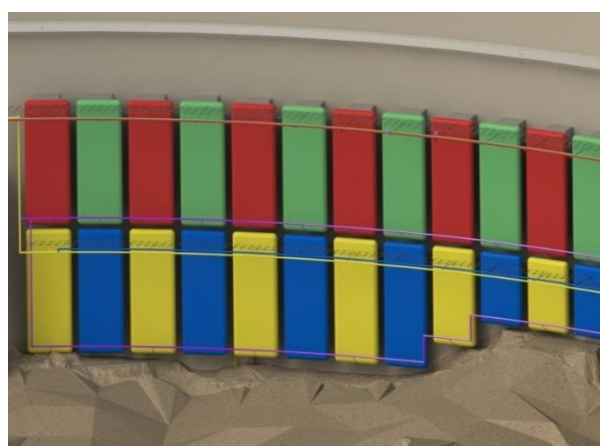


Figure 6. Layout of separate networks (each network has a different color).

Another fitting will be placed at the bottom of each bladder, for initial water filling.

The diameters of the pipes, hoses and fittings, and especially the ratio between them will determine the velocity in the different sections, and so the pressure drops along the hydraulic circuit. The diameters are thus defined by the acceptable losses of transferred loads for a given size of the failure point.

Our analysis leads to a diameter between 100 and 150 mm for the main pipes, 50 mm for the top pressurizing hoses, and 25 mm for the bottom filling fittings.

Depending on the specific environment of the dam, another function of the water supply network must also be to provide water treatment to avoid proliferation of bacteria and/or heating to prevent freezing. To that end, a closed loop water circulation can be achieved inside the bladders by using the bottom fittings.

3.3. INSTALLATION

The empty bladders will weigh about 1 ton each. Depending on the road accessibility to both the dam's crest and the crest of the reinforcement structure, the handling of the bladders can require the installation of permanent dedicated lifting tools. For instance, it can be a grappler on the dam's crest and a gantry crane on top of the reinforcement structure. In that case it is important to find a solution to limit the height of the bladders when packed for handling. One solution could be to roll them onto a reel. A low pressure air pre-filling will provide for correct shaping before water filling. Unless a bottom supporting cradle is installed, which seems unnecessary under working conditions, the handling fittings will have to support the weight of water required in order to achieve self-support by friction.

3.4. VANDALISM AND AGEING

One of the factors holding back the development of rubber dams in France is due to its (supposed) sensitivity to vandalism. In the case of inflatable bearing bladders, it is worth noticing that the bladders won't be reachable by passers-by, and can be easily fully protected by building a protection roof. Such a roof can also slow down the ageing of the rubber coating of the bladders by protecting them from UV, thermal and rain exposure.

4. QUALIFICATION TESTS

Several coated fabric products manufacturers have been contacted and have proposed solutions matching the project's strength and size requirements.

The next step now is to perform tests on full scale prototypes, that should start before the end of 2017. Beyond the questions of strength and water tightness of the bladders, the goal of these full scale tests will be to check some aspects difficult to accomplish on a small scale model. So the testing will require building a vertical dedicated testing bench in order to correctly simulate the behavior of the bladders and to check/adapt/define in particular:

- the handling and installation procedure;
- the filling procedure (how to control the final position of the bladder, to avoid the membrane folding and how to release the air during filling-up?);
- the actual final sizes, which depends on creep, friction/sliding;
- the need for a bottom supporting cradle (will the bladder progressively slide down?);
- the actual initial safety factor (on a smallest scale bladder).

Figure 7. shows the design of the testing bench. The physical bottom access will afford a good similarity to the on-site access conditions. The sidescuttles will afford a visual access to several points of one concrete/bladders' contact surface, that will allow to monitor sliding.



Figure 7. 3D views of the 13 m-high testing bench.

The qualification of the bladders will be completed by laboratory tests, with a special focus on ageing, and creep in particular.

5. CONCLUSIONS

The need for reinforcing existing dams will increase in the next decades because of ageing and increase in safety standards. Several projects involving the reinforcement of arch dams have been completed so far, and it often requires building a bracing structure downstream. The link between the existing dam and the new structure is a key issue and in most of the cases it has been designed as a rigid connection which does not allow adjusting or controlling the transferred loads. The Kölnbrein reinforcement project is, as far as we know, the only reference where adjustable devices have been used.

The new solution presented in this paper, is currently under development at a detailed stage and will enable transferring loads from an existing dam to a new supporting structure by using water-filled bladders. This new concept presents many benefits such as automatic adaptation of the load to the upstream water level, constant load regardless the differential displacement of the supports, and it does not constrain the normal operation of the existing dam for its implementation (no need for dewatering).

In order to demonstrate the feasibility of this solution, full scale prototypes will be tried on a test bench prior to their installation on an actual dam reinforcement project.

6. REFERENCES

1. Bärenthaler, G. et al. (1991), “*Remedial project for Kölnbrein arch dam – Design and construction*”, Österreichische Draukraftwerke, Carinthia, Austria.
2. Van Breukelen, M. (2013), “*Improvement and scale enlargement of the inflatable rubber barrier concept*”, MSc. Thesis, TU Delft, Netherlands.

Rockfill Dams Overtopping Risk Analysis

Ali. Komak Panah¹, Hamidreza. Rahmani²

1- Associate Professor, faculty of civil and environmental engineering, Tarbiat Modares University, Tehran, Iran

2- Phd candidate, faculty of civil and environmental engineering, Tarbiat Modares University, Tehran, Iran

Email: hr.rahmani@modares.ac.ir

Abstract

In hydraulic structures which are located in a natural environment, there is the possibility of system failure with increasing external forces acting on the structures. Stability and crest settlement of rockfill dams is a major factor in design which in some cases is very important (after construction and impoundment). Particle breakage in rockfill dams is the main cause of vertical deformations. Particle breakage changes resistance and deformation behavior of rockfill materials and this affects the performance of dams. For embankment dams the highest risk of damage is caused by water overtopping over the dams. The purpose of this research is to study rockfill dams settlement and freeboard height reduction that affect performance of dams, especially during the heavy flooding. Increasing in the probability of dams overtopping results in total destruction of the dam. In this research the overtopping risk analysis method has been studied and the effective parameters on overtopping risk analysis and the effect of particle breakage on overtopping risk of rockfill dams was investigated.

Keywords: particle breakage, rockfill dams, overtopping risk, Mahabad dam.

PREFACE

The risk concept has a long history and has been a main aspect of life since the beginnings of human experience. Applications of risk and safety analysis have been developed simultaneously by expanding various facets of technology in all branches of science, such as engineering and environment.

The main intentions of risk and safety analysis are to identify existing system threats and predict possible outcomes in the future to provide clearer ideas for making the best possible decisions. In other words, risk analysis not only provides quantitative support for decision makers, but also helps to find the most effective options for decision-making. For instance, engineers could never have designed systems such as great bridges, dams, sewer systems, and so on, without some form of risk assessment.

1. INTRODUCTION

1.1. DAM SAFETY

Dam safety is a major concern to the general public. In recent years, many countries have experienced frequent floods that may have overtop dams. Such deficiencies can cause dams to break and extreme floods to occur downstream. This leads to various problems such as loss of social capital, large scaled economical expenses, and the loss of life seriously [1,2]. In the case of modification of the structure, including repairs and reconstruction of the dam, economic feasibility and social goals need to be addressed. When evaluating the priority of the dam rehabilitation, a risk-based analysis is a potentially useful approach. Moreover, overtopping is one of the most important risk factors inducing dam failure. According to the International Commission on Large Dams [3] overtopping causes about 35% of all earth dam failures; seepage, piping, and other causes make up the rest. Accurate assessment of overtopping risk will provide useful information for managers in decision making such as formulating the emergency preparedness planning. For these reasons, dam overtopping risk analysis is very important to satisfy dam safety needs. In recent years, numerous studies have attempted to find and explore the possibility of a risk-based analysis in dam safety. Von Thun [4] studied the risk analysis method with U.S. Bureau of Reclamation (USBR) in order to estimate dam risk and risk expense. Cheng [5] estimated the dam overtopping risk considering the uncertainties of hydrology and hydraulics using the advanced first-order second-moment (AFOSM) method and fault tree analysis; Langseth and Perkins [6] proposed the procedure of dam risk analysis; Kwon and Moon [7] studied the dam overtopping risk using probabilistic concepts and the improved Monte Carlo

simulation was used to solve the hydrologic dam risk model; Kuo et al. [8] used five uncertainty analysis methods to calculate the overtopping risk and the results were compared with each other. Sun and Huang [9] established the overtopping risk model induced by concurrent flood and wind by considering the uncertainties of flood, wind wave, storage capacity of reservoir and discharge capacity; Mo et al. [10] established the overtopping risk model under the joint actions of flood and wind wave, and the Integrate-FOSM method was used to calculate the overtopping risk.

1.2. PARTICLE BREAKAGE IN ROCKFILL

Behavior of granular media is related to mineralogical composition, particle grading, size, shape, fragmentation and stress conditions. Breakage of the constituent components (grains) of a soil structure due to imposed stresses, called “particle breakage”, has arisen in many soil-rockfill masses such as rockfill dams and breakwaters as well as in many conventional laboratory tests under normal pressures. The related phenomenon has been studied in various laboratory tests, e.g., triaxial, consolidation and uniaxial [11,12,13,14], which showed that many engineering characteristics of granular materials such as strength (stress–strain behavior), deformability, pore pressure distribution and permeability are greatly influenced by the level of breakage of materials [11,15]. Marsal [13], perhaps the first to deal with the concept of crushing of particles, verified the breakage phenomena of particles in rockfill materials in a large-scale triaxial test, summarizing his study as follows: “It seems that phenomenon of fragmentation is an important factor that impacts shear resistance and potentiality of compaction of grain materials and this phenomenon is effective on aforesaid parameters in different conditions of implementing stresses such as confining pressure stage or stage of divertive loading in triaxial test.” Among other researchers [11,12,16], Varadarajan et al [17] presented the ratio of principal stresses (σ_1/σ_3) imposed on different rock materials at failure in triaxial tests. Also, many researchers demonstrated that particle breakage led to a reduction in void ratio, leading to compaction of the material. Marsal [13] believed that changes in void ratio were due to new arrangement of particles after breakage. Lade and Yamamuro [11] and Yamamuro and Lade [12] concluded from testing sand under different confining pressures (from 0.5 to 70MPa) that breakage of particles played the major role in changing the volume of the material.

Particle breakage index can be divided into different categories based on four methods. The first one is the PSD method, which is based on the differences of PSD before and after test. This method produced a single index, such as B15 [18], B10 [19], Bg [13] and Bt [20], and a global index, such as Br [21], BrE [22]. The second one is fine content (FC) method ($d < 0.075$ mm) [23]. The third one is area method [24,25,26], which is based on the increasing particle area during test and the last one is the discrete element method (DEM) [27,28,29,30], which simulates particle breakage by a discrete element software. The greater confining pressure, the more contact force among particles, which leads to the greater particle breakage. In addition, greater coefficient of uniformity C_u means more intermediate particles, and the PSD curve is distributed in a wider range, resulting in more contacts among particles. A decrease in the force of each particle due to increasing contacts causes decrease in the particle breakage.

The breakage is usually expressed quantitatively by the Breakage Index, Bg [13]. The value of Bg is calculated by sieving the sample using a set of sieves before and after testing. The percentage of particles retained in each sieve is determined at both stages. Due to the breakage of particles, the percentage of particles retained in the large size sieves will decrease and the percentage of particles retained in the smaller size sieves will increase. The sum of the decreases will be equal to the sum of the increases in the percentage retained. The decrease (or increase) is the value of the breakage factor, Bg. generally, the friction angle decreases with decreasing Bg. The effect of confining pressure on Bg is more significant for the high compacted materials.

1.3. MAHABAD DAM

The Mahabad storage dam specification presented in Table 1.

Table 1 . Mahabad dam specification

Type of dam	ECRD
Dam height	47.5 m
Crest length	700 m
Crest width	8 m
Dam body volume	1.66 Mm ³
Reservoir capacity	197.8 Mm ³
Power capacity	6 Mwat
Year of construction	1970

2. THE OVERTOPPING RISK MODEL FOR ROCKFILL DAM

2.1. OVERTOPPING RISK MODELING INDUCED BY CONCURRENT FLOOD AND WIND

Overtopping can be defined as when flood outlet works are notable to release water fast enough and the water level rises above the allowable safe height of the dam. To evaluate the overtopping risk associated with dam failure, we need to establish a method to transform the water surface level into overtopping probability. Assume that H_c is the dam height, H_0 is the initial water surface level, H_f and H_w is the increasing water surface level by the flood, wind respectively. Then, overtopping will happen when [31,32]

$$H_0 + H_f + H_w \geq H_c \quad (1)$$

Assume that H_0, H_f, H_w are independent variables, and they are all the function of time. Then, $H_0 + H_f + H_w$ can be expressed by a stochastic process of $H(t)$. Flood and wind can be considered as an annual periodic random process. However, the largest effective wind during flood season within a year is used in earth and rockfill dam overtopping risk evaluation. Flood discharge and storage capacity are constant random process. Therefore, $H(t)$ can be considered as an annual periodic random process. The dam overtopping risk can be defined as the probability that the water surface level of reservoir exceeding the dam height. Then, the formulation associated with MCS(Monte Carlo Simulation) for dam overtopping risk analysis induced by concurrent flood and wind can be represented as follows.

$$P_{FW} = P(H(t) \geq H_c) = P(H_0 + H_f + H_w \geq H_c) \quad (2)$$

The flowchart for dam overtopping risk analysis is illustrated in Fig. 1. As shown in Fig. 1, the procedure of this research includes three major steps [33,34]

(1) Identifying and assessing the important factors which may affect reservoir routing or overtopping. Fault tree analysis is adopted to assess the main important factors which may affect the risk of overtopping, and concluded with the following important uncertainty factors: initial water level, rainfall, T-year return period flood, wind velocity, dam height, and reservoir release, etc. (2) Data collection and analysis for reservoir routing and uncertainty analysis. Collecting the records of annual peak discharges and conducting a hydrological frequency statistical analysis to obtain return periods of discharges; using reservoir routing to calculate the highest water level during a flood; and defining the performance function and assigning distributional properties of uncertainty factors. (3) Performing reservoir routing incorporating uncertainty analysis and dam overtopping risk analysis. The uncertainty variable sets generated in step 2 are used in reservoir routing model that considers rainfall-runoff analysis, wind wave setup and run-up. The overtopping risk model are then analyzed to evaluate dam overtopping probability.

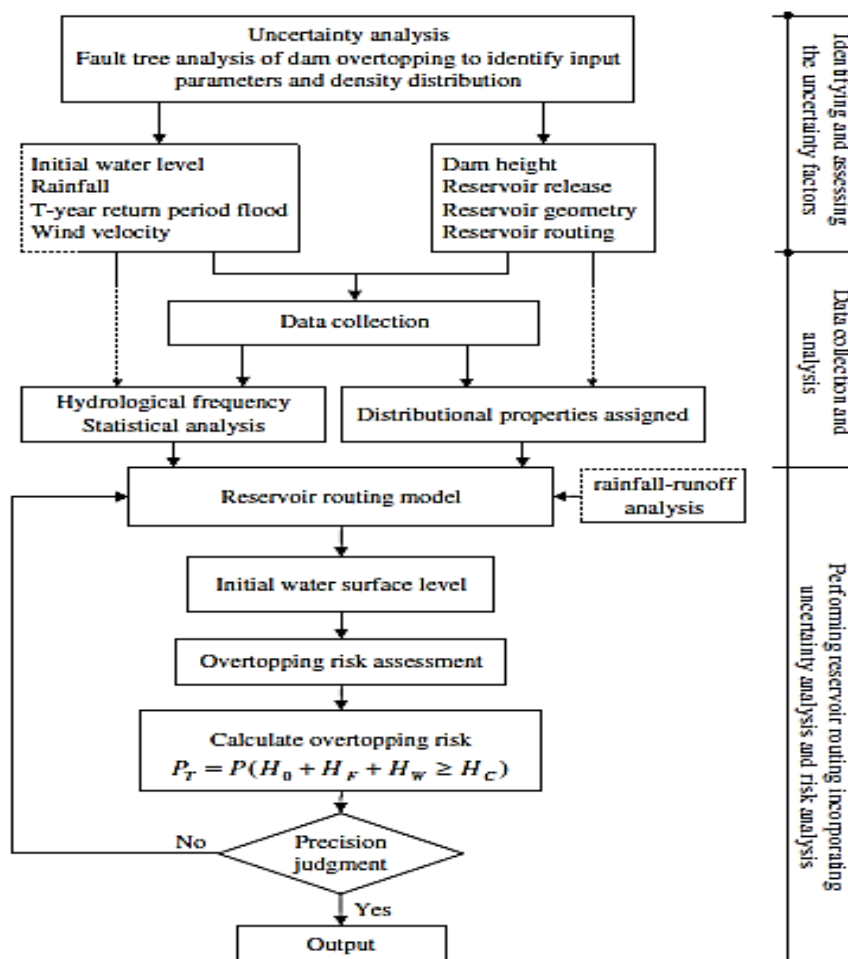


Fig1. Flowchart for calculating overtopping risk[35]

Overtopping happens when the flood outlet cannot release water fast enough and water rises above the dam and spills over (Fig. 2).

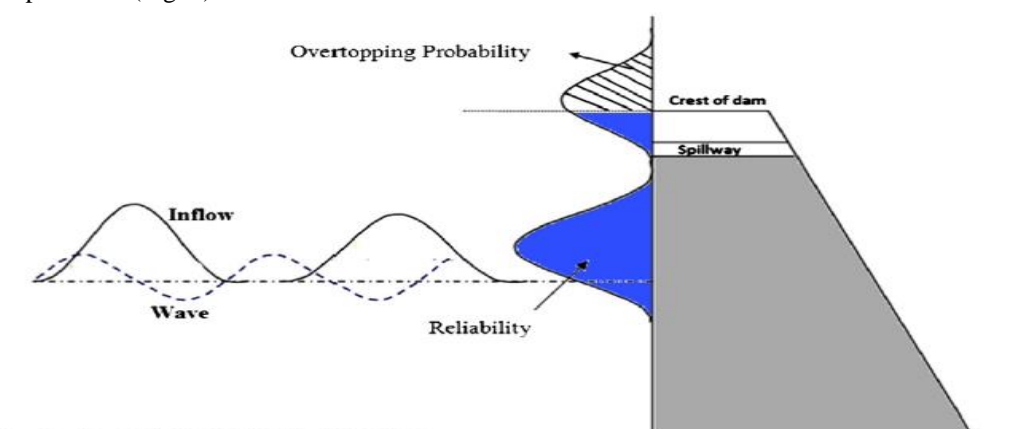


Fig 2. Overtopping risk concept based on probabilistic approach[36]

2.2. UNCERTAINTY ANALYSIS

Uncertainty is also called stochastic, which is a concept of stochastic mathematics. In this paper, the uncertainties of flood, wind wave, initial water surface level, and dam height are studied.

2.2.1. FLOOD

Flood of certain frequency is a stochastic event and it often follows distribution of P-III type. The increased water surface level H_f induced by flood can be calculated using water balance method[37]. For flood probability is assumed to follow distribution: Gumbel Max, General Extreme Value, Log-Logistic, Gamma, Log-Gamma, Pearson 5, Log-Pearson 3, Normal.

2.2.2. WIND WAVE

Wind velocity and wind direction can be considered as a stochastic process. So, the increased water surface level e and wave run-up h_p induced by wind are also random variables. Only the wind blowing to the dam during flood process, which is called “effective wind”, contributes to dam overtopping risk. Probability of maximum wind velocity W during certain time usually follows extreme type I distribution. The distribution function and distribution density function can be expressed by[38]. For wind wave probability is assumed to follow distribution: Gumbel Max, General Extreme Value, Weibull, Gamma, Log-Gamma, Normal, Log-Normal, Pearson 5, Log-Pearson 3.

2.2.3. INITIAL WATER SURFACE LEVEL

Uncertainty of initial water surface level is caused by operation, management, and so on. It is difficult to estimate the probability distribution to reflect the property of initial water surface level.

2.2.4. DAM HEIGHT

Uncertainty of dam height is induced by measure, construction error, and so on. Generally, dam height is assumed to follow normal distribution. The designed dam height is set to mean value, and the standard deviation is usually small [39]. Settlement and displacement inside the rockfill support shells during construction and operation not exceeding 0.6% to 0.8% and 0.1% and 0.2% respectively of the height of the dam. Relevant literature suggests settlement generally ranges between 1% and 3% during construction and between 0.2% and 1% during operation. Horizontal displacements are generally less than half of settlement. Settlement at a given time varied parabolically, with maximum settlement near the middle third of the dam; this is expected, since settlement is a function of the thickness of the compressible layer and the overburden[40].

3. SOLUTION METHOD OF DAM OVERTOPPING RISK MODEL

3.1. IMPROVED MONTE CARLO SIMULATION

The MCS method does not need to consider the complex interactions among random factors. The method is a statistical sampling technique that generates random variables according to the distributional property and provides numerical evaluations of the probabilistic features of the system response. The procedure for calculating dam overtopping risk by MCS is as follows: (1) generate random number corresponding to the probability distribution of each random variable; (2) substitute the random number into performance function and evaluation the system response; and (3) the dam overtopping risk is obtained after many times repeated test [41]. In MCS, it is important to generate random number that following the given probability distribution. Generally, simple random sampling is used to generate random number, and the sampling efficiency is low and unstable. It firstly generates random number between 0 and 1, and then generates sample value from the distribution function of random variables using reverse method and calculates the failure probability. Nevertheless, LHS method is an improvement of simple random sampling, and it is a statistical sampling method which has sample recording ability. The probability distribution of each variable is subdivided into N ranges with an equal probability of occurrence ($1/N$). Random values of the basic variable are efficiently simulated such that each range is sampled just once without repetition. LHS can be defined as follows [42,43]:

$$x_{i,j} = F_j^{-1}\left(\frac{1}{n} [P_{i,j} - r_{i,j}]\right) \quad (3)$$

where $r_{i,j}$ is the random number between 0 and 1 that follows the uniform distribution, and $P_{i,j}$ is random permutation.

The parametric method is usually used in dam overtopping risk evaluation. It reflects the linear relationship while neglects the important nonlinear characteristic of variables. Recently, nonparametric kernel

density estimation (NKDE) method has gained popularity in a variety of fields. This method has the advantage of not requiring assumptions about the distribution. The shapes of nonparametric density functions are directly determined by the data which avoid the difference between simulated probability density distribution and real distribution [43]. Kernel density estimation (KDE), a commonly used nonparametric density estimation method, is introduced by Rosenblatt [44]. By assuming that x is the real data where x_1, x_2, \dots, x_n are independent identically distributed real observations, $K(\cdot)$ is a kernel function, n is the sample size, and h is a bandwidth parameter assumed to tend to zero as n tends to infinity. The nonparametric density function can be defined as [43].

3.2. MEAN-VALUE FIRST-ORDER SECOND-MOMENT METHOD

MFOSM is an approximately analysis method and it assumes that the uncertainty features of a random variable can be represented by its first two moments [33]. This method is based on the Taylor series expansion of the performance function $Z = g(x_1, x_2, \dots, x_n)$ linearized at the mean value μ_{x_i} of the random variables. For most practical applications, information on higher-order moments and cross-product moments is not easily available. So, the first-order approximation of Z is used.

3.3. LATIN HYPERCUBE SAMPLING (LHS)

There are some reduction variance techniques to increase the precision of the Monte Carlo simulation outcome without needing to increase the sample size [45]. Some of the most important methods of variance reduction are antithetic variates technique, control variates, importance sampling technique, Latin hypercube sampling (LHS), correlated sampling, and stratified sampling technique [45]. LHS is one of the main variance reduction techniques that can increase the efficiency of the output statistics parameters. In this method, the range of each variable is divided into n non-overlapping intervals with the equal probability $1/n$. Then, a random variate is selected from each range with regards to the desire probability distribution [45].

4. THE RESULTS OF OVERTOPPING RISK ANALYSIS IN EMBANKMENT DAMS IN WORLD

Goodarzi et al [36] studied overtopping risk analysis about the Meijaran dam in Iran. From these results it can be concluded that rising water levels in the reservoir would result in the increasing overtopping probability based on both the MCS and LHS techniques. For instance, the probability of overtopping in $T = 20$ -year from $H_0 = 46$ to $H_0 = 49$ increased from $5.28E_{-10}$ to $1.82E_{-07}$ based on the MCS and LHS methods, respectively. On the other hand, the results revealed that wind speed could have a great impact on reservoirs situated in windy areas. Dam overtopping probabilities at $T = 20$ -year, $T = 2$ -year and $H_0 = 49$ were found to be 56.14% and 55.49% greater than the risk in the same condition without considering the wind effect.

Goodarzi et al [46] studied overtopping risk analysis about the Doroudzan dam in Iran. Based on the achieved results, by increasing the initial water level in each step, the probability of overtopping (in a constant return period) was raised for both uncertainty approaches adopted in this study. To show the effect of increasing initial water level in the reservoir on the risk of overtopping, the percentage of increasing risk in different water levels, On the other hand, the results revealed that wind speed could have a great impact on reservoirs situated in windy areas, and the probability of overtopping has been increased by increasing wind speeds in different return periods. Based on the results LHS method, the overtopping risk summary, the inclusion the uncertainty of key variables results in an expanded range of overtopping risks in different return periods, and provide significant information for decision makers to identify the critical parameters needed to effectively monitor, and detect the events that indicate a developing failure mode.

Chongxun et al [47] studied overtopping risk analysis about the Chengbihe reservoir in China. The results indicate that increasing the reservoir level by 0.40 m can increase storage by 16 million m^3 and lead to a corresponding mean annual direct economic profit of about 100 million CNY while at the same time protecting the reservoir dam from overtopping.

Sun et al [37] studied overtopping risk analysis about the Dongwushi reservoir in China. The application results show that the dam overtopping risk is calculated as $5.00 * 10^{-6}$ and $6.63 * 10^{-6}$ using the improved MCS method and MFOSM method, respectively. The overtopping risk computed by the improved MCS method is slightly lower than that computed by the MFOSM method. However, there are some limitations in this research. Only dam overtopping risk induced by concurrent flood and wind is studied in this paper.

5. MAHABAD DAM OVERTOPPING RISK ANALYSIS

Mahabad dam is the oldest rockfill dams in Iran that is located Orumieh lake basin. Since the dam after construction and impoundment have been much vertical settlement and horizontal displacements of the dam body and So far, two stages of rehabilitation has been done on the dam. Given that in most previous studies on the overtopping risk of earth dams vertical settlement and horizontal displacement of the dam is discussed less. We will discuss to evaluate the overtopping risk analysis of Mahabad dam based on the displacement which the impact of particle breakage and the results will be presented in the future.

6. CONCLUSION

Dam overtopping risk assessment and uncertainty analysis by mathematical and statistical methods provide useful information for managers. The paper demonstrates the procedure of evaluating overtopping probability considering the joint occurrence of wind and flood events subjected to uncertainties. The uncertainties of dam height, initial water surface level, precipitation, and wind velocity are considered in analyzing the overtopping risk.

We will discuss to evaluate the overtopping risk analysis of Mahabad dam based on the displacement which the impact of particle breakage and the results will be presented in the future.

7. REFERENCES

1. Yanmaz, A.M., Gunindi, M.E., (2008). "Assessment of overtopping reliability and benefits of a flood detention dam". Canadian Journal of Civil Engineering 35 (10),pp. 1177–1182.
2. Hsu, Y.-C., Tung, Y.-K., Kuo, J.-T., (2011). "Evaluation of dam overtopping probability induced by flood and wind". Stochastic Environmental Research and Risk Assessment 25 (1),pp. 35–49.
3. International Commission on Large Dams (ICOLD), (1973). "Lessons from Dam Incidents", reduced edition, Paris.
4. Von Thun, J.L., (1987). "Use of risk-based analysis in making decisions on dam safety". In: Duckstein, L., Plate, E. (Eds.), Engineering Reliability and Risk in Water Resources. M Nijhoff, Dordrecht.
5. Cheng, S.T., (1993). "Statistics of dam failure". In: Yen, B.C., Tung, Y.K. (Eds.), Reliability and Uncertainty Analysis in Hydraulic Design. ASCE, New York, NY, pp. 97–105.
6. Langseth, D.E., Perkins, F.E., (1983). "The influence of dam failure probabilities on spillway analysis". In: Proceedings of the Conference on Frontiers in Hydraulic Engineering. ASCE, pp. 459–464.
7. Kwon, H.-H., Moon, Y.-I., (2006). "Improvement of overtopping risk evaluations using probabilistic concepts for existing dams". Stochastic Environmental Research and Risk Assessment 20 (4), pp. 223–237.
8. Kuo, J.-T., Yen, B.-C., Hsu, Y.-C., et al., (2007). "Risk analysis for dam overtopping – Feitsui reservoir as a case study". Journal of Hydraulic Engineering – ASCE 133 (8), pp. 955–963.
9. Sun, Y., Huang, W.J., (2005). "Risk analysis on overtopping for operation management of reservoir". Journal of Hydraulic Engineering 36 (10), pp. 1153–1157.
10. Mo, C.X., Dong, Z.C., Ma, R.Y., et al., (2008). "Application study on overtopping risk analysis for Guangxi Chengbihe reservoir by integrate-FOSM method". Journal of Hydroelectric Engineering 27 (2), pp. 44–49.
11. Lade, P. V., Yamamuro, J. A., & Bopp, P. A. (1996). "Significance of particle crushing in granular materials". Journal of Geotechnical Engineering, 122(4), pp. 309–316.
12. Yamamuro, J. A., & Lade, P. V. (1996). "Drained sand behavior in axisymmetric tests at high pressures". Journal of Geotechnical Engineering, 122(2), pp. 109–119.
13. Marsal, R. J. (1967). "Large scale testing of rockfill materials". Journal of the Soil Mechanics and Foundations Division, Proceedings of the American Society of Civil Engineers, 93(SM2), pp. 27–43.
14. Marsal, R. J. (1973). "Mechanical properties of rockfill". In R. C. Hirshfeld & S. J. Poulos (Eds.), Embankment-dam engineering, casagrande volume (pp. 109–200). New York: John Wiley & Sons, Inc.
15. Lade, P. V., Yamamuro, J. A., & Bopp, P. A. (1996). "Significance of particle crushing in granular materials". Journal of Geotechnical Engineering, 122(4), pp. 309–316.

16. Indraratna, B., Wijewardena, L. S. S., & Balasubramaniam, A. S. (1993). “*Largescale triaxial testing of greywacke rock fill*”. Géotechnique, 43(1), pp. 37–51.
17. Varadarajan, A., Sharma, K. G., Venkatachalam, K., & Gupta, A. K. (2003). “*Testing and modelling two rockfill materials*”. Journal of Geotechnical and Geoenvironmental Engineering, ASCE, 129(3), pp. 206–218.
18. Lee KL, Farhoomand I. (1967). “*Compressibility and crushing of granular soil*”. Canadian Geotechnical Journal;4(1): pp.68-86.
19. Lade PV, Yamamuro JA, Bopp PA. (1996). “*Significance of particle crushing in granular materials*”. Journal of Geotechnical Engineering ;122(4):
20. Nakata AFL, Hyde M, Hyodo H, Murata H. (1999), “*A probabilistic approach to sand particle crushing in the triaxial test*”. Geotechnique 1999;49(5):567e83.
21. Hardin BO. (1985). “*Crushing of soil particles*”. Journal of Geotechnical Engineering;111(10).
22. Einav I. (2007a) “*Breakage mechanics -Part I: theory*”. Journal of the Mechanics and Physics of Solids 55(6).
23. Miura S, Yagi K, Asonuma T. (2003). “*Deformation-strength evaluation of crushable volcanic soils by laboratory and in-situ testing*”. Soils and Foundations;43(4): pp.47-57.
24. Miura N, Yamamoto T . (1976) Particle-crushing properties of sands under high stresses. Technology Reports of the Yamaguchi University.
25. Cristian JNG. (2011) “*Mechanical behavior of rockfill materials-Application to concrete face rockfill dams*”. PhD Thesis. Paris: Ecole Centrale Paris.
26. Russell AR, Khalili N. (2004). “*A bounding surface plasticity model for sands exhibiting particle crushing*”. Canadian Geotechnical Journal;41(6)
27. Cheng YP, Nakata Y, Bolton MD. (2003). “*Discrete element simulation of crushable soil*”. Geotechnique;53(7).
28. Lobo-Guerrero S, Vallejo LE, Vesga LF. (2006). “*Visualization of crushing evolution in granular materials under compression using DEM*”. International Journal of Geomechanics 2006;6(3): pp.195-200.
29. Bagherzadeh Kh A, Mirghasemi AA, Mohammadi S. (2011). “*Numerical simulation of particle breakage of angular particles using combined DEM and FEM*”. Powder Technology;205(1-3): pp.15-29.
30. Wang J, Yan H. (2012). “*DEM analysis of energy dissipation in crushable soils*”. Soils and Foundations 52(4).
31. Cheng, S.T., (1982). “*Overtopping Risk Evaluation for an Existing Dam*”. PhD Thesis, University of Illinois, Urbana.
32. Sun, Y., Huang, W.J., (2005). “*Risk analysis on overtopping for operation management of reservoir*”. Journal of Hydraulic Engineering 36 (10), pp. 1153–1157.
33. Kuo, J.-T., Hsu, Y.-C., Tung, Y.-K., et al., (2008). “*Dam overtopping risk assessment considering inspection program*”. Stochastic Environmental Research and Risk Assessment 22 (3), pp. 303–313.
34. Hsu, Y.-C., Tung, Y.-K., Kuo, J.-T., (2011). “*Evaluation of dam overtopping probability induced by flood and wind*”. Stochastic Environmental Research and Risk Assessment 25 (1), pp. 35–49.
35. Sun, Y., Chang, H., Miao, Z., Zhong, D., (2012), “*Solution method of overtopping model for earth dams*”. Safety Science, 50, 1906-1912.
36. Goodarzi, E., Lee, T. S., Ziaei, M., (2012), “*Dam overtopping risk using probabilistic concepts – Case study: The Meijaran Dam, Iran*”, Ain Shams Engineering Journal.
37. Li, Q.F., Long, S.J., (2006). “*Risk assessment of dam overtopping*”. Water Power 32 (7), pp. 20–22.
38. SL274-2001, (2001). “*Design Code for Rolled Earth-rock Fill Dams*”. China Water Power Press, Beijing.
39. Mo, C.X., Dong, Z.C., (2007). “*Application of interval analysis to evaluating overtopping risk*”. Water Power 33 (6), pp. 16–18.
40. International Commission On Large Dams ICOLD, (1993). “*Rock Materials for Rockfill Dams-Review and Recommendations*”, Bulletin92.

41. Ma, R.Y., (2004). "*Risk Analysis Methods and its Application for Dam*". Science Press, Beijing.
42. McKay, M.D., Beckman, R.J., Conover, W.J., (1979). "A comparison of three methods for selecting values of input variables in the analysis of output from a computer code". *Technometrics* 21 (2), pp. 239–245.
43. Langseth, D.E., Perkins, F.E., (1983). "The influence of dam failure probabilities on spillway analysis". In: *Proceedings of the Conference on Frontiers in Hydraulic Engineering*. ASCE, pp. 459–464.
44. Rosenblatt, M., (1956). "Remarks on some nonparametric estimates of a density function". *Annals of Mathematical Statistics* 27 (3), pp.832–837.
45. Tung YK, Yen BC, Melching CS. (2005) "*Hydro systems engineering reliability assessment and risk analysis*". New York: McGraw-Hill Professional.
46. Goodarzi, E., Lee, T. S., Ziaei, M., (2014), "Risk and uncertainty analysis for dam overtopping – Case study: The Doroudzan Dam, Iran", *Hydro-environment Research*, 8, 50-61.
47. Chongxun, M., Fanggui, L., Mei, Y., Rongyong, M., Guikai, S., (2008), "Risk analysis for earth dam overtopping", *Water Science and Engineering*, Vol.1, No.2, 76-87.

Study of the Sarough Dam Fusegates

Komeil Samet¹, Mojtaba Ahmadi², Mohammad Ashrafi³, Khosrow Hoseini⁴

1- Ph.D. student, Department of Water engineering and Hydraulic structures, Faculty of Civil engineering, Semnan University, Semnan, Iran.

1, 2 & 3- West Azerbaijan Regional Water Company, Iran.

4- Associate Prof. Department of Water engineering and Hydraulic structures, Faculty of Civil engineering, Semnan University, Semnan, Iran.

Email: k.samet@semnan.ac.ir

Abstract

Dam construction industry has concerned specific attention to engineering economy, over the past years; so in this direction the topic of emergency fusegates has considered as a new technology since 1989, in all over the world. Fusegate is a simple, safe, and robust structure in increasing live storage or spillway capacity and a mechanical equivalent of a fuse plug. Although the installation of gates with different types and heights might practically be difficult, but its lower annual cost, flexibility in operation and smaller wasted water resulting from gates tipping justifies their selection as a more desirable solution. In this paper, the fusegates of Sarough storage dam (Googerdchi) in West-Azerbaijan province is studied and analyzed. The fusegates are installed for the first time in Iran, on Sarough dam spillway instead of radial gates. By installing these gates, the storage capacity of the reservoir increased up to gates overhead level for about 10 mcm. Flood hydrograph in six different return periods (from 2 to 1000 years) of the dam, shows that dam capacity has increased by equipping with fusegates. In addition, a comparison discharge-time-reservoir level chart between 1st to 6th individual fusegate overthrow periods is done.

Keywords: Fusegates, Sarough Dam, Spillway Capacity, Flood.

1. INTRODUCTION

Increasing the storage capacity of existing reservoirs might be considered an economical and effective alternative for their alleviation. Fusegates installation is a comparatively new alternative, which has increased in popularity during recent years due to its numerous advantages. Since their first real-world application in the Lussas Dam in 1991, they have been widely used in over 50 dams all over the world and have gained considerable recognition as a safe and economical tool for providing extra water supply (Chevalier, 2004). Fusegates are essentially a technical method to increase the maximum water level without structural dam heightening. Fusegates may be efficiently implemented to increase spillway capacity without sacrificing existing reservoir storage. In fusegates system, gates are placed side-by-side to fill in the original spillway width. (Afshar and Takbiri, 2012). The fusegated spillway is favored to pass the design flood with maximum water level not exceeding that of original free spillway. Different gates combinations, their setting aprons, and varying routing characteristics of the fusegated spillway should be employed to fulfill this requirement. The principal advantage of fusegates over fuse plugs lies in their operational schedule. Fuse plugs completely fail when they overtop whereas a number of tipping fusegates depends on flooding conditions and design tipping head of the individual gates.

Fusegates were invented in 1989 by Francois Lemperiere as a simple, robust, and safe system to increase live storage or spillway capacity. The system has been patented by Hydroplus International in the United States, Europe, and most other countries. It is implemented in more than 40 dams in 14 different countries across 5 continents (Falvey and Treille, 1995). This system can be a good alternative for radial gates without any need to mechanical and electrical equipment and continuous maintenance; such a structure can be placed on running or even constructed dams separately. By installing this gate, the capacity of reservoir can be increased by maintaining safety factor and without any need to increase dam height. In some special cases this structure can be used to increase the capacity of overflow drain (discharge) without increasing the length of overflow threshold.

The fusegates will increase the capacity of the spillway without exceeding the flood pool level. Fusegates have the shape of a labyrinth weir and thus pass more flow than an equivalent straight crest. Among different type of spillways, the labyrinth one is a useful structure for the reservoirs having narrow floodways in which, by increasing the crest length in a constant width, the spillway enhances its conveyance capacity by maintaining upstream water level (Hosseini et al., 2015). A labyrinth weir (Fig. 1) is a type of polygonal overflow structure that has a distinct geometric shape (triangular, trapezoidal, or rectangular cycles in plan-view) and advantageous

hydraulic characteristics. Labyrinth weirs are used as primary or auxiliary spillways (new and rehabilitated structures) to increase discharge capacity, regulate water levels (e.g., intake ponds, residential areas, rivers with high max/min flow ratios), or as a cost-effective, passive-control alternative to gated control structures. (Crookston and Tullis, 2013). The most hydraulically efficient design of the labyrinth spillway is not always possible because of limited construction costs and/or implementation issues in construction procedure must be considered for the overall effectiveness of the project (Paxson et al., 2011). A labyrinth spillway is an overflow weir folded in plan view to provide a longer total effective length for a given overall spillway width. A labyrinth spillway has advantages compared to the straight overflow weir and the standard ogee crest. The total length of the labyrinth weir is typically three to five times the spillway width. Its capacity varies with head and is typically about twice that of a standard weir or overflow crest of the same width. (Tullis et al., 1995). The capacity of a labyrinth spillway is a function of the total head, the effective crest length, and the crest coefficient. The crest coefficient depends on the total head, weir height, thickness, crest shape, apex configuration, and the angle of the side legs. Another important variable that influences the general layout and economy of a labyrinth is the number of cycles, N . Ultimately, the design engineer should seek an economical layout with good hydraulic performance (Ghare et al., 2008).



Figure 1: Example of a labyrinth weir (after Crookston and Tullis, 2013)

The Fusegate System is based on the following concept:

- Fusegates are free-standing units installed side-by-side on a spillway sill to form a watertight barrier.
- They bear against small abutment blocks set in the sill to prevent them from sliding before they are required to rotate (under extreme flood conditions).
- There is a chamber in the base of each Fusegate, with drain holes to discharge incidental inflow (due to leaking seals for example).
- An inlet well on the upstream side of the Fusegate crest discharges water into the chamber when the headwater reaches a predetermined level (see figure 2).

In normal operating conditions, the Fusegates act as a watertight barrier. Medium to moderate floods are simply discharged above the Fusegate crest as they would do over a free weir (see figure 3).

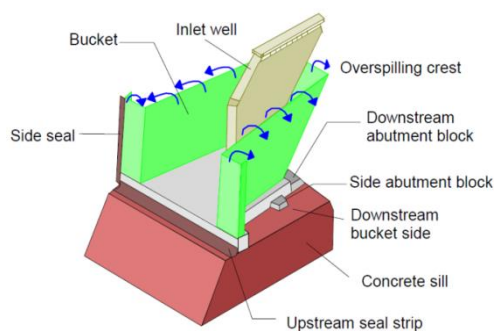


Figure 2: Typical 3D view of a Fusegate

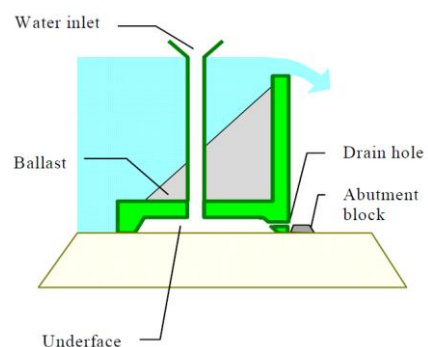


Figure 3: water spills over the Fusegate

If the reservoir level exceeds a predetermined value, water will flow into the inlet well and cause an uplift pressure to develop in the chamber (see figure 4). The uplift pressure, combined with the hydrostatic pressure (acting from left to right on the adjacent diagram) is sufficient to overcome the restraining forces and the imbalance causes rotation of the unit off the spillway. The Fusegate is then washed away clear of the spillway by the flood (see figure 5).

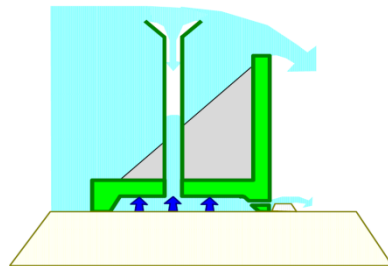


Figure 4: well-being fed

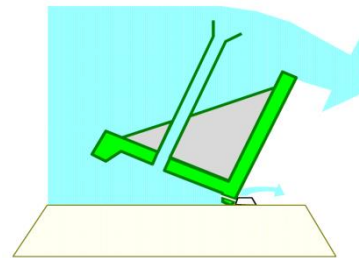


Figure 5: Fusegate tipping

2. MATERIALS AND METHODS

2.1. STUDY AREA

Sarough Reservoir Dam (Gugerdchi) is located in about 17 km north of the Takab city, in the West-Azerbaijan province, Iran, between $36^{\circ}30'54''$ N latitude and $47^{\circ}06'40''$ E longitude; Figure 6 shows its satellite picture and its position in the country. Its capacity is about 40 mcm (million cubic meters); It is a clay core rockfill dam and construction of the dam is conducted in order to meet the following objectives: - To supply 10.3 mcm drinking and industrial water. - Development of 40 mcm of water to irrigate 5500 hectares of ground area. Dam's spillway is showed in figure 7.

2.2. EQUATION

Hydraulic features of fusegates have obtained by hydraulic models in Europe and America laboratories and has



Figure 6: Study Area

conducted equal to special weather conditions for Sarough dam reservoir project. Adapted data from laboratory model roughly correspond with current standards. Flood discharge flow from crown to length is computed by following equation:

$$Q = \sqrt{2g} \mu h^{3/2} \quad \text{if } h < 0.27 \text{ m} \quad (1)$$

$$Q = (A.h + B).k \quad \text{if } h > 0.27 \text{ m}$$

Where h = Flow elevation upper than crown gate that make to pure; K , B , A and μ are constant values; S is determined due to physical parameters and physical conditions of flow. Constant values have implemented by experimental model in laboratories and has simulated for Sarough dam which is $A = 4.99$ and $B = -0.7$.

3. RESULTS AND DISCUSSION

3.1. HYDROGRAPH

The peak flood discharge of the Sarough dam reservoir for 2, 10, 20, 50, 100, 1000, and 10000 return period (years) is 78, 150, 187, 237, 270, 427, and 614 (m³/s), respectively; Design flood is 10000 years. The dam inflow hydrographs are displayed in the figure 7.

3.2. GEOMETRIC FEATURES OF FUSEGATES

Geometric features of Sarough dam fusegates are briefly presented in Table 1.

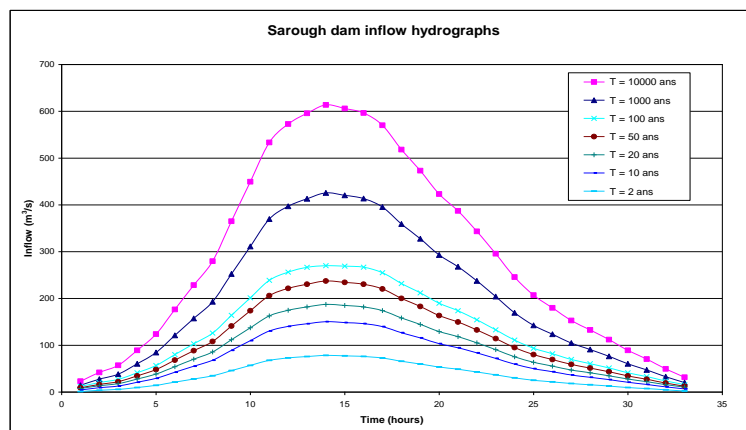


Figure 7: Hydro graphs flood with different return period in Sarough Dam

Table 1: Geometric features of fusegates Table 2: Determined reversal elevation for each gate

Gate Type	Snails with Average Height
Number of Gates	6
Gate Height	3.5 m
Gate Length	3.47 m
Real Gate Length	3.50 m
Crown Length of Spillway Gates	21 m
Gate Width	3.52 m
Base Elevation of Gate	1837.80 m
Crown Elevation of Gate	1841.30 m

Reversal Order	Gate	Reversal Elevation (m)	Elevation difference with crown gate (m)	Height difference with spillway crown elevation (m)
1	F1	1843.30	2	5.50
2	F2	1843.34	2.04	5.54
3	F3	1843.38	2.08	5.58
4	F4	1843.41	2.11	5.61
5	F5	1843.44	2.14	5.64
6	F6	1843.46	2.16	5.66

Figure 8: Laboratory Model



Figure 9: A view of gates swamp



3.3. REVERSAL SCHEME

Reversal elevation is increased level of dam's water area that lead to gate reversal. This elevation will be in the upstream of spillway; and in this step, velocity of inflow current is very low and specified reversal elevation to each gate is according to table 2.

Figure 8 displays a view of establishment of fusegate model at the threshold spillway, which is a part of implementation on an experimental model in the laboratory; Figures 9 shows a view of every six gates swamp.

A comparison discharge-time-reservoir level chart between first and 6th individual reversing fusegate are displayed in figure 10 and 11, respectively. The hydrograph of Sarough dam equipped with fusegates for 10 and 10000 years flood are shown in figure 12 and 13, respectively which 10000 years flood is design flood. The effect of fusegate installation are well illustrated, in these resent four figures.

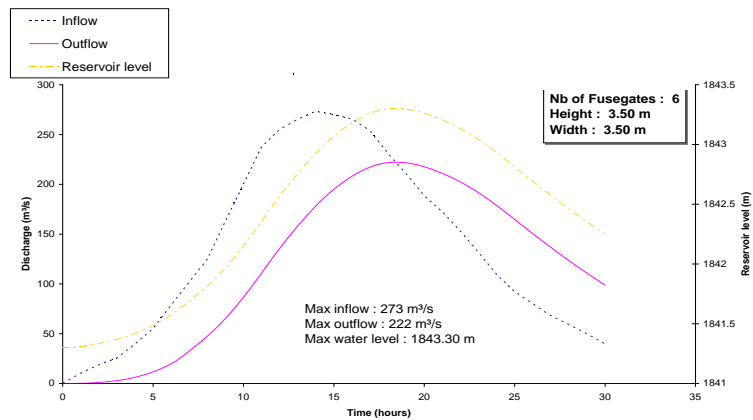


Figure 10: Dam equipped with fusegates just before 1st reversing

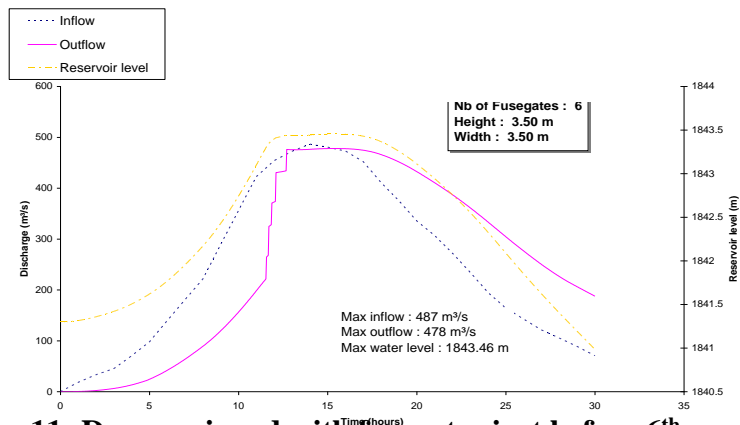


Figure 11: Dam equipped with fusegates just before 6th reversing

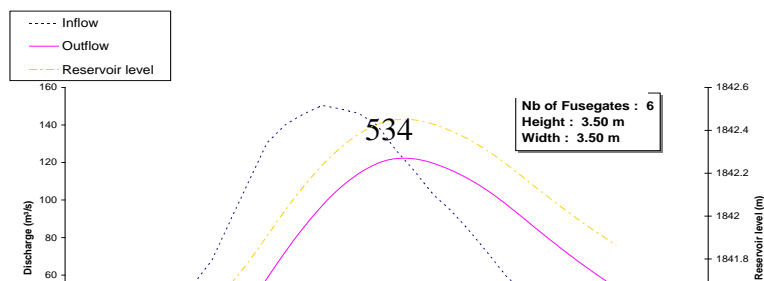


Figure 12: Dam equipped with fusegates for 10 years flood

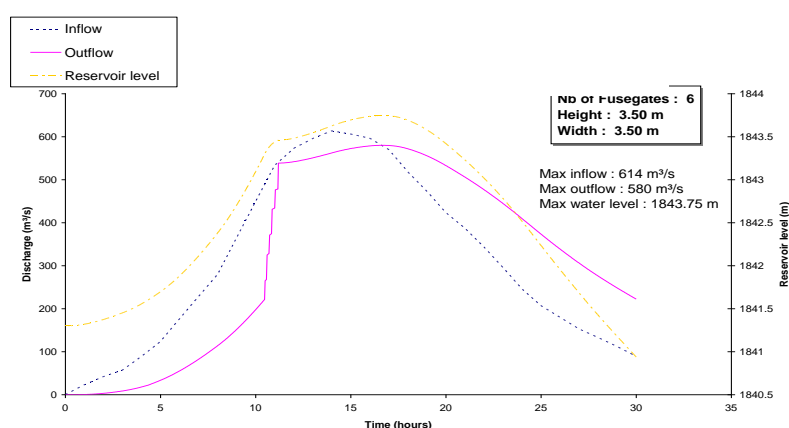


Figure 13: Dam equipped with fusegates for 10000 years flood (design flood)

4. CONCLUSIONS

Gates reversal are performed continuously one after the other and gates with average opening height will be able to overturn and empty by floods with return period of 100 years and less, easily. Without any additional operation, fusegates in comparison with mechanical errors or lack of access to electricity and other mechanical gates, can act as the simplest structure in safety and stability of dams and spillways against occurrence of large floods. With installing the mentioned gates, the reservoir storage capacity of dam has increased about 10 mcm until the align of gates crown.

By installing these gates, the storage capacity of the reservoir increased up to gates overhead level for about 10 mcm. Flood hydrograph in six different return periods (from 2 to 1000 years) of the dam, shows that dam capacity has increased by equipping with fusegates. In addition, a comparison discharge-time-reservoir level chart between 1st to 6th individual fusegate overthrow periods is done that illustrate the effect of these gates well.

5. ACKNOWLEDGMENT

The authors cordially thank the West Azarbayjan Regional Water Authority, for collecting and supporting by valuable field data. Writers are also immensely grateful to the editors and the reviewers for their guidance through comments on paper revision.

6. REFERENCES

1. Afshar, A., and Takbiri, Z. (2012). “*Fusegates selection and operation: simulation–optimization approach*”. Journal of Hydroinformatics. 14.2. P:464-477.
2. Chevalier, S. (2004). “*Fusegates mitigate silting at Beni Amrane reservoir*.” J. Hydropower & Dams 11 (5), 118–119.
3. Crookston, B. M., and Tullis, B. P. (2013). “Hydraulic Design and Analysis of Labyrinth Weirs. II: Nappe Aeration, Instability, and Vibration”. ASCE, Journal of Irrigation and Drainage Engineering, Vol. 139, No. 5, P:371-377.
4. Falvey, H. (2003). “*Hydraulic design of labyrinth weirs*”, ASCE Press Pub., Virginia, USA.
5. Ghare, A. D., Mhaisalkar, V. A., and Porey, P. D. (2008). “*An approach to optimal design of trapezoidal labyrinth weirs*”. World Applied Sciences Journal, Vol. 3, No. 6, pp. 934-93.
6. Hosseini, Kh., Jafari Nodoushan, E., Barati, R., and Shahheydari, H. (2015) “*Optimal Design of Labyrinth Spillways using Meta-Heuristic Algorithm*”. KSCE Journal of Civil Engineering (0000) 00(0):1-10. DOI 10.1007/s12205-015-0462-5.
7. Paxson, G., Campbell, D., and Monroe, J. (2011). “*Evolving design approaches and considerations for labyrinth spillways*.” USSD Conference, U.S. Society on Dams, San Diego, pp. 1645-166.
8. Tullis, J. P., Amanian, N., and Waldron, D. (1995). “*DESIGN OF LABYRINTH SPILLWAYS*”. ASCE, Journal of Hydraulic Engineering, Vol. 121. No.3, P:247-255.
9. Falvey, H. T., and Treille, Ph. (1995). “*HYDRAULICS AND DESIGN OF FUSEGATES*”. Journal of Hydraulic Engineering, ASCE. Vol. 121, No.7, P:512-518.
10. Crookston, B. M., and Tullis, B. P. (2013). “*Hydraulic Design and Analysis of Labyrinth Weirs. II: Nappe Aeration, Instability, and Vibration*”. ASCE, Journal of Irrigation and Drainage Engineering. Vol. 139, No. 5, P:371-377.

Design and Operation of Sustainable Reservoirs, a New Approach

Esmail Tolouie

**Ph. D. Civil (water Resources Development), University of Birmingham, UK
3rd flood, No. 26, 13th Alley, Shangarf Street, Mirdamad Avenue, Tehran-15486, Iran**

Email: etolouie@yahoo.com

Abstract

A reservoir is an artificial lake which begins to fill with sediment as soon as it is commissioned causing a gradual loss of storage capacity. Today, most dams of substantial size are engineered to have a practically unlimited life so far as the structure itself is concerned, provided it is given adequate maintenance. Modern geotechnics can be applied to dam site exploration and engineering skill in design reduces the risk of almost all types of structural and foundation failure. Present day knowledge of probable maximum precipitation (PMP) and probable maximum flood (PMF) has led to spillway design that leaves only a very small chance of failure from floods. Despite the above achievements, the reservoir sedimentation received less attention in study, design and operation stages. According to ICOLD sedimentation committee (March, 2009), the total storage capacity of the world reservoirs is about 7000 billion m³, of which 2000 billion m³ is the volume of deposited sediment, corresponding to an annual loss of .8%. It means that the half-life of the world's reservoirs in average is about 60 years, 2/3 of which is already past. Therefore it is very clear that the present rate of reservoir sedimentation along with such a huge amount of accumulated sediment will impose a very costly liability upon the next generation, hence a better understanding is urgently needed. The author believes that the present generation particularly those who are in the position of making key decisions must answer the following question. "What shall the future dam operators do while facing with the abandoned reservoirs full of sediment?" This paper describes a new approach of design and operation of dam reservoirs based on sustainable development principles, the reservoirs with almost unlimited life-cycles. The philosophy of the new approach is described as below.

1. A river system is a live element of the nature because it moves, it digs, it deposits, it carries, and it changes the environment to stabilize itself.

2. All the live elements of the nature need a part of their power to survive their live.

As a reservoir is a part of a river system, thus the above philosophy should be fulfilled in its design and operation. Steps taken in the new approach have been elaborated using 15 years field experiences on desiltation operations carried out at Sefidrud Reservoir, Iran.

Keywords: Required Trap Efficiency, Long-Term Capacity Ratio, Life-Cycle, Useful-Life, Rehabilitation Period.

1. INTRODUCTION

1.1. NEED FOR SUSTAINABLE RESERVOIRS

A reservoir is an artificial lake which begins to fill with sediment as soon as it is commissioned, causing a gradual loss of storage capacity.

Reservoir sedimentation affects the lives of the people who benefit from the stored water, and it may have both long-term and short-term consequences. In the short-term, the effect of sedimentation is the economics of the reservoir scheme. The rate of sedimentation may be so rapid as to prevent amortization of the cost of development. Most dams of substantial size are engineered to have a practically unlimited life so far as the structure itself is concerned, provided it is given adequate maintenance.

Today, modern geotechnics is applied to dam site exploration and engineering skill in design reduced the risk of almost all type of structural and foundation failure. Despite these measures, the useful life of the dam project can be greatly reduced by reservoir sedimentation. The most obvious effect is the depletion of storage capacity which prevents the reservoir from supplying the services for which it was designed, thus disturbing the economy of the region which it serves. Regulated water supply is also reduced by increased evaporation losses especially in arid and semi-arid regions, as the sediment accumulation will change the area-capacity relationship of the reservoir so that larger surface area is exposed for equal storage. The consequences of sediment accumulation in the upper reaches of a reservoir will reduce the flood routing efficiency and also flooding of upstream river valley developments, such as towns, highways, railroads, etc. an increase in the evapotranspiration

due to vegetation at the head of Elephant Butte Reservoir in USA, quoted by Murthy(1968), is about 37% of the evaporation losses from the reservoir surface.

The most favorable measure to control reservoir sedimentation may be watershed management, which is not always justified from technical and economical point of views, as the sediment yield is product of many natural and artificial interrelated factors such as rainfall characteristics, rainfall-runoff relationship, susceptibility of soil and valley alluvium to erosion, land use and density of vegetative cover on the watershed. Almost all of the significant factors mentioned above are worse in arid and semi-arid regions of the world, particularly in developing countries, where favorable natural conditions may be aggravated by the lack of programming and cooperation among the relevant authorities and the huge amount of capital and maintenance costs required in long-term plans.

Data collected by Murthy(1968) and Zhang-Qian(1985) with the Sefidrud Reservoir(Iran) added, are presented in Table 1.1. The table shows that reservoir sedimentation has not been avoided even in developed countries, so an improved understanding is needed.

The main goal of this paper is the steps in the study, design and operation stages necessary to minimize the capacity loss of reservoirs by controlling the trap efficiency, so that useful life of the reservoirs be prolonged, also the periodic rehabilitation of the reservoir capacity be possible, using hydrodynamic energy of the stored/inflow water to remove deposited sediment, thus achieving a sustainable development.

Table 1.1. Representative data of rates of reservoir sedimentation

COUNTRY	RESERVOIR	CATCHMENT AREA (KM ²)	PERIOD OF RECORD (YEAR)	ORIGINAL CAPACITY (MCM)	ANNUAL AVERAGE STORAGE LOSS (%)
1	2	3	4	5	6
USA	Boysen	20050	13	20	6.25
USA	Mississippi	308200	15	456	2.00
AFRICA	Lake Arthur	5880	10	78	4.10
AFRICA	Lake Mentz	12490	12	117	2.90
JAPAN	Soyama	1500	19	33	2.40
ITALY	Mont Reale	435	1	1.50	2.60
INDIA	Pahari	7840	28	47	2.19
CHINA	Qingtongxia	285000	12	620	6.52
CHINA	Yanguoxia	182800	18	220	4.04
CHINA	Sanmenxia ¹	688420	1.5	9640	10 ⁺
IRAN	Sefidrud ²	56200	17	1760	2.13 [*]

+ Normal operation period (1960-1962)

* Normal operation period (1963-1980)

Notes:

(1): The trap efficiency at Sanmenxia Reservoir in its normal operation period (1960-62) was 93.2%, but this value was reduced in subsequent years, due to de-siltation operations as below, Zhang and Long(1981).

- In the 1st stage of de-siltation operation (1962-66), TE=42%
- In the 2nd stage of de-siltation operation (1966-70), TE=18%
- In the 3rd stage of de-siltation operation (1970-73), TE=0.0%, no storage loss thereafter.

Originally the outlet system in Sanmenxia Dam was not capable to an efficient de-siltation operation, therefore an extensive structural measures have been taken.

(2): The trap efficiency at Sefidrud Reservoir during its normal operation period (1963-80) was 79%, but its value was reduced in the subsequent years due to de-siltation operations as described below, Tolouie(1989).

- In the 1st stage of de-siltation operation (Partial drawdown, 1980-82), TE=53%
- In the 2nd stage of de-siltation operation (empty flushing, 1982-90), TE=-75%

As a result of foregoing de-siltation operations, 358 mcm of the reservoir capacity was rehabilitated. It should be mentioned that the bottom outlet system at Sefidrud Dam was originally capable to partial drawdown/empty flushing of the reservoir, thus no structural measure was needed (5 bottom outlets with total capacity of 980 m³/s, 6.5 times the long-term average inflow discharge, located at about river bed elevation).

1.2. CONCEPTUAL DEFINITIONS

(1). Variation of traditional reservoir capacity against time (Fig. 1.1),

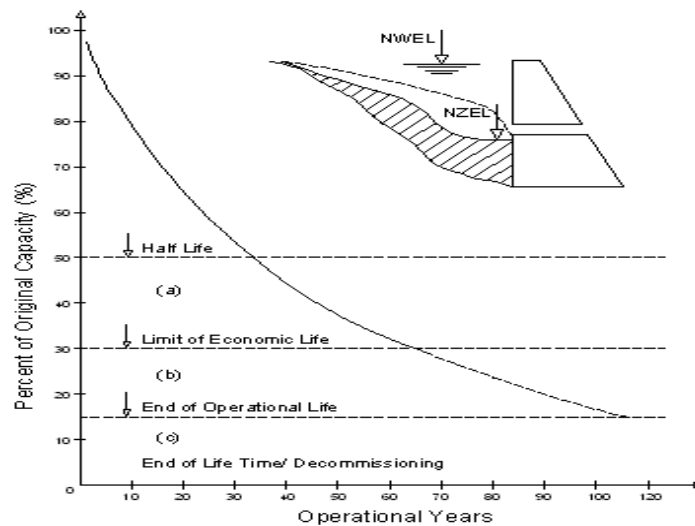


Figure 1.1. Typical variation of reservoir capacity against time, traditional design

Notes: NWEL = Normal Water Elevation, NZEL = New Zero Elevation

Fig. 1.1 shows that, in traditional design there is just one life-cycle which includes useful life/ economic life (a), uneconomic life (b), and abandonment of the whole facility or decommissioning stage (c). In addition, the volume of dead storage in traditional design which is usually allocated for deposition of 50 years inflow sediment may take up to 80% of the total original capacity of the reservoir, resulting high investment and environmental costs.

(2). Variation of sustainable reservoir capacity against time (Fig. 1.2),

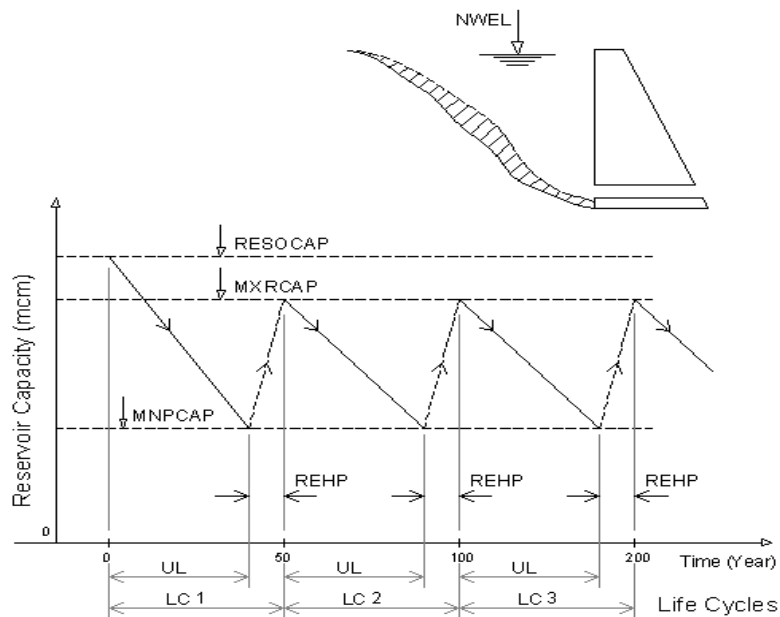


Figure 1.2. Typical variation of reservoir capacity against time, sustainable design

Notes:

RESOCAP = Reservoir Original Capacity, MXREHCAP = Maximum Rehabilitation Capacity
 MNPCAP = Minimum Permissible Capacity, REHP = Rehabilitation Period, UL = Useful Life
 LC = Life Cycle

Fig. 1.2 shows that in sustainable design, the reservoir operation can be carried out in different life-cycles as long as the structural life of the dam. In addition, no dead storage for sediment accumulation is required, so the height of the dam and the reservoir capacity is considerably reduced.

2. REQUIRED TRAP EFFICIENCY OF THE RESERVOIR

2.1. REQUIRED TRAP EFFICIENCY DURING USEFUL LIFE (RULTE)

The following steps are taken:

STEP 1: Plot long-term average demand shortage against trap efficiency of the reservoir for a certain value of useful life, say $UL = 40$ years (Fig. 2.1)

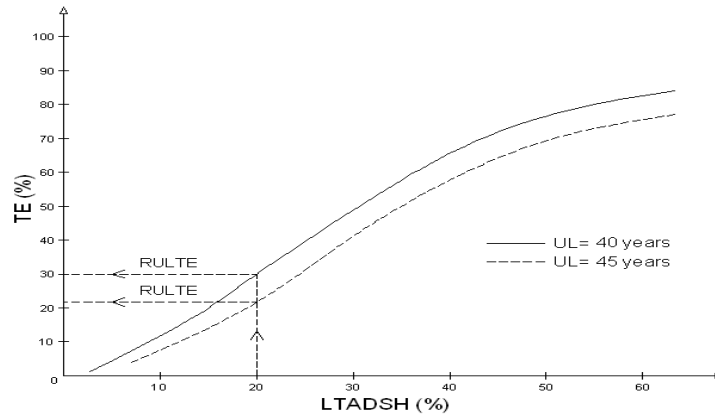


Figure 2.1. Typical variation of LTADSH against TE

Notes: TE = Trap Efficiency, RULTE = Required Useful Life Trap Efficiency, LTADSH = Long-Term Average Demand Shortage

STEP 2: From Fig. 2.1, find RULTE corresponding to the accepted value of LTADSH

2.2. REQUIRED TRAP EFFICIENCY DURING REHABILITATION PERIOD (RREHTE)

The following steps are taken:

STEP 1: Plot long-term capacity ratio of the reservoir against trap efficiency, for the same useful life as taken in Fig. 2.1, as shown in Fig. 2.2.

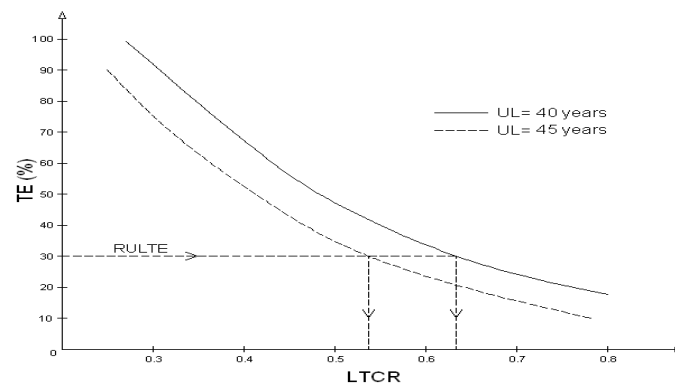


Figure 2.2. Typical variation of LTCR against TE

Notes: LTCR = Long-Term Capacity Ratio, the ratio of the reservoir capacity at the end of its useful life to the original capacity of the reservoir.

STEP 2: In Fig. 2.2, locate RULTE (found in paragraph 2.1) and find the corresponding value of LTCR.

STEP 3: Plot rehabilitation trap efficiency of the reservoir (REHTE) against LTCR for different values of rehabilitation periods (Fig. 2.3).

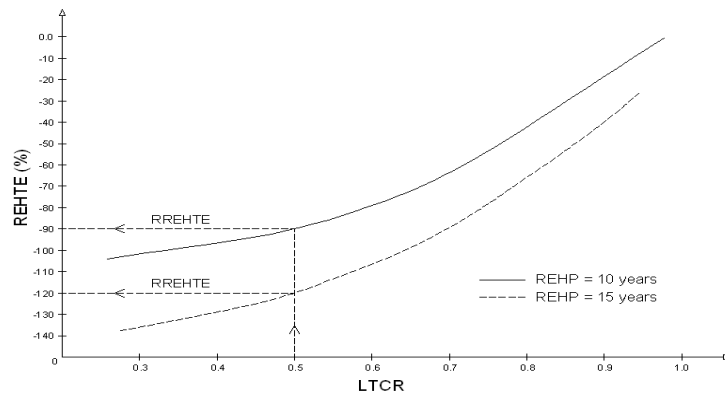


Figure 2.3. Typical variation of REHTE against LTCR for different values of REHP

Notes: REHP = Rehabilitation Period, REHTE = Rehabilitation Trap Efficiency, RREHTE = Required Rehabilitation Trap Efficiency

STEP 4: From Fig. 2.3, find RREHTE corresponding to the known values of LTCR and REHP.

STEP 5: Check feasibility of obtaining the calculated value of RREHTE, hence change the REHP and/or UL accordingly.

An example to calculate RREHTE

- Reservoir Original Capacity, RESOCAP = 500mcm
- Annual Average Inflow Sediment = 10 mcm/yr
- Long Term Capacity Ratio, LTCR = 0.6
- Available Capacity of the Reservoir at the end of its useful life = $500 * 0.6 = 300$ mcm
- Maximum extent of reservoir rehabilitation = 90%
- Maximum Recovered Capacity of the reservoir = MXRCAP = $500 * 0.9 = 450$ mcm

a: Reservoir Rehabilitation Period, REHP = 5 years

Total Outflow sediment during rehabilitation period = $5 * 10 + (450 - 300) = 200$ mcm

RREHTE = $(5 * 10 - 200) / (5 * 10) = -300\%$

b: Reservoir Rehabilitation Period, REHP = 10 years

Total outflow sediment during rehabilitation period = $10 * 10 + (450 - 300) = 250$ mcm

RREHTE = $(10 * 10 - 250) / (10 * 10) = -150\%$

c: Reservoir Rehabilitation Period. REHP = 15 years

Total outflow sediment during rehabilitation period = $15 * 10 + (450 - 300) = 300$ mcm

RREHTE = $(15 * 10 - 300) / (15 * 10) = -100\%$

Referring to Fig. 1.2, the Minimum Permissible Capacity of the Reservoir is,

MNPCAP = LTCR * RESOCAP = $500 * 0.6 = 300$ mcm

3. FEASIBILITY OF APPLYING DIFFERENT DE-SILTATION METHODS

3.1. OVERVIEW

Among the different de-siltation methods, the scope of the paper is utilization of hydraulic energy of the stored and / or inflow water to control the trap efficiency of reservoirs. That is, allocation a certain budget out of available water for conservation of the river system. In other words, those techniques such as dredging and siphoning are not considered as the main elements in de-siltation operations, but these techniques may be used as supplementary measures in small scales such as cleaning the areas around intakes or dredging a pilot channel along the impounded reservoirs to facilitate the passage of density-currents. Therefore, the paper will focus on density-current venting, sluicing, flushing, and bypassing (as an alternative to density-current).

3.2. ESTIMATION OF RESERVOIR TRAP EFFICIENCY BY DENSITY-CURRENT VENTING

Based upon the principle that density-current occurs during floods, the following steps are taken:

Step 1: Sort out monthly inflow discharges based on probability of occurrence, select base flow, hence split the long-term inflow discharge into base flow and flood discharge.

Step 2: Using a reliable simulation model, estimate long-term series of the following parameters:
 Sample of output files resulted from density-current simulation are represented in figures 3.1 to 3.5. The model (DENFLOW) was developed and calibrated during Sefidrud Reservoir de-siltation operations (1980 – 1994).

An example to calculate flood discharge (FDIS)

$$DFDIS = [MFLOW - BASFLOW * (30.5 - NOFD) / 30.5] / NOFD$$

$$FDIS = 11.57 * DFDIS$$

Where

DFDIS = Daily flood discharge in mcm/day

FDIS = Instantaneous flood discharge in m³/s

MFLOW = Monthly average flow in mcm/month

BASFLOW = Base flow in mcm/month

NOFD = Number of flood days per month

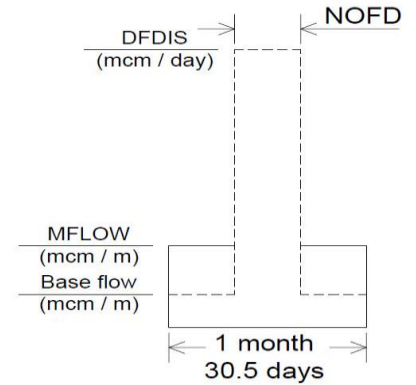
For example, MFLOW = 248 mcm/m

BASFLOW = 190 mcm/m, NOFD = 6

We have,

$$DFDIS = [(248 - 190 * (24.5 / 30.5)) / 6] = 15.9 \text{ mcm/day}$$

$$FDIS = 11.57 * 15.9 = 184 \text{ m}^3/\text{s}$$



Converting monthly av. flow (mcm/m) to instantaneous flood discharge (cms)

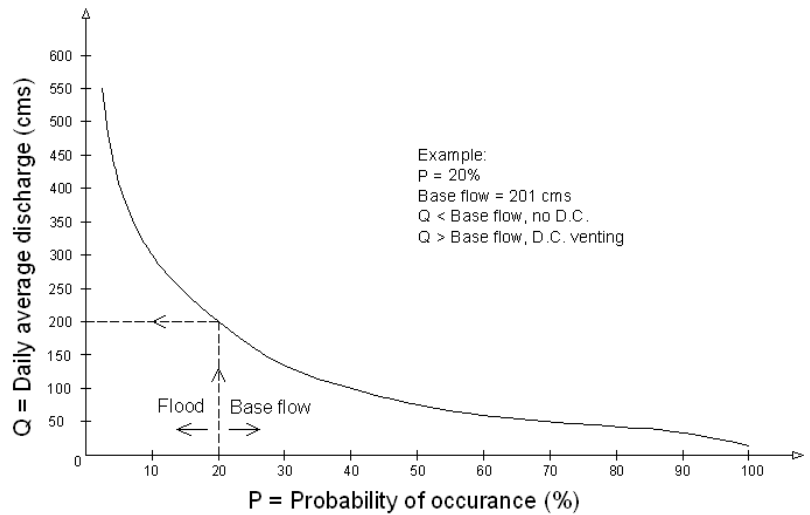


Figure 3.1. Flow – probability curve at SAMP Reservoir

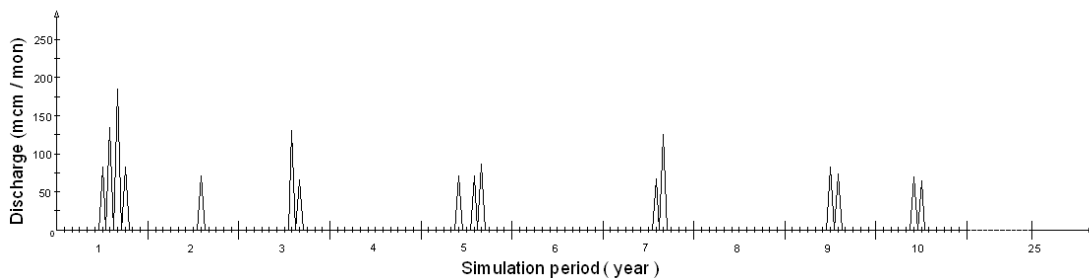


Figure 3.2. Density-current outflow discharge at SAMP Reservoir

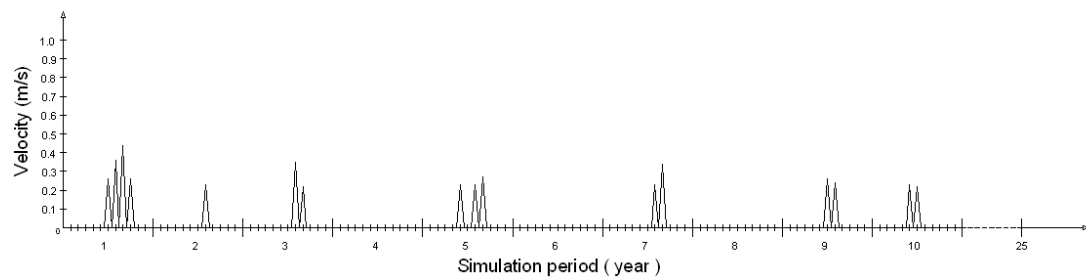


Figure 3.3. Density-current velocity at SAMP Reservoir

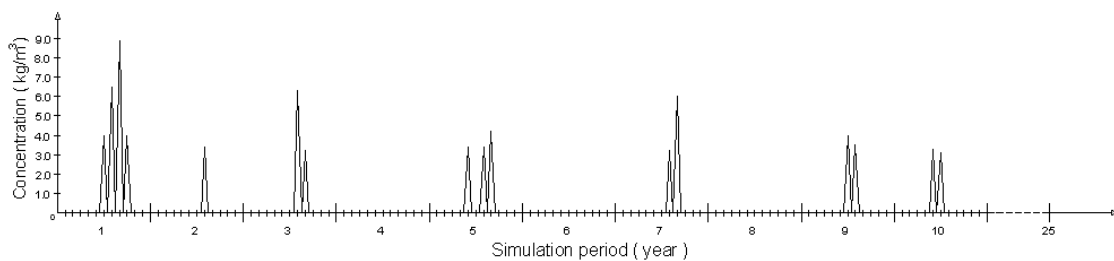


Figure 3.4. Density-current outflow concentration at SAMP Reservoir

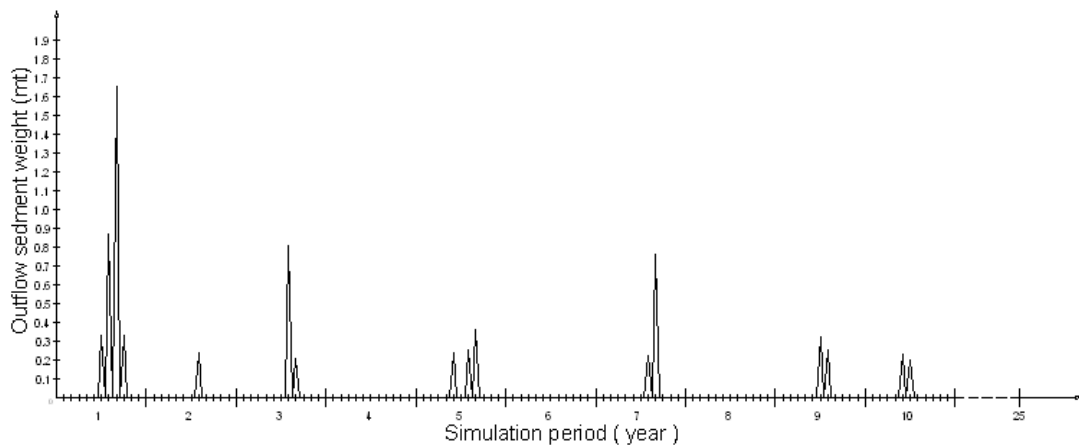


Figure 3.5. Density-current outflow sediment at SAMP Reservoir

3.3. ESTIMATION OF RESERVOIR TRAP EFFICIENCY BY PARTIAL DRAW DOWN FLUSHING

In partial draw down flushing (Sluicing), the reservoir water level is drawn down to minimum operating level, and the bottom outlets are opened allowing the development of a conical scour hole in front of the outlets. Maintaining the reservoir water level between the minimum operating level and the minimum draw down level, causes transport of the sediment from the upper reaches of the reservoir (where the river flow forms) towards the dam. This phenomenon is often more remarkable in hydropower reservoirs where the minimum operating level is relatively high.

Taking into consideration that drawdown flushing is more efficient during flood season, it will be clear that maintaining the reservoir water level in lower stages of the reservoir (between minimum operating level and minimum draw down level), necessitate high-capacity bottom outlets at low sill elevation. Draw down Ratio (DDR) is a criterion which defines a suitable stage of the reservoir during draw down flushing;

$$DDR = 1 - (HD / HH) > 0.7$$

Where,

HD = Reservoir water depth during draw down operation

HH = Hydraulic height of the dam (depth of water at normal water level)

That means, the depth of water behind the dam during draw down flushing should be maintained below 30% of the hydraulic height of the dm.

Alternative emptying and refilling of the reservoir within a certain range of water level, is also an effective measure to increase de-siltation efficiency in draw down flushing.

At Sefidrud Reservoir the draw down flushing was carried out in the first 2 years of de-siltation operations, but in subsequent years it was combined with the free flushing operations, in fact draw down flushing was a transient operation to empty flushing operation.

It should be mentioned that draw down flushing is generally not an effective flushing technique, but possibility of controlling outflow sediment concentration by proper maneuvering the bottom outlet gates, is an advantage of this technique as compared with free flushing operation. The said advantage is particularly valuable at those sites with downstream environmental limitations. Based on the field experiences at Sefidrud site, an empirical simulation model (SLUICE) was developed. The cone geometry in front of the bottom outlets is defined in the model based upon the field data.

A sample output file of the partial drawdown model (SLUICE), is represented as figure 3.6.

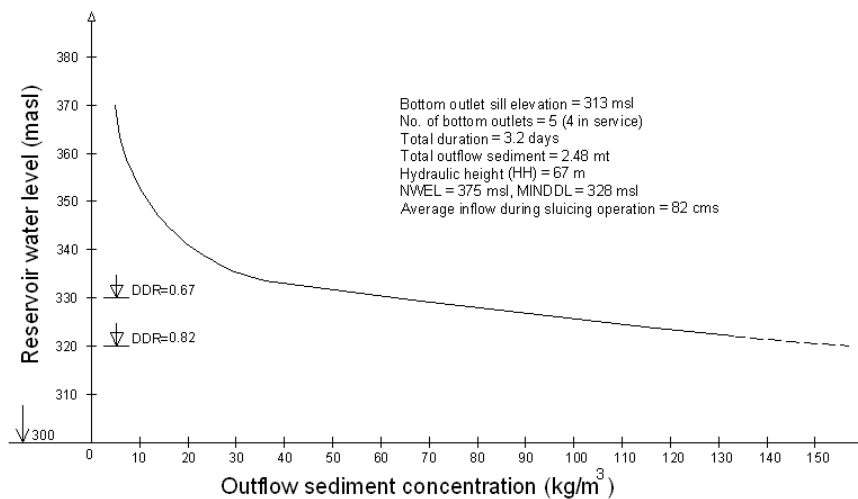


Figure 3.6. Result of partial drawdown (sluicing) operation at SAMP Reservoir

Notes: NWEL = 375 masl, MINDDL = 328 masl, Average inflow discharge during sluicing operation = 82cms
Sill elevation of bottom outlets = 313 masl, Number of bottom outlets = 5, Duration of operation = 3.2 days
Total outflow sediment = 2.48 mt

3.4. ESTIMATION OF RESERVOIR TRAP EFFICIENCY BY EMPTY FLUSHING

In empty flushing (complete drawdown), the flow regime along the reservoir changes to river flow, resulting a very high shear stress over the deposited sediment, hence increasing the outflow sediment concentration. In general, the efficiency of empty flushing depends on the following parameters;

- (1): Inflow water discharge.
- (2): Longitudinal slope of the water surface profile along the reservoir/ sill elevation of bottom outlets.

(3): Layout and capacity of bottom outlet system. As far as the layout is concerned, the concrete dams are more favorable as locating several outlets across the valley is possible. The in-service capacity of the bottom outlet system should be such that a river flow could be maintained during flushing operations and no back water is formed behind the dam.

A simulation model to estimate outflow sediment concentration in empty flushing operations "FLUSHING" was developed and calibrated using field data collected during 10 years of flushing operations at Sefidrud Reservoir. Three experimental sediment transport equations were found to be in good agreement with the field observations, these are;

1. Xia (1983) equation

$$QS_1 = 300 * Q^{1.6} * S_f^{1.2} / B^{.6} \quad [1]$$

where,

$$B = 12.8 * Q^{-5}$$

2. Fan and Jiang (1980) equation

$$QS_2 = .35 * Qw^{1.2} * (.8 * S_f * 10^4)^{1.8} \quad [2]$$

3. Rooseboom (1975) equation

$$QS_3 = 2 * 10^5 * (V_m S_f)^{.283} \quad [3]$$

where

$$V_m S_f = P * Qw^3 / (C^2 * A^4)$$

V_m = mean velocity

S_f = water surface longitudinal slope

P = wet perimeter

Qw = inflow water discharge

C = Chezy coefficient

A = wet area

4. Sefidrud – calibrated equation

$$QS_4 = .3 * (\text{Log}(1 + Qw)^{1.5} * S_f^{-.7}) \quad [4]$$

Out of the above equations, equation 4 yields lower results because of consolidated deposit at Sefidrud site, i.e. Starting flushing operation after about 20 years of commissioning.

Figures 3.7 and 3.8 illustrate the sample output files resulted by FLUSHING model.

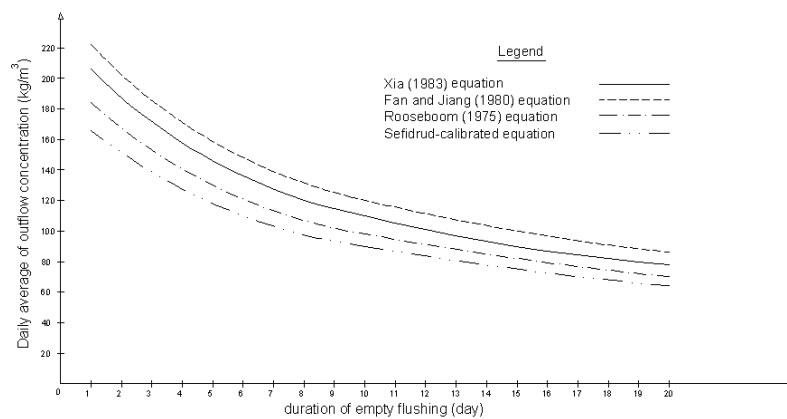


Figure 3.7. Outflow sediment concentration resulted by FLUSHING model at SAMP Reservoir

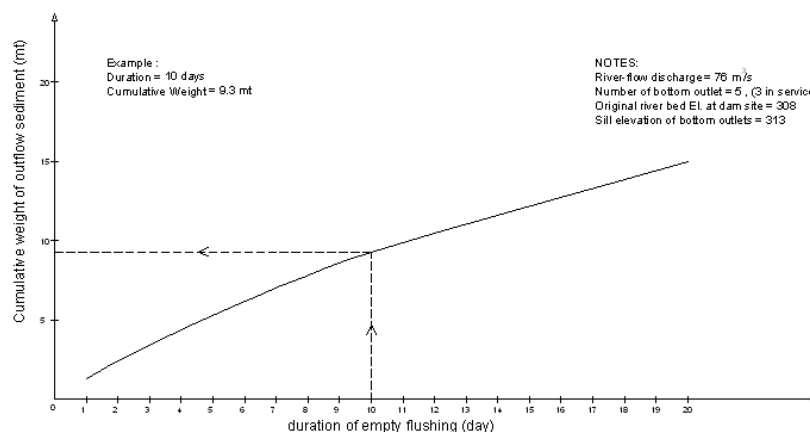


Figure 3.8. Weight of outflow sediment resulted by FLUSHING model at SAMP Reservoir

3.5. OVERALL TRAP EFFICIENCY OF SUSTAINABLE RESERVOIRS

Overall trap efficiency of a sustainable reservoir is the trap efficiency obtained by applying above mentioned de-siltation techniques, that is density-current venting, sluicing, and empty flushing. Summary of the results obtained by applying these techniques in a sample reservoir is represented in table 3.1. It is to be noted that, the outflow sediment resulted by density-current venting is for the entire simulation period, whereas those obtained by sluicing and empty flushing are just for a single operation.

Table 3.1. Summary of outflow sediments and resulted trap efficiencies in a sustainable reservoir in different alternatives

ALTER NATIVE	FLUSHING INTERVAL (YEAR)	FLUSHING DURATION (DAY)	WEIGHT OF OUTFLOW SEDIMENT (MT)				RESULTED TRAP EFFICIENCY (%)	REMARKS
			DENSITY-CURRENT VENTING	SLUICING	EMPTY FLUSHING	TOTAL		
1	1	5	37.4	62	134	233.4	-33	Inflow sediment = 7 mt/yr Sediment outflow in single sluicing operation = 2.48 mt Simulation period = 25 years
		10	37.4	62	230	329.4	-88	
		15	37.4	62	307	406.4	-132	
		20	37.4	62	373	472.4	-170	
2	2	5	37.4	30	67	134.4	+23	
		10	37.4	30	115	182.4	-4	
		15	37.4	30	153	220.4	-26	
		20	37.4	30	186	253.4	-45	
3	3	5	37.4	20	44	101.4	+42	
		10	37.4	20	76	133.4	+24	
		15	37.4	20	102	159.4	+9	
		20	37.4	20	124	181.4	-3	
4	4	5	37.4	15	33	85.4	+51	
		10	37.4	15	57	109.4	+37	
		15	37.4	15	77	129.4	+26	
		20	37.4	15	93	145.4	+17	
5	5	5	37.4	12	27	76.4	+56	
		10	37.4	12	46	95.4	+45	
		15	37.4	12	61	110.4	+37	
		20	37.4	12	75	124.4	+29	

According to table 3.1, the interval of empty flushing operations has got a very important role in overall trap efficiency of the reservoir. The table shows a very wide range of trap efficiencies from + 56% to – 170%. The negative trap efficiency indicates the rehabilitation of reservoir capacity therefore it is applicable in rehabilitation period of the life-cycle (see Fig. 1.2). Based on the field experiences at Sefidrud Site, an approximate estimation of the water-budget which should be assigned for implementation of de-siltation operations ranges from 15% to 20% of the annual water inflow, provided that a suitable arrangement of bottom outlet system is available (in fact this value at Sefidrud site was about 22% which was contributed to the consolidated deposit). This volume of water should be taken into account while studying water resources planning as well as during operation period of the project, as conservation water right.

4. REFERENCES

1. Fan J. and Jiang R. (1980). On methods for the de-siltation of reservoirs. International seminar of experts on reservoir de-siltation, Tunisia.
2. Murthy BN. (1968). Capacity survey of storage reservoirs. Publication No. 8, CBIP, New Delhi, India.
3. Rooseboom A. (1975). Sediment transport in rivers and reservoirs. D. Engineering dissertation, university of Pretoria.
4. Tolouie E. (1989). Reservoir sedimentation and de-siltation. A thesis presented to the faculty of engineering, university of Birmingham, UK.
5. Xia M. (1983). Sediment problems in design and operation of medium and small size reservoirs. Science press, Beijing, China.
6. Zhang Q. and Long Y. (1981). Sediment problems of Sanmenxia Reservoir. Proceeding international symposium on river sedimentation, Beijing, China.
7. Zhang R. and Qian N. (1985). Reservoir sedimentation. International research and training center on erosion and sedimentation. Beijing, China.

Rehabilitation of the Sylvenstein Dam, Germany Success Proof by Major Flood 2013

Peter Banzhaf

BAUER Spezialtiefbau GmbH, Bauer-Street 1, 86529 Schrobenhausen, Germany

Email: Peter.banzhaf@bauer.de

Abstract

Preventing flood damages is a central role of dikes and dams. The Sylvenstein Dam designed to manage the water level in the Isar River by mitigating flood damages downstream, for adequate low-tide-heightening of the river for better navigability and to generate electrical energy was built in the south of Germany in the 1950ies.

The Dam, with some upgrades over the years, performed very well its designated purposes. Preparing for presumed increasing flood events due to the climate change with higher and sudden precipitation, a restoration design for the Sylvenstein Dam was implemented between 2012 and 2014. The significant renovation part was the installation of a plastic concrete cut-off wall through the embankment dam core and into the alluvium filling the gorge created by the Isar River. In 2012, the wall was executed and completed. The Reservoir was partly impounded during the installation of the new barrier wall.

During heavy rainfalls in 2013, due to the flood retention capacity of the Sylvenstein reservoir, the peak discharge of the Isar River into the city of Munich could be significantly reduced thus no significant damage could be observed along the Isar River. Due to the new cut-off wall, it was possible to store a maximum of water for a longer period reducing the outflow from the dam essentially over the critical time-period, necessary, as dikes along the Danube were heavily burdened and even broke in two areas.

Keywords: Sylvenstein Dam, Dam Upgrading, Dam Rehabilitation, Plastic Concrete, Concrete Cut-off Wall.

1. INTRODUCTION

The Sylvenstein Reservoir was built between 1954 and 1959. For its reconditioning after 50 years of operation, it has been planned to strengthen the dam core by means of a deep concrete cut-off wall (COW) and to equip the dam with a state-of-the-art water collection system and a monitoring system for water seepage.

In this context, the Bavarian Ministry of Environment via its Bavarian State Office for Water Management in Weilheim (WWA-WM), the local Water Board, has entrusted Bauer with the construction of the 70 m deep and 1 m thick diaphragm wall forming the new seepage barrier in the embankment dam. The reservoir was originally meant for water augmentation to regulate the minimum low water flow of the Isar River. Meanwhile it has to deal with detention of water during flood seasons protecting the area of the city Bad Tölz and of Greater Munich from devastating floods like the one in 1999 and 2005. Furthermore, the refitting of the reservoir has to allow for prevention measures in case of climate changes.

The 42 m high and 180 m long earthen embankment dam is underlain by a 100 m deep gully formed into dolomite and filled by alluvial river sediments, which made it necessary during dam construction to perform grouting works to create a multi-layered sealing curtain of clay-cement grout.

The watertight thin core of the dam built in the early 50ties consists of a mix of gravel, fine sand, silt and bentonite sandwiched between filters of moraine gravel from both downstream and upstream sides.

The refit-design asked for a new sealing element by means of a 2-phase cut-off wall which had to be constructed as compensation to the core of the dam slightly towards the downstream side and had to key in to the steep rock flanks. The depth of the cut-off wall has been determined based on reconnaissance drillings performed down to 140 m deep in the substratum of the dam. Due to imbedded layers of gravel and rock sediments and to the fluctuating permeability in the bottom sealing, the cut-off wall had to be extended down to 70m below the dam crest (suffusion stability).

The 10,000 m² cut-off wall was constructed by Bauer Spezialtiefbau from dam crest which is stretching over 180 m. The edges of the wall had to be embedded in very hard rock. Particularly challenging was the timely execution from a restricted working platform width.

Due to the topography of the site and the restricted working space at the dam crest, logistic challenges had to be dealt with; concrete batching plants were installed downstream in the valley below the embankment

dam and the plastic concrete had to be pumped 50 m upwards. Moreover, the traffic on the adjacent scenic road could be kept up by means of a temporary road over the dam in direction towards the Achenpass, Austria.

2. FUNCTION OF THE EMBANKMENT DAM – REASONS FOR THE STRENGTHENING

The Sylvenstein Dam is the oldest water reservoir in the State of Bavaria. It has demonstrated its protective function during several floods at the rivers Isar, Dürnach and Walchen for the downstream communities and of the State Capital Munich.

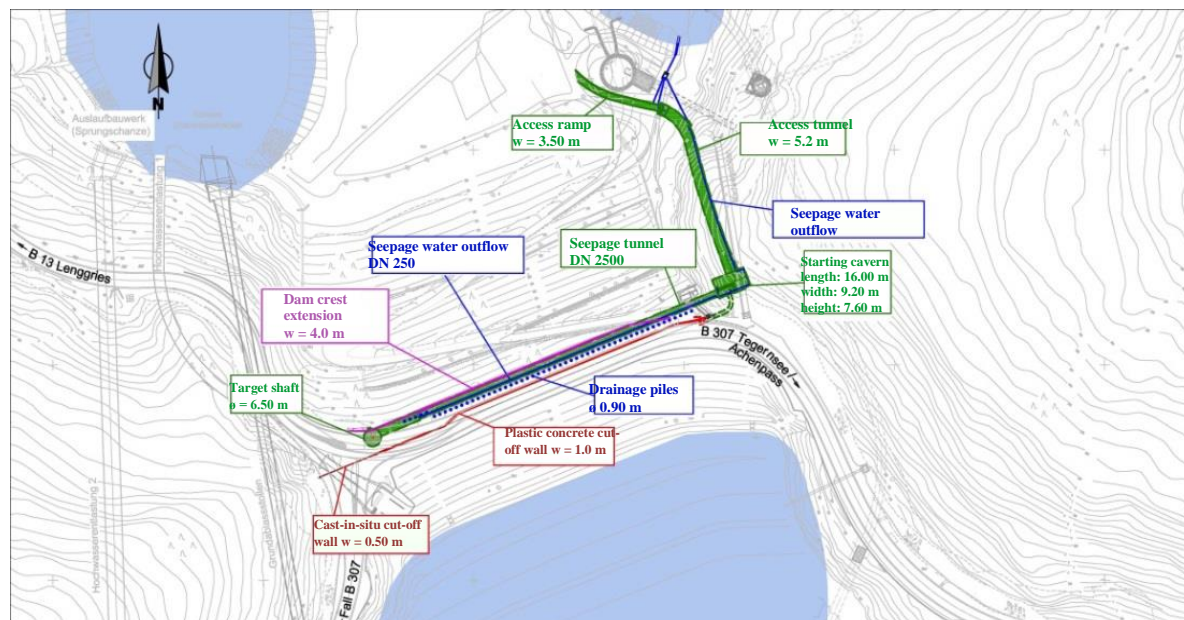


Figure 1. Layout of the rehabilitation concept (Source: WWA-WM)

Reasons for actual reconditioning of the sealing system were predominantly to improve the structure of dam and foundation; to strengthen the 50-year-old slim core; to install a new positive watertight sealing in the embankment dam. To achieve the targeted reconditioning, a design was awarded to CDM Smith Consult GmbH.

The designed plastic concrete cut-off wall has the functions: a) sealing the embankment dam, improving the existing aging core and b) sealing the underground structure to a designed depth of approx. 70 m below dam crest. Further a seepage collection tunnel and drainage piles downstream of the cut-off wall and a new seepage water measuring instrumentation was installed.

The following steps were essential to ensure long lasting functionality of the Sylvenstein dam:

The depth of the COW had to be designed in such a way that no damage will be caused by seepage in the substratum below the COW and that the assured embedment into the existing rock and concrete structure along the abutments of the embankment dam had to be watertight.

The presetting of the design asked for a two-phase diaphragm wall with a wall-thickness of 1 m; the material of the new barrier wall had to be plastic concrete assuring a permeability not exceed 1×10^{-9} m/s in the laboratory with a nominal tensile strength of 500 kN/m² and a maximum stiffness of 450 MN/m².

3. CUT-OFF WALL CHARACTERISTICS; CONSTRUCTION PROCESS; TECHNICAL FEASIBILITY

The new cut-off wall is required to seal the dam and the subsoil below to a defined depth. It was designed to implement a plastic or clay concrete cut-off wall which consists of natural aggregates without the use of artificial sealing material and additives. In order to guarantee the planned permeability of $k_f < 10^{-9}$ m/s full-face, a diaphragm wall of 1 m thickness was executed ensuring the designed continuity of the sealing system. In order to fully seal both the dam core and the subsoil, a tight embedment into the lateral sloped rock faces had to be implemented. For this reason, the use of a hydro-cutter was chosen. As a result of the expected long excavation periods of the individual diaphragm wall elements, the need to cut through boulders and into the sloped rock flanks, only the two-phase diaphragm wall system was feasible.

For the designed depth of the cut-off wall, it is decisive that there is no suffusion in the subsoil. A depth of 70 m was specified after having calculated the stability to suffusion and considering the soil analysis as interpreted by professional engineers. The new cut-off wall was to be embedded into the existing sealing blanket. In the original construction phase, some steel grout pipes remained in the subsoil. They posed a critical obstruction during the cut-off wall installation using a hydro-cutter. Therefore, in plan-view the cut-off wall was positioned downstream adjacent to the grout curtain. The old sealing core in the dam remains therefore largely untouched and effective. The dam crest had to be widened by 4.5 m to provide a sufficient working platform for the main equipment. However, it was only possible to operate the hydro-cutter equipment straddling across the wall axis parallel to the dam axis.

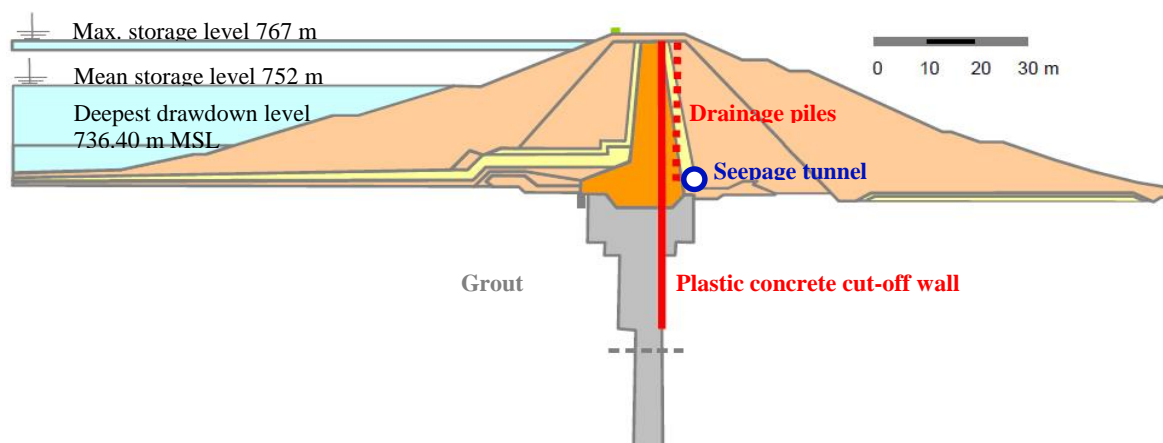


Figure 2. Standard cross section with cut-off wall, drainage piles and seepage tunnel

4. CONSTRUCTION OF THE CUT-OFF WALL

The diaphragm wall method has been proven for decades as the system to install concrete cut-off walls to greater depths. Grabs and hydro-cutters are being used with slurry supporting excavations, safely and successfully to remediate impounded embankment dams. Typically, clay concrete – so called plastic concrete – is chosen to install the durable and elastic seepage barrier.

For the Sylvenstein dam, on a limited working space, a hydraulic grab and the specially modified hydraulic cutter was chosen to install the wall to the satisfaction of the client, both in time and budget. The required slurry handling plant – consisting of mixing, storage and desanding units – had to be installed along the road to the dam crest. The concrete batching plant was placed downstream of the dam.

Pre-excavation with a grab is the method typically used for economic excavation of the panel elements in soil where depths usually do not exceed 40 m. The hydro-cutter technology is the established and tested method for cutting into rock and through boulders, ensuring a defined overlap between the individual panels for a continuous wall and for installing deep vertical panel elements.



Figure 3. Cut-off wall equipment on a limited working platform

The diaphragm wall executed at the Sylvenstein Dam had to reach a maximum depth of approximately 70 m below the dam crest as there are alternating layers of gravel and rock sediments and the highly varying permeability of the old underground sealing. Preparation works were executed with a grab in the upper part of the trench. Then, the diaphragm wall was installed, deploying a Bauer BC 40 Trench Cutter with a Bauer MC 128 base carrier. The wall is laterally embedded in very hard dolomitic limestone.

The location and natural surroundings of the project site were a challenge to logistics. As working space was limited on the dam crest the concrete mixing plant was assembled in the valley below the dam and the plastic concrete was pumped up 50 m to the work platform.

The mix design for the plastic concrete (clay concrete) was developed by the Technical University of Munich and conforms to the DIN EN 1538 standard. A permeability of $k_f < 10^{-9}$ m/s at a low stiffness was specified.

Table 1- Project specific mix design for plastic concrete / Clay concrete

Mix No.	H ₂ O (kg/m ³)	Binding agent (kg/m ³)	Clay powder (kg/m ³)	Gravel (kg/m ³)	Sand (kg/m ³)	Retarder [%]	Plasticizer [%]
H 0.57	375	125	220	521	782	4	1,5

The quality was assured through an intensive testing and control regime, all of which was defined by the Contractor in the project specific Quality Management Plan for approval by the Engineer.

5. CONSTRUCTION OF THE SEEPAGE TUNNEL SYSTEM AND COLLECTION PILES

Construction of the tunnel system started in May 2013. Firstly, the access tunnel and the starting cavern were driven by drilling and blasting and the target shaft was executed. The concrete pipes with a length of 2.8 m each were installed using a tunnelling machine with slurry supported working face. As the concrete cut-off wall was installed already, it was not necessary to lower the lake water level. The performance for the concrete pipe advancement was up to 5 pipes/24hours. The target cavern was reached with a deviation of less than 3 cm after 16 days. In 2014, the drainage piles are being constructed and connected to the tunnel by horizontal drills. Subsequently, the tunnel will be extended and the site instrumentation installed.

The rehabilitation package was started in 2011 and is planned to be completed by 2015. The total budget amounts to 24 million € and the costs will be shared equally by the Free State of Bavaria, Germany and the European Regional Development Fund (ERDF).

During the entire construction period the Sylvenstein Dam has to fulfil its core tasks which are flood protection and heightening of low water of the Isar River. Therefore, the reservoir was always partially impounded.



Figure 4. Cut-off wall installations with diaphragm wall grab, cutter and plants

6. FLOOD IN BAVARIA, GERMANY IN JUNE 2013

End of May 2013, with remarkably cool temperatures and constant rainfall, extensive heavy precipitation started, resulting in massive flood discharges and large scale flooding in Bavaria. Especially from May 30th to June 3rd the water levels reached record heights in many places resulting in catastrophic impacts in some areas. In the city of Passau, a new record height of almost 13 m above average was measured at the gauge Passau/Danube in the evening of June 3rd, (around 70 cm higher than during the Danube flood in 1954 - approx. 12.20 m), the highest Danube flood in the 20th century. This even exceeded the water levels of the highest known flood in the year 1501.

In Bavaria, the flood event caused damages amounting to about 1.3 Bio. Euro. The "disastrous flood" of 2013 once again drew the public's and media's attention to the flood issue. Apart from the enormous material damages, which considerably affected many citizens, Bavaria survived the flood relatively lightly. No loss of life was reported. The steps already taken within the scope of the flood protection programme 2020 for flood protection and risk management have proven effective and prevented more serious damage.

After the major flood events in May 1999 and August 2005, the June flood 2013 is already the third most significant event within the Isar catchment area, which severely strained the Sylvenstein Dam.

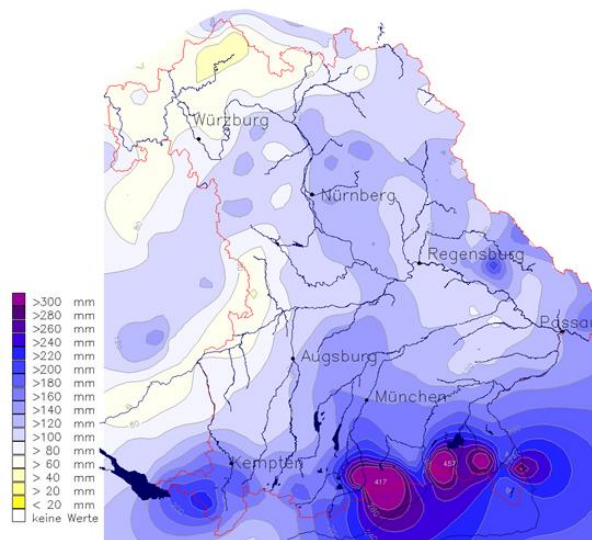


Figure 5. Precipitation volume of 26 May 2013 to 3 June 2013 in Bavaria

Other than at previous major floods during which mainly the discharge possibilities of the Alps and its edges contributed to the total flood runoff, here the complete Isar catchment area had rather uniform rainfall. Such rainfall could not be discharged in total in the Alps because the snow line during the flood was at approx. 1,800 m MSL. As the flood lasted so long, also the smaller Isar inflows contributed decisively to the flood peak. Thus, the return period of the Isar flood events increased downstream, starting near Munich.

The HQ-10 to HQ-20 inflow rate into the Sylvenstein Dam could be reduced downstream of the reservoir to an approximately HQ-10 inflow rate. Due to the enormous volume of inflow from the river Loisach (HQ-20), the river Amper (HQ-20 to HQ-50) and the massive rainfall on the interim area, the return periods starting from Munich increased. Below the inflow from the river Amper the return period was approximately at a HQ-100 level.

7. OPERATING THE SYLVENSTEIN DAM DURING THE 2013 FLOOD EVENT

The Sylvenstein Dam was hit by three inflow waves during the massive June 2013 flood. The first peak arrived at the reservoir in the morning of June 1st with about 300 m³/sec. The following day, the second wave reached the dam with approx. 550 m³/sec. After a very short subsiding phase (approx. ½ day) the highest inflow volume came with approx. 675 m³/sec; this figure corresponds near to that experienced every 20 years (HQ-20). On June 3rd, 99.7 % of the controllable water retention space of the Sylvenstein Dam was filled.

The old flood relief of the Sylvenstein dam became operational for the first time after its installation in 1954 from June 3rd to 4th. The volume of the flood event amounted to around 100 million m³ and thus exceeded the flood of 2005. Approximately 61 million m³ were retained, which is about 60 % of the total inflow waves. This is an excellent outcome in view of the extent and the duration of the flood wave; the standard floodwater retention space was used to almost full capacity.

It was only possible to manage floods such as in 1999, 2005 and 2013 by the dam rehabilitation measures taken from 1997 to 2001 (mainly by the construction of the second flood relief plant and by elevating the dam by 3 m). The current rehabilitation had set an essential milestone when installing the deep plastic concrete cut-off wall in 2012. Thus, due to the assured dam tightness after installing the new cut-off wall, it was possible to increase the impounded reservoir level to a record height and to keep it for an extraordinarily long time in order to drastically reduce the outflow considering the flood situation in lower lying areas.

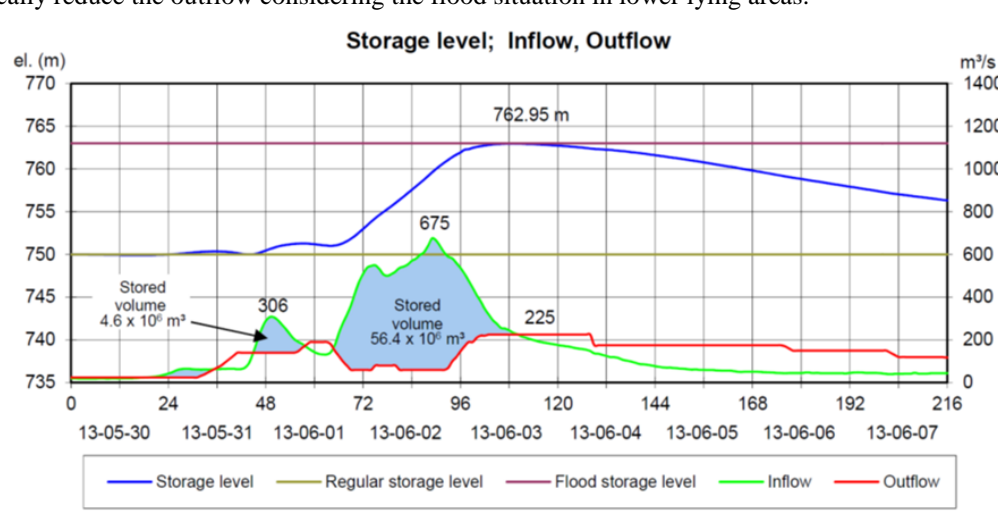


Figure 6. Storage management at Sylvenstein reservoir June 2013

At the dam itself, there was no major damage identified. However, the auxiliary dam (forebay reservoir) and the main reservoir had to be cleared of driftwood. During the flood the auxiliary dams retaining the bed-load again proved to work effectively. On the area with normal stored-up water level an echo sounder was used during a lake excursion. For the first time since the initial operation of the dam, the crest was measured during a flood. Although the reservoirs were completely filled, deviations of only a few millimetres were observed. The construction works (blasting) for the new seepage tunnel were interrupted for 10 days as a precautionary measure due to the full reservoirs at the Sylvenstein Dam.

8. CONCLUSIONS

The timing of the rehabilitation measures at the Sylvenstein Dam which started in 2011 was extremely opportune considering the flood of June 2013 because the centrepiece, (the installation of a diaphragm cut-off wall being up to 70 m deep in the dam core), was already successfully completed in 2012. Thus, the Sylvenstein Dam was capable of operating to its full potential. After the heightening of the dam in 1999, the financial means used for the Sylvenstein Dam again proved a resourceful investment considering the enormous damages which can be prevented in the complete Isar valley down to the city of Munich as well as the possibilities for relieving the water situation up to the Danube River.

9. ACKNOWLEDGMENT

The constructive and goal-focused cooperation between all parties involved including the head of the Water board, Weilheim, Germany Dr. Tobias Lang led to the successful completion of the plastic concrete cut-off wall in time. Tobias Lang and his team contributed as well in a significant way to the documentation of these works and the dam behaviour during the flood event 2013.

10. REFERENCES

1. Banzhaf, P.E.; Baltruschat, M.; Beutler, S.; Hechendorfer, S. (2013): Cut-off Wall for the Strengthening of the Sylvenstein Reservoir (70 km south of Munich, Germany) Cut-off Wall executed with BAUER cutter & grab and Plastic Concrete. Hydro 2013, Innsbruck, Austria.
2. Banzhaf, P.E.; Colmorgen, E. (2011): Reliable Seepage Control by Plastic Concrete Cut-off Walls, USSD 2011.
3. Banzhaf, P.E.; Lang, T. (2014): The performance of the Sylvenstein dam during the major flood event in June 2013. CDA 2014 Annual Conference, Banff, Alberta, Canada.
4. Langhagen, K.; Weiss, J.; Lang, T.: Ertüchtigung des Sylvensteinspeichers – Planung und Bau von Dichtwand und Sickerwassersammelsystem. In: Bautechnik 91 (2014), Heft 5, S. 347-353. (in German)
5. Lang T. et al.: Der Sylvensteinspeicher, (Hrsg.): Wasserwirtschaftsamt Weilheim, anlässlich der Feier '50 Jahre Sylvensteinspeicher', 2009, 88 S. (in German)
6. Nöll, H.; Dr. Langhagen, K.; Popp, M. and Dr. Lang, T. "Rehabilitation of the Sylvenstein Earth-Fill Dam – Design and Construction of the Cut-Off Wall", WasserWirtschaft 5/2013.
7. Overhoff, G.; Lang, T.; Popp, M.: Die geplante Ertüchtigung des Sylvensteinstaudamms. In: Wasserwirtschaft 100 (2010), Heft 4, S. 134-136. (in German)

Critical Success Factors in Construction or Rehabilitation Contracts Regarding Dams

Bettina Geisseler, GEISSELER LAW (Law firm), Germany

Email: geisseler@geisseler-law.com

Abstract

Constructing or rehabilitating a dam, be it for hydro power generation or other purposes such as flood control, drinking water supply or irrigation, is a complex project. Drafting adapted contracts taking into account and balancing the mutual interests of the contractual parties (the - future - owner as the “Employer” of the contract and the Contractor)¹ and aligning them with the requirements of other stakeholders of the project is a challenging task.

The critical success factors are:

- A clear-cut, unambiguous definition of the **Scope of Works**: this is *the* key provision of the contract and the benchmark, whether the works have been performed in compliance with the contract;
- Comprehensive rules regarding interface responsibilities and the **interface management**, be it between several Contractors, be it between the Employer and the Contractor; determination of the “rely upon information” to be provided by the Employer;
- A carefully drafted provision regarding the **allocation of typical risks** in case of unforeseen events during the erection phase;
- **Quality assurance**: an accurate documentation, the Employer’s approval-, inspection- and instruction rights and an adapted project organisation;
- Extensive **reporting obligations** to be complied with by the Contractor.

Keywords: Scope of Works, Interface Management, Allocation of Typical Risks, Quality Assurance, Reporting Obligations.

1. INTRODUCTION

Constructing or rehabilitating a dam, be it for hydro power generation or other purposes such as flood control, drinking water supply or irrigation, is a complex project. Drafting adapted contracts taking into account and balancing the mutual interests of the contractual parties (the - future - owner as the “Employer” of the contract and the Contractor) and aligning them with the requirements of other stakeholders of the project is a challenging task.

Critical success factor no. 1 of those contracts is a clear-cut, unambiguous definition of the Scope of Works. This is *the* core clause in the construction & erection contract.

The Scope of Works – including the quality requirements and a clear definition of the requested technical parameters – is the reference for evaluating whether the plant has deficiencies or not. And, it is the benchmark in disputes between the Employer and the Contractor if the latter asserts a claim for “EOT” (extension of time) and compensation of additional costs, alleging that works requested by the Employer are “extra work” requiring a so-called “Change Order”.

Critical success factor no. 2 are comprehensive rules regarding each of the parties’ responsibility in view of interfaces and the interface management. In complex projects with various lots there are a lot of interfaces and usually a great dependency between the works to be performed by different Contractors. The paper shows adapted contractual solutions.

Critical success factor no. 3 are provisions regarding an allocation of risks resulting from typical, but in the particular project unforeseen (and thus perhaps not calculated), events occurred during the erection phase such as bad quality of the rock, on which the foundations are built.

Quality assurance is the critical success factor no. 4: in complex projects it is of utmost importance to closely monitor the progress of the construction works in order to avoid bad performance and to be able to react quickly in case of discovered deficiencies. Usually the Employers reserve themselves the right to approve the design

¹. According to legal drafting standards some typical legal terms with an established meaning such as “Owner”, “Contractor”, “Scope of Works” are written in capital letters in the construction contracts and this paper.

documents, the engagement of subcontractors for major components or services and to exercise broad inspection and sometimes as well instruction rights. Furthermore, the establishing of an efficient project organisation combined with qualification requirements for the key personnel is substantial for the performance of the works in time and with the requested quality.

And last, but not least are ample reporting obligations by the Contractor essential. Only this will enable the Employer to closely monitor the project¹.

2. DEFINITION OF THE SCOPE OF WORKS

The definition of the Scope of Works is the core of the contract. Even in Turnkey Contracts where there is one single point of responsibility and the risk of incomplete supplies is much lower than in a multi-contracting structure, a precise definition of the Scope of Works together with the limits of supply and – as far as applicable – the definition of the parties' responsibility with regard to the interfaces is of utmost importance.

There are different approaches to define the Scope of Works. In countries with a long-standing experience in coordinating and supervising dam – and if applicable: hydro power plant - projects, state utilities seem to prefer to specify their requirements for the whole plant down to the smallest detail, e.g. down to the properties of the construction material to be used²; whereas in World Bank-financed projects Employers seem to prefer a more functional description of the plant to be delivered - leaving it up to the Contractor how to achieve this. An example are the JSCE specifications, which have developed in the past 20 years from rather prescriptive type specifications to more performance based specifications³ (*cf. JSCE Guidelines*). A certain caution is appropriate: An Employer stipulating detailed specifications risks bearing the responsibility that the specified parameters are “fit for the intended purpose.” In those cases, a Contractor might be released from its responsibility for the functioning of the equipment if he fully complies with the requested specifications.

While drafting the Scope of Works clause and setting up the Employer's Requirements, the parties need to avoid ambiguous expressions such as “of superior quality”, which can be interpreted in many ways. Other expressions like “state of the art” have – among experts – a clear meaning and can thus be used.

As far as the Contractor shall adhere to specific *technical standards*, guidelines or norms of national/international standardisation bodies such as ICOLD or DIN (e.g. the German DIN 19700, part 10 and 11) or the widely used USACE - US Army Corps of Engineers - standards, which are not legally binding, or to put it differently, do not directly result from the applicable laws⁴, those norms should be explicitly listed in the Employer's Requirements. I recommend this in order to avoid a dispute whether certain standards, which the Employer wants to have observed, are already “state of the art”, a general requirement, which each Contractor is obliged to comply with, or not. It is important to make reference to a specific edition (year) of an applicable standard and to avoid as far as possible contradictions while declaring various standards applicable – even if the contract provides for an order of precedence regarding the different annexes (*see figure 1*).

¹ The paper can only deal with some important contractual issues. Other important issues such as questions of the *applicable law* (not a “quantité négligeable”, because it will e.g. decide upon the available remedies and might contain mandatory legal provisions which the parties must consider while balancing their mutual interests!), or the *dispute resolution mechanism* (state courts vs. arbitration) could not be taken into consideration. The questions of the Employer's remedies in case of delay, defects or other non-compliance committed by the Contractor could not be addressed in this paper. The aim of this paper is to alert Owners / Employers or Contractors of critical issues potentially having a major (financial) impact on the execution of a dam / hydro power project, and to suggest, which critical issues should be considered and taken into account when drafting the contract. In no way shall it constitute and substitute for a specific legal advice, which will depend inter alia on the applicable law.

² *RWM Richtlinien für Werkstoffe in hydraulischen Maschinen des Verbands der Elektrizitätswerke Österreichs*, 2009

³ JSCE - Japan Society of Civil Engineers – Guidelines; e.g. the JSCE Guidelines for Concrete, no. 18 ‘Standard Specifications for Concrete Structures – 2007 ‘Dam Concrete’

⁴ As example for legally binding requirements: cf on an EU level the *BREF Documents (Best Available Technique Reference Documents)*, which substantiate the requirements of the *DIRECTIVE 2008/1/EC of the European Parliament and of the Council of 15 January 2008 concerning integrated pollution prevention and control* for the approval practice of the state authorities granting operation permits for industrial installations. The same applies in case of authorisations under the German environmental law: the *BVT Merkblätter* substantiate the “state of the art” requirement, stipulated by the relevant legal provisions.

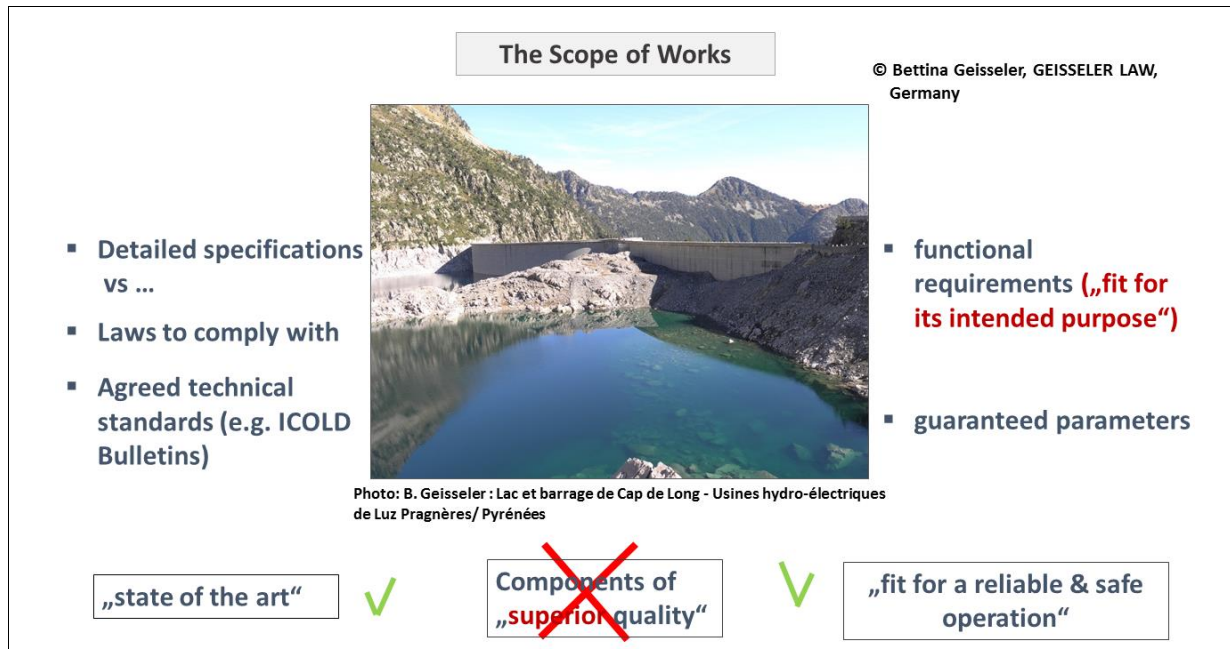


Figure 1. The definition of the Scope of Works

3. COPING WITH INTERFACES

Coping with interfaces first of all requires both from a technical point of view as well as from a contractual point of view to identify the interfaces.

In particular, in multi-contracting projects there are many interfaces between the different lots. However, there are also interfaces between the Employer and other stakeholders of the projects, and last, but not least the interfaces between the Employer and the Contractor. The role of the contract is to clearly attribute the respective responsibilities and to define the mutual obligations regarding the interfaces. Besides the definition of the Scope of Works the interface *management* is one of the most critical success factors of the project execution. While the Scope of Works determines the limits of supply, and thus determines which components found at the interfaces fall within the Contractor’s responsibility, the interface management relates to the question of which of the parties is responsible for coordinating the different lots. The parties need to decide who shoulders the risk if one lot upon which another lot is dependent is performed poorly or delivered too late.

Regarding interfaces, usually the Employer tries to minimize his risk by stipulating in a contract two obligations, which the Contractor has to fulfil: (i) the Contractor must deliver – within the limits of his Scope of Works - a complete work and he is obliged to perform all supplies and services which are necessary for the functioning of the plant even if they are not explicitly mentioned in the Employer’s Requirements; and (ii) the Contractor has to cope with the interfaces. It should be noted, that in case (i) this clause still requires Employers to clearly stipulate the limits of supplies or, differently spoken, the “Excluded Works” and that regarding case (ii) I would recommend to be much more specific. In such cases it can make sense to establish a detailed “Interface Matrix” in the annexes to the contract.

As shown below (see figure 2), one of several Contractors has no direct contractual relationship with anyone of the Employer’s other Contractors. Thus he cannot exercise and enforce any rights vis-à-vis his Co-Contractors. Unless specifically otherwise agreed upon in a contract, the respective rights and obligations only exist between the contracting parties. Therefore, it is typically - or should be, from a Contractor’s perspective - the Employer or his engineer (“Owner’s Engineer”) who assumes the interface *management* responsibility.

But of course other contractual solutions are possible: The Employer-friendliest I have ever seen in tender documents was: all Contractors had to organize the handling of the interfaces among themselves by guaranteeing all together the success of the works – though they were neither in a consortium nor another contractual relationship. It seems hard to imagine that one contractor accepted that clause!

The Employer himself has various other contractual/ legal relationships to other stakeholders of the project. He must comply with the conditions of the compulsory state permits and, as the case may be, the requirements of a hydro power plant or the possibility for ships / boats to be able to bypass the dam. He is well advised to pass on the requirements of these contractual relationships individually to each of his Contractors constructing the dam and make them an integral part of the respective contracts.

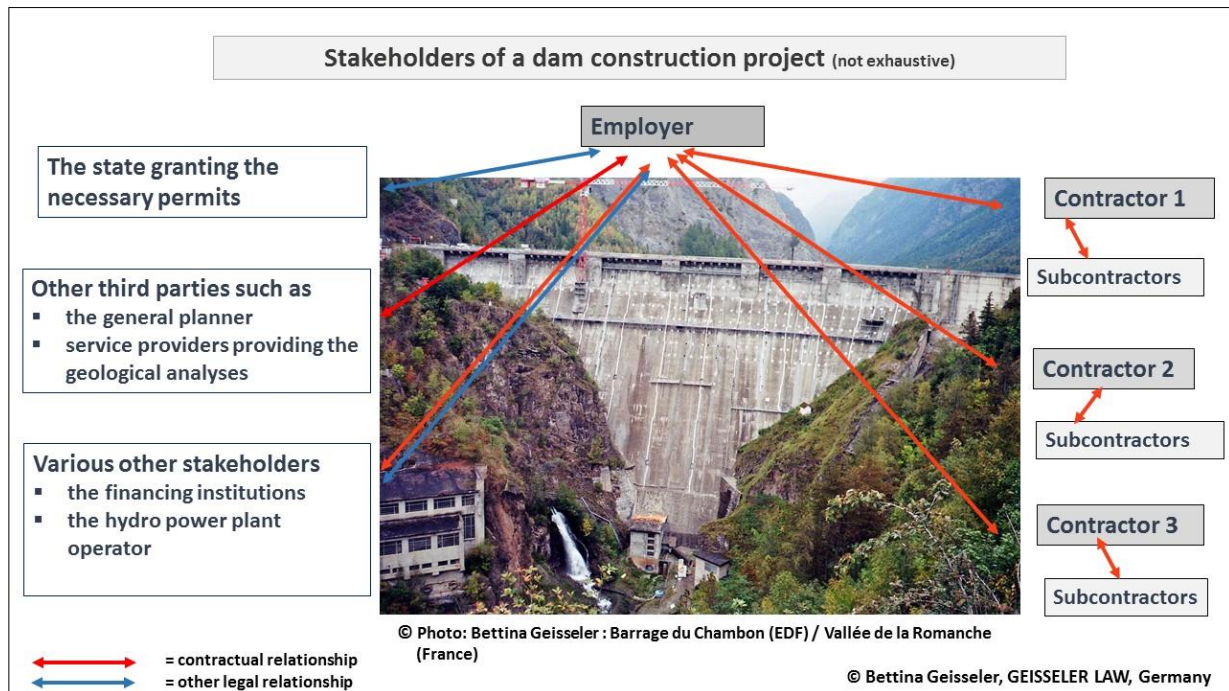


Figure 2. Interfaces – the stakeholders of a dam construction project

4. ALLOCATION OF TYPICAL RISKS – UNFORESEEN EVENTS

The more complex a project is, and the more stakeholders in the project exist, the more difficult it will be to balance the risks because the provisions of all the other related agreements have to be taken into account and aligned with each other.

In “BOT” (build – operate – transfer) schemes with the participation of the private sector the lending institutions and consequently the Employer want to have cost certainty. The financing banks have a vital interest that the Owner/ Employer does not assume risks which would endanger his possibility to comply with his obligations under the terms of the financing agreements and thus jeopardize the whole project.

The allocation of risks between the Employer and the Contractor and the balancing of the risks in view of the calculated and offered contract price is one of the most challenging and difficult tasks while drafting and negotiating a dam construction contract. Not only might it be difficult to clearly identify the potential risks and evaluate the risk exposure; sometimes it seems that the contractual parties do not have a clear idea of the legal consequences of a clear risk allocation, and in particular the cross-influence with a typical Force Majeure clause or, respectively, Force Majeure event. A Contractor who accepts a clearly identified risk (a) cannot claim EOT and / or compensation for higher costs in case of hindrances during the project execution due to the occurrence of that risk, and (b) still has the responsibility for “care and custody” of the plant. In the worst case the Contractor is obliged to rebuild parts of the already erected plant in the event that the risk materialises and leads to the (partial) destruction of the plant (see fig.3).

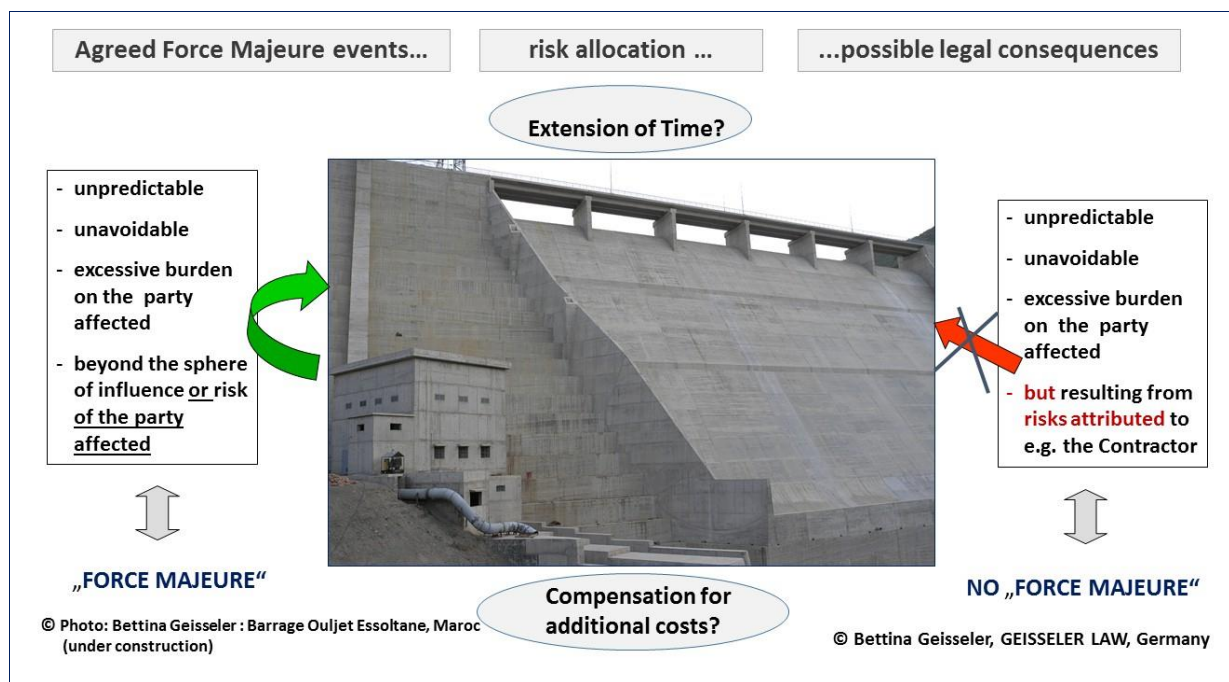


Figure 3. Allocation of risks – unforeseen events during the erection phase

There are typical risks in dam construction projects – or to put it differently: unforeseen conditions, where the risk that they materialise is considerable high. The materialisation of these risks might lead to considerable delays and in consequence considerably higher costs.

The contractual parties should identify and discuss in detail the major and typical project-related risks, such as the (remaining) risk of different geological subsurface conditions other than those investigated. They should carefully evaluate these risks and then allocate them to one of the parties – considering the provisions of the applicable contract law.

The probably highest risk in connection with the construction of a dam results from the geological conditions and in particular the quality of the subsoil. It should not be taken for granted that according to the applicable legal system it is the Owner/ Employer who bears the subsoil risk! Another typical risk is the flood risk during the construction/ erection phase.

In dam rehabilitation contracts there is a high risk that the condition of the existing dam is different from what one party/ the parties assumed. In this connection it is of importance to define to which extent the Contractor can rely on documents/ information given to him by the Owner/ Employer (so-called “rely-upon information”). Tender documents quite often contain (Employer-friendly) clauses such as “Contractor is thus deemed to be fully aware of all constraints, incidents, which may result from the natural site conditions (climatic, atmospheric, meteorological...), the nature of the ground and the subsoil and more generally from any elements and circumstances likely to have an influence on the performance of the Contractor's Works”. According to my experience it will depend not only on the applicable law but very much on the project, the negotiating position of either party, and the course of the negotiations, whether such a “catch-all” clause with a broad wording can allocate or, respectively, shift the total risk exposure for a majority of (quite important!) project-related risks to the Contractor in a legally valid way.

In a well - negotiated, balanced contract, the taking over of major risks with at least a medium probability of occurrence will normally lead to a proportionate increase of the contract price.

Within this context it should be reminded, that the contract law, i.e. the applicable law governing the contract, sometimes provides for solutions which the contractual parties do not like. In this case they explicitly have to derogate from the otherwise applicable provisions and stipulate provisions reflecting their intentions.

5. QUALITY ASSURANCE

5.1. DOCUMENTATION & SPARE PARTS

Like in all major infrastructure projects an accurate and actual documentation, including the "as built"-drawings is of great importance. Only then will the Owner/ Operator be in the position to maintain & rehabilitate the dam in an appropriate way. Regarding spare parts for critical components I recommend to agree contractually already in the construction contract on the issues that arise: shall the Contractor deliver an amount of spare parts to the site or keep in reserve a stock of spare parts; may the Owner use the construction drawings to have the dam maintained or rehabilitated by, as the case may be, having the spare parts re-constructed by a third manufacturer?

5.2. EMPLOYER'S APPROVAL, INSPECTION AND INSTRUCTION RIGHTS

Usually the Employer reserves the right to approve the design documents. It should be noted that the Employer's approval in no way relieves the Contractor from his own responsibility to deliver a work in accordance with the contract and in particular without any deficiencies. It should be clear that a non - approval can only be based on reasons of non - compliance of the design documents with the contractual requirements. A well - drafted contract should stipulate the deadlines, until when an Employer has to grant his approval.

Sometimes the Employers explicitly reserve themselves extensive rights to give detailed instructions regarding the execution of the works. Without prejudice to the question whether those instructions might be considered as Change Orders entitling the Contractor to an EOT and a price adaption, some caution is appropriate: in the case that the Contractor considers those instruction to jeopardize the success of the works, he must inform the Employer (I advise: in a written way) about his concerns. Only then he will be released from his responsibility for defects if the Employer insists on his instructions and thus forces the Contractor to follow them.

Typically, the contracts oblige the Contractors to seek the Employer's prior approval for the major subcontractors or suppliers of critical components. This can be done by way of approval in each particular case or by way of a list annexed to the contract establishing a number of pre-approved suppliers. From the Contractor's perspective a certain caution is appropriate in the latter case. In order not be faced with prices of the pre-approved sub-suppliers far beyond the usual market price, the Contractors should insist on a contractual clause allowing them to deviate in justified reasons from this list (under the condition that the alternatively engaged sub-supplier meets the quality requirements) and to state as one of the possible reasons the fact that the pre-approved sub-suppliers request prices being x % above the worldwide market price.

Other important instruments are broad inspection rights exercised by the Employer and the detailed specification of a quality assurance system/ quality assurance plan, which the Contractors are obliged to comply with and which they are to impose on each single subcontractor/ sub-supplier in the supply chain. A typical example in dam construction projects is the obligation of the Contractor to grant the Employer access to the Contractor's production sites for the purpose of inspections of the manufacturing process, especially of the manufactured (key) components before they are integrated into the plant during the erection process. Experience shows that it might be in the Employer's interest not to leave it to his Contractors to inspect the manufactured parts at the sites of their subcontractors, but to make large use himself of his rights and to double-check, even if the components in question are manufactured by a sub-sub-supplier and/ or in production sites 'at the other end of the world.

5.3. PROJECT ORGANISATION

The Employer should think about a project organisation on Contractor's side which will ensure an efficient project execution. The contract can and should contain provisions regarding the qualifications of the Contractor's Project Manager bearing the overall responsibility for the project progress.

Furthermore, the Employer is well - advised to determine the language skills of the key personal as well as the way of communication between the parties and on site. The same applies for the way in which the requested project - related documents should be delivered by the Contractor to the Employer – without prejudice to the official documents to be submitted to the state authorities.

6. CONTRACTOR'S REPORTING OBLIGATIONS

In complex and large-scale dam, or as the case may be, hydro power plant erection contracts, Employers are well advised to require from the Contractor continuous and regular, prompt, complete and accurate information

on the stage of completion of the design, manufacturing and erection process and in particular on the occurrence of hindrances having an impact on the price or the time for completion.

Only such a reporting system will enable the Employer to maintain control over the entire project and to notice at an early stage events having a negative impact on the time for completion and/ or the costs or the contract price. I have seen contracts (governed by a law of a civil law country) providing that the breach of those reporting obligations (e.g. the non-delivery of the requested weekly project reports) shall entitle the Employer to make use of a right of retention relating to due (payment) amounts up to a relatively high amount.

7. CONCLUSIONS

The purpose of a contract is to well balance the mutual interests of the contractual parties in view of potentially arising risks. The Parties are well - advised to carefully identify the typical risks, evaluate their mutual interests and to draft provisions reflecting their commercial intentions.

Analytical Solution for Level Pool Routing Equation Based on Various Inflow Hydrographs

Banafshe Nematollahi Sarvestani¹, Majid Niazkar², Nasser Talebbeydokhti³

1- PhD. student, Department of Civil and Environmental Engineering, School of Engineering, Shiraz University, Shiraz, Iran. E-mail: banafshe.nematollahi@gmail.com

2- PhD. Candidate, Department of Civil and Environmental Engineering, School of Engineering, Shiraz University, Shiraz, Iran. E-mail: mniazkar@shirazu.ac.ir

3- Professor, School of Engineering, Department of Civil and Environmental Engineering, Head of Environmental Research and Sustainable Development Center, Shiraz University, Shiraz, Iran. (Corresponding Author) E-mail: taleb@shirazu.ac.ir

E-mail: taleb@shirazu.ac.ir

Abstract

Reservoir routing is one of the most important issues in reservoir management. Estimating outflow from a dam outlet, which is the target of reservoir routing, is significantly vital since unpredicted floods can bring about severe damages to infrastructures and human beings downstream of storage reservoirs. In essence, general analytical computation of storage and outflow may be impossible in practice and subsequently, application of numerical methods seems to be inevitable for reservoir routing. However, analytical relations for temporal variation of water storage in a typical reservoir for several cases of inflow hydrographs including triangular, abrupt wave, flood pulse and broad peak hydrographs are derived in this paper. In these scenarios, an orifice was assumed for reservoir outlet. According to the literature, presented analytical solutions for the last three cases are proposed for the first time. The applicability of these analytical solutions is tested using four numerical examples while a robust numerical scheme, i.e., fourth-order Runge-Kutta, is also applied for solving these examples. The obtained results demonstrate that the recommended analytical solutions have a good agreement with the corresponding results of the utilized numerical scheme for all examples.

Keywords: Reservoir Routing, Analytical Solution, Inflow Hydrograph, Fourth-Order Runge-Kutta Scheme.

1. INTRODUCTION

Effective reservoirs which are decisive factors in water supply system in many communities usually have periodic high water levels. In order to not only maximize water usage but also prevent severe damages, hydraulic engineers are supposed to predict reservoir responses under various circumstances especially for high water levels [1]. From this point of view, reservoir routing is the process of determining the propagation corresponds to inflow hydrographs through reservoir [2]. Level pool routing is a robust tool for computation of outflow hydrograph from a single reservoir based on inflow hydrograph and the characteristics of the system [3]. In this regard, clarification of the hydraulic head equation with respect to time and detailed descriptions of hydrological characteristic related to the system play a key role in designing efficient reservoirs [4].

Various routing approaches can be classified into two main categories including (1) hydrologic routing and (2) hydraulic routing methods. The former employs continuity equation exclusively while the latter utilizes the continuity equation together with equation of motion [5-9]. This paper focuses on the hydrologic routing method which uses the nonlinear first-order ordinary differential equation.

The governing equation for level pool routing which is named as continuity equation is shown in Eq. 1:

$$\frac{dS}{dt} = I - Q \quad (1)$$

where S , I and Q are storage, inflow and outflow at time t , respectively.

Although there are numerous numerical solutions for the above mentioned equation [10-11], this equation can be analytically solved with some assumptions such as the hypothesis of power function for the storage-outflow relationship [12]. Furthermore, Paik [13] studied routing for a triangular inflow hydrograph in 2008. However, no recommendation is available for treating other types of inflow hydrographs in literature. In this study, it is tried to determine the analytical solution of outflow hydrograph for four common functions of inflow including triangular, abrupt wave, flood pulse and broad peak hydrographs.

The remainder of this paper is structured as follows: The methodology and governing equations of reservoir routing for various types of inflow hydrograph are developed in section 2. Afterwards, a comparison between obtained analytical solutions and numerical solutions of Runge-Kutta method is conducted for four numerical examples in section 3. Conclusion is given in the final section.

2. METHODOLOGY

The storage of a typical reservoir with constant area A may be computed as illustrated in Eq. 2.

$$S = Ah \quad (2)$$

where h is the hydraulic head of water.

The outflow from an orifice outlet can be computed using Eq. 3:

$$Q = \lambda Ca \sqrt{2gh} \quad (3)$$

where λ is the orifice formula error correction factor, C is the orifice coefficient, a is the total cross-sectional area of orifice outlet, and g is the gravitational acceleration.

By substituting Eq. 2 and Eq. 3 into the continuity equation (Eq. 1), a general form of routing equation of reservoirs with orifice outlets will be obtained, as shown in Eq. 4.

$$A \frac{dh}{dt} = I - \lambda Ca \sqrt{2gh} \quad (4)$$

The inflow hydrograph may have various types [14]. The solution of outflow hydrograph for 4 types of inflow hydrograph is proposed which are triangular, abrupt wave, flood pulse and broad peak. In the following, the analytical equations for hydraulic head and outflow of these inflow hydrograph are derived:

2.1. TRIANGULAR INFLOW HYDROGRAPH

The triangular inflow hydrograph (Fig. 1) function is expressed as follows:

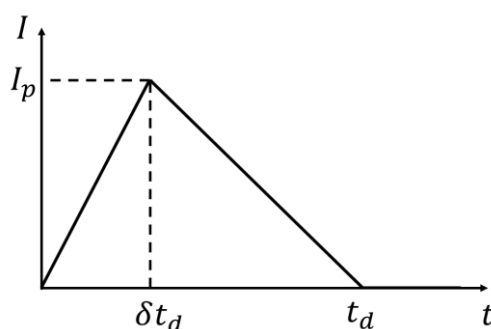


Figure 1. Triangular inflow hydrograph

$$I = \begin{cases} \frac{I_p}{\delta t_d} t & 0 \leq t < \delta t_d \\ \frac{I_p}{1-\delta} \left(1 - \frac{t}{t_d} \right) & \delta t_d \leq t < t_d \\ 0 & t \leq t_d \end{cases} \quad (5)$$

Thus, the outflow hydrograph can be divided into 3 parts: $0 \leq t < \delta t_d$, $\delta t_d \leq t < t_d$ and $t_d \leq t$. By substituting inflow for the first part into Eq. 4, the governing equation obtained as:

$$A \frac{dh}{dt} = \frac{I_p}{\delta t_d} t - \lambda Ca \sqrt{2gh} \quad (6)$$

Eq. 6 is in form of Abel differential equation [15]. By applying the initial condition of no initial storage ($h = 0$ at $t = 0$), the analytical solution of water head can be achieved as:

$$h = \frac{g}{8A^2} \left[\sqrt{(\lambda Ca)^2 + \frac{4AI_p}{\delta t_d g}} - \lambda Ca \right]^2 t^2 \quad (7)$$

Implementing Eq. 7 into Eq. 3 yields the analytical solution of first part of outflow hydrograph as:

$$Q = \frac{(\lambda Ca)^2 g}{2A} \left[\sqrt{1 + \frac{4AI_p}{\delta t_d g (\lambda Ca)^2}} - 1 \right] \times t \quad (8)$$

Eq. 8 reveals that the discharge from the orifice outlet increases linearly with respect to time t in the ascending limb of inflow hydrograph.

For the second part of outflow hydrograph, the governing equation is

$$A \frac{dh}{dt} = \frac{I_p}{1-\delta} \left(1 - \frac{t}{t_d} \right) - \lambda Ca \sqrt{2gh} \quad (9)$$

The initial condition of this part is the head water at time $t = \delta t_d$ which is:

$$h_{(t=\delta t_d)} = \frac{g \delta^2 t_d^2}{8A^2} \left(\sqrt{(\lambda Ca)^2 + \frac{4AI_p}{\delta t_d g}} - \lambda Ca \right)^2 \quad (10)$$

The analytical solution of this equation is not available but routing results from numerical methods show that the outflow hydrograph is nonlinear in this part.

Finally, the analytical solution of outflow hydrograph of third part is obtained by putting $I = 0$ in Eq. 4 as

$$h^{1/2} = -\sqrt{\frac{g}{2}} \frac{\lambda Ca}{A} t + J \quad (11)$$

where J is a constant that can be found by the initial condition of the third part, i.e., the head water at time $t = t_d$. Substituting Eq. 11 into Eq. 3 will result in a linear hydrograph similar to the first part.

2.2. ABRUPT WAVE INFLOW HYDROGRAPH

The mathematical expression of this type of hydrograph, which is shown in Fig. 2, is as follows

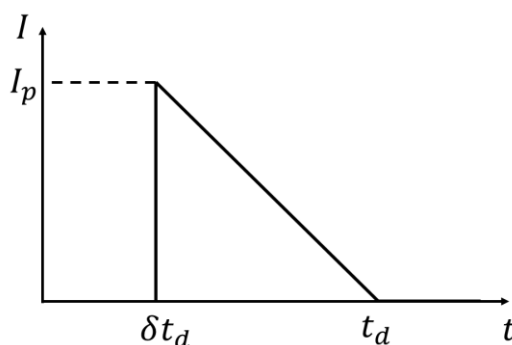


Figure 2. Abrupt wave inflow hydrograph

$$I = \begin{cases} 0 & 0 \leq t < \delta t_d \\ \frac{I_p}{1-\delta} \left(1 - \frac{t}{t_d} \right) & \delta t_d \leq t < t_d \\ 0 & t \leq t_d \end{cases} \quad (12)$$

First and third parts of this hydrograph are similar to the third part of triangular inflow hydrograph. Thus,

$$h^{1/2} = -\sqrt{\frac{g}{2}} \frac{\lambda Ca}{A} t + J \quad (13)$$

where J can be determined by initial condition of each part which are $h_{(t=0)} = 0$ and $h_{(t=t_d)} = h_d$, respectively.

The head water at time t_d can be found by solving the equation for second part of hydrograph. Similar to the second part of triangular hydrograph, there is no analytical solution for this part of hydrograph and it can be determined by numerical methods.

2.3. FLOOD PULSE INFLOW HYDROGRAPH

Third inflow hydrograph discussed in this paper is flood pulse hydrograph (Fig. 3). Similar to the previous types, it can be divided into 3 parts.

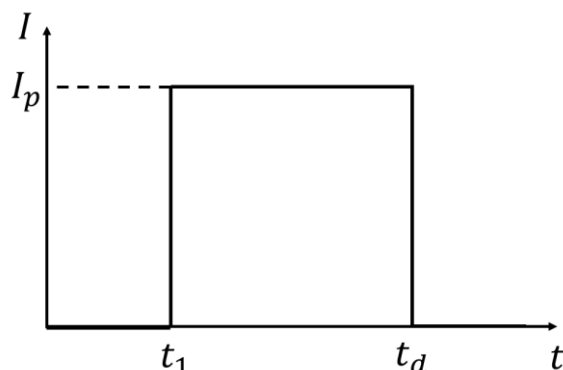


Figure 3. Flood pulse inflow hydrograph

$$I = \begin{cases} 0 & 0 \leq t < t_1 \\ I_p & t_1 \leq t < t_d \\ 0 & t_d \leq t \end{cases} \quad (14)$$

Substituting Eq. 14 into Eq. 4 will yield to analytical solution of each part of outflow. The first and third parts of this hydrograph are same as last part of triangular hydrograph with different initial conditions. Thus the analytical solution of head water is similar to Eq. 13. The initial conditions of these parts are $h_{(t=t_1)} = h_1$ and $h_{(t=t_d)} = h_d$. Eq. 15 and Eq. 16 are simplified equations of head water in the first and third part of hydrograph, respectively.

$$h^{1/2} = \sqrt{\frac{g}{2} \frac{\lambda Ca}{A} (t_1 - t)} + h_1^{1/2} \quad (15)$$

$$h^{1/2} = \sqrt{\frac{g}{2} \frac{\lambda Ca}{A} (t_d - t)} + h_d^{1/2} \quad (16)$$

Substituting the above equations into Eq. 3 will result in the linear relations for outflow which increase with time. The middle part of hydrograph with constant inflow results in Abel differential equation of the second kind [12]. Solving this equation results in the following equation

$$\frac{-\lambda Ca \sqrt{2g}}{2A} \times t = h^{1/2} + \frac{I_p}{\lambda Ca \sqrt{2g}} \ln \left(h^{1/2} - \frac{I_p}{\lambda Ca \sqrt{2g}} \right) + J \quad (17)$$

where J is a constant that can be determined by the one of the initial conditions mentioned in this section. However, because the natural logarithm argument is always negative, there is no analytical solution for this part of outflow hydrograph and should be determined by numerical methods.

2.4. BROAD PEAK INFLOW HYDROGRAPH

The last type of hydrographs discussed in this study is broad peak hydrograph which is shown in Fig. 4. Unlike three other types, this hydrograph should be divided into 4 parts (Eq. 18).

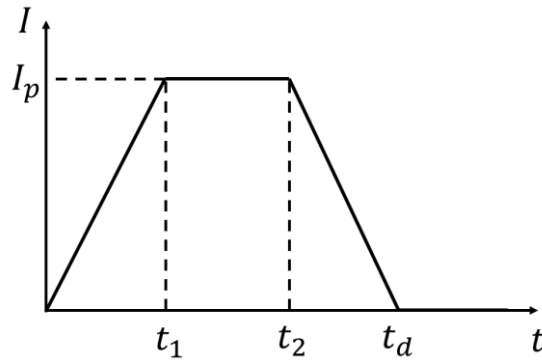


Figure 4. Broad peak inflow hydrograph

$$I = \begin{cases} \frac{I_p}{t_1} t & 0 \leq t < t_1 \\ I_p & t_1 \leq t < t_2 \\ \frac{I_p}{\left(1 - \frac{t_2}{t_d}\right)} \left(1 - \frac{t}{t_d}\right) & t_2 \leq t < t_d \\ 0 & t_d \leq t \end{cases} \quad (18)$$

By substituting inflow relation of each part into Eq. 4, the relation of outflow hydrograph can be obtained. The first part is same as the first part of triangular hydrograph with initial condition of $h_{(t=0)} = 0$ (Equ. 19).

$$h = \frac{g}{8A^2} \left[\sqrt{(\lambda Ca)^2 + \frac{4AI_p}{t_1 g}} - \lambda Ca \right]^2 t^2 \quad (19)$$

The second part is similar to the middle part of flood pulse hydrograph. Thus, there is no analytical solution for that.

As mentioned earlier, the descending limb of triangular hydrograph has not analytical solution. The descending part of Fig. 4 is same as the one in Fig. 1. Thus, the analytical solution of this part is not available and its outflow hydrograph is highly nonlinear.

Finally, the last part of inflow hydrograph which lies down on zero line, is like the last part of triangular hydrograph. The analytical solution of this part can be obtained by implementing the initial condition $h_{(t=t_d)} = 0$ to Eq. 13 as

$$h^{1/2} = \sqrt{\frac{g}{2}} \frac{\lambda Ca}{A} (t_d - t) \quad (20)$$

3. BENCHMARKS

In this section, the applicability of proposed formulations is demonstrated using four examples, one for each of inflow hydrographs. The analytical solutions are compared with results of a robust numerical method named as fourth order Runge-Kutta method which has shown good results in the literature [17]. Parameters of the orifice outlet and reservoir are listed in Table 1.

Table 1- Parameters of the model

Parameter	Value
λ	1
C	0.6
a (m ²)	2
A (m ²)	12000
Δt (s)	200

First, the triangular hydrograph with peak of $50\text{m}^3/\text{s}$ and total time of 7200s and $\delta = 0.5$ is assumed as input of the model (Gray dots in Fig. 5). As described in section 2, the ascending and zero limbs of inflow hydrograph result in linear outflow. Since there is no analytical solution for the second part of hydrograph, the results of the numerical solution in the result chart are used.

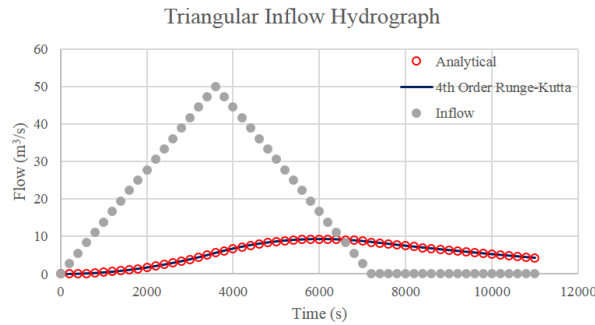


Figure 5. The outflow of triangular inflow hydrograph

Thereafter, hydrograph has zero value until 3600s . In the second part, it reduced linearly from peak of $50\text{m}^3/\text{s}$ to 0 and again it has zero value. According to the section 2, the first and third parts have analytical solution (Equ. 11) and there is no analytical solution for the second part.

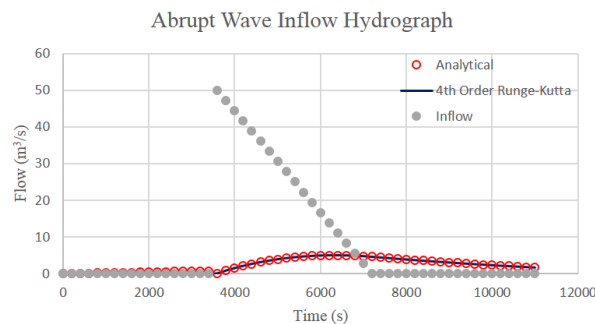


Figure 6. The outflow of abrupt wave inflow hydrograph

Flood pulse hydrograph composed of three constant parts. However, because the second part has non zero value, no analytical solution can be established and the numerical result is used for this part.

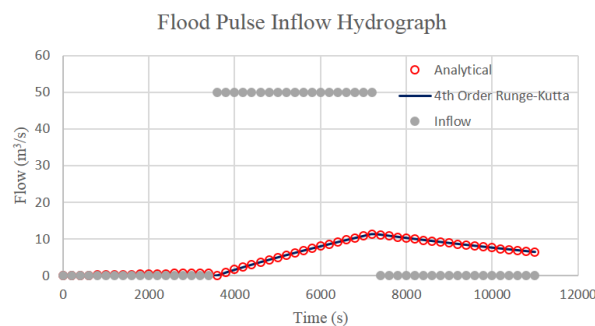


Figure 7. The outflow of flood pulse inflow hydrograph

The last inflow hydrograph shape is the broad peak hydrograph. It is a general trapezoid with an extended peak of $100\text{m}^3/\text{s}$ between a linear rise and descending parts. As an example, the hydrograph of two reservoirs in the historical 1997 flood of California can be approximated into this type of hydrograph [18].

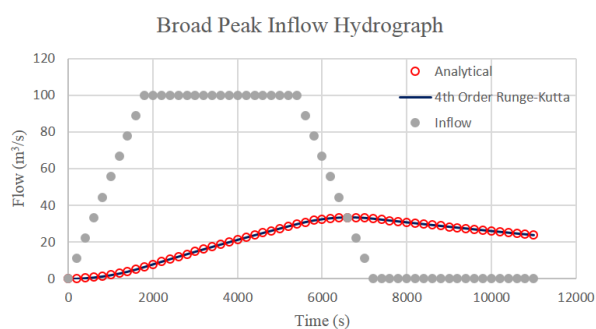


Figure 8. The outflow of broad peak inflow hydrograph

As illustrated in the above figures, the analytical solutions have very good agreement with numerical results. This good agreement indicates that the presented analytical solutions can be confidentially utilized for reservoir routing in cases in which the inflow hydrograph has similar shapes.

4. CONCLUSIONS

In this paper, analytical solutions for reservoir routing for several types of inflow hydrograph have been developed. According to the results, those parts of outflow hydrograph which has analytical solution are linear while those with no analytical solution are highly nonlinear. Compared with the results of Runge-Kutta method for four numerical examples, the analytical solutions have good agreement with the numerical method used for validation. It is obvious that general form of outflow hydrograph cannot be derived in practice. However, it may be possible to obtain analytical solution for special cases of inflow hydrograph and outlet conditions. Although, analytical solutions for four common types of hydrographs have been derived in this paper, seeking for analytical solution of other especial inflow hydrograph cases is suggested for future researches.

5. REFERENCES

1. Fenton, J.D. (1992), “*Reservoir routing*”, Hydrological Sciences Journal, **37** (3), pp. 233-246.
2. Fread, D.L. and Hsu, K.S. (1993), “*Applicability of two simplified flood routing methods: level pool and Muskingum-Cunge*”, In: Shen, H.W., Su, S.T. and Wen, F., editors. ASCE national hydraulic engineering conference. San Francisco, CA: ASCE, pp. 1564-8.
3. Chow, V.T., Maidment, D.R. and Mays, L.W. (1988), “*Applied hydrology*”, New York: McGraw Hill.
4. Leopold, L.B. (1997), “*Water, rivers and creeks*”, Sausalito, CA, USA: University science books.
5. Hossain, M.M. (2014), “*Analysis of flood routing*”, Dhaka University Journal of Science, **62** (2), pp. 69-73.
6. Niazkar, M. and Afzali, S. H. (2014), “*Assessment of Modified Honey Bee Mating Optimization for parameter estimation of nonlinear Muskingum models*”, Journal of Hydrologic Engineering ASCE, **20** (4), 04014055.
7. Niazkar, M. and Afzali, S. H. (2017), “*New nonlinear variable-parameter Muskingum models*”, KSCE Journal of Civil Engineering, **21** (7); DOI: 10.1007/s12205-017-0652-4.
8. Niazkar, M. and Afzali, S. H. (2016), “*Application of New Hybrid Optimization technique for parameter estimation of new improved version of Muskingum model*”, Water Resources Management, **30** (13), pp. 4713-4730.
9. Niazkar, M. and Afzali, S. H. (2016), “*Parameter estimation of an improved nonlinear Muskingum model using a new hybrid model*”, Hydrology Research, nh2016089; DOI: 10.2166/nh.2016.089.
10. Fread D.L. (1985), “*Channel routing*”, In: Anderson, M.G. and Burt, T.P., editors. Hydrological forecasting. New York: John Wiley and Sons, pp. 437-503.
11. Goodrich, R.D. (1931), “*Rapid calculation of reservoir discharge*”, Civil Eng., **1**, 5, pp. 417-8.
12. Yevjevich, V.M. (1959), “*Analytical integration of the differential equation for water storages*”, J. Res. Nat. Bureau Stand B Math Math Phys, **63B**, 1, pp. 43-52.
13. Paik, K. (2008), “*Analytical derivation of reservoir routing and hydrological risk evaluation of detention basins*”, Journal of Hydrology, **35** (2), pp. 191-201.
14. Hui, R. and Lund, J. (2014), “*Flood storage allocation rules for parallel reservoirs*”, Journal of Water Resources Planning and Management, **141**.
15. Polyanin, A.D. and Zaitsev, V.F. (1995), “*Handbook of exact solutions for ordinary differential equations*”, CRC Press, USA, pp. 29-31.
16. WWW.eqworld.ipmnet.ru, Abel differential equation, (2017)
17. Fiorentini, M. and Orlandini, S. (2013), “*Robust numerical solution for the reservoir routing equation*”, Advanced in Water Resources, **59**, pp. 123-132.
18. United States Army Corps of Engineers (USACE), (1997), “*Hydrologic engineering requirements for reservoirs.*”, Engineer Manual 1110-2-1420, Dept. of the Army, U.S. Army Corps of Engineers, Washington DC, USA.

Real Time Operation Model for Optimum Operation of Bukan Reservoir in Lake Urmia Basin

Kayhan Gavahi¹, S. Jamshid Mousavi²

1- MSc. Student, School of Civil and Environmental Engineering, Amirkabir University of Technology

2- Professor, School of Civil and Environmental Engineering, Amirkabir University of Technology

Email: jmosavi@aut.ac.ir

Abstract

This paper presents an adaptive forecast-based mathematical model for real-time operation of Bukan reservoir located in Lake Urmia (LU) Basin. The model consists of three modules: 1) a forecasting module that predicts future inflows to the reservoir up to the end of a year, 2) a reservoir operation optimization module determining optimum reservoir releases and 3) an updating module that updates inflow forecasts and optimal releases at the beginning of every time step. As the forecasting module, an adaptive neural-based fuzzy inference system (ANFIS) is trained and used to forecast future inflows. Having these future inflows, a linear optimization model is formulated and solved to find optimal reservoir releases in future time steps of the year. The objective function of the model is to maximize total volume of water received by the lake while supplying water for irrigation demands and instream flow. The model is tested for 2015-2016 water year and its performance is assessed. Results obtained are promising in terms of volumes of water allocated to different demand sectors and preventing downstream areas from flooding caused by uncontrolled spillage. This is important as the system has experienced a severe flood in this particular year resulting in significant damages.

Keywords: Lake Urmia, Bukan Reservoir, Real Time Operation, Optimization.

1. INTRODUCTION

Climate change and human related activities has severely affected total inflow received by the Lake Urmia (LU) in the Northwest of Iran. Construction of various dams on the main rivers flowing to the lake and domestic and agricultural developments, which has resulted in increasing water demands in the past decade, has decreased the water level of the lake by 90% in September 2015. Climate change and increased irrigation demands are two main reasons for reduction in inflows to the reservoirs and much less water received by the lake. In this critical situation, the issue of improved operation of reservoirs to better meet the LU share from upstream reservoir releases has become more significant. Most of these reservoirs are multipurpose reservoirs functioning for water supply for downstream consumptive and non-consumptive demands and flood control. A number of contradictory objectives exist for operation of reservoirs of the basin. The first one is to store water as much as possible at the beginning of May to meet agricultural demands of future months up to about middle of September (end of water year) and the other one requires water releases in order to reserve reservoir capacity for the incoming flood. On the other hand, most of water releases made during irrigation season (May-September) will not reach the LU, resulting in critical adverse conditions in the lake. In other words, retaining water behind dams in winter months, to achieve higher reliability in meeting irrigation water demands, also causes significant reduction in the annual volume of water received by the LU that ultimately culminate in water level decline of the lake being drying up. Therefore, more careful and planned reservoir release schedule is needed accounting for the aforementioned conflicting objectives. In this line, a real-time reservoir operation modeling approach benefiting from forecasts of future inflows to reservoirs could be of help on how to best operate the basin's reservoirs [1]. The framework can provide insight on how to make best possible release decisions based on the most recent knowledge of future inflows. Having the most recent state of the system, forecasting models can determine the future state with a reasonable degree of uncertainty. Although the inherent forecast uncertainty will directly affect the results of this kind of operational models, improvements is expected to attain because of step-by-step reduction of forecast uncertainty as more information and data are received and the release decisions are updated [2], [3].

Two types of real-time reservoir operation models has been used in the literature [4]. Standard real-time operation models in which a streamflow forecasting model estimates future inflows only one time up to a specified short-run time horizon, and the decisions will be made based on these estimated predictions. This type of real-time operation models is mostly used for flood management purposes [5]–[8]. The second type is adaptive real-time operation models where the inflow-to-reservoir forecasts are updated step-by-step at the beginning of each

time period of operation. It therefore has the chance to adapt itself to the most recent conditions and changes occurred in the system.

In this paper an adaptive real-time operation model is proposed for Bukan reservoir and its downstream system, which is the largest reservoir of the LU water basin built on the largest river of the basin, Zarinehrood, which provides nearly 40% of the total inflow to the lake. It is a multipurpose reservoir with the main objectives of water supply for agricultural, domestic and industrial uses, and controlling floods that occur mostly in spring season. Thus, a release schedule specifically accounting for the LU share is needed as a necessary requirement for the success of restoration plan of the lake. Therefore, the proposed modeling framework considers not only water supply to various demand sectors, it but also takes into account the LU water demand and share, especially in months prior to the crop season. The paper is organizing as follows: the proposed methodology is presented in section 2 with three subsections explaining inflow forecasting module, reservoir operation module and updating module, respectively. Section 3 introduces the case study and the data and information used followed by section 4 containing results obtained and discussing them. Finally, section 5 ends the paper by a summary and concluding remarks.

2. METHODS AND MODELING TOOLS

We explained that the real-time operation model consists of three modules. The forecasting module predicts the inflow to the reservoir up to a specified time horizon, T . Various types of forecasting methods including physics-based, time-series modeling and data-driven methods can be used in order to forecast future inflows to the reservoir. Having the future inflows, the reservoir operation module determines optimum releases in future months based on the water demands and various constraints of the system. Simulation, optimization or a combination of both could be used for this task. These two modules working together provide an efficient tool for making decision on how to operate the system in near future based on the most recent knowledge available. However, the longer the forecasting horizon of the prediction module, more uncertain future inflow forecasts will be. Therefore, the reliability of decisions made on future releases diminishes rapidly by heading toward the final time steps of the operation horizon (end of water year). This is where the last module plays an integral part by updating the model predictions at the beginning of each time step based on the most recent information received as the inputs for the forecasting module. The updating module also update the initial state of the system based on observed inflows and the latest changes in downstream demands and conditions.

Figure 1. illustrates how these three modules work together. We present the details of each module in the following subsections.

2.1. FORECASTING MODULE

An adaptive neural-based fuzzy inference system (ANFIS) model was developed and used as the forecasting module. ANFIS uses a combination of artificial neural network (ANN) and fuzzy logic approaches. It uses fuzzy inference system of Sugeno type to obtain final values of each decision variable [9], [10]. Using a hybrid learning mechanism that consists of the back-propagation gradient descent and a least squares methods, ANFIS determines the best possible set of parameters to map the given input-output set of data points. Thus model is a data-driven model that identifies the inherent function within a system without explicitly knowing the physical relationship between input and output variables.

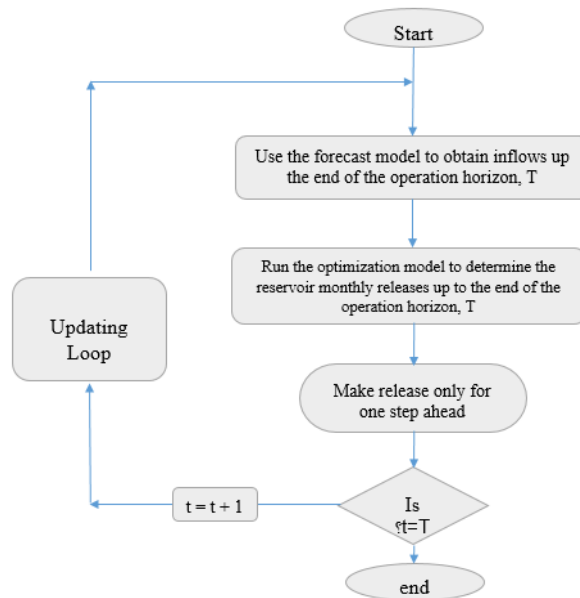


Figure 1. Flow diagram of the adaptive real-time reservoir operation model

Assuming a two dimensional input vector $[x, y]$, the equivalent ANFIS structure that derives the output function f will be a five-layer feed-forward network shown in Figure 2. More detailed presentation of ANFIS for forecasting hydrological time-series can be found in the literature [11]–[15].

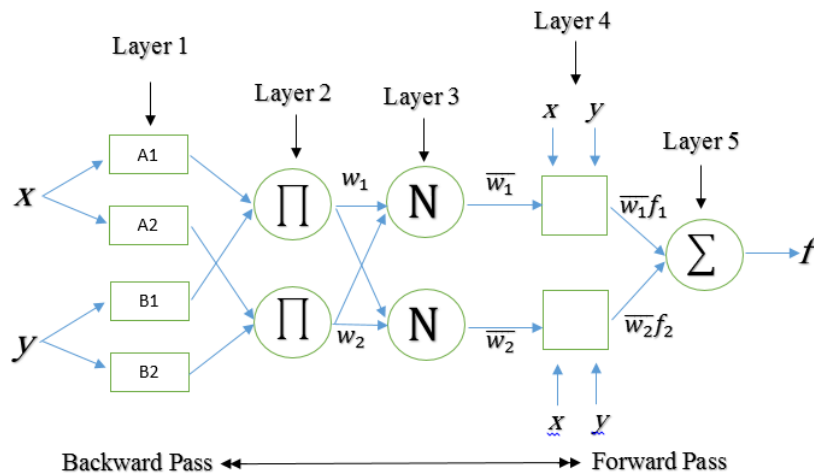


Figure 2. ANFIS structure for a two dimensional input vector $[x, y]$ and output function f

2.2. RESERVOIR OPERATION MODULE

Figure 3. shows a schematic view of the Zarinerood River system including Bukan Dam. Based on the sum of water demands for each sector that are directly supplied by the Bukan reservoir, we have developed a linear mathematical model optimizing the system operations.

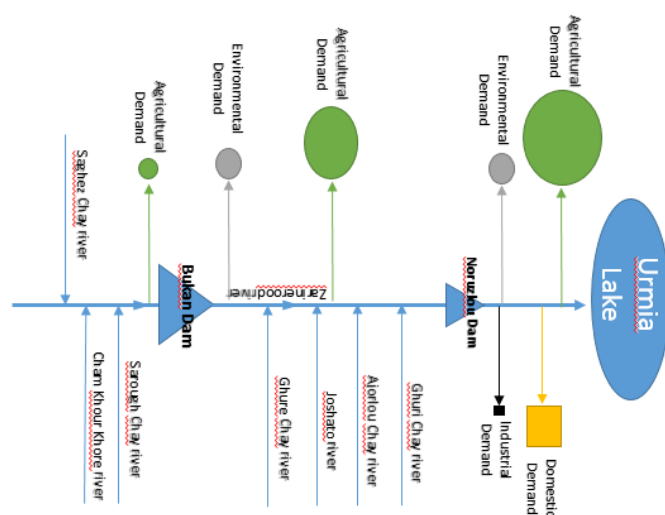


Figure 3. A schematic view of water inflows and withdrawals to the Zarinerood River downstream of Bukan Dam

The objective function of the proposed model is stated by equation 1. It is maximization of the benefits gained by releasing water for environmental instream flow, agricultural uses and the LU water demand. Each of these variables are accompanied by a priority coefficient. A larger coefficient for each user means a higher priority for water allocation to that user during shortages.

$$\text{Max } Z = \sum_{t=1}^n C_o R_{o_t} + C_a R_{a_t} + C_L R_{L_t} \quad (1)$$

In above equation n is the total number of time steps, C_o is the priority coefficient for environmental instream flow of Zarineroud River, C_a refers to priority coefficient for agricultural demands, and C_L is the priority coefficient for water received by the Lake Urmia. R_{o_t} , R_{a_t} and R_{L_t} are allocations for Zarineroud River, irrigation demands and the Lake Urmia, respectively. This objective function ensures that water is allocated first to minimum instream flow and minimum obligatory irrigation demands decreased by 40% compared to business-as-usual irrigation demands. After that the next priority is for the LU. Constraints of the mathematical program consist of water balance equations, upper bounds on water allocation values that must be less than the required demands and physical constraints regarding capacity of the reservoir and the downstream channels, especially at the inlet of Lake Urmia where fuse plugs are installed. They facilitate the release made for the lake reach the water body of the lake and prevent it from losing through seepage and evaporation in the buffer zone adjacent to the lake. Below is the set of constrains represented by equations 2 to 7:

$$S_1 \leq S_n \quad (2)$$

$$S_{t+1} = S_t + Q_t - R_{a_t} - R_{d_t} - R_{i_t} - R_{o_t} - R_{L_t} - E_t - spil_t \quad (3)$$

$$R_{a_t} \leq D_{a_t}, R_{d_t} = D_{d_t}, R_{i_t} = D_{i_t}, R_{o_t} \leq D_{o_t} \quad (4)$$

$$R_{L_t} + R_{o_t} = Cap_{fuz} \quad (5)$$

$$S_{\min} \leq S_t \leq S_{\max} \quad (6)$$

$$\frac{R_{a_t}}{D_{a_t}} = \frac{R_{a_{t+1}}}{D_{a_{t+1}}} \quad (7)$$

where S_t and Q_t are the beginning-of-month reservoir storage and inflow to reservoir in month t , respectively. E_t and $spil_t$ are evaporation and spillage from the reservoir, respectively. D_{a_t} , D_{d_t} , D_{i_t} and D_{o_t} are agricultural, domestic, industrial and minimum instream flow requirements, respectively. S_{\max} and S_{\min} are respectively upper and lower bounds on the reservoir storage volume, and Cap_{fuz} is the

capacity of the structures built at the inlet of the lake. Equation 7 ensures that if there exist any shortages and the annual irrigation demand cannot be fully met, shortages are distributed proportionately among irrigation months in an irrigation season [16]. Solution of this mathematical program contains optimum releases and allocation to different users.

2.3. UPDATING MODULE

According to figure 1, at the beginning of each time step, updating module will provide the ANFIS model with the most up-to-date observed data. These data include inflow to the reservoir, changes in downstream demands and also changes in downstream conditions that may result in changing the reservoir operation module coefficients. It also enables the ANFIS model to be trained once again in order to adapt itself and its parameters to observed inflows of previous time steps and therefore obtain higher performance in future inflow predictions. After forecasting future inflows of the next time steps up to the end of the operation horizon, T , the presented linear reservoir operation optimization model determines optimum releases and water allocations to different demands up to the end of the operation horizon. Since the forecasted inflows and therefore releases for more distant time steps are more uncertain and less reliable, only the reservoir release and water allocation for the immediate next time step ahead will be implemented. Having the observed inflow, the updating module simulates the system with actual values of inflow to the reservoir in order to determine the initial state of the system for the next time step.

Then if the model has not reached the final time step, the updating module collects the observed inflows and determines the initial state of the system, and forecasting and reservoir operation models are employed again. The procedure is repeated until reaching the end of operation time horizon that is the beginning of the next water year.

3. CASE STUDY

Lake Urmia (LU) water basin is located in northwest part of Iran. The basin takes its name from Urmia Lake located at the center of water basin. The lake suffers from dramatic decline in its water level and volume of water stored in it. In September 2015, the lake had only 10% of its potential storage capacity, a situation that seems to get worse if proper actions are not taken that could culminate in total loss of the lake. The largest river in the basin is Zarinerood River. This river starts from Zagros mountain range and drains to Lake Urmia after flowing for about 350 km distance. It passes through three provinces of Kordestan, West and East Azarbaijan and contributes to about 41% of total surface water inflow to the lake. The drainage area of Zarinerood River is about 12,000 km, and it crosses two cities of Shahindej and Miandoab [17]. Bukan reservoir as the largest reservoir in the basin has been constructed on this river for supplying water to agricultural, domestic and industrial water users. It has 810 million cubic meters (MCM) storage capacity and the long-term average annual inflow to the reservoir is about 1600 MCM. The outflows are distributed by the Norozlu diversion dam to about 85,000 hectares of Miandiab farming lands, and to three major cities such as Tabriz and its suburbs.

There are eight major dams being under operation in the basin discharging water to the lake and other demand points. The operation policies based on which the dams are operated directly affects the amount of water received by the lake throughout a year. Thus, it is important to use operation methods to account for downstream needs as well as considering the water required by the lake in order to survive. It should be noted that temporal variation of water released for LU is as important as the total quantity of water received. Releasing high amount of water in a shorter period of time not only can cause damages in downstream urban and agricultural areas, it but also results in damaging a number of structures and fuse gates built to facilitate transferring water to the main water body of the lake and prevent it from losing by evaporation.

4. RESULTS AND DISCUSSION

The proposed adaptive real-time model is tested for planning the operation of Bukan reservoir for a typical year. The operation horizon was considered to be one year with monthly time steps. However, the model has the ability to be used for any desired time horizon and time steps as long as the two first modules are adopted with the desired reliability. Using the 34 years available historical inflow time series, we trained and validated an ANFIS-based inflow forecasting model. Three previous monthly inflows were used as input to the model to forecast the future inflows to the reservoir. For example, if we are at the beginning of September, the ANFIS model uses inflows in June, July and August and predicts inflows to the reservoir during September. Having estimated inflows to the reservoir in September, August and July as inputs to the ANFIS model, the model will forecast October's inflow and so on. This procedure is continued up to the last month of the planning horizon until

inflow values of all future months are predicted. Note that the predicted inflow for September has a certain amount of error and uncertainty. This error will propagate through inflow forecast of all future months, therefore, forecast errors are accumulated as we go ahead. In this regard, the updating module helps us significantly reduce the forecast error and adapt the model to inflow changes by involving actual observed values into the model at the beginning of each time step.

Table 1. reports water demands for various users to be supplied exclusively by Bukan reservoir. Agricultural demands are about 58% of total water demand. Noting that the storage capacity of the reservoir is 810 Million Cubic Meters (MCM), volume of withdrawal for irrigation purposes is relatively considerable. Also 95% of annual irrigation demand belongs to the main crop season, i.e. May to September. Interestingly, only less than 15% of total annual inflow occurs in this period; therefore, the role of the reservoir storage to regulate natural inflows would be essential. Because of high water demands and farmers tendencies to use water in the crop season, releases made to reach LU (R_{L_t}) are more likely to reach the lake during time periods other than the crop season.

Table 1- Demands for various sectors downstream of Bukan Dam (all values are in MCM).

	Oct	Nov	Dec	Jan	Feb	Mar	Apr	May	June	Jul	Aug	Sep	sum
Agriculture Demand (Da)	1.9	18.3	0	0	0	0	0	51.2	90.9	81.6	99.5	72.8	416.2
Domestic Demand (Dd)	11.5	10.2	9.8	9.8	10.3	10.5	10.5	14.1	12.5	13.5	14	15.1	141.7
Industrial Demand (Di)	0.5	0.5	0.5	0.5	0.5	0.5	0	0	0	0	0	0	3
Environmental Demand (Do)	18.1	10	9	5	13.5	13.5	20	13.5	13.5	13.5	13.5	13.5	156.6

According to high priority of meeting domestic and industrial water demands, the reservoir releases for this type of demands are incorporated as rigid constraints of the reservoir operation module in the model (equation 4), so they must be met regardless of yearly variations of inflow to the reservoir.

The proposed model is tested for year 2015-2016 with monthly inflows shown in figure 4. It can be seen that inflow to reservoir in April is 517 MCM, which is 64% of total capacity of Bukan reservoir. This huge amount of input resulted in uncontrolled spillage and heavy damages downstream. The problem was mostly because of not having a suitable tool to forecast this event in advance and operate the reservoir smartly in such a critical situation. In this case, inflows in months prior to the crop season was stored and was not released on time to provide with enough storing capacity for incoming floods in Spring. It is of interest to test the proposed real time model and see if it can improve the situation in a real life operation context.

Table 2. presents the results obtained by the adaptive real-time operation model proposed. We can see that water demands for agricultural, domestic, industrial and environmental are completely met. Also the sum of spilled water is zero showing that it has successfully prevented unwanted spillage by releasing water for LU in January, February and March with the amounts of 156.4, 171.5 and 171.5 MCM, respectively. Therefore, the resulting end of month (EoM) storage of March is determined to be 422.5 MCM, which is nearly half of the capacity of Bukan reservoir. This allowed having enough space left for the incoming 517 MCM inflow in April and managing the flood occurred in this year with a volume of 300 MCM. This has been made possible mainly by the updating capacity of the proposed framework.

Table 2- Demands for various sectors downstream of Bukan Dam (all values are in MCM).

	Oct	Nov	Dec	Jan	Feb	Mar	Apr	May	June	Jul	Aug	Sep	sum
EoM storage	245.2	279.4	345.1	302	329	422.5	740.7	785.7	671.8	551.9	417.8	308.3	
Agricultural Release	1.9	18.3	0	0	0	0	0	51.2	90.9	81.6	99.5	72.8	416.2
Domestic Release	11.5	10.2	9.8	9.8	10.3	10.5	10.5	14.1	12.5	13.5	14	15.1	141.7
Industrial Release	0.5	0.5	0.5	0.5	0.5	0.5	0	0	0	0	0	0	3
Environmental Release	18.1	10	9	5	13.5	13.5	20	13.5	13.5	13.5	13.5	13.5	156.6
LU Release	0	0	0	156.4	171.5	171.5	165	76.2	15.7	0	0	0	756.2
Spillage	0	0	0	0	0	0	0	0	0	0	0	0	0
Env+LU Release	18.1	10	9	161.4	185	185	185	89.7	29.2	13.5	13.5	13.5	912.8

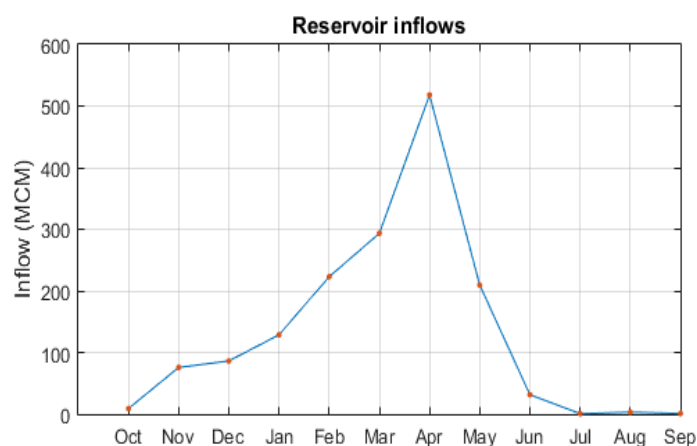


Figure 4. Monthly inflows to Bukan reservoir for the tested water year (2015-2016).

5. CONCLUSIONS

This paper presented an adaptive real-time operation framework proposed for forecast-based optimal operation of Bukan reservoir in Lake Urmia. It consists of a streamflow forecast module, a medium-term reservoir operation optimization module and an updating procedure to adjust the forecasted inflows and the reservoir releases as time moves forward and the planning horizon becomes shorter. Testing the proposed methodology, an adaptive network-based fuzzy inference system (ANFIS) developed for inflow forecasting coupled with a linear operation optimization model performed well enough for the Bukan system operation in year 2015-2016 in terms of supplying water for agricultural, domestic, industrial and environmental uses as well as controlling a severe flood experienced in this year. It provided LU with 756.2 MCM of water released in months prior to the crop season, which is the desired time period to make releases for LU.

6. REFERENCES

1. Nohara, D., & Hori, T. (2017). Integrated Reservoir Operation Considering Real-Time Hydrological Prediction for Adaptive Water Resources Management. In *Sustainable Water Resources Planning and Management Under Climate Change* (pp. 101-132). Springer Singapore.
2. Chen, L., Singh, V. P., Lu, W., Zhang, J., Zhou, J., & Guo, S. (2016). Streamflow forecast uncertainty evolution and its effect on real-time reservoir operation. *Journal of Hydrology*, 540, 712-726.
3. Nohara, D., Nishioka, Y., Hori, T., & Sato, Y. (2016). Real-Time Reservoir Operation for Flood Management Considering Ensemble Streamflow Prediction and Its Uncertainty. In *Advances in Hydroinformatics* (pp. 333-347). Springer Singapore.
4. Mujumdar, P. P., & Ramesh, T. S. V. (1997). Real-time reservoir operation for irrigation. *Water Resources Research*, 33(5), 1157-1164.
5. Unver, O. I., & Mays, L. W. (1990). Model for real-time optimal flood control operation of a reservoir system. *Water resources management*, 4(1), 21-46.
6. Wasimi, S. A., & Kitanidis, P. K. (1983). Real-time forecasting and daily operation of a multireservoir system during floods by linear quadratic Gaussian control. *Water Resources Research*, 19(6), 1511-1522.
7. Hsu, N. S., & Wei, C. C. (2007). A multipurpose reservoir real-time operation model for flood control during typhoon invasion. *Journal of Hydrology*, 336(3), 282-293.
8. Huang, W. C., & Hsieh, C. L. (2010). Real-time reservoir flood operation during typhoon attacks. *Water Resources Research*, 46(7).
9. Jang, J. S. (1993). ANFIS: adaptive-network-based fuzzy inference system. *IEEE transactions on systems, man, and cybernetics*, 23(3), 665-685.
10. Jang, J. S. R., Sun, C. T., & Mizutani, E. (1997). Neuro-fuzzy and soft computing: a computational approach to learning and machine intelligence.
11. Firat, M., Turan, M. E., & Yurdusev, M. A. (2009). Comparative analysis of fuzzy inference systems for water consumption time series prediction. *Journal of hydrology*, 374(3), 235-241.
12. Firat, M., & Güngör, M. (2008). Hydrological time-series modelling using an adaptive neuro-fuzzy inference system. *Hydrological Processes*, 22(13), 2122-2132.
13. Keskin, M. E., Taylan, D., & Terzi, O. (2006). Adaptive neural-based fuzzy inference system (ANFIS) approach for modelling hydrological time series. *Hydrological sciences journal*, 51(4), 588-598.
14. Zounemat-Kermani, M., & Teshnehlab, M. (2008). Using adaptive neuro-fuzzy inference system for hydrological time series prediction. *Applied Soft Computing*, 8(2), 928-936.
15. Nayak, P. C., Sudheer, K. P., Rangan, D. M., & Ramasastri, K. S. (2004). A neuro-fuzzy computing technique for modeling hydrological time series. *Journal of Hydrology*, 291(1), 52-66.
16. Ilich, N. (2011). Improving real-time reservoir operation based on combining demand hedging and simple storage management rules. *Journal of hydroinformatics*, 13(3), 533-544.
17. Yasi, M., & Ashori, M. (2017). Environmental Flow Contributions from In-Basin Rivers and Dams for Saving Urmia Lake. *Iranian Journal of Science and Technology, Transactions of Civil Engineering*, 41(1), 55-64.

Erosion of Channel Beds Covered by Cohesive Sediments

Hesam Fouladfar¹, Mahmoud Shafai Bajestan²

1- PhD, Head of river engineering department, IWPCO

2- Professor of faculty of Water Science Engineering of Ahvaz Chamran University

Email: h.fouladfar@iwpcو.ir

Abstract

A physically based model is developed for estimation of surface erosion flux of cohesive bed channels. Merit of the model, with respect to well-known formulas, is application of new approaches for estimation of erosion flux coefficient and critical shear stress. This model also accounts for stochastic behavior of the actual bed shear stress. It is assumed that the erosion flux coefficient is the same as entrainment flux of fluid mud layer. The critical shear stress has also taken to be proportional to bed shear strength. Rayleigh probability function has been proposed as the distribution of bed shear stress. The physical parameters needed for the model are effective sediment cohesion, volumetric concentration, entrainment velocity and gelling concentration. The statistical parameter of the model, named scale parameter, is applied to correlate the model, for practice. The experiments were conducted in a straight recirculating flume filled with natural cohesive sediments. It has been shown the scale parameter, regardless degree of consolidation, has a strong power relation with relative critical bed shear stress. This parameter can easily be determined by two fast erosion tests. The model estimated erosion flux has shown well agreement with experimental measurements.

Keywords: cohesive sediment, erosion flux, erosion coefficient, entrainment velocity, gelling concentration, shear stress, Rayleigh distribution, critical shear stress, effective cohesion, volumetric concentration.

1. INTRODUCTION

In most widely used resuspension formulations, the user calculates the erosion flux as a function of excess bed shear stress and up to three empirical material coefficients. Some frequently used approaches, define excess bed shear stress as current induced bottom shear stress minus critical shear stress below that no erosion occurs. Usually fitting models to short-term erosion experiments determine the empirical coefficients [1]. However, interpretation of data is often at least partially subjective, and frequently the results are specific to physical configuration and time history of the procedure used. These differences can lead to significant differences between derived parameters, even when the same sediments are tested [2]. Moreover, most of classical resuspension formulations try to give deterministic description of resuspension process. The bed shear stress as a main factor is however a stochastic variable. The relation between resuspension and bed shear stress is not necessarily linear. The stochastic behavior of turbulence is probably an important aspect in phenomenological description of resuspension. For this, the erosion flux results, obtained from different formulas, are very scattered and do not converge to reality. The aim of this study is to develop and verify a new physically based formulation for estimation of resuspension flux of beds covered with cohesive material. The proposed formulation must require minimum field and laboratorial measurements for a reasonable prediction of resuspension.

2. MATERIALS AND METHODS

It is proposed that resuspension flux formula framework to be the same as Partheniades' formula structure [3], which is multiplication of the erosion flux coefficient (M) and the probability of exceedence of actual instantaneous bed shear stress (τ_0) from critical shear stress (τ_{cr}).

$$E = M \times p(\tau_0 > \tau_{cr}) \quad (1)$$

In which, M equals to fluid mud entrainment rate, τ_{cr} equals to actual bed shear strength at the interface, τ_0 is instantaneous bed shear stress and p is the probability density function.

There is not any theoretical relationship for the erosion flux coefficient M . Clearly, this parameter is not larger than product of entrainment rate w_e (if the bed were fluid mud) and concentration of entrained fluid $c_{gel} = \rho_s \times \phi_{gel}$. The initial entrainment rates w_e of a fluid mud layer, has been investigated, both numerically and by means of experiments [4]. The M in the Partheniades equation is net erosion flux, while the M used in proposed resuspension formulation describes resuspension rate provided the bed shear stress exceeds the bed yield stress.

So one can expect the M used in this formulation to be higher than the traditional M . Some equations have been derived for entrainment of fluid mud layer by turbulent water layer above ([4], [5] [6]). An initial estimation for w_e is $w_e \approx 0.28u_*$ for low Richardson number [4].

It is proposed that the Rayleigh Probability Density Function (RPDF) is the distribution of actual bed shear stress at one moment in time and at one infinitesimal area of the bed, τ_0 .

$$f(\tau_0; \sigma) = \frac{\tau_0}{\sigma^2} \exp\left(-\frac{\tau_0^2}{2\sigma^2}\right), \quad \tau_0 \geq 0, \quad \mu = \sigma \sqrt{\frac{\pi}{2}} \quad (2)$$

For simplicity, a new scale parameter, β (Beta) is defined as:

$$\beta = \frac{1}{2\sigma^2} \quad (3)$$

So the RPDF can be rewritten as:

$$f(\tau_0, \beta) = 2\beta\tau_0 \exp(-\beta\tau_0^2) \quad \tau_0 \geq 0, \quad \mu = \frac{1}{2} \sqrt{\frac{\pi}{\beta}} \quad (4)$$

The cumulative density function is:

$$F(\tau_0) = 1 - \exp(-\beta\tau_0^2) \quad (5)$$

In the RPDF, when actual shear stress τ_0 is normalized by the regularly used bed shear stress τ_b , then regularly bed shear stress is related to the Beta as follows:

$$\mu = \frac{1}{2} \tau_b \sqrt{\frac{\pi}{\beta}} \quad (6)$$

One can see that the regularly used bed shear stress τ_b is not necessarily equal to the average of RPDF. Clearly, RPDF cannot simulate the turbulence flow accurately, but in practical point of view, RPDF contains only one argument, Beta. Thus only one parameter, has to be estimated when no data of the turbulence field are available. This reduces the chance of large mistakes. This distribution does not allow negative bed shear stress to act. So one has to deal with a probability of exceedence at one side of the bed shear stress spectrum. This makes the evaluation of the probability exceedence function easier.

In the proposed formulation, it is assumed that the critical shear stress to be the actual bed shear strength at interface. Obviously, the actual bed shear strength near the bed surface τ_y is at least equal to the critical shear stress and generally much higher. The reason of this assumption is that, one can calculate the τ_y as a function of density, effective stress and cohesion. Therefore, it can be considered as deterministic variable. Moreover, the burst mode of turbulence which is dominant phenomenon of resuspension on smooth bed like beds covered with cohesive materials happens rarely and corresponds to exceedence probability of higher value for critical shear stress. A relationship is derived between volumetric concentration of cohesive sediment ϕ and drained yield shear stress τ_c , in the failure layer in terms of microscopic properties [7]. The fractal description of material at micro-level is the basis of this relation. τ_c acts in the failure plane and reads:

$$\tau_c = c'\phi + \frac{1}{3} \tan \varphi' (1 + 2K_0) K_{\sigma,0} + \tan \varphi' \sigma'_v \quad (7)$$

The term $c'\phi$ is function of physico-chemical properties. τ_c is the yield stress in failure layer, while the τ_y is the yield stress parallel to the bed. Some simplifications are applied to Eq.7. The formulation will use the τ_y at the interface. At this level, the effective stresses are almost zero, so the effective stress term can be discarded. When substituting the constitutive relation of [8], $\sigma'_v = K_\sigma \phi^n - K_{\sigma,0} \approx 0$, Eq.7 becomes:

$$\tau_y = c'\phi + \frac{1}{3} \tan \varphi' (1 + 2K_0) K_\sigma \phi^n \quad (8)$$

The angle of internal friction φ' varies between 5° and 40° , and K_0 varies between 0.3 and 3.0. It means that $\tan \varphi' (1+2K_0)/3$ is of order one. Near the interface the effective stresses are zero, so the term $\sigma'_v = K_\sigma \phi^n$ is very small at the interface and the cohesion term $c'\phi$ dominates there. To this end, the proposed relation for critical shear stress, including a reduction factor, becomes:

$$\tau_{c,r} = 0.001 c'\phi \quad (9)$$

Water Research Institute of Ministry of Energy collected water and sediment samples from Sefidrud Dam Reservoir located 200 km north-west of Tehran, Iran. The laboratories of this institute measured physico-chemical properties, mineralogical composition, mechanical properties and grain size distribution of cohesive sediment samples.

A straight recirculating flume with width of 45cm and length of 12 m is used for experiments. Water depth was 0.2 m. Observing reach had length of 2 meter situated in downstream of the flume. The flume was filled with sand to improve the boundary layer in upstream of the observing reach. During erosion experiments, when a sediment layer was present, the water depth in the flume was constant and did not change during erosion process. A sediment mixing tank equipped with pumping system also was set.

Two series of tests were carried out to determine erosional characteristics of the sediment. The first experiment was performed on a sediment layer with consolidation period of one day and layer thickness of 0.07 m. In the second case, the consolidation period amounted to seven days resulting in a sediment layer of 0.055 m. The sediment beds were formed by deposition in still water after a mixing period of approximately 12 hours. The concentration of initial suspension was 50 kg/m³. The erosional behavior of each sediment layer were determined by increasing bed shear stress in successive steps of one hour.

The gelling concentration (structural density) was measured using settling column. The column had an internal diameter of 0.1 m and height of 1.5 m.

A turbidity meter, Analite 160, was used for measuring suspended sediment concentration during erosion tests. Furthermore, velocities were measured with an electromagnetic current meter. The bed shear stress was calculated in the flume using the relation between the depth-averaged flow velocity U and the friction coefficient C_f :

$$\tau_b = C_f \frac{1}{2} \rho U^2 \quad (10)$$

The Colebrook-White formula was used to estimate friction coefficients in fully-developed turbulent pipe and open channel flow. This formula for free-surface flow is presented as follows [8]:

$$\frac{1}{\sqrt{C_f}} = -4.0 \log \left(\frac{k_s}{12R} + \frac{1.25}{\text{Re} \sqrt{C_f}} \right) \quad (11)$$

Where k_s is the roughness height. The ultrasonic displacement sensor was used to measure surface profile of the bed after draining water from the flume. The volumetric concentration of the bed was determined in different consolidation period, by sampling of the bed after each test and measuring dry density of the bed. The bed sediment cohesion was measured by consolidated drained triaxial test.

3. RESULTS AND DISCUSSION

The resulting new resuspension expression reads:

$$E = 0.28 \times u_* \times C_{gel} \times \exp \left(-\beta \left(\frac{0.001 c' \phi}{\tau_b} \right)^2 \right) \quad (12)$$

Using Eq. 12, the following equation can be derived for Beta:

$$\beta = \ln \left(\frac{0.28 \times u_* \times C_{gel}}{E_{observed}} \right) \times \left(\frac{0.001 \tau_{cr}}{\tau_b} \right)^{-2} \quad (13)$$

The above equation shows power formed relation between Beta and relative critical shear stress, τ_{cr}/τ_b , with a bit difference with ordinary power equations. The difference is that, first term of equation is not constant for successive erosion tests and different shear stress. To evaluate the power regression between Beta and relative critical shear stress, the experimental data of [9], [10] and [11] were considered.

Fig.1-(a) illustrates the erosion flux as function of regularly bed shear stress for both experimental and formulation results, and for one-day consolidation. It is seen that there is good agreement between measured erosion flux data and formulation results. Root mean square error, RMSE = 4.2E-09 and Mean absolute relative error, MARE = 0.43. Fig. 1-(b) illustrates erosion flux as a function of regularly bed shear stress for both experimental and formulation results in seven days consolidation. Again, it is seen that there is good agreement between measured erosion flux and the formulation data. RMSE = 4. 1E-6 and MARE = 0.12. Fig. 1-(c) shows the erosion flux as a function of RBSS for both experimental and formulation results in seven days consolidation based on one day beta values. As it can be seen, still there is relatively good agreement between measured erosion flux and the formulation data. RMSE =2E-5 and MARE = 0.52.

4. Conclusions

A new formulation has been proposed for estimation of resuspension for channel beds covered with cohesive sediments. In the formulation, with more realistic and physical bases than before, one can estimate input parameters including resuspension flux coefficient and critical shear stress. In addition, the formulation has involved stochastic behavior of bed shear stress. The statistical scale parameter of the formulation which is a calibrating factor has a strong power relation with the relative critical shear stress. Since the degree of bed consolidation did not show a significant effect on the scale parameter, one can estimate it with two fast resuspension tests in laboratory or field. Comparison of the formulation estimated resuspension flux with current measurements and previous studies has shown a well agreement.

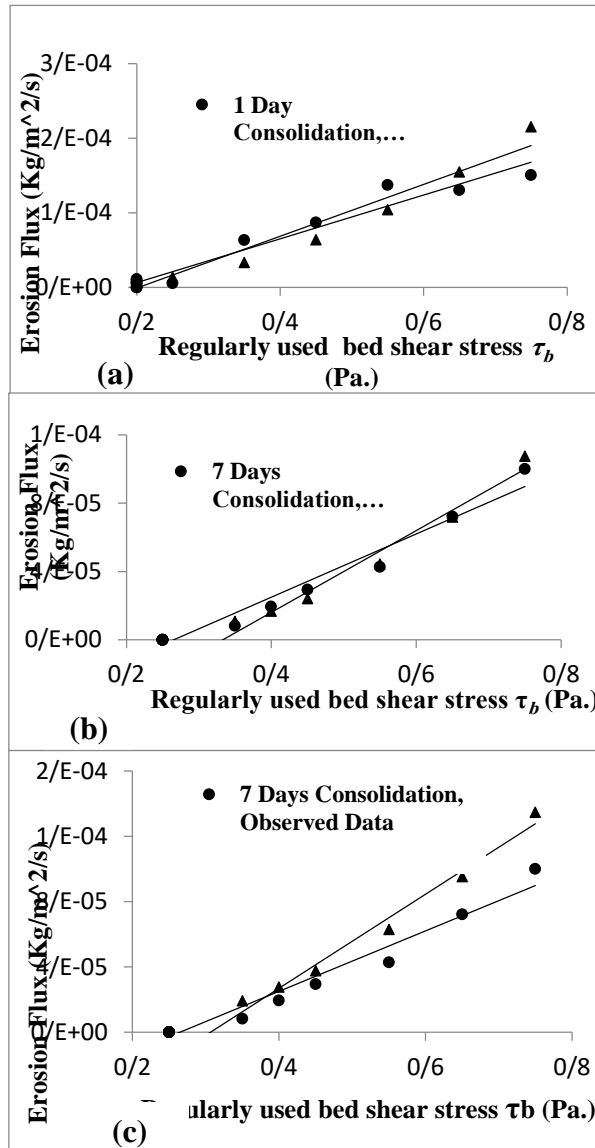


Fig.1 Comparison between experimental data of resuspension flux and formulation results

5. References

1. Winterwerp, J.C. and Van Kesteren, W.G.M. (2004). "*Introduction to the physics of cohesive sediment in the marine environment.*" Elsevier.
2. Sanford, L.P. and Maa, JPY. (2001). "A unified erosion formulation for fine sediments." *Marine Geology*, Vol. 179
3. Partheniades, E. (2009). "*Cohesive sediments in open channels*". Elsevier
4. Kranenburg, C., and Winterwerp, J.C. (1997). "*Erosion of fluid mud layers, I: Entrainment model.*" ASCE, *Journal of Hydraulic Engineering*, 123 (6): 504-511.
5. Kranenburg, C. (1994). "*An entrainment model for fluid mud. Communications on Hydraulic and Geotechnical Engineering.*" Faculty of Civil Engineering, Delft University of Technology, Report 94-10.
6. Bruens, A.W. (2003). "*Entraining mud suspensions.*" PhD thesis, Delft University of Technology, Department of Civil Engineering and Geosciences, The Netherlands.
7. Merckelbach, L.M. (2000). "*Consolidation and strength evolution of soft mud layers.*" Delft University of Technology, Faculty of Civil Engineering and Geosciences, Report 00-2, ISSN 0169-6548.
8. Henderson, F. M. (1966). "*Open Channel Flow*" Macmillan Publishing Co - New York.
9. Kuijper, C., Corneliesse J.M., and Winterwerp, J.C. (1990). "*Erosion and deposition characteristics of natural muds sediments from the Hollandsch Diep*, Rijkswaterstaat, Delft Hydraulics, Report 27.
10. Krishnappan, B. G., and Engel, P. (1994). "*Critical shear stresses for erosion and deposition of fine suspended sediments in the Fraser river.*" National Water Research Institute, Ontario, Canada.
11. Schaaff, E., Grenz, C., Pinazo, C., and Lansard, B. (2006). "*Field and laboratory measurements of sediment erodibility: A comparison.*" *Journal of sea research*, Vol 55.

Ageing Evaluation Model of Dams and Case Studies

Dong-Hoon Shin

K-water Institute, Korea Water Resources Corporation, Daejeon, Republic of Korea

Email: cute_lion@daum.net

Abstract

While many dams around the world are still under construction or planning, existing dams are ageing and becoming more degraded over time since their completion. Due to the relatively higher probability of failure during their remaining lifetime, ageing dams need to be properly maintained based on well-established inspection and evaluation systems. However, at present, it is not easy to know how seriously aged or degraded they are and when to take the action required to secure their safety at rational cost. In this paper, an ageing evaluation model (AEM) is suggested as a simple assessment method for dam ageing which can be used to determine the time for adequate maintenance work to extend the lifetime of dams. For the development of the AEM for existing dams, a variety of data showing any changes in integrity of the dam body since its completion were collected and analyzed. Some examples of ageing evaluation using the newly proposed AEM are presented here. It is expected that the proposed method may be useful to estimate the time for the opportune maintenance of existing dam facilities.

Keywords: Ageing, Evaluation Model, Deterioration, Existing Dams, Lifetime of Dam.

1. INTRODUCTION

Dams provide us with a variety of benefits such as hydropower, flood control, drinking water, irrigation, and recreation. However, as our population grows, their development continues and natural disasters are increasing due to climate change, thus they are sometimes a great threat to the public in respect of their hazard potential. Once a dam has been successfully built so that reservoir water can be safely stored (note that many dam failures occur either during construction or during or shortly after reservoir filling), its structure and component parts will begin to age with each structure ageing at a different rate in a different way. Some dams may remain safe for more than a thousand years, while others may start to be severely degraded and/or leak after less than a decade and consequently cause devastating damage and loss of property and life.

The Republic of Korea has around 15,000 facilities classified as “critical infrastructures” by the Korean government, and 9.3% of them are more than 30 years old. In the case of water infrastructure, around 56% of the classified dams are more than 30 years old (Kim, 2013). Around the world, some 5,000 large dams are now more than 50 years old, and the number and size of the dams have rapidly increased in the last half century. The average age of the 90,580 dams in the US is, as of 2016, around 56 years old. Around 80,000 of 98,000 dams in China were built in the 30 years between 1950 and the end of the 1970s, and among them, many have been identified as having a “high hazard potential” (Wang, 2017). In relation to the ageing issue of dams, it seems that every country is trying to develop technologies to identify defects or the possibility of dam failure at any age and to establish a number of institutional systems to maintain those ageing dams systemically.

In this paper, a theory or model developed to evaluate the degree of aging of dams is introduced and examples of the ageing evaluation of dams using it are described. It should be noted that while the newly propose evaluation model is one of a number of simple models by which quantitative evaluation can be made for ageing dams, a more generalized evaluation model should be developed to consider the more varied conditions that can be encountered during the ordinary operation of dams. Note that in this paper, according to the definition of the International Commission on Large Dams (ICOLD) Bulletin 93 (1994), the ageing of dams is defined as deterioration that occurs more than 5 years after the beginning of its operation and is a class of deterioration associated with time-related changes in the properties of the materials with which the structure and its foundations are constructed. Excluded are the effects of exceptional events. Under normal conditions during dam operation, structural ageing will usually affect the performance requirements and then later affect safety if corrective measures are not taken. However, in this paper, the author would like to use the term ‘degradation’ instead of ‘deterioration’, because it is considered that ‘degradation’ can more properly explain the cause-effect relationships regarding the reduction of performance or safety instigated by the results of ageing.

2. AN AGEING EVALUATION MODEL (AEM) FOR DAMS

Ageing as a cumulative degradation process occurring over time. It usually leads to degradation of materials subjected to service conditions and can cause a reduction in component and/or system safety margins if the degradation phase continues, eventually resulting in failure of the structure or else abandoning and demolishing it.

2.1. THE RELATIONSHIP BETWEEN PERFORMANCE (OR SAFETY) AND AGE

From the above perception of the ageing process of dams, the AEM can be expressed as a relationship between performance (or safety) and age (time), as shown in Figure 1.

Some typical types of ageing process encountered in practice are classified into **4 Types**. **Type 1** is the most common pattern in which ageing is detected after the first 5 years of operation. **Type 2** shows ageing at a slightly faster rate which begins within the first 5 years of operation (from the literature, it is well known that many dam failures occur during this period). **Type 3** is an unwanted case in which a dam shows anomalous behaviors such as excessive deformations or leakage during the first reservoir filling due to defects in design and construction, and in addition does not meet the design safety requirements. If the amount and rate of degradation are so big and rapid respectively, they may eventually result in catastrophic failure of the dam. **Type 4** is one of the worst cases in that a dam fails due to congenitally critical defects in design and construction.

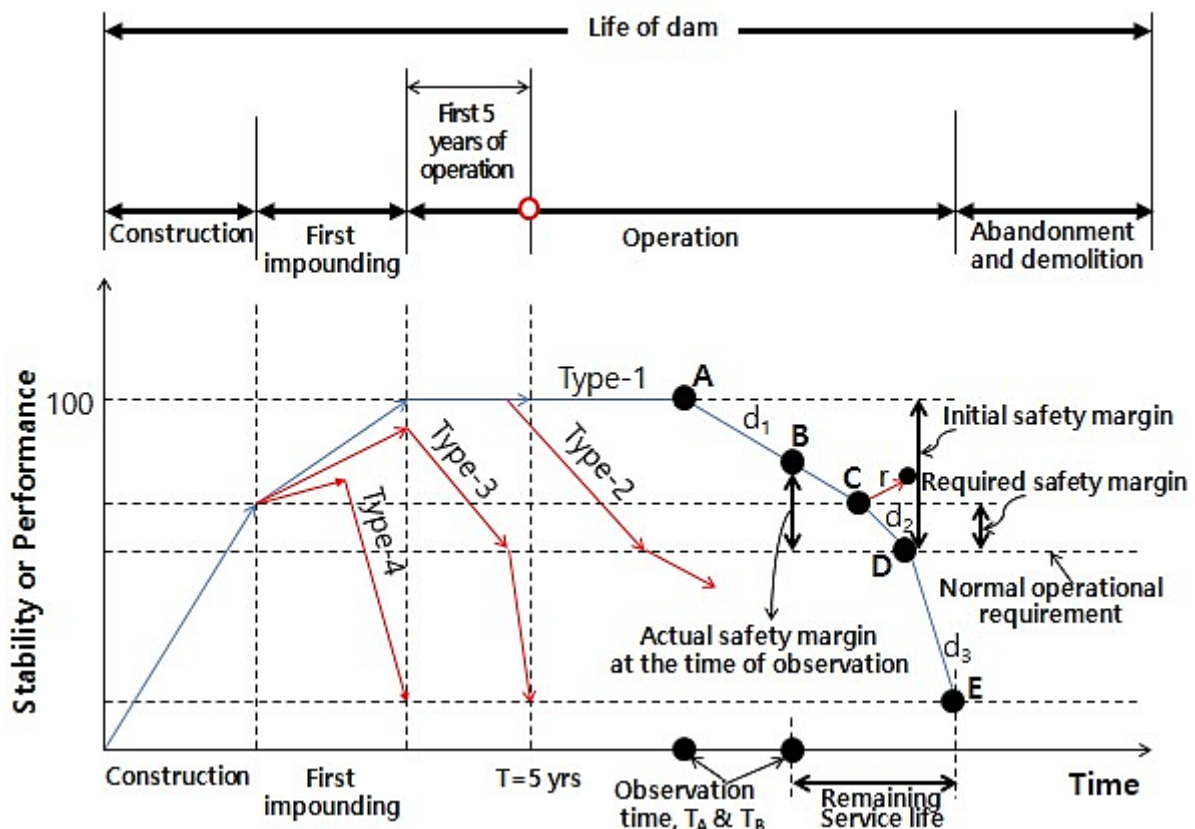


Figure 1. The relationship between performance and ageing of dams with time passage

2.2. A BASIC AEM

In Figure 1, the points **A**, **B**, **C**, **D**, and **E** indicate the level of performance or safety of a dam at a certain time point. Point **A** indicates the upper limit of performance and the starting point at which ageing begins. The dam at point **B** actually has a larger safety margin than is required and its performance is higher than the normal operational requirements. For the time T_B corresponding to point **B**, we can estimate the remaining service lifetime if the degradation rate is also known. Points **C** and **D** (where ageing occurs) are the upper and lower limits of the required safety margin, respectively. Point **E** means the lowest performance where the dam should be abandoned

or demolished without hesitation. In the same figure, **d₁**, **d₂** and **d₃** represent the rates of degradation of the dam. The ordinary ageing process will follow the **A-B-C-D-E** path if no mitigating work is taken. If any kind of rehabilitation work is carried out, then the dam's performance may increase along the path **C-r** (r denotes recovery), and consequently its remaining lifetime will be extended.

In order to establish the AEM, we need to essentially know the amount and rate of degradation, and the critical safety requirements such as allowable thresholds for deformation (mandatory), leakage (mandatory), strength (optional), pore pressure (optional), and so on. The amount of degradation and the rate of ageing can be theoretically quantified by long-term monitoring data including the results of surveillance activity. The ageing phenomena to be detected are summarized in Tables 1 and 2. Once we have assessed how far it has developed, then we can decide on appropriate corrective measures to extend the dam's lifetime. The rate of ageing can be calculated by directly monitoring or measuring changes in the dam's structural properties or performance over time:

$$P(t) = 1 - F(\text{time, (deformation, loss of strength, pore pressure increase, permeability change, etc.)}) \tag{1}$$

$$= 1 - \sum (F_{\text{deformation}}(t) + F_{\text{leakage}}(t) + F_{\text{strength}}(t) + F_{\text{pore pressure}}(t) + F_{\text{permeability}}(t) + \dots),$$

Where P(t) = Performance as a function of time t and F_{deformation}(t) = Reduction of deformation performance in which the rate of degradation is multiplied by the age (period) corresponding to the changes in deformation. The other terms for leakage, strength, pore pressure, and permeability are calculated in the same manner as in the term of deformation. It is assumed for simplicity that each degradation rate varies linearly with time.

Table 1- Major ageing symptoms for earth- and rockfill dams (ICOLD, 1994)

Dam Component	Symptom of Ageing
Foundation (soil or rock mass)	<ul style="list-style-type: none"> - Deformation - Loss of strength, uplift pressure increase, and change in stress state - Internal erosion - Foundation degradation - Ageing of grout curtains and drainage system*
Dam body (embankment materials)	<ul style="list-style-type: none"> - Deformation - Loss of strength - Pore pressure increase - Internal erosion - Leakage** - Embankment degradation - Surface erosion
Others	<ul style="list-style-type: none"> - Seepage through concrete faced rockfill dams - Permeability change - Loss of bond between concrete structures and embankment - Ageing of synthetic polymer materials

* and ** are symptoms added by the author

Table 2- Major ageing symptoms for concrete and masonry dams (ICOLD, 1994)

Dam Component	Symptom of Ageing
Foundation (rock mass)	<ul style="list-style-type: none"> - Loss of strength under permanent or repeated actions - Erosion and solution - Ageing of grout curtains and drainage system
Dam body (concrete or mortar and stone)	<ul style="list-style-type: none"> - Chemical reactions resulting in swelling - Shrinkage, creep, and reaction leading to contraction - Degradation due to chemical reactions of materials with the environment - Loss of strength under permanent and repeated actions - Poor resistance to freezing and thawing
Others	<ul style="list-style-type: none"> - Ageing of structural joints - Ageing of upstream facings - Ageing of pre-stressed structures

3. CASE STUDIES

Using the simplified AEM proposed by the author, the performance-age relationships of two earth and rockfill dams were analyzed.

3.1. THE ANGYE DAM CASE

Completed in 1971 to supply water to the Pohang industry complex located in the south east of Korea, the Angye dam is a 46-year-old center-cored earthfill dam with a height of 32.5 m, a length of 223 m, and a total reservoir capacity of 17 million m³ (Figure 2).

The dam is an example of ageing by loss of strength, deformation, and internal erosion. There have been two events showing that the dam body has been deteriorating for a long time: in 1985 (14 years after its completion) and 2003 (18 years after the first event) (Korea Water Resources Corp., 2009)

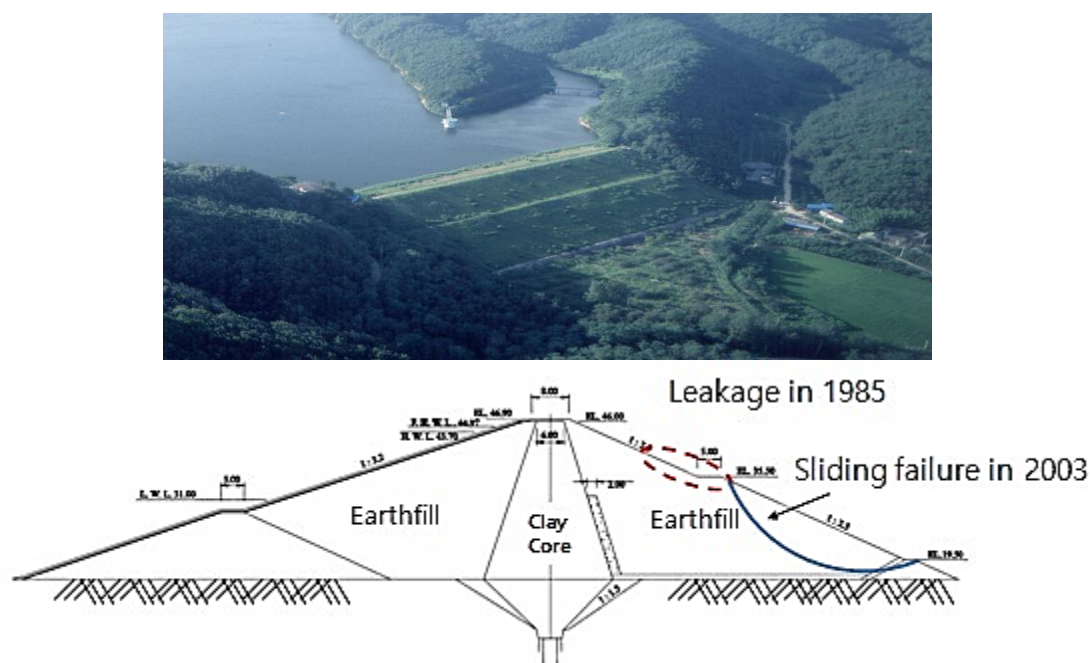


Figure 2. The Angye dam

The first evidence of ageing was detected in June, 1985 when leakage occurred from an area of around 20 m² at the downstream slope of the dam body. The amount of leakage was measured at as much as 50~200 ml/min. The results of a series of investigations on the cause of the leakage by drillings at the core zones and an electrical resistivity survey carried out 9 months after the first detection of the leakage implied that some parts of the core zone had loosened and permeability varied irregularly from $k=10^{-2}$ to 10^{-4} cm/s on the right side of the dam body. After that, 223 m-long curtain grouting was carried out as remedial work in 1986. The second event was the collapse of the downstream slope that occurred 8 years later in 2003, which is considered to have been associated with ageing as well as heavy rain at that time.

From the records of the two events and inspections, as shown in Figure 3, an ageing evaluation was carried out based on the performance-age relationship proposed by the author in Figure 1 and Equation (1). As of 2017, the Angye dam is showing sufficient performance above the required performance margin assumed by the author, and this case can be considered as **Type-1** ageing.

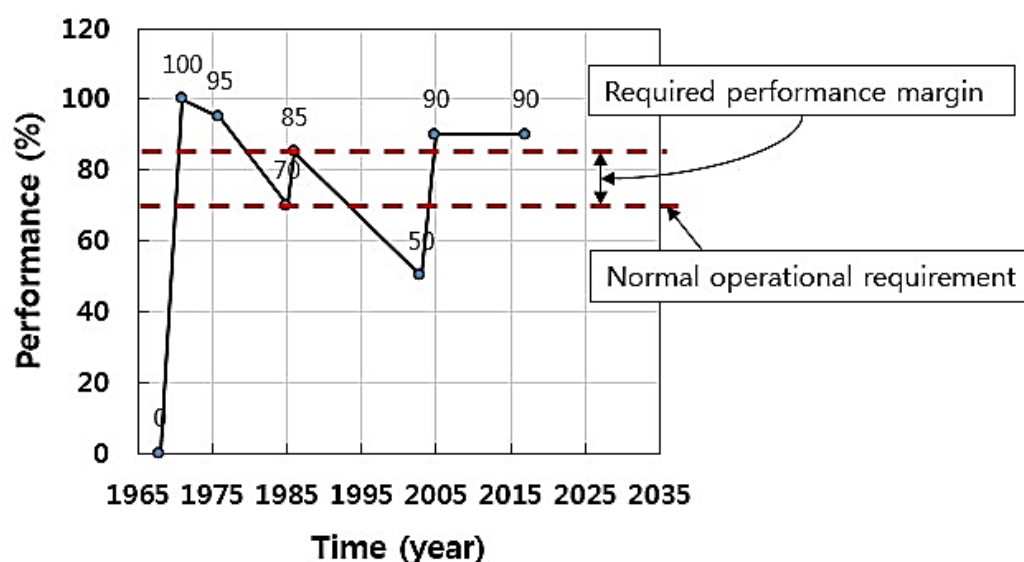


Figure 3. Ageing Evaluation of the Angye Dam

3.2. THE UNMUN DAM CASE

The Unmun dam was completed in September 1994 to supply 376,000 m³/day of municipal water to neighboring cities in the Kyungang-bukdo province in Korea. The dam, which is operated by K-water (Korea Water Resources Corporation), is a 23-year-old center-cored rockfill dam as of 2017 with a height of 55 m, a length of 407 m, and total reservoir capacity of 135 million m³ (Figure 4).

After the Unmun dam was first filled up to its normal high water level in 1998, the first accident of ageing occurred within 5 years after its completion, whereby its safety was seriously threatened by subsidence, sinkholes, and excessive leakage, which are all typical symptoms of ageing of rockfill dams (Korea Water Resources Corporation, 2005). A comprehensive investigation on the causes of such accidents revealed defects in design and construction of the core zone and its materials, and the core materials had been internally eroded due to gap-graded gradation and lead to development of sinkholes and subsidence at the dam crest (Figure 5). Based on the investigation, a compaction grouting method was applied to an 80 m-long strip of the core zone in 2000 as remedial work to extend the lifetime of the dam. However, the second event occurred around 1 year after the first remedial work when an unexpected spike of seepage measurement was recorded by the leakage monitoring system installed at the toe area of the dam. In addition, high turbidity was observed with some blue dye material intentionally mixed with clay materials to detect whether the seepage behavior was normal or not during the compaction grouting work after the first event in 2000. Thus, after more comprehensive investigations were conducted to find all of the defects in the dam safety, a permeation grouting method was applied to the entire length of the dam in 2003.

Using the records of these two important events and other investigations and maintenance, as shown in Figure 6, an ageing evaluation was made based on the performance-age relationship proposed by the author in Figure 1 and Equation (1). The rate of degradation in terms of internal erosion was considered as 'Slow' according to the classification method by Fell et al. (2003). The Unmun dam case is considered as **Type-2** ageing, and as of 2017, the dam is showing sufficiently good performance above the required performance margin assumed by the author.

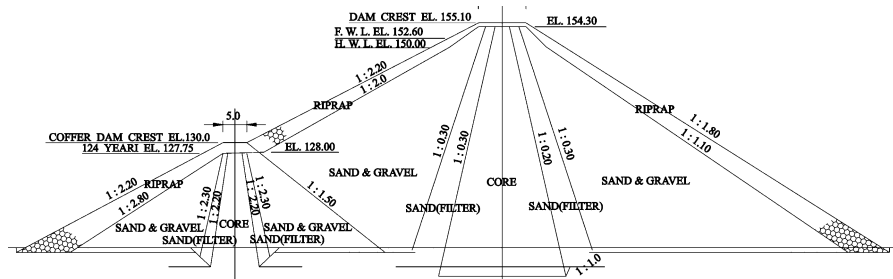


Figure 4. The Unmun dam before the sinkholes and excessive leakage accidents in 1998



Figure 5. A sinkhole as a consequence of ageing that developed on the crest of the Unmun dam in 1998

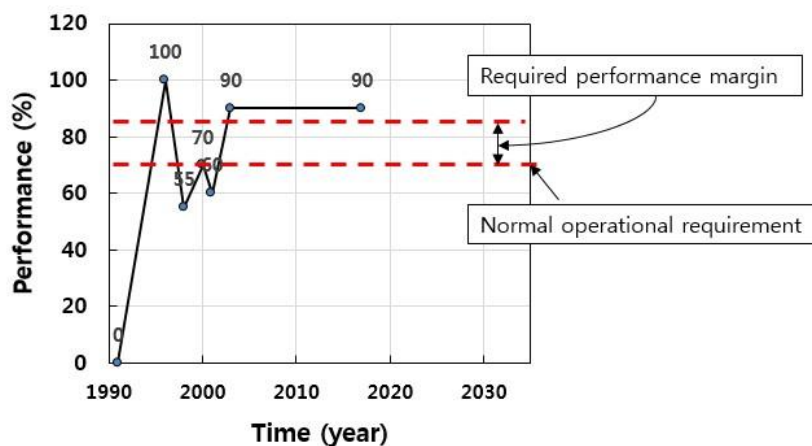


Figure 6. Ageing Evaluation of the Unmun Dam

5. CONCLUSIONS

In this paper, an AEM to assess the degree of aging of dams is introduced and two examples of the ageing evaluation of dams using the proposed model are described. According to the AEM, the ageing patterns of the Angye and Unmun dams are **Type-1** and **Type-2**, respectively, and with a more precise evaluation using data and

information collected from all kinds of investigations, inspections, and analyses, then the remaining lifetime of the dams could be more accurately estimated.

Therefore, it was confirmed that the AEM can well describe the entire lifetime of ageing dams. However, it should be noted that while the newly propose evaluation model is one of the simple and basic models by which quantitative evaluation of ageing dams can be made, a more generalized evaluation model should be developed to consider a wider variety of conditions encountered during the ordinary operation of dams. In a rational assessment of the ageing of dams, the realistic determination on a number of important criteria in dam performance such as the normal operational requirements and the required performance margin needs to be made based on the judgements by sufficiently experienced dam engineers.

6. ACKNOWLEDGMENT

This study was funded by the 2017 research grant from K-water Institute, Korea Water Resources Corporation. The author thanks for the support, and also would like to acknowledge the support from the Korea National Committee on Large Dams (KNCOLD).

7. REFERENCES

1. Kim, Dong-Ryeol (2013), "Current Status and Issues on Ageing of Infrastructures in Korea", The Weekly Economic Review, Hyundai Research Institute, Vol.536, pp.1-19, (in Korean).
2. Wang, Mi Xue (2017), "Safety Management and Evaluation Methods of Reservoirs and Dams in China," The Conference on Technology Exchange of Korea-China in 2017.
3. ICOLD Bulltin No. 93, "Ageing of Dams and Appurtenant Works," 1994.
4. Korea Water Resources Corporation (2004), "Review on Remedial Methods and Its Applicability to Unmun Dam," (in Korean)
5. Korea Water Resources Corporation (2009), "Report of the 2nd In-depth Diagnosis of Angye Dam," (in Korean).
6. Fell, Robin, Wan, Chi-Fai, Cyganiewicz, John and Foster, Mark (2003), "Time for Development of Internal Erosion and Piping in Embankment Dams," Journal of Geotechnical and Geoenvironmental Engineering, ASCE, Vol. 129, No.4, pp.307-314.

Introducing a New Long-Lead Hydrologic Forecasting System for Improving Reservoir Operation

Shahab Araghinejad¹, Saeed Jamali², Mohammad Hoseini Moughari³, Fereshteh Modaresi³

1-Associate Professor, University of Tehran, IRAN

2 Assistant Professor, Islamic Azad University, Central Tehran Branch, IRAN

3- University of Tehran, Tehran, IRAN

Email: araghinejad@ut.ac.ir

Abstract

Long-lead streamflow forecasting plays an important role in water resources planning and management. In this paper a new forecasting system named FARDA (Forecasting and Related Decision Analysis) is introduced. The results of the application of this system to two great river basins of Iran, namely Karkheh, and Karun are presented, briefly. Three data-driven models including K-Nearest Neighbor Regression (KNN), Artificial Neural Network (ANN), and monthly Rainfall-Runoff (R-R) models are performed within the system as individual forecasting models (IFMs). The fusion of all IFMs best outputs resulted from ordered series of model outputs is applied within the system to report the most reliable forecasts. All the forecasting models are presented in the model base of FARDA. Furthermore, the model base of the system consists of reservoir operation models which get benefit from the outputs of forecasting models to provide the best operating policies for the system of reservoirs. The inputs of those models are supported by the data base of the system which consists of different types of local and global hydro-climatological data as well as dams' data and information. This paper presents some characteristics of the system such as its conceptual model, the framework of its data and model base, and its specific graphical user interface. Some of the results of the application of the system in recent years is also presented.

Keywords: long-lead forecasting, model base, data base, graphical user interface, great Karun river basin, Karkheh river basin.

1. INTRODUCTION

One of the most important issues in long-term management of the surface reservoirs is the awareness of the amount of inflow to the reservoirs for better decision making. Decision making is one of the most significant challenges in the field of water resources and environmental engineering because of either the complexity around a problem or the un-predicted impacts of a decision. This challenge might be a result of multi-disciplinary problems, which may put some contrasting objectives in a competition that no compromising is allowed [1]. To overcome this challenge, new technologies have presented powerful tools to increase efficiency and accuracy of decisions and to accelerate the responses in facing with the real world problems. Decision Support Systems (DSSs) are one of the most efficient tools, with distinctive ability approval in the enormous engineering contexts. This paper presents a DSS namely FARDA which has been developed for long-lead streamflow forecasting, specifically.

A strategy for increasing the accuracy of long-lead forecasting results is to apply data-driven models such as Neural Networks (NN) [2,3], K-Nearest Neighbor regression (KNN) [4], and Support Vector Machines [5,6] which are able to recognize different relations between predictor and predicted variables for forecasting process. Nevertheless, each of those models contains estimation errors that are inevitable, and somehow lead to decline the accuracy of the forecasts.

In order to decrease the forecasting errors resulted from modeling, model fusion technique has been applied in a variety of fields for forecasting process such as cooling-load prediction [7], stock market forecasting [8,9], and wind power forecasting [10].

A forecasting model is developed to help solving a specific problem; however, in cases that we need to frequently face a generic forecasting problem and finding appropriate responses based on the current spatial and temporal state of a system, it is preferred to improve a model to a decision support system. Generally, the decision making procedure includes three main steps namely: data gathering, recognition of alternatives to solve a specific problem, and finally, selection of the best alternative. This procedure may be followed by two different approaches. In the first approach, well known mathematical formulation and decision rules are used algorithmically in different steps of solving a specific problem. Problems that are likely to be solved by this

approach are usually called structured problems. These kinds of problems could be possibly solved manually by the use of computer softwares, where no human judgment is needed. In contrast, in some problems, usually called unstructured problems, no decision rules and algorithmic procedure are defined and are dependent considerably to the human judgment to be solved. Decision support systems could be called as the second approach have been developed to be used in solving the latter.

Bonczek et al. [11] has defined DSSs as computer systems including three interactive components of user interface, a knowledge system, and a problem-processing system. Technology developments have changed slightly the definition of such systems in both holistic and detailed manner. Watkins and McKinney [12] have defined a DSS as a computer system which uses analytical models to help decision makers in defining and organizing various alternatives, and analyzing their impacts to choice most appropriate alternatives. In a general definition, the architecture of DSS consists of three components namely data base, model base, and user interface as shown in Figure 1.

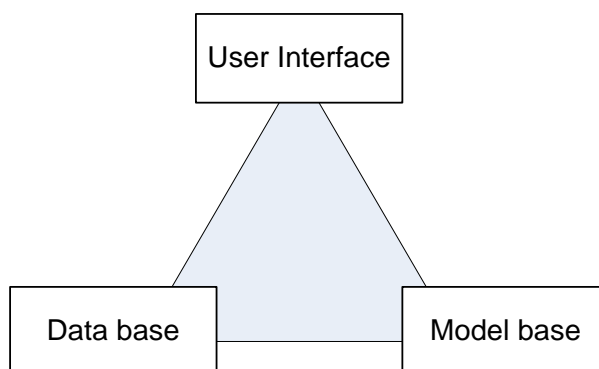


Figure 1. Main components of a decision support systems

DSSs usually are developed for a certain groups of decision makers. This needs a specific design such that decision maker could define new alternatives, and more importantly change an existing alternative to analyze that using the models embedded in the system. Since the delay in responding by the system is considered as an index of inefficiency, an interactive user interface, easy change of input parameters, and quick, understandable and managed output are considered as characteristics of a DSS. Next sections of the paper present the main components of FARDA DSS. The paper ends with the results of applying the system in hydrological forecasting in recent years. However, the system deals with the reservoir operation models either, the emphasis of this paper is on the hydrological forecasting.

2. FARDA: A LONG-LEAD HYDROLOGIC FORECASTING SYSTEM

2.1. CONCEPTUAL MODEL

To get benefit from the forecasting results in a real world system, the system has been developed which enables decision makers to have instant access to data, results of different models, applicable analysis, and saving the reports. As far as the general characteristics of the system is concerned, it is a platform to run different forecasting models, and integrating the forecasting results with reservoir operation models. The system is actually a combination of five following modules:

- Data Base,
- Long-lead forecasting models,
- Reservoir operation models,
- Management dashboard, and
- Report generation.

Figure 1 shows the conceptual model of the system demonstrating the relationship between different modules of the system.

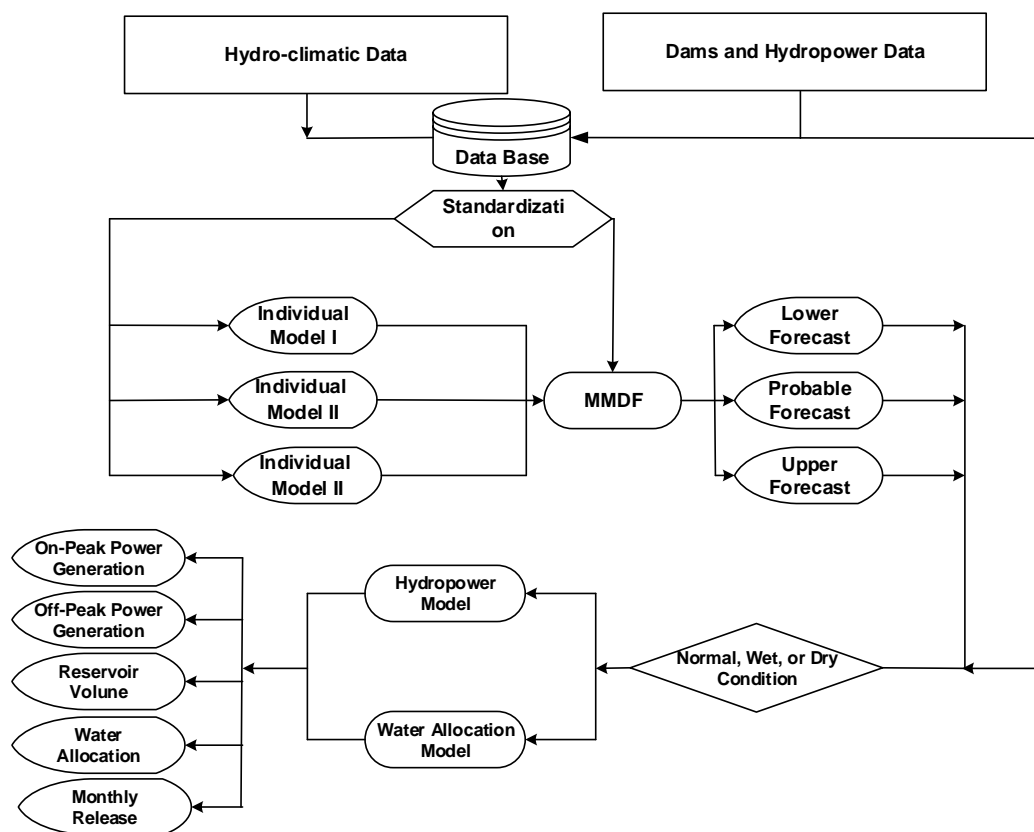


Figure 2. Conceptual model of FARDA system

2.2. DATA BASE AND MODEL BASE

Data base of the system consists of different local and global hydro-climatologic data and reservoir/hydropower data. Hydro-climatologic data of the system include:

- Tele-connection signals including Southern Oscillation Index (SOI), Northern Atlantic Oscillation (NAO), and Pacific Decadal Oscillation (PDO),
- Sea Surface Temperature (SST) data including Persian Gulf and Mediterranean SST,
- Rainfall data,
- Air temperature data,
- Snow cover data, and
- Historical inflow to the reservoirs.

Dam’s data include

- Elevation-area-volume curve of dams,
- Hydropower plants parameters, and
- Water demand values at downstream of each dam.

Model base of the system includes forecasting models and reservoir operation models. All forecasting models are employed through the forecasting module of the system. This module is categorized to two interrelated sections: individual models, and the fused model. In addition, all models have been developed in a way to generate, upper bound, lower bound, and most probable forecast values. A list of applied models within the system is presented in Table 1.

Table 1. Different forecasting models of the model base of the system

Category	Models	Name of the Model in the System
Individual Models	Artificial Neural Network	AI
	K-Nearest Neighborhood Regression	K-NN
	Monthly Rainfall-Runoff Model	R-R
Fused Model	Multi-Model Data Fusion Model [1]	MMDF

Due to the effect of available water on the hydropower generation and water allocation of reservoirs, a reservoir operation module has been designed within the system. This module is fed by the results of forecasting module, explicitly. Actually, the inputs to the reservoir operation model comes directly from what has been resulted by the forecasting models (Figure 2).

2.3. GRAPHICAL USER INTERFACE

Different graphical user interfaces in forms of interactive input/output forms, tables, graphs, and management dashboards have been designed and employed through the system. Examples of the graphical user interfaces are presented in this section.

Figure 3, shows the main page of the system. Different modules are presented in this page including:

- Data base,
- Forecasting,
- Reservoir Operation,
- Dashboard,
- System Management, and
- Help

Figure 4, demonstrates the interactive form for hydrologic data base of the system including meteorological data, hydrological data, climatic signals, sea surface e temperature, and reservoir data. Figure 5 shows the user interface designed to report the results of forecasting in a matrix form. By this matrix the user is able to monitor the forecast results for the entire water year in a monthly basis. Furthermore, the observed inflow to the reservoirs from the beginning of each water year to the current time is illustrated in this matrix. Figure 6 shows the management dashboard of the system which demonstrate the forecasting results in forms of informative gauges for months, seasons, half years, and annual basis. Each gauge demonstrate the situation of the forecasts in comparison with the historical experience of inflows to the reservoir. The user explores if the forecast values demonstrate a dry, normal, and wet situation at a glance. Seasonal and annual forecast are also shown in this dashboard. Furthermore, the details in seasonal and annual forecasts are reported in forms of graphs as shown in Figure 7.



Figure 3. Main Page of the System

The screenshot displays a data entry form with a tabbed interface. The active tab is 'Hydrologic Data'. The form is organized into two main sections: 'Inflow' and 'Snow'. Each section contains a label, a data entry field, a table with three columns (labeled 1, 2, and 3), and a 'Summary Statistics' button. The 'Inflow' section includes a 'Summary Statistics' button with a green checkmark and a red 'X' icon. The 'Snow' section also includes a 'Summary Statistics' button with a green checkmark and a red 'X' icon.

	1	2	3
Inflow the Reservoir	155.360	-999.999	12.254
Snow Area	-999.999	-999.999	-999.999

Figure 4. Interactive Form for Hydrologic Data Base of FARDA

Forecasting													
SolarMonth	Mehr	Aban	Azar	Dey	Bahman	Esfand	Farvardin	Ordibehe...	Khordad	Tir	Mordad	Shahrivar	Error
Mehr	19,575	44,943	51,633	58,558	158,738	227,830	129,433	99,823	46,923	29,433	27,120	36,700	0.00
Aban	24,000	53,940	50,505	63,678	158,620	239,768	95,813	76,893	46,903	35,945	34,220	31,338	-18.44
Azar	24,000	44,000	51,633	58,558	158,738	227,830	129,433	99,823	46,923	29,433	27,120	36,700	22.59
Dey	24,000	44,000	112,000	54,668	126,838	219,520	96,140	95,865	62,900	43,318	41,718	36,603	-53.90
Bahman	24,000	44,000	112,000	111,000	126,838	219,520	96,140	95,865	62,900	43,318	41,718	36,603	-50.75
Esfand	24,000	44,000	112,000	111,000	165,000	159,933	126,730	81,728	38,835	28,778	27,005	38,300	-23.13
Farvardin	24,000	44,000	112,000	111,000	165,000	250,000	127,058	100,700	32,330	36,150	34,903	31,665	-36.03
Ordibeheht	24,000	44,000	112,000	111,000	165,000	250,000	284,000	99,823	46,923	29,433	27,120	36,700	-55.26
Khordad	24,000	44,000	112,000	111,000	165,000	250,000	284,000	105,000	62,900	43,318	41,718	36,603	-14.45
Tir	24,000	44,000	112,000	111,000	165,000	250,000	284,000	105,000	32,000	28,778	27,005	38,300	184.36
Mordad	24,000	44,000	112,000	111,000	165,000	250,000	284,000	105,000	32,000	16,000	27,005	38,300	79.86

Figure 5. The reporting matrix of monthly/annual forecasts in FARDA

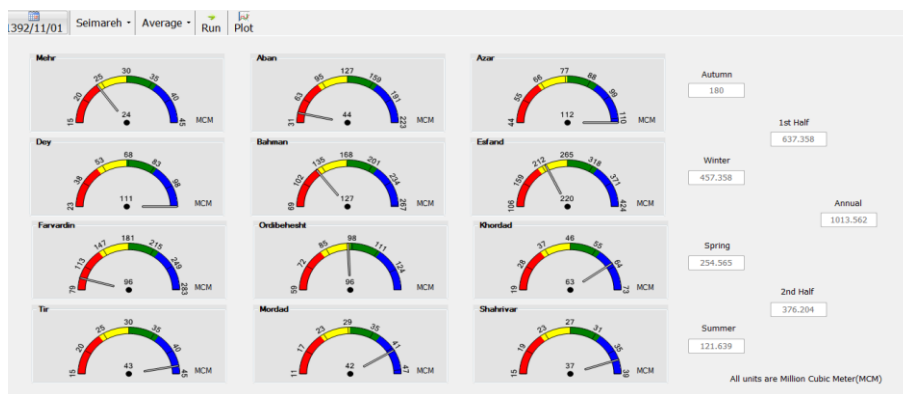


Figure 6. Long-Term forecasting Dashboard of FARDA

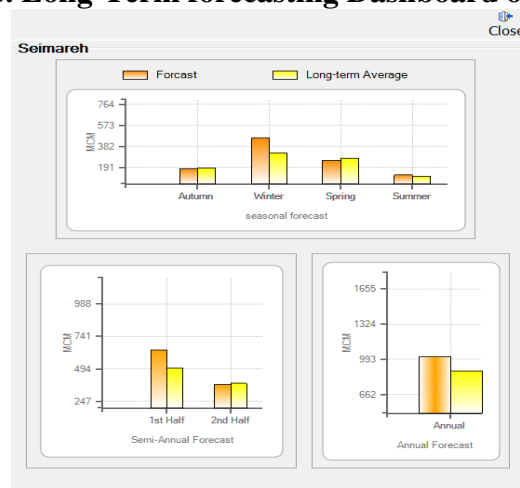


Figure 7. The graph of seasonal and annual forecasts in the system

3. CASE STUDY AND RESULTS

Forecasting of monthly to annual inflow to the Seimareh and Karkheh reservoirs in Karkheh river basin, and Karun VI, Karun III, Karun I, Godar, Gotvand and Dez reservoirs in Karun river in southwest of Iran, has been considered in the presented system. Figure 8 illustrates the location of those dams, rivers and their branches in Iran map. At the beginning of each month, a monthly hydrograph of inflow to each reservoir is forecasted by the end of the water year. While the inflow to the upstream reservoirs (Seimareh, Dez, and Karun VI) are forecasted as natural streamflow of the rivers, the inflow to the downstream series of reservoirs (Karkheh, and the remaining reservoirs on Karun river) are forecasted by the summation of river branches between two dams and the release by the upper dam.

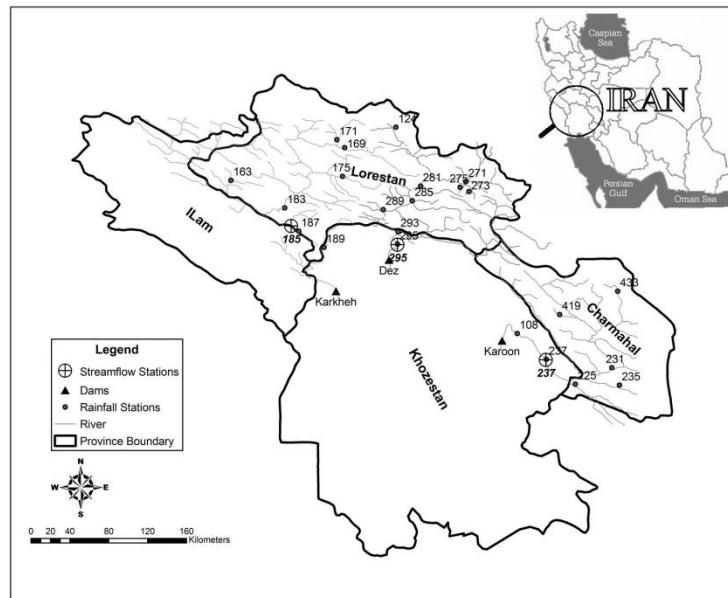


Figure 8. Location of Karkheh, Dez, and Karun I dams

Among the history of forecast values generated by the system, only a few of them is presented here as examples. Table 2 and Figure 9 show the forecast generated by the system for Seimareh dam in water year 2013-14. The forecast error of the system for this dam has been 27 percent as far as the annual forecast generated at the beginning of the water year (October 2013) is concerned. The forecasts became more accurate by the errors of 21 and 9 percent for the forecasts of January, and March 2014, respectively. It demonstrates the precision of forecast by the system as its getting better by receiving new data and establishment of the climate situation. A similar evidence is shown in Figure 10, where the forecast values is illustrated for Karun IV reservoir by the October 2011, and January 2012.

Table 2. Long-lead forecasts for Seimareh dam in water year 2013-14

Seimareh Dam	2013-14
Observed	1156
Forecast of October	850
Forecast of January	914
Forecast of March	1271

As an overall experience of applying the system, an average error of 25 percent is expected at the beginning of each water year, however, the forecast errors became less in recent years where tuning of the models have been applied after real world experience of the system.

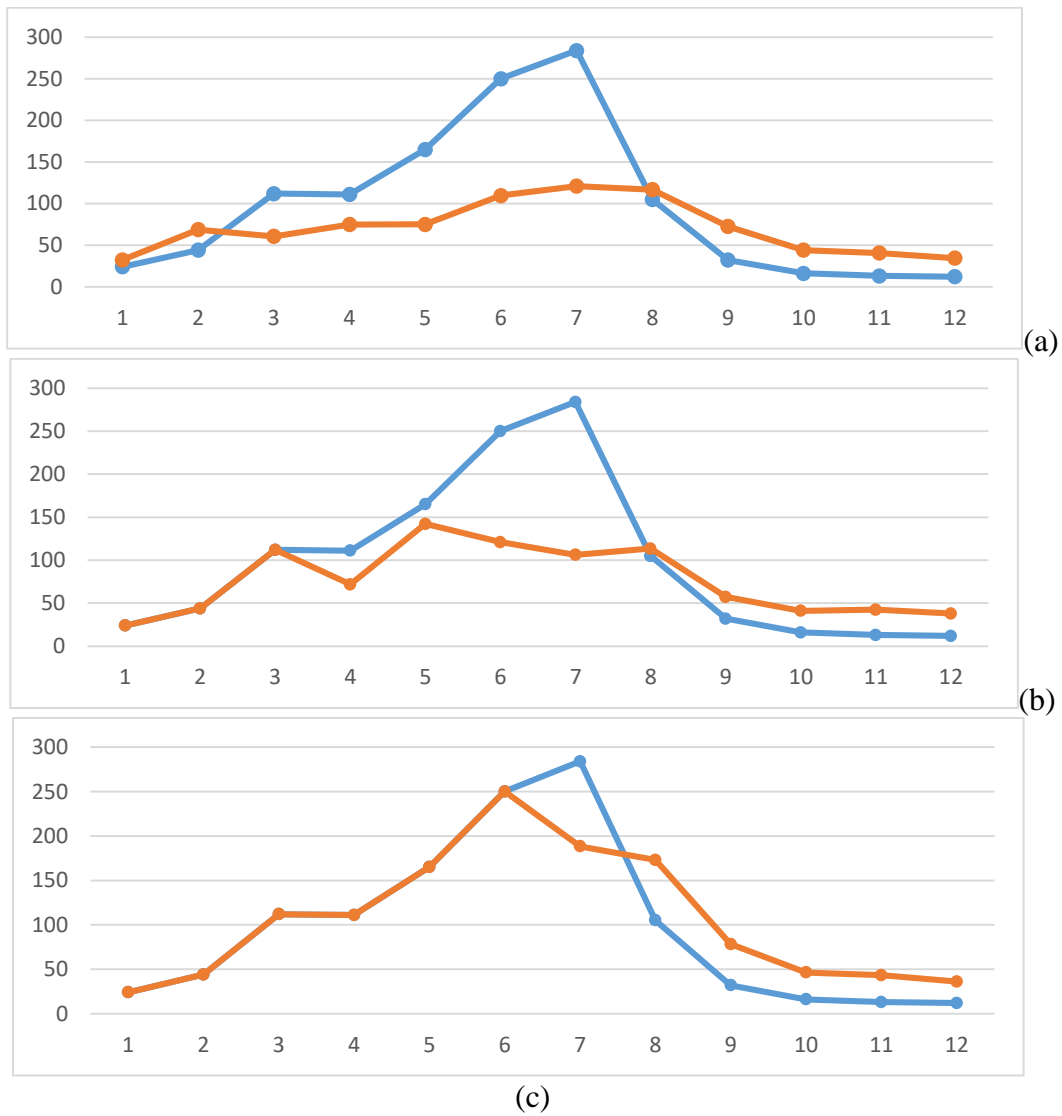


Figure 9. Long-lead forecast of inflow to the Seimareh reservoir generated at October 2013 (a) January 2014 (b), and March 2014 (c) (Red and Blue Lines demonstrate the forecast and observed values, respectively. The unit of the vertical axis is Million Cubic Meter)

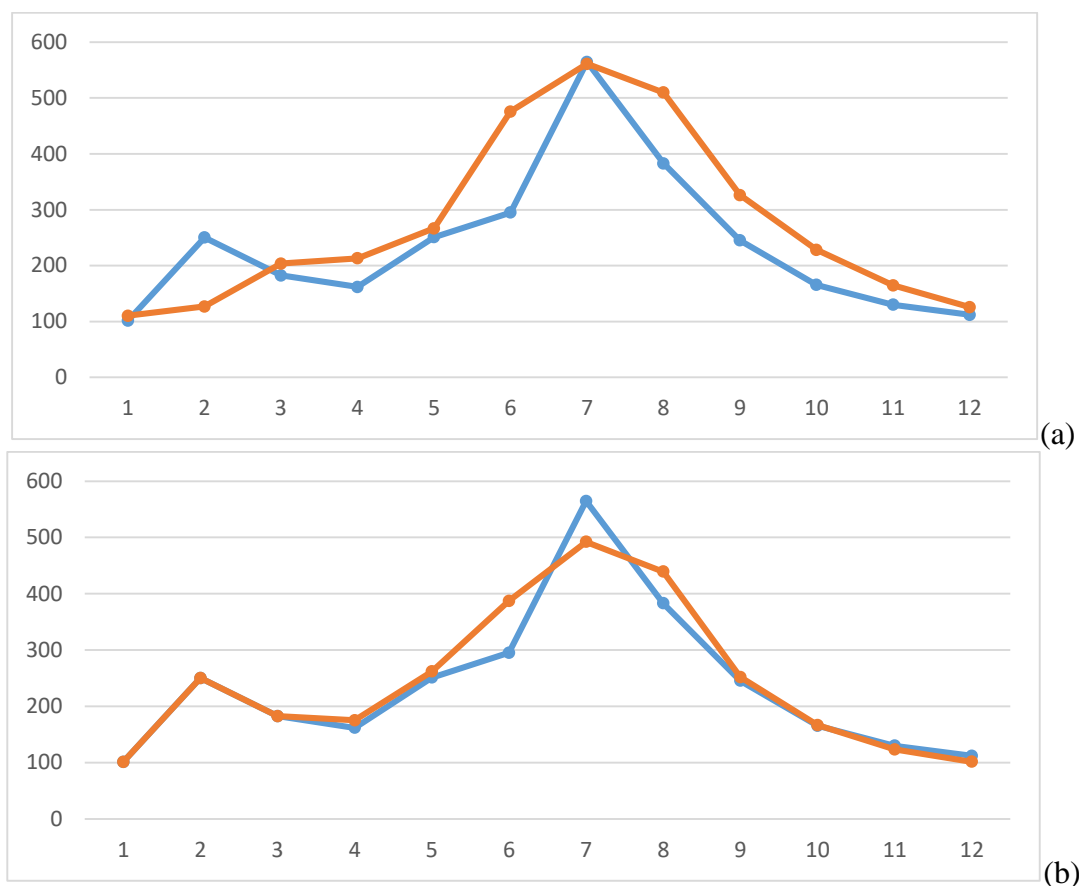


Figure 10. Long-lead forecast of inflow to the Karun IV reservoir generated at October 2011 (a) and January (b) 2012 (Red and Blue Lines demonstrate the forecast and observed values, respectively. The unit of the vertical axis is Million Cubic Meter)

4. CONCLUSIONS

The aim of developing this system was to apply different models which need to be used in a regular basis to forecast the future of hydrologic state of the system for an optimal operation of surface reservoirs. While it was important to develop an efficient system, it was a significant aim to develop a system which is rather user friendly. The system is developed on the basis of a decision support system. Conceptual model of the system was presented in the paper as well as the main framework of its data base and model base and examples of its graphical user interface. While the system deals with both forecasting and reservoir operation models, the focus of the paper was on the forecasting models. The novelty of the forecasting models of the system is the use of multi model fusion strategy which benefits from the skill of different individual forecasting models. The system was applied to the series of operating reservoirs in Karun and Karkheh river basins. The system could be applied to the other systems of reservoirs. The results of applying the system in real world experience demonstrate the efficiency of the system as an applicable tool for long-lead hydrologic forecasting.

5. ACKNOWLEDGEMENT

This study has been supported by a grant from Iran Water and Power Resources Development Company (IWPCo). The technical contributions of the staff of Technical and Research Division of IWPCo is hereby acknowledged.

6. REFERENCES

1. Araghinejad S (2014) *Data-Driven Modeling: Using MATLAB in Water Resources and Environmental Engineering*. Springer, Water Science and Technology Library, Volume (67).
2. Cigizoglu HK (2005) Generalized regression neural network in monthly flow forecasting. *Civil Engineering and Environmental System* 22(2): 71-81.
3. Chen S, Billings SA, Luo W (1989) Orthogonal least square methods and their application to nonlinear system identification. *International Journal of Control* 50: 1873-1896.
4. Meidani, E., and Araghinejad, S. (2014). "Long-Lead Streamflow Forecasting in the Southwest of Iran by Sea Surface Temperature of the Mediterranean Sea." *J. Hydrol. Eng.*, 19(8), 05014005.
1. Wang WC, Chau KW, Cheng CT, Qiu L (2009) A comparison of performance of several artificial intelligence methods for forecasting monthly discharge time series. *Journal of Hydrology* 374: 294-306.
2. Su, J., Wang, X., Liang, Y., and Chen, B. (2014). "GA-Based Support Vector Machine Model for the Prediction of Monthly Reservoir Storage." *J. Hydrol. Eng.*, 19(7), 1430–1437.
3. Hou, Z., Lian, A., Yao, Y., and Yuan, X. (2006). "Cooling-load prediction by the combination of rough set theory and an artificial neural-network based on data-fusion technique." *Appl. Energ.*, 83(9), 1033-1046.
4. Hassan, Md. R., Nath, B., and Kirley, M. (2007). "A fusion model of HMM, ANN and GA for stock market forecasting." *Expert. Syst. Appl.*, 33(1), 171-180.
5. Gunasekaran, M., and Ramaswami, K.S. (2011). "A fusion model integrating ANFIS and Artificial Immune Algorithm for forecasting Indian stock market." *J. Appl. Sci.*, 11(16), 3028-3033.
6. Vaccaro, A., Mercogliano, P., Schiano, P., and Villacci, D. (2011). "An adaptive framework based on multi-model data fusion for one-day-ahead wind power forecasting." *Elec. Power. Syst. Res.*, 81(3), 775-782.
7. Bonczek, R. H., C. W. Holsapple, and A. Whinston. (1981), "Foundations of Decision Support Systems." Academic Press, 1981.
8. Watkins, D.W., and D.C.Mckinney. (1995). "Recent developments associated with decision support systems in water resources." *Reviews of Geophysics (Supplement)*, July, 941-948.

Investigation on the Performance of Blanket, Cutoff Wall and Synthetic Cover for the Control of Seepage and Piping in Earth Dams

Hossein Khalili Shayan¹, Maryam Jamal¹, Faraz Rabeii Gholami²

1- Expert at Office of water resources basis studies, Iranian Water Resources Company, Tehran, Iran

2- Director General at Office of water resources basis studies, Iranian Water Resources Company, Tehran, Iran

Email: h_kh_shayan@ut.ac.ir

Abstract

This study firstly presents a review on the different methods for seepage and piping control of earth dams. Then, the capability of an upstream blanket, cutoff wall, and synthetic cover was compared for reducing of seepage discharge and exit gradient using SEEP/W software as a numerical simulation model. For this, a typical section of an earthen dam was considered. Totally, 54 tests were conducted under the different conditions of the upstream head, situation and depth of cutoff wall and upstream synthetic cover. For each test, the values of seepage discharge and exit gradient at the toe of earth dam were calculated. The results show that the presence of an upstream blanket cannot reduce the seepage discharge and exit gradient, significantly. For example, the design of upstream blanket with the length of 45 m, only reduces the seepage discharge and exit gradient about 0.3% and 7.3%, respectively. On the other hand, by using an upstream synthetic cover the seepage discharge and exit gradient can be more reduced about 67.5% and 65.5%, respectively. The results also show that the best situation of the cutoff wall for the control of seepage discharge and exit gradient is in the middle of the earth dam. This can reduce the seepage discharge and exit gradient about 40% and 23%, respectively. This study presents a comparison about reducing the seepage discharge and exit gradient by using a combination of a cutoff wall with an upstream blanket and synthetic cover as the two different cases. The seepage discharge (exit gradient) was reduced about 40.4% (10.6%) and 63.3% (44.6%) for the two above cases. It is concluded that the best way for reducing the seepage discharge is the use of upstream synthetic cover with a cutoff wall in the middle. It is believed that the optimal design of a drain hole reduces the seepage discharge and exit gradient, simultaneously which requires furthering studies.

Keywords: Seepage, Exit Gradient, Earth Dams, Cutoff Wall, Blanket, Synthetic Cover.

1. INTRODUCTION

Issues related to the security of earth dam while construction and also within operation have special important due to the effective role of those earth dams in supplying hydraulic requirements and also creating potential risks for residents of the downstream. There is the potential seepage water from the foundation and the bodies of these structures due to the difference in water head from the both sides of earth dams. Seepage effects in these structures could categorize into three parts, including uplift force, seepage flow and exit gradient. In designing earth dams, one purpose is achieving to the optimal design of dam section, in which the effects of seepage would be minimized. The aim of this study is evaluating the different methods for decreasing the seepage effects under the earth dams and determine the optimal model. Jaberi (1376) has considered water flow in a porous heterogeneous inconsistency environment [1]. Sedghiasl et.al (1384) have studied the effect of optimal position of cutoff walls in seepage decline under hydraulic structures using numerical model and concluded that the best position for decreasing the seepage discharge and exit gradient is at the toe [2]. Pakbaz et.al (2008) have considered constructing the plastic concrete cutoff wall using SEEP3D model for decreasing the water seepage at the right and left sides of the bearings of karkhe dam [4]. Their results show that by creating cutoff wall at the left and right sides, water seepage would decrease 60 and 20 percent, respectively.

2. MATERIALS AND METHODS

2.1. METHODS OF CONTROL AND DECREASE SEEPAGE EFFECTS

Generally, we could categorize different applied methods for either control or decrease seepage effects from the foundation and body into two groups: first group include methods for sealing or decrease seepage amount and second group include methods for control seepage and its effects. In first methods, components are designed such that the seepage amount decreased. However, in second methods main purpose is seepage effect, such as distribution of uplift pressure and leading leaked water flow in desired path, such that adverse effects be minimized. We could categorize combination of the above mentioned components for either decrease or control seepage effects into vertical (or diagonal) and horizontal components. It should be noticed that in most of cases, a combination of components of both recent groups might obtained optimal results. According to the above model, Figure 1 represents the most common methods which are applied in either decrease or control seepage. It should be mentioned that proper exploitation of these methods requires intensive field studies and identifying environmental conditions of constructing the structure.

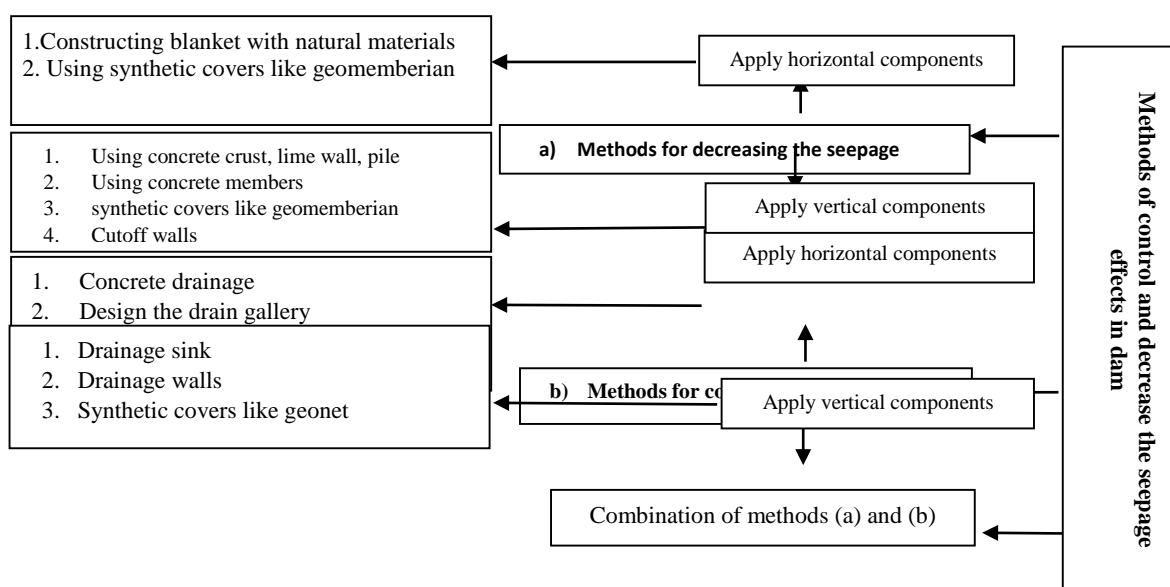


Figure 1. Methods of control and decrease the seepage effects in dam [5]

2.2. INTRODUCING SECTION OF UNDER STUDY DAM

In this study, the application of the mentioned methods for a section of a heterogeneous earth dam with represented dimensions in Figure 2 has evaluated. Specifications of used materials in foundation, shell, filter and core of the dam are presented in Table 1.

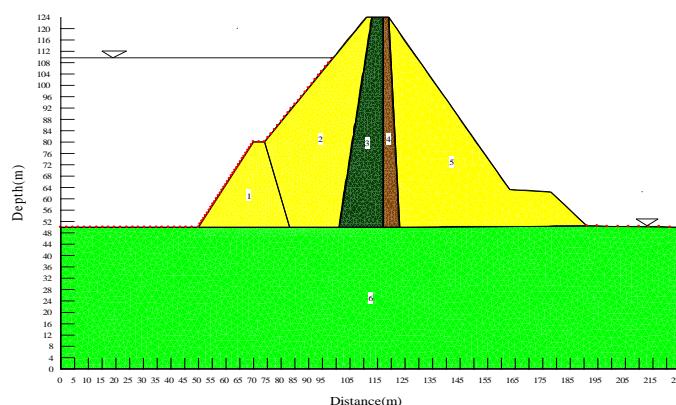


Figure 2. Section of under study dam

Table 1. Specifications of used materials in foundation, shell, filter and core of the dam

Region Number	Material	Saturated Hydraulic Conductivity, K_{sat} (m/s)
1,2,5	Shell	0.001
3	Filter	0.0001
4	Core	0.0000001
6	Foundation	0.00001

At first, water flow and exit gradient in lack of cutoff wall, clay blanket and synthetic covers were calculated using finite element method. Then, mentioned parameters were computed in different models such as the existence of a clay blanket with different length, cutoff wall in different position along the foundation and synthetic covers in different forms and combination of these components. It is not worthy to mention that we estimated above parameters in all modes in a condition that upstream water head and downstream water head was assumed 50 meters. Water flow and exit gradient in all modes were computed using finite element with seep/w software (type of GeoStudio 2004 software package).

2.3. BASIC EQUATIONS USED IN THE ANALYSIS

To find equation of water current in a porous environment, a small and saturated element with dimension of, dx and dy has considered and current speed along x and y axes are v_x and v_y , respectively. By ignoring changes in volume of an element due different factors like changes in effective tension and writing mass conservative rule, net value of input current into the element is [6]:

$$q_{net} = q_x + q_y + Q.dA = \left(-\frac{\partial v_x}{\partial x} - \frac{\partial v_y}{\partial y} + Q \right).dA \tag{1}$$

where q is net current in both sides and Q is produced water flow in element area. Using relations between rate of water mass changes in solid element and rate of changes in volume water content of solid element and mass conservation rule, we have:

$$-\frac{\partial v_x}{\partial x} - \frac{\partial v_y}{\partial y} + Q = \frac{d\theta}{dt} \tag{2}$$

Equation 2 is known as a differential equation of current continuity. By combination of Darsi relation and differential equation of current continuity, permeation differential equation is obtained:

$$\frac{\partial}{\partial x} \left(k_x \frac{\partial h}{\partial x} \right) + \frac{\partial}{\partial y} \left(k_y \frac{\partial h}{\partial y} \right) + Q = \frac{d\theta}{dt} \tag{3}$$

By enter special store confident in equation 3, we would have:

$$\overline{\nabla} \cdot (C \cdot \nabla h) + Q = m_w \cdot \gamma_w \cdot \frac{dh}{dt} \tag{4}$$

Equation 2 is Laplace differential equation, in which $\overline{\nabla} = \left\{ \frac{\partial}{\partial x}, \frac{\partial}{\partial y} \right\}$ and C is permeability matrix. As in stable currents, value of h doesn't change with time, permeation equation is simplified to:

$$\overline{\nabla} \cdot (C \cdot \nabla h) + Q = 0 \tag{5}$$

Finite element method is one of the strongest methods in numeral solving differential equations, such as permeation equation which has found many applications in engineering. In this method, problem area has been divided into limited parts and by assuming an approximate solution for differential equation and minimizing difference between approximate and real solution of the problem (minimizing system energy), the differential equation is transformed into integral form and unknown values in special positions which called nodes are

obtained. Using interpolation functions or shape functions and insert in derivative of Laplace differential equation and applying a border condition, the matrix form of permeation equation would obtain:

$$[K]\{H\} + [M]\{H\}_t = \{Q\} \quad (6)$$

Equation 6 is the general form of the Laplace equation in finite element method. As in steady analysis $\{H\}_t = 0$, Equation 6 is simplified to:

$$[K]\{H\} = \{Q\} \quad (7)$$

Above matrices are computed using numerical integration methods. To calculate above matrices and applying border conditions and solving equation systems, value of water head considering the location of network nodes is obtained.

3. RESULTS AND DISCUSSIONS

3.1. STUDYING THE EFFECT OF BLANKETS AND SYNTHETIC COVERS ON SEEPAGE AND EXIT GRADIENT

In order to study the effect of blankets and synthetic covers on seepage water flow and exit gradient, a blanket with four different lengths of 35, 25, 15 and 45 meters have considered in upstream. Blanket materials, clay and its hydraulic conductivity in horizontal and vertical directions equal to $2.5 \cdot 10^{-8}$ m/s have considered. Upstream water head in all modes is assumed 110 meters and values of water flow from foundation and body and exit gradient in both horizontal and vertical directions have computed. It has followed that:

- By increasing the length of the blanket, seepage is decreased, insignificantly, such that when there is a blanket with 45 meters length, water flow from foundation and body have decreased 0.08 and 2 %, respectively. Thus, total seepage has decreased 0.3% than basic condition. The reason could be found in less share of seepage flow from the foundation than from the body.
- Increase in blanket length could cause an increase in exit gradient in both horizontal and vertical directions. However, increasing in the exit gradient in horizontal direction is sharper than in the vertical direction. So, a blanket with 45 meters length cause approximately 23.5% and 7 % increase the exit gradient in horizontal and vertical directions, approximately (Figure 3). In total, exit gradient has increased 3%. However, by increasing the blanket length and as a result increase in length of current lines from foundation, it is expected that exit gradient decreased. Although, by decreasing in the permeability of foundation, congestion of speed vectors in the body has increased and finally causes increases in exit gradient.

Thus, if only there is a blanket in upstream for an earth dam with desired section, it is not an appropriate strategy for decreasing seepage and risk of piping in downstream.

3.2. STUDYING THE EFFECT OF SYNTHETIC COVERS ON CHANGES IN WATER FLOW AND EXIT GRADIENT

- horizontal synthetic cover: for this purpose, covers made of geo-synthetic with length of 35, 25, 15 and 45 meters in upstream of foundation have considered. Water head in upstream in all modes is constant and equal to 110 meters and values of seepage water flow and exit gradient in each mode have determined. Coefficient of cover permeability in horizontal and vertical directions is equal and has assumed 10^{-14} m/s. Figures 2 and 3 show that,
 - Horizontal synthetic covers cause an insignificant decrease in seepage from body and foundation. As a result, horizontal synthetic cover with 45 meters length causes approximately 0.42% and 0.35% decrease in seepage water flow from foundation and body, respectively, than basic condition. So, total seepage water flow in comparison with basic condition would decreased 0.36% (Figure 2).
 - Horizontal synthetic cover has insignificant effect on decrease in exit gradient in comparing with basic condition. For example, in situation that there is a horizontal synthetic cover with 45 meters length, exit gradient in both horizontal and vertical directions are decreased 0.35% and 0.45%, respectively, in comparison with basic condition.

Thus we could conclude that only existence of a horizontal synthetic cover couldn't have significant influence on the decrease in exit gradient and seepage water flow at the toe. Although it is more effective than condition with a blanket cover (Figure 3).

- b) Complete synthetic cover: complete synthetic cover is a combination of inclined cover in upstream and horizontal cover. Dimensions of horizontal cover is considered 35, 25, 15 and 45 meters, and content of water head in upstream in all modes is constant and equals to 110 meters. Values of seepage water flow and exit gradient are computed in each case and results are presented in diagrams.
- Complete synthetic cover has a significant effect on decrease seepage water flow from foundation and body, and by increasing the length of horizontal synthetic cover, it decreased more. So, in condition with complete synthetic cover with horizontal 45 meters length parts, seepage water flow from foundation and body would decrease 62.2% and 68.2%, respectively. In total, seepage water flow in comparison with the basic condition decreases 67.5% (Figure 2).
 - Complete synthetic cover is suitable strategy for decrease exit gradient and creating a piping phenomenon at the toe of the dam.

3.3. STUDYING THE EFFECT OF CUTOFF WALL POSITION ON CHANGES IN SEEPAGE FLOW AND EXIT GRADIENT

For this purpose, cutoff wall in positions of 50 (upstream), 70, 90, 110, 130, 150, 170 and 190 (downstream) meters was moved.

Materials of the cutoff wall include cement grout. Coefficient of permeability of materials in horizontal and vertical directions is considered constant and equal to 10^{-7} m/s. Depth of cutoff wall and upstream water head in all positions is constant and equal to 25 and 110 meters, respectively. Results of computing seepage water flow and exit gradient in all modes have presented in Figures 4 and 5.

- Water flow changes under the effect of cutoff wall position could be grouped into 3 parts (Figure 4):
 - 1- Content of seepage would decrease from the upstream to middle of foundation, intangibility.
 - 2- It is observed from the figure that seepage water flow from foundation and body when approaches to middle of the foundation, suddenly decreased. Intensity of seepage decrease while passing from the foundation; such that in position with 110 meters height, content of seepage water flow from body and foundation would decreased 18.8 and 43.4 %, respectively, and the content of total seepage water flow in comparison with basic condition would decreased 40.4%.

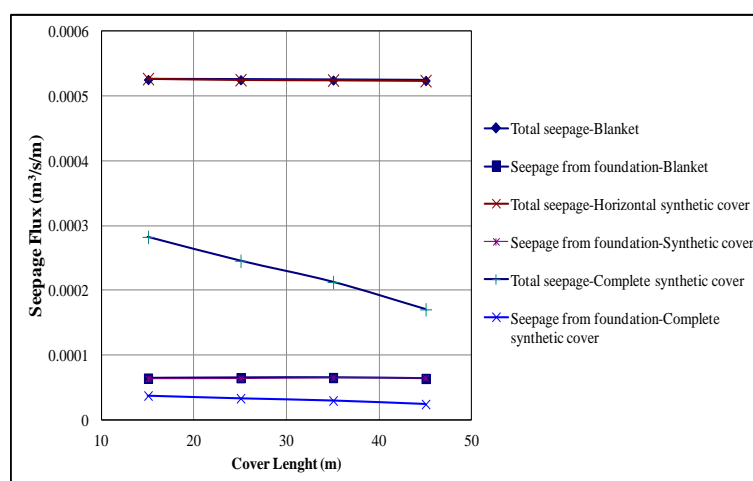


Figure 2. Effect of lengths of blanket, horizontal synthetic and complete on seepage flow

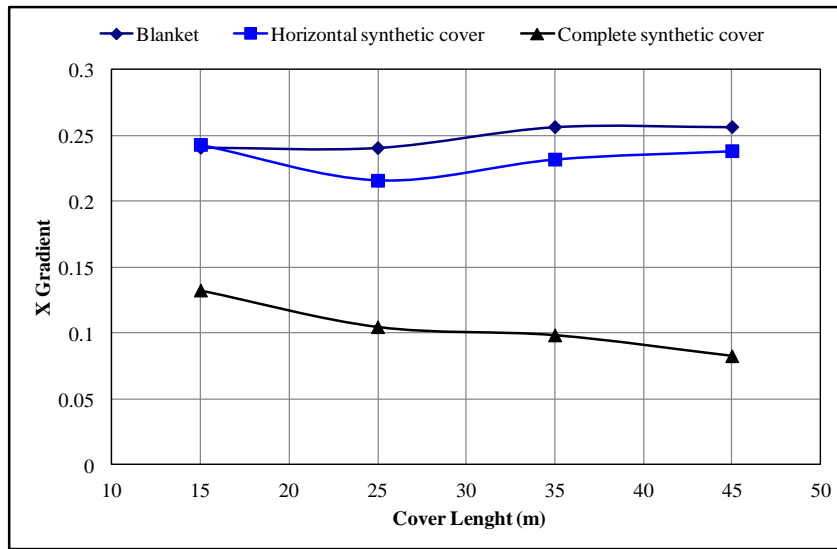


Figure 3. Effect of lengths of blanket, horizontal synthetic and complete on exit gradient

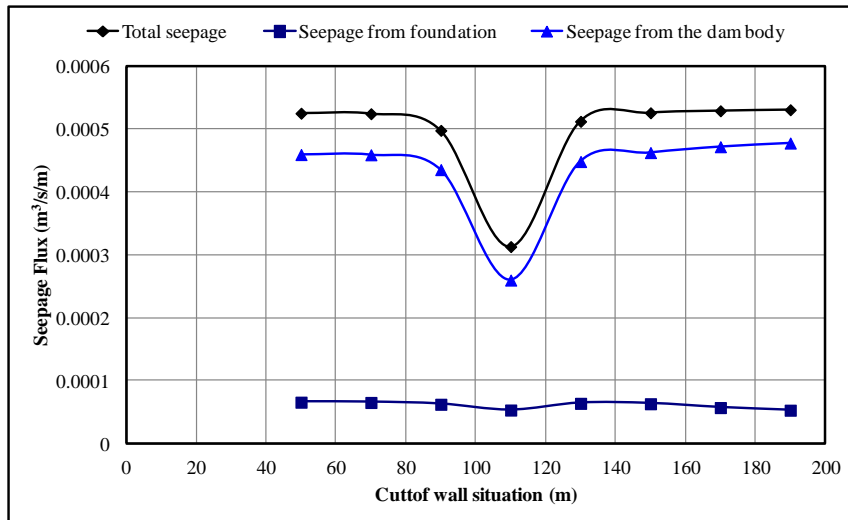


Figure 4. Effect of cutoff wall position on changes in seepage water flow and exit gradient

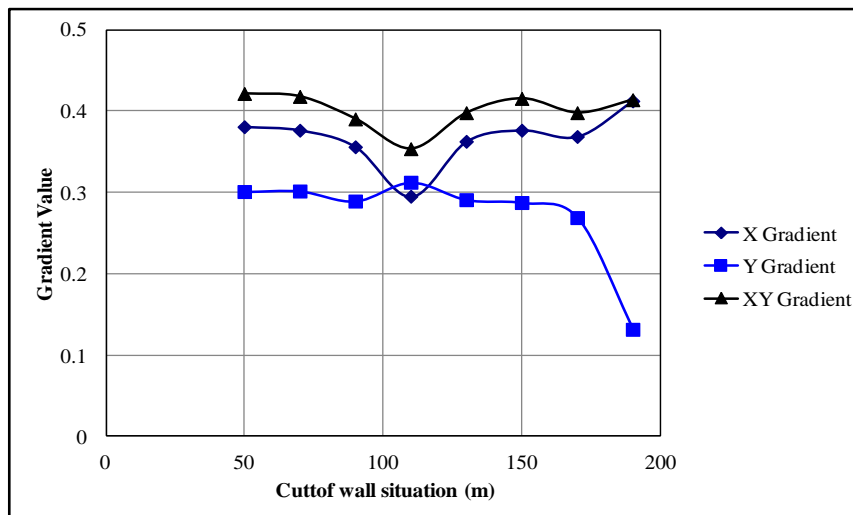


Figure 5. Effect of cutoff wall position on changes in vertical or horizontal exit gradient

3.4. STUDYING THE COMBINED EFFECT OF CUTOFF WALL AND BLANKET ON CHANGES IN SEEPAGE WATER FLOW AND EXIT GRADIENT

It has explained in section 3 that by approaching cutoff wall to middle of the foundation, content of seepage water flow and exit gradient would decrease, suddenly.

Purpose of this section is comparison the influence of blanket and cutoff wall, simultaneously, in condition that only cutoff wall is available. For this, cutoff wall moves in above mentioned positions. In all models, upstream water head and length of blanket have assumed 110 and 20 meters, respectively. Depth of cutoff wall was also assumed 25 meters.

At first section has discussed that blanket has insignificant effect on changes in seepage water flow. So, it is expected that the combination of blanket and cutoff wall for mentioned section has no influence on decrease in seepage water flow in compare with situation with only cutoff wall. It is presented in Figure 6.

- In section 3 it has presented that best position for placement of cutoff wall in order to control piping phenomenon is near middle of the foundation. However, blanket has no effect on decrease in seepage water flow than not using blanket. Although, it is observed from Figure 7 that the blanket along with cutoff wall in optimal position causes 27.6% decrease in horizontal exit gradient, 34.4% decrease in vertical exit gradient and totally 30.1% decrease in whole exit gradient in compare with lack of blanket situation.

3.5. STUDYING THE COMBINED EFFECT OF CUTOFF WALL AND SYNTHETIC COVER ON CHANGES IN SEEPAGE WATER FLOW AND EXIT GRADIENT

For this purpose, complete synthetic cover is considered with horizontal cover length of 25 meters and upstream water head of 110 meters. Cutoff wall moved in above mentioned positions. Depth of middle cutoff wall in all modes has assumed 25 meters.

- Synthetic cover with cutoff wall causes decrease in seepage water flow. When cutoff wall is placed in optimal position of 110 meters, synthetic cover causes 38.5% decrease in total seepage water flow, 36.2% decrease in seepage from foundation and 39% decrease in body seepage in compare with lack of synthetic cover (Figure 6).
- Synthetic cover with cutoff wall causes decrease in exit gradient. Intensity of this decrease is more than decrease in seepage water flow, such that while placing cutoff wall in position of 110 meters, causes 55% decrease in horizontal exit gradient, 59.5% decrease in vertical exit gradient and 56.7% decrease in exit gradient in plate (Figure 7).

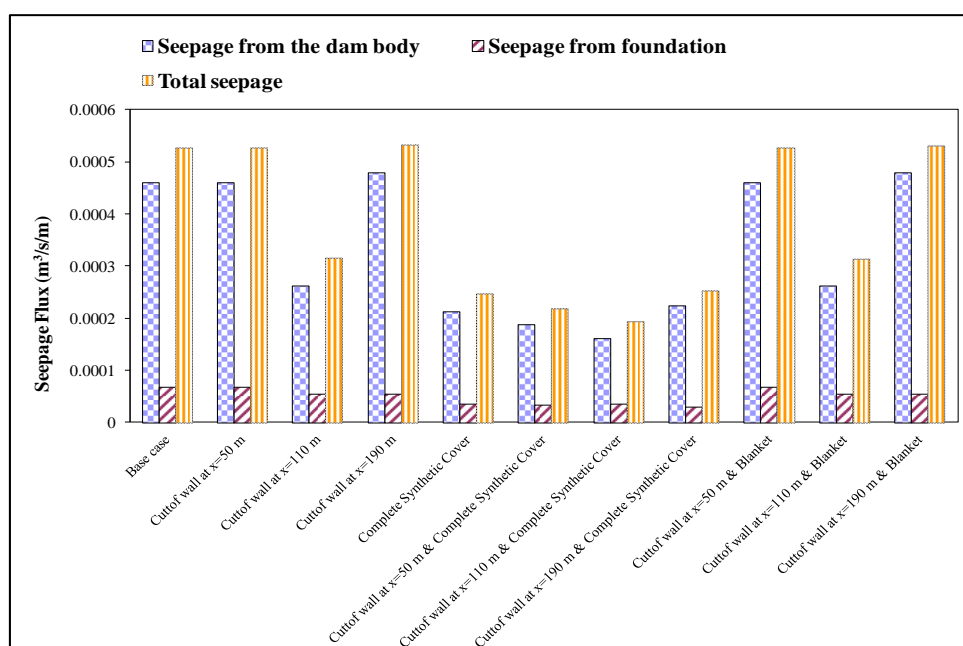


Figure 6. Comparison the combined effect of blanket, cutoff wall and synthetic cover on seepage from body and foundation

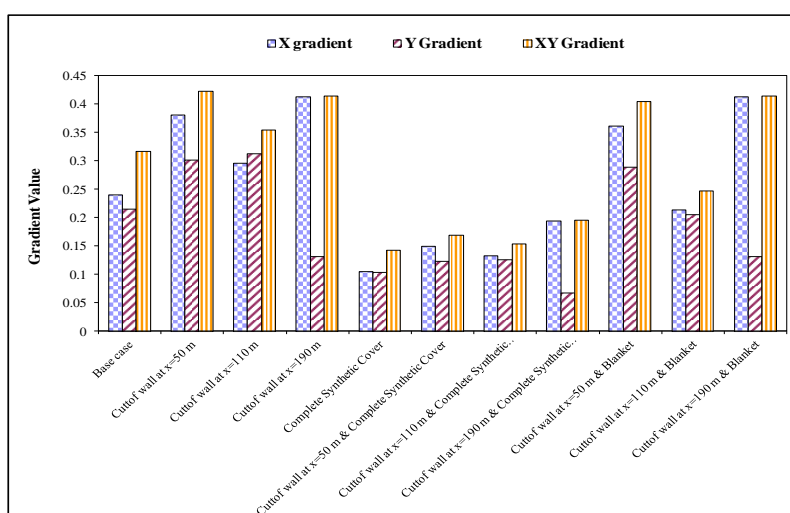


Figure 7. Comparison the combined effect of blanket, cutoff wall and synthetic cover on content of exit gradient

4. CONCLUSIONS

- 1) Only applying blanket in upstream for earth dam with proper section couldn't have significant influence on the decrease in seepage water flow and risks of piping in downstream.
- 2) Best position for cutoff wall to decrease in seepage water flow and risks of piping in downstream is middle of the foundation.
- 3) By ignoring economical, executive and local facilities, for mentioned earth dam, the best method for control seepage and exit gradient is applying cutoff wall in middle of the foundation along with complete synthetic cover.
- 4) Movement of cutoff wall from middle into downstream cause insignificant increase in seepage water flow from foundation and body. Moreover, cutoff wall in downstream in comparison with upstream cause 19.4%, 4% increase in seepage from the body and totally 1% increase in whole seepage.
- 5) Form of exit gradient changes under the effect of cutoff wall position is similar to form of seepage water flow changes. In this condition, moving cutoff wall toward the middle of foundation causes intense decrease in exit gradient.
- 6) Minimum of horizontal exit gradient and 2-dimensional exit gradient has obtained in position of 110 meters with cutoff wall. In this situation, horizontal exit gradient and 2-dimensional exit gradient have decreased 23.4% and 12% than basic condition, respectively.
- 7) Cutoff wall in downstream in comparison with the cutoff wall in upstream causes 5.6% increase in horizontal exit gradient, a 5.6% decrease in vertical exit gradient and 1.8% decrease in vertical exit gradient.

Thus, we could say that the best position for cutoff wall to decrease in seepage water flow and risks of piping in downstream is middle of the foundation.

5. REFERENCES

1. Jabari A. 1997. "Solution of three dimensional modelling of the steady flow at non homogenous enviroment with infinite volumes method". MSc. Theis, University of Tehran, Tehran, Iran.
2. Sedghi-Asl M., Rahimi H., Khaleghi H., Effect of cutoff wall's depth and situation on reducing seepage under hydraulic structures by using numerical method, 5th Iranian Hydraulic Conference, Iran, 2005 (In persian).
3. Yifeng C., Chuangbing Z., Hong Z. 2008. "A numerical solution to seepage problems with complex drainage systems". Computers and Geotechnics, 35(3), PP. 383-393.
4. Pakbaz M.S., Dardaei A., and Salahshoor J. 2009. "Evaluation of performance of plastic concert cutoff wall in karkheh dam using 3-D Seepage analysis and measurement". Journal of Applied Sciences, 9(4):724-730.
5. ICOLD, (2005), "Dam Foundations, Bulletin No.129".
6. Krahn, J., (2002), "SEEP/W version5 Manual", Calgary, Alberta, Canada.

Analyzing the Effect of Defect in the Upstream Impervious Blanket on the Seepage Behavior of Earthfill Dam

Hamed Farshbaf Aghajani¹, Majid Mahdavi²

1- Assistance professor, Department of Civil Engineering, Faculty of Engineering, Azarbaijan Shahid Madani University, Kilometer 35 of Tabriz/Azarshahr Road, P.O. Box 53714-161, Tabriz, Iran

2- M.Sc. student in Geotechnical Engineering, Azarbaijan Shahid Madani University, Tabriz, Iran

Email: h.farshbaf@azaruni.ac.ir

Abstract

This paper aims to thoroughly investigate the effect of weakness in the upstream impervious blanket of earthfill dam on the seepage behavior. For this end, a limited zone with high permeability is considered in various situations of impervious blanket. Then, for each situation, the discharge value and seepage pattern through the foundation is determined by performing 2D finite element seepage analysis via GeoStudio software.

Regarding to the analysis result, the location defected zone in upstream impervious blanket directly influences the seepage pattern through dam body and foundation. If the defected zone is occurred in the situations close to the dam core, escaping water from weakness zone of impervious blanket impact the clay core water tightening performance and water potential head drop is not completely occurred in clay core.

From the erosion potential view, the critical condition is directly depended on the foundation permeability. For most permeable foundation, the gradient of 5.6 is recorded for the defected zone located out of dam body in defected zone. For this type of dam, the gradient in foundation is insignificant. If the foundation has lower permeability and defected zone is occurred in impervious blanket next to clay core connection point, the foundation beneath the defected zone is susceptible to erosion.

Keywords: Defected zone, Seepage analysis, Upstream blanket, Earthfill dam.

1. INTRODUCTION

In all dam types, controlling and minimizing the discharge through dam foundation is emphasized by all dam designing bulletins and authorities [1]. One method for water tightening the foundation in the earthfill dams is the covering the upstream ground of reservoir bottom by means of an impervious blanket. The upstream impervious blanket is generally comprised of the materials with low permeability such as compacted clay soil, geomembrane and the asphalt material and applied in such cases where the ground surface has the relatively flat topography and the impervious strata of foundation is relatively located in deeper depth [2, 3, 4].

Regarding to the vital role of water barrier system of foundation in dam safety, any defect can avoid the appropriate functioning the barrier system and may lead to unfortunate consequents. Because the upstream impervious blanket is exposed at the ground surface, this type of water barrier system is fairly more susceptible to damage during operation phase [5, 6]. Besides, the defects in upstream blanket may be developed due to some weakness and shortages during the construction stage. If the clay blanket is compacted with the compaction degree lower than the minimum requirements or the unqualified or low quality material is used for the blanket material, the impervious blanket may be cracked and some weakness could be existed in a blanket. Also, if the clay material of blanket contains the soluble beds like the gypsum, the consequent dissolution of gypsum may lead to create some cavity within blanket and prepare some path for water flow [7].

In all of the instances mentioned above, the upstream impervious blanket is susceptible to impose a weakness in hydraulic barrier functioning. In other words, due to the aforementioned factors, some zones are developed within blanket which have the higher permeability rather than the original blanket material. These higher permeable zones provide short paths for concentrated flow of water from the dam reservoir into the foundation. Thus, even though upstream blanket is properly designed and constructed with adequate length to reduce the seepage, the defected zones in blanket causes for an unexpected increase in the discharge volume through dam foundation. The concentrated seepage through the defected zones is accompanying with a higher gradient leading to erosion in blanket material around the defected zone. Thus, by continuing the concentrated seepage, the dimension of defected zone is progressively increased and seepage magnitude is gradually enhanced [8, 9].

Even though the importance of defect in the water tightening system and preventing methods are thoroughly addressed in many dam design guidelines [1, 2], the hydraulic performance of defected zone and the effect geometry and situation of on the seepage behaviour have not been studied. Thus, this paper aims to thoroughly investigate the effect of weakness on the seepage behavior of the upstream blanket of an earthfill dam. For this end, a limited zone with higher permeability is considered as the representation of defected zone in various situation within upstream impervious blanket. Then, for each situation, the seepage through dam foundation is modelled by performing 2D finite element seepage analysis and compared with intact blanket.

2. NUMERICAL MODELLING

The seepage through the dam body and foundation are modeled in Geostudio software in the form of the two dimensional finite element seepage analysis. This software is a powerful means for analyzing the saturated and unsaturated flow in porous media and widely used in seepage analysis of dams [10].

The numerical model consists of a zoned earthfill dam located on the one-layer alluvial foundation. The dam body includes the clay core, shell and upstream impervious blanket. The slopes of dam face and clay core are 1V:2.5 H and 4V:1H, respectively. Three values of 20, 40 and 60 meters are selected for dam height. The depth of dam foundation is supposed equal to dam height. Besides, three various conditions are considered for foundation permeability. The upstream impervious blanket is comprised of compacted clay material which is connected to the clay core and extended toward the upstream of reservoir ground. The thickness of upstream blanket is 1 meter. For each dam with a specific height, several lengths are considered for impervious blanket and then the optimum length of impervious blanket is determined by numerical analysis in such a way that by increasing the impervious blanket more than the optimum length, seepage through foundation becomes almost constant.

For thoroughly investigating the effect of weakness in upstream blanket, a defected zone with constant width is considered in various situations along the upstream impervious blanket and in each situation; the total discharge through the foundation is determined. The X parameter is represented for situation of defected zone in blanket which is defined as the distance of defected zone from the connection point between impervious blanket and clay core. Moreover, for studying the dimension effect of defected zone, three values of 2, 4 and 10 meters are assigned for width of defected zone.

For the boundary condition, the hydraulic head equal to reservoir elevation is assigned to upstream face of dam and top surface of upstream blanket. All nodes on the downstream face of the ground have the zero water pressure head. The lower bound and sides of numerical model are closed with the zero flux boundary condition. All analyses are conducted as the steady state 2-D seepage analysis in Geostudio. The finite element meshing theme of numerical model is shown in Figure 1. The permeability of materials of dam body, foundation and intact upstream blanket and defaced zone of blanket is presented in Table 1. It is supposed that permeability of defected zone of blanket is almost 1000 times greater than the intact condition.

Table 1. The permeability of materials in numerical model

Material name	Clay core	Shell	Foundation	Intact upstream impervious blanket	Defected zone in upstream blanket
Permeability (m/s)	10^{-8}	10^{-3}	$10^{-2}, 10^{-4}, 10^{-6}$	10^{-8}	10^{-3}

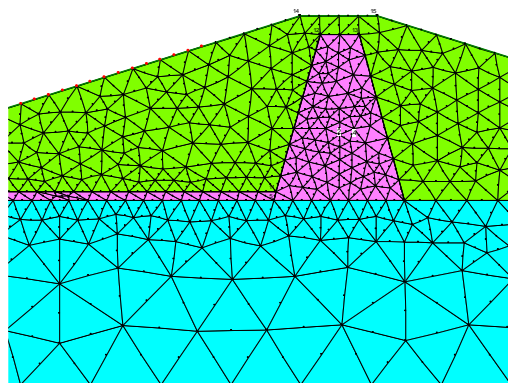


Figure 1. The finite element meshing of numerical model

3. NUMERICAL ANALYSIS RESULTS

For comparison of impervious blanket performance in both intact and defected conditions, the result of seepage analysis, including the phreatic line, equipotential lines and the flow directions are presented in Figure 2. The defected zone with width of $w=2$ m is located in three different locations of 1) next to clay core connection point ($X=0$), 2) inside the dam body ($X=40$ m) and outside of dam body ($X=60$ m). When weakness of impervious blanket is occurred next to the central clay core, some of water in dam body is flowed throughout the weakness area. In this condition, the weakness in upstream blanket impacts the water tightening performance of clay core. As seen, the whole of water energy drop is not dissipated in clay core and some of potential drop lines of water are established in dam shell and water flow vectors are concentrated toward weakness zone. Thus, the phreatic line in dam shell is not horizontal in equilibrium with reservoir and has a slight slope indicating drop of water energy and flowing in dam shell.

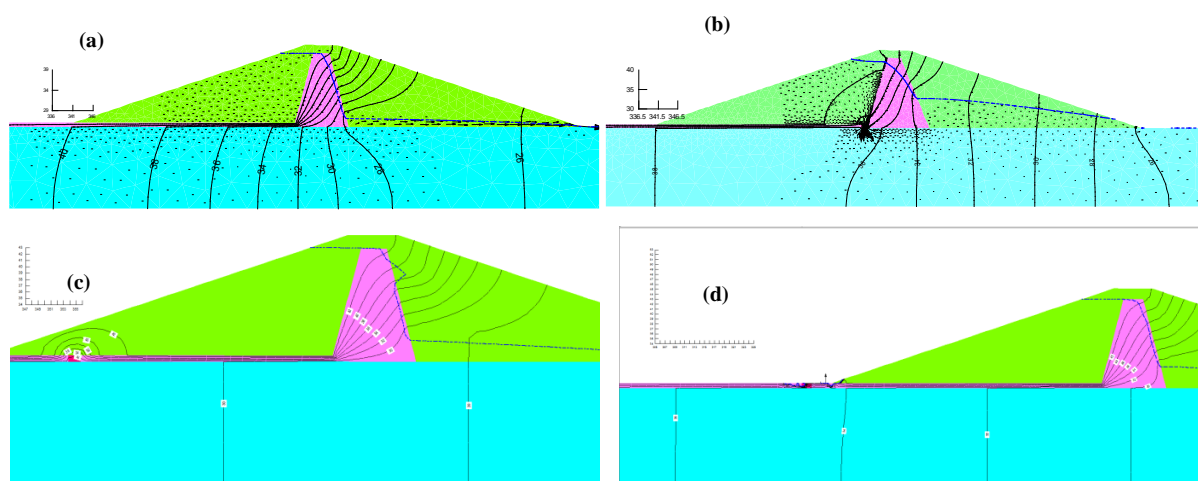


Figure 2. The flow pattern from seepage analysis of dam with height of 20m and foundation permeability of $K=10^{-4}$ m/s: a) intact impervious blanket, b) defected zone next to clay core connection point ($X=0$), c) defected zone inside the dam body ($X=40$ m), d) defected zone outside of dam body ($X=60$ m)

By increasing the distance of defected zone from clay core, the distribution intensity in water tightening performance of clay core is reduced and water is directly entered from dam shell to the foundation throughout the defected zone without any distribution in potential headlines in clay core. However, for a cases that defected zone is located inside the dam body, the drop of water head is found in dam shell and around the weakness zone which causes to establish a gradient force in an area around the weakness zone. This extra gradient may lead to erode the fine grained soil of blanket and will be discussed in later section.

By further increasing in distance of the weakness area in such a way that weakness zone is located outside of dam body (Figure 2-d), the effect of impervious blanket defect on the hydraulic performance of dam body is minimized and only the water is flowed toward the foundation. However, because of far distance of weakness zone, the resultant gradient of water flow in foundation is consequently low and the pattern of water potential head line drop in foundation is similar with the latter locations of weakness zone.

4. SENSITIVITY ANALYSIS

In this section, some sensitivity analyses are conducted to investigate the effect of defected zone in various conditions and determine which situation is the critical for defected zone of impervious blanket. Thus, in each sensitivity analysis, the specific conditions are supposed for dam body and foundation and then, seepage discharge through foundation is determined for various locations of defected zone along the impervious blanket. Then, the foundation seepage ratio parameter is defined as the ratio of the foundation seepage flux in defected condition to the intact condition of impervious blanket. By analyzing the graph of foundation seepage ratio versus defected zone distance from clay core connection point (X), the critical location of weakness zone in each sensitivity analysis is determined.

4.1. EFFECT OF DAM HEIGHT

The graph of foundation seepage ratio versus defected zone position (X) for three dams with heights of 20, 30 and 45 m is presented in Figure 3. In this sensitivity analysis, it is supposed that defected zone in upstream blanket is occurred with the width of 2 m and the foundation permeability is 1^{-4} m/s. Regarding to the results, imposing weakness and establishing defected zone in water tightening system causes to increase the flux through dam foundation in the order of 2.3 times greater than the regular condition. For all types of dams, the critical position of defected zone is occurred in situation of $X=0$ (adjacent to the connection point between clay core and upstream blanket) and by increasing the distance of defected zone from clay core, the effect of weakness in general performance of water barrier system is decreased. For extreme position of defected zone, the foundation seepage ratio approaches to 1 indicating that existing or not existing weakness zone in far way distance does not significantly influence the performance of impervious blanket.

The effect of the dam height on the defected zone performance can be investigated from two distinguished aspects. For situations that the defected zone is located inside the dam body, the traveling path of water from upstream slope face to the defected zone inside the dam body is somewhat short in dam with small height in comparison to the dam with greater height. Thus, because of comparatively greater gradient, more water escapes throughout the defected zone in smaller dam and therefore, for near distance of defected zone position, the foundation seepage ratio is maximum in dam with $H=20$ m. In contrast, when the defected zone is occurred outside of dam body, water is directly entered from reservoir into the foundation throughout the defected zone. For this condition, increasing the dam height directly increase the seepage flux through the defected zone and hence, for far distance of defected zone, the greatest values of foundation seepage ratio is occurred in highest dam (i.e. $H=45$ m).

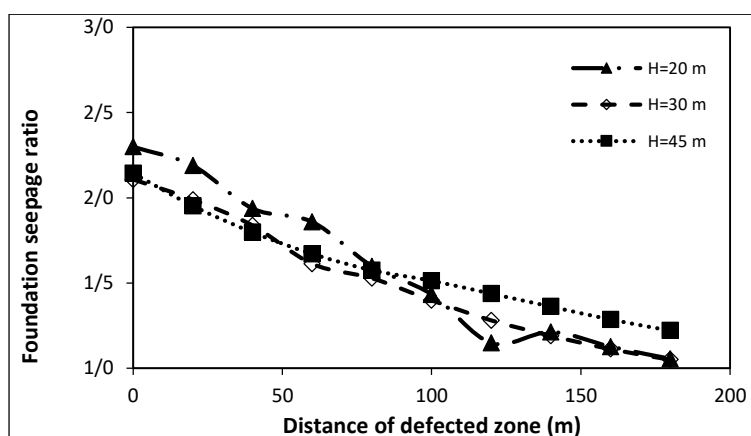


Figure 3. The graph of foundation seepage ratio versus defected zone location (X) in dams with different height (H) and foundation permeability of 1^{-6} m/s

4.2. EFFECT OF DEFECTED ZONE WIDTH

The variation of foundations seepage ratio versus defect location is determined by considering three different opening widths of 2, 4 and 10 m for defected zone and the graph is sketched in Figure 4 for dam with foundation permeability of 10^{-6} m/s and height of 20 m. Also, the foundations seepage ratio graph for dam with similar condition but different foundation with higher permeability is shown in Figure 5. As seen, when the foundation is low permeable, the dimension of weakness in water barrier system has no significant effect in enhancing the foundation seepage discharge and all three graphs of different weakness zone width are coincident. In other words, if foundation has lower permeability, the growing the defected zone may not be main concern and increasing the weakness dimension has no prominent role on enhancing the water escaping through defected zone. However, when the foundation has higher permeability and stopping the foundation seepage is directly depended on the water barrier system performance, growing the weakness dimension straightly increases the water escape throughout the defected zone and at particular location far from dam body, increasing the defected zone width significantly causes to increase the foundation seepage ratio. It should be noted that in higher permeable foundation, when the defected zone of upstream blanket is established in close distances and inside the dam body, the defected zone width has less influence on the foundation seepage ratio and all three graph are coincident for close locations of defected zone.

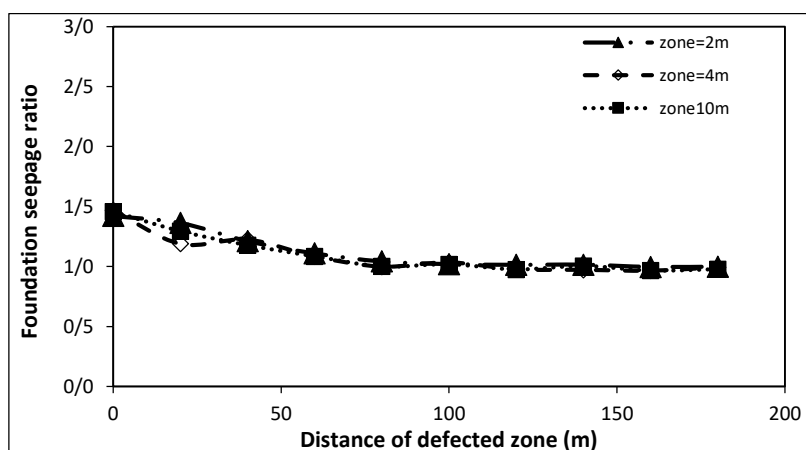


Figure 4. The graph of foundation seepage ratio versus defected zone location (X); the dam has height (H) of 20 m and foundation with permeability of 10^{-2} m/s and different width of defected zone in upstream blanket

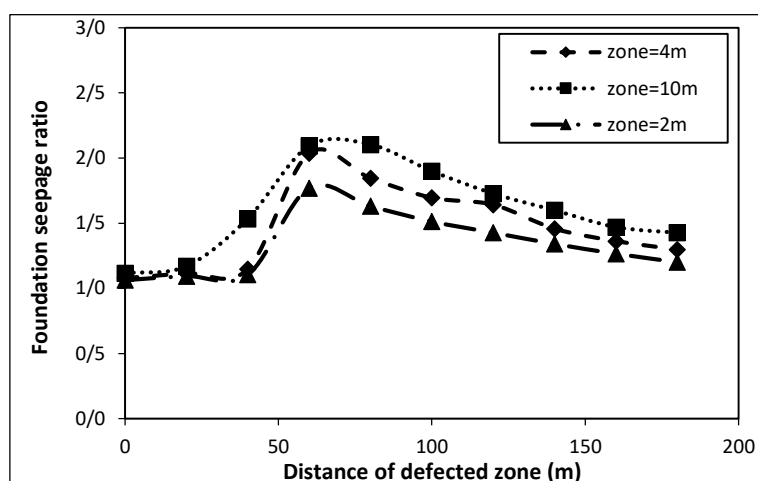


Figure 5. The graph of foundation seepage ratio versus defected zone location (X); the dam has height (H) of 20 m and foundation with permeability of 10^{-2} m/s and different width of defected zone in upstream blanket

5. CRITICAL GRADIENT IN DEFECTED BLANKET

In order to assess the erosion potential due to gradient forces, the maximum hydraulic gradient within defected zone is determined from numerical analysis and compared for different conditions. In dam with height of 20 m, the defected zone is situated in four locations of L1 to L4 (Figure 6). Then, for each situation of defected zone, the maximum hydraulic gradient within both defected zone and foundation beneath the defect is determined and presented in Table 2 and 3, respectively.

From view aspect of erosion, the critical condition is occurred in foundation with highest permeability where the great gradient is established within the defect zone. As compared the gradient in various locations of defected zone in dam with the foundation permeability of $K=10^{-2}$ m/s, it is recognized that by increasing the distance of defected zone from dam core, gradient is increased within the defected zone and when the defected zone is located outside the dam body (i.e. case of No. 4), the resultant gradient exceed unity and reaches the value of 5.6. In other hand, for other situations of defected zone inside the dam body, the gradient is lower than the unity. This consequent confirms with the trend of foundation seepage ratio graph for most permeable foundation. As mentioned in earlier sections, when foundation has the greatest permeability, the maximum value of foundation seepage ratio parameter is occurred for defected zone location that established out of dam body. The gradient in foundation beneath the defected zone for case of foundation permeability of $K=10^{-2}$ m/s is almost close and falls in narrow range between 0.28 and 0.38. The higher gradient within the weakness zone in No. 4 location is consequent of relative difference in permeability between the foundation and defected zone. When the

foundation is more permeable than the weakness zone of impervious blanket, more water energy head drop should be happened in defected zone to satisfy the continuity flow law of water discharge from defected zone into foundation. Thus, the higher drop of water head along a short path (equal to blanket thickness) causes to generate a higher magnitude gradient in defected zone in case of permeable foundation. The extra gradient of 5.6 for the defected zone location of No. 4 may lead to more erosion in defected zone which cause to develop the weakness zone and the weakness area is further enhanced. Also, as though earlier, enlarging the defected zone width in case of permeable foundation directly causes to increase the discharge and will be act as accelerate factor of defect. In contrast to the higher permeable foundation, if foundation has the lowest permeability (i.e. $K=10^{-6}$ m/s), insignificant gradient force is generated within the defected zone and, in turn, the extra gradient is developed in foundation beneath the defected zone. In this case, the critical condition occurs in defected zone location of No. 1 where the impervious blanket is connected to the clay core. For this location, the gradient of 2.8 is recorded in foundation. Furthermore, for defected zone located in mid width of dam body (i.e. location of No. 2), the gradient of 1.14 is recorded. For other locations, the gradient is relatively high, but less than unity. Generally, by increasing the distance of defected zone from dam core, the gradient in foundation is decreased. Existing extra gradient further than unity in foundation comprised of fine grained and low permeability soils implies that besides the weakness zone of impervious blanket, the foundation beneath the weakness zone is susceptible to erosion due to high gradient force and defect can be transmitted to foundation layer. The erosion in foundation may lead to extra local settlement beneath the impervious blanket and intensify the weakness zone in blanket.

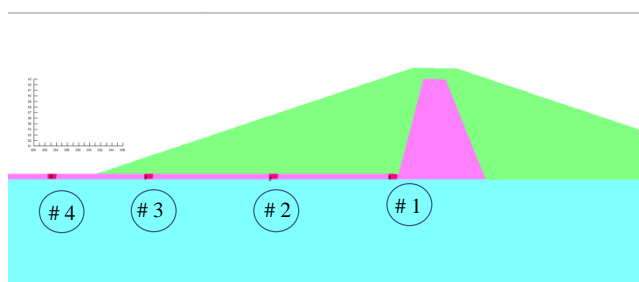


Figure 6. The location of defected zone that hydraulic gradient is measured

Table 2- The maximum hydraulic gradient within defected zone

Location No.	Distance from clay core (X) m	$K_{\text{foundation}}=10^{-2}$ m/s	$K_{\text{foundation}}=10^{-4}$ m/s	$K_{\text{foundation}}=10^{-6}$ m/s
1	0	0.4500	0.1500	0.0030
2	40	0.5000	0.1000	0.0015
3	60	0.5600	0.0900	0.0010
4	80	5.600	0.1000	0.0007

Table 3- The maximum hydraulic gradient in foundation beneath the defected zone

Location No.	Distance from clay core (X) m	$K_{\text{foundation}}=10^{-2}$ m/s	$K_{\text{foundation}}=10^{-4}$ m/s	$K_{\text{foundation}}=10^{-6}$ m/s
1	0	0.36	1.16	2.80
2	40	0.34	0.74	1.14
3	60	0.38	0.55	0.59
4	80	0.28	0.54	0.39

6. CONCLUSIONS

In this paper, the seepage through defected zone occurred in upstream water tightening blanket system is investigated. The following consequents from numerical analyses can be summarized:

- The location defected zone in upstream impervious blanket directly influences the seepage pattern through dam body and foundation. If the defected zone is occurred in the situations close to the dam core, escaping water from weakness zone of impervious blanket impact the clay core water tightening performance and water potential head drop is not completely occurred in clay core.
- If the permeability of foundation is high, the magnitude of water seepage discharge in foundation that entered through defected zone tended to increase by growing the defect zone area. In contrast, in dam

underlying on the foundation with lower permeability, the width of defected zone area has no effect on the enhancing the discharge through foundation.

- From the erosion potential view, the critical condition is the case that the defected zone in upstream blanket is occurred out of dam body and the foundation has the higher permeability. In this condition, the gradient of 5.6 is recorded in defected zone. For this type of dam, the gradient in foundation is insignificant.
- If the foundation has lower permeability and defected zone is occurred in impervious blanket next to clay core connection point, the foundation beneath the defected zone is susceptible to erosion due to significant extra gradient in this point that exceeds unity. By moving defected zone location far away the dam core, the hydraulic gradient in foundation tend to decrease and fall less than one.

7. REFERENCES

1. ICOLD, (2005), Bulletin No 129, “*Dam Foundations: Geologic Considerations, Investigation Methods, Treatment, Monitoring*”, International Commission on Large,
2. U.S. Army Corps of Engineers. (1993), “*SEEPAGE ANALYSIS AND CONTROL FOR DAMS*”, Engineer Manual EM 1110-2-1901, Washington, USA
3. Bennett, P.T., (1946), “*The effect of blanket on seepage through pervious foundation*”, Trans. ASCE, 3: 52-61.
4. Rezk, M.A.E.R.M. and Senoon, A.A.A., (2012), “*Analytical solution of earth dam with upstream blanket.*”, Alexandria Engineering Journal, **51** (1), pp.45-51.
5. Rezk, M. A. E. M., and Rabiea I. Nasr, (1991) “*Seepage from earth embankment with upstream blanket to a vertical crack extending to the impervious layer*”, Alex. Eng. Journal, Alex. Univ, **30** (4), C225-C231.
6. Yoshitake, Y., Kobayashi, N., Fujihara, M. and Nishiyama, T., (2011), “*An analytical solution of seepage discharge from a reservoir of embankment dam with triangular soil blanket and its applicability*”, Transactions of The Japanese Society of Irrigation, Drainage and Rural Engineering, **79** (2), pp.109-115.
7. Talouki, H. H., Lashkaripour, G. R., Ghafoori, M. and Saba, A. (2015),” *Assessment and presentation of a treatment method to seepage problems of the alluvial foundation of Ghordanloo dam, NE Iran*”, Journal of the Geological Society of India, **85** (3), pp 377-384
8. Foster, M., Fell, R. and Spannagle, M. (2000), “*The statistics of embankment dam failures and accidents.*” Canadian Geotechnical Journal, **37** (5), pp 1000–1024.
9. Rice, J. and Duncan, J. (2010), “*Findings of Case Histories on the Long-Term Performance of Seepage Barriers in Dams*”, Journal of Geotechnical and Geoenvironmental Engineering, **136** (1), pp 2-15.
10. GEOSLOPE International, (2004), “*GeoStudio software*”, <http://www.geo-slope.com/>

Field Seepage Tests on Discontinuity Structural Rocks in a Hydropower Project

Sihong Liu¹, Bin Zhou¹, Liping Weng², Meiqi Jiang³, Hanwen Xiong⁴

1-College of Water Conservancy & Hydropower Engineering, Hohai University, Nanjing 210098, China

2- Business school of Hohai University, Nanjing 210098, China

3-Zhejiang Hua Dong Construction Engineering Co., LTD, Hangzhou 310000, China

4-Water Resources Pearl River Planning Surveying & Designing Co., LTD, Guangzhou 510000, China

Email: sihongliu@hhu.edu.cn

Abstract

The permeability characteristics of the structural planes inside rock masses are of importance for the stability of hydropower station projects. In this paper, a large-scale in-situ seepage testing method was proposed and applied to the tests on the gently dipping structural plane (C2 zone) and the steep fault (F14) in the construction field of one hydropower station in China. The in-situ test results were compared with those of both the undisturbed and the reconstituted specimens. The test results indicate that the proposed in-situ testing method can be effectively used to determine the permeability characteristics of structural planes under the natural stresses with a relatively high accuracy. The critical hydraulic gradient of the structural planes is influenced by the natural stress of the surrounding rock mass, which cannot be reflected in the tests on the undisturbed and the reconstituted specimens.

Keywords: In-situ seepage test, permeability characteristic, rock discontinuity structural plane.

1. INTRODUCTION

The Baihetan project, located on Jinsha River and with a total installed capacity of 1,600 megawatts, is the second largest hydropower station currently under construction in China. A concrete double-curvature arch dam with a height of 289 m will be built. The Emeishan basalt rocks, in which many rock discontinuities such as the bedding fault zones, small faults and fractures, spread over the dam site, as shown in Fig.1. According to their inclinations, the rock discontinuities can be roughly classified into the gentle-dip bedding fault zones and the steep faults.

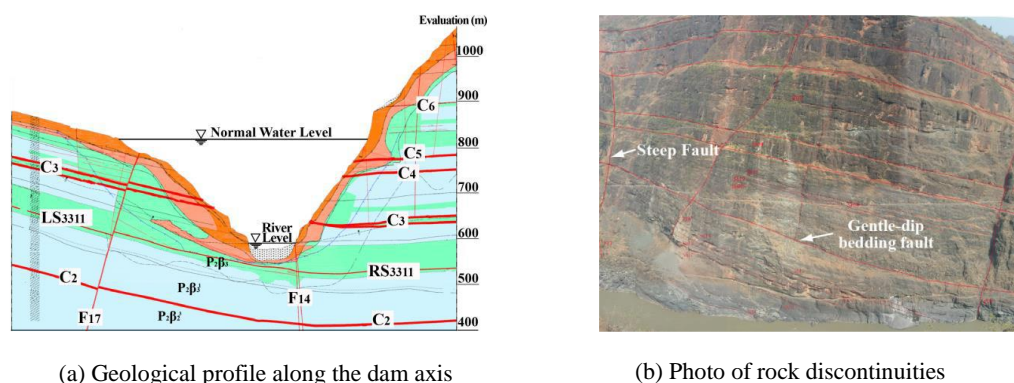


Fig.1 Rock discontinuities at the dam site of Baihetan project

Before the construction, most of the rock discontinuities are well above the groundwater or river level. After the completion of the project and the impounding of the reservoir, the water pressure within the rock discontinuities will significantly increase, resulting in the following two adverse effects on the project. One is the leakage of the reservoir water through the rock discontinuities; the other is the possibility of seepage deformation failures of the rock discontinuities and the subsequent failure of the dam foundation as well as the abutments. Therefore, the hydraulic properties of the rock discontinuities are crucial to the safety of the Baihetan project.

At present, the hydraulic properties of rock discontinuities are mainly determined through laboratory or field seepage tests and borehole water pressure tests. For laboratory tests, the sampling in the field will inevitably

disturb the rock discontinuities and the reliability of the test results depends on the specimen size and the sampling location. The small specimen will not be representative, and the large specimen will be difficult to be handed [1][2]; Borehole water pressure tests [3] are usually conducted in the boreholes with a depth of at least 5m and the test results reflect the average permeability of the fractured rock mass in a relatively wide range; The field seepage tests, usually conducted in adits, are probably the best approaches for investigating the hydraulic properties of rock discontinuities [4][5]. There are some reports on field seepage tests [6][7].

In this paper, we introduce a new in-situ seepage testing method for rock discontinuities, in which the stress environment of the specimen is closer to the natural situation and the specimen is more representative of rock discontinuities. The application examples in Baihetan dam site are presented.

2. PRINCIPLE OF IN-SITU SEEPAGE TEST

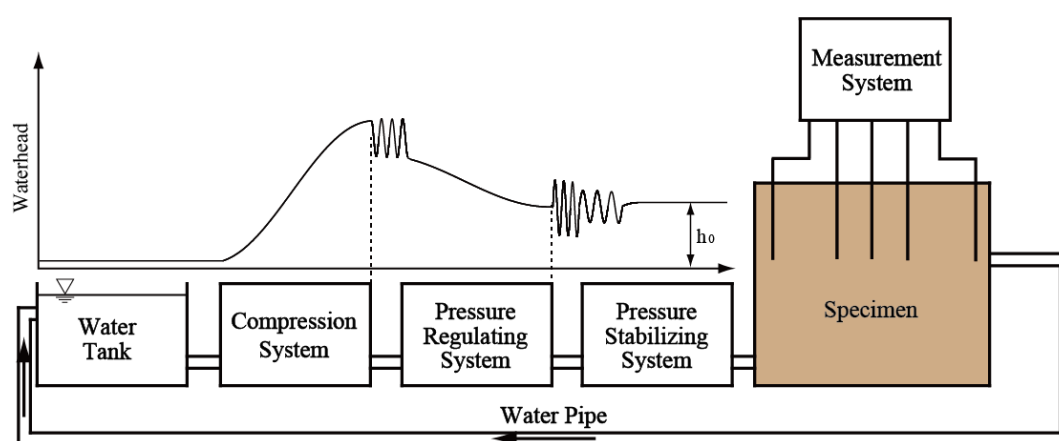


Fig.2 Principle of the in-situ seepage test

Fig.2 shows the principle of the new in-situ seepage tests on rock discontinuities. It consists of the water supply, the compression, the pressure regulating, the pressure stabilizing and the measurement systems. Through the compression system, the head of the water from a tank is raised to the rated maximum value of the centrifugal pump used in the test. Then, by means of the pressure regulating and the pressure stabilizing systems, the water head is regulated to a preset value h_0 at the inlet of the specimen. When the pressurized water flows through the specimen, the water temperature is recorded and the change of the water pressure within the specimen are measured with five piezometric tubes. The water flowing out of the specimen goes back to the tank through a pipe, achieving the cyclic utilization of the water. The inlet water pressure is gradually increased and applied onto the specimen through the pressure regulating and the pressure stabilizing systems. At one inlet water pressure, the measurement continues until the outlet flow per unit time reaches a stable value.

Figs.3 and 4 show the schematic views on gentle-dip bedding fault zones and steep faults, respectively. The tests are carried out in adits. Since the protolith surrounded the rock discontinuities is the compact and slightly weathered or fresh tuff in this project, it is considered to be nearly impermeable. For the gentle-dip bedding fault zones, the upper and lower parts of the specimen are the protolith and the two lateral sides (the inlet and the outlet) of the specimen are surrounded by the reinforced concretes (about 50cm thick). To prevent the contact leakage between the reinforced concretes and the specimen, a layer of plastic clay (about 5cm thick) is placed on the two side surfaces of the specimen before casting the reinforced concrete. For the deep faults, the two lateral sides of the specimen are the protolith and upper and lower parts of the specimen are isolated with reinforced concretes. The inlet and outlet of the specimen are sealed with reinforced concretes. Between the reinforced concretes and the specimen, the 30cm thick filter of sandy pebbles (the maximum grain size $d_{max}=2cm$) is placed to prevent the damage of the specimen by the pressurized water.

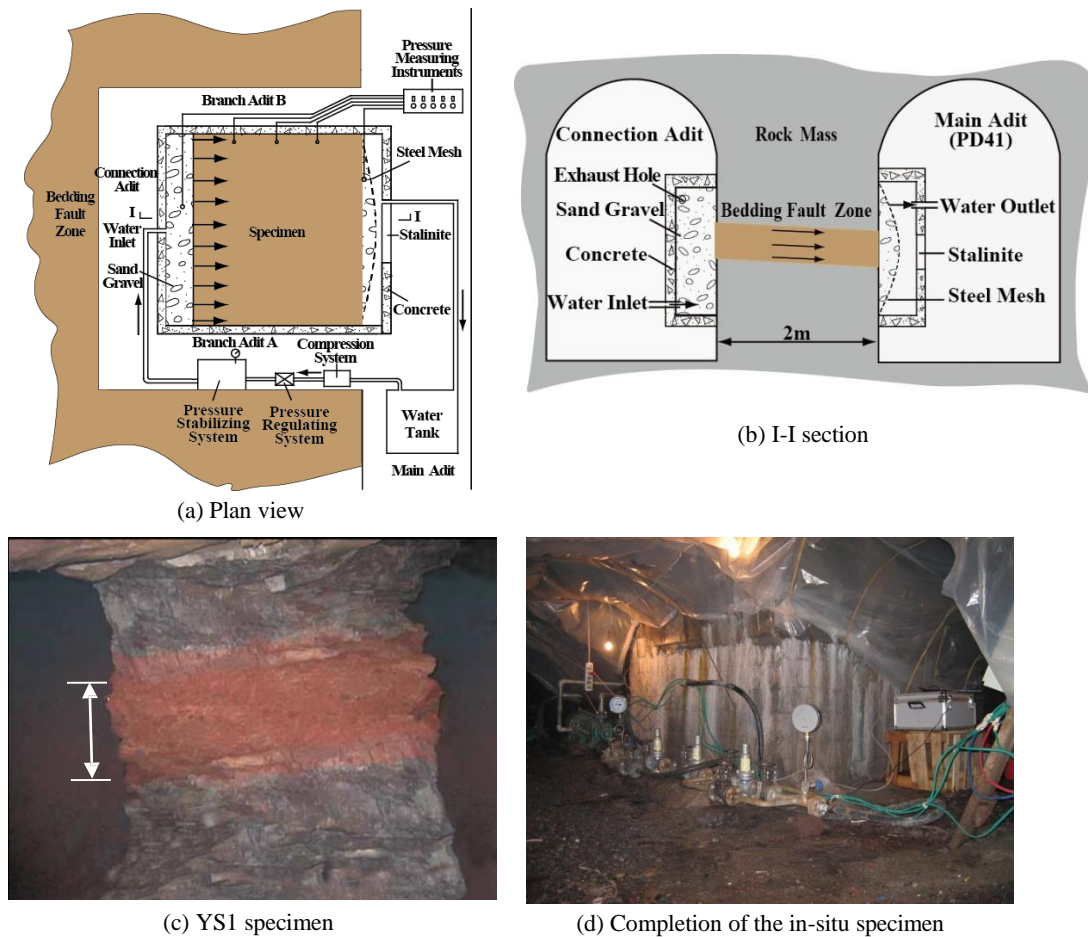


Fig.3 Schematic of in-situ seepage test on gentle-dip bedding fault zones

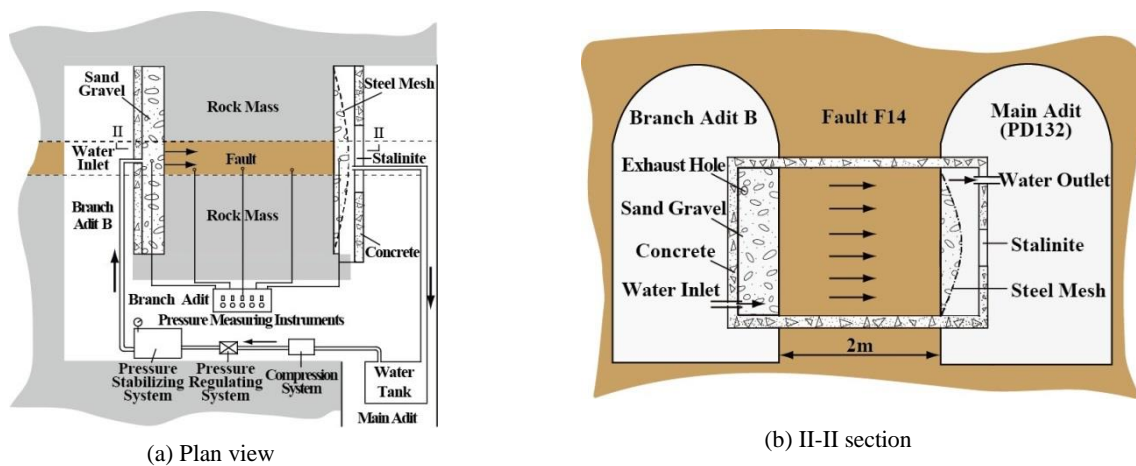


Fig.4 Schematic of in-situ seepage test on steep faults

3. APPLICATION EXAMPLES

Two application examples of the in-situ seepage tests on the gentle-dip bedding fault zone (C₃) and on the steep fault (F₁₄) in Baihetan dam site, respectively, are presented. The test procedures mainly include the specimen preparation, the specimen saturation, the seepage pressure application and the data acquisition. They are almost the same for the two application examples except the specimen preparation as illustrated in Figs.3 and 4.

The bedding fault zone (C₃) is palm red and has an average thickness of about 26 cm. It is the fractured tuff zone and filled with gravels, debris and some mud, with a natural void ratio ranging from 0.25 to 0.39. The filling materials within the bedding fault zone (C₃) has a good gradation with the characteristics of $d_{max}=60\text{mm}$, $d_{50}=0.1\text{mm}$ and $C_u=60$. The in-situ specimen of the gentle-dip bedding fault zone (C₃), denoted as YS1, has a seepage length of 200cm and a seepage section of 200cm×26cm, as shown in Fig.3.

The steep fault (F₁₄) is basically a fractured rock with breccia and gravels contained in its voids, and has an average width of 43cm. It is in a relatively dense state with a natural void ratio of about 0.15. The grains contained in F₁₄ are relatively uniform with a coefficient uniformity $C_u=4$. Their grain sizes mainly range from 4mm to 30mm and the fine grains ($d<0.1\text{mm}$) contained in F₁₄ are less than 5%. The prepared specimen of the steep fault (F₁₄), denoted as YS2, has a seepage length of 200cm and a seepage section area of 200cm high by average 45cm wide.

During the test, the seepage flux and the water heads at five piezometric tubes as well as the water temperature at the outlet chamber were measured every half an hour. Meanwhile, all phenomena, such as the turbidity and the bubbling within the seepage flow, and the suspension of the entrained fine particles in the outlet chamber, etc., were closely observed and timely recorded. The hydraulic gradient i and the seepage velocity v of the specimen at each staged pressure were calculated from the measurements of the water heads and the seepage flux. The hydraulic conductivity of the specimen at the test temperature was obtained from the Darcy's law and then converted to the equivalent one at a temperature of 20°C (denoted as k_{20}), expressed as:

$$k_T = \frac{v}{i}, \quad k_{20} = k_T \frac{\eta_T}{\eta_{20}} \tag{1}$$

where η_T and η_{20} are the coefficients of water dynamic viscosity at the test temperature T°C and 20°C, respectively.

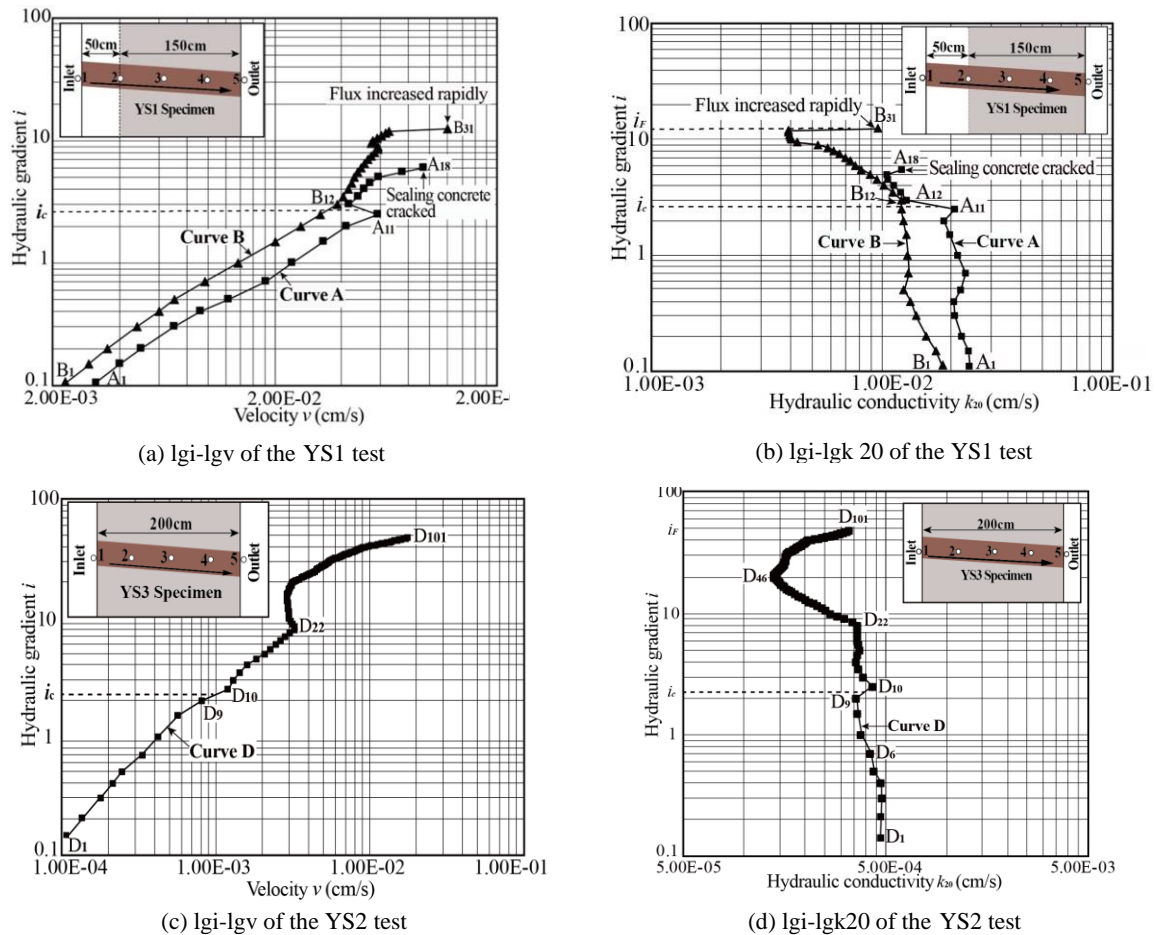


Fig.5 Results of the YS1 and YS2 tests

Fig.5 gives the results of the two tests with respect to the change of hydraulic gradient with the seepage velocity and the hydraulic conductivity in double logarithmic coordinates. The YS1 test was repeated twice because some cracks took place in the sealing concretes surrounding the specimen during the test. In YS1 test, very small hydraulic gradients had been measured between the piezometric tubes 1 and 2, indicating that the fractures may be well developed and the seepage channel is interconnected near the inlet chamber. Therefore, the hydraulic gradients in Figs.5(a) and (b) were obtained from the measurement of the piezometric tubes 2 and 5 as well as the corresponding seepage length. In Figs.5(a) and (b), the curves A and B represent the twice results of the YS1 test before and after the reinforcement of the sealing concrete of the specimen, respectively. Along the curve A in Fig.5(a), the hydraulic gradient i increases almost linearly with the seepage velocity v from points A₁ to A₁₁. At point A₁₁, the hydraulic gradient i is 2.5. When the hydraulic gradient i increases from 2.5 to 3.0 (point A₁₁ to point A₁₂), the seepage velocity v decrease slightly, indicating that the possible change of the internal structure of the specimen happens and some fine particles start to move along the seepage direction. The average value of the hydraulic gradients at points A₁₁ and A₁₂ could be regarded as the critical hydraulic gradient i_c , which is equal to 2.75. After the point A₁₂, the hydraulic gradient i increases further with the seepage velocity v until it reaches 6.0 at point A₁₈, where the cracking of the sealing concrete of the specimen happened and the test had to be stopped. From Fig.5(b), it can be seen that the hydraulic conductivity of the YS1 specimen changes slightly (ranging from 0.018 cm/s to 0.023 cm/s) before the point A₁₁. After the point A₁₁, the hydraulic conductivity decreases due to the increase of the fine particles along the seepage path. At the point A₁₈, the hydraulic conductivity increases suddenly as the cracking of the sealing concrete of the specimen happened.

As shown in Figs.5(a) and (b), the evolution of the curve B is similar to that of the curve A for the YS1 specimen. However, both the seepage velocity and the hydraulic conductivity in the curve B are slightly smaller than those in the curve A under the same hydraulic gradient because the partial seepage channel is blocked by the fine particles in the repeated test. When the hydraulic gradient i reached 12.50 at the point B₃₁, the seepage flow increased rapidly and it was observed that plenty of fine particles flowed out of the specimen in the outlet chamber. Therefore, the average value of the hydraulic gradients at points B₃₀ and B₃₁ was regarded as the failure hydraulic gradient i_F , which is equal to 12.25.

As the internal structure of the specimen may have changed after the critical hydraulic gradient i_c , the hydraulic conductivity of the specimen should be taken the value before i_c is reached. Thus, the hydraulic conductivity of the YS1 specimen should be taken from the curve A in Fig.5(b), which is about 2.13E-02cm/s by averaging the values from points A₁ to A₁₁.

For the YS2 specimen, it can be seen from Fig.5 (c) that the hydraulic gradient i increases almost linearly with the seepage velocity v from points D₁ to D₉. During the YS2 test, it was observed that the water level in the inlet chamber began to fluctuate and the seepage flow increased slightly when the hydraulic gradient reached 2.0 at point D₉. When the hydraulic gradient increased from 2.0 to 8.5 (from points D₉ to D₂₂), some fine particles flowed out of the YS2 specimen and the seepage water became turbid. However, the seepage water gradually changed from turbid to clear, together with the decrease of the seepage flow, from the points D₂₂ to D₄₆, indicating that the fine particles flowing out of the specimen decreased and a new stable state of the internal

Structure was achieved inside the specimen. After then, the further increase in the hydraulic gradient resulted in the movement of the fine particles again. When the hydraulic gradient reached 48.0 at point D₁₀₁, the water level in the inlet chamber varied greatly and plenty of fine particles flowed out of the specimen with a sudden increase of the seepage flow, leading to the seepage failure of the specimen.

As the fine particles began to move at point D₉ with a pronounced change of the slopes of both the $\lg i$ - $\lg v$ and the $\lg i$ - $\lg k_{20}$ curves in Figs.5(c) and (d), the critical hydraulic gradient of the YS2 specimen was taken as the average value 2.25 at the points D₉ and D₁₀. Accordingly, the hydraulic conductivity k_{20} was taken as the average value before the point D₉, i.e. 4.23E-4cm/s. The failure hydraulic gradient of the YS2 specimen was taken as the average values at the points D₁₀₀ and D₁₀₁, which was equal to 47.75.

The hydraulic properties of rock discontinuities are comprehensively influenced by their voids, grain sizes, gradations and so on. Usually, it is considered that the internal structure of the specimen starts to change when the hydraulic gradient reaches its critical one. As the filling materials within YS2 specimen are relatively uniform with a coefficient uniformity $C_u=4$ and the content of fine particles ($d<0.1\text{mm}$) is less than 5%, the skeleton pores formed by coarse particles cannot be fully filled with fine particles. Consequently, fine particles are more likely to migrate in the skeleton pores under seepage pressures, leading to a lower critical hydraulic gradient compared with YS1 specimen. As the natural void ratio of the filling materials in YS1 specimen is larger than that of YS2 specimen, it is easy to understand that the hydraulic conductivity of YS1 specimen is larger than that of YS2 specimen.

By the way, the measured seepage velocities v at point A₁₈ and D₁₀₁ are 0.098cm/s and 0.0177cm/s, respectively. The Reynolds numbers Re of the YS1 and YS3 specimens were calculated to be 86.21 and 15.53,

respectively, on the assumption that the kinematic viscosity of water equals to m^2/s , illustrating that the seepage flow both in YS1 and YS3 specimens is laminar flow and the Darcy's law holds. $1.31E-06$

4. CONCLUSIONS

In this study, an in-situ seepage testing method for large-scale rock discontinuities was introduced. It consists of the water supply, the compression, the pressure regulating, the pressure stabilizing and the measurement systems. In this testing method, the stress environment of the in-situ specimen is closer to the natural situation and the large-scaled specimen is more representative of rock discontinuities.

This new in-situ seepage testing method was firstly applied in Baihetan dam site. The determination of the in-situ specimen dimensions to be representative of rock discontinuities should be further studied. Also, the testing procedures and devices for this new method should be standardized.

5. ACKNOWLEDGEMENTS

The authors gratefully thank the anonymous reviewers for their kind efforts and valuable comments in improving this study. Special thanks are extended to Xu Jianrong, Tang Mingfa, Wang Xuyun, and Xu Gaofeng of Power China Huadong Engineering Corporation for their valuable discussion and great supports.

6. REFERENCES

1. Nastev, M., Savard, M.M., Lapcevic, P. (2004). "Hydraulic properties and scale effects investigation in regional rock aquifers, southwestern Quebec, Canada." *Hydrogeology J.*, Vol.12, pp.257-269.
2. Zhang, W., Chen, J.P., Liu, C., Huang, R., Li, M., Zhang, Y. (2012). "Determination of geometrical and structural representative volume elements at the Baihetan dam site." *Rock Mech. Rock Eng.*, 45(3), pp.409-419.
3. Hsieh, P.A., Neuman, S.P. (1985). "Field determination of the three-dimensional hydraulic conductivity tensor of anisotropic media." *Water Resource Research*, Vol.21, pp.1655-1665.
4. Cosenza, P., Ghoreychi, M., Bazargan-Sabet, B., De Marsily, G. (1999). "In-situ rock salt permeability measurement for long term safety assessment of storage." *Int. J. Rock Mech Min Sci.*, 36(4), pp.509-526.
5. Cook, P. (2000). "In-situ pneumatic testing at Yucca Mountain." *Int. J. Rock Mech Min Sci.*, 37, pp.357-367.
6. Zhou, Z.F., Yang, J., Yang, H. (1999). "A field test method for determining permeability parameters of gently dipping structural face in rock mass." *Journal of Engineering Geology* 7, pp.375-379.
7. Feng, S.R., Zhao, H.B., Jiang, Z.M. (2012). "Experimental study on seepage failure characteristics of broken rock mass in dam foundation at left bank of Xiangjiaba Hydropower Project." *Chinese Journal of Geotechnical Engineering*, 34, pp.600-605.

The Seepage Behavior of a High Concrete Face Rockfill Dam on Alluvium Deposit

Weijun Cen¹, Dengjun Li¹, Erich Bauer²

1- College of Water Conservancy & Hydropower Engineering, Hohai University, Nanjing, China

2- Institute of Applied Mechanics, Graz University of Technology, Graz, Austria

Email: hhucwj@163.com

Abstract

The nodal virtual flux method with a fixed finite element mesh is employed to investigate the non-confined seepage field of a high concrete face rockfill dam on an alluvium deposit layer after water impounding. Particular attention is also paid to the change of the seepage behavior caused by a local defect of the anti-seepage system located at the upstream side of the dam. The anti-seepage system considered consists of concrete face slabs, toe slabs connected with the grouting curtain in the dam foundation, and the seal system of the joints between the concrete slabs. For the intact anti-seepage system, the numerical results indicate that the seepage field is mainly concentrated in the dam foundation, and the location of the phreatic surface in the dam body is very low under normal conditions. Once a crack in the slab or a local failure of the concrete joint seal occurs the seepage behavior of the dam changes significantly. The concrete face slabs, joint seal and the sufficient depth of the grouting curtain are the significant anti-seepage barriers to control the seepage behavior of the dam, and particular attention should thus be paid to these elements for the design and construction of concrete face rockfill dams.

Keywords: CFRD, Alluvium Deposit, Seepage Behavior, Anti-Seepage System.

1. INTRODUCTION

The development of enhanced concepts for the construction of concrete face rockfill dams (CFRDs) started after the completion of Cethana CFRD in the 1960s. In China the application of modern construction concepts for CFRDs began relatively late, but over the past few decades, development has been very fast. Starting from one of China's first CFRD with a height of 95 m (begun in 1985 and completed in 1990 at Xibeikou) to the Shuibuya CFRD with a height of 233 m (completed in 2008), the number and height of Chinese CFRDs have made significant progress and has become one of the most competitive dam types in dam design, e.g. [1]. So far, there are approximately 40 CFRDs with heights of over 100 m. In the near future the height of CFRDs to be constructed such as the one in Rumei and Gushui will reach or exceed a height of 300 m. The safety of CFRDs can be strongly influenced by defects of the anti-seepage measures, which can lead to local erosion, collapse settlement and large creep deformation [2, 3]. In this context particular attention should already be paid in the design phase to the investigation of seepage fields under different scenarios. In the anti-seepage measures context, the CFRD is entirely different from the traditional earth-rock dam with a core wall. The anti-seepage system of a CFRD consists of the upstream concrete face slab, toe slab, joint seal and wave wall. As discussed in the present paper for a CFRD on an alluvium deposit, the grouting curtain or cut-off wall connecting with the toe slab is also needed to form a closed seepage control system. In particular, in the present paper a 138 m high CFRD located in Sichuan Province in China is considered for analyzing the seepage field in the CFRD and foundation under different boundary conditions. The investigations mainly focus on factors and scenarios affecting the seepage behavior such as the occurrence of cracks in concrete slabs, the permeability of cushion layers, the design depth of the curtain, and the permeability of the foundation. The location of the phreatic surface is computed using the virtual flux method for a finite element mesh fixed in space. The conclusions that can be drawn from the results of the present analysis may provide a useful reference for the design of CFRDs.

2. BASICS FOR MODELLING THREE-DIMENSIONAL SEEPAGE FIELDS

2.1. GOVERNING EQUATIONS AND BOUNDARY CONDITIONS

With respect to Darcy's law and the continuity condition for fluid flow through an anisotropic porous media, the governing equations of the three-dimensional steady-state seepage can be written as [4, 5]:

$$-\frac{\partial}{\partial x_i} \left(k_{ij} \frac{\partial h}{\partial x_j} \right) + Q = 0 \quad (1)$$

where x_i denotes the i coordinate ($i=1,2,3$); k_{ij} is coefficient tensor of permeability; the hydraulic head $h = x_3 + p/\gamma$ is the sum of the elevation x_3 and the pressure head p/γ ; and Q is the source or sink term.

The corresponding boundary conditions are as follows:

$$h|_{\Gamma_1} = h_1 \quad (2)$$

$$-k_{ij} \frac{\partial h}{\partial x_j} n_i|_{\Gamma_2} = q_n \quad (3)$$

$$-k_{ij} \frac{\partial h}{\partial x_j} n_i|_{\Gamma_3} = 0, h = x_3 \quad (4)$$

$$-k_{ij} \frac{\partial h}{\partial x_j} n_i|_{\Gamma_4} \geq 0, h = x_3 \quad (5)$$

where h_1 is the known hydraulic head; n_i is the exterior normal direction cosine of the seepage boundary surface, ($i=1, 2, 3$); Γ_1 , Γ_2 , Γ_3 and Γ_4 are the Dirichlet boundary, the Neumann boundary, the boundary of the free seepage surface, and the boundary of the seepage exit face, respectively; q_n is the normal flow, in which the sign of outflow is positive.

2.2. THE NODAL VIRTUAL FLUX PROCEDURE FOR A FIXED FINITE ELEMENT MESH

According to the variational principle, Eqs. (1)-(5) are equivalent to the following equations [6, 7]:

$$\prod(h) = \frac{1}{2} \int_{\Omega_1} k_{ij} \frac{\partial h}{\partial x_i} \frac{\partial h}{\partial x_j} d\Omega. \quad (6)$$

$$[K_1]\{h_1\} = \{Q_1\} \quad (7)$$

where $[K_1]$ is the conduction matrix of the seepage in real domain, $\{h_1\}$ is the nodal head array and $\{Q_1\}$ is the equivalent nodal flow array.

For unconfined seepage problems, the free surface of the seepage domain can be computed with help of the nodal virtual flux method. The corresponding iteration formula reads [8]:

$$[K]\{h\} = \{Q\} - \{Q_2\} + \{\Delta Q\} \quad (8)$$

where $[K]$ is the conduction matrix of total computational domain $\Omega = \Omega_1 + \Omega_2$; $\{h\}$ is the nodal head array; $\{Q\}$ is the equivalent nodal flow array. Ω_1 and Ω_2 are the real seepage domain and the virtual domain, respectively. The two domains are divided by the free seepage surface in seepage field Γ_3 . $\{Q_2\}$ is the equivalent nodal flow array in the virtual domain Ω_2 . The array $\{\Delta Q\} = [K_2]\{h\}$ denotes the virtual flux of the nodes of the virtual elements and transitional elements in the virtual seepage domain Ω_2 . The so-called transition elements are located in the virtual domain and crossed by the free water table Γ_3 [9].

2.3. LOCAL SEEPAGE BEHAVIOR IN CRACKS OF THE CONCRETE FACE SLABS AND LEAKING OF THE SEALING JOINTS

The analysis of CFRDs shows, that the concrete face slabs in the central riverbed are compressed, while the slabs near the abutments are pulled in the direction of the dam axial. The slabs on the top and bottom are also pulled, while in the central area the slabs are compressed along the dam slope. Based on the deformation characteristics of the entire structure, horizontal cracks can appear in the central part, and tensile cracks can appear near the abutments [8]. Because the concrete face slabs and toe slabs are connected to each other by joints, it can happen that the sealing will be pulled out in the peripheral joints close to the bottom and joints near the abutments will be opened. Once such defects occur, the seepage behavior changes significantly. In finite element simulations, thin-layer elements can be used to reflect the corresponding seepage behavior of cracks. To generate thin-layer elements a very fine discretization of the mesh is needed. In this context, however, the selection of the element

thickness and equivalent hydraulic conductivity are generally based on experience. In this paper, the plane joint element with zero thickness is used for the simulation of cracks or joints instead of thin-layer element [11, 12]. The local seepage behaviors due to cracks in concrete slabs or leakage of joint sealing can be described by the following relation [13]:

$$v_f = k_f J_f = \frac{g b_f^2}{12 \mu} J_f \quad (9)$$

where v_f , k_f , J_f are the average velocity within the joint, the equivalent hydraulic conductivity and hydraulic gradient respectively, b_f is the width of the cracks or joints, μ is the viscosity coefficient of water, and g is acceleration of gravity. The flow in plane cracks or joints can be written as:

$$-\frac{\partial}{\partial x_i^f} (k_{ij}^f \frac{\partial h}{\partial x_j^f}) = 0 \quad (i, j = 1, 2) \quad (10)$$

where k_{ij}^f is the coefficient tensor of permeability in the joint element; x_i^f is the local coordinate of the joint element.

3. CASE STUDY

3.1. GEOTECHNICAL CONDITIONS AND MATERIAL PARAMETERS

In this study a 138 m high CFRD located in Sichuan Province in China is considered. The dam height is 138 m. The crest width is 10 m and the length of dam axis is 292 m. Both upstream and downstream slope ratios are 1:1.4. The consolidation grouting depth under the toe slab is 10 m and the maximum depth of grouting curtain is 75 m. The typical cross section of the CFRD is shown in Figure 1. According to the geologic conditions and the dam profiles, a 3D finite element mesh is used to analyze the seepage field for the dam on alluvium deposit. The FE model is discretized by 36619 nodes and 34156 solid elements in form of hexahedra, prism or tetrahedral (Figure 2). A part of the mesh of the anti-seepage system is illustrated in Figure 3.

According to the laboratory experiments carried out with the dam materials, the coefficients of permeability of cushion layer (2A), special cushion layer (2B), transitional layer, main and secondary rockfill zones, filter layer, alluvium deposit layer are taken as 2.10×10^{-4} cm/s, 1.00×10^{-4} cm/s, 3.17×10^{-3} cm/s, 3.40×10^{-1} cm/s, 6.62×10^{-1} cm/s, 1.00×10^{-3} cm/s and 7.2×10^{-1} cm/s, respectively. The coefficients of permeability of face slab, toe slab and grouting curtain are taken as 1.00×10^{-7} cm/s and 3.00×10^{-5} cm/s, respectively. The coefficients of permeability of rock foundation above 10 Lu, between 10 Lu and 3 Lu, and less than 3 Lu are 1.00×10^{-3} cm/s, 2×10^{-4} cm/s and 3×10^{-5} cm/s, respectively.

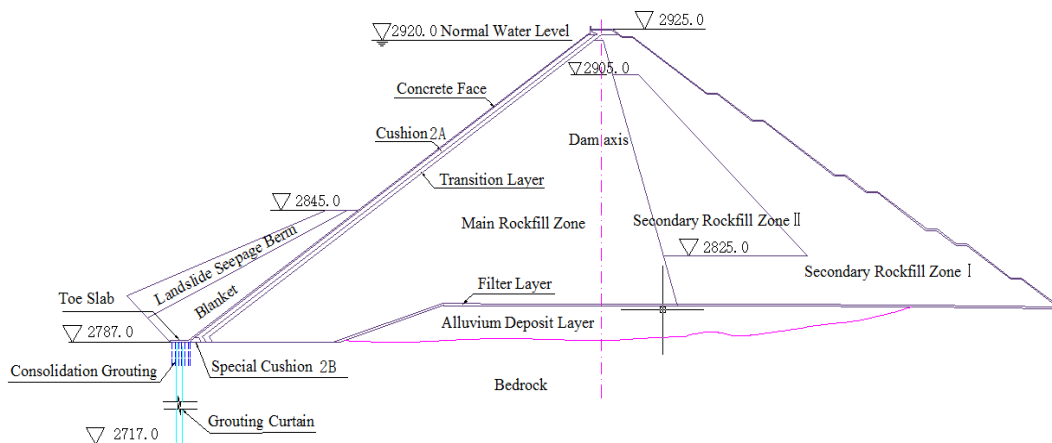


Figure 1. Cross section of the CFRD considered in the present study.

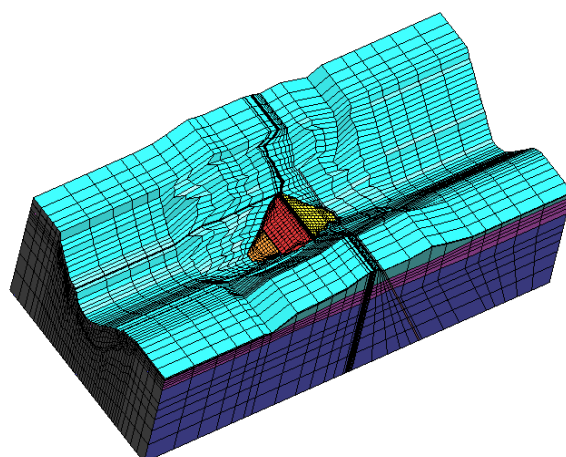


Figure 2. Finite element mesh of dam and foundation.

To investigate the relevance of the seepage control system under different working conditions and for reasonable local failure events numerical simulations were carried out with respect to different upstream and downstream water levels, reasonable cracking events in concrete slabs and local failure of the joint sealing, the depth of the grouting curtain, and the permeability's of the cushion layer and the bedrock.

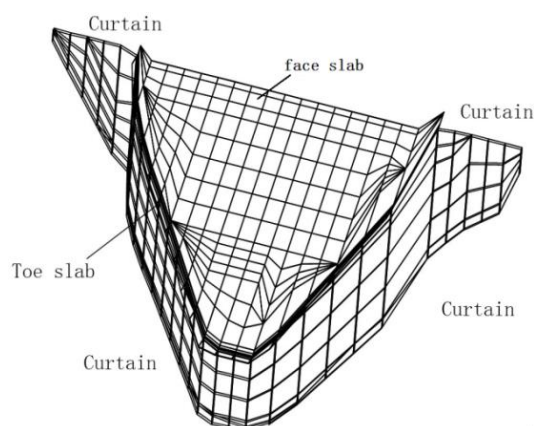


Figure 3. Finite element mesh of the anti-seepage system.

3.2. SIMULATION OF SEEPAGE BEHAVIOR OF THE DAM AND FOUNDATION FOR THE INTACT ANTI-SEEPAGE SYSTEM

In order to investigate whether specific anti-seepage measures are needed, the natural seepage behavior of the dam foundation is first analyzed. Numerical simulations show that for the existing geological condition and a water level of 2920 m in the reservoir, the total seepage flux will increase from 11414.6 m³/day (calculated for the CFRD with intact grouting curtain) to 26968.9 m³/day for the CFRD without grouting curtain. Thus, the flux of the dam foundation is doubled.

The seepage characteristics are significantly different in the left and right abutments. In particular, the seepage flow through the left abutment is about 59% of the total flux. If the coefficients of permeability of the dam foundation and alluvium deposit are assumed to increase by 30%, the flux increases up to approximately 24%. This indicates that the seepage occurs mainly in the dam foundation, thus suitable anti-seepage measures should be taken in the foundation.

For the intact seepage control-system with the grouting curtain the distribution of the total water head of dam and foundation at normal water level of 2920 m is shown in Figure 4. Higher gradients of the isolines can be detected mainly in the dam foundation. The phreatic surface in the dam body is located only a little higher than the downstream water level. The gradient of the isolines in the grouting curtain indicates that the curtain plays a key role in controlling the seepage field in the dam foundation. There are great differences for the leakage flow

through the dam body, the river bed and for the left and right abutments of the mountain which comprise 10%, 5%, 51% and 34% of the total seepage flux, respectively. From these together the total seepage flux through dam foundation and abutments is about 90%. This demonstrates the importance of seepage control measures for CFRDs in dam foundation and abutments despite the fact that the concrete face is in intact condition.

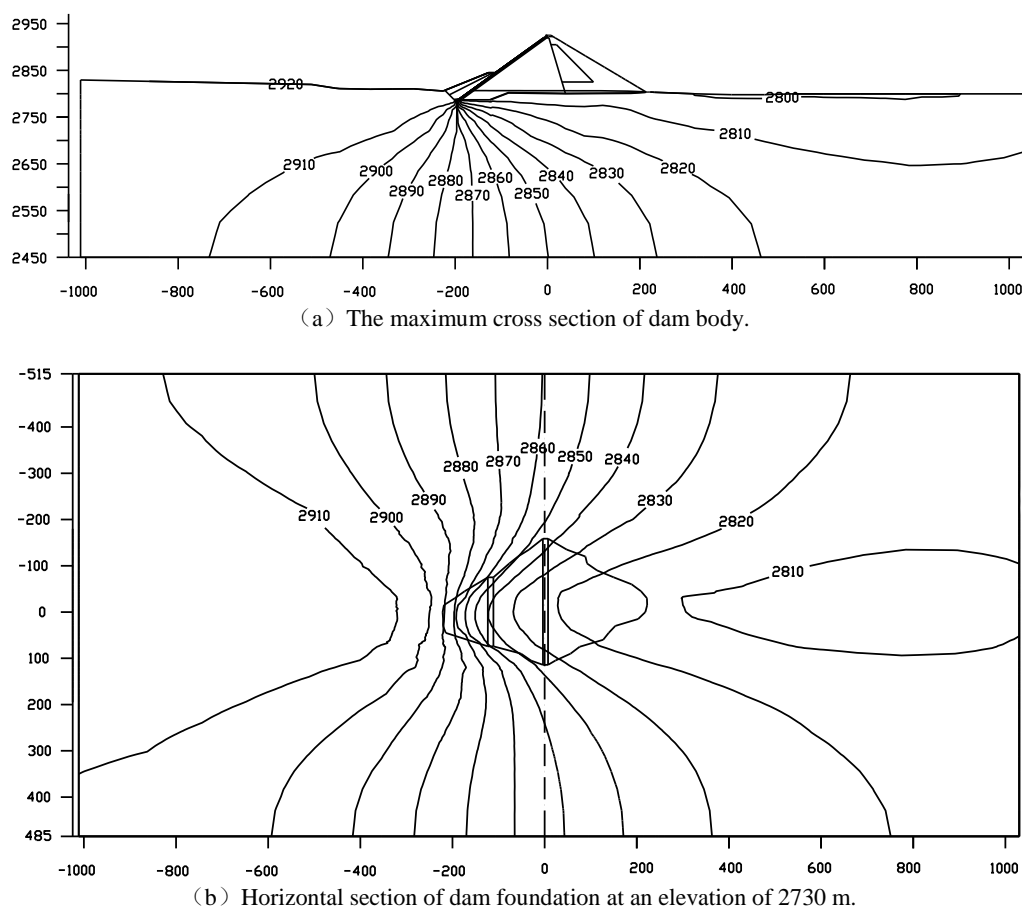


Figure 4. Isolines of the dam and foundation at normal water level of 2920 m in the reservoir (Unit: m)

3.3. SEEPAGE BEHAVIOR WITH LOCAL DEFECTS OF THE ANTI-SEEPAGE SYSTEM

Assume that the concrete face slab in the central riverbed is crushed along the vertical joint, water from the reservoir will flow through the crack into the dam body. As a consequence, the phreatic surface behind the crack will rise significantly. If the crack is assumed to be 1 mm wide and 1 m long the seepage flux will increase from 11414.6 m³/day to 17707.5 m³/day. Assume that the sealing of peripheral joints in the riverbed are in failure with a length of 1 m, the water head distribution of the seepage field changes only slightly and the increase of leakage flux does not exceed 5%. This is due to the low permeability of the special cushion layer. By contrast the cracking of face slabs and defects of the joint sealing above the special cushion has a much greater impact on both water head distribution and leakage flux of the seepage field. It is thus necessary to pay more attention to the seepage control design of these parts of the anti-seepage system. In addition, the sensitivity analysis of seepage flux of the concrete grouting curtain depth under normal design conditions shows that a good impermeable effect can be achieved as long as the curtain stretches between 1m and 2m below the 3Lu line of the rock foundation batholith zone.

3.4. SEEPAGE GRADIENT

The seepage gradients are large in the concrete face slab and concrete grouting curtain, but the values do not reach the permissible value for concrete.

Under normal conditions, the seepage failure will not occur in the transition layer, and the main rockfill zone for small seepage gradients. The secondary rockfill is almost in the dry zone and the maximum value of the seepage gradient is less than 0.001. Under normal working conditions the seepage gradients of the local cushion layer (2A) and special cushion layer (2B) reach 0.95 and 1.67 respectively.

If a face slab cracks or the seal ruptures, the cushion layer (2A) and special cushion layer (2B) can easily be destroyed due to an enormous increase of the seepage gradient. For the alluvium deposit the maximum value of the seepage gradient is less than 0.083 and thus, a seepage failure will not occur under the intact anti-seepage system. But if the grouting curtain is too short, the seepage gradient will increase to 0.201 and it is then possible that seepage failure may occur in zones with a gradient higher than the critical value. This also confirms the importance of appropriate installation of the grouting curtain.

3.5. SENSITIVITY ANALYSIS OF THE PERMEABILITY OF CUSHION LAYERS

If a crack in the concrete slab or a local failure of the joint sealing appears, the cushion layer (2A) and special cushion layer (2B) will function as seepage prevention due to their low permeability. In the design of CFRDs, this functionality is referred to as an auxiliary anti-seepage role. An analysis of the sensitivity of the permeability of the cushion layer (2A) was carried out for two different assumed coefficients of permeability and the results are compared with the original design value of 2.1×10^{-4} cm/s. The computed results show that the seepage gradients of the cushion layer reduce to 0.37 and 0.14 for a permeability of 7.1×10^{-4} cm/s and 2.1×10^{-3} cm/s, respectively. The distribution of isolines of the water head and the total seepage flux show no significant changes. It can be concluded that for the effective auxiliary seepage control measure, the semi-permeability of the cushion layer should be between 10^{-3} to 10^{-4} cm/s. In addition, the construction quality of the cushion layer (2A), the special cushion layer (2B) and the transition layer is also important to increase the required capacity of the auxiliary anti-seepage measure.

4. CONCLUSIONS

- (1) The sensitivity analysis shows that the coefficient of permeability of the bedrock and alluvium deposit have a great influence on the total seepage flux because the seepage field is mainly concentrated in the dam foundation.
- (2) The concrete grouting curtain strongly affects the seepage field in the foundation. In order to make sure that the work performance meets the design requirements, a sufficient depth of the curtain and also the quality of implementation is of importance.
- (3) Cracks in the concrete slabs and local leakage in the joint sealing leads to a rising of the phreatic surface and to a significant increase of seepage flux in the dam body.
- (4) If the coefficient of permeability of the cushion layer is too low, the seepage gradient in this zone will exceed the permissible value and can lead to seepage failure caused by internal erosion of the filling material. An appropriate higher permeability of the cushion layer will significantly reduce the seepage gradient, despite the fact that the dam leakage remains unchanged. Therefore, proper seepage properties of the cushion layer must be chosen in the design state of the CFRD to avoid seepage failure as a result of local imperfections in the seepage control system.
- (5) An intact concrete slab and joint seal system as also the effective operation of the underground concrete grouting system is of great importance in seepage control. For the intact anti-seepage system, the seepage field is mainly concentrated in the dam foundation and the greater part of the dam is in an almost dry or a moist state.

5. REFERENCES

1. Li, N.H. (2007), "*New Technologies of High Concrete Face Rockfill Dam*", Beijing, China Water and Power Press (in Chinese).
2. Alonso, E.E., Cardoso, R. (2010), "*Behavior of materials for earth and rockfill dams: perspective from unsaturated soil mechanics*", *Frontier of Architecture and Civil Engineering in China*, 4(1), pp. 1-39.
3. Bauer, E. (2009), "*Hypoplastic modeling of moisture-sensitive weathered rockfill materials*", *Acta Geotechnica*, 4, pp. 261-272.
4. Neuman, S.P. (1973), "*Saturated-unsaturated Seepage by Finite Elements*", ASCE, *Journal of Hydraulic Division*, pp. 2233-2250.
5. Neuman, S.P., Narasimhan, T.N., Witherspoon, P.A. (1977), "*Application of mixed explicit-implicit finite element method to nonlinear diffusion-type problems*", *Finite Elements in Water Resources*, Pentech Press, London, Plymouth.
6. Chen, S., Zhang, X. (2016), "*Seepage Control in a High Concrete Face-Rock Fill Dam Based on the Node Virtual Flow Method*", *The Open Construction and Building Technology Journal*, 10(1), pp. 547-560.
7. Zhu, Y.M., Gong D.Y. (2003), "*Solution to 3-D Unsteady Saturated-unsaturated Seepage Problem and Accurate Treatment of Saturated and Unsaturated Exit Surfaces of Seepage*", *Advances in Water Science*, 14(1), pp. 67-71, (in Chinese).
8. Zhu, Y.M., Wang, R.Y., Xu, H.B. (1992), "*Some Techniques for Solution to Free Surface Seepage Flow through Arch Dam Abutments*", In *Proc. of the International Symposium on Arch Dams*, Nanjing, China.
9. Zhu, Y.M., Sun, D., Bauer, E., Semprich, S. (2006), "*On refined FEM solution to seepage in arch dam foundation*", In *Rock Mechanics in Underground Construction: ISRM International Symposium 2006: 4th Asian Rock Mechanics Symposium*, 8-10 November 2006, Singapore (p. 441). World Scientific.
10. Cen, W.J., Wen, L.S., Zhang, Z.Q. (2016), "*Numerical simulation of seismic damage and cracking of concrete slabs of high concrete face rockfill dams*", *Water Science and Engineering*, 9(3), pp. 205-211.
11. Goodman, R. E., Taylor, R.L., Brekke, T.L. (1968), "*A model for the mechanics of jointed rock*", *Journal of Soil Mechanics & Foundations Div.*, 94, pp. 637-660.
12. Chowdhury, S.R., Narasimhan, R. (2000), "*A cohesive finite element formulation for modelling fracture and delamination in solids*", *Sādhanā*, 25(6), pp. 561-587.
13. Wittke, W. (1984), "*Felsmechanik-Grundlagen für wirtschaftliches Bauen im Fels*", Berlin, Springer Verlag (in German).

Numerical Analysis of Elastic Surface Settlement Due to Seepage Force

Abdollah Rohani Hajiagha¹, Abolfazl Riahi Nouri²

1- M.Sc., Department of Civil Engineering, Hormozgan University, Bandar Abbas

2- Assistant Professor, Department of Civil Engineering, West Tehran Branch, Islamic Azad University,

Email: sasanrohani@gmail.com

Abstract

In order to study elastic surface settlement owing to steady-state seepage condition, a tunnel subjected to water-flow was considered. The relationship between surface settlement in a block of soil due to seepage force and other parameters such as soil elasticity, permeability and tunnel diameter was explored. It was shown that elastic settlement due to seepage force can be remarkable to make damage on the building above the soil and soil permeability has major effect on differential settlement.

Keywords: Seepage, Elastic settlement, Numerical analysis.

1. INTRODUCTION

Water-flow can cause instability and deformation through soil in a region leading to damage on structures and their foundations. There are three common types of water-flow that bring such deformation and instability: (a) soil consolidation, (b) dewatering and (c) seepage flow (steady or non-steady).

A great deal of previous research into soil deformation due to water-flow has focused on soil consolidation and dewatering. In order to simulate gradual squeezing and settlement of one-dimensional saturated soil column, a physical model was introduced; this phenomenon named consolidation after Terzaghi [1]. The idea of consolidation developed mathematically for three-dimensional problems by Biot [2]. In addition, some authors utilized finite element method to model soil consolidation [3]. On the other hand, dewatering is inevitable in some projects which is being constructed below water-table. In such projects by designing cutoff wall and retaining wall systems are based on controlling base stability and deformation of excavated soil walls [4].

Although, some worthwhile studies have been performed on soil consolidation and dewatering, few studies have investigated soil settlement due to seepage [5]. understanding this type of settlement can play an important role in addressing the issue of damage in building in the exposure of such settlements. A related example is surface settlement owing to water-flow through tunnel face in tunneling underground water. It is still not known whether seepage forces can cause remarkable deformation and particularly differential settlement on the ground leading to damage and cracks on the buildings and structures as shown in figure 1.

In the present paper surface settlement due to water-flow thorough tunnel face investigated numerically. The relationship between surface settlement in a block of soil due to seepage force and other parameters such as soil elasticity and permeability and tunnel diameter was explored.

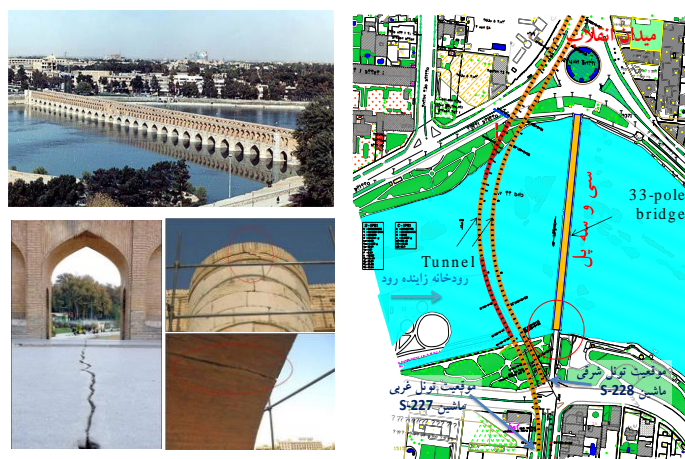


Figure 1. Detrimental effects of surface settlement on an ancient bridge

2. PROBLEM STATEMENT AND METHODOLOGY

A tunnel driven in a coarse-grained soil, and water-flow, was considered as shown in Figure 1, to determine the amount of elastic surface settlement owing to the seepage force in front of the tunnel face. It was assumed that the tunnel face is stable by applying sufficient amount of face support pressure on the tunnel face.

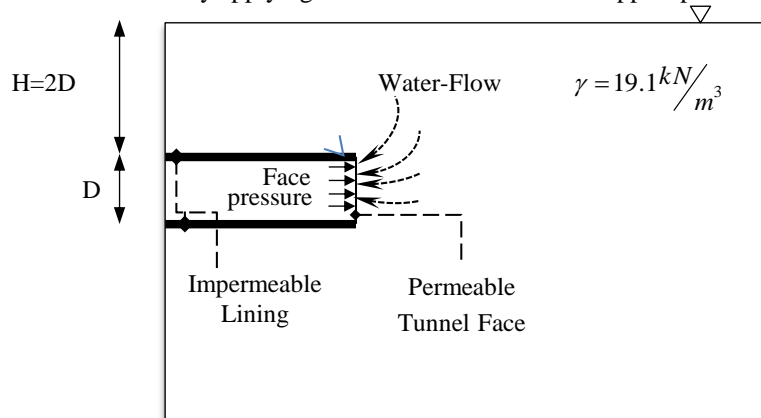


Figure 2. A typical shallow tunnel in saturated, permeable soil with water-flow

For simulating the above-mentioned tunnel, a number of fully-coupled 3D finite element analyses were performed employing ABAQUS software [6]. The geometry and dimensions of the soil around the tunnel are depicted in Figure 2. Due to the symmetry in the geometry of the model, only half of the geometry is simulated in the modeling process and symmetry boundary conditions are applied on the symmetry plane. After a number of analyses, outer boundaries are chosen far enough from the tunnel so that they have less effect on the results. The soil was modeled by 3D solid elements using reduced integration 20-node brick element with pore pressure (C3D20RP), while the lining was modeled using 8-node doubly curved shell elements (S8R) and embedded in the soil as shown in Figure 3.

The movement of nodes in vertical sides of the model in x or y direction are restrained. Besides, considering the bottom nodes, all degrees of freedom are fixed, while there is no constraint on the top nodes of the model. It is considered that there are "no-flow" conditions in vertical sides of the model. The water-table is located on top of the model and remains constant through the analyses. Lining of the tunnel is assumed waterproof, while, there is flow through the tunnel face to establish seepage condition.

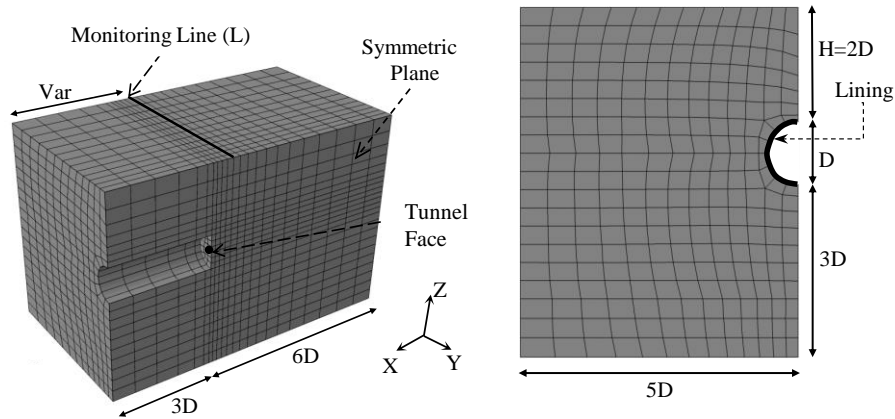


Figure 3. Finite element model of the simulated tunnel

3. NUMERICAL RESULTS AND DISCUSSION

In order to investigate the influence of physical parameters of soil such as elasticity and permeability, as well as other efficient parameters such as hydraulic head in the chamber and the tunnel diameter on the surface settlement, a parametric study was done as described in the following sections. In all cases the soil material is assumed elastic-perfectly plastic conforming Mohr-Coulomb criterion with non-associative flow rule. Figure 4. depicts total head distribution steady-state seepage condition established completely through the soil model.

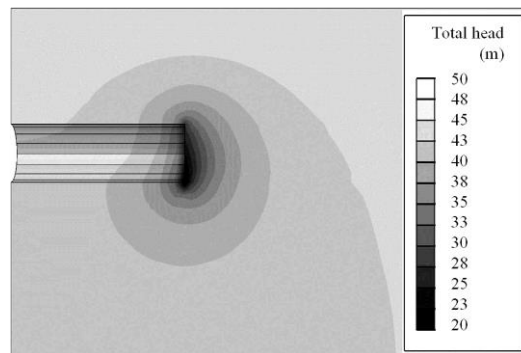


Figure 4. Hydraulic head distribution through model

3.1. EFFECT OF SOIL PHYSICAL PARAMETERS ON ELASTIC SETTLEMENT

To investigate the effect of soil elasticity and permeability on the ground surface settlement, a number of analyses were performed for soils with different values for modulus of elasticity ($E= 13$ and 25 MPa) and isotropic permeability coefficient ($k= 0.001$ and 1 m/sec). As shown in Figure 5 the greater elasticity coefficient leads to smaller surface settlement while soil permeability has no effect on the maximum surface settlement. However, miniscule soil permeability can cause differential settlement.

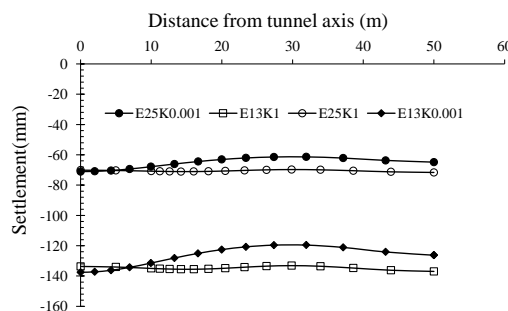


Figure 5. Elastic surface settlement for different modulus of elasticity (E) and permeability coefficients (k) of the soil

3.2. EFFECT OF TUNNEL DIAMETER AND HYDRAULIC HEAD ON ELASTIC SETTLEMENT

To study the effect of channel's dimension on the elastic settlement, three different tunnel diameters, i.e. 6m, 10m and 15m were considered. In all cases the proportion of tunnel cover (H) to diameter (D) ratio was 2. In addition, hydraulic head effect was studied by increasing pore water pressure in the chamber (tunnel face). In this regard parameter "dh" defined as follows:

$$dh = \frac{h}{h_{\max}} \quad (1)$$

Where h is the difference between hydraulic head in the tunnel face and ground surface and h_{\max} is maximum value for h which occurs for zero pore water pressure in the tunnel face the results in Figure 6 show that an increase in the channel diameter leads to greater surface settlement. In addition, the greater differential head, the greater surface settlement.

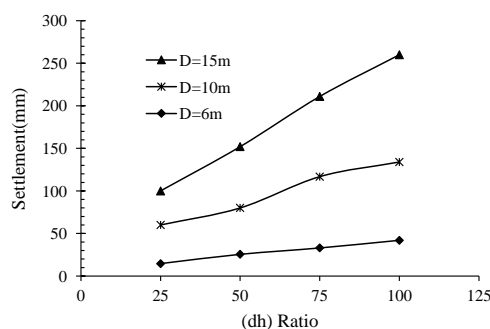


Figure 5. Elastic surface settlement for dimensions (D) of channel and differential heads (dh)

4. CONCLUSIONS

In order to illustrate elastic surface settlement because of seepage force, a tunnel under water-table was considered. Effect of some determining parameters such as soil elastic modulus and tunnel diameter and soil permeability on the settlement was studied. Based on the numerical results the following major conclusions were drawn:

- 1- Seepage force can cause remarkable elastic deformation in soil and corresponding surface settlement on the ground surface.
- 2- Elastic settlement has linear relationship with soil elastic modulus as 7cm and 13.6cm settlement occurred when the soil elastic modulus was 25 MPa and 13 MPa respectively.
- 3- When soil permeability is low enough about 0.001 m/sec, the ground surface experiences up to 2 cm differential settlements.
- 4- Greater tunnel diameter leads to higher surface settlement.

5. REFERENCES

1. von Terzaghi, C., *Erdbaumechanik auf bodenphysikalischer Grundlage*. 1925: Deuticke.
2. Biot, M.A., General theory of three-dimensional consolidation. *Journal of applied physics*, 1941. **12**(2): p. 155-164.
3. Sandhu, R.S., H. Liu, and K.J. Singh, Numerical performance of some finite element schemes for analysis of seepage in porous elastic media. *International Journal for Numerical and Analytical Methods in Geomechanics*, 1977. **1**(2): p. 177-194.
4. Wu, Y.-X., et al., Characteristics of groundwater seepage with cut-off wall in gravel aquifer. I: field observations. *Canadian Geotechnical Journal*, 2015. **52**(10): p. 1526-1538.
5. Chen, Y., et al., Modeling coupled processes of non-steady seepage flow and non-linear deformation for a concrete-faced rockfill dam. *Computers & Structures*, 2011. **89**(13): p. 1333-1351.
6. Manual, A.U.s., Version 6.8. Dassault Systems Simulia Corp., USA, 2008.

Earthquake Safety Evaluation for Dams in Upper Aras Basin, Turkey

Hasan Tosun

Professor, Eskişehir Osmangazi University, Batı Meşelik, Eskişehir, Turkey

Email: hasantosun26@gmail.com

Abstract

The Aras basin, which covers an area of 102,000 km², has the Aras river and many tributaries. The Aras river rises from eastern Turkey and drains the south side of the Lesser Caucasus Mountains, then joins the Kura River, which drains the north side of those mountains and joins Caspian sea after 1 072 km. It is a transboundary river, which flows in and along the countries of Turkey, Armenia, Azerbaijan, and Iran. There are so many small and large dams in the basin. However, eighteen of large dams, which are located on Upper Aras basin, were considered for this study. The heights of dams range from 25 to 157 m. The twelve of them are under operation stage while others are under construction and final design stages. Main part of this basin is located on active seismic region. It is clear that earthquake safety of dams is an important aspect in dam engineering and requires more comprehensive seismic studies for understanding the seismic behavior of dams subjected to severe earthquakes. This study evaluates the main concept of seismic hazard analysis and introduces results of analyses executed for dams of Upper Aras basin, Turkey. The analyses indicate that 75 percent of dams pose moderate hazard ratio and two of them are under near source effect when considered the updated seismic data.

Keywords: Earthquake, Aras basin, dam, seismic hazard.

1. INTRODUCTION

Seismic hazard rating of dam site and risk rating of the dam and appurtenant structures are the main factors acting on total risk for dam structures. The seismic hazard of a dam site can be based on the peak ground acceleration. This value derived from the defined design earthquake produces the main seismic loads. For preliminary study, the existing map of seismic zones can be used to estimate the seismic hazard of a dam site. However, the seismic hazard analysis should be performed for safety evaluation of existing dams. The risk rating of the dam can be based on the capacity of the reservoir, the height of the dam, the evacuation requirements and the potential downstream damages. In general, the seismic and risk ratings are evaluated separately [1]. These two factors were combined to define the total risk factor for dam structure [2]. Recently, the guidelines for selecting seismic parameters for large dams have been published by ICOLD [3].

Turkey is a rich country when considered projects in using land and water resources. The total number of large dams constructed throughout all country is over 1200. Most dams are of the embankment type. However, number of concrete dams and rolled compacted concrete dams increases recently. Most of the designers in Turkey believe the fact that embankment dams, which are well compacted according to the specification, are suitable type for regions having high seismic activity. In general, strong ground shaking can result in the instability of the embankment and loss of strength at the foundations. Active faults, which are very close to the foundation of dams, have the potential to cause damaging displacement of the structure. There is a good case in Turkey, which was damaged during the earthquakes, occurred in past [4]. Therefore, earthquake safety is an important concept for dams and their appurtenant structures. This paper deals with an evaluation of seismic hazard and total risk of the large dams, which have a structural height greater than 25 m, in the Upper Aras basin (Figure 1). In the basin, eighteen large dams have been designed to exploit energy and irrigational potential of the basin. Twelve of them are entirely completed.

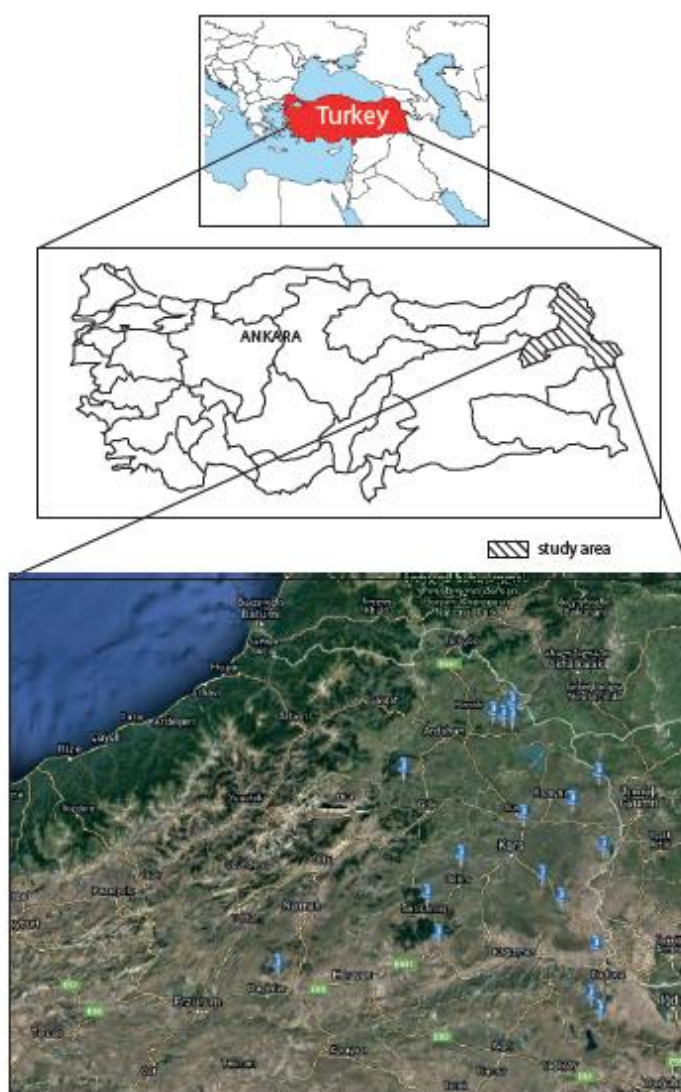


Figure 1. Location of dams considered for this study

2. METHODS OF ANALYSIS

The study of seismic activity is generally performed by means of deterministic and probabilistic seismic hazard analyses. The deterministic seismic hazard analysis considers a seismic scenario that includes a four-step process. It is a very simple procedure and gives rational solutions for large dams because it provides a straightforward framework for the evaluation of the worst ground motions. Due to the unavailability of strong motion records, various attenuation relationships were adopted to calculate the peak ground acceleration (PGA) acting on dam sites. Krinitzsky [5] states that deterministic seismic hazard analysis considers geology and seismic history to identify earthquake sources and to interpret the strongest earthquake with regardless of time. The probabilistic seismic hazard analysis is widely used and considers uncertainties in size, location and recurrence rate of earthquakes. Kramer [6] states that the probabilistic seismic hazard analysis provides a framework in which uncertainties can be identified and combined in a rational manner to provide a more complete picture of the seismic hazard.

For this study eight separate predictive relationships for horizontal peak ground acceleration were considered [7,8,9,10,11,12,13,14]. However, some data have been excluded for the study because of giving extreme values.

For the seismic hazard analysis of each dam site, all possible seismic sources were identified and their potential was evaluated in detail, as based on the guidelines [15] and the unified seismic hazard modeling for Mediterranean region introduced by Jimenez et al [16]. As a result of an extensive survey and a search of available literature, several sources have been identified to help analyzing the seismic hazard of dams in Turkey.

The data instrumentally recorded earthquakes for Turkey and vicinity collected by the National Disaster Organization were considered as a basis for the seismic hazard analyses. The earthquakes that occurred within the last 100 years were used for estimating seismic parameters. Throughout the study, seismic zones and earthquakes within the area having a radius of 100 km around the dam site were considered.

ICOLD states that the Maximum Credible Earthquake (MCE) is the largest reasonably conceivable earthquake magnitude that is considered possible along a recognized fault or within a geographically defined tectonic province [3]. According to this specification, the Safety Evaluation Earthquake (SEE) is defined as the maximum level of ground motion for which the dam should be designed or analyzed. For the dams with high total risk, it is recommended that the SEE should be characterized by a level of motion equal to that expected at the dam site from the occurrence of a deterministically-evaluated maximum credible earthquake or of the probabilistically-evaluated earthquake ground motion with a very long return period.

Earthquake definitions given by FEMA [17] were considered for seismic hazard analyses in this study. The Operating Basis Earthquake (OBE), which was defined by means of the probabilistic methods mentioned above, is the earthquake that produces the ground motions at the site that can reasonably be expected to occur within the service life of the project. MDE is normally characterized by a level of motion equal to that expected at the dam site from the occurrence of deterministically evaluated MCE. Safety Evaluation Earthquake (SEE) is the level of shaking for which damage can be accepted but for which there should be no uncontrolled release of water from the reservoir. Most of large dams in Turkey were analyzed by using these definitions in past [18].

3. SEISMIC HAZARD ANALYSES

For the seismic hazard analyses of the dam site in the Upper Aras basin, a detailed study was performed to identify all possible seismic sources, as based on the seismic zonation map of Turkey, given in Figure 2. The National Disaster Organization and other Institutes prepared the map for general use. But it was modified by the author and co-workers to use for dam projects at the Earthquake Research Center in Eskişehir Osmangazi University. Local geological features and seismic history were used to quantify the rate of seismic activity in the basin. As a result of detailed evaluation, total area covering all basins was separated into five seismic zones. Figure 3 introduces the model used for seismic hazard analyses of this study.

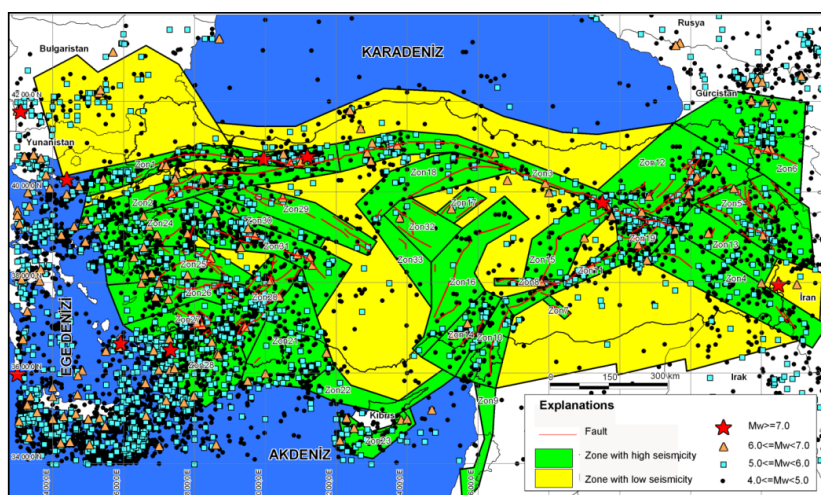


Figure 2. Seismo-tectonics model of Turkey

In Turkey, a new seismo-tectonic map was released to public by National Geological Survey [19]. In Turkey, a new seismo-tectonic map was released to public by National Geological Survey [19]. According to this map, only two dams considered for this study are under near source effect. ICOLD (2016) defined the near-field motion, which is ground motion recorded in the vicinity of a fault.

In this specification, a correlation between radius of near field area and earthquake magnitude is suggested as based on the cases on West United States. Author established limits of near-field motion for the investigation area. According to this model, there are two dams (Abbasgol and Unlendi), which are under the near-field motion. These two dams can be subjected to earthquake having a magnitude of 6.4 and 6.9 are the minimal distance to fault segment is 0.57 and 1.62 km, respectively. All dams excluding two dams discussed above are not under near-field motion (Table 1).

4. RESULTS AND DISCUSSION

There are important dam structures in Upper Aras basins such as Arpacay, Demirdöven, Karakurt, Kayabeyli, Koroglu, Kotanli, Sefakoy and Selim dams. The dams, which are located on the main river of the basin, can cause very serious conditions for downstream life and property, when they fail or are damaged. Therefore, their earthquake safety will be evaluated more detail as given below.

Arpacay dam is one of the main structures of the basin with volume of 0.53 hm^3 of concrete gravity type (Figure 4). It is located on the Arpacay river (the Armenia border) in Aras basin. Its construction was started in 1975 and finished in 1983. Its height from river bed is 50.9 m (DSİ, 2016). When the reservoir is at operation stage with maximum water level, the facility approximately will impound 525 hm^3 of water with a reservoir surface area of 42 km^2 . It is mainly designed to produce electricity with 13 MW of install capacity and to irrigate 70 520 ha of land. The alluvium on river bed was removed before beginning the construction of the main embankment. The seismic hazard analyses performed throughout this study indicates that this dam is one of safe dams within the Aras basin. It will be subjected to a peak ground acceleration of 0.106 g by an earthquake of 7.4 magnitude and it is only 47.4 km far away from an active fault.



Figure 4. A general view from Arpacay dam

Demirdöven dam is a earthfill dam 67-m high with a total embankment volume of $2\,500\,000 \text{ m}^3$. It is located on the Timar River in Upper Aras basin. Its construction was finished in 1996. When the reservoir is at operation stage with maximum water level, the facility approximately will impound 37.34 hm^3 of water. It was mainly designed to provide water for irrigation of 9 844 ha area. The crest length is 695 m and the side slopes of main embankment is 3.0H:1V for upstream and 2.5H:1V for downstream (H=horizontal and V=vertical). On the section there is a central impervious core, which is composed of compacted clay and a transition section of sand and gravel was designed between the core and earthfill materials for downstream part. The downstream shells are composed of natural earth materials with cover zone. The alluvium on river bed, which is composed of mixtures of fine to large size grains, was removed before beginning the construction of the main embankment. The seismic hazard analyses performed throughout this study indicates that Demirdöven dam is one of the safe dams within the basin. It will be subjected to a peak ground acceleration of 0.195g by an earthquake of 6.9 magnitude and it is not close to the fault segment (21.9 km).

The Karakurt dam is a rockfill dam with asphaltic core on the Aras River near Sarikamis County. It has a 137-m height from river bed. When the reservoir is at maximum capacity, the facility impounds 590 hm^3 of water. Its construction will be finished at the end of 2017. It was designed to produce electricity with an install capacity of 99.5 MW and flood controlling. The main embankment consists of crushed rock and transition zone to the central asphaltic core. According to the seismic hazard analyses of this study, it will be subjected to a peak ground acceleration of 0.148 g by an earthquake of 7.4 magnitude. It is identified as class III with high risk. Dam site is located 37.4 km for away from an active fault.

The Kayabeyli dam is a roller compacted concrete dam on the Kura River near Ardahan city in the Aras basin. It has a 155-m height and the facility impounds 148 hm^3 of water when the reservoir is at maximum capacity. Its construction was finished in 2016. It was designed to produce electricity with an install capacity of 87.5 MW. According to the seismic hazard analyses of this study, it will be subjected to a peak ground acceleration of 0.317g by an earthquake of 7.4 magnitude. Dam site is located 11.1 km for away from an active fault.

The Koroglu dam is a roller compacted concrete dam on the Kura River near Ardahan city in the Aras basin. It has a 170-m height and the facility impounds 73 hm³ of water when the reservoir is at maximum capacity. Its construction was finished in 2016. Its system was designed to produce electricity with an install capacity of 50 MW. According to the seismic hazard analyses of this study, it will be subjected to a peak ground acceleration of 0.206g by an earthquake of 7.4 magnitude. Dam site is located 20.7 km for away from an active fault.

The Kotanli dam is a roller compacted concrete dam on the Kura River near Ardahan city in the Aras basin. It has a 59.5-m height and the facility impounds 20.4 hm³ of water at maximum capacity of reservoir. Its construction was finished in 2016. This dam is a part of Koroglu-Kotanli energy system. According to the seismic hazard analyses of this study, it will be subjected to a peak ground acceleration of 0.254g by an earthquake of 7.4 magnitude. It is identified as class III with high risk. Dam site is located 15.3 km for away from an active fault.

Sefakoy dam is a earthfill dam 43-m high is located on the main river in Aras basin. Its construction was finished in 2012. When the reservoir is at operation stage with maximum water level, the facility approximately will impound 9.84 hm³ of water. It was mainly designed to provide irrigation water for lands of Kagizman plain. On the section there is a central impervious core, which is composed of compacted clay and a transition section of sand and gravel was designed between the core and shell materials. The alluvium on river bed, which is composed of mixtures of fine to large size grains, was removed before beginning the construction of the main embankment. The seismic hazard analyses performed throughout this study indicates that Sefakoy dam is one of the safe dams within the basin. It will be subjected to a peak ground acceleration of 0.157g by an earthquake of 6.9 magnitude and it is not close to the active fault segment (19.9 km).

Selim-Bayburt dam is a rockfill dam 57-m high with an embankment volume of 2.1 hm³. It is located on the Bozkus river in Aras basin. Its construction was finished in 2003. When the reservoir is at operation stage with maximum water level, the facility approximately will impound 52.43 hm³ of water. It was mainly designed to provide irrigation water for lands of Selim plain and domestic water for counties in the region. On the section there is a central impervious core, which is composed of compacted clay and a transition section of sand and gravel was designed between the core and shell materials. The seismic hazard analyses performed throughout this study indicates that Selim-Bayburt dam is one of the safe dams within the basin. It will be subjected to a peak ground acceleration of 0.123g by an earthquake of 7.4 magnitude and it is not close to the fault segment (32.5 km).

There are two dams, namely Abbasgol and Unlendi dams, are under the near-field motion when considered the new seismo-tectonic map of Turkey, introduced by MTA [19]. Abbasgol dam is not a very large dam when compared with others in the Basin and has risk class of II with moderate risk ratio. However, Unlendi dam is the most critical dam of the Aras basin. It is under near-field motion (1.62 km far away for critical fault segment).

5. CONCLUSIONS

For this study, eighteen large dams, which are located on different seismic zones of the Upper Aras basin, were analyzed to estimate their seismic hazard and risk classes, as based on the actual earthquakes occurred within the basin and structural features of dams. The most critical zone for the basin is Armenian Fault. As a result of this study, 75 % of the dams under operation stage have been identified as the dams in moderate hazard ratio. There are two dams (Abbasgol and Unlendi dams), which are under near-field motion in the basin. In other words, these dams are also under the impact of near source zone. However, other large dams are relatively safe structures when we consider public safety. This study also indicates that predictive relationship of Campbell and Bozorgnia [18] gives the PGA values with large variation for both deterministic and probabilistic analyses of the dams considered for this study. Author would like to point out a scientific fact that local predictive relationships or relationships, which were developed with considering similar seismo-tectonic environment, should be adopted to determine the seismic parameters to be used in dynamic analyses.

6. REFERENCES

1. ICOLD (1989). Selecting Parameters for Large Dams-Guidelines and Recommendations. ICOLD Committee on Seismic Aspects of Large Dams, Bulletin 72.
2. Bureau, GJ (2003). Dams and Appurtenant Facilities in Earthquake Engineering Handbook edited by Chenh, W.F and Scawthorn, C. CRS press, Bora Raton 26.1-26.47.
3. ICOLD (2016). Selecting Seismic Parameters for Large Dams-Guidelines. ICOLD, Bulletin 148.
4. Tosun, H (2002). Earthquake-Resistant Design for Embankment Dams: Publication of General Directorate of State Hydraulic Works, Ankara. 208 pp. (in Turkish).
5. Krinitzky, E. (2005). Discussion on Problems in the Application of the SSHAC Probability Method for Assessing Earthquake Hazards at Swiss nuclear power plants. Eng. Geol. 78 285-307; Eng.Geo. 82, 62-68.
6. Kramer, SL (1996). Geotechnical Earthquake Engineering: Prentice-Hall, Upper Saddle River, NJ 653 p.
7. Campbell, KW (1981). Near-Source Attenuation of Peak Horizontal Acceleration: Bulletin Seism. Soc. Am., V.71, N.6, 2039-2070.
8. Boore, DM, Joyner, WB. and Fumal, TE (1993). Estimation of response spectra and peak accelerations from Western North American earthquakes. An interim report. Open file report 93-509.U.S.G.S.
9. Ambraseys, NN (1995). The Prediction of Earthquake Peak Ground Acceleration in Europe. Earthquake Engineering and Structural Dynamics, V.24, 467-490.
10. Campbell, KW. and Bozorgnia, Y (1994). Near-source attenuation of peak horizontal acceleration from worldwide accelerograms recorded from 1957 to 1993: Proceeding of the Fifth U.S. National Conference on Earthquake Engineering. V.3, 283-292.
11. Boore, DM., Joyner, WB. and Fumal, TE (1997). Equation for Estimating Horizontal Response Spectra and Peak Acceleration from Western North American Earthquakes. A Summary of recent Work. Sesimological Reseach Letters, V.68, N.1, January /February, 128-153.
12. Gülkan, P and Kalkan,E (2002). Attenuation modeling of recent earthquakes in Turkey. Journal of Seismology, 6(3), 397-409.
13. Kalkan, E ve Gülkan, P (2004) Site-Dependent Spectra Derived from Ground Motion Records in Turkey, Earthquake Spectra, 20, 4, 1111-1138.
14. Ambraseys, NN., Douglas, J, Karma, SK and Smit, PM (2005). Equations for the Estimation of Strong Ground Motions from Shallow Crustal Earthquakes Using Data from Europe and the Middle East. Horizontal Peak Ground Acceleration and Spectral Acceleration, Bulletin of Earthquake Engineering, 3, 1-53.
15. Fraser, WA and Howard, JK (2002). Guidelines for Use of the Consequence-Hazard matrix and Selection of Ground Motion Parameters: Technical Publication, Department of Water Resources, Division of Safety of Dams.
16. Jiminez, MJ, Giardini, D and Grünthal, G (2001). Unified Seismic Hazard Modelling throughout the Mediterranean Region. Bolettino di Geofisica Teorica ed Applicata, Vol.42, N.1-2, Mar-Jun., 3-18.
17. FEMA (2005). Federal Guidelines for Dam Safety—Earthquake Analyses and Design of Dams.
18. Tosun, H and Tosun, V.T (2017). Total risk and seismic hazard analyses of large dams in northwest Anatolia, Turkey. ICOLD 85th Annual Meeting, July 3-7, Prague.
19. MTA (2013). Scale 1/1.125.000 Turkey Live Fault Map. General Directorate of Mineral Research and Exploration. Special publications series, Ankara, Turkey.
20. DSİ (2016). Dams of Turkey. TR-COLD, Ankara, 602 p.

Seismic and Geotechnical Aspects of the Large Earthfill Dam in a Seismically Active Region

Dariusz Belashi¹, Saeed Nayeb²

1- Geotechnical Engineer and Project Manager, Mahab Ghodss Consulting Engineering

2- Seismotectonics Expert, Mahab Ghodss Consulting Engineering

Email: dbelashi@yahoo.com

Abstract

The seismic and geotechnical aspects of 150M height Mixed-Clay core earthfill dam located in North of Iran in a severe seismic area near some main faults are discussed. As the dam is located in highly seismic area with some main faults, both ground shaking and fault movements in the dam foundation should be considered in the design. As a main fault is within a distance of about 1.5 km from the dam site, which can produce earthquakes with a magnitude up to 7.4, movements might be also anticipated along the minor faults or discontinuities in the bedrock. At least one minor fault (F1) cut the dam site. The design against multiple fault movements is considered so that after faulting and slip movements, adequate width of filter and transition zones are still available. The results of dynamic analysis are also presented to show the stability of the designed dam during earthquake loading. Sufficiency of designed filter and transition and considered freeboard is also concluded considering the results of dynamic analysis.

Keywords: seismic design, fault movement, dynamic analysis, permanent deformation.

1. INTRODUCTION

The earthquake hazard is a multiple hazard as besides ground shaking earthquakes can cause displacements along potentially active faults in the dam foundation or fault movements under the dam or in the reservoir. So the dam engineer should consider both shaking and movement effects for designing an embankment dam in a severe seismic area.

Haraz dam site is situated on the Haraz River on North Slope of Alborz Mountain Range in the North of Iran. It is located near to some major faults. So the dam should be designed considering existence of active faults. The dam site is located between North-dipping Chelav and Kelerd thrust Faults. The distance between hanging wall of Chelav Fault and the dam site is about 1 km. According to the seismotectonic studies, a major rupture of Chelav fault could induce some sympathetic movements along secondary faults which probably located along the river bed under the dam. So the dam and internal zones should be designed so that after fault movement the core of the dam beside the filter and transition zones have enough thickness.

The dam should also be designed to tolerate the acceleration of maximum credible earthquake during ground shaking. It is generally believed that a dam which is conservatively designed against strong earthquake shaking would probably also safely withstand moderate movements of foundation faults (Sherard, 1974)[1]. The seismic hazard assessment identified that Khazar Blind Fault is the source controlling maximum credible earthquake (MCE) for the dam site based on Magnitude of 7.4. The peak horizontal and vertical ground acceleration (PGHA and PGVA) for MCE are 0.8g and 0.73g, respectively. The Finite element dynamic analysis is performed for safety evaluation of the dam during earthquake.

2. GEOLOGICAL AND SEISMOTECTONIC CONDITIONS OF THE DAM SITE

Haraz Dam site is located on North Slope of Alborz Mountain Range in the North of Iran. The Alborz is a stack of thrust sheets, produced by late Cenozoic compressional deformation. Deformation is due to the North-South Arabia-Eurasia convergence, and westward motion of the adjacent South Caspian relative to Iran. Major thrust or reverse faults within the study area are generally located parallel to dam axis. The dam site is located between North-dipping Chelav and Kelerd thrust Faults which were considered as branches of North Alborz fault. The dam site locates on hanging wall of Chelav Fault about 1km north of its surface trace. The F1 fault is approximately parallel to the major joint sets at the dam site, so it is likely that F1 be a major joint set. On the other hand, other unknown faults and discontinuities might be under river bed.

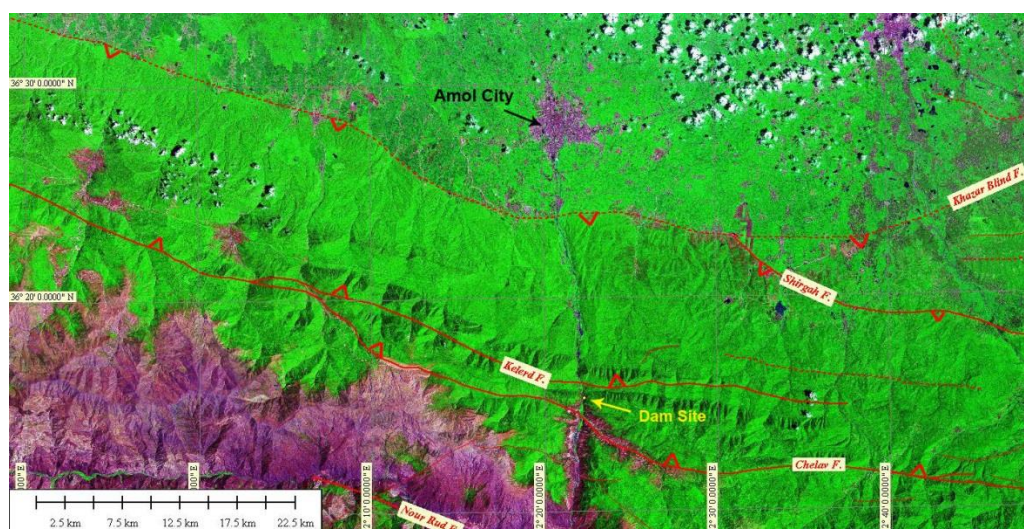


Figure 1. Illustration of Major Faults on LANDSAT Image

Generally, displacements on branch, Secondary or sympathetic faults are smaller than those on the generating fault. Potential displacement on a secondary fault decreases with increasing distance from the primary fault (McCalpin and Nelson, 2009) [2]. Based on engineering judgment and observations in other regions such as Bonilla 1967[3], displacement on secondary and sympathetic faults around the dam body can be up to 50% of displacement on the generating fault taking into account a distance of about 1km between the dam site and Chelav Fault. Therefore, in case the maximum co-seismic displacement along the Chelav Fault is assumed about 100 cm during an Ms 6.0 earthquake, the maximum displacement of 50 cm can be considered for secondary faults and discontinuity planes at the dam site.

As mentioned, Haraz earthfill dam is located in a severe seismic area. According to seismotectonic studies, the peak ground acceleration (PGA) for different levels of ground motion at the dam site using deterministic and probabilistic procedures are as follow:

Table 1. PGHA and PGVA at the dam site for different design earthquakes

	Return Period	PGA(Average)	
		PGHA(g)	PGVA(g)
1	150(OBE)	0.21	0.15
2	500(DBE)	0.32	0.21
3	2000(MDL)	0.47	0.30
4	10000(SEE-Prob.)	0.65	0.44
5	SEE (MCE-84%)	0.80	0.73

The seismic hazard assessment identified that Khazar Blind Fault is the source controlling maximum credible earthquake (MCE) for the dam site based on Magnitude 7.4 earthquake. PGHA and PGVA for MCE are 0.8 g and 0.73 g, respectively. In addition to PGA, the time history and frequency content of the design earthquake affect the dam response. The acceleration response spectra for different design earthquakes are presented in Figure 2.

For the safety check of a dam at least three different earthquakes shall be considered for the SEE ground motion. (ICOLD, Bulletin 148) [4]. Accelerograms of three earthquakes of Tabas, Loma prieta and Manjil are scaled for the dam site according to the response spectra of the site. Tabas scaled acceleration time histories in the SEE level is the critical one which is imported as design earthquake in this paper and presented in Figure 3.

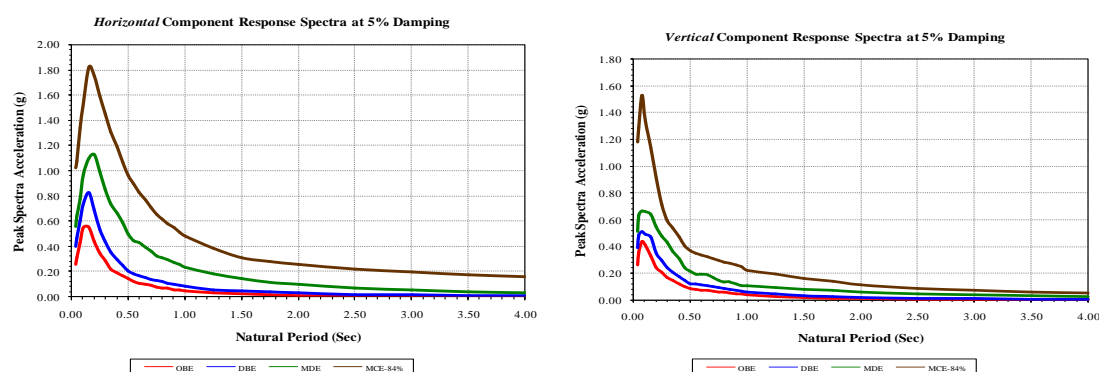


Figure 2. Acceleration Response Spectra for the dam site

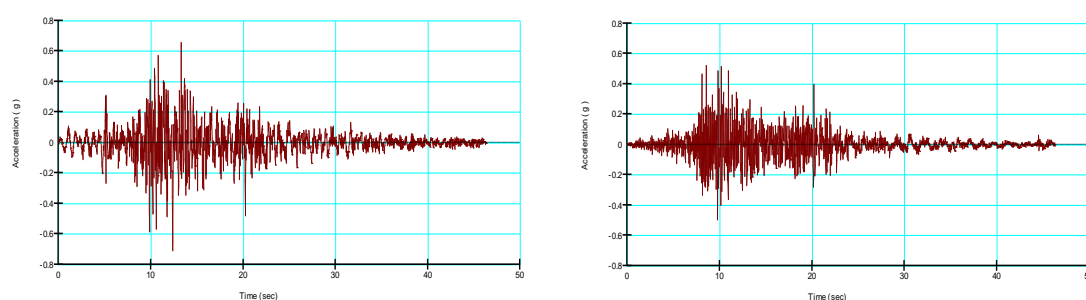


Figure 3. Horizontal (left) and vertical (right) acceleration time history (Tabas) in SEE level

3. GENERAL GUIDELINES FOR DESIGNING AN EMBANKMENT DAM NEAR AN ACTIVE FAULT

In 1998 the International Commission on Large Dams (ICOLD) published a guideline which addresses the issue of dams on active or potentially active faults (ICOLD, 1998, Bulletin 112) [5]. The basic statements relevant for the dam engineer given in the mentioned guideline can be summarized as follow:

1. When a major active fault is crossing the dam foundation the site should be abandoned and a more appropriate site should be looked for.

2. In highly seismic areas it may not be possible to find any site without fault slip hazard: In such a case, concrete dams should be avoided and preference be given to a conservatively designed embankment dam, designed with ample filter and transition zones, on both sides of a rather wide core, displaying ductile properties. There is a considerable confidence that such a structure can withstand, without failure, significant fault offsets.

3. If the seismotectonic conditions at a dam site are not clear, then the engineer should avoid concrete dams and select a conservatively designed embankment dam.

Sherard et al (1974) presented similar conclusions. Wieland et al (2008) [6] also state that concrete dams on active faults, or near some major active faults, are not advisable, and if a site with fault movements cannot be avoided then it is reasonable practice to construct a conservatively designed embankment dam.

According to the Wieland et al (2008) [6], the basic elements of an embankment dam, which can resist both differential ground movements and strong earthquake ground shaking, are the following:

1. Impervious core made of ductile material with a high failure strain to minimize the propagation of the rupture zone; prevention of internal erosion if core is cracked;
2. Thick filter and transition zones: about 50% shall still be available after faulting and slip movements;
3. Wide dam crest;
4. Flat slopes;
5. Generous freeboard: to prevent overtopping due to impulsive waves in reservoir and settlement of the dam crest;
6. Material selection and compaction of rockfill, etc.

The main concern of any embankment dam with impervious core is the erosion resistance of the core material. According to Sherard (1967) [7] ‘the filter and transition zones provide the first line of defense against earthquake induced concentrated leaks through the dam. If thick, adequately graded, cohesionless transitions are provided, a leak can only get out of control in extreme cases of embankment distortion caused by foundation movement’. ‘Where there is a choice between several types of materials for the core of a dam, which may be subject to an earthquake, it seems apparent that the resistance to concentrated leakage should be the main factor in the decision.’

An approximate classification of core materials on the basis of resistance to concentrated leaks was also made by Sherard as follow:

1. Very good materials: Very well-graded coarse mixtures of sand, gravel, and fines.
2. Good materials: Well-graded mixtures of sand, gravel, and clayey fines; highly plastic tough clay (CH) with plasticity index greater than 20.
3. Fair materials: Fairly well-graded gravelly, medium to coarse sand with cohesionless fines; clay of medium plasticity (CL) with plasticity index greater than 12, coarse mixtures of sand, gravel, and fines
4. Very poor materials are fine, uniform, Cohesionless silty sand; silt from medium plasticity to cohesionless (ML) (plasticity index less than 10) because these materials are highly erodible

4. DESIGN SPECIFICATIONS OF HARAZ DAM

The typical cross section of Haraz dam is shown in Figure 4. As seen a relative conservative design is adopted for Haraz dam in order to withstand ground shaking and tolerate fault movements during operation.

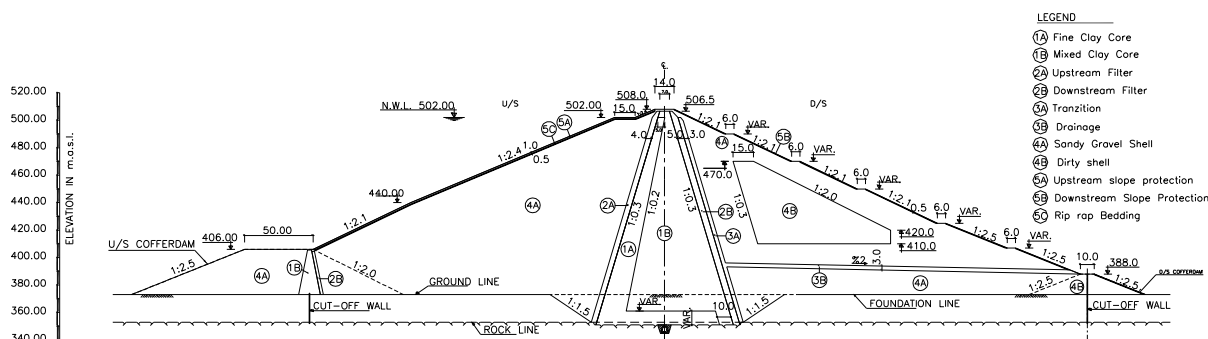


Figure4. Haraz dam typical section

The main features of Haraz dam are as follow:

A relative thick core is designed for Haraz Dam. The thickness of the core is 7 m at the crest elevation and the lateral slopes of the core is 1V:0.3H. The ratio of the core thickness (W) to the water height is about 65 percent. According to Sherard (1959) [8] cores with a width of 30 to 50 percent of the water head have proved satisfactory on many dams under different conditions. Probably a core with this width is adequate for any soil type and dam height. The core of the dam includes two main zones. A zone of fine clayey material (1A) in the upstream and lower elevations and a zone from well graded mixture of sand, gravel and clayey fines (1B) in the downstream and upper elevations of the core. These zones are designed considering the materials available in the site. The zone 1A includes medium to high plastic clay material in order to increase resistance of the core against concentrated leakage due to fault movements. The average of liquid limit and plasticity index of 1A zone is 42 and 18 respectively. The 1B zone on the other hand includes well graded mixture of sand, gravel and fines with average liquid limit and plasticity index of 32 and 12 respectively. The upstream and downstream filters are designed 5 and 4 m respectively. As the maximum displacement along secondary fault and discontinuity planes at the dam site is estimated about 50 Cm, considering a safety factor, minimum 2.5 to 3.0 m would be available after fault movement. A 15m berm is considered in the upstream at the Normal level elevation in order to decrease the permanent deformation near to the crest. The core is founded on groutable limestone and marly limestone sound rock. It means that all alluvial and weathered rock is excavated under the core of the dam. The upstream and downstream shell is founded on relative dense sandy gravelly alluvium. The 50m berm on the upstream is designed regarding limit equilibrium stability requirements.

5. NUMERICAL FINITE ELEMENT METHOD

Dynamic numerical methods utilize the time history of acceleration as direct input to the analysis. The dynamic analysis is carried out either in the time domain, or in the frequency domain using an equivalent linear or nonlinear method.

Over the years significant studies have been done in order to reach to more comprehensive understanding about the seismic behavior of earth and rockfill dams. Newmark (1965) and Seed (1966) were the first to propose methods of analysis to predict the permanent deformations of dams subjected to earthquake shaking. Various methods for predicting seismic deformation of earth structures have been developed based on Newmark’s method and its modified versions by Sarma (1975) [9] and Makdisi-Seed (1978) [10]. The empirical relations developed by Jansen (1990) [11], Swiasgood (1995) [12] and Bureau (1997) [13] are generally based on statistical analyses of data from a limited number of failure case histories. With the advent of fast computers and significant progress in nonlinear material modelling and testing, the embankment dams are increasingly being studied by finite element and finite difference methods with advanced nonlinear material models [14]. In some cases, experts have even recommended three-dimensional analysis to include effects of canyon, and other site-specific geometric irregularities on the dynamic stability of a dam. [14-15]

The equivalent linear is one of the preferred methods which are advised in ICOLD Bulletin (ICOLD, B52). In this method, a linear analysis is performed, assuming initial values of damping ratio and shear modulus for different materials. The maximum cyclic shear strain is then recorded for each element and new values for damping and modulus are determined with defined Equations or Graphs (Figure 5). In order to perform dynamic equivalent linear analysis, finite element software QUAKE/W which is part of GeoStudio is utilized. QUAKE/W is a geotechnical finite element software product used for the dynamic analysis of earth structures subjected to earthquake shaking. The combination of dynamic analysis results together with the Newmark Sliding Block concepts can be used to estimate the permanent deformation. In GeoStudio, SLOPE/W uses the QUAKE/W results to perform these calculations.

In order to perform dynamic analysis, it is necessary first to perform static analysis by simulating stage construction and impounding of the dam. After completion static analysis, the equivalent linear dynamic analysis is performed by introducing acceleration time history and corresponding material model and boundary conditions. In the last step, the results of a QUAKE/W analysis are used in conjunction with SLOPE/W to estimate the permanent deformations that may occur during the earthquake. As real laboratory tests for dynamic properties of different materials of Haraz Dam are now being performing, these specifications are estimated here based on literature studies. There are functions in Quake/w in order to estimate the dynamic properties including maximum shear modulus, G-reduction and damping ratio functions based on work by different researchers [16-17-18]. The functions which are used for different materials of Haraz dam based on QUAKE/W formulation are illustrated in Figure 5.

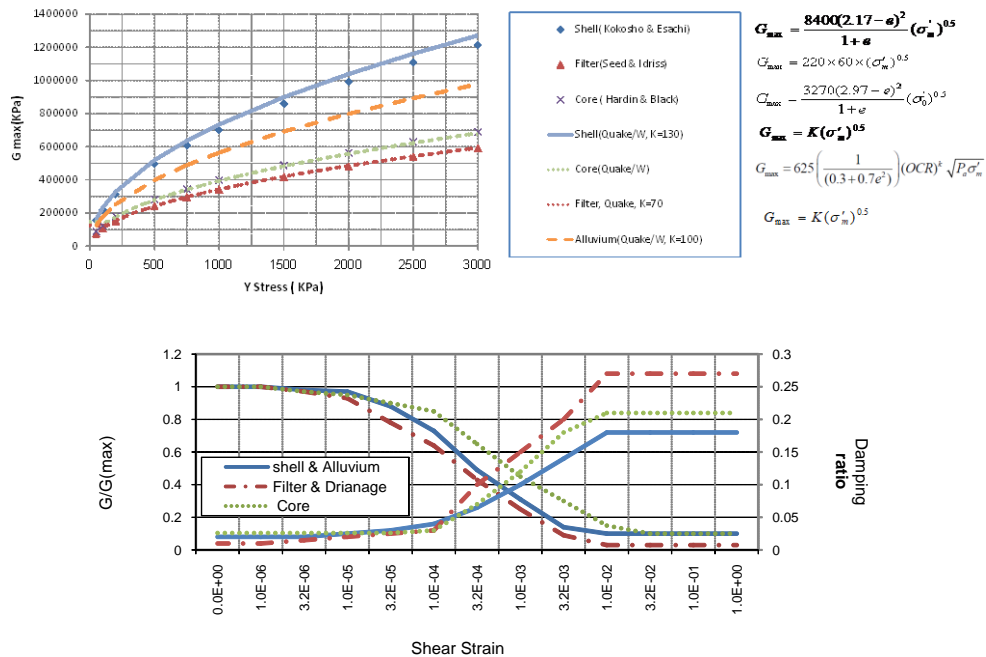


Figure5. G max, G/G max and damping ratio variation for different materials

6. PERMANENT DEFORMATION ESTIMATION

Permanent deformations are estimated according to the Newmark sliding blocks concept and presented in Figure 6. The maximum permanent displacement for near crest sliding block is about 155 cm for the design earthquake.

As seen in Figure 4, a 15 m thick berm is considered on the Normal elevation of the upstream side of the dam, in order to decrease the permanent deformation near crest of the dam. To study effect of the considered berm on the calculated permanent deformation, equivalent linear analyses are performed on the typical section without a berm on the upstream slope. The results have shown that the Maximum permanent deformation near crest is increased from about 155 cm to about 273 cm, if the considered berm is omitted on the upstream slope of the dam.

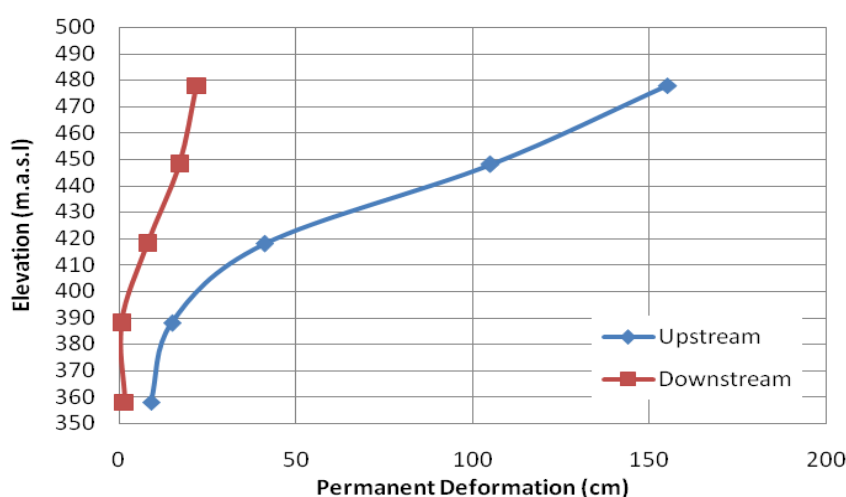


Figure6. Results of permanent deformation in different elevation- Haraz Dam

7. CONCLUSIONS

The seismic and geotechnical aspects of 150M height Mixed-Clay core earthfill dam located in North of Iran in a severe seismic area near some main faults are discussed. As the dam is located in highly seismic area with some main faults, both ground shaking and fault movements in the dam foundation should be considered in the design. The results of finite element dynamic analysis show that if the dam is designed to withstand permanent deformation imposed by design earthquake shaking, it would satisfy the criteria of designing the dam on the potentially active faults. The results also show that flattening the slopes near the crest of the dam or considering berm near the crest, has a significant effect in decreasing permanent deformation.

8. REFERENCES

1. Sherard, J.L, Cluf, L.S. and Allen, C.R (1974), “*Potentially Active Faults in Dam Foundations,*” Geotechnique, 24, No.3, pp. 367–428.
2. McCalpin, J. P. and Nelson, A.R. (2009), “*Paleoseismology,*” Chapter 1, Introduction to Paleoseismology, p.613.
3. Bonilla, M.G., (1967), “*Historic Surface Faulting in Continental United States and Adjacent Parts of Mexico*” A Factor in Nuclear Facility Siting and Design, USGS, TID-24124, p. 32.
4. ICOLD, (2010), “*Selecting Seismic Parameters for Large Dams Guidelines*” Bulletin 148, Committee on Seismic Aspects of Dam Design, ICOLD
5. ICOLD, (1998), “*Neotectonics and Dams*” Bulletin 112, Committee on Seismic Aspects of dam Design, ICOLD
6. Wieland, M., Brenner, R.P. and Bozovic, A. (2008), “*Potentially Active Faults in the Foundations of Large dam,*” Part2: Design aspects of dams to resist fault movements, 14th World conference on Earthquake Engineering, Beijing, China
7. Sherard, J.L (1967), “*Earthquake Considerations in Earth Dam Design.*” J. soil Mechanics and Foundation Division, ASCE, 83:SM-4, pp. 377-401
8. Sherard, J.L (1963), “*Earth and Earth-Rock Dams*” John Wiley
9. Sarma, S. K. (1975), “*Seismic Stability of Earth dams and Embankments*” Geotechnique 25(4): pp. 743-761
10. Makdisi F. I, Seed, H.B, (1978), “*Simplified Procedure for Estimating Dam and Embankment Earthquake Induced Deformations*” J. Geotech. Eng. Div. ASCE 104(7): pp. 849-867
11. Jansen, R. B, (1990), “*Estimation of Embankment Dam Settlement Caused by Earthquake,*” International Water power & Dam Construction 42(12): pp35-40
12. Swaisgood, J.R, (1995), “*Estimating Deformation of Embankment Dams caused by Earthquakes,*” ASDSO Western Regional Conf. Montana, USA pp. 1-7
13. Bureau, G. (1997), “*Evaluation Methods and acceptability of Seismic Deformations in Embankment Dams,*” Proc. 19th Cong. On large Dams, Florence, Italy, pp. 500-510
14. Sengupta, A. (2010), “*Estimation Permanent Deformation of the Tehri Dam in the Himalayas due to Future Strong Earthquakes,*” Indian academy of Science, Vol.35, Part:3, pp. 373-392
15. Gazetas, G. Dakoulas, P. (1992), “*Seismic Analysis and Design of rockfill Dams,*” State of the art. Soil Dynamics and Earthquake Eng. 11: pp. 27-61
16. Kramaer, S.L., (1996), “*Geotechnical Earthquake Engineering,*” Prentice Hall
17. Ishibashi, I., and Zhang, X., (1993), “*Unified Dynamic Shear Moduli and Damping Ratios of sands and Foundations,*” Soil and foundations, Vol.33, No.1, pp. 182-191
18. GEO-SLOPE International LTD, (2008), “*Dynamic Modeling with QUAKE/W 2007*”

Seismic Safety Aspects of Gated Spillways of Large Storage Dams

Martin Wieland¹, Sanaz Ahlehigh²

**1.Chairman, ICOLD Committee on Seismic Aspects of Dam Design, c/o Poyry Switzerland Ltd.,
Herostrasse 12, CH-8048 Zurich, Switzerland**

2.Structural Engineer, Poyry Switzerland Ltd. Tehran, Iran

Emails: martin.wieland48@gmail.com, sanaz.ahlehigh@poyry.biz

Abstract

Gated spillways of large storage dams must be operable after the safety evaluation earthquake (SEE) such that the reservoir level can be controlled and a moderate flood can be released safely. Consequently, the gates, motors, control units and power supplies including emergency power generators must be operable and the gates should not experience any inelastic deformations causing jamming of the gates. Moreover, the spillway piers shall not exhibit any inelastic deformation in the cross-river direction, which is the weak axis of typical spillway piers. The trunnions must be able to withstand the high hydrodynamic pressures acting on the gates. Thus these elements must be designed and checked for the SEE. Vulnerable to high seismic loads are gated crest spillways due to the amplification of the support motion with respect to the ground acceleration on the rock surface. The possible seismic hazards, the seismic performance criteria of gates and electro-mechanical equipment and the dynamic analysis of spillway structures are discussed.

Keywords: Earthquake safety, dam safety, spillway gates, spillway pier, dynamic stability analysis.

1. INTRODUCTION

In 2016, ICOLD has published new guidelines on the selection of seismic parameters for large dams [2], which include seismic design criteria for (i) the dam body and (ii) the safety-critical elements, such as spillways and low level outlets. The inclusion of the safety-critical elements is new and is the consequence of the following, very general, safety and performance criteria for large storage dams subjected to strong ground shaking resulting from the so-called Safety Evaluation Earthquake (SEE):

- (i) The dam must be able to retain the reservoir during and after the SEE (Note: Deformations and cracks in the dam body are accepted as long as the reservoir can be retained safely; the stability of the dam must be ensured).
- (ii) The dam operator must be able to control the water level in the reservoir after the SEE (Note: It may take several months until the earthquake damage of a large dam and/or its safety-critical elements has been repaired, therefore safe operation of the reservoir during this period is a must).
- (iii) It should be possible to lower the reservoir for the repair of a damaged dam and/or to increase the safety of a damaged dam or a dam, whose earthquake safety has been questioned, after an earthquake.

Item (i) has been the main concern of dam engineers since the 1930s when the first concrete and embankment dams were designed against earthquakes. However, the pseudo-static analysis method and the representation of the seismic hazard by a seismic coefficient - a value of 0.1 was used for most dams – are obsolete today and shall no longer be used, although engineers are still tempted to use this outdated concept.

Item (ii) requires the proper functioning of the spillway or a low level outlet as it has to be assumed that in a hydropower project the power plant is out of operation after the SEE. In general, ungated spillways are unproblematic if they are structurally safe. In the case of gated spillways it must be possible to open the gates such that a moderate flood with a return period of at least equal to the diversion flood can be released, as it may take several months until a storage dam project has been repaired or strengthened. The worst scenario is that shown in Fig. 1 where it was not possible to open any of the spillway gates of a run-of-river power plant, after the magnitude 8.0 Wenchuan earthquake in China in May 2008. As the structure of this power plant is made of reinforced concrete, overtopping is not a catastrophic event as it is unlikely that such a concrete structure will fail. However, overtopping of the concrete crest during extended periods of time could cause erosion damage, which may endanger the stability of the piers. Therefore, repairs must be carried out as quickly as possible. For example, progressive erosion of the rock surface was caused by the operation of the emergency spillway at Oroville dam in February 2017, threatening the stability of the emergency spillway.



Figure 1. Overtopping of run-of-river power plant due to failure of gate operation (left) and mud deposited on crest of overtopped run-of-river power plant (right) (Wenchuan earthquake in China)

Overtopping of an embankment dam, due to malfunction of spillway gates, is a far more serious safety problem than for a concrete dam, as this will ultimately lead to the failure of the dam and the catastrophic release of the reservoir. It should be added that depending on the reservoir level at the time of the earthquake and the inflow into the reservoir, it may take hours or days before the dam will be overtopped, if all gates are closed. Thus overtopping of the crest due to malfunction or inadequate spillway capacity will be a hazard that occurs after an earthquake and not during an earthquake.

Item (iii) is a matter of low level outlets, as by opening of the spillway gates, the reservoir can only be lowered to the elevation of the sill, assuming that the power plant is shut down. Although there are different opinions on the need of low level outlets of large storage dams, it is obvious that lowering of the reservoir after a damaging earthquake, increases the safety of the dam and lowers the risk for the people living downstream of a dam. For example, bottom outlets are compulsory for all dams in Switzerland. During the SEE, some structural damage may occur in the dam body (mainly cracks and joint opening in concrete dams, and cracks and deformations in embankment dams), however, this damage shall not jeopardize the global static stability of the dam or parts of it. To avoid overtopping of dams, it is necessary that the spillways be operable after the SEE and since the repair of a damaged dam or spillway may take several months or years it must also be possible to release a moderate flood.

The present paper is concerned with the seismic safety of the supporting civil structures (piers) of gated spillways. Typically, a spillway with radial gates consists of the following key elements that must function after the SEE:

- The steel gates with motors, hydraulic system or winches with counterweights etc., control unit, power supply, emergency power generator, redundant power supply, etc., and
- The concrete piers with supports of the steel gates and anchorage of the support forces.

The main static load for the design of spillway gates is the hydrostatic load. For the seismic load case the hydrodynamic pressure according to Westergaard [3] (is used, assuming that the gate is a rigid structure. In the pseudo-static analysis, the earthquake support motion of the gates is represented by a seismic coefficient. A value of 0.1 was usually considered. This pseudo-static concept used for the seismic design of the dam body and radial gates is obsolete today as it does not account for the dynamic characteristics of the dam and gates and the time-dependent nature of the earthquake ground motion.

In view of modern dam design concepts [2] [4] where two levels of earthquakes are specified, i.e. the Operating Basis Earthquake (OBE) and the SEE, the design of the hydro-mechanical and electro-mechanical equipment is often based on the OBE, following internationally accepted design codes or guidelines for hydro-mechanical equipment, assuming that the gate structure has sufficient reserves to cope with the SEE support motions.

This concept (design for OBE and neglecting the dynamic characteristics of the gates and the earthquake motion) is too optimistic, and there is no formal check done that the gates can be opened after the SEE. This is a systematic problem, which also includes all electro-mechanical equipment.

As a result of this concept the seismic support reactions and the anchorage forces in the spillway piers are underestimated and thus, the seismic safety of the spillway piers may not be sufficient.

The seismic design of the spillway gates must be consistent with the overall seismic safety concept of the storage dam, which is the key competence of the dam engineer [4] [5]. Therefore, any technical specifications for the seismic safety of hydro-mechanical and electro-mechanical equipment must comply with the overall seismic safety concept of the dam project. Unfortunately, technical specifications are often either copies of previous specifications, which have become obsolete, or the engineers in charge of the hydro-mechanical and electro-mechanical specifications do not communicate with dam engineers or are not familiar with the seismic design of equipment. Because of these reasons, it is not known, if the gated spillways of existing dams satisfy today's seismic safety requirements.

The present paper is only concerned with the seismic safety of the spillway piers; however, we must be aware that this cannot be treated independently from the gate design.

2. SEISMIC FAILURE MODES OF SPILLWAY GATES

The main seismic failure modes of gated spillways due to ground shaking are as follows:

- (i) Failure of the electro-mechanical equipment and/or failure of redundant power supply.
- (ii) Jamming of gates due to inelastic deformations of gate structure, caused by, e.g., large hydrodynamic forces or by seismic deformations of piers in cross-river direction resulting in pounding damage of the gate leaf close to the top part of the pier (Note: Gates with small gap between gate leaf and embedded steel frame are more vulnerable than older gates with larger gaps).
- (iii) Failure of counter weights or other components of gate operating system.
- (iv) Damage of gate caused by massive elements falling on the gate such as bridge girders, gantry cranes, motors, counter weights etc.
- (v) Jamming of gates due to inelastic deformations of spillway piers in cross-river direction.
- (vi) Failure of tension anchorage of gate support in spillway piers or large tensile cracks and deformations in under-reinforced piers causing jamming of gates.
- (vii) Jamming of gates due to differential joint movements, when structural joints in concrete are located between the two supports of, e.g. a radial gate.
- (viii) Damage of spillway chute, retaining walls, flip bucket, plunge pool etc. (Note: This damage may accelerate erosion damage during spillway operation after an earthquake, but should not have any impact on the functioning of the gates).
- (ix) Other failure modes depending on gate type.



Figure 2: Failure of two bays of the Shih-Kang weir caused by (mainly vertical) fault movements during the 1999 Chi-Chi earthquake in Taiwan

The most critical failure modes are those, which prevent opening of the spillway gates of an embankment dam project or a dam consisting of a concrete part and embankment dam sections after the SEE. As there are different types of gates, other failure modes may also have to be considered.

It is well known that for large dams the seismic hazard is a multi-hazard. Besides ground shaking the other seismic hazards must also be addressed, i.e. fault movement, and rockfalls and landslides (mass movements). If a concrete spillway is located on a fault, which can move during a strong earthquake, then the spillway will be destroyed as shown in Fig. 2. Rockfalls and landslides are important hazards, which have been underestimated during strong earthquakes. For example, during the magnitude 8.0 Wenchuan earthquake in China of May 12, 2008 and the magnitude 7.8 Kaikoura earthquake in New Zealand of November 14, 2016 about 100,000 mass movements were triggered.



Figure 3: Damage of spillway piers caused by rockslides during the 2008 Wenchuan earthquake in China

Figure 3 shows damage of spillway piers caused by mass movements during the Wenchuan earthquake. Mass movements are also visible in Fig. 1. Rockfalls are, however, a major problem for the unprotected electro-mechanical equipment of spillway gates and can also cause failure of radial gates as shown in Fig. 4. Mass movements can also block the spillway chute or in tunnel spillways the portal zones are those, which can be blocked or damaged by rockfalls.

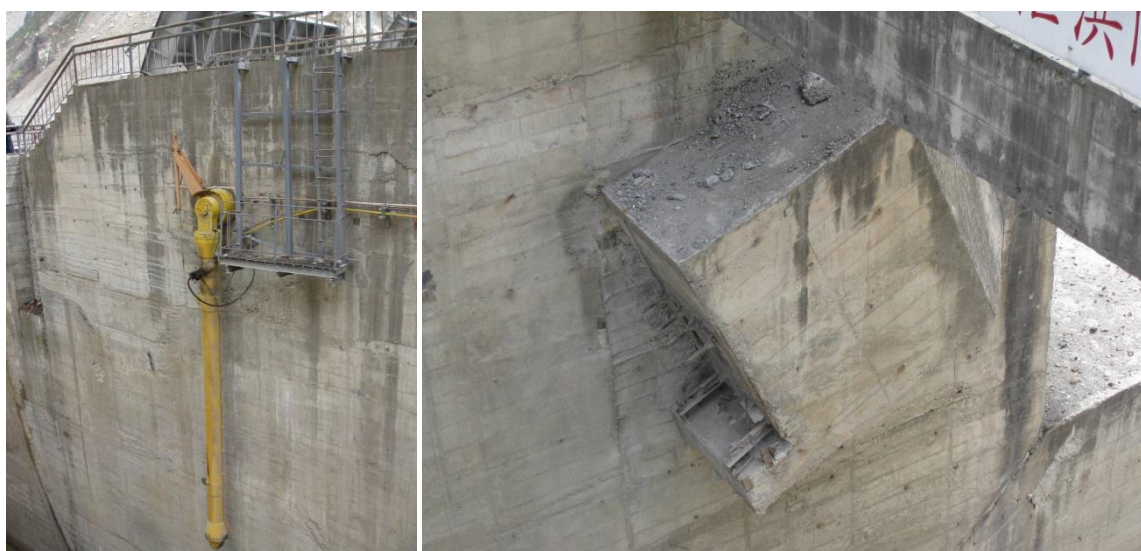


Figure 4: Left-over of radial gate destroyed by rockfall during Wenchuan earthquake in China [5]

In conclusion the main failure modes of spillways are those preventing opening of the spillway gates after a strong earthquake. This is of main concern for embankment dams as overtopping will ultimately lead to dam failure, but of lesser concern for concrete dams, where limited crest overtopping can be accepted. Failure modes, which include the failure of gates, as shown in Fig. 2, where water can escape through the open space, are less dangerous than those leading to an embankment dam failure. However, this failure mode is critical, when the water can escape through all spillway openings as it may create a flood similar to that expected during the passage of the safety flood (or probable maximum flood). This may be the worst case for concrete dams. Therefore, blockage of gates and full destruction of gates must be considered.

In the case of blockage of all gates the responsible parties like to refer to blasting of the gates as the last resort. But this has not been done yet in an emergency situation and, therefore, this option cannot be considered as a feasible option.

In most gated spillways, the gates are of the same type; therefore, if a gate or its electro-mechanical components should be damaged by ground shaking, then the other gates may have the same problem. Therefore, the redundancy principle, which is important in any probabilistic safety analysis, no longer holds and the probability that one or all gates fail during a strong earthquake is the same. This can also be seen in Fig. 1.

The structural failure mode analysed in this paper is failure mode (ii) and includes the seismic safety of the spillway piers subjected to ground shaking. However, this discussion shows that the seismic safety assessment of existing gated spillways and the design of new gated spillways may be a rather complex and comprehensive task. The analysis of functionality of a radial gate after a strong earthquake is mainly based on deformation analyses of the gates and piers, whereas the gate failure is mainly a problem of the gate support and the anchorage of the static and seismic support reactions, which can be done by the analysis of both the strength and deformations.

3. SEISMIC ANALYSIS OF SPILLWAY PIER

3.1. INTRODUCTION AND CASE STUDY

Spillway gates are vulnerable to inelastic deformations caused by strong earthquakes as they can be jammed due to additional hydrodynamic forces, which were not considered in the design, or due to cross-river deformations or inadequate sliding and overturning stability of the slender spillway piers.

Seismic design concepts and design criteria for large dam projects have undergone substantial changes since their first introduction in the 1930s, therefore the earthquake safety of gated spillways, built in the past, is uncertain.

The spillway piers were usually reinforced with minimum temperature and shrinkage reinforcement. In some construction practices a contraction joint is provided in the middle of the spillway pier, reducing the effective thickness of the pier to half. Deformations of the spillway pier in cross-river direction are important for operation of the radial gates. These deformations shall be limited so that the radial gates can be operated after

the SEE, provided that they do not experience any inelastic deformations and that all other equipment is functioning properly.

As a case study the spillway section, shown in Fig. 5 is investigated. The spillway system includes 7 radial gates located at the crest of an ogee spillway weir. The height of the spillway pier above ogee crest is 23.20 m. The width of each surface radial gate is 16.5 m and the piers in between are 6.0 m thick. Contraction joints are provided at the center of each pier. The spillway bridge is composed of simply supported precast bridge girders, therefore the transverse (in cross-river direction) deformations of the pier are not restrained by the spillway bridge. The vertical reinforcement of the spillway piers consists of diameter 25 mm bars at 200 mm spacing. No shear reinforcement is provided. The dynamic compressive and tensile strengths of concrete are taken as 31.5 and 3.4 MPa, respectively.

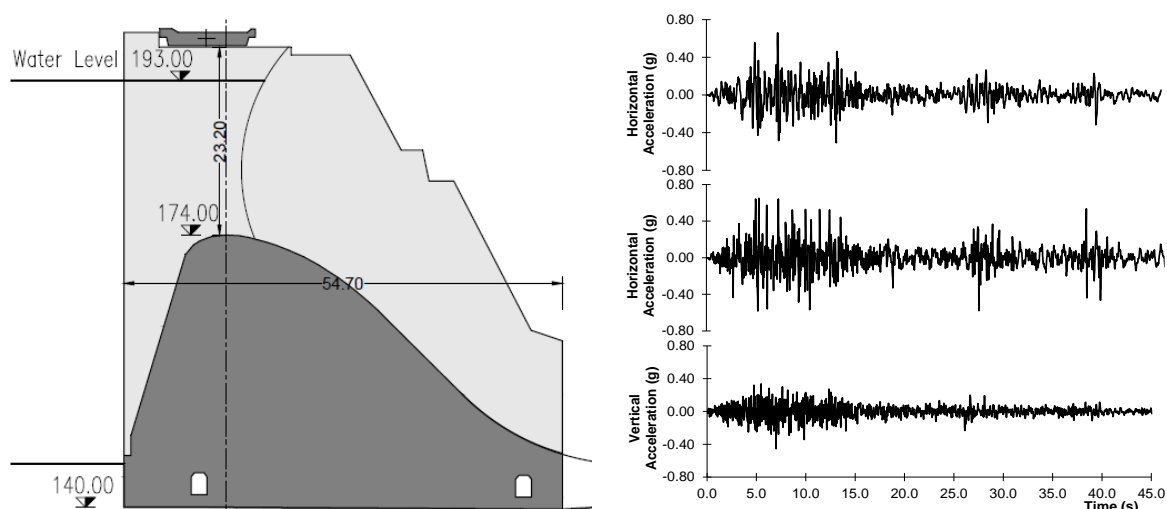


Figure 5: Cross-section of spillway pier with ogee, radial gate and bridge (left), and spectrum-matched acceleration time histories of horizontal and vertical components of the Safety Evaluation Earthquake with peak ground acceleration of 0.65 g (horizontal) and 0.45 g (vertical)

3.2. METHODOLOGY AND BASIC ASSUMPTIONS FOR SEISMIC ANALYSIS OF SPILLWAY PIER

The seismic behaviour of the pier was first investigated by a response spectrum analysis. This analysis was performed using linear material properties and the uncracked stiffness. The results showed that the spillway pier will experience significant seismic deformations at the top and the moment capacity of the pier is far more less than the seismic demand. Therefore, the pier will crack in flexure and considering the under reinforced pier, the tensile reinforcement will fracture. The crack may extend through the pier thickness which will detach the pier from the ogee mass concrete. As a result, a rigid body dynamic rocking analysis of the pier is performed in cross-river direction and the maximum displacement at top of the pier is computed.

Three sets of scaled acceleration time histories are used for the time history analysis of the pier. Each set includes the acceleration time histories of the two horizontal and vertical components of the SEE (Fig. 5).

The pier is assumed to be fixed at the connection with the ogee section. The hydrostatic water pressure on the radial gates is applied as a concentrated force at the location of trunnion supports. The added mass of water on gates in along-river direction is considered at the location of the trunnion. The added mass of water in cross-river direction is neglected. The mass of concrete bridge is applied at the nodes at the top of the pier. For the earthquake analysis the direct time integration method was used.

The acceleration time histories, peak accelerations and the acceleration response spectra at the trunnion elevation and at top of the pier, i.e. bridge support, are obtained from the time history analysis.

3.3. EIGENFREQUENCY ANALYSIS

In the first step of the dynamic analysis the vibration characteristics of the structure are computed, which include the eigenfrequencies and mode shapes. The natural periods of vibration of the four modes of vibration shown in Fig. 6 are 0.35 s, 0.20 s, 0.12 s and 0.09 s.

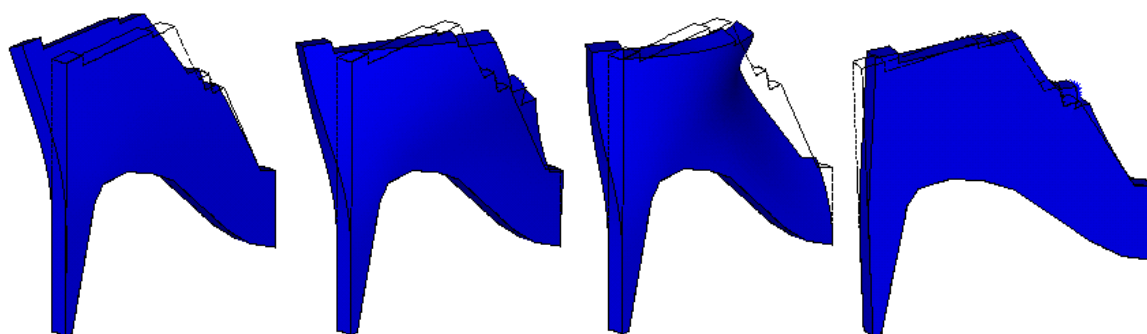


Figure 6: First four vibration mode shapes of the spillway pier

3.4. LINEAR TIME HISTORY ANALYSIS

The linear elastic dynamic analysis of the pier was carried out using three different acceleration time histories. Fig. 7 shows the time histories of the absolute acceleration and displacement in cross-river direction on top of the pier for one of the three ground motions. The maximum value of absolute acceleration is about 1.6 g, which is about 2.5 times the peak ground acceleration. The maximum top displacement of the slender pier is about 70 mm.

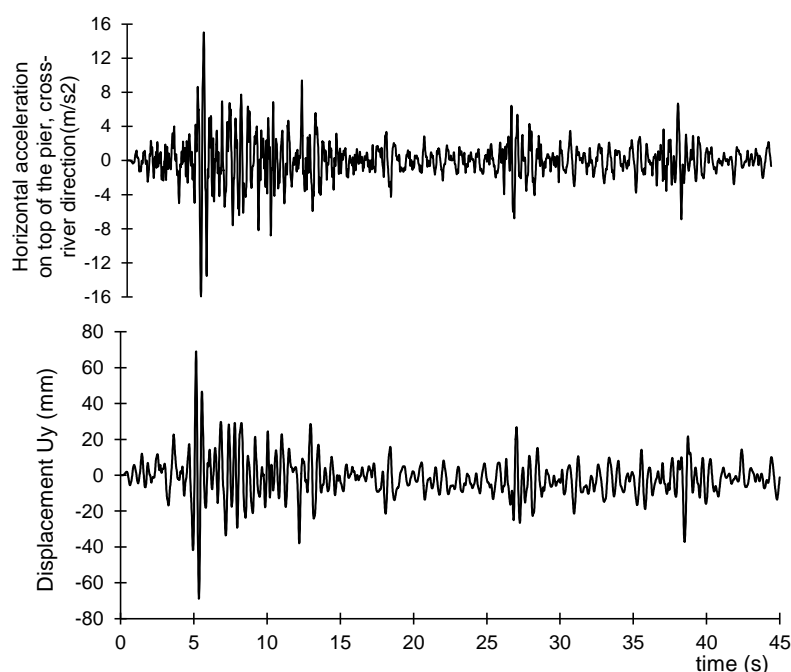


Figure 7: Time histories of absolute acceleration (top figure) and relative displacement (bottom figure) in cross-river direction on top of the spillway pier

Figure 8 shows the time history of the bending moment in the spillway pier at the ogee elevation as well as the dynamic cracking moment. For the axial compressive force of 1000 kN, the dynamic cracking moment of the 3.0 m thick concrete pier is 5600 kNm/m.

The spillway piers were normally reinforced with minimum temperature and shrinkage reinforcement. In the analyzed prototype the reinforcement at the location of the maximum bending moment (near the ogee crest) is diameter 25 mm at 200 mm spacing. For this section the nominal moment capacity of reinforced concrete section is less than the cracking moment of concrete. As yielding and nominal moment capacities of the pier are less than the cracking moment, brittle failure is expected.

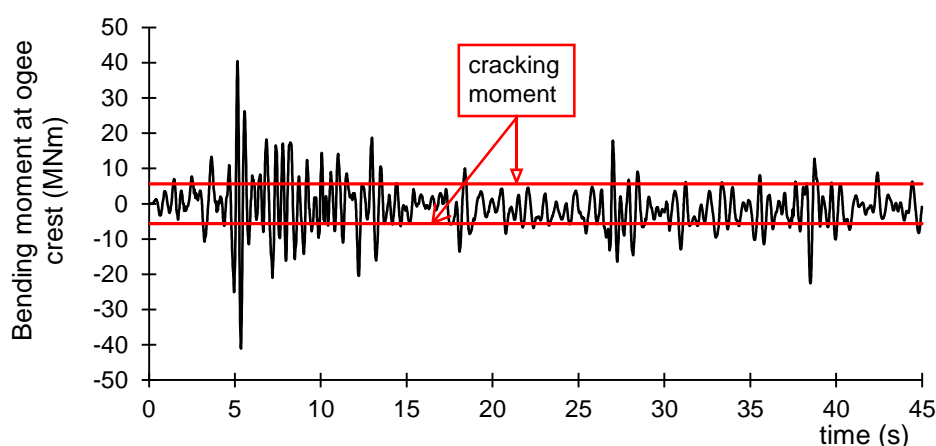


Figure 8: Bending moment time history at bottom of pier, dynamic cracking moment is shown in red

3.5. DYNAMIC STABILITY ANALYSIS OF SPILLWAY PIER IN CROSS-RIVER DIRECTION

The results of the linear-elastic time history analyses have shown that the concrete pier will crack in flexure and as the section is lightly reinforced, fracture of flexural reinforcement is probable. Therefore, it can be assumed that the pier will fracture at the elevation of horizontal lift joints close to the ogee crest and that the part of the pier above that crack is separated from the base of the spillway. Accordingly, a dynamic stability analysis was carried out for the separated concrete block of the spillway pier, including a rocking and sliding block analysis in cross-river and along-river directions, respectively. The concrete block separated by a horizontal crack is assumed to be rigid.

It is worth noting that in a seismic rigid body analysis several assumptions have to be made, especially those related to the crack separating the upper part of the pier from the lower one at ogee elevation.

The detached part of the spillway pier will eventually overturn if an overturning moment higher than the resisting moment is applied and sustained. However, under earthquake excitation, large overturning moments occur for only a fraction of a second in each cycle. Although rocking occurs, the structure may not become unstable as rocking motion about a horizontal surface is a reversible process.

Figure 9 shows the maximum cross-river displacement at the top of the detached pier obtained from a rigid body rocking analysis due to three sets of earthquake time histories. The maximum cross-river displacement varies from about 170 to 280 mm and occur at different times. In this figure also along-river sliding displacements obtained from a rigid body sliding analysis due to three sets of earthquake time histories are shown. The maximum residual displacement of about 75 mm is estimated assuming that the ogee block under the pier will not experience any displacements in case of earthquake.

From Fig. 9 it can be clearly seen that after the earthquake there is no residual tilting of the pier, however, sliding is a cumulative process, which continues if the duration of strong ground shaking would be extended. This is not the case for the rocking motion where the duration of strong ground shaking has hardly any effect on the maximum cross-river displacement.

These rigid body displacements may be different at the two supporting piers of the radial gate and may lead to gate damage and/or jamming of the gate.

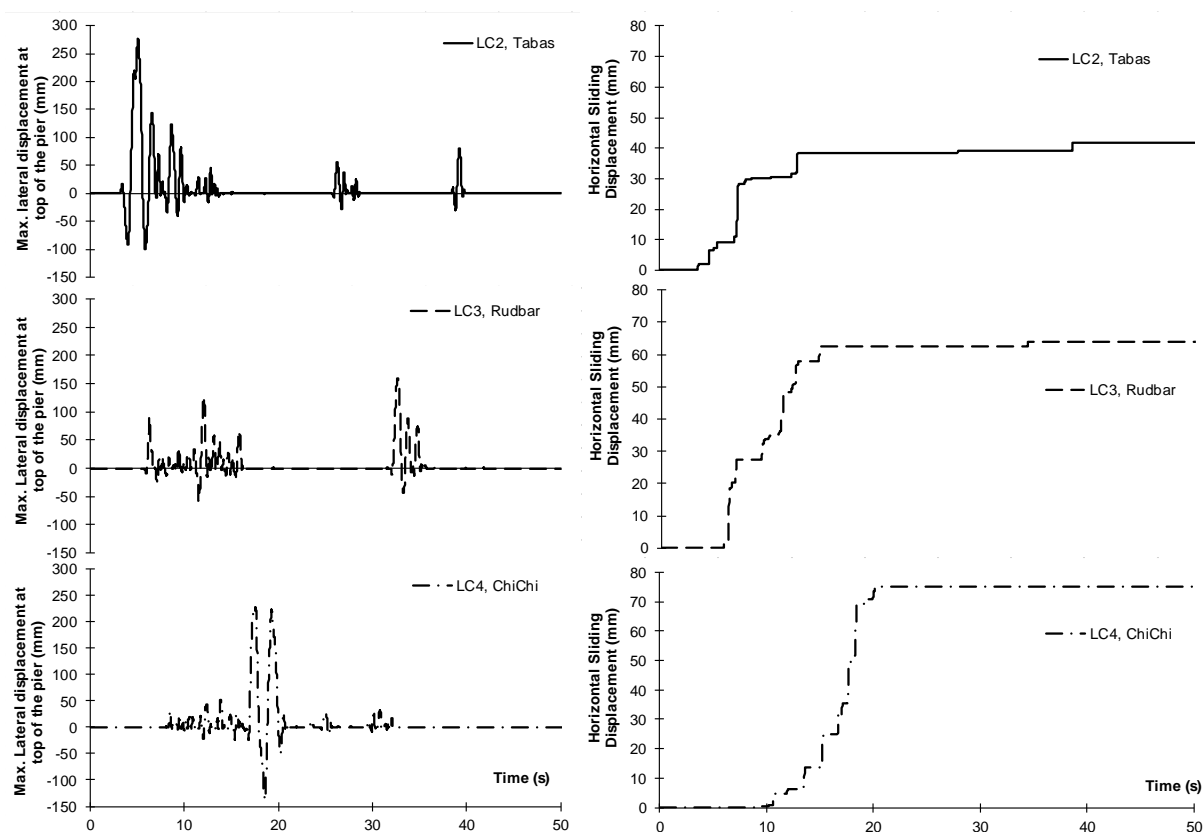


Figure 9: Rocking motion and sliding displacement of detached concrete pier: Time histories of cross-river displacement at top of spillway pier (left) and along-river sliding displacement (right) due to three spectrum-matched acceleration time histories with peak ground acceleration of 0.65 g

4. DISCUSSION OF SEISMIC PERFORMANCE OF SPILLWAY PIER

Inelastic deformations of the spillway pier in cross-river direction will endanger proper functioning of the spillway gates. The linear-elastic dynamic analysis of un-cracked pier of an existing spillway showed that the maximum dynamic cross-river deflection at the top of the pier can be about 70 mm during the SEE. This value will increase if the cracked stiffness of the pier is taken into account.

The maximum bending moment demand of the spillway pier exceeds the cracking moment capacity of concrete at the base of the pier. As the spillway pier analysed is under-reinforced, it is likely that cracks extend through the whole pier during SEE and the spillway pier be separated from the massive ogee structure by a horizontal crack. The maximum displacement of the rigid body rocking analysis of the detached concrete pier in cross-river direction is 280 mm while the horizontal sliding displacement in along-river direction is 75 mm.

The high deformations obtained from the dynamic analysis and high flexural demands signify the necessity of strengthening of the spillway piers.

5. CONCLUSIONS

The main seismic failure modes of gated spillways are (i) failure of opening of the gates after an earthquake causing overtopping of the dam body and failure of embankment dams - limited overtopping of concrete dams may be accepted -, and (ii) structural failure of the gates, resulting in uncontrolled release of water from the reservoir and flooding of the downstream region of the dam. Therefore, the following conclusions may be drawn:

- Spillway gates must be functioning after the safety evaluation earthquake (SEE), i.e. the seismic design criteria for the gated spillway must be the same as those for the dam body.

- The earthquake hazard is a multi-hazard and all hazards must be considered in the seismic safety check. Besides ground shaking, rockfalls may damage gates and or the electro-mechanical equipment and power supply needed for opening the gates.
- Appropriate methods of dynamic analysis must be selected, taking into account the dynamic characteristics of the gates and piers as well as the oscillating nature of the earthquake ground motion. The pseudostatic analysis method shall no longer be used as it is obsolete and gives incorrect results.
- Spillway piers must be able to withstand the seismic action in along-river and cross-river directions. The cross-river direction is most critical for slender piers. The resulting pier deformations may damage the gate due to pounding near the top, causing jamming. The cross-river component has been ignored in most existing spillways.
- In cases where the spillway gates and piers have been designed for the operating basis earthquake ground motion, a check for the SEE must be carried out as the gate must be functioning after the SEE.
- The dynamic rocking stability analyses show that the maximum cross-river deformation at the top of the pier depends strongly on the seismic input used, even for the case where the acceleration time histories match the same target response spectrum.

6. REFERENCES

1. ICOLD (1989), “*Selecting Seismic Parameters for Large Dams*”, Guidelines, Bulletin 72, Committee on Seismic Aspects of Dam Design, International Commission on Large Dams (ICOLD), Paris.
2. ICOLD (2016), “*Selecting Seismic Parameters for Large Dams*”, Guidelines, Bulletin 148, Committee on Seismic Aspects of Dam Design, International Commission on Large Dams (ICOLD), Paris.
3. Westergaard H.M. (1933), “*Water Pressures on Dams during Earthquakes*”, Transactions of American Society of Civil Engineers, 98(2): 418-433.
4. Wieland M. (2012), “*Seismic Design and Performance Criteria for Large Storage Dams*”, Proc. 15th World Conf. on Earthquake Engineering, Lisbon, Portugal, Sep. 24-28.
5. Wieland M. (2017), “*Seismic Aspects of Safety-relevant Hydro-mechanical and Electro-mechanical Elements of Large Storage Dams*”, Proc. Symposium, 85th Annual Meeting of International Commission on Large Dams, Prague, Czech Republic, July 3-7.

Spectrum Response Analysis of Concrete Face Rock Fill Dam, Case Study Bakun Dam

Behrouz Gordan¹, Azlan Adnan²

1. Civil Engineering Department, Islamic Azad University, Gorgan Branch, Iran

2. Engineering Seismology and Earthquake Engineering Research Group (e-seer), Universiti Teknologi Malaysia 81310 Skudai, Johor, Malaysia

Email: bh.gordan@yahoo.com

Abstract

The response spectrum analysis of the Bakun dam on the east of Malaysia is evaluated in this study. The scope of study is based on two macro zone maps with probability exceeding such as 10% (500 years) and 2% (2500 years) in 50 years. The response spectrum of the site is provided using ASCE7. In terms of spectrum response analysis, the Finite-Element method is applied using Ansys13 program. Based on the free vibration analysis, it can be concluded that the initial vibration mode was critical with respect to the minimum frequency. The relation between frequency and mode shape was the nonlinear trend. The maximum and minimum displacements were located on the site class (E) and (A) for both directions. This value was doubled in 2500 years in comparing to 500 years. The maximum horizontal and vertical displacements were at the crest and the upper half of upstream and downstream, respectively. The body crack was possible on the slope surface for 500 years based on the relative displacement. Consequently, the data monitoring is necessary in order to control dam.

Keywords: Spectrum, Modal, Displacements, CFRD dam, Crack.

1. INTRODUCTION

The dynamical analysis process was started after some huge damages of the earth dams. Much significant destruction during an earthquake was recorded. As a significant approach, the structural failure is a very critical aspect in the earthen dam. In the case of failure process, the basic role was based on some specific factors such as piping and overflow. Both of them are created by body crack. However, the body crack can be led by relative displacement. Therefore, reduction of the relative displacement in the structure is very important to control body crack. Besides, a construction method in earth dam is the gradual process. Therefore, the static settlement can be created during the consolidation development. Consequently, in order to generate relative displacement during an earthquake, the dynamical settlement can be made. According to the literature, the dynamical settlement is distinguished by experience and engineering opinion [1-3]. However, the prediction of dam behavior under the strong earthquake was necessary in the high seismic zones. The main concern in the design was the security while it was widely accepted that the (CFRD) performance under the earthquake was plastic deformation and settlement, but without a change of slope [4-7]. The concrete face rock-fill dam with additional challenges during an earthquake was designed while the physical face has been just a water stop and not a structural element of the dam's configuration. Therefore, the control of dam behavior is necessary at design stage. To date, the design effort is limited to avoid failure, minimize the crack making to ensure valid behavior of concrete joints. Moreover, materials are taken to avoid of the generate pore water pressures to develop in the dam's body during and after strong seismic loading [8]. Numerous studies have been attempted to explain some methods in order to evaluate the dynamic deformation range from simple analytical tools regard the three dimensional (3D) numerical models [4, 6, 7 and 8]. In terms of numerical analysis, some case studies were investigated widely. Recently, the numerical analyses are carried out to evaluate the structure (CFRD) during dynamical load [9, 10]. In addition, the dam was safe under the strongest earthquake, while it was well designed and compacted on the rock foundations [11]. In addition, settlement analysis of the Mornos earth dam was carried out with respect to the monitoring data [12]. This paper tried to evaluate the response spectrum analysis of the Bakun dam using ASCE7. In the case of this study, there are two main purposes. Firstly, the structural behavior can be estimated by response spectrum analysis. Secondly, the step by step of the design process can be reviewed using Finite-Element

Method (FEM). It should be noted that, this analysis included two periods such as 500 and 2500 years. Both periods were developed by macro zone maps in the case of 10% and 2% of probability in 50 years ground motions in the east of Malaysia [13].

2. BAKUN DAM

The hydroelectric dam on the river Balui in Belaga district of Sarawak in Malaysia since 1996 until 2011 was built. Respectively, the dam situation and dam perspective show in Figure 1 (a-b). There are some dams in the east of Malaysia. The location dams and stations network show in Figure 1(c). In order to distribute the station, there are two stations in the east of the map. It seems to be that, the stations in this area should increase in regards to the situation of the second highest earth dam that located in this zone.



Figure 1. a) Situation of Bakun dam (CRFD), b) The dam perspective before reservoir, c) Dams location of national seismological network, 8 dams and 14 stations in Malaysia

3. PEAK GROUND ACCELERATION

The peak ground acceleration (PGA) maps in Malaysia are available for two periods such as 500 years and 2500 years (Adnan et al, 2008). However, both macro zone maps for 10% and 2% probability of exceeding (PE) in 50 years ground motions in the east of Malaysia is available. It can be seen in Figure 2. In terms of the hazard level, the previous results indicated that the ground motions across the east Malaysia range between 60-120 (gal) for 10% in 50 years and 160-220 (gal) for 2% in 50 years.

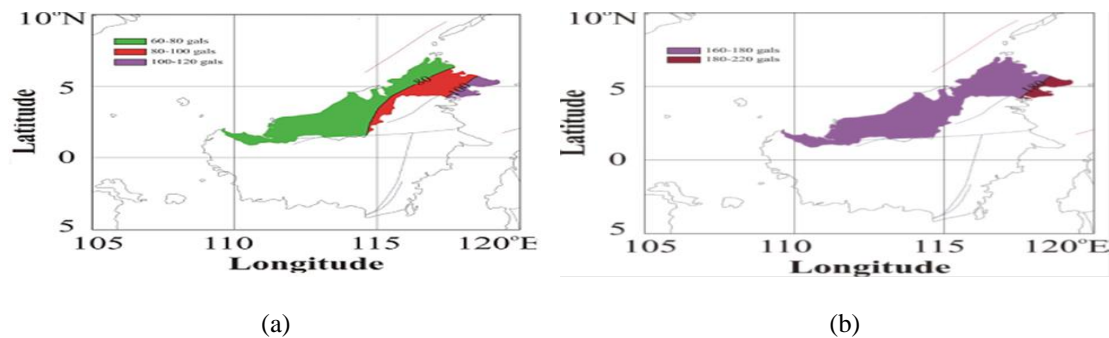


Figure 2: a) PGA map for 500 years, b) PGA map for 2500 years

4. RESPONSE SPECTRA ASCE

The input data for response spectra analysis is carried out using ASCE 7. It can be driven following below process.

4.1. SEISMIC GROUND MOTION PARAMETERS AND SITE CLASS

Both parameters S_5 and S_1 are determined from the 0.2 seconds and 1.0 seconds of the spectral response accelerations, respectively. The different site classes are classified based on the soil properties. Therefore, they have categorized [A, B, C, D, E, or F] that introduced strong soil to soft condition. It should be noted that while the soil properties have not known in sufficient detail to determine the site class, site class [D] should be used unless the authority having jurisdiction or Geotechnical data determines site class [E] or [F] soils are present at the site (ASCE7). The site classification presented in Table 1.

Table 1: Site classification

Site Class	h_s	R or R_{eq}	h_v
A. Hard rock	>5,000 ft/s	NA	NA
B. Rock	2,500 to 5,000 ft/s	NA	NA
C. Very dense soil and soft rock	1,200 to 2,500 ft/s	>50	>2,000 psf
D. Stiff soil	600 to 1,200 ft/s	15 to 50	1,000 to 2,000 psf
E. Soft clay soil	<600 ft/s	<15	<1,000 psf
	Any profile with more than 10 ft of soil having the following characteristics: - Plasticity index $PI > 20$, - Moisture content $\geq 40\%$, and - Undrained shear strength $h_u < 500$ psf		
F. Soils requiring site response analysis in accordance with Section 21.1	See Section 20.3.1		

4.2. SITE COEFFICIENTS AND ADJUSTED MAXIMUM CONSIDERED EARTHQUAKE (MCE) SPECTRAL RESPONSE ACCELERATION PARAMETERS

The MCE spectral response acceleration for two periods (S_{MS}) and (S_{M1}), adjusted for site class effects, shall be determined by equations 1-2, respectively.

$$S_{MS} = F_a * S_s \quad \text{When } T=0.2 \text{ second} \quad (1)$$

$$S_{M1} = F_v * S_1 \quad \text{When } T=1.00 \text{ second} \quad (2)$$

S_s = the mapped MCE spectral response acceleration at short periods of 0.20 seconds was specified 0.15 and 0.30 for 500-2500 years, respectively [14].

S_1 = the mapped MCE spectral response was acceleration in a period same 1.00 seconds. In case of 500 years or 2500 years (Adnan et al, 2005), this value 0.05 and 0.10 are respectively obtained. It should be noted that, the straight-line interpolation for intermediate values of S_s and S_1 can be used. Besides, two new parameters are shown using equation 3 and 4 in the case of acceleration spectrum curve.

$$S_{DS} = 2/3 * S_{MS} \quad (3)$$

$$S_{D1} = 2/3 * S_{M1} \quad (4)$$

Besides, both of the site coefficients such as F_a and F_v are driven by Table 2 and Table 3 respectively (ASCE7).

There are two key points at the top of spectrum response curve. These points are driven by both periods in equation 5 and equation 6.

$$T_0 = 0.2 * S_{D1} / S_{DS} \quad (5)$$

$$T_s = S_{D1} / S_{DS} \quad (6)$$

According to equations 1-6, the acceleration spectrum curve is obtained using ASCE 2007. Figure 3 shows this curve.

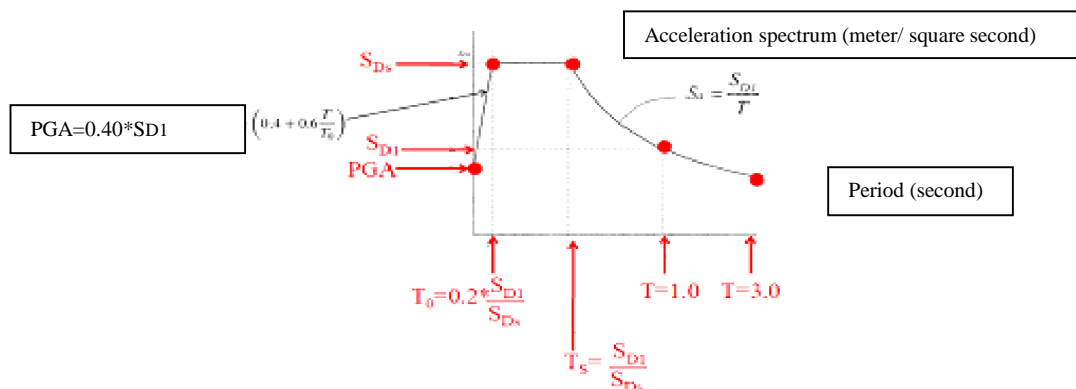


Figure 3: ASCE Acceleration spectrum curve. The period and acceleration spectrum was matched by horizontal and vertical axis

In terms of the response spectrum acceleration in Malaysia, both curves are computed and all factors are shown in tables 4-5.

Table 2: Site Coefficient, (F_a)

Site Class	Mapped Maximum Considered Earthquake Spectral Response Acceleration Parameter at Short Period (t=0.20 s)				
	$S_s = 0.25$	$S_s = 0.5$	$S_s = 0.75$	$S_s = 1.0$	$S_s = 1.25$
A	0.8	0.8	0.8	0.8	0.8
B	1.0	1.0	1.0	1.0	1.0
C	1.2	1.2	1.1	1.0	1.0
D	1.6	1.4	1.2	1.1	1.0
E	2.5	1.7	1.2	0.9	0.9
F	See Section 11.4.7 (ASCE 7 criteria)				

Table 3: Site Coefficient, (F_v)

Site Class	Mapped Maximum Considered Earthquake Spectral Response Acceleration Parameter at Period (t=1.00 s)				
	$S_s = 0.1$	$S_s = 0.2$	$S_s = 0.3$	$S_s = 0.4$	$S_s = 0.5$
A	0.8	0.8	0.8	0.8	0.8
B	1.0	1.0	1.0	1.0	1.0
C	1.7	1.6	1.5	1.4	1.3
D	2.4	2.0	1.8	1.6	1.5
E	3.5	3.2	2.8	2.4	2.4
F	See Section 11.4.7 (ASCE 7 criteria)				

Table 4: The acceleration spectrum factors for return period earthquake 500 years 2500 years

500 Years	A	B	C	D	E
(F_p)	0.8	1	1.7	2.4	3.5
(F_a)	0.8	1	1.2	1.6	2.5
SMs	0.12	0.15	0.18	0.24	0.375
SM1	0.04	0.05	0.085	0.12	0.175
SDs	0.08	0.1	0.12	0.16	0.25
SD1	0.02666	0.03333	0.05666	0.08	0.11666
TO	0.06666	0.06666	0.09444	0.1	0.09333
TS	0.33333	0.33333	0.47222	0.5	0.46666

Table 5: The acceleration spectrum for return period earthquake

2500 Years	A	B	C	D	E
(F_p)	0.8	1	1.7	2.4	3.5
(F_a)	0.8	1	1.2	1.56	2.34
SMs	0.24	0.30	0.36	0.46	0.702
SM1	0.08	0.10	0.17	0.24	0.350
SDs	0.16	0.2	0.24	0.31	0.468
SD1	0.05333	0.06666	0.11333	0.16	0.23333
TO	0.06666	0.06666	0.09444	0.10	0.099715
TS	0.33333	0.33333	0.47222	0.51	0.498575

The spectrum acceleration curves for different soils are provided, as can be seen in Figure 4. In the case of measurement unit, the horizontal and vertical axes are period (Seconds) and acceleration (gravity)

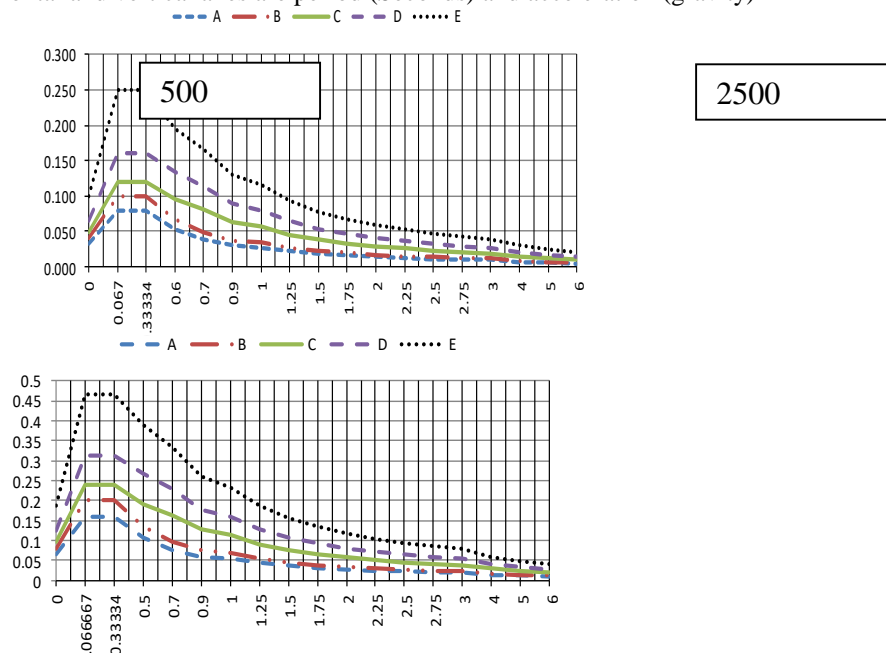


Figure 4. Acceleration spectrum, Vertical axis is acceleration, and horizontal axes is time

5. MODELING PROCESS

The modeling process was carried out following below process. The ANSYS program is based on the Finite - element method. A strong ability to compute the free vibration analysis is possible with respect to use modal analysis. In particular, it is one of the universal programs with high abilities for different analyses like response spectrum.

Moreover, other analysis like time-history is also available. Briefly, the result of free vibration analysis was used for response spectrum in this research.

5.1. ELEMENTS AND BOUNDARY CONDITIONS IN THE MODAL ANALYSIS

In the case of suitable element, solid42 in the model was applied. This element was recommended by help menu for 2D condition. The modal analysis was carried out while the model was coupled on the bedrock. Therefore, the both displacements for bedrock are assigned with zero value in order to effect of the degree of freedom.

5.2. CONFIGURATION, MATERIAL PROPERTIES OF DAM, MESH AND PROCESSING CHART

The dam is 205 meters height with a crest length of approximately 750 meters and tank volume of about 43.8 billion cube meter. To assess the road transport, the width at the crest was 12 meters. The face of rock-fill dam was built by concrete slab instead of riprap on the upstream. The different gradient was in both slopes. The upstream and downstream are located by 1.4H and 1.3H respectively, while 1v was fixed for both. The maximum section of dam with different zones shows in Figure 5. Furthermore, the concrete face with horizontal and vertical contraction joints shows in Figure 5. In terms of the material properties, the relative density and linear properties were used in this study. It is illustrated in Table 6. Based on the linear properties, the elasticity modulus and Poisson ratio for modal analysis and response spectrum analysis were used. Mesh process is possible with two methods such as regular and free based on the programming ability. Regular mesh to access the best interaction effect between different materials was used, as shown in Figure 5. Furthermore, Figure 6 shows the chart process in this study. Three steps are connected such as input data, free vibration analysis, and spectrum analysis.

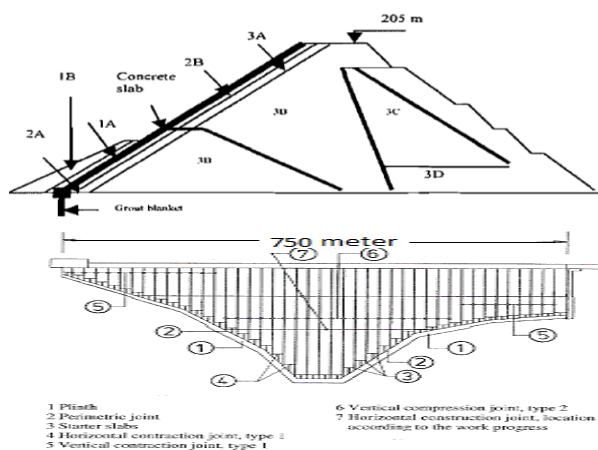
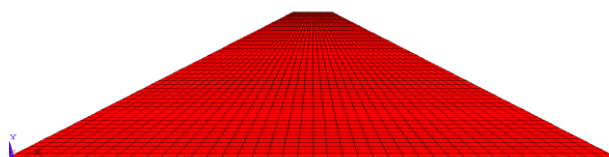


Figure 5: a) The dam section with different zones, b) Upstream face of dam,



c) Meshing

Table 6: Material properties

Zone	Elasticity modulus (Kg / m ²)	Poisson's Ratio	Relative Density (Kg / m ³)
Concrete slab Thickness (0.30m)	3.20E9	0.20	2400
2B-Cushion	3.20E7	0.30	2280
2A-Transition	1.60E9	0.30	2250
2B-Rockfill	1.00E9	0.30	2130
2C-Rockfill	1.00E9	0.30	2060
2D-Rockfill	1.00E9	0.30	2050

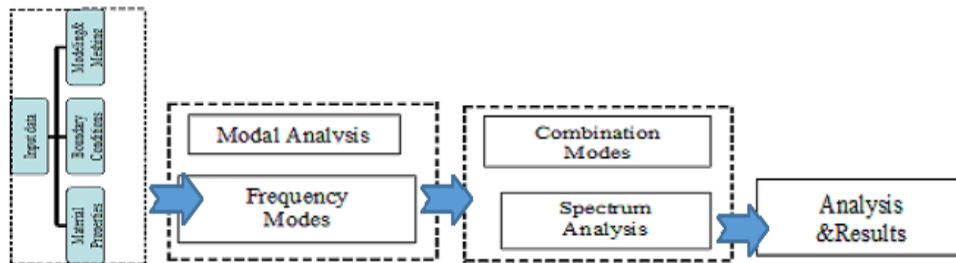


Figure 6. Chart Processing

6. ANALYSIS AND RESULTS

In the case of free vibration modes, the modal analysis was carried out using simulation. Generally, the best computational accuracy of the response spectrum was the main purpose. It was possible according to compute model with more vibration mode. In fact, the combination method is used for spectrum analysis. However, the spectrum analysis depends on the modal analysis in particular. In terms of frequency distribution, twenty vibration modes were collected as presented in Table 7.

Table 7: Frequency in twenty mode shapes of dam

Mode	Frequency	Mode	Frequency	Mode	Frequency	Mode	Frequency
1	1.222	6	3.233	11	4.775	16	5.691
2	1.823	7	3.563	12	4.961	17	5.810
3	2.152	8	3.816	13	5.051	18	6.275
4	2.658	9	4.251	14	5.464	19	6.571
5	3.182	10	4.439	15	5.661	20	6.648

The frequency trend indicated the incremental behavior when the vibration mode was increased. However, the relation between period and frequency is the reverse performance (See Equation 7). In the case of measurement unit, period is seconds and frequency is hertz.

$$T = 1 / f \tag{7}$$

In terms of dam behavior in different vibration modes, ten vibration modes are shown in Figure 7. It can be seen that; deformation is different for each mode. Besides, displacement in both directions and frequency are shown in the above on the left side in each mode. In fact, the maximum period is obtained in the first vibration mode with respect to the minimum frequency. Therefore, frequency was dominant in the first vibration mode.

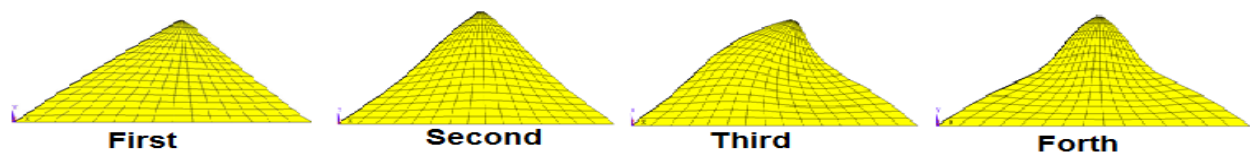


Figure 7: Different vibration modes

In addition, the frequency is expressed by equation 8 when the regression was at a high level of accuracy equal 0.997.

$$y = 1.21 x^{0.565} \tag{8}$$

The response spectrum analysis was carried out after collection results from modal analysis, as discussed. This analysis depends on frequency as distributed in different modes.

The Spectrum analysis was computed by the combination method with high level of accuracy. The input data were applied according to the response acceleration curves that shown in Figures 7-8. However, the square root sum of squares (SRSS) method in order to combine external data from modal analysis was used. This method is one of the full applicable approaches regarding program ability (ANSYS13). As a result, displacements in both periods such as 500 years and 2500 years are shown in Figures 8 for site class A. As shown, dam displacement illustrated in both directions. However, the horizontal displacement was maximized at the crest while it was the minimum value for bedrock. In addition, this value is increased while the site condition focuses on the soft soil. Furthermore, the peak level of vertical displacement is at both slopes while it is minimized in the bedrock. As a significant result, both displacements are decreased in this area. It means that the soil amplification was carried out. Besides, maximum vertical displacement occurred in the upper half of the gradient. Moreover, the maximum horizontal and vertical displacement show in Table 8. It was found that, the horizontal displacement is more than vertical displacement, significantly.

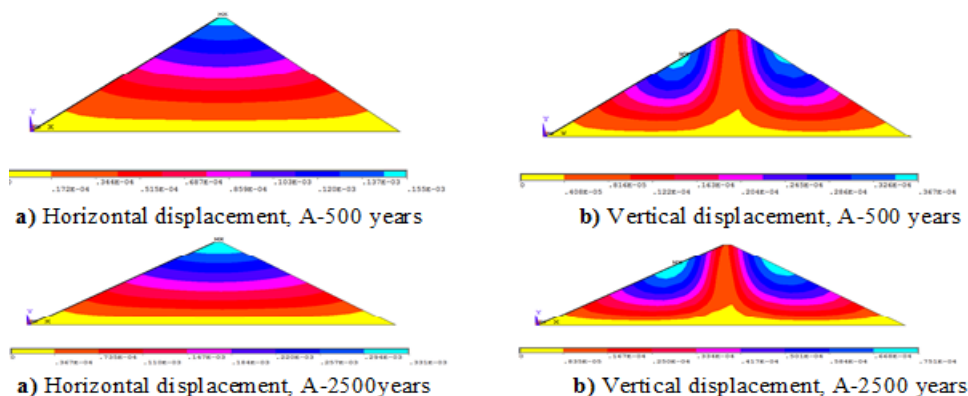


Figure 8. Distribution of displacements in different site class for 500 years returns earthquake period

Table 8: Maximum displacements in site classes (A to E) for 500 to 2500 years, measurement unit is meter.

Horizontal	500 years	2500 years	Vertical	500 years	2500 years
A	1.55E-04	3.31E-04	A	3.67E-05	7.51E-05
B	2.06E-04	4.12E-04	B	4.66E-05	9.36E-05
C	3.50E-04	7.02E-04	C	7.92E-05	1.59E-04
D	4.95E-04	9.90E-04	D	1.12E-04	2.25E-04
E	7.21E-04	1.44E-03	E	1.63E-04	3.28E-04

The distribution of displacement is shown in Figure 9 and Figure 10 in order to effect of the site classes (A- E). Both displacements were located more than quadruple on soft soil in comparison hard soil. The displacement ratio between both periods such as 500 and 2500 years was demonstrated double. Consequently, body cracks will be available by more probabilities due to the relative vertical displacements for 500 years. However, spectrum analysis is the prediction of dynamic behavior based on the linear method. On the other hand, one of the main concerns of the dam is the optimal utilization. It seems to be that; the installation of monitoring equipment is very useful suggestion to control dam. Finally, this project shows the design process, as can be used in the same structures step by step based on the response spectrum analysis.

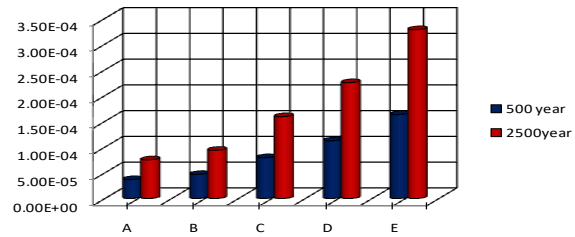
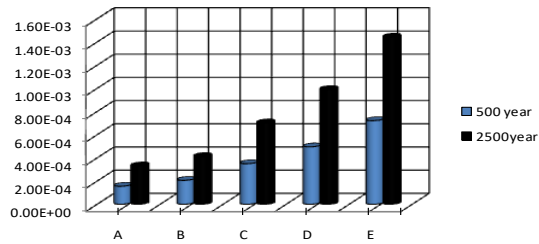


Figure 9. Maximum horizontal displacement **Figure 10: Maximum vertical displacement**

7. CONCLUSIONS

The response spectrum analysis of the CFRD dam (Bakun dam) case study was carried out using the Finite-Element method in the present study. According to the modal analysis, the dominant frequency was in the first vibration mode with minimum values. Frequency is increased with non-linear equation in different vibration modes. In terms of response spectrum analysis, horizontal displacement was maximum and minimum at the crest and bedrock, respectively. The peak of vertical displacement was at both slopes while in the bedrock was reduced significantly. In fact, the high rigidity in the case of the displacement reduction was observed in bedrock. Besides, the maximum vertical displacement was featured on the upper half of gradient surface. Both displacements were located more than quadruple on soft soil in comparison hard soil. The displacement ratio between both periods like 500 years and 2500 years, according to 10% and 2% probability of exceeding (PE) in 50 years was demonstrated double. The body crack was possible on the slope surface for 500 years with respect to assessment of the relative displacement. Consequently, the installation of monitoring equipment is very useful suggestion in the case of dam controlling.

8. REFERENCES

1. Cooke J. (1984). Progress in rock fill dams. ASCE JGE, 110(10), 1381-1414.
2. Cooke J. and Sherard J. (1987). Concrete-face rock fill dam: II. Design. ASCE JGE, 113(10), 1113-1132.
3. Núñez E. (2007). Uncertainties and approximations in geotechnics. Proc. XIII PCSMG, Margarita (Venezuela), 26-39.
4. Makdisi F. and Seed B. (1978). Simplified procedure for estimating dam and embankment earthquakes induced deformation. ASCE JGE, 104(7), 849-867.
5. Gazetas G. and Dakoulas P. (1992). Seismic analysis and design of rock fill dams: State of the art. Soil Dynamic Earthquake Engineering, 11(1), 27-61.
6. Newmark N. (1965). Effects of earthquakes on dams and embankments. Geotechnique 15(2), 139-160.
7. Seed H. (1979). Considerations in the earthquake-resistant design of earth and rock fill dams. Geotechnique 29(3), 215-283.
8. Sherard J and Cooke J. (1987). Concrete-face rock fill dam: I. Assessment. ASCE JGE, 113(10), 1096-1112.
9. X.j. Kong, Y. Zhou, b. Xu, d. g. Zou (2010). Analysis on Seismic Failure Mechanism of Zipingpu Dam and Several Reflections of Aseismic Design for High Rock-fill Dam. Earth and Space 2010: Engineering, Science, Construction, and Operations in Challenging Environments © 2010 ASCE <http://www.ascelibrary.org>
10. A. Bayraktar, M. Emre and Suleyman Adanur (2011). The effect of concrete slab–Rock fill interface behavior on the earthquake performance of a CFR dam. International Journal of Non-Linear Mechanics 46 (2011) 35–46 journal homepage: www.elsevier.com/locate/nlm
11. M. Wieland and P. Brenner. (2007). The Seismic performances of the concrete face rock fill dams under strong ground shaking, and discuss possible problems and deficiencies. International water power & dam construction, April 18-21.
12. V. Gikas and M. I. Sakellariou (2008). Settlement analysis of the MORNOS earth dam (Greece): Evidence from numerical model and geodetic monitoring. Journal homepage: www.elsevier.com/locate/engstruct Engineering Structures 30 (2008) 3074–3081
13. A. Adnan et al. (2008). Advances in earthquake engineering applications, chapter 1. Universiti Teknologi Malaysia.
14. A. Adnan et al. (2005). Seismic hazard assessment for Bakun hydroelectric Project. Structural earthquake Engineering Research, Faculty of civil engineering, Universiti Teknologi Malaysia. ASCE 2007.

Studying the Effects of Non-Uniform Earthquake Excitations on Dynamic Response of Concrete Arch Dams

Fateme Esmaili Soureh¹, Alireza Manafpour², Mohammad Manafpour²
1, 2- Department of Civil Engineering, Urmia University

Email: f.esmaili.68@gmail.com

Abstract

In structures with large dimensions such as bridges and dams, owing to the extent of supports, seismic ground motion at interface of different points of the structure and foundation might vary significantly. These real non-uniform motions in usual designs, due to analytical complexities, has been marginalized. While few studies reveal that for exact evaluation of seismic safety of dam, attention to non-uniform excitation is necessary. This paper studies the seismic response of dam-reservoir-foundation systems subjected to non-uniform motions. A high concrete arch dam is selected as the case-study example and its analytical model is subjected to seismic uniform and non-uniform motions. After performing finite element linear dynamic analysis, the results are compared and assessed. According to the results, imposing non-uniform excitation lead to significant differences in displacement responses and stresses.

Keywords: Non-Uniform Excitations, Linear Dynamic Analysis, Double Curvature Dam.

1. INTRODUCTION

Dams are strategic structures of high importance because of their key role in supplying water for people and agriculture and also generating electricity. Dam failure can cause immense property and environmental damages and take thousands of lives. Therefore, identification of all parameters affecting the safety of arch dams are important. Seismic load is one of the most essential loads which is considered in designing and analyzing processes.

Seismic analysis of dams is usually performed based on the assumption that the earthquake input motions are uniform at different supporting points [1, 2]. In large structures such as dams, long span bridges and piping systems, due to long structure-foundation interface, uniform seismic excitation assumption is not logical and can lead to inaccurate results [1, 3]. Recorded motions have revealed non-uniformity existing along dam-foundation interface at arch dams because of the finite speed of propagation of earthquake waves [1, 4]. Effective factors affecting the ground motion characteristics mainly stem from three mechanisms including “wave passage effect” due to differences in arrival time of waves at supporting points depending on their relative distances away from the source; “incoherency effect” due to reflections and refractions of seismic waves through the soil during propagation that causes changes in amplitude and frequency away from their source; and finally, the “site-response effect” due to differences in local soil conditions at the supporting points [5,6]. Nowak and Hall (1990) analyzed the seismic response of Pacoima dam in two parts and showed that the stresses for a full reservoir were higher than the stresses for an empty one and also non-uniformity in the stream component of the excitation reduced the response [2].

In recent years, few dams are equipped with accelerometers arrays. The accelerometers have been employed at different positions of the dam- foundation interface and have recorded several earthquakes ground motions [7]. Chopra and Wang (2010) computed the responses of two arch dams to spatially varying ground motions recorded during earthquake by developed linear analysis procedure considering dam-water-foundation rock interactions effects. They concluded that the influence of spatially varying ground motion for the same dam could differ from one earthquake to another, depending on the epicenter location and the focal depth of the earthquake relative to the dam site [8].

Sohrabi-Gilani and Gaemian (2012) investigated the seismic response of Karun III dam subjected to spatial variation of ground motions along dam-foundation interface. They studied topographic amplification between various points of the interface by obtaining ratios of the response spectral displacement and spectral pseudo acceleration. Time shift and amplification between stations show the non-uniform nature of ground motions. The results revealed that non-uniform ground acceleration can have extensive effects on dam behavior and can increase the responses [9]. Mirzabozorg et al (2013) investigated the seismic response of dam-reservoir- foundation system subjected to spatially varying ground motion. They utilized Monte Carlo simulation approach for generating spatially non-uniform ground motion. The results showed that the non-

uniform input response is substantially different from uniform input response and can increase the structural response of the system [10].

Research on the responses of dams to earthquake non-uniform support excitations in Iran is limited. So this study aimed to investigate and compare the seismic responses of Karun III dam to uniform and non-uniform support excitations.

2. KARUN III ARCH DAM

Karun III Dam, located in Khuzestan province, Iran, is a 205m high concrete double curvature arch dam. The dam was built with the aim of supplying electric power, flood control and increasing the potential water supply for drinking and agricultural utilization. Figure 1, a) shows a view of Karun III dam and Table 1 indicates the main characteristics of the dam.

An array of 15 accelerometers has been installed in Karun III dam to investigate the dam's response and characteristics of earthquake ground motions at the dam-foundation interface. As it is illustrated in Figure 1,b) channels S₀₁, S₀₂, S₀₃, S₀₅, S₀₆, S₁₁ and S₀₁₅ have been located at the dam-foundation interface and designed to record all three components of any probable acceleration. Channels S₀₄, S₀₇, S₀₈, S₀₉, S₁₀, S₁₂, S₁₃ and S₀₁₄ have been installed within the dam's body.

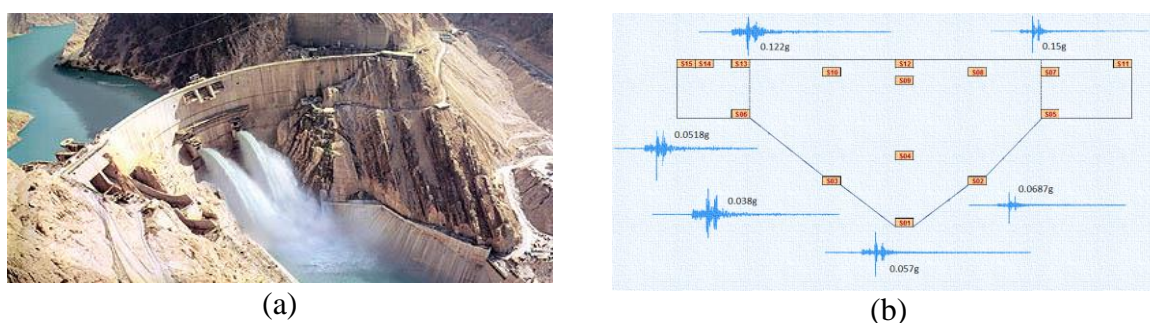


Figure 1. a) View of Karun III dam, b) Location of accelerometer installed on Karun III dam and upstream-downstream component of November 20, 2007 earthquake

Table 1- main characteristics of the dam

Crest level	850 m
Maximum height above the foundation	205m
Crest length	462 m
Crest width	5.5 m
Dam thickness at the base	29 m
Normal level of operation	845 m asl
Minimum level of operation	800 m asl
Reservoir capacity in normal level of operation	2970 Mm ³
Reservoir capacity in minimum level of operation	1250 Mm ³

3. CORRECTED RECORDED GROUND ACCELERATIONS AT DAM-FOUNDATION INTERFACE

A major event has been recorded by this array during dam operations on November 20 of 2007. The recorded ground motion had a PGA of 0.312g at the crest. All recorded accelerations at dam-foundation were corrected by Seismosignal Software, and the corrected records were matched with three seismic performance levels including DBE, MDE and MCE by Sismomatch Software. The PGA of the recorded and corrected ground motions are presented in Table 2.

Table 2- The PGA of the recorded and corrected ground motions

MCE	MDE	DBE	First intensity	Duration	Situation	Row
Corrected intensity	Corrected intensity	Corrected intensity				
0.62g	0.41g	0.275g	0.151g	11s	S07	1
0.58g	0.37g	0.25g		11s	S2-7	2
0.55g	0.34g	0.21g	0.068g	11s	S02	3
0.53g	0.33g	0.19g		11s	S1-2	4
0.5g	0.32g	0.177g	0.057g	11s	S01	5
0.48g	0.3g	0.15g		11s	S1-3	6
0.44g	0.28g	0.128g	0.038g	11s	S03	7
0.459g	0.29g	0.138g		11s	S3-6	8
0.47g	0.3g	0.157g	0.052g	11s	S06	9
0.536g	0.35g	0.2g		11s	S6-13	10
0.58g	0.37g	0.245g	0.122g	11s	S13	11

4. FINITE ELEMENT MODEL OF KARUN III DAM

Figure 2 shows the provided finite element model of the dam body and the reservoir of Karun III dam. Primary coordinates of the dam body, horizontal and vertical arch attributes were used to model the body and the main appurtenant structures like the spillway, the left and the right thrust blocks. Accordingly, the reservoir length was considered about 3.5 times of the dam height in the upstream direction. It is worth mentioning that the reservoir was modeled with the prismatic fixed section along its length. According to the particular topography of the region, the surrounding foundation rock was extended twice of the dam height in all directions.

3958 8-node solid elements are used for modeling the dam body, appurtenant structures, Foundation medium and there are 2302 8-node fluid elements in the reservoir [11]. Also the material properties for concrete and foundation briefly are presented in table 3.

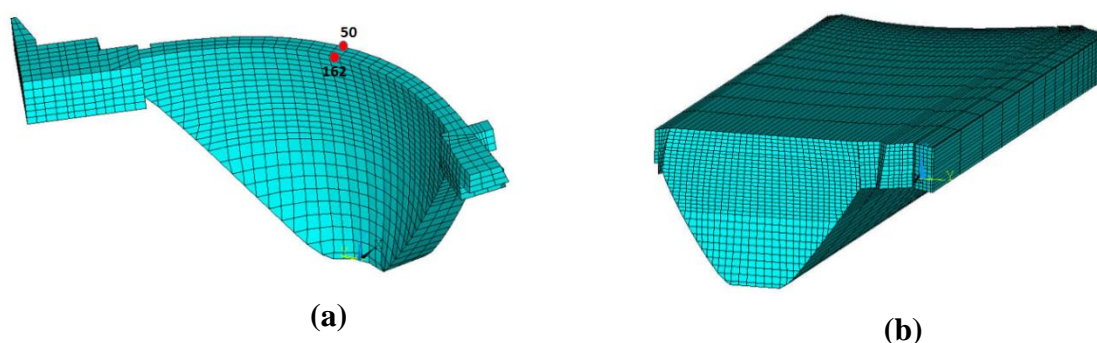


Figure 2. Finite element model of Karun III a) dam body, b) the reservoir

Table 3 Concrete and foundation parameters used in the finite element model

Concrete mass density	2400 kg/m ³
Concrete modulus of elasticity	30 GPa
Concrete Poison's ratio	0.2
Foundation deformation modulus	14 GPa
Foundation Poison's ratio	0.2

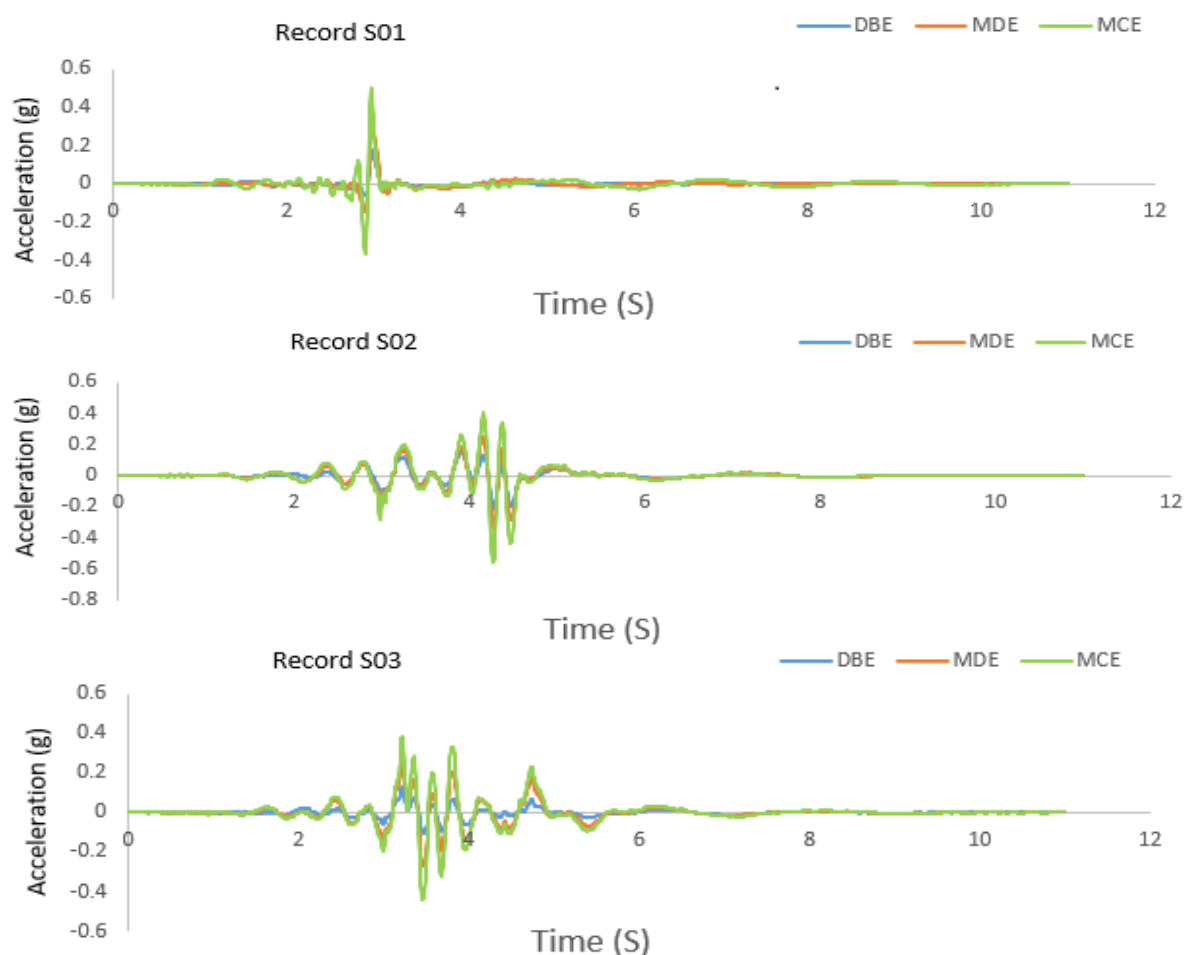
The recorded ground acceleration time histories used at dam-foundation interface in this study, therefore, in the finite element model, the foundation was excluded. The ground motion distribution across the thickness of the dam is considered uniform.

5. RESULTS AND DISCUSSION

In this section, responses of Karun III to uniform and non-uniform excitations of ground motions at three performance levels, including BDE, MDE and MCE, were studied, and compared with each other.

According to the displacement time histories in stream direction in the central crest for uniform and non-uniform excitation at three hazard levels (Fig.4), the results indicates that at three hazard levels, displacement values in uniform excitation was greater than non-uniform excitation. Increased hazard level can cause higher displacement. Also, the displacement pattern in the three levels was almost the same, and according to Fig.3, the peak of energy in both states of uniform (S13) and non-uniform was at intervals of 2-4 seconds. The maximum displacement also occurred at intervals of 2-4 seconds.

The minimum and maximum displacement of the central crest in two states of uniform and non-uniform for up-stream and down-stream faces (Table 4) revealed the displacement trend to down-stream face of dam. According to Table 5. In DBE level, the first principal stress (S1) and the third principal stress (S3) at non-uniform excitation is higher compared to the uniform excitation. Based on the results it can be concluded that by increasing in earthquake intensity, the values are increased.



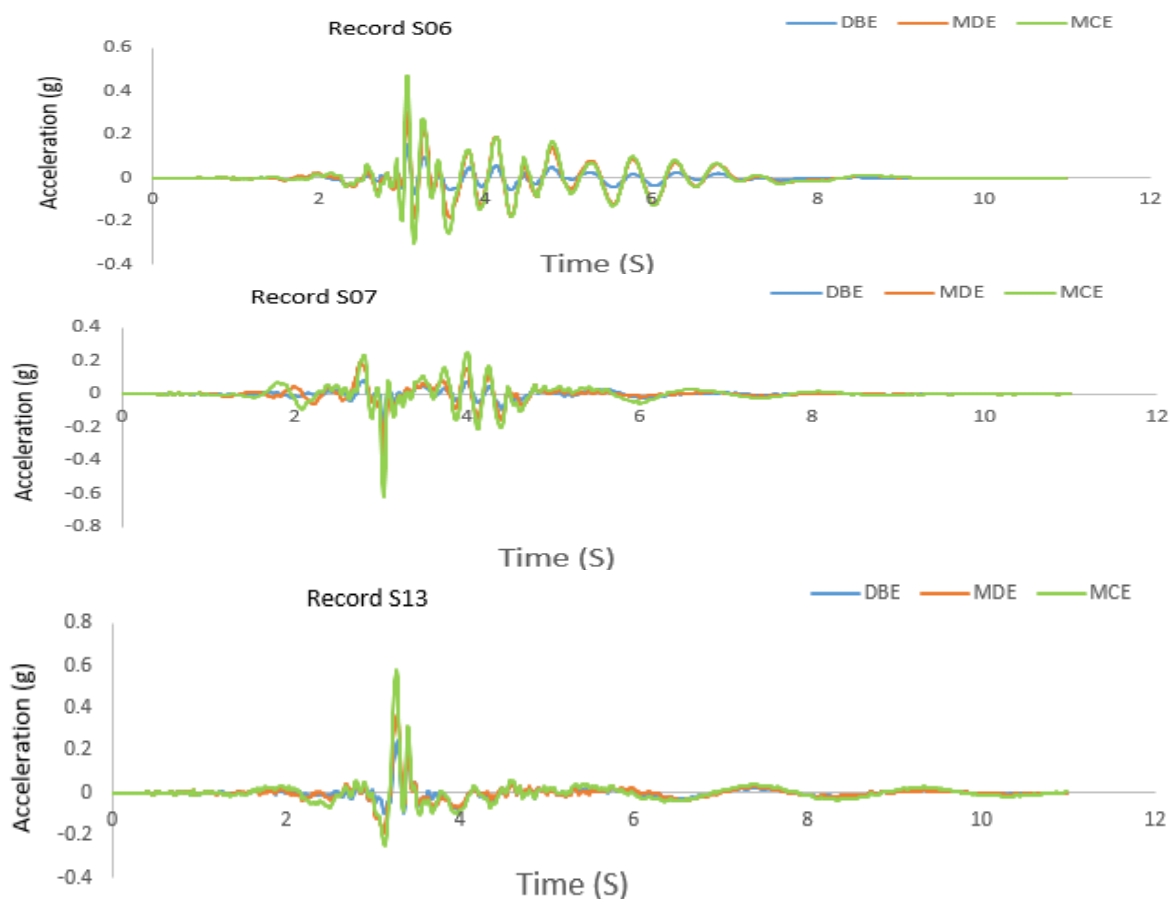
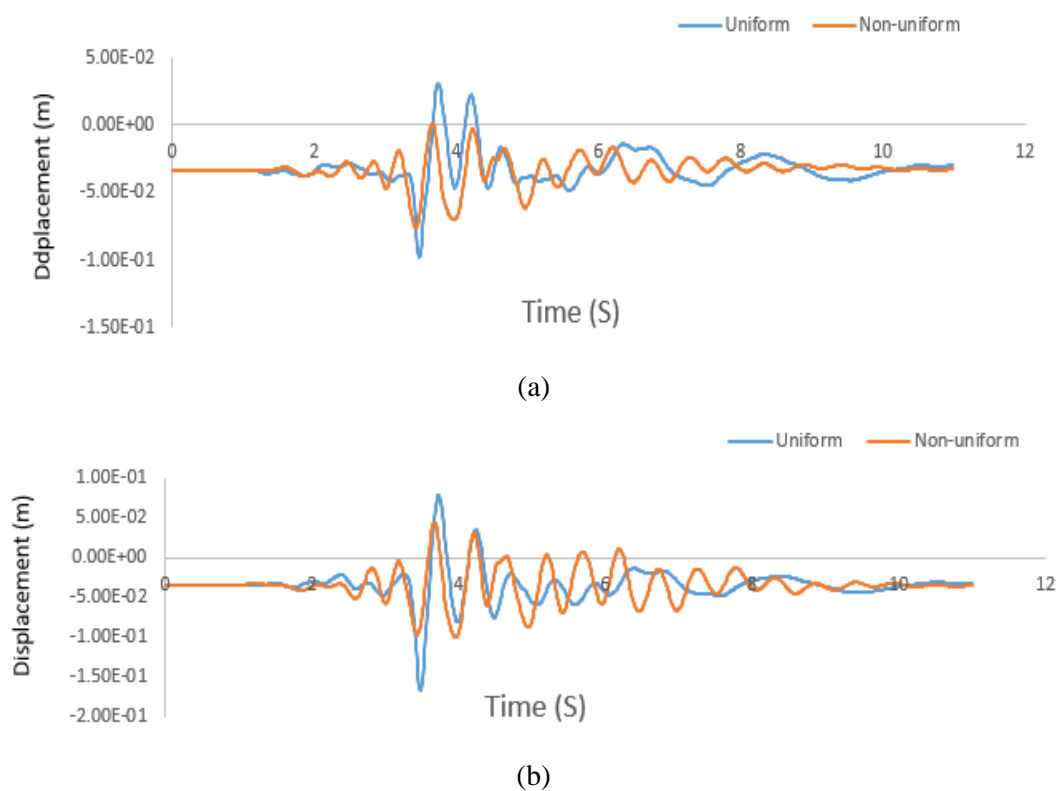
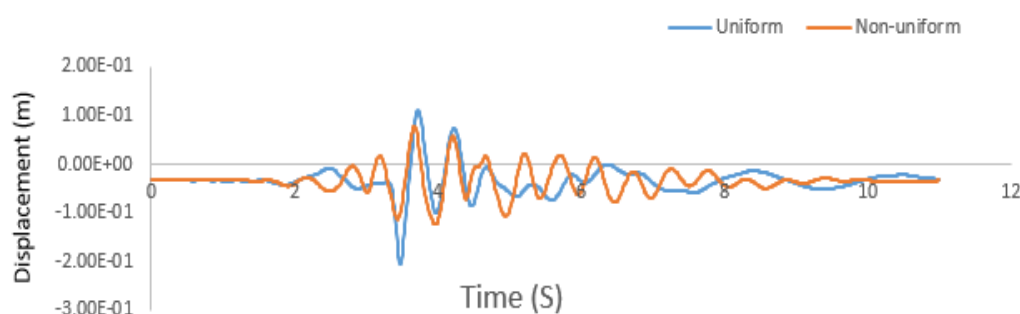


Figure 3. Comparison of records of main stations at three performance levels





(c)

Figure 4. Graph of comparison of displacement time histories in stream direction at central crest point for Uniform and Non-uniform records at three performance level a) DBE, b) MDE and c) MCE

Table 4. Maximum and minimum displacements of dam crest in stream direction for up-stream and down-stream faces

		DBE		MDE		MCE	
		Crest mid-point		Crest mid-point		Crest mid-point	
		US(cm)	DS(cm)	US(cm)	DS(cm)	US(cm)	DS(cm)
Uniform	min	-9.79	-9.84	-16.7	-16.75	-20.47	-20.53
	max	3.05	3.02	7.8	7.8	11.22	11.18
Non-uniform	min	-7.64	-7.68	-9.98	-10.02	-12.37	-12.42
	max	0.0918	0.0597	4.52	4.5	7.86	7.84

Table 5. Maximum and minimum principal stresses of dam at three performance levels

		S1 (MPa)	S3(MPa)
		BDE	Uniform
	Non-uniform	11.7	-19.6
MDE	Uniform	4.55	-11.8
	Non-uniform	17.4	-24.5
MCE	Uniform	4.18	-19.1
	Non-uniform	18.7	-27.3

6. CONCLUSIONS

This investigation studied the earthquake non-uniform excitation effects on dynamic response of arch dam. The Karun III concrete double curvature was selected as the case study for this purpose. The recorded ground motions were used at stations of dam-foundation interface on November 20, 2007. The recorded ground motion was corrected by Seismosignal Software, and the corrected records were matched with three seismic performance levels including DBE, MDE and MCE by Sismo Match Software. The earthquake horizontal component (stream direction) was applied as input in the ANSYS Finite Element Software. The corrected records at stations of dam-foundation interface was used as the non-uniform input and also one of the most intense records (S13) was applied as uniform input.

The obtained results indicate that displacement values in the uniform excitation at three performance levels were greater than the non-uniform excitation. With hazard level increasing, the displacement values enhanced. The non-uniform displacement ratio in compare with uniform increased at the levels DBE (22%), MDE (40.2%) and MCE (60.5%), respectively. However, the displacement pattern in three hazard levels was almost the same. Minimum and maximum displacement of central crest of cantilever at two modes of uniform

and non-uniform excitation for up-stream and down-stream faces showed the displacement trend to down-stream face of dam.

Based on the obtained results, maximum principal stress (S1) and minimum principal stress (S3) at non-uniform excitation is greater than uniform excitation and increase in hazard level can cause higher stress. It was generally observed that the non-uniform excitation had significant effect on structural responses of dam-reservoir-foundation system. Therefore, for more precise identification of dynamic behavior and reliable calculation of dam responses, the non-uniform excitation should be incorporated in seismic safety evaluation and seismic design of large dams.

7. REFERENCES

1. Alves, S.W. "Nonlinear analysis of Pacoima dam with spatially non-uniform ground motion", Earthquake Engineering Research Laboratory, California Institute of Technology, Report No. EERL 2004-11, Pasadena, Calif (2004).
2. Nowak, S. and Hall, J. "Arch dam response to non-uniform seismic input", J. Eng. Mech., 116(1), pp.125-139(2009).
3. Dumanaglu, A.A., Severn, R.T. and Taylor, C.A. "Effect of Asynchronous input on the response of dams", Proceedings 8th World Conf. On Earthquake Engineering, 6, San Francisco, pp. 127-134(1984).
4. Maheri, M.R. and Ghaffarzadeh, H. "Asynchronous and non-uniform support excitation analysis of large structures", JSEE, 4(2&3), (2002).
5. Zerva, A. Zervas, V. "Spatial variation of seismic ground motions", An Overview, Applied Mechanics Reviews. No.3, 55(2002) 271-97.
6. Der Kiureghian, A. "A coherency model for spatially varying ground motions", Earthquake Engineering and Structural Dynamics, 25(1996), 99-111.
7. Proulx, S., Darbre, G. and Kamileris, N. "A comparison of recorded and computed earthquake motions of large concrete dams", First European Conference on Earthquake Engineering and Seismology, Geneva, Switzerland, Paper No.627 (2006).
8. Chopra A, Wang J. "Earthquake response of arch dams to spatially varying ground motion", Earthquake Engineering and Structural Dynamics, No.8, 39(2010) 887-906.
9. Sohrabi-Gilani, M., and M. Ghaemian. "Spatial variation input effects on seismic response of arch dams." Scientia Iranica 19, no. 4 (2012): 997-1004.
10. Mirzabozorg, H., M. Akbari, and M. A. Hariri-Ardebili. "Nonlinear seismic response of a concrete arch dam to spatially varying earthquake ground motions." Asian Journal of Civil Engineering (BHRC) 14, no. 6 (2013): 859-879.
11. Mirzabozorg, H., M. A. Hariri-Ardebili, M. Heshmati, and S. M. Seyed-Kolbadi. "Structural safety evaluation of Karun III Dam and calibration of its finite element model using instrumentation and site observation." Case Studies in Structural Engineering 1 (2014): 6-12.

Global Sensitivity Analysis of Concrete Gravity Dams Subjected to Seismic Excitation

Mohammad Houshmand¹, Mohsen Ghaemian¹, Vahab Toufigh¹

1. Department of Civil Engineering, Sharif University of Technology, Tehran, Iran

Email: m.houshmand@alum.sharif.edu

Abstract

In this study, global sensitivity analysis is performed to determine relative importance of random variables and their interaction effects onto the response of concrete gravity dam model. The dam-foundation reservoir system is considered in this research to investigate the effect of input variables in the mentioned system. Material properties of concrete and foundation are assumed as random variables to tackle epistemic randomness involved in these models. The main novelty of this paper is to quantify the effect of each uncertain input variable and its interactions with other variables on the response of gravity dams. Most of the studies in the field of dam engineering focused on parametric or local sensitivity approaches. Nonetheless, these methods have the following drawbacks. First, they are based on only one point in the variable space. Second, the interaction between uncertain variables cannot be determined in parametric and local sensitivity analyses. On the other hand, in global sensitivity analysis, the interactions of random variable with other random variable are determined over the whole input space. In this research, variance-based sensitivity analysis is utilized as the model free global sensitivity approach to accurately quantify the effect of each random variable in the response of concrete gravity dams.

Keywords: Concrete Gravity Dam, Seismic Excitation, Global Sensitivity Analysis, Limit-State, Sensitivity Measure.

1. INTRODUCTION

The safety level of infrastructures is a critical concern and traditional methods consider simply safety factors for design and safety evaluation. As consequences of infrastructure including dams can be catastrophic, it is important to accurately evaluate the safety level of these systems. Furthermore, the failure of these infrastructures leads to substantial human casualties and economic losses. Consequently, employing more reliable approaches along with improved determination of loading conditions will result in more realistic assessments of safety. The complexity of Dam's behavior and a plethora of uncertainty involved in their numerical models has to be tackled specifically in seismic analysis. The probabilistic approach is an effective method to take into account the aforementioned difficulties. Uncertainties can be due to material properties, geometry of structure, environmental phenomenon, loads, and other factors. The sources of uncertainty can generally be categorized into aleatory and epistemic randomness. An aleatory uncertainty is irreducible randomness due to the nature of phenomenon, while an epistemic uncertainty is related to a lack of knowledge and is measurable and reducible.

Many previous studies have been determined an accurate assessment of dam safety under different failure modes, loading conditions, and various random variables were considered [1-4]. Nonetheless, many problematic issues have remained unsolved in these studies. They were unable to sufficiently determine the quantitative importance of the variables and utilized insufficient reliability methods and inappropriate performance criteria. Some studies used parametric analysis as a sensitivity analysis by applying perturbation to the mean of the random variables [5]. The local sensitivity analysis is based on the derivative of each random variable in a specific point, which can be the mean or the design point depending on the methods employed [6, 7]. In global sensitivity analysis, the influence of entire range of variables is neglected. In addition, crude sampling methods, such as MCS, require a large number of samples to obtain acceptable accuracy. Hence, employing more efficient sampling methods is inevitable and it is intended to implement a reliability method on models with an intrinsic high computational cost [8-9].

In this investigation, the relative importance of each random variable along with its interaction with other random variables is determined. The variance-based sensitivity analysis (VBSA) is used for quantifying the importance of random variables. As the computational cost of each deterministic analysis is high, it is inevitable to use efficient sampling as the basis of the VBSA. For this purpose, Latin Hypercube sampling which is an efficient less time consuming sampling method than MCS is used.

2. MODEL DESCRIPTION

For this research, the tallest monolith of the Pine Flat Dam, a concrete gravity dam in Central California, is selected as a case study. The geometry of dam's body and the elevation of the reservoir are presented in Figure 1(a). The concrete properties are assumed to be linearly elastic and isotropic. The Pine Flat dam is modeled using two-dimensional finite element method in a plane-strain analysis. The dam-foundation-reservoir interaction is considered in the model. The length of reservoir is assumed five times the dam height and non-reflective planar boundary condition is assigned as far-end boundary condition. The foundation rock is presumed to be massless. The finite element model of dam-foundation-reservoir is shown in Figure 1 (b). The material properties of concrete, water and rock foundation is presented in Table 1.

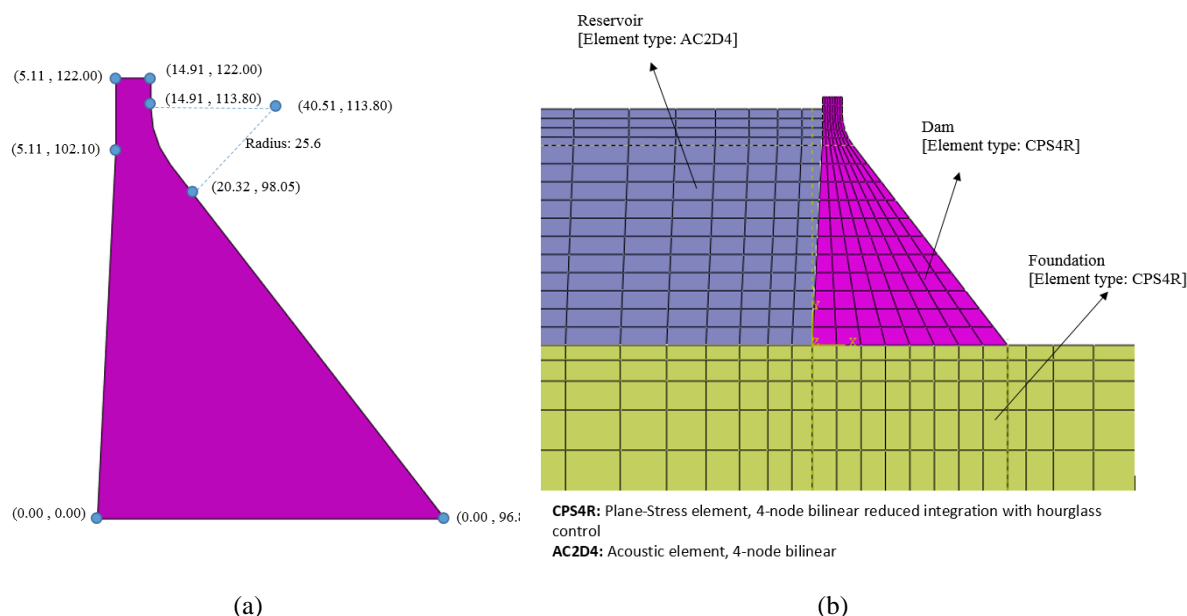


Figure 1. Geometry, finite element model and element type of the case study

Table 1- Material properties of dam-foundation-reservoir system

	Material	Value
Concrete	Elasticity modulus	30 (GPa)
	Poisson's ratio	0.2
	Density	2400 (kg/m ³)
	First and third mode damping ratio	5 %
Water	Density	1000 (kg/m ³)
	Bulk modulus	2.07 (GPa)
Foundation Rock	Elasticity modulus	30 (GPa)
	Poisson's ratio	0.33

For the seismic analysis, Taft ground motion, Kern County, 7/21/1952, Taft Lincoln School, 111, is utilized in three different level of intensity based on operating basis earthquake (OBE), maximum design earthquake (MDE) and maximum credible earthquake (MCE) having PGA of 0.18, 0.27 and 0.45 g, respectively. Based on damage index defined by Alembagheri and Ghaemian (2013), seismic performance of gravity dam can be pertinent to crest displacement. They utilized nonlinear static pushover and incremental dynamic analysis to quantify the crack state of Pine Flat gravity dam into crest displacement [10]. The crack initiation and ultimate state are considered for damage index determination. In their model, the concrete behavior in uniaxial tension is controlled by tension stiffening and tensile damage (d_t). The degradation of the material stiffness due to damage propagation in terms of cracking normal displacement is considered. Crack initiation state is defined by the first element of dam body, commonly the hill element, exceeding tensile damage. Besides, the ultimate state is indicated by the crack propagation of the dam's neck as well as the other cracked part of the dam body. In these states, the crest displacement has been considered as a performance criterion.

In this study, the performance criteria are defined using aforementioned damage index and tensile over-stressing indices as follows:

$$f_1(\mathbf{x}) = 1 - DI_c < 0 \tag{1}$$

$$DI_c = \frac{U_{\max}}{U_d} \tag{2}$$

$$f_2(\mathbf{x}) = S_{all} - S < 0 \tag{3}$$

Where $f_1(\mathbf{x})$ and $f_2(\mathbf{x})$ are the limit-state functions based on maximum crest displacement (MCD) and tensile over-stressing, respectively. U_{\max} and S are the maximum crest relative displacement and tensile stress, respectively. U_d and S_{all} are the thresholds corresponding to displacement and stress limit-states, respectively. The domain $f(\mathbf{x}) < 0$ represents the failure domain of the responses. These performance criteria controlling the maximum crest displacement and the tensile over-stressing are used to define limit-state functions that are required for the uncertainty analysis.

Material properties of dam and foundation rock are taken as random variables to quantify uncertainty in the current case study. According to engineering judgment and pertinent studies, these random variables are assumed to be uncorrelated and assigned probabilistic characteristics are shown in Table 2. Allocating nearly high value of standard deviation to the random variables is justified by large uncertainties involved in these variables due to lack of experimental and site data. In addition, influence of seismic randomness is assumed using parametric analysis to model uncertainty.

Table 2- Probabilistic characteristics of defined random variables

Random Variable	Mean	Standard Deviation	Probability Distribution
Concrete density (kg/m ³)	2400	480	Lognormal
Elasticity modulus of concrete (GPa)	30	0.6	Lognormal
Ratio of elasticity modulus of rock foundation to concrete (GPa)	0.625	0.216	Uniform
Concrete Poisson’s ratio	0.2	0.04	Uniform

3. METHODOLOGY

Variance-based sensitivity analysis (VBSA) determines the influence of each random variable and its interaction on the total variance of response, called first order (S_i) and total sensitivity (S_{Ti}) measures, respectively [11-15]. This method is appropriate for utilizing with complex nonlinear models. The main drawback of this method is its dependence on a number of random variables. The total number of analyses required for this approach is $(N/2)*M$. N and M represent the number of samples and random variables, respectively. VBSA was implemented using the Sobol method. The variance of output was decomposed to Sobol indices, which imply the first and total effect of each random variable. An analytical function, presented in Eq. 8, with three random variables has been selected to verify the accuracy of the implemented method. All random variables were uniformly distributed with a minimum and maximum value of $-\pi$ and π , respectively.

$$f(X_1, X_2, X_3) = \sin X_1 + a \sin X_2 + bX_3^4 \sin X_1 \tag{4}$$

In the above equation, a and b are constant parameters and assumed to be 7 and 0.1, respectively [16]. The main (first order) and total of Sobol’ indices were calculated for different numbers of samples, as demonstrated in Figure 2. In spite of slight differences between the exact and calculated indices, the performance of this implemented approach can be observed. For instance, importance measures for $N=1024$ were calculated and their comparison with exact values are presented in Table 3.

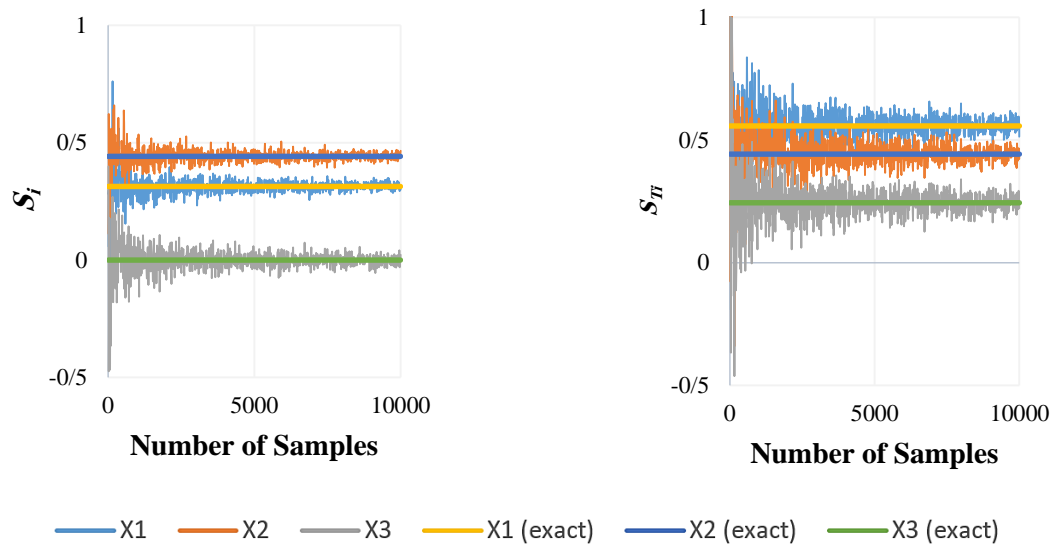


Figure 2. Verification of implemented VBSA (Sobol' indices) tested for equation 4.

Table 3- Comparison of exact and calculated Sobol' indices tested for equation 4.

	Exact value		Calculation for N=1024	
	S _i	S _{Ti}	S _i	S _{Ti}
X₁	0.3138	0.5574	0.3140	0.5351
X₂	0.4424	0.4424	0.4468	0.5002
X₃	0	0.2436	0.0064	0.2847

Utilizing Monte Carlo sampling in complex numerical models is not practical since a large number of samples are required to achieve an acceptable confidence level. Consequently, it is recommended to employ more efficient sampling approaches such as importance sampling, adaptive importance sampling, directional sampling, and Latin hypercube sampling (LHS) [17]. LHS was selected for this research since its efficiency and simplicity of implementation. On the other hand, the first step for implementation of importance and adaptive sampling is to find the design point, which is problematic as limit-state functions tend to be nonlinear.

The LHS is a stratified Monte Carlo sampling that results in filling all the areas of the sample space [18]. LHS was implemented by dividing the cumulative density function (CDF) of each variable into N non-overlapping intervals having equal probability as shown in Figure 3. A value for the corresponding variable was randomly selected in each interval. The number of samples was then equal to the number of intervals. The sample matrix was defined for all the variables and for each interval as follows:

$$x_{i,j} = F_j^{-1}(p_{i,j}) = F_j^{-1}\left(\frac{i-0.5}{N}\right) \tag{4}$$

$$i = 1, \dots, N; j = 1, \dots, M$$

where M is the number of random variables and F^{-1} is the inverse CDF of probability p .

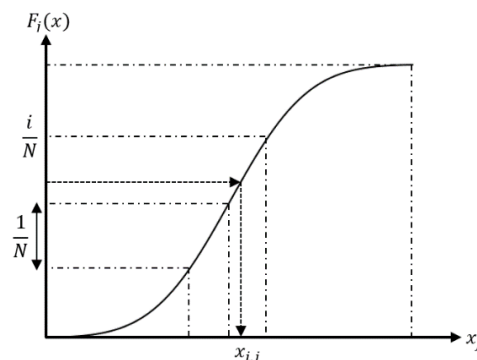


Figure 3. The algorithm of LHS

4. RESULTS

The global sensitivity analysis is performed in the model based on 1,000 samples generated using LHS. The results are obtained separately for two defined limit-states, maximum crest displacement and maximum tensile stress. The first order and total sensitivity measures along with total variance values are calculated based on crest displacement and tensile stress, see Figures 4 to 6.

The result of first order sensitivity measures indicate that for limit-state based on both MCD and maximum tensile stress, the most important variable is Young’s modulus of concrete. Furthermore, the second-ranked important variable in the results based on MCD is the ratio of Young’s modulus of rock to concrete but in the results based on maximum tensile stress is concrete density. All the results indicate that concrete Poisson’s ratio is the least important variables in this model. Despite the dam is asymmetric and also the seismic loading is not identical in U/S and D/S direction, the results of MCD for both of these directions are approximately the same. It implies that the importance measures are independent of these situation and they are only pertinent to the performance functions.

By comparing the first order and total sensitivity measures (in maximum tensile stress limit-state), it can be inferred that the elasticity modulus of concrete has higher impact on the results when its interaction with other variables is considered. For MCD limit-states, it is the ratio of Young’s modulus of rock to concrete is significantly affect the response of the dam and is the most important random variables. Based on the total sensitivity measures, the second-ranked important variables are Young’s modulus of concrete and the ratio of Young’s modulus of rock to concrete for limit-states based on MCD and maximum tensile stress, respectively. The total variance chart implies that the variance involved in the maximum tensile stress results is higher than MCD when considering first order effect. On the contrary, the total variance in total sensitivity calculation indicates that the variance involved in the maximum tensile stress is lower than MCD.

It is noteworthy that the results of model subjected to OBE, MDE and MCE earthquake determined to be identical. The reason is that the model is linear and the by increasing intensity of ground motions, what it is in OBE, MDE and MCE earthquake, only shifts backward and forward the results and the variance of the responses are not changed.

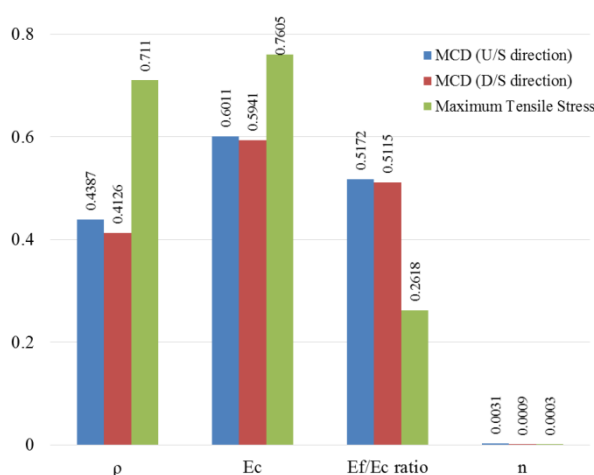


Figure 4. First order sensitivity measure results

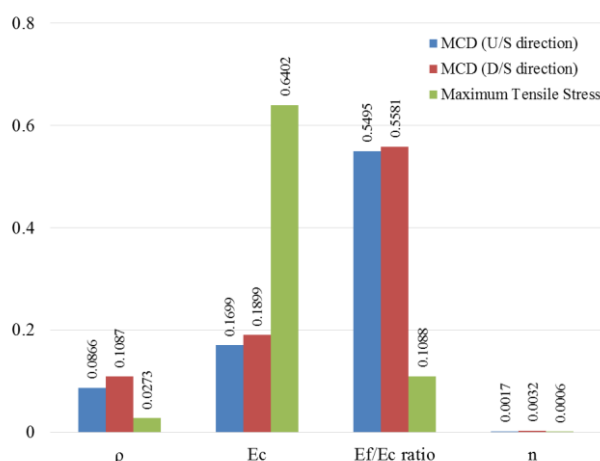


Figure 5. Total sensitivity measure results

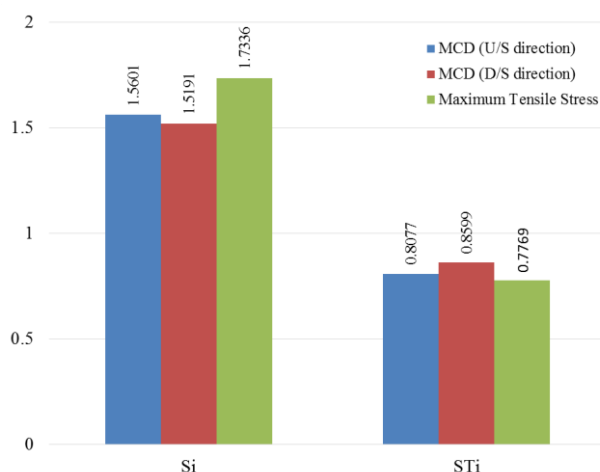


Figure 6. Total variance involved in the results

5. CONCLUSIONS

A probabilistic numerical model of concrete gravity dam subjected to seismic load is studied. In this study, the performance of concrete gravity dam is assumed to be associated with the maximum crest displacement and the maximum principal (tensile stress). For consideration of ground motion effects as a parametric study, the same ground motion with different intensity levels is applied to the model. The objective of this investigation is to accurately quantify the importance of random variables in the dam-foundation-reservoir system. For this purpose, global sensitivity analysis based on Latin Hypercube sampling is implemented. The sensitivity measures are calculated for different limit-state functions. The results indicate that the most important variable based on first order sensitivity measure is concrete Young's modulus. For results of total sensitivity measure, the most important variable is concrete Young's modulus for maximum tensile stress based limit-state and it is the ratio of Young's modulus of rock to concrete for MCD based limit-state.

6. REFERENCES

1. Hariri-Ardebili MA, Saouma VE. Probabilistic seismic demand model and optimal intensity measure for concrete dams. *Structural Safety*. 2016 Mar 31; 59:67-85.
2. Alembagheri M, Ghaemian M. Damage assessment of a concrete arch dam through nonlinear incremental dynamic analysis. *Soil Dynamics and Earthquake Engineering*. 2013 Jan 31; 44:127-37.
3. Kartal ME, Bayraktar A, Başağa HB. Nonlinear finite element reliability analysis of Concrete-Faced Rockfill (CFR) dams under static effects. *Applied Mathematical Modelling*. 2012 Nov 30;36(11):5229-48.
4. Lupoi A, Callari C. A probabilistic method for the seismic assessment of existing concrete gravity dams. *Structure and Infrastructure Engineering*. 2012 Oct 1;8(10):985-98.
5. Alembagheri M, Seyedkazemi M. Seismic performance sensitivity and uncertainty analysis of gravity dams. *Earthquake Engineering & Structural Dynamics*. 2015 Jan 1;44(1):41-58.
6. Sitar N, Cawfield JD, Der Kiureghian A. First-order reliability approach to stochastic analysis of subsurface flow and contaminant transport. *Water Resources Research*. 1987 May 1;23(5):794-804.
7. Castillo E, Hadi AS, Conejo A, Fernández-Canteli A. A general method for local sensitivity analysis with application to regression models and other optimization problems. *Technometrics*. 2004 Nov 1;46(4):430-44.
8. Cheng J, Druzdzel MJ. Latin hypercube sampling in Bayesian networks. In *FLAIRS Conference 2000* May 22 (pp. 287-292).
9. Helton JC, Davis FJ, Johnson JD. A comparison of uncertainty and sensitivity analysis results obtained with random and Latin hypercube sampling. *Reliability Engineering & System Safety*. 2005 Sep 30;89(3):305-30.
10. Alembagheri M, Ghaemian M. Seismic assessment of concrete gravity dams using capacity estimation and damage indexes. *Earthquake Engineering & Structural Dynamics*. 2013 Jan 1;42(1):123-44.
11. Homma T, Saltelli A. Importance measures in global sensitivity analysis of nonlinear models. *Reliability Engineering & System Safety*. 1996 Apr 30;52(1):1-7.
12. Saltelli A, Ratto M, Andres T, Campolongo F, Cariboni J, Gatelli D, Saisana M, Tarantola S. *Global sensitivity analysis: the primer*. John Wiley & Sons; 2008 Feb 28.
13. Sobol IM. Global sensitivity indices for nonlinear mathematical models and their Monte Carlo estimates. *Mathematics and computers in simulation*. 2001 Feb 15;55(1):271-80.
14. Tian W. A review of sensitivity analysis methods in building energy analysis. *Renewable and Sustainable Energy Reviews*. 2013 Apr 30; 20:411-9.
15. Saltelli A, Annoni P, Azzini I, Campolongo F, Ratto M, Tarantola S. Variance based sensitivity analysis of model output. Design and estimator for the total sensitivity index. *Computer Physics Communications*. 2010 Feb 28;181(2):259-70.
16. Ditlevsen O, Madsen HO. *Structural reliability methods*. New York: Wiley; 1996 Jan.
17. Rajabi MM, Ataie-Ashtiani B, Janssen H. Efficiency enhancement of optimized Latin hypercube sampling strategies: Application to Monte Carlo uncertainty analysis and meta-modeling. *Advances in Water Resources*. 2015 Feb 28; 76:127-39.
18. Dolsek M. Incremental dynamic analysis with consideration of modeling uncertainties. *Earthquake Engineering & Structural Dynamics*. 2009 May 1;38(6):805-25.

Earthquake Records on Concrete Dams in Japan: Comparison with Finite-Element Analyses

Emmanuel Robbe

Electricité de France - Hydro Engineering Center – Le Bourget du Lac

Email: emmanuel.robbe@edf.fr

Abstract

From 2014 to 2016, EDF was part of the cooperation between French (CFBR) and Japanese (JCOLD) committees on Large Dams occurred on the subject of dam’s behavior under earthquake. In Japan, seismic recordings have been conducted on existing dams and JCOLD released in 2014 an update of its databases of earthquake recordings on dams among them 135 gravity dams and 22 arch dams. The dynamic responses of gravity and arch dams are simulated by finite-element analyses using data recorded at the foundation and the responses are compared to the data recorded at sensor located at the dam’s crest. Comparisons between analyses and records confirm that the conventional massless foundation/added masses approaches with 5% concrete damping greatly overestimates the response of concrete dam, particularly in the case of gravity dams. The use of more advanced models taking into account the mass of the foundation, viscous-spring boundary input model and potential-based fluid finite elements with absorptive boundaries leads to more adequate values.

Keywords: Japan, Concrete, Earthquake, Analysis, Records.

1. INTRODUCTION

Based on seismic records from two existing dams, this paper presents several Finite Element Models (FEM) of these dams and their response to seismic solicitation; the open-source finite-element software Code-Aster is used. Conventional Westergaard added-mass with a massless foundation analyses are done followed by a more elaborate FEM taking into account soil-fluid-structure interaction by means of viscous spring boundary (VSB) and potential-based fluid. Results from both analyses are compared to the actual record at the crest of each dam to assess each method’s relevance.

2. PRESENTATION OF THE FLUID-STRUCTURE INTERACTION AND SOIL-STRUCTURE INTERACTION METHOD

In order to take into account the fluid-structure interaction, potential-based fluid finite elements are used. The assessment of this formulation for seismic analysis of dam-reservoir systems has been performed by the Ecole Polytechnique of Montreal 1.a.i.1 using test cases based on analytic solutions. The results from this test case have been reproduced using the finite element software Code-Aster used in this study. This formulation allows taking into account compressibility of the water, wave absorption at the end of the reservoir as well as partial absorption by sediments at the bottom of the reservoir.

In order to improve the soil-structure interaction method by taking into account absorption of the wave in the boundaries of the foundation, a viscous spring boundary model is implemented as proposed in 1.a.i.2 and 1.a.i.3, and briefly summarized in Figure 1. It is employed to absorb the wave energy radiating away from the dam and the foundation. A test case studying the reflection and absorption of a vertically propagating seismic shock in a rectangular foundation validated the viscous spring boundaries in Code-Aster.

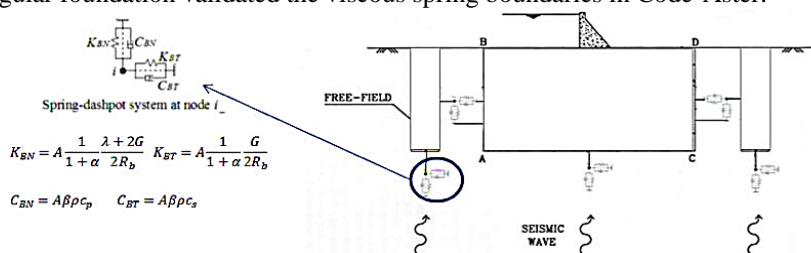


Figure 1: Viscous spring boundary model

The description of the VSB and fluid-structure interaction model is limited to this paragraph so as to allow the presentation of the results on the existing dams throughout the rest of this paper.

3. 2D APPLICATION ON A GRAVITY DAM

3.1. GEOMETRY OF THE GRAVITY DAM AND FINITE ELEMENT MODEL, RECORDING DEVICES

The gravity dam studied is 150 m high with a crest of 500 m long. It is equipped with four 3-directional sensor. They are positioned at elevation 515 (crest), 486, 444 and 399 (foundation). A 2D model of the dam that displays the sensors' locations is provided Figure 2.

This study makes use of an earthquake which was recorded at the dam on October the 23th, 2004. An estimation of the dam's first eigenfrequencies was performed using the data from this earthquake. Consequently, concrete's and rock's Young Modulus are set at $E_{\text{concrete}} = 40000 \text{ MPa}$, $E_{\text{rock}} = 35000 \text{ MPa}$.

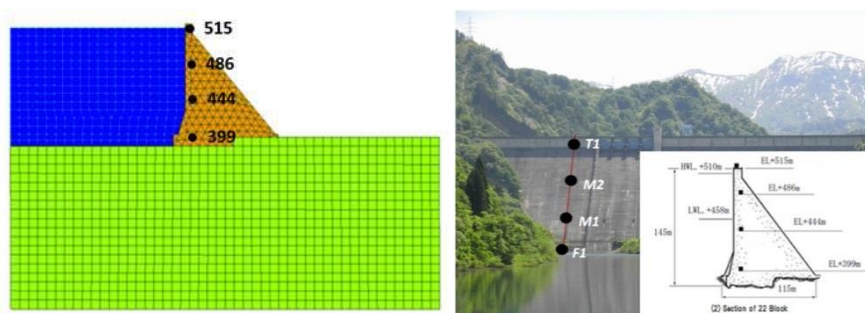


Figure 2 Geometry of the 2D model compared to the gravity dam

3.2. MASSLESS FOUNDATION AND ADDED MASSES APPROACH

First, a conventional analysis is conducted. The foundation is considered massless and Westergaard added masses are used to take into account the fluid-structure interaction. The concrete's damping value is set at 5 % of the critical value. The input accelerogram is taken at sensor 399.

Figure 3 shows the comparison between the crest acceleration (515) and the bottom acceleration (399); results are presented as Fourier spectra. Numerical results show a great overestimation of the computed response when compared to the recorded response. Overestimations occur mainly at 2.7 Hz (the first eigenmode) and at 6 Hz. Furthermore, the model is not able to reproduce the peak at the crest of 3.9 Hz, probably caused by the reservoir's mode.

3.3. VISCOUS SPRING BOUNDARY MODEL (VSB) AND POTENTIAL FLUID APPROACH

The improved FE method is used. Considering the introduction of damping in the model, the concrete damping is reduced to 1%, which seems more adequate regards to the low intensity of the earthquake. The following assumptions are considered for the fluid-structure interaction : full absorption of the wave at the upstream face of the reservoir (infinite propagation) and no absorption at the bottom of the reservoir by sediments.

The comparison between recorded and computed accelerations (Figure 3) shows a much better fit between recorded and calculated data than with the previous approach. The acceleration at the bottom and at the crest is on the same range of level and the FFT comparison shows:

- a slight overestimation of the peak around the first eigenfrequency,
- an underestimation of the peak around 4Hz,
- a slight underestimation of the calculated response at high frequencies (from 8Hz).

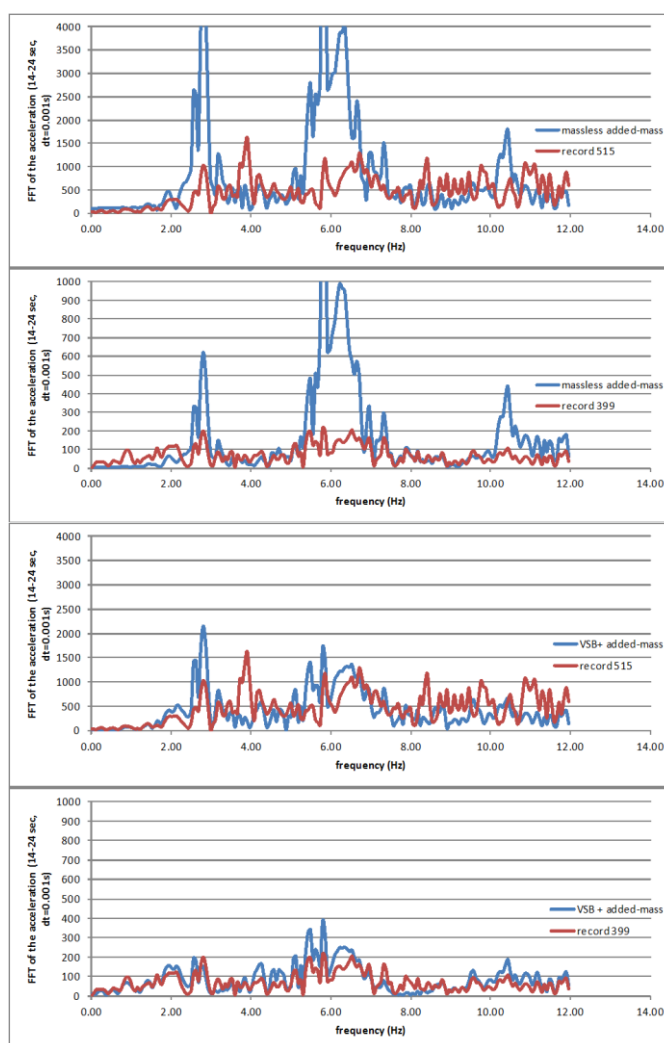


Figure 3 comparison of the FFT of the horizontal acceleration, recorded vs computed at the crest (top) and bottom of the dam (bottom) for Massless / added-mass model (left) and VSB / potential fluid model (right),

3.4. TRANSFER FUNCTION AND ESTIMATION OF THE DAMPING

In order to evaluate the damping introduced by the new soil-structure but also fluid-structure approaches in the FE analyses, transfer functions are computed (Figure 4) between the crest of the dam and the input (in that specific case, a white noise is used) in the following case :

- VSB model with added masses and no concrete damping,
- VSB model with potential fluid and no concrete damping.

Using the half-power bandwidth method, damping introduced by the absorbing boundaries in the foundation is evaluated around 10% for the first mode and up to 20% for higher frequencies. Introduction of the compressible fluid in the FE analyses (Figure 4) brings:

- A slight increase of the damping (around 2% additional damping on the first eigenmode evaluated with the half-power band method)
- A division of the first peak in 2 sub-ones: the first one is due to the structure while the other one comes from the reservoir mode,
- An increase of the dam's response around 8 Hz that might come, in that case, of the combination of structure and reservoir modes.

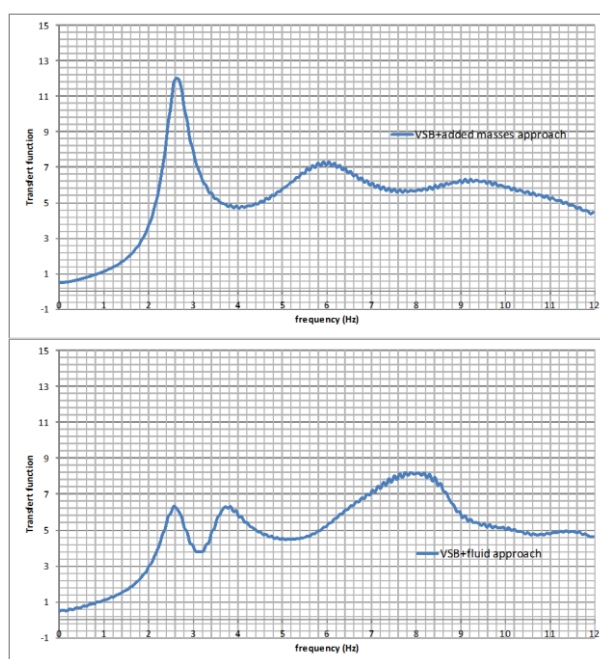


Figure 4. Transfer function: VSB/added masses (left) and VSB/fluid approach (right)

4. 3D APPLICATION ON THE ARCH DAM

Since the mechanical behaviour of an arch dam is strongly different than the behaviour of a gravity dam, the same type of analysis are lead on a 150 m high arch dam with a crest of more than 350 m long, in order to evaluate the numerical approaches in such a case.

4.1 EARTHQUAKE AND RECORDING DEVICES

Accelerometers are distributed on the dam (Figure 5). For the rest of the study, it should be noted that: X is the river direction, Y the bank to bank direction and Z the vertical direction. These devices recorded in the end of an earthquake which occurred off the coast Japan in the Sea of Japan with a high magnitude, on March, the 25th, 2007.

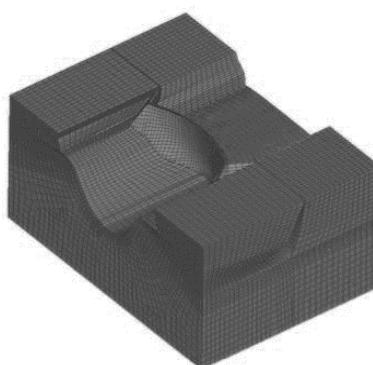


Figure 5 Mesh of the arch dam

4.2. PRESENTATION OF THE 3D MODEL OF THE ARCH DAM

In order to evaluate the response of the viscous-spring boundary / fluid potential model in the case of an arch dam, the dynamic linear analysis is performed with the mesh presented in Figure 5. Results from the massless foundation/Westergaard added masses approach are also presented for comparison. The maximal size of each element is around 20 m.

Earthquake records from the G2 sensor (in the right bank of the dam) are considered as input for the analyses. The response of the numerical analyses will mainly be evaluated by comparison of the recorded dam response at the crest of the dam, at the T1 sensor.

The following mechanical properties are taken into account: $E_{\text{concrete}} = 30000 \text{ MPa}$, $E_{\text{rock}} = 20000 \text{ MPa}$.

4.3. MASSLESS FOUNDATION AND ADDED MASSES APPROACH

First, a conventional analysis is provided considering the foundation massless and the Westergaard added masses to take into account fluid-structure interaction. A 5% Rayleigh damping (adjusted at the frequencies 3 and 13 Hz) is considered for the concrete. Figure 6 compares the recorded and computed acceleration (in the frequency domain) at the crest and at the right bank of the dam, where the input is coming from. This approach leads to rather good results in comparison with the record, particularly in the river direction for the first eigenmode of the dam. But it is also interesting to note that the FE model provides some peaks that do not appear in the records (around 5-6 Hz in every direction for example).

4.4. VISCOUS-SPRING BOUNDARY MODEL AND POTENTIAL FLUID APPROACH

Considering the results shown in the previous analyses with the VSB model, 1% concrete damping is taking into account in this approach, considering that this model introduces additional damping from the wave radiation at the boundaries (Figure 7). The introduction of the viscous-spring boundary model in the FE analyses brings first improvements of the results:

- The coherence between recorded and computed acceleration is good in the right bank. There is no need of adapting the input data using deconvolution
- The overestimated peak between 5 and 6 Hz are no present anymore
- The results are slightly overestimated at the first eigenmode around 2 Hz in the river direction but still underestimated it in the lateral direction.

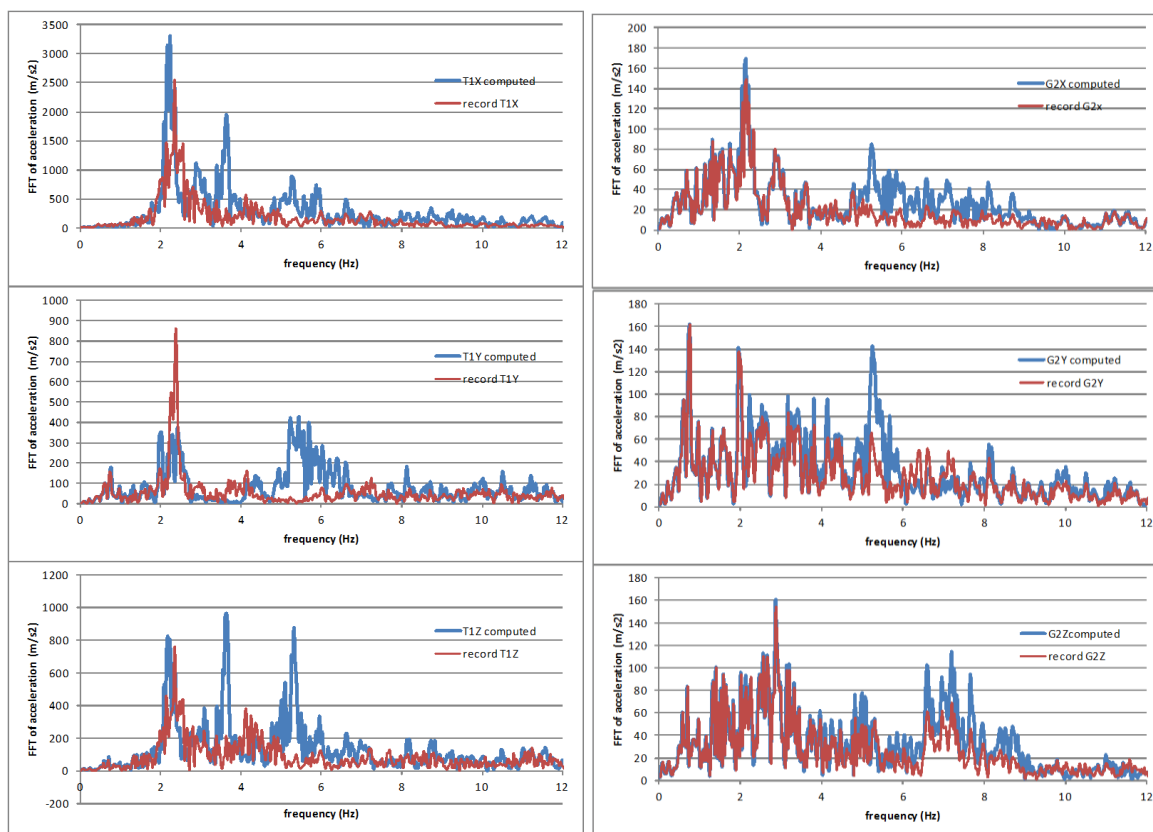


Figure 6. Massless added-mass, comparison of the FFT of the horizontal acceleration, T1 sensor (left) and G2 sensor (right), 3 directions u/s (top), dam axis (middle), vertical (bottom)

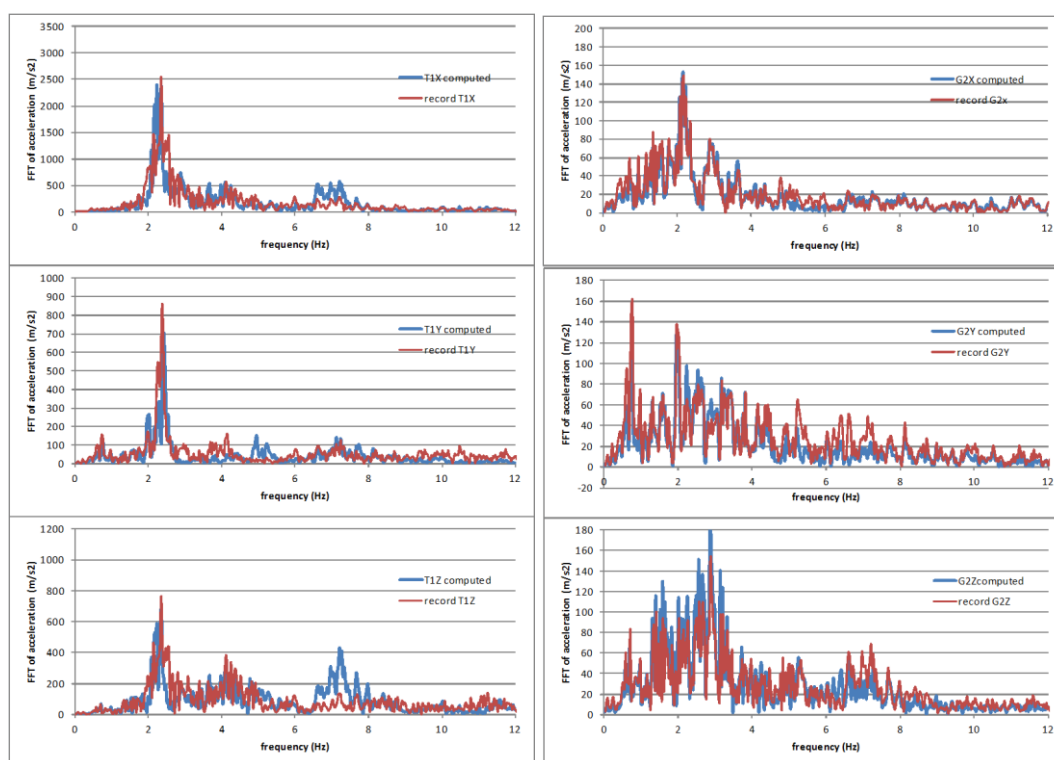


Figure 7 VSB/fluid approach, comparison of the FFT of the horizontal acceleration, T1 sensor (left) and G2 sensor (right), 3 directions u/s (top), dam axis (middle), vertical (bottom)

4.5. EVALUATION OF THE DAMPING

As previously done, and in order to evaluate the damping introduced by the new soil-structure in the FE analyses of the arch dam, transfer functions are computed between the crest of the dam and the input for the VSB/added-masses and the VSB/fluid with no concrete damping. The transfer functions are shown in Figure 8.

Using the half-power bandwidth method, the damping introduced by the absorbing boundaries in the foundation goes from 3% for the first peak to 1Hz for higher frequencies. That shows that in the case of the arch dam, damping coming from the soil-structure effect is of less importance than for the gravity dam (around 10%).

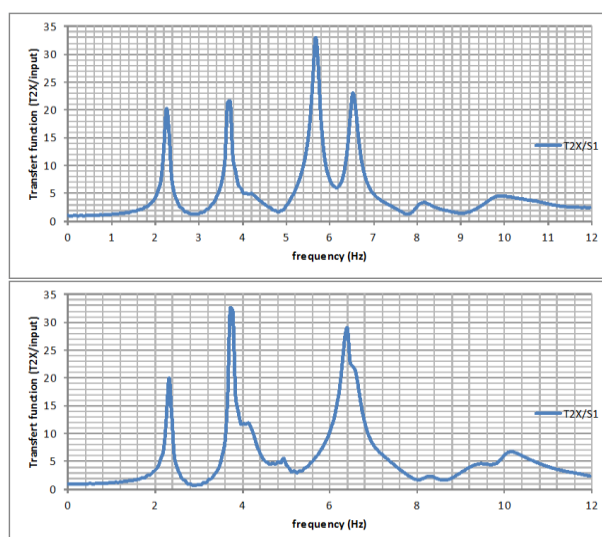


Figure 8. Transfer function: VSB and added masses (left), VSB and potential fluid approach (right)

5. CONCLUSIONS

This paper presents comparisons between recorded earthquake in Japan, on a gravity dam and an arch dam and FE analyses performed with different approaches in 2D and 3D: conventional analyses with massless foundation / Westergaard added masses are carried out, but also more accurate analyses with better soil-structure and fluid-structure interaction considering viscous-spring-boundaries and potential base fluid finite-element. These finite-element models have been based on the bibliography 1.a.i.1, 1.a.i.2, 1.a.i.3 and validated on test cases.

Comparisons between FE analyses and records confirm that the conventional massless foundation/added masses approaches with 5% concrete damping greatly overestimates the response of the dam, particularly in the case of gravity dams. The use of viscous-spring boundaries in the foundation (with its masse) and potential based fluid finite element to represent soil-fluid-structure interaction leads to very good results compare to the earthquake records on dams. With such method, a low damping value of the concrete (probably between 1 to 2-3 %) seems more adequate for low intensity earthquake, considering that geometrical damping introduced by the absorbing boundaries already increases the global damping of the FE model.

It seems also important to remind that in the case of more complexes models introducing the input as wave propagation through the foundation, there might be a need of deconvolution process in 3D analyses to be sure that the input earthquake is correctly applied at the feet of the dam.

6. ACKNOWLEDGEMENTS

The study conducted in this paper was made possible by a collaboration between the CFBR (Comité Français des Barrages et Réservoirs) and the JCOLD (Japanese Commission on Large Dams) that took place between 2014 and 2016.

The authors thank the JCOLD, J-Power and Kepco which provided the recorded data, plans and sensor's layout used in this study.

7. REFERENCES

1. Bouaanani N (2009): Assessment of potential-based fluid finite elements for seismic analysis of dam-reservoir systems. *Computer and structures*, **87** (3), 206-224
2. Liu YS, Chen DH (2013), Earthquake response analysis of a gravity dam considering the radiation damping of infinite foundation, *APCOM & ISCM*
3. Zhang C, Pan J (2009), Influence of seismic input mechanisms and radiation damping on arch dam response, *Soil Dynamic and Earthquake engineering*, **29** (9), 1282-1293
4. Japan Commission on Large Dams (2014): Acceleration Records on Dams and Foundations No.3.

Probabilistic-Based Analysis of Concrete Gravity Dams under Synthetic Ground Motion Excitation

Yasaman Afkhami¹, Mohammad Alembagheri²

1- Department of Civil Engineering, Sharif University of Technology, Tehran, Iran

2- Department of Civil and Environmental Engineering, Tarbiat Modares University, Tehran, Iran

Email: Yasaman_a44@yahoo.com

Abstract

This research investigates seismic analysis of concrete gravity dams subjected to synthetic ground motions in the uncertainty framework. Many studies focused on only epistemic randomness due to material properties of concrete gravity dams and the impact of aleatory randomness due to seismic excitation is neglected. The latter source of randomness can significantly affect the results of analyses. Hence, in the current study, uncertainty due to earthquake excitation is tackled using synthetic ground motions. In addition, probabilistic characteristics of materials are taken into account along with artificial ground motion to form the seismic probabilistic-based analysis. The dam-reservoir-foundation model is employed for the uncertainty analysis. Generation of synthetic accelerogram utilized in this study is an iterative process based on Fourier transformation and target spectrum as well as baseline and PGA correction. Latin Hypercube sampling is utilized for the purpose of reliability analysis because of its lower computational cost relative to crude Monte Carlo Simulation for the same accuracy. The utmost goal of this research is to determine the exceedance probabilities of defined limit-state functions as well as the probability distribution function of the dam's response.

Keywords: Concrete Gravity Dam, Seismic Analysis, Reliability, Synthetic Ground Motion, Exceedance Probability.

1. INTRODUCTION

As the dams are considered one of the critical infrastructures, the safety level and accurate simulation of these infrastructures are of paramount importance. Simulation of seismic loading in analysis of concrete dams has received considerable attention in recent studies, as it is one of the main factors causing extensive damages [1-4]. On the other hand, there is a great deal of uncertainty in concrete dam modeling which have to be taken into account. Hence, the aforementioned problem can be tackled by employing reliability approaches [5, 6]. Utilizing reliability approaches provide information about the safety level of the structures under the defined loading conditions. The first step toward uncertainty analysis is to have the comprehensive understanding of the source of randomness. The randomness is categorized into aleatory and epistemic. The aleatory randomness is irreducible and is related to the nature of the phenomenon. The epistemic randomness is due to lack of information which can be reduced by gathering more information on the subject [7]. In a seismic analysis, a primary source of modeling uncertainty lies in the ground motion characteristics. As a deduction, synthetic ground motions are used in seismic analysis to consider more realistic simulation of earthquake along with inherent randomness existing in earthquake nature. Moreover, the uncertainty in the model parameters (epistemic randomness) is taken into account by assigning probabilistic characteristics to them. The probabilistic characteristics of input parameters are defined through experiments, probabilistic modeling or engineering judgment.

Recently, the probabilistic analysis of concrete dams has received considerable attention from many researchers [8, 9]. Application of seismic reliability analysis to concrete dams with the consideration of epistemic randomness is reviewed in the literature [4, 10]. In these studies, the uncertainty due to seismic excitation was considered by applying a single record or a set of natural ground motion to the model. Moreover, the reliability method used in these researches was limited to crude Monte Carlo Simulation and the main drawback of this method is its high computational cost. By reviewing papers in the field of reliability methods, other approaches such as importance sampling, directional sampling, Latin Hypercube sampling (LHS), point-estimate method, first-order and second-order reliability method were widely used [11, 12]. Although these approaches were employed for the purpose of reliability analysis of miscellaneous structures, there are few studies considering these methods in the field of dam engineering. Utilizing the new approaches will lead to more accurate results along with less computational cost.

In this research, the aforementioned issues are handled using effective reliability method which is LHS and generating synthetic ground motions. Furthermore, the effect of foundation is considered in this study. The epistemic uncertainty is tackled by defining dam and foundation properties as random variables. Concrete density and Young's elasticity modulus of concrete and foundation are assumed as the source of epistemic randomness. Generation of synthetic accelerogram utilized in this study is an iterative process based on Fourier transformation and target spectrum as well as baseline and PGA correction. As the main potential failure mode of concrete gravity dams due under seismic excitation is due to tensile cracking, the performance function is defined by tensile overstressing of the dam body. The utmost goal of this research is to determine the exceedance probabilities of defined limit-state functions as well as the probability distribution function of the dam's response.

2. UNCERTAINTY APPROACH

The risk in dam safety analysis is affected by the combined impact of failure scenario, probability of occurrence and the associated consequences [1]. Therefore, the risk analysis of dams firstly requires identification of potential failure scenarios, and then quantification of the conditional probability of these scenarios for different loading conditions. The failure scenario can be presented as limit-state inequality given by:

$$g(\mathbf{x}) \leq 0 \tag{1}$$

where $g(\mathbf{x})$ is the limit-state (performance) function with the failure condition defined by the above inequality, and \mathbf{x} is the vector of random variables in the problem. $g(\mathbf{x}) = 0$ defines the failure or limit-state surface. The probability of occurrence of the failure scenario, $P_f [g(\mathbf{x}) \leq 0]$, which is equal to the exceedance probability of the corresponding limit-state function, can be computed through the probabilistic framework [10]

$$P_f [g(\mathbf{x}) \leq 0] = \int_{g(\mathbf{x}) \leq 0} h(\mathbf{x}) d(\mathbf{x}) \tag{2}$$

where $h(\mathbf{x})$ is the joint probability density function of the random variables. There are various statistical techniques to quantify the risk. These techniques, which are known as structural reliability methods, use different mathematical formulations. Assuming that the random variables are normally distributed, the reliability index, β , is defined as

$$\beta = -\Phi^{-1}(P_f) \tag{3}$$

where Φ is the standard normal cumulative distribution function.

The benchmark and most reliable method is sampling, such as Monte-Carlo method, which is used for its ease of application in problems formulated in terms of a performance function [12]. In Monte-Carlo method realizations of each random variable are generated, which form a simulation model, and then the model is analyzed to determine the thermal response. By repeating the process for thousands of sets of realizations, distribution of response results associated with the input random variables is determined [13]. The exceedance probability of failure scenario, P_f , is estimated by dividing the number of simulations where failure scenario occurred to the total number of simulations. While conceptually straightforward, the Monte-Carlo procedure can become computationally very intensive because the number of simulations performed should be large enough to capture the searched probability. The remedy can be using more efficient sampling methods, among them Latin hypercube sampling (LHS) is selected for this research because of its efficiency and simplicity. The LHS is a variance reduction sampling method that stratifies variable marginal distributions in order to fully cover the range of each variable in a more efficient way than pure Monte-Carlo sampling [14]. Unfortunately, the appropriate sample size N , cannot be formerly determined to achieve a certain confidence level. However, using a relatively high N that is substantially larger than the number of random variables will result in reasonably accurate estimates for practical purposes.

3. GENERATING SYNTHETIC GROUND MOTION

The calculation method used in this research is given by the algorithm which is described in the following [15]. The artificial accelerogram is defined starting from a synthetic one, compatible with the target spectrum, and adapting its frequency content using the Fourier Transformation Method.

The correction of the random process is carried on at every iteration using the relationship below [16]:

$$F(f)_{i+1} = F(f)_i [SRT(f)/SR(f)_i] \tag{4}$$

where $SRT(f)$ is the value of the target spectrum and $SR(f)_i$ is the value of response spectrum corresponding to the accelerogram of the current iteration for frequency f . $F(f)_{i+1}$ and $F(f)_i$ are the values of the accelerogram in the frequency domain for the current and previous iteration respectively. At each iteration a

Fourier Transformation is applied to move from time domain to frequency domain, where the correction to the accelerogram is carried on. Then an Inverse Fourier Transformation is applied in order to return to the time domain, where the corresponding spectrum is calculated, convergence is checked and it is evaluated whether or not further correction is needed. A schematic summary is given below.

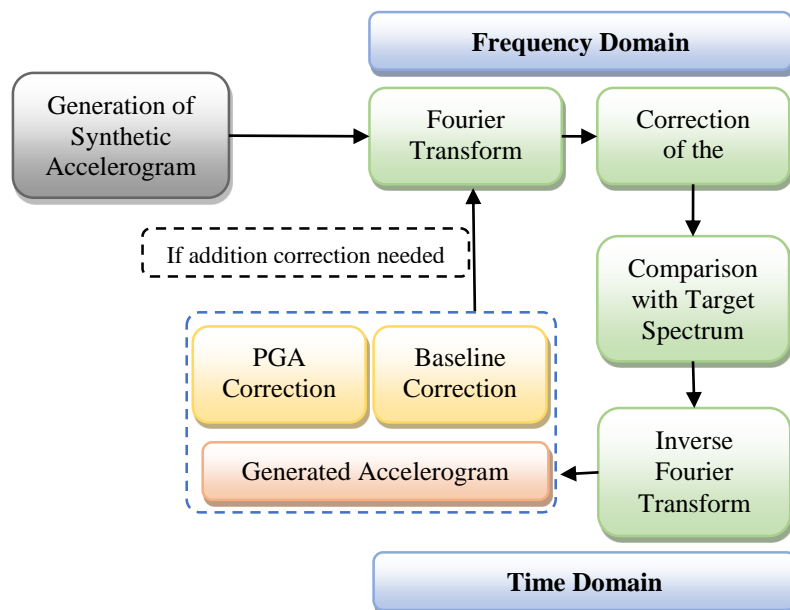


Figure 1. Algorithm of generating synthetic ground motion

In this calculation method framework, the Envelope Shape module is not explicitly shown to the user, since the procedure does not start from a random process, but rather from a synthetic accelerogram. The generation of the synthetic accelerogram starts from a Gaussian white noise which is multiplied by envelope shape and then adapted to a certain source spectrum [17]. The duration of the ground motion is calculated from the input parameters.

4. CASE STUDY: DETERMINISTIC AND PROBABILISTIC MODELING

In this study, Pine Flat concrete gravity dam is selected as the case study. The tallest monolith of the dam is used for the analyses. The geometry of the dam body and the finite element model of the dam-foundation-reservoir system are illustrated in Figure 2. The foundation rock is assumed as a homogeneous, isotropic, viscoelastic half-plane media. The foundation is extended twice the structural height of the dam in vertical direction, and five times in horizontal direction. The length of reservoir was assumed five times the dam height and non-reflective planar boundary condition was assigned as far-end boundary condition.

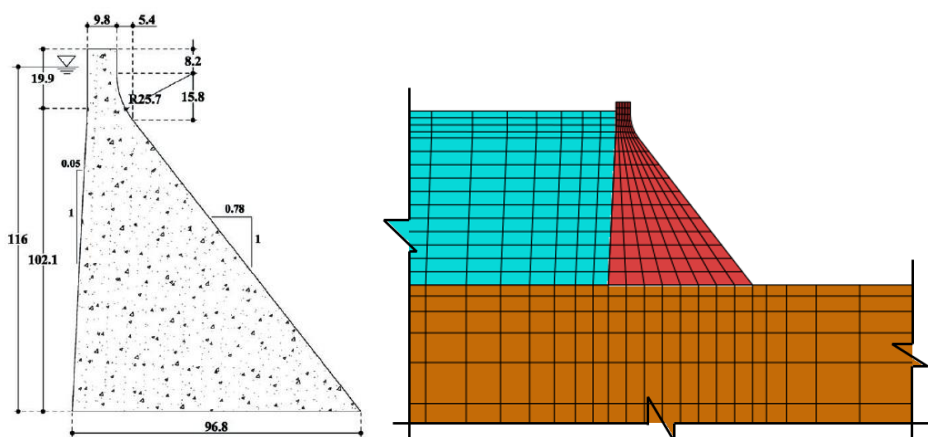


Figure 2. Geometry and the finite element model of the structure

The material and structural properties of the dam-foundation-reservoir system is given in Table 1. In the current research, concrete density and the Young’s elasticity modulus of the dam and foundation are assumed as random variables. The probabilistic characteristics of these random variables are shown in Table 1.

Table 1- Material and structural properties

		Mean Value	Distribution Type	Coefficient of Variation
Concrete	Young’s modulus (GPa)	30	Lognormal	10 %
	Poisson’s ratio	0.2	NA	
	Density (kg/m ³)	2400	Lognormal	15 %
	Rayleigh damping coefficients	$\alpha = 1.64$ $\beta = 0.0012$	NA	
	First and third mode damping (%)	5	NA	
Foundation Rock	Ratio of rock’s Young’s modulus to concrete	0.625	Uniform	34.64 %
	Young’s modulus	Range: [0.25-1]		
	Poisson’s ratio	0.33	NA	
Water	Density (kg/m ³)	1000	NA	
	Bulk modulus (GPa)	2.07	NA	

For the purpose of generating synthetic ground motion with the method described in previous section, Taft ground motion, Kern County, 7/21/1952, Taft Lincoln School, 111, is utilized. The spectrum of this record is employed so synthetic accelerogram can be generated as considering this target spectrum. Seven synthetic ground motions are generated and their statistics along with the characteristics of the target ground motion, Taft record, can be found in Table 2. As it can be noticed from Table 2, the mean error are below 10 percent and the arias intensity values are varied from 0.334 to 0.552.

Table 2- Statistical characteristics of generated ground motion

Synthetic Record No.	Mean Error (%)	CoV (%)	PGA (g)	PGV (cm/sec)	PGD (cm)	Arias Intensity (cm/sec)	Significant Duration (cm)
1	7.68	10.22	0.151	63.607	102.44 5	0.522	14.67
2	9.28	9.48	0.145	29.028	61.114	0.375	11.58
3	9.34	11.39	0.187	13.582	5.681	0.387	8.91
4	9.13	10.23	0.157	25.971	19.265	0.415	9.62
5	9.30	10.09	0.156	24.026	35.197	0.393	8.40
6	9.40	10.14	0.179	13.739	13.572	0.334	9.02
7	9.57	9.91	0.179	19.642	15.445	0.390	8.81
Taft Record	-	-	0.180	18.626	9.352	0.599	28.78

The only considered failure scenario for this model is the tensile overstressing which is quantified using the following limit-state function:

$$g(\mathbf{x}) = TS - \sigma_t \tag{5}$$

where TS is the concrete tensile strength, and σ_t is the peak value of the maximum principal (tensile) stress of the dam body. The performance index of this limit-state function can be in the form of:

$$g(\mathbf{x}) \leq 0 \tag{6}$$

which represents the exceedance of the maximum tensile stress in one or more elements within the dam body from the threshold value TS. Additional analyses have shown that the compressive overstressing is not a critical limit-state for the concrete gravity dam models under the seismic loading.

5. RESULTS

The exceedance probabilities for the defined limit-state are calculated using LHS with 1,000 realizations and the results are presented in Figure 3. The analyses are repeated for seven synthetic records and the probabilities are determined for different thresholds of the limit-state function. In the aforementioned figure, the exceedance probability curves illustrated for all synthetic records along with the mean, 84th and 16th

percentile values. The 84th and 16th percentile indicate the confidence interval and they are the mean value plus standard deviation and mean value minus standard deviation, respectively. It is concluded from exceedance probability curves that there are slight differences between the results for threshold values below 3 MPa. As the threshold values are increased, the differences are more obvious. The reason for this observation is since the larger thresholds values result in lower probabilities, the accuracy of the results are lower in the tail of the distributions which low probabilities are located there.

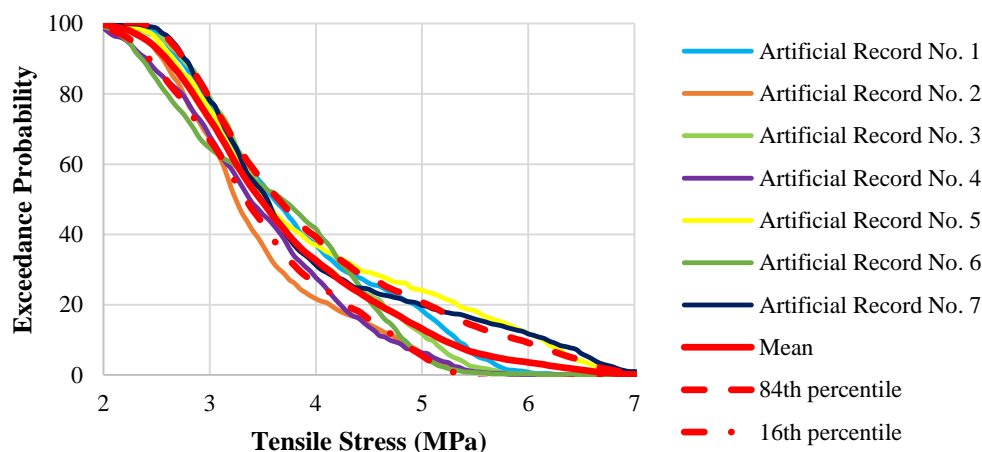


Figure 3. Exceedance probability curves for artificial records applied to the finite element model

Moreover, the results indicate that the confidence interval illustrated in Figure 3. encompass the results of all synthetic records. This means the further interpretation of the results will be more accurate considering the aforementioned confidence interval. In addition to these results, the histogram of the dam responses is depicted in Figure 4. These histograms indicate 1,000 results of the time history analysis of the Pine Flat dam under seven generated synthetic records. As mentioned earlier, the results are based on maximum tensile stress in the dam body under seismic excitation. The histograms imply that the maximum tensile stress in the dam body varies between 2 to 7 MPa.

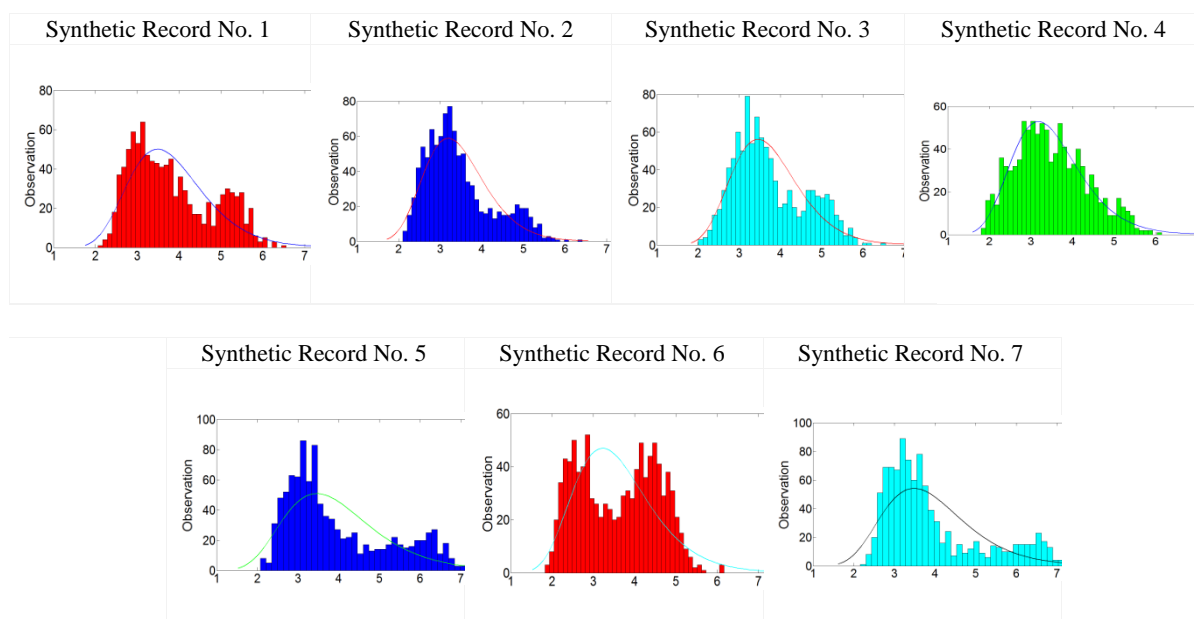


Figure 4. The histograms of the maximum tensile stresses obtained by LHS under synthetic ground motion excitation. The horizontal and vertical axes are the tensile stress (MPa) and number of observation, respectively.

Although the histograms reveal different pattern but the fitted distributions express identical results. The probabilistic characteristics of the results along with their fitted probability distribution are shown in Table 3. For the purpose of the goodness of fit tests, Anderson-Darling test is utilized. This procedure is a general test to compare the fit of an observed cumulative distribution function to an expected cumulative distribution function. Anderson-Darling test is the most standard way to control goodness-of-fitting for distributional models. According to the fitting results, the first three distributions which fit the observation the best is presented in Table 3. As it is obvious, Beta distribution is the best fitted distribution for all the results of the model under seven synthetic ground motions.

Table 3- Probabilistic characteristics and fitted distribution of the outputs

Synthetic Record No.	Mean (MPa)	Standard Deviation	Fitted Distribution		
			1 st rank	2 nd rank	3 rd rank
1	3.827	0.972	Beta	Gumbel Max	Lognormal
2	3.444	0.808	Beta	Gumbel Max	Lognormal
3	3.733	0.865	Beta	Gumbel Max	Lognormal
4	3.490	0.862	Beta	Gamma	Lognormal
5	3.977	1.274	Beta	Gumbel Max	Lognormal
6	3.607	0.948	Beta	Weibull	Normal
7	3.937	1.226	Beta	Gumbel Max	Lognormal

6. CONCLUSIONS

In this research, seismic reliability analysis of concrete gravity dam subjected to artificially generated earthquake is investigated. The aleatory randomness due to earthquake nature along with epistemic randomness is taken into account. The synthetic records are generated using a target spectrum with the algorithm based on Fourier transformation and target spectrum as well as baseline and PGA correction. The epistemic uncertainty is tackled by defining concrete density, Young's modulus of concrete and the ratio of Young's modulus of concrete to foundation rock as random variables. The dam-foundation-reservoir system is considered in this study. As the potential failure mode of concrete gravity dam due to ground motion is tensile cracking, the limit-state function is defined based on maximum tensile stress. The reliability methods employed in this investigation is Latin Hypercube sampling. With one thousands realizations, the exceedance probabilities of the defined thresholds are calculated and depicted as exceedance probability curves. Moreover, the histograms of the outputs are determined. The Anderson-Darling goodness of fit test indicates that for all outputs, the best fitted distribution is Beta. The results indicate that the confidence interval determined using exceedance probability curves, encompass the results of all synthetic records. This means the further interpretation of the results will be more accurate considering the aforementioned confidence interval.

7. REFERENCES

1. Altarejos-García, L., Escuder-Bueno, I., Serrano-Lombillo, A., & de Membrillera-Ortuño, M. G. (2012), "Methodology for estimating the probability of failure by sliding in concrete gravity dams in the context of risk analysis," *Structural safety*, 36, 1-13.
2. Gaspar, A., Lopez-Caballero, F., Modaressi-Farahmand-Razavi, A., & Gomes-Correia, A. (2014), "Methodology for a probabilistic analysis of an RCC gravity dam construction. Modelling of temperature, hydration degree and ageing degree fields," *Engineering Structures*, 65, 99-110.
3. Kartal, M. E., Bayraktar, A., & Başağa, H. B. (2012), "Nonlinear finite element reliability analysis of Concrete-Faced Rockfill (CFR) dams under static effects," *Applied Mathematical Modelling*, 36(11), 5229-5248.
4. Lupoi, A., & Callari, C. (2012), "A probabilistic method for the seismic assessment of existing concrete gravity dams," *Structure and Infrastructure Engineering*, 8(10), 985-998.
5. Vanmarcke, E. H. (1973), "Matrix formulation of reliability analysis and reliability-based design," *Computers & Structures*, 3(4), 757-770.
6. Ditlevsen, O., & Madsen, H. O. (1996), "Structural reliability methods (Vol. 178)," New York: Wiley.
7. Haukaas, T., & Der Kiureghian, A. (2004), "Finite element reliability and sensitivity methods for performance-based earthquake engineering (No. 14)," Pacific Earthquake Engineering Research Center, College of Engineering, University of California, Berkeley.
8. Mohammadi, P. M., Noorzad, A., Rahimian, M., & Omidvar, B. (2009), "The effect of interaction between reservoir and multi-layer foundation on the dynamic response of a typical arch dam to P and S waves," *Arabian Journal for Science and Engineering*, 34(1B), 92.
9. Hariri-Ardebili, M. A., & Saouma, V. E. (2016), "Probabilistic seismic demand model and optimal intensity measure for concrete dams," *Structural Safety*, 59, 67-85.
10. Alembagheri, M., & Seyedkazemi, M. (2015), "Seismic performance sensitivity and uncertainty analysis of gravity dams," *Earthquake Engineering & Structural Dynamics*, 44(1), 41-58.
11. Karamchandani, A., & Cornell, C. A. (1992), "Sensitivity estimation within first and second order reliability methods," *Structural Safety*, 11(2), 95-107.
12. Val, D., Bljucer, F., & Yankelevsky, D. (1997), "Reliability evaluation in nonlinear analysis of reinforced concrete structures," *Structural Safety*, 19(2), 203-217.
13. Liel, A. B., Haselton, C. B., Deierlein, G. G., & Baker, J. W. (2009), "Incorporating modeling uncertainties in the assessment of seismic collapse risk of buildings," *Structural Safety*, 31(2), 197-211.
14. McKay, M. D., Beckman, R. J., & Conover, W. J. (1979), "Comparison of three methods for selecting values of input variables in the analysis of output from a computer code," *Technometrics*, 21(2), 239-245.
15. Halldorsson, B., & Papageorgiou, A. S. (2005), "Calibration of the specific barrier model to earthquakes of different tectonic regions," *Bulletin of the Seismological society of America*, 95(4), 1276-1300.
16. Gomes, R. C., Santos, J., & Oliveira, C. S. (2006), "Design spectrum-compatible time histories for numerical analysis: Generation, correction and selection," *Journal of earthquake engineering*, 10(06), 843-865.
17. Rodolfo Saragoni, G., & Hart, G. C. (1973), "Simulation of artificial earthquakes," *Earthquake Engineering & Structural Dynamics*, 2(3), 249-267.

Probabilistic Analysis of Concrete Gravity Dams Owing to Foundation Inhomogeneity

Hamid Taghavi Ganji¹, Mohammad Alembagheri², Mohammad Houshmand²

1- Department of Civil and Environmental Engineering, Amirkabir University of Technology, Tehran, Iran

2- Department of Civil and Environmental Engineering, Tarbiat Modares University, Tehran, Iran

Email: h.taghavi.g@gmail.com

Abstract

Assumption of homogenous foundation would bring about a lot of hazardous consequences, although it might reduce the cost of designing. These hazardous consequences root in inhomogeneity of foundation which is caused by large joints or fissures in it. Even though it is impossible to extend a unique model of inhomogeneity to all dams, the effect of mechanical properties of coupled system of dam-foundation-reservoir would be evaluated by considering one of the most critical geological situations which lead to critical responses. In current study, seismic performance of Pine Flat dam founded on inhomogeneous foundation is studied by probabilistic analysis as case study. In this process, three different level of earthquake's intensity are imposed to the same models. Furthermore, the effect of deconvolution process is studied and the results have demonstrated importance of this process, especially in inhomogeneous cases.

Keywords: Concrete Gravity Dams, Inhomogeneous Rock Foundation, Probabilistic Analysis, Deconvolution, Levels of Earthquake's Intensity.

1. INTRODUCTION

The seismic safety of existing concrete dams and the risks posed by earthquakes has been a growing issue in the last decades. The main potential seismic failure modes of concrete gravity dams are tensile cracking and sliding along jointed sections specifically at the dam-foundation interface [1]. Gravity dams are usually evaluated using deterministic analysis methods; however, probabilistic and reliability methods are preferred due to the sources of uncertainty presented in earthquake ground motions and in parameters describing the structural system. Therefore, the seismic reliability assessment is employed as a useful tool in dam safety. This method of analysis for concrete dams is in its early development stage and examples are scarce [2, 3]. It requires an analytical or numerical model that robustly captures the nonlinear structural behavior, and explicit consideration of important sources of uncertainty. These uncertainties may be aleatoric (inherent randomness) or epistemic (lack of knowledge). In a nonlinear seismic analysis, a primary source of modeling uncertainty lies in definition of the analysis model parameters as compared to the components' actual behavior [4]. Application of seismic reliability analysis to gravity dams requires identification of potential failure modes presented as limit-state (performance) functions, and prediction of the conditional probability of limit-state exceedance under different earthquake events. This exceedance probability can be rigorously estimated using statistical techniques in probability analysis [5].

2. PROPOSED METHODOLOGY

The proposed methodology for deconvolution process would be elaborated in this section. For realizing the effect of foundation's mass in amplifying the free-field motion, this process is required. A schematic view of this process is illustrated in Figure 1. For this purpose, it is needed to be conducted in frequency domain by computing the transfer function TF, of the foundation medium through its finite element analysis by applying the available free-field record $a_{ff}(t)$, at the base and computing the acceleration time-history at the top of the foundation, $a_{top}(t)$. The foundation's TF is obtained as:

$$TF(\omega) = \frac{A_{top}(\omega)}{A_{ff}(\omega)} \quad (1)$$

where $A_{top}(\omega)$ and $A_{ff}(\omega)$ are Fourier transforms of the computed top and the applied free-field records, respectively. Then, the inverse of the foundation's TF is used to obtain Fourier transform of the required input base acceleration record, $A_{inp}(\omega)$:

$$A_{inp}(\omega) = \frac{A_{ff}(\omega)}{TF(\omega) + \varepsilon} \tag{2}$$

where ε is a regularization parameter avoids dividing by very low values. The input deconvolved base record $a_{inp}(t)$, that produces the free-field record at the top of the foundation is computed by the inverse Fourier transform of $A_{inp}(\omega)$. It is noteworthy that the foundation could be homogeneous or inhomogeneous but it should behave linearly so the deconvolution process can be applied. Also, because the properties of the foundation such as rock material properties may change in each sample, the deconvolution process should be repeated for each foundation sample to produce the correct free-field record at the top surface.

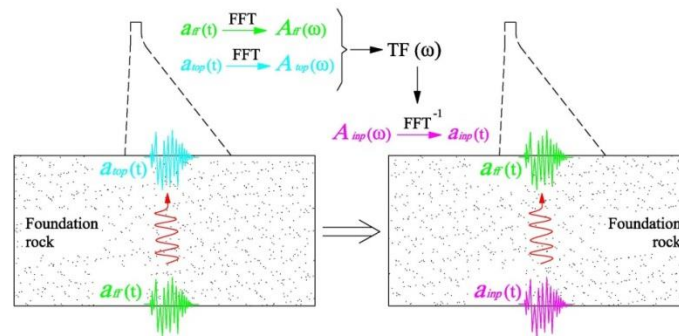


Figure 1. Schematic representation of the deconvolution process

3. APPLICATION EXAMPLE

3.1. PINE FLAT GRAVITY DAM

The proposed methodology is applied to Pine Flat gravity dam as case-study. The tallest non-over-flow monolith of the dam is selected, as shown in Figure 2(a), and numerically analyzed along with a portion of the full reservoir and the rock foundation using the finite element method. All components are modeled with eight-node continuum elements as illustrated in Figure 2(b). In addition, to assess the effects of foundation inhomogeneity on the seismic performance of the dam, three distinct rock regions are considered within the foundation as shown in Figure 2. This illustrative configuration has been selected based on primary analyses showing its high influence on the dam seismic performance. No joint or fault is considered between the rock regions. The inertia, flexibility, and damping of the foundation are taken into account. The radiation damping is modeled using infinite elements at the bottom and lateral sides of the foundation as shown in Figure 2(b) to avoid reflection of seismic waves back to the dam. The reservoir is assumed to be full, and linear elastic materials are used to model the behavior of the concrete, water and foundation rocks. The water's density and bulk modulus are 1000kg/m³ and 2.07GPa, respectively.

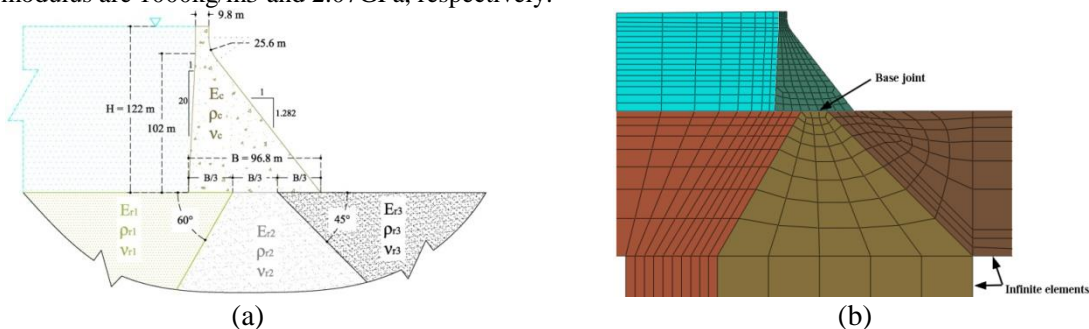


Figure 2. (a) Pine Flat dam with full reservoir and illustrative inhomogeneous foundation, (b) finite element mesh of the dam-reservoir-inhomogeneous foundation system.

There is a single interface in the contact between the dam and the foundation. This base joint which is shown in Figure 2(b) has no tensile strength but it can mobilize shear strength up to some extent. The sliding resistance is defined through the Coulomb model as a function of the friction coefficient μ [6]. The cohesion is neglected and no uplift pressure is considered in the analysis. Firstly, models are statically loaded and then they would be dynamically analyzed under the horizontal component of the deconvolved earthquake ground motions. A typical Rayleigh damping of 5% is used for the dam and the foundation.

3.2. PERFORMANCE FUNCTION

Multiple limit-states, related to structural failure modes, can be of interest for concrete gravity dams. As it was stated, the main potential seismic failure modes of gravity dams are tensile cracking, and movement along the prescribed joint at the dam-foundation interface. Hence, in this study, three different performance functions are defined. The first one is tensile overstressing of the dam body which would result in tensile cracking which is defined through subtracting the envelope maximum (tensile) principal stress within the dam body. The second and the third performance functions are related to the dam-foundation interface and are, respectively, sliding along the base joint, and opening of the base joint in its upstream end adjacent to the reservoir.

3.3. CONTROLLING EARTHQUAKES

For seismic analysis of gravity dams, the USACE guidelines [7] suggest return periods of 144-year, 950-year and 10'000-year for OBE, MDE and MCE records in a common service life of 100 years. Probabilistic seismic hazard analysis of the Pine Flat dam site shows that the peak horizontal accelerations to be expected at the site are 0.18g, 0.27g, and 0.45g corresponding to return periods for the OBE, MDE, and MCE ground motions, respectively [8]. They are proportional to hazard levels of 50%, 10% and 1% in a service life of 100 years, respectively. The Kern County earthquake of 1952 recorded at Taft Lincoln School Tunnel is selected as the free-field ground acceleration. It is scaled into three increasing PGA levels as stated above corresponding to the OBE, MDE and MCE records of the site. Their annual exceedance probability is 0.69%, 0.11% and 0.01%, respectively. The response spectra of the scaled records are shown in Figure 3.

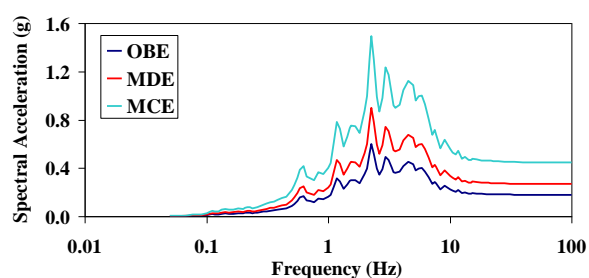


Figure 3. Response spectra of the selected earthquake ground motions

3.4. RANDOM VARIABLES

The random variables chosen are listed in Table 1 with their associated probability distribution function, mean, and coefficient of variation. The related domains are shown in Figure 2(a). As limited material investigations are available for the Pine Flat dam, most probability distributions are defined from empirical data of similar dams. The uncertainty in modeling parameters is mainly considered to be epistemic because of this lack of knowledge. The elastic moduli of the rock regions are related to the dam's one using the defined α ratios. The random variables are all assumed to be uncorrelated.

3.5. MONTE-CARLO WITH LHS

For Monte-Carlo simulation, statistically significant samples of the dam-foundation coupled system are derived using Latin Hypercube sampling (LHS). There is no predefined sample size N to achieve a certain confidence level, however, some formulas have been presented for various applications. One of the simplest formulas is [9]:

$$\lambda < 1 - e^{-N \cdot P_f} \quad (3)$$

where λ is the confidence level, and P_f is the exceedance probability of limit-state. Assuming a confidence level of $\lambda = 98\%$ and $P_f = 10^{-3}$, which is a reasonable value in dam engineering [10], about 4000 samples are required based on this convenient formula. To assess the number of samples, the LHS method is employed to obtain three different sets with 1000, 2000, and 4000 dam-reservoir-foundation samples by sampling the modeling parameters in Table 1. Each sample is then analyzed under the selected scaled ground motions. As there are three different earthquake records scaled to the given seismic intensities, total number of simulations is 42'000.

Table 1. Selected random variables; related domains and parameters are shown in Figure 2. (a)

Domain	Random variable	Unit	Distribution function	Mean	Coefficient of variation
Dam	Density, ρ_c	kg/m ³	Lognormal	2400	0.1
	Elastic modulus, E_c	GPa	Lognormal	30	0.2
Rock region 1	Density, ρ_{r1}	kg/m ³	Lognormal	2600	0.1
	Elastic modulus ratio, $\alpha_1 = E_{r1} / E_c$	---	Uniform	0.875	0.4
Rock region 2	Density, ρ_{r2}	kg/m ³	Lognormal	2600	0.1
	Elastic modulus ratio, $\alpha_2 = E_{r2} / E_c$	---	Uniform	0.875	0.4
Rock region 3	Density, ρ_{r3}	kg/m ³	Lognormal	2600	0.1
	Elastic modulus ratio, $\alpha_3 = E_{r3} / E_c$	---	Uniform	0.875	0.4
Base joint	Fiction coefficient, μ	---	Normal	1	0.2

4. RESULTS AND INTERPRETATION

The histograms of maximum seismic responses of the three sample sets under the OBE, MDE, and MCE ground motions are illustrated in Figure 4. Also shown is the best distribution fit using one of normal, lognormal, beta, and logistic fits. The distributions' mean and standard deviation, for each histogram is presented in Table 2. Regardless of the number of samples, the same distribution fit with very similar mean and standard deviation is obtained. Therefore, only one fit for the 1000-sample set is shown in Figure 4. As it is expected, when the applied earthquake becomes stronger, higher mean responses are generally captured. The mean responses are about 0.2, 0.7, and 4.8MPa for tensile stress under the OBE, MDE, and MCE, respectively. However, even up to 8MPa tensile stress may be observed under the MCE. The corresponding standard deviations also increase by increasing the earthquake intensity. So it seems that the tensile stresses spread in a wider range. But, the coefficient of variation of the tensile stress is about 1.10, 0.38, and 0.23 under the OBE, MDE, and MCE, respectively. So by increasing the earthquake intensity the lower dispersion of distribution is obtained.

About the base joint opening and sliding, the mean responses increase by increasing the earthquake intensity, but the standard deviation is the most under the MDE, then MCE, and then OBE. Moreover, same as tensile stress, more earthquake intensity causes lower coefficient of variation. Rather high values of the coefficient of variation show that large uncertainties are controlling the results, no matter what number of samples is being used. Even with low coefficient of variation, the base sliding more than 60cm may occur under the MCE. Based on the results obtained, it is important to increase the amount of information about the sources of uncertainty affecting the seismic responses.

From the histograms, it is possible to compute the exceedance probability of the limit-states P_f , for varying threshold values using equation (3). The varying threshold values describe various damage levels. The obtained exceedance probability (EP) curves are plotted in Figure 5 for the defined performance functions. As it is observed, the EP curves are very similar regardless of the number of samples used. As the earthquake record becomes more intensive, the related EP curve will be shifted to the right side which shows higher exceedance probabilities. For example, considering threshold value of 2.25MPa for the overstressing performance function, the exceedance probabilities would be 2%, 37% and 93% for the OBE, MDE and MCE, respectively. This threshold is a common value of the dynamic tensile strength of dam concrete [11], so exceeding this value means tensile cracking of the dam body, however it is not coincident with the total failure of the dam.

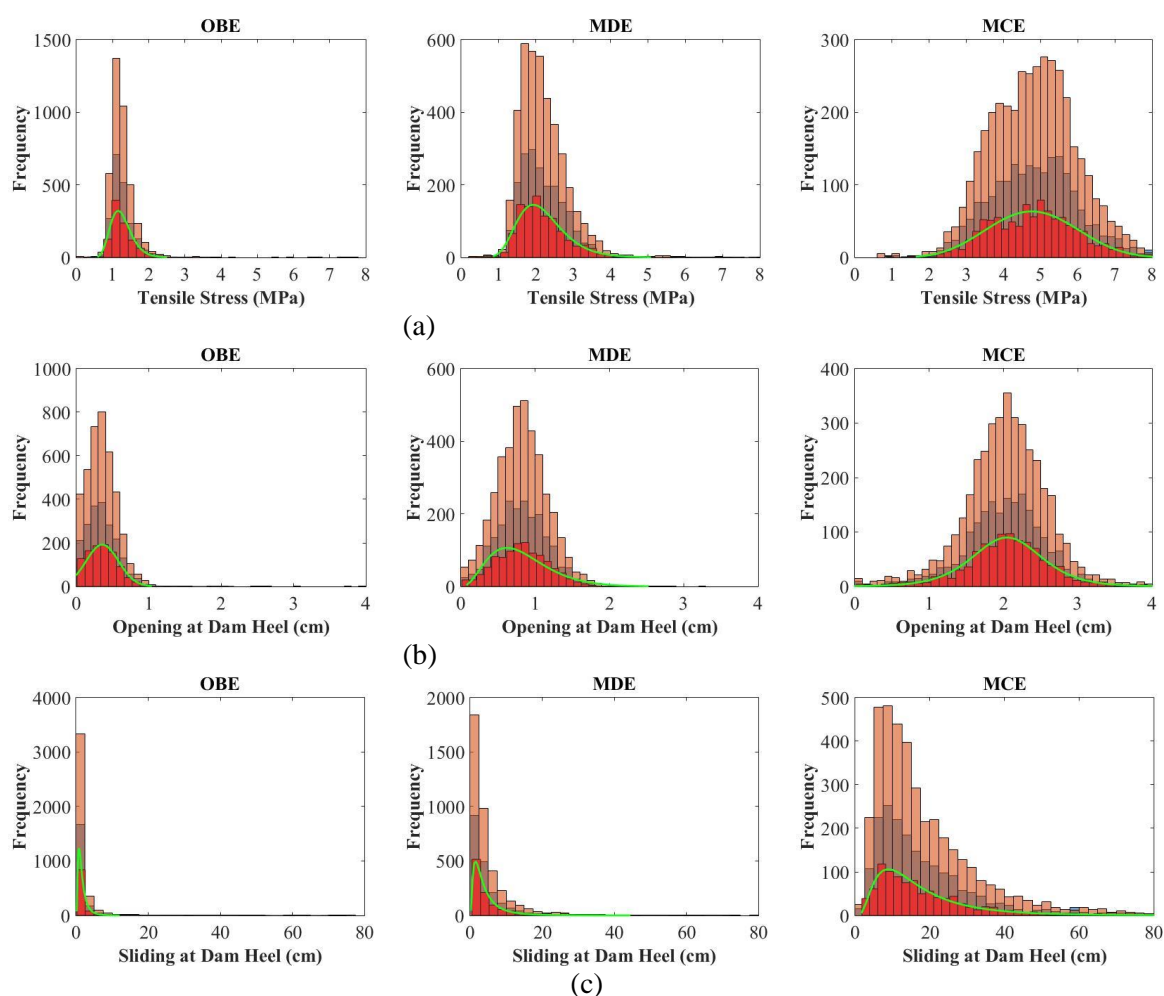


Figure 4. Histograms of seismic analysis output for the three sets of samples under different ground excitations. (a) maximum tensile stress, (b) base joint opening, and (c) base joint sliding. The results of 1000, 2000, and 4000-sample sets are shown in red, brown, and light brown, respectively.

Table 2. Mean and standard deviation of distribution fits on the output histograms

Seismic output	Ground motion	Distribution	Number of samples					
			1000		2000		4000	
			Mean	STDEV	Mean	STDEV	Mean	STDEV
Tensile stress	OBE	lognormal	0.197	0.232	0.204	0.221	0.197	0.217
	MDE	lognormal	0.733	0.276	0.739	0.266	0.734	0.263
	MCE	beta	4.787	1.149	4.808	1.152	4.802	1.132
Base joint opening	OBE	normal	0.349	0.204	0.349	0.201	0.349	0.198
	MDE	beta	0.820	0.346	0.818	0.333	0.820	0.334
	MCE	logistic	2.032	0.316	2.020	0.306	2.001	0.330
Base joint sliding	OBE	lognormal	0.261	0.676	0.288	0.701	0.284	0.702
	MDE	lognormal	1.130	0.850	1.139	0.861	1.140	0.868
	MCE	lognormal	2.674	0.710	2.683	0.718	2.648	0.787

The base joint opening is observed even for low seismic intensities. Because the opening is measured at the upstream end of the base joint adjacent to the reservoir, it may result in water to penetrate inside the base joint that endangers the dam stability. The probability of maximum opening to exceed 1cm is 0%, 29% and 97% under the OBE, MDE and MCE, respectively. Minor, moderate and severe damage will be imposed to the dam's drain system for incipient, 2.5cm and 5cm base sliding, respectively [12]. The moderate and severe damage probabilities are 16% and 8% under the OBE, respectively, while they are 53% and 29% under the MDE, and more than 90% under the MCE. A sliding displacement of 15cm would cause unacceptable differential movements with the adjacent monoliths and could, eventually, cause loss of reservoir control [2]. The probability of exceeding from this high sliding is 3%, 8% and 50% for the OBE, MDE and MCE, respectively.

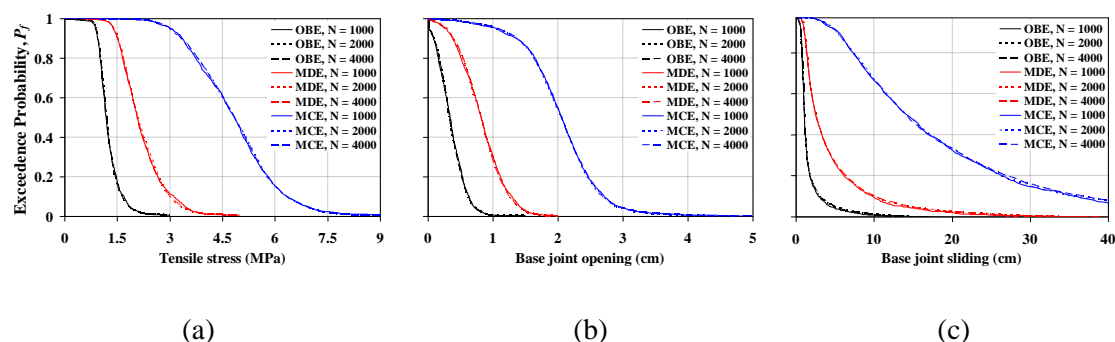


Figure 5. EP curves of the three sets of samples under increasing ground excitation intensities for: (a) overstressing, (b) base joint opening, and (c) base joint sliding performance functions.

All in all, considering two seismic failure modes of tensile overstressing and movement along joints, the dam will undergo severe damage level with the probability more than 90% under the MCE ground motion, while this probability is below 5% for the OBE. Approaching coincidentally to two failure modes will probably cause the total failure of the dam under intense earthquake ground shakings; however, the dam will safely survive light earthquakes in order of OBE. It should be noted that the computed conditional probabilities do not provide much information on dam total safety because it has to be multiplied by the probability of the seismic loadings [5]. In this way, the total annualized probability of failure is computed by summing the products of the probability of the seismic event by the conditional probability of failure for all potential failure modes.

5. SENSITIVITY TO EARTHQUAKE DECONVOLUTION PROCESS

To investigate the effects of the deconvolution process, the 1000-sample set is re-analyzed under the OBE, MDE and MCE deconvolved using the foundation with mean values for the random variables of the rock regions. The deconvolution process is done only once for each earthquake, and it is not repeated for every sample. So the same ground motion is applied to all samples. The new computed EP curves are compared with obtained curves in last section in Figure 6. The difference between the EP curves increases by increasing the earthquake intensity. So the deconvolution process is more important for larger earthquakes. However, the maximum difference between the estimated P_f values in all threshold levels is up to 12% for the defined performance functions. Excluding the deconvolution process for each sample flattens the EP curve, and the mean values are shifted into lower values. It shows that the obtained results are more sensitive when the deconvolution process is considered for each sample.

In the next step, the 1000-sample set is re-analyzed under the MDE which is applied without any deconvolution in the free-field condition to the model base. The resulted EP curves are illustrated in Figure 7 against the EP curves obtained considering the deconvolution of the MDE. Ignoring the deconvolution and applying the ground motion in the free-field condition totally underestimates the exceedance probabilities in entire threshold range for all failure modes. The difference is more for lower threshold values. It is expected that magnifying the earthquake intensity would increase this underestimation. Hence, the earthquake records should be deconvolved when analyzing dam-foundation systems considering inertia and inhomogeneity of the rock.

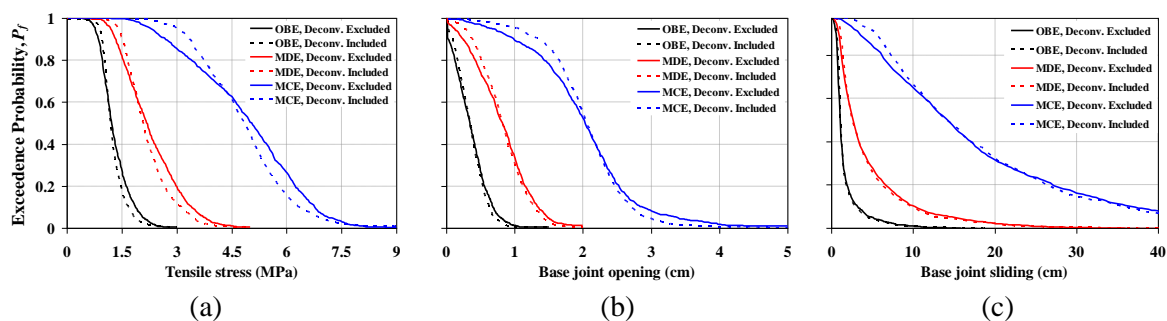


Figure 6. Effects of the earthquake deconvolution process on the EP curves for (a) overstepping, (b) base joint opening, and (c) base joint sliding performance functions

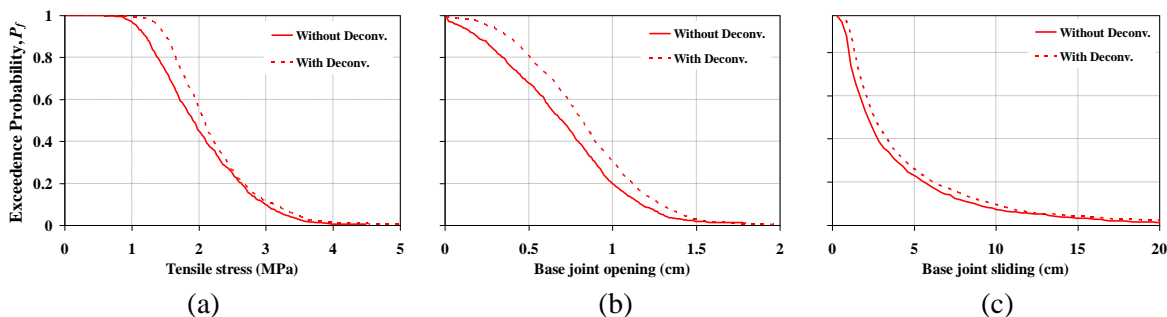


Figure 7. Comparison of the EP curves of the 1000-sample set under the MDE with and without deconvolution: (a) overstepping, (b) base joint opening, and (c) base joint sliding

6. CONCLUSIONS

In this study, a methodology was proposed to evaluate the seismic reliability of gravity dam-reservoir-foundation coupled systems. The uncertainties associated with modeling parameters were incorporated in nonlinear time history analysis to realistically quantify their effects on the seismic performance of the system. The system was analyzed under the OBE, MDE, and MCE records of the dam site. The deconvolved-base-rock input model was utilized as earthquake input mechanism. The same distribution fit with very similar parameters and approximately the same exceedance probability curves were obtained for seismic output results regardless of the number of samples. So in this type of analysis, the number of simulations can be reduced in order of four, from 4000 to 1000, with the same estimation of probability. Higher mean responses were obtained under larger earthquake, but the coefficient of variation decreased by increasing the earthquake intensity. However, high values of the coefficient of variation showed that large uncertainties are controlling the results. It was shown that considering two seismic failure modes of tensile overstepping and movement along joints, the dam will undergo severe damage level with the probability more than 90% under the MCE, while this probability is below 5% for the OBE. Approaching coincidentally to two failure modes will probably cause the total failure of the dam under intense earthquake ground shakings; however, the dam will safely survive light earthquakes in order of OBE.

About the deconvolution process, it was found that it is more important for larger earthquakes. Excluding the deconvolution process for each sample flattened the EP curve, and the mean values were shifted into lower values. The obtained results were more sensitive when the deconvolution process was considered for each sample. Ignoring the deconvolution and applying the ground motion in the free-field condition totally underestimated the exceedance probabilities for all failure modes. Hence, the earthquake records should be deconvolved when analyzing dam-foundation systems considering inertia and inhomogeneity of the rock.

7. REFERENCES

1. ICOLD (2001), Design features of dams to resist seismic ground motion: Guidelines and case studies. Bulletin No. 120, Paris.
2. Bernier C, Padgett J.E, Proulx J, and Paultre P. (2016), “*Seismic Fragility of Concrete Gravity Dams with Spatial Variation of Angle of Friction*”, Journal of Structural Engineering, **142** (5).
3. Alembagheri M, and Seyedkazemi M. (2015). “*Seismic performance sensitivity and uncertainty analysis of gravity dams*”, Earthquake Engineering and Structural Dynamics, **44** (1), pp 41-58.
4. Liel A.B, Haselton C.B, Deierlein G.G, and Baker J.W. (2009), “*Incorporating modeling uncertainties in the assessment of seismic collapse risk of buildings*”, Structural Safety, **31** (2), pp 197-211.
5. Altarejos-García L, Escuder-Bueno I, Serrano-Lombillo A, and de Membrillera-Ortuño M.G, (2012), “*Methodology for estimating the probability of failure by sliding in concrete gravity dams in the context of risk analysis*”, Structural Safety, **36-37**, pp 1-13.
6. Alembagheri M, and Ghaemian M. (2013), “*Incremental dynamic analysis of concrete gravity dams including base and lift joints*”, Earthquake Engineering and Engineering Vibration, **12** (1), pp 119-134.
7. USACE (2003), Time-history dynamic analysis of concrete hydraulic structures. EM-1110-2-6051, Washington, DC.
8. USBR (2003), Upper San Joaquin River Basin Storage Investigation, Raise Pine Flat Dam. Surface Storage Option Technical Appendix to the Phase 1 Investigation Report. In Coordination with: The California Bay-Delta Authority.
9. Broding W.C, Diederich F.W, and Parker P.S. (1964), “*Structural optimization and design based on a reliability design criterion*”, Journal of Spacecraft and Rockets, **1** (1), pp 56-61.
10. Chauhan S.S, and Bowles D.S. (2003), “*Dam safety risk assessment with uncertainty analysis*”, Proceeding of Australian Committee on Large Dams Risks Workshop, Australia.
11. Harris D.W, Mohorovic C.E, and Dolen T.P. (2000), “*Dynamic properties of mass concrete obtained from dam cores*”, Materials Journal, **97** (3), pp 290-296.
12. Fenves G.L, and Chavez J.W. (1996), “*Evaluation of earthquake induced sliding in gravity dams*”, 11th World Conf. on Earthquake Eng., International Association for Earthquake Engineering, Tokyo.

Hydrodynamic Sub-Pressure Incremental Pattern in Dam-Reservoir Interaction System Subjected to Far Field and Near Field Ground Motions

Mohammad Manafpour¹, Arman Roshanravan²

1- Assistant Professor, Faculty of Civil Engineering, University of Urmia

2- PhD student, Faculty of Civil Engineering, University of Urmia

Email: Arman.roshanravan@gmail.com

Abstract

Hydrodynamic pressure distribution on upstream face of the dam depends on several parameters such as distance from fault, natural frequency of dam and etc. distance from fault cause significant effect on amplitude and frequency content of the motions. Frequency contents could cause significant effects on dam responses and hydrodynamic pressure distribution which is main goal of this paper. In hydrodynamic pressure fluctuations, sub-pressure occurrence cause cavitation problem on upstream face of the dam. Although cavitation effects in this case could not cause severe damage on dam body but it is not negligible especially near outlet structures. Results show frequency contents of the ground motion has a significant effect on hydrodynamic pressure distribution and sub-pressure occurrence.

Keywords: hydrodynamic sub-pressure, cavitation, dam-reservoir interaction, near field, far field.

1. INTRODUCTION

Dynamic analysis of dam-reservoir-foundation system and dam responses highly depends on frequency contents of the ground motions. Frequency contents of the ground motions also depends on several parameters. Distance from fault is the most important parameter which affect the frequency contents of the recorded motions. Far field recorded motions have wider frequency contents than the near fields motions.

Chopra et al in 2001, investigated on the effect of near field and far field ground motions on the behavior of the structures. They concluded, structures near the fault need more resistance to ground motions than the far structures [1]. Bayraktar et al in 2009 investigated on the effect of near field and far field motions on response of concrete gravity dam. The results show, displacements and stresses in dam body are greater in case of near field motions [2]. Hajihoseini et al in 2011, investigated on the damage pattern on concrete gravity dams due to near field and far field ground motions. They considered Koyna dam on rigid body and concluded the dam body cracked under near field recorded motions of Bam earthquake. The cracks located on downstream face where the slope changes [3]. Zhang et al in 2013 studied the effect of near field and far field ground motions on dynamic response of dam-reservoir-foundation system. They selected Koyna dam as their case study and the results show displacement response of the dam in case of near field motions are completely different with far field motions [4]. Roshanravan et al in 2015 studied the recorded vibrations on Karun3 dam using system identification and continues wavelet transform (CWT) [5].

In this paper, hydrodynamic Sub-pressure and cavitation occurrence on upstream face of the dam for near field and far field ground motions investigated. Frequency of hydrodynamic pressure also calculated.

2. CONTINUES WAVELET TRANSFORM (CWT) METHOD

CWT is a mathematical transform which can analyze signals in both time and frequency domain with variable resolution. The main equation of CWT is:

$$CWT_x^\psi(a, b) = \frac{1}{\sqrt{a}} \int_{-\infty}^{+\infty} x(t) \bar{\psi}\left(\frac{t-b}{a}\right) dt \quad (1)$$

Where “b” and “a” are translation and scale parameters respectively. “x” is signal and “t” indicates that the signal is in time domain and “ψ” is wavelet function. In this research the modified Morlet wavelet is used as wavelet function. Mathematical representation of modified Morlet wavelet is:

$$\psi(t) = \frac{1}{\sqrt{\pi f_b}} e^{i2\pi f_c t} e^{-t^2/f_b} \quad (2)$$

Where f_b and f_c are band pass and central frequency of wavelet respectively.

As mentioned above Wavelet transform is a multi-resolution transform that resolutions are depend on wavelet parameters. Wavelet time and frequency resolutions represents as:

$$\Delta t_i = \frac{f_c \sqrt{f_b}}{f_i^2} \quad (3)$$

$$\Delta f_i = \frac{f_i}{f_c 2\pi \sqrt{f_b}} \quad (4)$$

As is clear by changing the value of f_b and f_c , different resolutions obtained. So these parameters should be optimized to obtain better results. Here, a trial and error process hired to optimize wavelet parameters. The requested domain for wavelet parameters should satisfy Equation5 [6].

$$\sqrt{f_b} f_c = (2\alpha) \frac{f_{i,i+1}}{2\pi \Delta f_{i,i+1}} \quad (5)$$

Where α is the parameter defining the overlap between the adjacent Gaussian windows of the modified Morlet wavelet. Kijewski and Kareem suggested the empirical value $\alpha=2$ is generally sufficient to distinguish two adjacent frequency components [7].

3. FINITE ELEMENT MODEL

The Koyna Dam is one of the largest dams in India. The dam has withstood many earthquakes in the recent past, including the devastating 1976 Koynanagar earthquake, resulting in the dam developing some cracks. Dam height, crest length and reservoir capacity of the dam are 103 m 807.2 m and 2.8 MCM respectively. Koyna dam-reservoir-foundation system modeled using ABAQUS software. Finite element model of the Koyna dam showed in figure 1. Reservoir length and foundation depth are considered 3 times and 2.5 times of the dam height respectively.

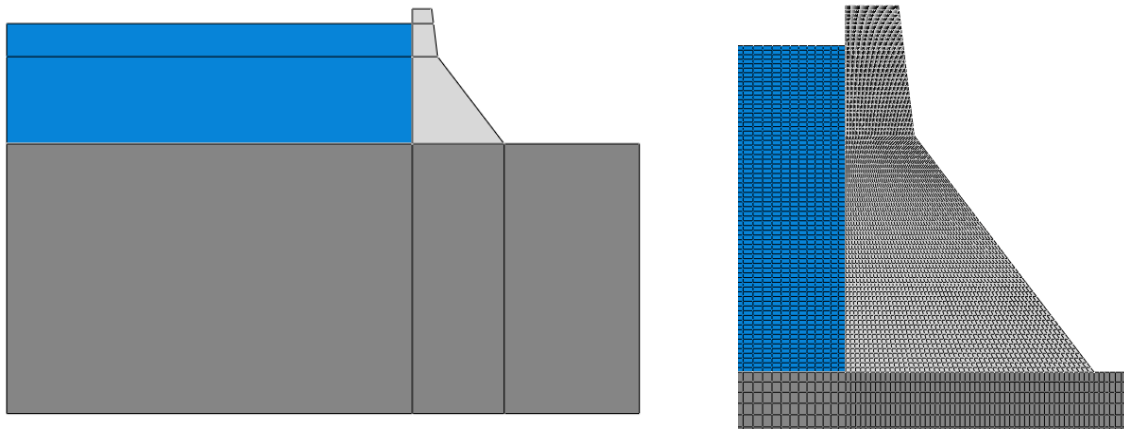


Figure 1-Finite element model of dam-reservoir-foundation system

4. GROUND MOTIONS

As discussed above, the main goal of this paper is to investigate the sub-pressure on upstream face of the dam due to near field and far field ground motions and compare them to each other. So near field and far field recorded motions of Kobe earthquake hired to analyze the finite element model. Horizontal and vertical components of the ground motions and their frequency contents showed in figures 2 to figure 9.

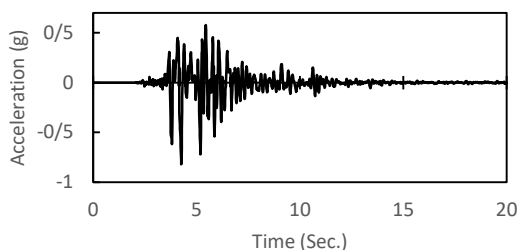


Figure 2-Horizontal component of Kobe near field motion

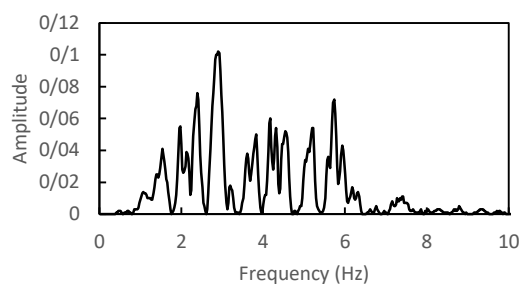


Figure 3-PSD spectrum of horizontal component of Kobe near field motion

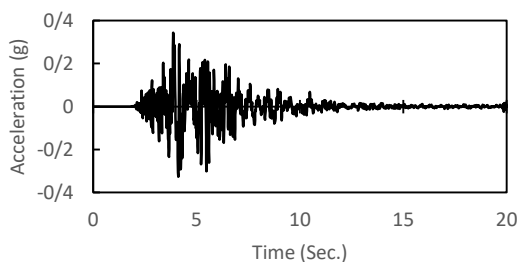


Figure 4-Vertical component of Kobe near field motion

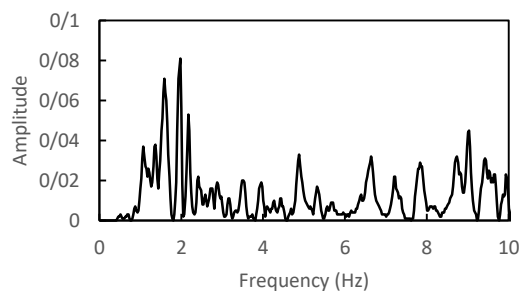


Figure 5-PSD spectrum of vertical component of Kobe near field motion

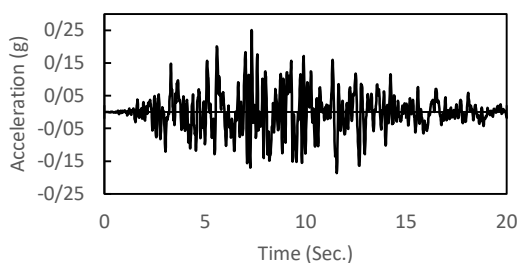


Figure 6-Horizontal component of Kobe far field motion

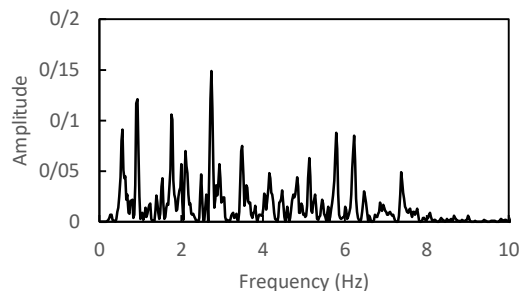


Figure 7-PSD spectrum of horizontal component of Kobe far field motion

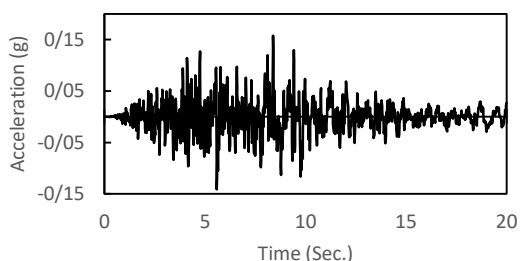


Figure 8-Vertical component of Kobe far field motion

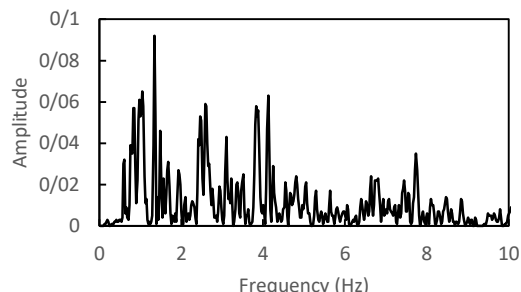


Figure 9-PSD spectrum of vertical component of Kobe far field motion

Far field recorded motion belongs to Kakogawa station which is 22.5 km far from the site and near field recorded motion belongs to Kijma station which is 1 km far from the site.

5. RESULTS

Recorded motions showed in previous section applied to finite element model of Koyna dam-reservoir-foundation system. transient stress distribution in dam body and hydrodynamic pressure fluctuations in the reservoir achieved. Hydrodynamic pressure time history and its frequencies presented below. Location and magnitude of maximum hydrodynamic sub-pressure on upstream face of dam body also discussed later.

5.1. FLUCTUATION FREQUENCY OF HYDRODYNAMIC PRESSURE

Hydrodynamic pressures on upstream face of the dam are due to impact of dam to water behind it. So it is expected that identified frequency of dam motions and hydrodynamic pressure be the same. The frequency of hydrodynamic pressure fluctuations also highly depends on the frequency contents of the ground motions. In fact, hydrodynamic pressure fluctuations depend on both dam body natural frequencies and ground motion frequency contents.

Hydrodynamic pressure time history at dam heel due to Kobe near field is showed in figure10 and its identified frequency using CWT presented in figure11. Hydrodynamic pressure time history at dam heel due to far field motions and its CWT also presented in figure12 and figure 13 respectively.

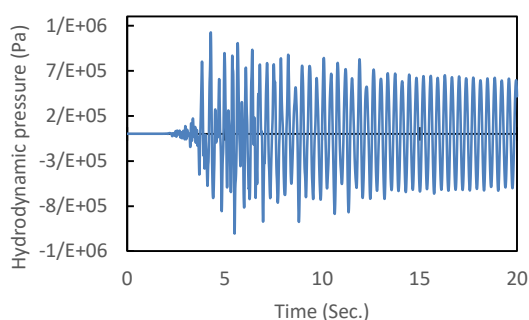


Figure 10-Hydrodynamic pressure at dam heel due to Kobe near field motion

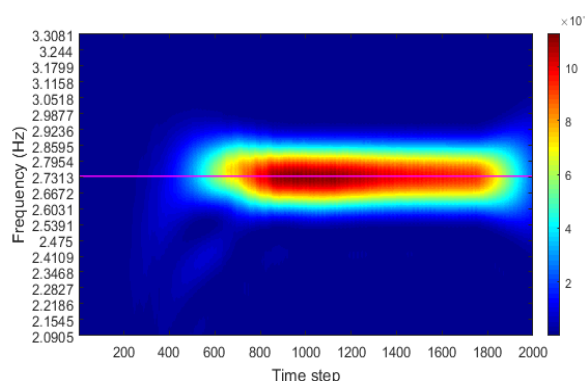


Figure 11-CWT of hydrodynamic pressure at dam heel due to Kobe near field motion

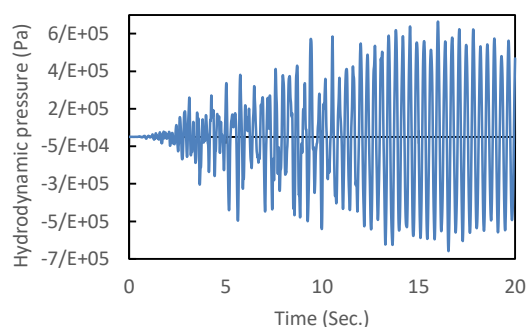


Figure 12-Hydrodynamic pressure at dam heel due to Kobe far field motion

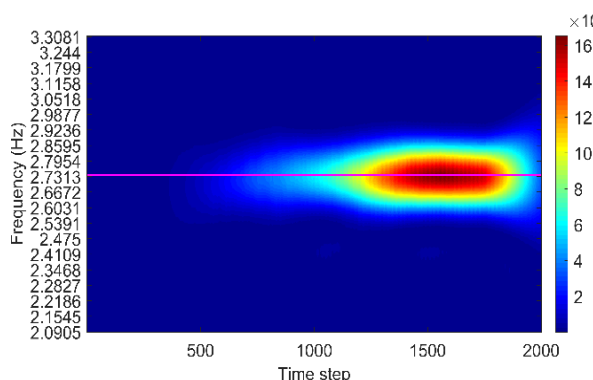


Figure 13-CWT of hydrodynamic pressure at dam heel due to Kobe far field motion

From the figure 10 to figure 13, it is obvious that hydrodynamic pressure due to far field motions have wider frequency contents and also it takes more time to take a constant frequency. On the other hand, hydrodynamic fluctuations in case of near field motions have a constant frequency in most of the earthquake duration. It is related to far field input motions which have wider frequency contents than the near field motions. Both figure 11 and figure 13 show similar frequency which is about 2.73 Hz. It shows in both cases, dam body motions frequency converged to 2.73 Hz in lapse of time.

5.2. HYDRODYNAMIC PRESSURE INCREMENTAL PATTERN

In previous section, hydrodynamic pressure time history at dam heel presented. Here, hydrodynamic pressure time history on upstream face of the dam presented as an incremental pattern in figure 14 and figure 15. These patterns show hydrodynamic pressure on upstream face of dam body in all time steps.

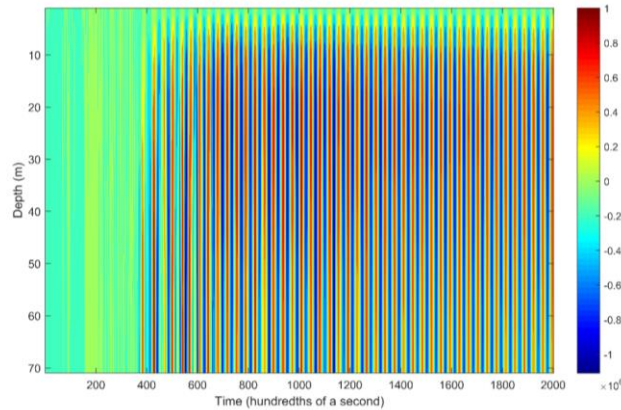


Figure 14-Incremental pattern of hydrodynamic pressure distribution due to Kobe near field motion

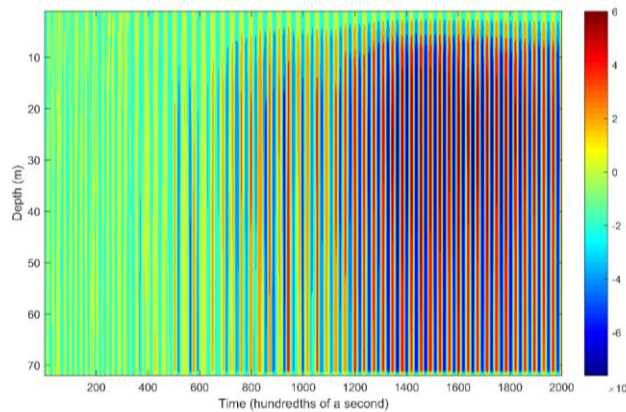


Figure 15-Incremental pattern of hydrodynamic pressure distribution due to Kobe far field motion

As shown in figure 14, the fluctuations are approximately uniform which means in a specific time, all dam upstream face is under either positive or negative pressure. In another word, there is no time step in which positive and negative pressure occur simultaneously. Maximum hydrodynamic sub-pressure in case of near field ground motion occurred in 5.51 s at dam heel. But in the case of far field ground motion, the maximum hydrodynamic sub-pressure occurred in 13.63 s at dam mid height. With respect to figure 11 and figure 13 these time steps are those in which hydrodynamic pressure fluctuations take 2.73 Hz as constant frequency.

5.3. STRESS DISTRIBUTIONS AND HYDRODYNAMIC CONTOURS

Stress distribution in dam body and hydrodynamic pressure distribution in reservoir, at the maximum hydrodynamic sub-pressure time step, due to near field and far field ground motions are presented in figure 16 to figure 19.

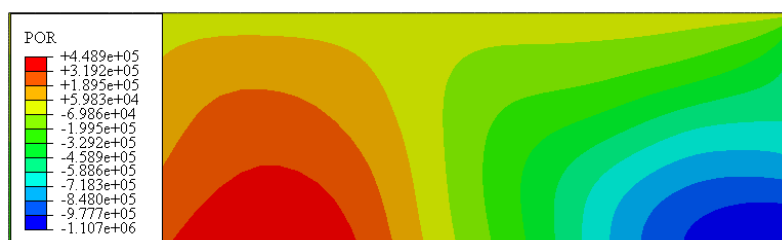


Figure 16-Contours of hydrodynamic pressure in 5.51 second due to Kobe near field motion

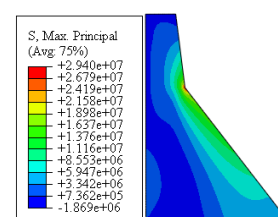


Figure 17-Contours of max principal stress in 5.51 second due to Kobe near field motion



Figure 18-Contours of hydrodynamic pressure in 13.63 second due to Kobe far field motion

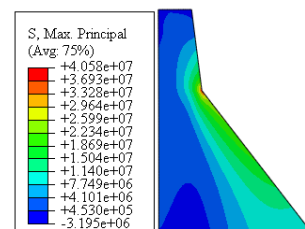


Figure 19-Contours of max principal stress in 13.63 second due to Kobe far field motion

6. CONCLUSIONS

Hydrodynamic pressure distribution on upstream face of the dam has been studied in this paper. The main goal of this paper is to investigate the effect of near field and far field ground motions on hydrodynamic sub-pressure which cause cavitation on upstream face of the dam. For this purpose, Kobe earthquake records hired to analyze Koyna gravity dam. Far field ground motions have wider frequency contents and also lower amplitude. Because of these differences in frequency contents, they could affect different modes of the dam. In case of near field motion, in the initial time steps hydrodynamic pressure shows a constant frequency of 2.73 Hz but on the other hand in case of far field motion, it takes time to show constant frequency of 2.73 Hz. It is because of wider frequency range of far field motion. In addition, the results show maximum hydrodynamic sub-pressure occurred just when hydrodynamic pressure fluctuations converged to constant frequency of 2.73 Hz which happen in 5.51 s and 13.63 s for near field and far field motion respectively. Wider frequency content for far field motion also caused hydrodynamic pressure in low amplitude in initial time steps. Another difference between these two cases is about location of maximum hydrodynamic pressure which is in dam heel for near field motion and mid height of the dam for far field case.

7. REFERENCES

1. Chopra, A. K., & Chintanapakdee, C. (2001). Comparing response of SDF systems to near-fault and far-fault earthquake motions in the context of spectral regions. *Earthquake engineering & structural dynamics*, 30(12), 1769-1789.
2. Bayraktar, A., Altunişik, A. C., Sevim, B., Kartal, M. E., Türker, T., & Bilici, Y. (2009). Comparison of near-and far-fault ground motion effect on the nonlinear response of dam-reservoir-foundation systems. *Nonlinear Dynamics*, 58(4), 655-673.
3. Hajihoseini, J. and Moradloo, J. (2011), "Investigation of damage pattern in concrete gravity dams due to far and near field ground motions" Proc. Of the 6th national congress on civil engineering, Semnan University, Semnan. (In Persian)
4. Zhang, S., & Wang, G. (2013). Effects of near-fault and far-fault ground motions on nonlinear dynamic response and seismic damage of concrete gravity dams. *Soil Dynamics and Earthquake Engineering*, 53, 217-229.
5. Roshanravan, A. (2015), "modal identification of arch dam based on the time-frequency domain decomposition" M.Sc. thesis, Tabriz University.
6. Tarinejad, R., Damadipour, M., 2014, Modal identification of structures by a novel approach based on FDD-wavelet method, *Journal of Sound and Vibration*, Vol. 333: 1024-1045,
7. Kijewski, T., Kareem, A., 2003, Wavelet transforms for system identification in civil engineering, *Computer-Aided Civil and Infrastructure Engineering*, Vol. 18: 339-355,

The Study of Site Effects on Seismic Response of Adjacent Rectangular Valleys

Behrouz Gatmiri^{1, 2}, Zahra Khakzad³

1- Department of Civil Engineering, University of Tehran, Tehran, Iran

2- Cermes, Ecole Nationale des Ponts et Chaussées, Paris, France

3- Department of Structural Civil Engineering, Islamic Azad University of Roodehen, Tehran, Iran

Email: z.khakzad@yahoo.com

Abstract

A numerical analysis on the seismic site effects due to ground irregularities is performed. Two dimensional (2D) rectangular configurations under incidence of vertically propagating SV waves is modeled with the aid of HYBRID program, combining finite elements in the near field and boundary elements in the far field. In fact, this paper aims to study the adjacency effects of two rectangular valleys on the ground amplification at various points across the valleys. Valleys are characterized by their depth, H and their half width at the surface, L and the calculations are made for different depth ratios $H/L = 0.2, 0.4, 0.6, 1$. Finally, some practical graphs are proposed in terms of engineering applications to assess the spectral response at the surface of rectangular valleys.

Keywords: Site Effect, Seismic Response, Hybrid Numerical Method, Adjacent Valleys, Filling Ratio.

1. INTRODUCTION

It has been recognized that effects of geometrical of a site can significantly affect the nature of strong ground motion during earthquakes. The modification of the seismic movement due to local topographical and geotechnical conditions is called site effect. Certainly in the recent past, there have been numerous cases of recorded motions and observed earthquake damage pointing towards geometrical and geotechnical amplification as an important effect. Thus study of site effects is one of the most important topics in earthquake engineering. Geometrical of a site modify the nature of seismic waves in transition from depth to the surface. The majority of seismic codes rest on seismic site effects by using one-dimensional (1D) model. The purpose of this paper is study of site effects in two-dimensional (2D) non-curve adjacent valleys in a building code. The 2D wave scattering is studied with a hybrid numerical method, combining finite elements in the near field and boundary elements in the far field (FEM/BEM). This program has been developed by Gatmiri and his coworkers [1, 2, 3, and 4].

2. SUMMARY OF PREVIOUS STUDY

Gatmiri et al have performed several parametric analyses of site effects. In order to better clarify the usage of HYBRID program, some of these studies are mentioned in the following. It should be noted, that sediments are modeled by finite elements and substratum is represented by boundary elements, which is adapted to the study in the far field. Gatmiri et al., studied various configurations and considered the influence of configuration of irregularities, slope angle of irregularities and dimensionless frequency of incident wave. The several salient features of topographic effects obtained are as follows [3, 4]:

The seismic ground motion was amplified at the crest of ridges, at the upper corner of slopes and at the edges of canyons; it was systematically attenuated at the base of these reliefs. This conclusion was normally verified for the cases of low dimensionless frequency. The ground motion as not homogeneous as in case of the half-space, but it strongly varied on the free field. There were successive regions that movements of round ere attenuated. The magnitude of response at a location on the top surface was dependent on the distance from this location on the relief. This distance was a function of the frequency content of the relief itself.

The effects of topography were also influenced by the slope angle of the relief. Generally, the stiffer the slope of the relief was, the more the effects of topography due to this relief were accentuated. The topographic effects of a relief on the seismic response of that relief strongly depended on the frequency content of the excitation. In general, the higher the excited frequency was the more significant and complex were the site

effects due to relief, and the wider the region influenced by the presence of the relief was, especially for the wavelengths comparable to or lower than the characteristic dimension of the relief. Gatmiri and Arson, studied several parametric analyses in order to characterize the combined effects of topographical irregularities and sedimentary filling on ground motion under seismic solicitation due to vertically incident SV Ricker wave [4].

Indeed, the horizontal displacement in a canyon tend to be attenuated at the centre and slightly amplified at the edge but in an alluvial basin, horizontal displacements are amplified at the centre and can be locally attenuated near the edge if depth is large enough. A qualitative comparison between seismic response of the filled and empty was carried out suggesting that 2D geotechnical effects increase with depth and steep sidedness.

Gatmiri et al., studied acceleration response spectra of different empty valleys. Curves were collected on a unique figure, which characterized topographical effects in a quantitative and qualitative way in the spectral domain. The results showed that maximum amplification was reached at the edge point of valleys. The spectral acceleration responses were classified according to a unique geometrical criterion except for elliptical valleys: the “S/A” ratio (where S is the area of the valley opening, and A indicates the angle between the horizontal line and slope in the above corner) (Fig. 1). The spectral response increased by increasing the parameter of S/A, in elliptical valleys for each depth ratio [5, 6].



Figure 1. Definition of parameters S, A [5, 6]

New criteria were offered in order to develop simple methods to incorporate 2D combined site effects in building codes. Filling ratio effects of Non-curved alluvial valleys and the influence of the changes in impedance ratio between sediments and the bedrock were investigated. The derived conclusions are presented briefly as follows [7]:

Existence of sediments could smooth valley’s response at the edge and amplify it at the centre. When combining the depth and shape effects, two geometrical parameters S/A and $\sin(A)$ were presented; by increasing S/A, $SR \cdot \sin(A)$ increased (S and A are similar to prior work). In order to combine filling ratio and depth ratio effects, the two geometrical parameters S_1/A and H/L were considered. As increasing the S_1/A , $SR \cdot H/L$ increased (S_1 , the area which was occupied by sediment, and H/L was the valley’s depth ratio) (Fig. 2). Spectral ratio had an inverse relation to impedance ratio. By sediment softening in comparison to rocky bed, the spectral ratio increased and the seismic response of a configuration became more and more complicated and the data sequencing became more and more difficult. Finally, variation $S_1/A \cdot n_1/\beta$ as a function of dimensionless parameter $SR \cdot \sin(A) \cdot H_1/L$ (H_1 was sediments depth) was plotted as a linear trend.



Figure 2. Definition of parameters S1, H/L [7]

3. PROBLEM PARAMETERS

3.1. GEOMETRICAL PARAMETERS

In order to evaluation of influence of shapes of empty non-curved adjacent valleys on the site effects the shapes of rectangular valleys was modelled. Valleys are characterized by their depth, H and their half width at the surface, L (Fig. 3). Simulations are carried out with depth ratios, H/L, equal to 0.2, 0.4, 0.6, 1. The value of L for all of the valleys is kept equal to 100m.

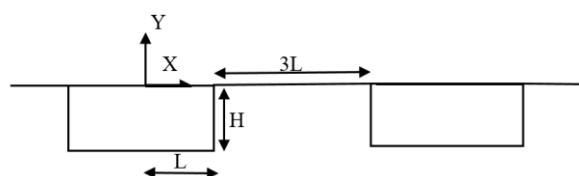


Figure 3. Adjacent rectangular valley

3.2. MECHANICAL PARAMETERS OF THE MATERIAL

In adopted models, the rocky bed is assumed to be homogeneous linear elastic materials. The main parameters of the bedrock are given in Table 1. The data used as input in this research are the digits and numbers considered for simulation in this program and their practical application calls for assessment of the extent by which they are factual and statistical as well as their sensitivity of results to these parameters, an assessment which is beyond the scope of objectives of this study.

Table 1. Mechanical characteristics of bedrock

E(MPa)	v	$\rho(\text{kg/m}^3)$	C(m/s)
6720	0.4	2450	1000

3.3. INCIDENT WAVE CHARACTERISTICS

The main focus of this work is the study of the effect of 2D geometrical irregularities on modification of seismic response and this study relies on simplified geometrical conditions as seismic loading is considered to be the simplest one; vertically incident SV Ricker wave. Imposed displacements are therefore expressed as [8];

$$u(t) = A_0(a^2 - 0.5) \exp(-a^2)$$

Were

$$a = \pi \frac{t - T_s}{T_p}$$

Amplification A_0 is constant value of 1; predominant frequency (f) is thus equal to 2 Hz; and $T_P = T_S = 0.5\text{s}$. The incident signal lasts 3s, but it can be seen from Fig. 2 that amplitude is nearly zero as soon as it reaches $t = 1\text{s}$. That is why the window has been defined from $t=0$ to $t=3\text{s}$ (Fig. 4). It should be noted, in all the models above, vibration is applied to the base of the left valley (Fig. 5).

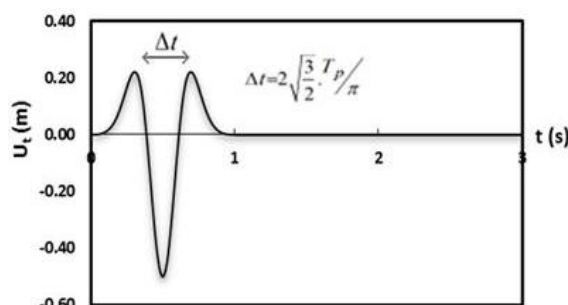


Figure 4. Incident Ricker signal [8]

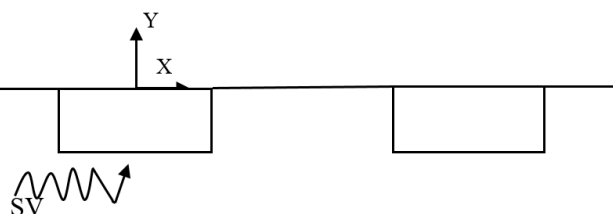


Figure 5. Point of the wave diffusion

4. 2D SITE EFFECTS IN NON-CURVED ADJACENT VALLEYS

The aim of this section is compare of influence of non-curved adjacent valleys on the seismic response of valleys with different ratios of H/L . The geometrical characteristics of valleys are displayed in Figure 1. In rectangular valley, L is half of the width of the valley and is equals to 100 m for all the valleys, as well as the distance between the adjacent valleys was determined $3L$ and the depth of valleys are H . In the present work, simulations are carried out with a depth (H) equal to 20, 40, 60, and 100 m and for different ratios (H/L) equal to 0.2, 0.4, 0.6, and 1. The spectral ratio in rectangular valleys in depth 6 is show in figure 6. According to the following graph, the results of non-curved adjacent rectangular valleys show a general trend that spectral ratio is increased with increasing H/L ratio, and this increase is more evident in the inner edge of the valleys. The spectral ratio at the inner edge of rectangular valleys in depth 1 is more critical than spectral ratio at the inner edge of depth 0.2, 0.4, 0.6. (Fig. 7).

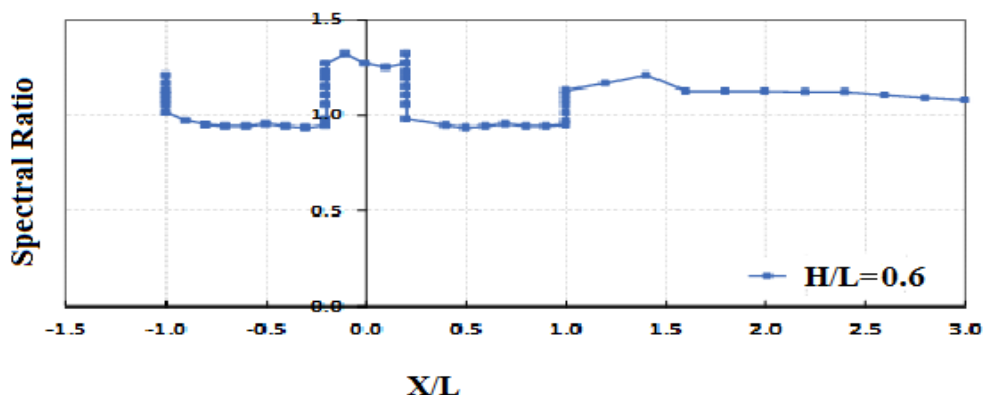


Figure 6. The results of Rectangular model in 0.6 depth

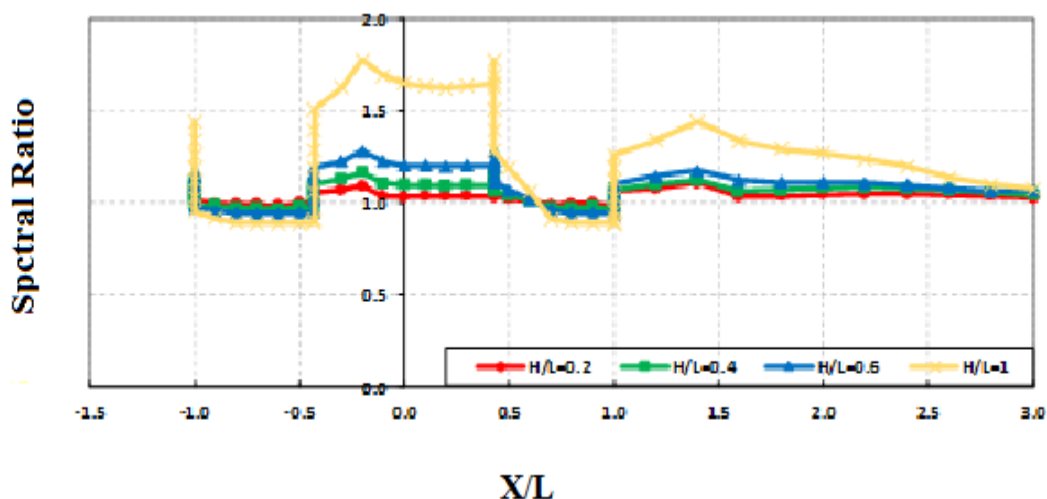


Figure 7. The results of Rectangular model in different depth

5. CONCLUSIONS

Site effects in non-curve adjacent valleys are studied by means of a hybrid numerical technique. The main results of this study are:

- Spectral ratio is increased with increasing H/L ratio.
- In the constant H/L ratio, spectral ratio at the adjacent rectangular valleys in H/L=1 is more than spectral ratio at the H/L=0.2, 0.4, 0.6.
- According to the results, the spectral ratio at the inner edge of all valleys is more critical and the value of that is nearly uniform, between two adjacent valleys.

6. REFERENCES

1. B. Gatmiri and M. Kamalian, (2002). “Two-dimensional transient wave propagation in an elastic saturated porous media by a hybrid FE/BE method”, Proceedings of the fifth European conference of numerical methods in geotechnical engineering, Paris, France, 947–56.
2. B. Gatmiri and K. Dehghan, (2005). “Applying a new fast numerical method to elasto-dynamic transient kernels in HYBRID wave propagation analysis”, Proceedings of the sixth conference on structural dynamics (EURODYN2005), Paris, France, p.1879–84.
3. KV. Nguyen and B. Gatmiri, (2007). “Evaluation of seismic ground motion induced by topographic irregularity”, Int J Soil Dyn Earthquake Eng 27:183–8.
4. B. Gatmiri, C. Arson and KV. Nguyen, (2008). “Seismic site effects by an optimized 2D BE/FE method I. Theory, numerical optimization and application to topographical irregularities”, Int J Soil Dyn Earthquake Eng 28:632–45.
5. B. Gatmiri, P. Maghoul and C. Arson, (2009). “Site-specific spectral response of seismic movement due to geometrical and geotechnical characteristics of sites”, Int J Soil Dyn Earthquake Eng 29:51–70.
6. B. Gatmiri, S. Lepense and P. Maghul, (2011). “A multi-scale seismic response of two dimensional sedimentary valleys due to the combined effects of topography and geology”, J Multi scale Model 03:133–49.
7. B. Gatmiri and T. Foroutan, (2012). “New criteria on the filling ratio and impedance ratio effects in seismic response evaluation of the partial filled alluvial valleys”, Int J Soil Dyn Earthquake Eng 41:89–101.
8. B. Gatmiri and D. Amini, (2014). “Impact of geometrical and mechanical characteristics on the spectral response of sediment-filled valleys”, Int J Soil Dyn Earthquake Eng 67, 233-250.

Comparison of 2D and 3D Seismic Analysis of Concrete Face Rockfill Dams in Narrow Canyons

1. Babak Mahmoodi¹, Ali Asghar Mirghasemi¹

1- School of Civil Engineering, College of Engineering, University of Tehran, Tehran, Iran.

Email: aghasemi@ut.ac.ir

Abstract

Concrete Face Rockfill Dam (CFRD) is a type of rockfill dam with a concrete slab as its impervious part. CFRD is a popular choice in countries with high seismic activity because of its great flexibility under seismic loading and ease of construction especially in rainy regions. Seismic response of rockfill dams is usually evaluated through two dimensional dynamic analyses on the maximum cross-section of the dam. This type of analysis needs sufficient insight regarding the effects of canyon geometry on seismic behavior of dam. This 3D effect is the subject of this study. Using 2D and 3D FEM simulations, we have extracted maximum values of acceleration, displacements and stresses throughout dam body and face slab. Comparison of this results for different canyon geometries has resulted in interesting and useful findings about the effects of canyon geometry on CFRD's seismic behavior. The results indicate that in canyons wider than 5 times of the dam's height, 2D and 3D results have good compliance for a middle section of the dam. Results also show that in some geometries especially canyons with mild side slopes, the most critical section of the dam is not necessarily its middle section (section with the max height).

Keywords: Concrete Face Rockfill Dam, Dynamic Analysis, Canyon Geometry Effects.

1. INTRODUCTION

Concrete face rockfill dam (CFRD) is a popular choice in some countries because of its certain advantages over the clay-core earthfill and concrete dams. The structural and geotechnical design of CFRDs are based on precedence with little emphasis on using analytical tools to predict the performance of the face slab [1]. By ensuring the stability of the embankment using conventional slope stability analyses, the thickness of the face slab, as well as the reinforcement ratio, is usually chosen based on empirical formulas [2]. Recent cases of performance of rockfill dams under earthquake excitations show us that even though they are inherently resilient against dynamic forces due to their great flexibility, still some aspects of their behavior are not clear and have been subject of many researches for the last two decades. Understanding the behavior of a CFRD is a challenging task as the behavior is shaped by the complex interaction between various components of the dam, namely the rockfill, the cushion layer-face slab interface and the concrete face slab. Another important characteristic of a CFRD is the canyon's 3D geometry. The span of the canyon and the inclination angle of its slopes have a significant effect on the static and seismic behavior of a CFRD located in that canyon. In this paper, the aforementioned effect has been studied using 2D and 3D FEM simulation of different CFRD models. Comparison of the results of different analysis points out the effect of the canyon geometry on Dam's seismic behavior. In order to investigate the effect of 3D canyon geometry on CFRD's seismic behavior, 54 three-dimensional and 6 two-dimensional analyses have been implemented. These models are different in dam height, canyon span and abutment angle. Three different heights of 70, 100 and 130 meters have been used. Also for defining canyons geometry, the L/H parameter has been introduced in which L is canyon span and H is the height of the dam. For this study we have used 1, 3, 5 and 7 as different values for L/H. Another characteristic of dam that combined with height and L/H ratio completely defines the dam's geometry, is abutment angle (the angle between canyon side slope and horizontal imaginary plane). In this study we've used the abutment angle of 63 degrees for L/H=1 ratio, 45 and 60 degrees for L/H=3, and 30, 45 and 60 for both L/H=5 and L/H=7. For 2D models, we just had the variable of dam height for which we used 70, 100 and 130 meters. In summary, there are 27 different 3D and 3 different 2D geometries. We investigated the seismic behavior of these models under two different earthquakes which resulted in 54 three-dimensional and 6 two-dimensional FEM seismic analysis respectively.

2. FEM MODELING

Simulation of CFRDs under seismic loading has been implemented using a FEM commercial software. All models include static and dynamic stages with comprehensive attention to the construction and impounding phases. All the intricate details of FEM seismic analysis of geostructures is taken into account in this study. Followings are the number of most important features of FEM models used in this study:

2.1. GEOMETRY

Figure 1 shows an example of 2D and 3D geometries used for seismic analysis of the CFR dams. For 3D models, in order to decrease the analysis time of the FEM software, half model has been used. Since the 3D dam model is symmetrical with respect to the river axis and also the seismic excitation is being imposed parallel to the river axis, using half model is completely warranted.

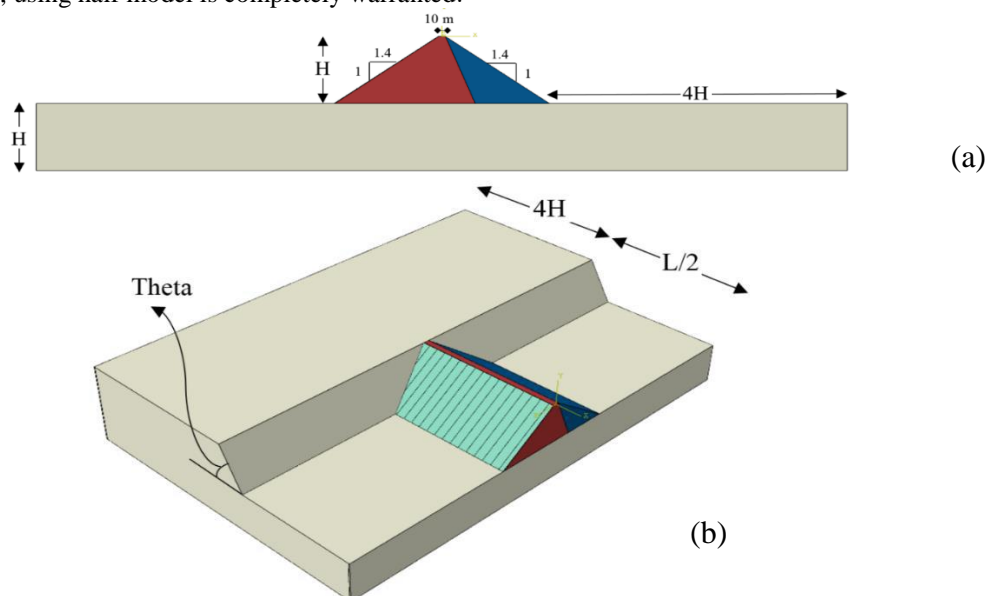


Figure 1- 2D (a) and 3D (b) FEM models of CFRD

2.2. MATERIAL PROPERTIES

For foundation and abutment, properties of good quality rock have been used as is the case with most CFRDs. For rockfill materials typical CFRD properties have been used and finally for face slab, the properties of a reinforced concrete with compressive strength of 24 MPa was inserted in the model. Material properties for different parts of dam models are summarized in Table 1. The other important aspect of dam materials are their constitutive models. In this study three different constitutive models have been used. For foundation and abutment, we have used elastics model because of rock's high stiffness. For rockfill material that constitutes dam body, we have used the elastic-perfect plastic Mohr-Coulomb model which takes into account the plastic strains of rockfill materials under loading. The most important part of the CFRD is face slab, so special emphasis has been put on its constitutive model.

Table 1- Material Properties

Zone	Density (kg/m ³)	Young Module (MPa)	Poisson Ratio	Cohesion (kPa)	Friction Angle (°)	Dilation Angle (°)
Face Slab	2640	31000	0.2	-	-	-
Foundation and Abutment	2500	20000	0.25	-	-	-
3B (Red area in Figure)	2100	200	0.35	0	50	15
3C (Blue area in Figure)	1900	150	0.35	0	45	10

We used the state of the art Plastic-Damage model for face slab [3]. This model completely simulates the complex behavior of the reinforced concrete under cyclic loading and takes into account the stiffness degradation of the concrete resulted from cracks created. Another important dynamic property of materials is

their damping. Damping of material in this study has been introduced into models using Rayleigh’s α and β coefficients [4].

2.3. INPUT EARTHQUAKE RECORD

The 1983 earthquake of Coalinga in California with magnitude of 6.4 has been selected as an excitation input. Two different versions of this record have been used in seismic analysis with their max acceleration scaled to 0.3g and 0.6 g.

Figure 2 [5] shows the acceleration record of this earthquake with maximum acceleration of 0.3g.

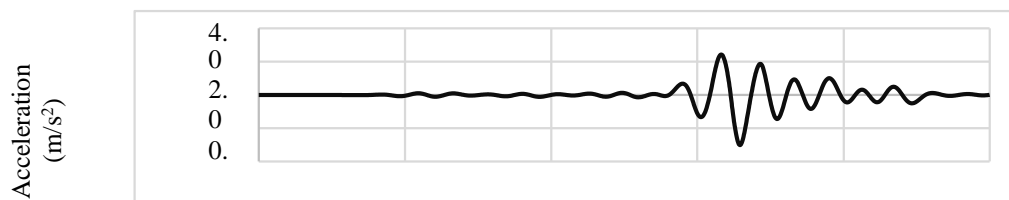


Figure 2- Acceleration Record of Input Earthquake with Peak Acc. Equal to 0.3g

2.4. BOUNDARY CONDITIONS

From wave propagation theories we know that waves tend to reflect upon reaching a boundary. Using conventional rigid boundaries in dynamic analysis, raise this problem in FEM analysis. After earthquake waves reach model boundaries, they reflect toward center of the model and cause extra strains and deformation. In reality we do not encounter this phenomenon because there are no such boundaries in vicinity of a real dam. One way to overcome this problem is to increase the distance between dam and model boundary which is not applicable to most of the cases since it makes the model too large for FEM dynamic analysis. Another way and the one used in this study, is introducing viscose dashpots at model boundaries to absorb coming waves and prevent them from returning to the dam body. Therefore, two perpendicular dashpots have been added to the model boundaries using suggestion of Lysmer [6] for their damping properties.

2.5. INTERACTION

Considering the construction stages of CFRD, we know that face slab and body parts of dam are not completely connected and they can move relative to each other. Also the face slab is not continuous itself and consists of a number of vertical segments. Therefore, interaction properties had to be introduced into the models. The friction coefficients have been set equal to $\mu=0.5$ and $\mu=0.7$ for slab-rockfill interaction and slab-slab interaction respectively [7].

3. THE EFFECT OF DAM HEIGHT ON SEISMIC BEHAVIOR

The height of a dam plays an important role on its seismic response since it affects dam flexibility and hence changes its fundamental frequency. Using 2D finite element analysis we’ve calculated natural frequency of a CFRD with three different heights and also extracted their seismic response under two different seismic excitations. The Type 1 earthquake record has dominant frequency of 4.16 Hz and maximum acceleration equal to 0.3g while the Type 2 earthquake has the dominant frequency the same as Type 1 earthquake but with maximum acceleration of 0.6g. The extracted data have been summarized in Table 2 for both Type 1 and Type 2 excitations.

Table 2- Seismic Response of 2D CFRD Models

Dam’s Height (m)	Dam’s Natural Frequency (Hz)	Max. Acceleration of Crest (m/s ²)		Dominant Frequency of Dam’s Response (Hz)	
		E.Q. Type 1	E.Q. Type 2	E.Q. Type 1	E.Q. Type 2
70	0.866	6.13	7.45	4.16	4.16
100	0.630	5.34	7.05	3.84	3.84
130	0.488	2.80	4.69	3.22	3.22

According to Table 2, it can be deduced that increasing dam’s height will result in lower natural frequency or higher natural period. In other words, increasing dam’s height makes the dam body more flexible. Results from Table 2 show that more flexible dams undergo a lower acceleration. This phenomenon can be justified using the frequency content chart of input earthquake. It is evident from Figure 3 that around dam’s natural frequency values, as we decrease the frequency, the spectral acceleration will decrease.

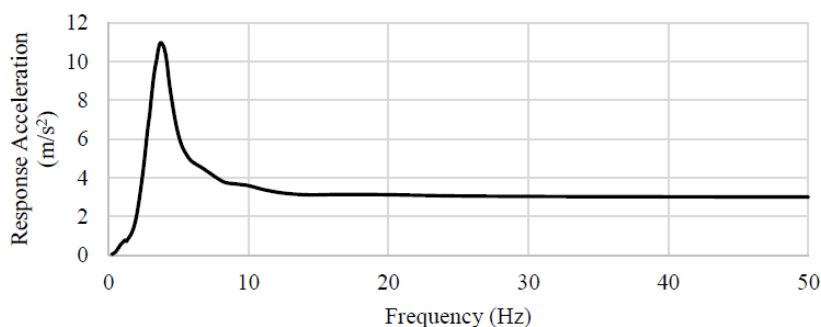


Figure 3- Spectral Acceleration of Type 1 Earthquake (Peak Acc. Equal to 0.3g)

4. THE EFFECT OF CANYON GEOMETRY ON FUNDAMENTAL FREQUENCY

Canyon Width, is a key factor in seismic response of dams. CFR dams located in wide canyons show different responses compared to dams located in narrow ones. Because of the confinement and stiffening effect of the narrow canyons, the fundamental natural periods of CFRDs with the same height vary with varying canyons width. Results show that studying the effect of canyons geometry on dam’s response is best regulated using the parameter L/H (the ratio of canyon’s width to dam’s height). We extracted the fundamental period for different dams with different canyons geometries and the results are shown in Figure 4. It can be seen that increasing the L/H ratio (widening the canyon) results in reduction of the dam system’s natural frequency. In other words, as we make the canyon wider, the dam behaves in a more flexible manner and this means lower frequency. Furthermore, 3D frequency of dams with any geometry is always higher than its 2D frequency, which indicates that canyons always have stiffening effect.

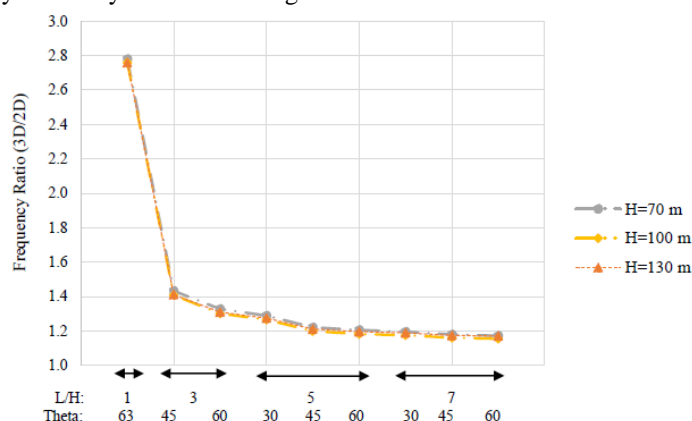


Figure 4- Effect of Canyon Geometry on Fundamental Frequency of CFR Dams

5. THE EFFECT OF CANYON GEOMETRY ON THE SEISMIC BEHAVIOR OF DAM BODY

Seismic behavior of dam body in CFR dams includes accelerations, displacements, strains, etc. In this study, horizontal acceleration and horizontal displacement of different dam models, have been presented. Two type of comparison has been made between results for better illustration of the differences between 2D and 3D behavior of the dam under earthquake excitation. In one type, we’ve compared the maximum values of acceleration (ordisplacement) at crest for 2D models with values at crest (middle canyon section) in 3D models. This way we can verify with what accuracy, 2D models represent 3D behavior of dams. In another type of comparisons, we’ve extracted maximum values throughout whole dam and have compared it with max values from 2D analysis and max values from middle section of 3D analysis. This second type of comparison,

illustrates the real 3D behavior of dam and the fact that in some cases of CFRDs under seismic loading, the middle section of dam, is not necessarily the most critical section.

5.1. MAX VALUES OF HORIZONTAL ACCELERATION

Figure 5 shows that dam with L/H greater than or equal to 5, have good conformity between 2D and 3D models. Also from Figure 66 we understand that max horizontal acceleration of dam body does not necessarily occur in middle section of dam. This is especially noticeable in dams located in canyon with low Theta.

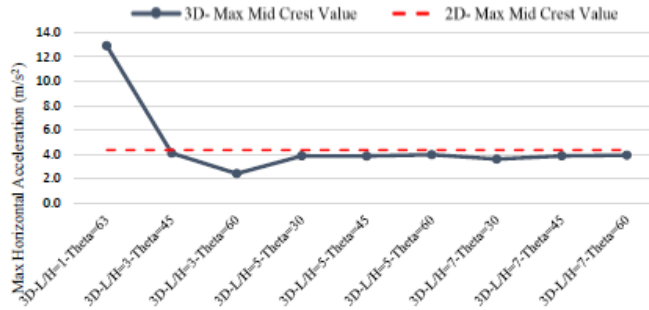


Figure 5- Comparison of 3D and 2D Results for Max Dam Crest Horizontal Acceleration at Middle Section under PGA=0.3g Earthquake

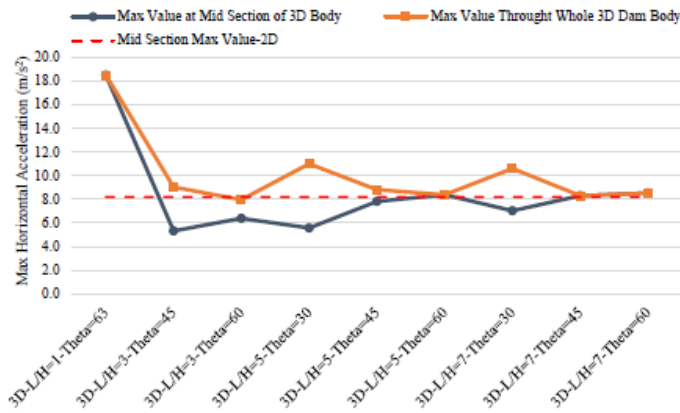


Figure 6- Comparison of Max Horizontal Acceleration Value at Different Locations of Dam Body for 3D and 2D Analysis under PGA=0.3g Earthquake

5.2. MAX VALUES OF HORIZONTAL DISPLACEMENT

Except for the dam with triangular section (L/H=1), according to Figure 7 results of the max horizontal displacement from 2D and 3D models are quit identical.

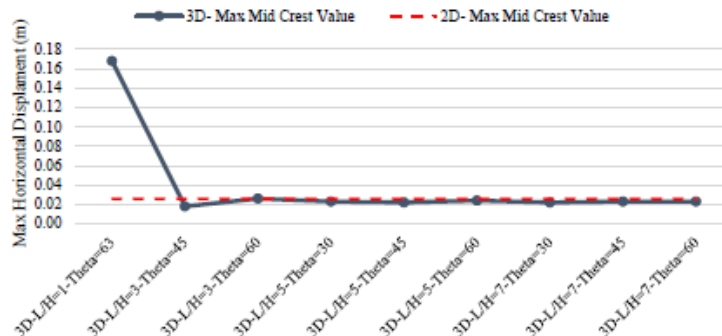


Figure 7- Comparison of 3D and 2D Results for Max Dam Crest Horizontal Displacement at Middle Section under PGA=0.3g Earthquake

Figure 8 gives us another interesting aspect of dam’s behavior. It shows that even though the max 2D and 3D results comply in middle section, still the max value occurs someplace other than middle section. In this particular case it occurs near abutment. So we find out that sections with max height do not necessarily give the most critical results.

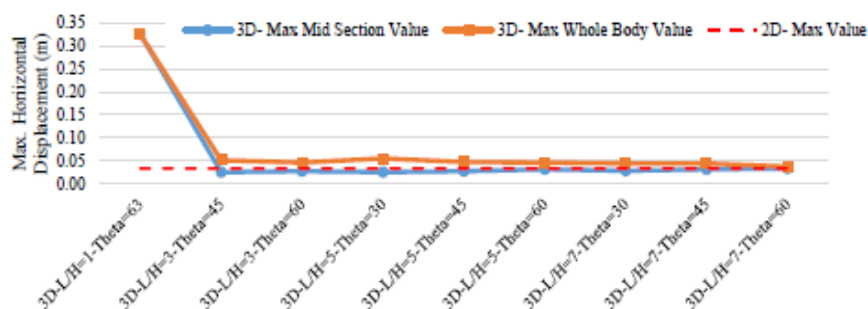


Figure 8- Comparison of Max Horizontal Displacement Value at Different Locations of Dam Body for 3D and 2D Analysis under PGA=0.3g Earthquake

6. THE EFFECT OF CANYON GEOMETRY ON SEISMIC BEHAVIOR OF FACE SLAB

The most important section of CFRD is its face slab, so its behavior is crucial to dams’ safety and performance. Seismic loading of the dam induces compressive and tensile stresses in face slab that may result in its rupture and failure. In this study we extracted maximum compressive and tensile stresses in face slab in 2D and 3D models. Figure 9 shows that canyon geometry affects max tensile stresses induced in face slab. Its effect is more intense in lower half of the slab where higher water pressure does not allow slipping of the slab relative to the rockfill. Also 2D models tend to underestimate the max tensile stress at bottom of the dam. Figure 9 illustrates the max compressive stress of face slab. There is good compliance between 2D and 3D results. But again dam located in triangular canyons behaves completely different from other geometries. Higher values in dam with L/H=1, can be explained considering stiffening effect of very narrow canyon. In this narrow geometry, slab is completely confined between hard rock boundaries and this cause it to undergo high stresses.

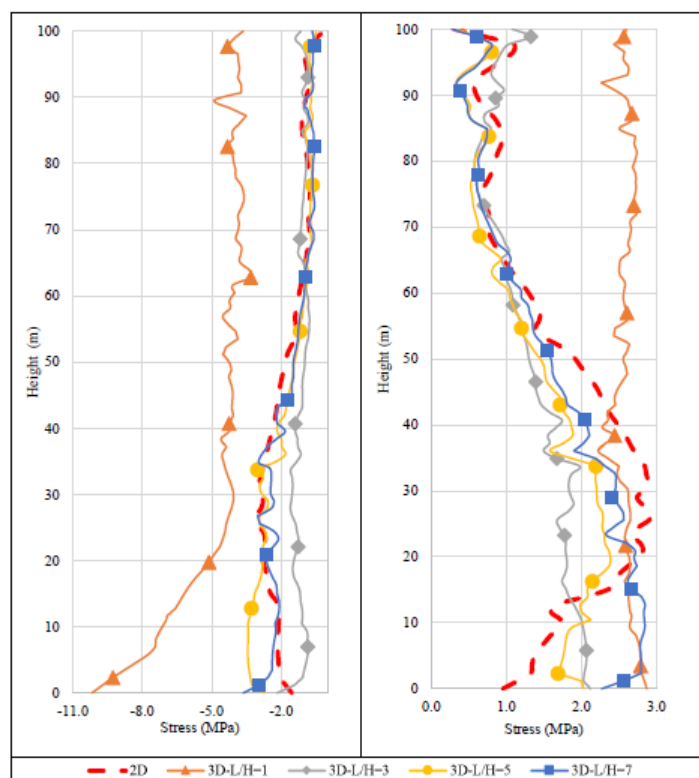


Figure 9- Maximum Compressive Stress (Left) and Tensile Stress (Right) of Face Slab

7. CONCLUSIONS

□ Increasing dam's height results in more flexible dam structure which yields lower fundamental frequency. Increasing L/H ratio has the same effect. Change in fundamental frequency has significant effect on dam seismic behavior.

□ 3D analysis always shows higher frequency than 2D analysis for a dam with the same height. Also the ratio of 3D frequency to 2D frequency for a specific L/H ratio does not depend on dam's height.

□ Results of max horizontal acceleration developed in dam body shows that for dam geometries with L/H ratio higher than or equal to 5, for middle section of dam body, 3D and 2D analysis concur. On the other hand, for dam with L/H=1 and other with canyons slope angle (Theta) equal to 30°, the highest acceleration does not occur within middle section of the dam. In other words, in some geometries, the most critical section is not necessarily the middle section. Result of the max horizontal displacement of dam body also confirm this statement.

□ From results of the max compressive and tensile stresses induced in face slab, it can be deduced that stresses in lower half on slab is more sensitive to the canyon geometry. Also 2D analysis tend to underestimate the max tensile stress in this part of the slab. For compressive stress, 2D and 3D analysis are in great agreement except for triangular geometry (L/H=1).

□ For dam with L/H ratio equal to 1, very narrow geometry of canyon results in more confinement. Slabs that are confined show more stiffness and undergo higher stresses.

8. REFERENCES

1. J. L. Sherard and J. B. Cooke, "Concrete-face rockfill dam: I. assessment," J. Geotech. Eng., vol. 113, no. 10, pp. 1096–1112, 1987.
2. ICOLD, "Concrete Face Rockfill Dams," ICOLD, no. November, 2004.
3. J. Lee and G. L. Fenves, "Plastic-damage model for cyclic loading of concrete structures," J. Eng. Mech., vol. 124, no. 8, pp. 892–900, 1998.
4. S. L. Kramer, Geotechnical Earthquake Engineering: Pearson New International Edition. Pearson Education, Limited, 2013.
5. Peer.berkeley.edu, "PEER Strong Ground Motion Database."
6. J. Lysmer and R. L. Kuhlemeyer, "Finite dynamic model for infinite media," J. Eng. Mech. Div., vol. 95, no. 4, pp. 859–878, 1969.
7. P. Dakoulas, "Nonlinear seismic response of tall concrete-faced rockfill dams in narrow canyons," Soil Dyn. Earthq. Eng., vol. 34, no. 1, pp. 11–24, 2012.

Seismic Response Analysis of High Arch Dams to Spatially-Varying Ground Motions

Jin-Ting Wang¹, Feng Jin¹, Chu-Han Zhang¹

1. Department of Hydraulic Engineering, Tsinghua University, Beijing 100084, China

Email: wangjt@tsinghua.edu.cn

Abstract

The failure of a large dam can be catastrophic to human life and property downstream. Therefore, the seismic safety is of particular concern for high dams in seismically active regions. This paper addresses the seismic response analysis of high arch dams due to spatially-varying ground motions. Firstly, a comprehensive analysis model developed at Tsinghua University is presented, which takes into account radiation damping effect of semi-unbounded canyons, dynamic interaction of dam-water, opening of contraction joints, seismic damage cracking and strengthening of dam concrete, and nonlinearity of foundation rock. Subsequently, the seismic damage of Pacoima dam during the 1994 Northridge earthquake is qualitatively analyzed by the developed analysis model. The results agree with the actual damage observed after the earthquake. Most of the contraction joints opened and closed during the earthquake, and a larger residual opening occurred at the thrust block joint after the earthquake. The cracks continue from the bottom of the thrust block joint in three directions: diagonal, horizontal, and vertical. Finally, a large-scale numerical simulation of seismic ground motion from source rupture to dam canyons is introduced, which can simulate the characteristics of near-field ground motions at dam sites by considering the effect of source mechanism, propagation media, and local site.

Keywords: Concrete dam, seismic damage, spatially-varying ground motion, source to site.

1. INTRODUCTION

Earthquakes can cause damage to dams, such as Xinfengjiang buttress dam (105 m high, 1962 Xinfengjiang earthquake), Koyna gravity dam (103 m high, 1967 Koyna earthquake), Pacoima arch dam (113 m high, 1971 San Fernando earthquake and 1994 Northridge earthquake), Rapel arch dam (112 m high, 1985 Rapel Lake earthquake), Sefid Rud buttress dam (106 m high, 1990 Manjil-Rudbar earthquake), Shihgang dam (25 m high, 1999 Chi-Chi earthquake), and Zhipingpu concrete-faced rockfill dam (156 m high, 2008 Wenchuan earthquake). Therefore, the seismic safety of arch dams is a widely-concerned topic. During last several decades, considerable research efforts have been devoted to seismic safety study of arch dams, and many numerical models have been developed to analyze seismic response of arch dams, such as [1-8]. However, due to the complexity of arch dam-reservoir-foundation rock systems, the numerical models are inevitably filled with assumptions. Determining the extent to which the developed numerical models may be truly representative of the actual systems is still a challenging problem.

A major difficulty lies in rationally defining the variations in ground motions along dam-foundation interfaces. The ground motions recorded at several arch dams, such as Pacoima dam [9], Mauvoisin dam [9] and Ertan dam [10], provide an opportunity to verify the effectiveness of numerical models. Chopra and Wang [9] investigated the linear response of Pacoima dam to the spatially-varying ground motions recorded during earthquakes. Wang et al. [5] investigated the earthquake damage of Pacoima dam in the 1994 Northridge earthquake of magnitude 6.7 using a comprehensive analysis model, which the semi-unbounded size of foundation rock and compressible water, the opening of contraction joints, the cracking of dam body, and the spatial variation of ground motions. The joint opening and the concrete cracking may be roughly reproduced when the ground motion excitation is spatially defined based on the acceleration records at the dam-rock interface.

However, most high dams, particularly new dams, lack appropriate strong motion records at dam-canyons for seismic safety evaluation. Recently, He et al. [11] and Wang et al. [12] investigated the ground motions at dam sites by numerically simulating the whole propagation process of seismic waves from fault rupture to dam site. The physics-based numerical simulation may take into account the effects of source, propagation path and local sites, and thus offer a potential way for predicting ground motions at dam sites.

This paper summarizes some of the above-mentioned work. Firstly, a comprehensive analysis model developed at Tsinghua University is presented. Subsequently, the damage of Pacoima dam during the 1994

Northridge earthquake is qualitatively analyzed by the developed analysis model. Thirdly, a large-scale numerical simulation of seismic ground motion from source rupture to dam canyon is introduced.

2. EARTHQUAKE DAMAGE ANALYSIS MODEL OF DAM-WATER-FOUNDATION SYSTEMS

The arch dam-water-foundation rock system considered is composed of a concrete dam with contraction joints, semi-unbounded foundation rock, and semi-unbounded reservoir, as shown in Figure 1. A comprehensive analysis model [5, 13-18] has been developed by the research group on earthquake resistance of high dams at Tsinghua University, which takes into account radiation damping effect of semi-unbounded canyons, dynamic interaction of dam-water, opening of contraction joints, seismic damage cracking and strengthening of dam concrete, and nonlinearity of foundation rock.

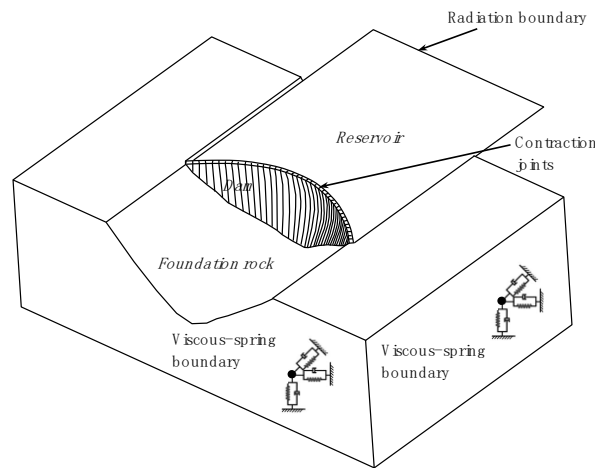


Figure 1. Sketch of the arch dam-water-foundation rock system

(1) Radiation damping model of semi-unbounded foundation rock:

The semi-unbounded foundation rock is truncated in a certain region. Zhang et al. [13] applied the viscous-spring boundary condition [19] to the truncated foundation boundary to simulate the radiation damping of the semi-unbounded foundation rock. In the viscous-spring boundary input model, pairs of dashpots and springs are installed in all nodes of artificial boundaries as shown in Figure 1. Each node on the artificial boundary contains three pairs of dashpots and springs, i.e. one in the normal direction of the boundary plane and the other two in the tangential directions. The parameters of springs and dashpots on the artificial boundary are given as the following:

$$K_n = a \cdot \frac{\lambda + 2G}{r} \quad C_n = b\rho V_p \quad (1)$$

$$K_s = a \cdot \frac{G}{r} \quad C_s = b\rho V_s \quad (2)$$

where subscripts n and s refer to the normal and tangential directions of the artificial boundary surfaces; K is the elastic stiffness of the spring, C is the viscous damping, λ and G are the Lamé's constants; V_p and V_s denote the propagation velocity of P- and S-waves, respectively; ρ is the mass density; r is the distance from the wave source, which takes the approximate value of the perpendicular distance from the center of the structure to the nodes of artificial boundary; and a and b are modification coefficients, which may be determined from parameter analysis.

(2) Modeling of semi-unbounded reservoir:

The impounded water is assumed to be inviscid, irrotational, and compressible. Similar to the semi-unbounded foundation rock, the semi-unbounded reservoir is truncated at a certain distance in the upstream direction. Wang et al. [15] used the plane-wave radiation condition at the truncated water boundary to simulate the fluid wave that propagates along the upstream direction. The plane-wave radiation equation [20] is expressed as

$$\frac{\partial p}{\partial n} = \frac{\cos \theta}{V_w} \dot{p} \quad (3)$$

where p is the hydrodynamic pressure of the impounded water, and the superposed dot indicates the partial differentiation with respect to time; n is the inward normal direction of the truncated reservoir boundary, θ is the incident angle from the inward normal; and V_w is the velocity of pressure waves in the water.

(3) Modeling of contraction joints:

The nonlinear response of high-arch dams due to contraction joint opening during earthquakes is significant. It is of importance to appropriately model the behavior of interaction between monoliths. Zhang et al. [13] improved a contact boundary [21] provided in ABAQUS to simulate the opening-closing behavior of contraction joints.

(4) Damage model of concrete:

Dam concrete may crack during a strong earthquake because of excessive stress. For example, Pacoima dam suffered severe damage during the 1994 Northridge earthquake. Pan et al. [14] adopted the elastic-plastic damage model [22] to simulate the nonlinearity of concrete material during strong earthquakes. Considering that dam safety is usually controlled by tensile stresses during earthquakes, only the tensile damage of concrete is considered. Moreover, compressive stiffness is assumed to fully recover upon the closure of cracks when load changes from tension to compression. Based on these assumptions, the uniaxial stress-strain relationship of concrete is shown in Figure 2, where σ and ε are concrete stress and strain, respectively; E_0 is the initial (undamaged) elastic modulus; d_t is the tensile damage factor that varies from 0 (undamaged material with elastic behavior) to 1 (fully damaged material); G_f is the fracture energy; f_t is the tensile strength; ε_t and ε_f are the maximum elastic and limiting tensile strains, respectively; ε_p is the equivalent plastic strain; and l_c is the characteristic length of concrete (commonly defined as three times the maximum aggregate size).

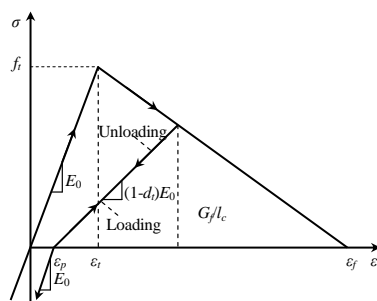


Figure 2. Softening curve of concrete under uniaxial cyclic loading

(5) Earthquake input model:

Two earthquake input methods may be used in the dynamic analysis of arch dams to consider the radiation damping of semi-unbounded foundation rock [15]. As schematically shown in Figure 3, one is the incident wave model, and the other is the free-field model. The incident wave model defines the seismic input at the foundation base boundary. To maintain the consistency of the motions at the base boundary with the specified free-field surface motions, the input excitation at the foundation base is usually determined by a deconvolution analysis. The incident wave is a uniform input at the base, but spatially varying ground motions are generated at the dam-foundation rock interface due to the scattering effect of canyon topography on the earthquake waves. In the free-field model, the specified free-field motions are imposed as direct input to the dam-foundation interface. Therefore, spatially varying free-field input could be considered if it is available. Wang et al. [5, 15] developed an equivalent force scheme based on the similar idea to achieve the free-field input when the radiation damping of semi-unbounded foundation rock is taken into account. It is worth noting that the artificial boundary condition at the foundation base is essential in simulating the semi-unbounded of the foundation rock for these two input models in the finite element analysis.

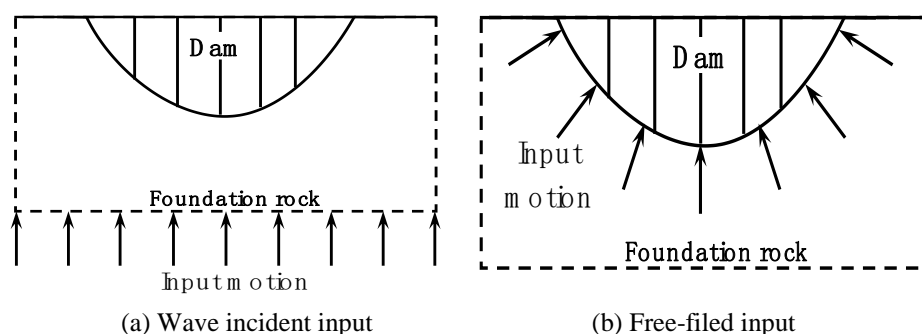


Figure 3. Earthquake input mechanism

3. EARTHQUAKE DAMAGE ANALYSIS OF PACOIMA DAM

Located in the San Gabriel Mountains near Los Angeles, Pacoima dam is 113 m high and 180 m long at the crest. The thickness at the crown section varies from 3 m at the crest to 30 m at the base. A thrust block supports the dam at the left abutment. Pacoima dam was shaken by the 1971 San Fernando earthquake of magnitude 6.6 and the 1994 Northridge earthquake of magnitude 6.7. Figure 4 shows the observed damage of Pacoima dam in the Northridge earthquake [23]. The thrust block joint opened and remained open after the earthquake by about 50 mm at the crest level. This opening continued downward and decreased to 5 mm at the bottom of the joint. The rest of the contraction joints were closed after the earthquake. However, there were indications that some of joints opened and closed during the earthquake. A crack diagonally extended from the open joint through the thrust block into the abutment. Several fine cracks were also observed in the dam body adjacent to the thrust block. A permanent horizontal offset 10 mm to 15 mm occurred along the horizontal joint about 15 m below the crest. The top block moved downstream relative to the bottom block.

The seismic response of Pacoima dam to the 1994 Northridge earthquake is analyzed using the procedure presented in Section 2 [5]. The applied static loads include the deadweight of the dam, and the hydrostatic pressure of the reservoir. The ground motions that are spatially varied along the dam-foundation rock interface are defined based on the earthquake records [9]. Figure 5 presents the joint opening envelope, the residual joint opening, and the damage distribution on the downstream face during the earthquake excitation.

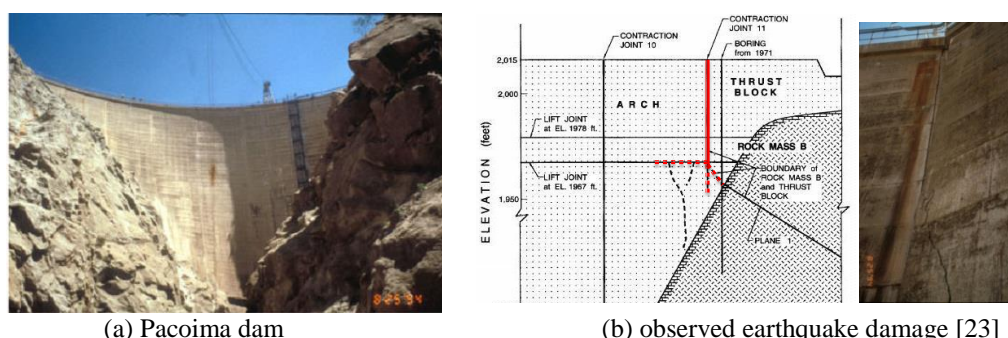


Figure 4. Observed damage of Pacoima dam in the Northridge earthquake

From Figure 5, it is clearly observed that most of the joints are open during the earthquake. Some of the joints open downward about half the height of the dam. On the downstream face, the maximum opening 36.0 mm occurs at the crest level of the thrust block joint. The thrust block joint remains open about 15 mm at the crest level. This opening continues downward and decreases to 5 mm at the bottom. These scenarios are qualitatively similar to the actual observation after the 1994 Northridge earthquake, wherein some of the joints opened during the earthquake and the thrust block joint remained open after earthquake.

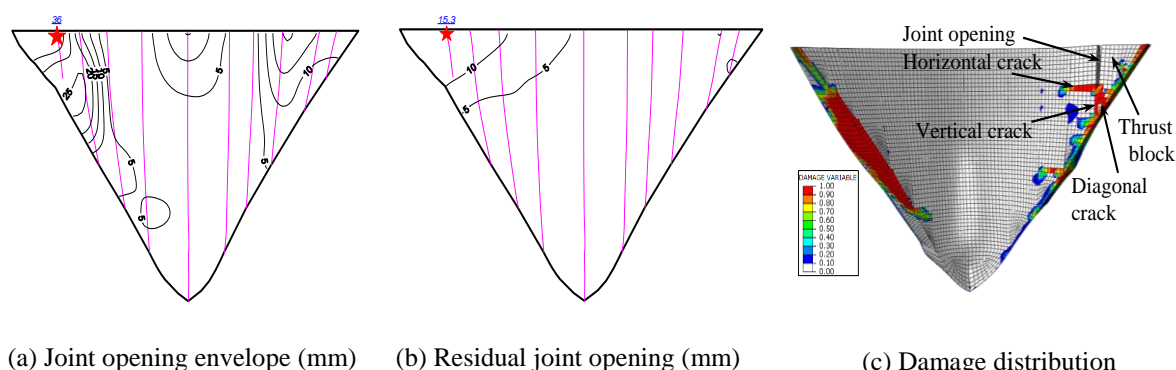


Figure 5. Computed response of Pacoima dam due to Northridge earthquake

The calculated damage distribution (Figure 5(c)) indicates that the severe damage occurs under the earthquake excitation. The damage appears in the dam body adjacent to the thrust block and to the foundation rock. The damage extends from the bottom of the thrust block joint in three directions. A crack diagonally extends from the bottom of the open joint into the left abutment. A crack horizontally stretches out from the open joint into the dam body. In addition, damage extends downwards along the vertical contraction joint. These damage modes agree with the actual cracks observed after the 1994 Northridge earthquake.

Figure 6 shows the seismic damage on the downstream face of Pacoima dam when the input ground motion is defined by the two methods commonly-used in the current engineering practice, respectively. The first one is the free-field input, in which uniform ground motion is input at the dam-foundation interface. The second one is the incident wave input, in which the ground motion with the amplitude halved is vertically incident from the bottom of the foundation rock. It is obvious that the earthquake input mechanism has a significant influence on the damage distribution of Pacoima dam. The uniform free-field input and the incident wave input cannot achieve the damage mode that occurred during the 1994 Northridge earthquake.

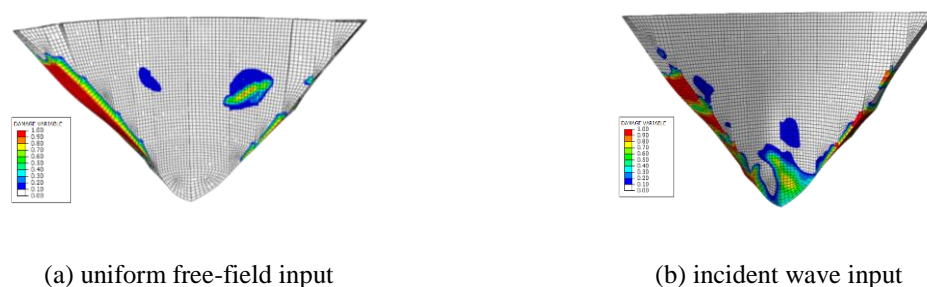


Figure 6. Dam damage with different earthquake input mechanisms

4. LARGE-SCALE NUMERICAL SIMULATION OF GROUND MOTIONS AT DAM CANYONS

Ground motions recorded exhibit spatial variation along the dam-foundation interface, which may have a significant influence on the seismic response of high arch dams. From the seismic response analysis of Pacoima dam [5], it is clearly shown that the seismic responses resulting from the recorded ground motions are quite different compared with conventional assumptions. However, it is difficult to rationally define such variation in practice engineering because the available ground motions at the dam-foundation interface are limited.

With the significant improvements in the seismological methods, numerical simulation techniques and large-scale computing, it is promising to simulate the whole process of seismic waves from fault rupture to sites. Therefore, we proposed a “rupture-site” approach to generate spatially-varying ground motions along dam canyons [11, 12]. As schematically shown in Figure 7, the fundamental idea is to build a realistic fine model integrated of seismic source, propagation path and local site to simulate the whole propagation process of the seismic wave from the fault rupture to the dam site based on large scale high-performance computing. This physics-based approach may take into account the effects of source mechanism, propagation path, and local site on the seismic response of dams, and thus predict ground motion for a specific dam.

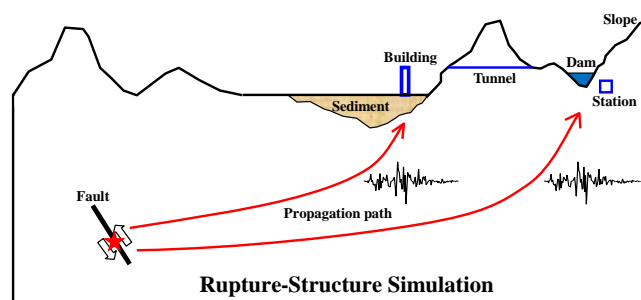


Figure 7. Schematic of numerical simulation of seismic waves from source

Next, the ground motions at the Dagangshan dam site in Southwest China is simulated as an example [12]. The closest active fault is only 4.5 km away from the dam site, and it has an upper bound magnitude of M_w 7.4. Figure 8 shows the numerical model and 9 receivers deployed along the dam base. The rupture area is assumed to be 60 km in length and 28 km in width. From the profile of the fault, it can be seen that the whole rupture is discretized into an array of point sources and each point source represents a sub-fault. Both the velocity structure and surface topography are included in the simulation. Summaries of the global model information are as follows: $288 \times 240 \times 40$ spectral elements are distributed on 120 processors; the total DOFs add up to 0.54 billion; and the whole computation takes 2.7 hours to finish 20,000 time steps.

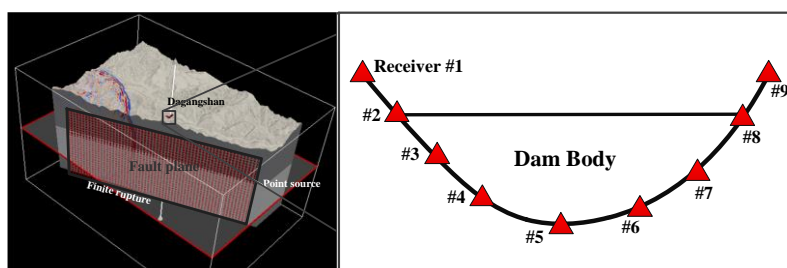


Figure 8. Three dimensional numerical model of Dagangshan dam site

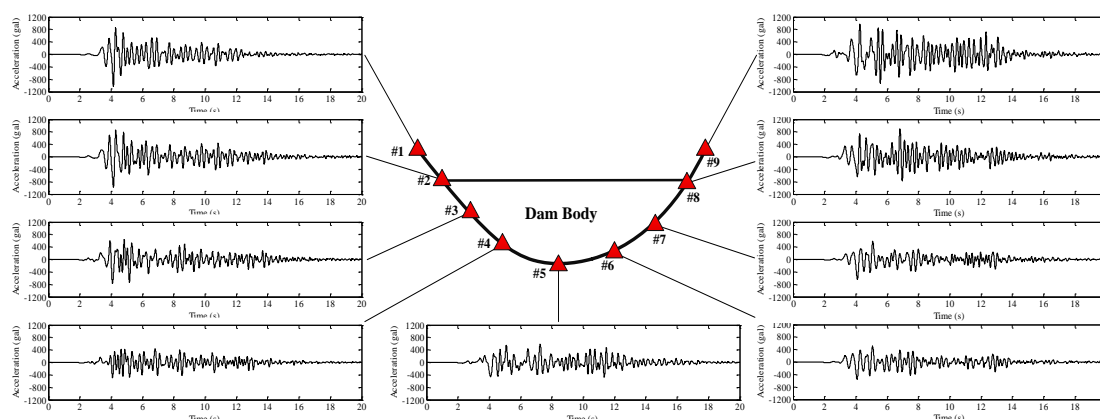


Figure 9. North components of the 9 receivers at dam canyon

Upon the numerical simulation, the acceleration time histories at all the nodes in the SEM model are computed in three components. The north components of the 9 receivers deployed along the canyon are plotted in Figure 9. It is apparent that the ground motions are different at the 9 receivers. The peak value of the north acceleration component at the bottom of the dam canyon (Receiver #5) is 593 cm/s^2 . However, the east acceleration component has a peak value of 390 cm/s^2 at the same point. This indicates that ground motions vary along different directions. This phenomenon is conventionally not taken into consideration in earthquake-resistant design, which may have a significant effect on the seismic response of high dams.

5. CONCLUSIONS

The damage of Pacoima dam occurred in the 1994 Northridge earthquake is qualitatively reproduced by the comprehensive analysis model developed at Tsinghua University. This verifies the effectiveness of the analysis model. Therefore, we may conclude that the comprehensive analysis procedure can represent the real behavior of arch dams to a certain extent. One key issue is the spatially-varying ground motions along the dam-foundation interface, which has a significant influence on the seismic damage mode. However, the variation of ground motions along the dam-foundation is usually unavailable for most dams, particularly new dams under construction or planned.

The physics-based “rupture-site” approach can simulate the rupture process of the causative fault and take into account the velocity structure of propagation path and realistic topography, and thus predict site-specific ground motions for high dams. Therefore, it is a promising method for predicting the ground motions at dam sites due to maximum credible earthquake. However, the accuracy of the numerical simulation of seismic waves heavily relies on the models describing the source and propagation path. Therefore, more efforts are needed from researches in both seismological and engineering fields.

6. ACKNOWLEDGMENT

The authors gratefully acknowledge the financial supports provided by the National Natural Science Foundation of China, under granted No. 51639006. Appreciation is expressed to Prof. Yan-Jie Xu and Dr. Jian-Wen Pan for their valuable discussion and suggestions. The authors are also grateful to Professor Anil K. Chopra, University of California at Berkeley, for helpful advice and comments on the earthquake input models.

7. REFERENCES

1. Zhang, C., Jin, F. and Pekau, O. A. (1995), “*Time Domain procedure of FE-BE-IBE coupling for seismic interaction of arch dams and canyon*,” *Earthquake Engineering and Structural Dynamic*, **24**, pp. 1651-1666.
2. Maeso, O., Aznarez, J. J. and Dominguez, J. (2004), “*Three-dimensional models of reservoir sediment and effects on the seismic response of arch dams*,” *Earthquake Engineering & Structural Dynamics*, **33**(10), pp. 1103-1123.
3. Du, X. and Tu, J. (2007), “*Nonlinear seismic response analysis of arch dam-foundation systems-part II opening and closing contact joints*,” *Bulletin of Earthquake Engineering*, **5**, pp. 121-133.
4. Wang, J. and Chopra, A. K. (2010), “*Linear analysis of concrete arch dams including dam-water-foundation rock interaction considering spatially varying ground motions*,” *Earthquake Engineering & Structure Dynamics*, **39**(7), pp. 731- 750.
5. Wang, J., Lv, D., Jin, F. and Zhang C. (2013), “*Earthquake damage analysis of arch dams considering dam-water-foundation interaction*,” *Soil Dynamics and Earthquake Engineering*, **49**, pp. 64-74.
6. Alembagheri, M, and Ghaemian, M, (2013), “*Damage Assessment of a concrete arch dam through nonlinear incremental dynamic analysis*,” *Soil Dynamics and Earthquake Engineering*, **44**, pp. 127-137.
7. Mircevska, V., Nastev, M., Hristovski, V. and Bulajic, I. (2014), “*Arch dam-fluid interaction considering reservoir topology*,” *Journal of Earthquake Engineering*, **18**(7), pp. 1083-1101.
8. Omid, O. and Lotfi, V. (2017), “*Seismic plastic-damage analysis of mass concrete blocks in arch dams including contraction and peripheral joints*,” *Soil Dynamics and Earthquake Engineering*, **95**, pp. 118–137.
9. Chopra, A. K. and Wang J. (2010), “*Earthquake response of arch dams to spatially-varying ground motion*,” *Earthquake Engineering & Structural Dynamics*, **39**(8), pp. 887-906.
10. Yang, J., Jin, F., Wang, J. and Kou L. (2017), “*System identification and modal analysis of an arch dam based on earthquake response records*,” *Soil Dynamics and Earthquake Engineering*, **92**, pp. 109-121.
11. He, C., Wang, J., Zhang, C., and Jin, F. (2015), “*Simulation of broadband seismic ground motions at dam canyons by using a deterministic numerical approach*,” *Soil Dynamics and Earthquake Engineering*, **76**, pp.136-144.

12. Wang, J., He, C. and zhang C. (2017), "*Large-scale wave propagation simulation from fault rupture to dam structures*," Proceedings of 16th World Conference on Earthquake Engineering, Paper No. 3311, Santiago Chile.
13. Zhang, C., Pan, J. and Wang, J. (2009), "*Influence of seismic input mechanisms and radiation on arch dam response*," Soil Dynamics and Earthquake Engineering, **29**(9), pp.1282-1293.
14. Pan, J., Zhang, C., Wang, J. and Xu, Y. (2009), "*Seismic damage-cracking analysis of arch dams using different earthquake input mechanisms*," Science in China Series E: Technological Sciences, **52**, pp. 518-529.
15. Wang, J., Zhang, C. and Jin, F. (2012), "*Nonlinear earthquake analysis of high arch dam–water–foundation rock systems*," Earthquake Engineering and Structure Dynamics, **41**(7), pp. 1157–76.
16. Long, Y., Zhang, C. and JIN F. (2008), "*Numerical simulation of reinforcement strengthening for high-arch dams to resist strong earthquakes*," Earthquake engineering and Structure Dynamics, **37**: 1739-1761.
17. Pan, J., Xu, Y., Jin, F. and Wang, J. (2015), "*Seismic stability assessment of an arch dam-foundation system*," Earthquake Engineering and Engineering Vibration, **14**(3), pp. 517-526.
18. Song, L., Wu, M., Wang, J. and Xu, Y. (2016), "*Seismic damage analysis of the outlet piers of arch dams using the finite element sub-model method*," Earthquake Engineering and Engineering Vibration, **15**(3), pp. 617-626.
19. Liu, J, and Li, B. (2005), "*A unified viscous-spring artificial boundary for 3-D static and dynamic applications*," Science in China Series E: Engineering & Materials Science, 48(5), pp. 570-584.
20. ABAQUS Inc. (2007), "*Abaqus Theory Manual. Version 6.7*", ABAQUS, Inc., Providence, RI, USA.
21. Bathe, K. J. and Chaudhary, A. (1985), "*A solution method for planar and axisymmetric contact problems*," International Journal for Numerical Methods in Engineering, **21**(1), pp. 65–88
22. Lee, J. L. and Fenves, G. L. (1998), "*Plastic-damage model for cyclic loading of concrete Structures*," Journal of Engineering Mechanics, ASCE, **124**(3), pp. 892–900
23. Ghanaat, Y. (2004), "*Failure modes approach to safety evaluation of dams*," Proceedings of 13th World Conference on Earthquake Engineering, Paper No. 1115, Vancouver, Canada.

Three-Dimensional Effects on the Dynamic Response of the Dariyan Dam

Davood Salehi

Head of Earthfill Dam Design Group, Mahab Ghodss Consulting Engineers, Tehran, Iran

Email: Dav.salehi@gmail.com

Abstract

The Dariyan dam with 180m height is one of the highest rockfill dams in IRAN. The dam is located in high seismic zone. The ratio of crest length to the dam height is a little over 2. So, three dimensional effects of the valley on the dynamic response of the dam are not negligible. To study the dynamic response of the dam in three-dimensional conditions, linear and nonlinear dynamic analyses were performed by means of FLAC3D software. These analyses have been demonstrated that the maximum crest acceleration in three-dimensional analysis is much higher than 2D analysis and also permanent displacements of the dam body in 3D analysis are increased.

Keywords: Rockfill dam, Dynamic analysis, Three-dimensional analysis, Nonlinear analysis.

1. INTRODUCTION

The Dariyan dam is constructed on Sirvan River which is located in north-west of IRAN. The dam is one of the most important components of the Garmsiri project. Since the dam is located in a relatively narrow valley and in a high seismic zone, the three dimensional effects will not be negligible in earthquake conditions. Therefore, 3D dynamic analysis was performed by FLAC3d software in order to make a more accurate evaluation of the dam body behavior during seismic loading.

Developing more sophisticated softwares makes it possible to perform more realistic analyses. However, most studies in this field specially in academic activities have been focused on the effect of the shape of valley on dambody response and less attention has been paid to the amount of deformation. In most cases, the studies have been done by using linear or equivalent linear analyses. For instance, Ambraseys & Hatanaka in 1960 compared result of 2D and 3D analyses in rectangular shape of the valleys. They concluded that the results of the 3D analysis in L/H greater than 4 are similar to the results of 2D analysis. A similar study was performed by Makdisi in 1982 on triangular shape of valley that shows more Differences between the results of two and three-dimensional analyses. A more comprehensive study in this field was performed by Gazetas and Dakoulas in 1992. The results are summarized in Figure 1. As can be seen, in L/H ratios larger than 6, 3D effects are somewhat negligible. Based on these studies, natural period of the dam could be decreased 50 percent in very tight valleys.

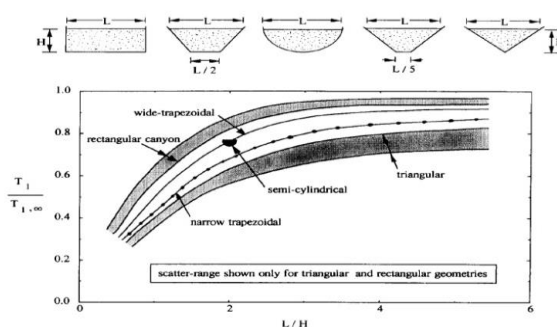


Figure 1. Comparing the 3D to 2D natural period of the dambody in different L/H [10]

2. CONSTITUTIVE MODELING AND ANALYSIS APPROACH

Cyclic loads in the unloading and reloading stress paths often create hysteresis loops. In equivalent linear method of analysis, area of a hysteresis loop represents energy dissipation factor or damping ratio and inclination of a hysteresis loop represents equivalent shear stiffness of the material. However, under realistic

triaxial conditions, not only the damping and the stiffness changes with increasing shear strain during unloading-reloading condition but also plastic strain could occur due to loading. Actual behavior of a soil sample under cyclic loading compared to equivalent linear behavior is shown in figure 2 schematically. According to the above description, combination of equivalent linear parameters with a non-linear model is closer to real behavior of the material under cyclic loads. Thereupon, Mohr-Coulomb elasto-perfectly plastic model with adjustment of the stiffness and damping ratio for every element was used in nonlinear analysis. Unfortunately, because of numerical instability, it was not possible to perform fully non-linear analysis with strain hardening model.

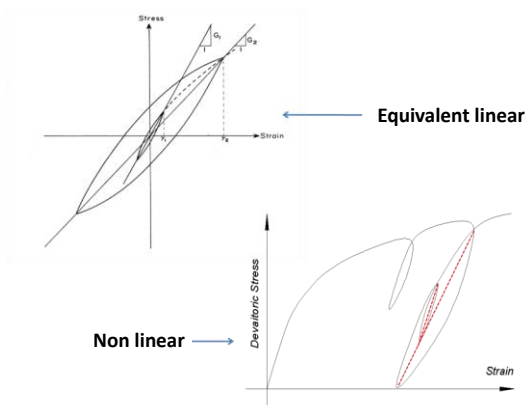


Figure 2. Comparison of equivalent linear behavior and actual behavior of materials in cyclic loading

3. ZONING AND GEOMETRY OF THE NUMERICAL MODEL

Cross section of the dam which is considered in two-dimensional analysis is shown in Figure 3. By some simplifications, dam body and the abutments are modeled in 3D analysis. Finite difference mesh of 3D model is shown in Figure 4. The model is composed of 19310 elements.

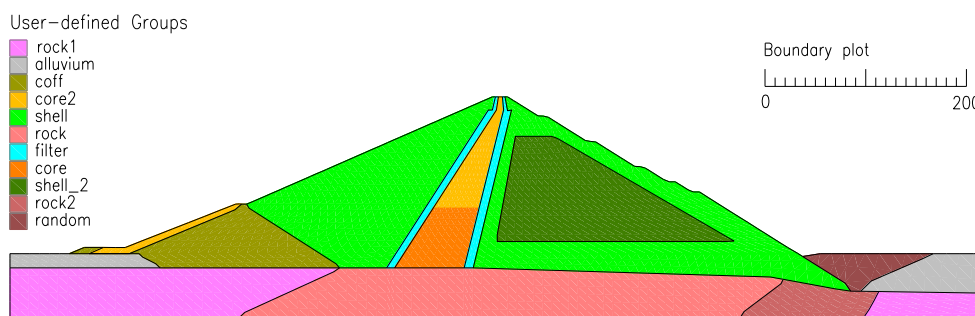


Figure 3. Cross section of the dam in two dimensional analyses

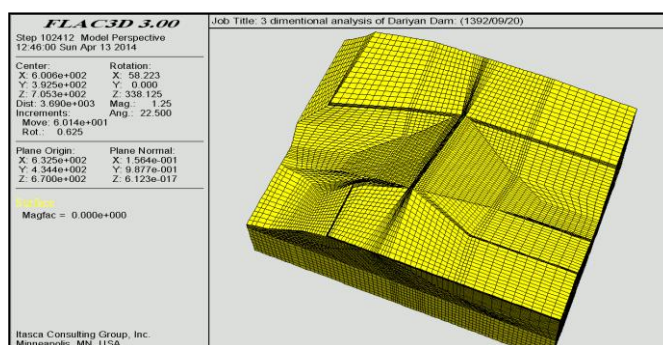


Figure 4. FDM mesh of the dam and abutments in 3D model

Numerical model shown in figure 4 was used in Static analyses including the construction stages and impounding. Since dynamic analysis of the dam body and foundation together was very time consuming, in dynamic stage the foundation and abutments of the model were removed and the scaled time histories of acceleration components were applied to the boundary of the dam body and foundation. In dynamic analysis, time step is dependent on the element size and stiffness. The time of calculations not only increases with increasing number of elements but also increases when the time step decreases. Therefore, analysis that considers the abutments took several months to perform. Shear modulus of the foundation is very high compared to the dam body material, therefore, considering top of the foundation as a seismic base is a reasonable assumption. Obviously, by removing the abutments, amplification effects of the abutments are neglected.

4. INPUT PARAMETERS

Table 1 presents the assumed shear strength parameters for different zones of the model.

Table 1- Shear strength parameters of dam body zones

Zone	ρ_d (gr/cm^3)	C (KPa)	ϕ_f (deg)
(Shell)	2.2	70	39.5
(Shell_2)	2.2	60	38
(Core)	1.75	10	25
(Core2)	1.65	20	21.5
(Filter)	1.8	0	32
(Alluvium)	1.7	5	16.5

Maximum shear modulus (G_{max}) for different materials were defined as follows:

$$G_{max} = 13000 \frac{(2.17 - e)^2}{1 + e} \times (\sigma'_{ave})^{0.55} \quad (kokusho \& Esashi, 1981) \quad \text{Rockfill (Shell)} \quad (1)$$

$$G_{max} = 3270 \frac{(2.97 - e)^2}{1 + e} \times (\sigma'_{ave})^{0.5} \quad (Hardin \& Black, 1968) \quad \text{Clay Core} \quad (2)$$

$$G_{max} = 220 \times 60 \times (\sigma'_{ave})^{0.5} \quad (Seed \& Idris, 1970) \quad \text{Filter} \quad (3)$$

$$G_{max} = 220 \times 90 \times (\sigma'_{ave})^{0.5} \quad (Seed \& Idris, 1970) \quad \text{Alluvium} \quad (4)$$

In equations (1) to (4) e is void ratio which was considered 0.4, 0.3 and 0.2 for Core, filter and shell material, respectively. Poisson's ratio was assumed equal to 0.3 for core and filters materials and equal to 0.2 for the rockfill shells. Variation of shear modulus and damping ratio versus cyclic shear strain are shown in figure 5.

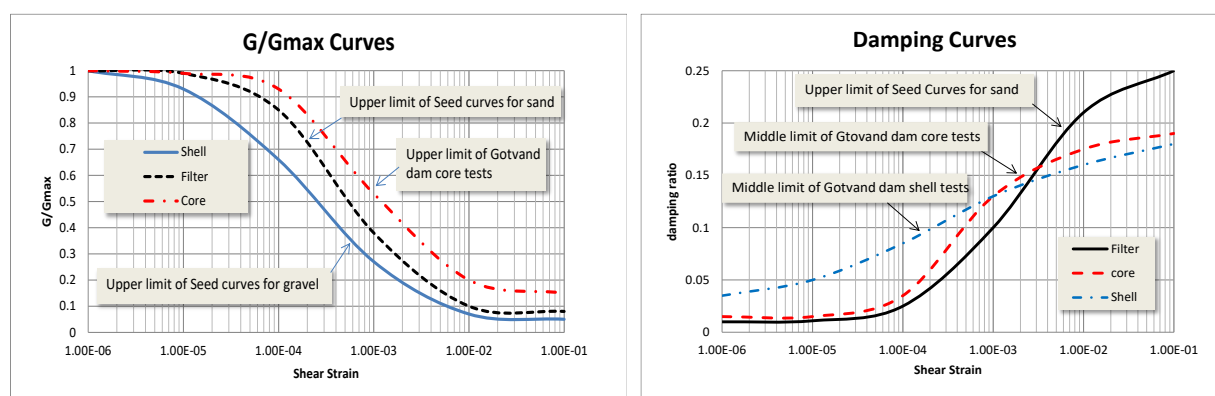


Figure 5. Damping ratio and G/G_{max} versus cyclic shear strain

5. INPUT MOTIONS

Khorgu scaled time history for Safety evaluation was used in the analyses. Horizontal and vertical components of acceleration are shown in figure 6. Maximum horizontal and vertical acceleration components are almost equal to 0.6g.

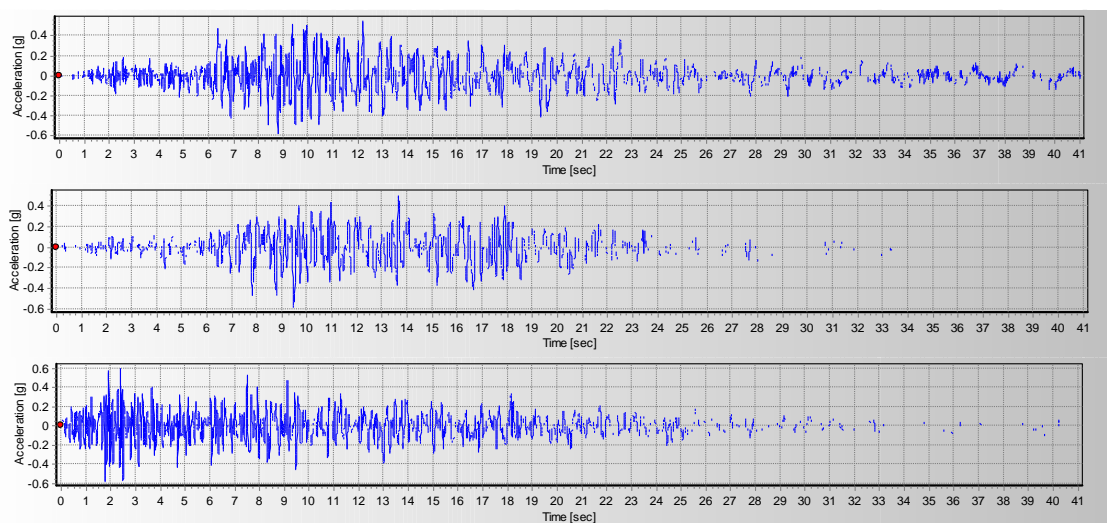


Figure 6. Khorgu scaled accelerograms components in the MCL

6. EQUIVALENT LINEAR ANALYSIS

Using the equivalent-linear method (Seed and Idriss 1969), a linear analysis was performed with some initial values assumed for damping ratio and shear modulus in the various regions of the model. By reference to defined curves that relate damping ratio and secant modulus to amplitude of cycling shear strain, the maximum cyclic shear strain was recorded for each element and used to determine new values for damping and modulus. The new values of damping ratio and shear modulus were then used in a new analysis of the model. The whole process is repeated several times, until there is no further changes in properties.

The G/G_{max} ratio contours at the end of equivalent linear analysis at the middle section of the model are shown in figure 7. The Damping ratio contours are shown in figure 8. As can be seen, minimum G/G_{max} ratio in the dam body is calculated less than 0.3. Maximum damping ratio is about 13% and 10% for core and shell respectively. Horizontal and vertical components of acceleration at the middle of the dam crest are shown in figure 9. Maximum horizontal acceleration at the middle of dam crest is estimated more than 3.1g and 2.5g for upstream to downstream direction and for the direction parallel to the dam axis, respectively. Maximum vertical component aligned with the Earth's gravity is calculated more than 2.1g. While, based on 2D analysis, maximum horizontal and vertical components of the crest acceleration were calculated equal to 1.4g and 0.8g, respectively. Maximum acceleration in different elevations of the core axis for 2D and 3D analysis are compared in figure 10. In 2D analysis amplification of acceleration occurs near to the dam crest while in 3D analysis, the acceleration was amplified strongly even in middle of the dam height.

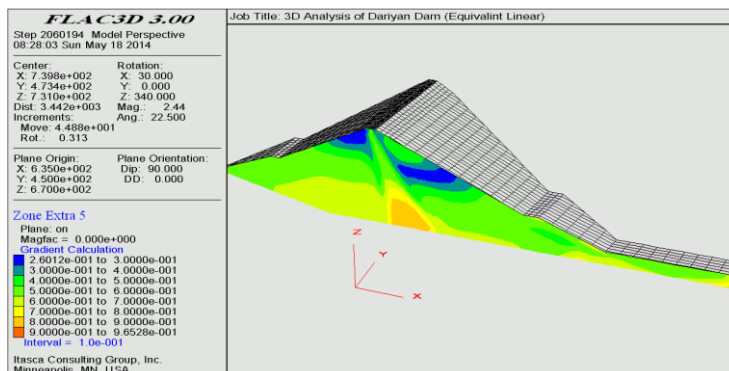


Figure 7. The G/G_{max} ratio contours at the end of equivalent linear analysis

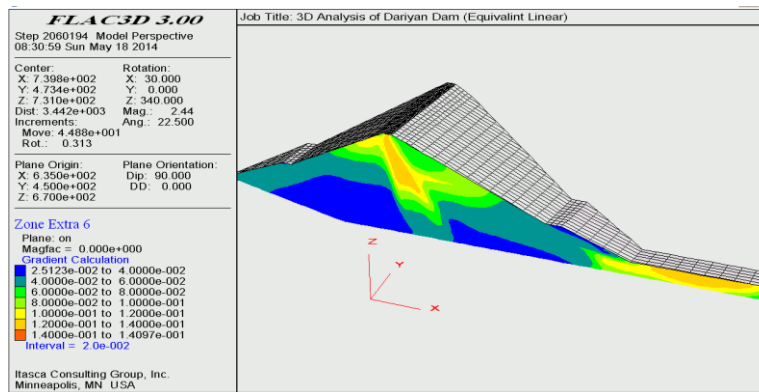


Figure 8. The Damping ratio contours at the end of equivalent linear analysis

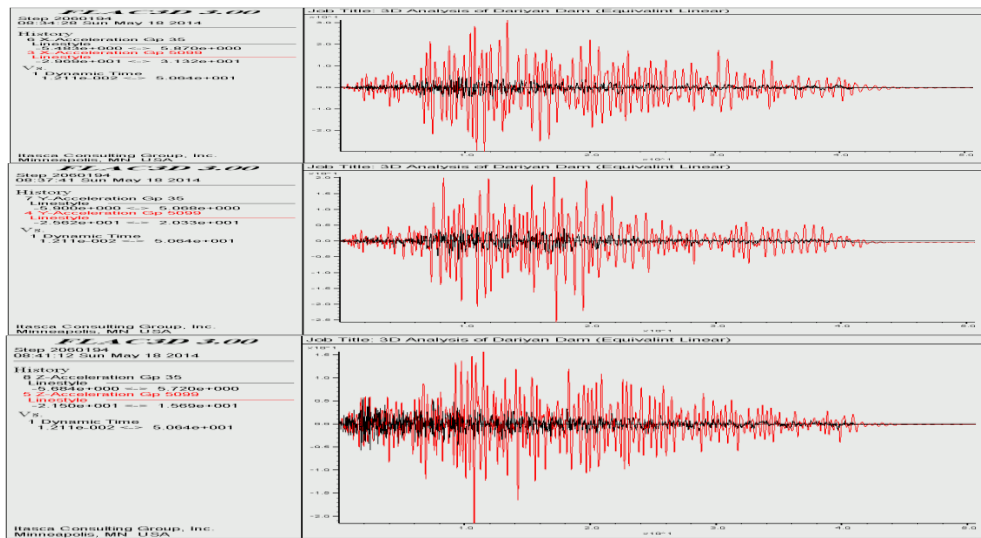


Figure 9. Crest acceleration components records

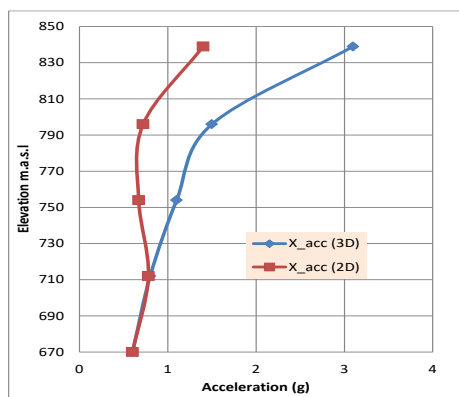


Figure 10. Comparison between 2D and 3D analysis (Maximum horizontal acceleration of different elevations of the core)

7. NONLINEAR ANALYSIS

In a nonlinear analysis, permanent displacements of every nodes at the end of the dynamic analysis will be directly visible. Mohr-Coulomb elasto-perfectly plastic model was used in nonlinear analysis. The results of this analysis are presented in Figure 11. In this figure, the horizontal displacement contours along with displacement vectors are shown on the middle cross section of the dam. The result of 2D analysis is shown

in Figure 12. As can be seen, the pattern of displacements of 3D analysis is similar to the 2D analysis. The crest settlement in 3D analysis is estimated about 2.2 m which is about 20% higher than the 2D analysis. Main features of 2D and 3D analysis results are summarized in table 2. Based on nonlinear analysis, maximum horizontal acceleration at the middle of dam crest is estimated more than 2.0g and 1.6g for upstream to downstream direction and direction parallel to the dam axis, respectively. Maximum vertical component in the opposite direction of gravity is calculated more than 2.6g and in the direction of gravity, it is close to 1.2g. The acceleration components near the dam crest are strongly amplified in 3D condition. According to the literature, Natural period of the dambody in 3D condition reduced and resonance condition is occurred. In addition, by applying another component of acceleration, the input energy increases. Despite the significant increasing of the crest acceleration response in 3D condition, the permanent displacement was increased to a lesser extent.

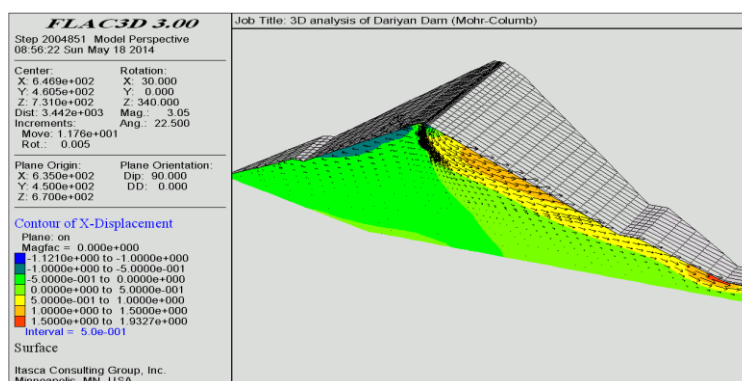


Figure 11. Horizontal displacement contours with displacement vectors on the middle cross section of the dam

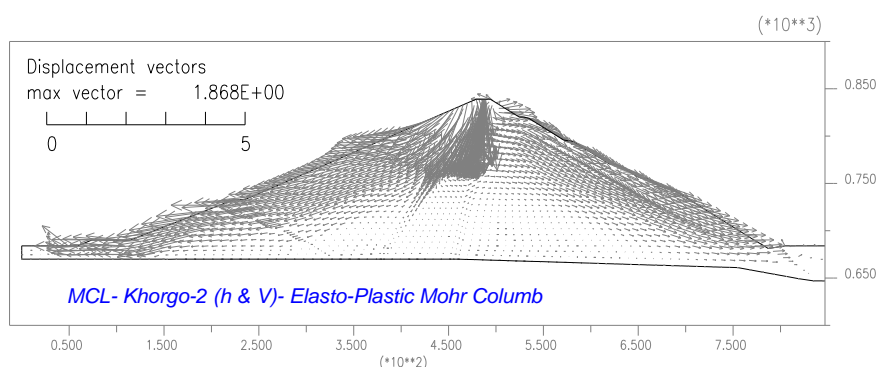


Figure 12. Displacement vectors of 2D analysis

Table 2- Summary of 2D and 3D linear and nonlinear dynamic analyses

Main features		unit	Equivalent linear			Nonlinear(Mohr Coulomb)		
			2D	3D	3D/2D	2D	3D	3D/2D
Maximum crest acceleration	horizontal (cross)	(g)	1.50	3.10	2.07	1.60	2.00	1.25
	horizontal (axis)		-	2.50	-	-	1.60	-
	vertical		0.80	2.10	2.63	1.00	2.60	2.60
Maximum U/S berm acceleration	horizontal (cross)	(g)	1.30	1.80	1.38	0.80	1.28	1.60
	horizontal (axis)		-	1.55	-	-	1.20	-
	vertical		0.40	0.85	2.13	0.70	0.75	1.07
Maximum D/S berm acceleration	horizontal (cross)	(g)	1.50	1.30	0.87	0.90	1.10	1.22
	horizontal (axis)		-	1.90	-	-	1.40	-
	vertical		0.55	1.40	2.55	1.00	1.00	1.00
Crest settlement		(m)	-	-	-	1.80	2.20	1.22
Maximum Horizontal Displacement	U/S face	(m)	-	-	-	1.00	1.50	1.50
	U/S berm		-	-	-	1.20	2.00	1.67
	D/S face		-	-	-	0.55	1.20	2.18

8. CONCLUSIONS

Considering the three-dimensional effects of the valley, leads to a further increase in dam crest acceleration. The ratio of amplification of 3D analysis to 2D analysis was more than 2. Both reducing of natural period of the system and inducing of input energy can explain the differences. However, in the 3D analysis acceleration near the dam crest was increased more than 2 times (compared to 2D analysis), the crest settlement has increased by about 20 percent. It should be noted that because of the densification of the rockfill materials due to shaking, the displacements may be actually higher than the calculated values. Although, the amount of displacements is higher than some of recommendations presented in the technical literature, since there is enough freeboard (11m), there will be no great concern about the dam safety during earthquake loading.

9. ACKNOWLEDGMENT

The author would like to acknowledge the valuable assistance given by my colleagues at the Soil and Rock Mechanics department and Dariyan dam site staff of the MahabGhodss Consulting Engineers and also the Dariyan projects staff at Iran Water and Power Resources Development Corporation (IWPC).

10. REFERENCES

1. Itasca Consulting Group, Fast Lagrangian Analysis of Continua in 3 Dimensions (FLAC3D), Minneapolis, Minnesota, USA, 2002
2. Prakash Sh. , "Soil Dynamics", McGraw-hill,Inc.,1981
3. Das, B. M., (1993). Principle of soil dynamics, PWS-KENT publishing company. Kramer S. L., "Geotechnical Earthquake Engineering" Prentice-Hall, Inc., Upper Saddle River, NJ, 1996
4. Seed H. B., Idriss I. M., (1970). Soil moduli and damping factores for dynamic response analyses. Report EERC 70-10, Earthquake Engineering Research Center. University of California, Berkeley, CA.
5. Lo Presti D. C. F., Jamiolkowski M., Pallara O., Cavallaro A. and Pedroni S. "Shear Modulus and Damping of Soils" Geotechnique 47, No. 3,603-617 ,1997
6. Makdisi, F. I., and Seed, H.B.(1978). "Simplified procedure for estimating dam and embankment earthquake-induced deformation," Journal of the geotechnical engineering division, ASCE, 104(GT7), pp.849-859.
7. Newmark, N. (1965) "Effect of Earthquakes on Dams and Embankments", J. Geotechnique 15, 139-160.
8. Sarma, S.K. (1981). "A simplified method for earthquake resistant design of embankment dams." Dams and Earthquake, TTL, London.
9. Salehi D. and Mahinroosta R., "Evaluation of Different Methods for Dynamic Stability Analysis of Embankment Dams", 73rd Annual Meeting of ICOLD, Tehran, IRAN, May 1-6, 2005, Paper No. : 063-W4
10. Gazetas G. and Dakoulas P., "Seismic Analysis and Design of Rockfill Dams, State of the Art. Elsevier: Soil Dynamics and Earthquake Engineering, 1992, Vol. 11.
11. MahabGhodss Consulting Eng. "Dynamic parameters of dambody materials of upper Gotvand dam", Phase II, September 2007 (Persian)
12. IISE., "The results of dynamic testing of core materials of upper Gotvand dam", International Institute of Seismology and Earthquake Engineering, October 2006 (Persian)
13. BHRC., "The results of dynamic testing of shell materials of upper Gotvand dam", Building and housing research center, 2009 (Persian)
14. Salehi D. and Tabibnejad A., "Experimental study and numerical modeling of the dynamic behavior of core mixture materials of Gotvand dam", The 4th International Conference on Soil Mechanics and Geotechnical Engineering, Tehran, Iran, November 2010 (Persian)
15. Mirghasemi A. and Shahbazi R. "Comparison of 2D and 3D dynamic analysis of earth dam with clay core in the narrow valleys" MA thesis of Civil Engineering - Soil Mechanics and Foundation branches, Faculty of Tehran University, September 2012 (Persian).

Nonlinear Dynamic Analysis of Concrete Gravity Zavin Dam

Behzad Najmoddini ¹, Abbasali GhezelSofloo ²

1- M.Sc. in Civil Engineering, Khavaran Institute of Higher Education, Mashhad, Iran

2- Assistant Professor, Department of Civil Engineering, Islamic Azad University of Mashhad, Iran

Email: behzad.nj55@yahoo.com

Abstract

In recent decades, the issue of seismic safety of concrete dams, attention has been paid. The main reason for this may be economic plan and also the lifetime of existing dams. Thus fondness engineering community to develop and use a powerful process for nonlinear analysis and as much as possible close to reality as concrete dams under different loads, especially dynamic loads generated by earthquakes can be seen. In this paper, nonlinear dynamic analysis of concrete gravity dams before cracking with regard to interaction Dam - Lake - the foundation is done. The Smeared crack model for nonlinear analysis of concrete gravity dams and cracks has been used to determine the position and orientation. The research has been modeled Zavin Dam, in North-East of Iran. Nonlinear Dynamic Analysis of this research under three different earthquakes with same PGA around 0.5g and frequency varies done and PGA been given that the earthquake in almost same vibration and power can have a different story and this suggests that factors other than PGA in the destructive power of earthquakes are effective. Dynamic interaction of dam and lake, with Zangar method is the model and for nonlinear model of concrete in Nonlinear Dynamic Analysis of Rupture criterion Drucker - Prager has been used. After dynamics analyzing in Zavin dam in the cracked presence the horizontal and the vertical crown displacement and tensile stress major at the end and leave amounts of strain plastic bottom left along x and y obtained. Fissuring results show that the tensile cracking of concrete dams' behavior important factor is nonlinear. Responses obtained from nonlinear analysis Zavin dam, crack without and after crack completely left disagree.

Keywords: Concrete Gravity Dam, Displacement, Tensile Stress, Earthquake, Nonlinear Dynamic Analysis.

1. INTRODUCTION

Dam Building industry has started with modern methods using dams with large scales about three decades ago in Iran. Study and design of large dams started around the year 1948 and their construction began in late 1950s and entered a new era with the advent of the Iranian Islamic revolution and the country's water industry has been aimed at being self-efficient in this ground. The most important factor in reducing the useful life of a concrete dam is water settlement and one of the major causes of water settlement is cracking of concrete. As a result, it is necessary to attempt to prevent cracks in parts of the structures that are exposed to water pressure and consider the risk of cracks. Therefore, when preparing the concrete mix design, the construction and operation of the dam and during the construction and development, usually conventional cracks in the concrete dams and methods of prevention of such cracks in such structures are discussed. One of the most important risks that threaten the stability of a concrete dam and may also lead to the failure of the dam and endanger many lives is the cracks in the concrete dam body and its development in various directions. These cracks cause by water infiltration into the dam body and through creating additional pressure within the body lead to the growth of the cracks downwards and will finally lead to the slipping of the isolated parts of the dam. To familiarize with the cracks, it should be noted that the physical and mechanical properties of concrete and its composition and behavior play a very important role at the time of cracking, the type of cracks and how it is spread.

2. REVIEW OF THE LITERATURE

Research conducted to predict the cracks' expansion in concrete gravity dams is restricted to the cracks at the junction of the dam to foundation. In the concrete gravity dams for the crack considered at the dam to the foundation area there is linear elastic failure mechanical conditions (LEFM) because the length of the damaged area of the tip of crack will be small compared to the dimension of the structure and it will be negligible. With concrete dams' aging and the progress in human societies, the need for safety analysis of the dams is felt more than before. In this regard in recent years, great efforts are made in modeling the nonlinear behavior particularly

under seismic loads and several models are provided for the non-linear behavior and using them the non-linear behavior of the concrete dams is evaluated under the static and seismic loads. Modeling the cracks' profiles in concrete dams under static and heat loads has attracted the attention of some investigators. In the field of the non-linear behavior of dams during earthquakes it is possible to refer to USCOLD publications [10]. In the study of seismic behavior and predicting cracks in dams it is possible to indicate the work of Chopra et al (1972) as the first step in which using the linear elastic analysis the situations in which cracks may appear are specified. In this study gravity dams of Koyna in India and Pine flat in the United States are studied regardless of the effect of interaction between the lake and foundation under the Koyna earthquake (1967). The first nonlinear FEM analysis was performed by Pal on concrete gravity dams. In this study Koyna Dam is analyzed regardless of the lake and assuming a solid foundation using the expanded crack model to simulate the progress of the crack with the fracture resistance of materials criterion. Some researchers have applied a combination of continuous, CCPM and discrete models for the seismic analysis of gravity dams [2]. In this study the equivalent tensile strength measure is used for the onset and expansion of cracks in which the crack expands on a plane perpendicular to the main tensile stress. Among the studies in which the discrete crack model is used include the work presented by Tinawi and Guizani (1994) in which the hydrodynamic pressure inside cracks has been investigated on the seismic response of concrete dams [5].

3. ZAVIN KALAT CONCRETE GRAVITY DAM

The dam is located at 95 kilometers northeast of the city of Mashhad and Kalat and 1.5 kilometers from the Olia village at a place called Doabi on a River called Zavin as one of the main streams of the Qarah Tikan border river. The dam has a height of 51.2 meters from the foundation and the crest length of 132 meters. Zavin dam lake capacity in maximum level is 3000000 cubic meters and 2690000 cubic meters at normal level. The dam is capable of setting more than three million cubic meters of water for agricultural purposes. The regulated water is capable of irrigating more than 440 hectares of up and down Lavin village lands. This river is a permanent river and its runoff is 8.1 million cubic meters annually. Zavin dam on this river is designed to save the river to supply water for agricultural lands near water, coastal villages, drinking water and industrial estate [8]. Figure (1) presents Zavin concrete gravity dam in the city of Kalat.



Figure 1. The image of Zavin concrete gravity dam in the city of Kalat

4. THE BASIC APPLIED NUMERICAL METHODS

In this study predicting the life span of the cracks and the two-dimensional modeling of the crack growth is done by the Abaqus using the finite element methods. Abaqus software is a set of engineering simulation software programs based on the finite element method which is able to solve a wide range of engineering problems from the simple linear to the complex nonlinear simulations. Abaqus has an extensive library of different types of elements as well as a wide collection of models of different materials for modeling most common engineering materials. This software is capable of performing the structural analyses (stress/displacement) as well as thermal, electric soil mechanics, and mass transfer and the interaction analyses such as structure-fluid interaction. In the nonlinear analyses Abaqus has automatically selected loading and convergence tolerance and sets them continuously so that a detailed response is obtained.

5. MATERIAL AND METHODS

In the present study Abaqus program is used for modeling and analysis of concrete gravity dam. In this study the analyses are conducted on Zavin dam. This dam is a concrete gravity dam. Table (1) shows the elastic properties of concrete used in dam construction:

Table 1. The elastic properties of concrete used in body and dam foundation [8]

Concrete specific weight	$2400(\frac{kg}{m^3})$
Concrete compressive strength	$200(\frac{kg}{cm^2})$
Modulus of elasticity of concrete	$15100(\frac{kg}{cm^2})$
Tensile strength of concrete	$2.1e5(\frac{kg}{cm^2})$
Poisson's ratio	0.17
Concrete failure energy	$100(\frac{n}{m})$
Saturated specific weight of bedrock	$2660(\frac{kg}{m^3})$
Modulus of elasticity of the bedrock	$4.2e5(\frac{kg}{cm^2})$
Poisson's ratio of the bedrock	0.2

The loads applied on the structure in modeling Zavin dam include the gravity load of the body, hydrostatic water pressure in normal mode (normal level) and flood (maximum level), sediments pressure, uplift pressure, hydrodynamic pressure and seismic forces on the dam body. To perform the body and dam foundation loading the specific weight presented in Table (1) is used. In this loading the weight of the peripheral equipment such as valves is ignored. The total mass of the dam body at the depth unit is 2812800 kg and the total mass of dam foundation at the depth unit is 1,634,676.4 kg. According to the Water normal level (1302 m) the hydrostatic pressure of each point at the upstream is calculated according to its height. For loading the earthquake in the dynamic analysis of the dam the horizontal component (longitudinal) of three earthquakes is used. Japan's Kobe earthquake with PGA = 0.503, USA's Loma earthquake with PGA = 0.501 and Aryan Turkey's earthquake with PGA = 0.496; Zavin dam is dynamically analyzed under these earthquakes.

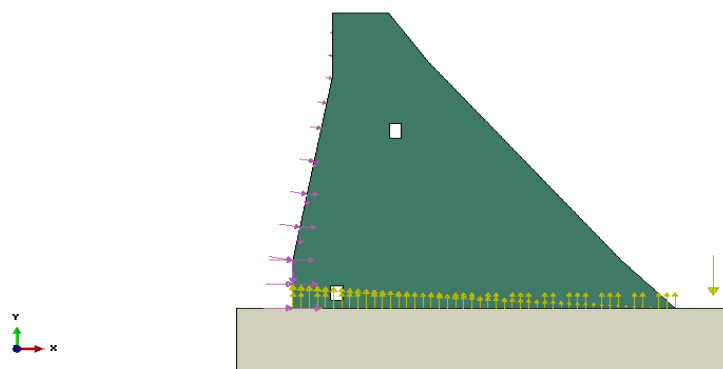


Figure 2. Different loading mode of Zavin concrete gravity dam

6. FINITE ELEMENT MODEL

Abaqus is general software based on Finite element method (FEM) and it is one of the most powerful software programs in general areas. The static and dynamic analyses of the materials are done by this software in Zavin dam. The correct meshing and choosing the right elements are the most important steps in finite element analysis. The dimensions and type of meshing depend on the type of analysis, modeling and the accuracy of the output results. For example, the size of the elements in the nonlinear analysis is usually much smaller than linear analysis. In finite element analysis usually by reducing the size of the elements the accuracy of the results is increased but this increases the number of elements and their analysis time exponentially. In order to model the body and the foundation of the dam Abaqus Software and for meshing the body and foundation the SOLID 4node CPS4R element is used. In the area near the contact area of the dam and

foundation, where there is the possibility of cracking and cracking is considered, the smaller element is used to both prevent the cracking of the element and after cracking its stress distribution to the adjacent elements is managed properly.

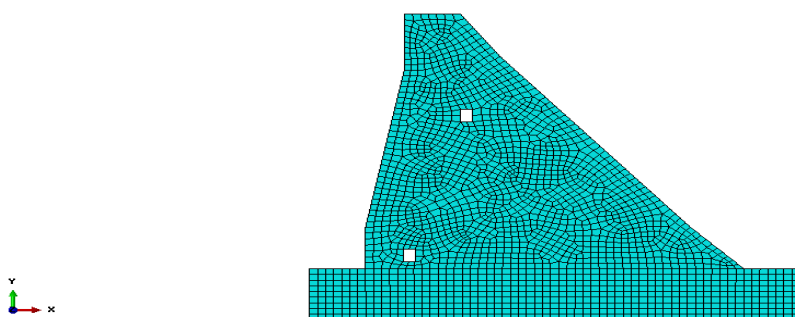


Figure 3. Meshing by finite element analysis of Zavin concrete gravity dam

7. THE METHOD OF MODELING THE EFFECT OF LAKE'S HYDRODYNAMIC PRESSURE ON THE DAM RESPONSE TO THE EARTHQUAK

Vibrations caused by earthquakes can cause tremors and movement in the dam and its foundation towards the reservoir and the water in it is applies its additional pressure by its inertia against this motion. The exact determination of the hydrodynamic pressure distribution curve and its value is difficult for various reasons and then usually the simple methods are used to estimate the hydrodynamic pressure, the resultant force and the moment cause by it. Different studies such as Zangar (1975) show that the hydrodynamic pressure distribution caused by earthquake on the dam is almost parabolic (semi-parabolic semi-elliptical) Figure (4) and the following equation can be used to find the pressure intensity level used for each section to a depth Z [1]:

$$P_{ez} = C_e \alpha_h \gamma_w \cdot h \quad (1)$$

Where: α_h is the horizontal earthquake acceleration coefficient to the gravity acceleration, h is the water level at the section under study (from the bottom to the water level), γ_w water specific weight and C_e is dimensionless coefficient which depends on the water height, upstream slope of the dam body and the Z value which is obtained by the following equation:

$$C_e = \frac{c_m}{2} \left[\frac{z}{h} \left(2 - \frac{z}{h} \right) + \sqrt{\frac{z}{h} \left(2 - \frac{z}{h} \right)} \right] \quad (2)$$

Where: C_m is the maximum C_e obtained as follows:

$$c_m = 0.735 \left(\frac{90 - \phi}{90} \right) \quad (3)$$

ϕ is the angle between the upstream side and the vertical line. According to the above equations the hydrodynamics force is calculated at each point.

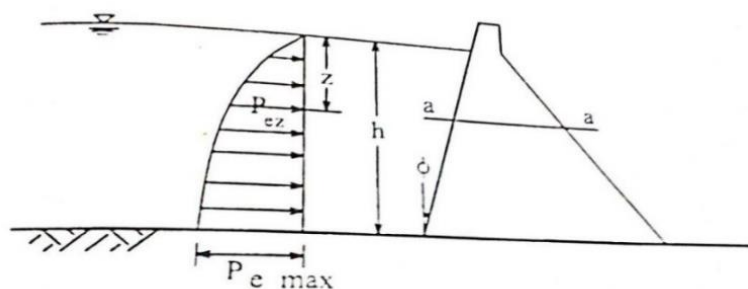


Figure 4. Distribution of hydrodynamic pressure on Dam [1]

Table 2. The values of hydrostatic and hydrodynamic pressures at different levels

Level	Hydrostatic pressure (pa)	Hydrodynamic pressure (pa)*
51.2	0	0
50	11772	975.6
45	60822	4946.36
40	109872	6269.76
35	158922	7218.72
30	207972	8000.88
25	257022	8677.44
20	306072	9278.88
15	355122	9846.40
10	404172	10365.92
5	453222	10847.76
0	502272	11304.96

*Hydrodynamic pressure is obtained by the Zangar formula.

Usually modal analysis is the starting point of dynamic analysis for determining the structural response against dynamic loads in which the natural frequencies and vibration modal form of the system are determined. In this study before performing the dynamic analyses the modal analysis and parameters are considered to determine the attenuation coefficients.

Table 3. The results of modal finite element analysis of Zavin dam with and without cracks

Frequency without crack ($\frac{cycles}{time}$)	9.4795	18.126	20.637	27.794
Frequency with crack ($\frac{cycles}{time}$)	9.3894	18.004	20.373	27.349

8. NONLINEAR DYNAMIC ANALYSIS

For loading the earthquake in the dynamic analysis of the dam the horizontal component (longitudinal) of three earthquakes is used. Japan’s Kobe earthquake with PGA = 0.503, USA’s Loma earthquake with PGA=0.501 and Aрызkan Turkey's earthquake with PGA = 0.496.

The results of nonlinear dynamic analysis of Zavin dam with crack under the effects of the earthquakes are listed as follows:

Table 4. Maximum main tensile stress at the end of crack in nonlinear response of Zavin dam under different earthquakes

Effective earthquakes	The maximum tensile stress at the end of crack in the nonlinear response (Mpa)
Kobe Earthquake	4.4663
Loma Earthquake	2.7416
Aрызkan Earthquake	2.0153

Table 5. The results of nonlinear dynamic analysis of Zavin dam under Kobe earthquake

Kobe earthquake	Nonlinear response of the dam without crack	Nonlinear response of the dam with crack
The maximum horizontal displacement of dam crest (m)	0.3937	0.0225
The maximum vertical displacement of dam crest (m)	0.1125	0.0238
Maximum plastic strain in the direction of x at the tip of the crack	-----	0.0326
Maximum plastic strain in the direction of y at the tip of the crack	-----	0.1391

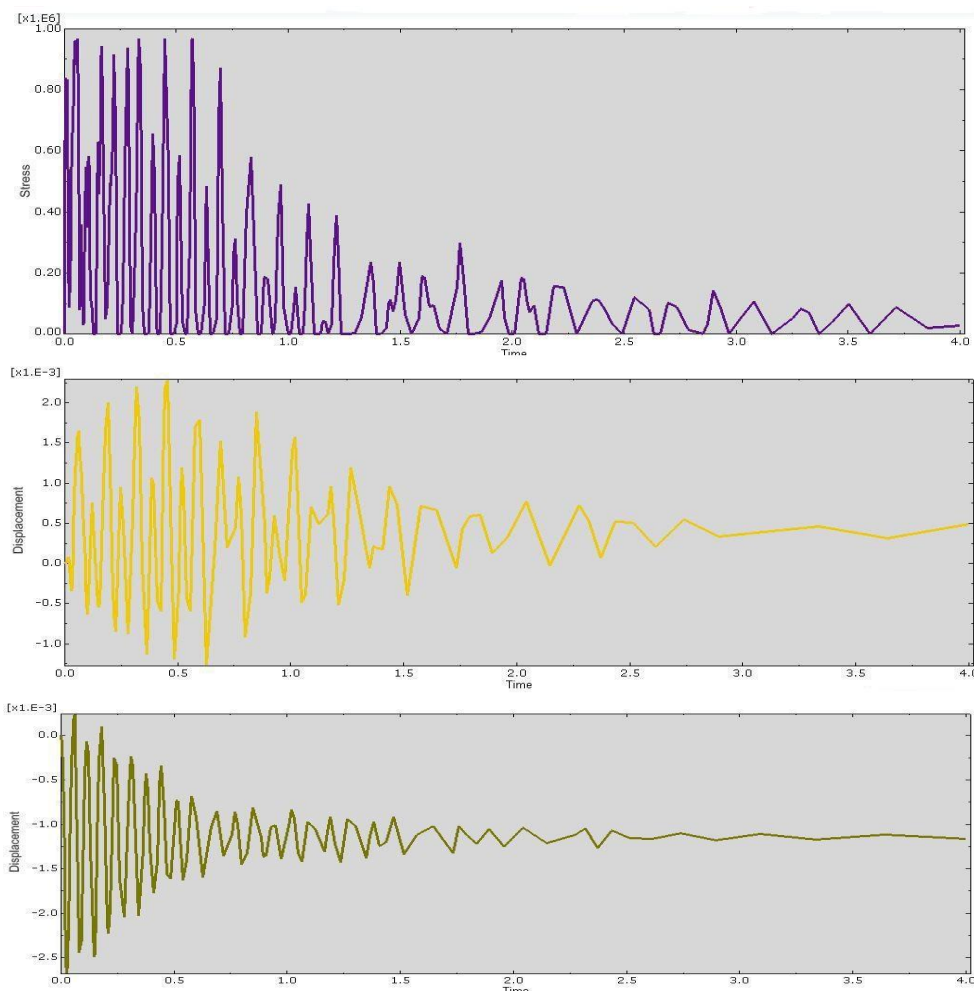


Figure 5. The time history of stress in dam heel, horizontal and vertical crest displacement under Kobe earthquake

9. VALIDATION

For this purpose, the method of analysis mode using reservoir interaction is utilized using the method of Zangar and in it the frequency of the dam in the first four modes is compared with the results obtained by Chopra and Chakrabarti (1972) these results are in Table (6) shows that the model is in accordance with normal conditions [4].

Table 6. Compare natural frequency results in software Abaqus

Mode	Natural frequency ($\frac{cycles}{time}$)	
	Abaqus	Chopra and Chakrabarti
1	9.4795	10.562
2	18.126	19.271
3	20.637	22.501
4	27.794	28.732

10. CONCLUSIONS

In this study the nonlinear dynamic analysis of Zavin dam is done under three different earthquakes with PGA of about 0.5g using Drucker- Prager failure criterion for nonlinear modeling of concrete and the Zangar method is used to model the dynamic interaction between the dam and reservoir. The results of this study may be summarized as follows:

- Reservoir sediments have a huge impact on earthquake energy absorption and dynamic response of the system through the absorption of hydrodynamic compressive waves' energy absorption and response reduction of the system under the vertical ground acceleration and this is also important for the ground horizontal acceleration.
- The reservoir depth has a significant impact on dam system response and this response is higher in the response to the vertical component than the response to the horizontal component.
- Reducing the frequency of dynamic response in nonlinear mode with cracking indicates that as the result of plasticity of some elements the dam hardness is reduced and their displacement is increased.
- In nonlinear dynamic analysis of concrete gravity dam with cracks the horizontal and vertical displacements of the dam crest are much less than the horizontal and vertical displacements of the dam crest in nonlinear dynamic analysis of concrete gravity dam without cracks and this indicates that in the cracked state a part of energy is absorbed by the crack and this leads to the displacement.

11. ACKNOWLEDGEMENT

We would like to acknowledge Razavi Khorasan Water Co. for data of Zavin Kalat Dam.

12. REFERENCES

1. Abrishami J., Wahab Rajaei N, (2010). "*The design and implementation of concrete dams*", 4th edition, Astan Ghods Razavi.
2. Bahattacharjee SS, Leger p., (1993). "*Seismic cracking and energy dissipation in concrete gravity dams*" earthquake Engineering & structure Dynamic, 22,991-1007.
3. Bahattacharjee SS, Leger p. (1994). "*Application of NLFM Models to predict Cracking in Concrete Gravity dams*". Journal of Structural Engineering, ASCE, 120 (4), 1255-1271.
4. Chopra, A.K. & Chakrabarti, P., (1972). "*The earthquake experience at Koyna dam and stresses in concrete gravity dams*", Earthquake Eng. Struct. Dynamics, 1(2):151-164.
5. Fenves G., Vargas- loli LM, (1988). "*Non-linear Dynamic analysis of flue - structure System*". Journal of engineering mechanics. ASCE, 114,219-239.
6. Ghrib F., Tinawi R., (1995). "*Nonlinear behavior of Concrete Dams using damage mechanics*," journal of Engineering mechanics, ASCE, 121 (4), 513-526.
7. Ghrib F., Tinawi R., (1995). "*Application of damage mechanics for Seismic analysis of concrete gravity dams*" Engineering & structure Dynamics, 24, 157-173.
8. Heyrani Z., Ghaemian M., Summer (2010). "*Nonlinear seismic analysis of concrete gravity dams considering dam-reservoir- foundation interaction*", Journal of Civil Engineering, Islamic Azad University.
9. Khorasan Regional Water Authority, December (2001). Zavin Dam three-dimensional analysis report, Pooy Water Consulting Engineers.
10. Lohrasbi, R. attarnejad R., (2008). "*Crack Growth in Concrete Gravity Dams Based on discrete crack method*" American Journal of Engineering and Applied science, 1 (4), 318-323.
11. United States Committee of large dams (USIcold), (1984). "*Bibliography on performance of dam's during earthquake*". Committee on earthquake.
12. VE Saouma, Hansen E., & B. Rajagopalan, (2001). "*Statistical and 3D Nonlinear Finite Element Analysis of Schlegels Dam*," Technical Report, University of Colorado.

Seismic Vulnerability Assessment of a Set of Concrete Gravity Dams

Saeid Ghasemi Gavabar¹, Mohammad Alembagheri², Behrang Esmi¹

1- M.Sc., School of Civil Engineering, University of Tehran, Tehran, Iran

2- Assistant Professor, Department of Civil and Environmental Engineering, Tarbiat Modares University, Tehran, Iran

Email: ghasemisaeid@ut.ac.ir

Abstract

Since dams are very important structures, vulnerability assessment and evaluation of their safety against destructive phenomena are significant. Vulnerability assessment and prediction of dam's damage due to earthquake with a variety of intensities can provide helpful information that would be very useful and effective in the proper management of probable crises. One of the useful tools in assessing earthquake damage in concrete dams is the production of their related fragility curves. Due to the vulnerability of concrete dams to tensile cracking, a new concept of damage index (DI) according to tensile cracking has been developed. Also because of dependency of fragility curve to limit states of engineering demand parameters (EDP), limit states have been defined according to tensile cracking in dams. Studies on the production of fragility curves on concrete gravity dams are very limited and mostly not comprehensive in a way fragility curve are normally produced only for one type of dams or with one height and one figuration. In this paper, fragility curves have been plotted for a set of concrete gravity dams, such as Pine Flat, Koyna and Shafarood. Through extensive studies on different sample dams' structural performances comparisons are made possible using fragility curve.

Keywords: concrete gravity dams, damage index, nonlinearity, fragility curve, seismic vulnerability.

1. INTRODUCTION

About 10% of high dams in the world are concrete gravity dams [1]. They impound large reservoirs of water and play a key role in water management, flood prevention and power generation. The consequences of failure of a high concrete dam could be very catastrophic. Hence, assuring their proper performance specifically during extreme events like earthquakes is of great importance. Yet, many dams are aging and most were designed at a time with limited seismic field data. Most of the existing dams have been in service for several years and the effect of age has made them too vulnerable to endure severe natural hazards like earthquake. Therefore, seismic vulnerability assessment of concrete gravity dams is very important now. Due to new design guidelines for severe earthquake conditions and dams, most of the existing dams fail to provide the safety criteria of new design guideline [2].

Damage index (DI) measures the amount of damage and degradation rate that is inflicted to a structure. The idea of describing the damage states of the structure with one number is marvelous because of its plainness [3]. DIs are obtained with empirical and theoretical approaches. In the case of concrete gravity dams, because there is a limited data base of field and experimental observation of damages, the numerical methods for estimation of DI are preferred. One well-known method for computing the structural capacities is the incremental dynamic analysis (IDA) [4]. In an IDA, the intensity of ground motion applied to the base of the structure is incrementally increased until the structure collapses [5].

Damage indexes are usually normalized so that they have zero value when the structure is in no-damage state and unit value when failure or total collapse of the structure occurs. The damage state of the structure can be defined in several ways: a binary damage state (failure/no failure) and a discrete valued damage state by using qualitative indicators such as none, minor, repairable, severe and failure [4]. In concrete gravity dams due to lack of empirical data, determining such qualitative indicators of damage for gravity dams is not easily possible.

The DIs are divided into two general categories: local and global DIs. A local DI is an indicator of damage for a part of a structure, whereas a global DI gives an estimate of overall damage imposed on the structure. In addition, the DIs are separated into cumulative and non-cumulative ones. Those indexes that can consider the accumulation effect of seismic excitation to structural damages are called cumulative indexes [4].

Concrete gravity dams can be divided into three major zones on the basis of crack propagation; (i) base/dam-foundation interface region, (ii) main body of dam, and (iii) around neck region. Among all these three regions (i) and (iii) are most likely to have cracks; however, in some rare cases under extreme events, region (ii) can also undergo cracks [2]. Therefore, in this paper a damage index has been proposed to monitor tensile damage (d_t) in concrete gravity dams.

Fragility curves describe the probability of damage in a structure at various levels of earthquake. It is the best way to estimate and evaluate the vulnerability of potential damage in future earthquakes. Fragility curves can also be used for prioritizing retrofiting, pre-earthquake planning, and loss estimation tools. The development of fragility or vulnerability assessment function is generally based on expert opinion, analytical methods, and the damage data of structures from past events [6].

The past vulnerability data are very scarce in case of concrete dams. Therefore, analytical methods have been used to obtain fragility curves. There are two approaches used for the development of analytical fragility curves (a) based on demand of structures [9, 10] and (b) based on damage indexes [11, 12]. The first approach is suitable for design purposes [13] while the second methodology is appropriate for the damage evaluation due to its ability to define damage states [24]. In the present paper, incremental dynamic analysis (IDA) method is used for the categorization of the limit states on engineering demand parameters and development of fragility curve by considering 30 earthquake ground motions [2]. Two local and one global damage indexes have been developed according to tensile damage in base and around the neck of the dams.

This study is an attempt to determine the limit states and define a new local and global damage index (DI) for a set of concrete gravity dams and plot their related fragility curves according to their limit states. Using Pine Flat, Koyna and Shafarood dams as case study, their numerically modeled along with its full reservoir utilizing finite element method in three analysis cases (Pine Flat, Koyna and Shafarood) to assess the performance of the dam's structure in intact situations. Only material nonlinearity is considered in modeling. The dam-reservoir system is modeled based on Eulerian-Lagrangian approach. Thirty proper ground motion records are selected for the purpose of analysis. Several EDPs for each case are calculated in terms of IMs. Limit states are defined in every level of $S_a(T_1)$ according to progress of tensile damage in base or neck of the dams. Finally, the seismic fragility curves of every EDP and EDPs for a set of concrete gravity dams are generated.

2. INCREMENTAL DYNAMIC ANALYSIS

Incremental dynamic analysis is a parametric analysis that estimates more thoroughly structural performance under seismic loads. It involves subjecting a structural model to some ground motion records, each scaled to multiple levels of intensity, thus producing some curves of response parameterized versus intensity level [18]. As mentioned earlier, the IDA approach involves performing nonlinear dynamic analyses to a structure under a suite of ground motion records; each of the selected records is scaled to several intensity levels. Herein, the spectral acceleration at the natural period of the concrete gravity dam structure ($S_a(T_n)$) is selected as an intensity measure (IM) used to describe ground motion characteristics. The first reason behind this selection is that seismic demand estimates are strongly correlated with the linear-elastic spectral acceleration at natural period of the structure (T_n). Moreover, based on 4 criteria (i.e. practicality, sufficiency, effectiveness and efficiency) Hariri et al. showed that $S_a(T_n)$ is an optimal IM for seismic performance assessment of concrete gravity dam structures [7]. Each of the records has been scaled to multiple levels of $S_a(T_1, 5\%)$ from zero to 1 g that have been arranged in 0.1 g steps. A set of incremental time history analyses was performed by applying scaled ground motions and desired EDP values were monitored during each analysis.

3. GRAVITY DAM-RESERVOIR NONLINEAR NUMERICAL MODELS

The tallest non-overflow monolith of concrete gravity dams is chosen along with its full reservoir, as shown in Figure 1. The two-dimensional dam-reservoir system is numerically analyzed using the finite element method based on Eulerian formulation (pressure-based elements) for the reservoir, and Lagrangian formulation (displacement-based elements) for the dam body in plane-stress manner. The foundation is assumed rigid. The reservoir length is considered to be five times the dam height and transmitting boundary condition is assigned to its truncated far-end. A pressure-free condition is assumed for the free surface of the reservoir. The finite element equations of the dam body are coupled with the finite element equations of the reservoir through a coupling matrix which relates the hydrodynamic pressure of the reservoir to the equivalent forces on the dam structure. For a detailed description of these models, one can refer to [19]. The selected earthquakes are uniformly applied to the rigid foundation beneath the dam body.

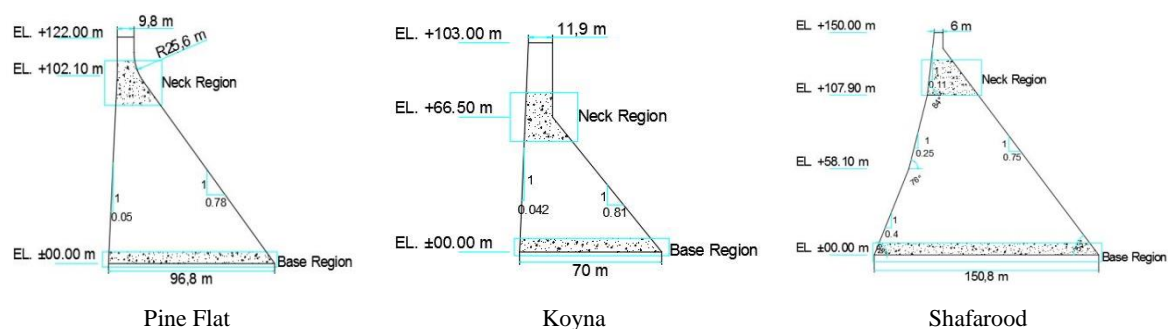


Figure 1. (a) Tallest non-over-flow monolith of Pine Flat dam, Koyna dam and Shafarood dam

Only material nonlinearity is taken into account. The material nonlinearity of mass concrete is modeled using plastic-damage method which is a continuum homogeneous damage mechanics approach. Considering only the tensile damage as the main material failure for the gravity dam, the stiffness degradation of mass concrete in tension, beyond the tensile strength (f_t) is modeled as:

$$E = (1 - d_t)E_0 \tag{1}$$

where E_0 is the initial (undamaged) modulus of the material, and d_t is the tensile damage parameter which is assumed to be a function of the plastic strains. The tensile damage parameter can take values from zero, representing the undamaged material, to one, which represents total loss of strength [20]. For a detailed description of the model, one can consult [21]. The considered constitutive behavior of mass concrete in this study is shown in Figure 2. The curve and parameters have been selected based on the experimental data [22]. The material properties for all three models are tabulated in Table 1. They are assumed the same for both static and dynamic analyses.

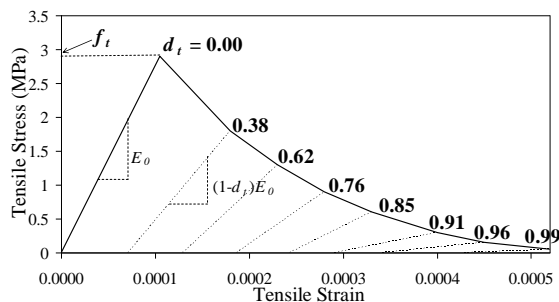


Figure 2. Constitutive behavior of mass concrete in uniaxial tension

Table 1. Material properties used in this study

Material	Property	Value
Concrete	Mass density (kg/m ³)	2400
	Undamaged Young's modulus (GPa)	27.58
	Poisson's ratio	0.2
	Tensile strength (MPa)	2.9
Water	Mass density (kg/m ³)	1000
	Bulk modulus (GPa)	2.07

3.1. LOCAL AND GLOBAL DAMAGE INDEX

During seismic events, the dam body may separately crack from its base or neck. Hence, based on the plastic-damage model for cracking response of the concrete, two damage-based indices can be locally defined on the cracking-susceptible sub-regions of the dam body. These sub-regions were depicted in Figure 3 as base and neck regions. The local damage indices, DI , for both regions can be defined as:

$$DI_i = \frac{\sum_{e \in i} d_{t|e} A_e}{\sum_{e \in i} A_e} \quad i = \text{base or neck} \quad (2)$$

where $d_{t|e}$ is the tensile damage of element e with area of A_e . The summation is done on the entire region i . It simply calculates the weighted average of the damage variables over the prescribed base or neck regions. Therefore, it is a measure of the amount of damage that the dam may locally experience. $DI_i = 0$ means that no element cracks. $DI_{\text{base}} = 1$ shows that the crack has penetrated through the entire dam base, and $DI_{\text{neck}} = 1$ shows total complete damage of the dam neck, however, this diffused cracking is not a realistic cracking pattern for mass concrete structures like gravity dams. If damage index had been provided for the entire dams, it would present global damage index. The energy-based EDPs include the energy dissipated through cracking damage process, ED , which can also be considered as a global measure of damage imposed to the dam body.

3.2. REPRESENTATIVE EDPs

The EDPs are the outcome of the nonlinear finite element analysis of the models that classify the dams seismic demand. The adopted EDPs for each case are described in Table 2. They are categorized in three groups: (1) deformation-based, (2) damage-based, (3) energy-based. The deformation-based EDPs are crest maximum relative displacement. Because the dam body has un-symmetric geometry, the crest relative displacements can be separately monitored into the upstream (US) or the downstream (DS) directions.

Table 2. The adopted EDPs for all analyses model

Category	EDP	Explanation
Deformation-based	D_{us}	Crest maximum relative displacement in the US direction
	D_{ds}	Crest maximum relative displacement in the DS direction
	D_{max}	Crest maximum absolute relative displacement
Damage-based	$DI_i, i = \text{base or neck}$	Local damage index
	DI_{Total}	Global damage index
Energy-based	ED	Energy dissipated through cracking damage

4. NAMING OF CREATED DAMAGE PATTERNS

According to propagation of tensile damage imposed on concrete gravity dams in different intensities of ground motion, three limit states have been defined.

a: This letter represents the initiation of the tensile damage (cracking) at the first element in the base of the dams. Within this time dams have completely a linear behavior named immediate occupancy (IO).

b: This letter represents the initiation of tensile damage (cracking) at the first element in the neck area of the dams. In all of the models this type of damage occurs after initiation and propagation tensile damage in the base of the dam named medium damage (MD).

c: this letter defines a throughout cracking line that has occurred along the neck area. Due to sliding the monolith that is located above cracking line, this situation is very critical for the dam and downstream of the dam. Therefore, this type of damage has been named high damage (HD).

5. LIMIT STATES ACCORDING TO DRIFT

In table 3 the comparison of the dam's drift according to different intensities have been demonstrated. All the numbers in table 3 are presented in percent (%). As shown here, the initiation of tensile cracking has occurred in Drift_{us} , 0.014%, 0.01% and 0.007% and in $\text{Drift}_{\text{max}}$, 0.016%, 0.031% and 0.018% for Pine Flat, Koyna and Shafarood respectively. Also, the initiation of tensile cracking around the neck has been in Drift_{us} , 0.023%, 0.012% and 0.016% and in Drift_{us} , 0.036%, 0.057% and 0.030% respectively for the mentioned dams. Finally, the ultimate value for Drift_{us} are 0.026%, 0.015% and 0.019% and for $\text{Drift}_{\text{max}}$ are 0.053%, 0.070% and 0.35% respectively for Pine Flat, Koyna and Shafarood dam.

Table 3. Comparison of dam’s drift

S _a (T ₁)	Drift _{us} %			Drift _{ds} %			Drift _{max} %		
	PineFlat	Koyna	Shafarood	PineFlat	Koyna	Shafarood	PineFlat	Koyna	Shafarood
0.1g	-0.007	-0.008	-0.003	0.009	0.022	0.010	0.009	0.022	0.010
0.2g	-0.014	-0.010	-0.005	0.016	0.031	0.014	0.016	0.031	0.014
0.3g	-0.019	-0.011	-0.007	0.025	0.042	0.018	0.025	0.042	0.018
0.4g	-0.023	-0.012	-0.010	0.036	0.056	0.022	0.036	0.057	0.022
0.5g	-0.026	-0.015	-0.013	0.053	0.070	0.026	0.053	0.070	0.026
0.6g	-0.029	-0.016	-0.016	0.078	0.094	0.030	0.078	0.094	0.030
0.7g	-0.032	-0.020	-0.019	0.099	0.108	0.034	0.099	0.108	0.035
0.8g	-0.034	-0.022	-0.023	0.129	0.181	0.039	0.129	0.181	0.040
0.9g	-0.036	-0.023	-0.027	0.163	0.242	0.045	0.164	0.242	0.047
1g	-0.030	-0.027	-0.036	0.239	0.319	0.050	0.239	0.319	0.054

6. FRAGILITY CURVE DEVELOPMENT

In this study, the probability of exceeding a damage state given a level of ground motion (i.e. seismic fragility) is calculated for three previously defined limit states.

Having previously defined bounds of three damage states and seismic demand values (resulted from IDA), seismic fragility of the damage state D_i is the conditional probability that a concrete dam has a state of damage exceeding the damage state D_i at a specific S_a level, which is shown in closed form as Eq. (3).

$$[D > d | S_a] = P[X > x_i | S_a] = 1 - \phi\left[\frac{\ln(x_i - \alpha)}{\beta}\right] \quad (3)$$

$$\alpha = \ln \mu - \frac{1}{2} \beta^2 \quad (4)$$

$$\beta = \sqrt{\ln\left[1 + \left(\frac{\sigma}{\mu}\right)^2\right]} \quad (5)$$

Where $\phi(\cdot)$, is the standard normal cumulative distribution function and X_i is the upper bound for each damage state as presented in section 5.

The parameters α and β as defined in Eqs. 4 and 5 depend on the S_a level. σ and μ are respectively the mean and standard deviation of seismic demand values in each S_a level.

6.1. FRAGILITY CURVE DEVELOPMENT FOR A SET OF CONCRETE GRAVITY DAM

The purpose of this study is to provide fragility curves for a set of concrete gravity dams whose heights are between 100 m to 150 m.

All of the limit states for the plotting of the figure 3 are the average of the three dams limit states. And also, the standard normal cumulative distribution function parameters have been obtained with the averaging of three models. Table 4 represents three limit states for a set of concrete gravity dams as (IO, MD and HD).

Table 4. Limit states for concrete gravity dams with the height between 100-150 m

	D _{us} (cm)	D _{ds} (cm)	D _{max} (cm)	DI _{base}	DI _{neck}	DI _{Total}	E _D (j)
IO	-1.22	2.62	2.62	0.1283	0	0.00062	6525
MD	-2.14	4.86	4.86	0.2884	0.0177	0.0191	29042.7
HD	-2.54	6.27	6.31	0.3352	0.0334	0.0272	44651.38

As seen in figure 3, the Pine Flat and Koyna EDPs fragility curves moved forward but Shafarood EDPs fragility curves were transferred to the rear side. Finally, the concrete gravity dams' probability of exceedance with height ranging between 100 to 150 meters are summarized in the following.

The D_{us} (figure 3 (a)) probability of exceedance for three average limit states are 99%, 72% and 55% respectively according to $S_a=0.6g$. Also, the D_{ds} and D_{max} (figure 3 (b, c)) probability of exceedance for three average limit states are 100%, 88% and 56% respectively based on $S_a=0.6g$. DI-base fragility curves have been demonstrated in figure 3 (d) whose the probability of exceedance for three limit states are 100%, 89% and 61% respectively based on $S_a=0.6g$. figure 3 (e) represented the DI_neck fragility curves whose the probability of exceedance for two limit states are 74% and 50% respectively according to $S_a=0.6g$. The DI_Total (figure 3 (f)) probability of exceedance for three limit states are 100%, 73% and 55% respectively according to $S_a=0.6g$. And finally ED fragility curves are demonstrated in figure 3 (g) whose the probability of exceedance for three limit states are 100%, 80% and 54% respectively based on $S_a=0.6g$.

7. CONCLUSIONS

In this paper, the seismic behavior of a set of concrete gravity dams has been studied through nonlinear dynamic analyses. The dams were modeled along with their reservoirs utilizing the finite element method. The material nonlinearity was considered in all models. Thirty far-field ground motion records were selected for the purpose of analysis. Concrete dams were subjected to selected earthquakes which scaled according to spectral acceleration from 0.1g to 1g. Seven EDPs have been defined in the finite element model. Two local and one global damage indexes have been introduced according to tensile damage (d_t) and element areas. Three limit states have been defined according to propagation of tensile cracking in the base and around the neck of the dams. That Shafarood behavior is nearly linear compared with two other dams due to the former's shape and large width. According to the defined limit states for EDPs, the seismic fragility curve that estimates the conditional exceeding probability of damage at a given ground motion intensity has been plotted for all EDPs in three models whose Shafarood EDPs probability of exceedance are less than the two others' same EDPs probability of exceedance. Finally, because of having a collectivity of fragility curves for concrete gravity dams with 100-150 meters height, fragility curves have been developed for seven EDPs according to spectral acceleration which can be useful for vulnerability assessment of existing concrete gravity dams which experience a lot of earthquakes.

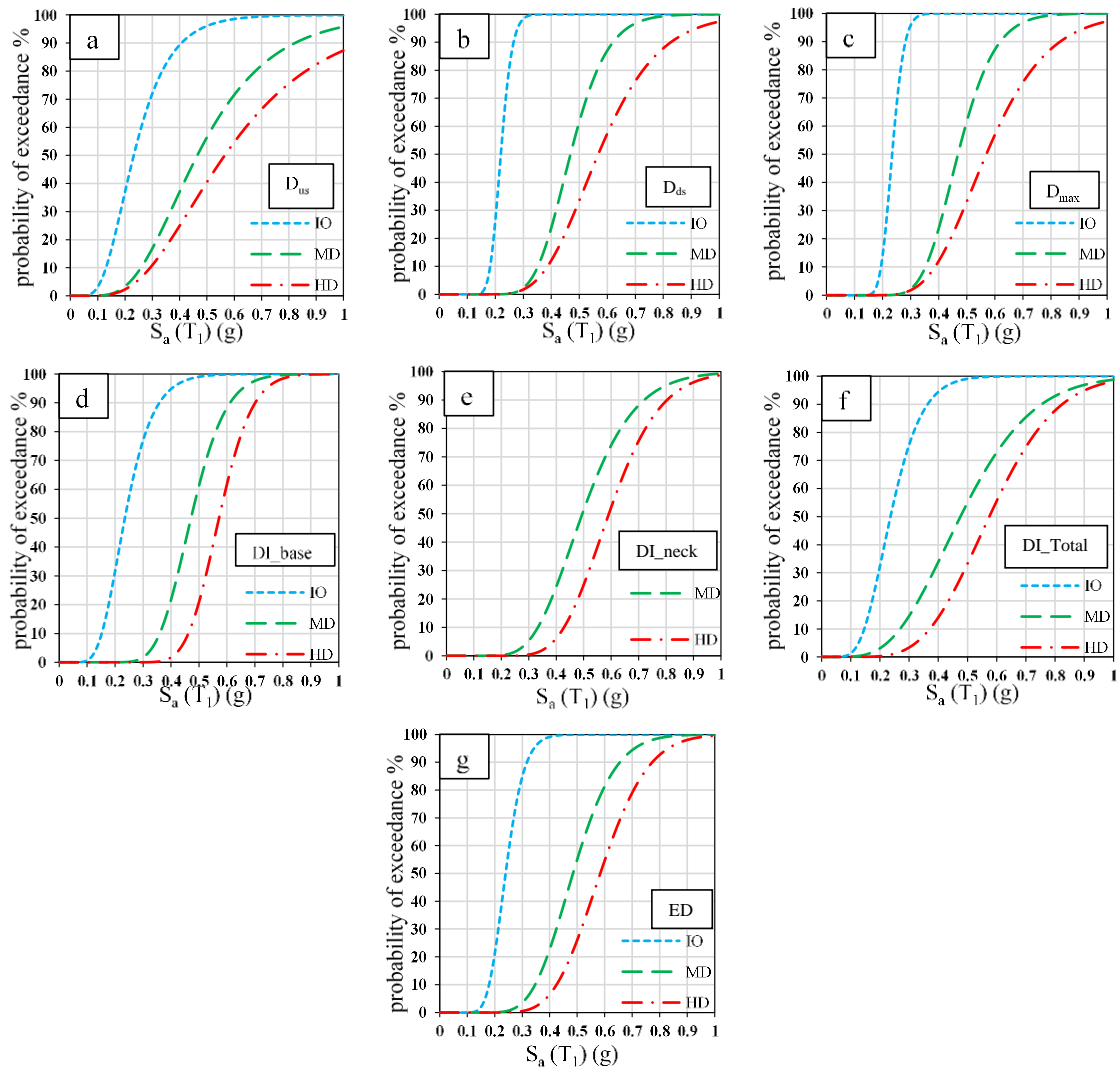


Figure 3. Fragility curves for a set of concrete gravity dams EDPs according to three limit states

8. REFERENCES

1. International Commission on Large Dams (2016) Selecting seismic parameters for large dams - Guidelines, ICOLD Bulletin 148.
2. Ansari MI, Agarwal P. Categorization of damage index of concrete gravity dam for the health monitoring after earthquake. *Journal of Earthquake Engineering*. 2016 Nov 16;20(8):1222-38.
3. Ghobarah A, Abou-Elfath H, Biddah A. Response-based damage assessment of structures. *Earthquake engineering & structural dynamics*. 1999 Jan 1;28(1):79-104.
4. Alembagheri M, Ghaemian M. Seismic assessment of concrete gravity dams using capacity estimation and damage indexes. *Earthquake Engineering & Structural Dynamics*. 2013 Jan 1;42(1):123-44.
5. Vamvatsikos D, Cornell CA. Incremental dynamic analysis. *Earthquake Engineering & Structural Dynamics*. 2002 Mar 1;31(3):491-514.
6. Porter KA, Kiremidjian AS. Assembly-based vulnerability of buildings and its uses in seismic performance evaluation and risk-management decision-making. SPA Risk LLC; 2000.
7. Hariri MA, Saouma VE (2016) Probabilistic seismic demand model and optimal intensity measure for concrete dams. *Structural Safety* 59:67-85
8. Ghanaat Y (2004) Failure modes approach to safety evaluation of dams. In: *Proceedings of 13th World Conference on Earthquake Engineering*, Vancouver, B.C., Canada.
9. Shinozuka M, Feng MQ, Lee J, Naganuma T. Statistical analysis of fragility curves. *Journal of engineering mechanics*. 2000 Dec;126(12):1224-31.
10. Dimova SL, Hirata K. Simplified seismic fragility analysis of structures with two types of friction devices. *Earthquake engineering & structural dynamics*. 2000 Aug 1;29(8):1153-75.
11. Smyth AW, Deodatis G, Franco G, He Y, Gurvich T. Evaluating earthquake retrofitting measures for schools: a cost-benefit analysis. *School Safety and Security: Keeping Schools Safe in Earthquakes*. 2004 Aug 4:208-16.
12. Karim KR, Yamazaki F. A simplified method of constructing fragility curves for highway bridges. *Earthquake engineering & structural dynamics*. 2003 Aug 1;32(10):1603-26.
13. Bazzurro P, Cornell CA, Menun C, Luco N, Motahari M. Advanced Seismic assessment guidelines. Report for Pacific Gas and Electric-PEER Lifelines Program, Task, pp: 507.
14. Lupoi A, Callari C. The role of probabilistic methods in evaluating the seismic risk of concrete dams. In *Protection of Built Environment Against Earthquakes 2011* (pp. 309-329). Springer Netherlands.
15. FEMA (2003) NEHRP recommended provisions for seismic regulations for new buildings and other structures (FEMA 450). National Earthquake Hazards Reduction Program, Part 1: PROVISIONS. Prepared by the Building Seismic Safety Council for the Federal Emergency Management Agency, Washington, DC, USA.
16. PEER (Pacific Earthquake Engineering Research Center). (2014). "Ground motion database." CA.
17. Hariri-Ardebili MA, Saouma VE. Collapse Fragility Curves for Concrete Dams: Comprehensive Study. *Journal of Structural Engineering*. 2016 Apr 28;142(10):04016075.
18. Vamvatsikos D, Cornell CA. Incremental dynamic analysis. *Earthquake Engineering & Structural Dynamics*. 2002 Mar 1;31(3):491-514.
19. Heidary-Torkamani H, Bargi K, Amirabadi R, McClough NJ. Fragility estimation and sensitivity analysis of an idealized pile-supported wharf with batter piles. *Soil Dynamics and Earthquake Engineering*. 2014 Jul 31; 61:92-106.
20. Calayir Y, Dumanoğlu AA, Bayraktar A (1996) Earthquake analysis of gravity dam-reservoir systems using the Eulerian and Lagrangian approaches. *Computers & Structures* 59:877-890
21. Alembagheri M, Ghaemian M (2016) Seismic performance evaluation of a jointed arch dam. *Structure and Infrastructure Engineering* 12:256-274
22. Lee J, Fenves GL (1998) A plastic-damage concrete model for earthquake analysis of dams. *Earthquake Engineering and Structural Dynamics* 27:937-956

Dynamic Analysis of Embankment Dams Under Strong Seismic Excitation and a Case Study

Hasan Tosun¹, Turgut Vatan Tosun²

1- Professor, Eskisehir Osmangazi University, Turkey
2- Civil Engineer, Dam Safety Association, Ankara, Turkey

Email: hasantosun26@gmail.com

Abstract

It is a well-known fact that ground motion induced at the dam site by an earthquake located at some distance from the dam can result damages to dams and their appurtenant facilities. Also direct fault movement across the dam foundation can create displacements, which result to more serious problems for embankments and their appurtenant structures. Especially active faults on or near dam sites can cause to damaging deformation of the embankment. Therefore, meaningful seismic parameters are needed to perform a satisfactory evaluation of dam structure. Turkey has so many dams, which are under the influence of near source zone. One of them is Bebekli dam, which has an earth fill embankment having a 34.0 m height from river bed, located at the western part of Turkey. A seismic evaluation of dam site was performed in detail. For the dam site, a seismic-hazard source was obtained as based on local seismic events and a ground motion model was produced by means of the appropriate attenuation relationships. The dynamic analysis of 2-D finite element model of dam-foundation system shows that the maximum value of settlement is 58.5 cm on the crest under the loading of Maximum Design Earthquake.

Keywords: Earthquake, Embankment Dams, Seismic Analysis, Stability Analysis.

1. INTRODUCTION

Earthquakes can result in damages or failures for dam structures. Case studies about the seismic performance of dams under large earthquakes are available in the literature. Tosun [1] states that earthquake safety of dams is an important phenomenon in dam engineering and requires more comprehensive seismic studies for understanding the seismic behavior of dams subjected to severe earthquakes. It is a well-known phenomenon that earthquakes can result damages and failures for dams and their appurtenant structures.

Earthquake effects on dams mainly depend on dam types. Tosun et al [2] stated that safety concerns for embankment dams subjected to earthquakes involve either the loss of stability due to a loss of strength of the embankment and foundation materials or excessive deformations such as slumping, settlement, cracking and planer or rotational slope failures. Safety requirements for concrete dams subjected to dynamic loadings should involve evaluation of the overall stability of the structure, such as verifying its ability to resist induced lateral forces and moments and preventing excessive cracking of the concrete [3].

In the world there are some important cases, which subjected to damages and failures after earthquake, Lower San Fernando Dam in USA is first example failed as a result of liquefaction phenomenon under the earthquake loading conditions. In case of the May 12, 2008 Wenchuan earthquake in China many dams and reservoirs had been subjected to strong ground shaking. So many dams and hydropower plants were damaged. During the 2001 Bhuj earthquake in Gujarat, India, 245 dams had been affected and rehabilitated or strengthened after the earthquake. Also, in the case of the March 11, 2011Tohoku earthquake in Japan, damages were observed about 400 dams and the 18 m high embankment dam failed and 8 people lost their live [1].

In general, strong ground shaking can result in the instability of the embankment and loss of strength at the foundations However, embankment dams, which are well compacted according to the specification, are suitable type for regions having high seismic activity. Well-compacted embankment dam can withstand moderate earthquake shaking, with peak accelerations of 0.2g and more, with no detrimental effects [4,5]. According to Parish and Abadi [6], the well-compacted modern dams can withstand substantial earthquake shaking with no detrimental effects. Performance of well-compacted embankment dams have also been good in general after the 1999-Kocaeli earthquake, Turkey. Recently we have seen from some cases that active faults, which are very close to the foundation of dams, have the potential to cause damaging displacement of the structure.

2. MATERIAL AND METHODOLOGY

The deterministic and probabilistic seismic hazard analyses are commonly used to relieve the seismic activity for a dam site. The deterministic seismic hazard analysis considers a seismic scenario and includes four-step process. It is very simple procedure and gives rational solutions for large dams because of providing a straightforward framework for evaluation of worst ground motions. The probabilistic seismic hazard analysis is widely used and considers uncertainties in size, location and recurrence rate of earthquakes.

ICOLD [7] states that the Maximum Credible Earthquake (MCE) is the largest reasonably conceivable earthquake magnitude that is considered possible along a recognized fault or within a geographically defined tectonic province. In this study, earthquake definitions given by FEMA [8] were considered for seismic hazard analyses. Most of large dams in Turkey were analyzed by using these definitions in past.

The probabilistic hazard calculation was performed to obtain 5 percent damped elastic hazard pseudo-acceleration spectra and to generate the response spectrum compatible acceleration time histories for time domain analyses. The elastic hazard acceleration spectra on the basis of Boore et al [9] were obtained. For generating the acceleration time histories, a software program TARSCTHS was used [10].

Pseudo static analysis was performed for the case study. A 2-D finite element model for the maximum section of the dam and soil profile including bedrock was developed by Plaxis software [11] for the dynamic analysis. Once the model was defined to represent the layered construction technique, then it was modified for dynamic loading conditions. Standard fixity elements were considered along the base and vertical sides of the model. It was assumed that the ground motion acts uniformly along the fixed boundaries.

3. CASE STUDY

Bebekli dam is an earthfill dam, which is situated at the western part of Turkey. The main section of the dam is high from foundation and 35.5 m long. The embankment cross section includes a central core zone flanked on both side by shell zones. The outer slopes of dam are inclined at 3:1 (horizontal: vertical) for upstream and downstream. The cross section includes a transition filter zone between core and shell materials on both sides and a blanket drain system on downstream to collect seepage through the dam and foundation. A toe drain for seepage collection is also included on the downstream toe of dam. The upstream slope of the dam is covered with a layer of riprap to provide wave protection. It rests on the hard bed rock. The alluvium soil on river bed is removed before beginning to embankment constructions.

Table 1. Properties of Bebekli Dam

Properties	Value
Location	West of Turkey
Type	Zoned earthfill
River	
Volume of embankment	348 255 m ³
Beginning to construction	2012
Completion of construction	2016
Crest elevation	684.00 m
Crest length	236.20 m
Height from foundation	35.5 m
Geological formation of foundation	schist
Maximum Water Level	682.60 m
Minimum water level	669.30 m
Reservoir capacity at Maximum Water Level	0.932 hm ³

3.1. SEISMIC HAZARD ANALYSES

The seismic hazard parameters were obtained from the magnitude-frequency relation of Gutenberg-Richter for two different linear seismic zone [12]. The seismic hazard analysis was performed for the dam by means of two separate methods. The deterministic seismic hazard analysis shows that the PGA values for 50 percentile range from 0.193 to 0.327 while those for 84 percentiles they are between 0.338 and 0.491. They average to 0.244 for 50 percentiles and 0.406 for 84 percentiles. These PGA values are high. Because the fault is very close to the dam site. Its distances to the possible fault, the Quaternary fault and the main Holosen fault are 4.07, 6.07 and 9.36 km, respectively (Figure 1).

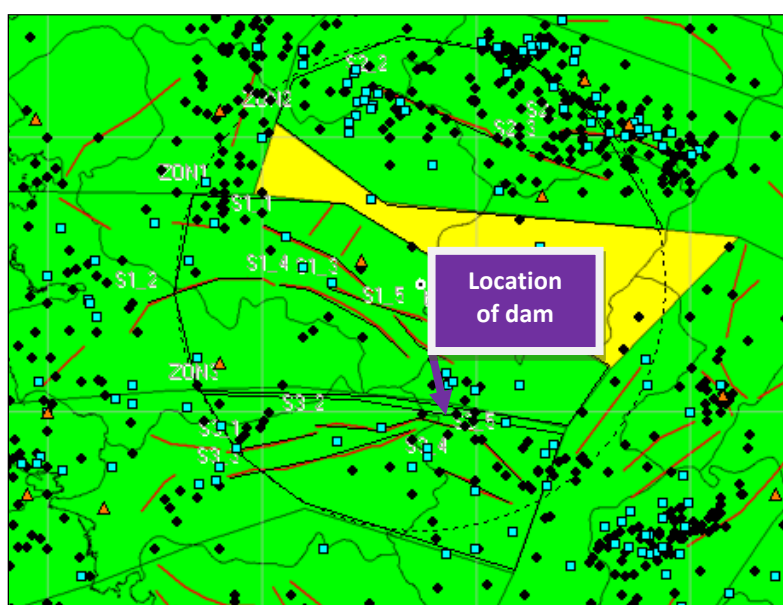


Figure 1. The model used for seismic hazard analyses

The results of probabilistic seismic hazard analysis indicate that peak ground acceleration (PGA) changes within a wide range for all earthquakes levels. For OBE, MDE and SEE, the PGA value averages to 0.300g, 0.405g and 0.566g, respectively. These values mainly depend to the predictive relationships. In this study six separate relationships were considered for determining horizontal peak ground acceleration [12].

As based on this study, Total Risk Factor (TRF) value is 90.5 and it is identified as risk class of II of Bureau method [13]. It means that it has moderate risk potential for downstream life and structures. According to the risk classification adopted by DSI [14], It is categorized as class III with high risk. The seismic hazard analyses performed throughout this study indicates that Bebekli dam is one of the most critical dams within the basin when considered downstream life.

3.2. ANALYTICAL AND NUMERICAL ANALYSES

For this study, earth fill stability of Bebekli dam have been investigated as defining a factor of safety for different loading condition by means of pseudo-static analysis (table 2). At the beginning of this study, seismic coefficient was determined for pseudo-static analysis as based on the approach given in DSI specification [14].

According to this approach seismic coefficient ranges from 0.20 to 0.25. For this study, it was selected as 0.20. Analyses have been executed by means of a software, namely GSTABIL7. The safety factors were calculated by the Modified Bishop Method. The value of seismic coefficient (k) was determined as 0.27 for limit equilibrium condition ($F_s = 1.0$). An example from analyses is introduced in figure 2.

Table 2. Safety factors of pseudo-static analysis for separate loading conditions

Case	Description	Slope	Factor of Safety	
			Required	Calculated
I	End-of Construction	Downstream	1.3	2.19
		Upstream		2.92
II	Rapid drawdown	Upstream	1.1-1.3	1.99
III	Operation	Downstream	1.4-1.5	2.04
		Upstream		2.24
IV	Earthquake	End-of Construction	1.0	
		Downstream		1.38
		Upstream		1.71
		Operation		
		Downstream		1.19
		Upstream		1.28

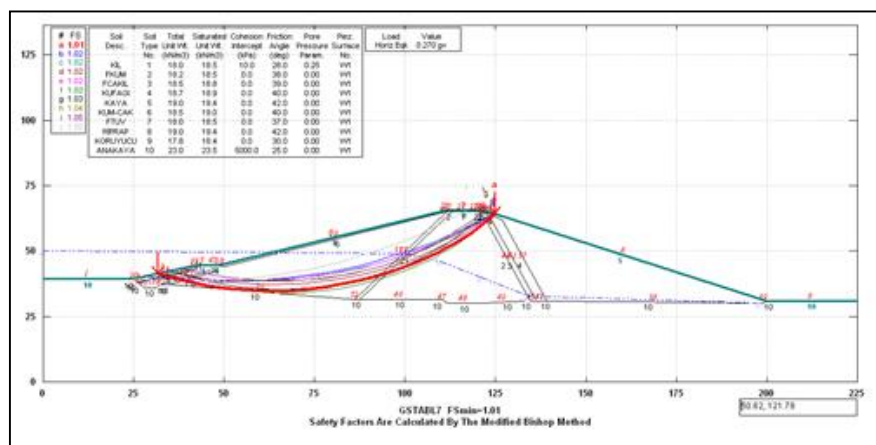


Figure 2. An example of slope stability analyses for Bebekli dam embankment

The parameters of dynamic analysis were selected after defining the OBE and MDE values for the dam site. The probabilistic hazard calculation was performed to obtain 5 percent damped elastic hazard pseudo-acceleration spectra and to generate the response spectrum compatible acceleration time histories for time domain analyses. For generating the acceleration time histories, a software program TARSCHTS was used. The output of time history record of dam site for OBE level is given in Figure 3.

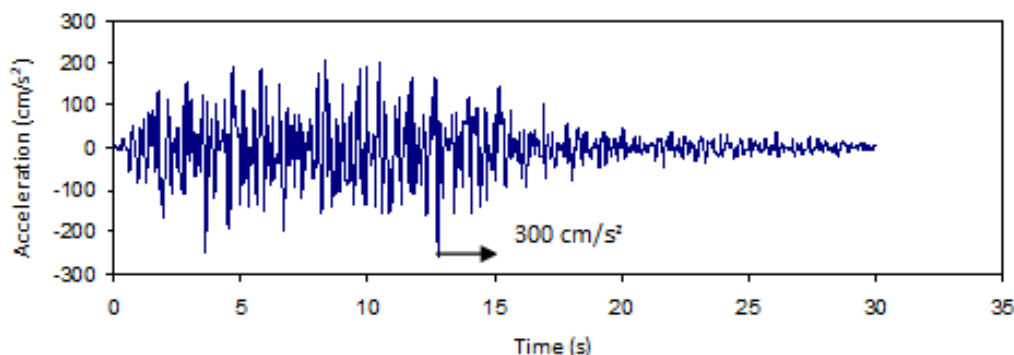


Figure 2. Synthetic acceleration-time history of OBE plot for input motions used in the dynamic analysis of Bebekli dam.

The 2-D finite element model for the maximum section of the dam and soil profile including bedrock and alluvial soil is given in Figure 4. The model consisted of 8905 nodal points and 1090 six-node plane-strain elements. Standard fixity elements were considered along the base and vertical sides of the model. It was assumed that the ground motion acts uniformly along the fixed boundaries. The hardening soil model was selected to define soil properties for all models discussed here.

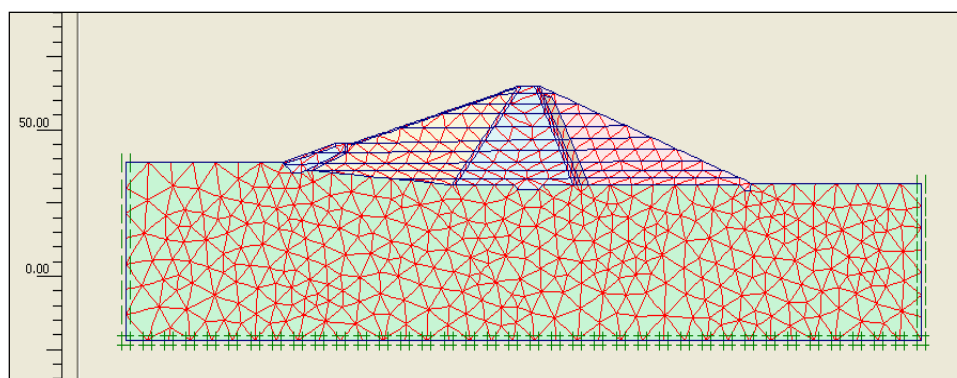


Figure 4. The finite element model of the embankment

The finite element model used in this study is composed of five different materials including the diaphragm wall. The bedrock is also considered as a rigid element with high deformation modulus. The parameters used in the model were considered from the laboratory tests and the literature survey [15,16,17]. For the analysis, the deformation moduli of impervious zone and semi-pervious zone were taken into account as 30 000 and 55 000 kPa, respectively.

As a result of this analysis, maximum vertical settlement was predicted as 40 cm for dynamic loading of MDE level (Figure 5). The horizontal displacements are little greater than vertical displacements. Figure 6 introduces the distribution of horizontal displacement on the model during the dynamic time.

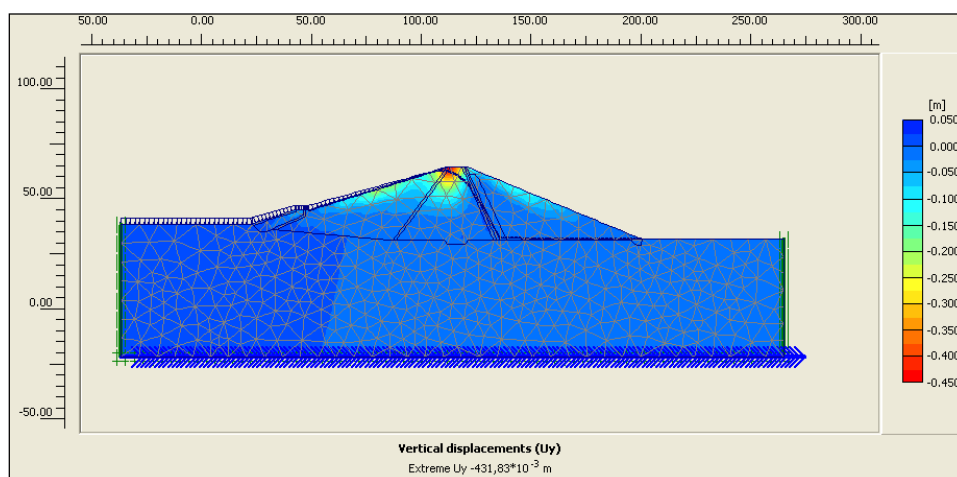


Figure 5. Distribution of vertical displacement for MDE loading condition

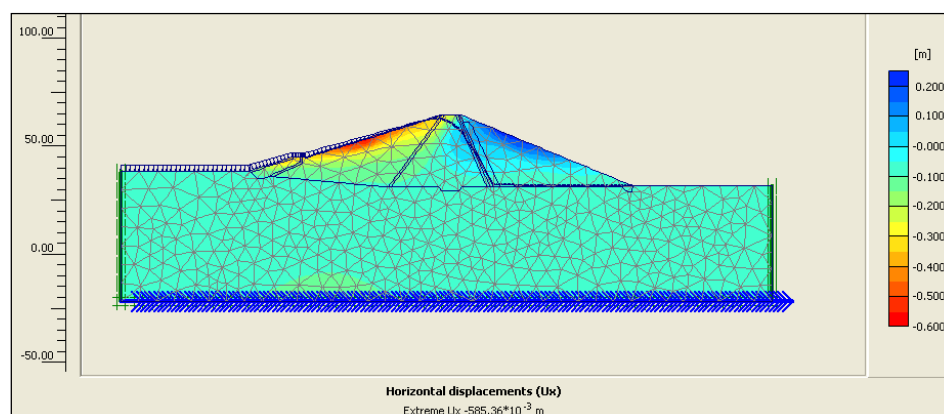


Figure 6. Distribution of Horizontal displacement for MDE loading condition

4. RESULTS AND DISCUSSION

The pseudo-static analysis indicates that both slopes of embankment are safe. The value of seismic coefficient was obtained as 0.27 for limit equilibrium condition. As a result of numerical analysis, maximum vertical settlement was predicted as 43.1 cm for dynamic loading of MDE level, while it obtains as 58.5 cm for horizontal section. The vertical and horizontal displacements are given in table 3 for OBE and MDE conditions.

Table 3. Summary of displacements for different loading conditions

Loading conditions	Vertical Displacement (m)	Horizontal Displacement (m)
OBE	0.195	0.185
MDE	0.431	0.585

As a result of finite element analysis, the horizontal component of acceleration was obtained for different level of embankment. Figure 7 introduces the horizontal acceleration on dam crest with input ground motion. In this figure, red line represents horizontal peak ground acceleration on the base rock, while blue line represents same parameter on the crest of dam, but both for MDE.

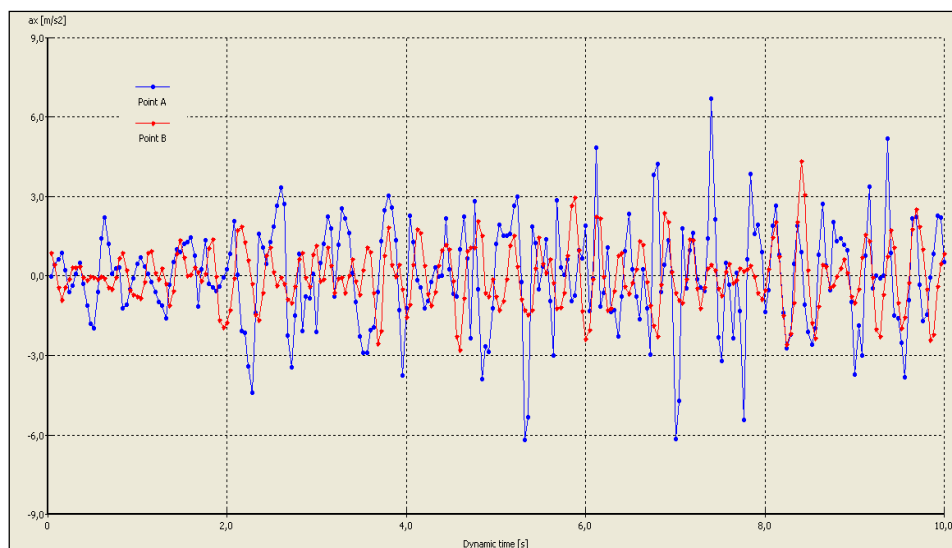


Figure 7. Horizontal acceleration on crest of embankment for MDE.

5. CONCLUSIONS

Bebekli dam site is located on very active seismic region of Turkey. It is under near field motion according to the updated seismic data. The slopes of embankment are safe when considered the pseudo analyses. The dynamic analysis of 2-D finite element model of dam-foundation system indicates that the maximum value of displacement is only 58.5 cm on the crest under the loading of Maximum Design Earthquake. The permanent deformation for this model was obtained between 7 and 15 cm by means of semi-empirical methods. These results indicate that local sliding problem can be seen during the loading of MDE condition, not failure of dam.

6. ACKNOWLEDGMENT

Authors would like to thank DSI General Director, who is the owner of state dams and TVT Hydrotech Bureau, which is responsible for designing the dam.

7. REFERENCES

1. Tosun, H. (2015), “*Earthquakes and Dams*”, in Earthquake Engineering-Seismology to Optimal seismic design of engineering structures (edited by A. Moustafa), Intec Publication ISBN 978-953-51-2039-1.
2. Tosun, H., Zorluer, I., Orhan, A., Seyrek, E., Savaş, H. and Türköz, M. (2007), “*Seismic Hazard and Total Risk Analyses for Large Dams in Euphrates Basin, Turkey*”. Engineering Geology, 89, 155-170.
3. Jansen, R.B., (ed.) (1988), “*Advanced Dam Engineering for Design, Construction and Rehabilitation*”, Van Nostrand Reinhold, New York, 884p.
4. Seed, H. B and Makdisi, F. I. and De Alba, P. (1978), “*Performance of Earth Dams During Earthquakes*”, Journal of Geotechnical Engineering, American Society of Civil Engineers, Vol, 104, No. GT7, pp. 967-994.
5. Seed, H.B. (1979), “*Considerations in the Earthquake-Resistant Design of Earth and Rockfill Dams*”, 19th Rankine Lecture of the British Geotechnical Society, Geotechnique, Vol XXIX, No. 3, pp. 215-263.
6. Parish, Y. and Abadi, F.N. (2009), “*Dynamic Behaviour of Earth Dams for Variation of Earth material Stiffness*” International Scholarly and Scientific Research & Innovation 3(2) 446-451.
7. ICOLD (2016), “*Selecting Seismic Parameters for Large Dams-Guidelines*”, ICOLD Bulletin 148.
8. FEMA, (2005), “*Federal Guidelines for Dam Safety-Earthquake Analyses and Design of Dams*”.
9. Boore, D.M., Joyner, W.B., and Fumal, T.E. (1997), “*Equations for estimating horizontal response spectra and peak acceleration from Western North American earthquakes*” A summary of recent work. Seismological Research Letters, 68, 128-153.
10. Papageorgiou, A., Halldorsson, B. and Dong, G. (2000), “*Target Acceleration Spectra Compatible Time Histories*”, University of Buffalo, Dept. of Civil, Structural and Environmental Engrg., NY.
11. Plaxis, (2008), Plaxis “*V8 Professional Version-User Manual*” (Edited by Brinkgreve, R.B.J., Broere, W., and Waterman, D.), Netherlands.
12. DSİ, (2011), “*Seismic Hazard Analysis of Bebekli Dam*”, State Hydraulic Works, Ankara (in Turkish).
13. Bureau, GJ (2003), “*Dams and Appurtenant Facilities in Earthquake Engineering Handbook*” (edited by Chenh, W.F and Scawthorn, C.), CRS press, Bora Raton 26.1-26.47.
14. DSİ (2012), “*Selection of Seismic Parameters for Dam Design*”, State Hydraulic Works, Ankara, 29 p (in Turkish).
15. Seed, H.B., Wong, R.T., Idriss, J.M. and Tokimatsu, K. (1984), “*Moduli and damping factors for dynamic analysis of cohesionless soils*”, Report No: UCD/EERC-84-14, Earthquake Engineering Center, University of California.
16. Hunter, G. and Fell, R. (2003), “*Rockfill modulus and settlement of concrete faced rockfill dams*”, J. Geotech. And Geoenviron. Engrg. 129, 2003.
17. Brenner, R.P., Wieland, M. and Malla, S. (2005), “*Large-diameter cyclic triaxial tests for seismic safety Assessment*”, 16 th ICSMGE, Osaka.
18. Makadisi, F.I and Seed, H.B. (1978), “*Simplified procedure for estimating dam and embankment earthquake-induced deformations*”, J. Geotech. Eng. Div. ASCE 104(7): 849-867

Finite Element Analysis of Multi-Tiered Reinforced Soil Walls Of Gotvand Dam Powerhouse under Earthquake Loading

Amir Mohsen Safae¹, Ali Noorzad², Ahmad Reza Mahboubi-Ardakani²

1- Ph.D. Candidate, 2- Associate Professor

Department of Civil, Water and Environmental Engineering, Shahid Beheshti University, Tehran, Iran

Email: a_safae@sbu.ac.ir

Abstract

Multi-tiered reinforced soil walls are now an innovation technology for the solution of earth retaining wall problems. This paper is focused on the numerical modeling of a reinforced soil wall with steel strip soil reinforcement taken from a series of structures constructed at the powerhouse of Gotvand dam located in south of Iran.

In this paper details of the numerical simulation and specifications of the materials that are used in a 31 m high reinforced soil wall that was built in 5-tiered configuration and located above the powerhouse of Gotvand dam are described. This paper presents the wall responses to a typical seismic loading. The lessons learned here have applications to other types of multi-tiered reinforced soil walls and are of value to designers who wish to: explore the mechanical behavior of these systems under static and earthquake loading and to generate data to fill the gaps in performance data from the limited number of monitored structures reported in the literature.

Keywords: Finite element method, Seismic analysis, Multi-tiered reinforced soil walls, Earthquake loading, Gotvand dam, Soil reinforcement, Powerhouse.

1. INTRODUCTION

Mechanically stabilized earth (MSE) walls also called reinforced soil walls, constructed with steel strip reinforcing elements and segmental concrete facing panels, are now an accepted technology in world-wide. The first wall of this type in Japan was constructed in 1972 (Hirai et al., 2003). There are now estimated to be more than 30,000 of these structures in Japan (Ochiai, 2007). A useful history of the development of this technology and relevant codes of practice in Japan can be found in the paper by Miyata and Bathurst (2012a). The first instrumented steel strip wall in Japan was constructed in 1978 that is 6m in height (Chida and Nakagaki, 1979) [9].

The behavior of MSE walls is complicated, and performing an accurate simulation of these walls using numerical modeling techniques (e.g., finite element and finite difference methods) is a challenge [11]. This challenge is due to the complex interactions between the soil and there in forcing elements, the soil and the facing panels and the segmental construction technique. A recent case study was reported by Damians et al. (2015) who used the finite element method to simulate the performance of a well-instrumented 17-m-high steel strip wall constructed in the USA (Runser et al., 2001). The numerical results were judged to be in reasonable agreement with a range of measured response features [12]. In contrast, there are many examples in the literature of numerical simulations of instrumented reinforced soil walls constructed with extensible polymeric reinforcement materials using the finite element method (Karpurapu and Bathurst, 1995; Rowe and Skinner, 2001; amongst others) and the finite difference method (Hatami and Bathurst, 2005, 2006; Huang et al., 2009, 2010; Abdelouhab et al., 2011; amongst others).

There are many situations where reinforced soil walls are constructed in a tiered configuration for variety of reasons such as aesthetic, stability and construction requirement. Current design of reinforced soil walls shows that multi-tiered wall has a better performance in comparison to single tiered walls, especially when it is necessary to construct the high reinforced soil retaining wall with stable, economic and aesthetic consideration.

The current study presents the development and validation of a numerical model to reproduce the static and seismic responses of multi-tiered wall at the end of construction subjected to earthquake loading. Investigation of reinforced soil walls in multi-tiered configuration that built in water and power resources projects (multi-tiered reinforced soil walls that in powerhouse of Gotvand dam) is the most important goal of this study. The paper is to describe the methodology used to select the optimum material properties, to

maximize the accuracy of the numerical predications, and to demonstrate the sensitivity of the numerical outcomes to arrange of input parameter values. The numerical finite element method program, ABAQUS (Version 6.11), has been used to perform the numerical simulations.

2. PROBLEM DEFINITION AND MODEL PARAMETERS

2.1. MULTI-TIERED REINFORCED SOIL WALLS

A 31 m high steel-reinforced soil wall in multi-tiered configuration (Figure 1) was built in 2004 that was located above the powerhouse of Gotvand dam (one of the biggest water & power project in south of Iran). These walls are in 5-tiered configuration and the facing of the walls was constructed using 1.5 m high cruciform-shaped concrete panels with a thickness of 180 mm. In the current study, comparisons between the static and seismic wall performance are restricted to the end of construction and dynamic loading was applied. The walls were reinforced by smooth steel strips that were 50 mm wide and 5 mm thick. The length of the steel strips varied with the elevation as given in Table 1.

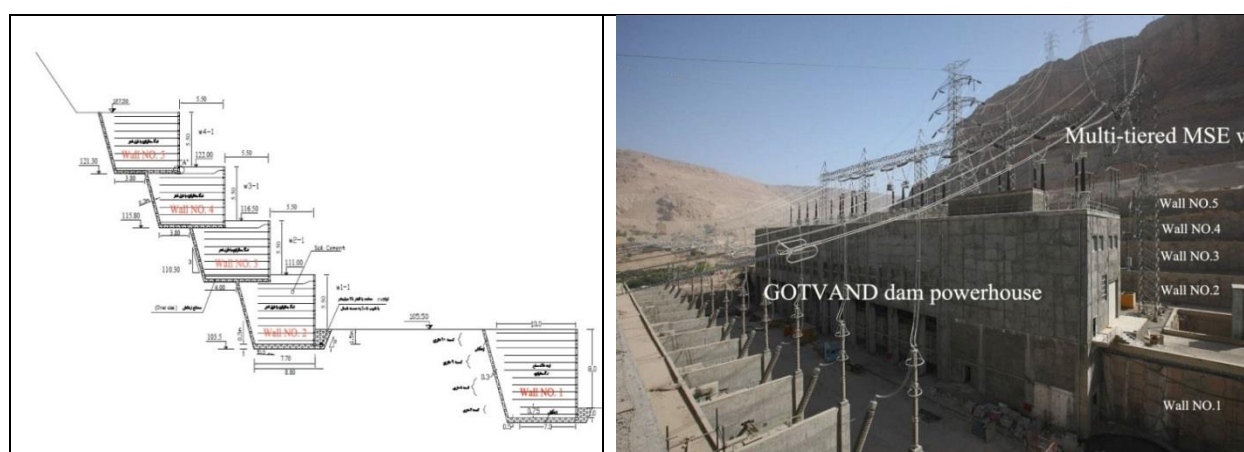


Figure 1. View and cross section of multi-tiered reinforced soil walls in Gotvand dam powerhouse

Table 1. Characteristic of each stage of multi-tiered reinforced soil walls in Gotvand dam powerhouse

Name of wall	Wall No. 1	Wall No. 2	Wall No. 3	Wall No. 4	Wall No. 5
Height (m)	9	7.5	6.2	6.2	6.2
Berm length (m)	33	5.5	5.5	5.5	5.5
Number of reinforcement layers	12	9	7	7	7
Length of reinforcement layers (m)	7, 8, 9, 10	7	8	7	7
Vertical space of reinforcement layers (m)	0.75	0.75	0.75	0.75	0.75

The specifications of backfill and retained soil, reinforcements, and concrete facing panels which were used in numerical simulations are presented in Table 2-4.

Table 2. Characteristic of soils and rock

Parameter	Symbol	Unit	Rock	Soil (2)	Soil (1)
Soil Type	Type	-	-	Un-drained	Drained
Dry unit Weight	γ_{unsat}	kN/m ³	20	20	18.5
Saturated unit Weight	γ_{sat}	kN/m ³	21	21	20
Constitutive model of soil	Model	-	MC	MC	MC
Elastic modulus	E	MPa	1.7	0.1	0.1
Poisson's ratio	ν	-	0.462	0.3	0.3
Cohesion	C	kN/m ²	120	30	1
Internal friction angle	ϕ	Degree	36	36	36
Dilation angle	ψ	Degree	6	6	6
Cutoff tensile stress	$\sigma_{cutoff-t}$	kN/m ²	120	30	1

Table 3. Characteristic of steel strips reinforcements

Parameter	Unit weight	Elastic modulus	Poisson's ratio	Thickness	Dimensions
unit	kN/m ³	GPa	-	m	mm
quantity	78.5	210	0.25	0.18	5×50

Table 4. Characteristic of facing concrete panels

Parameter	Unit weight	Elastic modulus	Poisson's ratio
unit	kN/m ³	MPa	-
quantity	24	66.7	0.15

2.2. SEISMIC LOADING

The acceleration-time history employed is the horizontal component of the El-Centro earthquake of 1940, with a peak horizontal acceleration of 0.40g, as shown in Figure 2. Acceleration history was applied for 32 seconds for want of more computer time.

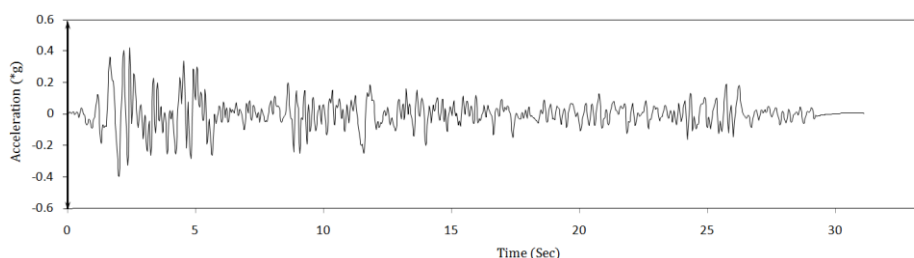


Figure 2. Time history of base reference input acceleration, (El-Centro earthquake, 1940)

3. FINITE ELEMENT METHOD PROCEDURE

The numerical simulations were performed using the 2-D finite element computer program ABAQUS 6.11. Figure 3 shows the ABAQUS numerical network used in this study. Plane strain conditions were assumed in this study and the finite element simulations were carried out. Wall geometry, arrangement of wall reinforcements, backfill and foundation soil properties, and facing type were simulated as were reported in the original case study [8]. The construction process was modeled using sequential bottom-up numerical network increments of 0.25 m thick.

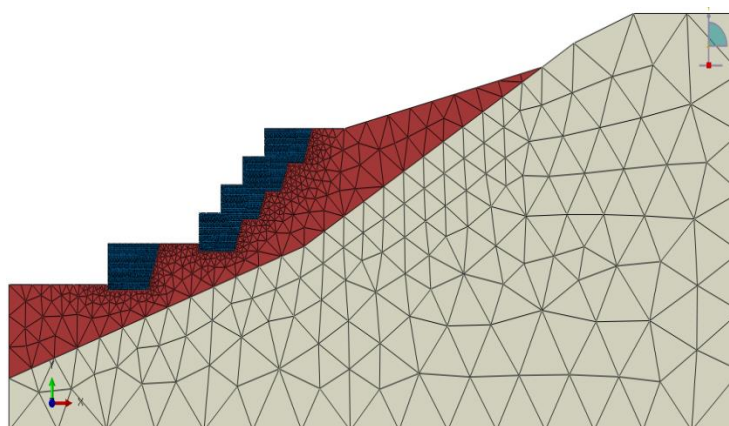


Figure 3. View of numerical grids

4. NUMERICAL RESULTS

In this section, comparison between static and seismic analyses for steel-reinforced soil walls is done. The results of seismic analysis are presented and the different analysis parameters are compared.

4.1. DISTRIBUTION OF LATERAL PRESSURE

Figure 4 shows the horizontal stress in walls at the end of construction for static analysis (Figure 4-a) and dynamic loading (Figure 4-b). It can be observed that the horizontal stress fluctuated near the lines of the active earth pressure. The fluctuation of the horizontal stress distribution in the numerical analysis is thought to be caused by the dynamic shearing forces between the horizontal soil layers.

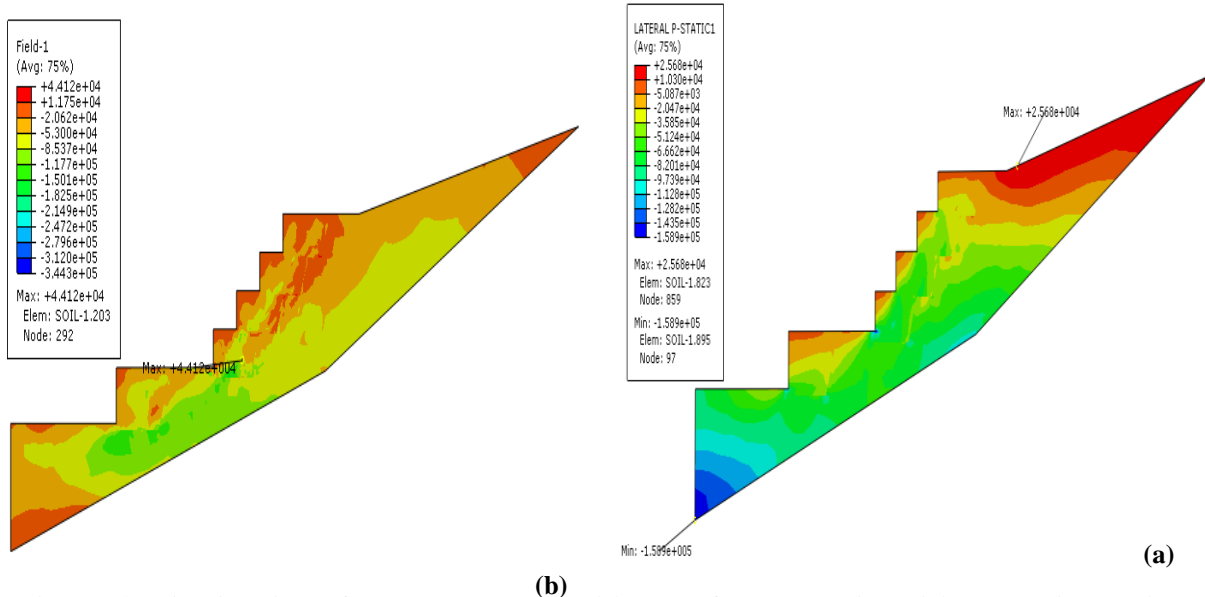


Figure 4. Distribution of lateral pressure: (a) end of construction, (b) dynamic loading

4.2. DEFORMATION OF BACKFILL SOIL

The residual horizontal displacements of backfill soil in static and dynamic loadings are displayed in Figure 5. The seismic analysis results have larger horizontal displacement than the statically analysis, implying that the dynamic excitation has a slight influence on the overall horizontal displacement, especially in high elevation in multi-tiered walls.

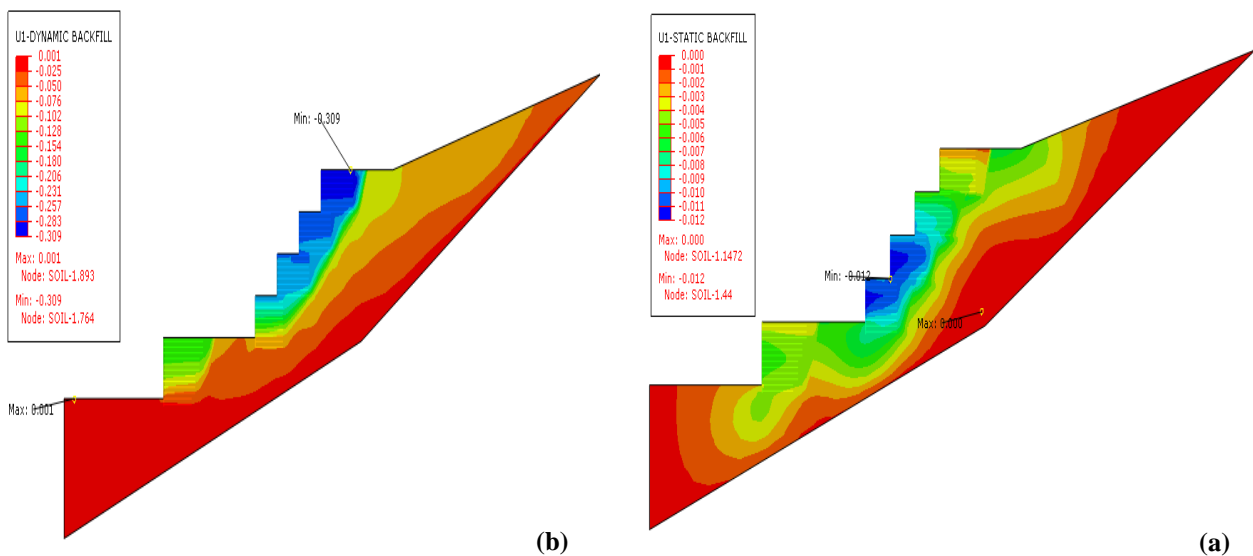


Figure 5. Horizontal displacement of backfill soil: (a) end of construction, (b) dynamic loading

4.3. DISTRIBUTION OF TENSILE FORCE IN REINFORCEMENTS

Figure 6 indicates the calculated tensile forces along the steel strips at the end of static and dynamic analysis. It can be observed that the dynamic analysis gives slightly higher values than static analysis in the upper part of the wall, and give slightly lower values than those in the lower part of the wall. However, because the tensile forces are relatively small, the difference was only about 15% of the strength of reinforcements. As shown in Figure 6-b in seismic analysis, maximum tensile load is occurred in the first stage of multi-tiered walls.

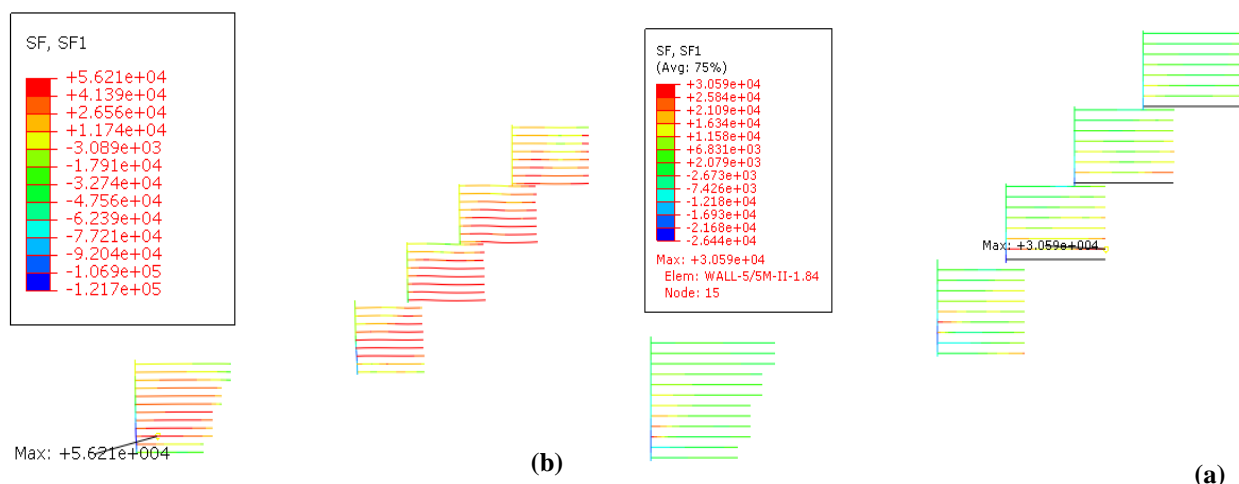


Figure 6. Distribution of maximum tensile forces at different heights in walls at: (a) end of construction, (b) dynamic loading

4.4. STRAIN OF REINFORCEMENTS

Figure 7 illustrates the strains of steel-strips at different layers of wall No.1 to wall No.5 at the end of the construction (Figure 7-a) and at the end of earthquake loading (Figure 7-b). In both loadings the maximum strain of reinforcements is occurred in the first reinforcement layer of wall No.2.

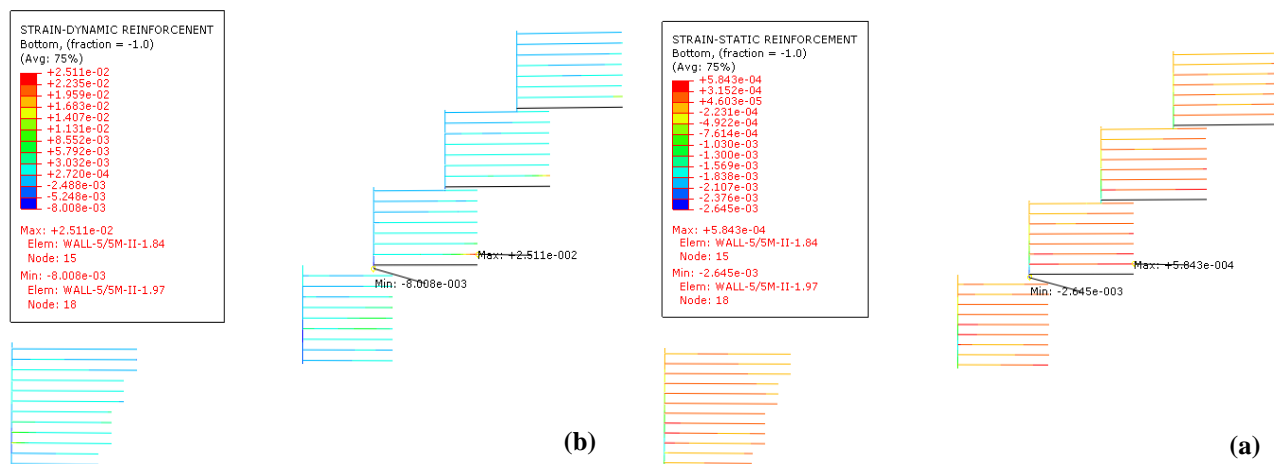


Figure 7. Strains of the reinforcements: (a) end of construction, (b) dynamic loading

4.5. SHEAR ZONE

Figure 8 shows typical plots of shear zones in the multi-tiered reinforced soil walls for seismic conditions. In this numerical study, there was no evidence of a well-defined failure surface intersecting all reinforcement layers as may be expected from conventional tied-back wedge and nonlinear slip surface methods

of analysis (Bathurst and Alfaro 1997). This was true even for models with the lowest reinforcement stiffness. Rather, the reinforced soil zone acted as a parallel-sided monolithic mass. Further study is required to determine if the pattern of internal failure will change with greater reinforcement spacing [5].

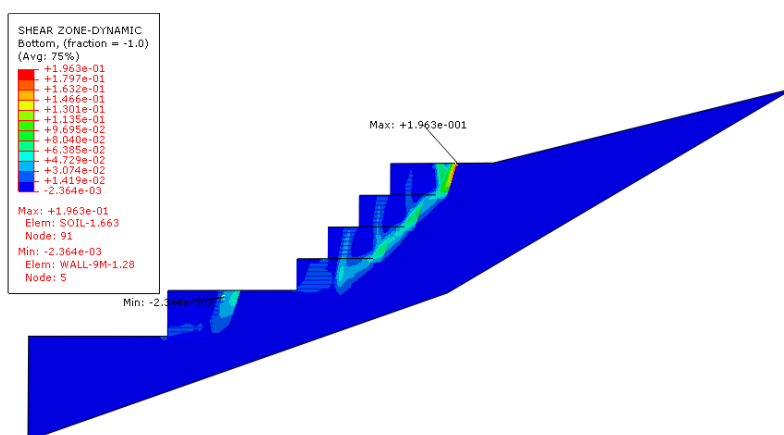


Figure 8. Shear zone at end of dynamic loading

4.6. DISTRIBUTION OF BACKFILL ACCELERATIONS

Figure 9 shows the accelerations at different elevations of the reinforced soil area, whose locations are depicted in Figure 9, during the second vibration stage. It can be observed from the results that the accelerations were amplified along with the increase of height, which is also coincident with the numerical analysis. These results again proved the fact that the accuracy of the dynamic FEM analysis conducted in this paper is quite high. The distribution and magnitude of peak accelerations in the backfill soil is of interest in pseudo-static seismic design methods because a coherent distribution of the ground acceleration is considered to be responsible for the additional destabilizing force that must be resisted by reinforced structures during a seismic event [4].

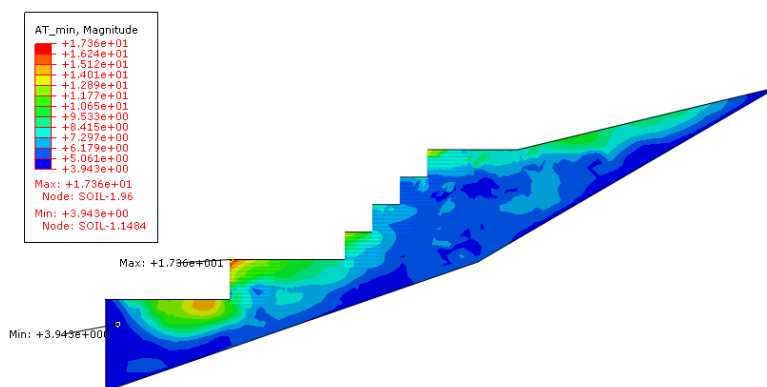


Figure 9. Acceleration responses subjected to reinforced soil walls during seismic loading

5. CONCLUSIONS

In this research, a multi-tiered reinforced wall with steel strip soil reinforcement was designed and built in 2004, is investigated under seismic loading. The results of static analysis are compared to seismic analysis using the finite element program ABAQUS. In this paper, the static and dynamic analyses on reinforcement forces and numerical analysis using finite element method, and the results have been presented.

1. Based on the obtained results, the backfill lateral pressure due to seismic loading is two times more. Also the location of maximum backfill soil lateral pressure is differed from reinforced soil at wall No.5 under static loading to reinforced soil at wall No. 2 under dynamic loading.
2. In seismic analysis results, the maximum magnitude of strain of reinforcements, deformation of reinforced backfill soil, the maximum magnitude of reinforcements tensile force is respectively 100, 11, 1.84 times more than static analysis. The location of maximum magnitude of strain of

reinforcements is in second layer of reinforcements in both static and dynamic analysis, the maximum deformation of reinforced backfill soil is in wall No.5 in both static and dynamic analysis and location of reinforcements tensile force maximum is differed from second layer at wall No.3 under static loading to third layer at wall No. 1 under dynamic loading.

3. The reinforcement loads increased from top of the wall to base in each single wall and with increasing height from wall No.1 to wall No.5. At the region of one third of base of the wall, the reinforcement forces were bigger than the top.
4. Dynamic loading induces more forces in reinforcement in comparison to static loading. At the top of the wall, the dynamic and static forces were almost similar, but with an increase in depth, the difference became slightly more. This result is similar to increasing the height of wall by increasing the number of stages in multi-tiered walls. The earthquakes with maximum base input acceleration had more effect on the difference between static and dynamic forces.
5. The magnitude of strip-backfill soil interface stiffness had a minor effect on both the tensile loads in the steel strips and the vertical facing load at the toe.
6. Backfill soil horizontal accelerations due to dynamic analysis is 3.4 times more than maximum time history accelerations that applied to numerical model, that it shows the resonance in some points of reinforced soil mass.

6. REFERENCES

1. Bathurst, R.J. and Cai, Z. (1995), "Pseudo-static seismic analysis of geosynthetic reinforced segmental retaining walls," Geosynthetics International, Vol. 2(5), pp. 789-832.
2. FHWA. (2001), "Mechanically stabilized earth walls and reinforced soil slopes: design and construction guidelines", Publication FHWA NHI-00-43, Federal Highway Administration and National Highway Institute, Washington, DC, USA.
3. Hatami, K. and Bathurst, R.J. (2000), "Effect of structural design on fundamental frequency of reinforced-soil retaining walls," Soil Dynamics and Earthquake Engineering, Vol. 19, pp. 137-157.
4. Koseki, J. Tatsuoka, F. Munaf, Y. Tateyama, M. and Kojima, K. (1998), "A modified procedure to evaluate active earth pressure at high seismic loads," Soils and Foundations, Special Issue on Geotechnical Aspects of the January 17 1995 Hyogoken-Nambu Earthquake, Vol. 2, pp. 209-216.
5. Ling, H. Liu, H. Mohri, M. (2006), "Parametric Studies on the Behavior of Reinforced Soil Retaining Walls under Earthquake Loading," Journal of Engineering Mechanics, Vol. 44, ASCE, pp. 1056-1065.
6. Ren, F. Zhang, F. gXu, C. Wan, G. (2016), "Seismic evaluation of reinforced-soil segmental retaining walls," Geotextiles and Geomembranes, Vol. 44, Elsevier, pp. 604-614.
7. Sakaguchi, M. (1995), "A study of the seismic behavior of geosynthetic reinforced walls in Japan," Geosynthetics International, Vol. 3, No. 1, pp. 1-18.
8. Safaee, A.M. (2012), "Seismic Analysis of Mechanically Stabilized Earth Wall (MSEW) Case Study: MSEW of Upper Gotvand Powerhouse," M. Sc. Thesis, Power and water university of technology (PWUT), Faculty of Water & Environmental Engineering, Tehran, (in Persian).
9. Sahara, K. (2012), "Investigation of damage to reinforced earth walls in the great east Japan earthquake and related maintenance," Proc. of the International Joint Symposium on Urban Geotechnics for Sustainable Development, JS-Seoul, pp. 2-26.
10. Stuedlein, A.W. Allen, T. Holtz, R. Christopher, R. (2012), "Assessment of Reinforcement Strains in Very Tall Mechanically Stabilized Earth Walls," Journal of geotechnical and geo-environmental engineering, Vol. 138, Issue 3, ASCE, pp. 345-356.
11. Stuedlein, A.W. Bailey, M. Lindquist, D. (2010), "Design and Performance of a 46-m-High MSE Wall, Journal of geotechnical and geoinviornmental engineering," Vol. 136, No. 6, ASCE, pp. 786-796.
12. Watanabe, K. Munaf, Y. Koseki, J. Tateyama, M. Kojima, K. (2003), "Behaviors of several types of model retaining walls subjected to irregular excitation," Soils and Foundation, Vol. 43, No. 5, pp. 13-27.

Investigation of the Effect of Seismic Loading on Displacements of Multi-Tiered Reinforced Soil Walls in Iran Major Hydropower Projects

Amir Mohsen Safaee¹, Ali Noorzad², Ahmad Reza Mahboubi-Ardakani²

1- Ph.D. Candidate, 2- Associate Professor

Department of Civil, Water and Environmental Engineering, Shahid Beheshti University, Tehran. Iran

Email: a_safaee@sbu.ac.ir

Abstract

Reinforced Soil Wall (RSW) is one of the flexible structures that have good performance during earthquakes. Investigating the displacement behavior of RSWs in earthquake is an important issue in dynamic behavior of these structures. In this paper, one of the reinforced soil walls that are constructed in IRAN major hydropower projects is selected. These walls are modeled in Finite element method (FEM) based software, and the performance analysis in several conditions included: end of construction, statically analysis, dynamic analysis are done. In order to investigate the effect of different seismic loadings, two earthquake records of seismic loading are applied to numerical simulations. Comparing the results of seismic analysis of walls illustrates difference of seismic performance of reinforced soil wall under different seismic loadings specially in displacements of these structures.

Keywords: Multi-tiered Reinforced Soil Walls, Seismic Displacement, Dynamic Analysis, Finite Element Method, Gotvand dam.

1. INTRODUCTION

There are different types of retaining walls (e.g. gravity, cantilever and tieback walls) and they are used to secure embankments against sliding, or as key elements of harbors. Tall retaining walls are often constructed as what is called reinforced soil retaining walls or in multi-tiered configuration [3]. This type of retaining wall consists of a facing with a reinforced soil zone behind it (Kramer, 1996). Reinforced soil walls are mechanically stabilized earth retaining systems that are technically proven and a cost effective alternative to the conventional concrete walls [1]. Traditionally, the reinforcements are consisted of thin steel elements but today the use of geogrids is becoming more common. During an earthquake, the retaining wall is subjected to inertial forces due to the backfill inertia. Reinforced soil walls must be designed to withstand the static lateral earth pressure, in addition to forces that are applied in case of an earthquake (Kramer, 1996). As summarized in Rowe and Ho (1998), lateral facing displacement consists of the contributions from deformation of reinforced soil zone, displacement at the back of reinforced soil zone, displacement due to foundation yielding (Skinner and Rowe, 2003, 2005; Rowe and Taechakumthorn, 2008; Bergado and Teerawattanasuk, 2008; Li and Rowe, 2008; Viswanadham and König, 2009; Huang and Luo, 2010; Rowe and Taechakumthorn, 2011), compaction (e.g., Hatami and Bathurst, 2006; Bathurst et al., 2009), slack in reinforcement connection, and dislocation of facing blocks. With proper quality control, slack in reinforcement connection and block dislocation can be minimized [12].

Reinforced soil walls are often used along coastal highways and riverbanks, for docks, sea walls, dams and spillways [2]. Flooding, tides, impounded water and rapid water level drawdown all create complex hydraulic loading conditions that benefit from the open facing joints and free-draining backfill characteristics of reinforced soil walls. In addition, the precast facing panels can move slightly relative to each other, giving the wall system flexibility, resiliency, and the ability to resist storm-driven waves, debris and even pack ice. Investigation of reinforced soil walls that built in water and power resources (e.g. dams and powerhouses) projects shows that the main applications of these structures are as below:

1. Soil slope stability
2. Construction of bridge abutment
3. Protection soil and rock slopes against sliding
4. Soil improvement for construction or development of main or access roads

Some of the reinforced soil walls that were designed and constructed in IRAN dam projects are given in Table 1 and Figure 1.

Table 1- A number of the most important reinforced soil walls that were designed and constructed in Iran dam projects

No.	Project name	Location	Date of completion	Total area (m ²)
1	Powerhouse of Seymareh dam	Iran, Eilam	2010	500
2	Rural road in Alborz dam	Iran, Mazandaran	2004	2708
3	Access road to Cham Gordalan dam	Iran, Eilam	1999	538
4	Khoda Afarin dam	Iran, Tabriz	2005	1270
5	Powerhouse of Gotvand Dam	Iran, Khozestan	2004	6000
6	Development of access road in Bakhtiari dam	Iran, Ahwaz	2012	4200
7	Retaining wall in Lorestan Roodbar dam	Iran, Lorestan	2012	2000
8	Geogrid MSE walls in Dorood dam	Iran, Lorestan	2014	2000



Figure 1. Pictures of reinforced soil walls in Iran dam projects

2. CHARACTERISTICS OF MATERIALS, ASSUMPTIONS AND ANALYSIS METHOD

2.1. CHARACTERISTICS OF MATERIALS

Materials used for modeling the multi-tiered reinforced soil walls, is defined according to prototype condition [15]. Three type of materials is modeled including: two types of granular soil that are used to modeling backfill soil (soil type 1) and retained and foundation soil (soil type 2), one type of rock to modeling bed rock, one type of concrete to modeling segmental facing panels and one type of steel to modeling reinforcements. Physical and mechanical properties of backfill soil, reinforcements, and concrete facing panels which were used in numerical modeling are shown in Table 2-4. It is worthy to note that the ground water table level is -82.5 m that has no effect on soil parameters.

Backfill soil

Design codes typically recommend that the backfill soil is a granular soil so that it is free draining. A number of possibilities exists with respect to choice of constitutive model for the soil. In the present paper linear elastic-plastic with Mohr-Coulomb failure criterion is considers.

Table 2- Characteristic of soil and rock

Parameter	Symbol	Unit	Rock	Soil (2)	Soil (1)
Soil condition	Type	-	-	Un-drained	Drained
Dry unit Weight	γ_{unsat}	kN/m ³	20	20	18.5
Saturated unit Weight	γ_{sat}	kN/m ³	21	21	20
Constitutive model of soil	Model	-	MC	MC	MC
Elastic modulus	E	MPa	1.7	0.1	0.1
Poisson's ratio	ν	-	0.462	0.3	0.3
Cohesion	C	kN/m ²	120	30	1
Internal friction angle	ϕ	Degree	36	36	36
Dilation angle	ψ	Degree	6	6	6
Cutoff tensile stress	$\sigma_{cutoff-t}$	kN/m ²	120	30	1

Reinforcements

Steel-strips with 5mm×50mm area and 5mm thickness were used for reinforcement of the backfill soil. The wall comprises several layers of steel strips that are extended.

Table 3- Characteristic of steel strips reinforcements which were used in numerical modeling

Parameter	Unit weight	Elastic modulus	Poisson's ratio	Thickness	Dimensions
unit	kN/m ³	GPa	-	m	mm
quantity	78.5	210	0.25	0.18	5×50

Facing

Segmental concrete panels with 1.5m×1.5m area and 0.3m thickness were used for construction of the multi-tiered reinforced soil walls that are considered as case study in this paper.

Table 4- Characteristic of facing concrete panels which were used in numerical modeling

Parameter	Unit weight	Elastic modulus	Poisson's ratio
unit	kN/m ³	MPa	-
quantity	24	66.7	0.15

2.2. SEISMIC LOADING

Acceleration that used in this dynamic analysis belongs to Coalinga, El-Centro earthquakes. It was an attempt to use accelerations that were registered on stone base so that it may be consistent with rigid foundation in the models (Figure 2). These two earthquake have same frequency content and different time duration and same peak ground acceleration (PGA) equal 0.4g.

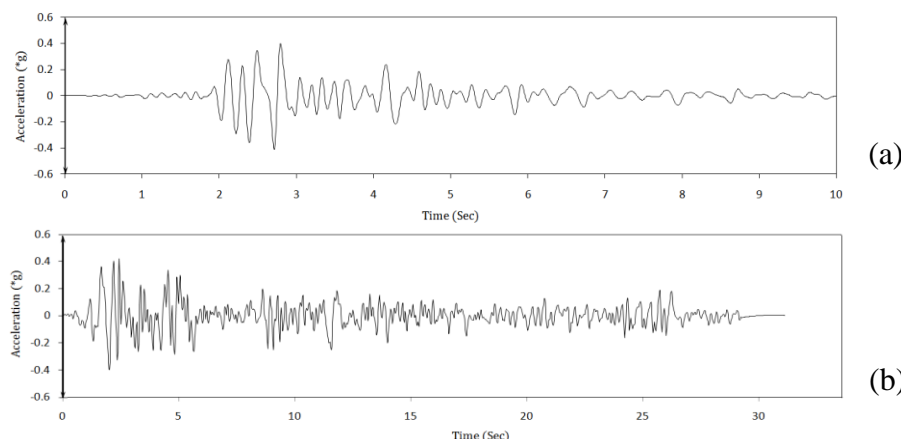


Figure 2. Time-acceleration diagram for: a-Coalinga earthquake (1983), b-El-Centro earthquake (1940)

2.3. ASSUMPTIONS

For dynamic analysis some assumptions included below items as are considered. The dry materials, Mohr-Coulomb for constitutive model of soil and rock, rolled connection as connection of reinforcement to facing panels and nonlinear dynamic analysis is assumed in numerical modeling.

3. THE CASE STUDY

In this paper, one of the highest reinforced soil walls in multi-tiered configuration is selected that are designed and constructed in one of the Iran major hydropower projects. This 31-m-high multi-tiered wall is built to support the soil slopes that are around the powerhouse of Gotvand dam project. Figure 3 shows a typical view of multi-tiered reinforced soil walls around the Gotvand dam powerhouse.

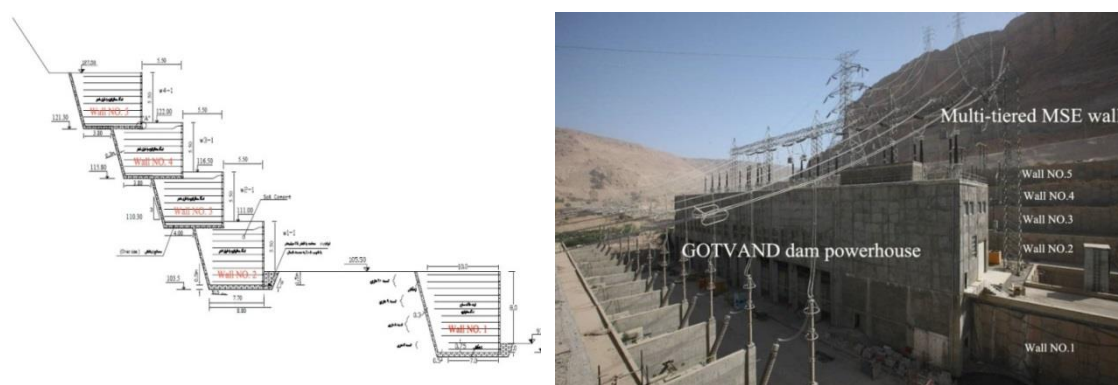


Figure 3. View and cross section of multi-tiered reinforced soil walls in Gotvand dam powerhouse

4. METHOD OF SEISMIC ANALYSIS

The finite element package ABAQUS Explicit, version 6.11 was used to perform two dimensional finite element analysis. The mesh of the wall without facing units, includes 1346 elements and 2035 nodes, and the wall with facing has 402 elements and 608 nodes (Figure 4). The wall is 31 m height in 5-tiered configuration and comprises concrete masonry units connected together by a cementing material, a uniform granular backfill, and several layers of steel-strip reinforcement extending into the backfill soil (Figure 1). The elements are discretized into 3-node quadrilateral elements (triangular) for backfill soil and facing panels and 2-node quadrilateral elements (beam) for reinforcement elements.

Multi-tiered soil walls reinforced with steel-strips, are analyzed in 3 steps as below:

1. Static analysis
2. Frequency analysis is done for detecting the model basic frequencies and Rayleigh (seismic) coefficients.
3. Seismic analysis is done to study the walls dynamic performance.

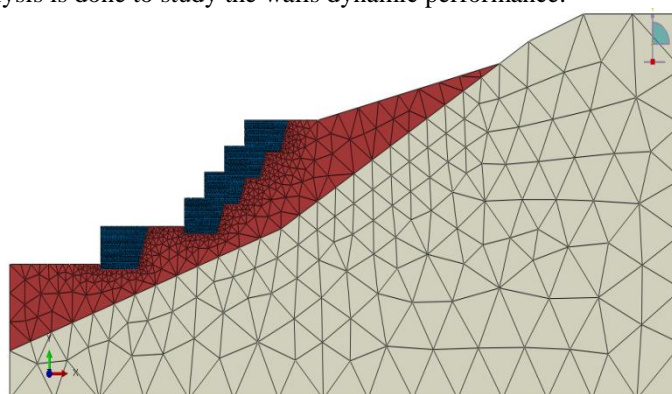


Figure 4. View of numerical grids

5. NUMERICAL RESULTS

Dynamic finite element analyses were carried out to simulate earthquake loading on a multi-tiered reinforced soil wall subjected to earthquake. The numerical analysis was carried out to investigate the dynamic behavior of multi-tiered reinforced soil wall. The comparison between the other previous results and the numerical calculation shows that the numerical method proposed in this paper can properly describe the seismic behavior of multi-tiered reinforced soil wall with sufficient accuracy. Some relevant physical mechanical parameters, such as the horizontal displacement of the facing segmental panels, the settlement of the backfill surface, the lateral earth pressure acting on the facing panels, the tensile forces in the steel-strips and the acceleration response, were all reproduced well by the numerical analysis. In the main part of numerical analyses, the influences of earthquake loading, specially deformation of walls, is investigated by comparing of first and second dynamic analysis results. Thus, the proposed numerical method in this paper can provide an effective evaluation method for the dynamic design of multi-tiered soil walls reinforced with steel-strips. The numerical results of seismic analyses can be explained in the following sections as below.

5.1. MAXIMUM OF SEISMIC ANALYSIS PARAMETERS

The maximum value of the most important seismic analysis parameters that obtained from dynamic analysis is presented in Table 5.

Table 5- Maximum values of seismic analysis parameters

Parameter	Unit	Coalinga earthquake	El-Centro earthquake
Maximum horizontal displacements of walls	m	-0.197	-1.073
Maximum settlements of walls	m	-0.127	-0.506
Maximum strain along reinforcements	%	+0.800	+3.700
Maximum horizontal displacement of walls during earthquake	m	-0.210	-1.100
Maximum horizontal displacement of facing walls during earthquake	m	-0.210	-1.100

5.2. HORIZONTAL DISPLACEMENTS OF WALLS

The magnitudes of deformation occurred during and after construction subjected to earthquake loading is important in the performance of reinforced soil walls. However, there is no standard method for prediction of the lateral deformations [11]. Horizontal movements depend on compaction, reinforcement extensibility, reinforcement length, reinforcement to facing connection details, and deformability of the facing system (Mitchell and Christopher, 1990). The contour of horizontal displacements of walls after is presented in Figure 5.

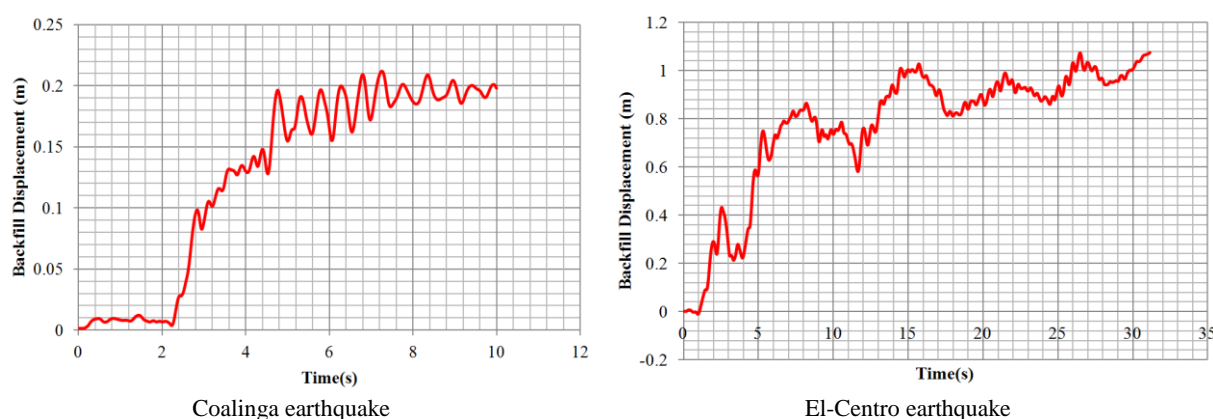


Figure 5. Horizontal displacements of walls

Two shapes of a deformed reinforced soil wall, named bulging and tilting were observed in the typical dynamic analyses [4]. The shape of a deformed wall depends to the dynamic loads and wall characteristics. Tilting shapes are created when the earthquake is very strong and/or the wall is not stiff. Bulging shapes could

be seen when the earthquake is not strong and/or the wall is very stiff .Typical wall deformation in this study is bulging shape and is shown in Figure 6.

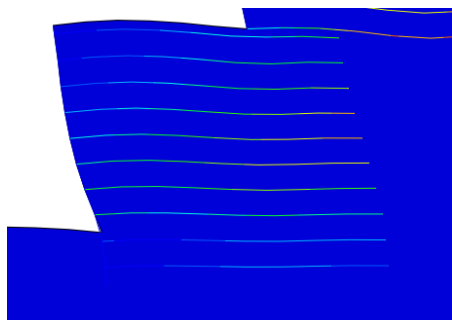


Figure 6. View of typical wall deformation

5.3. SETTLEMENTS OF WALLS

The vertical deformation of reinforced soil wall depends on the ground condition supporting the wall. In real situation, the settlement of reinforced soil walls does not significantly cause the failure, if the settlement is even throughout the wall elevation and at the backfill zone [13]. However, differential settlement of wall on localized spot area in the wall elevation may cause the opening between the interlocking concrete facing panels. In 2D finite element analysis, where the plane strain assumption is applied, differential settlement along wall elevation is unable to be predicted. On the other hand, vertical deformation along cross sectional of wall can be modeled. The contours of wall settlements subjected seismic loading (after first and second seismic loading) are illustrated in Figure 7.

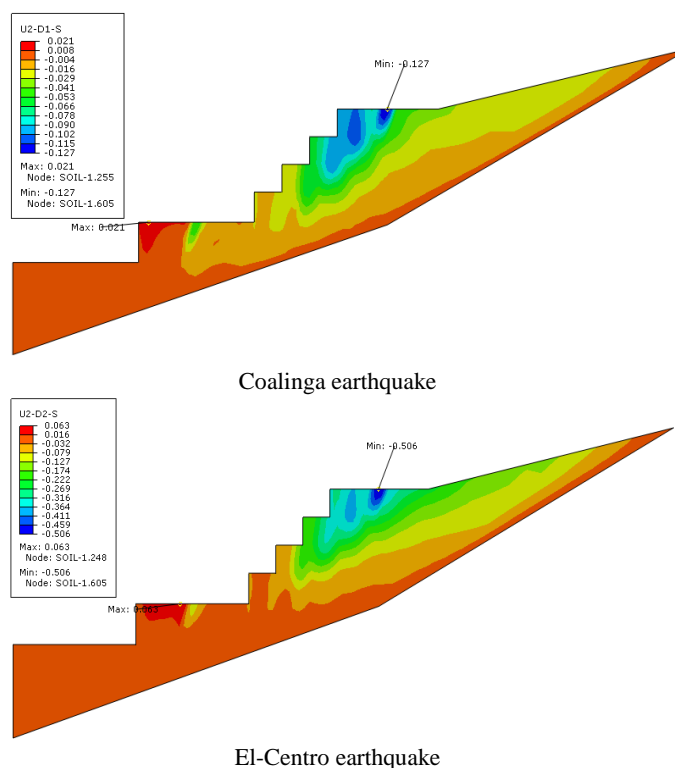


Figure 7. Contour of horizontal settlement of walls

5.4. MAXIMUM HORIZONTAL DISPLACEMENTS OF WALLS DURING EARTHQUAKE

This section gives the deformed shape of the diaphragm wall at different time steps in the dynamic analyses. It gives the information about relative permanent displacement and permanent tilt of the gravity wall. This information is useful for displacement base design procedures. Figure 8 shows the maximum horizontal displacements of walls during earthquake at first and second seismic loading.

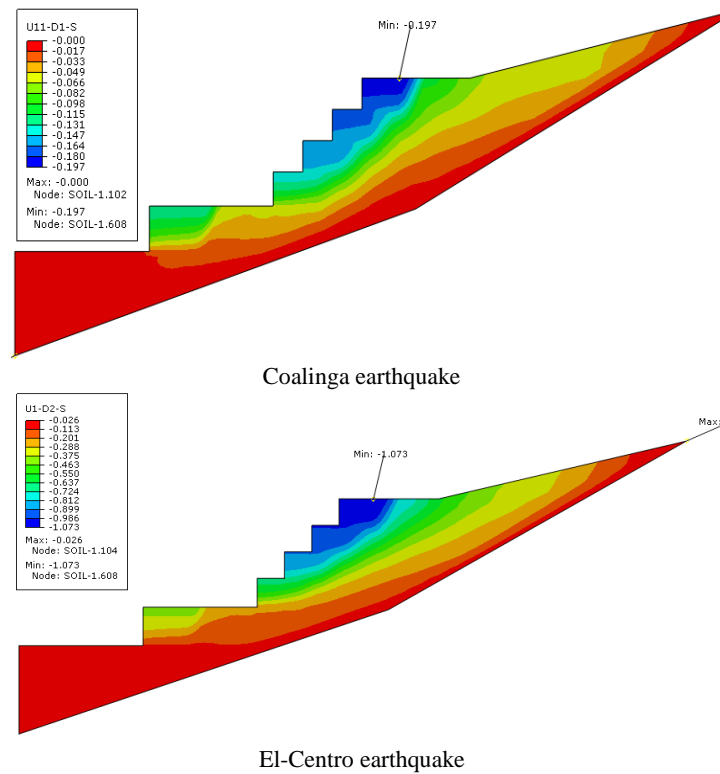


Figure 8. Contour of horizontal displacements of walls

5.5. MAXIMUM HORIZONTAL DISPLACEMENTS OF FACING PANELS DURING EARTHQUAKE

The time history of maximum horizontal displacements of facing panels in multi-tiered reinforced soil walls subjected to 0.40g excitation that is graphed in Figure 9, shows that the displacements around static displacement over the ground motion duration, and are not permanent at the end of the excitation. As is graphed in Figure 9 is the fluctuating displacement at the middle level of the wall. The increasing in the displacement of the top, rightly so, results from the increasing acceleration along the wall height.

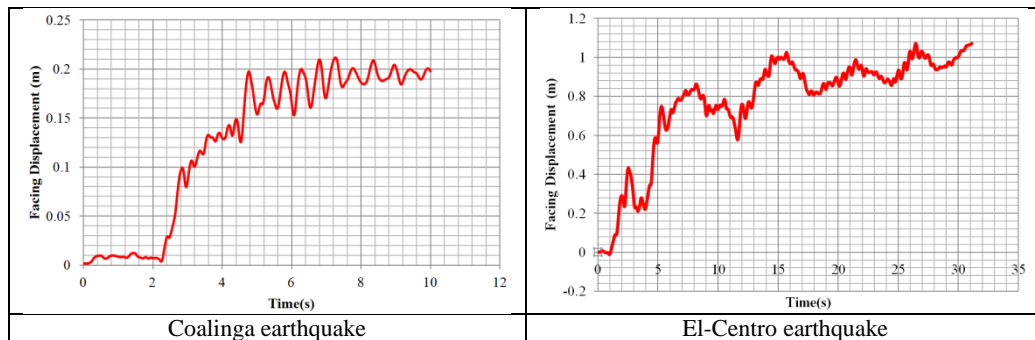


Figure 9. Time history diagram of maximum horizontal displacements of facing panels during earthquake

5.6. MAXIMUM STRAIN OF REINFORCEMENTS AFTER EARTHQUAKE

Figure 10 shows the distribution of reinforcement strain after seismic loading. In each part of this figure, maximum strain of reinforcements after seismic analysis in one stage of multi-tiered soil wall is presented (wall No.1 to wall No.2). As shown in Figure 10, with increasing the height of walls, the value of reinforcement strain is increasing because of ground horizontal amplification. The value of reinforcement strain in first layer of steel-strips is about zero because of their high stiffness and reinforcement strain is increasing with increasing the wall height and reinforcements elevations as is shown in Figure 10.

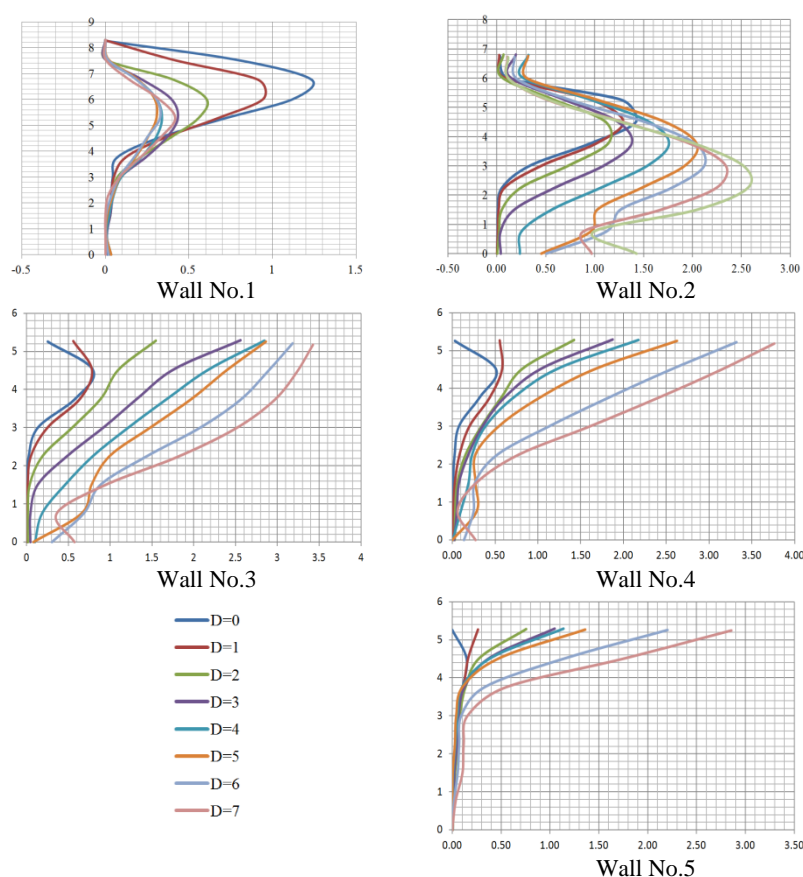


Figure 10. Maximum strain of reinforcement along wall height in each stage of multi-tiered soil walls after El-Centro earthquake

6. CONCLUSIONS

This paper describes the results of the numerical study of multi-tiered reinforced soil in Gotvand dam powerhouse. The analyses are performed using the finite element methods as describes section 4. Based on the obtained results, the following conclusion may be drawn.

1. It was found that deformations of reinforced soil zone and displacement at the back of reinforced soil zone are the two main components of lateral facing displacement for medium-high to high reinforced soil walls. The deformation of reinforced soil zone was only slightly affected by reinforcement length, but was largely determined by reinforcement spacing and reinforcement stiffness that can be unified by the global reinforcement stiffness.
2. Reinforced soil walls can undergo large displacements due to resonance, when exposed to earthquakes with significant energy content at frequencies similar to their first-mode of response, even when the total energy content of the earthquake is not large. It is very important in reinforced soil walls in multi-tiered configuration and tall wall specially.
3. Soil stiffness played an important role in the lateral deformation when soil strength was not mobilized owing to large reinforcement stiffness and/or small reinforcement spacing (Leshchinsky and Vulova, 2001). Soil strength took over as the important role when soil deformation was large due to higher soil stress because of low stiffness reinforcement, large reinforcement spacing or high retaining wall.
4. In typical seismic analysis of reinforced soil wall two shapes of a deformation, named bulging and tilting were observed. Bulging shapes could be seen when the earthquake is not strong and/or the wall is very stiff. Typical wall deformation in this study is bulging shape.
5. The most important parameters that are affecting the value of reinforcement strain are: the layout of reinforcements, reinforcement axial stiffness (EA), wall elevation, wall surcharge and etc.

6. The results state that the assumptions of available seismic design codes are highly conservative, due to ignoring allowable displacements after earthquake occurrence. Consequently, performance based design concept would result in more suitable and economical structure.
7. The displacement based performance of single reinforced soil walls is differed from multi-tiered reinforced soil walls [13]. Therefore multi-tiered reinforced soil and their seismic performance must be analyzed and investigated before designing and construction.

7. REFERENCES

1. Bathurst, R.J. and Alfaro, M.C. (1997), "Review of seismic design, analysis and performance of geosynthetic reinforced walls," Slopes and embankments, Earth Reinforcement, Balkema, Vol. 2, pp. 887-918.
2. Bathurst, R.J. (1998), "NCMA segmental retaining wall seismic design procedure – supplement to design manual for segmental retaining walls," National Concrete Masonry Association, Herndon, VA, 187 p.
3. Bhattacharjee, A. Krishna, A. M. (2015), "Strain Behavior of Backfill Soil in Rigid Faced Reinforced Soil Walls Subjected to Seismic Excitation," International Journal of Geosynthetics and Ground Engineering, Vol. 14, pp. 1-14.
4. Brabhaharan, P. Fairless, G.J. Chapman, H.E. (2003), "Effect of vertical earthquake shaking on displacement of earth retaining structures," 2003 Pacific Conference on Earthquake Engineering, New Zealand, pp. 1-8.
5. Cia, Z. Bathurst, R.J. (1996), "Seismic-include permanent displacement of Geosynthetic-reinforced segmental retaining Walls," Geotech Journal, Vol. 33, pp. 937-955.
6. El-Emam, M. and Bathurst, R.J. (2004), "Experimental design, instrumentation and interpretation of reinforced soil wall response using a shaking table" International Journal of Physical Modeling in Geotechnics, Vol. 4, pp. 13-32.
7. Hatami, K. and Bathurst, R.J. (2000), "Effect of structural design on fundamental frequency of reinforced-soil retaining walls" Soil Dynamics and Earthquake Engineering, Volume 19, pp. 137-157.
8. Koseki, J. and Hayano, K. (2000), "Preliminary report on damage to retaining walls caused by the 1999 Chi-Chi earthquake," Bulletin of ERS, Institute of Industrial Science, Univ. of Tokyo, 33, pp. 23-34.
9. Ling, H. Liu, H. Kaliakin, V. Leshchinsky, D. (2004), "Analyzing Dynamic Behavior of Geosynthetic Reinforced Soil Retaining Walls," Volume 130, No. 8, ASCE, pp. 911-920.
10. Miyata, Y. Bathurst, R.J. Miyatake, H. (2015), "Performance of three geogrid-reinforced soil walls before and after foundation failure," Geosynthetics International, Vol. 22, Elsevier, pp. 311-326.
11. Onodera, S. Fukuda, N. Nakane, A. (2008), "Long-term Behavior of Geogrid Reinforced Soil Walls," Public Works Research Institute, Tsukuba, Japan, pp. 1-10.
12. Tatsuoka, F., Koseki, J., Tateyama, M., Munaf, Y. and Horii, N. (1998), "Seismic stability against high seismic loads of geosynthetic-reinforced soil retaining structures," Proc. 6th Int. Conf. on Geosynthetics, Atlanta, Vol. 1, 103-142.
13. Stuedlein, A.W. Bailey, M. Lindquist, D. (2010), "Design and Performance of a 46-m-High MSE Wall, Journal of geotechnical and geoinviornmental engineering," Volume 136, No. 6, ASCE, pp. 786-796.
14. Sahara, K. (2012), "Investigation of damage to reinforced earth walls in the great east Japan earthquake and related maintenance," In: Proceedings of the International Joint Symposium on Urban Geotechnics for Sustainable Development. JS-Seoul, pp. 2-26.
15. Safaee, A.M. (2012), "Seismic Analysis of Mechanically Stabilized Earth Wall (MSEW) Case Study: MSEW of Upper Gotvand Powerhouse," M. Sc. Thesis, Power and Water University of Technology (PWUT), Faculty of Water & Environmental Engineering, Tehran, (in Persian).

Dynamic response of concrete dams

Shiva Khosravi¹, Reza Kamyab Moghadas¹

1- The Iranian Academic Center for Education, Culture and Research, Kerman, Iran

Email: Shivakhosravi@ymail

Abstract

Dams are constructed to serve a variety of purposes such as supply of drinking and irrigation water, generation of electric power, flood protection. During this century, increasing numbers of concrete dams have been constructed, and more are expected to be built, in seismic regions. Sooner or later these dams will be exposed to major earthquakes in addition to the usual sources of potential damage. Because millions of people live in the floodplains downstream of these dams, it is essential that increasing attention be given to the earthquake safety of these structures. Dynamic response of concrete dams including dam-water-foundation rock interaction subject to earthquake loading is the main of the study. In this study, first the concrete dam-water-foundation rock system has been simulated using the finite element method. Then dynamic analysis of dam-water-foundation rock system is performed. The results of the seismic response for dam-water-foundation model have also been discussed.

Keywords: Concrete dams, Earthquakes, Dynamic response.

1. INTRODUCTION

Gravity dams are fluid–structure–soil interaction problems. It is obvious that the foundation and water reservoir affect the dynamic response of gravity dams during earthquakes. Many factors have influence the dynamic response concrete gravity dams against earthquake motion. Some of these factors included dam-reservoir-foundation interaction, sediments at the bottom of the reservoir and nonlinear behavior of concrete gravity dams. Usually to compute the dynamic response of the dam, the concrete dam and the foundation rock are modeled by standard finite elements, whereas for the interaction effects of the water, there are several methods to investigate the dynamic response of the mentioned systems. The dam reservoir interaction problems can be analyzed using the three famous approaches: Westergaard approach: the dynamic effect of the reservoir is modelled as added masses. Eulerian approach: since in this approach the displacements are the variables in the structure and the pressures are the variables in the fluid, a special purpose computer program is required for the solution of the coupled systems. Lagrangian approach: In this approach the behavior of the fluid and structure is expressed in terms of displacements. For that reason, compatibility and equilibrium are automatically satisfied at the nodes along the interfaces between the fluid and structure. This makes a Lagrangian displacement based fluid finite element very desirable; it can be readily incorporated into a general purpose computer program for structural analysis; because special interface equations are not required. The first presented solution was based on the added mass method. In this approach, the only effect of fluid was the portion of fluid mass which was added to the solid. The stiffness and damping effects of the fluid was ignored. In this state, the solid was solved without considering the fluid, and the solid mass matrix was modified by a portion of fluid mass. This method was used to analyze stiff and flexible structures such as dams and water reservoir. In general, this method gives overestimated results, but is still useful for pre-analysis procedures. The first research on the analysis of concrete gravity dam has been done by Westergaard in 1930 and its analysis response for hydrodynamic pressure on the dam face was clear [1]. The original added mass concept is based on simplifying assumptions of vertical upstream face, rigid dam section, and incompressible water but was modified by Kuo (1982) for other orientations of the upstream face and in the linear and nonlinear responses dam-reservoir system approximated dam equation by adding some mass [2]. Both approaches, however, ignore compressibility of water and the energy loss due to radiation of pressure waves in the upstream direction and due to reflection and refraction at the reservoir bottom. Chopra and his coworkers (1981) the complete system is considered as composed of three substructures, the dam, represented as a finite element system, the fluid domain, as a continuum of infinite length in the upstream direction, and the foundation rock region as a viscoelastic half-plane. The foundation region may also be idealized as a continuum or as a finite element system. The continuum idealization permits the continuum idealization permits accurate modeling of the structure-foundation interaction when similar materials extend to large depths. For sites where soft rock or soil

overlies harder rock at shallow depths, a finite element idealization of the foundation region is more appropriate, but at low depths the rock and rigid layer should be modeled with finite element method [3].

In addition to dam-reservoir-foundation interaction, the effect of seismic waves absorption by the reservoir bottom sediments on the response of the dam have been studied. Dam-reservoir-foundation-sediment interaction has been investigated by many researchers. Among other, Fenves and Chopra (1984, 1985) presented a model which includes reservoir bottom absorption for the seismic analysis of gravity dam by the means of an absorbing boundary condition. The study concluded that the sediment could significantly reduce the hydrodynamic pressure effect on the seismic response of the dam [4,5].

Singhal (1991), the effect wave reflection coefficient (α) on maximum values crest displacement and maximum stress at the heel of the dam investigated. The (α) is the ratio of the amplitude of the reflected hydrodynamic pressure wave to the amplitude of a vertical propagating pressure wave incident on the reservoir bottom ($0 < \alpha < 1$). A value of $\alpha = 1$ indicates that pressure waves are completely reflected, and smaller values of α indicate increasingly absorptive materials. The results show that increasing the wave reflection coefficient increases the maximum values crest displacement and maximum stress at the heel of the dam [6].

Many researches, studied this problem using the computer programs for analysis 2D Finite Element Method of gravity dams. For example, the computer program EAGD-84 (Fenves and Chopra, 1984) is a two-dimensional finite element method of analysis for gravity dams which includes dam-water interaction with water compressibility, dam-foundation rock interaction, and reservoir bottom absorption due to reservoir bottom sediments [7]. Lotfi (2003, 2007) a new technique is proposed for earthquake analysis of concrete gravity dams, which is referred to as decoupled modal approach. A special computer program "MAP-76" is used as the basis of this study. The program was already capable of analyzing a general dam-reservoir system by direct approach in the time domain and frequencies of the dam - reservoir found. The main advantage of this modal technique is that it employs eigenvectors of the decoupled system, which can be easily obtained by standard eigen-solution routines [8,9]. Akkose (2010), the seismic nonlinear behavior of the concrete gravity dams to earthquake ground motion near and far fault including dam-reservoir-sediment-foundation rock interaction is investigated and using a computer program NONSAP modified System frequencies dam - reservoir received. The program is modified for elasto-plastic analysis of fluid-structure systems and employed in the response calculations [10].

In this paper, we study the dam-reservoir-foundation interaction during an earthquake. For this purpose, model of two-dimensional finite element that is included dam, reservoir and foundation be provided using the finite element software (ANSYS). In order to check verify of modeling and ensured used assumption during the modeling, dam is intended in 4 different cases: 1. Dam with empty reservoir and rigid foundation. 2. Dam with empty reservoir and flexible foundation. 3. Dam with full reservoir and rigid foundation. 4. Dam with full reservoir and flexible foundation. The modal analysis and mode shapes results of the Pine Flat is studied and the results obtained, verify the accuracy of the modeling against available reference results.

2. FINITE ELEMENT MODEL OF DAM-RESERVOIR- FOUNDATION SYSTEM

To modeling concrete gravity dam-reservoir-foundation problem using the finite element procedure, the discretized dynamic equations of the fluid and structure including dam and its foundation need to be considered simultaneously to obtain the coupled fluid-structure-foundation.

2.1. THE DISCRETIZED FLUID EQUATION

Assuming that water is linearly compressible and neglecting its viscosity, the small amplitude irrotational motion of the water is governed by the two-dimensional wave equation [11]:

$$\nabla^2 p = \frac{1}{c^2} \frac{\partial^2 p}{\partial t^2} \tag{1}$$

Where c is the speed of pressure wave, P is the acoustic hydrodynamic pressure; t is time and ∇^2 is the two-dimensional Laplace operator.

As shown in Figure 1, some boundary conditions may be imposed on the fluid domain as follows:

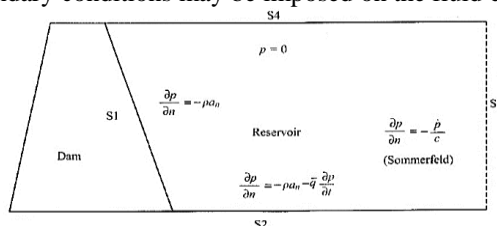


Figure 1. The boundary conditions of the fluid domain [12]

(S1), at the fluid–structure interface:

$$\frac{\partial p}{\partial n} = -\rho \alpha_n \quad (2)$$

Where n is a unit normal vector to the interface, α_n is the normal acceleration on the interface and ρ_w is the mass density of water.

(S2), at the bottom of the fluid domain:

$$\frac{\partial p}{\partial n} = -\rho \alpha_n - \bar{q} \frac{\partial p}{\partial t} \quad (3)$$

Where \bar{q} is the damping coefficient characterizing the effects of absorption of hydrodynamic pressure waves at the reservoir boundary[4] and α is the wave reflection coefficient, which represents the ratio of the amplitude of the reflected wave to that of the normally incident pressure wave. α is related to \bar{q} by the following expressions:

$$\alpha = \frac{1 - \bar{q}c}{1 + \bar{q}c} \quad (4)$$

It is believed that a Value from 1 to 0 would cover the wide range of materials encountered at the boundary of actual reservoirs. The value of the wave reflection coefficient α that characterizes the reservoir bottom materials should be selected based on their actual properties, not on properties of the foundation rock. Materials on the reservoir bottom has great influence in absorbing of earthquake waves and decreases the system response under the vertical component of the earthquake and this effect is also important for horizontal component.

(S3), at the far-end of the fluid domain a Sommerfield-type radiation boundary condition [11] may be implemented, namely

$$\frac{\partial p}{\partial n} = -\frac{1}{c} \frac{\partial p}{\partial t} \quad (5)$$

(S4), at the free surface when the surface wave is neglected, the boundary condition is easily defined as:

$$p = 0 \quad (6)$$

Eqs. (2)– (6) can be discretized to get the matrix form of the wave equation as [13]:

$$M_f \ddot{P}_e + C_f \dot{P}_e + K_f P_e + \rho_w Q^T (\ddot{u}_e + \ddot{u}_g) = 0 \quad (7)$$

Where M_f , C_f and K_f are the fluid mass, damping and stiffness matrices, respectively, and P_e ; \ddot{u}_e and \ddot{u}_g are the nodal pressure, relative nodal acceleration and nodal ground acceleration vectors, respectively. The term $\rho_w Q^T$ is also often referred to as coupling matrix.

2.2. THE DISCRETIZED STRUCTURAL EQUATION

The discretized structural dynamic equation including the arch dam and foundation rock subject to ground motion can be formulated using the finite-element approach as:

$$M_s \ddot{u}_e + C_s \dot{u}_e + K_s u_e = -M_s \ddot{u}_g + Q p_e \quad (8)$$

Where M_s , C_s and K_s are the structural mass, damping and stiffness matrices, respectively, u_e is the nodal displacement vector with respect to ground and the term $Q p_e$ represents the nodal force vector associated with the hydrodynamic pressure produced by the reservoir.

2.3. THE COUPLED FLUID–STRUCTURE-FOUNDATION EQUATION

Eqs. (7) and (8) describe the complete finite-element discretized equations for the dam-water–foundation rock interaction problem and can be written in an assembled form as:

$$\begin{bmatrix} M_s & 0 \\ M_{fs} & M_f \end{bmatrix} \begin{Bmatrix} \ddot{u}_e \\ \dot{P}_e \end{Bmatrix} + \begin{bmatrix} C_s & 0 \\ 0 & C_f \end{bmatrix} \begin{Bmatrix} \dot{u}_e \\ \dot{P}_e \end{Bmatrix} + \begin{bmatrix} K_s & K_{fs} \\ 0 & K_f \end{bmatrix} \begin{Bmatrix} u_e \\ P_e \end{Bmatrix} = \begin{Bmatrix} -M_s \ddot{u}_g \\ -M_{fs} \ddot{u}_g \end{Bmatrix} \quad (9)$$

Where $K_{fs} = -Q$ and $M_{fs} = \rho_w Q^T$.

Eq. (9) expresses a second order linear differential equation having unsymmetrical matrices and may be solved by Means of direct integration methods. In general, the dynamic equilibrium equations of systems modelled in finite elements can be expressed as:

$$M_c \ddot{u}_c + C_c \dot{u}_c + K_c u_c = F(t) \tag{10}$$

Where M_c , C_c , K_c and $F(t)$ are the structural mass, damping, stiffness matrices and dynamic load vector, respectively.

3. MODELLING OF DAM-RESERVOIR-FOUNDATION SYSTEM

The objective of this work is to study the effects of dam-reservoir-foundation interaction on modal behaviour of gravity dams. The computer program used to model and analyzes the dam-reservoir- foundation system was ANSYS (APDL language programming). Pine flat Dam are analyzed to evaluate the accuracy and efficiency of the present model finite element. For dam body modelling four nodes element of Plane 42 (structural 2D solids) are used. The dam and foundation elements are in a state of plane-stress. The reservoir is assumed to be of uniform shape and four-noded FLUID29 element is used to discretize the fluid medium and the interface of the fluid-structure interaction problem. The element has four degrees of freedom per node: translations in the nodal x, y and z directions and pressure. The translations, however, are active only at the nodes that are on the interface. In order to consider the damping effect arising from the propagation of pressure waves in the upstream direction, instead of a Sommerfield-type radiation boundary condition, the reservoir length is selected as one and a half times the reservoir depth and zero pressure is imposed on all nodes of the far end boundary. In this study, foundation rock treating as a linearly elastic structure is represented via a four-noded Plane 42 element as well. The foundation rock is assumed to be massless in which only the effects of foundation flexibility are considered and the inertia and damping effects of the foundation rock are neglected. The foundation rock is extended to one and a half times dam height in upstream, downstream and downward directions [14].

The dam body is assumed to be homogeneous, isotropic and elastic properties for mass concrete. The foundation rock is idealized as a homogenous, isotropic media. The foundation model was constructed using solid elements arranged on semicircles having a radius one and a half times base of the dam. The impounded water is taken as inviscid and compressible fluid.

In the present study, to create the gravity dam geometry, nine geometry variables are considered. With the defined geometry variables in APDL ansys a 2D shape of gravity dam body is created. Shape of the dam with nine geometry variables is presented in Figure (1).

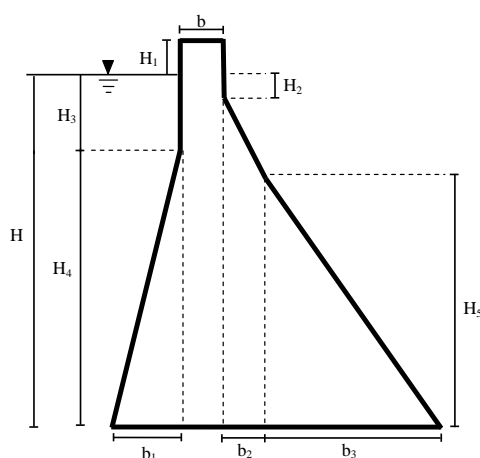


Figure 1. Geometrical model of concrete gravity dam

4. FINITE-ELEMENT MODEL OF PINE FLAT DAM

In this section, the analysis of Pine Flat Dam is considered as a verification example. The dam is 121.92 m high, with the crest length of 560.83 m and its basis has a length of 96.80 m. It is located on the King’s River near Fresno, California.

The material properties of the dam, water and foundation rock are given in Table 1 [15,16].

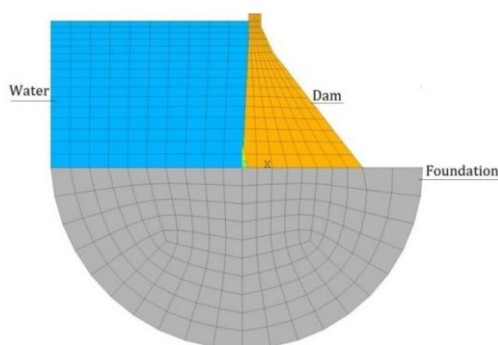


Figure 2. Finite element model of Pine Flat dam-water-foundation rock system

Table 1. The properties of materials

Concrete	Elasticity modulus of concrete (MPa)	22400
	Poison's ratio of concrete	0.2
	Mass density of concrete (kg /m ³)	2430
Water	Mass density of water (kg /m ³)	1000
	Wave velocity (m/s)	1440
	Wave reflection coefficient	0.817
Foundation	Elasticity modulus (MPa)	68923
	Poison's ratio	0.3333

The natural frequencies for Cases 1-4 from the finite element model and the literature are given in Table 2[16]. It can be observed that a good conformity has been achieved between the results of present work with those of reported in the literature [16]. Also, the very small percentage error showed excellent accuracy of the proposed model for dam-reservoir-foundation system.

Table 2. A comparison of the natural frequencies from the FE model with the literature

Case	Foundation	Reservoir	Natural frequency (Hz)		
			Chopra [16]	The present work	Error (%)
1	Rigid	Empty	3.1546	3.152	0.082
2	Rigid	Full	2.5189	2.522	0.123
3	Flexible	Empty	2.9325	2.930	0.085
4	Flexible	Full	2.3310	2.340	0.386

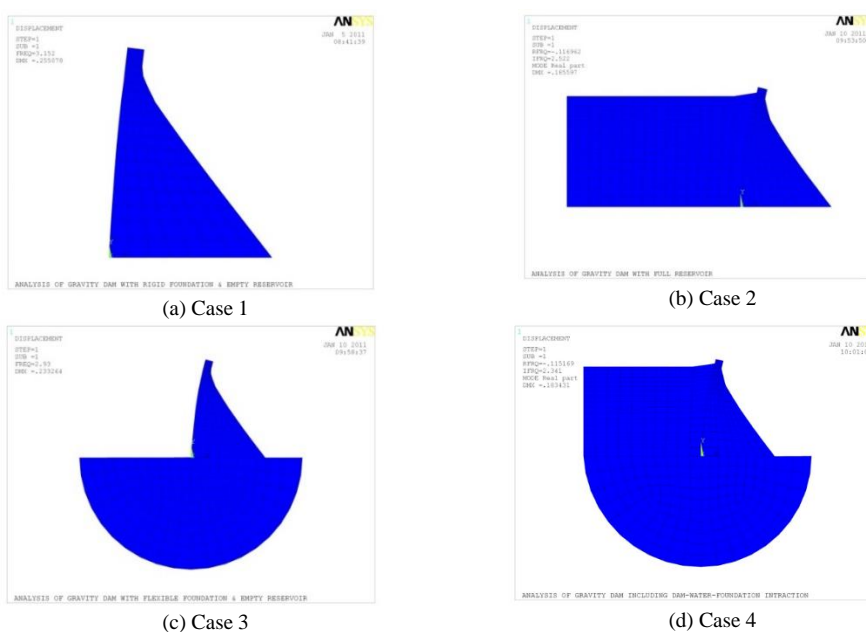


Figure 3. The first mode shape of the dam for different Cases

The result of transient analysis shown in Figure 5 and 6.

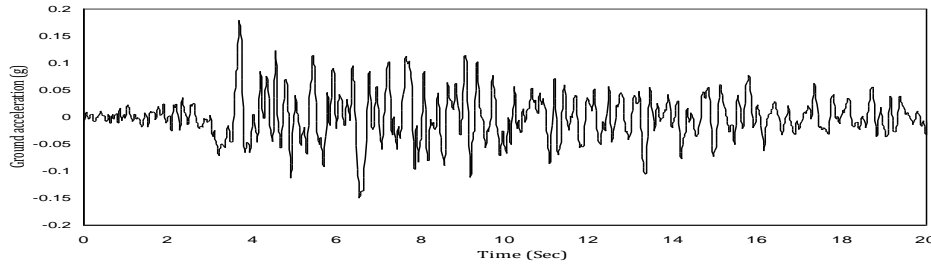


Figure 4. Ground motion at Taft Lincoln Tunnel; Kern country, California, 1952

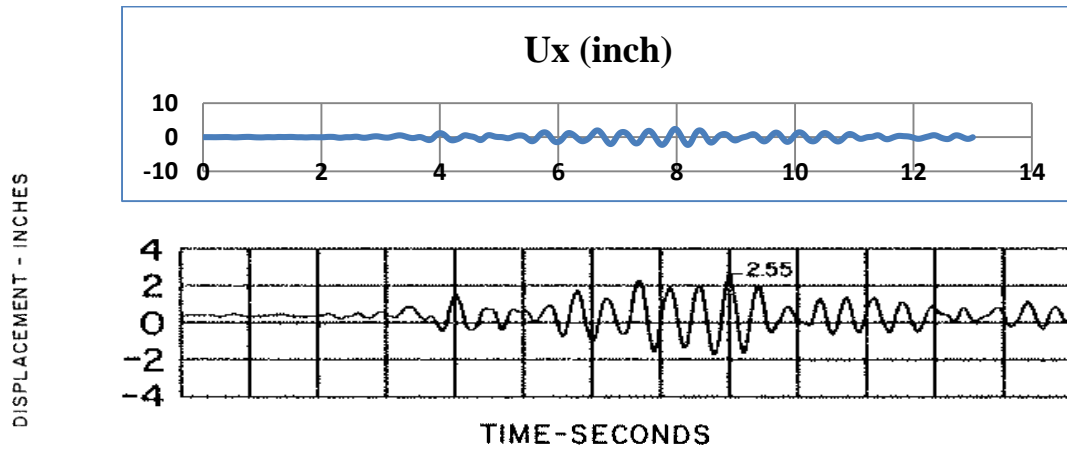


Figure 5. Crest displacement of Pine flat dam [16]

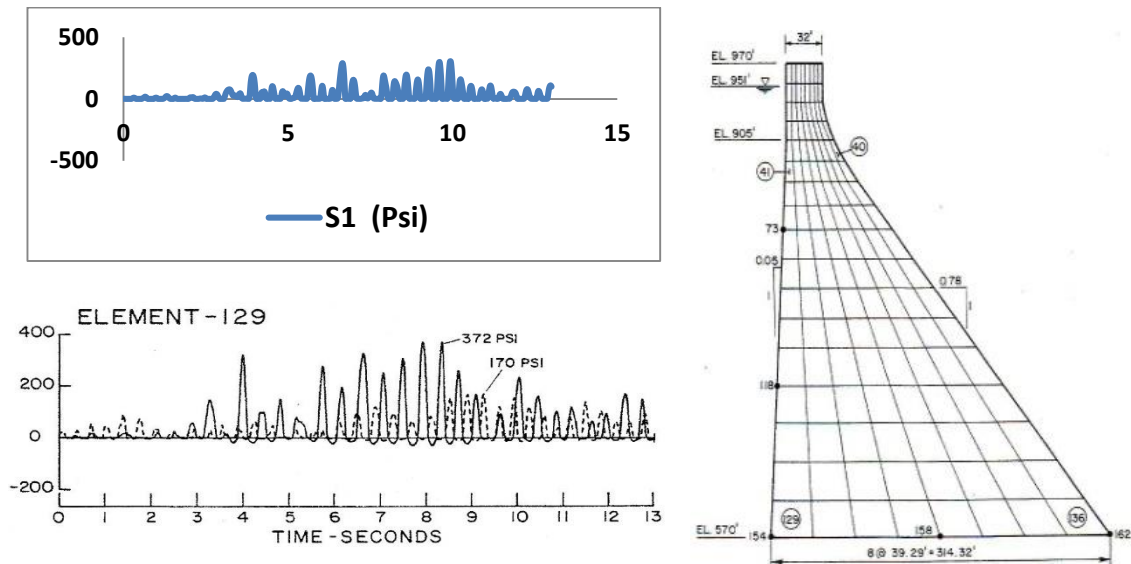


Figure 6. Stress of Pine flat dam [16]

5. CONCLUSIONS

Dynamic response of concrete dams including dam-water-foundation rock interaction subject to earthquake loading is the main of this study. To achieve this aim, a 2D finite element model has been established for the modal analysis of Concrete gravity dams -reservoir–foundation rock system with APDL language. To create the gravity dam geometry, nine geometry variables are considered. With the defined geometry variables in APDL/ANSYS a 2D shape of gravity dam body is created.

In order to validate FEM with the employed assumptions in this study, the first natural frequency of FEM of the gravity dam for four cases are determined from the frequency response function. The results of first

natural frequency for four design cases are compared with those of reported in literature and its performance is verified.

It is observed that the gravity dam–foundation rock interactions have an important role in the design of dams and neglecting these effects can lead to an improper design. Also, it can be observed that when the reservoir is empty and the foundation is rigid (Case 1) main frequency of the dam is maximal. Furthermore, a minimum value for the main frequency is obtained when the dam–water–foundation rock interaction (Case 4) is considered.

It is also found that considering the dam–water–foundation rock interaction has an important role for safely designing a gravity dam.

6. REFERENCES

1. Westergaard, H.M. (1933), “*Water pressures on dams during earthquakes*,” Transactions of ASCE 98, pp. 418-427.
2. Kuo, J.S.H. (1982), “*Fluid–structure interactions: Added mass computation for incompressible fluid*,” UCB/EERC-82/09 Report. University of California, Berkeley, USA.
3. Chopra, A.K and Chakrabarti P. (1981), “*Earthquake response of concrete gravity dams including dam-water- foundation rock interaction*,” Earthquake Engineering and Structural Dynamics Vol 9, pp. 363-383.
4. Fenves G .and Chopra A.K. (1983), “*Effects of reservoir bottom absorption on earthquake of concrete gravity dams*,” Earthquake Engineering and Structural Dynamics, pp.11, 809-829.
5. Fenves G .and Chopra A.K. (1984), “*Earthquake analysis of concrete gravity dams including reservoir bottom absorption and dam-water-foundation rock interaction*,” Earthquake Engineering and Structural Dynamics, **12**, pp. 663-680.
6. Singhal A.C. (1991), “*Comparison of computer codes for seismic analysis of dams*”, Computers & Structures, 38, pp.107-112.
7. Fenves G .and Chopra A.K. (1984), “*EAGD-84: A computer program for earthquake analysis of concrete gravity dams*,” UCB/EERC-84/11 Report. University of California, Berkeley, USA.
8. Lotfi V. (2003), “*Seismic analysis of concrete gravity dams by decoupled modal approach in time domain*,” Electronic Journal of Structure Engineering, **3**, 102-116.
9. Samii A .and Lotfi V. (2007), “*Comparison of coupled and decoupled modal approaches in seismic analysis of concrete gravity dams in time domain*,” Finite Elements in Analysis and Design 43, 1003-1012.
10. Akkose M .and Simsek E. (2010), “*Non-linear seismic response of concrete gravity dams to near-fault ground motions including dam-water-sediment–foundation interaction*, Applied Mathematical Modelling,” **34**, pp. 3685-3700.
11. Kucukarslan S., Coskun B. and Taskin B. (2005), “*Transient analysis of dam-reservoir interaction including the reservoir bottom effects*,” Journal of Fluids and Structures ,20, pp.1073-1084.
12. Kucukarslan S. (2003), “*Dam –reservoir interaction including the reservoir bottom effects in time domain*,” 16th ASCE engineering mechanics conference, July 16-18.
13. Seyedpoor S.M., Salajegheh J .and Salajegheh E .(2009), “*Shape optimal design of arch dams including dam-water-foundation rock interaction using a grading strategy and approximation concepts*,” Applied Mathematical Modelling, **34**, pp. 1149-1163, 2009.
14. Seyedpoor S.M. (2009), “*Optimum Design of arch dams Using Approximation Methods*”, PhD Thesis, Department of Civil Engineering, University of Kerman, Kerman, Iran.
15. Vargas-Loli L. and Fenves G. (1989), “*Effects of concrete cracking of the earthquake response of gravity dams*,” Earthquake Engineering and Structural Dynamics, **18**, pp.575-592.
16. Chopra A.K .and Chakrabarti P. (1980), “*Earthquake response of concrete gravity dams including hydrodynamic foundation interaction effects*,” UCB/EERC-80/01 Report. University of California, Berkeley, USA.
17. Sarkar, R. (2007), “*Influence of reservoir and foundation on the nonlinear dynamic response of concrete gravity dams*,” ISET Journal of Earthquake Technology, 44, pp.377-389.
18. Arjomandi S.A. and Lotfi V. (2007), “*Dynamic analysis of structures in frequency domain by utilizing a new set or ritz rectors*,” Journal of faculty of engineering (University of Tehran); 41(1 (103)): pp/1-10.
19. Fathi, A. (2004), “*Dynamic analysis of weight concrete dams by using combination of finite elements method and boundary element method*.” Master of Science thesis, Amir Kabir, University of Technology.
20. EAGD-84, Available from: <[http://nisee.berkeley.edu/elibrary/ Software / EAGD84PZIP](http://nisee.berkeley.edu/elibrary/Software/EAGD84PZIP)>.
21. EAGD-PC, Available from: <[http://nisee.berkeley.edu/elibrary/Software /EAGD84PCZIP](http://nisee.berkeley.edu/elibrary/Software/EAGD84PCZIP)>.

Seismic Analysis of Rockfill Dam, a Case Study of Ghoocham Dam

Hooman Rezaee¹, Hamidreza Hajihassani², Shahram Mahzarnia³

1- Rock mechanics engineer of Tahkimkav Consulting Engineers Company

2- Project Manager of Tahkimkav Consulting Engineers Company

3- Project Manager of Iran Water and Power Development Company

Email: Hooman.rezaee@mi.iut.ac.ir

Abstract

Ghoocham dam is 45 m height ECRFD type with a vertical clay core and soft alluvial and rock foundation under construction in west of Iran. The study of the seismic response of rockfill dams is a complex problem that generally requires the use of dynamic methods of analysis. The non-linear analysis is established to calculate the permanent deformation caused by the earthquake. In this paper, the seismic analysis of Ghoocham dam based on non-linear approach is presented. The dynamic analyses were conducted as non-linear two-dimensional analyses using the Fast Lagrangian Analysis of Continua (FLAC) computer code. The initial condition of stress and pore pressure is performed for the steady state condition. The initial condition of stress and pore pressure calculated in construction stage was performed for analysis at steady state condition. Time-acceleration histories of two different earthquakes with a magnitude of 6.9 in Richter scale and the maximum peak acceleration (PGA) of 0.47g were applied in analysis. The maximum deformation and the failure pattern are obtained through the non-linear analysis. The analysis results show that permanent deformation is in the acceptable range and stability of dam is secured after the earthquake.

Keywords: Rockfill dam, seismic analysis, non-linear analysis, numerical analysis.

1. INTRODUCTION

Dams play a significant role in fulfilling the increasing demand of water for municipal and agricultural purposes. Embankment dams have become very popular among dam engineers since available materials of different types at site could be used in appropriate zones of dam. Safety of rockfill dams depends on the proper analysis, design, construction and monitoring of actual behaviour during the construction and the operation of the structure. The stability of dam during and after earthquake is a very important safety issue. The solution of geotechnical engineering problems is complicated. One of the reason is the geotechnical problems generally involve large nonhomogeneous structures. The solution of dynamic problems is complicated because soil exists in general as a multi-phase solid-fluid system. Further, the behaviour of the soil is highly nonlinear, anisotropic and hysteretic [1-2]. Under these conditions, the analytical solutions of geotechnical problems have necessarily involved many simplifying assumptions. However, the development of computing facilities has now made it possible to solve these complicated problems more exactly using numerical methods. Nowadays the non-linear dynamic analysis approach is common regarding the development of computational methods and advanced numerical analysis. In this category of analysis, an appropriate constitutive model can be assigned to soil materials and, moreover, a real acceleration-time history is used to calculate the seismic deformations. Considering these factors, the results of the non-linear method are supposed to reflect the real dynamic behavior of soil materials. Ghoocham dam is an ECRFD type which is under construction in west of Iran. In this paper, to obtain the seismic response of Ghoocham dam during and after earthquake, the seismic analysis was done based on non-linear approach.

2. GEOMETRY

Ghoocham dam is an ECRD with vertical clay core material with 45 m height. The length of dam crest is 1820 m at the elevation 1856 m.a.s.l. The slopes of both dam abutments are gentle, around 12%-15% and 600 m of the central part of dam foundation is almost flat. Upstream and downstream slopes of rockfill shell are 1:1.7 and 1:1.5 (V:H), respectively. The slope of central core is 1:0.35(V:H).

Due to weak rock foundation, two stabilizing berms at upstream and downstream of dam with 16 & 50 m width have been designed in central part of dam. At maximum height section of dam, two 3 m and 2 m width

fine filter and transition zone are considered at both upstream and downstream of core with the same slope of central core. Figure 1 shows the typical cross section of Ghoocham dam. Shell materials are obtained from two limestone and andesite-bazalt quarries close to the dam site. Materials for zones 4, 5A, filter and transition are obtained from limestone quarry, and material for zones 4A and 4B are from andesite-bazalt quarry. Zone 7 material is from mandatory excavation of fine alluvial and rock foundation of dam body. Foundation of dam consists of 4-14 m thickness alluvial material and weak rock of tertiary quaternary unit of sanandaj-sirjan zone underneath.

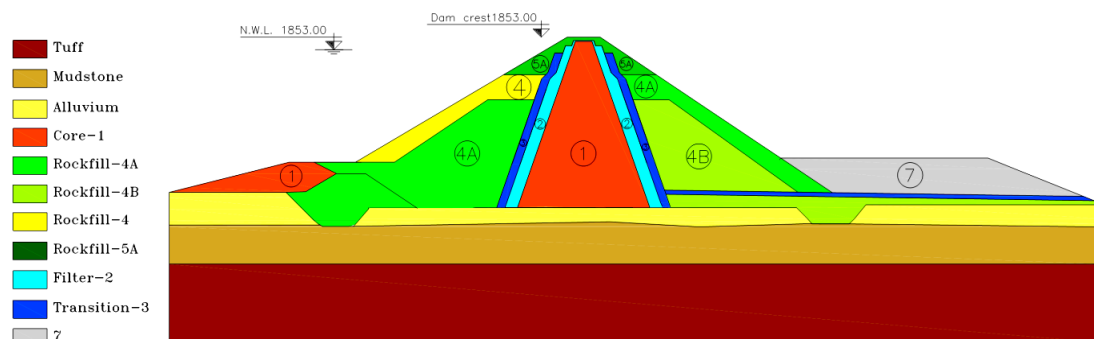


Fig 1. Typical cross section of Ghoocham dam

3. FOUNDATION AND DAM BODY MATERIAL

3.1. OVERBURDEN AND FOUNDATION

The overburden of Ghoocham site with 4-14 m thickness consists of alluvial, slopewash and residual soils. The type of soil is majority silt, clay with a thin layer of sand and gravel. The Consistency of overburden is classified as stiff to hard based on standard penetration test (SPT). A complete set of site and laboratory tests have been performed on these materials. Summary of overburden material parameters is shown in table 1.

Table 1. Geomechanical parameters of overburden.

Materials	d (kg/m ³) γ	E (MPa)	ν	C (KPa)	ϕ	k (cm/sec)
Alluvium	1800	10 - 40	0.25	34	19	3×10^{-7}

Rock types of foundation at Ghoocham dam site are mudstone, tuff and weak conglomerate. The average of rock quality designation (RQD) of rock is 81. The different types of foundation rock parameters are shown in table 2. Based on this table, the cohesion of rock is 40-50 KPa, internal friction angle is 22-25 degree and deformation modulus ranges between 470-800 MPa. The permeability of the rock is around 3×10^{-7} cm/s.

Table 2. Geomechanical parameters of dam foundation.

Materials	d (kg/m ³) γ	E (MPa)	ν	C (KPa)	ϕ	k (cm/sec)
Tuff	2400	470	0.3	40	22	3×10^{-7}
Mudstone	2180	800	0.3	50	25	3×10^{-7}

3.2. DAM BODY MATERIAL

Clay material of central core has been obtained from 0.5-1.5 Km upstream borrow areas in dam reservoir. The core material is classified as CL based on unified classification, average PI of material is 22 and compacted with 2-3 percent moisture more than optimum water content. The maximum size of core material aggregates is 25 mm. fine and coarse filters at both upstream and downstream of core zone are processed from limestone quarry. D₁₅ of fine filter is 0.45 mm with 10 mm maximum size aggregate (MSA). The MSA of

coarse filter is 50 mm. The upstream outer shell zone (zone 4) and upper elevation shell (5A) are from limestone quarry. The other shell zones (4A & 4B) are andesite-bazalt type rock from basalt quarry. The layer thickness of zones 4, 4A and 4B is 60 cm. The maximum percent of passing sieve no.200 for zones 4 and 4A materials is 5 percent and for zone 4B material is 15 percent. The filling of shell zones has been done with wet procedure. A complete series of laboratory tests including large scale triaxial, shear and index tests performed on shell materials. Geomechanical parameters of different zones of dam body are listed in table 3.

Table 3. Geomechanical parameters of dam body

Materials	γ (kg/m ³)	ν	C (KPa)	ϕ	k (cm/sec)
Core	1650	0.35	41	28.8	4×10^{-7}
Filter & Drainage	1900	0.25	0	38	1×10^{-3}
Rock fill(4)	2150	0.25	38	43	1×10^{-5}
Rock fill(4A)	2150	0.25	0	43.2	1×10^{-5}
Rock fill(4B)	2150	0.25	0	43.2	1×10^{-5}
Rock fill(5A)	2150	0.25	38	43	1×10^{-5}
Zone7	1900	0.25	30	30	1×10^{-5}

Adequate information on dynamic soil properties, including dynamic shear modulus, damping ratio, pore pressure response and cyclic strength, are more essentially considered in ground response and soil–structure interaction problems. Dynamic behaviour of soils under cyclic load is different from static behaviour. The soils have a non-linear behaviour under cyclic load. As shown in Fig. 2 the shear modulus (G_{max}) of soil in cycle number 1 is decreased to (G_1) and (G_2) in cycle number 2 and 3 [1-2]. An accurate dynamic analysis needs to obtain the soils parameters such as shear modulus, damping and etc. The shear modulus can be determined from field measurement techniques, such as down-hole, up-hole, cross-hole, seismic refraction surveys or from the tests such as resonant column and ultrasonic wave propagation in the laboratory. Cyclic triaxial, cyclic simple shear and hollow cylindrical simple shear tests on the other hand, are suitable for the strain levels on the order of 10^{-3} to 10^{-2} [1]. Many researchers have suggested equations based on laboratory and field measurements, to evaluate the maximum shear modulus [1-3-4]. Table 4 shows the equations which used in this paper to calculate the maximum shear modulus of dam body and foundation. Dynamic response of earth and rock fill structures is very dependent on an amount of energy internally dissipated through the soil during shaking. This mechanism of energy dissipation is commonly referred to as damping. Damping in soil is caused by viscous properties and plastic deformation during the shaking and it is to cause energy losses of dynamic load. In general, the initial damping ratio of soils material is assumed between 2% to 5%.

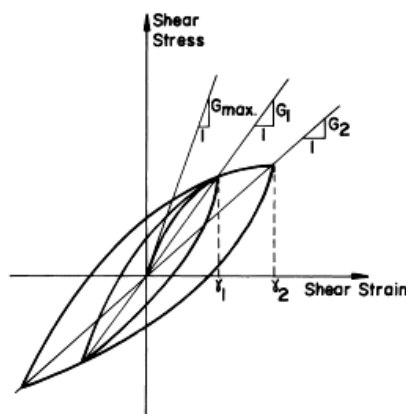


Fig 2. Nonlinear cyclic stress–strain relationship of soils [1]

Table 4. Maximum shear modulus equations of materials

Materials		Shear Modulus
(1)	Rockfill	$G_{max} = 13000 \frac{(2.17-e)^2}{1+e} \times (\sigma'_{ave})^{0.55}$ [3]
(2)	Core	$G_{max} = 3270 \frac{(2.97-e)^2}{1+e} \times (\sigma'_{ave})^{0.5}$ [3]
(3)	Filter & Drainage	$G_{max} = 220 \times 60 \times (\sigma'_{ave})^{0.5}$ [4]
(4)	Alluvium	$G_{max} = 220 \times 90 \times (\sigma'_{ave})^{0.5}$ [4]

4. NUMERICAL ANALYSIS

Numerical analyses were conducted using the finite difference program FLAC^{2D} based on a continuum finite difference using the Lagrangian approach. The maximum cross section of the dam was selected to analyze. Fig. 3 shows the finite difference mesh of Ghoocham dam. The boundary condition of the model is fixed at the base at which the seismic loading is applied, and is free field at laterals to prevent wave reflection from the sides. Kuhlmeier and Lysmer (1973) showed that for an accurate representation of the wave transmission through the soil model, the spatial element size ΔL, must be smaller than approximately one-tenth to one-eighth of the wavelength associated with the highest frequency component of the input wave [5]. In the numerical model the element size is about 2m.

$$\Delta L \leq \lambda/10 \tag{1}$$

λ is the wave length associated with the highest frequency component that contains appreciable energy.

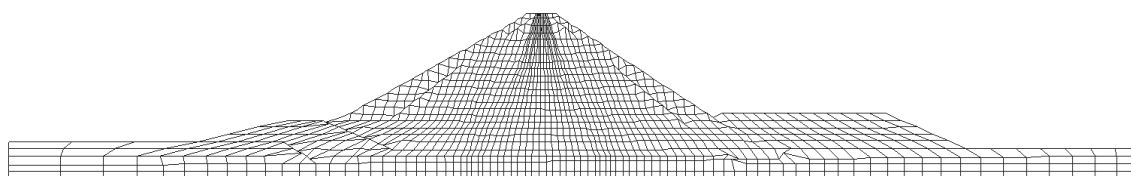


Fig 3. Finite difference mesh

The initial condition of stress and pore pressure is performed for the steady state condition. The steady state condition is reached after a layer by layer construction analysis by a combination of non-linear elastic Duncan and Chang model and elastic-perfectly plastic Mohr-coulomb constitutive model following by an impounding analysis [6]. The nonlinear stress-strain behavior of materials can be represented more accurately by cyclic nonlinear models that follow the actual stress-strain path during cyclic loading. After completion of the static stages, the dynamic analyses were performed. The elasto-plastic model (Mohr-Coulomb) was used for all materials incorporated in of the dam body. These analyses were performed for maximum credible earthquake (MCE) by two acceleration time histories, Khoorgo and Cape Mendocino with the maximum peak ground acceleration of 0.47g with the duration of 41 and 36 sec. The acceleration time histories of the earthquakes are illustrated in Fig. 4 and Fig. 5.

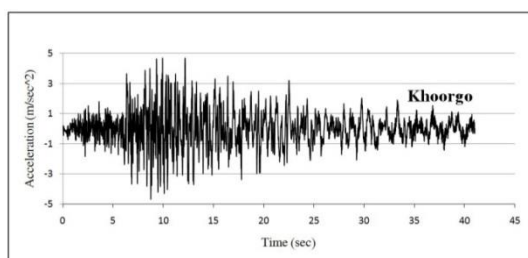


Fig 4. Khoorgo input acceleration time history

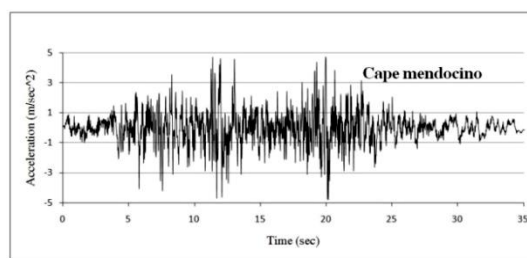


Fig 5. Cape Mendocino input acceleration time history

To dynamic analysis of dam needs to calculate the shear modulus and damping. Many researchers have been proposed equations and curves to estimate the shear modulus and damping based on shear strain [4-7]. In the first step, the analysis was done by elastic model and the shear modulus and damping was assumed as table

4 and 5%, respectively. The maximum shear strain of each element was recorded during the analysis and the shear modulus and damping ratio are updated with respect to the maximum shear strain of each element. In this paper was used the curves proposed by Seed et al. 1984. Fig. 6 shows the shear modulus and damping ratio curves. This procedure was repeated until the shear strain converged to a constant value. In final step, the analysis was conducted by elastic-perfect plastic Mohr-Coulomb constitutive model and final shear modulus and damping to estimate permanent deformation in dam body.

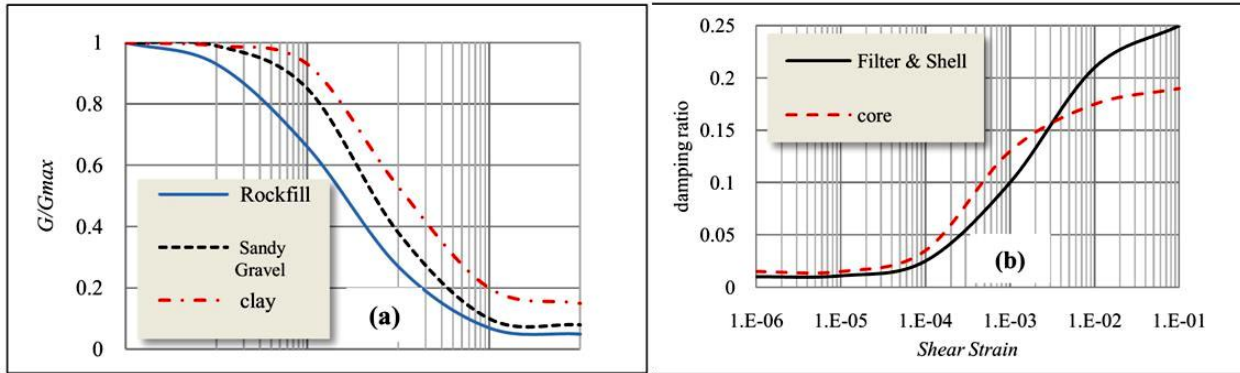


Fig 6. a) shear modulus curves of dam body materials, b) damping ratio curves of dam body materials

Dynamic loading from an earthquake changes the stress states within an embankment, causing permanent deformation. The maximum displacement vector of Khoorgo earthquake is illustrated in Fig. 7 and it is equal to 1.155 m. As shown in Fig. 8 and Fig. 9 the maximum vertical and horizontal displacements at the end of Khoorgo earthquake are 1.1 m and 60 cm, respectively. Fig. 10 shows the dam crest acceleration history. As shown the maximum crest acceleration is 5.96 m/s^2 equal to 1.29 resonance coefficient.

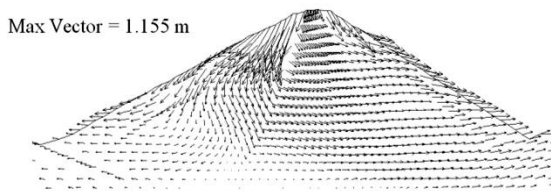


Fig 7. Maximum displacement vector of Khoorgo earthquake

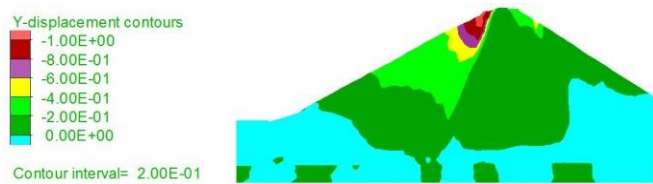


Fig 8. Vertical displacement contours of Khoorgo earthquake

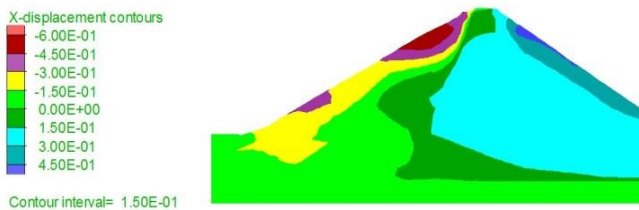


Fig 9. Horizontal displacement contours of Khoorgo earthquake

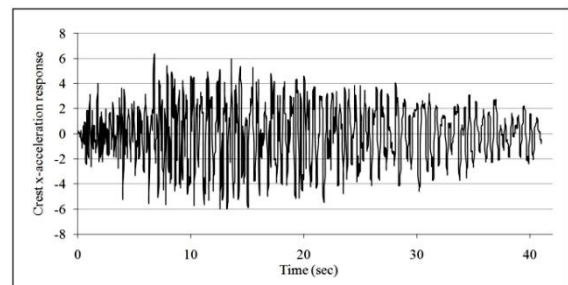


Fig 10. Crest acceleration time history of Khoorgo earthquake

Fig. 11 shows the maximum displacement vector of Cape Mendocino earthquake and it is equal to 0.582 m. As shown in Fig. 8 and Fig. 9 the maximum vertical and horizontal displacements at the end of Cape Mendocino earthquake are 55 cm and 35 cm, respectively. Fig. 14 shows the dam crest acceleration history. As shown the maximum crest acceleration is 5.2 m/s^2 equal to 1.14 resonance coefficient.

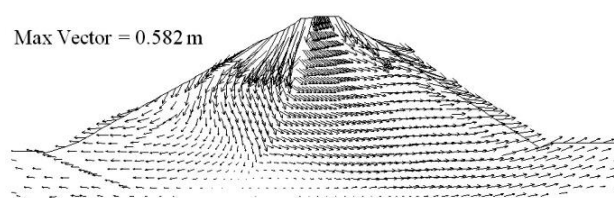


Fig 11. Maximum displacement vector of Khoorgo earthquake



Fig 12. Vertical displacement contours of Khoorgo earthquake



Fig 13. Horizontal displacement contours of Khoorgo earthquake

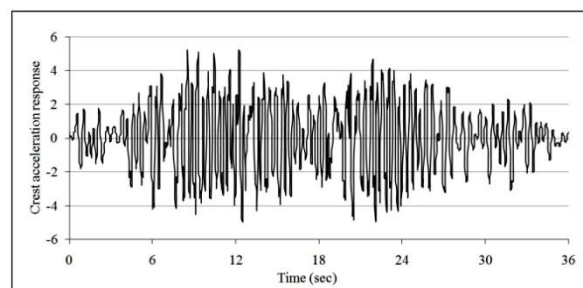


Fig 14. Crest acceleration time history of Khoorgo earthquake

5. CONCLUSIONS

This paper presents nonlinear dynamic behavior of rockfill dams using finite difference method. A simple elastic-perfectly plastic constitutive model with Mohr-Coulomb failure criterion is used to describe the stress-strain response of the soil. The analysis was done by earthquake loading condition for MCL by two acceleration time histories, Cape Mendocino and Khoorgo earthquake with the peak ground acceleration of 0.47g. Based on engineering codes such as ICOLD, USBR and DSOD a general criterion to evaluate damage to embankment dam is the proper continuity and workability of different part of dam such as filters, core, freeboard and etc. after the earthquake. The analysis results show maximum displacement of Khoorgo and Cape Mendocino earthquake are 1.15 m and 58 cm. The upstream and downstream filters are first line of defense against leakage through the dam. The results show the deformation in filters zones is quiet small therefore, the continuity of filters is appropriate. Regarding analysis results, the maximum settlement in dam body is 1 m therefore, the height of freeboard (3m) is adequate. As a conclusion, the non-linear dynamic analysis of Ghoocham dam shows after the earthquake performance of different parts of dam is suitable.

6. REFERENCES

1. Yener Ozkan. M. (1998), "A review of considerations on seismic safety of embankments and earth and rock-fill dams," Soil Dynamics and Earthquake Engineering, 17, PP. 439–458.
2. ABOUSEEDA. H. and DAKOULAS. P. (1998), "Non-linear dynamic earth dam-foundation interaction using a BE-FE method," Earthquake Engineering & Structural Dynamics, 27, PP. 917–936.
3. Kokusho, T. and Esahsi, Y. (1982), "Cyclic triaxial testing on sands and coarse materials," Proc. 10th Int. Conf on Soil Mechanics and Foundation Engrg., 1, PP. 673–676.
4. Seed, H. B., and Idriss, I. M. (1970), "Soil Moduli and Damping Factors for Dynamic Response Analysis," Earthquake Engineering Research Center, University of California, Report No. EERC 75-29.
5. Kuhlmeier, R. L. and Lysmer, J. (1973), "Finite Element Method Accuracy for Wave Propagation Problems," J. Soil Mech. Foundations Div., ASCE, 99(SM5), PP. 421–427
6. Duncan, J.M., and Chang, C. Y (1970), "Nonlinear analysis of stress and strain in soil. Journal of the Soil Mechanics and Foundation Division," ASCE, Vol. 96. No. SM5, PP. 1629-1653.
7. Seed, H.B., Wong, T.W., Idriss, I.M. and Tokimatsu, K. (1986), "Moduli and damping factors for dynamic analyses of cohesionless soils," J. Geotechnical Engrg., ASCE, 112(11), PP. 1016–1032.

Seismic Performance Evaluation of Salman Farsi Dam with Considering the Influence of Sediment

Sahar Rezaei Koujani¹, Zahra Heirany²

1-Dept. of Civil Engineering, Islamic Azad University, Estahban Branch, Estahban, Iran

2-Dept. of Civil Engineering, Islamic Azad University, Parand Branch, Parand, Iran

Emails: rezaei.sr@gmail.com, zheirany@yahoo.com

Abstract

In this study, a three-dimensional finite element software was used to investigate a concrete arch gravity dam through a nonlinear time history analysis method. The system is subjected to a scaled horizontal component of Manjil earthquake accelerogram and decreasing coefficient of 0.1 and 0.6. The lake is modeled with Eulerian elements and nonlinear effects of dam body are included. Besides, the effects of existing interactions between dam, sediment and lake are also considered. The analyses were done at sediment heights of 0, 2, 5, 10, 25, 50 m under reservoir conditions at normal water levels of 60 m and without water. The results showed that low earthquake accelerograms reduced displacement of dam body. The results indicate that low height sediments in the reservoir could initially increase displacement of dam body, however, as the height of sedimentation is increased, displacements will be reduced.

Keywords: Nonlinear dynamic analysis, Concrete arch gravity dam, Finite element software.

1. INTRODUCTION

Given the importance of dam safety during earthquakes, investigation of seismic behavior of concrete dams and their seismic safety assessment has been attracted many researchers; because destruction of these structures caused by earthquakes can have adverse economic and social consequences. One of the most important issues affecting the seismic behavior of dams is dam-reservoir-sediment interaction. In addition to the hydrostatic pressure, the interaction of dam and reservoir produces hydrodynamic pressure, as well. The hydrodynamic pressure is caused by dam movement and the force is imposed by dam on the reservoir. Similarly, sedimentation increases the inertia imposed on dam due to the displacement of water and soil particles. Considering such effects, it is clear that precise seismic analysis of dams is a complex process.

Amin Mahmoudi, Mohammad Reza Gholami and Morteza Asadollahi (2015) investigated the effects of increasing the height of sediments inside the reservoir on stability of a concrete gravity dam using CADAM software and concluded that as sediments increase, stability decreases. Changing drainage heights, however, it was observed that the best point for drainage ditch is 50 meters from the heel [1].

Sadeghioun et al (2015) examined sediments of Salman Farsi Dam reservoir hydraulically. In this research, the sediment volume deposited in the reservoir of Salman Farsi Dam located in Fars province was calculated using Karoon92-salam software. The amount of sediment at Salman Farsi Dam site was estimated 10.8 MTPA (million tons per annum) and total sediment volume deposited in the reservoir during the 50-year period was estimated at 540 MTPA [2].

Ghaemian et al (2015) surveyed seismic analysis of a concrete gravity dam taking into account the effect of sediment layers using finite element method. In this study, the interactions between components of concrete dam system were evaluated. Researchers mainly emphasized on the effects of sediment layer on dam response, to this end, the developed model was analyzed at different heights of sediment layer from various types using ABAQUS software. The results of analysis suggested that not only the type but also elevation (height) of sediment layer affects concrete dam response. Thus, both effects of type and height of sediment layer must be included when it analyzes concrete dam system [3].

Seyfi et al (2016) studied the influences of sedimentation inertia on seismic performance of a concrete gravity dam with regards to the impact of interactions. To examine seismic behavior, sedimentation of the reservoir floor was modeled regarding to equivalent fluid pressure assumption. Considering the complexity of dam-reservoir-foundation-sediment system, finite element method was used for modeling and analysis as it is suited to apply different boundary conditions. To perform the seismic analysis of the system, a finite element model was developed using ANSYS software. When extracting domains governing equations, the effects of interactions between dam, reservoir, foundation and sediment were included in the model and various boundary

conditions were foreseen to be imposed on the system. Further, time domain analysis was employed in terms of dynamic stimuli and then Newmark's method was used to solve dynamical equations, that are an unconditionally and numerically stable technique. To demonstrate the impacts of sedimentation inertia on seismic response of a concrete gravity dam, Pine Flat Dam was selected as a case study and 20 El Centro earthquakes accelerogram was applied as simulating seismic input. The developed model was analyzed and compared in two states of reservoir without sediment and with a volume percentage of sediment. According to the results of analyzes, the inertia of sediment deposited in the reservoir increased seismic response of concrete gravity dam [4].

Garci et al (2014) examined geometric properties of the reservoir and their effect on seismic performance of arch dams using finite element method. It was determined that smaller reservoirs decreased dam response and deformations of the crest of the dam depend on the reservoir geometry in the upstream face and sediments of the floor [5].

Sharafi and Mohammadi (2016) evaluated occurrence of damage mechanisms in Karun-3 Dam. In this study, the impact of earthquake accelerograms on seismic behavior of the concrete arch dam was investigated. In this regard, Karun-3 concrete arch dam was modeled and simulated in ABAQUS finite element software and accelerograms of Tabas and Northridge earthquakes were imposed on it, where the model was subjected to hydrodynamic pressures caused by fluid. The results indicate that major damages were imposed on Karun-3 dam by Tabas earthquake. The reason is simply that this earthquake is much stronger than the other. Upstream face and crest of the dam were seriously damaged and cracked [6].

Rezaei and Heirany (2017) surveyed the evaluation of seismic behavior of arch concrete dams including the effects of reservoir conditions using finite element method. The results indicate that low height sediments in the reservoir initially increased displacement of dam body; however, as the height of sedimentation is increased, displacements will be decreased [7].

2. ASSUMPTIONS

In this section, structural and hydrodynamic considerations of the problem are formulated. Then, the effect of sediments deposited in the reservoir as elastic solids on the reservoir is demonstrated. At the same time, the water inside the reservoir is assumed to be a non-sticky, incompressible fluid with small displacements. The dam is also considered as a solid plastic damage model. Eulerian-Lagrangian formulation method was employed to solve the water-structure interaction problems. In this method, hydrodynamic pressure of the reservoir is imposed on the dam as an equivalent nodal force. This technique was performed due to the importance of fluid behavior and pressure parameters in dam modeling [8].

3. GOVERNING EQUATIONS

The equation governing dam behavior is called equation of motion. To take into consideration and define the fluid-structure interaction, however, the load applied by fluid's hydrodynamic pressure to the point where structure and fluid meet must be added to the structural equations.

$$M\ddot{u} + C\dot{u} + Ku = M\ddot{u}_g + F^{PF} \quad (1)$$

Where, M represents mass matrix, C is damping matrix and K structural stiffness matrix. In addition, u is relative displacement vector, \dot{u} is the velocity vector, \ddot{u} is the structural motion acceleration vector, \ddot{u}_g ground acceleration vector and F^{PF} is the hydrodynamic pressure vector loaded from the reservoir on the dam at contact point.

4. MODEL ANALYSIS

To perform the seismic analysis of the concrete arch gravity dam, ABAQUS software was used. This software is suited for seismic analysis taking into account the irregular geometry of domains and reservoir-dam interaction effects. The effects of surface water waves are neglected due to the depth and high elevation, instead the effects of dam-reservoir-sediment interaction are considered. Given the conditions governing the behavior of concrete arch gravity dam and geometric shape of the reservoir, dam model developed here was deemed as a simplified three dimensional model and the effect of interaction with foundation were eliminated. The 8-node 6-face brick element (C3D8R) was employed to perform dam body and sediment finite element model. To mesh the reservoir, Eulerian's flowing elements (EC3D8R) was used which are suited for modeling water.

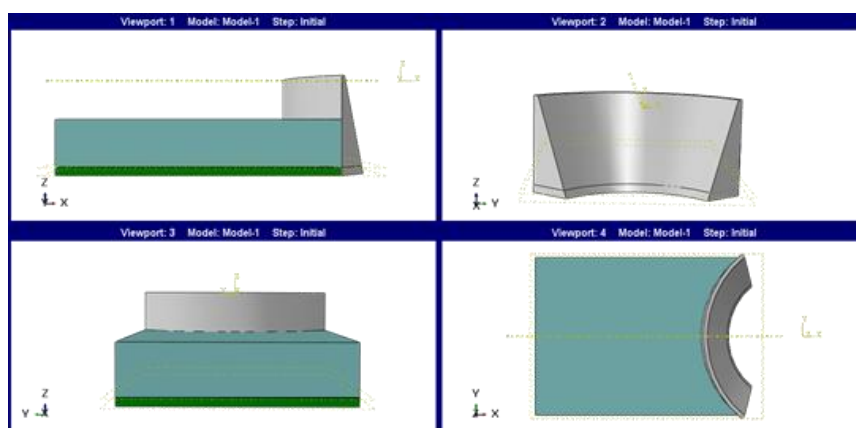


Figure 1. The model designed in the software

In order to demonstrate the capability and applicability of the model provided while investigating the seismic behavior of a concrete arch gravity dam located in seismically active regions, Salman Farsi storage dam (Ghir) was chosen to be studied which is located 180 km south of Shiraz and about 20 km northeast of Ghir town in Mond watershed areasouthwest of Shiraz built on Qare Aqaj River in a place called Tang Karzin with a watershed area of 11800 km². Geographically, dam limits chosen in this study is between 28° 30' and 28° 45' eastern longitude and 53° 20' north longitude. The bed level f the dam is 833 m above the free water level and is defined parabolically in the plan. The height of the dam from the base is 125 m and crest central brink has a 7-meter thickness. Dam's height at the lowest level is 58 m upstream and that makes' the dam look like a vertical cylinder. The radius of the dam is 175 m with an angle of 105° and the length of dam's crest is 320 m.

It should be noted that the materials used to construct the dam is concrete with a density of 2400 kg/m³, an elastic modulus of 27 GPa, a Possion coefficient of 0.29 and deflection angle of 36°. Assuming solidity of sediment in the reservoir, density of sedimentation is 1300 kg/m³, Possion coefficient is 0.2 and elastic modulus is equal to 20 GPa. Moreover, the water stored in the reservoir has a density of 1000 kg/m³, dynamic viscosity of 0.001 Ns/m³, and the fluid sound velocity is 1500 m/s. In order to perform the analysis process, scaled horizontal accelerogram of Manjil earthquake was applied.

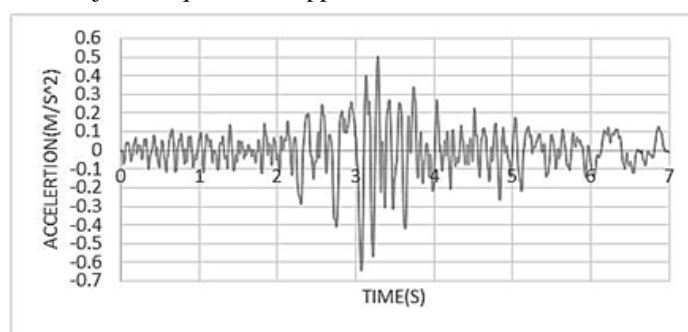


Figure 2. Manjil earthquake scaled horizontal accelerogram (PGA0.5)

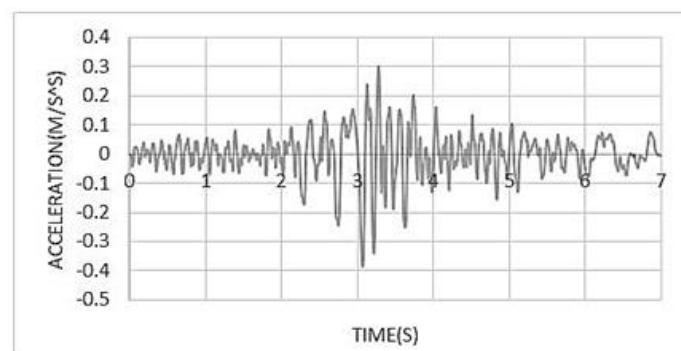


Figure 3. Manjil earthquake scaled horizontal accelerogram and decreasing coefficient of 0.6 (PGA0.3)

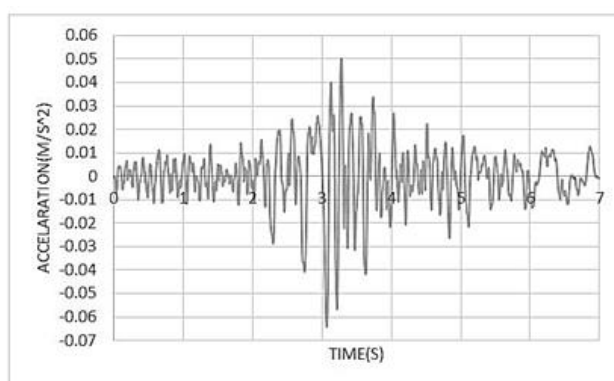


Figure 4. Manjil earthquake scaled horizontal accelerogram and decreasing coefficient of 0.1 (PGA0.05)

Riley's damping method was used to apply the damping coefficients. Further, the Sommerfeld method was used to measure reservoir's far-reaching boundary conditions where time step of $\Delta t = 0.02$ is considered. The non-massive foundation and dam-sediment interaction were employed in the analyzes. According to the research, it is clarified that dam's seismic response is affected by the amount and volume of sediment deposited in the reservoir.

To investigate the exact dynamic behavior of a concrete arch gravity dam, a through model was developed in this study. Dynamic analysis was carried out through a time-domain model. To this end, various boundary conditions such as nodal displacements and nodal forces can be regarded in the finite element model proposed. The interaction between domains of dam, reservoir and sediment is well predicted in the model. Regarding the selection of finite element method and its capabilities, complicated geometries can be studied by the model provided. The interaction between dam and foundation was eliminated in this study.

5. CONCLUSIONS

After modeling and dynamic analysis completed, the results of responses to displacements and stresses imposed on the dam body were extracted. Considering that the main objective of this study was to investigate the effect of sediment on seismic performance of Salman Farsi concrete arch gravity dam, the model was analyzed at 6 different sediment heights of 0,2,5,10,25 and 50 m at two reservoir heights of 60 applying Manjil earthquake scaled horizontal accelerogram and decreasing coefficient of 0.1 and 0.6 and the results were represented as time history (results of horizontal displacement of the dam crest center from the ground).

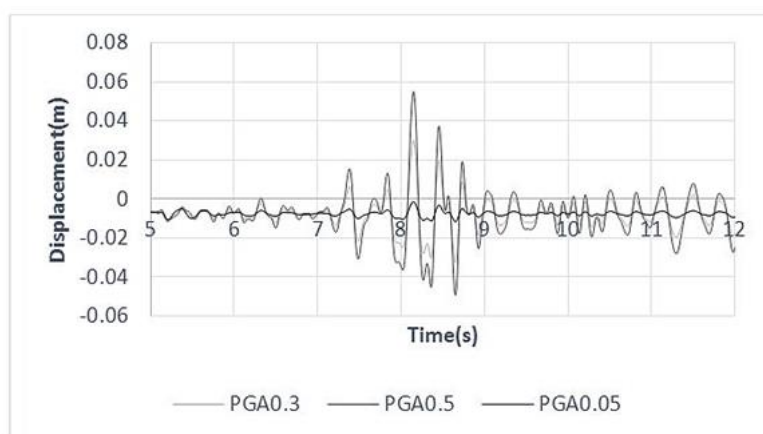


Figure 5. Displacement of the node in the dam crest center from the ground in the empty reservoir state

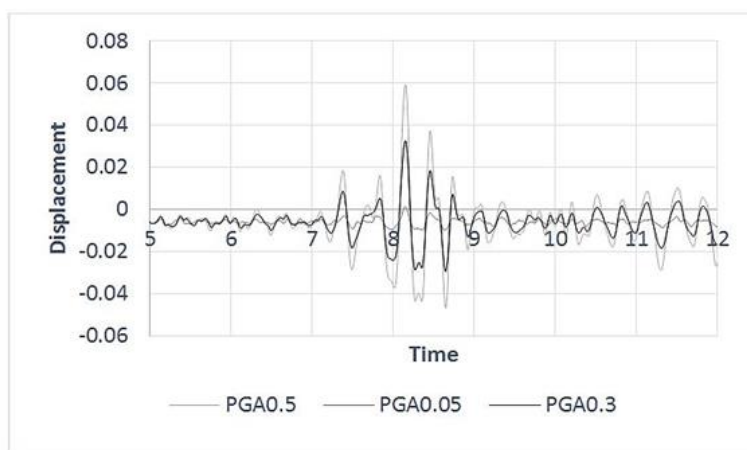


Figure 6. Displacement of the node in the dam crest center from the ground with a water depth of 60 m

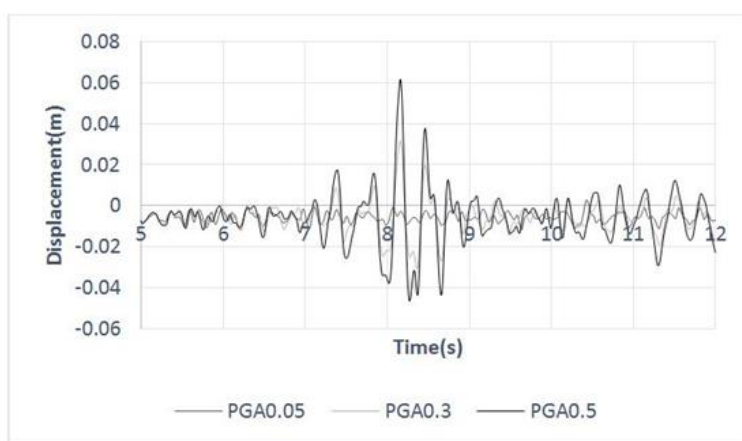


Figure 7. Displacement of the node in the dam crest center from the ground with 60-meter water depth and 2-m sediment height

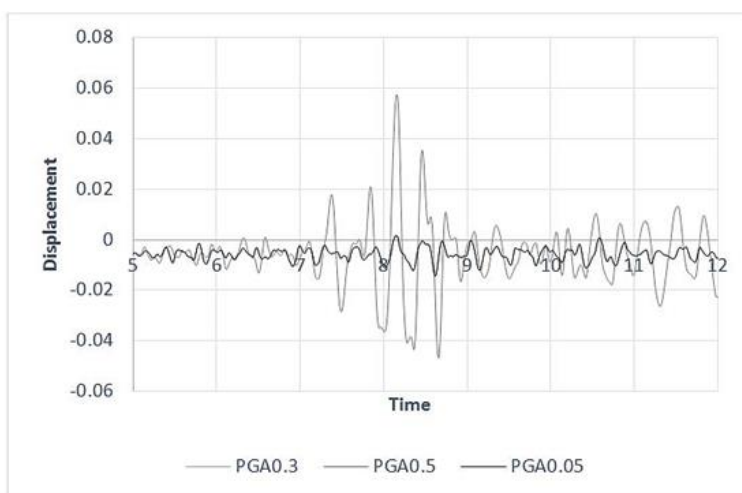


Figure 8. Displacement of the node in the dam crest center from the ground with a water height of 60 m and a sediment height of 5 m

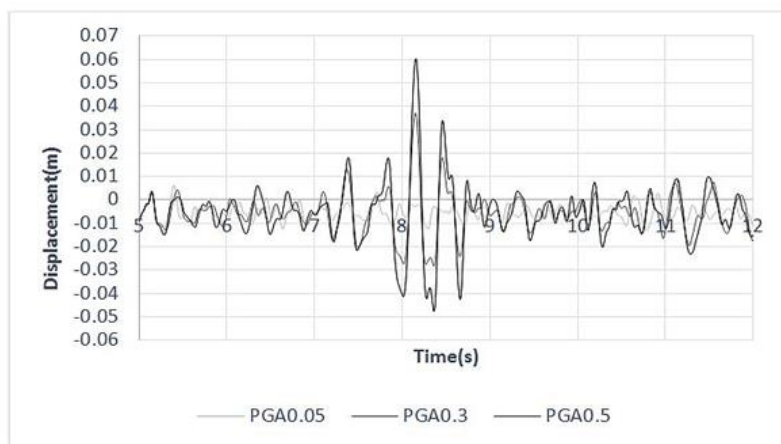


Figure 9. Displacement of the node in the dam crest center from the ground with the water height of 60 m and a 10-m sediment height

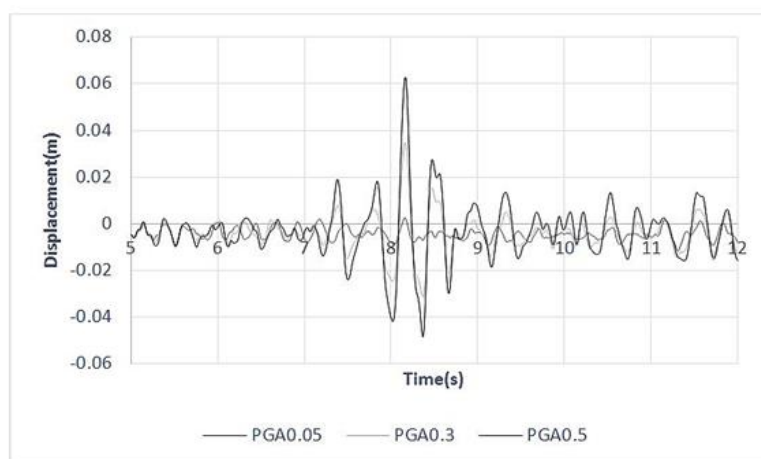


Figure 10. Displacement of the node in the dam crest center from the ground with the water height of 60 m and a 25-m sediment height

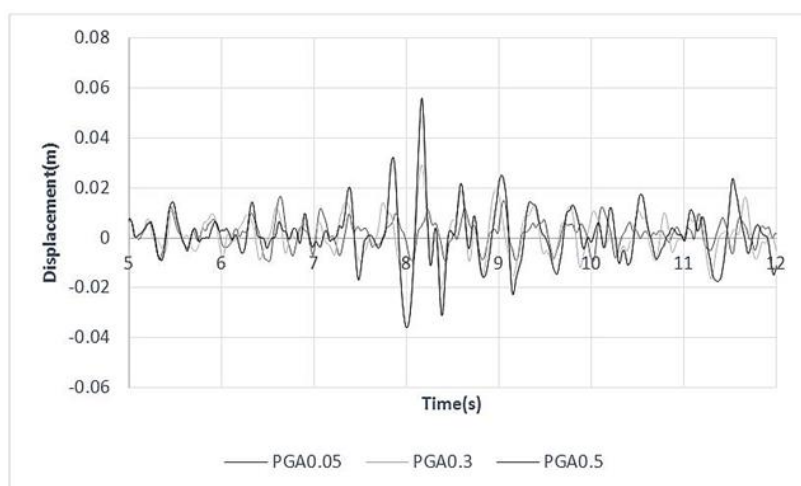


Figure 11. Displacement of the node in the dam crest center from the ground with the water height of 60 m and a 50-m sediment height

In order to reach precise results in this study, 12 models representing sediment height changes with water level of 60 was employed the last of which is performed with a 50-m sediment height. In real situation,

such volume of sediment in the reservoir damages the operational ability of the dam and it is only used here to obtain more accurate results. As observed in Figures 5 to 11, low earthquake accelerograms, displacements will be lowered in the center of the crest. The results indicate that the acceleration of the earthquake mapping increases, the damage to the dam will also be greatly increased. The results indicate that low height sediments in the reservoir initially will increase displacement of dam body, however, as the height of sedimentation increases, displacements will reduce.

6. REFERENCES

1. Mahmoudi, A., Gholami, M., and Asadollahi, M. (2015). "*Effect of increasing the height of sediments inside reservoir on stability of concrete gravity dam using CADAM software.*" 14th Hydraulic Conference of Iran, Zahedan.
2. Molazadeh Sadeghioun, A., Derakhshan Alamdarloo, P., and Azizian, G. (2015). "*Hydraulic survey of sediments in dam reservoir (case study: Salman Farsi Dam).*" 14th Hydraulic Conference of Iran, Shahid Nighbakht Engineering School, Zahedan.
3. Ghaemian, M., Rouh Zamin, A., and Sotoudeh, P. (2015). "*Seismic analysis of concrete gravity dam considering the effect of sediment layer using finite element method.*" 10th International Congress on Civil Engineering, Faculty of Civil Engineering, Tabriz.
4. Seyfi, L., Khiavi Pasbani, M., and Ali Ghorbani, M. (2015). "*Effect of sediment inertia on seismic response of concrete gravity dam using finite element method.*" Journal of Dam and Hydroelectric Power Station. Vol. 2, No. 4, pp. 34-45.
5. Garcia, F., Aznarez, J., Cifuentes, H., Medina, F., and Maeso, O. (2014). "*Influence of reservoir geometry and conditions on the seismic response of arch dams.*" Soil Dynamics and Earthquake Engineering, Vol. 67, pp. 264-272.
6. Sharafi, H., and Mohammadi, H. (2016). "*evaluated damage occurrence mechanisms in Karun-3 Dam.*" The 3rd International conference on science and engineering. istanbul-turkey.
7. Rezaei kojani, s., Heyrani shabani por, z. (2017). 4th Comprehensive Conference on Disaster Management &HSE. Tehran University, pp. 141.
8. Soroushnia, S., Najafi, H., Mamaqani, M., and Mehrvand, M. (2016). "*ABAQUS most complete reference.*"

Assessment of Newmark Methods for the Prediction of Deviatoric Displacement of Earth Dams Using Energy Approach

Reza Karimi Moghadam¹, Mohammad Hassan Baziar²

1- M.sc. Graduated Student, School of Civil Engineering, Iran University of Science and Technology, Tehran, Iran

2- Professor, School of Civil Engineering, Iran University of Science and Technology, Tehran, Iran

Email:baziar@iust.ac.ir

Abstract

In this research, permanent earthquake-induced deformations of earth dams using Newmark methods are investigated. For this purpose, the errors of all sliding block methods for the prediction of the permanent deformation of 25 real earth dams are discussed in the time domain. Also, the importance level of some related parameters, discussed by previous studies, is scrutinized using energy approach. The results of the study revealed that, the energy value, related to the velocity time history, not only acts as a separator parameter between conservative and non-conservative predictions of sliding block methods but also has a significant impact on the prediction of permanent earthquake-induced deformations of earth dams.

Keywords: Energy Approach, Earth Dams, Newmark Methods.

1. INTRODUCTION

Since Newmark's 1965 rankine lecture[1], prediction of the earthquake-induced permanent deformation of earthen structures using sliding block method has been discussed by many researchers. Many investigators, taking different approaches, further modified Newmark model. All the methods proposed by different researchers can be categorized in two classes of "the methods which do not consider the sliding block response (Rigid approach)" and "the methods which consider the sliding block response (Decoupled and Coupled approaches)". Advantages and disadvantages of each approach have been discussed by previous studies in detail.

Bray and Rathje [2] indicated that the results of the original method led to non-conservative predictions when the fundamental period of the system is close to the mean period of the acceleration time history. On the other hand, this approach resulted in conservative predictions for large values of period ratio (for example $T_s/T_m = 4$). In addition, when yield acceleration is greater than PGA, the estimated deformation using rigid approach inherently is equal to the zero. Although decoupled approach eliminated some deficiency of rigid approach, it has its own disadvantages. The results of the study by Kramer and Smith [3] revealed that the decoupled approach estimated very conservative results when T_s/T_m ratio was less than one. Lin and Whitman [4] studied the decoupled approximation using a lumped mass shear beam model with linear elastic material properties. They analyzed shallow, deep, and intermediate sliding systems. They indicated that at k_y/k_{max} value of 0.5 and material damping ratio of 15%, the decoupled approximation overestimated the exact displacement, (exact displacement obtained from coupled approach) by an average of 20%. However, this finding did not indicate that the decoupled approach was always conservative. Moreover, they did not investigate when k_y/k_{max} exceeded 0.5, how would be the calculated displacement. However, Rathje and Bray 1999 [5] concluded that the above conservatism decoupled approximation was right only for small ratio of k_y/k_{max} (for example $K_y/K_{max}=0.6$) and T_s/T_m of less than 2. Furthermore, for large values of k_y/k_{max} or T_s , prediction of decoupled approximation may be non-conservative. Nevertheless, for large values of both ratios, it is expected that the calculated permanent deformations, using both coupled and decoupled approaches, are naturally small. Bray and Rathje [6] also indicated that nonlinearity of slippage behavior is more important than nonlinearity of material behavior in the cases of T_s/T_m less than one. On the other hand, for large values of T_s/T_m , the nonlinearity of material behavior can have significant impact on the permanent displacement prediction using coupled approach. Such nonlinearity also can cause an increase in the fundamental period of the system due to decrease in the shear modulus of material. Hence, Bray and Travarasrou [7] used $1.5T_s$ instead of T_s for the development of a new nonlinear coupled method by running 55000 analysis and using 688 records related to 41 earthquakes. Then, they calibrated their model using 16 case studies. Their method eliminated almost all the deficiencies of previous methods.

More recently, Garini et al.[8] studied rigid sliding block system under near-field motions by discussing the sequence of high-duration pulses importance. Afterward, Voyagaki et al. [9] by applying near-field normalized pulses on sliding block system concluded that for constant values of PGA and material shear strength, existence of half-cycle pulse may result in larger permanent deformation compared to full-cycle pulse. This conclusion contradicted the common understanding, such as e.g. Yegian et al. [10]. Later, Gazettas et al. [11], applied number of records containing forward directivity and fling step effects on sliding system and discussed slip nature and its relation with PGV, dominant period of the velocity pulse and polarity of velocity pulse. They also indicated that vertical component of the applied strong motion had no significant effect on the sliding systems. It is worth noting that, researchers such as Franklin and Chang [12]; Yegian et al. [13]; and Kramer and Lind wall [14], have previously mentioned some of these finding. Following previous studies, Garini and Gazettas [15] indicated that the damage potential of the near-field strong motions may be much greater than what was previously considered. So, they defined an upper bound for deformation of rigid sliding systems under near-field ground motions. However, the accuracy of this method was not examined using real case studies.

However, some other studies such as Meehan and Vahedifard [16], which discussed performance of the methods using case studies, indicated that some developed methods (which did not include Garini and Gazettas method[12]) may underestimate results despite their complexity in calculation and analysis, especially for large values of occurred deformations. However, none of these type of studies introduced a clear separator parameter for the definition of a boundary between conservative and non-conservative predictions in time or frequency domains.

In the present study, the calculated deformation obtained by Newmark methods, for ten real cases are discussed in detail. In order to achieve this goal, all the Newmark methods were classified in two groups: 1-Methods which do not consider response of sliding system (the methods which are derived from rigid approach)& 2-Methods which consider response of sliding system (the methods which are derived from decoupled and coupled approaches). Then, a total of 10 earth dams, which experienced known amount of displacements during a known earthquake, were selected. The strong motions used for analyzing the earth dams were the same recorded motion at the dam site. All the required parameters including yield acceleration, PGA, PGV, Arias Intensity, Initial fundamental period (Ts), earthquake Magnitude, Distance between site and energy source, Sa(1.5Ts) and etc. for calculation of the permanent deformation of the earthen structures using all the simplified and rigorous Newmark methods were obtained directly for each case. The permanent deformation of these case studies were estimated by 32 values of 26 methods. The predicted values were compared with deviatoric deformation of the recorded cases to determine conservative and non-conservative method. So, the error between predicted and observed deformations for each method has been discussed in time domain for this group of case studies and consequently, an effective parameter has been introduced. Finally, for the sake of checking the results of Group 1, a total of 15 earth dams, included in Group 2 of earth dams, have been analyzed using sliding block methods. The necessary parameters for analyzing Group 2 of case studies, mainly have been obtained from previous studies and attenuation relationships. The results of Group 2 have confirmed the conclusions made for the analysis of Group 1.

2. DISCUSSION OF FUNDAMENTAL CONCEPTS

2.1. NEWMARK FAMILY METHODS

All the Newmark methods are categorized and introduced in tables 1, 2. As indicated, 32 predicted values resulted from 26 (rigorous and simplified) methods within two categories are discussed in this research.

Table 1. List of the methods which do not consider response of sliding block system

1.Rigorous Method (Newmark 1965)	2.Newmark Simplified (mean): by Newmark	3.Newmark Simplified (mean): by Cai 1996
4.Franklin & Chang- (Whitman & Liao 1977)	5.Ambraseys & Menu (Median) 1988	6.Jibson et al (1993)
7.Jibson et al 1998 & 2000	8.Jibson et al (2007) (a)	9.Jibson et al (2007) (b)
10.Jibson et al (2007) (c)	11.Jibson et al (2007) (d)	12.Watson-Lamprey and Abrahamson(2006)
13.Saygili & Rathje (2008) (a)	14.Saygili & Rathje (2008) (b)	15.Saygili & Rathje (2008) (c)
16.Saygili & Rathje (UpperBound.)2009	17.Ebling (Mean) 2009	18.Rathje and Antonakos (PGA,M) a
19. Rathje and Antonakos (PGA,PGV)a	20. Garini and Gazettas 2012–Upper Boundb	
Methods 18 & 19 are unified methods. Initial values of these methods are estimated by method 16 and final values are obtained using decoupled approach.		
Method 20 is developed by applying Near-Field strong motions on rigid sliding system.		

Table 2. List of the methods which consider response of sliding block system

21, 23.Seed and Makdisi 1978 (Upper Bound & Lower Bound)	22.Seed and Makdisi 1978 (Mean: by Gazettas & Dakoulas 1992)
24.Hynes-Griffin & Franklin1984 (mean)	25.Bray 1998
26.Rigorous Linear Elastic Decoupled (Bray & Rathje 1999a)	27.Rigorous Equivalent Linear Decoupled (Bray & Rathje 1999a)
28.Rigorous Linear Elastic Coupled (Bray & Rathje 1999a)	29.Rigorous Equivalent Linear Coupled (Bray & Rathje 1999a)
30, 31, 32.Bray and Travasarou 2007 (Upper Bound, Mean and Lower Bound)	

2.2. YIELD COEFFICIENT(K_Y)

The pseudo-static analysis was applied in this study, for all methods, to obtain yield coefficient. The Morgenstern-Price's Method was used as a limit equilibrium method in pseudo-static analysis. All the properties of the dams are obtained from their real conditions during the earthquake and analysis were performed in total stress or undrained condition as recommended by Newmark [1]. Finally, due to the effects of cyclic loading, the yield acceleration, calculated by the pseudo-static analysis, has been reduced by 10 percent[17]. Therefore, all the yield accelerations used in this study were the theoretical yield accelerations that were obtained from the mentioned procedure and other type of procedures such as back-analysis and lab-tests were not considered in the present study.

2.3. OBSERVED DEVIATORIC DEFORMATION

Observed deviatoric deformations, including both deformations related to the sliding block movement on the inclined slip surface and also related to the volumetric contraction of sliding block, have been calculated in the present study for all cases by distributing the values of the observed max horizontal and max vertical deformations on the related inclined slip surface and then accumulating of distributed deformation. It is worth noting that the obtained deviatoric deformation by this procedure is mainly related to horizontal component of the observed deformations [18].

2.4. INITIAL FUNDAMENTAL PERIOD (T_s)

The expression of $T_s=2.6H/V_s$ has been used in order to estimate initial fundamental period of sliding block wedge. Note that H is the sliding block depth which the geometry of sliding block has been obtained by pseudo-static analysis, as mentioned in section 2.2. Therefore, the height of sliding mass when sliding is triggered is considered as H. In addition, V_s is the average shear wave velocity of the sliding mass.

3. DISCUSSION OF RESULTS:

The results of this study are presented in two parts of 3.1 and 3.2 for Group 1 and 2, respectively.

3.1. ANALYZING GROUP 1 OF CASE STUDIES (10 EARTH DAMS)

3.1.1. GROUP 1 OF CASE STUDIES

The Group 1 of case studies (table 3) includes 10 dams, all located up to 15 kilometers from the related fault, and were shaken with an earthquake of $M_w > 5.8$. In addition, none of these cases have experienced liquefaction or failure phenomenon during the related earthquake. In other words, all the displacements for the ten cases were related to the movement of sliding block wedge during related earthquake. Also, all the properties of these 10 dams such as recorded strong motion, material properties, geometry and etc. were precisely available. In other words, their deformations can be predicted using all the 26 methods (all the rigorous and simplified methods of tables 1 and 2) using precise parameters. For this group of case studies, all the required parameters such as yield acceleration, ground motion parameters and etc. were calculated in this study. The details of earth dams included in Group 1, are presented in table3.

Table 3. The detail of Group1 of case studies

Case No.	Case Name	Height (m)	Earthquake	Mw	Closest Distance to Fault(km)	Displacement (mm)	
						Horizontal	Vertical
1	Anderson Dam	72	Morgan Hill 1984	6.1	3.3	9	15
2	Cogswell Dam	81	Sierra Madre 1991	5.8	4	41	16
3	Coyote Lake Dam	43	Morgan Hill 1984	6.1	1.5	37	67
4	La Villita Dam	60	Mexico 1975 (15 Nov)	5.9	10	16	24
5	Lexington Dam	63	Loma Prieta 1989	7.0	5	76	259
6	Long Valley Dam	38	Mammoth Lake 1980 (main shock)	6.1	15	Minor 1	
7	Los Angles Dam	40	Northridge 1994	6.7	6	55	90
8	Matahina Dam	86	EDGE CUMBE 1987	6.5	12	268 Dst	102
9	Oroville Dam	235	Oroville 1975	6.0	8	15	10
10	Whittier Narrows Dam	29	Whittier Narrows 1987	6.1	7	Minor	

Minor Means <5mm

As mentioned above, strong motions used for analyzing Group 1 earth dams, were the same motions recorded at the dam sites during the related earthquake. It is worth noting that the applied record for each earth dam, for using in the Newmark family method analysis, was calculated at the base of sliding block using numerical analysis when the height of sliding wedge was less than the height of dam.

Note that the recorded strong motion in the south-west abutment of coyote lake dam during Morgan Hill 1984 earthquake, in the transverse direction had a PGA equal to 0.65g. However, the base acceleration for the coyote lake dam has been scaled down to PGA=0.36g, as recommended by Boore et al [19] for this dam site. In addition, the strong motion used for analyzing Whittier Narrows dam was the strong motion recorded at the crest of dam. However, this record was scaled to a target response spectrum which was obtained from attenuation relationship developed by Ambraseys & Douglas [20] for Near-Field Regions. The details of mentioned recorded strong motions in the transverse component are presented in table 4.

Table 4. Strong motions recorded at the dam site, used as the horizontal transverse base record

Case No. due to Table 6	Station in the dam site	Comp.	Operations on Record	SED (cm2/s)	SMV (cm/s)	PGV (cm/s)
1	Down-Stream toe	250	--	322	15.21	27.6
2	Right Abutment	60	--	34	3.71	9.55
3	South-West Abutment	195	Scaled to the target response spectrum which obtained from attenuation relationship recommended by Ambraseys & Douglas 2003 for Near-Field Regions (D<15KM)	342	15.77	26.8
4	Berm (Near the Toe)	S05E	--	24	4.391	5.11
5	Left Abutment	0	--	3102 (3116) a	35.25 (36.00)	84.7 (86.03)
6	Down-Stream toe	90	--	135	6.38	17.8
7	Foundation (on free field)	334	--	3210	31.54	62.2
8	Down-Stream Toe	353	--	1290 (12266)	17.43 (49.24)	20.6 (71.54)
9	Seismological Station	N37E	--	1.4 (15)	1.23 (2.71)	2.25 (4.03)
10	Crest	303	Scaled by the same way which was applied for case number 3	48	6.02	11.3

Values in brackets are related to the records at the base of sliding blocks (for cases: block height/dam height)

PREDICTION OF THE DEFORMATIONS FOR GROUP 1

The details of sliding block calculated for each case of Group 1 are presented in table 5. The performance of each method regarding the prediction of the observed max deviatoric deformations of the earth dams, presented in table 3, has been discussed in the following.

Table 5. Details for sliding wedge of case studies obtained from limit-equilibrium analysis

Case No. due to Table 6	Static Factor of Safety ^a	Yield Coefficient (Ky)			Sliding Wedge ^c	
		Calculated by this study ^b	Calculated by other studies		height (m)	Description
			Ky	Reference		
1	1.197	0.059	0.03 for Upstream	USCOLD: J.Ryan et al.2013	72	Deep
2	1.465	0.150	0.15	Singh & Roy 2009	81	Shallow
3	2.346	0.288	--	--	45	Deep
4	1.808	0.198	0.2	-Singh & Roy 2009 -Bray & Travarasrou 2007	65	Deep
5	1.814	0.230	0.23	Santa Clara Valley Water District 2004 Report No. LN-4	25	Deep
6	2.046	0.243	0.23	Singh & Roy 2009	36.3	Shallow
7	2.269	0.198	0.15	Singh & Roy 2009	45	Deep
8	1.641	0.153	0.17	Singh & Roy 2009	15	Shallow
9	1.692	0.198	0.21	Singh & Roy 2009	106	Shallow
10	2.386	0.315	--	--	16.3	Deep
Using Morgenstern-Price's Method Using Pseudo-Static a Details of all analysis have been explained in the thesis published in IUST: "Evaluation of sliding block methods performance for the estimation of permanent deformation of earth dams located in Near-field regions" By Reza Karimi Moghaddam 2017						

In order to analyze each earth dam, the strong motion, recorded in the dam site, has been used as mentioned above. Then, the permanent deformation for each case has been calculated using the recorded strong motion using all the simplified and rigorous Newmark methods (32 values of 26 methods). Finally, the errors between observed and predicted permanent deformations, using all the methods, have been discussed.

The performance of the methods are indicated in figures 1 and 2. Figure 1 is related to the methods which do not consider the response of sliding systems (Rigid-based methods), while figure 2 is related to the methods which consider response of sliding block system (Decoupled-based and Coupled-based methods). The vertical axis of these figures are calculated deformations by the methods and the horizontal axis are observed deviatoric deformation for each earth dam. Also, the 45 degree lines have been drawn to separate conservative and non-conservative predictions. Hence, it is clear that the points, located at the top of 45' lines, are related to the conservative predictions and on the contrary, the points located at the bottom of 45' lines are related to the non-conservative predictions.

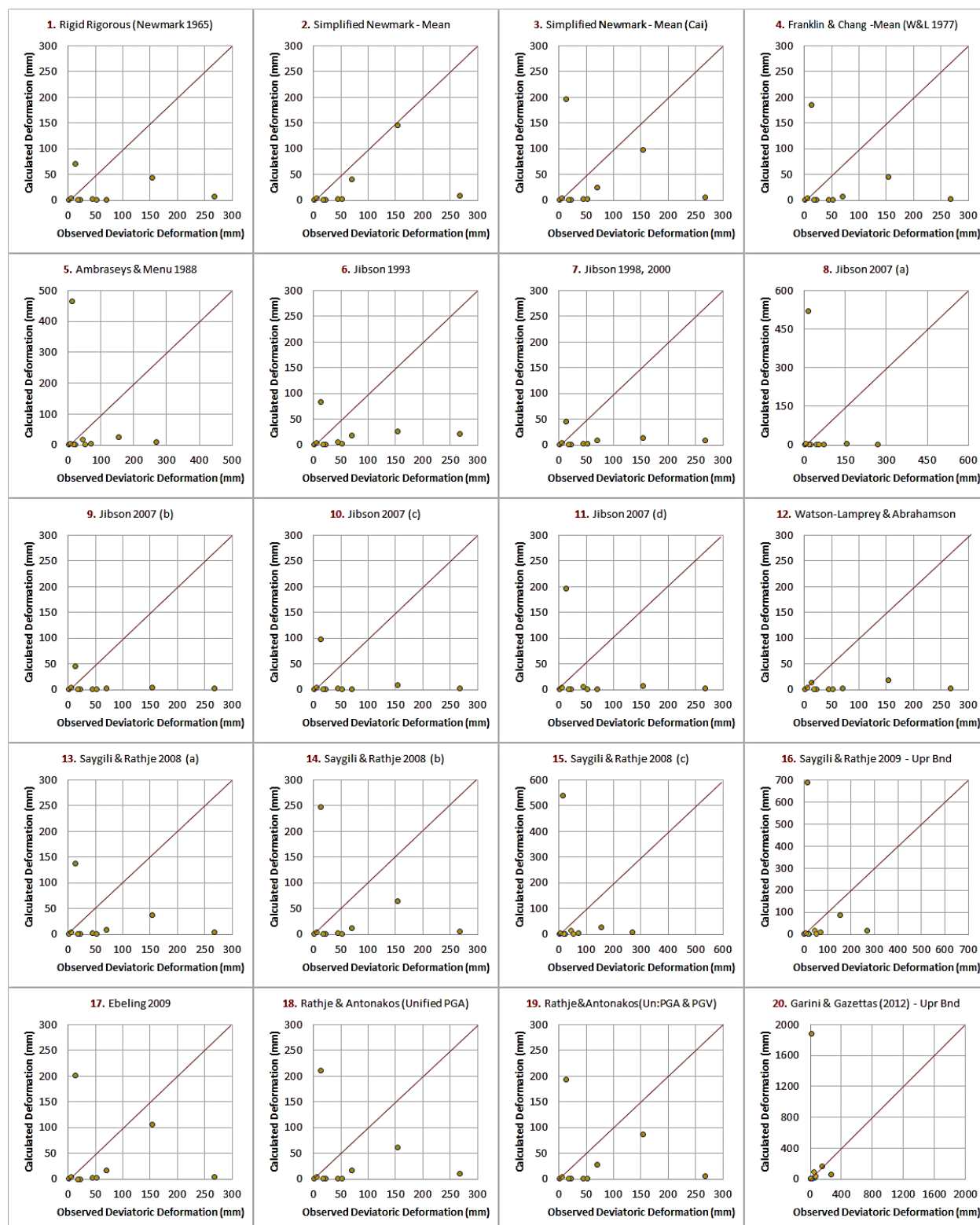


Figure 1. Calculated displacement by different rigid-based, Unified and Near-Field methods versus observed max Deviatoric deformation of 10 case studies (Group 1)

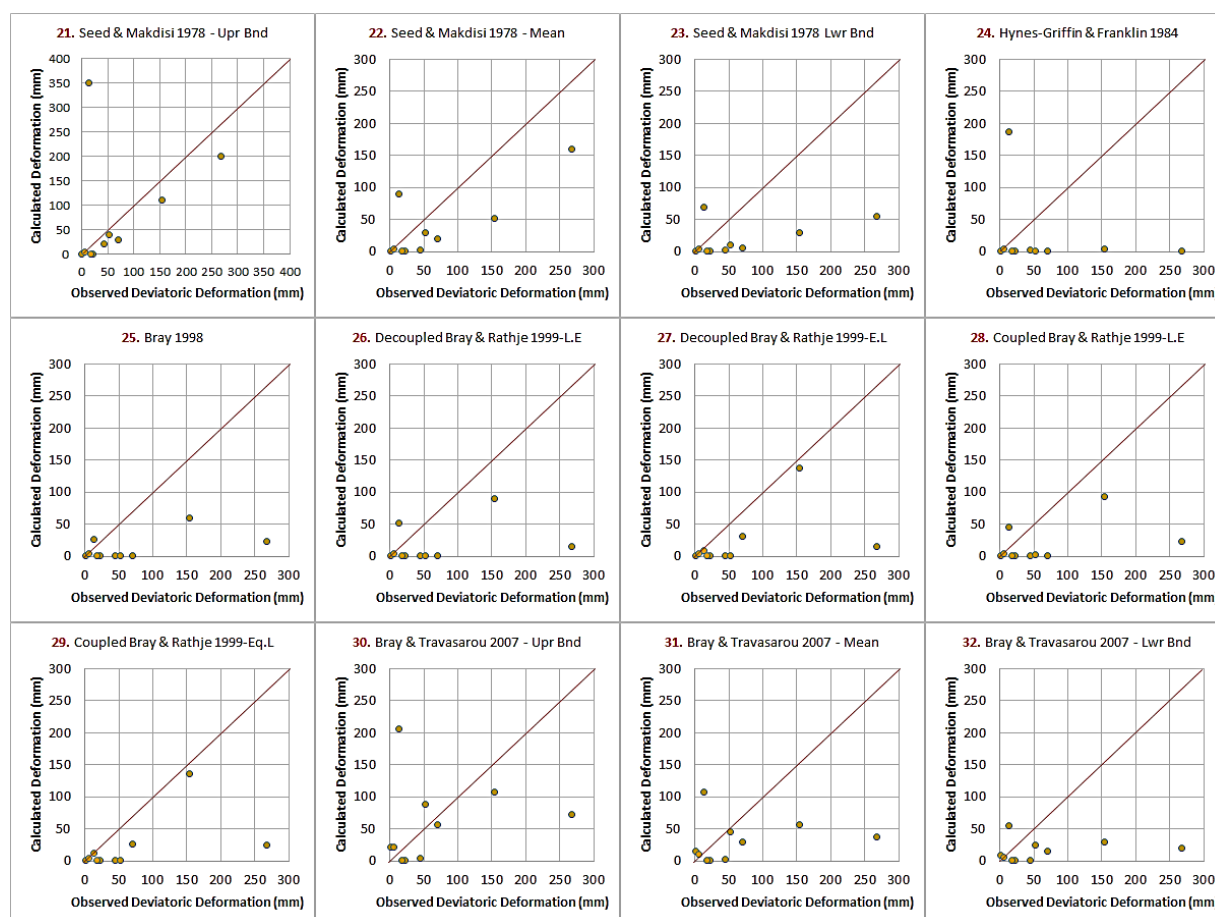


Figure 2. Calculated displacement by different decoupled-based and coupled-based methods versus observed max Deviatoric deformation of 10 case studies (Group 1)

DESIGNEE METHOD

As seen in figures 1 and 2, the method developed by Bray and Travararou 2007 [7] estimates the best results and so, this method is known as the designee method in this study. This method has the highest number of acceptable (conservative) predictions and lowest rate of negative errors (the lowest error when is underestimated) among all the methods for the prediction of permanent deformation of the earth dams. Note that also, the method developed by Garini and Gazettas 2012 [15] has equal number of conservative predictions compared with this method. However, the absolute amount of negative errors for Garini and Gazettas [15] method are higher than Bray and Travararou [7] method. This means that when two methods result in underestimated predictions, the Garini and Gazettas [15] method is more non-conservative than the Bray and Travararou [7] method. Also, the upper bound of Seed and Makdisi 1978 method and the upper bound of Saygili and Rathje [22] method have the best results among decoupled and rigid methods, respectively.

DISCUSSION OF THE RESULTS FROM THE ENERGY POINT OF VIEW

It is well known that the near-field strong motions are different in content compared with far-field motions. The energy generated by an earthquake is depreciated by the earthquake wave travelling from near-field to far-field. The orientation of site toward the wave emission direction has also its own impact on the accumulation of energy in the near-field regions as well as rupture velocity. It is well accepted that the earthquake energy can present the effect of an earthquake in a site better than other parameters such as PGA or PGV. In fact, the accumulation of energy in a site is a generic parameter for defining effect of an earthquake in any site.

To express energy concept in time domain in this study, the cumulative squared velocity of recorded strong motion in the dam site is used. This parameter is also known as recorded specific energy density which is derived from the site specific energy density [23].

$$\text{Site Specific Energy Density} = \frac{\beta s \cdot \rho s}{4} \int v^2(t) dt \tag{1}$$

$$\text{Recorded S.E.D} = \text{Cumulative Squared Velocity} = \int V^2(t) d(t) \tag{2}$$

The values of specific energy density, computed for all the earth dams of table 3, are indicated in table 4. The absolute errors of Bray and Travasarou [7] method (Designee method in this study) versus SED are depicted in figure 3 using the below expression:

$$\text{Absolute Error (\%)} = D_{\text{Calculated}} - D_{\text{Observed}} \tag{3}$$

Note that, vertical axis of figure 3 is absolute error which is calculated by equation (3). It is obvious that in this figure, the positive errors are related to the conservative and the negative errors are related to the non-conservative predictions. Also, horizontal axis of this figure is SED which is calculated for each earth dam using equation (2). The velocity time history used in equation (2) is obtained from the recorded strong motion acceleration at the base of related sliding block.

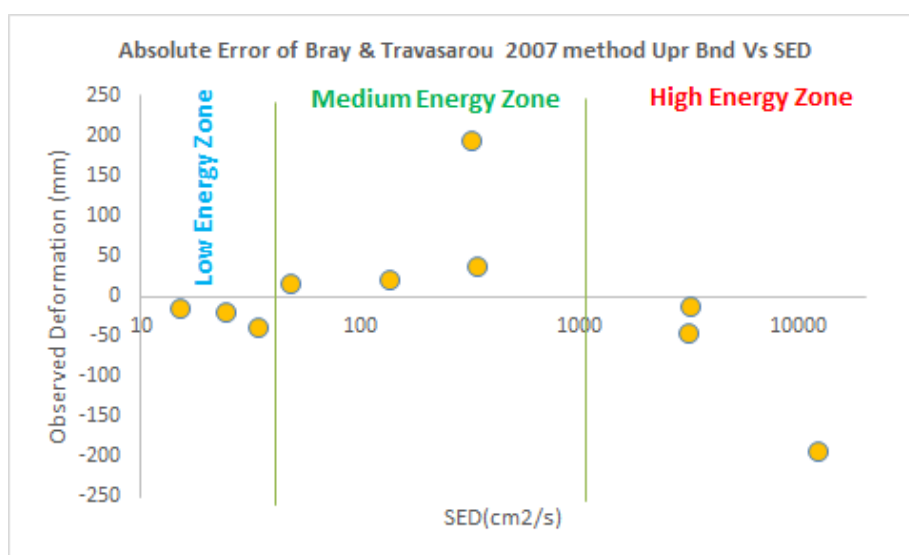


Figure 3. The absolute errors of the upper bound values of Bray and Travasarou 2007 coupled-based method (the designee method), for estimating max deviatoric deformations versus SED of the Group 1 case studies

As illustrated in figure 3, the predictions of designee method are non-conservative for high values of SED (i.e. SED > 1000 cm²/s) and for small values of SED (i.e. SED < 50 cm²/s). On the other hand, this method predictions are generally conservative in the medium values of SED. Although figure 3 only proves the mentioned conclusion about Bray and Travasarou [7] method, but this conclusion is also valid about all the methods of tables 1 and 2. In addition, although the figure 3 only depicts the errors of max deviatoric deformation predictions, but this conclusion is also valid about max horizontal and max overall deformations. (Max overall deformation is defined as the maximum of max horizontal and max vertical deformations).

Since SED is directly calculated from a velocity time history, it is expected to have a rational relationship with PGV for an earthquake. However, since SED is obtained from the square root of the velocity time series, it is logic to say that PGV does not present the full content of SED. In addition, since SED concept considers the amount of PGV in positive and negative positions, it seems that the parameters, such as sustained maximum velocity (SMV) which are associated with velocity time history and related cycles, to act partly the same way which SED does. Note that, SMV gives the sustained maximum velocity during three cycles, and is defined as the third highest absolute value of velocity in the time-history (note: in order for an absolute value to be considered as a "maximum", it must be larger than values 20 steps before and 20 steps after). The SMV values, computed for all earth dams of table 3, are indicated in table 4. In figure 4, absolute error of Bray & Travasarou [22] method (designee method in this study) for all 10 earth dams is also depicted against SMV. As it is depicted in this figure, the Designee method results in conservative predictions only in medium values of SMV which shows the same trend as is established for SED.

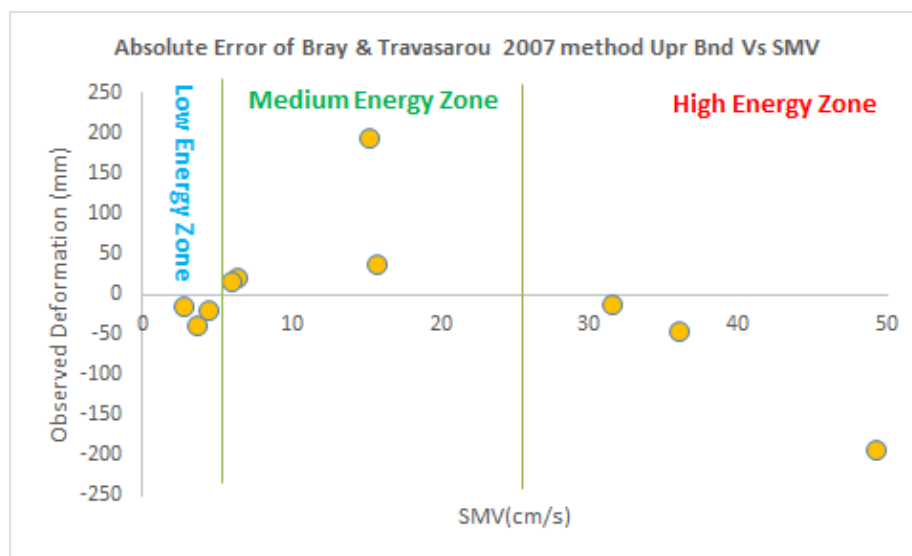


Figure 4. The absolute errors of the upper bound values of Bray and Travarasrou 2007 coupled-based method (the designee method), for estimating max deviatoric deformations versus SMV of the Group 1 case studies

Although figure 4 only depict Bray and Travarasrou [7] method, but this conclusion is also valid for all the methods of tables 1 and 2 and also about max horizontal and max overall deformations.

Furthermore, although SED and other parameters such as SMV which are related to the experienced energy in a site, act as a separator parameter between conservative and non-conservative results in time domain, it seems that they have a direct impact on occurring permanent deformation of earthen structures during an earthquake as well as other parameters such as K_y . Figure 5 indicates observed deviatoric deformations (Vertical axis) against associated SED (Horizontal axis). Despite the fact that other parameters such as K_y and T_s affect deformation of earth dams, figure 5 indicates that observed deviatoric deformations increase with increasing SED of transverse component of base motion. For the cases with low and medium values of SED, small values of deviatoric deformations occur (for example <5cm) despite having different values of k_y in the range of 0.06-0.32. On the other hand, the large values of permanent deformations occur in the large values of SED. Figure 6 indicates observed deviatoric deformations (Vertical axis) against associated SMV (Horizontal axis). As it is seen in figure 6, all above discussions are valid about SMV too.

Overall, it seems rational that considering energy concepts can eliminate some errors related to calculation of earthquake-induced permanent deformation of earthen structures.

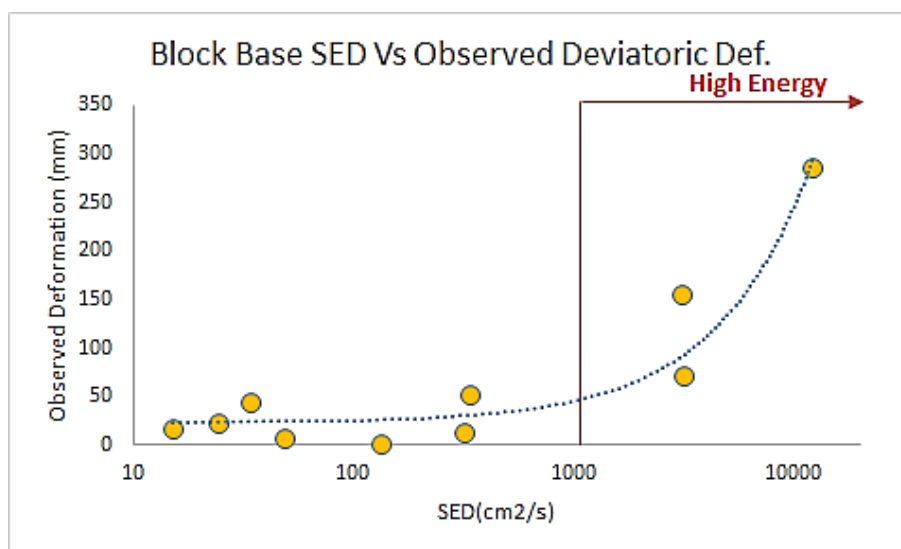


Figure 5. Observed deviatoric deformations versus Specific Energy Density (SED) for Group 1 case studies

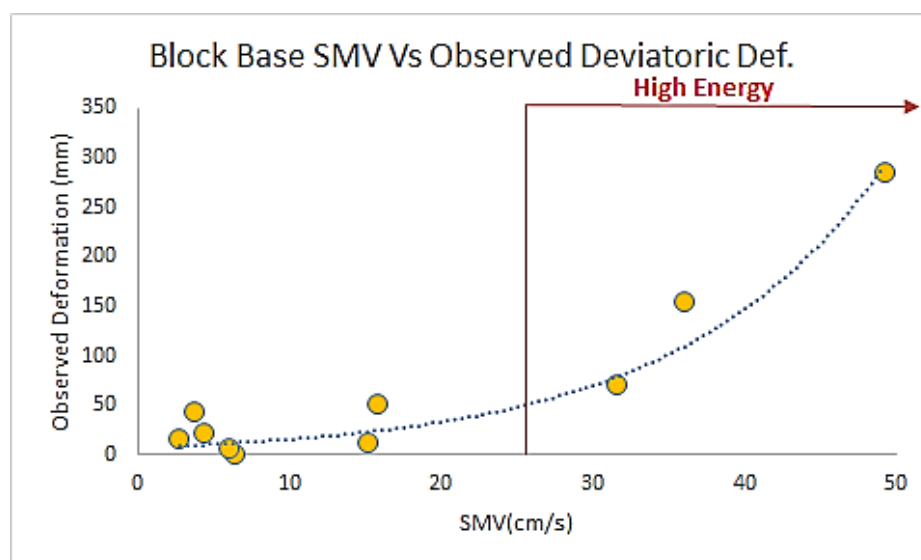


Figure 6. Observed deviatoric deformations versus SMV for Group 1 case studies

ANALYZING GROUP 2 OF CASE STUDIES (15 EARTH DAMS)

The list of 15 earth dams, as Group 2, are presented in table 6. All the necessary parameters for the purpose of analysing Group 2 earth dams, were obtained from previous studies. However, in order to estimate the response of the sliding systems, attenuation relationships were used. However, since PGAs of the strong motions for Group 2 of case studies were available (or suggested by previous studies), the attenuation relationships used in this study were recalibrated using sigma parameter which was obtained from try and error process. For this purpose, first, the sigma parameter of an attenuation relationship was changed enough to achieve the desired PGA. Then, the exact response of the system was calculated using the attenuation relationship and the obtained sigma. The calculated response, in this way, had the least error such that the results of various attenuation relationships were almost identical in value. However, the relationship developed by Campbell, K.W [24] was used for estimating the response of the systems for the distances of less than 40 kilometers. Also, the relationship developed by Crouse [25], was used to estimate the response of the systems for the distances of more than 40 kilometers. Furthermore, the PGV for each earth dam was calculated using previous mentioned procedure related to attenuation relationships.

Table 6. The details of case studies of Group2

Case Name	EQ Date	M	Dist. (KM)	PGA (g)	Estimated PGV (cm/s)	Height (m)	Ky (g)	Max Deformation (mm)	
								Hor.	Ver.
La Villita	3.14.79	7.6	124	0.1	4.9	60	0.2	12	13
Asagawara	10.23.04	6.8	24	0.12	5.2	56.4	0.08	400	700
El Infiernillo (D/s)	3.14.79	7.6	110	0.23	8	148	0.55	34	46
La Villita	10.25.81	7.3	121	0.174	8.5	60	0.2	24	114
Demi	1.26.01	7.6	90	0.2	11.3	17	0.26	100	50
Sasoi	1.26.01	7.6	120	0.2	12.1	20	0.3	90	25
Surgu	5.5.86	6.6	10	0.21	13.1	55	0.15	1	150
Tapar	1.26.01	7.6	43	0.15	18.4	15.5	0.12	500	800
Chabbot	4.18.06	8.3	32	0.57	28.4	43.3	0.12	225	450
Lower SanFernando	1.17.94	6.9	11	0.32	32.3	32.8	0.15	150	150
Shin Yamamoto	10.23.04	6.8	6	0.55	33.7	44.5	0.36	20	20
Kashi	8.23.85	7.4	21	0.25	34.1	16	0.14	300	400
Kashi	9.12.85	6.8	16	0.5	45.2	16	0.14	1000	1500
Austrian	10.17.89	7	11	0.575	58	21.5	0.21	305	789
Suvi	1.26.01	7.6	37	0.42	62	15	0.09	4000	1100

PREDICTION OF THE DEFORMATIONS FOR GROUP 2

Deformation of the Group 2 earth dams were estimated by the best method of each approach (four methods), introduced in section 3.1, and are indicated in figure 7.

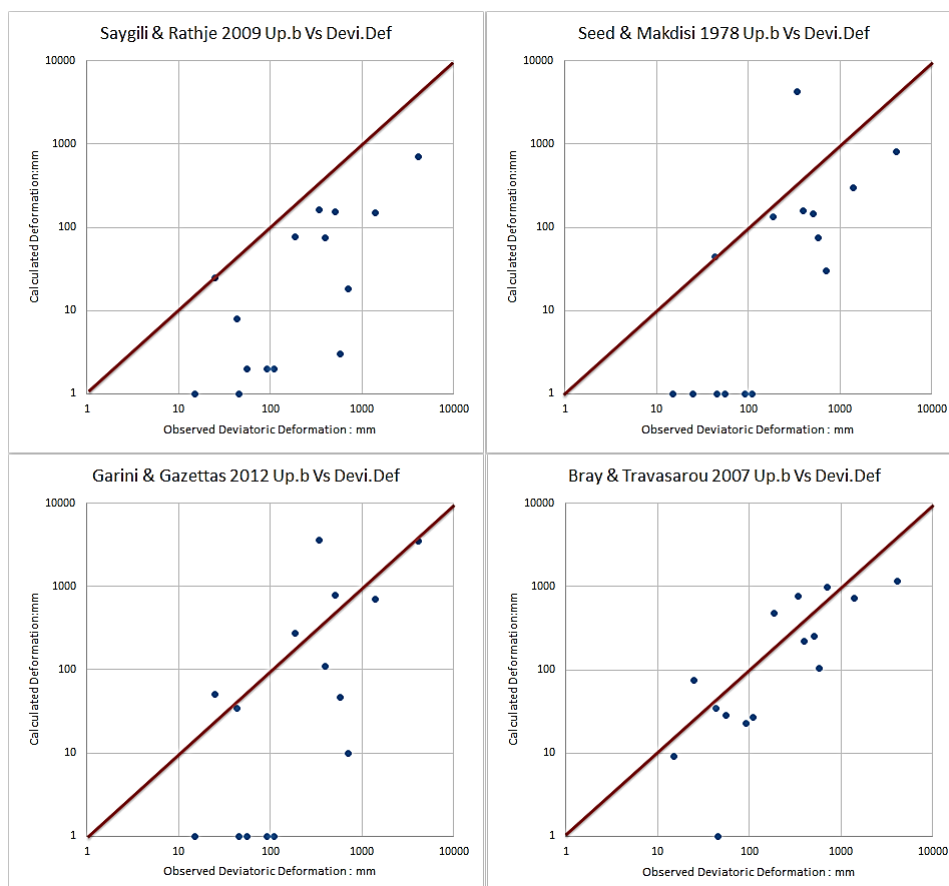


Figure 7. The performance of the sliding block methods for the prediction of observed max Deviatoric deformation of 15 case studies (Group 2)

As it is clear in figure 7, the method developed by Bray and Travararou [7] estimates the best results as the same was established for the prediction of Group 1 deformations. This method has the highest number of acceptable (conservative) predictions and the lowest absolute values of negative errors. Note that, the method developed by Garini and Gazettas [15] has also equal number of acceptable predictions compared with Bray and Travararou [7] method. However, the absolute amount of negative errors for Garini and Gazettas [15] method are higher than Bray and Travararou [7] method.

4. DISCUSSION OF THE RESULTS FROM THE ENERGY POINT OF VIEW

Since the Energy representative parameters such as SED are unknown for Group 2 of case studies, PGV parameter is considered as the closest parameter in content and concept to the SED which can be estimated for Group 2, using attenuation relationships. PGV values are drawn against SED (Figure 8-a) and SMV (Figure 8-b) for Group 1 of case studies. As it is indicated in these figures, PGV has a direct relationship with SED and SMV so that PGV values increase by increasing SED or SMV values. Therefore, it is expected that almost large amounts of PGV to be associated with high SED values and small amounts of PGV to be associated with low SED values. However, because of the unknown relationship between PGV and SED or SMV, it cannot be said that all of the medium PGVs can generate a medium SED. It seems that it depends on many unknown parameters such as the number of half-cycles, significant duration and etc. Therefore, a medium PGV can create a medium, a low or a high SED in various conditions. The PGV values for the case studies of Group 2 was calculated using mentioned procedure for obtaining response of sliding systems by attenuation relationship. PGV values for Group 2, are presented in table 6.

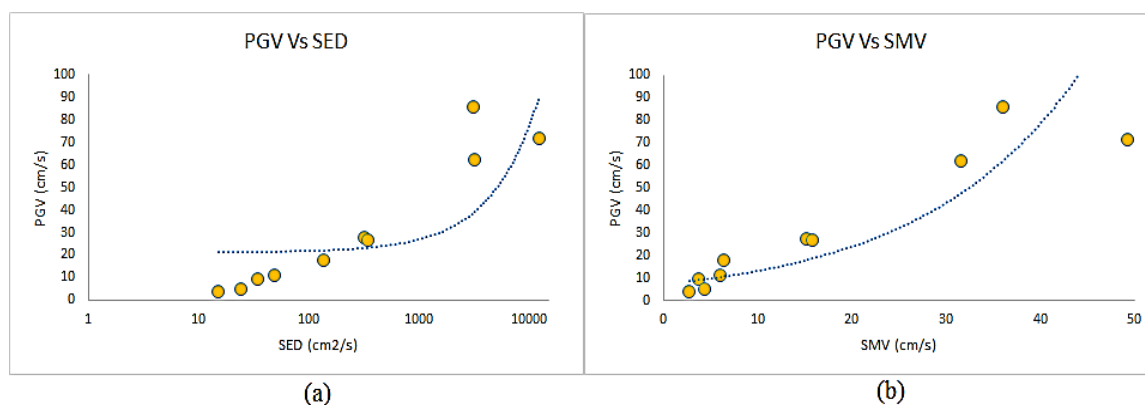


Figure 8. PGV versus energy representative parameters for Group 1 earth dams
(a): PGV Vs SED / (b): PGV Vs SMV

Relative errors between observed deviatoric deformations of Group 2 and calculated deformation by upper bound of Bray and Travararou [7] method (designee method in this study) are depicted against PGV, in figure 9 using below equation:

$$\text{Relative Error (\%)} = \frac{D_{\text{calculated}} - D_{\text{observed}}}{D_{\text{observed}}} \times 100 \quad (4)$$

Note that the vertical axis of figure 9 are relative error which are calculated by equation (4). It is obvious that the positive errors are related to the conservative results and the negative errors are related to the non-conservative results. Hence, the positive part of diagrams may gain a high value (For example > 100%) for a very conservative result while, the negative part of diagrams can have the maximum of 100% negative error when calculated deformation is equal to zero. Also, the horizontal axis of these figures are PGV which are calculated for each case using attenuation relationships as mentioned previously.

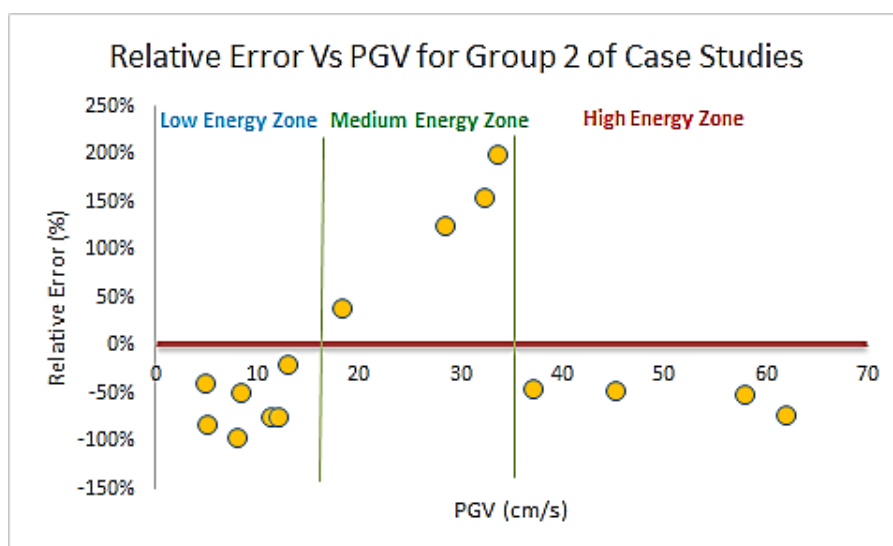


Figure 9. The relative errors of the upper bound values of Bray and Travararou 2007 coupled-based method (the designee method), for estimating max deviatoric deformations versus PGV of the Group 2 case studies

As illustrated in figure 9, Bray and Travararou [7] method (which is a non-linear coupled method) results in non-conservative predictions for small and large values of PGV which are related to low and high levels of energy respectively. On the other hand, this method results in conservative predictions only in the medium values of PGV. Although the figure 9 only depict the errors of max deviatoric deformation predictions, but this conclusion is also valid about max horizontal and max overall deformations.

It should be noted that although error values in low energy zone are larger than error values in high energy zone, but the absolute error values in high energy zone are larger. Therefore, as it is indicated in figure 10, not considering parameters related to energy concept in high energy zone is more critical. Note that the vertical axis of this figure is absolute errors which is calculated from equation (3) for Group 2 of earth dams, and the horizontal axis of this figure is PGV.

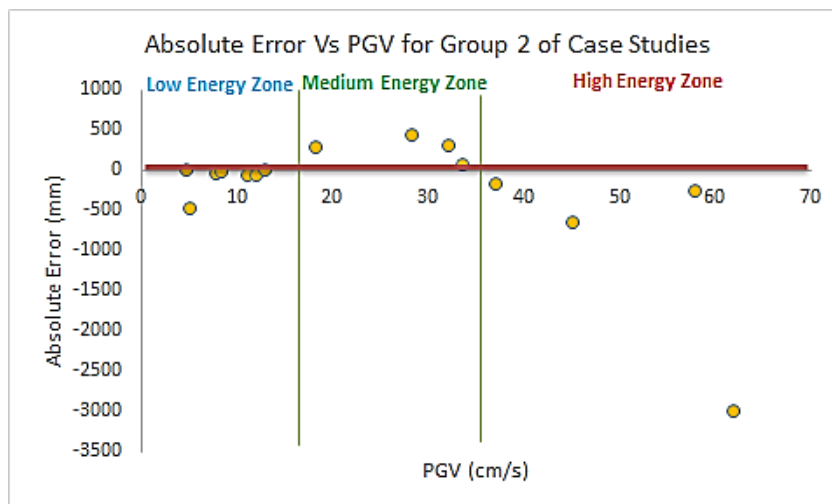


Figure 10. The absolute errors of the upper bound values of Bray and Travasarou 2007 coupled-based method (the designee method), for estimating max deviatoric deformations versus PGV of the Group 2 case studies

5. CONCLUSIONS

- a. Applying all the 26 simplified and rigorous methods for 25 real Earth dams, it is observed that the method developed by Bray and Travasarou [22] which is a simplified non-linear coupled method, predicts the displacements better than other methods. This method has the highest number of acceptable (conservative) predictions and the lowest absolute values of negative error among all of the Newmark sliding block family methods. Note that also, while the method developed by Garini and Gazettas [15] has equal number of conservative predictions with this method, but the absolute values of negative error of Garini and Gazettas [15] method are higher than Bray and Travasarou [22] method. This means that when two methods result in the underestimated predictions, the Garini and Gazettas [15] method is more non-conservative than the Bray and Travasarou 2007 method.
- b. Energy representative parameters such as SED and SMV act as separator parameters so that the predictions of the methods are underestimated in the low and high levels of energy and also the conservative predictions of the methods occur only in the medium levels of energy.
- c. It seems that energy has a key role in the occurrence of the permanent deformation of earthen structures so that the large values of observed deviatoric deformation of case studies occurred in large values of energy.
- d. In conclusion, considering SED as an energy representative parameter may eliminate some errors of sliding block methods due to following observations:
 - SED separates conservative and non-conservative deformation prediction using sliding block methods
 - Some of important parameters such as PGV and SMV are included in SED content
 - Deformation of earth dams increase by increasing SED values so that large values of permanent deformations occur in large values of SED. On the other hand, the cases with low and medium values of SED, experienced small values of deformations despite having wide range of K_y (between 0.06 and 0.32).

6. REFERENCES

1. Newmark, N. M. (1965) "Effects of earthquakes on dams and embankments," *Geotechnique* 15(2), 139-160.
2. Rathje, E. and Bray, J. (1999) "Two dimensional seismic response of solid-waste landfills," Proc. of second International Conference on Earthquake Geotechnical Engineering, Lisbon, Portugal, June, pp. 655–660.
3. Kramer, S.L. and Smith M.W. (1997) "Modified Newmark model for seismic displacements of compliant slopes", *Journal of Geotechnical and Geoenvironmental Engineering*, 123 (7), pp. 635-644
4. Lin, J. S. and Whitman, R. V. (1983) "Decoupling approximation to the evaluation of earthquake-induced plastic slip in earth dams," *Earthquake engineering and structural dynamics* 11(5), 667-678.
5. Rathje, E. M. and Bray J. D. (1999) "An examination of simplified earthquake-induced displacement procedures for earth structures" *Canadian Geotechnical Journal*, 36(1): 72-87.
6. Rathje, E. M. and Bray J. D. (2000) "Nonlinear coupled seismic sliding analysis of earth structures", *Journal of Geotechnical and Geoenvironmental Engineering* 126 (11), 1002-1014.
7. Bray, J. D. and Travasarou, T. (2007) "Simplified procedure for estimating earthquake-induced deviatoric slope displacements," *Journal of Geotechnical and Geoenvironmental Engineering* 133(4), 381-392.
8. Garini Ev., Gazetas G., and Anastasopoulos I., (2007) "Rupture-Directivity and Fling-Step Effects on Newmark Block Sliding", *Proceedings of the 4 th International Conference on Earthquake Geotechnical Engineering*, Thessaloniki.
9. Voyagaki, E. Mylonakis, G. Psycharis, I. N. (2008) "Sliding Blocks under Near-Fault Pulses: Closed-Form Solutions," *Geotechnical Earthquake Engineering and Soil Dynamics IV* 181, 1-10.
10. Yegian, M. Marciano, E. Ghahraman, V. G. (1991) "Earthquake-induced permanent deformations: probabilistic approach," *Journal of Geotechnical Engineering* 117(1), 35-50.
11. Gazetas, G. Garini, E. Anastasopoulos, I. Georgarakos, T. (2009) "Effects of near-fault ground shaking on sliding systems," *Journal of Geotechnical and Geoenvironmental Engineering* 135(12), 1906-1921.
12. Franklin, A. and Chang, F. (1977) "Earthquake resistance of earth and rockfill dams," Misc: Paper S-17-17. US Army Waterway Experiment Station, Vicksburg, Miss.
13. Yegian, M. Marciano, E. Ghahraman, V. (1991) "Seismic risk analysis for earth dams," *Journal of Geotechnical Engineering* 117(1), 18-34.
14. Kramer, S. L. and Lindwall, N. W. (2004) "Dimensionality and directionality effects in Newmark sliding block analyses," *Journal of Geotechnical and Geoenvironmental Engineering* 130(3), 303-315.
15. Garini, E. and Gazetas, G. (2012) "Destructiveness of earthquake ground motions: "Intensity Measures" versus sliding displacement," Proc. of the second international conference on performance-based design in earthquake geotechnical engineering, Taormina, Italy, pp 886–899.
16. Meehan, C L., Vahedifard, F. (2013) "Evaluation of simplified methods for predicting earthquake-induced slope displacements in earth dams and embankments", *Engineering Geology*, 152(1), 180-193
17. Makdisi, F.I. and Seed, H.B. (1978) "Simplified procedure for estimating dam and embankment earthquake-induced deformations," *Journal of Geotechnical Engineering* 104 (7), 849–867.
18. Bray, J.D., (2007). "Simplified seismic slope displacement procedures". In: Pitilakis, K.D. (Ed.), 4th Int. Conf. on Earthq. Geotech. Eng., Invited Lectures. Springer, pp. 327–353.
19. Boore, D. M. Graizer, V. M. Tinsley, J. C. Shakal, A. F. (2004) "A study of possible ground-motion amplification at the Coyote Lake Dam, California," *Bulletin of the Seismological Society of America* 94(4), 1327-1342.
20. Ambraseys, N. and Douglas, J. (2003) "Near-field horizontal and vertical earthquake ground motions," *Soil dynamics and earthquake engineering* 23, 1-18.
21. Ambraseys, N. and Menu, J. (1988) "Earthquake-induced ground displacements," *Earthquake engineering & structural dynamics* 16(7), 985-1006.

22. Saygili, G. and Rathje, E. M. (2009) “*Probabilistically based seismic landslide hazard maps: An application in Southern California*,” *Engineering Geology* 109(3), 183-194.
23. Sarma S. K. (1971) “Energy flux of strong earthquakes,” *Tectonophysics* 11(3), 159-173.
24. Campbell, K.W. (1997)“*Empirical Near-Source Attenuation Relationships for Horizontal and Vertical Components of Peak Ground Acceleration, Peak Ground Velocity, and Pseudo-Absolute Acceleration Response Spectra*,” *Seismological Research Letters*, 68, 154–179.
25. Crouse, C.B. (1991)“*Ground Motion Attenuation Equations for Earthquakes on the Cascadia Subduction Zone*,” *Earthquake Spectra*, V. 7, No. 2, p. 201-236.
26. Bray, J. D. (2007) “*Chapter 14: Simplified seismic slope displacement procedures*.” Proc.of the fourth International Conference on the Earthquake Geotechnical Engineering, Vol. 6, Springer, New York, pp. 327–353
27. Cai, Z. and Bathurst, R. (1996) “*Deterministic sliding block methods for estimating seismic displacements of earth structures*,” *Soil dynamics and earthquake engineering* 15(4), 255-268.
28. Ebeling, R. M. Fong, M. T. Yule, D. E. Chase Sr, A. Kale, R. V. (2009) “*Permanent seismically induced displacement of rock-founded structures computed by the Newmark program*,” ERDC TR-09-2. U.S. Army Corps of Engineers, Flood and Coastal Storm Damage Reduction Research and Development Program.
29. Hynes-Griffin, M. E. and Franklin, A. G. (1984) “*Rationalizing the seismic coefficient method*,” Misc: Paper GL-84-13, US Army Corps of Engineers Waterways Experiment Station. Vickburg, Miss.
30. Jibson, R. W. (2007) “Regression models for estimating coseismic landslide displacement,” *Engineering Geology* 91(2), 209-218.
31. Jibson, R. W. and Jibson, M. W. (2003) “*Java programs for using Newmark's method and simplified decoupled analysis to model slope performance during earthquakes*,” Open-File Rep. No.03-005, U.S.Geological Survey, Denver.
32. Jibson, R. W. Harp, E. L., Michael, J. A. (2000) “*A method for producing digital probabilistic seismic landslide hazard maps*,” *Engineering Geology* 58(3), 271-289.
33. Jibson, R. W. Harp, E. L. Michael, J. A. (1998) “*A method for producing digital probabilistic seismic landslide hazard maps: an example from the Los Angeles, California, area*,” Open-File Rep. No. 98-113, US Department of the Interior, US Geological Survey.
34. Jibson, R. W. (1993) “*Predicting earthquake-induced landslide displacements using Newmark's sliding block analysis*,” *Transportation research record* 1411, 9–17.
35. Makdisi, F.I. and Seed, H.B. (1978) “*Simplified procedure for estimating dam and embankment earthquake-induced deformations*,” *Journal of Geotechnical Engineering* 104 (7), 849–867.
36. Rathje, E. M. and Antonakos, G. (2011) “*A unified model for predicting earthquake-induced sliding displacements of rigid and flexible slopes*,” *Engineering Geology* 122(1), 51-60.
37. Rathje, E. M. and Saygili, G. (2008) “*Probabilistic seismic hazard analysis for the sliding displacement of slopes: scalar and vector approaches*,” *Journal of Geotechnical and Geoenvironmental Engineering* 134(6), 804-814.
38. Rathje, E. M. and Saygili, G. (2011) “*Estimating fully probabilistic seismic sliding displacements of slopes from a pseudoprobabilistic approach*,” *Journal of Geotechnical and Geoenvironmental Engineering* 137(3), 208-217.
39. Saygili, G. and Rathje, E. M. (2008) “*Empirical predictive models for earthquake-induced sliding displacements of slopes*,” *Journal of Geotechnical and Geoenvironmental Engineering* 134(6), 790-803.
40. Watson-Lamprey, J. and Abrahamson, N. (2006) “*Selection of ground motion time series and limits on scaling*,” *Soil dynamics and earthquake engineering* 26(5), 477-482.

Numerical Earthquake Response Analysis of the Earth Dams

Babak Ebrahimian^{1,2}, Ali Noorzad¹

1- Faculty of Civil, Water and Environmental Engineering, Abbaspour School of Engineering, Shahid Beheshti University (SBU), Tehran, Iran

2- The Highest Prestigious Scientific and Professional National Foundation, Iran 's National Elites Foundation (INEF), Tehran, Iran

Emails: ebrahimian.babak@gmail.com; b_ebrahimian@sbu.ac.ir

Abstract

Numerical investigations are carried out to consider the seismic behavior of earth dams. A fully nonlinear dynamic finite difference analysis incorporating an elastic perfectly plastic constitutive model is taken into account to describe the stress-strain response of the soil during earthquakes. In addition, Rayleigh damping is used to increase the level of hysteretic damping in numerical analyses. The Masing rules are implemented into the constitutive relations to precisely explain the nonlinear response of soil under general cyclic loading. As a result, the soil shear stiffness and hysteretic damping can change with loading history. The constructed numerical model is comprehensive calibrated via the centrifuge test data as well as the field measurements of a real case history both in the time and frequency domains. Good agreements are shown between the computed and measured quantities. It is confirmed that the proposed numerical model can predict the essential fundamental aspects of nonlinear behavior of earth dams during earthquakes. Then, a parametric study is conducted to identify the effects of dam height and input motion characteristics on the seismic response of earth dams. To this end, three real earthquake records with different intensities and PGAs are used as the input motions.

Keywords: Numerical Modeling, Nonlinear Response, Seismic Behavior, Earth Dam.

1. INTRODUCTION

The performance of earth dams subjected to seismic actions can be evaluated through different approaches including the force-based pseudo-static methods as the simplest one, displacement-based sliding block methods and fully nonlinear dynamic analyses as the most complicated one [1,2]. The most common method named pseudo static approach is largely used in engineering practice to assess the seismic stability of earth dams. This approach is quite simple since it attempts to represent complex dynamic behavior in terms of static forces. Then, stability is expressed in terms of an overall factor of safety. However, dam response to an earthquake may be related to many factors such as dam geometry, mechanical properties of construction soils, static stresses and pore water pressures inside the dam, and input motion characteristics. Most of these factors are partially or totally neglected by the approaches traditionally adopted to assess the seismic safety of earth dams. The pseudo-static approach [3], for instance, ignores some earthquake parameters such as frequency content and duration, known to significantly influence the soil response. In fact, study of seismic response of earth dams is a complex problem that generally requires the use of dynamic methods of analysis with different levels of sophistication in terms of proper problem formulation, characterization of material properties and modeling of stress-strain soil behavior. On the other hand, numerical methods allow the most comprehensive analyses of the response of earth dams to seismic loading. Progress in the area of geotechnical computation and numerical modeling offers powerful facilities to analyze the seismic response of dams considering complex issues such as soil nonlinearity, evolution of pore pressure during dam construction and real earthquake records.

The current study paper presents numerical modeling of the seismic behavior of earth dams overlaying bedrock subjected to real earthquake records using fully nonlinear dynamic analysis approach. The effect of nonlinear soil behavior is then accounted in the analyses from the early beginning of earthquake loading. The numerical analyses are carried out using an elastic perfectly plastic soil model, capable to reproduce some basic features of cyclic soil behavior. A critical review of the role of hysteretic damping introduced by the model and the viscous damping artificially added in the analyses is addressed. First, the proposed numerical model is comprehensively calibrated against centrifuge model test data and field measurements of the Long Valley (LV) earth dam as a real case-history. In this regard, some important aspects of model calibration are discussed and emphasized. Comparison between the obtained numerical results and experimental observations shows that the current numerical procedure can accurately capture the fundamental aspects of the seismic behavior of earth

dams. Then, through a parametric study the effects of dam height and input motion characteristics are considered on the seismic response of earth dam.

2. NUMERICAL MODELING PROCEDURE

Numerical analyses are carried out using the finite difference program FLAC based on a continuum finite difference discretization using the Lagrangian approach [4]. Every derivative in the set of governing equations is replaced directly by an algebraic expression written in terms of the field variables (e.g. stress or displacement) at discrete point in space. For dynamic analysis, it uses an explicit finite difference scheme to solve the full equation of motion using lumped grid point masses derived from the real density surrounding zone. The calculation sequence first invokes the equations of motion to derive new velocities and displacements from stresses and forces. Then, strain rates are derived from velocities, and new stresses from strain rates. Every cycle around the loop correspond to one time step. Each box updates all of its grid variables from known values that remain fixed over the time step being executed (Figure 1).

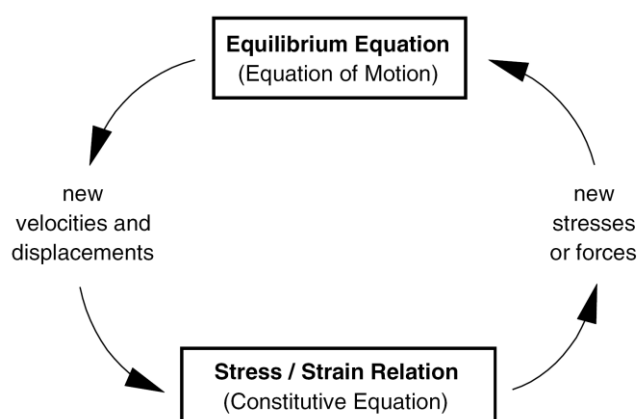


Figure 1. Basic explicit calculation cycle [4].

In simplest form, the equation of motion relates the acceleration, $d\dot{u}/dt$, of a mass, m , to the applied force, F , which may vary with time. Newton's law of motion for the mass-spring system is

$$m(d\dot{u}/dt) = F \quad (1)$$

To analyze a problem, the strain rate tensor and rotation rate tensor, having the velocity gradient, can be calculated from the following equations:

$$e_{ij} = \frac{1}{2} \left[\frac{\partial \dot{u}_i}{\partial x_j} + \frac{\partial \dot{u}_j}{\partial x_i} \right] \quad (2)$$

$$\omega_{ij} = \frac{1}{2} \left[\frac{\partial \dot{u}_i}{\partial x_j} - \frac{\partial \dot{u}_j}{\partial x_i} \right] \quad (3)$$

where, e_{ij} are the components of the strain rate and \dot{u}_i are the components of the velocity. To obtain the stress tensor, the specific mechanical relationships are used which in general are as below:

$$\sigma_{ij} = M(\sigma_{ij}, \dot{e}_{ij}, \kappa) \quad (4)$$

where, M is the specific rule of behavior and κ is the history parameter (based on the specific rules which may or may not exist).

The selected problem is a simplified representation of a typical earth dam geometry. The dam section is a symmetric zone section with central clay core resting on bedrock as shown in Figure 2. Five earth dam cross sections with different heights i. e., $H= 40, 80, 120, 200$ and 280 m are analyzed in this study.

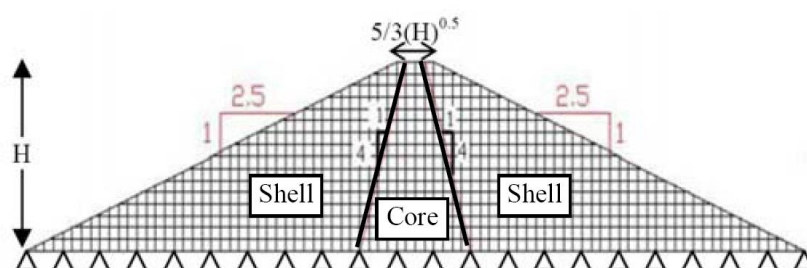


Figure 2. Geometry of dam

Mohr-Coulomb constitutive relation is used to model the soil behavior. The failure envelope for this model corresponds to a Mohr-Coulomb criterion (shear yield function) with tension cutoff (tensile yield function). The stress-strain relationship is linear elastic-perfectly plastic. The linear behavior is determined by elastic shear and bulk modulus. The plastic behavior is defined by the angle of internal friction and cohesion of soil. The shear modulus of sandy soil as shell materials is calculated with the formula given [5]:

$$G_{\max} = 8400 \frac{(2.17 - e)^2}{1 + e} (\sigma'_m)^{0.6} \quad (5)$$

where, G_{\max} is the maximum (small strain) shear modulus in kPa, e is the void ratio and σ'_m is the mean effective confining stress in kPa. The Poisson's ratio for shell materials is taken as 0.3. The shear modulus of clayey soil as core materials is calculated with the following formula [6]:

$$G_{\max} = 3270 \frac{(2.973 - e)^2}{1 + e} (\sigma'_m)^{0.5} \quad (6)$$

The Poisson's ratio for core materials is taken as 0.45.

To provide constitutive relations that can better fit the curves of shear modulus degradation and damping ratio increase derived from the experimental tests data, two different modifications are implemented into the FLAC soil model to assess the potential for predicting the seismic behavior and associated deformations. To represent the nonlinear stress-strain behavior of soil more accurately that follows the actual stress-strain path during cyclic loading, the masing behavior is incorporated into FLAC via a FISH subroutine as a first modification. Since, there is a need to accept directly the same degradation curves derived from the test data in fully nonlinear method and to model the correct physics, the second modification is related to incorporate such cyclic data into a hysteretic damping model for FLAC. Modulus degradation curves imply a nonlinear stress-strain curve. Shear modulus and damping of soils are strain dependent. Shear modulus decreases with increasing shear strain and damping increases with increasing strain. In this study, the shear modulus degradation and Damping ratio increase curves for sandy soils proposed by Seed and Idriss [7] and for clayey soils proposed by Vucetic and Dobry [8] are adopted as a reference. Geotechnical properties used in the analyses are presented in Table 1 for the earth dam materials.

Kuhlemeyer and Lysmer [9] showed that for an accurate representation of the wave transmission through the soil model, the spatial element size must be smaller than approximately one-tenth to one-eighth of the wavelength associated with the highest frequency component of the input wave i.e.,

$$\Delta L = \frac{\lambda}{9} \quad (7)$$

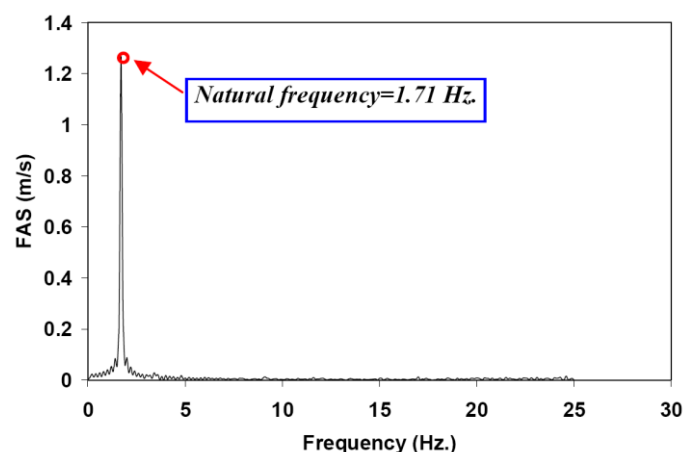
where, λ is the wave length associated with the highest frequency component that contains appreciable energy. Considering above criteria, element size is defined small enough to allow seismic wave propagation throughout the analysis. Rayleigh damping $R_d = 5\%$ is used in the analyses to compensate for the energy dissipation through the medium [4]. The natural frequency of the dam is determined by a Fourier analysis of the free response of the dam (Figure 3). It shows a fundamental frequency $f_1 = 1.71 \text{ Hz}$ for the dam with height of 40 m. The fundamental frequencies of dams with different heights are summarized in Table 2.

Table 1- Geotechnical soil properties

Region	γ_{wet} (kN/m ³)	γ_{sat} (kN/m ³)	ν	Porosity (n)	C (kPa)	Φ degree	K (cm/s)
Core	20	20.5	0.45	0.41	80	8	10^{-7}
Shell	22	23	0.30	0.33	-	40	10^{-2}

Table 2- Fundamental frequency

Frequency (Hz)	Dam Height (m)				
	40	80	120	200	280
f_1	1.7	0.88	0.60	0.36	0.26


Figure 3. Fourier amplitude spectrum of free horizontal motion at the dam crest

In this paper, three different real acceleration time histories including Tabas (PGA=0.93g in MCE level), Naghan (PGA=0.72g in MDE level) and San Fernando (PGA=0.21g in DBE level) are selected from a database of earthquake records [10]. In the dynamic analyses of dams, the scaled records have been filtered to a maximum frequency of 10 Hz, transferred to the “inside” bedrock formation through a standard de-convolution analysis and applied at the base of the numerical model. Pertinent information on the earthquake records are summarized in Table 3, and the corresponding acceleration time histories and Fourier amplitude spectra are depicted in Figure 4.

In the nonlinear analysis which is used in this investigation, the nonlinear stress-strain relationship is followed directly by each element. The damping ratio and shear modulus of the materials at different strain levels are calculated automatically. The real behavior of soils is nonlinear and hysteretic under cyclic loading. This behavior can be simulated by the Masing model [11], which is capable of modeling the dynamic behavior of soils. The shear behavior of the soil, in this model, may be explained by a backbone curve:

$$F_{bb}(\gamma) = \frac{G_{max}\gamma}{1 + (G_{max} / \tau_{max})|\gamma|} \quad (8)$$

where, $F_{bb}(\gamma)$ is the backbone function, γ is the shear strain amplitude, G_{max} is the initial shear modulus and τ_{max} is the maximum shear stress amplitude.

Table 3- Earthquake records data

Earthquake	Station	Date	M	Closest Distance (km)	PGA (g)	PGV (cm/s)	PGD (cm)
Tabas	Tabas	1978	7.4	94	0.93	121.4	94.58
Naghan	Naghan	1977	5.4	75	0.72	46.20	61.00
San Fernando	Pasadena	1971	6.6	19	0.21	10.90	2.320

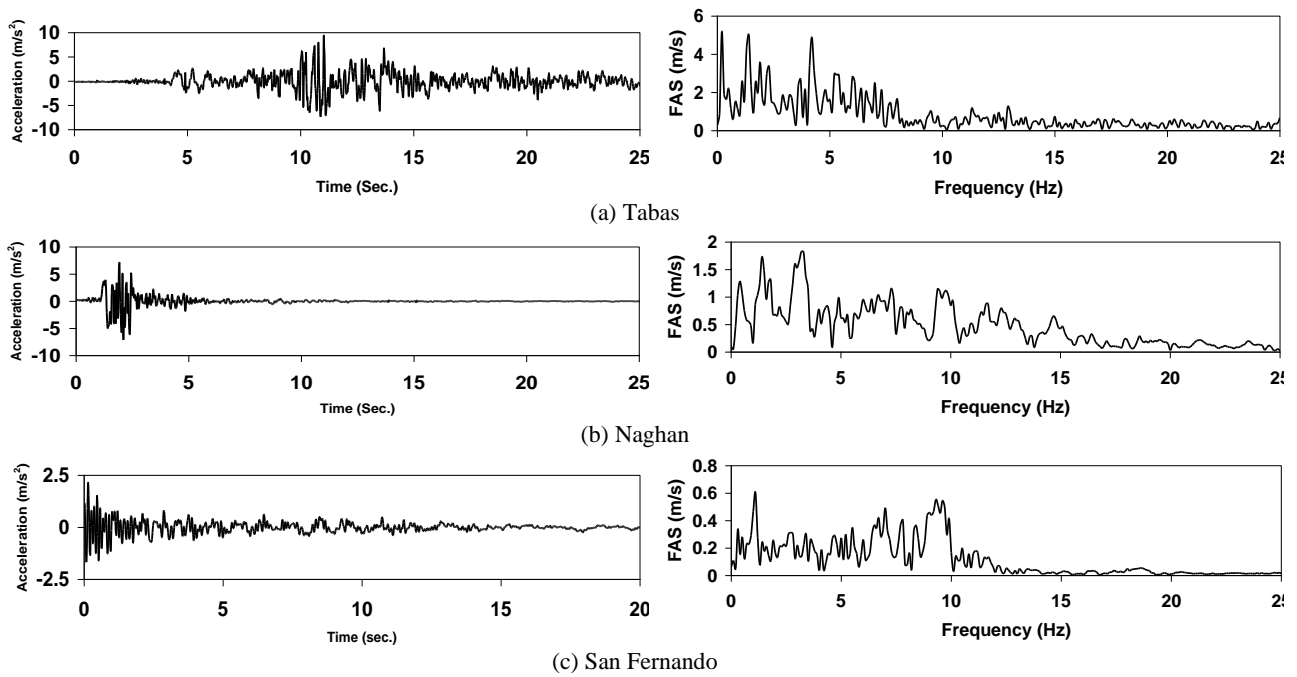


Figure 4. Input acceleration time histories and Fourier amplitude spectra

The stress-strain curve follows the backbone curve in the first loading, but to explain the unloading-reloading, the above equation has to be modified. If the stress returns from point (τ_r, γ_r) , the stress-strain curve follows the path below:

$$\frac{\tau - \tau_r}{2} = F_{bb} \left[\frac{\gamma - \gamma_r}{2} \right] \quad (9)$$

In other words, the unloading-reloading curves have the same shape as the backbone curve except the fact that its origin is displaced towards the stress returning point and they have been magnified by a factor of 2 (Figure 5). The Masing rules seem not to be enough to precisely explain the soil response under general cyclic loading. Finn et al. (1977) developed modified rules to describe the irregular loading [12]. They suggested that unloading and reloading curves follow the two rules; If the new unloading or reloading curve exceeds the last maximum strain and cut the backbone curve, it will follow the backbone curve till it reached the next returning point. If a new unloading or reloading curve passes through the previous unloading or reloading curve, it will follow the former stress-strain curve. According to this model, the tangent shear modulus can be defined as below at a point on the backbone curve:

$$G_t = G_{\max} \left/ \left[1 + \frac{G_{\max} |\gamma|}{\tau_{\max}} \right]^2 \right. \quad (10)$$

The tangent shear modulus, at a point on the new reloading-unloading curve can be also defined by the following equation:

$$G_t = G_{\max} \left/ \left[1 + \frac{G_{\max}}{2\tau_{\max}} |\gamma - \gamma_r| \right]^2 \right. \quad (11)$$

Based on research results, as the number of load cycles increase, the shear stress decreases; that means the shear stress-strain curves get more inclined. To simulate the nonlinear shear stress-strain relationship in this study, the Masing rules have been implemented into FLAC via a series of FISH functions.

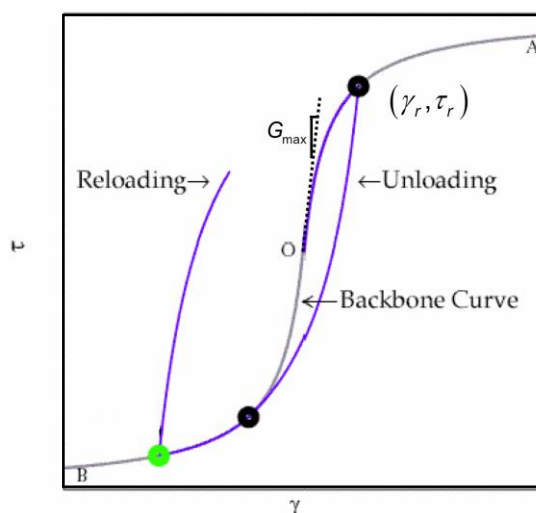


Figure 5. General pattern of loading and unloading of soils

3. VALIDATION ANALYSES

To validate the implementation of the Masing rules in FLAC program, the simulation of one-zone sample with the implemented rules is conducted by using a unit cell as shown in Figure 6 (a). The one-zone sample is modeled with FLAC which consists of a sandy soil and a periodic motion is exerted at its base. Vertical loading is established by gravity only. Equilibrium stresses are installed in soil. The stress-strain loops of the one-zone sample for several cycles are shown in Figure 6(b). It can be observed that shear modulus decreases with increasing shear strain. The hysteretic model seems to handle multiple nested loops in a reasonable manner. There is clearly energy dissipation and shear stiffness degradation during dynamic loading.

To evaluate the applicability of the proposed model, the results obtained from numerical analyses are compared with the experimental counterparts. One of the centrifuge tests related to the embankment performed in VELACS project (VERification of Liquefaction Analysis using Centrifuge Studies [13,14]) is chosen to calibrate the constructed numerical model in FLAC and also consider the ability of the constitutive model in predicting the dynamic response of the dam during seismic loading. It is attempted to create almost similar conditions between laboratory model test and numerical model. The model test configuration is depicted in Figure 7(a). The numerical model constructed in FLAC is shown in Figure 7(b). The numerical results are presented and compared to those of centrifuge test data. Comparisons between the computed and measured results (computed: numerical and Measured: centrifuge test results) are made in Figure 8. The comparisons show that the reference numerical model can predict the dynamic behavior of the earth dam in terms of acceleration and displacement in a rational way.

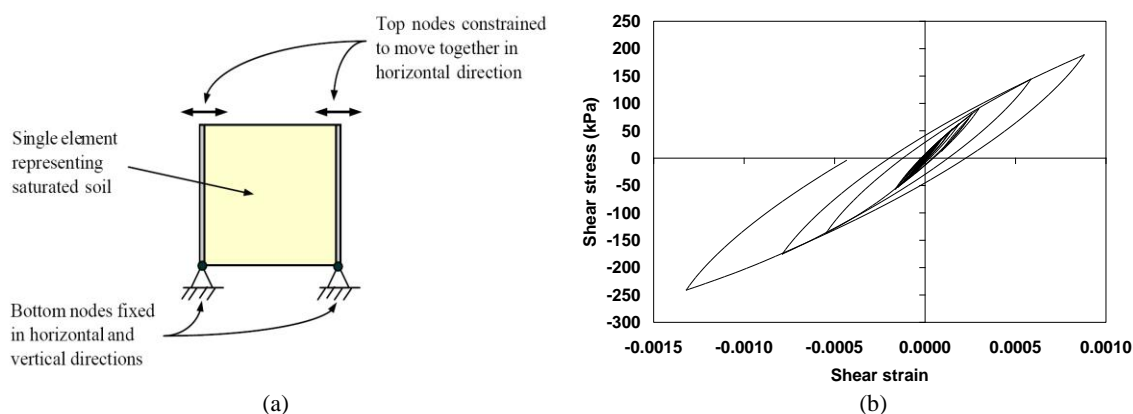


Figure 6. Simulation of cyclic simple shear test of one-zone sample in FLAC: (a) applied boundary conditions, and (b) Hysteresis loops

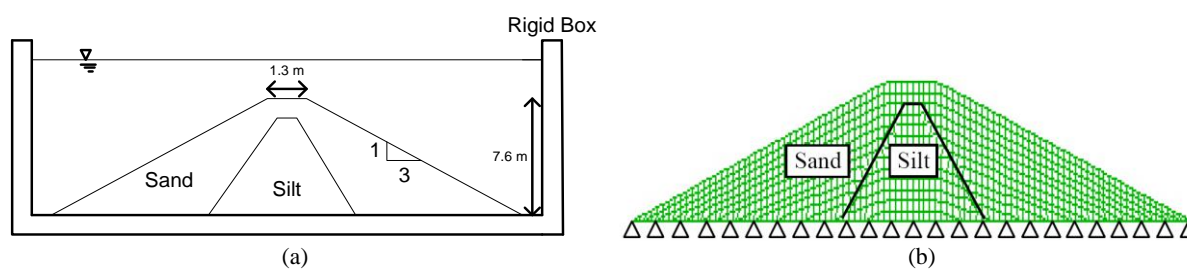


Figure 7. Model configuration in rigid container: (a) centrifuge test, and (b) numerical grid constructed in FLAC

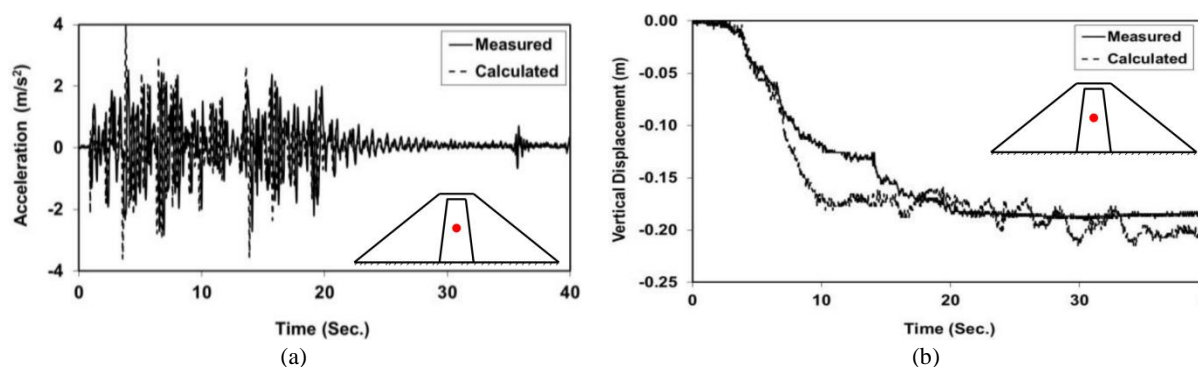


Figure 8. Measured versus calculated results of centrifuge modeling: (a) acceleration, and (b) displacement time histories at the middle of dam height

The last verification of the proposed numerical model is performed through a real well-documented case history in order to show the ability of the model in simulating the seismic behavior of earth dam during a real earthquake. To this end, the results of non-linear seismic analyses of the Long Valley (LV) earth dam in California subjected to the 1980 Mammoth Lake earthquake are presented and compared with the real measurements recorded at the site [15]. Herein, the results of the previous investigations in the literature have been also presented for comparison purposes. The details information about LV dam can be found in [15]. The LV dam is located in the Mammoth Lake area (California) in the close proximity of active faults. The dam is a rolled earth-fill with an impervious zone that forms the major portion of it. The dam has a maximum height of 55 m, a length of 182 m at the crest, and upstream and downstream slopes of 3h/1v. The LV dam was instrumented in the 1970's with a multiple-input-output array consisting of 3 accelerometer stations to monitor the boundary conditions and 5 stations to record the dam response (Figure 9). Thus, the array comprised a total of 22 accelerometers linked to a common triggering mechanism. LV dam cross section is shown in Figure 10(a). The numerical model constructed in FLAC is presented in Figure 10(b). In May 1980, a series of 6 earthquakes occurred in the Mammoth Lakes area. The magnitudes of these earthquakes were ranged from $M_L = 4.9$ to $M_L = 6.7$, and the induced peak accelerations at the crest center reached 0.5g in the upstream-downstream direction (x direction, Figure 9) during the strongest event. An extensive array of 22 input-output (excitation-response) accelerations was recorded, providing a valuable source of information on the dam seismic response over a wide range of deformation levels. In this study, the LV dam is subjected to the input motion recorded downstream at the outlet during Mammoth Lake earthquakes. The first 12 seconds of the recorded acceleration is used with data point at 0.02 second intervals and peak acceleration equal to 0.135g in the upstream-downstream direction and 0.084g in the vertical direction. The input accelerations are applied in the horizontal and vertical directions of the model base. Of particular interest is the computed acceleration at the crest which can be compared directly with the measured ones. Previous analyses of the LV dam have been reported by Griffiths and Prevost [15], Lai and Seed [16], Yiagos and Prevost [17], Woodward and Griffiths [18]. The first natural frequency obtained from the current study is presented in Table 4 and compared with the other solutions available in literature. The present study gives reasonably close agreement with the other numerical investigations. The crest acceleration responses of the LV dam are computed and compared with the motions recorded at the site in the both time and frequency domains.

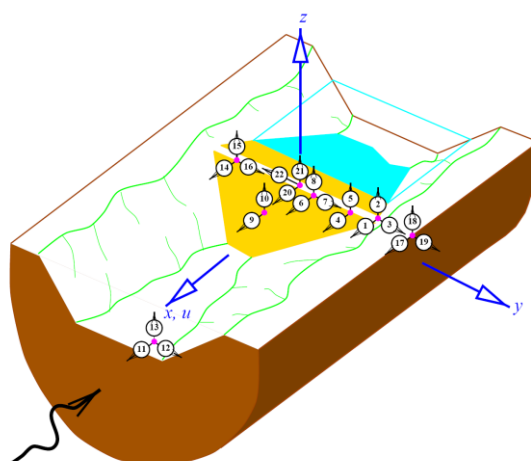


Figure 9. A schematic view of Long Valley canyon and earth dam, and installed instrumentation array [15]

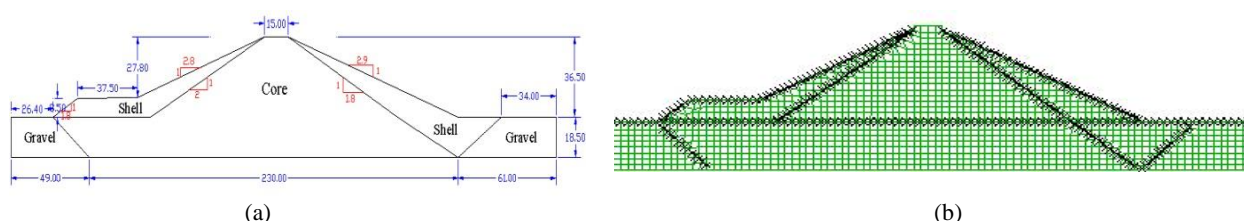


Figure 10. Long Valley earth dam cross section: (a) dimensions in meter, and (b) numerical grid for seismic analysis

Table 4- First natural frequency of LV dam

Mode	Spectral Analysis	2D FE Analysis	3D FE Analysis	Elasto-plastic FE Analysis	Elasto-plastic FE Analysis	Present Study
	Griffith & Prevost	Griffith & Prevost	Griffith & Prevost	Yiagos & Prevost	Woodward & Griffiths	
	Ref. No. [15]	Ref. No. [15]	Ref. No. [15]	Ref. No. [17]	Ref. No. [18]	
1	1.85	1.76	1.95	1.987	1.79	1.71

Figure 11(a) shows the computed horizontal acceleration of the crest. The peak amplitude at the crest has a magnification factor of about 5.47 over the peak base amplitude. The computed response of the crest in the horizontal direction is compared with the measured ones in Figure 11(b). The computed response is plotted with a dashed line. Excellent overall agreement is achieved, with the computed values giving somewhat higher amplitudes. The frequency content of the two time records is compared in the form of a Fourier amplitude spectrum (FAS) in Figure 11(c). The peaks are in close agreement although the computed values show rather more energy associated with the fundamental frequency around 1.8 Hz. The frequency content of the up/down stream motion presented in Figure 11(c) shows that the energy is concentrated at a frequency of just under 2 Hz.

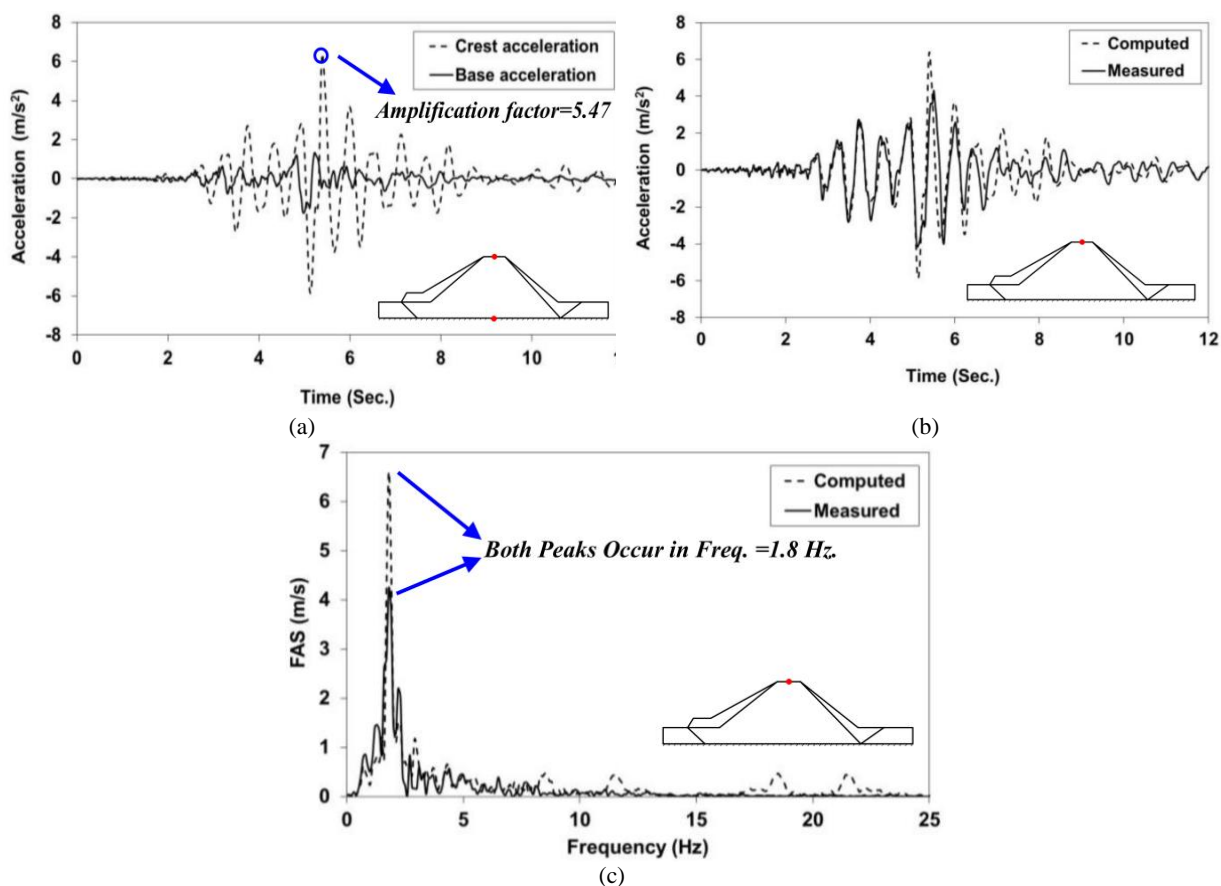


Figure 11. Comparison between computed and measured values of LV dam in horizontal direction at: (a) crest and base, (b) crest acceleration time histories, and (c) Fourier amplitude spectrums

The calculated acceleration in the vertical direction shows less agreement with the measured values. This excitation is noisier than that of horizontal direction and is less intensive. The maximum recorded vertical acceleration at the crest is 0.172g compared with 0.64g in the horizontal direction. The computed accelerations in the vertical direction are compared with the measured ones in Figure 12. The computed values show generally lower amplitudes than the measured ones. The Fourier amplitude spectrum of these time histories is given in Figure 12(c) and the measured values indicate a broad band of frequencies with no particular frequency dominating the situation. The computed values also contain a broad band of frequencies, but with clear peaks in the ranges 2-3 Hz and 5-6 Hz. The frequency content of the vertical acceleration in the form of Fourier response spectra indicates that the computed values do not reproduce the higher frequencies present in the broad band of measured frequencies. It is noticed that the time and frequency-domain results give good agreement and high correlation in the horizontal direction than those of the vertical direction.

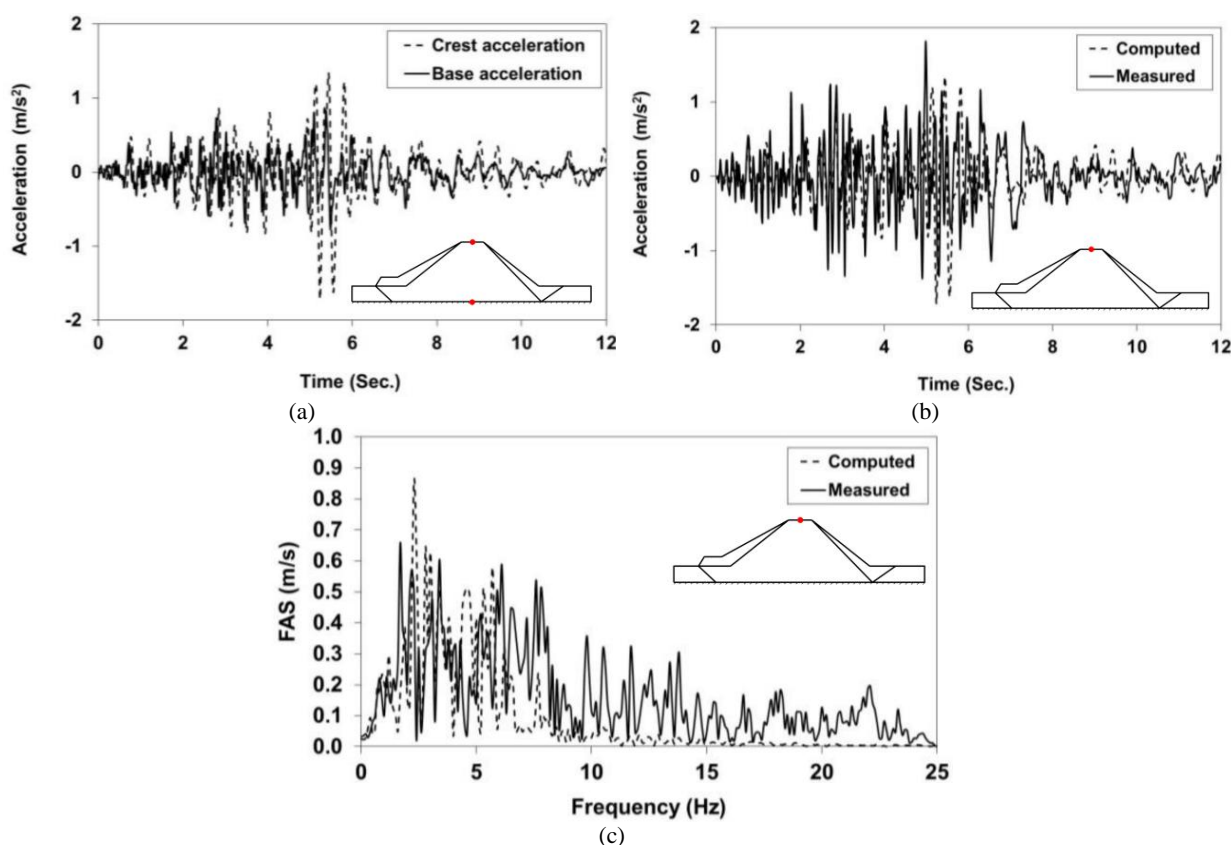


Figure 12. Comparison between computed and measured values of LV dam in vertical direction at: (a) crest and base, (b) crest acceleration time histories, and (c) Fourier amplitude spectrums

The results obtained from validation analysis of the LV dam in term of crest acceleration are compared with those of other previous numerical results available in the literature and summarized in Table 5. These Comparisons show that the current numerical procedure can capture the essential fundamental aspects of the seismic behavior of earth dams very well. It can be concluded that due to the satisfactory modeling of the validation cases, the numerical model is then employed to perform a parametric study on the hypothetical earth dam, as described earlier.

4. NUMERICAL RESULTS AND DISCUSSIONS

Numerous analyses are carried out to investigate the effects dam height and input motion characteristics on the seismic behavior of earth dams. The effects of different types of earthquake on the horizontal deformations at the crest of dams with different heights are shown in Figure 13(a). Besides the displacements, the relevant shear strains are also presented in Figure 13(b). It is clear that the shear strain variation is similar to that of displacement. The horizontal displacements and shear strains in the dam body are increased with increasing dam height. The calculated quantities are much higher for Tabas earthquake and failure occurs in the dam body. Figure 13(a) shows that the computed maximum horizontal displacement at the dam crest is about 94 cm at the end of Tabas earthquake. It can be observed that an increase in the input motion energy leads to a significant increase in the displacements and shear strains. Figure 13(c) illustrates the coupled effects of the dam height and the type of earthquake on the induced maximum acceleration at the dam crest. It is noticed that the crest acceleration is reduced when the dam height increases and no amplification is observed. The reason may be attributed to more flexible behavior, higher damping ratio and larger plastic zones which observed in higher dams. Thus, there is more energy absorption in higher dams with respect to smaller dams due to these factors. It can be seen that the reduction of accelerations in dam crest is more pronounced for the higher dam comparing with the smaller ones.

Table 5- Comparison between numerical studies of LV dam

	Yiagos & Prevost	Woodward & Griffiths	Present Study	Measured values
	Ref. No. [17]	Ref. No. [18]		
Maximum horizontal Acceleration (m/s ²)	0.53g	0.80g	0.61g	0.40g
Minimum horizontal Acceleration (m/s ²)	-0.65g	-0.68g	-0.50g	-0.50g

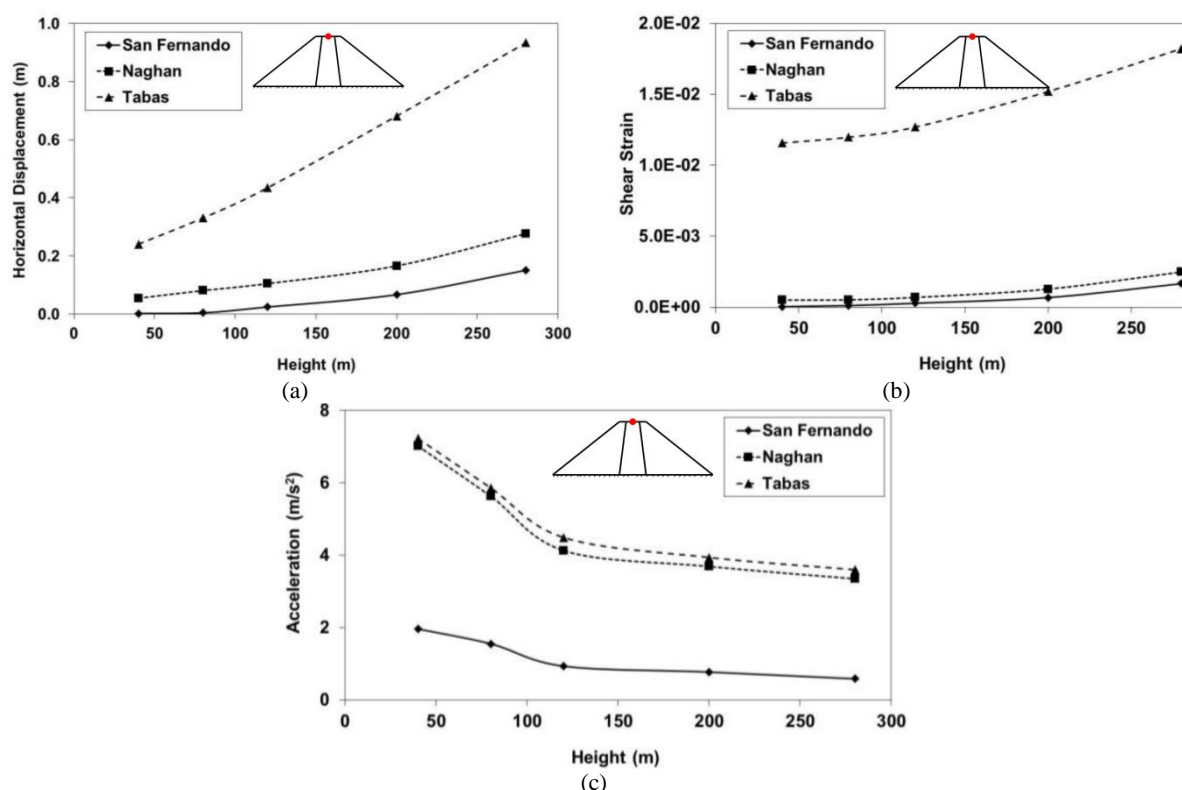


Figure 13. Effect of dam height and input motion characteristics: (a) permanent horizontal displacements, (b) permanent shear strains, and (c) induced maximum accelerations at the dam crest versus dam height for different earthquakes

The pattern of failure mechanism with permanent shear strain contour in the dam body is shown in Figure 14 for two different heights at the end of Naghan earthquake. It is seen that failure occurs in higher dam (280 m) comparing with the smaller one (120 m). The slip surface in 280 m dam is much deeper and clearer than in 120 m. It is noteworthy that the PGA of Naghan earthquake (0.72g) is much higher than San Fernando earthquake (0.21g) but the created displacements and shear strains in dam crest due to Naghan earthquake is close to those obtained from San Fernando input motion. It can be concluded that the PGA is not a sufficient parameter for considering the potential of a particular earthquake on the permanent deformations and the other earthquake parameters such as effective duration, intensity, magnitude, frequency content should be taken into account.

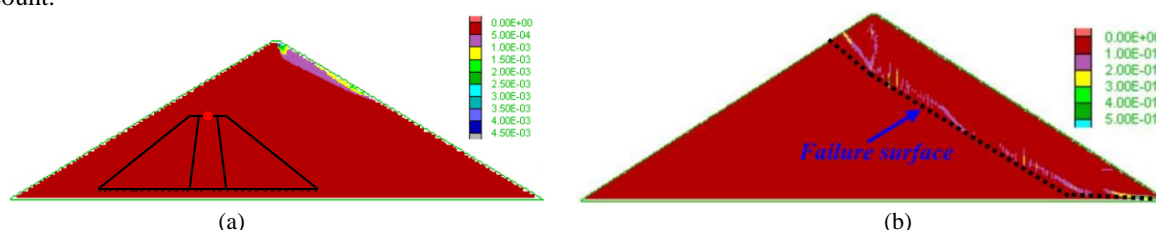


Figure 14. Pattern of failure mechanism in dam body at the end of Naghan earthquake: (a) dam height=120 m, (b) dam height=280 m

5. CONCLUSIONS

This paper presents the nonlinear seismic analyses of earth dams using finite difference method. An elastic perfectly plastic constitutive model with Mohr-Coulomb failure criterion is used to describe the stress-strain response of the soil. Rayleigh damping is utilized to increase the level of hysteretic damping. The Masing rules are implemented into the constitutive relations to precisely explain the nonlinear soil response under general cyclic loading. The numerical model is comprehensively calibrated against the centrifuge test data as well as the field measurements of a real case history both in the time and frequency domains. The numerical analysis is shown to reproduce well the overall behavior of the dam under the earthquake loading qualitatively as well as quantitatively. After validation, a parametric study has been performed to evaluate the influence of real earthquake loading and dam height on the seismic response of the earth dams. Particular attention is given to the influence of dam height on the dynamic seismic of dam. If the dam materials keep their elastic behavior, then the horizontal acceleration becomes larger along the dam height (from the base to the top). In this case, the higher dams show larger amplification, especially if the natural period of dam body coincides to the periodical nature of earthquake motions. As the dam body behaves as a non-linear or even plastic material when a strong earthquake influences the dam, the attenuation of waves becomes more effective, and consequently the earthquake accelerations descend in magnitude when passing from the base towards to the top. Nonlinear elasto-plastic analyses show that the strongest seismic loading (Tabas earthquake) induces plasticity in a large part of dam body when the height of the dam increases. In fact, the stronger earthquakes are more effective to change the material behavior from elastic to plastic in comparison with the rather weak earthquakes. The higher dams are more flexible than the smaller ones, as a result it affects the shear strains which influence the shear modulus and the attenuating coefficient, and all these effects are on the trend of weakening the accelerations along the height. When the dam is subjected to the earthquake with lower energy, the dam body behaves as an elastic material and thus the induced seismic accelerations inside the dam body become larger from the base to the top. In this case, small plasticity zones are developed in the dam body and then the dam remains safe during earthquake loading.

6. ACKNOWLEDGMENT

The first author wants to express his sincere gratitude to the Iran's National Elites Foundation (INEF) for his moral support and encouragement.

7. REFERENCES

1. Seed, H.B., Lee, K.L., Idriss, I.M. and Makdisi, F.I. (1975), “*The Slides in the San Fernando Dams during the Earthquake of February 9, 1971*”, J Geotech Eng Div, ASCE, Vol. 101(GT7), pp. 651–88.
2. Sherard, J.L. (1967), “*Earthquake Considerations in Earth Dam Design*”, J. Soil Mech. Found. Div. – ASCE, Vol. 93, pp. 377–401.
3. Ambraseys, N.N. (1960), “*The Seismic Stability of Earth Dams*”, In: Proc. of the Second World Conference on Earthquake Engineering, Tokyo, Japan, pp. 1345–63.
4. Itasca, (2002), “*FLAC User’s Guide, Version 4.0*”, Itasca Consulting Group. Inc, Minnesota, USA.
5. Kokusho, T. and Esashi, Y. (1981), “*Cyclic Tri-axial Test on Sands and Coarse Material*”, In: Proceedings of 10th International Conference on Soil Mechanics and Foundation Engineering, 1981, (Quoted by Ishihara 1986).
6. Hardin, B.O. and Black, W.L. (1968), “*Vibration Modulus of Normally Consolidated Clay*”, J. Soil Mechanics & Foundation Engineering, ASCE, 84(2), pp. 1531-1537.
7. Seed, H.B., Wong, R.T., Idriss, I.M., Tokimatsu, K. (1986), “*Moduli and Damping Factors for Dynamic Analyses of Cohesionless Soils*”, J. Geotech. Engrg., ASCE, 112 (11), pp. 1016-1032.
8. Vucetic, M. and Dobry, R. (1991), “*Effects of the Soil Plasticity on Cyclic Response*”, J. Geotech. Engrg ASCE, 117, pp. 89–107.
9. Kuhlmeier, R.L. and Lysmer, J. (1973), “*Finite Element Method Accuracy for Wave Propagation Problems*”, Journal of the Soil mechanics and Foundation Division, ASCE, 99(SM5), pp. 421-427.
10. www.nisee.berkeley.edu
11. Masing, G. (1926), “*Eigenspannungen und Verfestigung beim Messing*”, Proc. 2nd Int. Congress on Applied Mechanics, Zurich.
12. Finn, W.D.L., Lee, K.W. and Martin, G.R. (1977), “*An Effective Stress Model for Liquefaction*”, J. Geotech. Engrg. Div., ASCE, Vol 103 (6), pp. 517-553.
13. Arulanandan, K. and Scott, R.F. (1993), “*Verification of Numerical Procedures for the Analysis of Soil Liquefaction Problems*”, Conference Proceedings, Balkema, Rotterdam, Vol. 1.
14. Arulanandan, K. and Scott, R.F. (1994), “*Verification of Numerical Procedures for the Analysis of Soil Liquefaction Problems*”, Conference Proceedings, Balkema, Rotterdam, Vol. 2.
15. Griffith, D.V. and Prevost, J.H. (1988), “*Two- and Three-dimensional Dynamic Finite Element Analyses of the Long Valley Dam*”, Geotechnique Vol. 38, pp. 367-388.
16. Lai, S.S. and Seed, H.B. (1985), “*Dynamic Response of Long Valley Dam in the Mammoth Lake Earthquake Series of May 25-27 1980*”, Report No. UCB/EERC-85/12, Earthquake Engineering Research Center.
17. Yiagos, A.N. and Prevost, J.H. (1991), “*Tow-phase Elasto-plastic Sseismic Response of Earth Dams : Applications*”, Soil Dynamics and Earthquake Engineering Vol. 10, No. 7, pp. 371-381.
18. Woodward, P.K. and Griffiths, D.V. (1996), “*Non-linear Dynamic Analysis of the Long Valley Dam*”, Compute Methods and Advances in Geomechanics Vol. 11, No. 6, pp. 635-644.

Numerical Analysis of Soil Liquefaction Induced Failure of Earth Dams

Babak Ebrahimian^{1,2}, Ali Noorzad¹

1- Faculty of Civil, Water and Environmental Engineering, Abbaspour School of Engineering, Shahid Beheshti University (SBU), Tehran, Iran

2- The Highest Prestigious Scientific and Professional National Foundation, Iran 's National Elites Foundation (INEF), Tehran, Iran

Emails: ebrahimian.babak@gmail.com; b_ebrahimian@sbu.ac.ir

Abstract

This study presents numerical modeling of the dynamic behavior of an earth dam rested on a liquefiable foundation. Numerical simulations are carried out using effective stress-based, fully coupled nonlinear dynamic analysis approach. The Finn-Byrne model with extended Masing rules is employed to model pore pressure generation in the liquefied soils. In this regard, Masing rules are implemented into the constitutive relations to precisely explain the nonlinear response of soil under general cyclic loading. As a result, the soil shear stiffness and hysteretic damping can change with loading history. Pore pressure is accumulated as a function of the cyclic shear strain amplitude. The procedure of calibrating the constructed numerical model with well-documented centrifuge test data is addressed. Acceptable agreements are shown between the results obtained from the current investigation and those of experimental observations available in the literature. Afterwards, the dynamic response of an earth dam founded on a liquefiable sandy soil foundation is evaluated and discussed. Special emphasis is given to the computed excess pore water pressures, deformations and accelerations during dynamic loading. It is shown that the numerical model can predict the essential aspects of liquefaction phenomenon occurred in the earth dam-foundation system during dynamic loading.

Keywords: Numerical simulation, nonlinear dynamic response, liquefaction, earth dam.

1. INTRODUCTION

Soil structures such as embankments and earth dams have been frequently damaged during past major earthquakes in seismically active regions of the world due to the liquefaction of dam materials and/or foundation soils. Many liquefaction induced dam failures or near-failures have been reported during various previous earthquakes [1]. In most cases, large deformations have been occurred due to the liquefaction of the supporting loose cohesionless foundation soil [2]. Experimental studies including shaking table tests [3-4] and centrifuge tests [5-6] and numerical investigations [7-8] related to the liquefaction assessment in embankments and earth dams have been conducted. According to these studies, a complete representation of the failure mechanism usually requires using comprehensive constitutive models accompanied by numerical techniques to account for the effect of generation and dissipation of pore pressure within the dam body and foundation soil and its impact on the variation of shear strength which, in turn, will lead to permanent deformations.

In the current study, the dynamic behavior of an earth dam rested on a liquefiable foundation is numerically simulated by an effective stress-based, fully coupled nonlinear analysis approach. In the following, the numerical modeling procedure is briefly described and then, some aspects related to calibration of the numerical model by using the centrifuge test data are discussed. After verification, a reference model is constructed to represent the basic of dynamic behavior of earth dam founded on a liquefiable soil. A comparative study is performed to identify the effects of liquefiable soils location (in dam, in foundation or in both of them) on the permanent deformations of earth dam, accelerations, pore pressure, liquefaction potential and failure modes of earth dam-foundation system.

2. REVIEW OF NUMERICAL MODELING

In this research, a two-dimensional (2D) reference model is developed to simulate the dynamic behavior of an earth dam founded on liquefiable soil. Nonlinear time history dynamic analysis is conducted using computer program FLAC 2D (Fast Lagrangian Analysis of Continua) [9]. This program is based on a continuum finite difference discretization using the Lagrangian approach. For dynamic analysis, it uses an

explicit finite difference scheme to solve the full equation of motion using lumped grid point masses derived from the real density surrounding zone.

Finn and Byrne model is modified and used to carry out coupled effective stress dynamic calculations [10]. The model takes into account the effects of dynamically induced pore water pressures to investigate the degree and extend of liquefaction. First, a static analysis considering the effect of gravity loading is conducted to simulate the stress conditions before the dynamic loading. Once, the initial stress state is established in the model, the reservoir is placed behind the dam. It is noted that the dam and foundation are modeled in several stages corresponding to the stage construction procedure of earth dams. Afterwards, the soil model is changed to a pore pressure generation constitutive model; the effective stress fully coupled dynamic analysis is recalled and started. During the dynamic analysis, the excess pore water pressures are allowed to generate and also the dissipation of these pore pressures is simulated. The selected reference model is a simplified representation of typical earth dam geometry with a symmetric zone section. The numerical grid used in the current study is illustrated in Figure 1.

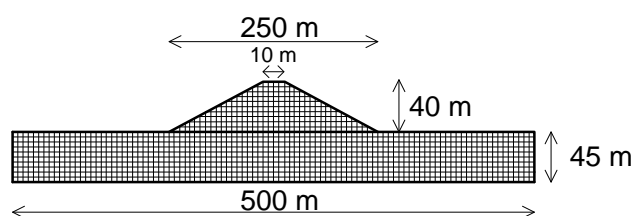


Figure 1. Numerical grid of the dam-foundation system

In static analysis, Mohr-Coulomb constitutive relations are used to model the behavior of sandy soil. The linear behavior is defined by the elastic shear and drained bulk modulus. The shear modulus of sandy soil is calculated with the formula given by Seed and Idriss [11]:

$$G_{\max} = 1000k_{2\max} (\sigma'_m)^{0.5} \quad (1)$$

where, G_{\max} is the maximum (small strain) shear modulus in pounds per square foot, *psf* (it is later converted to *kPa* to be consistent with the metric units being used), $K_{2\max}$ is the shear modulus number (Seed and Idriss [15]), and σ'_m is the mean effective confining stress in *psf*. The Poisson's ratio for sandy soil is taken as 0.3.

For pore water generation during dynamic analysis, the updated model proposed by Byrne [10] is incorporated to account the development of pore water pressure build-up as an effect of volumetric strain induced by the cyclic shear strain using the following formulation:

$$\Delta\varepsilon_v = C_1 \exp(C_2 \varepsilon_v / \gamma) \quad (2)$$

where, $\Delta\varepsilon_v$ is the increment in volumetric strain that occurs over the current cycle, ε_v is the accumulated volumetric strain for previous cycles, γ is the shear strain amplitude for the current cycle, and C_1 and C_2 are constants dependent on the volumetric strain behavior of the sand. According to Byrne [10], the constant C_1 in Equation (2) controls the amount of volumetric strain increment and C_2 controls the shape of the volumetric strain curve. These constants are estimated using:

$$C_1 = 7600(Dr)^{-2.5} \quad (3)$$

$$C_2 = 0.4/C_1 \quad (4)$$

where, Dr is the relative density of the soil in percent.

To provide a constitutive model that can better fit the curves of shear modulus degradation and damping ratio increase derived from the experimental tests data, two different modifications are implemented into the FLAC soil model as a part of this research to more precisely assess the potential for predicting liquefaction process and associated deformations. To represent the nonlinear stress-strain behavior of soil more accurately that follows the actual stress-strain path during cyclic loading, the masing rules are implemented into FLAC which works with Byrne model by a FISH subroutine as a first modification. Since, there is a need to accept directly the same degradation curves derived from the test data in fully nonlinear method to model the correct physics, so, the second modification is related to incorporate cyclic data into a hysteretic damping model in FLAC. Modulus degradation curves imply a nonlinear stress-strain curve. An incremental constitutive relation can be derived from the degradation curve, described by $\tau/\gamma = M_s$, where τ is the normalized shear stress, γ is the shear strain and M_s is the normalized secant modulus. The normalized tangent modulus, M_t , is described as

$$M_t = d\tau/d\gamma = M_s + \gamma \cdot dM_s/d\gamma \quad (5)$$

The incremental shear modulus in a nonlinear simulation is then given by GM_t , where G is the small-strain shear modulus of the material. Shear modulus and damping of soils are strain dependent. Shear modulus decreases with increasing shear strain and damping increases with increasing strain. In this study, the shear modulus reduction and Damping ratio increase curves for sandy soils propose by Seed and Idriss are adopted [11]. Geotechnical properties used in the analyses are presented in Table 1 for foundation soil and earth dam materials.

Table 1- Geotechnical soil properties

	γ_d (kN/m ³)	G (MPa)	K (MPa)	Friction (degree)	C ₁	C ₂
Dam	1520	40	87	30	0.185	2.15
Foundation	1600	60	195	35	0.43	0.93

After static equilibrium is achieved (end of static construction stage), the full width of the foundation is subjected to the variable-amplitude harmonic ground motion record illustrated in Figure 2. The mathematical expression for input acceleration is given by:

$$\ddot{U}(t) = 0.6 \times \sqrt{\beta e^{-\alpha t} t^\eta} \sin(2\pi f t) \quad (6)$$

where, $\alpha=3.3$, $\beta=1.3$ and $\eta=10$ are constant coefficients, f is the base acceleration frequency and, t is the time.

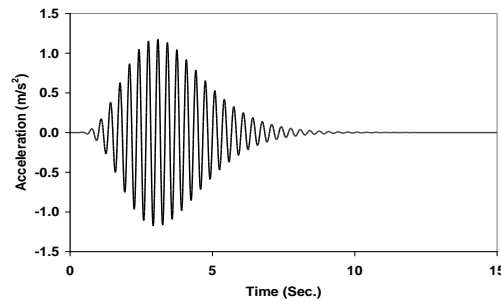


Figure 2. Seismic excitation applied to the bottom of the numerical model

During the static analysis, the bottom boundary is fixed in the both horizontal and vertical directions and the lateral boundaries are just fixed in the horizontal direction. In dynamic problems, fixed boundary condition will cause the reflection of outward propagating waves back into the model. Therefore, during the dynamic analysis, the lateral boundary conditions are changed to the FLAC free-field boundary to eliminate wave reflections from the truncated boundaries [10].

In each dynamic analysis, 5 percent Rayleigh damping which is a typical value for geologic materials [13] is included for the soil elements in addition to the hysteretic damping already incorporated in the nonlinear stress-strain model. The damping frequency is chosen by examining the undamped behavior of the numerical model. A damped frequency of 1.8 Hz is used for the present model.

To avoid the numerical distortion of the propagating wave in dynamic analysis the spatial element size, Δl , must be smaller than approximately one-tenth to one-eighth of the wavelength associated with the highest frequency component of the input wave (Kuhlemeyer and Lysmer [12]):

$$\Delta L = \lambda/9 \quad (7)$$

In general, the cut-off frequency for geotechnical earthquake engineering problems should be not less than 10 Hz [13]. Considering above criteria, element size is defined small enough to allow seismic wave propagation throughout the analysis.

3. VERIFICATION ANALYSIS

To validate the implementation of the masing rules and hysteretic damping in FLAC program via a series of FISH function, the simulation of one-zone sample with modified Byrne model is conducted by using the unit cell incorporated with the implemented rules as shown in Figure 3. The one-zone sample is modeled

with FLAC which consists of a sandy soil and a periodic motion is exerted at its base. Vertical loading is established by gravity only. Equilibrium stresses and pore pressures are installed in the soil, and pore pressure and effective stress (mean total stress minus the pore pressure) are created within the soil. The results are shown in Figures 4 and 5. Figure 4 indicates the pore pressure build-up in a single zone. It can be seen that the effective stress reaches zero after about 20 cycles of shaking (2 seconds, at 5 Hz). At this point, liquefaction can be said to occur. The stress/strain loops of the one-zone sample for several cycles are shown in Figure 5. It can be observed that shear modulus decreases with increasing shear strain. The hysteretic model seems to handle multiple nested loops in a reasonable manner. There is clearly energy dissipation and shear stiffness degradation during seismic loading.

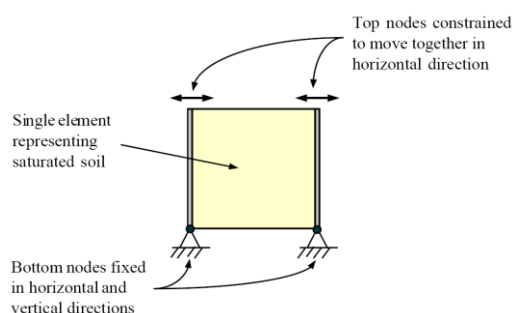


Figure 3. One-zone model in FLAC for simulating cyclic simple shear test

To evaluate the applicability of the effective stress-based analysis by FLAC, the results obtained from numerical analyses are compared with the experimental counterparts. One of the centrifuge tests related to the embankment performed in VELACS project (VERification of Liquefaction Analysis using Centrifuge Studies [6], [7]) has been chosen to evaluate the ability of the constitutive model in predicting the liquefaction phenomenon during seismic loading. It is attempted to create almost similar conditions between laboratory model test and numerical model.

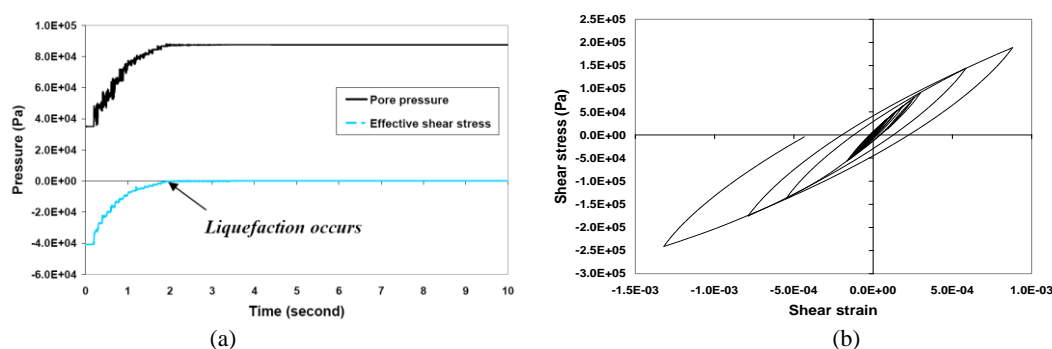


Figure 4. Simulation of cyclic simple shear test of one-zone sample in FLAC: (a) pore pressure generation and effective stress time histories during the dynamic loading, and (b) hysteresis loops

The model test configuration is depicted in Figure 5(a). The numerical model constructed in FLAC is shown in Figure 5(b). The numerical results are presented and compared to those obtained from the corresponding centrifuge test. Comparisons between the computed and measured results are made in Figure 6. These comparisons show that the reference numerical model can predict the dynamic behavior of an earth dam in a reasonable manner. Due to the satisfactory modeling of the validation cases, the numerical model is then used to perform comparative study on the earth dam, as described earlier.

4. NUMERICAL RESULTS AND DISCUSSIONS

Three sets of analysis are conducted to cover all the basis of liquefaction phenomenon occurred within the earth dam and its foundation and also to evaluate the overall performance of the dam–foundation system due to the liquefaction during dynamic loading. These analyses are assigned as: Case (1): Both the dam and its foundation are susceptible to liquefaction. Case (2): Only the foundation has liquefaction potential. Case (3): Only the dam has liquefaction potential. The responses of earth dam during dynamic loading in terms of acceleration, deformation, excess pore water pressure (U_e) and excess pore water pressure ratio (R_u) are

considered. The failure mechanism of the dam can be observed in the plot of deformed grid after the dynamic loading, presented in Figure 7. It is clear that according to the simulations, the failure occurs as a progressive movement in the dam body. In Case (3), failure is observed in the both upstream and downstream slopes of dam. The overall deformation patterns of the models are the same. Horizontal displacement attained maximum values at downstream slope of the dam. The maximum horizontal and vertical displacements occur in Case (1). The shear strain increments contours are shown in Figure 8. The progressive failure is observed in slopes for all cases and failure surfaces are completely clear in the dam body. It is of interest to observe that the computational results show larger downstream lateral movements compared to the upstream side. This may be attributed to the presence of the laterally varying phreatic surface. The variable water table induced: (1) a fluid seepage force in the upstream–downstream direction and (2) a higher initial (static) shear stress distribution on the downstream side of the dam. The quantities of shear strain increments are higher for Case (1) in comparison with the other cases.

The normalized excess pore pressure ratio, (or cyclic pore pressure ratio, U_e/σ_c) is used to identify the region of liquefaction in the model. Where U_e is the excess pore pressure and σ_c is the initial effective confining stress. Note that a liquefaction state is reached when $U_e/\sigma_c = 1$. Contours of the cyclic pore pressure ratio greater than 0.99 are plotted in Figure 9. These contours show that the extent of the liquefied soils have been primarily established in the upstream region. Significant amounts of pore pressure developed after the dynamic loading can be seen in the majority of the soil material located in the upstream face and close to the dam heel. There is a larger zone of liquefaction in Case (1) rather than the other cases.

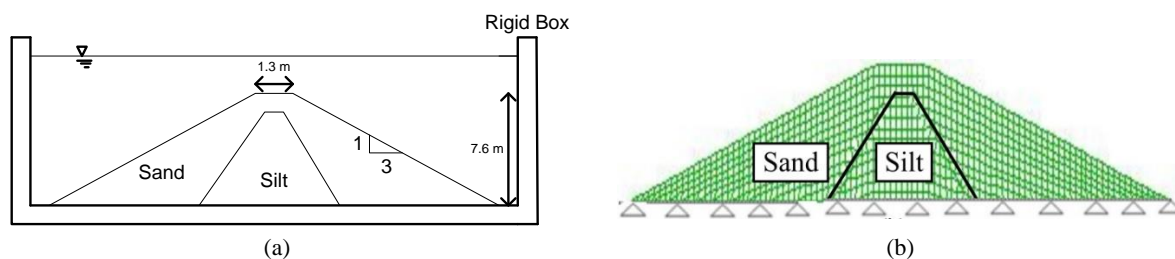


Figure 5. Model configuration in rigid container: (a) centrifuge test, and (b) numerical grid constructed in FLAC

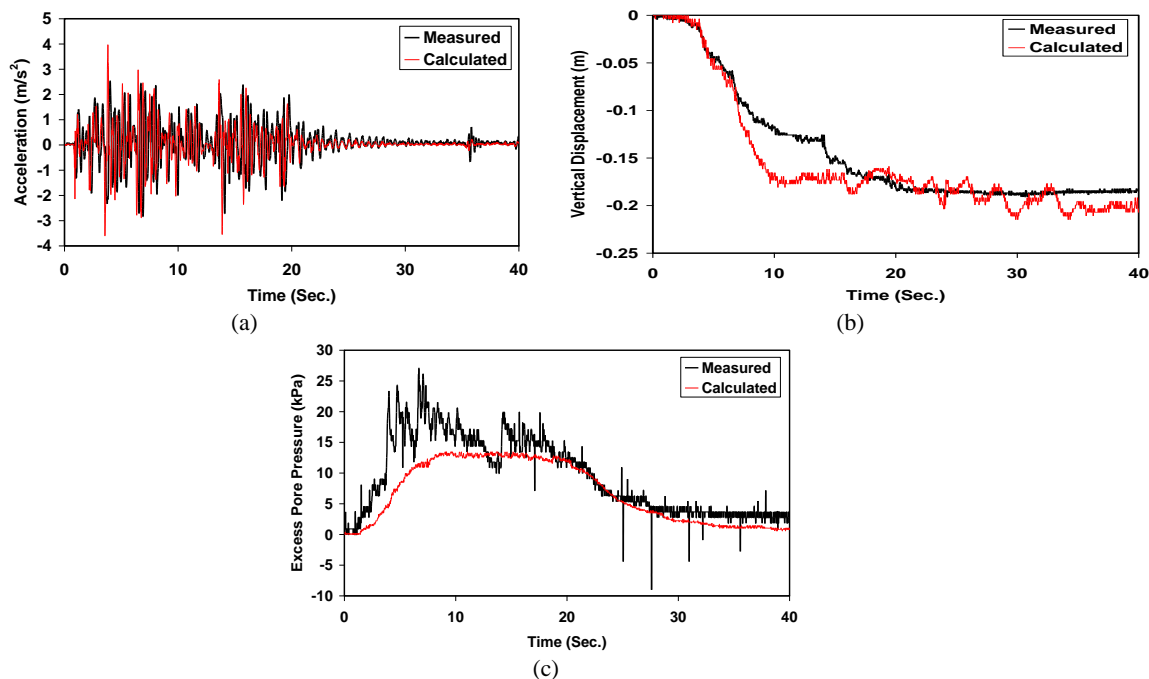


Figure 6. Comparison between obtained numerical results and centrifuge test data: measured versus calculated (a) acceleration time histories, (b) displacement time histories, and (c) excess pore pressure time histories at the middle of dam height

Figure 10 (a) shows the horizontal displacement computed at the downstream slope of dam. In all cases, the horizontal displacement is seen to accumulate on a cycle-by-cycle basis. In general, lateral movements are seen to increase when the liquefaction occurs in the both dam and foundation materials. The maximum horizontal displacement (within the downstream slope) is about 1.4 m. The vertical displacement computed at the dam crest is shown in Figure 10(b). In general, maximum settlements take place in the crest of dam. The maximum vertical settlement at the crest is about 0.85 m. Figure 10(c) shows the predicted acceleration time histories at the crest of dam for all cases. It indicates that the input motion is amplified in all cases. The maximum amplification occurs in Case (3) at 3.75 seconds. The computed acceleration time histories at the crest show that the input motion is amplified at the crest of dam about 1.8, 1.7 and 2 times for Cases (1), (2) and (3), respectively.

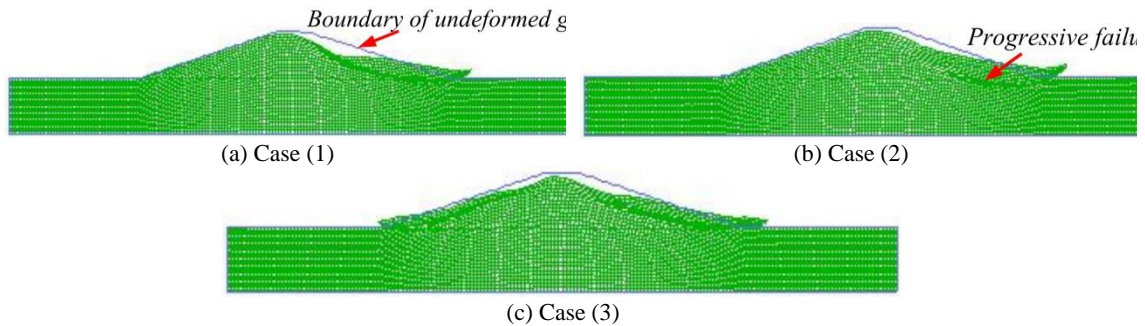


Figure 7. Computed deformed configuration at the end of dynamic loading (magnified by factor of 5 for clarity)

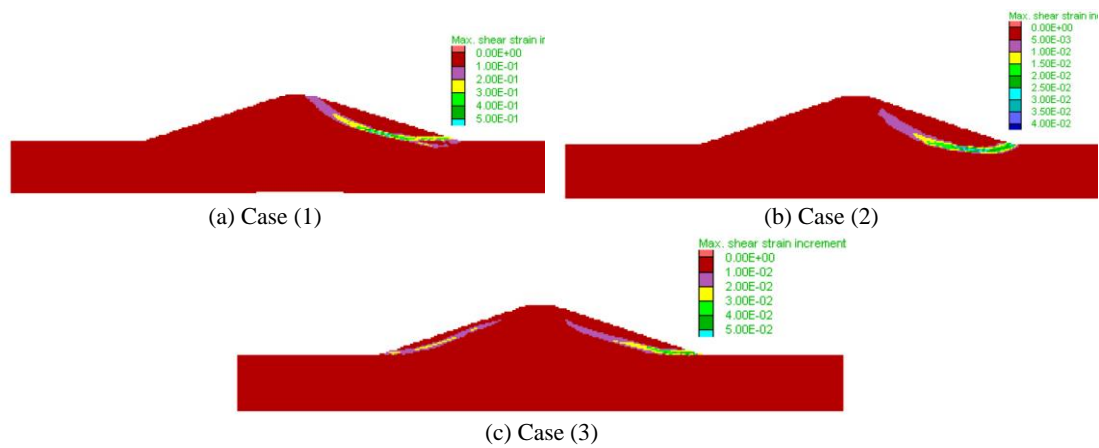


Figure 8. Computed shear strain increment contours at the end of dynamic loading

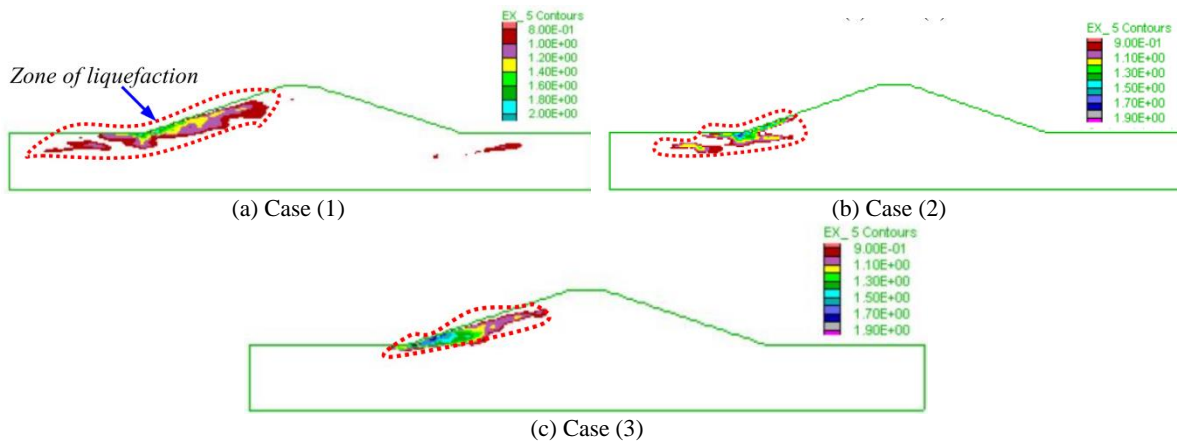


Figure 9. Contours of cyclic pore pressure ratio at the end of dynamic loading (values greater than 0.99)

Predicted excess pore pressures (U_e) as a function of time are shown in Figure 11(a) recorded in the zone of liquefaction at a nearby location of dam heel in foundation. It can be seen that the pore pressures increase rapidly in the time of 1 to 4 s, corresponding to the period of strong shaking, and then level off. However, the computed results of Case (1) are higher in the residual state comparing with the other cases. Figure 11(b) shows the evolution of the excess pore water pressure ratio (R_u) during the dynamic loading in the zone of liquefaction at a nearby location of dam heel in foundation. The excess pore water pressure ratio (R_u) increases significantly from the second 0.7 to 2.5 and then becomes constant. $R_u = 1$ represents a condition of 100 % pore pressure ratio and complete liquefaction.

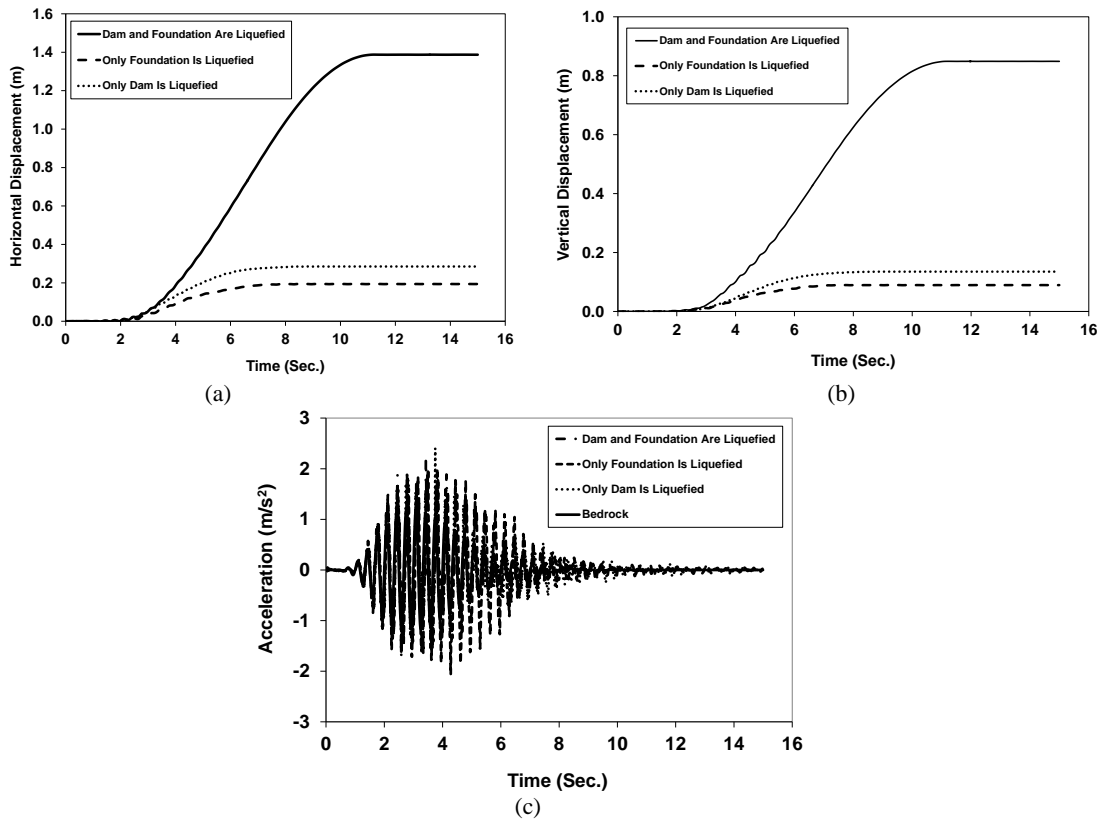


Figure 10. Computed results: (a) horizontal displacement time histories at the downstream slope of dam, (b) vertical displacement time histories, and (c) acceleration time histories at the crest of dam

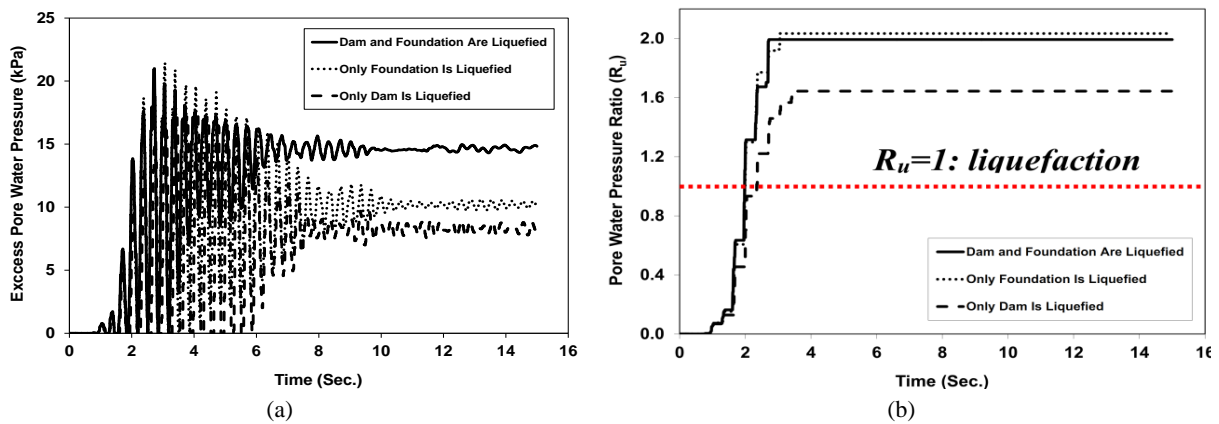


Figure 11. Computed results: (a) excess pore water pressure (U_e), and (b) excess pore water pressure ratio (R_u) time histories at the zone of liquefaction

5. CONCLUSIONS

A fully coupled nonlinear effective stress-based approach is applied to the dynamic behavior and deformation analyses of earth dam–foundation system that experiences induced liquefaction. The Finn-Byrne model with extended Masing rules is incorporated in FLAC and used for the analyses. The soil stiffness reduction and hysteretic damping changes are considered during the dynamic loading. The model's capability is demonstrated by comparing the numerical simulations with the centrifuge test results. It is observed that the numerical simulation models reasonably well the dynamic behavior of the earth dam during liquefaction phenomenon and therefore, its applicability is confirmed. It is found that, in the analyses, when liquefaction occurs in the both dam materials and foundation soils; liquefied zone at a nearby location of dam heel becomes larger and also maximum horizontal and vertical displacements occur for this case. There are larger downstream lateral movements compared to the upstream side. This may be attributed to the presence of the laterally varying phreatic surface and a higher initial (static) shear stress distribution on the downstream side of the models. The maximum amplification for acceleration occurs in the case that only the dam materials are liquefied.

6. ACKNOWLEDGMENT

The first author wants to express his sincere gratitude to the Iran's National Elites Foundation (INEF) for his moral support and encouragement.

7. REFERENCES

1. Seed, H.B. (1968), “*Landslides During Earthquakes due to Soil Liquefaction*”, Journal of Geotechnical Engineering Division, American Society of Civil Engineering Vol. 94(5), pp. 1055–1123.
2. Krinitzky, E.L. and Hynes, M.E. (2002), “*The Bhuj, India, Earthquake: Lessons Learned for Earthquake Safety of Dams on Alluvium*”, Eng. Geol. (Amsterdam), Vol. 66(3–4), pp. 163–196.
3. Koga, Y. and Matsuo, O. (1990), “*Shaking Table Tests of Embankments Resting on Liquefiable Sandy Ground*”, Soils and Foundations Vol. 30(4), pp. 162-174.
4. Park, Y.H., Kim, S.R., Kim, S.H. and Kim, M.M. (2000), “*Liquefaction of Embankments on Sandy Soils and the Optimum Countermeasure Against the Liquefaction.*” In: Proceeding of 7th International Conference on Computer Methods and Advances in Geomechanics. Balkema, Rotterdam, Vol. 2, pp. 869-874.
5. Arulanandan, K. and Scott, R.F. (1993), “*Verification of Numerical Procedures for the Analysis of Soil Liquefaction Problems*”, Conference Proceedings, Balkema, Rotterdam, Vol. 1.
6. Arulanandan, K. and Scott, R.F. (1994), “*Verification of Numerical Procedures for the Analysis of Soil Liquefaction Problems*”, Conference Proceedings, Balkema, Rotterdam, Vol. 2.
7. Elgamal, A., Yang, Z. and Parra, E. (2002), “*Computational Modeling of Cyclic Mobility and Post-liquefaction Site Response*”, Soil Dynamics and Earthquake Engineering. Vol. 22(4), pp. 259–271.
8. Yang, Z., Elgamal, A.H., Adalier, K. and Sharp, M.K. (2004), “*Earth Dam on Liquefiable Foundation and Remediation: Numerical Simulation of Centrifuge Experiments*”, Journal of Engineering Mechanics Vol. 130(10).
9. Itasca, (2002), “*FLAC User's Guide, Version 4.0*”, Itasca Consulting Group. Inc, Minnesota, USA.
10. Byrne, P. (1991), “*A Cyclic Shear-volume Coupling and Pore-pressure Model for Sand*”, In Proceedings: Second International Conference on Recent Advances in Geotechnical Earthquake Engineering and Soil Dynamics (St. Louis, Missouri), Paper No. 1.24, pp. 47-55.
11. Seed, H.B. and Idriss, I.M. (1970), “*Soil Moduli and Damping Factors for Dynamic Response Analyses*”, Report EERC 70-10, Earthquake Engineering Research Center. University of California, Berkeley, CA. (as cited in Kramer, 1996).
12. Kuhlemeyer, R.L. and Lysmer J. (1973), “*Finite Element Method Accuracy for Wave Propagation Problems*”, Journal of Soil Mechanics and Foundations. ASCE Vol. 99, No. SM4, pp. 421-427.
13. American Society of Civil Engineers, (2000), “*ASCE 4-98 Seismic Analysis of Safety-related Nuclear Structures and Commentary*”, ASCE, Virginia, USA.

Numerical Analysis of Granular Soil-Structure Interface Behavior at Large Shearing Displacement: Evolution and Characterization

Babak Ebrahimian^{1,2}, Ali Noorzad¹

1- Faculty of Civil, Water and Environmental Engineering, Abbaspour School of Engineering, Shahid Beheshti University (SBU), Tehran, Iran

2- The Highest Prestigious Scientific and Professional National Foundation, Iran's National Elites Foundation (INEF), Tehran, Iran

Emails: ebrahimian.babak@gmail.com; b_ebrahimian@sbu.ac.ir

Abstract

This paper presents the interface behavior between cohesionless granular soil and moving bounding structure using finite element method and a micro-polar elasto-plastic continuum model. The focus of investigation is on the consideration of rough, medium rough and relatively smooth interfaces. In this regard, plane monotonic shearing of an infinite extended narrow granular soil layer between two parallel rigid boundaries of varying surface roughness is simulated under the conditions of constant vertical pressure and free dilatancy. To describe the essential mechanical properties of granular soil, an elasto-plastic single hardening soil model enhanced by polar quantities i.e., Cosserat rotations, curvatures, and couple stresses is employed. Furthermore, the mean grain diameter as the material characteristic length is implemented in the model to properly predict the thickness of shear band formed along the interface as well as to consider the scale effect in the simulations. Particular attention is paid to the influence of boundary condition on the shear behavior of granular soil layer. In this regard, the additional micro-polar kinematical boundary conditions along the boundaries allow more detailed description of the surface roughness of adjoining structure. It is shown that the assumed boundary conditions have strong influences on the granular soil behavior in terms shear band thickness and mobilized interface friction angle. For large shearing, the shear deformations and polar quantities are localized within a narrow zone, called shear band, parallel to the direction of shearing and the state quantities tend towards a stationary state. It is also revealed that the location of shear bands is different in an infinite or finite shear layer.

Keywords: Micro-polar continuum, elasto-plasticity, interface shearing, granular soil, finite element.

1. INTRODUCTION

The serviceability of a wide range of engineering structures involving interfaces between their structural elements and adjoining soil bodies is highly dependent on the behavior of soil layer forming close to the surface of bounding structure. Due to the shear movement of bounding structure, the intense shear deformations are localized within the interface, in the form of an induced single shear band [1]. The localized shearing mechanism mainly governs the interface behavior and controls the overall performance of structure having interaction with the soil body [2]. The investigations of soil-structure interface behavior have attracted great attentions of many researchers in recent years. Field observations, laboratory experiments and numerical simulations have been conducted in order to gain insights into the complex phenomena occurred in the soil bodies close to the surface of bounding structures. In this regard, the development of strain localization and shear banding occurring along the interface and the relevant micro-mechanical mechanisms are still not fully known. Most of the previous studies on interface behavior between granular media and rough surfaces have focused on exploring and quantifying factors influencing peak and steady state strength along the interface [3-9]. However, very limited experimental works have been published on shear deformation of interface due to difficulty in collecting microscopic information, at the scale of soil grains, interior to the soil samples [10-11].

In this paper, shear behavior of interface between granular soil body and moving bounding structure is analyzed using FEM and micro-polar continuum approach. To this end, a micro-polar elasto-plastic single hardening soil model is applied to simulate the mechanical behavior of cohesionless granular materials like sand [12-13]. Plane monotonic shearing of an infinite long and narrow granular soil layer, located between two parallel rigid boundaries of varying surface roughness, is investigated under constant vertical pressure and free dilatancy. In FE analyses, the emphasis is given to the influence of bounding structure's surface roughness on the shear band thickness as well as the mobilization of shear strength along the interface. Furthermore, the

distribution and evolution of polar quantities and state variables are mainly focused to precisely consider the interface shear behavior of granular soil layer in contact with a bounding structure. Micro-polar kinematical boundary conditions are introduced to describe different roughness values of interface. Such conditions take into account Cosserat rotation, displacement along the boundary, surface roughness of bounding structure, and the ratio between slip and corresponding Cosserat rotation along the boundary. Following the relevant literature, this research presents the first numerical simulation systematically addressing the effect of continuum surface roughness on the shear behavior of neighboring micro-polar elasto-plastic granular material. Furthermore, the numerical results obtained in this study can be considered as a basis to be compared with the future laboratory experiments and DEM-simulations.

2. REVIEW OF CONSTITUTIVE MODEL

Cosserat continuum kinematics are distinguished from classical continuum theory by introducing an extra rotational degree of freedom of a body-point, independent of translational degrees of freedom [14]. For plane strain problems, each material point has three degrees of freedom, two translational represented and one rotational. In Cosserat continuum stress and strain tensors are generally non-symmetric due to the existence of couple stresses and curvatures. According to [14], the objective or Cosserat strain rate tensor now can be redefined as

$${}^{n+1}\dot{\gamma}_{ij} = {}^{n+1}\dot{E}_{ij} + ({}^n\dot{\Omega}_{ij} - {}^n\dot{\Omega}_{ij}^c) \quad (1)$$

$$\dot{\Omega}_{ij} = \frac{1}{2}(v_{i,j} - v_{j,i}) \quad (2)$$

$$\Omega_{ij}^c = -e_{ijk}\omega_k^c \quad (3)$$

$${}^n\kappa_{ij} = {}^n\omega_{j,i}^c \quad (4)$$

where, \dot{E}_{ij} is classical strain-rate tensor; Ω and Ω^c are classical spin and Cosserat spin tensors, respectively; e_{ijk} is the Ricci permutation tensor; and κ_{ij} curvature vector of deformation or the gradient of grain rotation. The single hardening Lade's model enhanced with Cosserat rotations, curvatures and couple stresses [12-13], is used in this study. The model is obtained through extending non-polar Lade constitutive relations [15-17] by Cosserat quantities. Lade's model is an elasto-plastic soil model with single yield surface expressed in terms of stress invariants. The employed micro-polar Lade's model is enhanced through the second stress and deviatoric stress invariants in order to incorporate the material characteristic length. The model formulations are very briefly discussed here to make this paper self-contained and more details are found in [12-13]. The constitutive constants of micro-polar Lade's model can be determined by the simple standard laboratory experiments. The model has totally 16 material constants, for 11 of which (M_L , λ , ν , m , η_1 , μ , ψ_2 , h , α , C and P) the calibration procedure are conducted based on the experimental data of three conventional CD triaxial tests and one isotropic compression test. These 11 constants are calibrated similarly in both micro- and non-polar version of Lade's model because the micro-polarity is not affected for purely homogeneous and co-axial deformations with zero couple stresses. The definition of material constants and calibration procedure are presented in [12-13]. Non-linear elasticity modulus is as follows:

$$E = M_L P_a \left[\left(\frac{I_1}{P_a} \right)^2 + \left(6 \frac{1+\nu}{1-2\nu} \right) \frac{J_2'}{P_a^2} \right]^\lambda \quad (5)$$

where, P_a is a reference pressure used for normalizing the stress invariants (this pressure is assumed as atmospheric pressure); I_1 is the first invariant of stress tensor ($I_1 = \sigma_{ii}$; where, $i = 1, 2, 3$); M_L and λ are dimensionless material parameters, determined by a series of simple experiments of loading-unloading-reloading cycles (for more details see [15]); ν is constant Poisson's ratio; and J_2' is the second invariant of deviatoric stress tensor according to [14]. The mentioned invariant is enhanced to account for the couple stress effect and expressed as:

$$J'_2 = \left\{ \left[(\sigma_{11} - \sigma_{22})^2 + (\sigma_{33} - \sigma_{22})^2 + (\sigma_{11} - \sigma_{33})^2 \right] + \left(\frac{\sigma_{12} + \sigma_{21}}{2} \right)^2 \right\} + \frac{(m_1^2 + m_2^2)}{l^2} \quad (6)$$

where, σ_{ij} and m_i are stress and couple stress, respectively; and l is the internal length scale.

The second invariant has been enhanced to incorporate the effect of couple stresses (m_i) and expressed as follows:

$$I_{II} = \frac{1}{2} (\sigma_{12}\sigma_{21} - \sigma_{11}\sigma_{22} - \sigma_{11}\sigma_{33} - \sigma_{22}\sigma_{33}) - \frac{m_1 m_2}{l^2} \quad (7)$$

Stress tensor is expressed in the 2D Cosserat continuum in the vector form as follows:

$$\{\sigma\} = \left\{ \sigma_{11} \quad \sigma_{22} \quad \sigma_{33} \quad \sigma_{12} \quad \sigma_{21} \quad \frac{m_1}{l} \quad \frac{m_2}{l} \right\}^T \quad \text{or} \quad \{\Sigma\} = \left\{ \sigma \right\} \quad (8)$$

Similarly, the objective strain vector, including strain and curvature of rotations, is non-symmetric and defined as:

$$\{\gamma\} = \{\nabla U\} = \left\{ \gamma_{11} \quad \gamma_{22} \quad \gamma_{33} \quad \gamma_{12} \quad \gamma_{21} \quad l\kappa_1 \quad l\kappa_2 \right\}^T \quad \text{or} \quad \{\gamma\} = \left\{ \begin{matrix} \varepsilon \\ \kappa \end{matrix} \right\} \quad (9)$$

In FE implementation, each node has the following degrees of freedom in the plane strain Cosserat continuum as:

$$\{U\} = \left\{ u_1 \quad u_2 \quad \omega_3^c \right\}^T \quad (10)$$

The following constitutive law can be used:

$$\{\dot{\sigma}\} = [D] \{\dot{\gamma}\} \quad (11)$$

where, [D] is elasto-plastic stiffness matrix.

A quadrilateral isoparametric 4-node element is used in this study. Gaussian integration technique [18] has been applied to achieve numerical integration of surface and volumetric integrands. Static equilibrium equations are fulfilled using Newton-Raphson method. In this investigation, the proposed micro-polar Lade's single hardening model is implemented into a non-linear FE program in order to investigate the interface shear behavior between granular soil and bounding structure under motion.

3. MODELING INTERFACE BEHAVIOR

The interface behavior between granular soil layer and bounding structure under large shearing movement is investigated using finite element method. In this regard, a section of lateral infinite extended narrow granular soil layer located between two parallel rigid boundaries of varying surface roughness is considered under free dilatancy and constant vertical pressure (Figure 1). The granular layer is modeled with the proposed micro-polar elasto-plastic Lade's model described in Section 2. The prescribed interface conditions are related to the surface roughness of top and bottom boundaries and the properties of granular medium. Apart from stress and displacement boundary conditions of non-polar conventional continuum, additional non-standard micro-polar kinematical boundary conditions, i.e. couple stress and Cosserat rotation, must also be introduced along the boundaries of Cosserat granular layer.

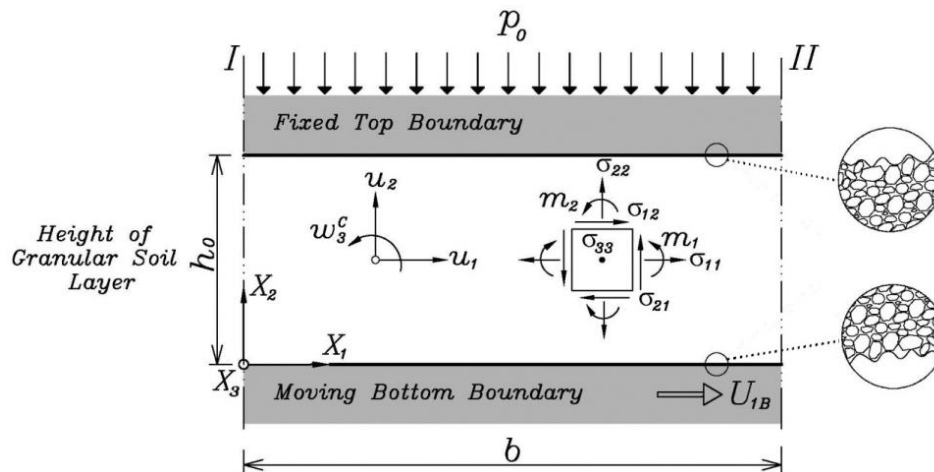


Figure 1. Modeling plane shearing of granular material under constant vertical pressure: section of extended infinite granular soil layer located between two parallel rigid boundaries of varying surface roughness along with kinematics and static quantities of micro-polar material under plane strain condition

In this study, the relation proposed by Tejchman (1997) [1] is used between Cosserat rotation and shear displacement at the top and bottom boundaries of granular soil layer to describe the interface behavior:

$$\omega_3^c = -f u_{1B} / d_{50} \quad (12)$$

The above kinematic boundary condition is proposed in the form of a constant ratio of Cosserat rotation to the displacement, occurred along the top and bottom boundaries of layer, to describe different roughness values. In fact, Cosserat boundary conditions allow different boundary roughnesses with considering grain rotations. The interface coefficient (f) depends on the interaction between soil grains and boundaries. The dimensionless factor (f) denotes u_{1B} fraction, transmitted to the soil grains in the form of rotation. This factor can determine the behavior of interface between granulate and surface of bounding structure. In the numerical calculations, presented in this paper, different values are chosen for the interface coefficient to account for the influence of surface roughness of top and bottom boundaries on the shear behavior of granular soil layer. The calculations are performed for rough, medium rough and relatively smooth interfaces. In the following, it is assumed that relatively smoother bounding interface is corresponded to a higher value of f . In fact, smooth interface shear behavior is observed when boundary soil grains are large relative to any counterface topography. On the other hand, full shearing of the material is assumed ($\omega_3^c = 0$) along a rigid surface for modeling very rough interfaces [12]. A slip occurs along a very rough surface if the surface friction angle reaches its residual value with no simultaneous deformation [19]. Up to this point, the material experiences shearing. It is noted that the shear displacement (u_{1B}) can be viewed as a relative displacement between top and bottom boundaries. Therefore, a similar proportional relation is assigned to Cosserat rotation on the top and bottom surfaces. In the present FE calculations, the proportional relation given in Equation (12) is described for the rates of Cosserat rotation (micro-curvature), on the bottom and top surfaces, and applied shear displacement (displacement gradient) and presented as follows:

$$x_2 = 0: \quad \dot{\omega}_{3B}^c = -f_B \frac{\dot{u}_{1B}}{d_{50}} \quad (13)$$

$$x_2 = h: \quad \dot{\omega}_{3T}^c = -f_T \frac{\dot{u}_{1B}}{d_{50}} \quad (14)$$

where, f_B and f_T are interface coefficients reflecting the interface conditions between surface grains and boundaries at the bottom and top surfaces of granular soil layer, respectively. In the above relations, h represents the thickness of soil layer; d_{50} is the characteristic length of granular soil; where $h \gg d_{50}$ is assumed so that the top boundary of granular soil layer has little influence on the formation of shear band along the bottom boundary.

In this study, all calculations are performed for a shear layer with an initial height of $h_0 = 4 \text{ cm}$ and the width of $b = 10 \text{ cm}$ and starting from same homogeneous and isotropic states: initial void ratio (e_0) = 0.6; initial

pressure (p_0) = 100 kPa ; stresses (σ_{ij}) = P_0I ; and couple stresses (m_i) = 0. The mentioned boundary conditions also imply zero assumption of shear stresses and couple stresses in the initial state. The layer is discretized by 4-node elements, each with the dimensions of 1.25 mm × 1.25 mm. Particularly, the boundary conditions assumed along the top and bottom surfaces of granular soil layer are:

$$u_1(x_1, 0) = u_{1B}, u_2(x_1, 0) = 0, \omega_3^c(x_1, 0) = \omega_{3B}^c$$

$$u_1(x_1, h) = 0, u_2(x_1, h) = u_2(x_1 + \Delta x_1, h), \omega_3^c(x_1, h) = \omega_{3T}^c, \sigma_{22}(x_1, h) = -p_0 = -100 \text{ kPa}$$

The vertical displacements of top surface of granular soil layer are obtained as a result of dilatancy or contractancy behavior within the whole layer. A vertical pressure of $p_0 = 100 \text{ kPa}$ is kept constant at the top surface. Therefore, the initial height of shear layer is not kept constant during shearing and can change as the result of dilatancy or contractancy of material under shearing. Along the bottom boundary ($x_2 = 0$), the vertical displacement (u_2) is zero and the applied horizontal displacement is the same for bounding structure (U_{1B}) and bottom surface of granular layer (u_{1B}). This assumption implies that the possibility of relative displacement, resulted from lower skin frictions, is not considered along the surface of bounding structure [19]. A shear deformation is initiated by applying horizontal node displacements ($U_{1B} = u_{1B}$). The material behavior to be described is rate independent; therefore, time increment can be related, for instance, to the increment of initiated shear displacement. The calculations are performed for large deformations using an Updated Lagrangian formulation. The symmetry condition of a lateral infinite extended narrow granular soil layer can be modeled by applying constraint conditions to the side nodes of its FE mesh. It means that each node on the left boundary is controlled to have the same displacements and Cosserat rotation as the corresponding node with the same vertical coordinate on the right boundary [12-13]. Therefore, the numerical results are independent of horizontal coordinate as well as the width of FE mesh. Regarding the infinite shear layer, the field quantities are independent of coordinate in the shearing direction with respect to the coordinate system, shown in Figure 1. Field quantities are also independent of the coordinate x_3 in the plane strain condition. Kinematic quantities are displacements (u_1 and u_2) and micro-rotation (Cosserat rotation, ω_3^c); and non-zero static quantities are stress components ($\sigma_{11}, \sigma_{22}, \sigma_{33}, \sigma_{12}, \sigma_{21}$) and couple stress components (m_1, m_2) in the plane strain conditions, concerning Cartesian coordinate system, Figure 1. The calibrated material constants given in Table 1, for a dense silica sand [12-13], are used in numerical simulations of subsequent sections.

Table 1- Lade’s model parameters for dense silica sand

Elastic properties			Failure criterion		Plastic potential		Yield criterion		Yield criterion	
M_L	λ	ν	m	η_1	μ	ψ_2	h	α	C	P
292.6	0.25	0.13	0.37	84.1	2.2	-3.06	0.95	0.3	7e-5	2.6

This paper presents the influence of interface condition (various interface roughness values) between granular soil layer and moving bounding structure on the shear behavior of layer. The distribution and evolution of state variables and polar quantities are proposed for the first time for an infinite elasto-plastic micro-polar shear layer in contact with a continuum of different surface roughness values. This issue is studied here under large shear displacements to precisely investigate the interface shear behavior of granular soil. Special attention is paid to rough, medium rough and relatively smooth interfaces under pure translatory motion. The effects of rotation resistance of soil grains are studied in the form of various surface roughness values along the interface, considering three different micro-polar kinematical boundary conditions (Cases 1-3). The descriptions of their surface roughness values are summarized in Table 2. The results obtained from numerical simulations of these cases are presented and discussed in the following. The cases, called Case (1) to (3), give a representative collection of interface condition for granular soil layer in contact with rigid boundaries of various surface roughness values at the top and bottom surfaces of soil layer.

Table 2- Description of surface roughness in different simulated cases

Case	Boundary Condition along Top Surface	Top Surface Roughness Description	Boundary Condition along Bottom Surface	Bottom Surface Roughness Description
1	$f_r = 0$	very rough	$f_b = 0.0001$	rough
2	$f_r = 0$	very rough	$f_b = 0.01$	medium rough
3	$f_r = 0$	very rough	$f_b = 0.5$	relatively smooth

4. NUMERICAL RESULTS AND DISCUSSIONS

In *Cases 1-3*, locked Cosserat or micro-rotations have been assumed along the top surface of shear layer in order to model a very rough surface condition [12]. While a certain coupling between Cosserat rotation and horizontal displacement of bounding structure is assumed along the bottom surface of layer indicating rough, medium rough or relatively smooth interfaces. Therefore, micro-polar boundary conditions are non-symmetric in the entire layer for the mentioned cases.

The distribution of normalized horizontal and vertical displacements (u_1/h_0 , u_2/h_0), and void ratio (e) across the normalized height of infinite granular soil layer (x_2/d_{50}) is plotted in Figure 2. Unlike earlier investigations of the authors for very rough surfaces along the bottom and top boundaries of granular soil layer [12], in *Cases 1-3*, the location of shear band deviates from the middle of shear layer for rough, medium rough and relatively smooth interfaces. For very rough surfaces, no grain sliding and rotating may occur along the bottom and top boundaries of layer. Thus, the resulting shear localization is within a narrow zone in the middle of layer for large shearing. This implies that the location of localized deformations significantly depends on f values, representing the surface roughness of top and bottom boundaries. According to Figure 2(a), the horizontal displacement gradient close to the interface decreases as f increases. In *Cases 1-3*, as the bottom surface roughness decreases which corresponds to higher values of f_B , the horizontal displacement of granular soil layer relative to the bounding structure is limited to a narrower zone near the bottom bounding structure. Then, the displacement decreases rapidly with increasing its distance from the structure. In the mentioned cases, u_1/h_0 is approaching to zero at the parts farther from the bounding structure or interface. In *Case 1* (rough bottom interface: $f_T = 0$ and $f_B = 0.0001$), shear band is located near the middle of layer. In *Case 3* (relatively smooth bottom interface: $f_T = 0$ and $f_B = 0.5$), it is formed along the bottom adjacent to the moving boundary of soil layer with the thickness of about $2d_{50}$, confirmed by the experiments [1]. Unlike non-polar continuum, in the proposed micro-polar continuum approach the normalized horizontal displacement field (u_1/h_0) across x_2/d_{50} is no longer linear from the beginning of shearing, Figure 2. The deformations are inhomogeneous from the beginning of shearing, Figure 2. The distribution of displacement field (u_1/h_0 , u_2/h_0) varies significantly within the layer as f_T and f_B increase, Figure 2(a,b). According to Figure 2(A), the surfaces with higher roughness which can fully mobilize the granular soil strength will develop the thickest shear bands (e.g., *Case 1*: $f_T = 0$ and $f_B = 0.0001$). The surfaces with lower roughness will sustain a lower stress ratios (e.g., *Case 5*: $f_T = f_B = 0.1$) and accordingly, develop the shear bands with lower intensity and thickness, Figure 2(C). The higher and lower values of void ratio (e) are obtained within and outside the shear band, respectively, Figure 2(c). Void ratio significantly increases within the shear band. Maximum void ratio values increase in the shear band as U_{1B}/h_0 increases. As f increases, the zone of higher void ratio moves from the middle of layer towards the bottom interface, Figure 2(c). The distribution of quantities across the height of shear layer is strongly affected by the interface behavior between granular soil layer and bounding structure, Figure 2. According to Figure 2, the location and evolution of shear band strongly pertain to the magnitude of interface coefficients (f_T and f_B) or surface roughness described along the top and bottom surfaces of layer. It seems that the granular soil behavior in the narrow layer is drastically affected by the rotation resistance of soil grains along the interface. According to [1], the interface behavior is significantly affected by the boundary conditions of entire system. This fact is confirmed by this research as well. According to the mentioned figure, shear band is closer to the smooth bottom boundary with higher rotation resistance of soil grains comparing to rough bottom boundary with lower rotation resistance.

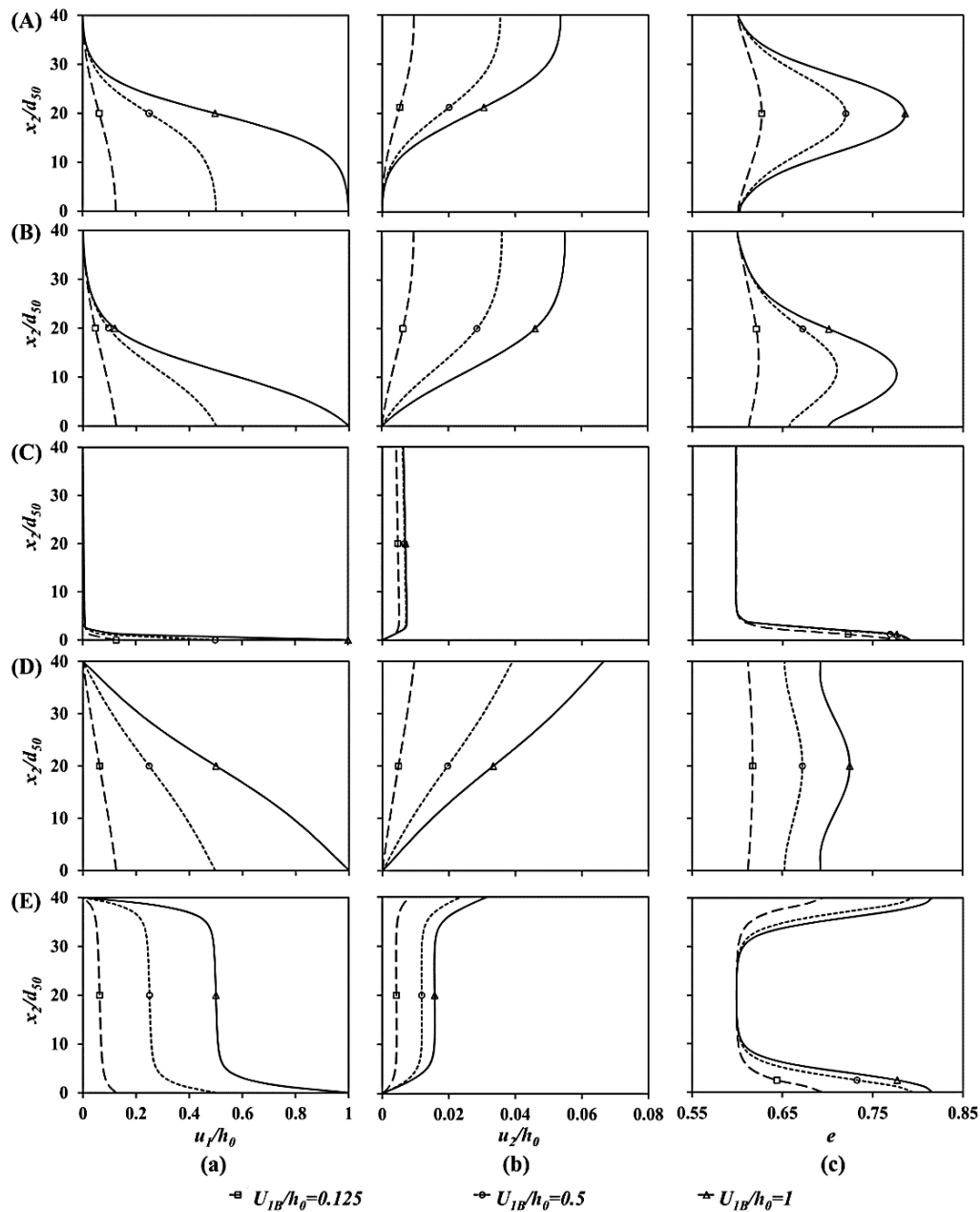


Figure 2. Distribution of (a) u_1/h_0 , (b) u_2/h_0 and (c) e across x_2/d_{50} at different U_{1B}/h_0 for: (A) Case (1): $f_T = 0$ and $f_B = 0.0001$, (B) Case (2): $f_T = 0$ and $f_B = 0.01$ and (C) Case (3): $f_T = 0$ and $f_B = 0.5$

Figure 3 shows the profile of Cosserat rotation (ω_3^c), normalized micro-curvature ($\kappa_2^* = l \cdot \kappa_2, (l = d_{50})$) and normalized couple stress ($m_2^* = m_2 / (l \cdot \sigma_{22}), (l = d_{50})$) during shearing across x_2/d_{50} . According to Figure 3(a), Cosserat rotations have high values within the shear band and nearly zero value outside it. As U_{1B}/h_0 and f increase, Cosserat rotation increases inside the shear band while outside shear band these quantities remain almost unchanged. Based on the results obtained from numerical simulations, the zone of strain localization is no longer located in the middle of shear layer, Figure 3(E). These results indicate that the location of shear localization in the granular material can be influenced by the interface behavior as well as the rotation resistance of soil grains in contact with the surface of moving bounding structure. According to Figure 3, the shear bands developed along the surfaces with smaller roughness (Case 3) are much thinner than those of greater roughness (Cases 1,2). Numerical simulations with different boundary constraints for ω_3^c show that the location and thickness of shear band are influenced by interface conditions between granular medium and boundaries. The interface conditions are related to the surface roughness of boundaries and properties of granular medium. The

thickness of localized zone is lower in *Case 3* than those of *Cases 1,2* comparing Figure 3(a-C) with Figure 3(a-A,a-B). The lower the rotation resistance, the closer the localized zone to the bounding structure surface. This result generally shows that shear deformations are concentrated in the areas with large soil grain rotations. Significant grain rotations, accompanied by dilatancy, are observed within the shear band (Figures 2(b,c),3(a)). The development of Cosserat rotation outside the shear band is nearly stopped as shear deformations are localized. High Cosserat rotation, manifested in shear band, is closer to the smooth bottom boundary compared to rough bottom boundary. Shear band thickness is significantly lower in the smooth interfaces, $f_B \geq 0.5$, (about $2d_{50}$), comparing to that of rough interfaces, $f_B \leq 0.0001$, (about $32.5d_{50}$). In turn, the maximum Cosserat rotation is larger and more concentrated (due to the lower shear band thickness) in the smooth interfaces, comparing to that of rough interfaces. Figure 3(b) shows normalized micro-curvatures (κ_1^*, κ_2^*), distributed across x_2/d_{50} . According to this figure, the values of κ_1^* are zero across the height in all magnitudes of U_{1B}/h_0 and f . However, the values of κ_2^* are noticeable in the shear band during shearing and increase as U_{1B}/h_0 and f increase. Oppositely, κ_2^* has extremely lower values approaching to zero outside the shear band. In parts where κ_2^* is nearly zero, the material behaves as a rigid body. The highest values of κ_2^* in the thinnest shear band (around $2d_{50}$ thickness) corresponds to relatively smooth surface condition (i.e., *Case 3*: $f_T = 0$ and $f_B = 0.5$). Fig. 4(c) shows the distribution of normalized couple stress components (m_1^*, m_2^*) across x_2/d_{50} . The values of m_1^* are zero across the height for all magnitudes of U_{1B}/h_0 and f . In general, couple stress and micro-curvature are zero in the middle of shear band, regardless the amount of shearing, Figure 3(b,c). The profile of normalized couple stress (m_2^*) across x_2/d_{50} shows highly non-linear patterns in all cases, Figure 3(c). According to this figure, the distribution of m_2^* changes drastically when f increases. The variation of m_2^* depends significantly on the values of U_{1B}/h_0 and f . For relatively smooth interface condition (*Case 3*: $f_T = 0$ and $f_B = 0.5$), zero values of couple stresses across a large part of layer height correspond to the presumption of classical continuum; i.e. grain rotations (Cosserat rotations) are equal to macro-rotations (continuum rotations). In this case, couple stress (m_2^*) has almost constant values across the height excluding the upper and lower boundaries of soil layer. The sign of normalized couple stresses is switched at the middle of shear band in all magnitudes of U_{1B}/h_0 and f . However, the highest values of normalized couple stress (m_2^*) occur along the interface ($x_2 = 0$) for smooth interfaces ($f_B \geq 0.5$) within a narrow band of $2d_{50}$ thickness.

Figure 4 shows the evolution of normalized normal and shear stress components ($\sigma_{11}^*, \sigma_{22}^*, \sigma_{33}^*, \sigma_{12}^*, \sigma_{21}^*$) as well as mobilized interface friction angle (φ_m) versus normalized horizontal displacement of bounding structure (U_{1B}/h_0) at different positions across x_2/h_{50} . All shear stress-displacement curves first increase up to a peak value higher than the limit shear stress. Then, they are followed by softening and a reduction to a steady state shear stress, Figure 4. The limit resistance is achieved once the stationary state is reached in the shear band. According to this figure, normal stress components approach to same limit value of P_0 . The evolution of σ_{12}^* is the same across the height in all elements, while that of σ_{21}^* is different based on the position of elements across the layer height, Figure 4(A). A pronounced difference between σ_{12}^* and σ_{21}^* can be observed after peak. Two stages, characterized as steep increase and then gradual decrease, can be distinguished in Figure 4.

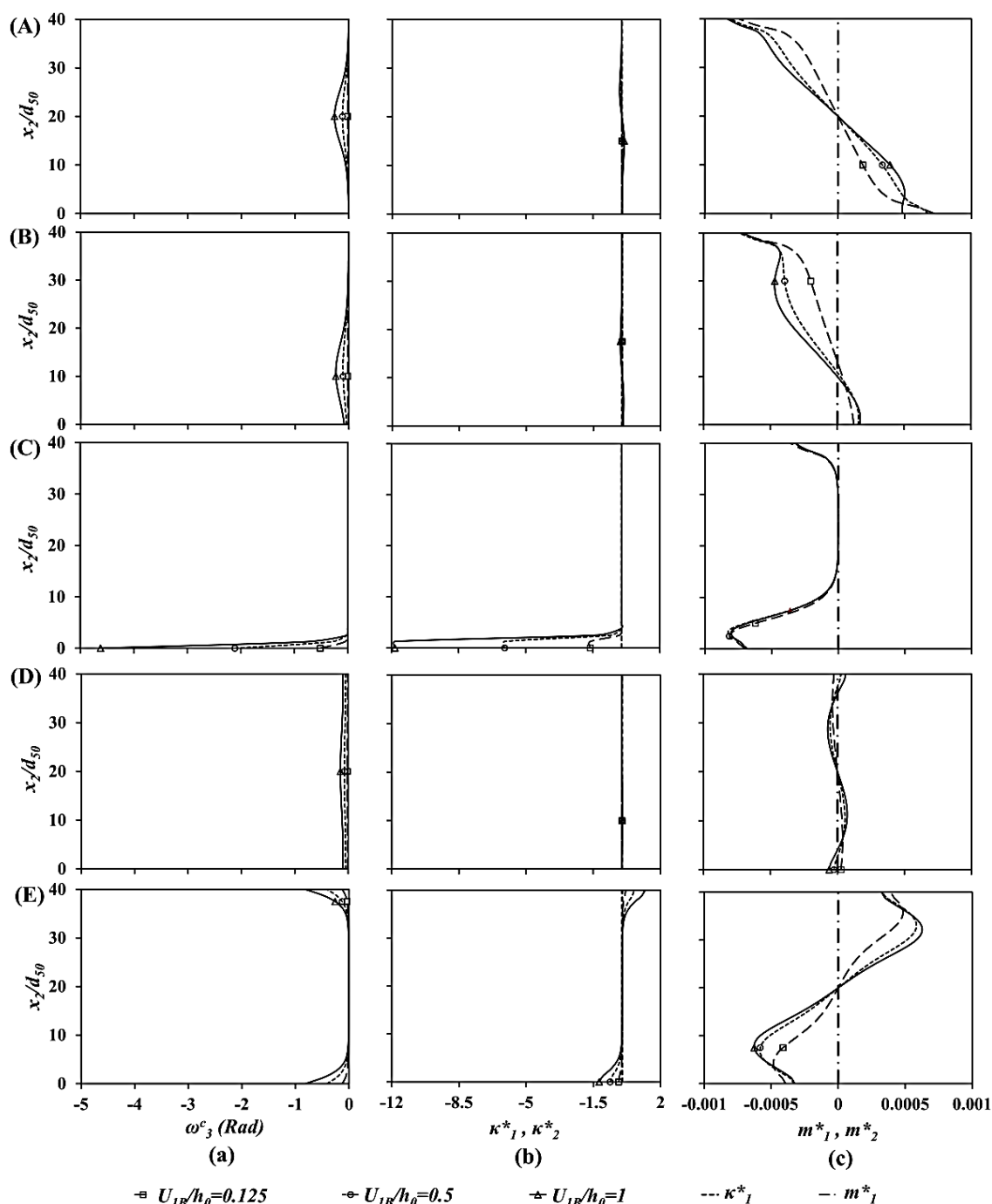


Figure 3. Distribution of (a) ω_3^c , (b) $\kappa_{1,2}^*$ and (c) $m_{1,2}^*$ across x_2/d_{50} at different U_{1B}/h_0 for: (A) Case (1): $f_T = 0$ and $f_B = 0.0001$, (B) Case (2): $f_T = 0$ and $f_B = 0.01$ and (C) Case (3): $f_T = 0$ and $f_B = 0.5$

The interface coefficient (f) has a strong influence on the resistance magnitude of bounding structure against shearing. For large displacements of bounding structure, normalized shear stresses tend towards a stationary value which depends on the assumed stress limit condition. As surface roughness increases or f decreases, peak and residual shear strengths increase. It is shown in Figure 4 that the surface roughness has a controlling effect on the shear strength along the interface. The rougher interface (e.g., Case 1) exhibits a higher strength compared to the smoother interface (e.g., Case 3). This is reasonable because the rougher interfaces are more interlocked with the soil grains and thus more resistant to shear, Figure 4(B). Distinct post-peak strain softening to steady state is observed in Case 1 ($f_T = 0$ and $f_B = 0.0001$) due to the low value of f_B , Figure 4(a). Rough interfaces exhibit post-peak displacement-softening behavior and smooth interfaces approximately post-peak plastic behavior. The yielding of smooth interfaces is almost elastic-perfectly plastic. Figure 4(B) shows

the evolution of mobilized interface friction angle (φ_m) versus normalized horizontal displacement of bounding structure (U_{1B}/h_0). φ_m is related to the entire granular soil layer, as the stresses (σ_{12} and σ_{22}) are constant across the height and along the length of layer. φ_m first goes sharply up towards its peak, and then decreases gradually to meet its stationary value in the shearing under constant vertical pressure, $P_0 = 100 \text{ kPa}$. The highest peak shear strength is achieved in *Case 1* when the interface is roughest, Figure 4(B-a).

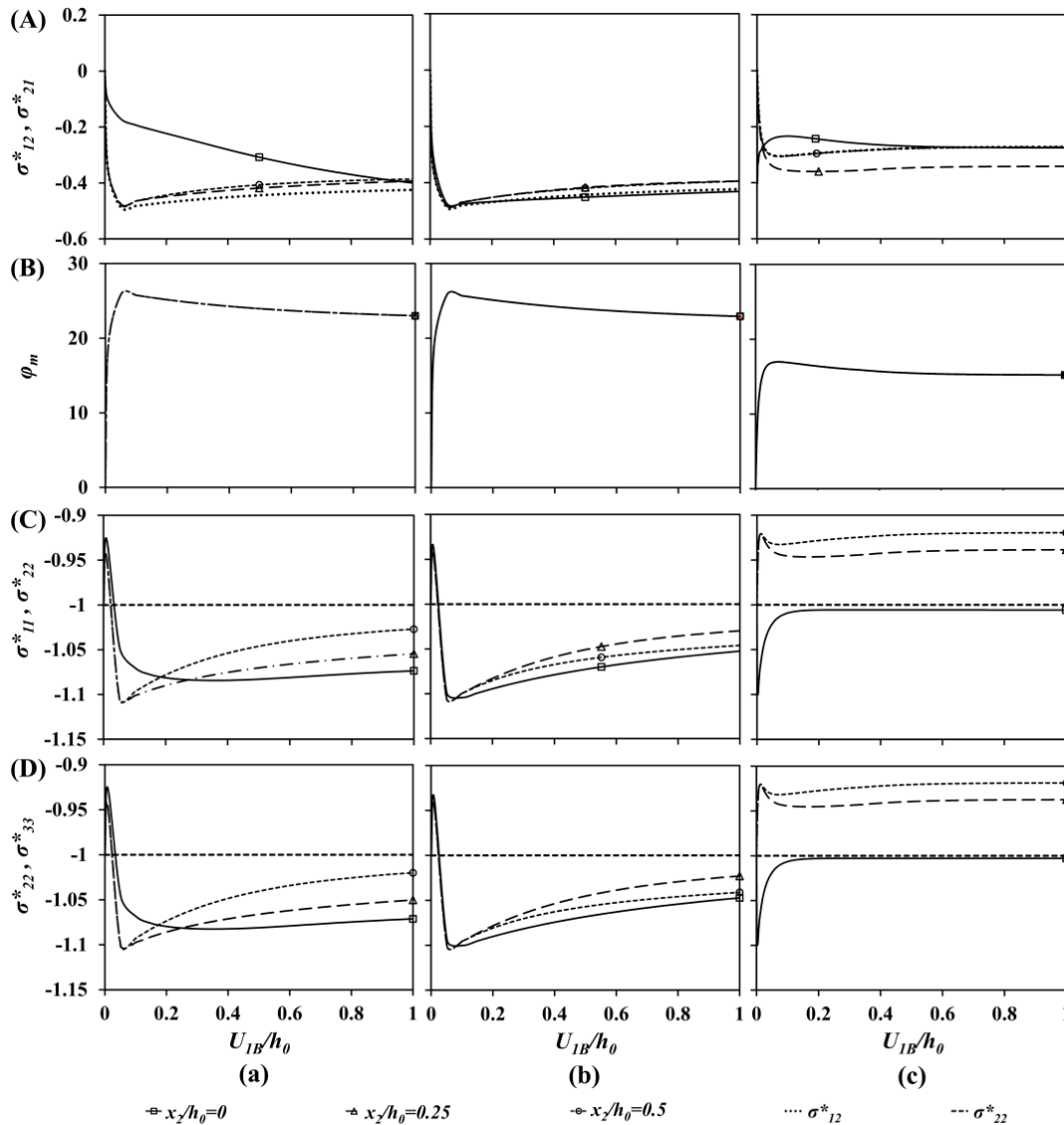


Figure 4. Evolution of (A) $\sigma_{12}^*, \sigma_{21}^*$, (B) φ_m , (C) $\sigma_{11}^*, \sigma_{22}^*$ and (D) $\sigma_{22}^*, \sigma_{33}^*$ at different x_2/h_0 for: (a) *Case (1)*: $f_T = 0$ and $f_B = 0.0001$, (b) *Case (2)*: $f_T = 0$ and $f_B = 0.01$ and (c) *Case (3)*: $f_T = 0$ and $f_B = 0.5$

Considering the quantities of horizontal shear stress (σ_{12}^*), the mobilized peak and residual interface friction angles are $\varphi_m = 26.0^\circ$ and 23.0° , 25.8° and 22.8° , 16.4° and 15.2° for *Cases 1* to *3*, respectively, Figure 4(B). Similar to shear stresses, the mobilized interface friction angle (φ_m) also shows a steeply increase phase followed by a very gradual decrease toward stationary value, Figure 4(B). According to this figure, the magnitude of φ_m directly depends on the surface roughness of top and bottom boundaries.

Figure 5 presents the deformed granular soil layer along with the contour plot of void ratio after the horizontal shear displacement of $U_{1B}/h_0 = 1.0$ for different values of interface roughness (f). The brighter zones, in the plots, are corresponded to the higher void ratios or where failure may start. Shear band is fully developed at the steady state, having higher void ratios than other parts of the layer due to the dilation, Figure 5. It is found that the shearing mechanism of granular soil–structure interface is dramatically changed with the magnitude of cf . Comparing the deformed configurations, presented in Figure 5, the location and thickness of shear bands depend significantly on the described interface coefficient (f) in the form of surface roughness. As f increases,

the localized shear deformation zone moves from the middle of layer to the bottom surface of the layer adjacent to bounding structure. Shear band is located in the vicinity of interface in *Case 3* ($f_T = 0$, $f_B = 0.0001$) and close to the mid-height of soil layer in *Case 1* ($f_T = 0$ and $f_B = 0.0001$). The predicted thicknesses of shear band, derived from the distributions of void ratio and Cosserat rotation, are about $32.5d_{50}$, $25d_{50}$, $2.5d_{50}$ for *Cases 1* to 3, respectively. Numerical simulations with different boundary constraints for ω_3^c show that the location and thickness of shear band are influenced by the interface conditions between granular medium and boundaries. The interface conditions are related to the surface roughness of boundaries and the properties of granular medium. It is found that boundary effects play significant roles in the interface shear behavior of granular soil.

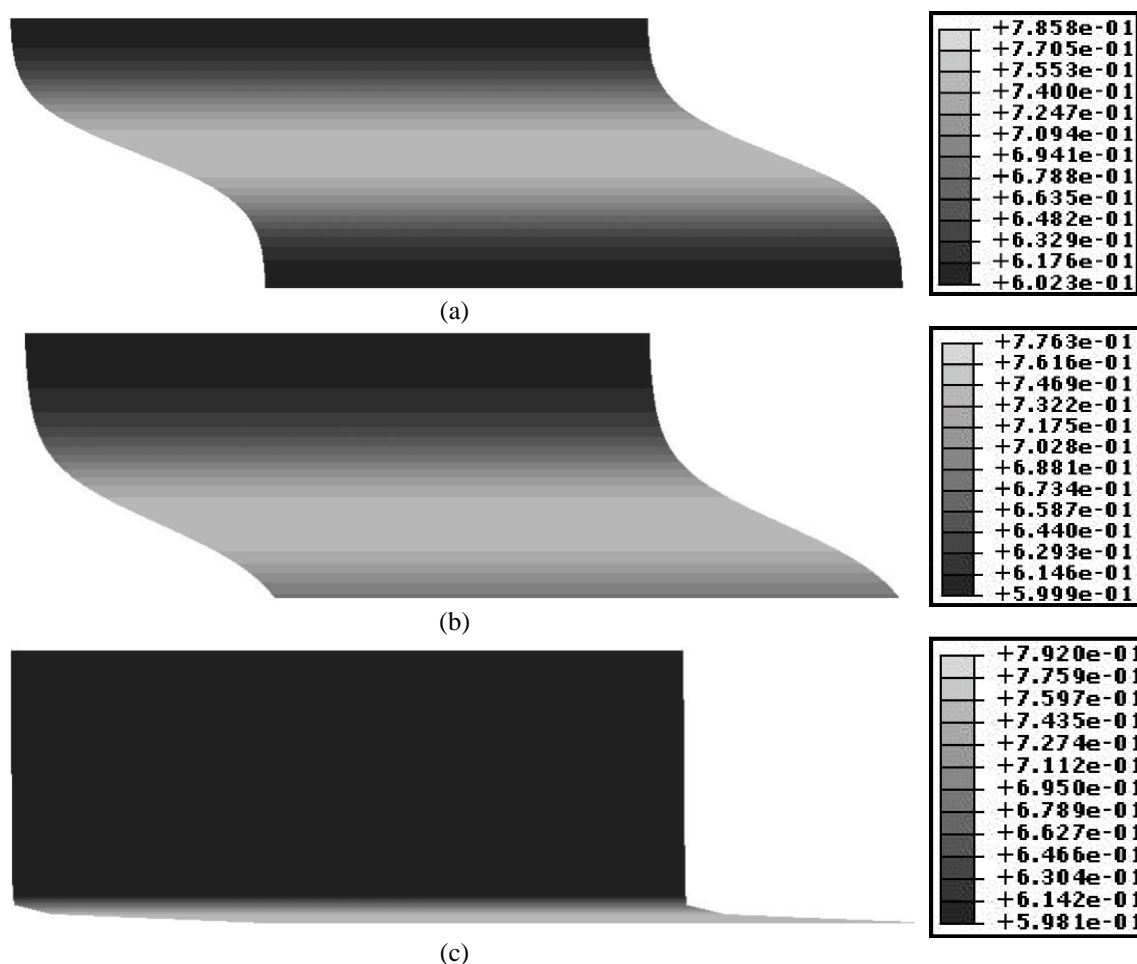


Figure 5. Deformed shape of granular soil layer along with contour plot of void ratio after $U_{IB}/h_0 = 1.00$ for: (a) *Case 1*): $f_T = 0$ and $f_B = 0.0001$, (b) *Case 2*): $f_T = 0$ and $f_B = 0.01$ and (c) *Case 3*): $f_T = 0$ and $f_B = 0.5$

5. CONCLUSIONS

This paper has quantified how the interface roughness between granular soil layer and rigid bounding structure influences the shear behavior of particulate-continuum interface system. The main findings can be summarized as follows:

- Boundary effects and soil grain rotation resistance are two major factors which influence the response of infinite granular soil layer in contact with bounding structure under plane quasi-static shearing. The results reveal the micro-structural and boundary effects on soil behavior at the very beginning of shearing.
- The pattern, location and thickness of shear band(s) depend on the roughness of top and bottom boundaries, specimen size and boundary conditions of the whole system. Strain localization is formed near the boundary with large Cosserat rotations at the boundary surface. When Cosserat rotations are locked or very small, then the zone of strain localization is formed far away from the boundary. Localized zone occurs in the middle of

shear layer for locked Cosserat rotations along the top and bottom of shear layer. Otherwise, it is located close to the boundary with higher Cosserat rotations. Particularly, if the top or bottom boundaries are smooth, shear band is created directly at the boundaries. If the boundaries are very rough, then shear band occurs in the mid-height of granular soil layer. Regarding rough boundaries, it forms close the mid-height and in medium rough boundaries between the middle and bottom of layer. Shear band thickness, or the zone with intense shear strain, increases with increasing surface roughness or decreasing interface coefficient (f). The values of shear band thickness, obtained in this study, are ranged from negligible ($1-2d_{50}$) for relatively smooth interface up to maximum ($32.5d_{50}$) for rough interface. As a result, the surfaces with greater roughness generally sustain higher stress ratios and develop thicker shear bands. The most intense shear band with maximum thickness of $32.5d_{50}$ is developed by the surfaces which can fully mobilize the material strength.

- The effect of interface roughness on the strength mobilized along the interface as well as on the shearing mechanism is taken into account, using additional micro-polar boundary conditions. However, mobilized shear strength along the interface does not only depend on interface roughness and but also on the boundary conditions of the whole system. Mobilized interface friction angle is derived as natural outcome rather than described when using micro-polar boundary conditions; i.e. no special interface element is needed. The peak and residual mobilized interface friction angles decrease with decreasing interface roughness or increasing interface coefficient (f). When free dilation is allowed, as in the case of shearing under constant normal pressure, the shear resistance reaches its peak value and then approaches toward stationary status for continuous shearing.

6. ACKNOWLEDGMENT

The first author wants to express his sincere gratitude to the Iran's National Elites Foundation (INEF) for his moral support and encouragement.

7. REFERENCES

1. Tejchman, J. (1997), “*Modelling of shear localisation and autogeneous dynamic effects in granular bodies*”, Publication Series of the Institute of Soil and Rock Mechanics, vol. 140, Gudehus, G., Natau, O., (Eds.), Karlsruhe: University Karlsruhe, pp. 1-353.
2. Gudehus, G. (2008), “*Physical Soil Mechanics*”, Springer, Heidelberg.
3. Potyondy, J.G. (1961), “*Skin friction between various soils and construction materials*”, Géotechnique 2(4), pp. 339–353.
4. Vermeer, P.A. (1983), “*Frictional slip and non-associated plasticity*”, Scand. J. Metall. 12, pp. 268–276.
5. Desai, C.S., Zaman, M.M., Lightner, J.G. and Siriwardane, H.J. (1984), “*Thin-layer element for interface and joints*”, International Journal for Numerical and Analytical Methods in Geomechanics 8, pp. 19-43.
6. Boulon, M. (1989), “*Basic features of soil structure interface behaviour*”, Computers and Geotechnics 7, pp. 115-131.
7. De Gennaro, V. and Frank, R. (2002), “*Elasto-plastic analysis of the interface behaviour between granular media and structure*”, Computers and Geotechnics 29(7), pp. 547-572.
8. Hu, L. and Pu, J. (2003), “*Application of damage model for soil-structure interface*”, Computers and Geotechnics 30, pp. 165-183.
9. Liu, H., Song, E. and Ling, H.I. (2006), “*Constitutive modeling of soil-structure interface through the concept of critical state soil mechanics*”, Mechanics Research Communications 33, pp. 515-531.
10. Zhang, G., Liang, D. and Zhang, J. (2006), “*Image analysis measurement of soil particle movement during a soil-structure interface test*”, Computers and Geotechnics 33, pp. 248-259.
11. DeJong, J.T. and Westgate, Z.J. (2009), “*Role of initial state, material properties, and confinement condition on local and global soil-structure interface behavior*”, Journal of Geotechnical and Geoenvironmental Engineering ASCE 135(11), pp. 1646-1660.
12. Ebrahimiyan, B., Noorzad, A. and Alsaleh, M.I. (2012), “*Modeling shear localization along granular soil-structure interfaces using elasto-plastic Cosserat continuum*”, International Journal of Solids and Structures 49 , pp. 257–278.
13. Ebrahimiyan, B., Noorzad, A. and Alsaleh, M.I. (2017), “*Modeling interface shear behavior of granular materials using micro-polar continuum approach*”, Continuum Mechanics and Thermodynamics, <https://doi.org/10.1007/s00161-017-0588-4>.
14. Vardoulakis, I. and Sulem, J. (1995), “*Bifurcation Analysis in Geomechanics*”, Blackie Academic & Professional (an imprint of Chapman & Hall): Glasgow, London, U.K.
15. Lade, P.V. and Nelson R.B. (1987), “*Modeling the elastic behavior of granular materials*”, International Journal for Numerical and Analytical Methods in Geomechanics 11, pp. 521-542.
16. Lade, P.V. and Kim, M.K. (1988), “*Single hardening plasticity model for frictional materials*”, Computers and Geotechnics 6, pp. 13-29.
17. Kim, M.K. and Lade, P.V. (1988), “*Single hardening constitutive model for frictional materials*”, Computers and Geotechnics 5, pp. 307-324.
18. Belytschko, T., Liu, W.K. and Moran, B. (2000), “*Nonlinear Finite Elements for Continua and Structure*”, John Wiley & Sons, LTD.
19. Ebrahimiyan, B. and Bauer, E. (2012), “*Numerical simulation of the effect of interface friction of a bounding structure on shear deformation in a granular Soil*”, International Journal for Numerical and Analytical Methods in Geomechanics 36(2), pp. 1486-1506.

On Sensitivity Analysis of a Nonlinear Gravity Dam Model

M.A. Hariri-Ardebili¹, S.M. Seyed-Kolbadi²

1- Department of Civil Engineering, University of Colorado, Boulder, USA

2- Iranian National Committee on Large Dams, Tehran, Iran

Email: mahdi_kolbadi@sina.kntu.ac.ir

Abstract

This paper investigates the sensitivity of the nonlinear responses in a gravity dam to the variability of the input parameters. For this purpose, the classical finite element analysis of coupled system is adopted. The coupled dynamic interaction of dam-foundation-reservoir system is modeled based on Lagrangian-Eulerian approach while the reservoir is modeled as a compressible medium and the foundation is assumed to be massless. The non-linearity in the concrete is originated from an adopted/extended rotating smeared crack model. The finite element model is excited using both the near-fault and far-field ground motions. The global parameters such as modulus of elasticity ratio, reservoir bottom absorption, reservoir length and height, earthquake intensity and etc. are assumed to be random variables. Finally, the sensitivity of the nonlinear responses in terms of crack propagation and crest displacement is assessed. Results of this research can be used in global uncertainty reduction and developing a robust probabilistic models.

Keywords: Concrete dam; seismic; crack; random variable; parametric study; probabilistic.

1. INTRODUCTION

There are several important factors that influence the finite element analysis of concrete gravity dams [1]. These factors are the semi-unbounded size of the reservoir and foundation rock domains; dam-reservoir interaction; wave absorption at the reservoir boundary; water compressibility; dam-foundation rock interaction; spatial variations in ground motion at the dam-rock interface, complex nature of material and loads and also their interaction in dam-reservoir-foundation coupled system. However, it is worthy to mention that the integrative seismic analysis of a dam is combination of all these aspects which are required for realistic assessment of a coupled system [2].

In the present paper only the potential failure modes due to earthquake shaking on gravity dams are investigated. The major potential failure modes in gravity dams are due to overstressing, sliding along cracked surfaces in the dam or planes of weakness within the foundation, and sliding accompanied by rotation in the downstream direction. The consequence of cracking, if extended through the dam section, may lead to sliding or rotational instability of the separated block [3].

In the following sections, parametric finite element analysis of a concrete gravity dam is performed. The main contribution of the authors is to investigate crack behavior of the coupled system under different types of input excitations. Different finite element models are provided for this purpose taking into account both the internal and external effects. The paper discusses on each parameter individually and investigates the relative importance of each one. Finally, results are compared in terms of displacement and crack profile and an optimum numerical model is recommended. This conference paper is, in fact, a short summary of a peer-reviewed journal paper [4] already published by the authors.

2. MODELS AND MATERIALS

Koyna dam in India is selected as the case study in this investigation. The existing Koyna dam is rubble concrete gravity dam of 853 m length and 103 m height, its thickness at the base and at the crest are 70.2 m and 12.1 m, respectively for the central non-overflow monoliths. Usually due to large dimension of gravity dams in cross-stream direction the assumption of plane strain is acceptable and so gravity dams are analyzed as 2D structures [5]. In the present study one of the non-overflow blocks is modeled. The finite element model of 2D dam and its dimensions is shown in Fig. 1a. Furthermore, Fig. 1b shows the coupled dam-reservoir-foundation system. Fluid and solid elements are in interaction with each other at the interface of dam and reservoir as well as reservoir and foundation. Table 1 represents the mechanical and strength properties of the mass concrete and foundation rock. These properties are used for analysis of the base model and they may change during the parametric analyses.

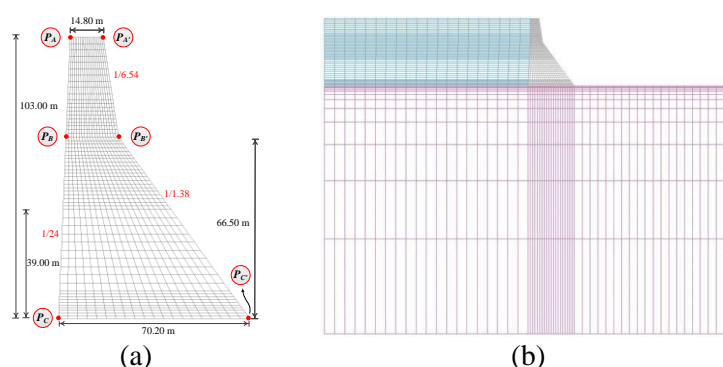


Figure 1: Numerical model of Koyna dam (a) 2D mesh, (b) coupled system

Table 1: Mechanical properties of mass concrete and foundation rock

	E_c (GPa)	ρ_c (kg/m ³)	ν_c	f'_t (MPa)	f_c (MPa)	G_f (N/m)	E_f (GPa)	ρ_f (kg/m ³)	ν_f
Static	31.0		0.2	2.4	24	-			
Dynamic	35.7	2643	0.14	3.6	36	200	16.9	2700	0.33

Applied loads on the system are dam body self-weight, hydrostatic pressure and seismic loads. In the case of bi-directional seismic analysis, both components are applied simultaneously to the system. The excitations are applied at the base of the foundation model. It is noteworthy that the nonlinearity of the system is originated from a co-axial rotating smeared crack approach for the concrete. This model has already been developed and tested on a gravity dam by the authors [6]. The five-parameter Willam-Warnke [7] failure criterion is used in this model.

3. LOADS AND METHODS

Considering that in this paper a set of ground motions other than the original Koyna ground motion is used, hence, the smoothed response spectrum of the Koyna ground motion is used as the target one. The other ground motions are scaled in such a way to match the target spectra reasonably.

The Pacific Earthquake Engineering Research (PEER) Center ground motion database (version beta) was used for preliminary selection of two appropriate ground motions (far-field and near-fault) based on the general site characteristics of the Koyna dam [8]. Imperial Valley-06 ground motion recorded at the Victoria Station was chosen as far-field motion. Its magnitude, M_w , closest distance to co-seismic rupture, R_{rup} , and fault mechanism, F_{mech} , are 6.53, 31.9 km, and strike-slip, respectively. On the other hand, the Imperial Valley-06 event recorded at El Centro Array#5 Station was selected as near-fault motion. Its M_w , R_{rup} , F_{mech} , and the predominant period, T_p , are 6.53, 4.0 km, strike-slip, 4.0 s, respectively. Figs. 2a and 2b show the scaled acceleration time histories of the selected motion. In order to reduce the computational efforts in nonlinear analyses only the strong ground motion part of the records were selected (which includes at least 90% of the Arias intensity of the motion).

4. RESULTS

In this section the importance of the different parameters on nonlinear seismic response of a typical gravity dam-reservoir-foundation system is investigated. Changes in response due to changes made in the considered parameter are studied. In assessing the effects of the considered parameter, all other parameters are kept unchanged. The Newmark- β time integration method is utilized to solve the coupled nonlinear problem of dam-reservoir-foundation system. The displacement and flow characteristics are chosen as the convergence criteria in each load step of the dynamic analysis.

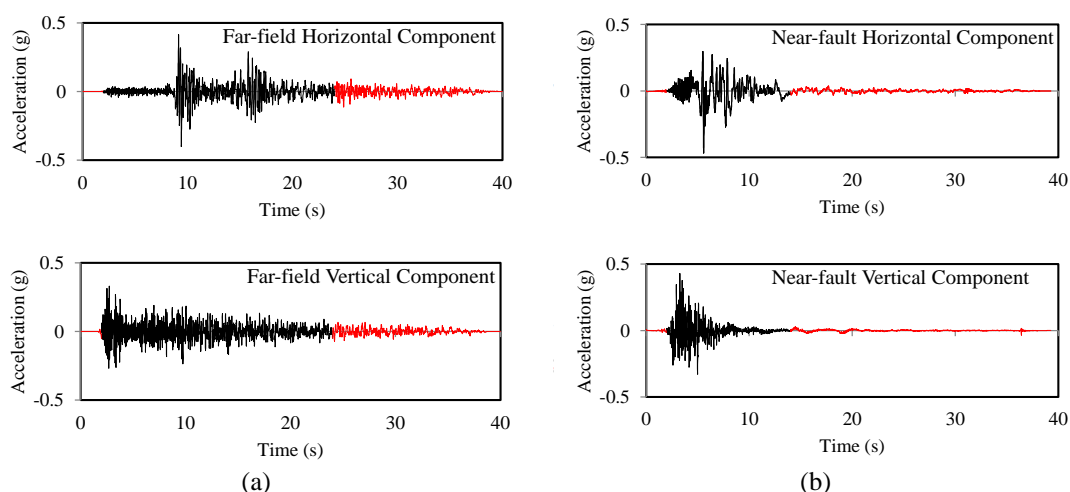


Figure 2: Truncated ground motion time histories (a) far-field; (b) near-fault

Based on the extensive literature survey explained in the first section and also the authors' experiences in seismic analysis of concrete dams, a base (pilot) model is chosen first. The responses of different parametric models are evaluated with respect to the base model. Considering total height of the gravity dam to be H_0 , the length of the reservoir finite element model is assumed to be $3H_0$ and the water level is $0.95H_0$. The massless foundation model is assumed and the material properties are used based on Table 1. Wave reflection coefficient at the reservoir bottom is assumed 0.8. A $\xi = 5\%$ damping ratio is used in dynamic analyses. Table 2 is summarized different models used for parametric-sensitivity studies. The varying parameter in each group is highlighted.

Considering that the continuum crack model is used in the present paper, the failure of the dam is judged based on the following two criteria: (1) having at least one unstable crack through (upstream-downstream) within the dam, and (2) exceeding the maximum displacement, u_{max} , of the cracked segment from the unacceptable ultimate displacement, u_{ult} . The value of the u_{ult} was suggested to be 0.1% of H_0 in [9]. This value for Koyna dam is about 100 mm. It means that in nonlinear analysis of Koyna dam, if there is a through crack in dam body and the crest displacement (as an index point) exceeds $u_{ult} = 100$ mm, the case is judged to be failed.

Table 2: Summary of models used for parametric study

Group ID	1	2	3	4	5	6	7	8		
Reservoir length	Varying	$3H_0$ Reservoir level	$0.95H_0$	Varying	$0.95H_0$	$0.95H_0$	$0.95H_0$	$0.95H_0$	$0.95H_0$	$0.95H_0$
Reservoir absorption	0.80	0.8	Varying	0.8	0.8	0.8	0.8	0.8		
Foundation model	Massless	Massless	Massless	Varying	Massless	Massless	Massless	Massless		
Foundation flexibility	~ 0.5	~ 0.5	~ 0.5	~ 0.5	Varying	~ 0.5	~ 0.5	~ 0.5		
Damping ratio	5%	5%	5%	5%	5%	Varying	5%	5%		
GM components	H+V	H+V	H+V	H+V	H+V	H+V	Varying	H+V		
GM intensity	Spectrum-based	Spectrum-based	Spectrum-based	Spectrum-based	Spectrum-based	Spectrum-based	Spectrum-based	Varying		

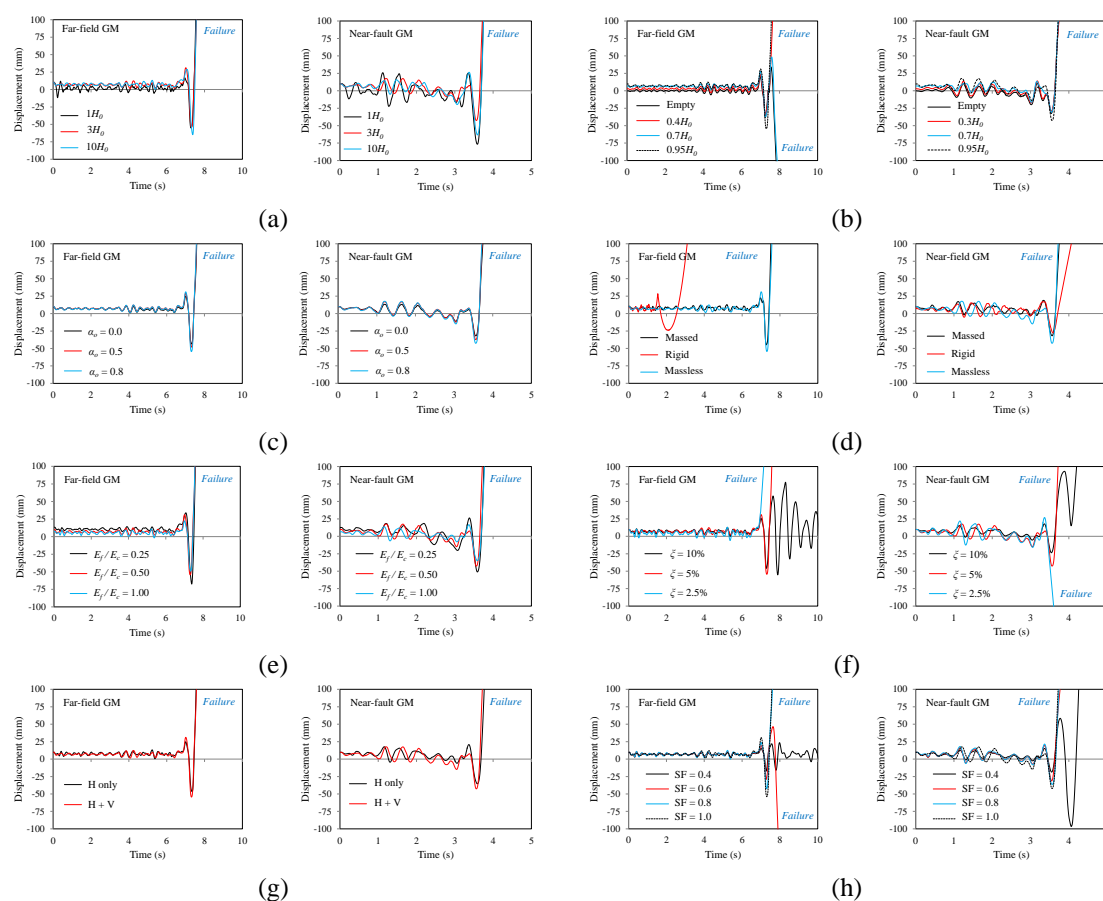


Figure 3: Impact of variable parameter on horizontal displacement time history of crest, (a) reservoir length, (b) water level, (c) reservoir bottom absorption, (d) foundation model, (e) foundation flexibility, (f) damping ratio, (g) GM component, (h) GM intensity

4.1. RESERVOIR WATER LENGTH

The length of the reservoir finite element model is assumed to be $1H_0$, $3H_0$, and $10H_0$. Fig. 3a shows the time history of crest (P_A) displacement in stream direction for the three cases. As seen, modeling the reservoir length equal to the reservoir height leads to a slightly different crest displacement than two other models. Both models with the length $3H_0$ and $10H_0$ lead to almost the same drift response. Thus, the reservoir with the length $3H_0$ can be the computationally optimal model. Similar conclusions derived by Bayraktar et al. [10] and Attarnejad and Lohrasbi [11]. Fig. 4a shows the crack propagation for all models. In all cases the cracks start at the slope discontinuity of the downstream face and propagate toward upstream. Under the near-fault ground motion, cracks are also propagating on the lower parts of the body in downstream face. It seems that increasing the reservoir length leads to increasing the cracked lengths; however, the crack profile of the model with the reservoir length $3H_0$ is similar to that obtained from the model with $10H_0$.

4.2. RESERVOIR WATER LEVEL

Four cases are considered for the water level, i.e. $0H_0$ (empty reservoir), $0.4H_0$, $0.7H_0$, and $0.95H_0$. Fig. 3b shows the displacement time history of the crest (P_A) point for different water levels. Increasing water level increases the initial displacement of the dam due to hydrostatic pressure. Higher water level leads to higher displacement during the seismic excitation. One cycle prior to failure, the model with $0.95H_0$ has a considerably larger displacement than the others. Fig. 4b shows the crack propagation in which reduction of water level reduces the cracked length at the dam-foundation interface. This also changes the crack profile of the neck area.

4.3. RESERVOIR BOTTOM ABSORPTION

Three cases are considered for the reservoir bottom absorption. The wave reflection coefficient, α_o , is assumed to be 0, 0.5, and 0.8. Based on Fig. 3c, the bottom wave reflection coefficient does not have a meaningful effect on displacement response of the dam. However, increasing the wave reflection coefficient increases the hydrodynamic pressure and consequently increases the displacement one cycle before failure, especially for near-fault ground motion. The results of this study are in agreement to those by Gupta and Pattanur [12]. Fig. 4c shows the crack profiles for three models. Under the far-field ground motion, the amount of the cracked elements at the neck area is almost the same; however, increasing the wave reflection coefficient increases the base cracking.

4.4. FOUNDATION MODEL

Three types of foundation models are assumed for the system, i.e. rigid, massless, and massed foundation with infinite elements. Fig. 3d shows the displacement time history. Comparing the massless and massed foundation models reveals that they have almost the same trend; however, considering the radiation damping (massed foundation) decreases the response values compared to standard massless model. A similar response was observed by Hariri-Ardebili and Saouma [13]. Seismic response of the dam under far-field ground motion and using rigid foundation model has a substantial difference with the two others. In this condition, dam fails earlier than the others. Fig. 4d shows the crack profile of the dam body. Again, comparing the massless and massed foundation models shows less cracked elements for the massed foundation. Rigid foundation model leads to extensive cracking at the base of the dam. Under the far-field ground motion, there is a large cracked area around the heel of the dam; however, under the near-fault motion a through crack is generated at the dam-foundation interface.

4.5. FOUNDATION FLEXIBILITY

Three different foundation flexibilities are tested. Ratio of the foundation modulus of elasticity to the concrete is assumed to be 0.25, 0.50 and 1.0. Fig. 3e shows the displacement time history. Increasing the modulus of elasticity of foundation leads to decreasing both the initial static displacement due to hydrostatic pressure and dynamic displacement of the dam. This observation is similar to those reported by Hall [14]. Fig. 4e shows the crack profile of the dam. As seen, in general, increasing the modulus of elasticity of the foundation leads to increasing the number of cracked elements at the lower parts of the dam especially at dam-foundation interface. However, crack profile of the neck is decreased slightly. In the case of E_f equal to E_c , almost the entire dam-foundation interface is cracked. This observation matches well with the research by Motamedi et al. [15] on seismic response of PineFlat gravity dam.

4.6. DAMPING RATIO

Three different structural damping ratios are taken into account, i.e. $\xi = 2.5\%$, $\xi = 5\%$ and $\xi = 10\%$. Considering that the bounded Rayleigh damping formulation is used in the present study, three different pairs of α_M and β_K are computed. Fig. 3f shows the displacement time history of the crest point for different values of the damping. It can be concluded that using higher damping ratio decreases the displacement response almost during whole range of dynamic excitation. Using $\xi = 2.5\%$ leads to early failure of the model at least one cycle prior to the model with $\xi = 5\%$ fails. This observation satisfies well with those reported by Chuhan et al. [16] for arch dams. Fig. 4f shows the crack profile resulted from different damping ratios. As seen, increasing the damping ratio leads to decreasing the damaged area and reduces the crack profile of the dam. The reduction in number of cracked elements is perspicuous in the neck area for far-field ground motion and in the dam-foundation interface for the near-fault ground motion.

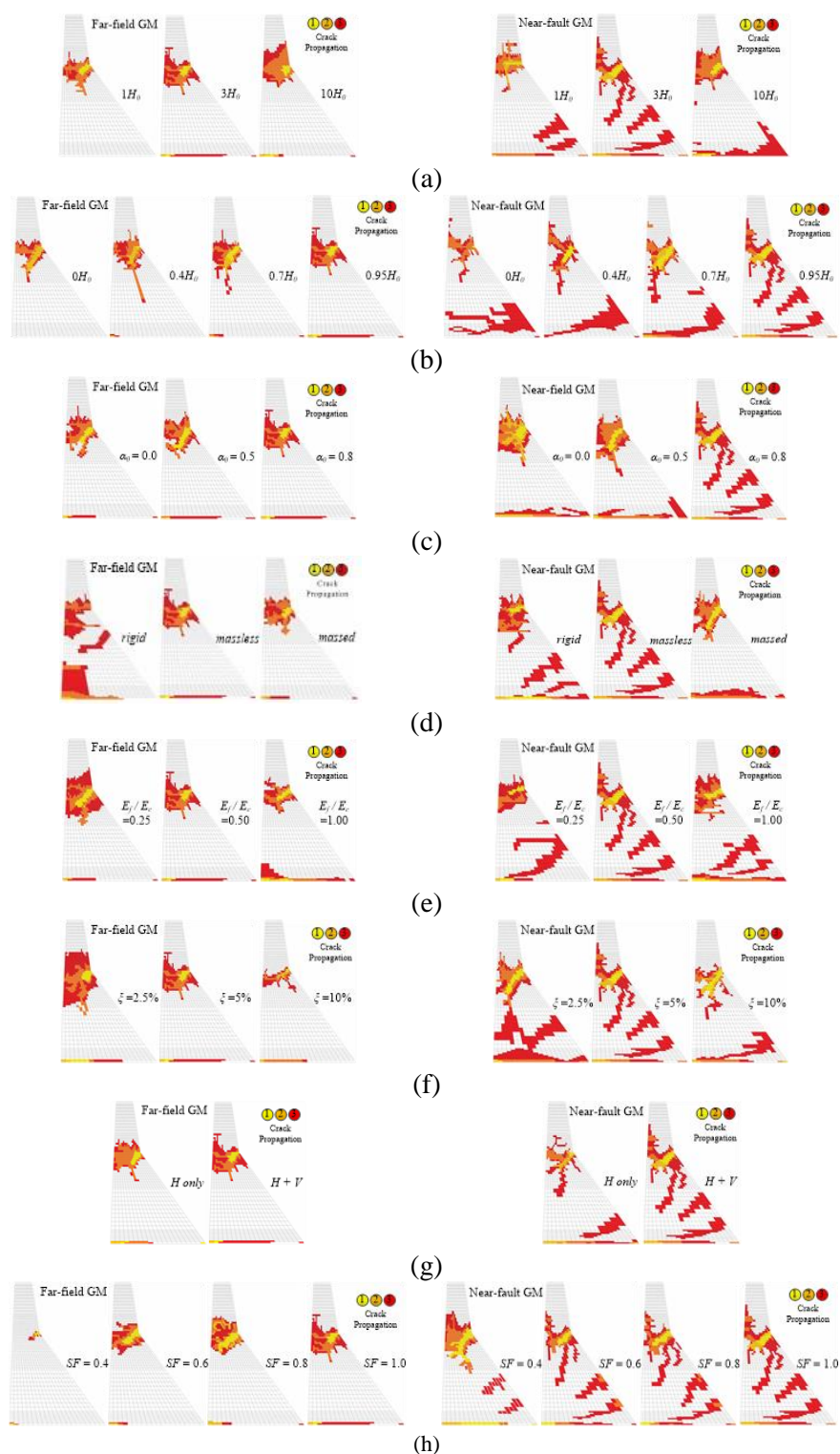


Figure 4: Impact of variable parameter on crack propagation in dam, (a) reservoir length, (b) water level, (c) reservoir bottom absorption, (d) foundation model, (e) foundation flexibility, (f) damping ratio, (g) GM component, (h) GM intensity

4.7. GROUND MOTION COMPONENTS

In this case, the finite element model is kept unchanged and only the input ground motion is changed. In the first model, only the horizontal component is used. In the second model, both the horizontal and vertical components are applied simultaneously. Fig. 3g shows the comparison between the displacement time histories.

As seen, there is a small difference between two models. The difference is much clear for the far-field ground motion. It seems that the effect of vertical component intensifies the crack process. These observations match well with those reported by Lee and Fenves [17]. Fig. 4g shows the crack profile of the dam subjected to different ground motion components. In the case of far-field ground motion, the final crack profiles are close together; however, applying only the horizontal ground motion leads to slightly less cracked elements especially in the dam-foundation interface. In the case of near-fault ground motion, applying the horizontal and vertical components increases cracked elements.

4.8. GROUND MOTION INTENSITY

The original scaled ground motions are assumed to have the scale factor (SF) of unity. Consequently, other pairs of ground motions are generated using a linear SF of 0.8, 0.6, and 0.4. Equal SF is used for both the horizontal and vertical components in each case. Fig. 3h shows the displacement time history. In the linear (pre-cracking) region, the displacement has a direct relation with the intensity of the applied load. Higher intensity motions lead to higher displacement response. The far-field ground motion with SF = 0.4 leads to some small cracking in the crack area; however, no failure occurred in this case (Fig. 4h). The ground motion with SF = 0.6 leads to failure of the model one cycle after the base model (SF = 1.0). Based on Fig. 4h, increasing the seismic intensity level under far-field ground motion does not have a considerable effect on final crack profile of the neck area (because in the case of Koyna dam, this section of the dam is most vulnerable); however, increases cracking in the dam-foundation interface.

5. CONCLUSIONS

This paper studies the parametric finite element analysis of a concrete gravity dam. Nonlinear behavior of the dam is originated from concrete smeared crack. The following conclusions can be drawn from this research:

- Increasing the water level leads to increasing the vibration period.
- Increasing the reservoir water length from $1H_0$ to $3H_0$, leads to increasing the crack profile; however, any further increase in reservoir length does not have considerable effect on crack profile and displacement response.
- Increasing the reservoir water level leads to increase in both the static and dynamic displacements. Crack profile especially in the dam-foundation interface also increases.
- Increasing the wave reflection coefficient leads to increase in both the hydrodynamic pressure and the displacement one cycle prior to failure, especially for near-fault ground motion.
- Using the standard massless foundation model increases the displacement and cracked area.
- Rigid foundation model leads to extensive cracking at the dam-foundation interface.
- Increasing the flexibility of the foundation leads to reduction in both the initial static and dynamic displacement of the dam.
- A flexible foundation increases the number of cracked elements at the dam-foundation interface; however, crack profile of the neck reduces slightly.
- Increasing the damping ratio leads to reduction in the displacement almost during the entire range of dynamic excitation. Also it leads to reduction of both the damaged area and the crack profile of the dam.
- Impact of vertical component of ground motion is almost negligible in the linear elastic range; however, cracking of concrete intensifies the effect of vertical component.
- High intensity motions usually dominant the neck cracking, however, the low intensity motions usually dominant heel cracking.
- In most cases, near-fault excitation leads to a different crack profile than the far-field motion. Pulse-like motion leads to additional cracks at the lower parts of the body which starts at the downstream face and proceeds in an almost inclined line toward upstream.

6. REFERENCES

1. Chopra AK (2012) Earthquake analysis of arch dams: factors to be considered, *Journal of Structural Engineering*, 138:205-214.
2. Hariri-Ardebili MA, Kianoush MR (2014) Integrative seismic safety evaluation of a high concrete arch dams, *Soil Dynamics and Earthquake Engineering*, 67:85-101.
3. Ghanaat Y (2004) Failure modes approach to safety evaluation of dams, *Proceedings of the 13th World Conference on Earthquake Engineering*, Vancouver, Canada.
4. Hariri-Ardebili MA, Seyed-Kolbadi SM, Kianoush MR (2016) FEM-based parametric analysis of a typical gravity dam considering input excitation mechanism, *Soil Dynamics and Earthquake Engineering*, 84:22-43.
5. Fenves G, Chopra AK (1984) EAGD-84: A computer program for earthquake response analysis of concrete gravity dams (Report No. UCB/EERC-84/11), 102 pp. Berkeley: Earthquake Engineering Research Center, University of California, US.
6. Hariri-Ardebili MA, Seyed-Kolbadi SM, Mirzabozorg H (2013) A smeared crack model for seismic failure analysis of concrete gravity dams considering fracture energy effects, *Structural Engineering and Mechanics*, 48(1):17-39.
7. Willam KJ, Warnke EP (1974) Constitutive model for tri-axial behavior of concrete, *International Association for Bridges and Structural Engineering*, Italy.
8. PEER (2012), http://peer.berkeley.edu/peer_ground_motion_database/
9. Hariri-Ardebili MA, Saouma VE (2014) Quantitative failure metric for gravity dams, *Earthquake Engineering and Structural Dynamics*, doi:10.1002/eqe.2481.
10. Bayraktar A, Turker T, Akkose M, Ates S (2010) The effect of reservoir length on seismic performance of gravity dams to near- and far-fault ground motions, *Natural Hazards*, 52:257-275.
11. Attarnejad R, Lohrasbi AR (2008) Reservoir length effect in calculation accurate of dam-reservoir interaction, *Proceedings of 14th World Conference on Earthquake Engineering*, Beijing, China.
12. Gupta ID, Pattanur LR (2013) Investigation of reservoir bottom absorption effects on stochastic seismic response of gravity dams, *ISH Journal of Hydraulic Engineering*, 19(3):282-290.
13. Hariri-Ardebili MA, Saouma VE (2014) Impact of near-fault vs. far-field ground motions on the seismic response of an arch dam with respect to foundation type, *Dam Engineering*, 24(1):19-52.
14. Hall JF (1986) Study of the earthquake response of pine flat dam, *Earthquake Engineering and Structural Dynamics*, 14(2):281-295.
15. Motamedi MH, Amini A, Ghaemian M (2008) The study of the foundation role in the seismic nonlinear behavior of concrete gravity dams, *Proceedings of the 14th World Conference on Earthquake Engineering*, Beijing, China.
16. Chuhan Z, Jianwen P, Jinting W (2009) Influence of seismic input mechanisms and radiation damping on arch dam response, *Soil Dynamics and Earthquake Engineering*, 29(9):1282-1293.
17. Lee J, Fenves GL (1998) A plastic-damage concrete model for earthquake analysis of dams, *Earthquake Engineering and Structural Dynamics*, 27:937-956.

Durability Enhancement of Concrete Dams by Controlling and Mitigating Aar Problem

Ramezaniapour, Ali Akbar¹, Ramezaniapour, Amir mohammad²

1. Professor, Amirkabir University, Concrete Technology and Durability Research Center

Amirkabir University, Tehran, Iran

2. Assistant professor, Tehran University

Email: aaramce@aut.ac.ir

Abstract

Many concrete dams have suffered from heavy deterioration due to Alkali Aggregate Reaction (AAR). The alkali aggregate reaction occurs between the alkalis in cement paste and reactive minerals in the aggregate produces expansive gel resulting in map cracking and low service life of concrete dams. Researches show that a solution for controlling or mitigating this problem is the usage of appropriate supplementary cementing materials in the mixture design of concretes. This paper discusses the effectiveness of various artificial and natural pozzolans as supplementary cementing materials in controlling AAR expansion for various reactive aggregates. Petrographic examination of aggregates was carried out to determine the types of active minerals. Accelerated mortar bar and concrete prism methods were used to evaluate the reactivity of aggregates. Results of the tests show that for each pozzolan there would be an optimum content to be effective in suppressing AAR expansion in accelerated test method. Results of the long-term prism method show that the expansion is not only related to the type and quantity of the supplementary cementing materials but also depends upon the type and the minerals of the aggregates. However, reactivity of some aggregates may be controlled by the optimum content of each pozzolanic materials. It is also concluded that individual evaluation test method may not be suitable for some aggregates and final assessment should be based on different test methods.

Keywords: Alkali Aggregate reaction, concrete Dams, Mitigation, Deterioration, Pozzolans.

1. INTRODUCTION

The alkali-silica reaction (ASR) that occurs between the alkali hydroxides in cement paste and reactive minerals in the aggregate produces expansive gels that cause cracking and displacement in concrete structures. Preventive methods for protecting concrete from the onset of alkali-silica reaction include limiting the use of reactive aggregates, using low-alkali cements, and application of chemical and mineral admixtures. One of the best methods for improving the quality of concrete and controlling deleterious ASR is through the use of supplementary cementing materials. Many different mechanisms have been proposed to explain the effectiveness of supplementary cementing materials against alkali aggregate reactivity, namely higher strength, lower permeability, consequent lower ion mobility, portlandite reduction in the cement paste and alkali reduction in the pore solution are all important factors. The most critical of these factors includes total alkali reduction of the cement matrix and consequent pH decrease in the pore solution as a result of alkali reduction of or entrapping of alkali ions in calcium silicate hydrate [1,2,3]. It is important to note that these materials must be used correctly and in recommended dosages.

Mineral pozzolanic admixtures such as fly ash, silica fume (SF), natural pozzolan, slag, rice husk ash, and highly reactive metakaolin (HRM) have been recommended and used for the mitigation of the deleterious effects of ASR in concrete [4,5] have shown that silica fume (SF) must be used at replacement levels exceeding 10% by mass of cementing materials. Replacement levels in excess of 50% FA or 10% SF may not be acceptable for many construction purposes and this presents a barrier to the wider use of these materials for controlling ASR.

It is generally accepted that the use of natural pozzolans in cement or concrete systems results in low alkali-silica activity [5,6]. In a study carried out by Uzal et al. [7], natural pozzolan has the potential to be used at higher volumes in blended cements for structural concrete applications. They showed that blended cements containing 35%, 45%, and 55% natural pozzolan has excellent performance for suppressing the expansions caused by alkali-silica reaction.

Natural pozzolans are available at limited regions of the world. Chemical properties and the Pozzolanic activities of natural pozzolans vary depending on the region of the source [5]. All natural pozzolans are not equally

effective in combating alkali-carbonate and alkali-silica expansions. The importance of using natural pozzolans in the cement industry requires a complete evaluation of their effects on concrete.

Iran is rich in natural pozzolans such as volcanic tuffs (Trass), pumicite (Taftan and Sabalan) and some diatomaceous earths (Mamaghan, Azarshahr) deposits. Some of these natural pozzolans are currently being used to produce blended cements by local cement manufacturers. According to the previous studies[8], Iranian natural pozzolans are competitive with other natural pozzolans in the world because of high amount of active silica and also the high alumina content. The effect of natural Iranian pozzolans on mitigation of alkali-carbonate and alkali-silica reactions has not been well documented; despite the limited works conducted on the use of natural pozzolans as a cement replacement material in concrete. Also the mechanism by which natural pozzolans affect the alkali-carbonate reactions is not yet fully understood.

Many test methods and guidelines for the prevention of alkali aggregate reaction in new concrete structures have been adopted by various national and international organizations around the world [9]. Most of these standards and guidelines are dealing with alkali-silica reaction. The tests are usually carried out by a number of accelerated and long term laboratory methods. Prior to mortar bar and concrete prism tests, petrography examination, chemical tests are carried out. They have given satisfactory results for some aggregates, while in a number of cases and for aggregates in different parts of the world test results were not reliable [10].

A large number of concrete dams and other concrete structures in the world are suffering from deterioration induced by AAR reaction that impair the durability, serviceability, and also endanger the safety of the structures in future. Most of the aggregates used for the construction of these structures and those for dams to be constructed in the future are reactive aggregates.

The aim of this investigation is to study the effectiveness of natural pozzolans to control the alkali-silica reaction of some reactive aggregates from different sources, which have been considered as concrete aggregates for construction of dams. petrographic examination, accelerated mortar bar test, and concrete prism test were used throughout this investigation.

The use of natural pozzolans as a reasonable method to control the expansion of concretes as a result of ASR has been studied in accordance with ASTM C 1293 and ASTM C 1260, however the accelerated mortar bar test method (ASTM C 1260) has been recognized not to be suitable to determine the effect of cement replacement materials and also it is recommended to measure the expansion of concrete prisms at least for two years [11,12]

2. TEST RESULTS AND DISCUSSION

Results of the expansion of mortar bar specimens containing various aggregates are illustrated in Figs.1 and 2. The length changes of at least two specimens for each aggregate are shown in these figures. It can be seen that the expansion of mortar bars containing fine and coarse aggregates have exceeded 0.25 percent after 14 days. Thus from the results of the mortar bar accelerated test, three aggregates were classified as highly reactive.

In order to investigate the effect of natural pozzolans on mitigation of alkali aggregate reaction, mortar bar test was carried out on specimens containing pozzolanic cements at 15 and 30 percent replacement level. Test results are depicted in Figs.3 and 4. From the results it is obvious that significant reduction in expansion can be obtained in all concrete mixtures containing natural pozzolans. Mortar mixtures containing natural pozzolans at the 15% replacement level have shown expansion higher than 0.1 percent limitation after 35 days. However, in mortar mixtures containing higher amounts of natural pozzolans (30%), the expansion is below 0.1 percent which indicates the ability of pozzolans to control ASR in accelerated mortar bar test.

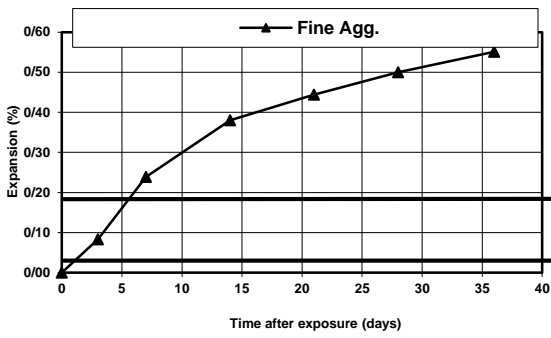


Figure 1. Expansion of mortar bars made with Fine Agg

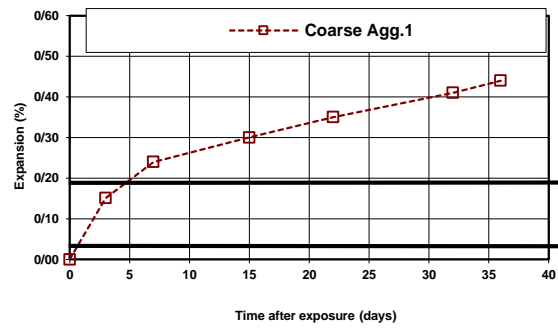


Figure 2. Expansion of mortar bars made with Coarse

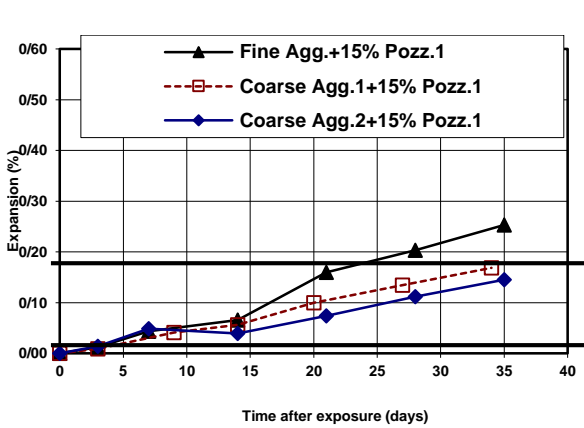


Figure 3. Expansion of mortar bars made with 15% pozzolan

Agg.1

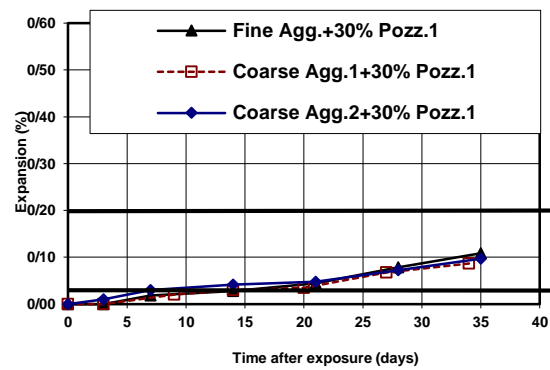


Figure 4. Expansion of mortar bars made with 30% pozzolan

Results of expansion of concrete prisms incorporating reactive sand with and without natural pozzolans at various ages up to 270 days are illustrated in Figs.5 and6. In specimens containing natural pozzolans, 30 percent pozz-1 natural pozzolan was replaced with cement. It is clearly seen that in concrete mixtures containing 30 percent natural pozzolans, expansions of all specimens are less than 0.04 percent at this age. However, expansions after one and two years will show how pozzolans can control the ASR.

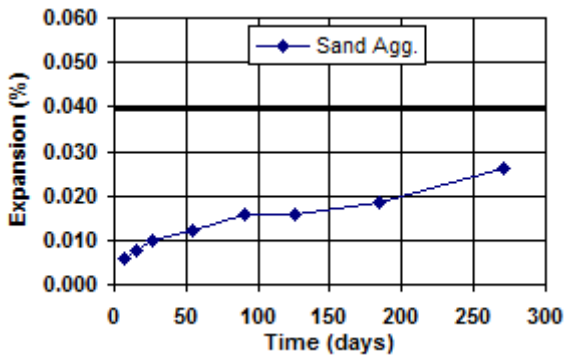


Figure 5. Expansion of prisms made with sand

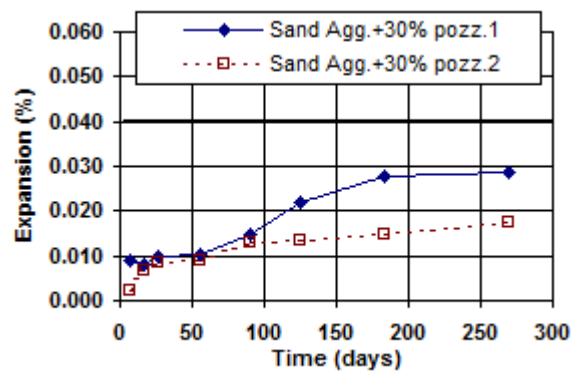


Figure 6. Expansion of prisms made with 30% pozzolan

In another research, results of 56-day mortar bar expansion of specimens containing various amounts of natural pozzolan and a reactive carbonate aggregate are presented in Fig 7.

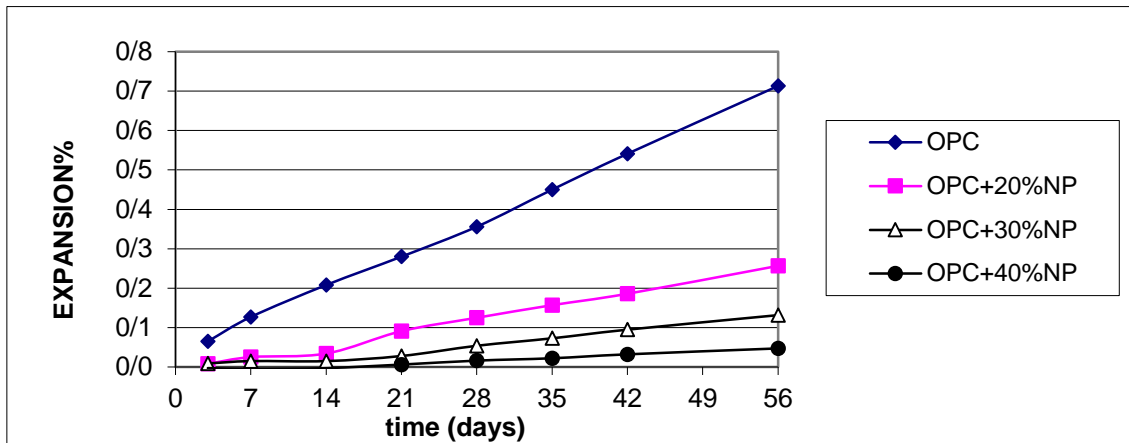


Figure 7. Results of accelerated mortar bar tests containing natural pozzolan

As seen in Fig 7, the expansion rate of the control sample is about 0.21% for 14 days which is categorized as extremely reactive aggregates based on ASTM C1260 standard. This sample expands about 0.71% at 56 days and will expand more at longer ages.

Mortar bars containing natural pozzolan have lower expansion at all ages and show a reduction of 64%, 79% and 93% for pozzolan's content of 20%, 30% and 40% respectively after 56 days under ASTM C1260 standard. This reduction in expansion is about 84%, 89% and 99% after 14 days respectively. The results of one-year test based on ASTM C1293 shows that natural pozzolan has marginally reduced the expansion (see Fig.8).

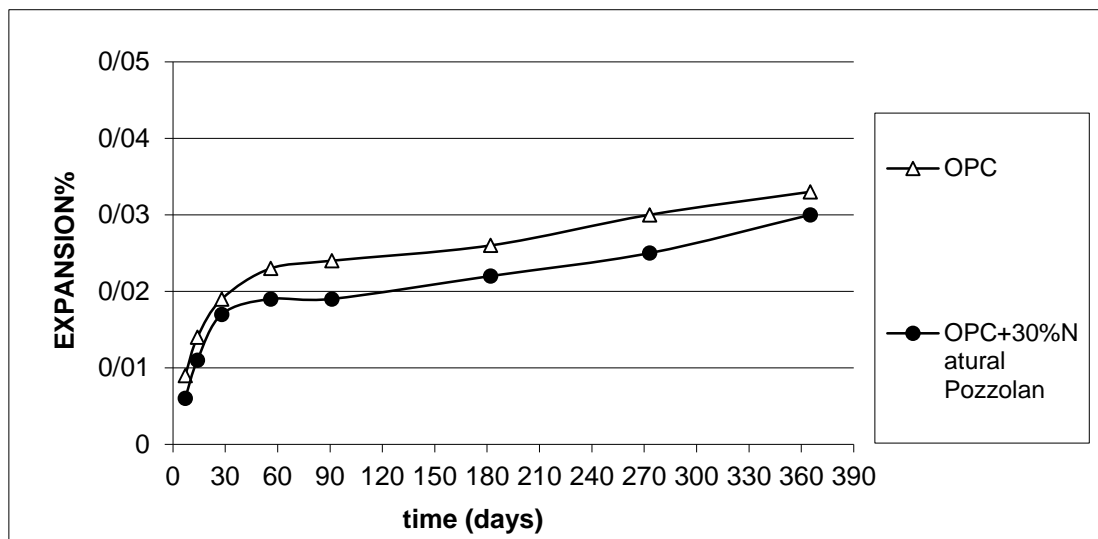


Figure 8. Results of long term expansion of specimens containing natural pozzolan

In an investigation the results of concrete prism test indicate that the expansion of specimens can be controlled by addition of trass as a natural pozzolans at 20 and 30 percent replacement [66]. This is clearly seen in Figure 9. In general, the effect of natural pozzolans to suppress alkali silica reaction depends on the reactivity of aggregate, the level of natural pozzolan replacement, the equivalent alkali content of cementitious composition and the activity index of natural pozzolan. The maximum reduction of concrete prism expansion compared with control sample increases with an increase in activity index of natural pozzolan. It was also concluded that the expansion of specimens is declined by increase of natural pozzolan replacement level, while in some cases a pessimum amount in natural pozzolan replacement level exists.

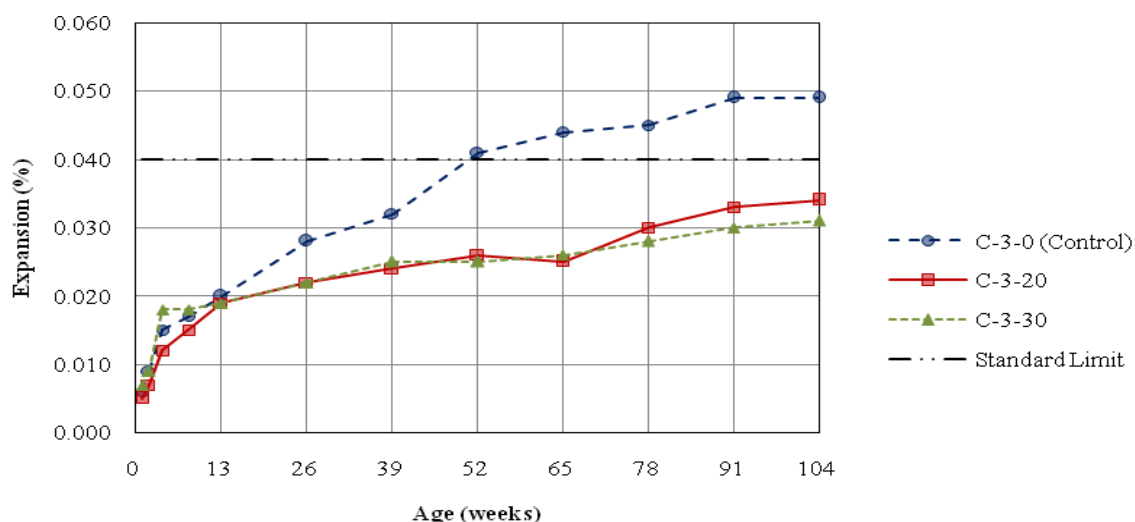


Figure 9. Effect of a natural pozzolan on expansion reduction of concrete prisms up to 2 years

3. CONCLUSIONS

From the test results obtained in this investigation, the following conclusion can be drawn:

1. For the assessment of alkali silica reaction of siliceous aggregates, the application of the ASTM C 289 chemical test method should be followed by the accelerated mortar bar and concrete prism tests.
2. Incorporating natural pozzolans in the mixes can reduce the expansion of mortar specimens containing highly reactive aggregates.
3. The use of 15% natural pozzolans in the mixtures seems to be not sufficient to control the expansion of mortar bars in accelerated tests.
4. When using highly reactive aggregates, it is recommended to incorporate 30 percent or more natural pozzolans in concrete mixtures to control the alkali silica reaction.
5. The results of accelerated mortar bar test method are approximately the same for a constant natural pozzolan replacement with an individual aggregate. It means that this test method is not an appropriate method to assess the influence of natural pozzolans replacement on expansion due to ASR. Nevertheless, the AMBT method is a suitable accelerated method to distinguish reactive aggregates.
6. The results of concrete prism test indicates that the expansion of specimens does not cease at 52 weeks. The growth of expansions, however, is declined significantly at the age of 104 weeks. Therefore it is recommended to measure the expansion of concrete prisms which contain natural pozzolans as a part of their cementitious composition up to two years.
7. In general, the effect of natural pozzolans to suppress alkali silica reaction depends on the reactivity of aggregate, the level of natural pozzolan replacement, the equivalent alkali content of cementitious composition and the activity index of natural pozzolan.
8. The maximum reduction of concrete prism expansion increases with an increase in activity index of natural pozzolan.
9. The expansion of specimens is declined by increase of natural pozzolan replacement level, while in some cases a pessimum amount in natural pozzolan replacement level exists.

4. REFERENCES

1. Bérubé, M. A. and Duchesne, J., "The effectiveness of silica fume in suppressing expansion due to alkali-silica reaction", Proceeding of CANMENT/ACI International workshop on the use of silica fume in concrete, Washington D.C., 1991, pp. 255-304.
2. Bérubé, M. A. and Duchesne, J., "Effectiveness of supplementary cementing materials in suppressing expansion due to alkali-silica reactivity", part 1 and 2, Cement and Concrete Research, Vol. 24, No.1 and 2, pp. 73-82 and pp. 221-230.
3. Ramezani pour, A. A., Raiss ghasemi, "Evaluation of alkali-aggregate reactions with the effect of silica fume in the construction of dams in Iran", 11th International Conference on Alkali-Aggregate Reaction, Quebec, Canada, 2000, pp. 733-741
4. Fournier B., Bilodeau A., Malhotra, V.M. CANMET "Industry research consortium on alkali- aggregate reactivity, in", CANMET/ACI International Workshop on Alkali-Aggregate Reactions in Concrete, Natural Resources, Canada, 1995, pp. 169- 180.
5. Ramezani pour, A.A. "Cement Replacement Materials", properties, durability, sustainability, Springer publication, 2014
6. ACI Committee 232 Report, "Use of natural pozzolans in concrete", ACI Mater. J. 91 (4) (1994) 410-426.
7. B. Uzal, L. Turanli, Studies on blended cements containing a high volume of natural pozzolans, Cement and concrete research, (11) (2003) 1777- 1787
8. Ramezani pour, A.A. "Evaluation of Pozzolans of Iran", Building and Housing Research Center of Iran, Publication No. 153, 1992.
9. Berube, M. A. and Fournier, B., "Accelerated Test Methods for Alkali-Aggregate reactivity", Advances in Concrete Technology, CANMET-Ottawa, Canada, 1992, pp. 583-627.
10. Hooton, R. D. and Rogers, C.A., "Evaluation of Test Methods for Detecting Alkali-Reactive Aggregates", Proceedings of the 8th International Conference on Alkali Aggregate Reaction in Concrete, Kyoto, Japan, 1989, pp. 439-444.
11. Ramezani pour AA, Shafikhani M, Nili M., "The effect of natural pozzolans on controlling expansion of concrete due to alkali-silica reaction", Proceedings of International Conference on Concrete and Reinforced Concrete, Moscow, 2005.
12. Ramezani pour, A.A. M. Shafikhani, "ASR Test Methods Evaluation for Concretes Containing Natural Pozzolans", 14th International Conference on AAR in concrete Austin, June 2012, Texas, USA

A Probabilistic Approach to Define the Reliability of Gates at Dams and Weirs

Adrian Lindermuth¹, Barbara Brinkmeier², Markus Aufleger³

1-3- Unit of Hydraulic Engineering, Institute for Infrastructure, University of Innsbruck
Technikerstraße 13, 6020 Innsbruck, Austria

Email: Adrian.lindermuth@uibk.ac.at

Abstract

The safety of a dam depends, among other things, on the functionality and the hydraulic ability of the gates. Therefore, a literature study was undertaken by observing national and international research to receive actual failure frequencies of gates and weirs. This information is necessary to extend the so called (n-1)-condition in the actual dimensioning process from a deterministic design concept towards a probabilistic approach. Because of the determined lack of data, a kind of semi-probabilistic approach was developed, to treat varying failure probability of different gate types. The basic principle is to generate an evaluation matrix to assess different gate structures relating to their failure patterns. The result should be a defined “basic-value” for each gate type, which reflects the overall susceptibility. Furthermore, there should be a possibility for design engineers and operators of dam structures to intervene the dimensioning process through an “individual value”.

Keywords: reliability analyses, weir, gates, probabilistic approach, (n-1)-condition.

1. INTRODUCTION

The functionality and the hydraulic ability of gates are essential for the operational and overall safety of dams and weirs. Therefore, a reduction of the discharge capacity, through accidental or scheduled blockage, is mandatory in the dimensioning process. In Germany and Austria these requirements are taken into account through a deterministic design concept which includes the so called (n-1)-condition [1]. According to this concept, the design flood must be able to pass the weir with one gate out of function. The probabilistic approach behind this concept is that the coincidence of a blockage of two or more gates with a design flood is very unlikely.

Accidental blockage of a gate can be caused by a variety of mechanical and electronical malfunctions. In the following chapters these eventualities of unavailability are briefly summarized by the term “failure”.

2. PSEUDO-PROBABILISTIC APPROACH

In literature the (n-1)-condition usually aims at maintenance activities which lead to an unavailability of the gate [2]. With regard to the editors of DVWK 1990 also the case of an unavailability caused by failure of relevant components should be taken into account through this approach. Therefore the formula was extended by a term considering the maintenance and another one the failure probability [3].

$$(n - a_R - a_S) \times B_F \rightarrow HQ_b \quad (1)$$

where n is the number of gates, a_R is a factor considering the failure of the gate, a_S considering the maintenance, B_F is the clear width of one gate and HQ is the design flood discharge, which has to pass through the total clear width of the structure.

This consideration could result in thoughts, there should be two gates in redundancy, but this is in general not necessary because of the fact that a negative impact only arises if the following three aspects appear at the same time [3]:

- maintenance of one gate,
- failure of another gate and
- the occurring amount of water cannot be discharged by the remaining gates and the safety margin of the construction is insufficient.

3. RELIABILITY ANALYSIS AND DATA ACQUISITION

Over the last decades, reliability analysis has gained more and more acceptance in academic circles. These methods consider a probabilistic approach for the design of structures by defining a reliability index or a probability of failure instead of a deterministic factor of safety. To specify a limit state equation that governs the behavior of the structure, for every random variable a probability of failure has to be defined. Therefore, a literature study was undertaken by observing national and international research to receive actual failure frequencies of gates and weirs.

At the moment only a few reliable publications relating to this scientific issue are available [4–9]. An attempt to compare the individual results failed because of the widely varying methodologies of the single analysis.

4. SEMI-PROBABILISTIC APPROACH

Because of the lack of data and analysis, another approach to treat varying failure probability of different gate structures has been developed. The basic principle is to generate an evaluation matrix to assess different gate structures relating to their failure patterns. The result should be a defined “basic value” for each gate type, which reflects the overall susceptibility.

Furthermore, there should be a possibility for design engineers and operators of dam structures to intervene the dimensioning process by increasing the safety. For example, if a structure is equipped with a redundancy measure, the “basic value” can be reduced by an “individual value”.

$$(n - (a_B - a_I)) \times B_F \rightarrow HQ_b \quad (2)$$

Where n is the number of gates, a_B is the “basic value” considering the vulnerability to fail, a_I is the “individual value”, which can be influenced by the engineers and operators, B_F is the clear width of one gate and HQ is the design flood discharge.

a. BASIC VALUE

The concept is to determine a basic value a_B for each gate type which describes the susceptibility of failure. This is done through assessing the individual structure by a defined valuation scheme, which focuses on the complexity of the components. The consideration behind this is, that with an increasing level of complexity also the vulnerability to fail rises.

Five main categories have been specified and rated inspired by literature mentioned in chapter 3. The categories were then further divided to accomplish a detailed rating system (see Table 1).

The first category “control system” includes all kind of electronic devices which are responsible for acquisition, processing and transfer of data, information and signals. According to the probabilistic approach, the likelihood to fail rises with the amount of components. Thus, two subcategories “simple” and “complex” have been defined. The same concept was considered for splitting the second category “mechanics”. The subcategories were defined sufficiently abstract to simplify the allocation of components of different weir systems.

A power unit failure, which is mentioned in category three, only includes mechanical or hydraulic infirmities of the drive system. An interruption of the energy supply is not considered, because the probability is independent from the weir type. Therefore, it is important, if during a break down, a release of the gate with a redundant device (e.g. truck-mounted crane) is possible.

The category “abrasion” aims at assessing the resilience of the structure with regard to the applied materials. As an example, a corrosion-resistant metal drum gate is much more resistant to abrasion through flood debris, than a common inflatable rubber weir.

The last category focuses on the revision period, which leads to an unavailability of the weir. To distinguish between different gate types, it is important to characterize the necessary interval and duration of typical revision procedures.

Table 1 - Main categories and subdivisions for the evaluation and determination of the basic value a_B

<i>Control system</i>	<i>Mechanics</i>	<i>Failure of power unit</i>	<i>Abrasion</i>	<i>Revision time</i>
simple	weir body	weir moveable	low	short
complex	force transmission	weir immovable	high	average
	support			long
	pressure pipes and valves			
	seals			

b. INDIVIDUAL-VALUE

As already mentioned, engineers and operators should have the possibility to influence the basic value through measures which improve the structure. The individual value a_I depends on the following five categories:

- Number of gates
- Year of construction
- Further redundancy (beyond the state of the art)
- Revision concept
- Possibility to unblock the gate in case of a revision

As already mentioned in DVWK 1990, the failure probability rises with the number of gates installed at one plant. With regard to river characteristics in central Europe the (n-1) approach is valid for up to six gates per facility. Furthermore, a linear growth of the default criterion is assumed, so that in case of twelve weirs, two with failure are suggested [3].

Also the year of the construction can play an important role, although the opinion of experts on this topic varies widely. On the one hand, the technical development reduces the vulnerability of electrical and mechanical components[8], on the other hand there are reports of plants that have worked without problems over the last decades.

As already mentioned, design engineers and operators of dam structures should have the possibility to increase the overall safety of the structure by assembling further redundancy, beyond the required extent. This could be an additional power unit or a gantry crane.

In addition, risk minimization could be achieved by generating a revision plan, which focuses on a reduction of the time period with the weir out of function [10]. Also the possibility to unblock the gate during a revision is significant to reduce the risk. This presupposes that - apart from releasing the actual weir - also the revision gate, which provides dry working conditions, can be opened.

5. CONCLUSIONS

Because of the increasing demand to implement probabilistic approaches to the design of gates at weirs and dams, a literature study was undertaken to obtain information about the failure probability. At the moment only a few publications concerning this issue are available. Furthermore, an attempt to compare the results failed because of the widely varying methodologies behind the individual analysis. To avoid the lack of data, another semi-probabilistic approach was developed. For each gate type a “basic value” was defined by assessing the complexity of the structure. To enable engineers and operators of dam constructions to influence the dimensioning process a further “individual value” was introduced. Through measures, which improve the structure safety, the “basic value” can be improved. This approach is going to be discussed and evolved by an expert committee and could be included in a new guideline for gate dimensioning at weirs and dams.

6. REFERENCES

1. Normausschuss Wasserwesen. DIN 19700-13 2004.
2. Vischer D. Hydrologische Grundlagen, Elemente des Wasserbaues, Nutz- und Schutzbauten an Binnengewässern 1985.
3. DVWK. DVWK Merkblatt 216, Betrachtungen zur (n-1)-Bedingung an Wehren 1990.
4. Heuberger K. Die (n - 1)-Bedingung im Kontext der Sicherheitsphilosophie der DIN 19700. Technische Universität München, 2017.
5. Franke J. Einfluss der Überwachung auf die Versagenswahrscheinlichkeit von Staustufen. Universität Stuttgart, 2011.
6. Barker M, Vivian B, Matthews J, Oliver P. Spillway Gate Reliability and Handling of Risk for Radial and Drum Gates. NZSOLDANCOLD 2003 Conf. Dams, 2003.
7. Estes AC, Foltz SD, McKay DT. Estimating Risk from Spillway Gate Systems on Dams Using Condition Assessment Data. US Army Corps Eng Eng Res Dev Cent 2005:97.
8. Pohl R. Failure frequency of gates and valves at dams and weirs 2000.
9. Kalantarnia M. Reliability analysis of spillway gate systems. McGill University, Department of Civil Engineering and Applied Mechanics, 2013.
10. Pohl R. Funktionsicherheit von stahlwasserbaulichen Verschlüssen 2014;104:21–7.

A Case Study on the Deformation Behaviour of Asphalt Concrete Core Dams (ACRD) with Different Core Inclinations

Peter Tschernutter¹, Adrian Kainrath¹

1- Tschernutter Consulting GmbH, Villach, Austria

Email: office@zt-tschernutter.at

Abstract

Asphalt concrete cores in dams as sealing barrier provide a cost-effective and highly flexible solution even for high dams. Within this study an intense numerical analysis is performed to study the stress and deformation behaviour of asphalt concrete core dams with different core inclinations. Therefore three models of an 128 m high rockfill dam with different designs (vertical, inclined and partially inclined core) are introduced in the current paper. Based on numerical analyses the stress and deformation behaviour of the dam and the core are studied in order to demonstrate differences between the core designs. The analyses showed only small deviations of the vertical deformation behaviour of the dam for the core designs examined in this study. The highest horizontal core deformations were obtained with the vertical core. The inclined and partially inclined core showed considerable lower horizontal deformations. With regard to the stress state in the core, the lowest principal stress is obtained with the inclined core.

Keywords: Asphalt Concrete Core, Rockfill Dam, Vertical Core, Inclined Core, Deformation Behaviour, Numerical Analysis.

1. INTRODUCTION

An existing 128 m high rockfill dam with an asphalt concrete core as sealing element and barrier has been selected for numerical analysis to study the stress and deformation behaviour of asphalt concrete core rockfill dams with different core inclinations. A soft material behaviour, steep upstream and downstream slopes as well as the height of the dam are particularly well suited for the case study. Figure 1 shows the zoning of the cross section of the dam. The foundation of the dam is assumed to be on stiff rock. The upstream dam slope was designed with 1:1.5 (V:H) and the downstream slope with an inclination of 1:1.4. The width of the vertical asphalt core is at the bottom 95 cm, decreasing gradually to 50 cm, which is maintained for the top 50 meters. The cross section depicted in Figure 1 is used as basis for the case study and two alternative designs with different core inclinations were analysed. Figure 2 shows an alternative design of the dam with a core inclination of 11V:1H, while Figure 3 shows the design with a vertical core for the lower two thirds of the height and an inclination of 5V:1H in the upper part. All three core designs are analysed by means of stress and deformation behaviour in order to provide general design considerations.

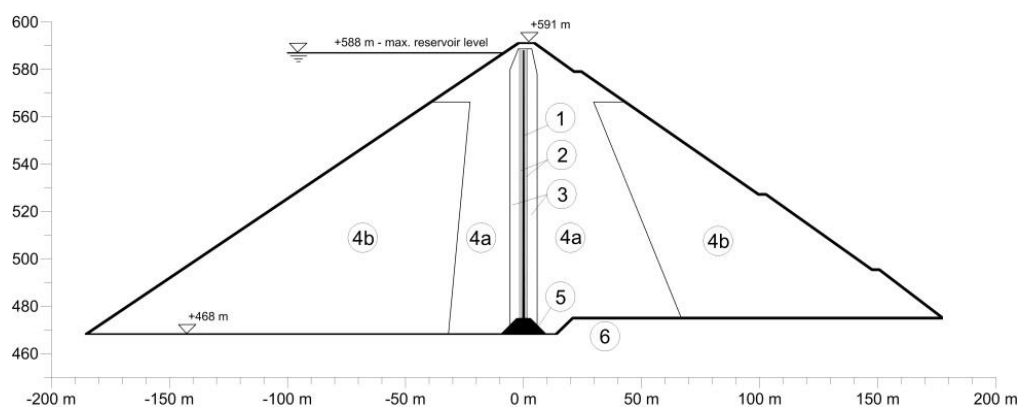


Figure 1. Original section of the dam with a vertical asphalt concrete core

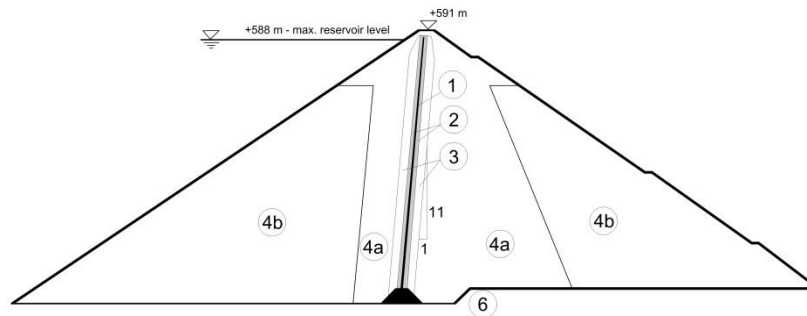


Figure 2. Design with inclined core

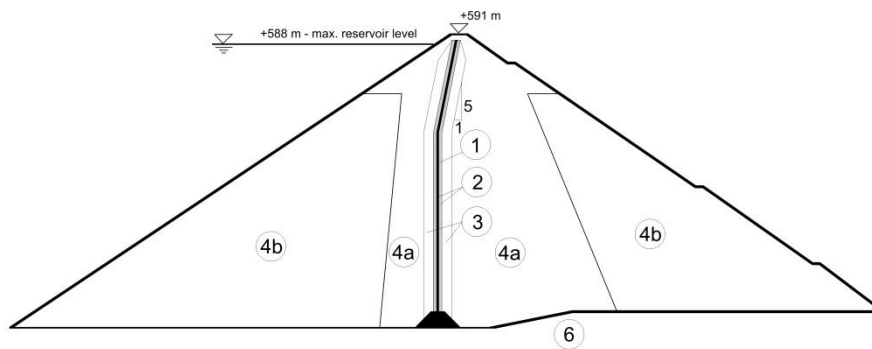


Figure 3. Design with partially inclined core

2. NUMERICAL ANALYSIS AND PARAMETERS

The finite element program Plaxis 2D, which has been developed for the analysis of geotechnical structures, was used throughout this analysis. The simulations were carried out with a 2D-plane strain model. Three models have been created with different core inclinations according to Figure 1, Figure 2 and Figure 3. The models used for the current study consist of about 30,000 15-node triangular elements, which have 12 interior stress points situated at different positions. The average element size was around 1.4 m. The finite element mesh of the original dam (model 1) is shown in Figure 6. The model's horizontal expansion amounts to 870 m, which is 2.6 times the model's vertical expansion of 326 m. The hardening soil model [4] implemented in PLAXIS was used for the numerical analysis. It is a modified version of the hyperbolic model. The hardening soil model supersedes the hyperbolic model by far, using the theory of plasticity rather than the theory of elasticity, including soil dilatancy, and introducing a yield cap. The hardening soil model accounts for the stress dependence of the soil stiffness for oedometric and deviatoric loading as well as for primary loading, unloading and reloading. The stress dependency is modeled with three different stiffness moduli: E_{50}^{ref} for primary loading, E_{ood}^{ref} for oedometric loading, and E_{ur}^{ref} for unloading and reloading, and the parameter m for the amount of the stress dependency. The stress dependency of the stiffness is nonlinear and given by the following equation:

$$E_{50} = E_{50}^{ref} \left(\frac{\sigma_3 + c \cdot \cot \varphi}{p^{ref} + c \cdot \cot \varphi} \right)^m \quad (1)$$

where c is the cohesion; φ is the friction angle; p^{ref} is the reference stress; σ_3 is the minor principal stress, which is the effective confining pressure applied in a triaxial test; and E_{50}^{ref} is the reference stiffness modulus corresponding to the reference stress p^{ref} , which is determined from a triaxial stress-strain curve for a mobilization of 50% of the maximum shear strength. The unloading/reloading path is modelled as purely (linear) elastic with the reference Young's modulus for unloading/reloading E_{ur}^{ref} .

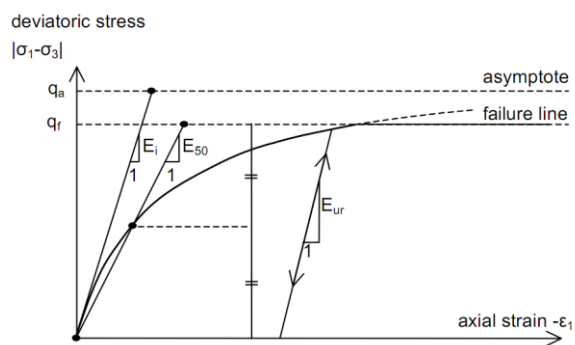


Figure 4. Hyperbolic stress-strain relation

In the hardening soil model, two different hardening mechanisms (i.e., isotropic and deviatoric) account for the history of stress paths. Therefore, a shear hardening yield surface (cone) as indicated in Fig. 5 is introduced. For isotropic stress paths, a cap-type yield surface is used to close the elastic region. Due to shear hardening, the shear yield locus can expand up to the Mohr-Coulomb failure surface while the cap expands due to volumetric hardening as a function of the pre-consolidation stress. A detailed description of the hardening soil model can be found in [4].

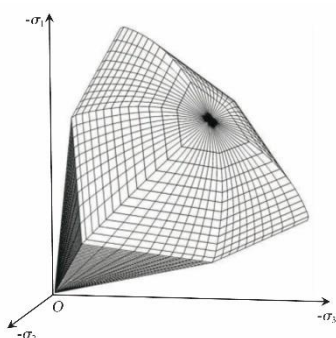


Figure 5. Yield contour of the hardening soil model in total stress space

Figure 1-3 depicts the zoning of the models which were taken into account with seven different zones. For all dam zones, the hardening soil model was used. The bedrock as well as the concrete plinth was implemented with a linear elastic relationship. Since no test data for the dam materials were available the parameters have been derived from [5, 6, 8]. The parameters used in the current study are shown in Table 1. The construction of the dam in the numerical model was carried out in sequential steps with a layer thickness of about 5 meters. The reservoir level was sequentially increased in the numerical model with the dam height.

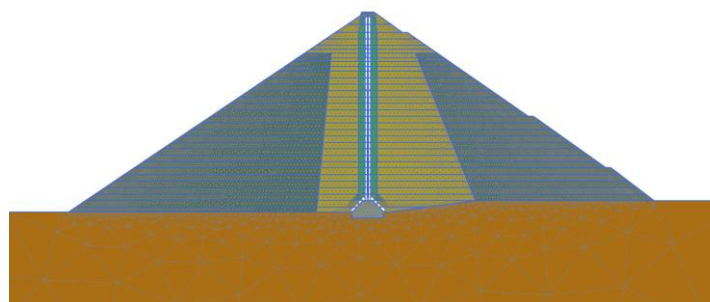


Figure 6. Numerical model with vertical core

Table 1- Parameters for the numerical simulation

Zone		Bedrock	Concrete	Asphaltic Core	Transition Zone Gravel	Transition Zone crushed rock	Shoulder rockfill – well compaction	Shoulder rockfill – bad compaction
Zone		1	2	3	4	5	6	7
Model		LE	LE	HS	HS	HS	HS	HS
E	[kN/m ²]	300000	30000000	-	-	-	-	-
ν	[-]	0,3	0,15	-	-	-	-	-
E_{50}^{ref}	[kN/m ²]	-	-	15000	76000	95250	76200	50000
E_{oed}^{ref}	[kN/m ²]	-	-	14.000	60.000	57000	68000	43000
E_{ur}^{ref}	[kN/m ²]	-	-	30000	210000	300000	210000	120000
m	[-]	-	-	0,21	0,48	0,25	0,45	0,4
ϕ	[°]	-	-	45	45	45	45	45
c	[kN/m ²]	-	-	580	1	1	1	1
ψ	[°]	-	-	2	7	7	7	7
ν_{ur}	[-]	-	-	0,2	0,2	0,2	0,2	0,2

LE...Linear Elastic model, HS...Hardening Soil model

3. RESULTS OF THE STRESS ANALYSIS

Figure 7 shows the vertical and horizontal effective stress distribution for all three core types at maximum reservoir level. It can be clearly seen from the plots, that the downstream zone adjacent to the core undergoes a reduction of the vertical stress, accompanied by a significant increase of horizontal stress. In those areas the plots indicating a strong rotation of the principal stress directions. Due to the high horizontal stress, it is obvious that the quality and compaction of this area mainly influence the shear deformation of the core. In general, only slight differences can be seen from the vertical and horizontal stress distribution of the three different core designs.

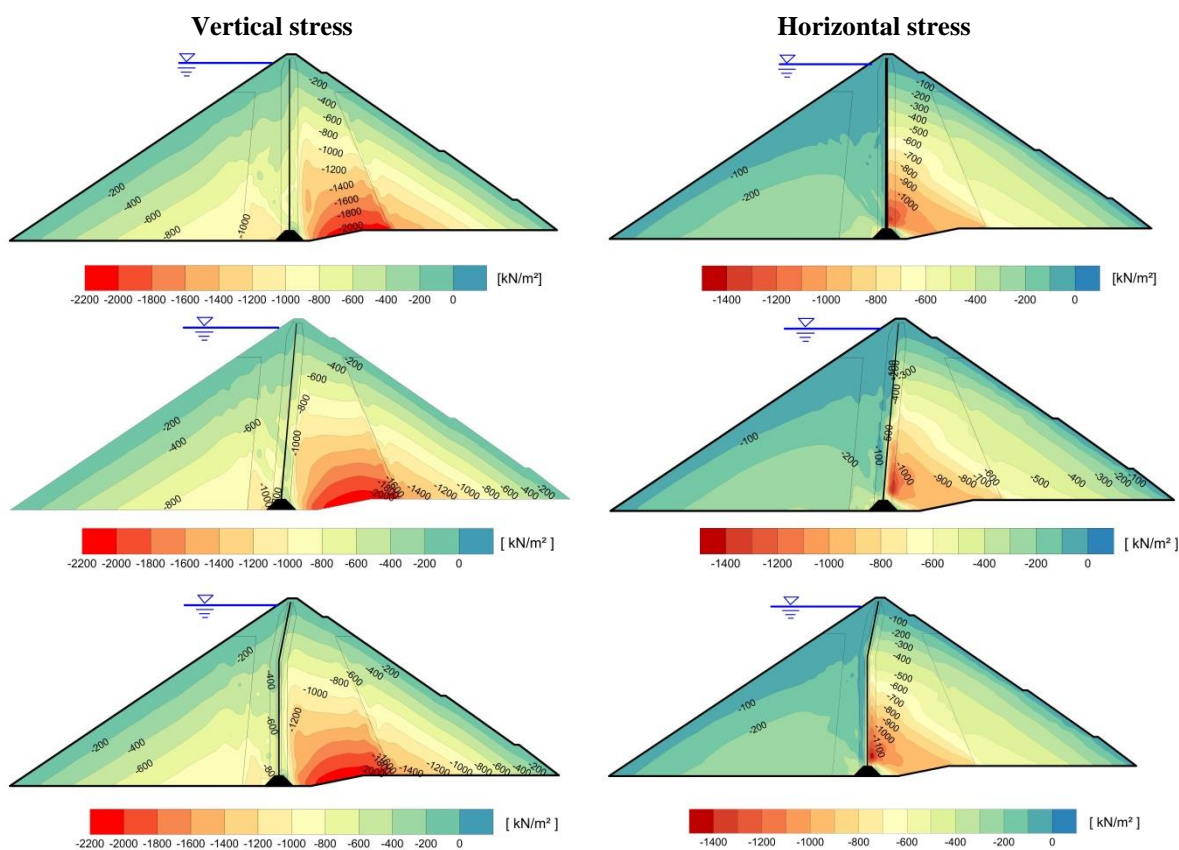


Figure 7. Vertical and horizontal stress

4. RESULTS OF THE DEFORMATION ANALYSIS

Figure 8 shows the vertical and horizontal deformation for the three different core designs caused by construction and impounding. The graphs show, that the highest vertical deformation occurs in the upstream shoulder, adjacent to the core. The highest settlements are achieved with a vertical core, followed by the partially inclined core. The model with the inclined core shows the lowest settlements. With regard to the horizontal displacements, the partially inclined core shows the lowest values.

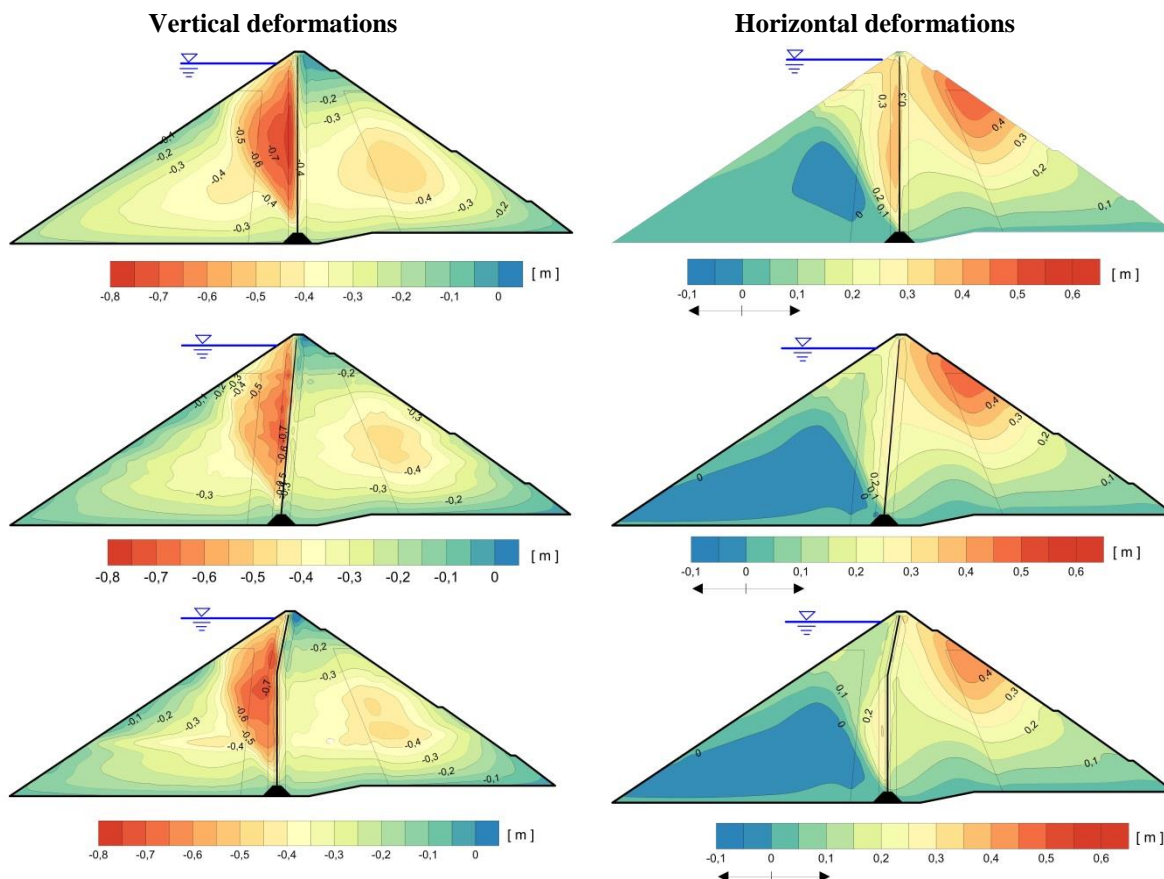


Figure 8. Vertical and horizontal deformation

The shear strains after impounding are depicted in Figure 9. It can be seen from the graphs that different shear zones occur in the upstream shoulder. The zones develop because of the horizontal deformation of the core during impounding. The water pressure acting on the impermeable core leads to a horizontal core deformation and subsequently a stress reduction in the upstream zones adjacent to the core. For the vertical core, only one big shear zone occurs, while for the inclined core smaller local shear zones are distribute over the height.

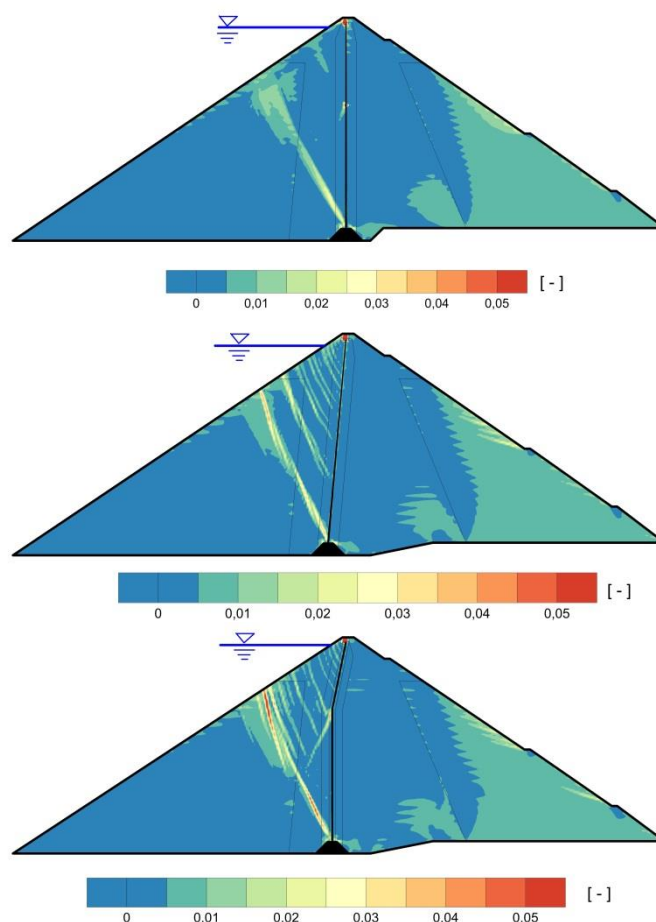
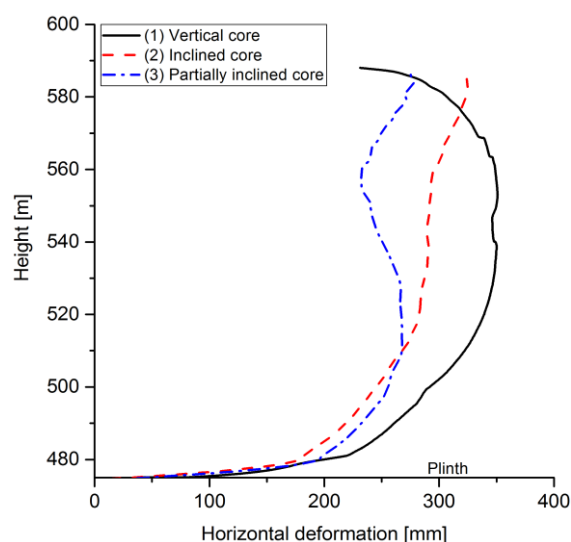
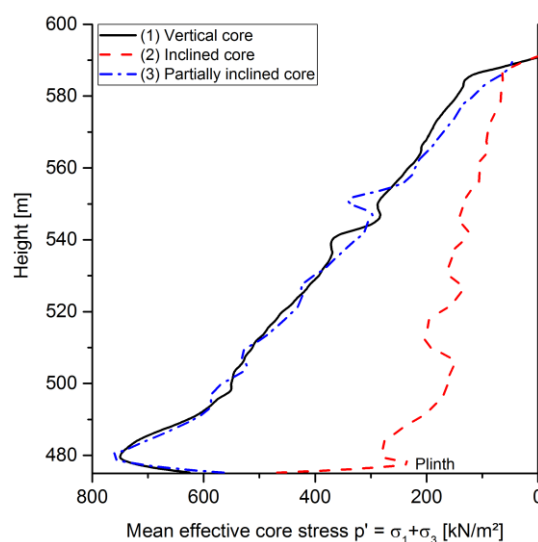


Figure 9. Shear strains after impounding

The horizontal core deformations of all three core types are depicted in Figure 10. The model with the vertical core shows the highest horizontal deformation of about 350 mm at mid height. The model with the partially inclined core gives the lowest horizontal core deformations. Figure 7 and Figure 10 show that the lowest part of the core needs a high transversal deformation to balance the stress differences between the upstream and downstream side. In this area the core undergoes a high shear deformation to arouse a downstream resistance against the high horizontal stress.

Figure 11 depicts the mean effective stress in the core for all three models. The graph clearly indicates the differences between the vertical core and the inclined core. For the inclined core, the mean effective stress p' in the core is about half the stress of the vertical core. The inclination of the upper part of the core has only a slight influence on the stress state in the asphalt concrete core.


Figure 10. Horizontal core deformation

Figure 11. Mean effective core stress

5. CONCLUSIONS

A numerical analysis on a 128-meter-high rockfill dam has been conducted to study the influence of different core designs on the stress and deformation behaviour of the dam. Therefore vertical, inclined and partially inclined core were investigated. The results of the presented study show only minor differences in the vertical deformation behaviour of the dam for the three models. The settlements of a dam with an inclined core are slightly smaller, compared to a similar dam with a vertical core. In contrast to this, an inclined or partially inclined core considerably reduces the horizontal core deformations. The mean effective stress in the core is about half the stress of a vertical core.

6. REFERENCES

- Höeg, K. (1993). "Asphaltic concrete cores for embankment dams". Stikka Press, Oslo, Norway.
- Hoeg, K., Valstad, T. and Kjaernsli, B. (2007), "Asphalt core embankment dams: Recent case studies and research". *Hydropower & Dams*, 13(5), pp. 112-119.
- Hoeg, K., Wang W. (2017), "Design and construction of high asphalt core embankment dams". 85 Annual Meeting on International Commission on Large Dams, Prague, Czech Republic.
- ICOLD. (1992) "Bituminous cores for fill dams". Bulletin 84. International Commission on Large Dams (ICOLD), Paris.
- Schanz, T., Vermeer P.A. and Bonnier B.G. (1999), "Formulation and verification of the Hardening-Soil Model". Beyond 2000 in Computational geotechnics, Amsterdam.
- Smesnik M., Tschernutter P., and Hofko B. (2017), "Laboratory method to simulate short-term aging of hot mix asphalt in hydraulic engineering". *Construction and Building Materials* 150, page 435-441.
- Tschernutter, P. and Kainrath, A. (2016), "Design considerations and behavior of reinforced concrete core dams during construction and impounding". *Water Science and Engineering*, 9(3), pp. 212-218.
- Tschernutter, P. and Nackler, K. (1991), "Construction of Feistritzbach Dam with Central Asphaltic Concrete Membrane and the Influence of Poor Quality Rock on Fill Behaviour". Proceedings of the XVII ICOLD Congress, Vienna, pp. 435-442.
- Tschernutter, P. (2009), "Influence of soft rock-fill material as dam embankment with central bituminous concrete membrane". LTBD09, Graz, Austria.
- Wang, W. (2008). "Research on the suitability of asphalt concrete as water barrier in dams and dikes". Ph.D. thesis, University of Oslo, Oslo, Norway.

Thermal Analysis of Roller Compacted Concrete Dams

Mohammad Mousavi¹, Majid Pasbani Khiavi², Mortaza Ali Ghorbani³

1- M. Sc. Student of Hydraulic Structure, Faculty of Engineering, University of Mohaghegh Ardabili

2- Associate Professor of Civil Engineering, Faculty of Engineering, University of Mohaghegh Ardabili

3- Assistant Professor of Civil Engineering, Faculty of Engineering, University of Mohaghegh Ardabili

Email: pasbani@uma.ac.ir

Abstract

Concrete is a material with weak against tension strength. Due to the change in the volume caused by the temperature variations, tensile stresses appear that cause cracks in critical situations. For this reason, the issue of thermal stresses and cracks have great importance in design of roller compacted concrete (RCC) dams. In this paper, thermal analysis of RCC dams is considered to show the effect of temperature change which induced the tension stresses in the body. For modeling and transient analysis of case model of RCC dams, Ansys Workbench software based on finite element method has been used. Different conditions of concreting such as beginning in hot and cold seasons and stopping in hot and cold months of year, pre-cooling of materials are considered as effective conditions. Obtained results illustrate the distribution of temperature and induced stresses in dam body.

Keywords: RCC dams, environmental conditions, finite element, tensile stress.

1. INTRODUCTION

In the building of RCC dams, the concreting of the dam body is carried out on a vast surface containing several blocks. After pouring concrete, transverse joints are performed. The roller compacted concrete dams do not carry longitudinal joints and usually do not have cooling system. In implementing of RCC dam, precise and continuous monitoring of parameters such as concreting speed, bonding between layers, thickness of layers, concrete start time and time interval between layers is considered.

The basic requirement in the design of concrete dams is to ensure the integrity, sealing and durability of the dam structure. Concrete cracking is a factor that threatens the above cases. Therefore, new methods in building of dam should include measures to limit the possibility of cracking, especially cracks resulted by heat.

The Simulation of the thermal behavior of the dam during construction and operation years are done with the using of a set of mathematical models based on finite element method. Therefore, one, two, and three-dimensional models have been used in different length of time and place for different purposes for the study and thermal analysis of dams.

The effect of environmental heat and cement hydration on a roller concrete dam was conducted by Ahmadi and Heidari (2011). In their study, besides the changes in the properties of the concrete relative to the time, the dam construction process is also modeled. For different levels, the boundary conditions for radiation, convection and solar radiation and for the adiabatic boundary threshold are considered.

Thermal cracking of concrete dams has been done by finite element method by Nurzad and Nemati Chari (2006). In their research, the application of the finite element method in the calculation of the risk of thermal cracking of the bulk dam structure has been investigated. Also, production and distribution of heat in bulk concrete have been investigated. By describing of induced thermal stresses and effective factors, the method of control of conventional thermal stresses, especially the use of post-cooling pipes in concrete was defined. The results showed that preventing thermal cracking can be obtained by appropriate pre-cooling and post-cooling.

The thermal analysis for RCC roller concrete dam was performed by Malkawi (2003) using the Ansys finite element program. The purpose of research was to provide the distribution of temperature in the body of the gravity dam and to investigate the thermal response of the dam using the Ansys software.

In the following, Luna and Yong Wu (2000) considered the properties of concrete as a time function and suggested that if the dam was constructed in cool seasons, the maximum temperature of the dam will be reduced. Also, according to the Hinks and Copley models (1999) that take into account the effect of solar radiation, the speed of execution is lower than the planned speed in hot air, causing a higher temperature than the predicted temperatures, and by reducing the length of the concreting blocks, there is no rapid drop in maximum stresses. Servera (2002, 2003) illustrated that although the pre-cooling of the concrete before pouring in specified location,

the temperature clearly will be lower than the final distribution. But the efficiency of this method is very limited. For the case model, only 20% is evaluated, and the worst possible scenario is the start the project in the summer. Among the factors that affect the cracking of concrete dams are environmental factors. Therefore, an analytical model by Aguado and et al. (1995) simulated the thermal behavior of dams that are exposed to environmental conditions during operation.

2. HEAT TRANSFER

2.1. EFFECTIVE ENVIRONMENTAL PARAMETERS AFFECTING TEMPERATURE VARIATIONS IN THE DAM BODY

The environmental parameters affecting temperature variations in the dam body are: Ambient temperature, wind speed, radiation, insulation and rainfall. The most important of which is the ambient temperature which is investigated by thermal analysis. Lack of data about other parameters and the impossibility of their accurate prediction cause the effects of phenomena such as displacement or wind speed can't be predicted in models. However, their effect on the final results is lower than the ambient temperature. In model simulation, cooling during construction as well as future years, the temperature curves of the environment are always used, which is the result of statistical work on the data obtained from the dam site.

2.2. HEAT EFFECTS IN CONCRETE DAMS

The concrete dams are the largest bulky concrete structures exposed to cracking caused by various phenomena. It is difficult to find a gravity dam that is not in some way affected by cracking. Extreme cracks in dams, other than those caused by earthquake loading, have resulted by climatic conditions. The Daniel Johnson dam in Quebec, Canada, is an example of a large dam that has been damaged by thermal cracking. In this dam, due to temperature changes, thermal cracks appeared at a time when the dam was not yet intact.

The FONTA dam in the U.S is another example of heat cracking. In the finite element analysis performed on this dam, the cracking mechanism was changed due to the combination of two following phenomena. One is the thermal expansion of the concrete in the downstream side and the second is the increasing of concrete temperature due to the hydration of the cement. Department of pathology of dam and reservoir of the great Dams committee announced in a report, temperature variations in the environment and the periods of freezing and melting are one of the most important deterioration factors in concrete dams. In a gravity concrete dam, the upstream procedure is affected by seasonal variations in water temperature variation, which changes with the depth of water in the reservoir. Usually the above temperatures are stabilized at the bottom of the reservoir at 4 C. The downstream side of the dam is affected by seasonal and daily changes in temperature.

Finally, during the process of fixing and hardening of new concrete, the heat caused by hydration will increase the internal temperature of the concrete, which will start to cool over time. The above temperature changes lead to non-uniform volumetric changes in the concrete, which is proportional to the thermal gradient between the core of the dam and its surfaces. When the thermal stress exceeds the capacity of concrete tensile strength, the cracks form in the dam that can cause further damage to the structure. Weather conditions can be damaged during the useful life of the dam, even when the effect of the heat of hydration has been lost.

2.3. THERMAL ANALYSIS

In this research, Ansys workbench software is used for analysis and modeling. The software is based on finite element method for modeling and analysis. The finite element method has been developed to solve complex problems with the geometry, type of material, and custom loading.

2.4. GOVERNING EQUATIONS AND BOUNDARY CONDITIONS

A conduction heat transfer for a two-dimensional, transient and isotropic state can be described mathematically in the Cartesian coordinates as described below.

$$\frac{\partial}{\partial x} \left(K_x \frac{\partial T}{\partial x} \right) + \frac{\partial}{\partial y} \left(K_y \frac{\partial T}{\partial y} \right) + \frac{\partial}{\partial z} \left(K_z \frac{\partial T}{\partial z} \right) + Q = \rho C \frac{\partial T}{\partial t} \quad (1)$$

T :District temperature [$^{\circ}K$]

ρ : Density $\left[\frac{kg}{m^3} \right]$

C : Specific Heat $\left[\frac{J}{kg^\circ K} \right]$

K_x, K_y, K_z : Thermal conductivity coefficient $\left[\frac{W}{m^2^\circ K} \right]$

Q : The internal heating rate for the unit volume $\left[\frac{W}{m^3} \right]$

Equation (1) must be solved under the initial conditions and appropriate boundary conditions. The boundary conditions for this equation are given in the form of the following equations.

$$T = \bar{T} \tag{2}$$

$$-\left(K_x \frac{\partial T}{\partial x} n_x + K_y \frac{\partial T}{\partial y} n_y + K_z \frac{\partial T}{\partial z} n_z \right) = -q_a + q_c + q_r \tag{3}$$

q_a : The intensity of the heat flow is entered $\left[\frac{W}{m^2} \right]$

q_c : Condensation current intensity $\left[\frac{W}{m^2} \right]$

q_r : Intensity of the radiation flux $\left[\frac{W}{m^2} \right]$

n_x, n_y, n_z are Normal surface vectors in the present study. $Q, \Gamma_T, \Gamma_q, \bar{T}$ Accordingly, the representative of the rate of heat output of hydration, the common boundary of the dam and concrete, the open-air boundary, the temperature of dam's foundation and the intensity of the thermal current input from the solar radiation and q_c Condensation current intensity and q_r The intensity of the radiation flux is output from the surface.

2.5. HEAT TRANSFER THROUGH CONVECTION

The heat exchange carried out by convection resulting from the temperature difference between Γ_q and the ambient air temperature is obtained by Newton's cooling law as follows:

$$qc = hc(T - T_a) \tag{4}$$

hc : Convection coefficient $\left[\frac{W}{m^2^\circ K} \right]$

T : Boundary temperature Γ_q $[\text{K}]$

T_a : Ambient temperature $[\text{K}]$

V : Air velocity in the surroundings $[\frac{m}{sec}]$

3. MODELING AND CASE STUDY

3.1. MODEL GEOMETRY AND MATERIALS SPECIFICATIONS

To conduct this analysis, the Jhave roller compacted concrete dam has been selected as case study. This dam is located in Kurdistan province on the Jhave river.

In the mixing plan of the Jhawe RCC dam, Portland cement of Urmia has been used. The diagram of increasing adiabatic temperature of the dam mix with 25% of the pozzolan is figure 1.

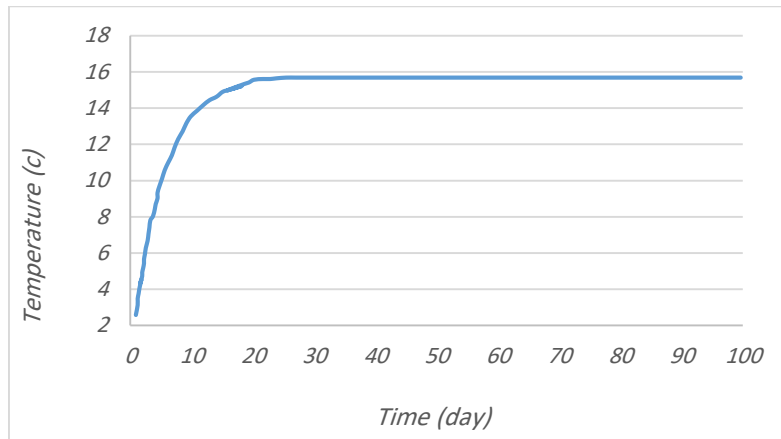


Fig.1. Adiabatic temperature rise due to hydration heat.

The temperature of the dam in the site, according to the reports of the Mashanir Water Resources Department, has been illustrated in figure 2.

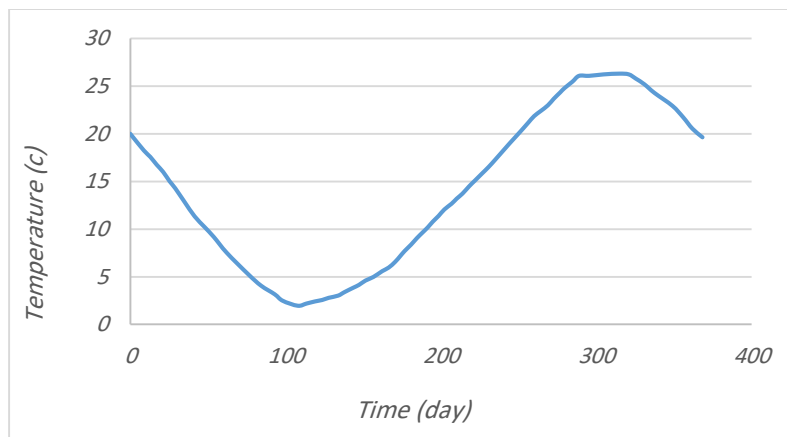


Fig.2. Air temperature in place of construction.

In this research, the initial temperature of the concrete is 15°C and the average annual temperature is 13.8°C and The interval time between two consecutive layer 3-day runs is considered. To solve and analyze the considered model, concrete dam and foundation materials are assumed to have homogeneous, linear and isotropic behavior. All dimensions are based on the SI system. The bulk modulus of elasticity, concrete density and Poisson ratio are 25 GPA, 2450 kg / m^3 , 0.37 respectively. The parameters required to define the thermal behavior of the materials are summarized in Table 1.

Tab.1.Properties of the materials considered

Variable	Value	Unit
Isotropic Thermal Conductivity	2.96	$W/m * ^\circ C$
Specific Heat	970	$J/kg * ^\circ C$
Film Coefficient	1500000	$J/m^2 * day * ^\circ C$
Thermal Conductivity	10670	$J/m * h * ^\circ C$

4. Thermal Analysis Results

The Ansys workbench software based on finite element method has been used for thermal analysis. To do this analysis, first the layering was carried out according to the criteria for the implementation of the dam then the time step was set for each layer. In this analysis, the weight of layers was not considered and only the effect of heat and its tensions was investigated. Figure 4 shows that the concrete temperature is not even higher at 21 °C even mid-time during construction.

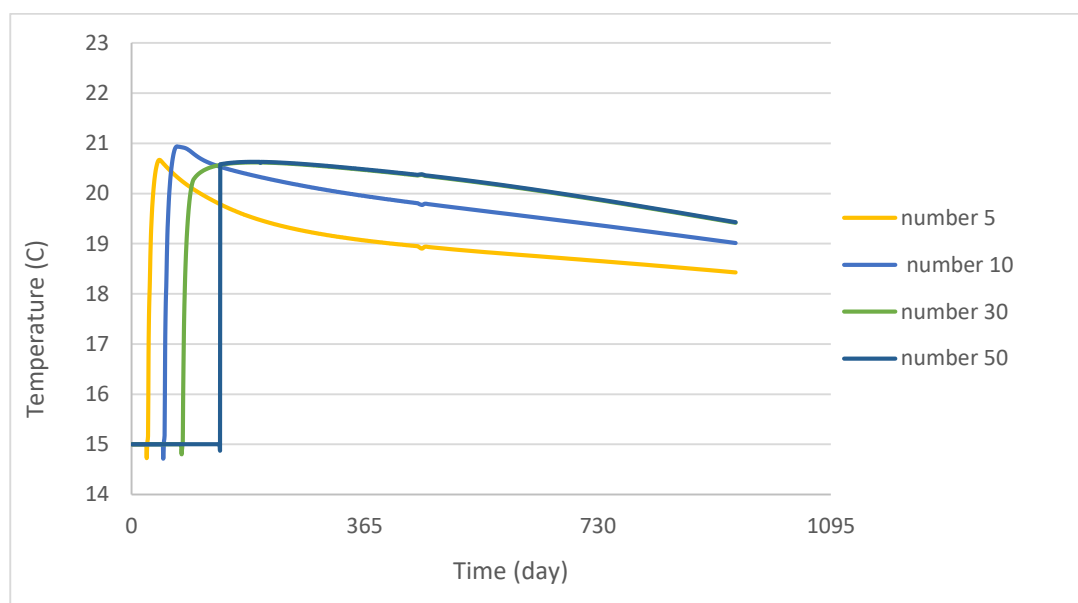


Fig.4. Rcc temperature at different layers during construction

Figures 5 to 9 show how to create and change temperature during construction and concreting of different layers of the dam. It is observed that the body of the dam begins to cool with the passage of time and to the concrete, the new layers from areas exposed to the environment. By the end of 05/03/2009, the end of the concreting and construction work, all the outer parts of the dam begin to decrease the temperature. This decreasing in the following days is the completion of the construction process it continues.

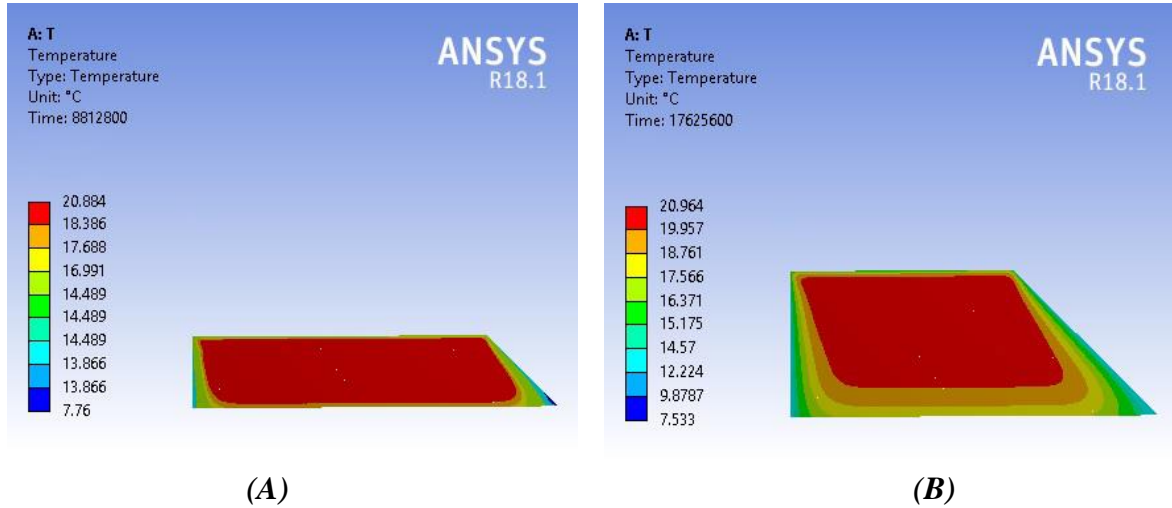


Fig.5. Temperature in °C during construction on 02.01.2008 (A) and 13.04.2008 (B)

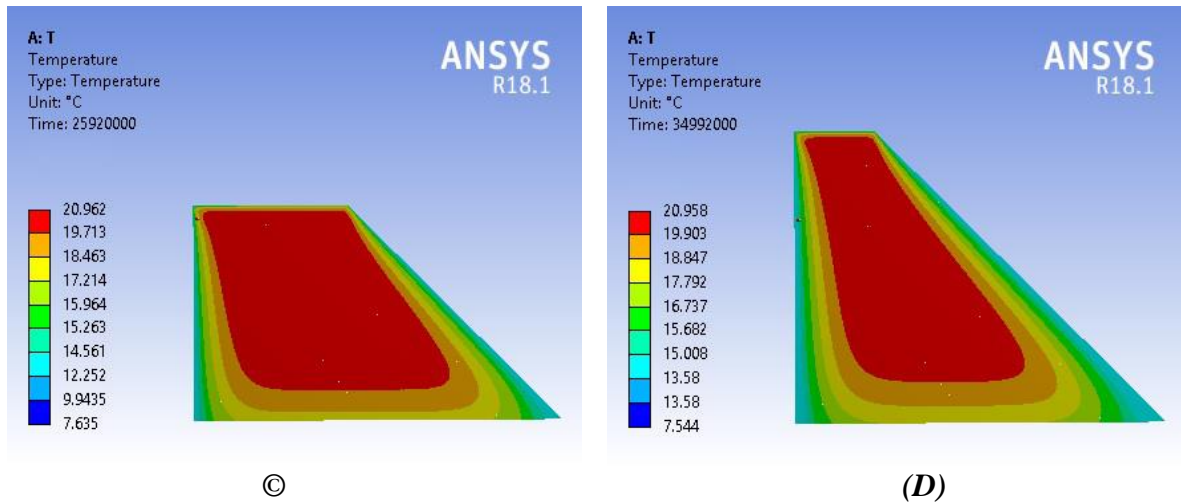


Fig.6. Temperature in °C during construction on 22.07.2008(C) and 05.10.2008(D)

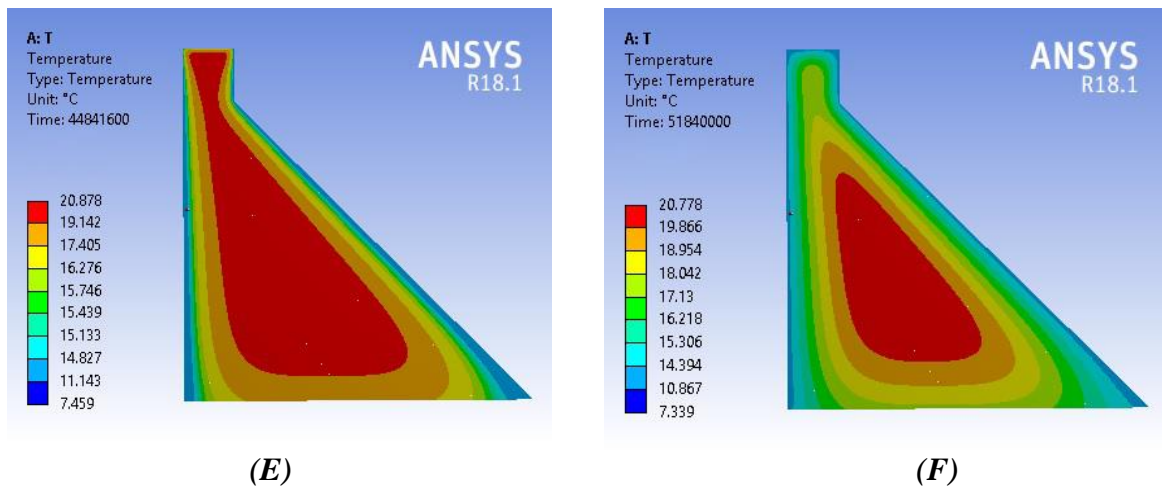


Fig.7. Temperature in °C during construction on 27.01.2009 (E) and 16.05.2009 (F)

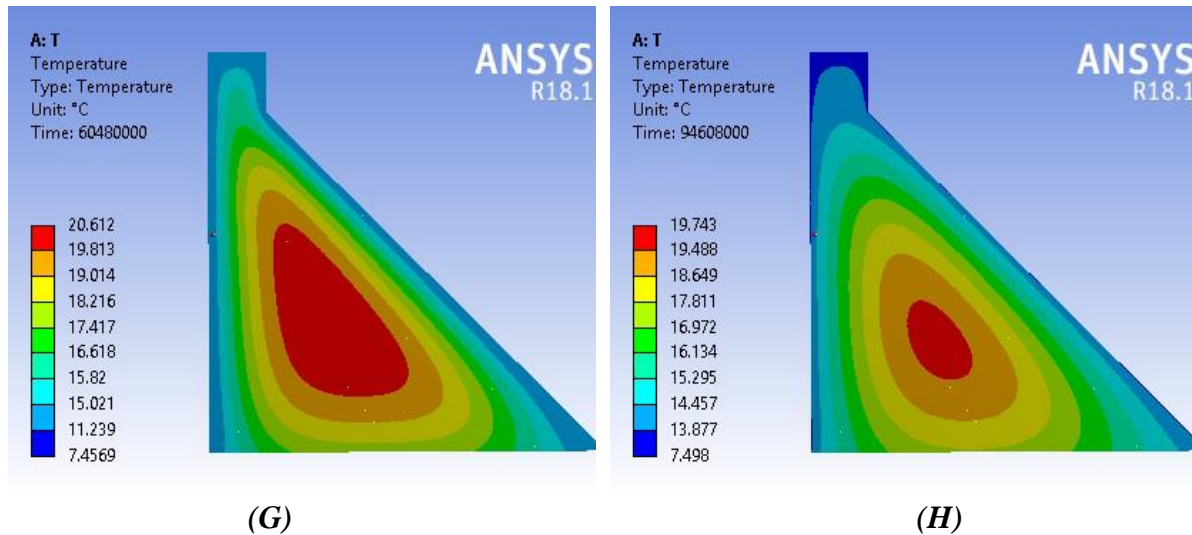


Fig.8. Temperature in °C during construction on 25.08.2009 (G) and 02.04.2010 (H)

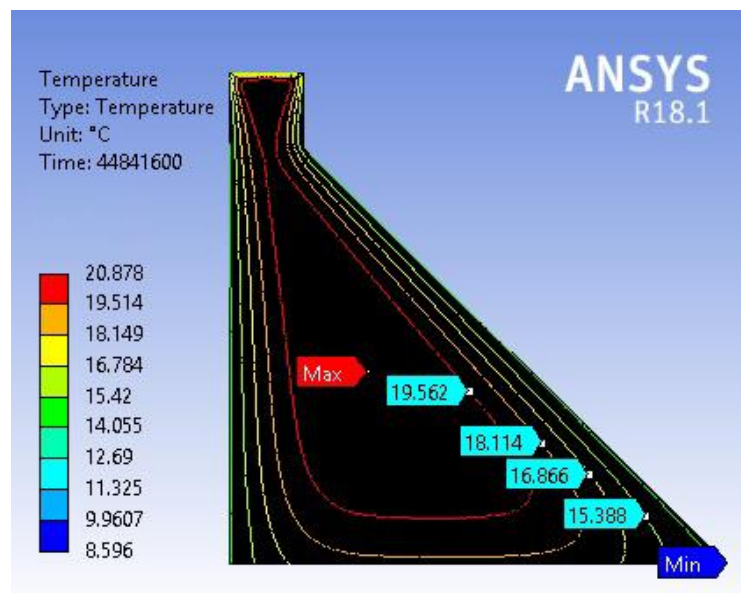


Fig.9. Temperature in °C during construction on 27.01.2009.

5. Stress Analysis Result

Figures 10 and 11 show the amount of tension stresses and how it changes in the dam body. These tensions are solely due to the heat created during the dam. And the weight of the dam is not considered. The maximum amount of tension occurs at the points located on the heel and the toe of the dam. And as we move towards the center of the dam, the tensions are reduced.

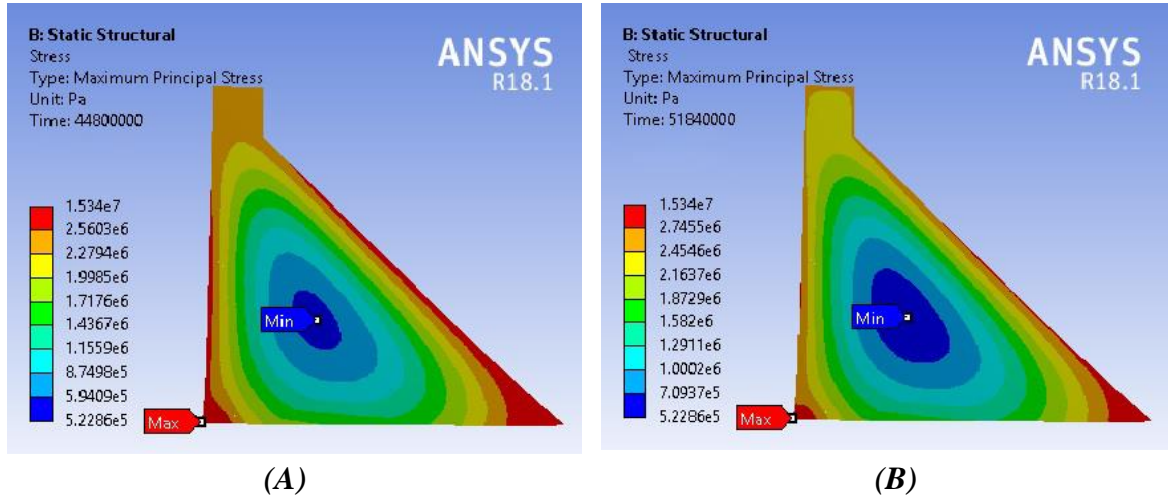


Fig.10. Maximum principal stress distribution (Pa) on 27.01.2009(A) and 16.05.2009 (B)

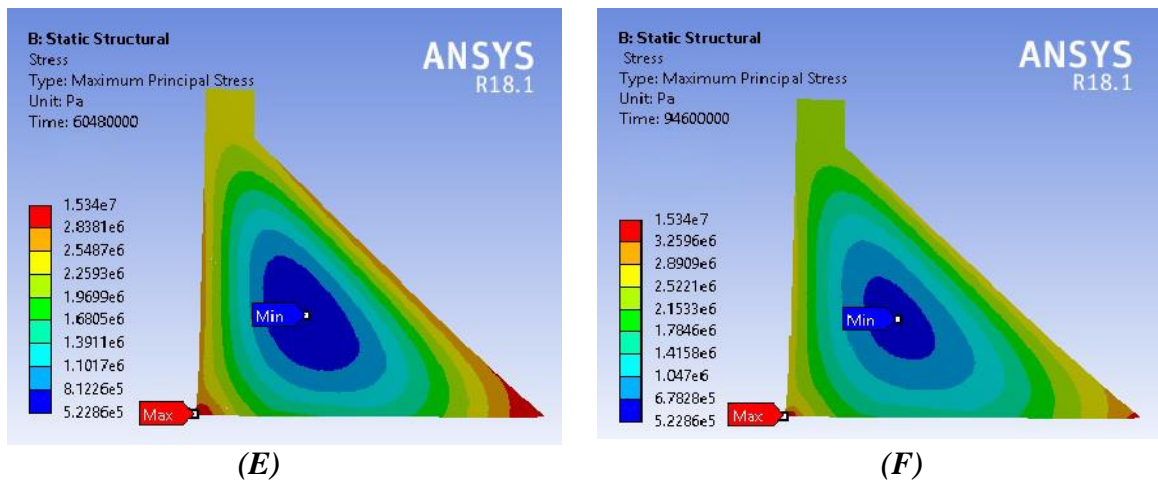


Fig.11. Principal stress distribution (Pa) on 25.08.2009 (E) and 02.04.2010 (F)

As expected, the maximum deformation of the dam is due to heat during the concrete (Regardless of the weight of the layers) there is a crown dam in the crater and equal to 12 mm.

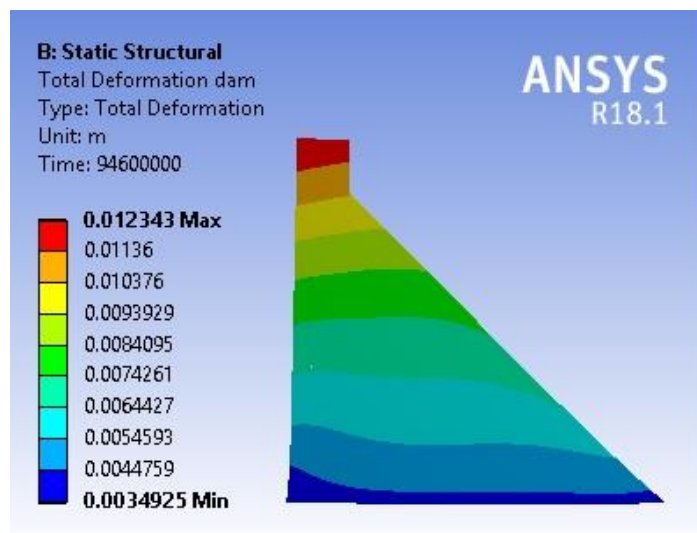


Fig.11. Total deformation rate (m) in the end of construction

6. CONCLUSIONS

In this research thermal analysis of case model of RCC dam with 86.5m height during and after construction. The following conclusions may be stated:

- For RCC dams the temperature of each thin layer after its placement can be significantly reduced by the water evaporating on the upper face. For conventional dams, this phenomenon is of lesser importance due to the greater thickness of the layers and because of the limited extension in space of its influence.

- RCC dams are hardly subjected to thermal cracking if the external temperature is more or less constant, as in tropical climate, and the initial concrete temperature is not very different of the air.

- Obviously, by significant seasonal variation, crack may appear at the faces of a thick RCC gravity dam during the following winter if the placing occurred at summer time. The cracking is caused by the temperature increase in the interior of the dam combined with the fast cooling of the surface in winter.

- The temperature of the core of the thick gravity dam requires a long time to drop to the final equilibrium state.

7. REFERENCES

1. Luna R. and Wu Y., “*Simulation of temperature and stress field during RCC dam construction*”, Journal of Construction Eng. and Management, ASCE Sep. /Oct. (2000), PP. 381-388
2. Cervera M., Oliver J., Prato T., “*Simulation of construction of RCC dams: I- temperature and aging, II: stress and damage*”, J. Struc. Eng., ASCE, Sep. 2000, PP. 1053-1069
3. Cervera M., Goltz M., “*A modified 1-D strip model for thermo-mechanical analysis of RCC dams*”, Roller Compacted Concrete Dams, Berga et al. (eds) (2003) Swets & Zeitlinger, PP. 579-588
4. Malkawi, A. I. H., Mutasher, S.A. and oiu, T. J, Thermal-Structural Modeling and Temperature Control of Roller Compacted Concrete Gravity Dam, Journal of Performance of constructed facilities, ASCE, November (2003), pp. 177-187., 2003
5. J.Noorzaei , K.H.Bayagoob , W. A. Thanoon, M.S.Jaafar.”*Thermal and Stress Analysis of Kinta RCC Dam*”. ENGINEERING STRUCTURES. 28(2006)1795-1802
6. Agullo L, Aguando A. & Mirambell E. (1995), Thermal behavior of Concrete Dam Due to Environmental Action, Dam engineering.
7. N. Heydari , M. T. Ahmadi. “*Advanced Analysis of Ambient and Cement Hydration Thermal Effects on a RCC Dam Considering Construction Schedule.*” Modares Civil Engineering Journal (M.C.E.L.), (2011)

Flow Pattern and Delta Characteristics in a Dam Reservoir

Kazem Gomar¹, Masoud Ghodsian², Seyed Ali Ayuobzadeh³

1- PhD Student, Civil and Environmental Engineering Department, Tarbiat Modares University

2- Professor, Water Research Institute, Tarbiat Modares University

3- Professor, Agriculture Department, Tarbiat Modares University

Email: k.gomar@modares.ac.ir

Abstract

Floods, with huge amount of water and sediment, play an important role in deposition and distribution of sediment in reservoirs. In this paper, the flow pattern and characteristics of delta in a reservoir are experimentally studied using steady and unsteady flows of water and sediment. The experiments were carried out using triangular and trapezoidal hydrographs. The bed load sediment particles were deposited in the reservoir mouth forming a delta. Investigating the flow pattern revealed that, in spite of the full symmetry in geometry and hydraulic conditions of upstream flow, the flow in the reservoir was asymmetric. It was found that although the characteristics of delta depend on the flow pattern, but the flow pattern may be in turn affected by the sedimentation. Sedimentation lead to formation of unstable flow due to fluctuation in flow direction in the reservoir. The specification of delta including: deviation of delta, its length and shape was also addressed in this paper. An exponential equation was developed to predict the length of delta.

Keywords: Flow Pattern, Sedimentation, Reservoir, Flood Flow, Unsteady Flow

1. INTRODUCTION

The distribution of sediment in reservoirs as a function of reservoir geometry, inflow hydraulic conditions and sediment characteristics is one of the important issues in designing and managing dam reservoirs. Extensive research on sedimentation and formation of delta carried out in the second half of the 20th century, such as Chang et al. [1], Sugio [2], Fan and Morris [3] and Morris and Fan [4] among others. They studied, qualitatively and quantitatively, the geometric characteristics of the delta formed in different geometric and hydraulic conditions. Shieh et al. [5] investigated the longitudinal and transverse development of delta in a laboratory model. Kostic and Parker [6] investigated, experimentally and numerically, the effects of density current on the delta characteristics. Lai and Capart [7, 8, 9] investigated effects of density current and rising reservoir water level on the delta. They also studied effect of channel slope and sediment flow rate on delta morphology over rocky beds. Researchers such as Dewals et al. [10], Dufresne et al. [11, 12, 13] and Camnasio et al. [14, 15] studied effects of sedimentation on the flow pattern in rectangular reservoirs. These studies showed that under certain geometric conditions, despite the presence of symmetric geometry, an asymmetric flow is created in the reservoir. Laboratory observations of Mamizadeh et al. [16] showed that the flow and sediment distribution is symmetric in a reservoir with sudden expansion.

Although most of sediments are carried to reservoirs by means of unsteady flows, but majority of earlier researches were carried out under steady flow conditions. Few researchers such as Sediqkia [17] and Heydari [18] investigated specifications of delta under flood conditions. In the present study, the flow pattern and sediment deposition in a dam reservoir are investigated experimentally. The experiments are performed in steady and unsteady conditions while the flow is completely turbulent, and the sediments is transported as bed load. Further details of the laboratory model and experiments are given in the next section.

2. MATERIALS AND METHODS

2.1. EXPERIMENTAL SETUP

The model (Figure 1) consisted of an upstream channel as the river model (with length of 3.0 m, width of 0.3 m and slope of 0.007) followed by reservoir model with length of 5.0 m, initial width of 0.3 m and a terminal width of 2.0 m. The slope of the reservoir bed is 0.75 and angle of the side walls of reservoir θ equals to 11.8 degrees (the side slope is 0.21). The bed of the channel and the reservoir is made of smooth steel and the walls are made of glass. For the generation of unsteady flow, a system including: pump, inverter, control & programming device was used. The flow rate was measured by ultrasonic flowmeter with accuracy of 1%, and the data was transferred to the flow generation system. The sediment was injected by a sediment feeder at a distance of 2.0 m from the

reservoir mouth in the upstream channel. The sediment feeder was able to feed sediment particles in steady or unsteady rate into the flow. The bed topography (sedimentation/delta) was recorded by a mechanical point gage with a precision of ± 0.05 mm. The sedimentation and flow pattern were also recorded by a 30 fps camcorder.

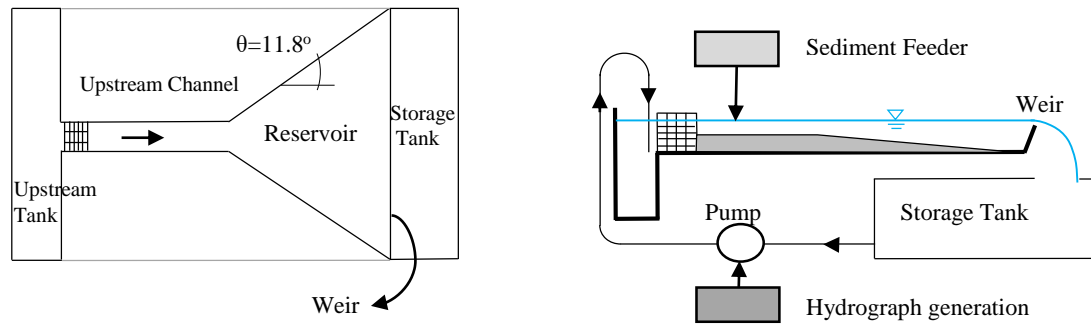


Figure 1. The scheme of laboratory model (not to scale)

The flow and sediment discharge were selected in such a way that the sediment moves as a bed load and no deposition occurred in the upstream channel, so that the entire volume of injected sediment was deposited in the reservoir. The critical discharge (minimum flow discharge for initiation of motion of sediment particles) was found to be equal to 10 l/s. Uniform Silica with mean diameter of 0.480 mm was used as non-cohesive particles. The relation between flow and sediment discharges was obtained experimentally as given by equation 1.

$$Q_s = (6 \times 10^{-7}) Q_w^{6.07} \quad (1)$$

Where Q_w is the flow discharge (l/s) and Q_s is sediment discharge (g/s).

2.2. EXPERIMENTS

Experiments were conducted under steady and unsteady flow conditions. Each series of steady and unsteady flow experiments includes several experiments with the same characteristics but different durations. In other words, each experiment was carried out several times with different duration and therefore different amount of sediment transport (M_s). The different durations for the unsteady flow means the implementation of successive identical hydrographs. Details of steady and unsteady flow experiments are given in Tables 1 and 2. In this table S represent the steady flow and U represent the unsteady flow. Unsteady flow experiments were carried out with two types of hydrographs; triangular (Tri.) and trapezoidal (Trap.), as schematically shown in Figure 2. The adjacent numbers to S and U represents the flow rate (l/s). Since the base flow discharge for unsteady flow experiments was equal to the critical discharge (i.e. 10 l/s), therefore no sediment was transported by the base flow.

The dimensionless numbers in Tables 1 and 2 are obtained from the following equations:

$$V^* = \frac{(u_p h_p - u_0 h_0) t_r}{h_p^2} \quad (2)$$

$$P = \frac{(h_p - h_0)}{u_p t_r} \quad (3)$$

$$T^* = \frac{ut}{h} \quad (4a- \text{for steady flow})$$

$$T^* = \frac{u_p t_r}{h_p} \quad (4b- \text{for unsteady flow})$$

Where V^* , P and T^* are, respectively, dimensionless volume of the hydrograph, unsteady parameter of hydrograph and time scale. The parameters u , h and t are, respectively, upstream flow velocity, upstream flow depth and time. The subscripts p , 0 , and r represent, respectively, the peak value, the base flow and the rising limb of the hydrograph.

Table 1- Details of steady flow experiments

Experiment Series	Q _w (l/s)	Q _s (g/s)	Upstream Froude number	Flow deviation	T [*]
S-12	12	0.6	0.43	N	-
S-14	14	1.5	0.51	N	-
S-16	16	5.0	0.60	Y	8411
S-18	18	10.5	0.71	Y	1237
S-20	20	19.0	0.83	Y	2330

Q_w and Q_s are, respectively, water and sediment discharge. T^{*} is the time scale when the flow starts to fluctuate. Y means the occurrence of flow deviation and N means no flow deviation.

Table 2- Details of unsteady flow experiments

Experiment Series	m _s (kg)	Q _p (l/s)	Q ₀ (l/s)	t _d (s)	t _r (s)	P*1000	V*	Flow deviation	T [*]
U-Tri. 0.5	0.5	15.3	10.0	360	180	0.088	708.4	Y	81800
U-Tri. 1	1.0	17.5	10.0	360	180	0.125	844.4	Y	7881
U-Tri. 2	2.0	20.0	10.0	360	180	0.150	986.2	Y	6060
U-Tri. 4	4.0	20.0	10.0	720	360	0.075	1972.4	Y	5424
U-Tri. 8	8.0	20.0	10.0	1440	720	0.037	3944.8	Y	9862
U-Trap. 0.5	0.5	15.3	10.0	256	90	0.175	653.3	N	-
U-Trap. 1	1.0	17.5	10.0	236	90	0.250	684.9	Y	11625
U-Trap. 2	2.0	20.0	10.0	232	90	0.299	778.0	Y	8876
U-Trap. 4	4.0	20.0	10.0	463	180	0.150	1550.5	Y	6651
U-Trap. 8	8.0	20.0	10.0	926	360	0.075	3101.0	Y	5917

m_s is the sediment mass transported by one hydrograph, Q_p and Q₀ are, respectively, peak and base flow discharge, t_d and t_r are, respectively, total duration and rising limb duration of the hydrograph. T^{*} is the time scale at the instant when the flow starts to fluctuate. Y means the occurrence of flow deviation and N means no flow deviation.

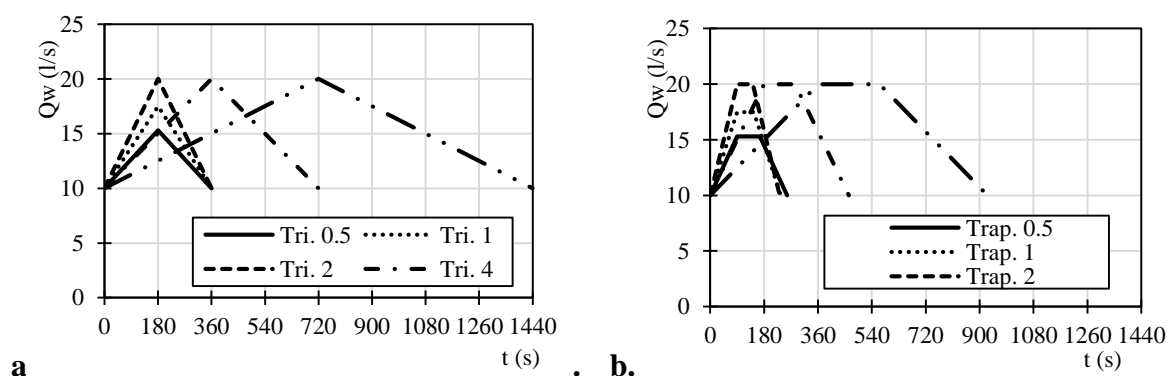


Figure 2. Different hydrographs used in unsteady experiments: (a) triangular hydrographs and (b) trapezoidal hydrographs

3. RESULTS

3.1. FLOW PATTERN

Laboratory observations revealed that although sedimentation pattern follows the flow pattern, but flow pattern may be in turn affected by sedimentation. Therefore, in following, the non-sediment (clear water) flow pattern is investigated at first and then the flow pattern after deposition of sediments/formation of delta is discussed.

3.1.1. CLEAR WATER FLOW PATTERN

Several primary experiments were carried out without sediment injection to investigate the flow pattern in the reservoir. Colored strings were floated on the water surface to observe the direction of the flow in the reservoir. The schematic diagram of the flow pattern observed in the laboratory is shown in Figure 3. As this figure shows, with the arrival of the flow in the reservoir, despite the full symmetry in the upstream, the flow is diverted to one of the side walls and, therefore, the asymmetric flow is formed. The formation of asymmetric flow, consequently, leads to formation of a vortex in the reservoir.

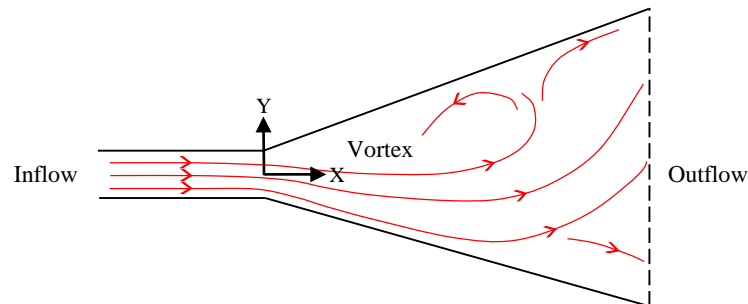


Figure 3. Schematic diagram of flow deviation and vortex formation in the reservoir

The direction of the flow and formation of vortex in the reservoir are completely random but stable. In other words, by entering the flow into the reservoir, the flow is randomly diverted to the left or right walls of the reservoir, but the direction of deviated flow did not change during the experiment, which means the flow is stable. It was observed that the turbulence caused by the entry of successive hydrographs in non-sediment flow experiments does not change the direction of deviated flow. A clockwise or counterclockwise vortex is then formed in the reservoir according to the direction of flow.

In the present experiments, the inflow Reynolds number was in the range of 33000 to 66000, which produced an asymmetric flow. This is in accordance with the results of the studies on flow pattern in a channel with converging side walls (Cherdron et al. [8], Durst et al. [9], Sobey [10], Fearn et al. [11], Shapira et al. [12], Chiang et al. [13]). These researchers concluded that the flow in a reservoir is symmetric if approach Reynolds number is low, while it is asymmetric if approach Reynolds number is high. The occurrence of asymmetric flow has been also reported in rectangular shallow reservoirs by other researchers such as Stovin and Saul [14], Dewals et al. [10], Dufresne et al. [11, 12, 13] and Camnasio et al. [15].

3.1.2. FLOW PATTERN AFTER SEDIMENT DEPOSITION

As already mentioned, the initial direction of the deviated flow is completely random. Therefore, in order to make the initial conditions for all the experiments identical, the initial flow direction was deliberately diverted to the left side before the beginning of the experiment. The recording of data was started after the stabilization of the flow direction.

In the steady flow experiments, it was observed that by entering the sediment into the reservoir, the depositional pattern of sediments follows the flow pattern and the sediments are initially deposited in the reservoir in the same direction as the main flow (to the left). In the low rates of flow (i.e. $Q_w=12$ and 14 l/s), the flow direction was fixed initially (to the left) during the experiment and no fluctuation in flow direction was observed after deposition of the sediments. Therefore, the flow pattern is stable even after sedimentation in low rates of steady flow. But in higher amounts of steady flow (i.e. $Q_w=16$, 18 and 20 l/s), the deposition of sediments gradually affects the flow pattern and causes the flow not to be stable further. In the experiment S-16 ($Q_w=16$ l/s), sedimentation causes fluctuation in the direction of flow, but the fluctuation gradually decreases with the delta development. In the experiments S-18 and S-20 ($Q_w=18$ and 20 l/s), the flow direction becomes rapidly symmetrical with a slight fluctuation, and then the flow remains to be symmetrical until end of the experiments. The vortex flow in the reservoir disappears when the symmetry flow occurs. It is clear from Table 1 that the possibility of fluctuation in the steady flow depend on the upstream Froude number, although there is no explicit relationship between them. There was no fluctuation in the flow for Froude numbers less than 0.51 (i.e. for experiments S-12 and S-14), but with increase of Froude number, beyond 0.60, there is a flow fluctuation for the experiments S-16, S-18 and S-20.

In the unsteady flow also, the sediment deposition following the flow pattern is initially deviated to the left, but the deposition gradually fluctuates in the flow direction. Figure 4 shows a typical flow deviation in a U-Tri. experiment. The flow, which is marked with red string on the water surface, is diverted to the right at the

beginning of the falling limb of hydrograph. The direction of sediment path has also diverted to the right with a spatial delay relative to the flow.

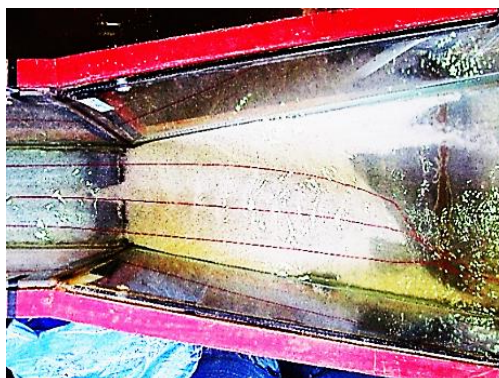


Figure 4. The flow and sediment diverted to the right in falling limb of the hydrograph (Flow from left to right)

From table 2, it is clear that the dimensionless volume of the hydrograph (V^*) is an effective factor influencing fluctuation of the flow direction. The time scale at which the flow starts to fluctuate (T^{**}) decreases in both triangular and trapezoidal hydrographs by increasing V^* (with the exception of the U-Tri. 8 experiment). In U-Trap. 0.5 experiment, with the lowest value of V^* , no fluctuation was observed. Also, in U-Tri. 0.5, the flow fluctuation occurs at longer duration as compare to other experiments.

The flow fluctuation was recorded during unsteady flow experiments in 90 seconds intervals, with the sign +1 for flow deviation to the right, 0 for symmetrical flow and -1 for flow deviation to the left. The fluctuation of flow for both types of hydrographs is depicted in Figure 5. It is observed that after the first change in direction of flow, the flow is no longer stable and the flow direction is continuously fluctuating by the entry of successive hydrographs into the reservoir.

The observations revealed that the flow is diverted to the central line of the reservoir, with a short delay after the peak of hydrograph. Then the flow direction may change to the opposite direction in the falling limb of the hydrograph, or return to its original direction again. The former was usually observed in the triangular hydrographs, and the later was usually observed in the trapezoidal hydrographs. Thus, the flat peak of the trapezoidal hydrograph leads to a weak flow fluctuation and further stabilization of flow, as seen in figure 5.

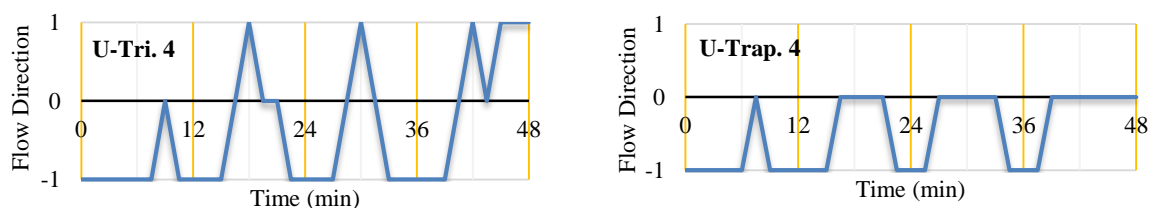


Figure 5. Fluctuations in flow direction for unsteady flow experiments

3.2. SEDIMENTATION PATTERN

For low rates of steady flow, the delta direction was always toward the left side (Figure 6a, b). While for higher values of steady flow rates ($Q_w=16, 18$ and 20 l/s), the delta direction, following the flow, changed gradually to symmetrical state. Figure 6c, d, e. shows the symmetry in delta at the end of experiment.

For unsteady flow, the fluctuation of delta direction decreases with development of delta, although the flow continuously fluctuates. This means that the dependency of the delta direction on the flow direction decreases gradually. To describe the sediment pattern in more details, some specifications of delta including the delta deviation parameter, delta length and delta convexity parameter are investigated.

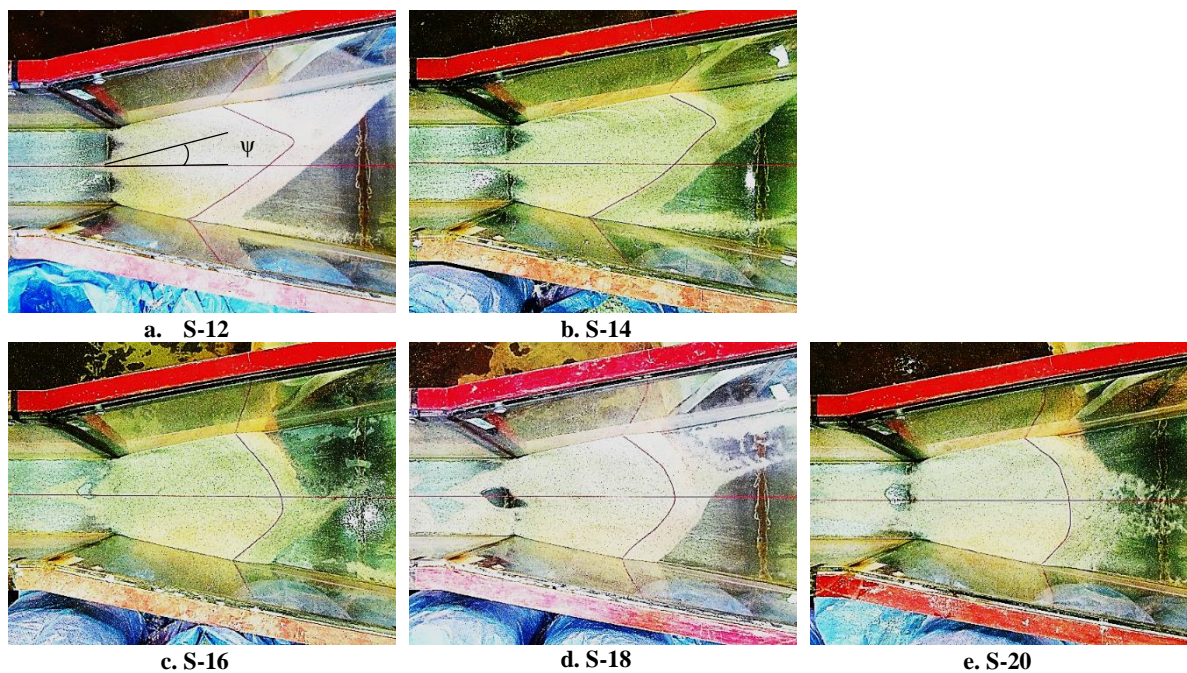


Figure 6. Delta direction in steady flow (Flow from left to right)

3.2.1. DELTA DEVIATION PARAMETER (Ψ)

In order to estimate deviation of the delta from the central line of reservoir, the parameter ψ is introduced, which is equal to the slope of the line connected the delta forehead and the center line of the channel (see Figure 6a). Deviation of the delta is obtained from equation 5, where, Y_t is the transverse distance of the delta forehead from the channel center line and X_t is the length of the delta. The value of ψ can be positive, negative or zero, which in turn means the direction of the delta to the right, left or symmetric.

$$\psi = \frac{Y_t}{X_t} \quad (5)$$

The variation of the parameter ψ versus the dimensionless mass of sediment transported into the reservoir (M_s^*) is depicted in Figure 7. The dimensionless mass of the sediment is calculated by equation 6, where M_s is the total mass of sediment transported into the reservoir, ρ_s is the sediment specific mass, g is the gravity acceleration and h is the flow depth. The peak flow depth is used in equation 6 for unsteady flow.

$$M_s^* = \frac{M_s}{\rho_s g h^3} \quad (6)$$

Figure 7 shows that ψ is negative at small values of M_s^* , which means that the delta initially is deviated to the left. For steady flow (Figure 7.a), the parameter ψ remains negative for experiments S-12 and S-14, fluctuates around the horizontal axis for experiment S-16, and gets close to zero for experiments S-18 and S-20. High fluctuations of ψ in experiments with triangular hydrograph (Figures 7.b) are observed, while the fluctuations are reduced significantly for the trapezoidal hydrograph (Figure 7.c). Less fluctuations in trapezoidal hydrograph is due to weak flow fluctuations resulted from the flat peak of the trapezoidal hydrograph. Note that the value of ψ is always negative for U-Trap. 0.5, because the flow direction never changes for this type of hydrograph. The absolute value of delta deviation parameter, when the sediment mass increases and the delta is developed, remains less than 0.21 which is equal to the side wall diversion angle of the reservoir.

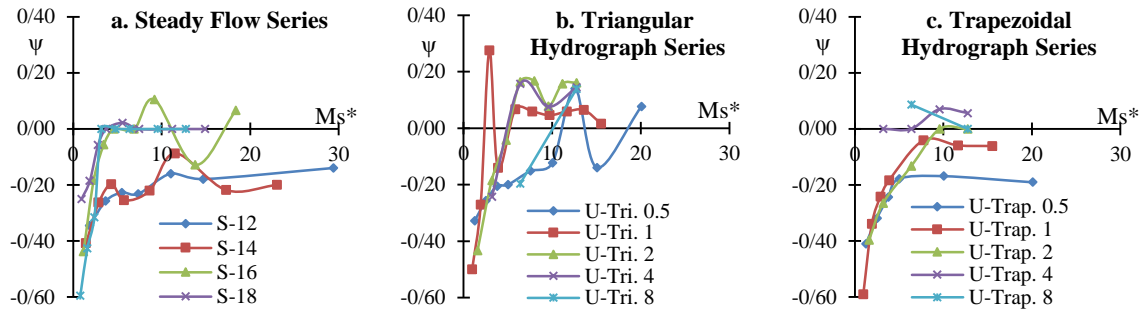


Figure 7. Variations of deviation of delta with mass of sediment

3.2.1.1. LENGTH OF DELTA (X_T)

The analysis demonstrated that despite of different sediment patterns formed under different upstream hydraulic conditions, the length of delta is almost identical. The relation between the dimensionless length of delta ($X_t^* = X_t/h$; where h represents the flow depth for steady flow and peak flow depth for unsteady flow) and the dimensionless mass of sediment (M_s^*) is depicted in figure 8 for steady and unsteady flows. It is clear that dimensionless length of delta in all experiments increases exponentially with increasing the dimensionless mass of sediment. The following equation was considered for the dimensionless length of delta:

$$X_t^* = a(M_s^*)^b \tag{7}$$

in which a and b are empirical values obtained by using the experimental data as given in Table 3. The mean absolute prediction error (MAPE) calculated from equation 8 is also included in this table. Here M_i and P_i are, respectively, the measured value and the predicted value, and n represents the number of data.

$$MAPE = \frac{1}{n} \sum_{i=1}^n \left| \frac{P_i - M_i}{M_i} \right| \tag{8}$$

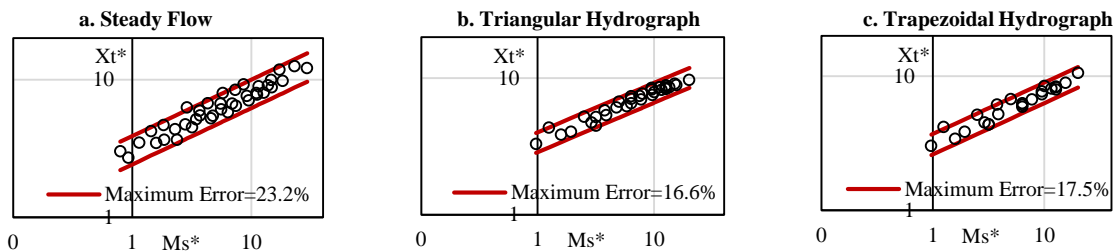


Figure 8. Length of delta versus mass of sediment

The small values of MAPE given in Table 3 reveals that equation 7 is a reliable to predict the length of delta.

Table 3- The values of a and b and MAPE for Equation 7

Series	a	b	MAPE
S	3.155	0.409	0.09
U-Tri.	3.442	0.362	0.05
U-Trap.	3.159	0.383	0.07

3.2.2. DELTA CONVEXITY PARAMETER (η)

The forehead of the delta is a convex curve while the convexity depends on the upstream flow conditions. The parameter η is defined by equation 9 to estimate the convexity of delta, where X_r and X_l are the length of delta at right and left sides, respectively. The value of this parameter is always between 0 and 1, while bigger values represents further convexity at forehead of delta and vice versa. For the extreme conditions, where the length of delta at the right and left sides are equal to the central length of delta, the forehead of delta is perpendicular to the delta central line. In this case, the convexity parameter is zero. The variations of the parameter η versus the dimensionless sediment mass is plotted in Figure 9.

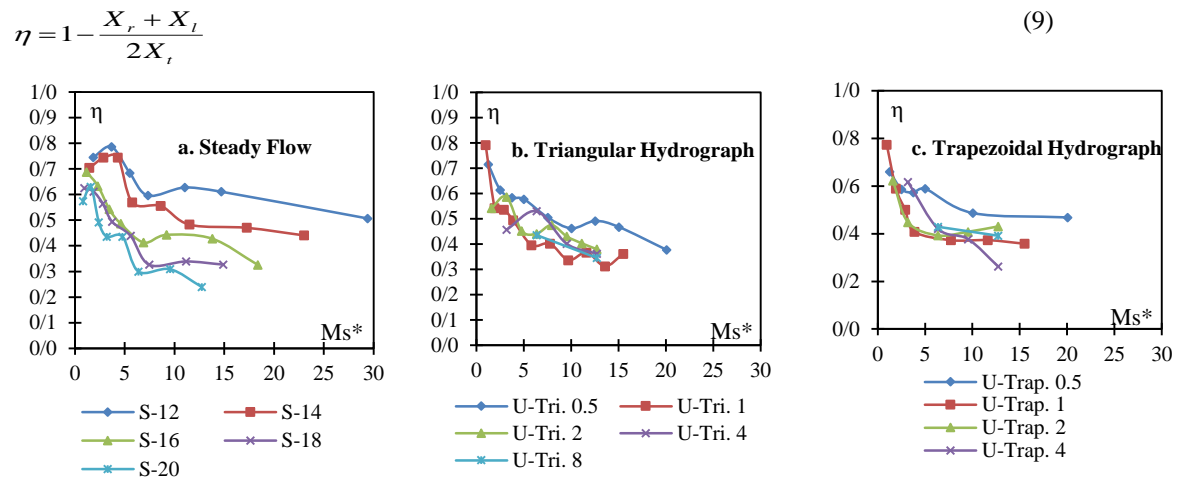


Figure 9. Variations of the convexity parameter versus sediment mass

It is observed that value of the maximum convexity is about 0.8. Furthermore, irrespective of the fluctuations in the graphs, the delta convexity has a decreasing trend with increasing M_s^* . Decreasing the convexity means faster growth of the left and right sides of delta than its central line. Therefore, the delta develops in the longitudinal direction in the early stages, and then gradually develops in transverse as well as in longitudinal directions. In other words, with development of delta, its enlargement becomes more uniform in a transverse direction leading to decrease of convexity.

The fluctuations in the convexity graphs indicate that the delta is not uniformly developed in the longitudinal direction. In the other words, the delta develops in longitudinal direction in one step and then develops in the transverse direction in the next step, while these steps are alternately repeated.

4. CONCLUSION

In this research, the flow and sedimentation pattern in dam reservoir is investigated under steady and unsteady flows. For this purpose, a laboratory model including two separate systems for generating hydrographs and sediment graphs was used. The results were discussed in two sections of flow pattern and sedimentation pattern. The observations revealed that the symmetric inflow, was randomly diverted to the left or right side of the reservoir and created a clockwise or counterclockwise vortex flow in the reservoir. The deposition of sediments may lead to change of flow pattern by fluctuations in flow direction. The sedimentation in the steady flow leads finally to a symmetrical flow. But in the unsteady flow, at the beginning of the falling limb of the hydrograph, a deviation in direction of flow occurred and, by passing successive hydrographs, the vortex direction changed frequently. This unstable flow pattern causes the delta direction to change with a small temporal and spatial delay relative to the flow. The analysis of the results showed that, unlike other delta specifications, delta length is an exponential function of the volume of sediments transported into the reservoir. A delta convexity parameter was introduced to explain the shape of the delta. It was found that the maximum delta convexity value is equal to 0.8 while it decreases with development of delta, which means growth of sides of the delta is faster than its central line. The delta develops in longitudinal direction and then in the transverse direction alternately.

5. REFERENCES

1. Chang, H.Y., Simons D.B. and Brooks R.H. (1967), “*The Effect of Water Detention Structures On River and Delta Morphology,*” Symp. On River Morphology, General Assembly Iugo, Bern, Switzerland.
2. Sugio, S. (1972), “*Laboratory study of degradation and aggradation a discussion,*” Proc. ASCE, Vol. 98, No. WW4.
3. Fan, J. and Morris, G. (1992), “*Reservoir sedimentation. I: delta and density current deposits,*” Journal of Hydraulic Engineering, Vol. 118, pp. 354-369.
4. Morris, G. and Fan, J. (1998), “*Reservoir Sedimentation Handbook, Design And Management Of Dams, Reservoirs, And Watersheds For Sustainable Use,*” McGraw- Hill companies, Washington. 1800p.
5. Shieh, C., Tseng, C., and Hsu, M. (2001), “*Effect Of Sediment Gradation On The Geometry Of River Deltas,*” International Journal of Sediment Research, vol.16, pp. 45-59.
6. Kostic, S. and Parker, G. (2003), “*Progradational Sand-Mud Deltas in Lakes and Reservoirs, Part 2, Experimental and Numerical Simulation,*” Journal Of Hydraulic Research, Vol.4, No.2, P.P. 127-140.
7. Lai, S. Y. J. and Capart, H. (2007), “*Two-Diffusion Description of Hyperpycnal Deltas,*” J. Geophys. Res., 112, F03005.
8. Lai, S. Y. J. and Capart, H. (2008), “*Response of Hyperpycnal Deltas to A Steady Rise in Base Level,*” 5th IAHR Symposium on River, Coastal and Estuarine Morphodynamics.
9. Lai, S. Y. J. and Capart, H. (2009), “*Reservoir Infill by Hyperpycnal Deltas Over Bedrock,*” J. Geophys. Res. Lett., 36, L08402.
10. Dewals, B.J., Kantoush, S.A., Erpicum, S., Piroton, M. and Schleiss, A.J. (2008), “*Experimental and numerical analysis of flow instabilities in rectangular shallow basins,*” Environ Fluid Mech. 8:31–54.
11. Dufresne, M., Vazquez, J., Terfous, A., Ghenaïm A., Poulet, J.B. (2009), “*Experimental investigation and CFD modelling of flow, sedimentation, and solids separation in a combined sewer detention tank,*” Computers & Fluids, Vol. 38, pp. 1042–1049.
12. Dufresne, M., Dewals, B.J., Erpicum, S., Archambeau, P. and Piroton, M. (2010), “*Experimental investigation of flow pattern and sediment deposition in rectangular shallow reservoirs,*” International Journal of Sediment Research, Vol. 25, No. 3, pp. 258–270.
13. Dufresne, M., Dewals, B.J., Erpicum, S., Archambeau, P. and Piroton, M. (2010), “*Classification of flow patterns in rectangular shallow reservoirs,*” Journal of Hydraulic Research, Vol. 48, No. 2, pp. 197–204.
14. Dufresne, M., Dewals, B.J., Erpicum, S., Archambeau, P. and Piroton, M. (2011), “*Numerical Investigation of Flow Patterns in Rectangular Shallow Reservoirs,*” Engineering Applications of Computational Fluid Mechanics, Vol. 5, No. 2, pp. 247–258.
15. Camnasio, E., Orsi, E. and Schleiss, A.J. (2011), “*Experimental study of velocity fields in rectangular shallow reservoirs,*” Journal of Hydraulic Research, Vol. 49, No. 3, pp. 352–358.
16. Camnasio, E., Erpicum, S., Orsi, E., Piroton, M., Schleiss, J. and Dewals, B. (2013), “*Coupling between flow and sediment deposition in rectangular shallow reservoirs,*” Journal of hydraulic research, Vol. 51, No. 5, pp. 535–547.
17. Mamizadeh, J., Ayyoubzadeh, S.A. and Banihashemi, M.A. (2012), “*Experimental study of hydraulic-sediment properties on deltaic sedimentation in reservoirs,*” International Research Journal of Applied and Basic Sciences, Vol., 3 (4), 810-816.
18. Sediqkia, M. (2011), “*Experimental study on the Effect of Inflow Hydrograph and Non-uniform Graded Sediment Particles on the Rate of Progression and Delta Pattern in Reservoir,*” MSc Thesis, Tarbiat Modares University (in Persian).
19. Heydari, M. (2013), “*Experimental study of the effect of internal flood hydrograph and non-uniform graded sediment particles on the rate of progression and delta pattern,*” MSc Thesis, Tarbiat Modares University (in Persian).
20. Cherdron, W., Durst, F. and Whitelaw, J.H. (1978), “*Asymmetric flows and instabilities in symmetric ducts with sudden expansions,*” Journal of Fluid Mech., 84(1), 13-31.

21. Durst, F., Melling A. and Whitelaw J. H. (1974), "*Low Reynolds number flow over a plane symmetric sudden expansion*," J. Fluid Mech., Vol. 64, part 1, pp. 111-128.
22. Sobey, I. J. (1985), "*Observation of waves during oscillatory channel flow*," J. Fluid Mech. 151,395-426.
23. Fearn, R. M., Mullin, T. and Cliffe, K.A. (1990), "*Nonlinear flow phenomena in a symmetric sudden expansion*," J. Fluid Mech., 211, 595-608.
24. Shapira, M., Degani, D. and Weihs D. (1990), "*Stability and existence of multiple solutions for viscous flow in suddenly enlarged channels*," Computers & fluids, 18, 3,239-258.
25. Chiang, T.P., Sheu, W.H. and Wang, S.K. (2000), "*Side wall effects on the structure of laminar flow over a plane-symmetric sudden expansion*," Computers & Fluids, 29, 467-492.
26. Stovin, V. R. and Saul, A. J. (1994), "*Sedimentation in Storage Tank Structures*," Water Science and Technology, Vol. 29. No. 1-2. pp. 363-372.
27. Stovin, V. R. and Saul, A. J. (2000), "*Computational Fluid Dynamics and the Design of Sewage Storage Chambers*," Water and Environment Journal, Vol. 14, pp.103–110.